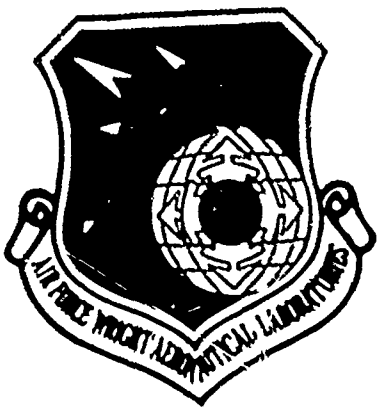
VOLUME 1

AFWAL-TR-86-3059



AD-A173 902

DAMPING 1986 PROCEEDINGS

May 1986

Summary Report for Period February 1984 - February 1986

Approved for public release; distribution unlimited.

DTIC FILE COPY

DTIC ELECTE NOV 1 2 1986 S D E

FLIGHT DYNAMICS LABORATORY
AIR FORCE WRIGHT AERONAUTICAL LABORATORIES
AIR FORCE SYSTEMS COMMAND
WRIGHT-PATTERSON AIR FORCE BASE, OHIO 45433

86 11 12 119

NOTICE

When Government drawings, specifications, or other data are used for any purpose other than in connection with a definitely related Government procurement operation, the United States Government thereby incurs no responsibility nor any obligation whatsoever; and the fact that the government may have formulated, furnished, or in any way supplied the said drawings, specifications, or other data, is not to be regarded by implication or otherwise as in any manner licensing the holder or any other person or corporation, or conveying any rights or permission to manufacture, use, or sell any patented invention that may in any way be related thereto.

This report has been reviewed by the Information Office (OI) and is releasable to the National Technical Information Service (NTIS). At NTIS, it will be available to the general public, including foreign nations.

This technical report has been reviewed and is approved for publication.

Lynn Rogers

LYNN ROGERS, Ph.D., P.E.
Project Engineer
Director, DAMPING 86

Lawrence R. Phillips

LAWRENCE R. PHILLIPS, Acting Program Mgr
Advanced Metallic Structures ADPO
Structures & Dynamics ADP Branch

FOR THE COMMANDER

R J Hegstrom

ROGER J. HEGSTROM, COL, USAF
Chief, Structures & Dynamics Division

If your address has changed, if you wish to be removed from our mailing list, or if the addressee is no longer employed by your organization please notify AFWAL/FIBA ,W-PAFB, OH 45433 to help us maintain a current mailing list

Copies of this report should not be returned unless return is required by security considerations, contractual obligations, or notice on a specific document.

UNCLASSIFIED

SECURITY CLASSIFICATION OF THIS PAGE

AD-A173 905

REPORT DOCUMENTATION PAGE

1a. REPORT SECURITY CLASSIFICATION: UNCLASSIFIED	1b. RESTRICTIVE MARKINGS
2a. SECURITY CLASSIFICATION AUTHORITY	3. DISTRIBUTION/AVAILABILITY OF REPORT: Approved for public release; distribution unlimited.
2b. DECLASSIFICATION/DOWNGRADING SCHEDULE	
4. PERFORMING ORGANIZATION REPORT NUMBER(S): AFWAL-TR- 86-3059	5. MONITORING ORGANIZATION REPORT NUMBER(S)
6a. NAME OF PERFORMING ORGANIZATION: Advanced Metallic Structures Adv. Development Prog.Office; 6b. OFFICE SYMBOL (If applicable): AFWAL/FIBAA	7a. NAME OF MONITORING ORGANIZATION
6c. ADDRESS (City, State and ZIP Code): Wright-Patterson Air Force Base OH 45433	7b. ADDRESS (City, State and ZIP Code)
8a. NAME OF FUNDING/SPONSORING ORGANIZATION; 8b. OFFICE SYMBOL (If applicable)	9. PROCUREMENT INSTRUMENT IDENTIFICATION NUMBER
8c. ADDRESS (City, State and ZIP Code)	10. SOURCE OF FUNDING NOS.

PROGRAM ELEMENT NO.	PROJECT NO.	TASK NO.	WORK UNIT NO.
632)11F	486U	11	02

11. TITLE (Include Security Classification): (UNCLASSIFIED) Damping 1986 Proceedings	
12. PERSONAL AUTHOR(S)	
13a. TYPE OF REPORT: Summary; 13b. TIME COVERED: FROM Feb 84 TO Feb 86	14. DATE OF REPORT (Yr., Mo., Day): 1986 May; 15. PAGE COUNT: 1319
16. SUPPLEMENTARY NOTATION	

17. COSATI CODES			18. SUBJECT TERMS (Continue on reverse if necessary and identify by block number)
FIELD	GROUP	SUB. GR.	
			Vigration damping, controls/structure interaction.

19. ABSTRACT (Continue on reverse if necessary and identify by block number)

Individual papers of Damping 86 held 5-7 March 1986 in Las Vegas NV are presented. The subjects included: mechanical properties of polymers, experimental methods, damping in metal matrix composites, friction damping, design of damping structure, modal damping values, and applications of damping, etc.

20. DISTRIBUTION/AVAILABILITY OF ABSTRACT: UNCLASSIFIED/UNLIMITED ☒ SAME AS RPT. ☐ DTIC USERS ☐	21. ABSTRACT SECURITY CLASSIFICATION: UNCLASSIFIED

22a. NAME OF RESPONSIBLE INDIVIDUAL	22b. TELEPHONE NUMBER (Include Area Code)	22c. OFFICE SYMBOL
Dr Lynn Rogers	(513) 255-5664	AFWAL/FIBAA

DD FORM 1473, 83 APR ... EDITION OF 1 JAN 73 IS OBSOLETE.

UNCLASSIFIED

SECURITY CLASSIFICATION OF THIS PAGE

FOREWORD

This publication includes the individual papers of Damping 86 held 5-7 March 1986 in Las Vegas NV. The Workshop was sponsored by the Flight Dynamics Laboratory, Air Force Wright Aeronautical Laboratories, Structures and Dynamics Division, Advanced Metallic Structures, Advanced Development Program Office (AFWAL/FIBAA).

It is desired to transfer vibration damping technology in a timely manner within the aerospace community thereby stimulating research, development, and applications.

Accession For	
NTIS GRA&I	X
DTIC TAB	☐
Unannounced	☐
Justification	
By	
Distribution/	
Availability Codes	
Dist	Avail and/or Special
A-1	

TABLE OF CONTENTS*

BEGIN VOLUME 1 — Page

The Department of Defense Science and Technology Program in Spacecraft Materials and Structures (Keynote Address)
J. Persh — A-1

*Standard Graphical Presentation of Complex Modulus and Processing Methodology
J. B. Layton, J. Eichenlaub and Dr. L. C. Rogers — AA-1

Comparison of Damping Material Properties by Various Test Methods
M. F. Kluesener — AB-1

Viscoelastic Characteristics of an Elastomeric Isolator
Dr. R. S. Fersht, S. N. Fersht, and M. Denice, Jr. — AC-1

*RELSAT Damping Material Data
M. L. Parin — AD-1

PACOSS Damping Material Measurements
M. L. Parin — AE-1

Design Oriented Measuring Techniques for Determining the Mechanical Properties of Rubber
Dr.Ir. B. Devis, Dr.Ir. C. DeMeersman, and Prof.Ir. J. Peters — AF-1

*Selected Complex Modulus Data
C. Chesneau and B. Duperray — AG-1

On The Fractional Calculus Model of Viscoelastic Behavior
Maj. R. L. Bagley and Dr. P. J. Torvik — AH-1

*A Critique of Complex Modulus Test Methods
Dr. D. I. G. Jones — AI-1

Hubble Space Telescope Reaction Wheel Assembly Vibration Isolation System
L. P. Davis, J. F. Wilson, R. E. Jewell, and J. J. Roden — BA-1

*Gasdynamic Damping Properties of Steam Turbine Blades
Dr. N. F. Rieger — BB-1

*A Layered Notch Filter for High Frequency Isolation
Prof. J. L. Sackman, Prof. J. M. Kelly, and A. E. Javid, — BC-1

*Not available for publication.

TABLE OF CONTENTS (Continued)

	Page
Analytical and Experimental Studies of Structures with Coulomb Friction Elements Prof. S. F. Masri, O. T. Hata, and J. A. Malthan	BD-1*
Is It Damping or Nonlinearity? Prof. R. A. Ibrahim	BE-1
Damping in Elastic Systems Prof. E. Dowell	BF-1*
Viscosity and Damping as the Diabolic and Roguish Cause for Instability Prof.Dr.rer.nat. H. F. Bauer	BG-1
Damped Optics Design M. J. Laughlin	CA-1
Viscoelastic Component Damper Design Problems C. W. White	CB-1
The Effects of Bond Imperfections on the Dynamic Response of Laminated Beams Prof. P. G. Reinhall and R. N. Miles	CC-1
Method of Predicting Damping in Stiffened Structures Dr. J. Soovere	CD-1
Implementation of Modal Strain Energy Method Using MSC/NASTRAN and Post-Processing Utility Programs N. K. Frater	CE-1
Influence of Temperature on Structural Joints with Designed-In Damping J. Prucz, P. Smith, L. W. Rehfield, and A. D. Reddy	CF-1
Dynamics of Viscoelastic Structures Dr. K. J. Buhariwala and Prof. J. S. Hansen	CG-1
On the Virtues and Prospects for Passive Damping in Large Space Structures Prof. H. Ashley and Dr. D. L. Edberg	DA-1
Investigation of Passive Damping of Large Space Truss Structures Dr. J. M. Hedgepeth and Dr. M. Mobrem	DB-1

END VOLUME 1

*Not available for publication.

TABLE OF CONTENTS (Continued)

BEGIN VOLUME 2

	Page
Damping Characteristics of the Solar Array Flight Experiment E. D. Pinson	DC-1
Resonant Shift Modal Testing Method for Viscous Damping Coefficient Estimation Dr. D. W. Nicholson, Dr. M. G. Prasad, and R. H. Lin	DD-1
Prediction of Spacecraft Damping Dr. B. K. Wada	DE-1
On-Orbit Flexible Body Parameter Identification for Space Station Dr. F. Y. Hadaegh, Dr. D. S. Bayard, and D. R. Meldrum	DF-1
Design and Analysis of the PACOSS Representative System D. R. Morgenthaler and R. N. Gehling	DG-1
Robust Control Design for Vibration Suppression of Large Space Structures Dr. R. K. Yedavalli	EA-1
Active Augmentation of a Passively Damped Representative Large Space System R. N. Gehling	EB-1
Active Control for Vibration Damping Lt. P. J. Lynch and Dr. S. S. Banda	EC-1
A New Approach to Modeling Linear Viscoelastic Damping for Space Structures P. C. Hughes, D. McTavish, K. W. Lips, and F. R. Vigneron	ED-1
Experimental Investigations Into Passive and Active Control Using Space-Realizable Techniques D. W. Miller and Dr. E. F. Crawley	EE-1
Distributed, Active Damping of Multiple Modes Dr. T. J. Brennan, P. R. Dahl, and J. J. Gerardi	EF-1*
Active Damping Augmentation by Pole Allocation Methods Dr. E. F. Berkman	EG-1*

*Not available for publication.

TABLE OF CONTENTS (Continued)

	Page
A Unified Approach to Model Reduction and Robustness Dr. L. R. Fasseron and B. J. Sevennec	EH-1*
Eigenstructure and Control of Damping and Vibrations Dr. A. N. Andry, Jr., Dr. E. Y. Shapiro, and Dr. K. M. Sobel	EI-1*
Material Damping in Aluminum and Metal Matrix Materials Dr. E. F. Crawley and M. C. van Schoor	FA-1
Material Damping in Space Structures Dr. S. P. Rawal and M. S. Misra	FB-1
Specific Damping Capacity of Metal-Matrix Composites in Tension-Tension Fatigue A. K. Ray, Prof. V. K. Kinra, Dr. S. P. Rawal, and M. S. Misra	FC-1
Response Suppression in Composite Sandwich Shells Prof. R. Vaicaitis and Prof. D. A. Bofilios	FD-1
Prediction of Material Damping of Laminated Polymer Matrix Composites Prof. C. T. Sun, J. K. Wu, and Prof. R. F. Gibson	FE-1
The Influence of Fiber Length and Fiber Orientation on Damping and Stiffness of Polymer Composite Materials Prof. S. A. Suarez, Prof. R. F. Gibson, Prof. C. T. Sun, and S. K. Chaturvedi	FF-1
A Review of the Damping Mechanisms in Advanced Fibre-Reinforced Composites Dr. R. D. Adams	FG-1
A Design Methodology for Estimating the Damping in Laminated and Fibre-Reinforced Plates Dr. R. D. Adams and R. F. Lambert	FH-1
Damping Measurements by Hilbert Transform on Composite Materials A. Agneni and Prof. L. B. Crema	FI-1
A Comparison Among Damping Coefficients on Several Aerospace Composite Materials Prof. L. B. Crema and A. Castellani	FJ-1

*Not available for publication.

TABLE OF CONTENTS (Continued)

	Page
Vibration Damping of Solid Propellant Rocket Motors Prof. R. A. Heller and Prof. M. P. Singh	GA-1
Damping Predictions Using Material Properties from Various Test Methods M. L. Drake and M. F. Kluesener	GB-1
The Prediction of Total Loss Factors of Coupled Structures Dr. J. M. Cuschieri and Prof. E. J. Richards	GC-1
Identification of Modal Damping of Flexible Spacecraft Appendages Using Substructure Techniques L. Slivinski, G. A. Clark, and Dr. F. H. Chu	GD-1
Construction of a Consistent Damping Matrix Dr. K. J. Buhariwala and Dr. J. S. Hansen	GE-1
Damping Identification from Nonlinear Random Responses Using a Multi-Triggering Random Decrement Technique Prof. S. R. Ibrahim, K. R. Wentz, and J. Lee	GF-1
Design and Testing of a Sixty-Foot Damped Generic Space Truss Dr. C. D. Johnson and Dr. D. A. Kienholz	HA-1
The Design of Viscoelastic Passive Damping Treatments for Satellite Equipment Support Structures Dr. R. Ikegami and D. W. Johnson	HB-1
Shock and Vibration Attenuation in Viscoelastic Damped Structure C. J. Beck, Jr.	HC-1
Vibroacoustic and Shock Performance of Damped Spacecraft Equipment Panels C. V. Stahle, Jr., J. A. Staley, and J. C. Strain	HD-1
Design and Experimental Verification of Damped Spacecraft Equipment Panels C. V. Stahle, Jr., J. A. Staley, and J. C. Strain	HE-1
Fabrication of Damped Spacecraft Equipment Panels K. A. Schmidt, F. P. Curtis, E. F. Muziani, and L. Amore	HF-1
Registrants for DAMPING 86	R-1

*Not available for publication.

KEYNOTE ADDRESS

"THE DEPARTMENT OF DEFENSE SCIENCE AND TECHNOLOGY PROGRAM IN SPACECRAFT MATERIALS AND STRUCTURES"

By

Jerome Persh

Staff Specialist for Materials and Structures
Office of the Under Secretary Defense
Research and Engineering
Research and Advanced Technology
Military Systems Technology
The Pentagon, Washington DC

Good morning ladies and gentlemen. I am delighted to be here at this "Vibration Damping Workshop II" and share with you some of my thoughts on this very important technology area.

In this presentation, rather than dealing with vibration damping in a technical sense, I plan to interpret the expression more in a broad sense. The technical presentations that will be given during your meeting provide a true snapshot of where the U.S. stands technologically in this essential area and there is little that I could contribute to the information the fine speakers are presenting here at this workshop. Therefore, rather than risking the danger of technical involvement, my intuition tells me to stay clear.

But first before getting into the subject of this workshop let me tell you briefly how the Department of Defense is structured and where this technology area fits into the overall scheme of things. My first illustration (Chart 1) displays an overall organization of the DOD with the group that I work in highlighted. This highlighted box is further expanded on Charts 2 and 3.

The responsibilities of the Military Systems Technology Office are shown on Chart 4. The overall mission of the Research and Advanced Technology Office is displayed on Chart 5 and its in-house laboratory coverage is displayed on Chart 6. The proposed fiscal year 1987 budget for the R&AT organization is shown on Chart 7. For those not familiar with DOD funding categories, I have included Chart 8 which shows the breakdown of DOD budget categories.

Of the total R&AT Science and Technology Program I showed on Chart 7, that allocated to the materials and structures area is displayed on Chart 9. With this funding, our responsibilities covers practically every mission area of the DOD as shown on Chart 10. It is to be noted that the subject of this workshop impacts the spacecraft mission area principally

although work is on-going in other mission areas as well. As such, it is distributed throughout the overall program but the spacecraft area has maximum visibility. Of the total materials and structures budget shown on Chart 9, it would be extremely difficult to isolate those dollars allocated to vibration damping, although it is known that work is continually on-going. It should also be noted that work on metal-matrix composites is underway in practically all of the mission areas.

To complete the overall picture, let me outline in very broad terms where I see the Department of Defense Materials and Structures Science and Technology Program is going. (Chart 11) Certainly the overall philosophical direction is towards more and more technical sophistication. The "handwriting was on the wall" when we started our Rapid Solidification Technology (RST) program in 1980. We were then dealing with micron size powder particles, now we are headed towards sub-micron particles. We are involved in the exciting areas of sol-gel processing and organometallic synthesis.

Processing science is another important area of research. That is the understanding of the effect of processing variables on the generation and development of property-controlling microstructures of constituent materials. This can only lead to the development of unique structures and properties precisely tailored the needs.

The materials development direction is clearly towards composites. Not only are the fiber reinforced organic, metal, ceramic and carbonaceous matrix composites being developed, but also those in which the reinforcement is produced simultaneously with the matrix. Key research areas include the fiber interface regions and mechanisms and concepts to achieve precisely the structural properties desired.

The final general direction in which we are headed is toward demonstration. We have found that it is unsatisfactory to stop our work with a new materials development. It has to be demonstrated on a structural or functional component that closely simulates the final use to which it is intended to be put. I am sure you have noticed that over the past number of years more and more sub-scale and full scale components are being subjected to real environmental testing and followed up with detailed analysis leading to understanding of the results. It is this procedure that leads to accurate performance predictions in systems use. Before we consider we have finished our job these things must be done. This is a fundamental change in the overall character of our programs that has taken place over the past ten or fifteen years.

Along with each of these directions we have found that it is insufficient to carry any new materials and structures development through demonstration without the establishment of a knowledgeable government, industry, and academia "team". This is why you see so many of our "thrust" programs in discrete technological areas. If new developments are to be used for advanced military hardware, we have to show that it does what we say it will do, and have the "team" in place to provide the expertise to do the explaining. This is definitely a consequence of the ever increasing sophistication. Whether this is "good" or "bad" is another question. It is just the way it is now.

Now that I have placed in perspective just where this technology area fits in the overall DOD scheme of things, I would like to discuss just where the subject of this workshop fits into the picture. As I said at the outset I do not plan on getting into the technical aspects because you are much more qualified to discuss these matters and will have ample opportunity during the course of this workshop.

Now, recalling Chart 9 which showed an overall breakout of the Science and Technology (S&T) funding for materials and structures, I have plotted the overall dollars against fiscal years on the next chart (Chart 12) and indicated that portion of the overall devoted to composite materials. Also indicated on this chart is an estimate of how much of the total program has been dedicated to the space mission of the Navy and Air Force. It is obvious that this represents only a very small fraction of the total effort. Then along came the Strategic Defense Initiative (SDI) whose investment in related S&T far overwhelms our investment. This is indicated on the overlay on Chart 12. Of course what I am showing here are overall totals for the related S&T work. It is not possible to break out the funding allocation for vibration damping but you can imagine that it must be a very small number compared to the total. My next chart (Chart 13) shows a display of the broad categories of space S&T work for both our S&T program and the SDI. I have indicated on the overlay to this chart, those areas where efforts in the S&T program complement and feed basic generic technology to the SDI program.

Now to get to the subject of damping in space.

I have to start this discussion by stating flatly that the military is ever increasing its dependence on space assets for both tactical and strategic warfare situations. Because of this growing dependence there is a demand for vastly increased capability which leads to greater complexity and in turn requires attention to all of the detailed aspects of a space vehicle. This is easily illustrated by considering potential requirements that future spacecraft will have to be moved or pointed in different directions to accomplish certain missions. Moreover, survivability in hostile environments is also becoming a more important factor in spacecraft design. This requirement may also mean movement of the spacecraft. Since the spacecraft may not be able to perform its information acquisition or transmission function while it is moving, it is an obvious requirement that loss of operational time be as short as possible. What these thoughts add up to is that greater and greater consideration must be given to the intrinsic materials properties and dynamic behavior of structural systems than has been done in the past when the structure was only a support system for the sophisticated sensors. In the past spacecraft designers generally paid attention to the dynamic behavior of the spacecraft structure only after the materials were selected. Therefore spacecraft control has depended on use of complex active systems. Now I believe that it is essential for the future to factor in the fundamentals of the behavior of spacecraft materials and structures before the spacecraft is designed. This means that a great deal of very sophisticated technology must be developed if we are to be able to fulfill the missions that are confronting us.

As I indicated, it is only logical that if one wishes to move a spacecraft to either fulfill a sensor mission or avoid some hostile action, the need to start and stop its motion in minimum time is extremely important. It is unreasonable to assume that this can always be accomplished totally passively.

Some sort of active damping will certainly have to be used for many missions, but one would hope that as much as possible can be done passively to decrease complexity and weight as well as increasing overall spacecraft reliability. To date there has been minimal effort to understand the role of materials and structures on spacecraft damping. But for the future, damping may have the same degree of importance in spacecraft structures as dimensional stability and specific stiffness. (Chart 14). Optimization of materials and structures for passive damping will require a great deal of technological understanding which we do not now have. We certainly can get more payoff from the materials.

Let me briefly discuss some of the conflicting needs that must be considered. Probably one of the most important is joints in space structures. On one hand there is a need for extreme dimensional accuracy and stability which translates to very tight joints. This means that the helpful damping we depended upon in joints may not be available because of this requirement.

The only way I know to address this problem is head-on. The technology to provide a detailed understanding of joint damping-including test methods and techniques must be obtained. In a similar vein, the dynamics of the interfacial region between the fiber and matrix in a composite, whether metal, organic or carbonaceous must be known if one is to be able to design passive damping into spacecraft. (Chart 15). There are numerous other examples of unknown areas that have to be investigated.

One thing we do know. The lighter the structure, the easier it is to move it and stop it from moving. This fact leads naturally to the use of composites, which by their very nature are much more difficult to understand than homogeneous materials. But it has to be done. Here again an example will illustrate the point. Consider a metal-matrix composite utilizing magnesium as the matrix reinforced with very high modulus pitch (graphite) fibers. It is relatively easy to visualize that the greater the stiffness of the fibers, the fewer of them will be needed to achieve equal stiffnesses. Since the weight (density) of graphite is greater than magnesium, it is obvious that the direction to go is to the highest stiffness fiber available to provide for the lightest weight structure. (Chart 16). And this naturally translates back to the requirements for damping the system in the shortest time with the minimum of complexity. Much work remains to be done in this area.

Clearly, what I have attempted to illustrate is that if we are to fulfill our future spacecraft mission requirements with the most efficient structures, we must have basic understanding of intrinsic materials related factors and their dynamic behavior when fabricated into structures. One has to very seriously consider all of the aspects of the total system. There is a great deal of technology yet to be developed. I feel certain

that we can develop this technological understanding, but it will take time and much work.

While I am sure that this audience has a deep appreciation of the magnitude and difficulty of the effort that needs to be done, I am uncertain as to whether the spacecraft development and procurement communities understand. There will have to be some fundamental and conceptual changes in the way we do business in this arena because as I indicated earlier, the allocation of funding for spacecraft in the overall materials and structures S&T program is minimal at best. The other traditional mission responsibilities of the military departments must be dealt with in priority order. This means that a much greater responsibility for fundamental spacecraft technology must be assumed by the project officers. There is just no way that the S&T program is going to develop the needed understanding in a time frame required for such programs as the strategic defense initiative. We can help, but certainly not provide a package of the needed technology. Recognition of this reality must be taken into account in future program planning.

In closing, I have tried to give a broad picture of the challenges facing this community and the directions I see the Department of Defense Materials and Structures Program going in. I am confident that we will do what we have to do in the years to come. This workshop is one of the essential steps to getting us there.

OFFICE OF THE SECRETARY OF DEFENSE

Chart 1

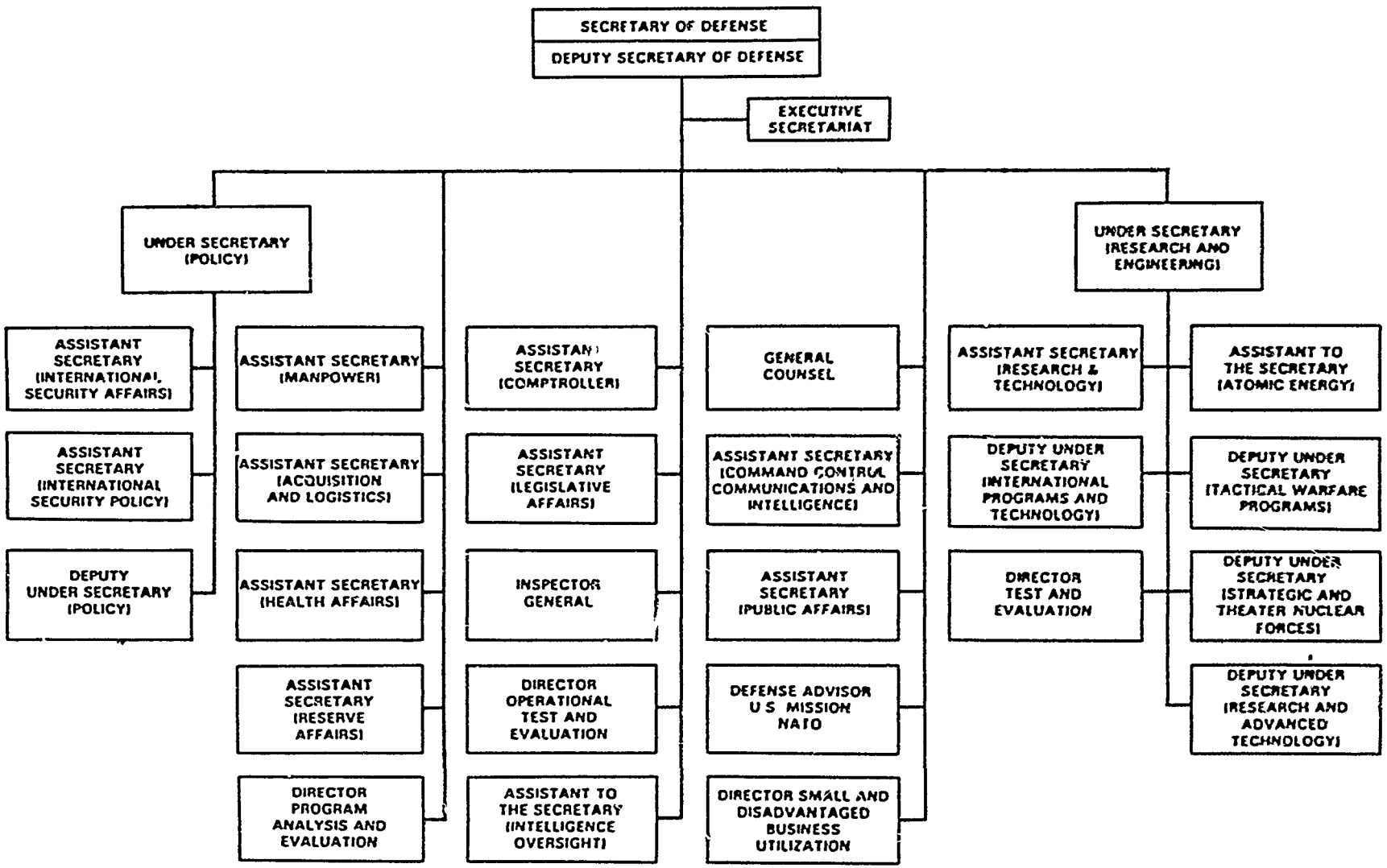
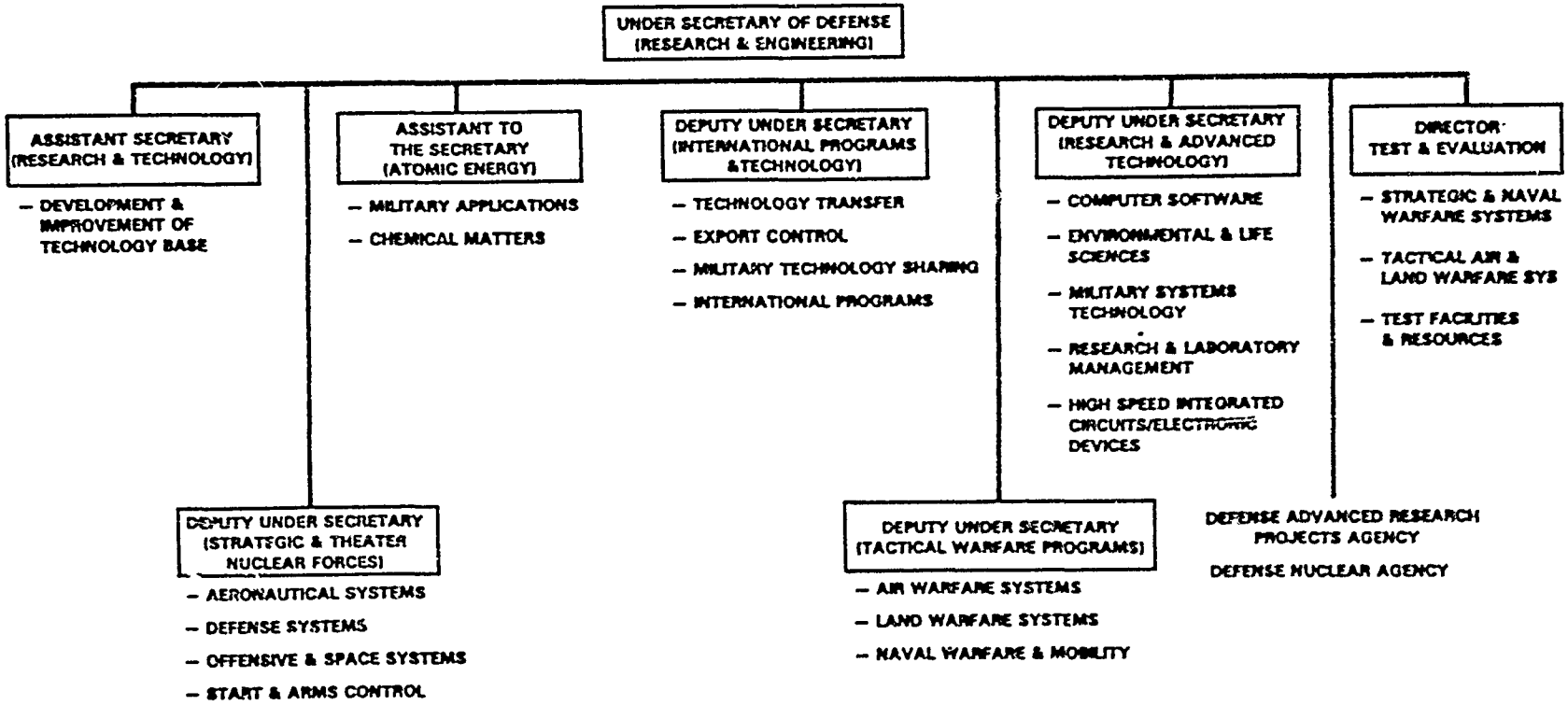
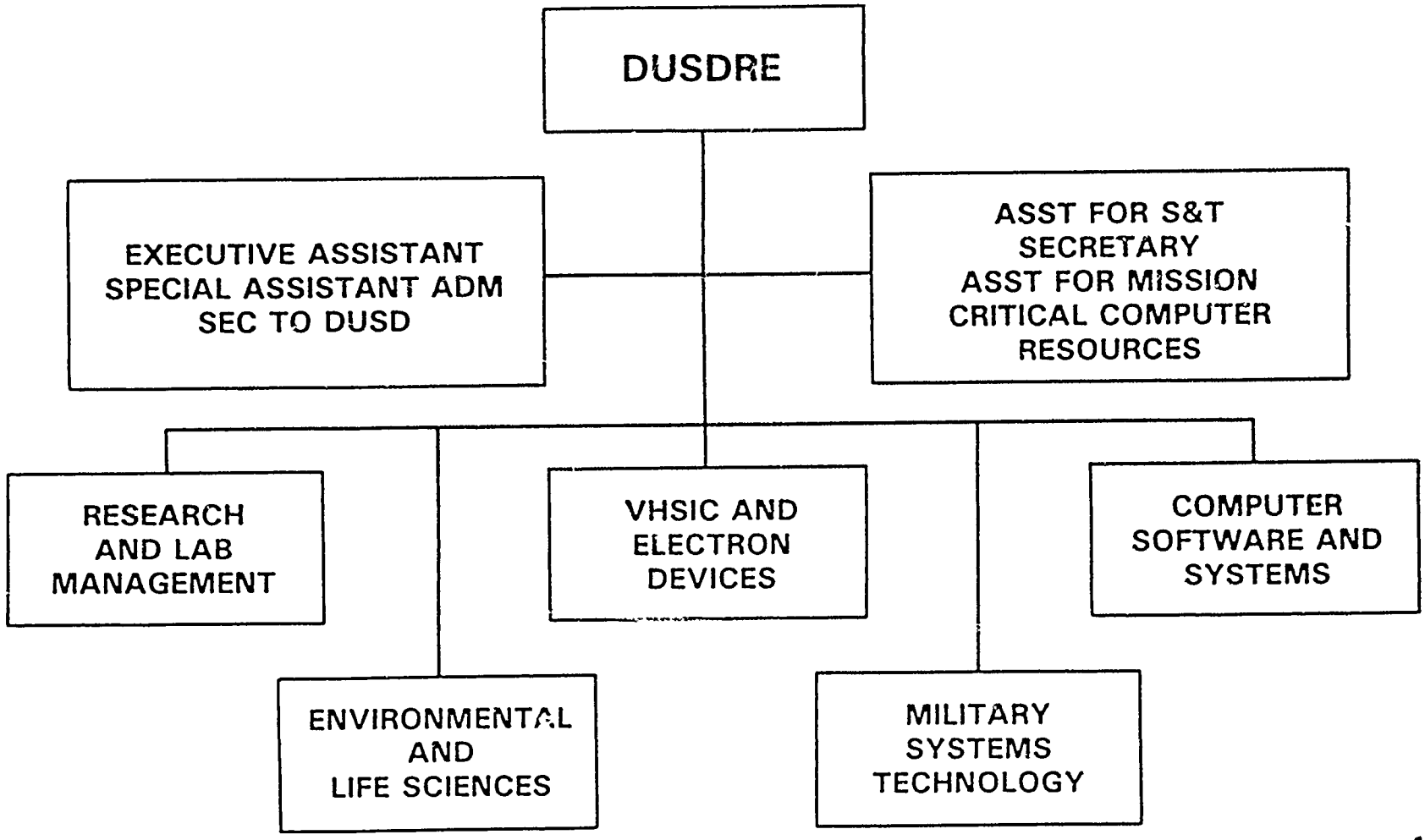


Chart 2


UNDER SECRETARY OF DEFENSE (RESEARCH & ENGINEERING)
ASSISTANT SECRETARY (RESEARCH & TECHNOLOGY)
– DEVELOPMENT & IMPROVEMENT OF TECHNOLOGY BASE
ASSISTANT TO THE SECRETARY (ATOMIC ENERGY)
– MILITARY APPLICATIONS
– CHEMICAL MATTERS
DEPUTY UNDER SECRETARY (INTERNATIONAL PROGRAMS &TECHNOLOGY)
– TECHNOLOGY TRANSFER
– EXPORT CONTROL
– MILITARY TECHNOLOGY SHARING
– INTERNATIONAL PROGRAMS
DEPUTY UNDER SECRETARY (RESEARCH & ADVANCED TECHNOLOGY)
– COMPUTER SOFTWARE
– ENVIRONMENTAL & LIFE SCIENCES
– MILITARY SYSTEMS TECHNOLOGY
– RESEARCH & LABORATORY MANAGEMENT
– HIGH SPEED INTEGRATED CIRCUITS/ELECTRONIC DEVICES
DIRECTOR TEST & EVALUATION
– STRATEGIC & NAVAL WARFARE SYSTEMS
– TACTICAL AIR & LAND WARFARE SYS
– TEST FACILITIES & RESOURCES
DEPUTY UNDER SECRETARY (STRATEGIC & THEATER NUCLEAR FORCES)
– AERONAUTICAL SYSTEMS
– DEFENSE SYSTEMS
– OFFENSIVE & SPACE SYSTEMS
– START & ARMS CONTROL
DEPUTY UNDER SECRETARY (TACTICAL WARFARE PROGRAMS)
– AIR WARFARE SYSTEMS
– LAND WARFARE SYSTEMS
– NAVAL WARFARE & MOBILITY
DEFENSE ADVANCED RESEARCH PROJECTS AGENCY
DEFENSE NUCLEAR AGENCY

R&AT ORGANIZATION

Chart 3



MILITARY SYSTEMS TECHNOLOGY
AREAS OF RESPONSIBILITY

Chart 4

- ELECTRONIC SYSTEMS
  - SEARCH, SURVEILLANCE, FIRE CONTROL, C^3 AND EW
- COMBAT VEHICLES
  - AIRCRAFT, SHIPS, SUBMARINES, TANKS, TRUCKS
- PROPULSION AND FUELS
  - GAS TURBINES, DIESELS, RAMJETS, ROCKETS, TRANSMISSIONS
- CONVENTIONAL WEAPONS
  - GUIDED WEAPONS, GUNS, PROJECTILES, BOMBS, FUZES, EXPLOSIVES
- MATERIALS AND STRUCTURES
  - COMPOSITES, ARMOR, RAPID SOLIDIFICATION ALLOYS, E/M WINDOWS

A-9

Chart 5

DEPUTY UNDER SECRETARY FOR RESEARCH AND ADVANCED TECHNOLOGY

THE DoD SCIENCE AND TECHNOLOGY PROGRAM INCLUDES RESEARCH (6.1), EXPLORATORY DEVELOPMENT (6.2), AND ADVANCE TECHNOLOGY DEVELOPMENTS (6.3A)

RESPONSIBILITIES

- POLICY
- GUIDANCE
- OVERSIGHT

ROLES

- SCIENTIFIC ADVISOR FOR USDRE

DoD POINT OF CONTACT FOR SCIENTIFIC COMMUNITY

FUNCTIONS

- STRUCTURE S&T PROGRAM ACROSS SERVICES
- RESOLVE TECHNICAL DIFFERENCES
- ENHANCE RETURN ON INVESTMENT

IN-HOUSE LABORATORIES

Chart 6

LABORATORIES	74
PEOPLE	60,000
PROFESSIONALS	27,000
PROPERTY & EQUIPMENT	$4 BILLION

A-11

SCIENCE AND TECHNOLOGY PROGRAM
FY 1987 BUDGET SUBMISSION
(DOLLARS IN MILLIONS)

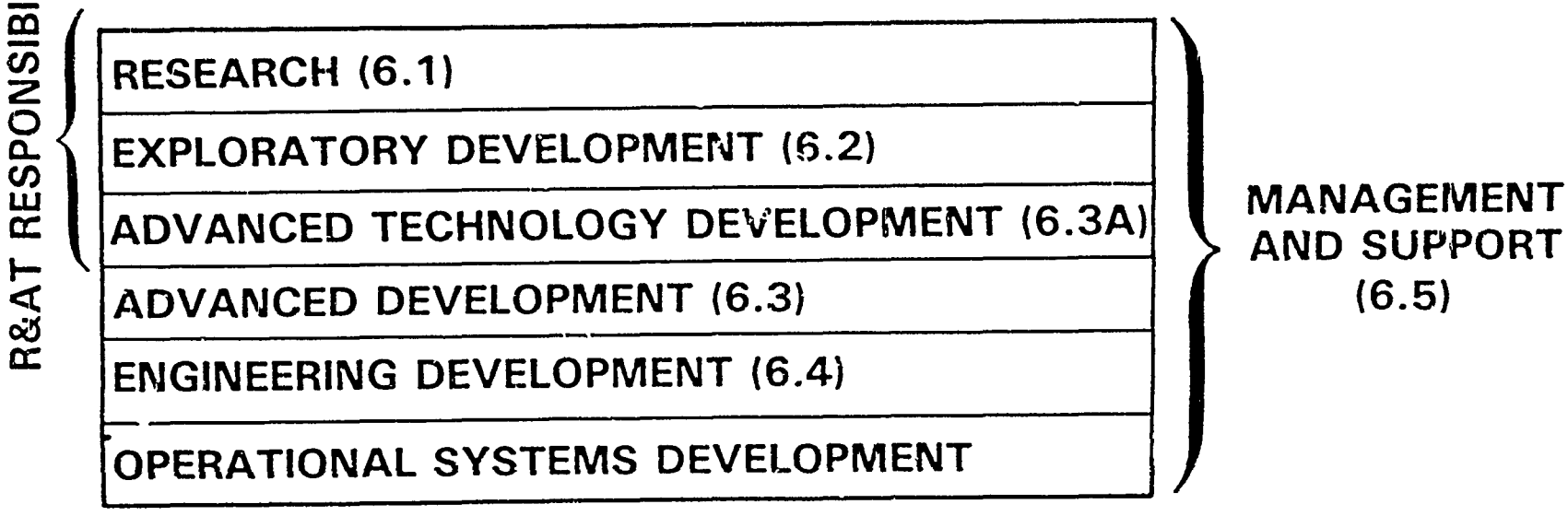
Chart 7

	FY 1986	FY 1987 REQUEST
RESEARCH	1,024	986
EXPLORATORY DEVELOPMENT	2,425	2,599
ADVANCED TECHNOLOGY DEV.	1,488	1,790
TOTAL SCIENCE AND TECHNOLOGY	4,937	5,375
STRATEGIC DEFENSE INITIATIVE	2,746	4,785

STRUCTURE OF THE RDT&E PROGRAM

Chart 8

TO FACILITATE MANAGEABILITY, THE RDT&E PROGRAM IS DIVIDED INTO THE FOLLOWING SIX CATEGORIES OF EFFORT:



DoD MATERIALS AND STRUCTURES SCIENCE AND TECHNOLOGY PROGRAM

Chart 9

MISSION AREAS		TECHNOLOGY NEEDS	THRUSTS
STRATEGIC OFFENSE • REENTY VEHICLES • PROPULSION SYSTEMS	• MATERIALS PROPERTIES • LOADS AND ENVIRONMENTS • CHARACTERIZATION • NON-DESTRUCTIVE EVALUATION	• ALL WEATHER CAPABILITY • MANEUVERING CAPABILITY • EFFICIENT ROCKET NOZZLES • LIGHTWEIGHT UPPER STAGES	• CARBON/CARBON COMPOSITES • METAL-MATRIX COMPOSITES
SPACE • SATELLITE STRUCTURES • PROPULSION SYSTEMS • MIRRORS—OPTICAL STRUCTURES • ANTENNAS		• SURVIVABILITY • NO OUTGASSING • THERMAL/ELECTRICAL CONDUCTIVITY • DIMENSIONAL STABILITY • HIGH STIFFNESS • DAMPING	• METAL-MATRIX COMPOSITES • CERAMIC MATRIX COMPOSITES • CARBON/CARBON COMPOSITES
LAND WARFARE • TANKS • VEHICLES • MOBILITY		• IMPROVED ARMOR • GUN BARREL EROSION • GROUND VEHICLE SURVIVABILITY	• METALS, CERAMICS, ORGANICS • METAL-MATRIX COMPOSITES
AIR WARFARE • AIRCRAFT • TACTICAL MISSILES		• DURABILITY OF COMPOSITES • HIGH STRENGTH "FORGIVING" METALS • LONG LIFE HIGH TEMPERATURE GAS TURBINE COMPONENTS • ALL WEATHER CAPABLE SEEKER DOMES	• ORGANIC MATRIX COMPOSITES • METAL-MATRIX COMPOSITES • CERAMIC MATRIX COMPOSITES
NAVAL WARFARE • MINES AND TORPEDOES • SHIPS SURVIVABILITY • SUBMARINES		• HIGH STRENGTH "FORGIVING" METALS • COMPOSITES • JOINING TECHNIQUES	• METALS • METAL-MATRIX COMPOSITES • WELDING
RESEARCH		• UNDERSTANDING STRUCTURAL RESPONSE • ENERGY INTERACTIONS • SYNTHESIS NEW MATERIALS	• MICRO/MACRO MECHANICS • FRACTURE MECHANICS

Chart 10

DoD MATERIALS AND STRUCTURES SCIENCE AND TECHNOLOGY PROGRAM FUNDING

WHO, WHAT, AND HOW MUCH	$ MILLIONS						
	FY 1980	FY 1981	FY 1982	FY 1983	FY 1984	FY 1985	FY 1986
MATERIALS TECHNOLOGY	108.0	118.8	136.4	145.6	155.3	186.4	230.0
STRUCTURES TECHNOLOGY	65.4	109.1	121.8	127.0	96.4	75.3	58.8
RESEARCH (6.1)	54.2	70.9	81.1	83.8	77.7	82.7	102.2
EXPLORATORY DEVELOPMENT (6.2)	94.4	115.7	128.3	120.0	132.4	141.0	142.2
ADVANCED TECHNOLOGY DEVELOPMENT (6.3A)	27.8	36.5	45.1	63.4	63.7	46.7	40.4
MANUFACTURING SCIENCE (6.1)	—	4.8	3.7	5.4	9.6	9.1	4.0
INFORMATION ANALYSIS CENTERS (6.5)	1.5	1.0	1.5	1.8	2.0	2.0	2.0
ARMY	33.3	39.9	49.2	48.6	69.2	73.6	51.9
NAVY	56.7	72.1	76.6	83.4	73.1	80.2	73.1
AIR FORCE	66.0	94.3	105.3	111.3	109.4	107.9	122.3
DARPA	17.4	21.6	27.1	29.3	35.0	38.3	41.5
DLA	1.5	1.0	1.5	1.8	2.0	2.0	2.0
TOTAL	174.9	228.9	259.7	274.4	288.7	302.0	290.8

io-1502

BASIC CHARACTER AND TRENDS IN MATERIALS AND STRUCTURES SCIENCE AND TECHNOLOGY IN THE DEPARTMENT OF DEFENSE

Chart 11

PHILOSOPHICAL DIRECTION → SOPHISTICATION

- SOL – GEL PROCESSING
- ORGANOMETALLIC SYNTHESIS
- SUB-MICRON PARTICLE SYNTHESIS
- PROCESSING SCIENCE-MICROSTRUCTURE CONTROL
- COMPOSITES INTERFACE PHENOMENA
- UNDERSTANDING RESPONSE TO ENVIRONMENT
- TAILORING TO NEEDS

MATERIAL DIRECTION → COMPOSITES

- ORGANIC MATRIX
- METAL MATRIX
- CERAMIC MATRIX
- CARBON/CARBON
- HYBRIDS

→ PARTICLE REINFORCEMENT

→ CONTINUOUS FIBER REINFORECEMENT

PROGRAMMATIC DIRECTION → DEMONSTRATION

- SUB AND FULL SCALE COMPONENTS
- REAL ENVIRONMENT TESTING
- UNDERSTANDING OF RESULTS
- ESTABLISHMENT OF "TEAMS"

542 6

MATERIALS AND STRUCTURES TECHNOLOGY BASE FUNDING TRENDS

Chart 12

ARMY + NAVY + AIR FORCE + DARPA (6.1 + 6.2 + 6.3A)

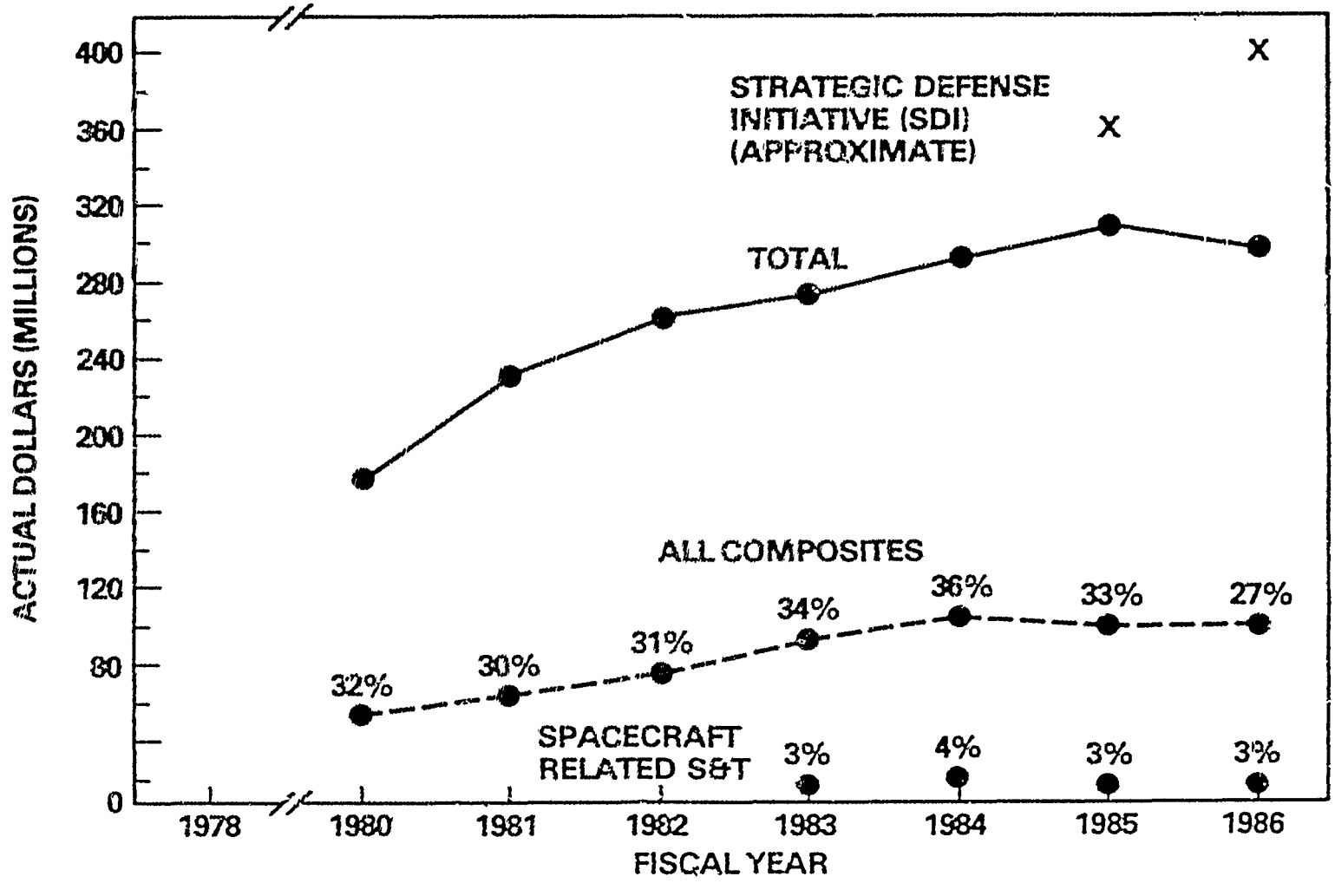
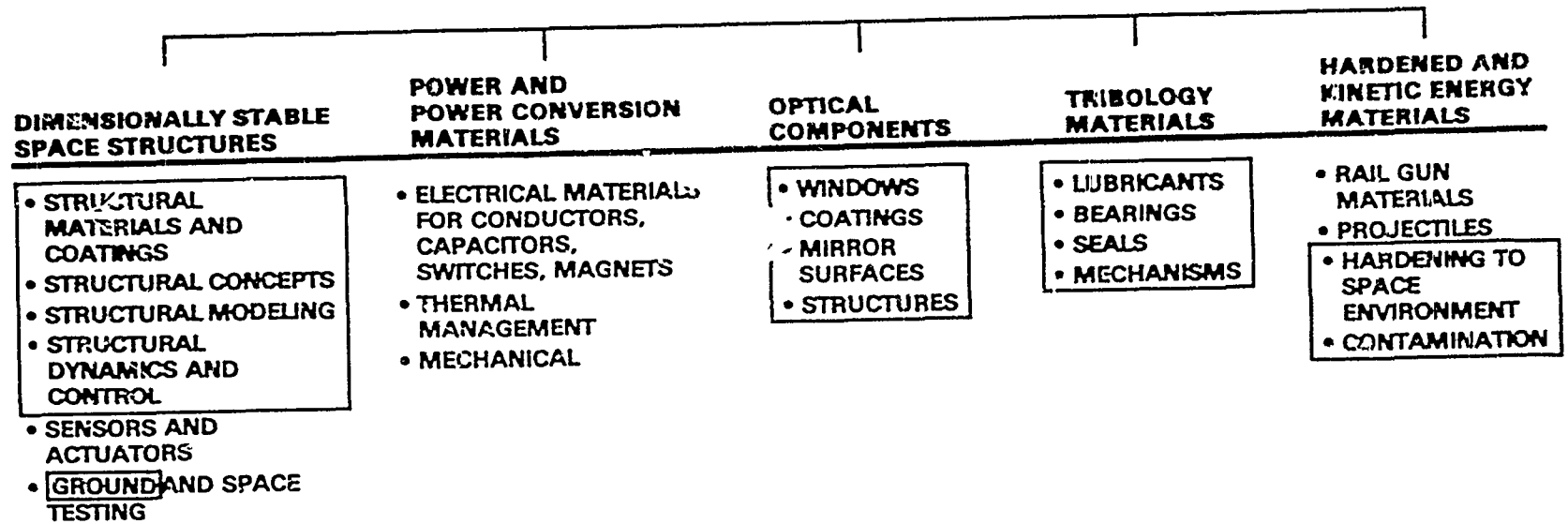


Chart 13

STRATEGIC DEFENSE INITIATIVE AND S&T MATERIALS AND STRUCTURES AREAS



ESSENTIAL CONSIDERATIONS FOR FUTURE SPACECRAFT MATERIALS AND STRUCTURES

Chart 14

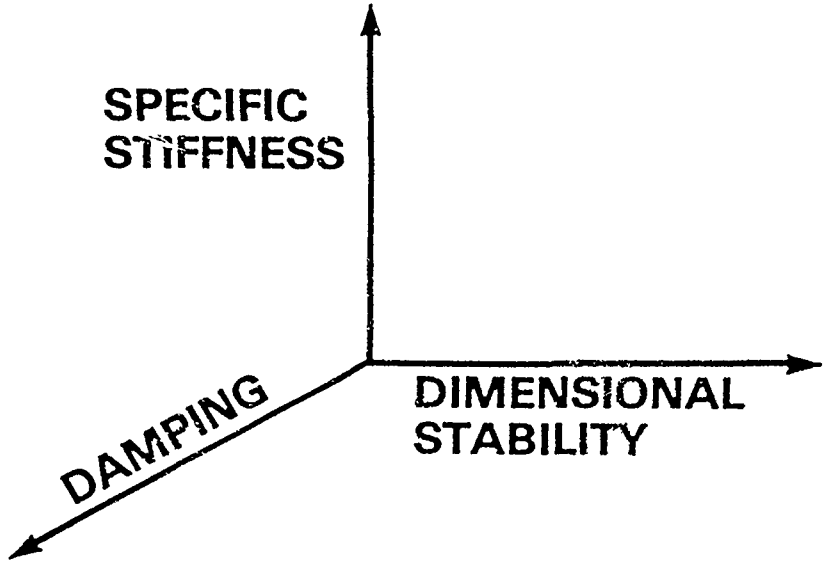


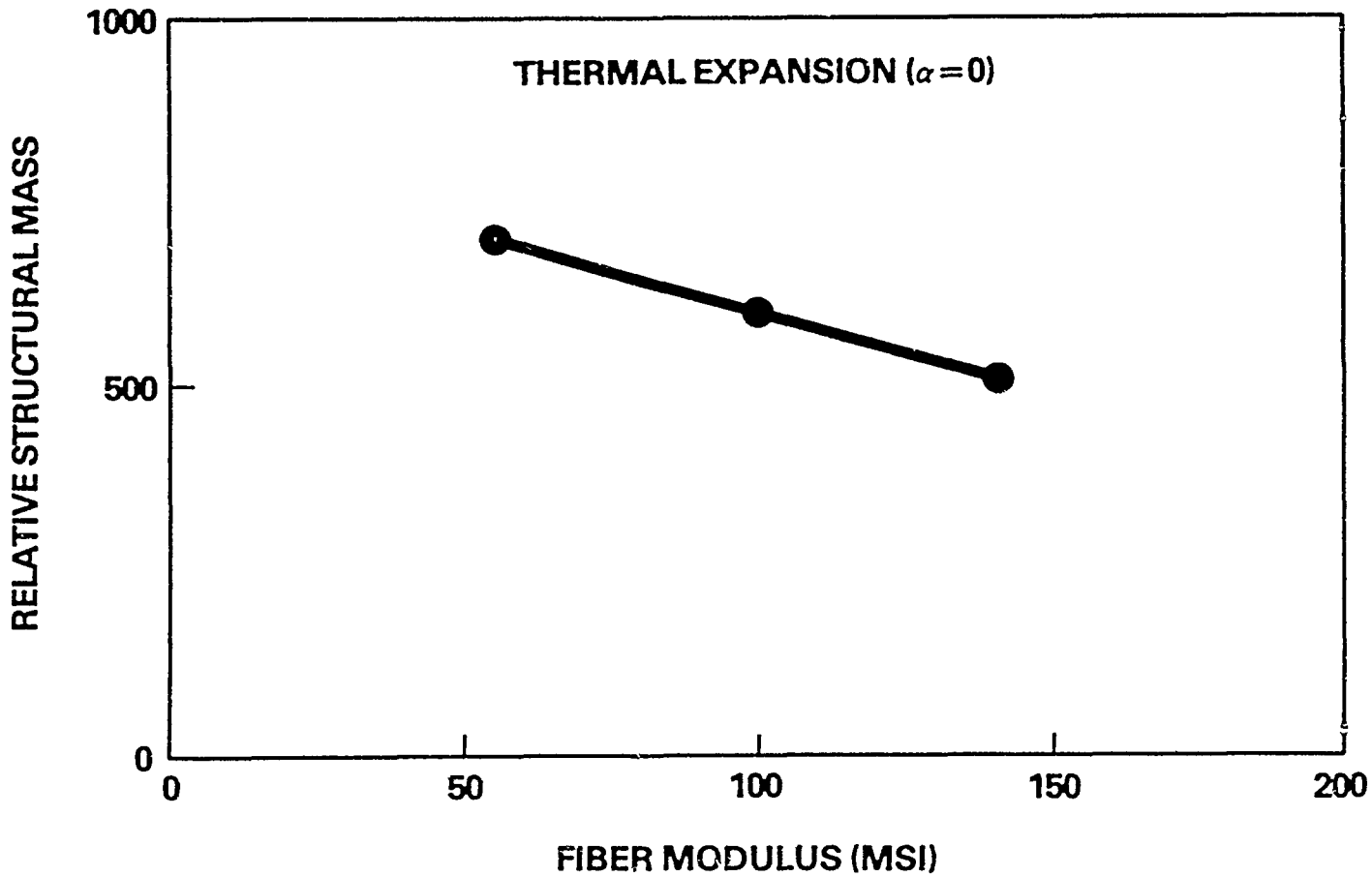
Chart 15

SOME COMPOSITE VARIABLES RELATED TO DAMPING

- MATRIX COMPOSITION AND STRUCTURE
- FIBER MODULUS
- FIBER/MATRIX INTERFACE CHARACTER
- NUMBER OF INTERFACES

Chart 16

STRUCTURAL MASS DEPENDENCE ON FIBER MODULUS



STANDARD GRAPHICAL PRESENTATION OF COMPLEX MODULUS AND DATA PROCESSING METHODOLOGY

Lynn Rogers and James Eichenlaub
AFWAL/FIBA
Wright-Patterson Air Force Base

and

Jeffrey B. Layton
Purdue University

ABSTRACT

Present practice for data processing, storing, retrieving, and transmitting damping material complex modulus is summarized. Appendix A is a reasonably mature draft standard for the graphical presentation of complex modulus data. Appendix B proposes a procedure for obtaining an initial estimate for the temperature shift function for a set of data, especially useful when the range of experimental frequency is marginal. The flow of data processing is described and individual steps are presented in some detail.

INTRODUCTION

A key to the advancement and implementation of damping technology is accurate and efficient data processing, modeling, presentation, dissemina ' ı, storage, retrieval, and utilization for vibration damping or viscoelastic materials (VEM). The graphical presentation of complex modulus data is useful as an interface between the VEM supplier and user (designer or analyst) as well as other purposes; Appendix A is a reasonably mature draft of a proposed standard.

Finding the appropriate temperature shift function is central to all handling of complex modulus data; Appendix B makes a case for considering the slope of the temperature shift function. It also presents some relevant mathematical relationships.

The present paper gives a procedure to obtain an estimate for the temperature shift function and estimated parameter values for the particular equation used to analytically represent the complex

modulus. Obviously, once initial estimates are obtained, improvements may be made iteratively either by qualitative judgement or by some regression technique.

BASIC EQUATION

The utility and economy of fractional calculus for complex modulus representation was developed by Bagley [1], while the use of Bode diagrams (from control system methodology) and the current notation were developed by the present author [2]. The simplest equation of current interest is

$$G = (G_e + G_g z)/(1 + z) \qquad E1$$

where

$$z = (jr)^{\beta} \; ; \; r = f_R/f_{RO} \qquad E2$$

and

$$f_R = f_{\zeta_T} \; ; \; \log f_R = \log f + \log \zeta_T \qquad E3$$

E1 is shown in F-B4 for typical values. Many damping materials have this general character. E1 is the basis for the initial approximation to the temperature shift function and is the initial analytical fit to the complex modulus. Iterations and refinements may be necessary.

It may be shown that the maximum loss factor from E1 is

$$\eta_{max} = \frac{(1 - 1/A) \tan \beta\pi/2}{1 + 1/A + 2A^{1/2} \cos \beta\pi/2} \; ; \; A = G_g/G_e \qquad E4$$

QUALITY CHECK

Some indication of quality of the set of complex modulus data is given by a plot of log loss factor (i.e., tan δ) vs. log modulus magnitude, e.g. F-A1, which is analogous to the Nichols plot used in control system methodology. From F-A1 estimates of G_e,

G_g, and η_{max} are obtained, and β estimated using E4. This is typically an excellent estimate for β.

Other estimates for G_e and β may be obtained by considering the projected rubbery intercept on a Cole-Cole [3] diagram (linear imaginary modulus vs. linear real modulus), e.g. F1. The curve in the rubbery region is given by imaginary and real components of E1 over the range

$$0.01\ (G_e/G_g)^{1/\beta} < r < 100\ (G_e/G_g)^{1/\beta} \qquad \text{E5}$$

Quite often E1 does not fit data in the glassy region; an improved model is [4]

$$G = G_e + \frac{G_g - G_e}{1 + a\ (jr)^{-\alpha_1} + (jr)^{-\beta}} \qquad \text{E6}$$

An estimate for α_1 (not to be confused with a_T) and another estimate for G may be obtained from consideration of the projected glassy intercept in F1. This region is given by E6 with

$$0.01 < r < 100 \qquad \text{E7}$$

TEMPERATURE SHIFT FUNCTION

The presently favored expression for the temperature shift function is

$$\log a_T = a(1/T - 1/T_z) + 2.3(2a/T_z - b)\log T/T_z + (b/T_z - a/T_z^2 - S_{Az})(T - T_z) \qquad \text{E8}$$

which is based on fitting its slope through the three points (see Appendix B)

$$(S_{AT}, T_z)\ ;\ (S_{AR}, T_H)\ ;\ (S_{AG}, T_L) \qquad \text{E9}$$

The log loss factor vs. temperature, e.g. F2, is plotted. T_L is the lowest experimental temperature rounded down to the nearest temperature in degrees Kelvin divisible by 10, T_H is the highest

experimental temperature rounded up, and T_z is selected between T_L and T_H, hopefully at the maximum experimental loss factor, and rounded to the nearest 5°K. If the experimental temperature range covers the transition, T_L, T_z and T_H should represent the glassy, transition, and rubbery regions respectively.

The imaginary component from E1 is

$$G_I = (G_g - G_e)(\sin 90\beta)r^{\beta}/(1 + 2\cos 90\beta r^{\beta} + r^{2\beta}) \qquad E10$$

or approximately

$$G_I = (G_g - G_e)\sin 90\beta r^{\beta} \; ; \quad r < 0.01 \qquad E11$$

from which

$$\log G_I = \log(G_g - G_e)\sin 90\beta + \beta \log r \; ; \quad r < 0.01 \qquad E12$$

It may be seen that E12 is the straight line portion in F-B4.

Solving E11 for r, and making substitutions E2 and E3 yields

$$\frac{a_T(T_i)}{f_{RO}} = \frac{1}{f_i}\left(\frac{G_{Ii}}{(G_g - G_e)\sin 90\beta}\right)^{1/\beta} \qquad E13$$

The initial estimate for the a_T curve in the transition and rubbery regions is that which shifts individual points horizontally to fall on the straight line portion of E12. The results from E13 are plotted in F3 for a set of data. Obviously, a judgement must be made to select a temperature below which points are not considered. Since from E8, a_T is unity at T_z, the reciprocal of f_{RO} is indicated at T_z by the points in F3. Values for S_{AT} and S_{AR} in E8 are selected to fit the remaining points. Initially the apparent activation energy is taken as a constant (see Appendix B) at T_L presumed to be in the glassy region.

COMPLEX MODULUS

At this juncture, the experimental points G_R, G_I and η should be plotted vs. f_R, e.g. F-A3a, and examined. Assuming low scatter data and that the material is thermorheologically simple, the data

points will define low scatter curves in the rubbery region depending on S_{AR}, in the transition region depending on S_{AT}, and in the glassy region depending on S_{AG}. One attractive feature of E8 is that these regions are uncoupled. The a_T is now established for the particular set of data. If the range of experimental frequency is less than 3 decades, the choice of a_T depends on satisfying the analytical representation of complex modulus.

Estimated values for all parameters in the analytical representation of complex modulus, E6, have been obtained except for a_1; a good initial estimate is

$$1.0 < a_1 < 2.5 \qquad \text{E14}$$

Parameter values can now be adjusted on the basis of interactive graphics and operator qualitative judgement or on the basis of some regression analysis with possibly some values held fixed.

Future work will no doubt lead to an equation which will be an improvement to E6.

DISCUSSION

Ultimately, the application, which may be unsophisticated and have limited objectives, pays for the complex modulus data. Therefore the transition may not be well defined, and experimental ranges of temperature and frequency may be limited. This situation often clouds the data analysis and processing. Regardless, existing data may be useful, perhaps only for material screening.

This paper is possibly the beginning of a standard for defining the temperature shift for a set of data when the experimental frequency range is marginal or inadequate. Crucial to this procedure is selection of an appropriate complex-valued analytical representation of complex modulus; and improvements are needed in the form of the equation.

When data fully defines the rubbery, transition, and glassy regions with 3 or more decades of experimental frequency, these procedures will not be needed. Meanwhile, the standard cautions against extrapolating in frequency and temperature must be observed.

REFERENCES

1. R. L. Bagley, "Applications of Generalized Derivatives to Viscoelasticity," AF Materials Lab TR-79-4103, November 1979. (Available from Defense Technical Information Center as ADA 081131.)

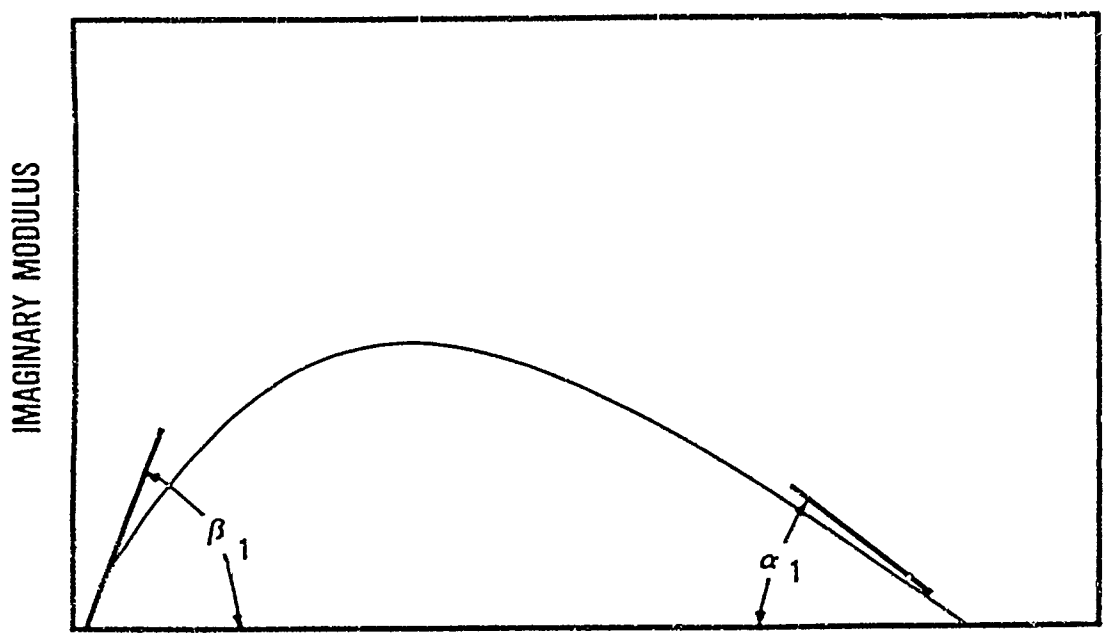
2. L. Rogers, "Operators and Fractional Derivatives for Viscoelastic Constitutive Equations," J. Rheology, 27(4), 351-372 (1983).

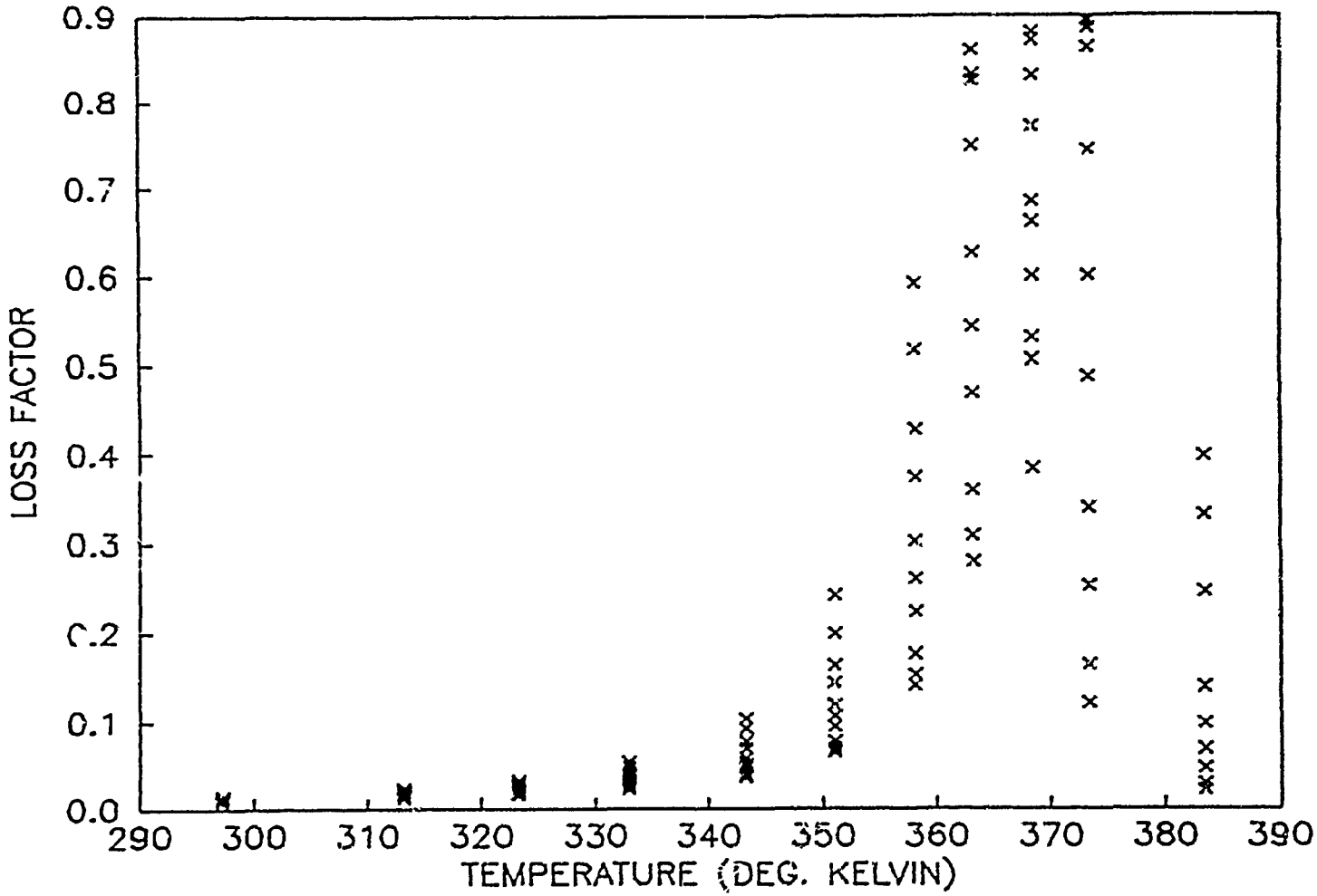
3. K. S. Cole and R. H. Cole, J. Chem. Phys., 9, 341-351 (1941).

4. M. Salvia, "Proprietes Dynamiques des Propergols Solides Composites," These Doc. Ing., L'Universite Claude Bernard Lyon I, France, 1981.

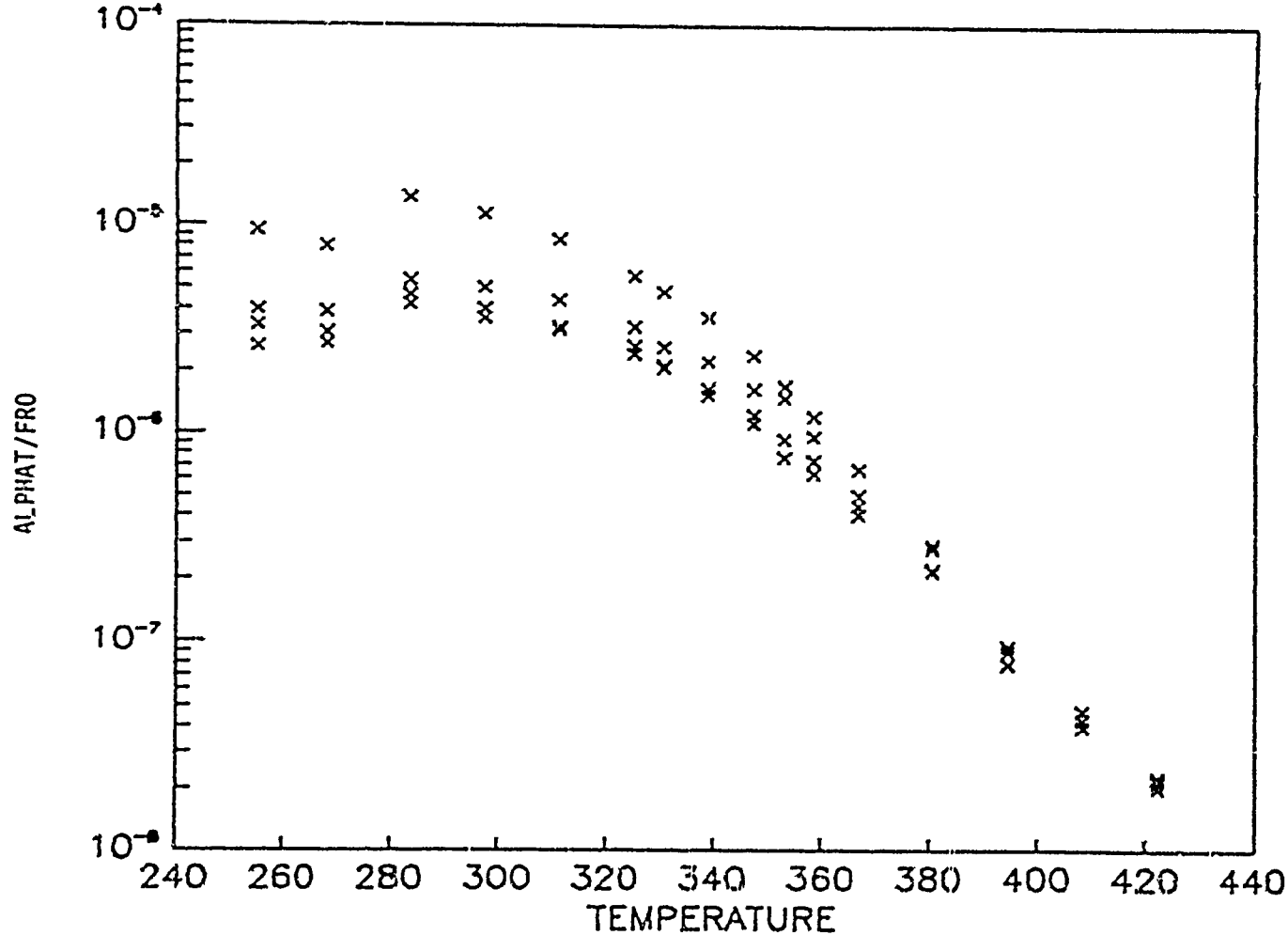
F1

RUBBERY AND GLASSY INTERCEPTS





F2 LOSS FACTOR VS TEMPERATURE



F3 DATA FOR INITIAL ESTIMATE OF ALPHAT

CXSTD REV 860505.1102

GRAPHICAL PRESENTATION OF DAMPING MATERIAL COMPLEX MODULUS

Proposed Standard

ASA/S2 - 73

ISO/TC108/WG13

Dr Lynn Rogers
AFWAL/FIBA
Area B - Building 45 - Room 257
Wright-Patterson AFB OH 45433-6553 USA
(513) 255-3738

1. INTRODUCTION

Damping is one potential approach to reducing vibration levels in a structural system. Damping is the dissipation of vibratory energy by converting it into heat, as distinguished from transporting it to another part of the system. When the damping is due to internal energy dissipation within a material which is part of the structural system, and when the damping is of engineering significance, the material is called a vibration damping material. The energy dissipation is due to the stress-strain hysteresis loop of the vibration damping material. Other possible sources of damping, such as plastic deformations in the joints, relative slip at joints, air pumping in the joints, acoustic radiation of energy, eddy current losses, etc., are not due to the material and are not covered in the present document.

2. SCOPE

The preferred nomenclature (parameters, symbols and definitions) and graphical presentation of the complex modulus of viscoelastic vibration damping materials which are macroscopically homogenous, linear and thermorheologically simple are given; the complex modulus may be Young's modulus, bulk modulus, longitudinal wave propagation modulus, or Lamé modulus. This graphical presentation is convenient and sufficiently accurate for many vibration damping materials.

The primary purpose is to improve communication among the diverse technological fields concerned with vibration damping materials.

3. RELATED DOCUMENTS

ISO/31 7 - 1978 Quantities, Units, Symbols, Conversion Factors and Conversion Tables (ISO TC 12)
ISO 2041 - 1986 Shock and Vibration Vocabulary (ISO TC 108)
ISO 2856 - 1981 Elastomers - General Requirements for Dynamic Testing (ISO TC 45)
ISO/TR 4137 - 1978 Plastics - Determination of Modulus of Elasticity by Alternating Flexure (ISO TC 61)
ISO 472/DAD 8 (1984) Plastics-Vocubulary-Damping Terminology (ISO TC 61)

4. TERMS AND DEFINITIONS

4.1 COMPLEX MODULUS

The operator form of the constitutive equation for the linear, isothermal, isotropic, macroscopically homogenous, thermorheologically simple (defined after E7) viscoelastic material being deformed in shear is [Ref. 1]

$$P(p_R)\tau(t) = Q(p_R)\gamma(t) \qquad (E1)$$

where $r(t)$ is the shear stress, $\gamma(t)$ is the strain, $P(p_R)$ and $Q(p_R)$ are polynomials in p_R, the operator defined as

$$p_R = d/dt_R \tag{E2}$$

where the reduced time is

$$t_R = t/a_T(T) \tag{E3}$$

where t is time and $a_T(T)$ is the temperature shift function dependent on temperature,T[Ref.2]. The fourier transform (f.t.) of E1 leads to the definition of the complex shear modulus valid for steady state sinusoidal stress and strain

$$G(j\omega_R) = r^*(j\omega_R)/\gamma^*(j\omega_R) = Q(j\omega_R)/P(j\omega_R) \tag{E4}$$

where $r^*(j\omega_R)$ denotes the f.t. of $r(t)$ and the reduced radian frequency is

$$\omega_R = \omega a_T(T) = 2\pi f_R = 2\pi f a_T(T) \tag{E5}$$

which is a product of ω, the radian frequency in radians/sec and the dimensionless temperature shift function, while f_R and f are in Hz.

The complex shear modulus

$$G = G(j\omega_R) = G(j\omega a_T(T)) \tag{E6}$$

is dependent on both temperature and frequency

$$G = G(\omega, T) \tag{E7}$$

in a very specific way, i.e.,E6 applies; a material obeying E6 is called thermorheologically simple(TRS). Further, the above equations apply only to linear conditions.

Alternatively, this case may be considered as starting with a viscoelastic material element undergoing a sinusoidal shear strain[Ref. 3]

$$\gamma = \gamma_A \sin\omega t \tag{E8}$$

which lags the sinusoidal shear stress

$$r = r_A \sin(\omega t + \delta_\sigma) \tag{E9}$$

by phase angle δ_σ. The sinusoidal strain and stress may be represented in complex notation as

$$\gamma^* = \gamma_A e^{j\omega t} \tag{E10}$$

$$r^* = r_A e^{j(\omega t + \delta_\sigma)} \tag{E11}$$

and the complex shear modulus,G,equivalently defined

$$G = r^*/\gamma^* = r_A e^{j\delta_\sigma}/\gamma_A = G_M e^{j\delta_\sigma} = G_M \cos\delta_\sigma (1 + j\tan\delta_\sigma) = G_R + jG_I = G_R(1 + j\eta_\sigma) \tag{E12}$$

where

G_M is the magnitude of the shear modulus,

G_R is the real (storage) modulus,

$G_I = G_R\eta_\sigma$ is the imaginary (loss) modulus, and

$\eta_\sigma = \tan\delta_\sigma$ is the material loss factor in shear.

Similar developments apply to the Young's modulus,E, to the bulk modulus, K, to the longitudinal wave propagation modulus,W, and to the Lamé modulus,λ.

A thermorheologically simple material is a material for which the complex modulus is a complex valued function of one independent variable, namely reduced frequency; reduced frequency in turn is a function of frequency and temperature. (In the past the real modulus and the material loss factor sometimes have been treated as independent functions of reduced frequency; while this has facilitated some satisfactory applications, it is a conceptual error.) The complex modulus evaluated at a given temperature and a given frequency represents both the magnitude and the phase relationships between sinusoidal stress and strain.

4.2 DATA CHECK

This document presumes that a set of valid complex modulus data (e.g., T1) has been obtained in accordance with good practice[e.g., Ref.4]. It is recommended that each set of data be routinely and carefully scrutinized. As a minimum, the log η_a vs log G_M, e.g. F1, should be plotted. If the set of data represents a thermorheologically simple material, if a "vertical shift" is not appropriate and if it has no scatter,it will plot as a curve of vanishing width. A temperature value and a frequency value together lead to a reduced frequency value, which corresponds to a unique location along the arc of the curve; however, this is not considered in this plot. The material loss factor and the modulus magnitude are cross-plotted, and the reduced frequency, temperature, and frequency parameters do not occur explicitly. No part of any scatter in this plot can be attributed to an imperfect temperature shift function.

The log loss factor vs log modulus magnitude plot can reveal valuable information regarding scatter of the experimental data. The width of the band of data as well as the departure of individual points from the center of the band are indicative of scatter. Acceptable scatter depends on the application. Nothing is revealed about the accuracy of the temperature and frequency measurements.

4.3 TEMPERATURE SHIFT FUNCTION

The set of complex modulus data itself implicitly defines the temperature shift function, $a_T(T)$, provided the experimental ranges of temperature and frequency are adequate. It is assumed that a single temperature shift function is adequate.

Because the temperature shift function,$a_T(T)$, has historically had a central role, because its slope, $d(log a_T)/dT$, is the crucial feature that causes data to be correctly shifted, and because the apparent activation energy [Ref. 2]

$$\Delta H_A = 2.303RT^2 d(log a_T)/dT \qquad (E13)$$

where the gas constant is

$$R = 0.00828\ newton \cdot km/gram \cdot mole \cdot degK \qquad (E14)$$

is of interest, it is recommended that these three functions be plotted,e.g.,F2a.

4.4 GRAPHICAL PRESENTATION

A set of complex modulus data is presented in F3a using the recommended format. The left vertical logarithmic scale axis is provided for the real and the imaginary modulus components in megaPascal (MPA) units and for the dimensionless loss factor. The horizontal logarithmic scale axis is reduced cyclic frequency, f_R, in Hz. The reduced frequency for the i-th experimental point is given by

$$f_{R_i} = f_i a_T(T_i) \qquad (E15)$$

where f_i is the experimental frequency and T_i is the experimental temperature.

4.4.1 JONES TEMPERATURE LINES

In F3a the right hand side (RHS) vertical logarithmic scale is cyclic frequency in Hz. The nonuniformly spaced diagonal isotherm lines together with the horizontal reduced frequency axis and the RHS vertical frequency axis provide a temperature- frequency-reduced frequency nomogram[Ref. 5]. Taking the logarithm of E5 gives

$$log f_R = log f + log a_T(T) \qquad (E16)$$

which is the equation for a straight line on F3a. Values of temperature in degrees Kelvin divisible by 10 (alternatively, 5, 20 or any other convenient integer) are chosen. The set of isotherm lines implicitly defines the temperature shift function used. The range of the diagonal isotherm lines should be chosen to be the same as the experimental temperature range of data to preclude unintentional and possibly highly erroneous extrapolation. Similarily, the RHS frequency scale should include only the decades of experimental frequency

To follow the illustration included in F3a, enter at a frequency of 200 Hz and proceed horizontally to the intersection with the diagonal line representing 280 degK; the intersection defines a reduced frequency

of 12000 Hz; where this vertical reduced frequency line crosses the curves, a real component of 136. MPA, an imaginary component of 116. MPA, and a loss factor of 0.854 are read on the left scale.

4.5 ANALYTICAL REPRESENTATION

While manual processing and interpretation are adequate for some purposes, computerization offers considerable efficiency. Furthermore, analytical representation of the temperature shift function and of the complex modulus provides increased efficiency for design studies. If available, analytical representations should be given, e.g., F2b and F3b In the event analytical representation is used in design, care must be taken to not extrapolate inadvertently.

4.6 REFERENCES

1. L Rogers, "Operators and Fractional Derivatives for Viscoelastic Constitutive Equations," *J.Rheology*, 27(4), 351-372 (1983).

2. J.D.Ferry, *Viscoelastic Properties of Polymers*, 3rd ed, Wiley,1980.

3. A.D. Nashif, D.I.G. Jones, and J.P.Henderson, *Vibration Damping*, Wiley, 1985.

4. Standard Method for Measuring Vibration-Damping Properties of Materials, American Society for Testing and Materials, ASTM E 756-83,1983.

5. D.I.G.Jones, "A Reduced Temperature Nomogram for Characterization of Damping Material Behavior", *Shock and Vibration Bulletin*, 48(2), pp13-22, 1978.

ISSUES

G^* *vs* G

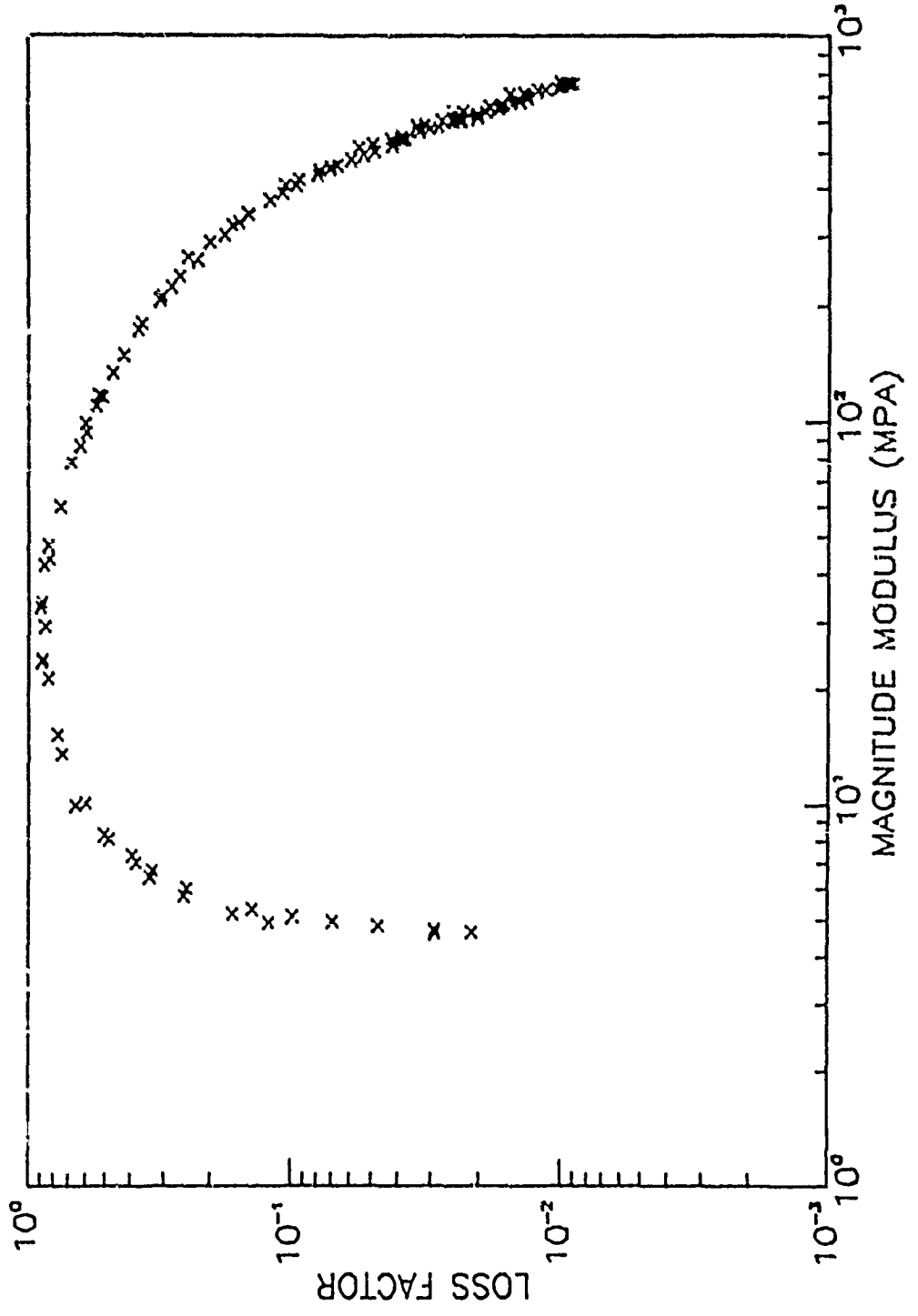
G', G'' *vs* G_R, G_I

i *vs* j

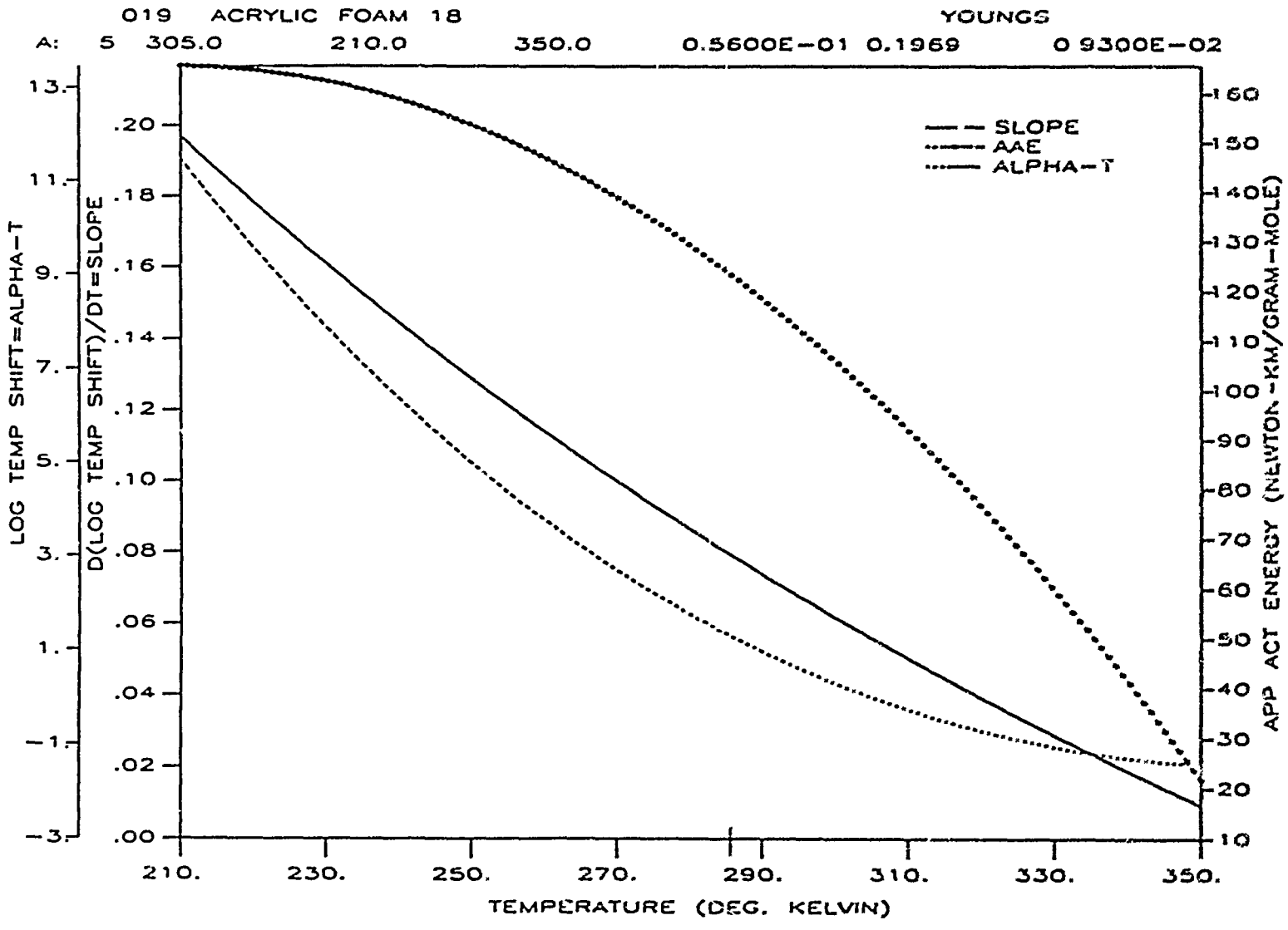
η *vs* d

T1 COMPLEX MODULUS DATA

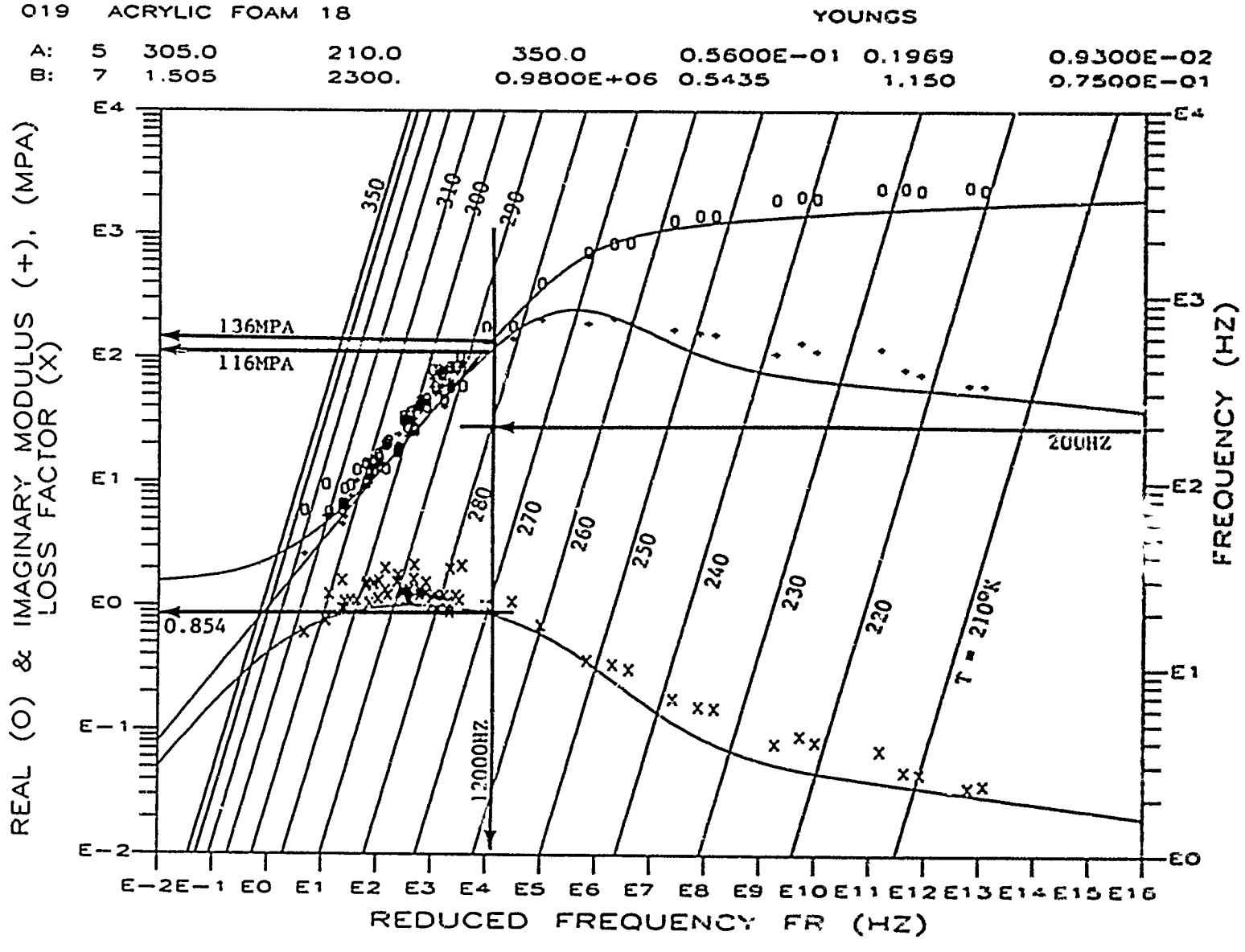
T Deg K	f Hz	G_R MPA	G_I MPA	η	T Deg K	f Hz	G_R MPA	G_I MPA	η
340.4	95.91	4.398	2.002	.4551	261.5	993.7	637.8	147.0	.2305
340.4	267.2	4.264	3.973	.9318	249.3	214.7	976.0	130.8	.1340
340.4	522.9	6.567	4.591	.6991	249.3	617.9	1063.	122.6	.1153
340.4	803.1	9.346	7.705	.8312	249.3	1213.	1068.	119.9	.1123
340.4	1273.	10.44	11.41	1.093	236.5	252.1	1438.	84.27	.0586
340.4	1791	10.76	12.20	1.134	236.5	716.9	1516.	102.9	.0679
325.4	90.65	7.092	4.042	.5700	236.5	1386.	1470.	87.91	.0598
325.4	269.4	6.990	5.832	.8344	224.8	276.0	1772.	92.32	.0521
325.4	525.0	7.254	8.320	1.147	224.8	770.5	1788.	62.58	.0350
325.4	870.8	12.47	10.66	.8546	224.8	1481.	1713.	57.21	.0334
325.4	1291.	15.90	14.56	.9157	218.2	778.5	1830.	47.40	.0259
316.5	90.41	4.924	4.019	.8163	218.2	1487.	1726.	46.95	.0272
316.5	271.0	9.241	7.340	.7943	295.4	5.930	4.915	3.494	.7108
316.5	533.9	14.99	15.05	1.004	295.4	77.74	23.19	22.15	.9551
316.5	873.1	13.04	15.19	1.165	295.4	154.3	31.37	28.74	.9167
316.5	1305.	20.73	17.77	.8571	295.4	260.3	59.28	44.69	.7538
316.5	1830.	19.40	31.12	1.604	295.4	385.0	54.31	45.48	.8374
305.9	97.37	9.077	10.19	1.123	295.4	545.2	62.26	46.94	.7539
305.9	274.0	13.92	18.57	1.334	295.4	5.920	4.458	5.354	1.201
305.9	540.1	20.01	24.79	1.239	295.4	28.08	11.53	13.80	1.197
305.9	903.5	29.88	34.57	1.157	295.4	78.20	25.02	25.17	1.006
305.9	1886.	34.23	30.92	.9033	295.4	155.2	33.34	33.44	1.003
295.4	100.6	25.07	25.32	1.010	295.4	260.4	59.48	51.90	.8725
295.4	289.8	43.67	39.55	.9056	295.4	387.4	56.64	45.63	.8057
295.4	504.7	43.51	65.22	1.499	295.4	546.4	63.13	42.01	.6655
295.4	929.0	44.29	70.24	1.586	293.7	27.88	9.512	14.42	1.516
283.7	110.1	77.00	64.49	.8375	293.7	78.64	26.78	22.59	.8437
283.7	331.8	132.4	99.79	.7537	293.7	155.8	34.61	32.89	.9503
273.2	119.6	134.3	109.2	.8134	293.7	260.2	59.19	41.01	.6929
273.2	398.7	299.5	157.1	.5246	293.7	392.6	61.73	50.52	.8184
261.5	171.5	534.0	145.8	.2730	293.7	546.8	63.42	57.74	.9105
261.5	505.5	630.2	159.9	.2537					



F1 DATA QUALITY CHECK



F2A TEMPERATURE SHIFT FUNCTION AND ITS PROPERTIES



F3A GRAPHICAL PRESENTATION OF DAMPING MATERIAL COMPLEX MODULUS

$$\log a_T = a(1/T - 1/T_R) + 2.303\,(2a/T_R - b)\log T/T_R + (b/T_R - a/T_R^2 - S_{AR})(T - T_R)$$

$$-d(\log a_T)/dT = a(1/T - 1/T_R)^2 + b\,(1/T - 1/T_R) + S_{AR}$$

Slope thru the three points:

$$T_R = A(1) = 300.,\quad S_{AR} = A(4) = 0.002$$

$$T_L = A(2) = 220.,\quad S_{AL} = A(5) = 0.173$$

$$T_H = A(3) = 340.,\quad S_{AH} = A(6) = 0.018$$

$$C_A = (1/T_L - 1/T_R)^2$$

$$C_B = 1/T_L - 1/T_R$$

$$C_C = S_{AL} - S_{AR}$$

$$D_A = (1/T_H - 1/T_R)^2$$

$$D_B = 1/T_H - 1/T_R$$

$$D_C = S_{AH} - S_{AR}$$

$$D_E = D_B\,C_A - C_B\,D_A$$

$$a = (D_B\,C_C - C_B\,D_C)/D_E$$

$$b = (C_A\,D_C - D_A\,C_C)/D_E$$

F2b Analytical Representation of the Temperature Shift Function

$$G = G_e + G_1/[1 + c_1\,(jf_R/f_1)^{-\alpha_1} - (jf_R/f_1)^{-\beta_1}]$$

$$G_e = B(1) = 1.8$$

$$G_1 = B(2) = 2130.$$

$$f_1 = B(3) = 0.22E6$$

$$\beta_1 = B(4) = 0.6$$

$$c_1 = B(5) = 2.2$$

$$\alpha_1 = B(6) = 0.16$$

F3b Analytical Representation of the Complex Modulus

TEMPERATURE SHIFT CONSIDERATIONS FOR DAMPING MATERIALS

Dr. Lynn Rogers
AFWAL/FIBA
Area B - Bldg. 45 - Rm. 257
Wright-Patterson AFB, OH 45433
(513) 255-3738 or -5664

Presented at the 56th Shock and Vibration Symposium
October 1985

For the temperature shift function for a particular damping material to be obtained, it must be implicitly defined by a set of complex modulus data. Historical procedures have been marginal because frequency ranges have not been adequate. A new procedure for such data is proposed based on the slope of the temperature shift function, on a fractional model of complex modulus and on apparent activation energy considerations.

INTRODUCTION

For many viscoelastic damping materials, or at least as a first approximation, the dynamic mechanical properties are thermorheologically simple. In particular, the complex modulus

$$G^* = G^*(f_R) \qquad E1$$

is a function of the reduced frequency

$$f_R = f a_T \qquad E2$$

which is a product of the actual frequency and the well-known temperature shift function. It is often desirable to divide by a reference reduced frequency and use logarithmic scales

$$\log(f_R/f_{RO}) = \log f + \log a_T - \log f_{RO} \qquad E3$$

Expressions for the partial derivatives

$$\partial \log G^*/\partial T = (d \log G^*/d \log f_R)(\partial \log f_R/\partial T) = (d \log G^*/d \log f_R)(d \log a_T/dT) \qquad E4$$

and

$$\partial \log G^*/\partial \log f = (d \log G^*/d \log f_R)(\partial \log f_R/\partial \log f) = d \log G^*/d \log f_R \qquad E5$$

will be needed.

In the typical explanation of frequency-temperature equivalence [1], a temperature shift curve or function is constructed for each particular set of complex modulus data. The real part (R), the imaginary part (I), and the material loss factor (η) of the complex modulus data are plotted as a function of the reduced frequency. For convenience, the expression for the temperature shift function is usually taken to be unity at the reference temperature. With reference to E1 and E3, the effect of a constant in the temperature shift function, a_T, is to shift the experimental data horizontally, whereas the effect of a reference reduced frequency is to shift any analytical representation horizontally. Historically, the a_T for a particular damping material has been defined empirically by the experimental complex modulus data. The value of a_T at each experimental temperature is selected such that it simultaneously shifts horizontally the three complex modulus data points (R,I,η) to define curves and minimize scatter.

With usage of computers it is convenient to fit the empirical a_T curve with a suitable analytical function.

By contrast to the historical focus on a_T, the present focus is on its slope. Consider complex modulus data taken at the three temperatures, T_1, $(T_1 + \Delta_{1a})$, and $(T_1 - \Delta_{1b})$. For both the data taken at $(T_1 + \Delta_{1a})$ to be shifted to that at T_1,

$$\text{shift } (\Delta_{1a}) = \log a_T(T_1) - \log a_T(T_1 + \Delta_{1a})$$

and the data taken at $(T_1 + \Delta_{1b})$ to be shifted

$$\text{shift } (\Delta_{1b}) = \log a_T(T_1 + \Delta_{1b}) - \log a_T(T_1)$$

and from calculus approximations to derivatives, it follows that

$$\frac{\log a_T(T_1 + \Delta_{1a}) - \log a_T(T_1)}{\Delta_{1a}}$$

$$= \frac{\log a_T(T_1) - \log a_T(T_1 - \Delta_{1b})}{\Delta_{1b}}$$

$$= \left.\frac{d \log a_T}{dT}\right|_{T = T_1}$$

The satisfactory horizontal shift of complex modulus curve segments is clearly dependent on the slope or derivative of a_T rather than the value of a_T, and that the slope is also a function of T.

WLF EQUATION

A commonly used representation for the temperature shift function is the WLF equation

$$\log a_T = - C_1 D_T/(C_2 + D_T); \quad T > T_Z - C_2; \quad D_T = T - T_Z \qquad E6a$$

which may be written

$$\log a_T = - S_{AZ} D_T/(1 + D_T/C_2) \qquad E6b$$

where

$$S_{AZ} \equiv C_1/C_2 \qquad E7$$

Taking the derivative of E6b yields

$$- d(\log a_T)/dT = S_{AZ}/(1 + D_T/C_2)^2 \qquad E8$$

The slope given by E8 is normalized and plotted in F1 for representative values of the parameter.

EXPONENTIAL EQUATION

Another expression is the exponential

$$\log a_T = - N \log(1 + D_T/C_e); \quad T > T_Z - C_e \qquad E9$$

which may be written

$$\log a_T = -2.3\, C_e S_{AZ} \log(1 + D_T/C_e) \qquad E10$$

where

$$S_{AZ} \equiv N \log e/C_e \qquad E11$$

The slope corresponding to the exponential is

$$- d(\log a_T)/dT = S_{AZ}/(1 + D_T/C_e) \qquad E12$$

and is plotted in F2.

ARRHENIUS EQUATION

The Arrhenius equation is written in the form

$$\log a_T = a_2 R_T \qquad E13$$

where

$$R_T = 1000/T - 1000/T_Z; \quad T > 0 \qquad E14$$

and using

$$S_{AZ} = 1000\, a_2/T_Z^2 \qquad E15$$

may be written

$$\log a_T = (S_{AZ}T_Z^2/1000)R_T \qquad E16$$

from which

$$-d(\log a_T)/dT = S_{AZ}/(1 + D_T/T_Z)^2 \qquad E17$$

and this is plotted in F1. Alternatively E17 may be written

$$-d(\log a_T)/dT = S_{AZ}T_Z^2/T^2 \qquad E18$$

APPARENT ACTIVATION ENERGY

For some purposes, it is of interest to display the apparent activation energy [2, p. 289, (44)]

$$\Delta H_A = -2.303\, R\, T^2\, d\log a_T/dT \qquad E19$$

where the gas constant is

$$R = 0.00828 \text{ Newton·kilometers/gram·mole·°K}$$

In general, the apparent activation is a function of T. When E18, the slope for the Arrhenius equation, is substituted into E19, we obtain

$$\Delta H_A = 2.303\, R\, S_{AZ}\, T_Z^2 \qquad E20$$

which is independent of temperature, the standard result for the Arrhenius form.

SLOPE QUADRATIC IN 1/T

This paper proposes the representation for the derivative or slope

$$-d(\log a_T)/dT = a(1/T-1/T_Z)^2 + b(1/T-1/T_Z) + S_{AZ} \qquad E21$$

as the most workable for many damping materials.

Integrating the above representation leads to

$$\log a_T = a(1/T-1/T_Z) + 2.303(2a/T_Z - b)\log T/T_Z + (b/T_Z - a/T_Z^2 - S_{AZ})(T-T_Z) \qquad E22$$

where the constant of integration has been chosen for convenience to make a_T unity (or log zero) at the reference temperature. The coefficients may be evaluated by fitting the slope through the three points

Slope	Temp	
S_{AZ}	T_Z	E23a
S_{AL}	T_L	E23b
S_{AH}	T_H	E23c

The form of the equation E21 inherently satisfies E23a. Substituting E23b and c results in

$$a(1/T_L-1/T_Z)^2 + b(1/T_L-1/T_Z) + S_{AZ} = S_{AL} \qquad E24a$$

$$a(1/T_H-1/T_Z)^2 + b(1/T_H-1/T_Z) + S_{AZ} = S_{AH} \qquad E24b$$

Letting

$$C_A = (1/T_L - 1/T_Z)^2 \qquad E25a$$

$$C_B = (1/T_L - 1/T_Z) \qquad E25b$$

$$C_C = S_{AL} - S_{AZ} \qquad E25c$$

$$D_A = (1/T_H - 1/T_Z)^2 \qquad E26a$$

$$D_B = (1/T_H - 1/T_Z) \qquad E26b$$

$$D_C = S_{AH} - S_{AZ} \qquad E26c$$

$$D_E = D_BC_A - C_BD_A \qquad E27$$

it follows that the coefficients are evaluated

$$a = (D_BC_C - C_BD_C)/D_E \qquad E28a$$

$$b = (C_A D_C - D_A C_C)/D_E \qquad E28b$$

If it happens that

$$a = S_{AZ} T_Z^2; \quad b = 2 S_{AZ} T_Z \qquad E29$$

then this representation reduces to the Arrhenius case. This is a major attraction.

The apparent activation energy for this case is found by substituting E21 into E19

$$\Delta H_A = 0.001907 \left[a\left(1 - \frac{T}{T_Z}\right)^2 + bT\left(1 - \frac{T}{T_Z}\right) + S_{AZ}T^2\right] \qquad E30$$

SPECIFIC CURVES [3]

Two specific curves used for vibration damping materials were developed empirically and the convenient exponential equation (E9) was adapted. One curve was developed for use with polymers and is designated "ADN" with the parameters

$$N = 11$$

$$C_e = 175.6064/1.8 = 97.5591 \approx 100.$$

$$S_{AZ} = 0.0489676 \approx 0.05 \qquad E31a$$

The WLF equation approximates this curve when

$$C_1/C_2 = 9/175 = 0.0514 \approx 0.05$$

$$C_2 = 315/1.8 = 175. \qquad E31b$$

The "DIGJ" curve was developed for the larger temperature ranges required by enamels and is given by

$$N = 14$$

$$C_e = 278/1.8 = 154.44 \approx 155.$$

$$S_{AZ} = 0.03937 \approx 0.04$$

$$C_1/C_2 = 12/291.7 = 0.04114 \approx 0.04$$

$$C_2 = 525/1.8 = 291.7 \approx 290. \qquad E32$$

The exponential slope E12 is compared in F3 for the two sets of parameter values given by E31 and E32. It may be seen that the slopes as a function of temperature, T, (rather than of D_T) can be caused to approximate each other more closely by an appropriate choice of T_Z. These two curves are defined by the exponential representation. The curves were determined empirically, and the exponential equation and the parameter values are also empirical. The quadratic in 1/T is an adequate approximation over some range of D_T (probably sufficient for engineering interest) because the curves are themselves approximations as noted above.

DETERMINATION OF THE TEMPERATURE SHIFT FUNCTION

The temperature shift function is implicitly defined by the set of complex modulus data. Historically, the function has been found by shifting data horizontally until curves were defined and scatter minimized; where there is a marginal experimental frequency range, this is not completely satisfactory. It happens that there are theoretical relationships that may be used to determine the slope of a_T from experimental data. The basis of this procedure is the hypothesis that the complex modulus as a function of reduced frequency is adequately approximated in the range of interest by

$$G^* = [G_e + G_g(jr)^\beta]/[1 + (jr)^\beta]; \quad r = f_R/f_{RO} \qquad E33$$

which contains fractional powers [4]. Note that as shown by F4, the slope of the magnitude, real and imaginary, in the transition region is a constant. Because the slope of the imaginary is also constant below the transition, it is more convenient and is used. The imaginary component of E33 is

$$G_I = \sin 90\beta (G_g - G_e) r^\beta / (1 + 2\cos 90\beta\, r^\beta + r^{2\beta})$$

which in the range of interest is proportional to

$$G_I \cong r^\beta; \quad r < 0.01$$

It follows that

$$\log G_I \cong \beta \log f_R;$$

$$d \log G_I / d \log f_R = \beta \qquad E34$$

This result may be substituted into the imaginary part of E4 to give

$$(\partial \log G_I/\partial T) = \beta(d \log a_T/dT) \qquad E35$$

The desired slope is evaluated once the two quantities $\partial \log G_I/\partial T$ and β are determined.

The complex modulus (i.e., the real modulus, the imaginary modulus, and their ratio or loss factor) depends on both temperature and frequency. Temperature is dominant; and the present context is that experimental frequency is marginal (at least to determine a_T). It is necessary to adjust experimental data for the effect of frequency

$$G_I(f_{exp}, T_{exp}) \rightarrow G_{IA}(f_A, T_{exp}) \qquad E36a$$

$$G_R(f_{exp}, T_{exp}) \rightarrow G_{RA}(f_A, T_{exp}) \qquad E36b$$

$$\eta(f_A, T_{exp}) = G_{IA}/G_{RA} \qquad E36c$$

where f_A is a frequency representative of a particular data set, e.g., a geometric average of experimental frequencies. In order to make these adjustments, E34 is substituted into E5

$$\partial \log G_R/\partial \log f = \beta;$$

$$\partial \log G_I/\partial \log f = \beta \qquad E37$$

or approximately

$$\log G_{RA} - \log G_{Rexp} = \beta(\log f_A - \log f_{exp})$$

or

$$G_{RA} = G_{Rexp}(f_A/f_{exp})^{\beta} \qquad E38a$$

and similarly

$$G_{IA} = G_{Iexp}(f_A/f_{exp})^{\beta} \qquad E38b$$

and therefore in the middle of the transition region

$$\eta_A = \eta_{exp}$$

This last equation indicates the validity of fitting a polynomial in temperature

$$\eta = \sum_{k=o}^{N} C_{D_k} T^k \qquad E39$$

and determining η_{max} and T_Z and its temperature. Accurate representation of properties in the transition is of interest because of possible engineering applications in this region; consequently, the temperature of η_{max} is chosen as the reference.

The next step is to determine β. The expression for η_{max} may be developed from E33

$$\eta_{max} = \frac{(1 - 1/A)\tan\beta\pi/2}{1 + 1/A + 2/A^{1/2}\cos\beta\pi/2};$$

$$A = G_g/G_e \qquad E40$$

Numerically this equation may be solved iteratively, and the parameter A may be approximated from experimental data.

With β known the imaginary modulus may be adjusted using E38b and fitted to a polynomial

$$\log G_{IA} = \sum_{k=o}^{N} C_{Ak} T^k \qquad E41$$

and the slope

$$\partial \log G_I/\partial T = d \log G_{IA}/dT = \sum_{k=1}^{N-1} k\, C_{Ak} T^{k-1};$$

$$T \geq T_Z \qquad E42$$

evaluated s a function of T or at specific points such as T_Z and at a higher temperature, T_H.

It follows that

$$S_{AZ} = (d \log G_{IA}/dT\Big|_{T = T_Z})/\beta \qquad E43$$

and

$$S_{AH} = (d \log G_{IA}/dT\Big|_{T = T_H})/6 \quad E44$$

At this juncture, two points (T_Z, S_{AZ}) and (T_H, S_{AH}) have been defined, and a third relationship is required. It is supplied by hypothesizing that at T_L, a temperature in the glassy region, the apparent activation energy, is a constant, or the derivative

$$d\Delta H_A/dT \propto 2a(T/T_Z - 1)/T_Z + b(1 - 2T/T_Z) + 2TS_{AZ} \quad E45$$

is set equal to zero at T_L

$$a(2T_L/T_Z^2 - 2/T_Z) + b(1 - 2T_L/T_Z) + 2T_L S_{AZ} = 0 \quad E46$$

This may be used as one of two equations

$$C_A = 2(T_L/T_Z - 1)/T_Z \quad E47a$$

$$C_B = 1 - 2T_L/T_Z \quad E47b$$

$$C_C = -2T_L S_{AZ} \quad E47c$$

in lieu of E25. F5 characterizes a temperature shift function obtained by this procedure.

NON-MONOTONIC SLOPE

It is possible to choose values for the WLF parameters S_{AZ}, C_2, and T_Z in E8 to give specified values of slope at three temperatures only if the slope is monotonic as in F1. The same conclusion applies to the exponential parameters in E12 and F2. Some materials possess temperature shift curves with a slope which has an upright "U" shape or an inverted "U" shape. These functions cannot be represented by conventional expressions, but can be easily described by the quadratic in 1/T.

DISCUSSION

Very limited usage with experimental complex modulus data together with engineering judgment suggests that the quadratic in 1/T as determined by the slopes is accurate and efficient. The greatest advantage is that the various temperature regions of data may be considered independently or in uncoupled fashion. That is, the parameter determining slope in only the glassy region, or the transition, or the rubbery, may be determined while not affecting the others.

Another very obvious advantage is representation of a much more general type of slope curve than has been possible in the past. Only experience with viscoelastic materials of interest will determine general adequacy.

It is worthy of note that the reference temperature has no physical significance here; it should be considered to be an empirical parameter which happens to have units of temperature.

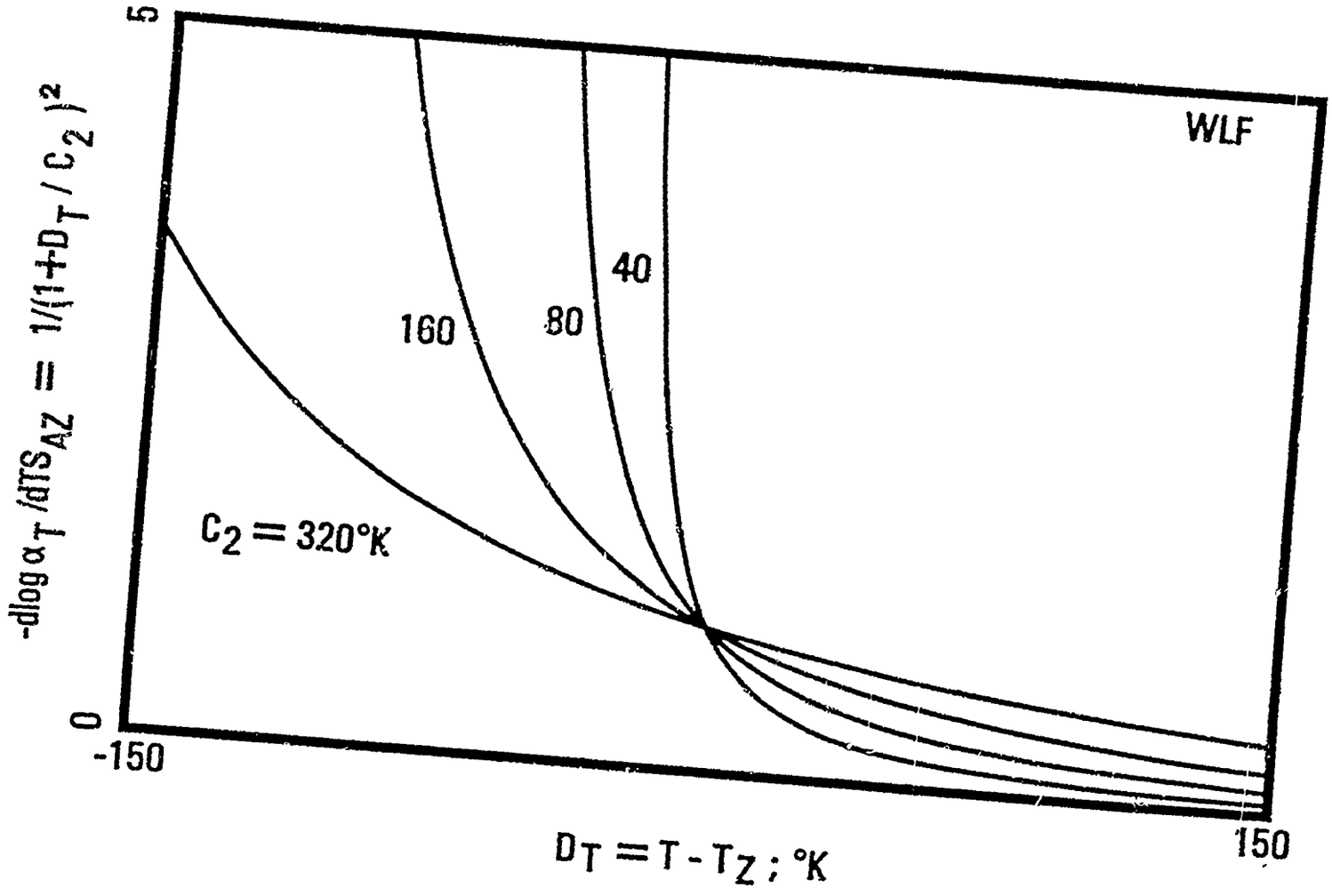
REFERENCES

1. Jones, D. I. G., "Temperature-Frequency Dependence of Dynamic Properties of Damping Materials," Journal of Sound and Vibration, Vol. 22, n. 4, 1974, pp 451-470.

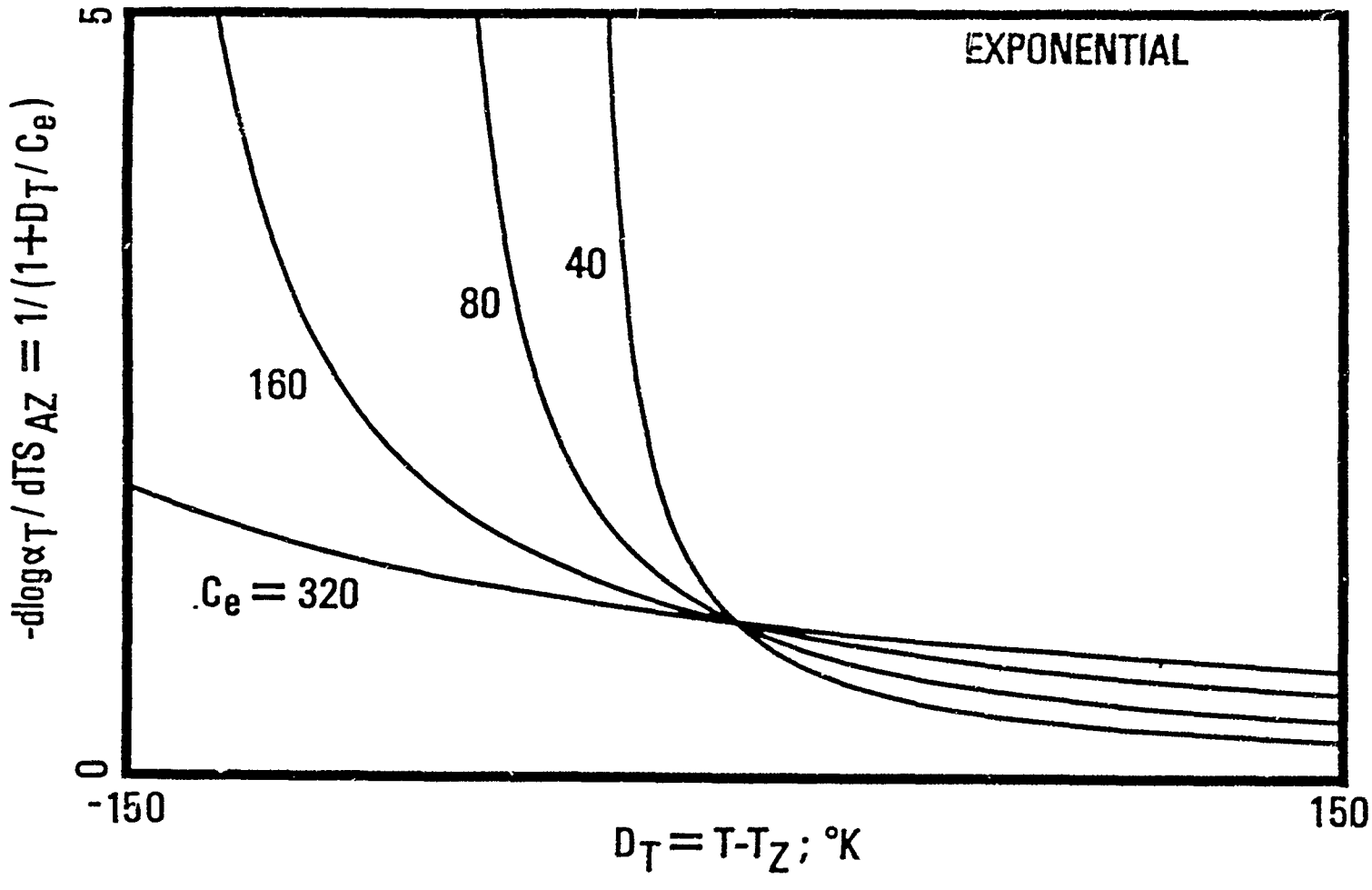
2. Ferry, John D., Viscoelastic Properties of Polymers, John Wiley and Sons, 3rd ed., 1980.

3. Rogers, Lynn and Ahid D. Nashif, "Computerized Processing and Empirical Representation of Viscoelastic Material Property Data and Preliminary Constrained Layer Damping Treatment Design," The Shock and Vibration Bulletin, No. 48, September 1978, Part 2, pp 23-37.

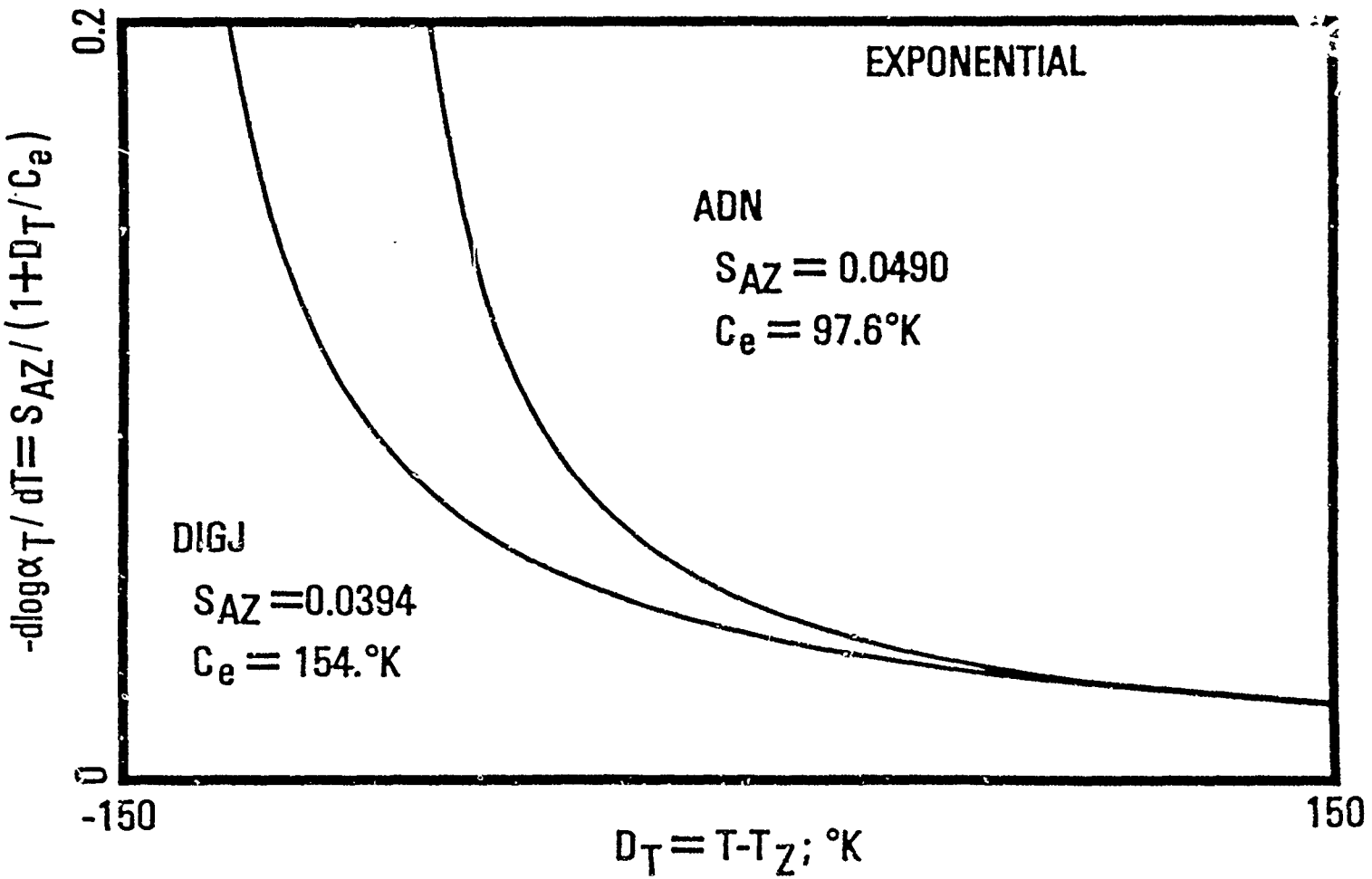
4. Rogers, Lynn, "Operators and Fractional Derivatives for Viscoelastic Constitutive Equations," J. Rheology, 27(4), pp 351-372 (1983).



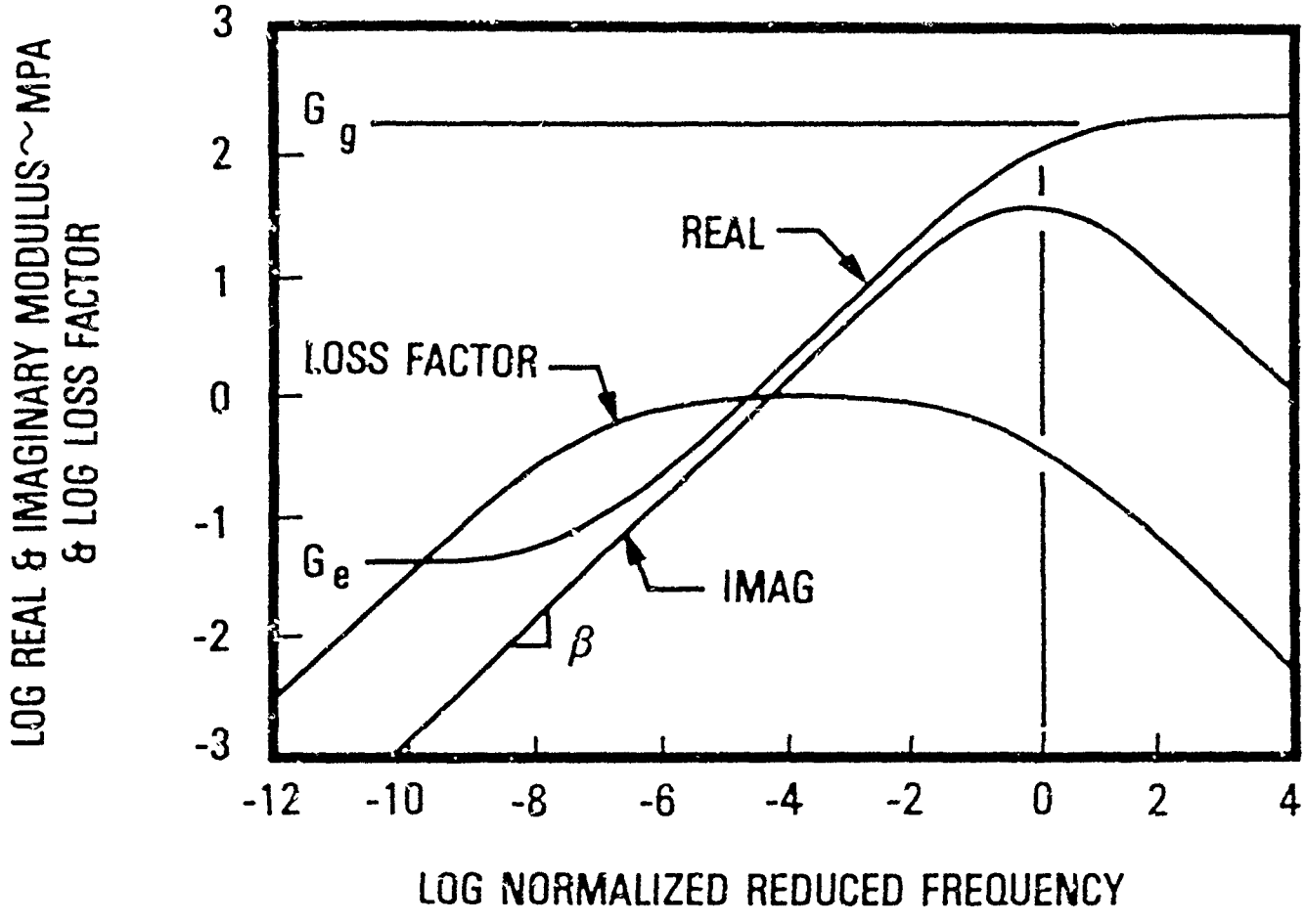
F1 WLF NORMALIZED SLOPE VS TEMPERATURE DIFFERENCE



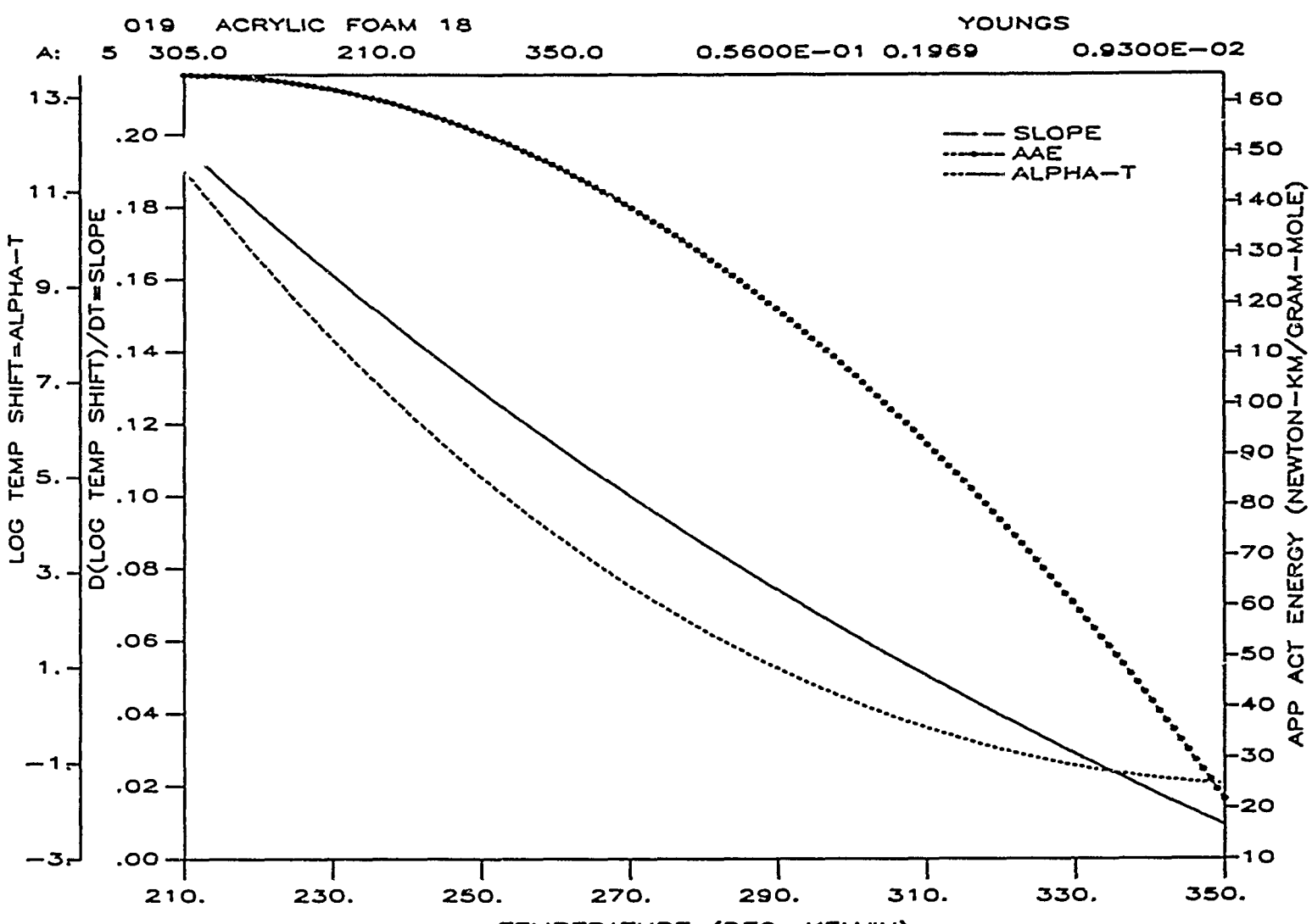
F2 EXPONENTIAL NORMALIZED SLOPE VS TEMPERATURE DIFFERENCE



F3 EXPONENTIAL SLOPE VS D_T FOR TWO SPECIFIC CURVES



F4 COMPLEX MODULUS



F5 TEMPERATURE SHIFT FUNCTION AND ITS PROPERTIES

COMPARISON OF DAMPING MATERIAL PROPERTIES BY VARIOUS TEST METHODS

Matthew F. Kluesener, P.E.
University of Dayton
Research Institute
Dayton, Ohio

ABSTRACT

Two viscoelastic damping materials, G.E. SMRD 100F90A and 3M ISD-112, were evaluated using five different test methods or instruments. The methods/instruments were the Resonant Beam Test, The DuPont Dynamic Mechanical Analyzer (DMA), the Imass Autovibron, the Rheometrics Mechanical Spectrometer (RMS), and the Stress Relaxation Test. All results are compared to curves fit to the beam test data and are presented on the reduced temperature nomogram. The beam test yielded results from the glassy region into the rubbery region. The DMA gave results significantly different from the other methods and does not give any data in the rubbery region. The Autovibron and RMS require two samples to define the entire modulus range and the results agreed with the other methods in various regions. The Stress Relaxation Test defined data only in the rubbery region and the high temperature end of the transition region and agreed well with the other methods.

INTRODUCTION

Two viscoelastic damping materials, General Electric's SMRD 100F90A and 3M's ISD-112, were evaluated by five test methods and/or instruments. The methods/instruments were the Resonant Beam Test (Beam Test), the DuPont Dynamic Mechanical Analyzer (DMA), the Imass Autovibron, the Rheometrics Mechanical Spectrometer (RMS), and the Stress Relaxation Test. At room temperature, SMRD 100F90A is a moderately stiff, epoxy-like material and ISD-112 is a very soft, self-adhesive material, thus providing a large range of properties being determined.

In order to show the differences in material properties determined by the various methods, all data are compared to curves which are based largely on the beam test data, with results from other test methods being used to help define the rubbery region. All data are presented in metric units on the reduced temperature nomogram using the Jones[1] α_T relationship. The reference temperature T_0 = 79°C, for SMRD 100F90A was selected by considering the Autovibron and Beam test results; for ISD-112, T_0 = 75°C, was selected by considering the RMS and Beam Test results.

The DMA and Autovibron determine the complex Young's modulus. These results were converted to shear modulus by assuming the Poisson's ratio to be 0.5 which gives the relationship G = E/3.

The following paragraphs give a brief description of each test method, discuss the error sources and limitations of each, and present the results of the tests on SMRD 100F90A and ISD-112.

RESONANT BEAM TEST

The resonant beam test technique forms the basis of ASTM standard E756-83 for determining the vibration damping properties of materials. In the resonant beam test, the viscoelastic material is applied to either the outside surface(s) of the beam (Oberst configurations) or in between matched beam pairs (symmetric sandwich configuration). The symmetric sandwich configuration was used for the materials evaluated herein, and is shown in Figure 1 along with the dimensions of the specimens. As its name suggests, data is taken only at the natural modes of vibration of the built-up structure. The test data is reduced using fourth order beam theory.[2]

The beam test, using the symmetric sandwich configuration is applicable for materials with a Young's modulus of less than $1x10^8$ Pa and can be conducted over the temperature range from -73 to 232°C.

Sources of error in the measured complex modulus can result from poor specimen preparation, poorly matched beam pairs, and extraneous damping sources such as damping in the fixture. For the beam test, as with all the methods considered herein, errors in temperature measurement and control are also sources of error. One of the largest sources of error, albiet usually only near the rubbery region comes from an instability in the data reduction equations which leads to magnification of the measurement errors. The error magnification factors have been determined for the free layer beam test[3] but not for the symmetric sandwich beam test.

The main limitation of the Beam test is in the definition of the rubbery modulus plateau. With the symmetric sandwich beam test it is usually possible to define the high temperature end of the transition region and the beginning of the rubbery plateau. Sometimes only a limited amount of data in the transition region is obtainable, because the damped beam specimens are so highly damped that the resonances are hard to excite, and only one or two modes may be measurable instead of the usual 4 or 5 modes.

BEAM TEST

The results of the Beam Tests on SMRD 100F90A and ISD-112 are shown in Figures 2 and 3 respectively. Almost the entire modulus range was defined for both materials using a single pair of specimen beams. There is considerable scatter in the loss factor data for SMRD 100F90A. The curves which are fit to the Beam Test data points are used in the nomograms from the other test methods that follow, in order to show difference in the measured properties.

DUPONT DYNAMIC MECHANICAL ANALYZER

The mechanical portion of the DMA consists of two parallel balanced sample support arms which are free to oscillate around flexure pivots. The arms are connected to the sample forming a compound resonance system, the resonant frequency of which is dependent almost entirely (because of the low natural frequency of the arm-pivot system) on the configuration and modulus of the sample. In oscillation, the sample is deformed via the geometry shown in Figure 4.

The DMA is applicable to materials with a Young's modulus between 1.8E7 to 2E11 Pa and testing can be conducted from -120 to 450°C. The frequency range is generally 2 to 30 Hz and the samples are usually rectangular.

Error sources in the DMA include thermal lag (caused by too thick of a sample or sweeping temperature at faster than 2°C per minute), improper alignment of the sample and buckling of the sample. The manufacturer of the DMA states that the precision of the modulus measurement is 5% in the frequency range 5 to 30 Hz.

A major limitation of the DMA is that for the two materials tested, and presumably for many other damping materials, the end of the transition region and the beginning of the rubbery plateau is not defined because the material becomes too soft. This results in only a few data points above the temperature of peak damping. The limiting modulus value seems quite clear, because the tests on SMRD 100F90A and ISD-112 both stopped at a shear modulus of approximately 6E6 Pa.

Another limitation of the DMA test is that is is conducted over a very limited frequency range (2 to 30 Hz), and at each temperature measurement point, data at only one frequency is obtained. Therefore the DMA data appears to be free of scatter; however, the absence of data scatter should not be assumed to indicate accurate material data.

The results for the two materials are shown in Figures 5 and 6 for SMRD 100F90A and ISD-112, respectively. For both materials the rubbery region was not defined. For SMRD 100F90A, the glassy modulus agrees with the Beam Test but the transition region is at a higher temperature. For ISD-112, the modulus curve is significantly different from the Beam Test curve and the peak damping is lower. ISD-112 is believed to be too soft to test on the DMA.

IMASS AUTOVIBRON DYNAMIC VISCOELASTOMETER

The Imass Autovibron is an automated Toyo Baldwin DDV-II-C Rheovibron. A sinusoidal tensile strain applied at one end of the test sample in the longitudinal direction generates a sinusoidal stress at the other end. There is a phase difference between the two signals of δ. From these measurements the modulus and loss factor are determined. The sample, which is a thin flat strip, is held at each end by spring loaded clips on slender rods which are attached to the driver and transducers. This arrangement is shown in Figure 7.

The Autovibron is applicable to materials with a Young's modulus of 1E5 to 1E13 Pa and the temperature range is -40°C to 200°C. The instrument operates at the fixed frequencies of 3.5, 11, 35 and 110 Hz.

Misalignment and poor condition of the grips can cause errors in the loss factor measurement. Also, the error in measuring the phase angle has a larger effect at low values of loss factor than at high values. Lastly, if the material sample becomes too stiff relative to the compliance of the instrument, errors in the glassy modulus can occur.

The limitations of the Autovibron include the limited frequency range of operation and the fact that two sample sizes or geometries are necessary to define the entire modulus range. For instance, very soft materials cannot be tested using a tensile specimen, because it can stretch significantly under the applied load; they must be tested using shear grips. Shear grips were not available at the time these tests were run.

The Autovibron results for SMRD 100F90A and ISD-112 are shown in Figures 8 and 9, respectively. For SMRD 100F90A the rubbery data and the peak loss factor agree well with the Beam Test, but the transition region is shifted to a higher temperature. The glassy modulus is low because the sample became too stiff. The sample length or cross sectional area needed to be changed to determine the glassy modulus more accurately.

Only partial results were obtained for ISD-112 because the sample stretched more than 10% percent of its original length. Shear grips would have yield additional data, but were not available. The glassy modulus determined was nearly the same as that for the Beam Test.

RHEOMETRIC MECHANICAL SPECTROMETER (RMS)

The RMS subjects the sample to torsional forced vibration. The form of the sample can be either a rectangular bar or a thin flat circular disk, the former being used for rigid materials and the latter being used for softer materials which are mounted between serrated parallel plates. The sample geometries are shown in Figure 10. At each temperature,

measurements are taken at four frequencies, 0.0159, 0.159, 1.59 and 15.9 Hz (corresponding to 0.1, 1.0, 10.0 and 100.0 radians per second). Since the tests are performed in torsion, the results are shear modulus, shear loss modulus and loss factor.

The RMS can test materials with a Young's modulus between 1.7E6 to 6.9E9 Pa over a temperature range of -150 to 300°C. This was the only instrument to cover 3 decades of frequency.

Errors can come from several sources. When using a thin disk sample on the serrated parallel plates, slippage can occur when the material becomes stiff at low temperatures resulting in scatter in the loss factor data. Also at low temperatures, the relative compliance between the instrument and the sample can cause errors in the modulus. With the rectangular bar sample, if the material becomes too soft there can be considerable scatter in the data. The main limitation of the RMS is that two samples, the rectangular bar and thin disk, are probably necessary to determine the entire modulus range from glassy to rubbery for most viscoelastic materials.

The SMRD 100F90A data from the RMS is shown in Figure 11. The Beam Test curve is not shown because a different T_0 was required to properly shift the RMS data. The glassy modulus is the same as the Beam Test, but the transition region occurs at a lower temperature. The data scatter above the temperature of peak damping occurred as the material became too soft for the rectangular bar sample. Changing to the thin disk sample would have been necessary to obtain data into the rubbery region.

The ISD-112 data, shown in Figure 12, agreed well with the Beam Test data in the transition region. The scatter in the data toward the glassy region is probably due to slippage of the sample on the serrated parallel plates. A rectangular bar sample would have been necessary to define the rest of the transition region and the glassy region.

STRESS RELAXATION

In a stress relaxation test, the sample is rapidly taken from an undeformed state to a deformed state. An MTS test machine, with servo hydraulic controls, was used to accomplish this. As the sample is maintained in the fixed strain position, the force decays with time. Since data is taken over a time span of approximately 0.25 to 100 seconds, and since the frequency is taken as the reciprocal of time, this corresponds to low frequencies, 4.0 to 0.01 Hz. Therefore, the method is most suitable for determining modulus data in the rubbery and low transition region. From the plot of force (or stress) versus time, the storage modulus is obtained as described in Ferry.[4]

The temperature range over which this method can be used is limited by the particular equipment available, but -73 to 150°C is a reasonable range.

Sources of error in the Stress Relaxation Test include the load cell and the extensometer, both accurate to ±1% of full scale. Another source of error may be the transformation process itself, but this is not discussed by Ferry.[4]

The materials were tested in a double lap shear fixture, shown in Figure 13, to determine their shear modulus. For the SMRD 100F90A and ISD-112, the stress relaxation tests were conducted at -4°C, 24°C, and 52°C. The imposed shear strain for SMRD 100F90A ranged from 0.2 to 2.0 percent, and for ISD-112, the imposed shear strain was 5.6 percent at all temperatures.

The modulus data points are shown on the reduced temperature nomograms in Figures 14 and 15 for SMRD 100F90A and ISD-112, respectively. In both cases the data lay on the rubbery plateau although some data from ISD-112 was also in the transition region. These data were in fact used to define the rubbery plateaus of the Beam Test curves shown in these and all previous nomograms.

CONCLUSION

As was seen from the foregoing discussion, the measurement of accurate damping material properties is not a trivial matter, and there can be a large variation in results. However, it should be remembered that the modulus of a typical viscoelastic material can vary by almost a factor of 10,000 from the rubbery to glassy state, so the difficulty of measuring these properties accurately should not surprise us.

Although individual test methods may have errors in certain regions such as the glassy, rubbery or transition region because of inherent limitations or improper sample geometry, the author feels that the large differences between methods may be the nomogram presentation of the material properties. The nomograms presented in this paper used the Jones[1] α_T shift factor relationship. It should be noted that the test methods considered in this paper determined material properties from approximately .01 Hz (for the RMS) to greater than 5000 Hz (for the BEAM). Representing results from such a broad frequency range using the Jones α_T relationship may be stretching the range of applicability of this relationship since it was developed from data in the 100 to 5000 Hz range. Techniques are being developed which generate a shift factor for each material which may make the properties from various tests compare more favorably.[5] An investigation using these new techniques was not included in the scope of the program under which this work was conducted.

If one is given different properties for the same material from different test methods, how does one know which properties are correct? One way to determine which properties are correct is to do a comparison between experimentally measured modal characteristics (natural frequency and damping) of a simple damped system and analytically determined modal characteristics using a mathematical model of the damped system with the measured material properties as input.

Naturally, the most accurate properties should yield the smallest error between measured and predicted results. Interested parties are referred to a companion paper[6] in these proceedings which shows the Beam test to have the lowest root mean squared error.

ACKNOWLEDGMENTS

This work was performed by the University of Dayton Research Institute as a subcontractor to General Electric Space System Division, which was prime contractor on the Relsat program (Reliability for Satellite Equipment in Environmental Vibration), Air Force Contract F33615-82-C-3223.

REFERENCES

1. King C., "Computerized Processing and Graphic Representation of Viscoelastic Material Property Data," AFML-TR-79-4099, Wright-Patterson AFB, 1979. Available from Defense Technical Information Center as ADA079914.

2. ASTM E756-83, Standard Method for Measuring Vibration-Damping Properties of Materials.

3. Pritz, T., Analysis of Errors in Investigating the Complex Modulus of Viscoelastic Materials by the Coated Beam Method, Journal of Sound and Vibration, 1978, 60(3), 319-334.

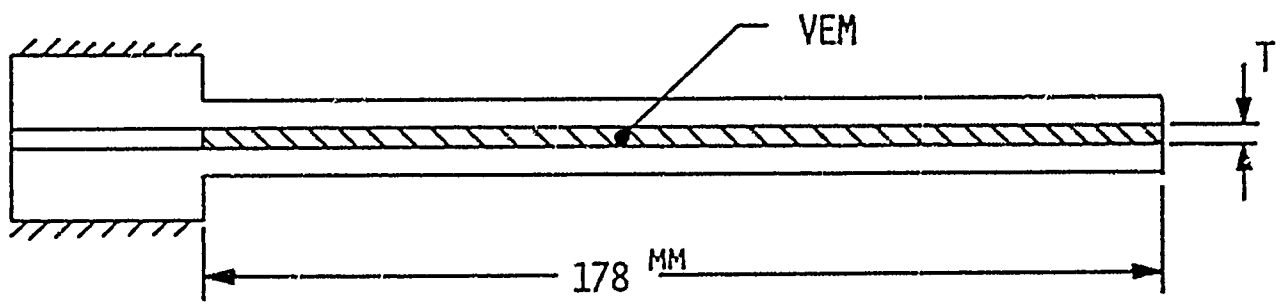
4. Ferry, John D., Viscoelastic Properties of Polymers, 3rd Edition, John Wiley & Sons, Inc., New York, New York, 1980.

5. Rogers, L., private communications.

6. Drake, M. L., and Kluesener, M. F., "Damping Predictions Using Material Properties from Various Test Methods," presented at the Vibration Damping Workshop II, March, 1986, and published in proceedings.

RESONANT BEAM TESTS

SYMMETRIC SANDWICH CONFIGURATION



$T_{SMRD\ 100F90A} = 1.0$ MM

$T_{ISD-112} = .13$ MM

Figure 1 Symmetric Sandwich Test Beam for SMRD 100F90A and ISD-112

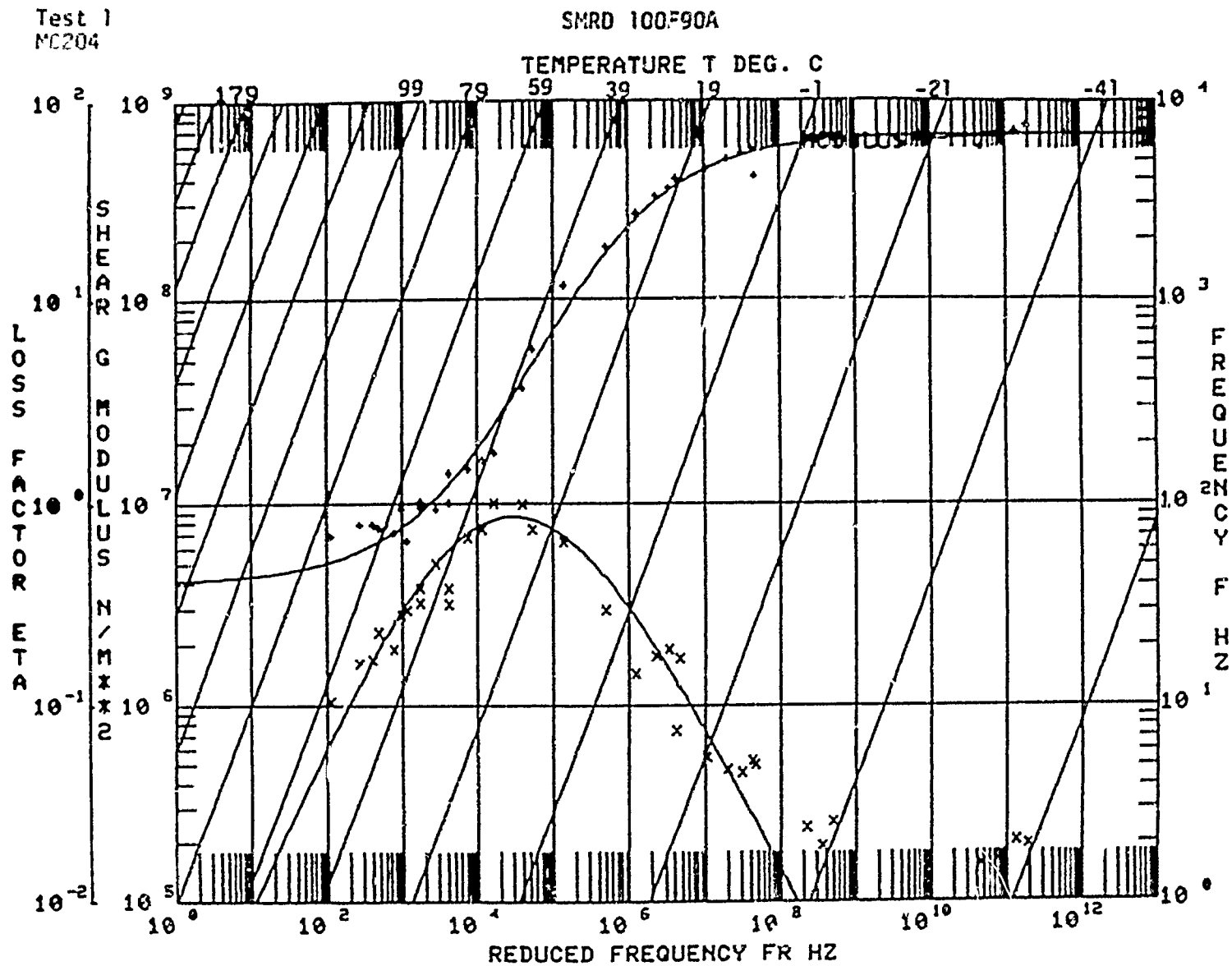


Figure 2 SMRD 100F90A Shear Test Data and Curve

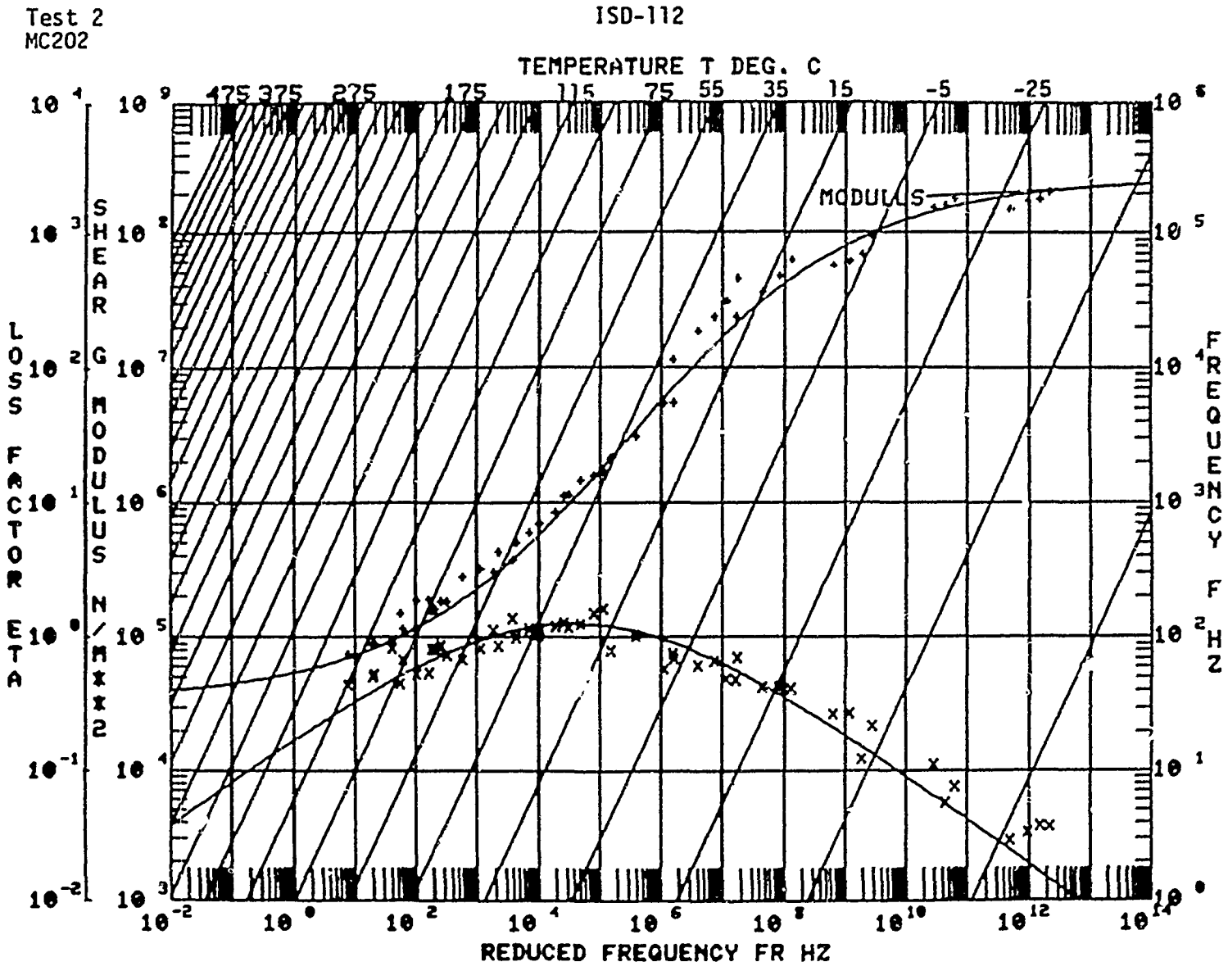


Figure 3 ISD-112 Beam Test Data and Curve.

DYNAMIC MECHANICAL ANALYZER (DMA)

FORCED FLEXURAL VIBRATION

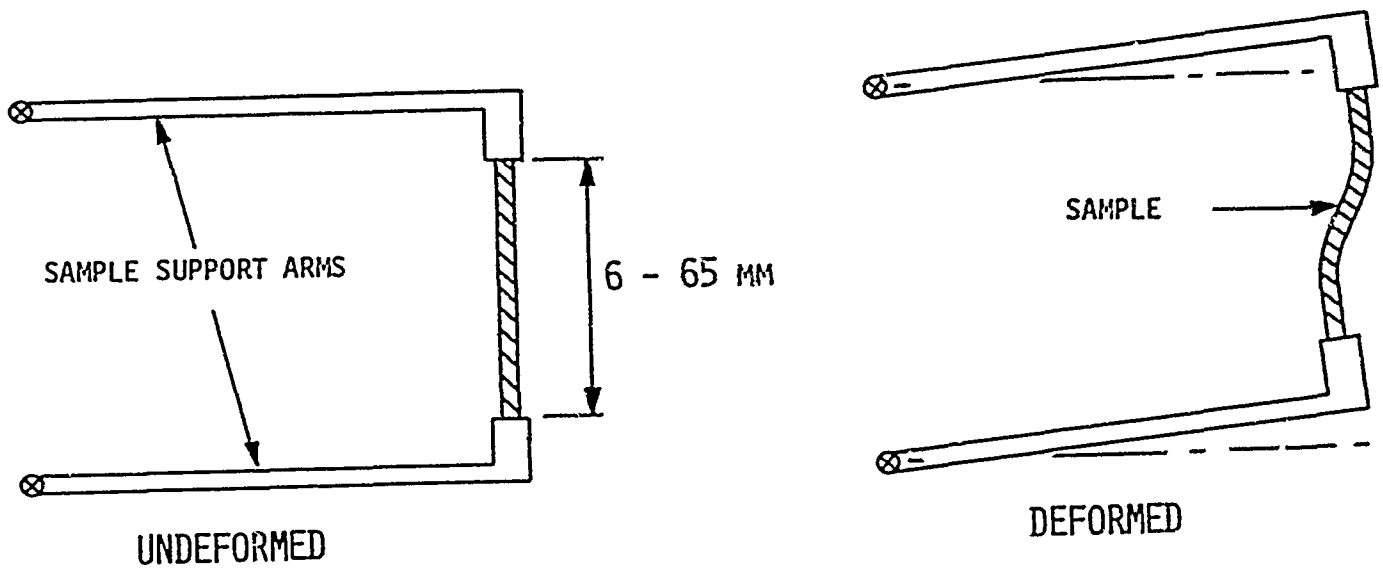


Figure 4 Dynamic Mechanical Analyzer Sample Geometry and Deformation

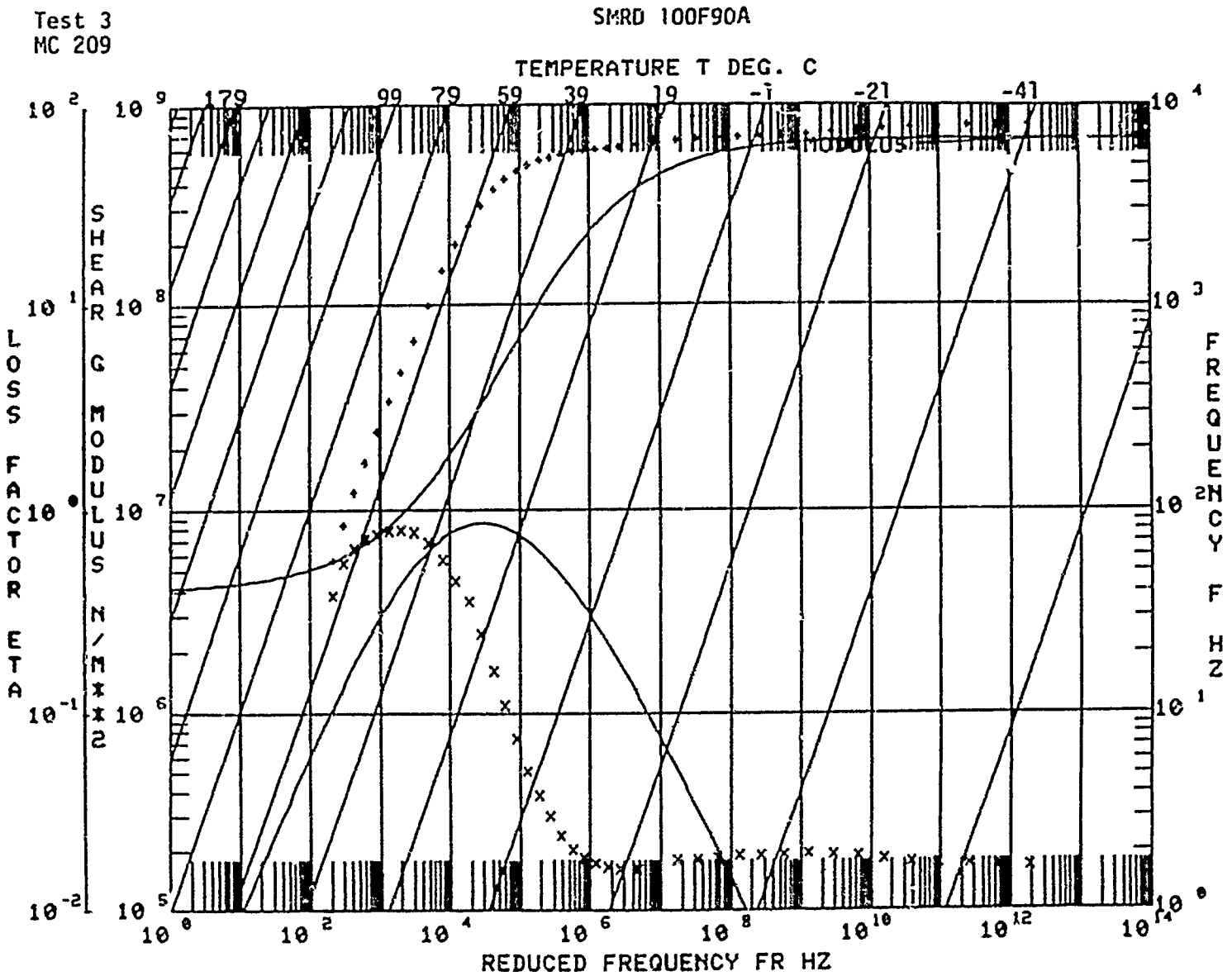


Figure 5 SMRD 100F90A DMA Data with Beam Test Curve.

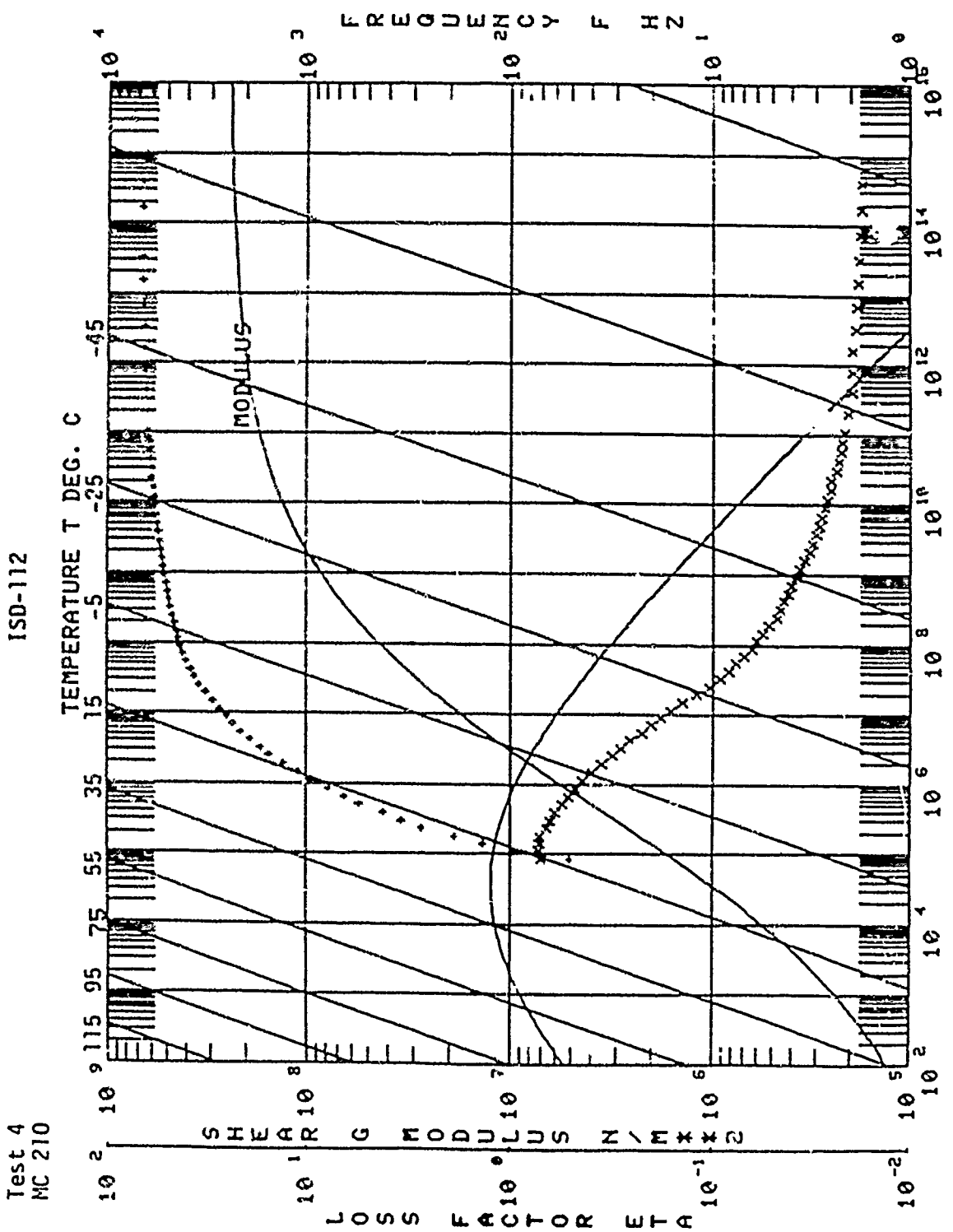


Figure 6 ISD-112 DMA Data with Beam Test Curve.

AUTOVIBRON
(RHEOVIBRON)
TENSILE SPECIMENS USED

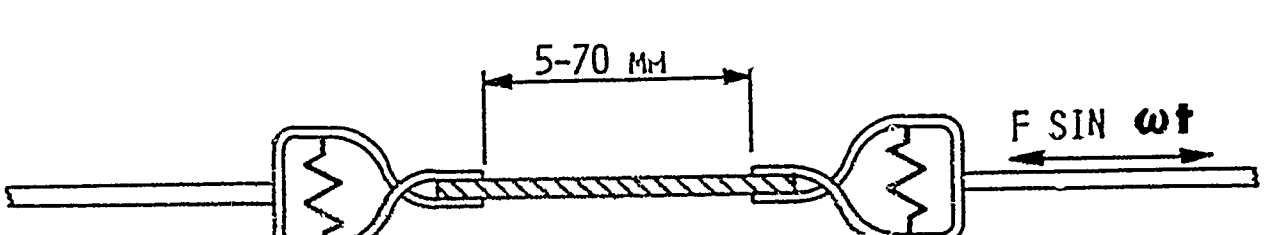


Figure 7 Autovibron Tensile Specimen Geometry

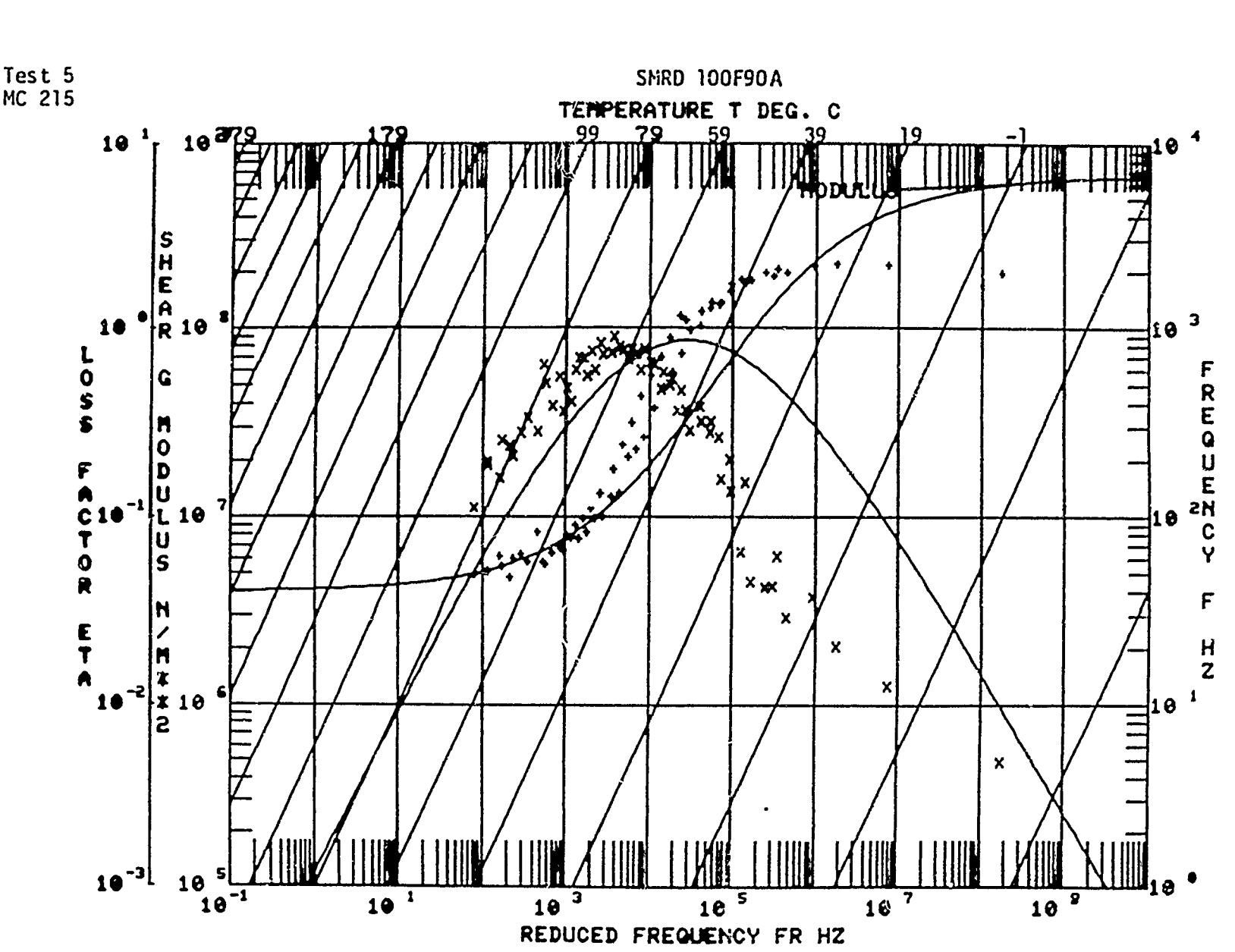


Figure 8 SMRD 100F90A Autovibron Data with Beam Test Curve.

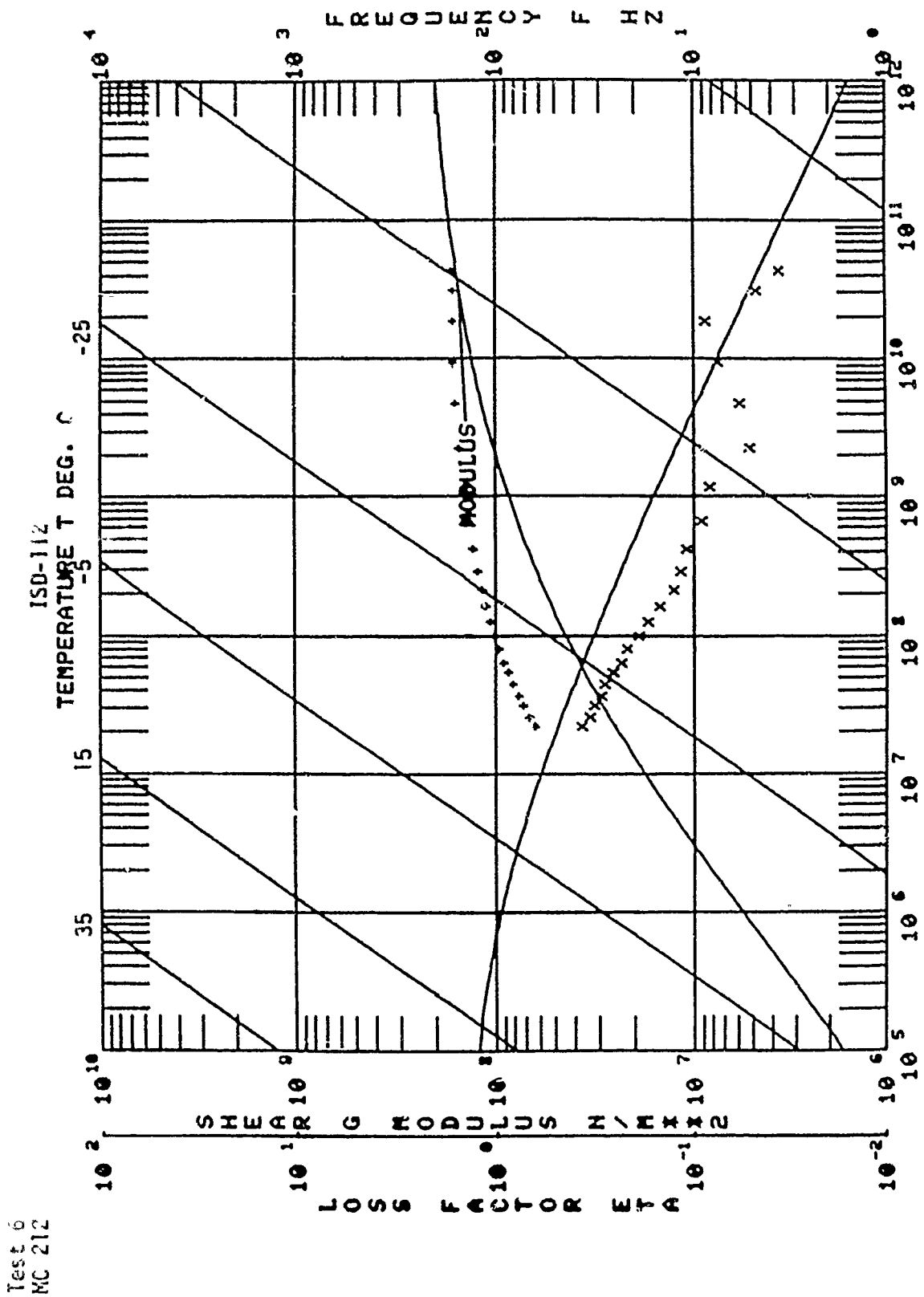
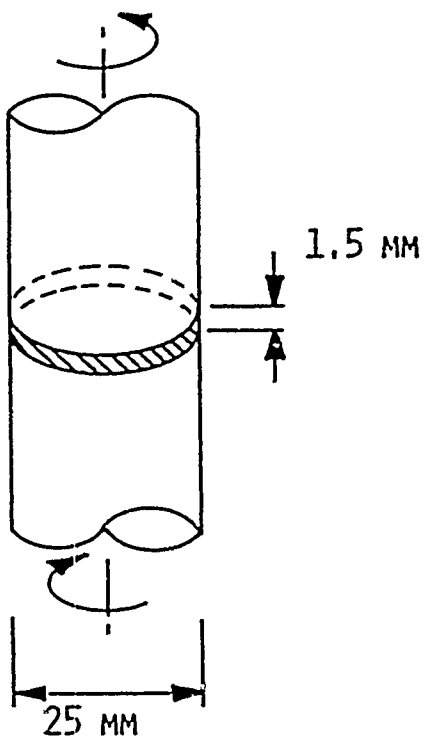


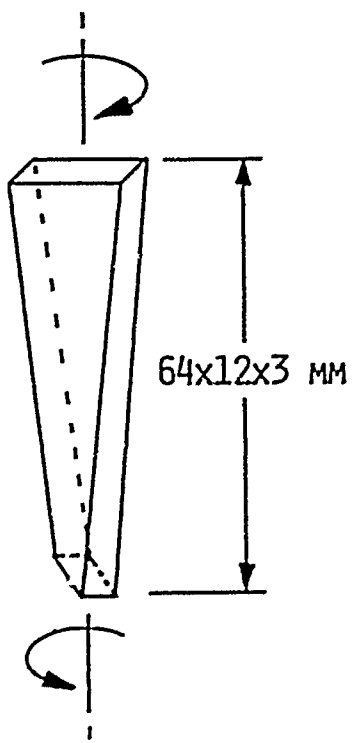
Figure 9 ISD-112 Autovibron Data with Beam Test Curve.

RHEOMETRICS MECHANICAL SPECTROMETER (RMS)

FORCED TORSIONAL VIBRATION



ISD-112



SMRD 100F90A

Figure 10 Rheometrics Mechanical Spectrometer Sample Geometries

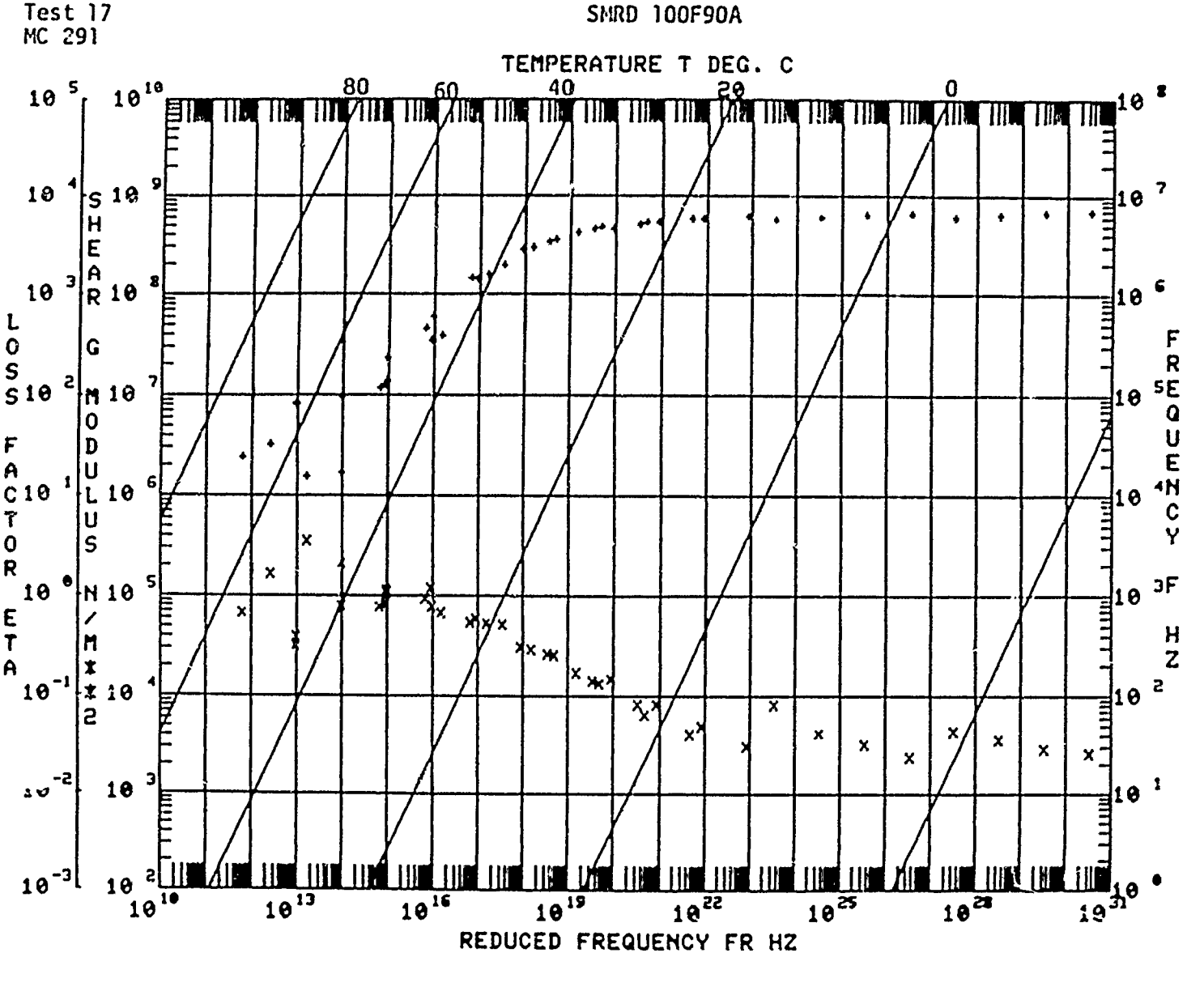


Figure 11 SMRD 100F90A Rheometrics Mechanical Spectrometer Data with T_0 = 180°C

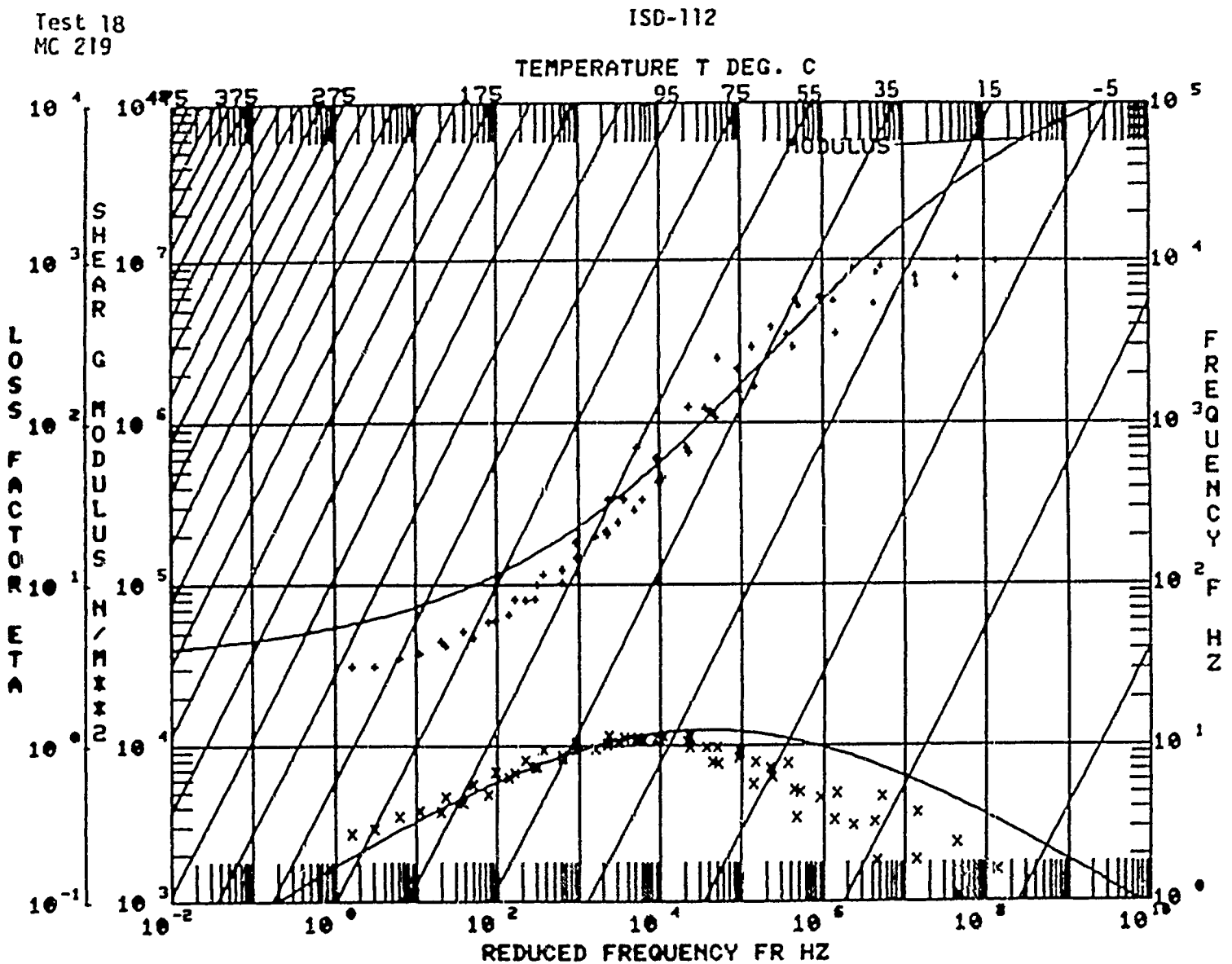
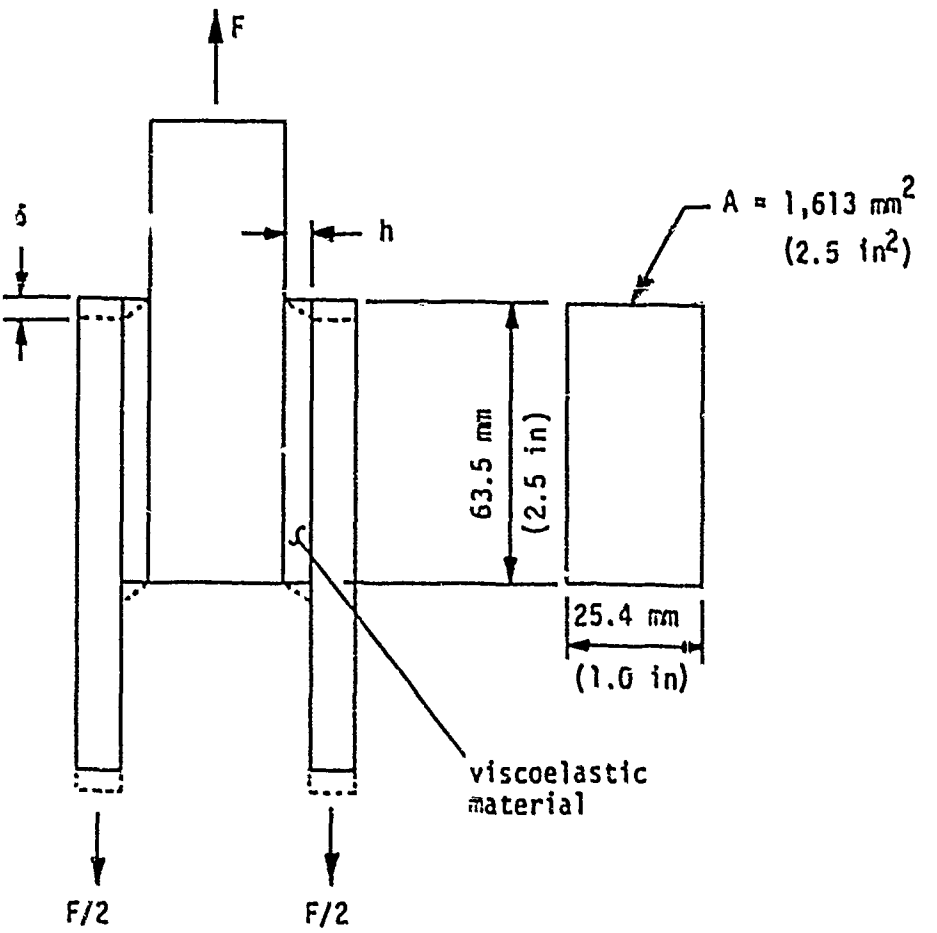


Figure 12 ISD-112 Rheometrics Mechanical Spectrometer Data with Beam Test Curve.



δ = displacement

h = material thickness

F = force

A = area

h = 6.22 mm (.245 in.) for SMRD 100F90A

h = 4.50 mm (.177 in.) for ISD-112

Figure 13 Stress Relaxation Test Fixture

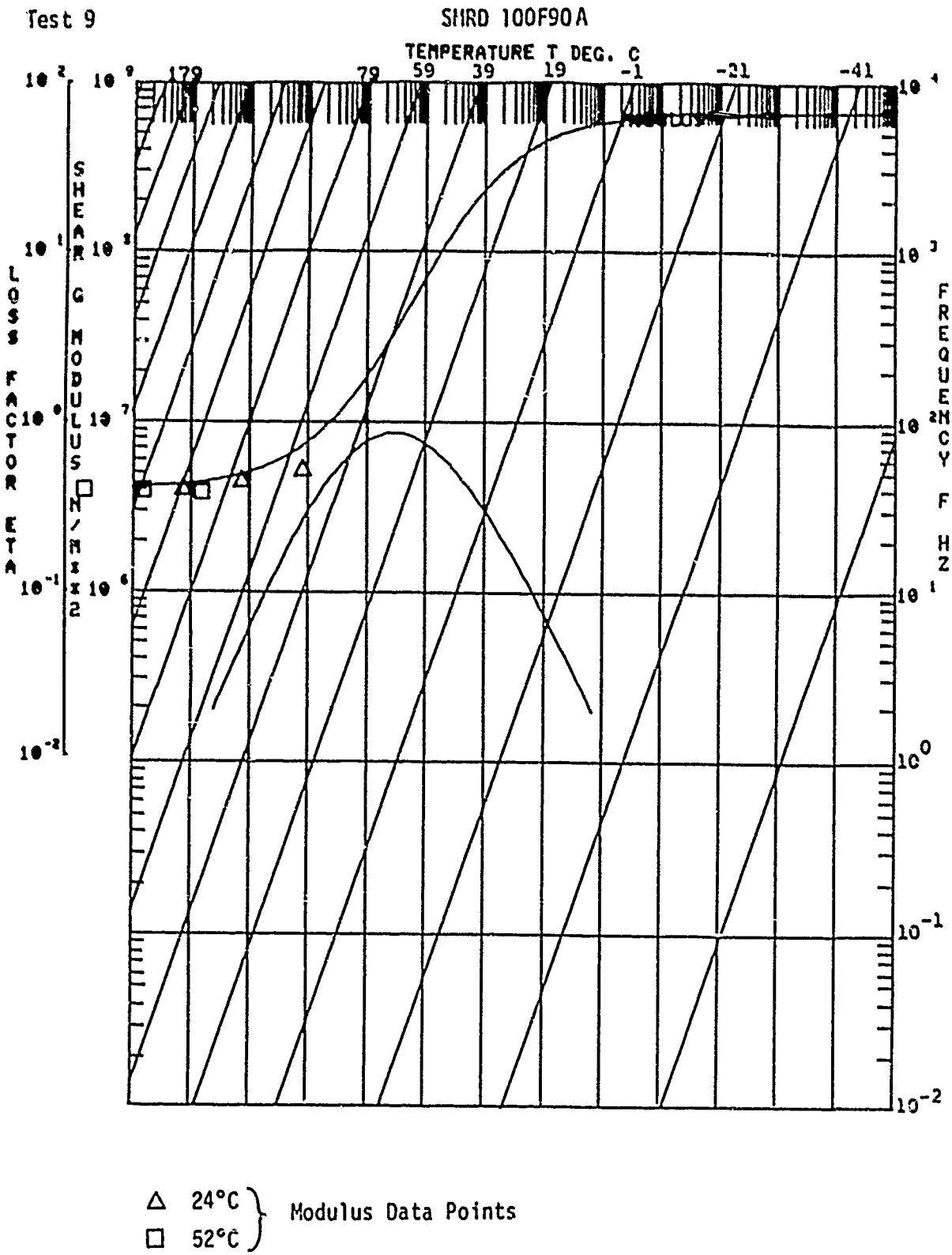


Figure 14 SMRD 100F90A Stress Relaxation Data with Beam Test Curve.

Test 10 ISD-112

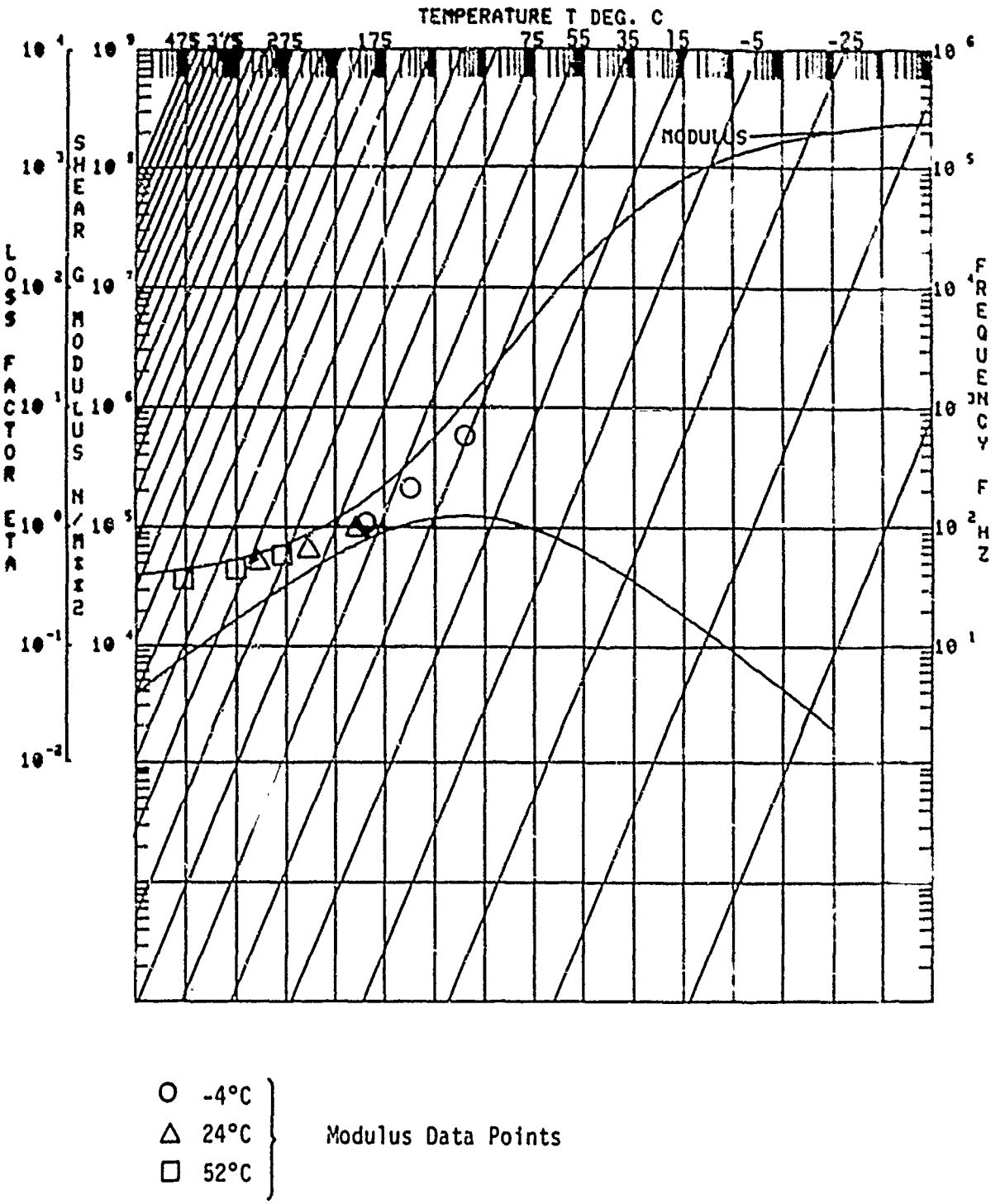


Figure 15 ISD-112 Stress Relaxation Data with Beam Test Curve.

VISCOELASTIC CHARACTERISTICS

OF AN

ELASTOMERIC ISOLATOR

R. SCHER FERSHT
S. N. FERSHT
M. DENICE, JR.
LITTON GUIDANCE &
CONTROL SYSTEMS

ABSTRACT

An experimental investigation was conducted to identify the transmissibility characteristics, in terms of the storage and loss functions of an elastomeric type isolator, over a broad range of temperatures. The prime concern here is the definition of the complex transmissibility function away from the resonant frequencies where they interact with instrument rotational vibration modes. Contrary to what is commonly known, indications are that transmissibility characteristics are amplitude dependent in small motions, thus refuting the assumption of elastomers being a linear viscoelastic material. Furthermore, vibration time length clearly has an impact on the impedance function of the elastomeric isolators.

PROBLEM DESCRIPTION

Mechanical gyros were used for many years as the main angle rate measurement inertial device. In the last two decades, new angle and angle rate devices were developed using non-mechanical phenomena. The best known instrument is the Ring Laser Gyro, or in short RLG, where two counter rotating, gas discharge glow beams of light are generated in a closed loop rotating resonance cavity.

As the cavity rotates, the light beam travelling in the rotation direction has a longer distance to travel than that in the opposite direction; this rotational effect is known as the Sagnac Effect. The small frequency difference that develops between the two counter rotating beams can be detected and scaled upon beam interference, thus measuring the instant rotation of the cavity by beat count. The Sagnac effect is general relativistic and leads to a scale factor which is not dependent on the refractive properties of the medium in which the light beams are propagating.[1,2]

In reality, as the rotation of the cavity decreases beyond a certain level, a lockin phenomena sets in which diminishes the beat pattern. To overcome this deficiency, RLGs are often rotationally dithered about their input axis. Efficient dithering is secured by mounting the gyro on a flexure which is alternately stressed in bending at the natural frequency of the combined system. Since the rotational flexure has low material damping, forced dithering at resonance consumes minimal power. A ring laser gyro cluster, consisting of three gyros mounted on a single instrument block with input axes mutually perpendicular, is a typical strapdown triad configuration measuring 3 dimensional rigid body rotation. The instrument block in most practical designs is supported on elastomeric isolators. This system, upon dithering, sets the instrument block in motion which in turn causes a time phase shift in its rotation about different axes, thus resulting in block coning at the dither frequency. Instrument coning is an error source which often cannot be compensated for.

The elastomeric isolators, needed for controlling adverse environmental effects such as shock and vibration, are the prime contributor to the phase shifting causing the coning error. It became therefore essential to study the behavior of the isolators at the dither frequencies, 300 to 450 Hz. The ultimate objective here is to minimize dither instrument error by proper modelling of the isolators and by conducting an extensive, dynamic system analysis. The definition of viscoelastic characteristics of the isolators is the subject matter of the present investigation, focusing specifically on the frequency band of 200 to 600 Hz.

INTRODUCTION

The sensor assembly of an inertial measurement unit is typically suspended in its chassis by a set of elastomeric isolators. Isolators are used on the sensor assembly to: 1) protect the instruments (gyros and accelerometers) from damage due to handling and operational shock and vibration; and

2) attenuate shock and vibration environments to levels acceptable to meet instrument performance requirements. Elastomeric isolators, in particular, are used so as to provide necessary damping in addition to compliance in a relatively small, lightweight, and inexpensive package. The disadvantage is that their dynamic behavior is sensitive to temperature, strain, and frequency. New programs generate new requirements creating the need for new isolator designs. Since many performance criteria must be met throughout the temperature range (typically -65° to 160°F) and for all the many dynamic environments of the program spec, there is a need to predict the behavior of an elastomer for the entire environmental envelope. The use of simple viscous theory, as is presently commonplace, has severe shortcomings. It does not predict isolator performance with sufficient accuracy. Selecting a proper isolator becomes a series of design, build, and test iterations. This wasteful method has created a need to better understand the behavior of an elastomeric isolator and to better model and predict its performance.

TEST SETUP

Test data was obtained for two elastomeric isolators, identical except for the type of elastomer. A sketch and cutaway view of the isolator is shown in Figure '. Both elastomers are silicon based and have approximately the same room temperature stiffness but, because of additional ingredients, they exhibit different dynamic behavior. Each isolator, with a suspended test mass, was vibrated by means of an electromagnetic shaker. The input was a 1g sine wave, sweeping from 30 to 1000 Hz at 3 octaves/min. The absolute transmissibility and phase were recorded by means of piezoelectric accelerometers located on the shaker head and on the suspended test mass. A temperature chamber surrounding the test setup maintained isolator temperatures between -55°F and 160°F, which is the typical operating range for our application of isolators. A schematic of the test setup is shown in Figure 2.

TEST RESULTS

Transmissibility and phase test results are plotted in Figures 3 through 6 and 7 through 10 for elastomers type A and B, respectively. Results are shown for two temperatures, 75°F and -55°F. Superimposed with test results are theoretical results for both a 1 DOF viscous damped model and a viscoelastic damped model.

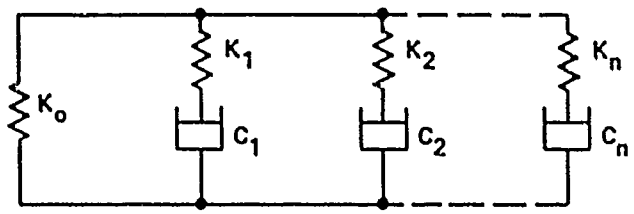
The test results are also presented as the storage modulus (G') and loss modulus (G") plotted as a function of the reduced frequency. These are shown in Figures 11 and 12 for the two elastomer types. The storage and loss moduli were calculated from the transmissibility and phase test data for temperatures between -55°F and 160°F and excitation frequencies of 30 to 1000 Hz.

MODELLING

Attempts to theoretically predict the dynamic behavior of elastomeric isolators in the past have been made with a simple viscous model consisting of

a spring and damper in parallel. This model has proven to be totally inadequate.

In an effort to improve our prediction capability, the isolator was modelled as a viscoelastic system. The general short time[3] (measured in milliseconds) viscoelastic model often used for elastomeric materials consists of a main spring, K_o, and an infinite number of elastically coupled dampers in parallel with K_o.



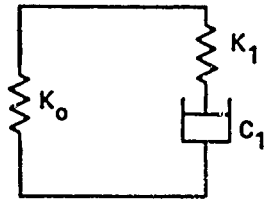
GENERAL VISCOELASTIC MODEL

The equation of motion is the form

$$G(i\omega) = G'(\omega)+iG''(\omega) = K_o + \sum_{r=1}^{n} \frac{i\omega C_r}{\left(1+i\omega \frac{C_r}{K_r}\right)} \qquad (1)$$

where $G'(\omega)$ is the total storage function and $G''(\omega)$ is the total loss function.

As a first step a simplified version of the general viscoelastic model was examined. This consisted of a single elastically coupled damper:



The equation of motion thus becomes

$$G(i\omega) = K_o + \frac{i\omega C_1}{\left(1+i\omega \frac{C_1}{K_1}\right)} \qquad (2)$$

In Figures 3 through 10, transmissibility and phase test data are compared to theoretical results of both the viscous damped and viscoelastic damped models. The natural frequency, ω_n, used in the theoretical models, was determined by the peak in the transmissibility test curve. The damping ratio, η, was chosen so the theoretical results approximately matched the transmissibility at resonance of test data. For the viscoelastic model, the stiffness ratio of the damper coupling spring to the main spring is 1 as this provided the best match of phase with the test data.

Correlation of the results of the viscoelastic model with phase test data is very good, and greatly improved over that of the simple viscous model for frequencies above the resonance, particularly in the frequency range of interest, 200 to 600 Hz. Correlation of the viscoelastic model with transmissibility test data is also improved although not as dramatically as with the phase data. What is important to note here is that the slope of the transmissibility curve at frequencies above resonance for the viscoelastic model closely matches the test data, whereas that of the viscous model is drastically different.

Thermal dependance of the storage and loss moduli are presented in Figures 11 and 12, showing a high level of scattering. Indications are, based on a limited amount of data, that elastomeric materials are not necessarily rehologically simple in a regular sense.

CONCLUSIONS

Viscoelastic modelling of elastomeric isolators appears to be the proper direction to take. The important conclusion from the work done so far is that even with the simplest viscoelastic model, correlation with test data is greatly improved over the viscous damped model. The next step will be to expand the simple viscoelastic model to include additional elastically coupled dashpot elements, the object being to create a model that will sufficiently predict the dynamic behavior of an elastomeric isolator.

There are also indications that the elastomeric medium exhibits nonlinear behavior, with strong frequency dependency. Though in the present experiments nonlinear response parameters were quantitized, it was not the objective of the present study to carefully evaluate this nonlinear phenomena. This subject will be addressed in a future study.

REFERENCES

1. Coccoli, J. D., Feldman, J., and Helfant, S., Ring Laser Gyros, in IEEE Transactions on Aerospace and Electronic Systems, Vol. AES-20, No. 4, July 1984.

2. Chow, W. W., et. al., The Ring Laser Gyro, in Reviews of Modern Physics, Vol. 57, No. 1, January 1985.

3. Williams, M. L., Structural Analysis of Viscoelastic Materials, in AIAA Journal, Vol. 2, No. 5, May 1964.

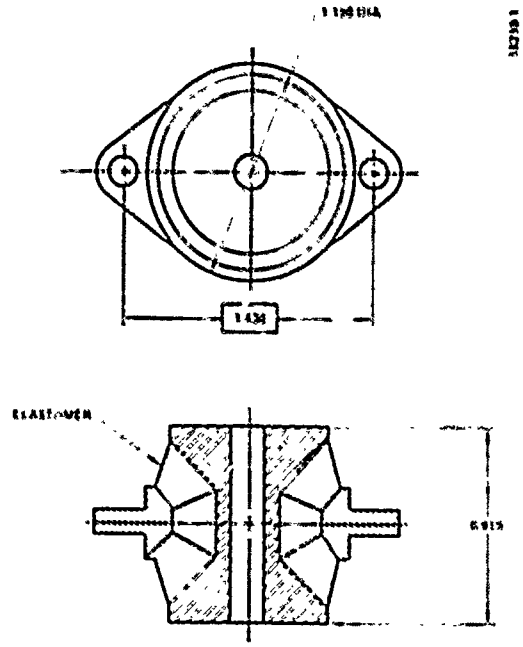


Figure 1. Elastomeric Isolator

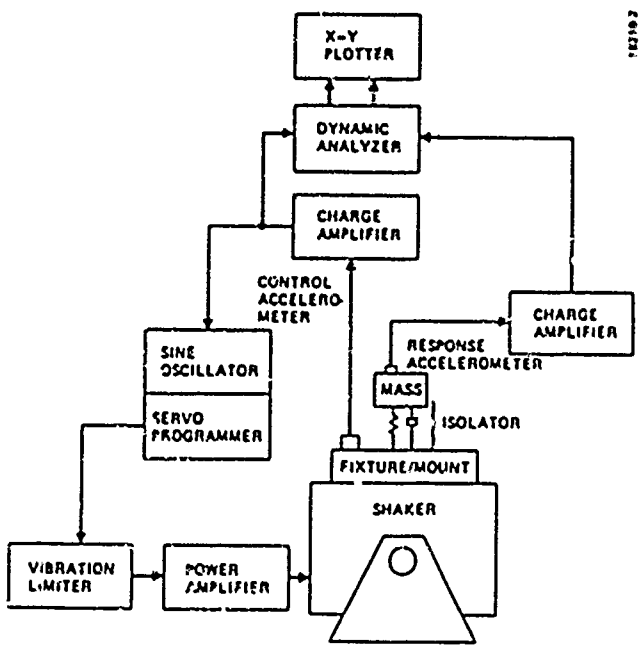


Figure 2. Vibration Test Set-Up

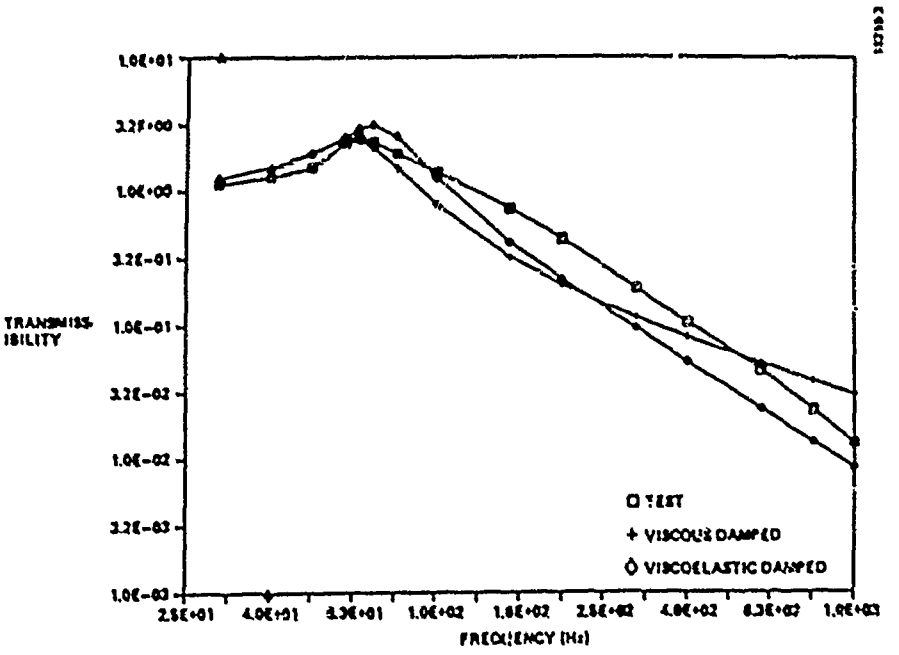


Figure 3. Test of an Elastomeric Isolator - Type A at 75°F

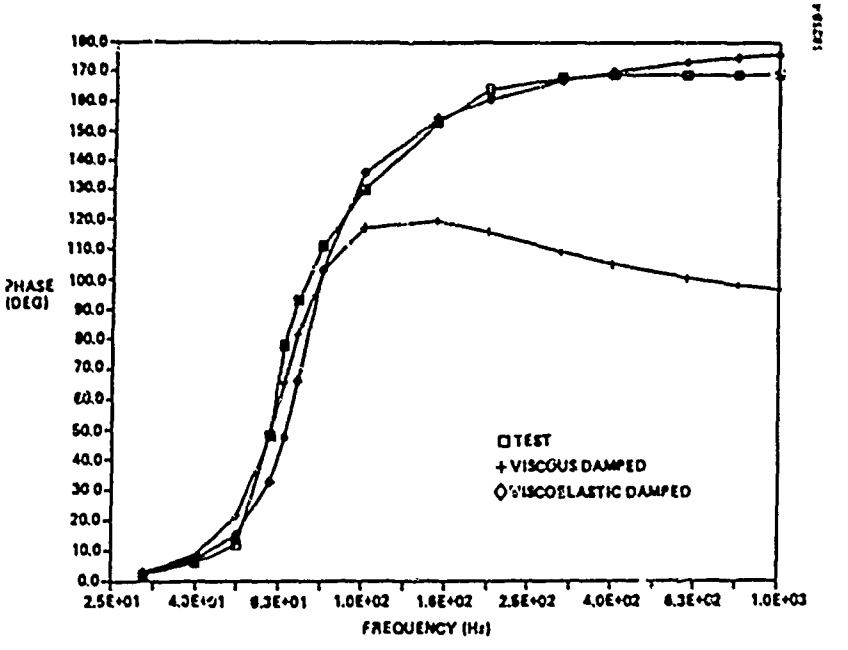


Figure 4. Test of an Elastomeric Isolator - Type A at 75°F

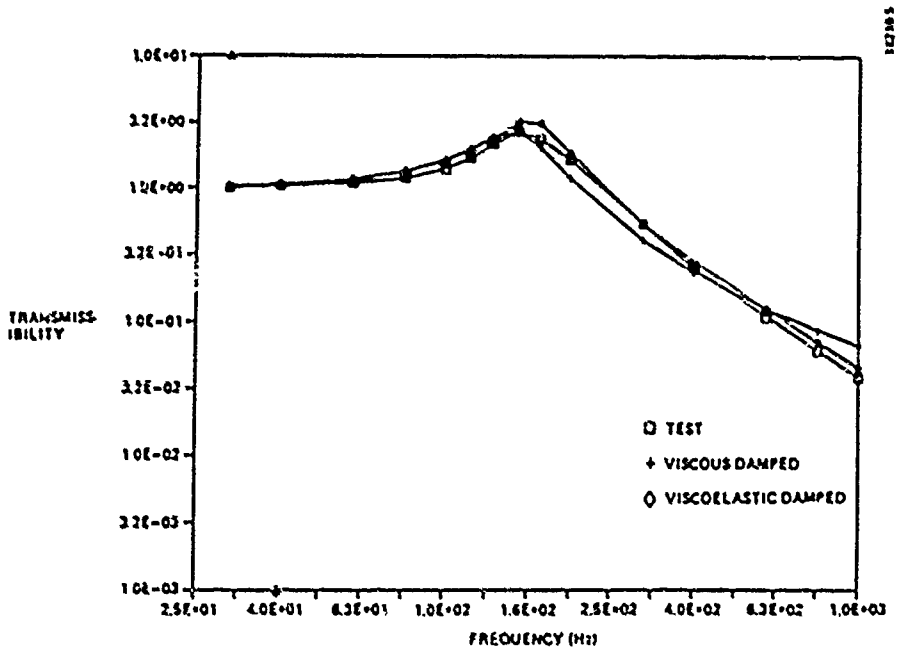


Figure 5. Test of an Elastomeric Isolator - Type A at -55°F

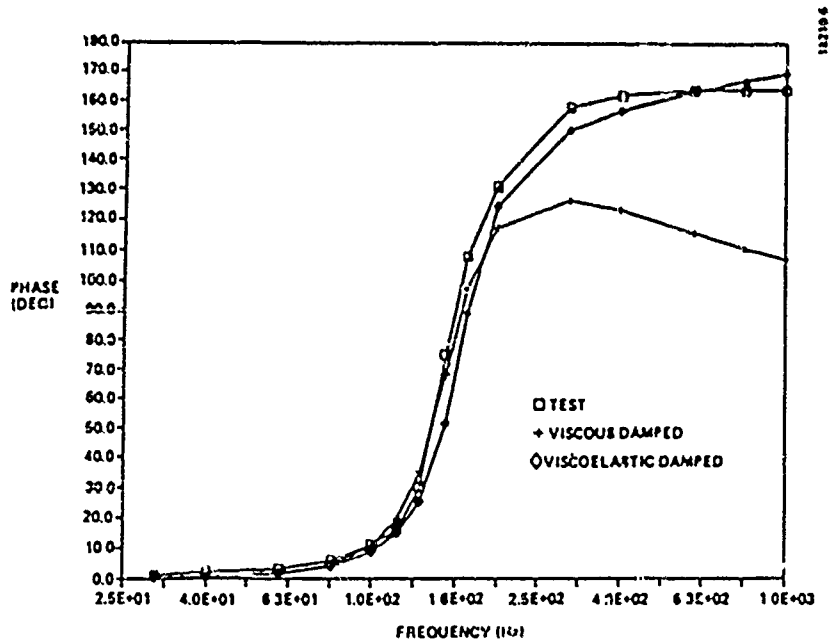


Figure 6. Test of an Elastomeric Isolator - Type A at -55°F

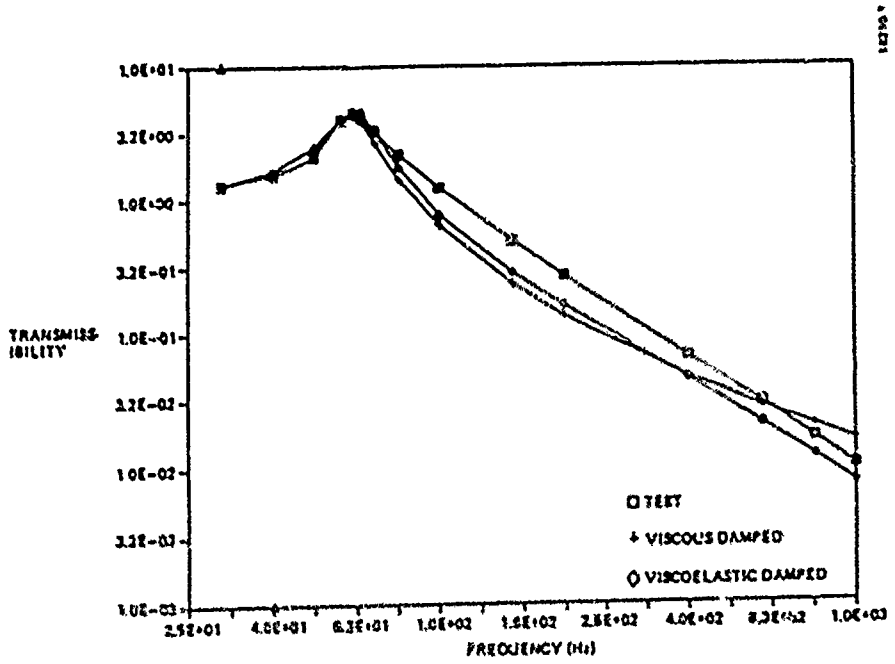


Figure 7. Test of an Elastomeric Isolator - Type B at 75°F

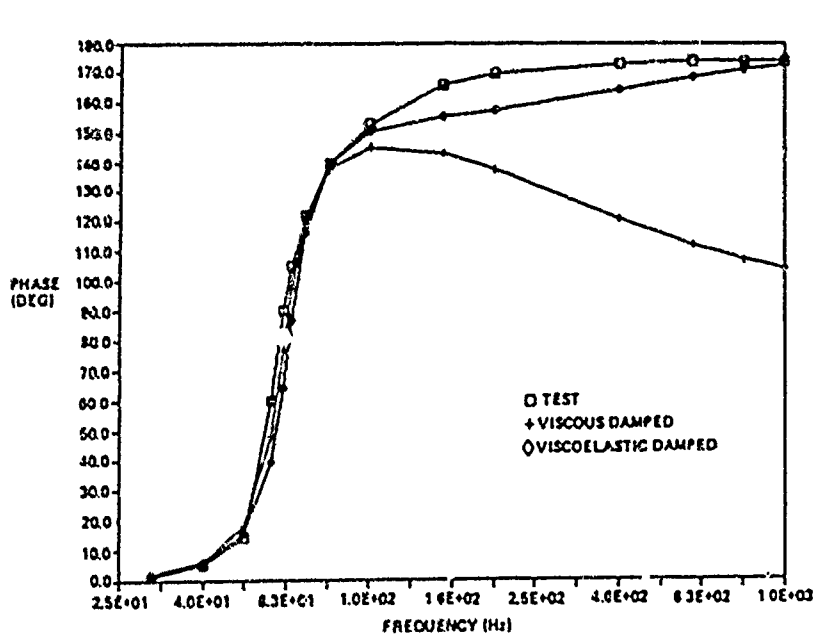


Figure 8. Test of an Elastomeric Isolator - Type B at 75°F

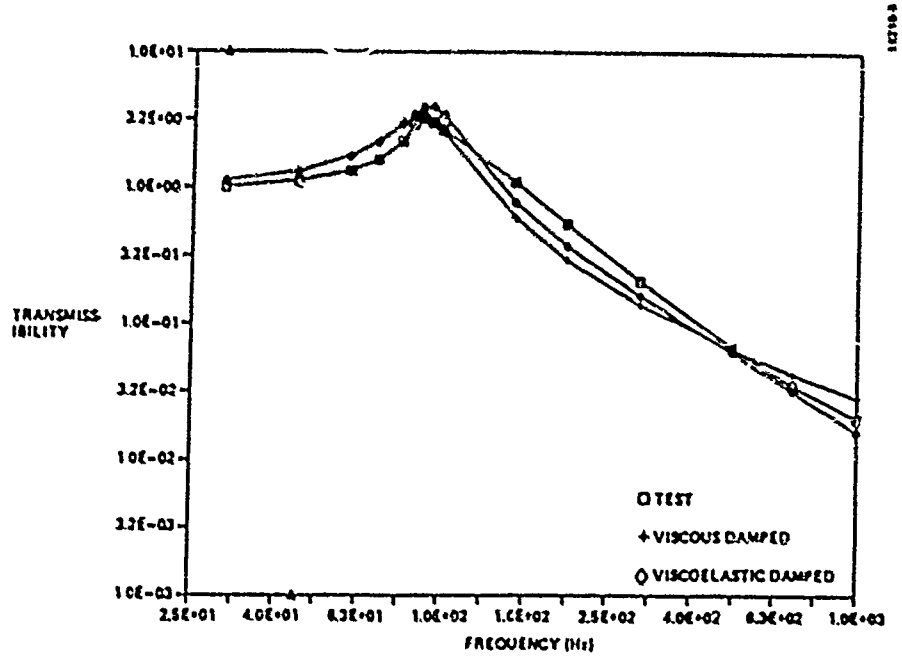


Figure 9. Test of an Elastomeric Isolator - Type B at -55°F

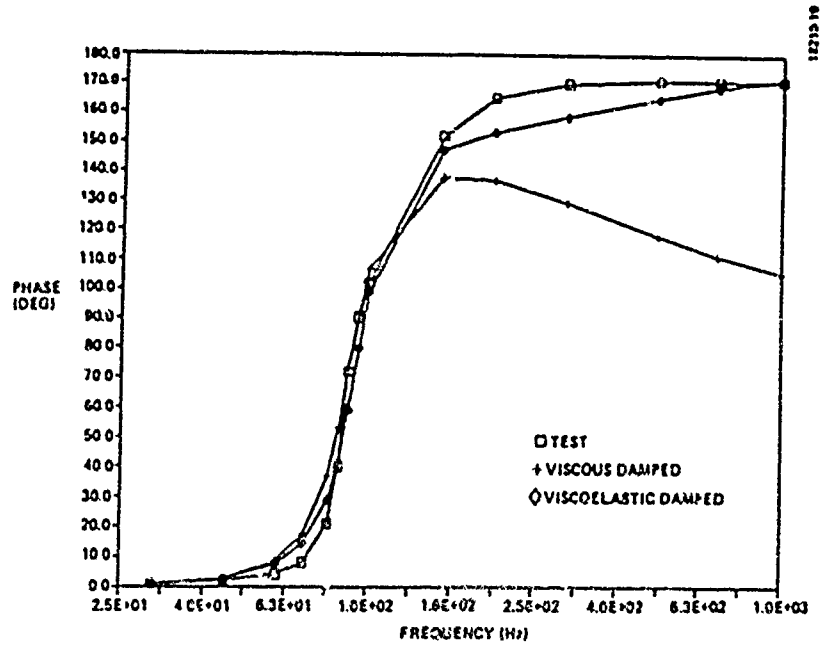


Figure 10. Test of an Elastomeric Isolator - Type B at -55°F

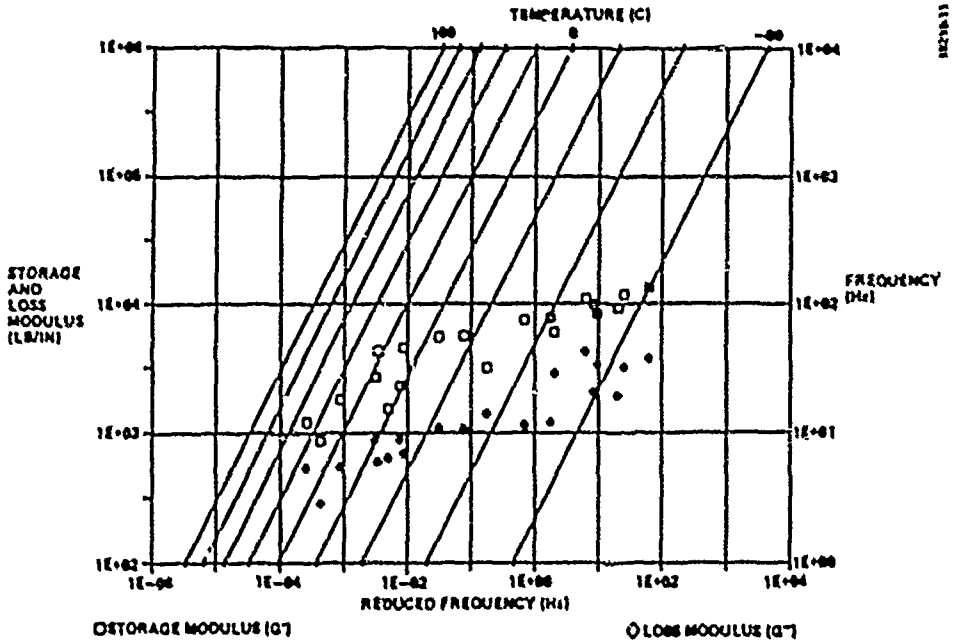


Figure 11. Test of an Elastomeric Isolator - Type A

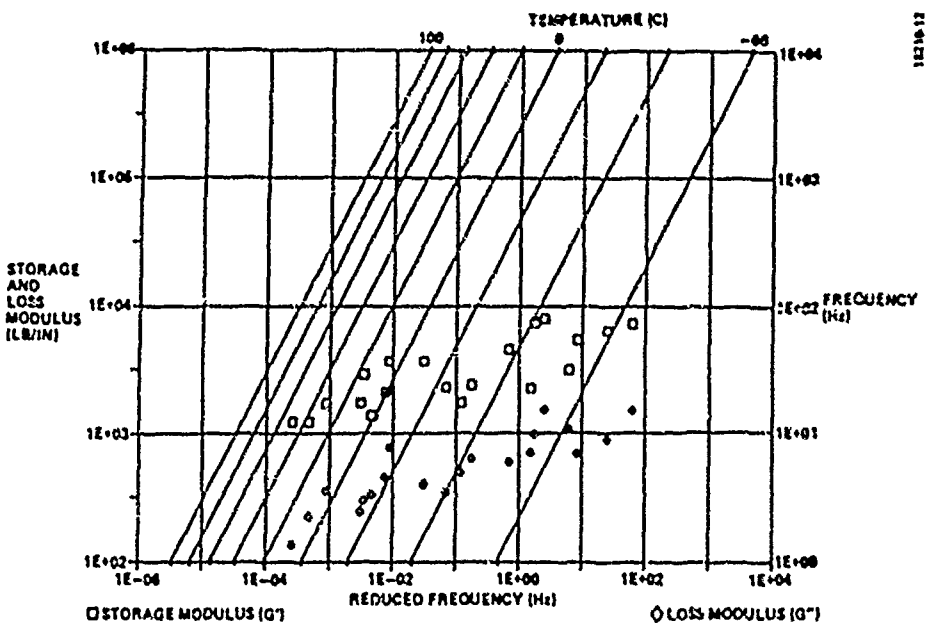


Figure 12. Test of an Elastomeric Isolator - Type B

RELSAT DAMPING MAYERIAL DATA

For
VIBRATION DAMPING WORKSHOP II
"DAMPING 86"

MARCH 5-7, 1986

RIVIERA HOTEL AND CONVENTION CENTER
LAS VEGAS, NV

AUTHORS: M.L. PARIN
A.D. NASHIF
T.M. LEWIS
ANATROL CORPORATION
10895 INDECO DRIVE
CINCINNATI, OH 45241
(513) 793-8844

ABSTRACT

The damping properties of two materials, one a structural expoxy and the other a pressure sensitive film adhesive evaluated for Boeing Aerospace Company, were presented and discussed. The damping properties were evaluated and corrolated using one or more test procedures. These include the resonant, vibrating beam, mechanical impedance, and relaxation test techniques. The test methods and data analysis were discussed in relation with the damping properties of 3M Co. AF-32 structrual adhesive and 3M Co. No. 966 transfer adhesive. The results show that by properly applying the temperature frequency superposition principle to the measured properties, the dynamic mechanical properties can be correlated over a wide range of frequencies and temperatures. The dynamic storage modulus (both shear and Young's), material loss factor, and Poisson's ratio for the materials are presented.

I. INTRODUCTION

The damping properties for viscoelastic materials are generally characterized using a number of different experimental test methods that are selected based on the environmental conditions of interest. For example, the vibrating beam approach [1-4] is often used to characterize the linear damping properties in terms of frequency and temperature for both shear and/or extensional types of deformation, while the impedance [5,6] and resonant [2,7,9] techniques are used for determining the non-linear effects of strain amplitude, and static preloads. Long term stability is usually investigated using relaxation and/or creep procedures. The combined results of these different test methods can then be used to develop analytical [10] and also graphical [11,12] representations of the dynamic mechanical properties in terms of the various environmental factors.

This paper discusses the merits and limitations of the resonant beam, mechanical impedance resonance, and relaxation test methods. The damping properties of materials that were measured by various techniques will be presented and discussed. The results show that the dynamic mechanical properties can be measured and correlated over a wide range of temperatures and frequencies for different states of stress. From the experimental data, analytical and graphical representations of the material's damping properties can then be developed that include the environmental effects. This will include the dynamic storage modulus (both Young's and shear), loss factor, and Poisson's ratio for both materials.

II. MEASUREMENT TECHNIQUES

Many techniques have been used to measure the dynamic properties of elastomers, the discussion in this paper will be limited to the vibrating beam, impedance, resonance, and relaxation techniques. The vibrating beam technique is an indirect method that does not require an accurate measurement of the excitation force or the response displacement.

Vibrating Beam Technique

The analysis developed by Ross, Ungar, and Kerwin [13] can be used to calculate the damping properties of elastomeric materials from measurements made on the composite beam system. To use the analysis in its general form, iterative procedures must be used because the equations are coupled. However, for special cases, the equations can be simplified and only these will be presented here.

The technique is based upon utilization of the elastomeric material in conjunction with vibrating metal beams either in shear or extension. If the material is applied to the outside of the metal beam, then the properties can be obtained in extension, whereas if the material is sandwiched between two metal beams, then the properties can be obtained in shear. By studying the various resonances of the damped beam, the effect of frequency on the properties of the material can be established. Also, by placing the system inside an environmental chamber, the effects of temperature can be investigated.

This procedure has been adopted by the American Standard Testing Material as the preferred method for determining the damping properties of materials. The details of this procedure are found in ASTM E-756-83.

Description of Specimens

Any type of beam specimens can in principle be used to make measurements on the dynamic properties of elastomeric materials, previous experience has concentrated mainly on cantilever beams. This is because of the simplicity of the set-ups for such beams, and also because at least one end can be simulated properly, namely the free end. This implies that careful attention must be applied to insure that the boundary condition at the other end is fully fixed. The same approach is used for other types of beams, with clamped-clamped, simply supported, or free-free boundary conditions. In making dynamic measurements on materials, using vibrating beam tests, it is necessary to apply the elastomeric

material on the metal beam and make measurements on the composite system. Usually the elastomeric material is combined with a metal beam in different configurations depending on the properties of the material of interest. The four main combinations, illustrated in Figure 1 are:

1. The homogeneous beam. This type is used for measuring the dynamic properties of metal alloys and composites. Such materials are usually stiff on their own and do not require combination with a metal beam.

2. The Oberst or externally coated beam, named for Dr. Oberst [14] who developed this technique for making measurements on the dynamic properties of stiff elastomeric materials under extensional deformation.

3. The symmetric free layer beam. This is a modified Oberst beam, where the material is coated on both sides. Again, the properties are determined for extensional deformation. This beam allows for a simplification in the equations and data reduction, and it circumvents some experimental difficulties.

4. The sandwich beam. This technique is used to determine the dynamic properties of elastomeric materials under shear deformation, and is usually employed for soft materials.

From Figure 1, it can be seen that all beams have massive roots, necessary to properly simulate the fixed boundary condition at the root of the cantilever beam, which is usually clamped in a rigid fixture. These roots can be either integrally machined as part of the beam, welded to the beam, or epoxied to the beam. It is emphasized that, for most measurements, the roots are essential for generating useful and accurate data.

The damping material is usually bonded to the metal beam by means of an epoxy adhesive which must have a modulus higher than that of the viscoelastic material. Also, the thickness of the epoxy layer must be kept to a minimum in general and small in comparison with the thickness of the damping material. If these two rules are not followed [15], deformation will occur in the epoxy layer as well as in the elastomeric layer, and erroneous data will result. In some cases the elastomeric material is, or can be, of the self-adhesive type and in that case there will be no need of an epoxy layer.

The type of metal used for the beams is usually steel or aluminum. Typical dimensions, used previously, and found to be successful, are a width of 0.5 inches, a free length of 7 to 10

inches, a root length of 1 inch, and a thickness of 0.04 to 0.125 inches. The thickness of the elastomeric material can vary according to the specific properties of the material and the temperatures and frequencies of interest. The beam geometry used in the measurements are found in Tables 1 and 2.

Instrumentation and Set-up

When using the beam specimens of Figure 1 to make measurements of the dynamic properties of materials one usually requires two types of transducer. One is needed to apply the excitation force, and the other to measure the response of the beam. Because, when making such measurements, it is necessary to minimize all extraneous sources of damping, apart from that of the material to be investigated, it is essential to use transducers that are light in weight or of the non-contacting type.

The beam is mounted in a heavy, rigid, fixture which can provide sufficient clamping force around the root of the beam to simulate a fixed end boundary condition. Either a sinusoidal or random signal can be applied to the excitation transducer via a power amplifier. The response of the beam is measured by the second transducer, and is processed through signal conditioning equipment, and the resulting response is stored in a computer or on an X-Y recorder plot for later analysis. The set-up is usually mounted inside an environmental chamber in order to study such environmental factors as temperature, vacuum, etc. A schematic of such a set-up is illustrated in Figure 2.

Data Reduction

For all types of beams, the response of the specimen is measured as a function of frequency. From such a response spectrum, the frequencies and damping values of the various modes of vibration of the specimen are determined at each selected temperature. By varying the temperature of the environmental chamber, these tests are repeated at various temperatures to investigate the effects of temperature. The response of the undamped beam is also needed. Before this data can be processed, it is necessary to have three sets of information, as follows:

1. The frequency and the loss factor of the damped beam for each mode of vibration.

2. The frequencies of the undamped beam for the same modes of vibration, as for the damped beam.

3. The geometrical properties of the damped and undamped beams, along with the densities of the materials.

The following data reduction process is used to calculate the damping properties of materials from measurements conducted on the four types of beams outlined previously.

Homogeneous Beam Technique

The system loss factor and Young's modulus E of the beam can be calculated from

$$\eta = \Delta f_n / f_n \tag{1}$$

and

$$E = \rho b H L^4 \omega_n^2 / (a_n^2 I) \tag{2}$$

where f_n is the nth natural frequency, ω_n is the nth circular frequency $(2\pi f_n)$, ρ is the mass density, L is the length of beam, a_n is the characteristic number of the nth mode, I is the second moment of area and Δf_n is the half-power bandwidth.

Oberst Beam Technique

The properties of the damping material are computed from the measured values of the composite beam using the following equations:

$$(\omega_n/\omega_{1n})^2(1+h_2\rho_r) = \frac{1 + 2e_2h_2(2+3h_2+2h_2^2) + e_2^2h_2^4}{1 + e_2h_2} \tag{3}$$

$$\eta/\eta_2 = \frac{e_2h_2(3 + 6h_2 + 4h_2^2 + 2e_2h_2^3 + e_2^2h_2^4}{(1+e_2h_2)\ (1+4e_2h_2+6e_2h_2^2+4e_2h_2^3+e_2^2h_2^4)} \tag{4}$$

where $e_2 = E_2/E_1$, E_1 is the Young's modulus of the metal beam, $h_2 = H_2/H_1$, H_2 is the thickness of the damping material, H_1 is the thickness of the metal beam, $\rho_r = \rho_2/\rho_1$, ρ_2 is the density of the damping material, ρ_1 is the density of metal beam, η is the loss factor of the composite beam in the nth mode, η_2 is the loss factor of the damping material, ω_{1n} is the nth circular frequency of the metal beam and ω_n is the nth circular frequency of composite beam.

It should be noted that significant errors can be introduced

when

$$(\omega_n/\omega_{in})^2(1+\rho r h_2) < 1.1$$

Symmetric Free Layer Beam Technique

The equations used for symmetric beams are:

$$E_2 = \frac{[(\omega_n/\omega_{1n})^2(1+2h_2\rho_r) - 1]\, E_1}{(8h_2^3 + 12\, h_2^2 + 6h_2)} \qquad (5)$$

$$\eta_2/\eta = \frac{E_1}{(8h_2^3 + 12\, h_2^2 + 6h_2)\, E_2} + 1 \qquad (6)$$

The same error problems as noted for Oberst test results can occur for this technique if

$$(\omega_n/\omega_{in})^2(1+2\rho_r h_r) < 1.10$$

Sandwich Beam Technique

The following relations for the shear modulus and loss factor of the damping material are used for sandwiched beams:

$$G_2 = \frac{(A-B) - 2(A-B)^2 - 2(A\eta)^2}{(1-2A+2B)^2 + 4(A\eta)^2} \times \frac{E_1 H_1 H_2 a_n}{L^2} \qquad (7)$$

$$\eta_2 = \frac{A\eta}{A - B - 2(A-B)^2 - 2(A\eta)^2} \qquad (8)$$

where

$$A = (\omega_n/\omega_{1n})^2 \ (2 + \rho_r h_2) \ (B/2) \tag{9}$$

$$B = 1/6(1+h_2)^2 \tag{10}$$

and G_2 is the shear modulus of the damping material

For the sandwich beam technique

$$(\omega_n/\omega_{in})^2(2+\rho_r h_2)>1.10$$

to minimize numerical errors in the calculations.

Since the properties of damping materials can be computed for different modes of vibration, and at different temperatures, the effects of both frequency and temperature can be established.

Usually, the loss factor of the composite beam is measured by the half-power bandwidth method. This is not the only method to measure the damping for a given resonant condition of the beam, and other techniques can be used equally well, within their limitations, such as decay, modal curve-fitting, Nyquist diagrams, etc.

Assumptions

As with all techniques and analyses, certain important assumptions have to be made and are listed here. They should be kept in mind when making damping measurements on materials.

1. All damping measurements made by beam tests must be made in the linear range. It is important to select a force level that will be meaningful, because the analysis for the data reduction will otherwise not be applicable.

2. For the Oberst and symmetric free layer specimens, the analysis is the classical analysis for beams. It does not include the effects of rotatory inertia or shear deformation. The analysis assumes that plane sections remain plane and, therefore, care must be taken not to use specimens with a damping material thickness that is greatly exceeds that of the metal beam.

3. The equations presented for computing the properties of damping materials in shear do not include the extensional terms of the damping layer. This is a good assumption as long as the stiffness of the damping layer is considerably lower than that of the metal beam. Also, these equations were developed and solved using sinusoidal expansions for the mode shapes. For cantilever beams, this approximation is good only for the higher modes. For the first mode, it does not apply and an equivalent wavelength of vibration must be assumed empirically, to generate useful data. It has been the common practice to ignore the first mode results for sandwich cantilever beams.

4. The loss factor of the metal beam(s) is assumed to be zero. This is usually a good assumption because steel and aluminum have loss factors of the order of 0.0001 or less, which is significantly lower than those of the composite damped beams. This point should be kept in mind if other beam materials are used, such as plastic or epoxy.

5. The damping introduced by the mounting conditions is also assumed to be very low. This is usually a good assumption provided: a) the clamping configuration has sufficient mass and stiffness to counteract the moments introduced by the specimen; and b) the clamping surfaces are flat and paralled so that the clamping forces are uniformly distributed and minimize slip.

Impedance Technique

The impedance technique is usually used to generate the material properties continuously with frequency and is especially useful to investigate the effects of preloads on the dynamic properties. By this technique, a known force is applied to a given specimen and the resulting displacement is measured. The amplitudes of the two signals and the phase angle between them are then used to compute the material properties.

Since most of today's vibration testing is carried out using fast Fourier analyzer systems, it is necessary to adapt the impedance technique to such systems. Of particular importance is that the vibration data is processed on the analyzer using complex algebra. Thus to compute the dynamic properties of elastomers it is necessary to work with the real and imaginary components of the frequency response measurements made on the material of interest. To illustrate this, consider the single degree-of-freedom system illustrated in Figure 3. The compliance X/F for such a system can be written as:

$$\frac{X}{F} = \frac{1}{k - m\omega^2 + ik\eta} \tag{11}$$

If the compliance is defined in terms of its real part R and its imaginary part I then equation (11) can be rewritten as:

$$R + iI = \frac{1}{k - m\omega^2 + ik\eta} \tag{12}$$

The real and imaginary parts of equation (12) can now be used to solve for the two unknowns k and η or:

$$k = m\omega^2 + \frac{R}{R^2 + I^2} \tag{13}$$

$$\eta = \frac{-I}{m\omega^2(R^2+I^2)+R} \tag{14}$$

Description of Specimens

Elastomeric materials are usually tested in tension-compression or in shear states of stress by the impedance technique. Figures 4 and 5 represent some of the ways for combining the material and the mass to simulate a single degree-of-freedom system. Although the cross section of the elastomeric material could be of any shape, it has been common to use specimens having retangular or circular sections.

Instrumentation and Setup

Similar instrumentation to that of the vibrating beam technique is used for the impedance technique in order to apply a force to the specimen and measure its response. Typically, the force is applied by either a shaker or an impact transducer while the response is measured by an accelerometer. By controlling the amplitude of the applied force, the non-linear effects on the dynamic properties can be investigated. Also by preloading the specimens, such effects can be studied.

Data Reduction

Equations (13) and (14) can be used to compute the dynamic properties of elastomeric materials when tested either in

shear or tension-compression states of stress as illustrated for both specimens of Figures 4 and 5. For either type the loss factor is computed directly from equation (14) while the modulus needs to be computed from the specimen stiffness k of equation (13).

Shear Specimen

The shear modulus of the elastomeric material is determined after the stiffness value k has been established by using the following expression:

$$G = \frac{kH}{A} \tag{15}$$

where H is the height of the specimen and A is its cross-sectional area.

Tension-compression Specimen

Shape factors are usually considered [16] in reducing the data generated on tension-compression specimens to account for the Poisson's effects. In such cases Young's modulus, E, of the elastomeric material is given by:

$$E = \frac{kH}{A[1+\beta(A/A')^2]}$$

where A' is unloaded area of the specimen and β is a material constant equal to 1.5 or 2.0, depending on whether the material is filled or an unfilled elastomer, respectively.

Assumptions

The major point for consideration in making impedance measurements is that the state of stress should be well defined. Unfortunately, this is difficult unless extreme care is taken in designing the specimen and making measurements on it. Specifically, the following points should be kept in mind.

1. To minimize the effects of free edges on the measured values for the shear specimen it is recommended that the height to thickness ratio of the specimen be greater than 4.

2. To minimize the effects of shape factors on tension-compression specimens it is necessary to make the loaded area small in comparison with the unloaded area.

3. The type of excitation and pickup methods and locations should be selected to avoid rocking motions.

4. Although measurements could be made over a wide frequency range using the impedance technique, it has been found that in order to minimize the effects of error magnification factors on the computed properties it is necessary to limit the frequency range to that around the resonance frequency only. Practically, it has been demonstrated, with current equipment, that the frequency range could be as wide as a decade with the specimen resonant frequency approximately in its center. Thus different masses are needed to consider different frequency ranges.

Resonance Technique

The resonance technique is a special case of the impedance one where measurements and analysis of the data is restricted to the resonant frequency. Thus different masses and/or specimen geometries are needed to investigate the frequency effects. Although this technique is restricted to one frequency it is very useful because of its simplicity and the fact that high amplification at resonance help in studying the effects of dynamic nonlinearities on the material properties.
As far as the analysis for this technique, it is sufficient to keep in mind that at resonance:

$$\omega_n = \frac{k}{m} \tag{16}$$

in order to compute the specimen stiffness. The loss factor of the specimen can be measured by many methods such as the half-power bandwidth method or by the following formula:

$$\eta = \frac{1}{\sqrt{Q^2 - 1}} \tag{17}$$

where Q is the amplification factor at resonance.

All points considered for the impedance technique apply equally well for the resonance one.

Relaxation Technique

By this technique the material is subjected to a constant displacement and the change in the force is monitored over a period of time. The time interval where a noticeable change in force occurs depends on the temperature range where the material is being tested. For example, if the material is tested in its rubbery region, then the force can reach equilibrium in a short time. However, as the test temperature causes the material to reach its transition and glassy regions, longer time periods will be needed since the force will continue to change with time for longer periods.

Figure 6 illustrates the measurements made by the relaxation technique. The elastomeric sample having a length of L is mounted to a rigid fixture on end and to a force transducer on the other. The specimen is stretched by displacement ΔL and the force signal can thus be monitored with time and recorded.

The time domain relaxation modulus can then be described as

$$E(t) = \frac{F(t)\, L}{A\, \Delta L} \qquad (18)$$

where F(t) is the load, A is the loaded area, L is the sample length, and ΔL is the displacement.

The time domain relaxation modulus can then be transformed into the frequency domain by [17].

$$E(i\omega) = i\omega \int E(\theta)\, e^{-i\omega\theta}\, d\theta \qquad (19)$$

where

$$\theta = (t-t') \qquad (20)$$

and t' is some past time and t is present time. Rewriting this equation for the storage (E_R) and loss modulus (E_I) gives:

$$E_R(\omega) = \omega \int E(\theta) \sin\omega\theta\, d\theta \qquad (21)$$

$$E_I(\omega) = \omega \int E(\theta) \cos\omega\theta\, d\theta \qquad (22)$$

Equations (21) and (22) can then be used, along with the time domain loading history and specimen geometry, to compute the

dynamic properties for viscoelastic materials in either shear or tension-compression states of stress by applying numerical integration procedures. The loss factor is then determined by taking the ratio of equation (22) to equation (21).

III. RESULTS AND DISCUSSION

Tables 1 and 2 summarize the different specimens that were used to determine the damping properties of AF-32 structrual adhesive. As can be seen from Table 1 a variety of speciman geometries were used for the 966 materials so that the properties could be correlated over a wide range of frequencies for both shear and tension/compression states. The specimen used to determine the properties of AF-32 were limited to sandwich and free layer beams.

All the experimental data was analyzed using the equations presented in the previous section. The damping properties for 966 and for AF-32 are plotted in Figures 20, 21, 22, 23, 24, 25, 35, 36, 45, 46, 59, 52, 57, 58, 59, and 60 in terms of reduced frequency using the temperature/frequency equivalance principles. For comparison purposes, the dynamic Young's and Shear modulus data for 966 are superimposed onto the single graph shown in Figure 59. Figure 60 shows the same comparison for AF-32.

Figures 53, 54, 55, and 56 present the dynamic Shear and Young's modulus material properties of 966 in formats that eliminate both temperature and frequency [18]. The purpose for using these formats is two fold. First, both the modulus vs. loss modulus and modulus magnitude vs. loss factor plots can be used to identify points that diverge from the general trends of the data. These plots can, thus, be used as a tool to identify data points that fall outside some established acceptance ban.

These points can then be eliminated prior to developing the analytical models for the modulus and loss factor.

The data presented in Figure 60 for AF-32 and in Figure 59 for 966 illustrates good correlation over a wide range of reduced frequencies. The 966 data also shows excellent correlation between the various test methods. Also, the loss factor for both shear and tension/compression states of stress are essentially the same for the AF-32 and the 966 materials. The data also shows that for both the AF-32 and the 966 that the Young's modulus is approximately three the shear modulus in the rubbery and transition zones and then fall to approximately 2.7 times in the glassy zone. This indicated a Poisson's ratio very close to .5 for the rubbery region and the transition region and approximately 0.34 for the glassy regions.

IV. SUMMARY AND CONCLUSIONS

Different techniques for measuring the dynamic properties of elastomers have been presented and discussed. The dynamic properties for the elastomer have been measured by the various techniques and correlated over wide frequency and temperature ranges. It was found that there is good agreement in the results of the various techniques.

REFERENCES

1. "Standard for measuring vibration damping properties of materials," American Society for Testing and Materials, E756-80.

2. D.I.G. Jones, "Temperature-frequency dependence of dynamic properties of damping materials," J. Sound Vib., 33(4), pp 451-470, 1974.

3. A.D. Nashif, "A new method for determining the damping properties of viscoelastic materials," Shock and Vibration Bulletin, 36, pp 37-47, 1967.

4. F.S. Owens, "Elastomers for damping over wide temperature ranges," Shock and Vibration Bulletin, 36, Part 4, pp 25-35, 1967.

5. J.L. Edwards and D.R. Hicks, "Useful range of a mechanical impedance technique for measurement of dynamic properties of materials," J.A.S.A., 52, pp 1053-1056, 1972.

6. D.I.G. Jones and A. Muszynska, "On the modal identification of multiple degree of freedom systems from experimental data," Shock and Vibration Bulletin, 53, 1983.

7. C.M. Cannon, A.D. Nashif, and D.I.G. Jones, "Damping measurements on soft viscoelastic materials using a tuned damper technique," Shock and Vibration Bulletin, 38, Part 3, pp 151-163, 1968.

8. D.L. Hunston, W.D. Bascom, E.E. Wells, F.D. Fahey, and J.L. Bitner, "Viscoelastic characterization of structural adhesive via forced oscillation experiments," Adhesion and Absorption of Polymers (ed. Lieng-Huang Lee), Plenum Publishing Corporation, New York, 1980.

9. G.E. Warnaka and H.T. Miller, "Strain-frequency temperature relationships in polymers," J. Eng. for Industry, Tran. ASME, 1967.

10. L.C. Rogers, "Operators and fractional derivatives for viscoelastic constitutive equations," Journal of Rheology, 27(4), pp 351-372, 1983.

11. D.I.G. Jones, "A reduced-temperature nomogram for characterization of damping material behavior," Shock and Vibration Bulletin, 48, Part 2, pp 13-22, 1978.

12. D.I.G. Jones, "An attractive method for displaying material damping data," AIAA Journal, 18(8), pp 644-649, 1981.

13. D. Ross, E.E. Ungar, and E.M. Kerwin, Jr., "Damping of Plate Flexural Vibrations by Means of Viscoelastic Laminate," Section III of Structural Damping, ASME, pp. 49-88, 1959.

14. H. Oberst and K. Frankenfeld, "Uber die Dampfung der Biegeschwingungen dunner Bleche durch festhaftende Belage," Acustica, Vol. 2, pp. 181-194, 1952.

15. G.E. Warnaka, "Effect of Adhesive Stiffness on Extensional Damping" ASME, 1967.

16. J.C. Snowdon, Vibration and Shock in Damped Mechanical Systems, Wiley, New York, 1968.

17. M.P. Blake, and W.S. Mitchell, Vibration and Acoustic Measurement Handbook, pp. 214-224.

18. L.C. Rogers, J. Eichenlaub, and J.B. Layton, "Standard Graphical Presentation of Complex Modulus and Processing Methodology," Damping 1986, AFWAL Technical Report.

TABLE 1

SPECIMEN DESCRIPTION 3M 966

Technique	Specimen
Vibrating Beam Vibrating Beam	10" Length Sandwiched Beam 5" Length Sandwiched Beam
Vibrating Beam Vibrating Beam	10" Length Sandwiched Beam 5" Length Sandwiched Beam
Resonance-Impedance	.25" Length/.8125"OD-.375"ID Tension-Compression Link .020" Thick/8in^2 Shear Joint
Relaxation	5.5" Length/.28125in^2 Tension Sample 4.5in^2 Shear Joint

TABLE 2

SPECIMEN DESCRIPTION 3M AF-32

Technique	Specimen
Vibrating Beam	10" Length Sandwiched Beam
Vibrating Beam	10" Length Mod Oberst Beam

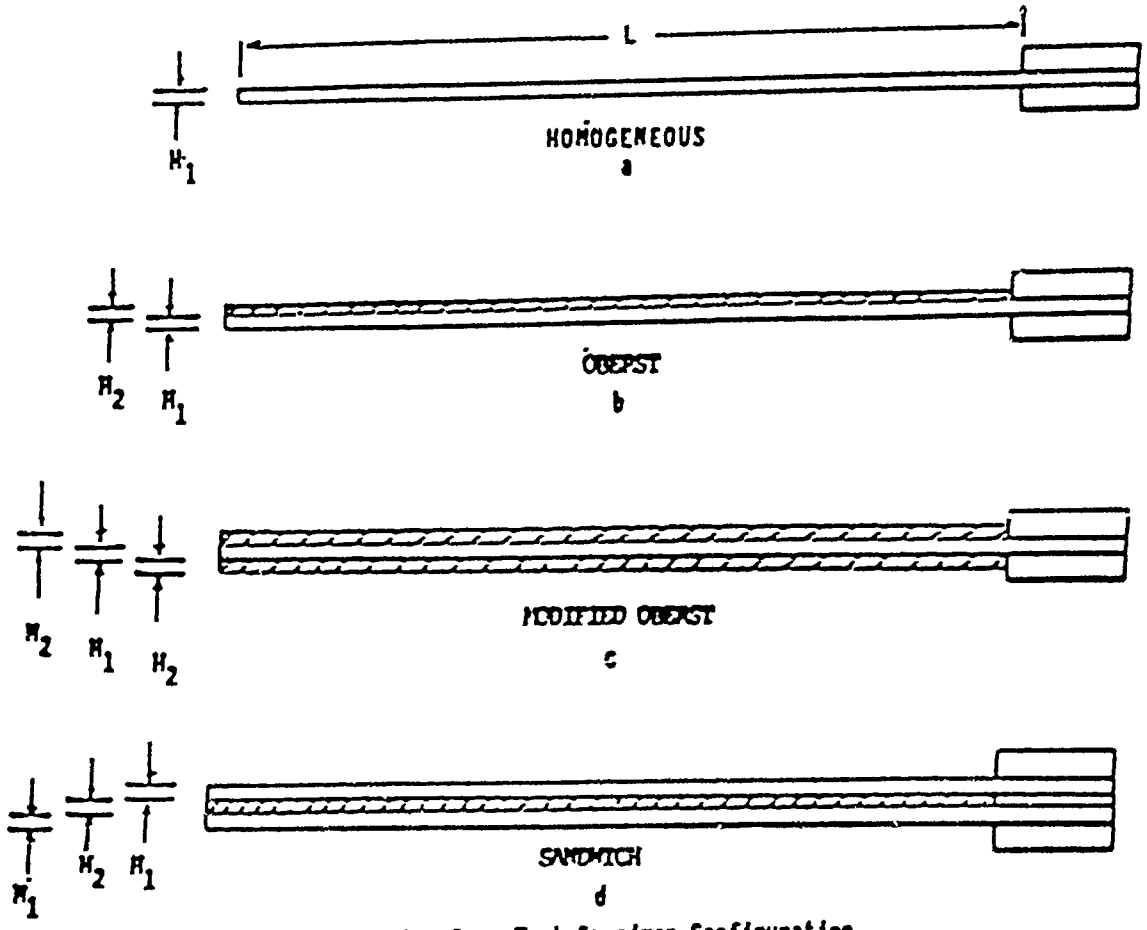


Figure 1: Beam Test Specimen Configuration

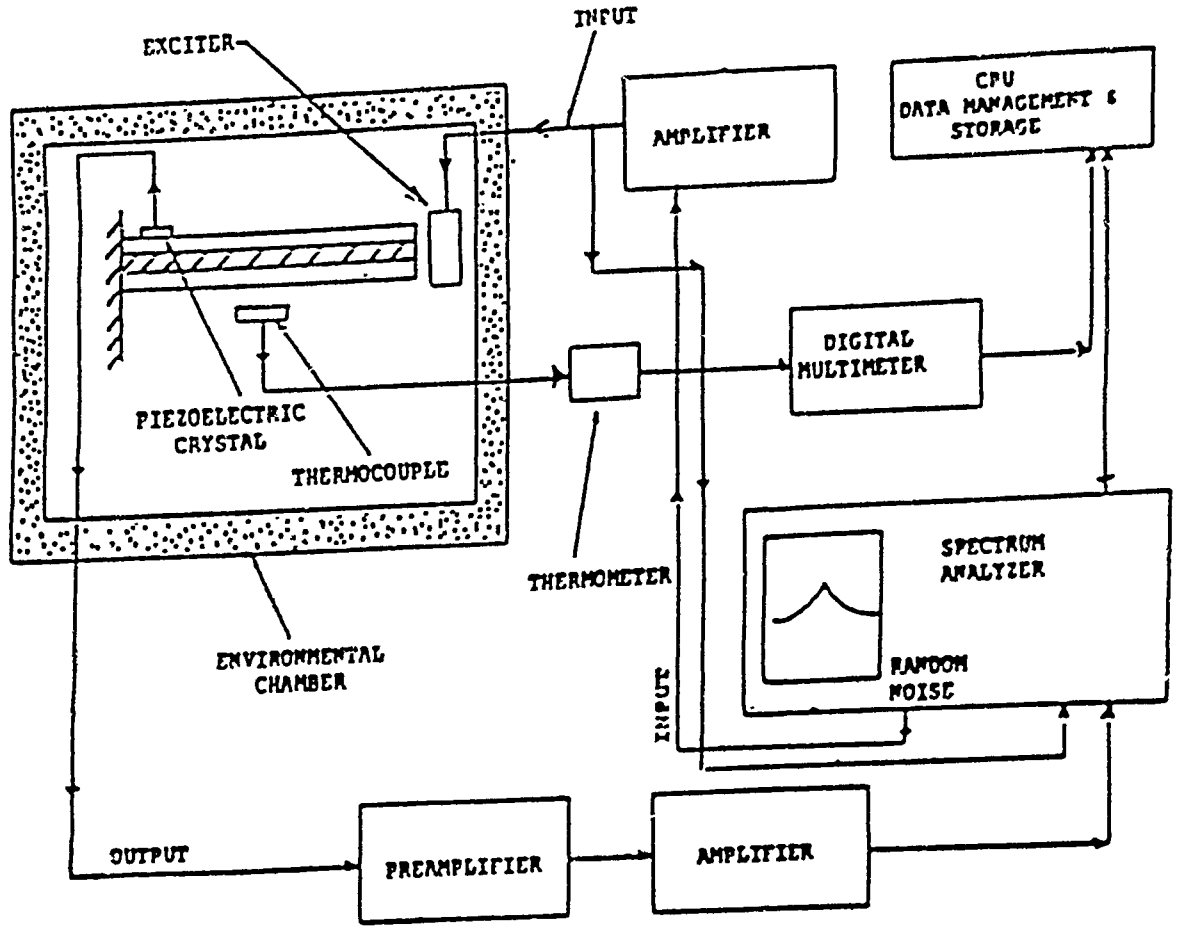


Figure 2: Block Diagram of Typical Laboratory Test Setup for Vibration Beam Tests

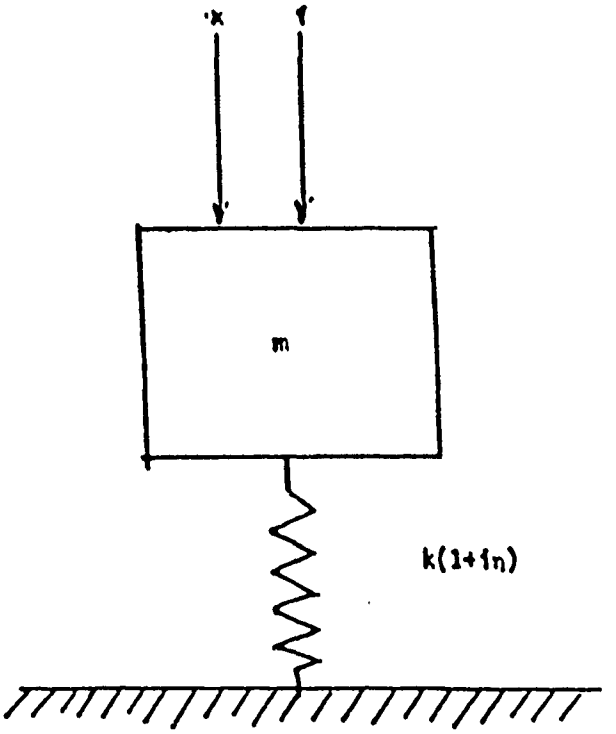
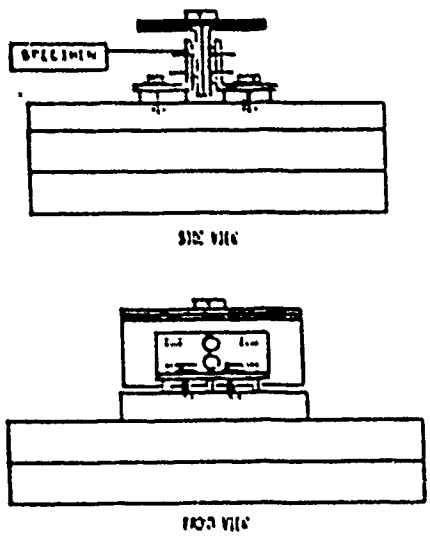


Figure 3: Schematic of Impedance Measurement

SHEAR MECHANICAL IMPEDANCE BREAKDOWN



SHEAR MECHANICAL IMPEDANCE SETUP

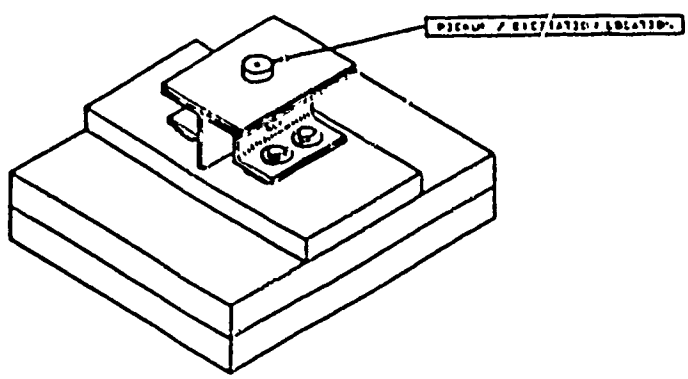


Figure 4: Typical Test Specimen Setup for Resonant and Mechanical Impedance Shear Test Techniques

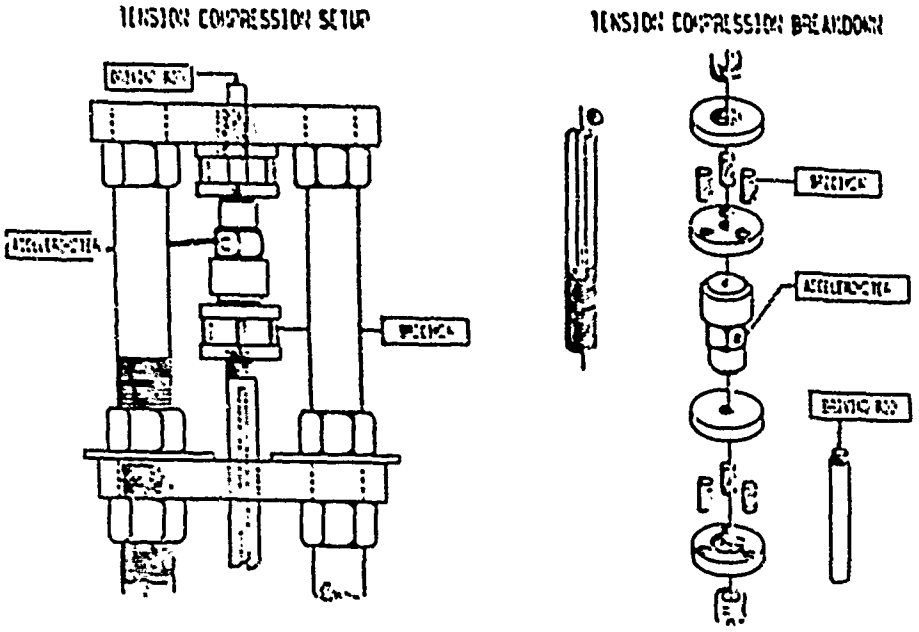


Figure 5: Test Setup for Resonant and Mechanical Impedance Tension-Compression Test Techniques

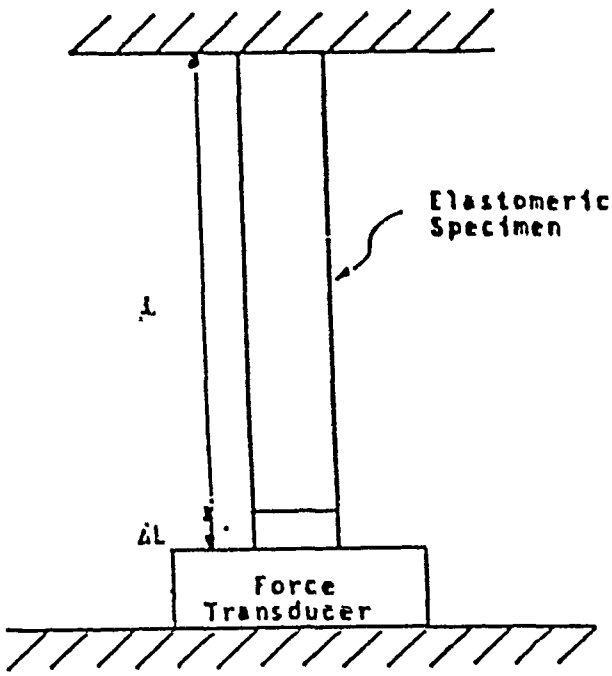


Figure 6: Schematic of Relaxation Measurements

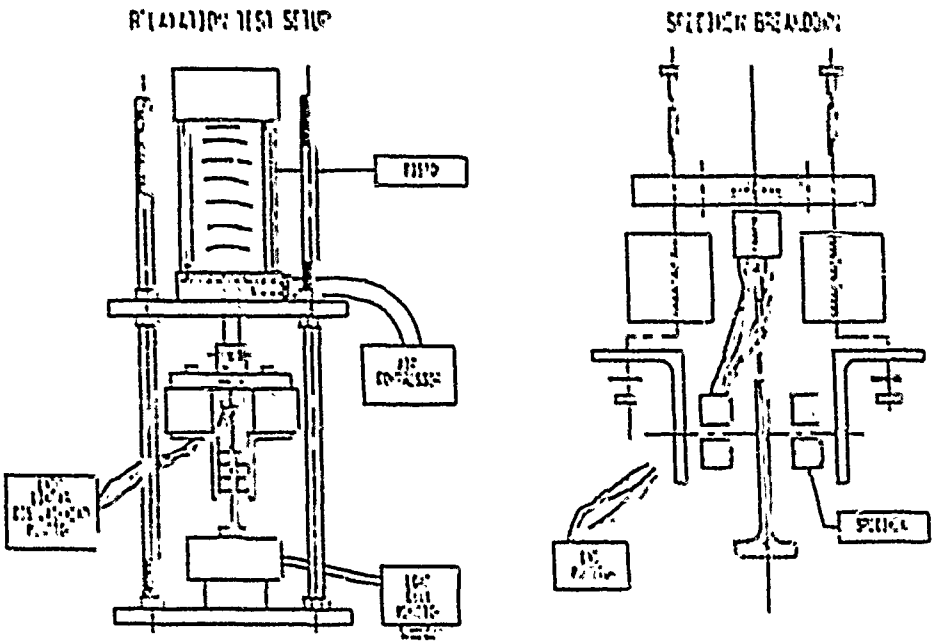


Figure 7: Shear Relaxation Test Measurement System

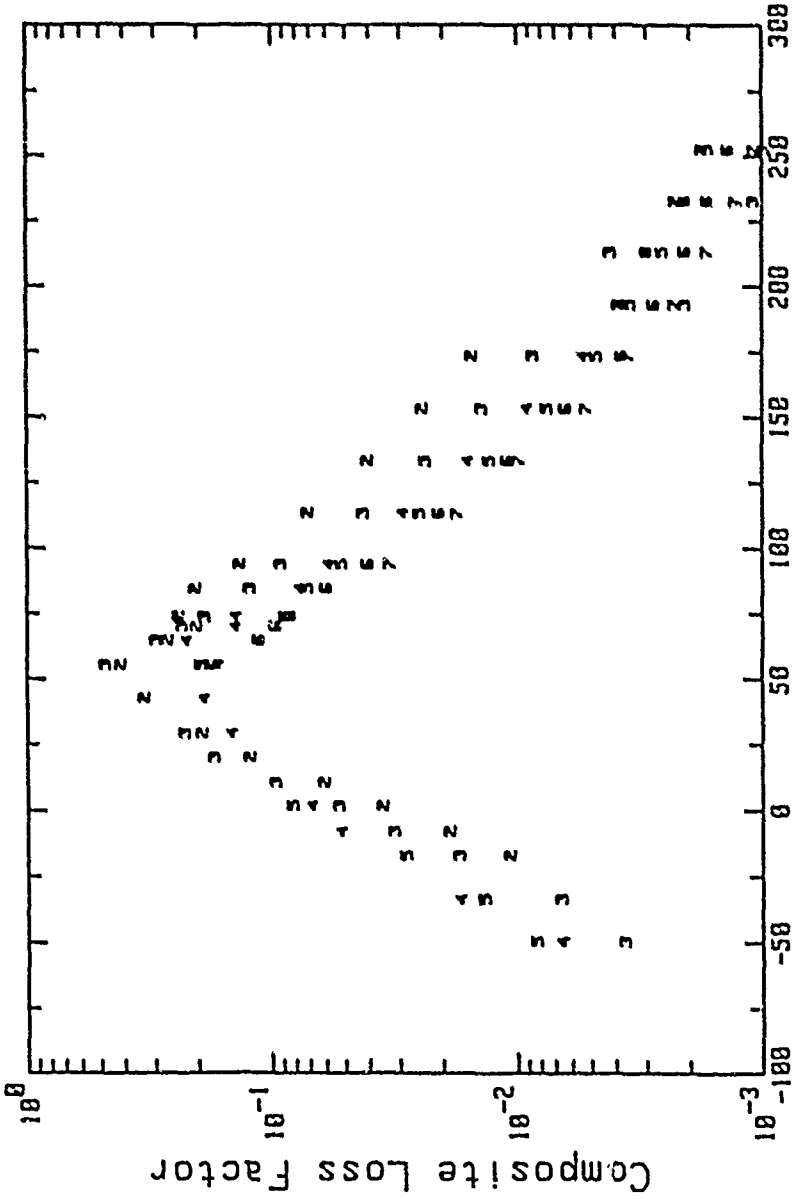


Figure 8: 10" Sandwich Beam - Variation of the Composite Beam Loss Factor with Temperature for the Indicated Modes of 966 Specimen

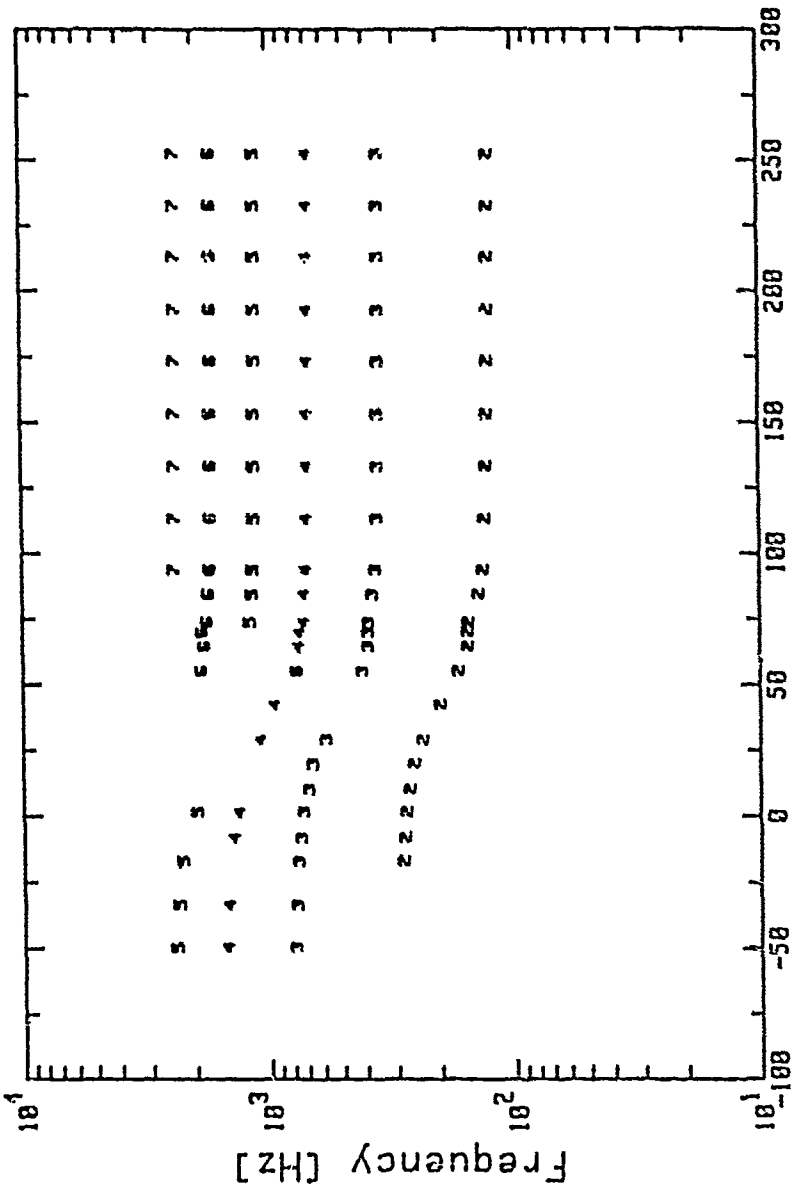


Figure 9: 10" Sandwich Beam - Variation of the Composite Beam Resonance Frequency with Temperature for the Indicated Modes of 966 Specimen

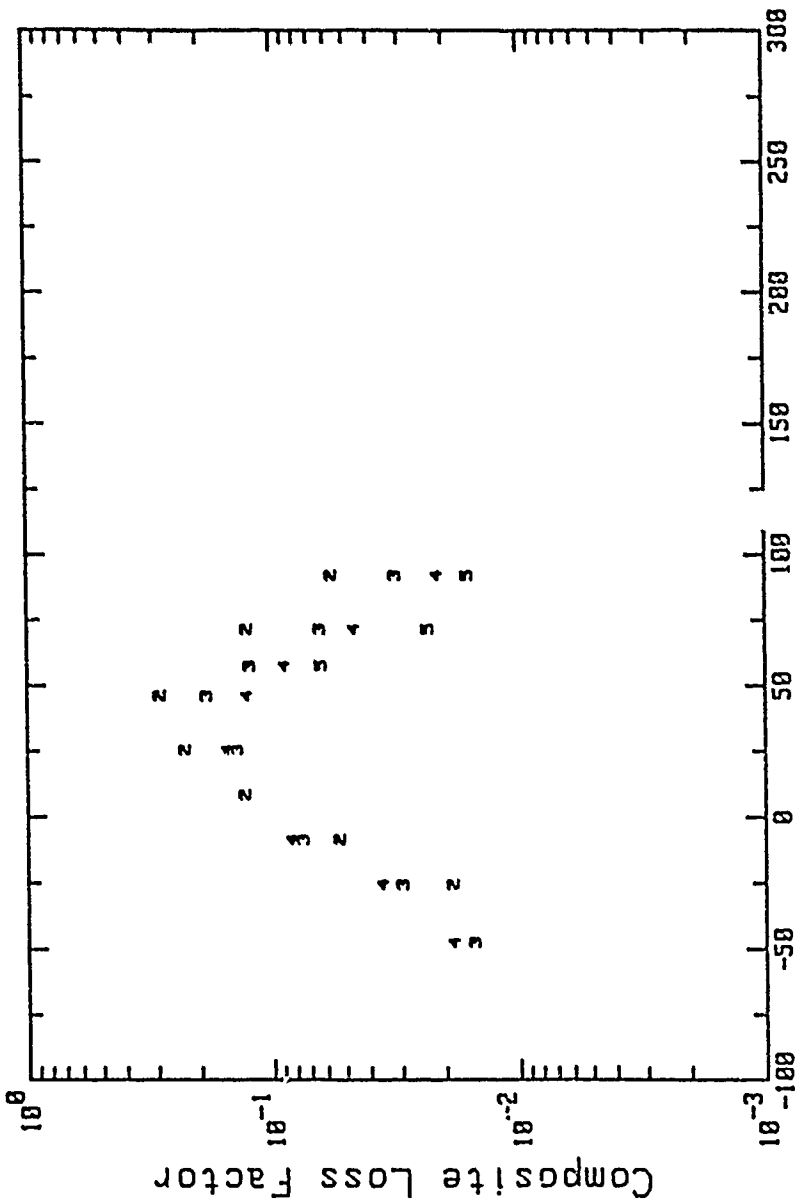


Figure 10: 5" Sandwich Beam - Variation of the Composite Loss Factor with Temperature for the Indicated Modes of the 966 Specimen

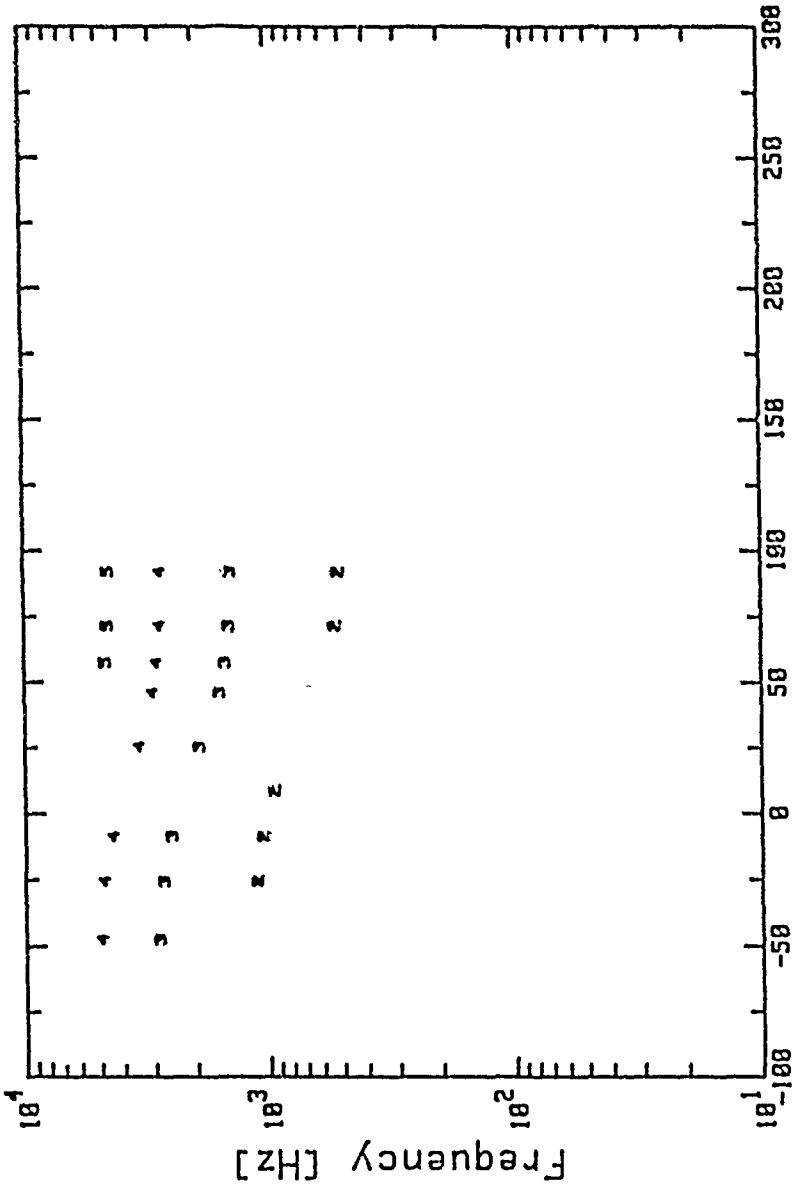


Figure 11: 5" Sandwich Beam - Variation of the Resonance Frequency with Temperature for the Indicated Modes of a 966 Specimen

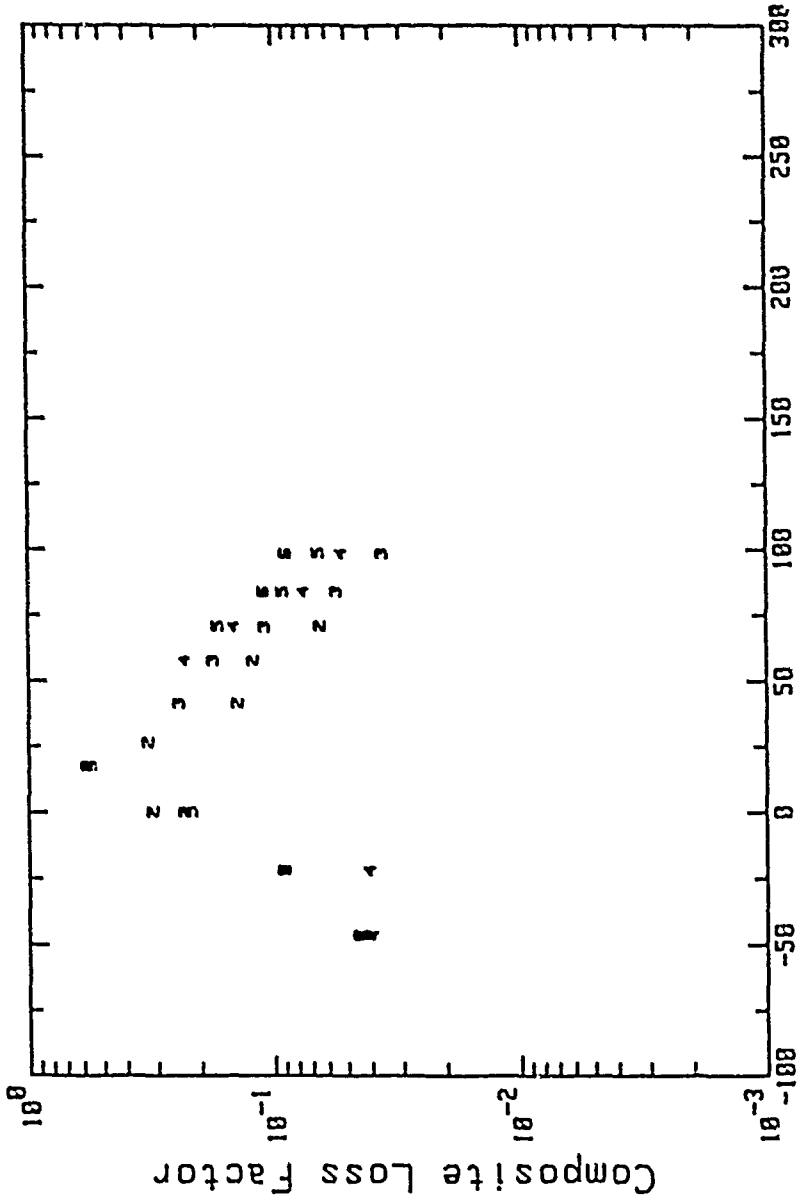


Figure 12: 10° Modified Oberst Beam - Variation of the Composite Loss Factor with Temperature for the Indicated Modes of a 966 Specimen.

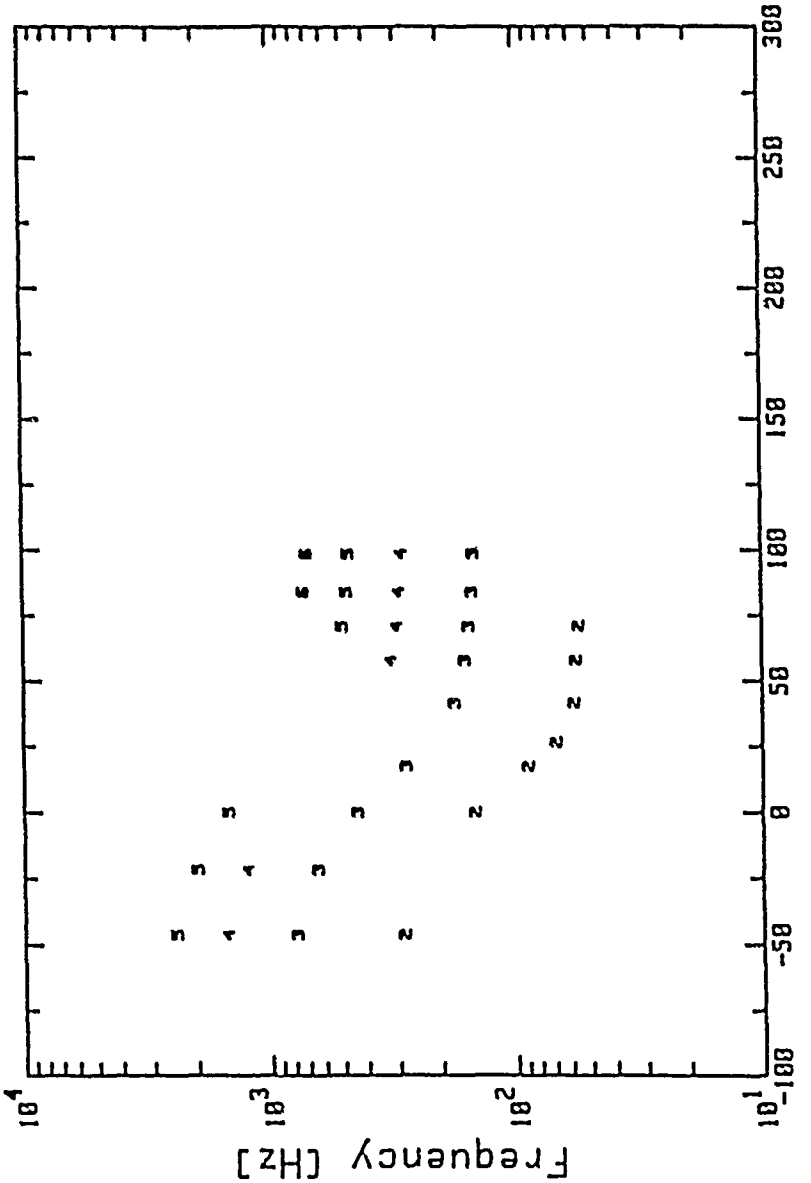


Figure 13: 10" Modified Oberst Beam - Variation of the Resonance Frequency with Temperature for the Indicated Modes of a 966 Specimen

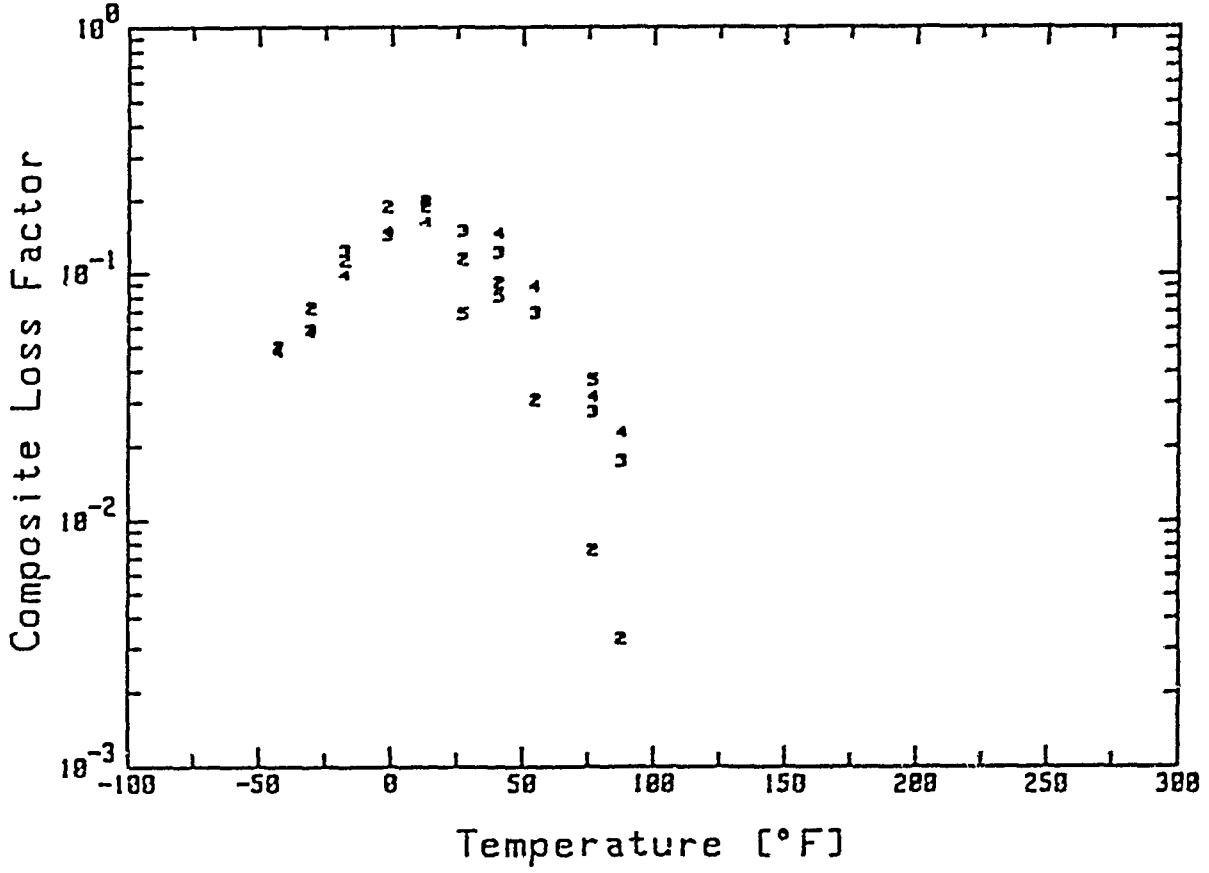


Figure 14: 5" Modified Oberst Beam - Variation of the Composite Beam Loss Factor with Temperature for the Indicated Modes of a 966 Specimen

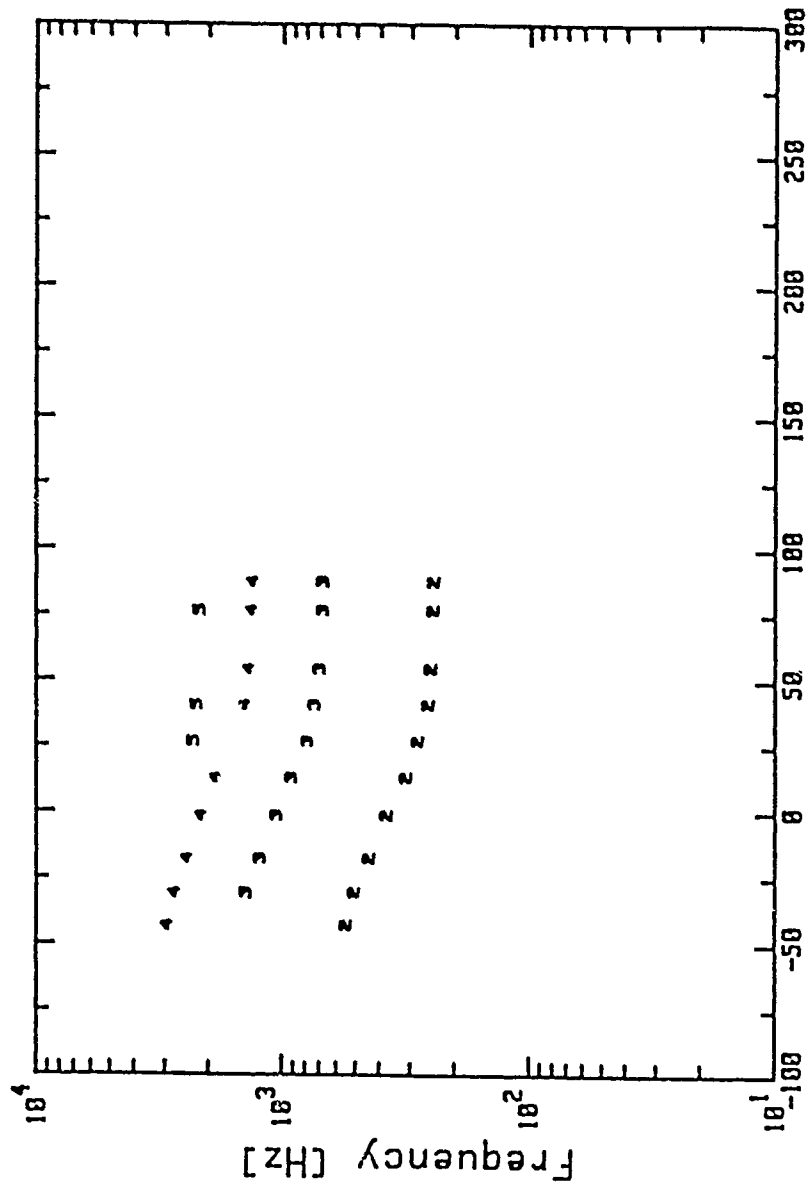


Figure 15: 5" Modified Oberst Beam - Variation of the Resonance Frequency with Temperature for the Indicated Modes of a 966 Specimen

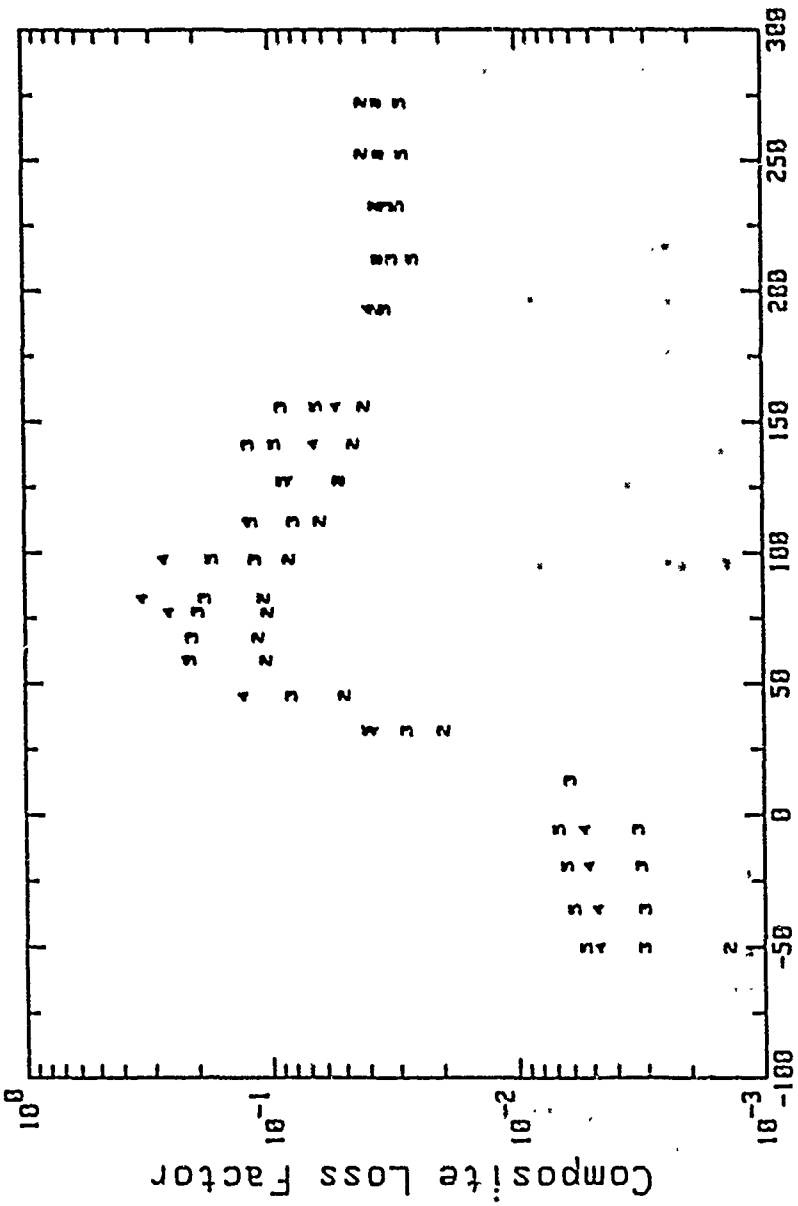


Figure 16: 10" Sandwich Beam - Variation of Composite Beam Loss Factor with Temperature for the Indicated Modes of an AF-32 Specimen

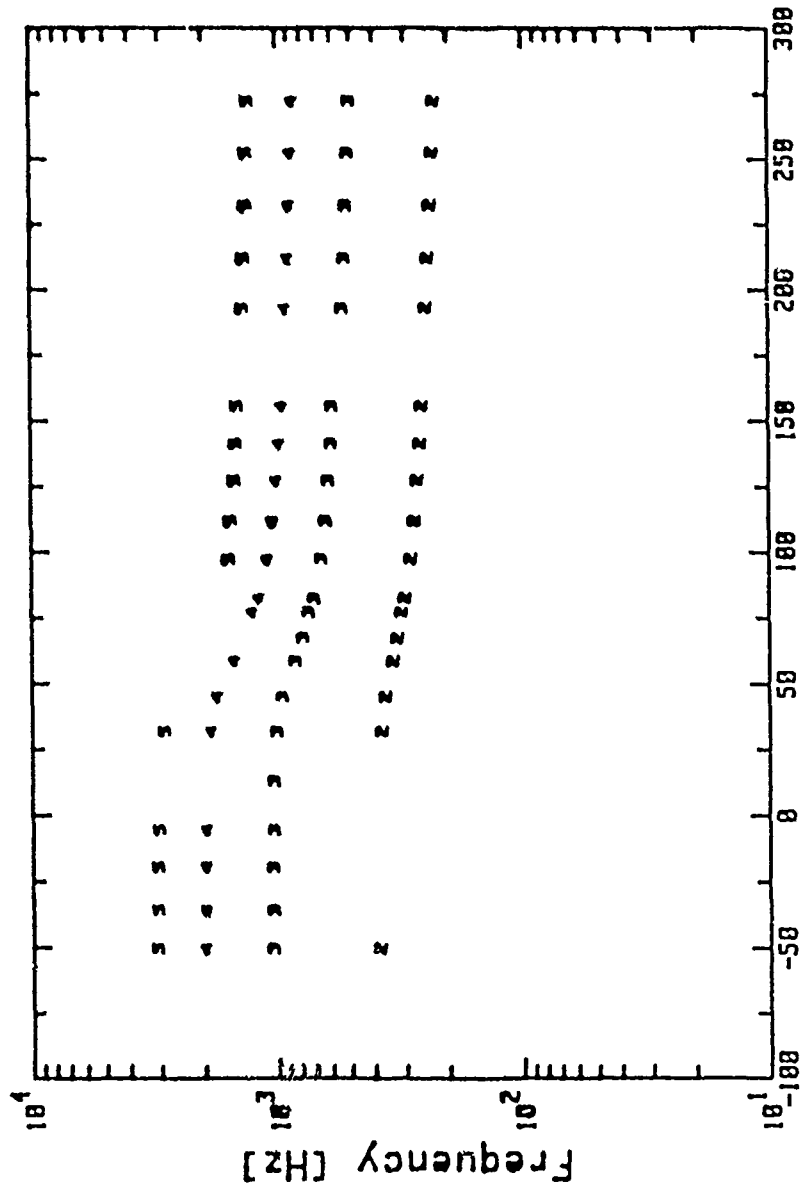


Figure 17: 10" Sandwich Beam - Variation of Resonant Frequency with Temperature for the Indicated Modes of an AF-32 Specimen

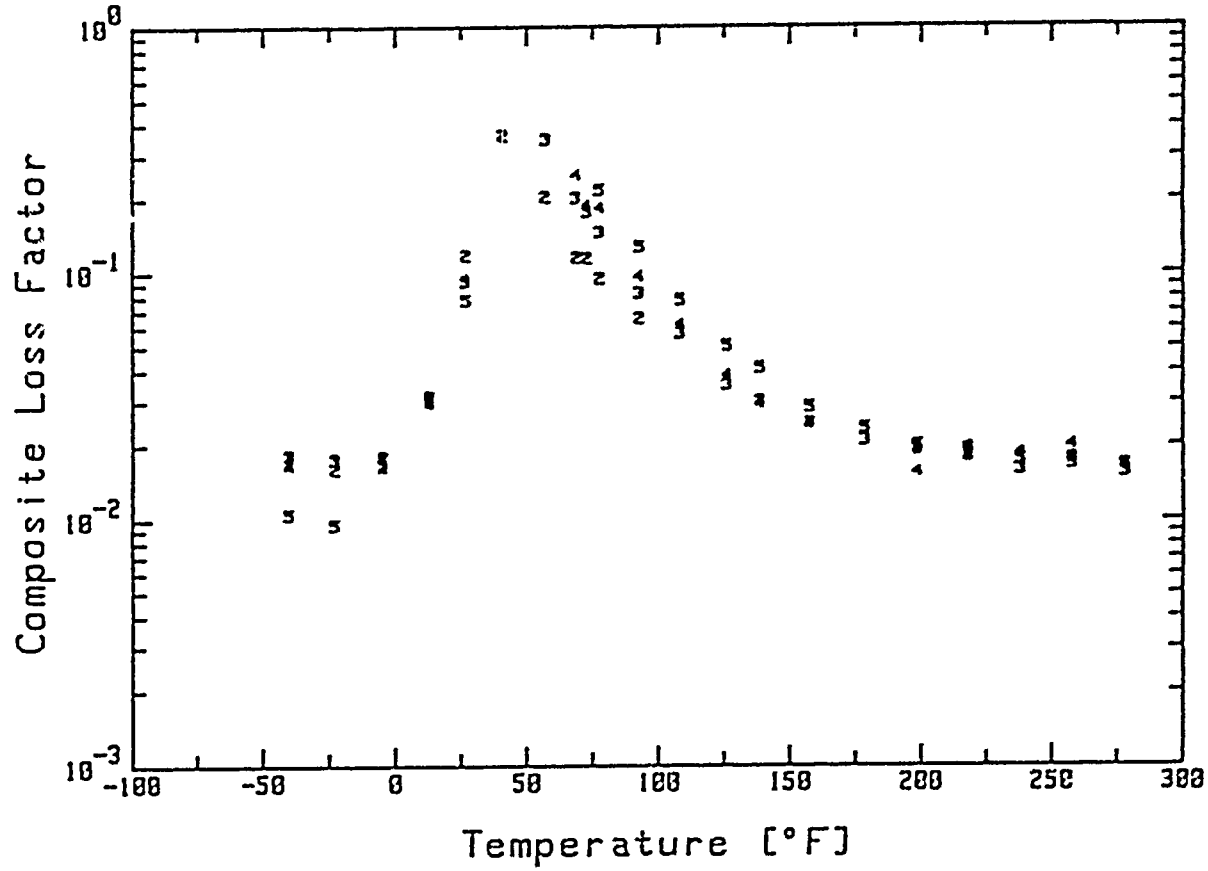


Figure 18: 10" Modified Oberst Beam - Variation of Composite Loss Fator with Temperature for the Indicated Modes of and AF-32 Specimen

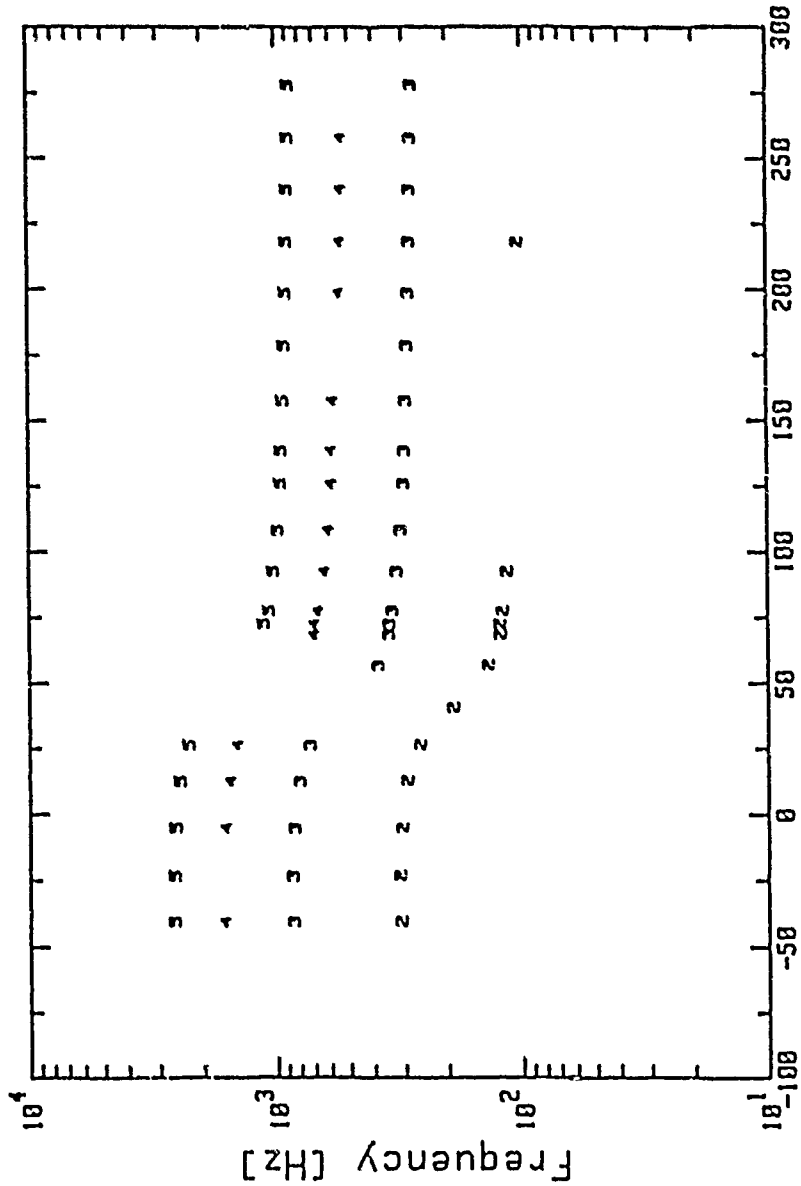


Figure 19: 10° Modified Oberst Beam - Variation of Resonant Frequency with Temperature for the Indicated Modes of an AF-32 Specimen

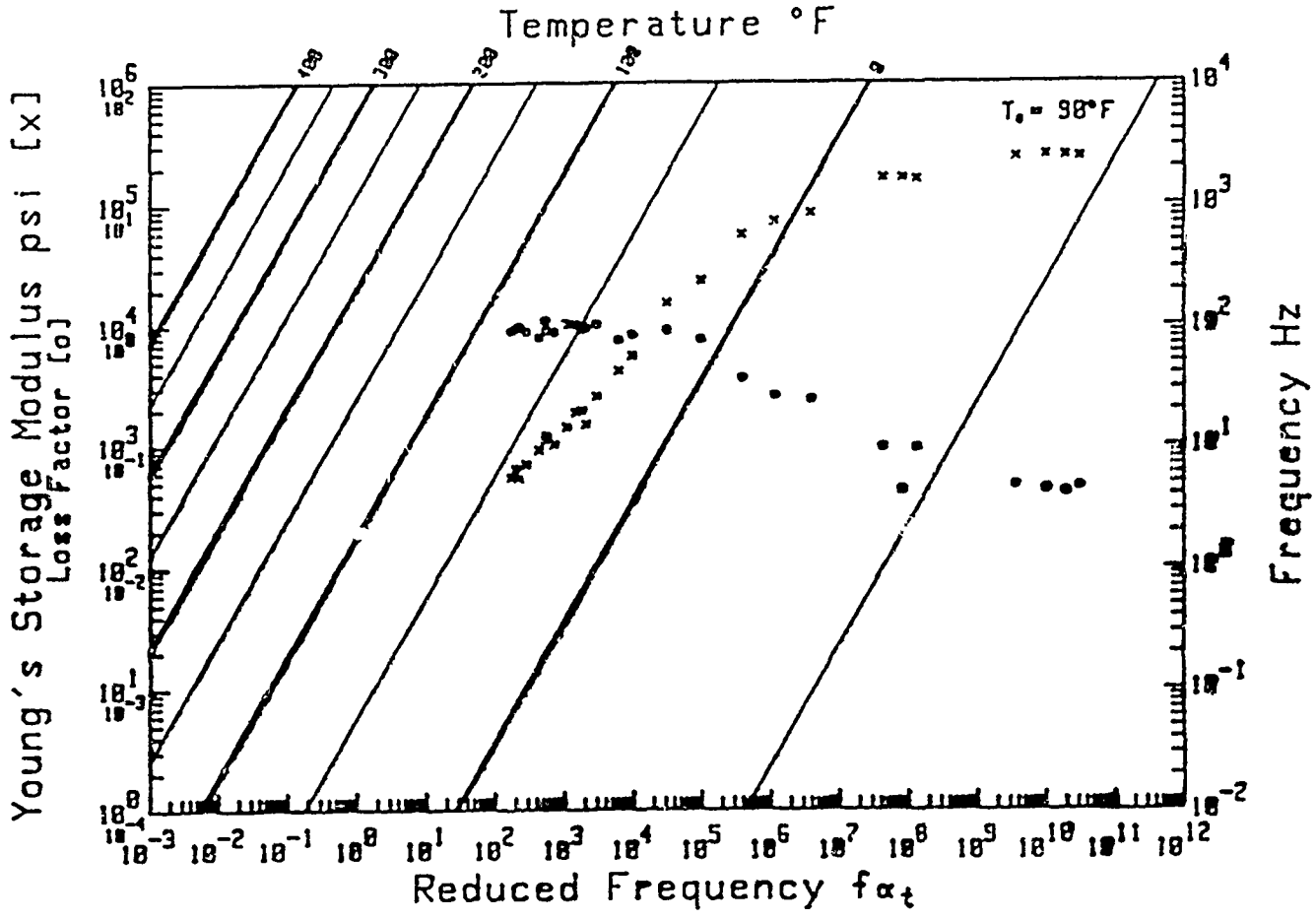


Figure 20: 10" Modified Oberst Beam - Reduced Frequency Nomogram for 966

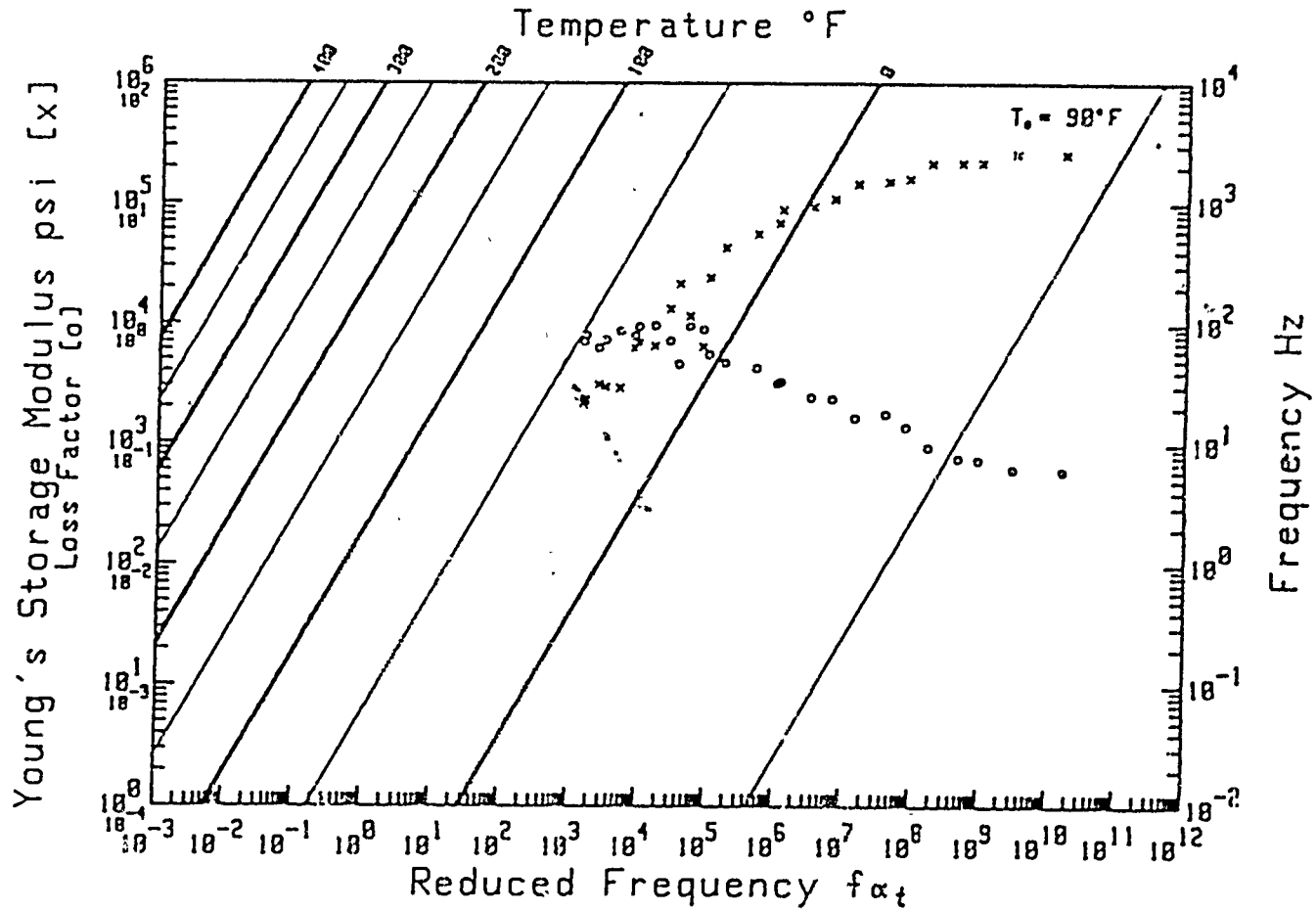


Figure 21: 5" Modified Oberst Beam - Reduced Frequency Nomogram for 966

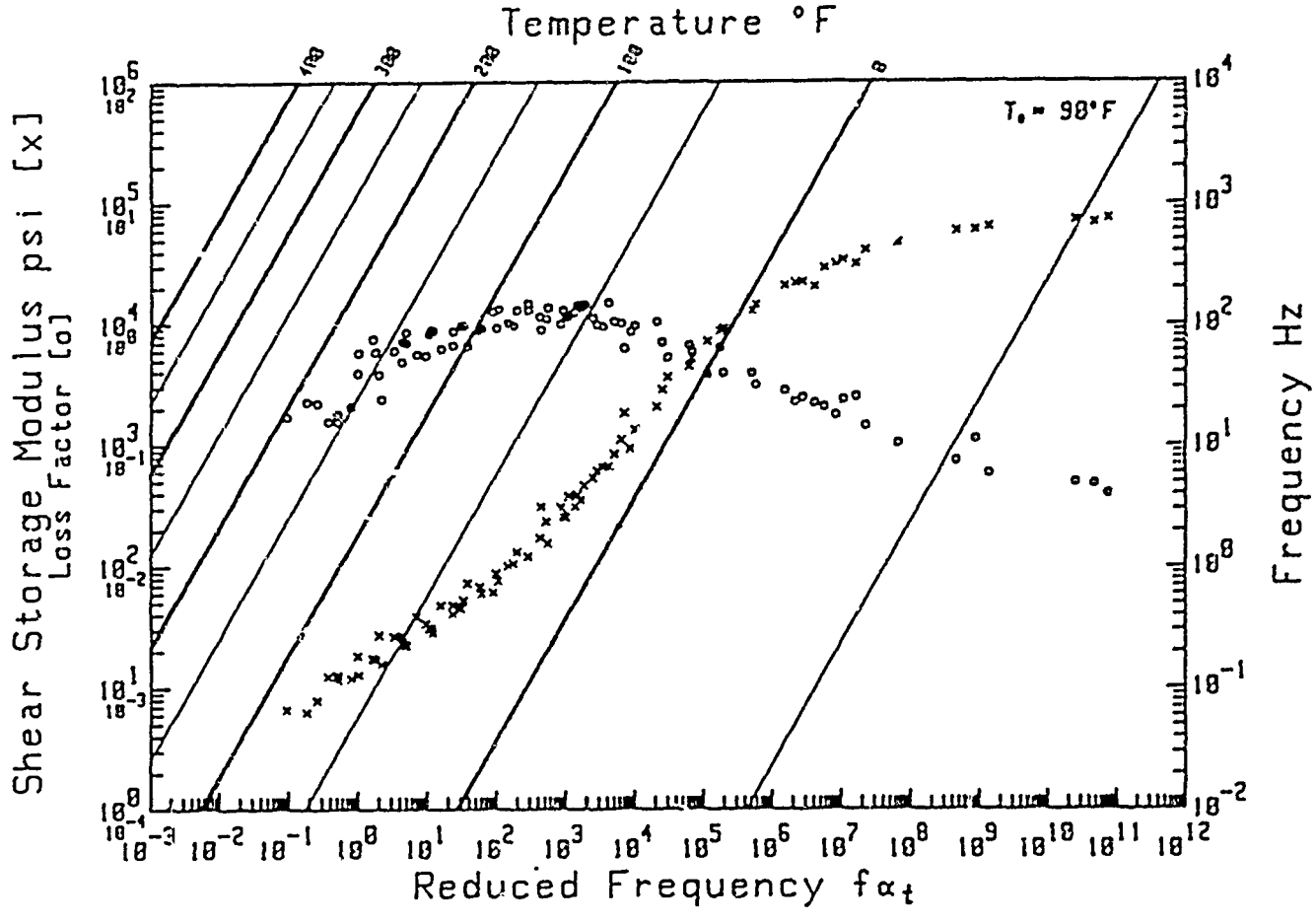


Figure 22: 10" Sandwich Beam - Reduced Frequency Nomogram for 966

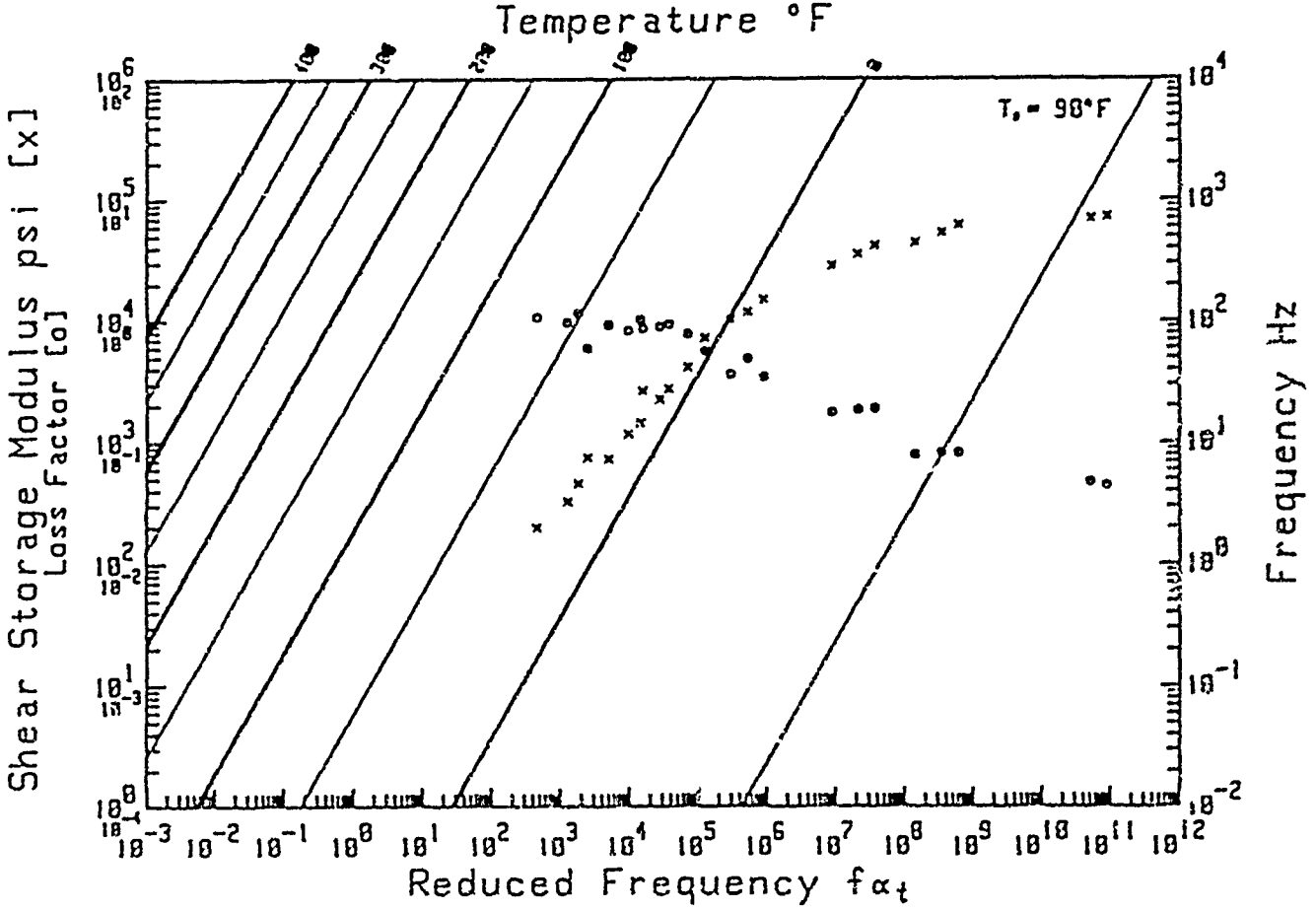


Figure 23: 5° Sandwich Beam - Reduced Frequency Nomogram for 966

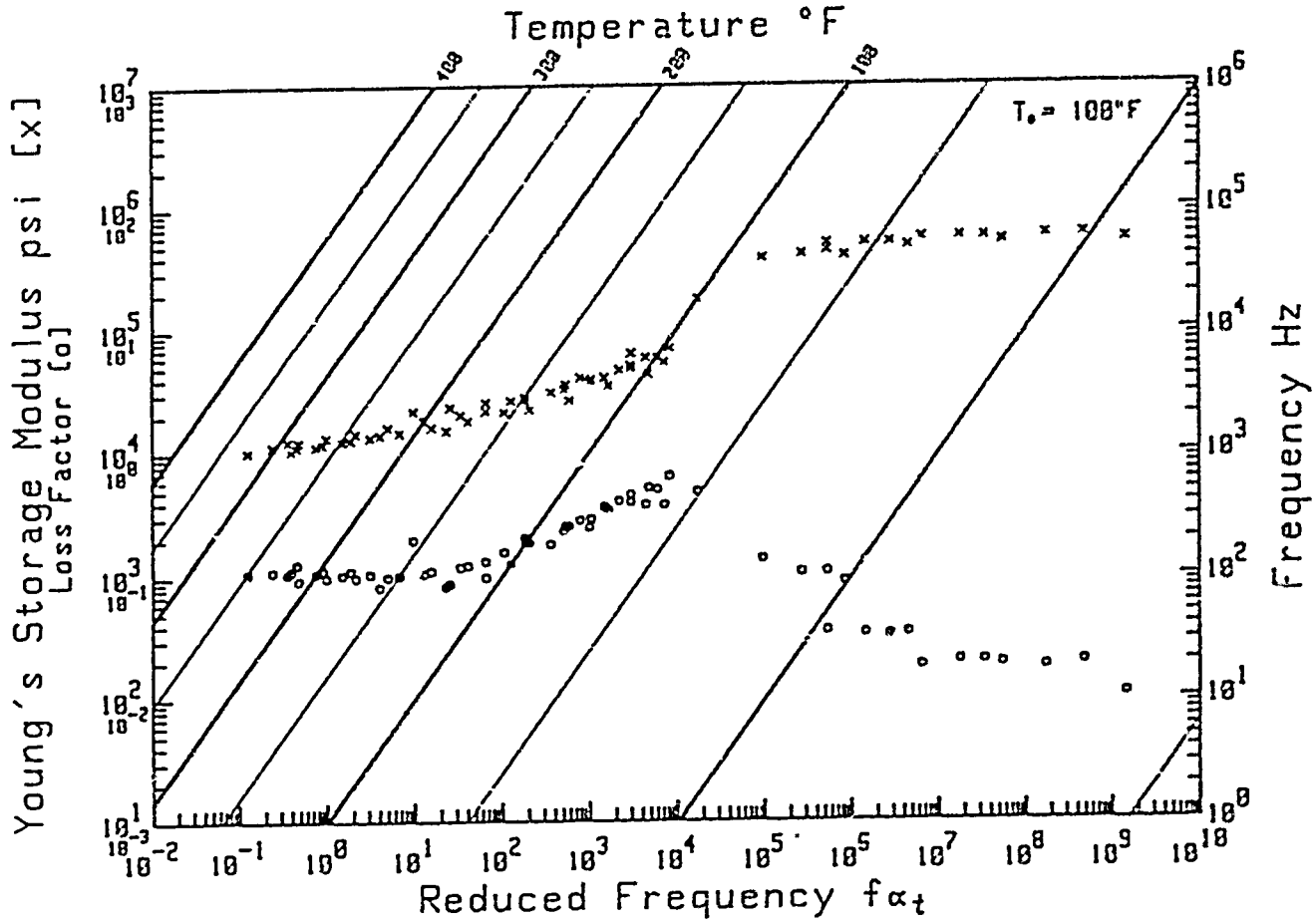


Figure 24: 10" Modified Oberst Beam - Reduced Frequency Nomogram for AF-32

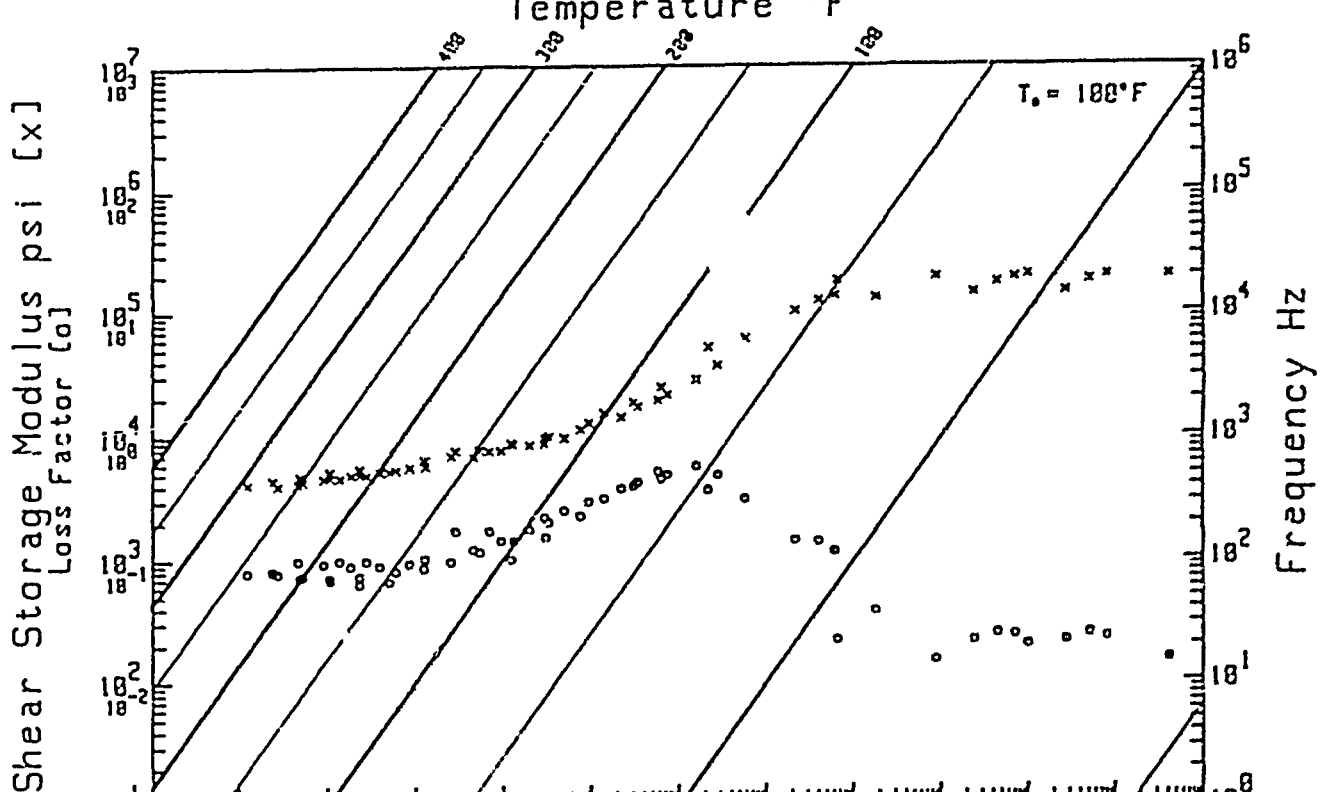
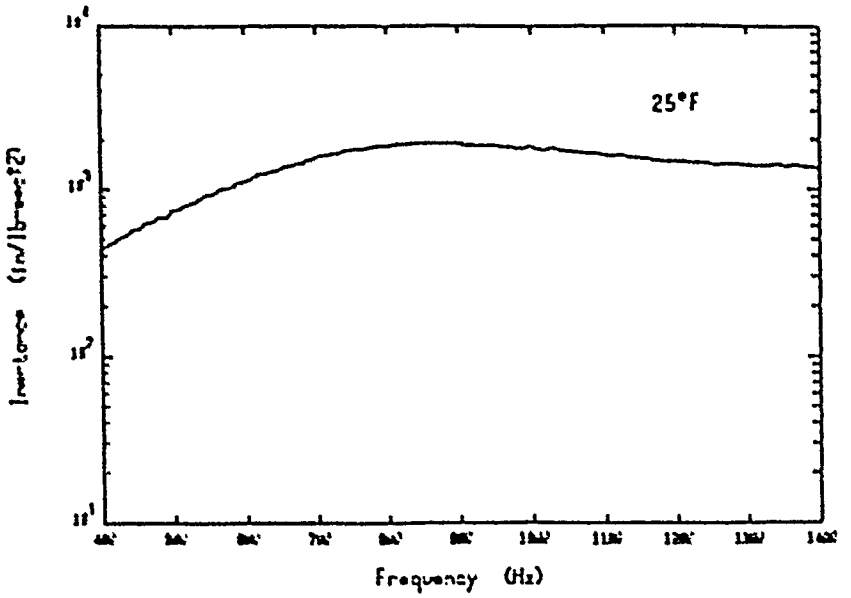


Figure 25: 10" Sandwich Beam - Reduced Frequency Nomogram for AF-32



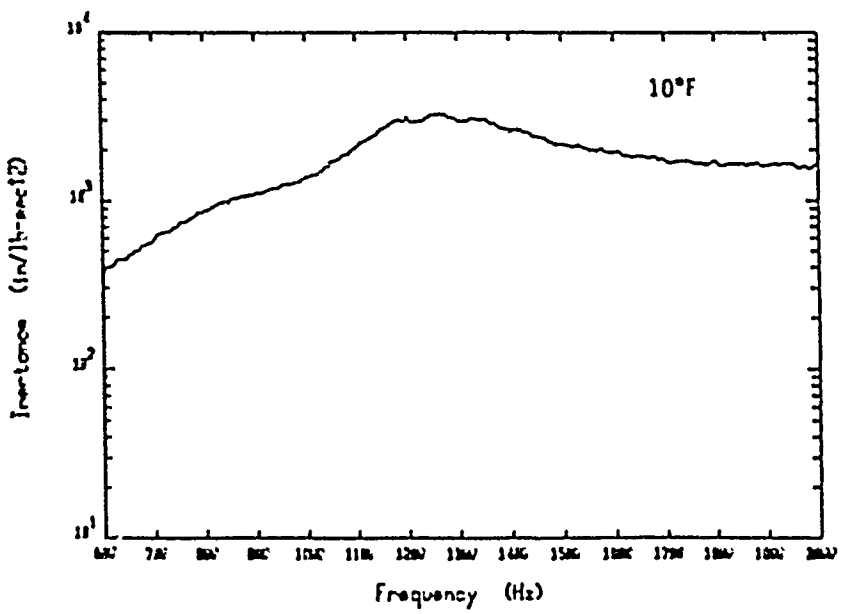


Figure 26:
Tension-Compression: Frequency Response Measurements Used in the Resonance and Impedance Techniques for 3M 966

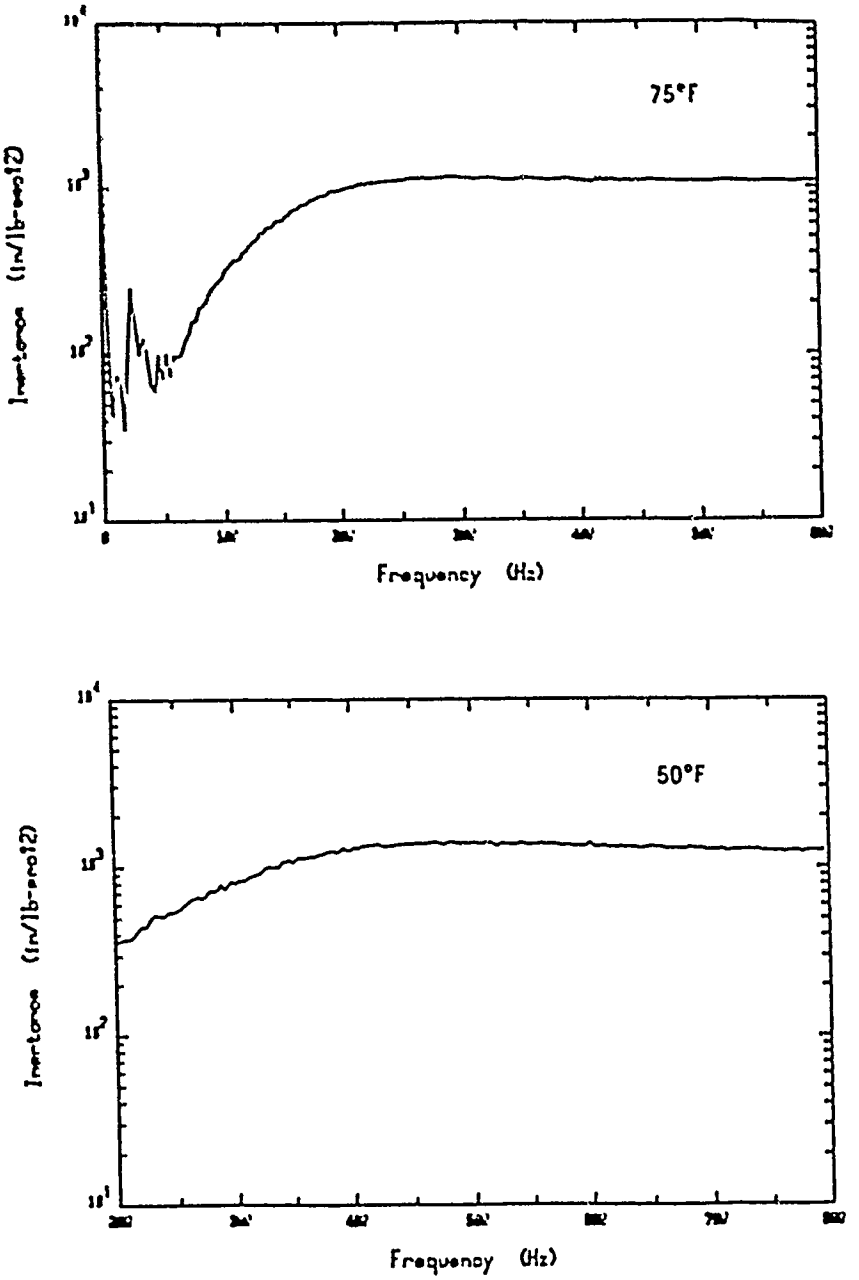


Figure 27:
Tension-Compression: Frequency Response Measurements Used in the Resonance and Impedance Techniques for 3M 966

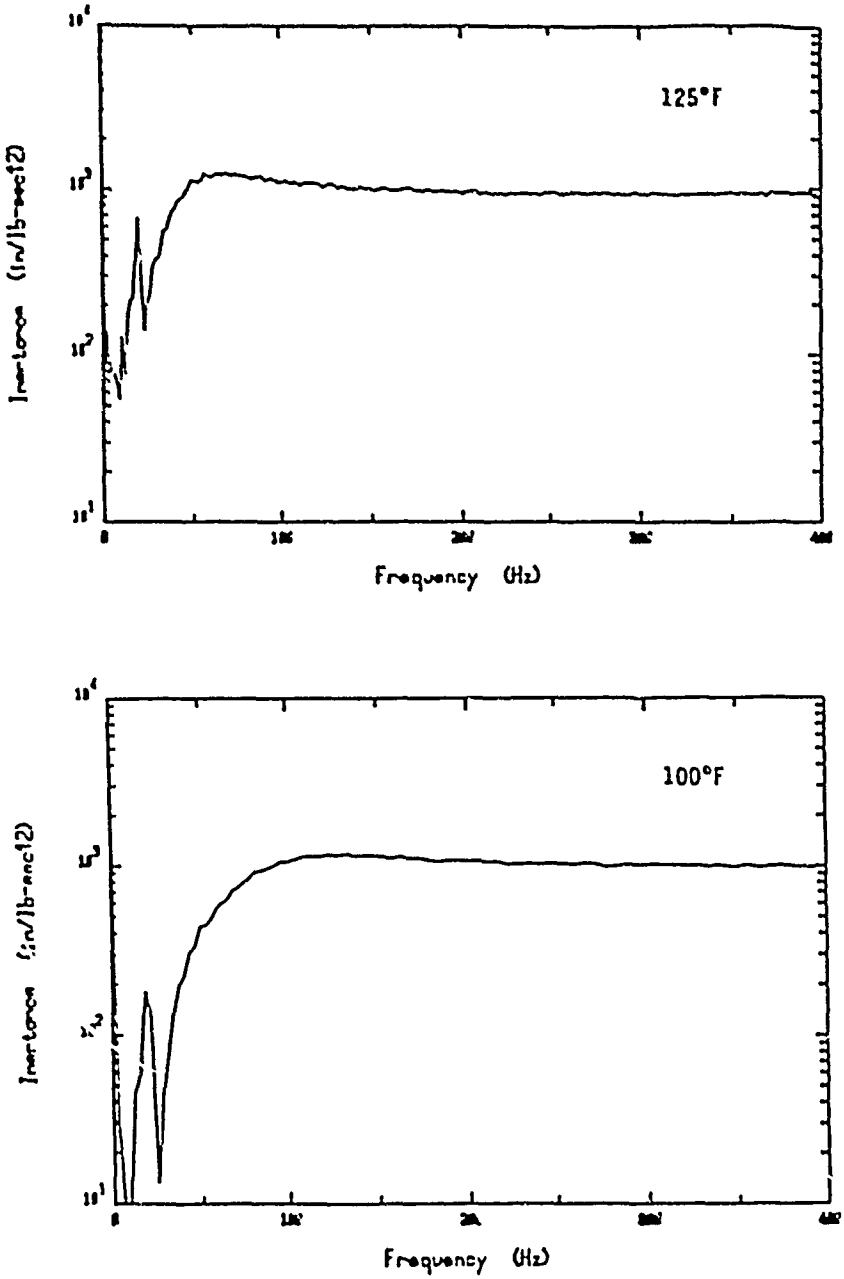
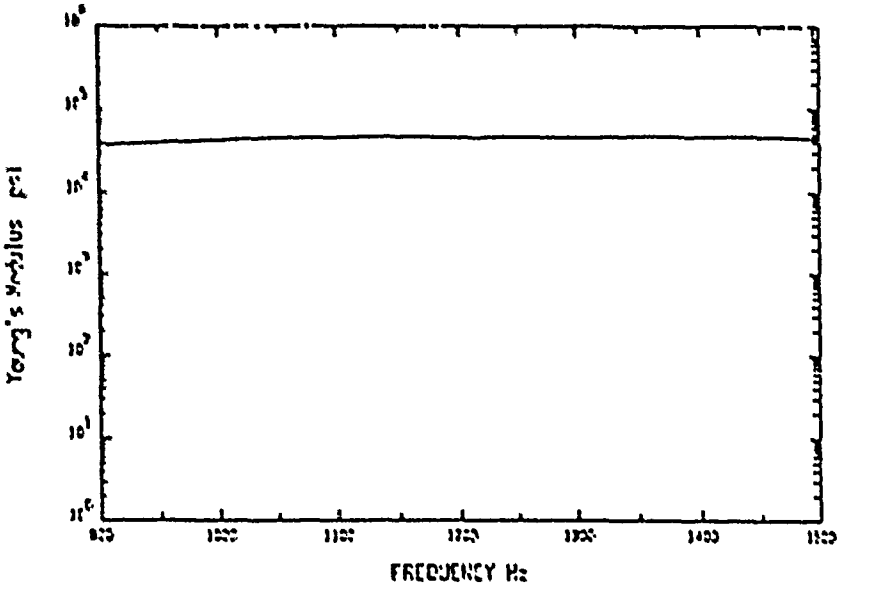


Figure 28:
Tension-Compression: Frequency Response Measurements Used in the Resonance and Impedance Techniques for 3M 966



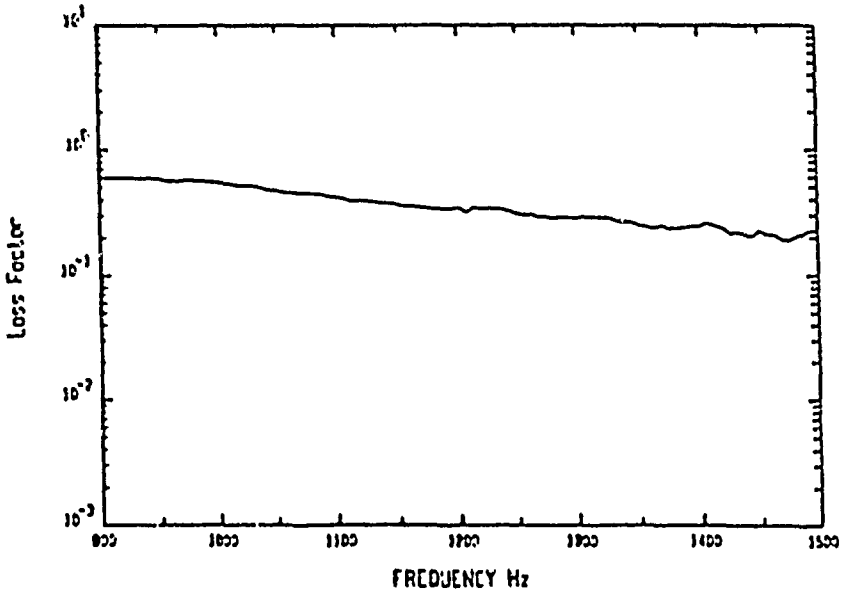
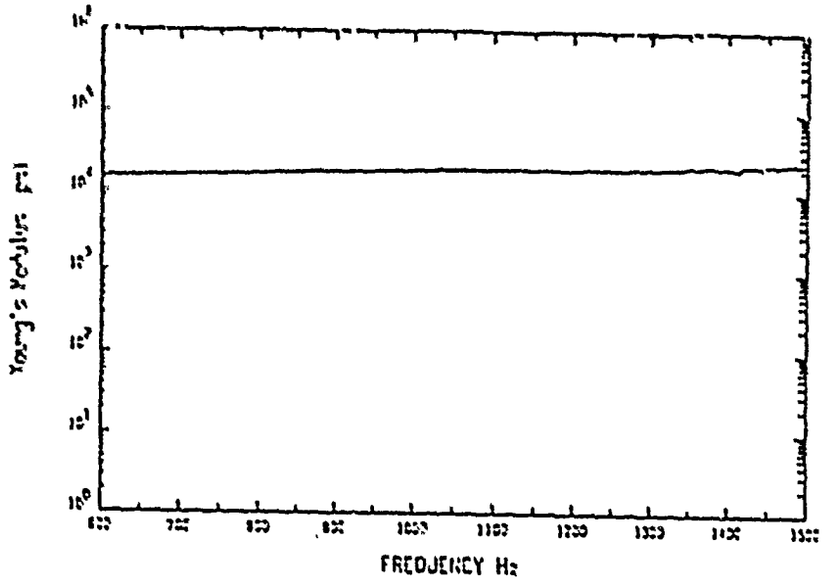


Figure 29:
Tension-Compression: Material Properties at 10°F Using the Impedance Technique for 3M 966



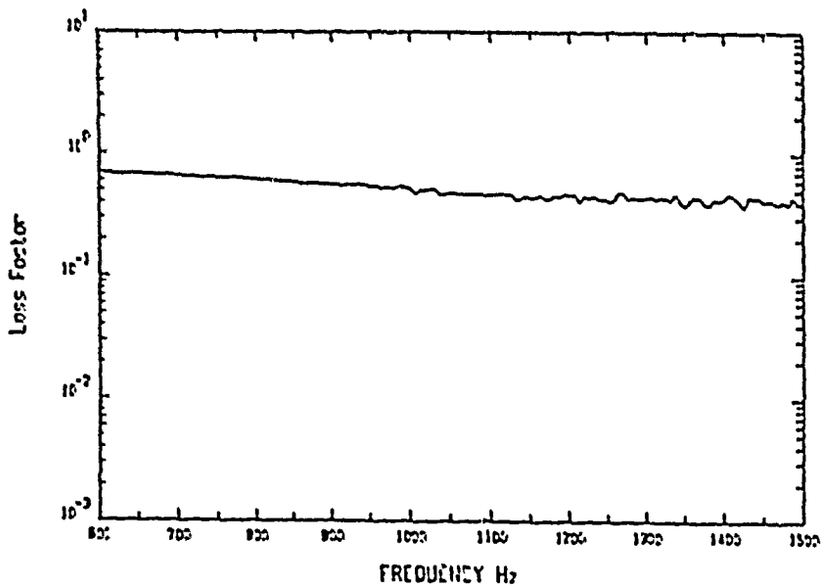
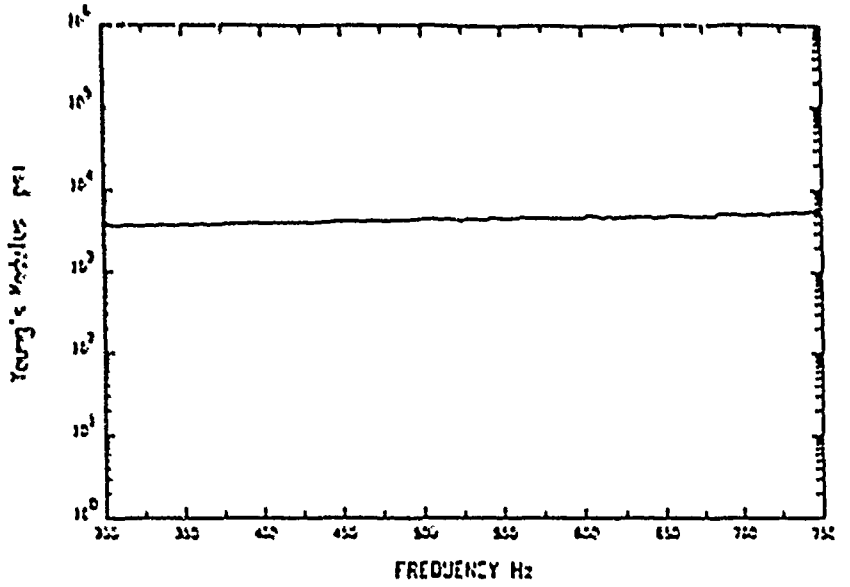


Figure 30:
Tension-Compression: Material Properties at 25°F Using the Impedance Technique for 3M 966



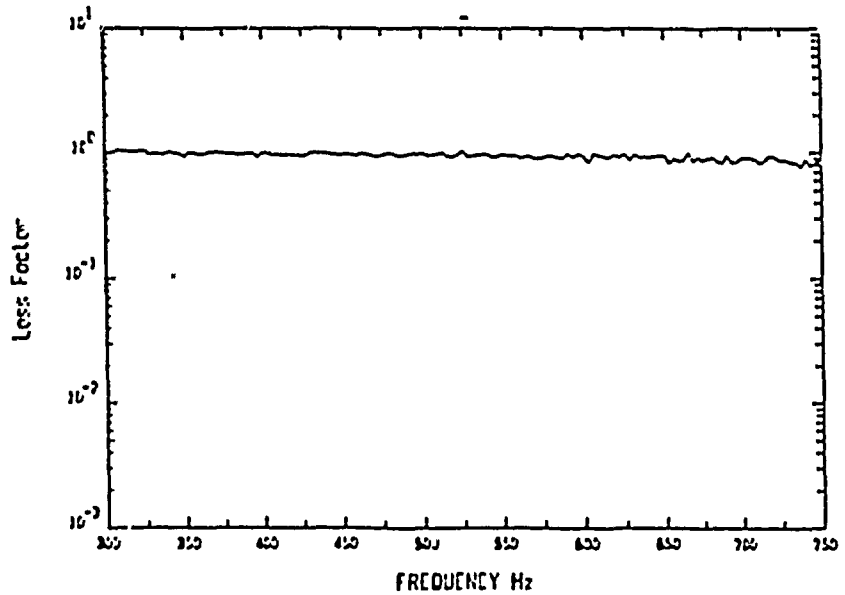
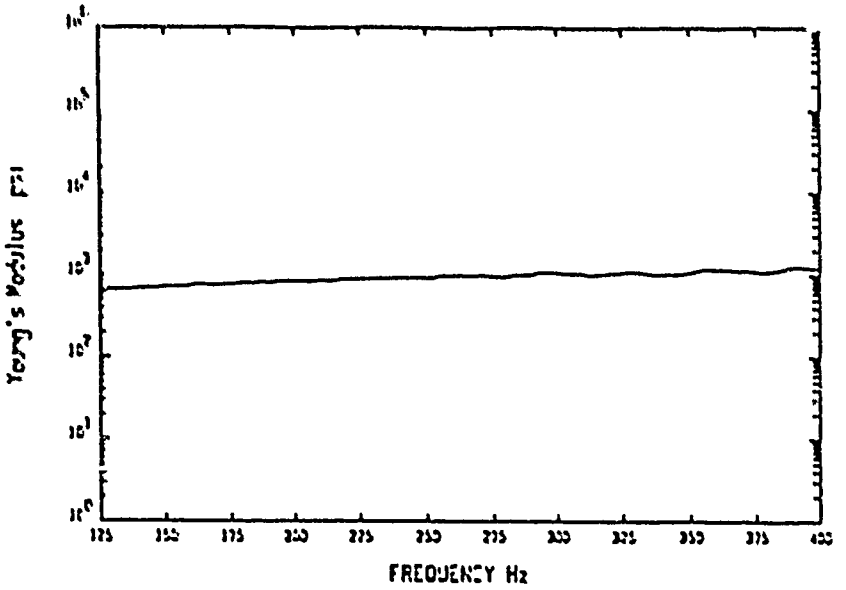


Figure 31:
Tension-Compression: Material Properties at 50°F Using the Impedance Technique for 3M 966



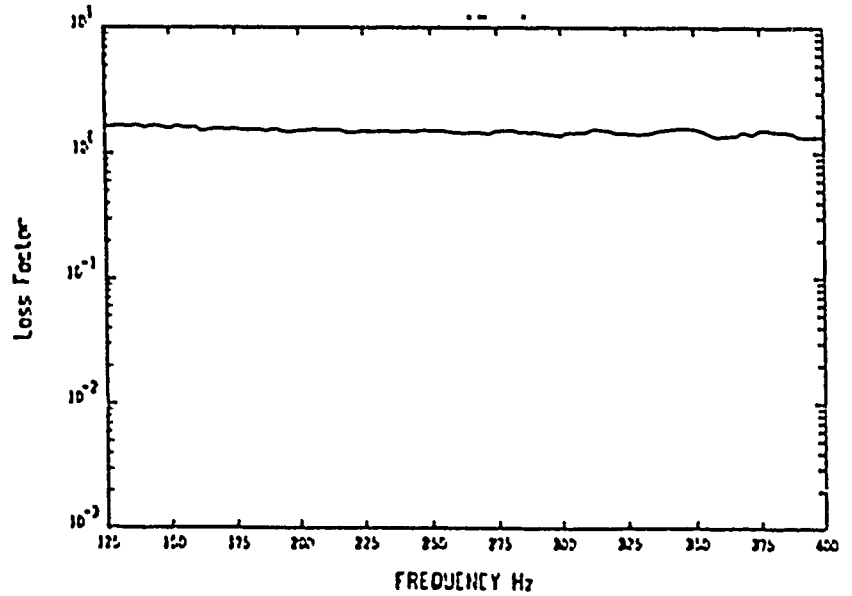
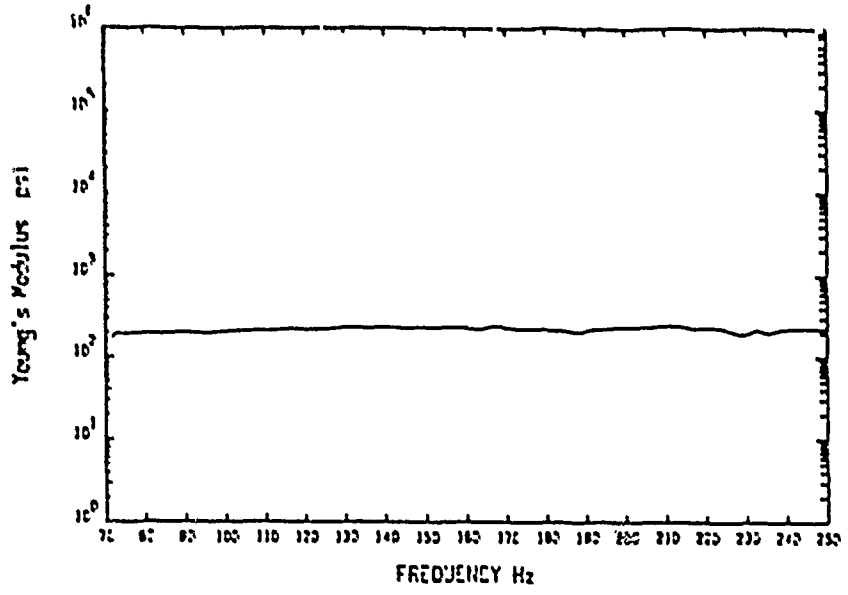


Figure 32:
Tension-Compression: Material Properties at 75°F Using the Impedance Technique for 3M 966



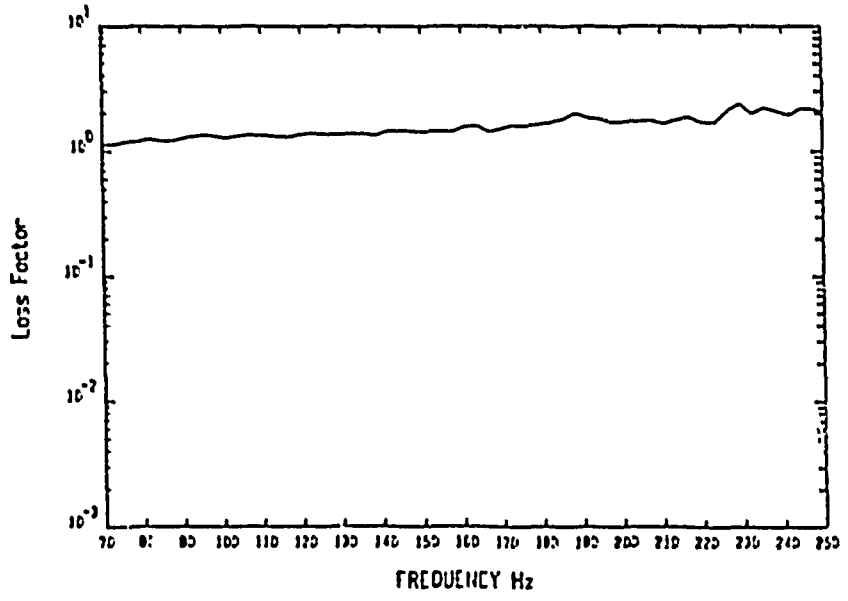
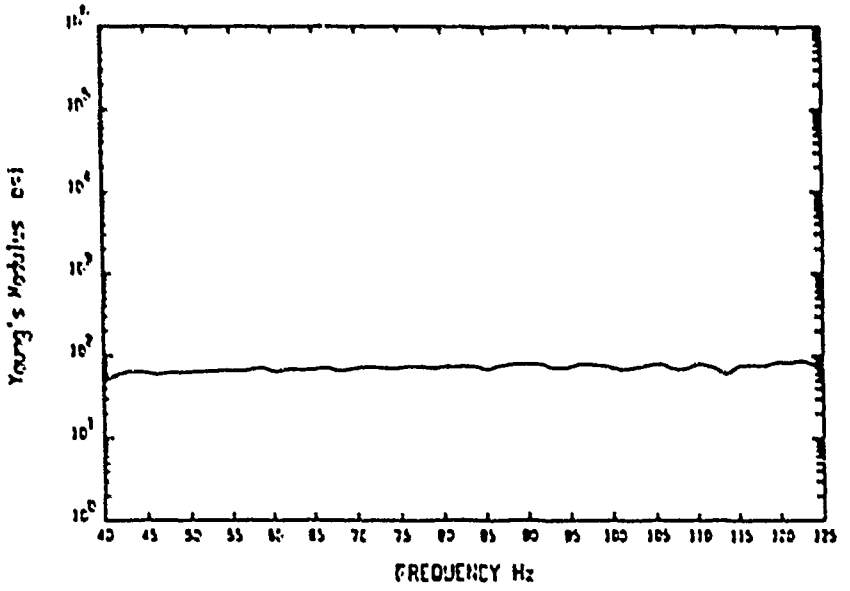


Figure 33:
Tension-Compression: Material Properties at 100°F Using the Impedance Technique for 3M 966



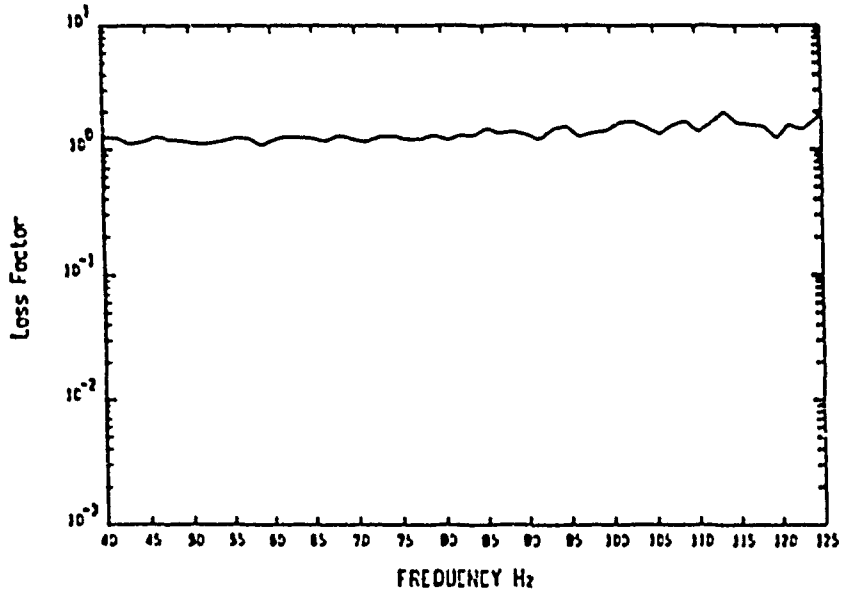


Figure 34:
Tension-Compression: Material Properties at 125°F Using the Impedance Technique for 3M 966

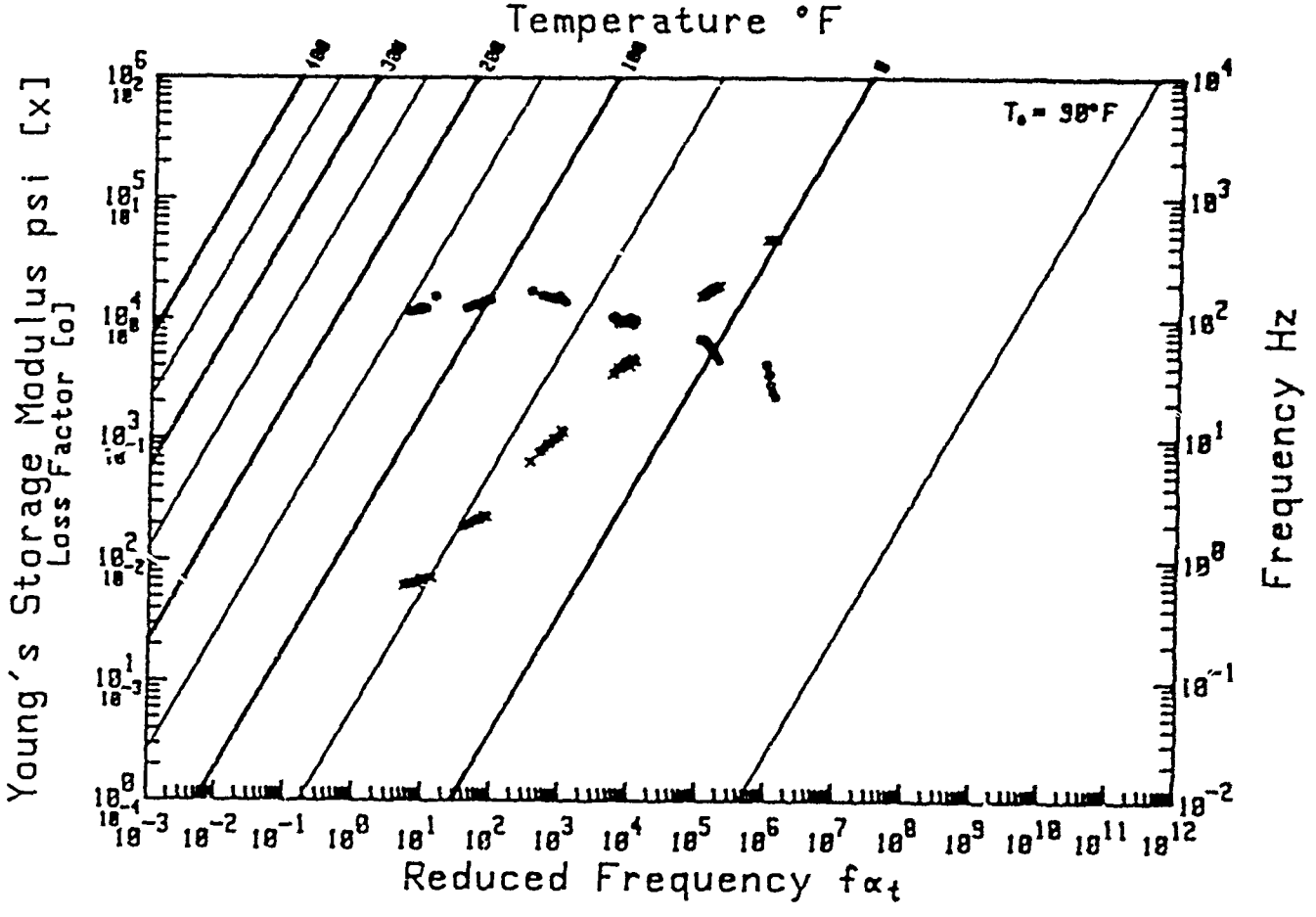


Figure 35: Reduced Frequency Nomogram for 966 using the Tension/Compression Impedance Technique

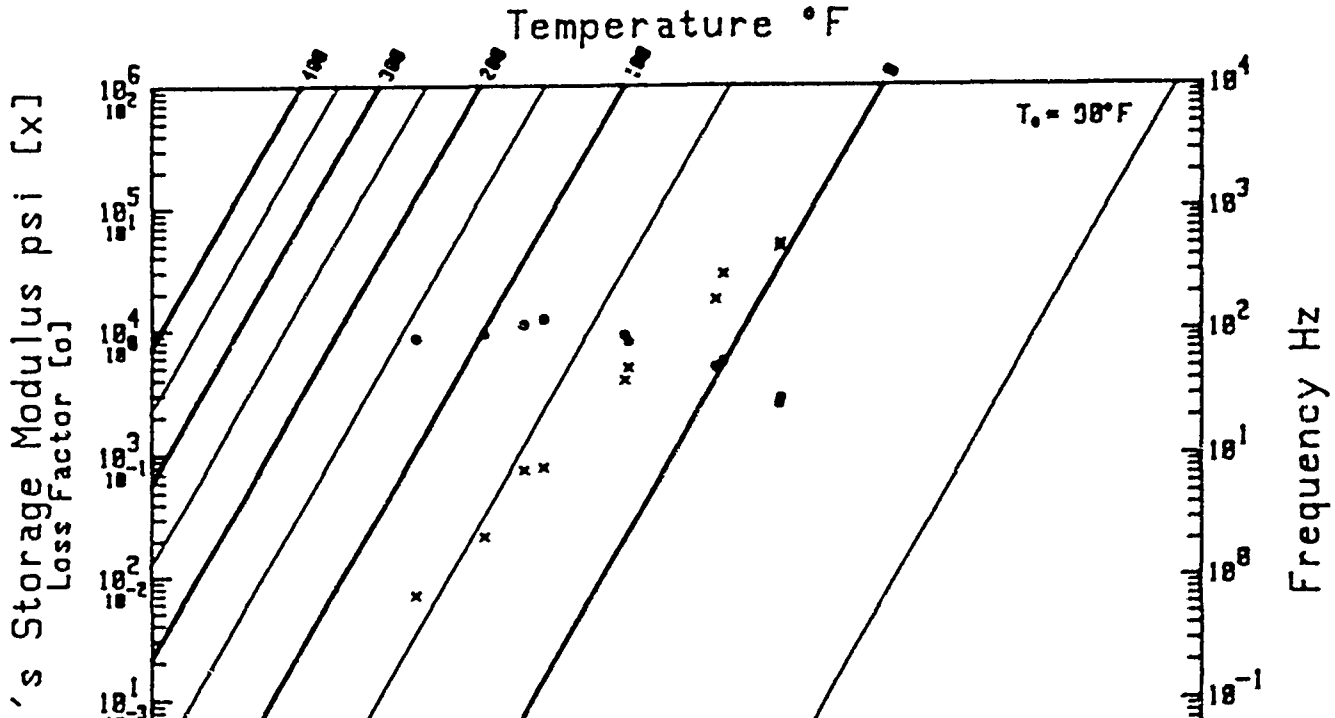
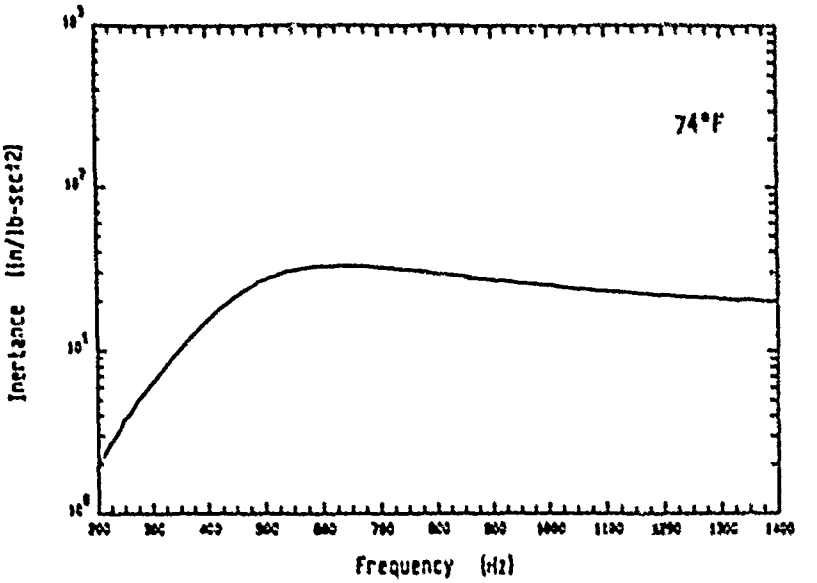


Figure 36: Reduced Frequency Nomogram for 966 using the Tension/Compression Resonance Technique



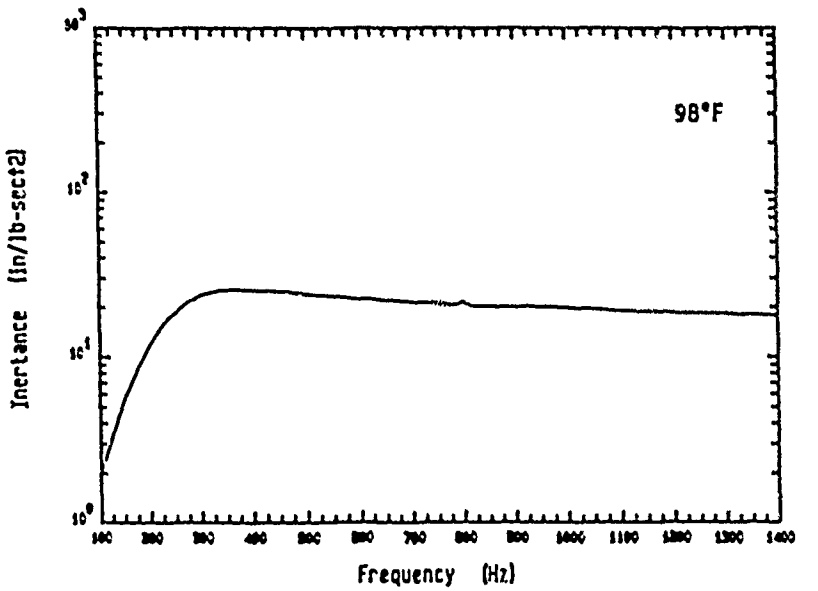


Figure 37: Frequency Response Measurements used in the Shear Impedance Technique for 3M Co. 966

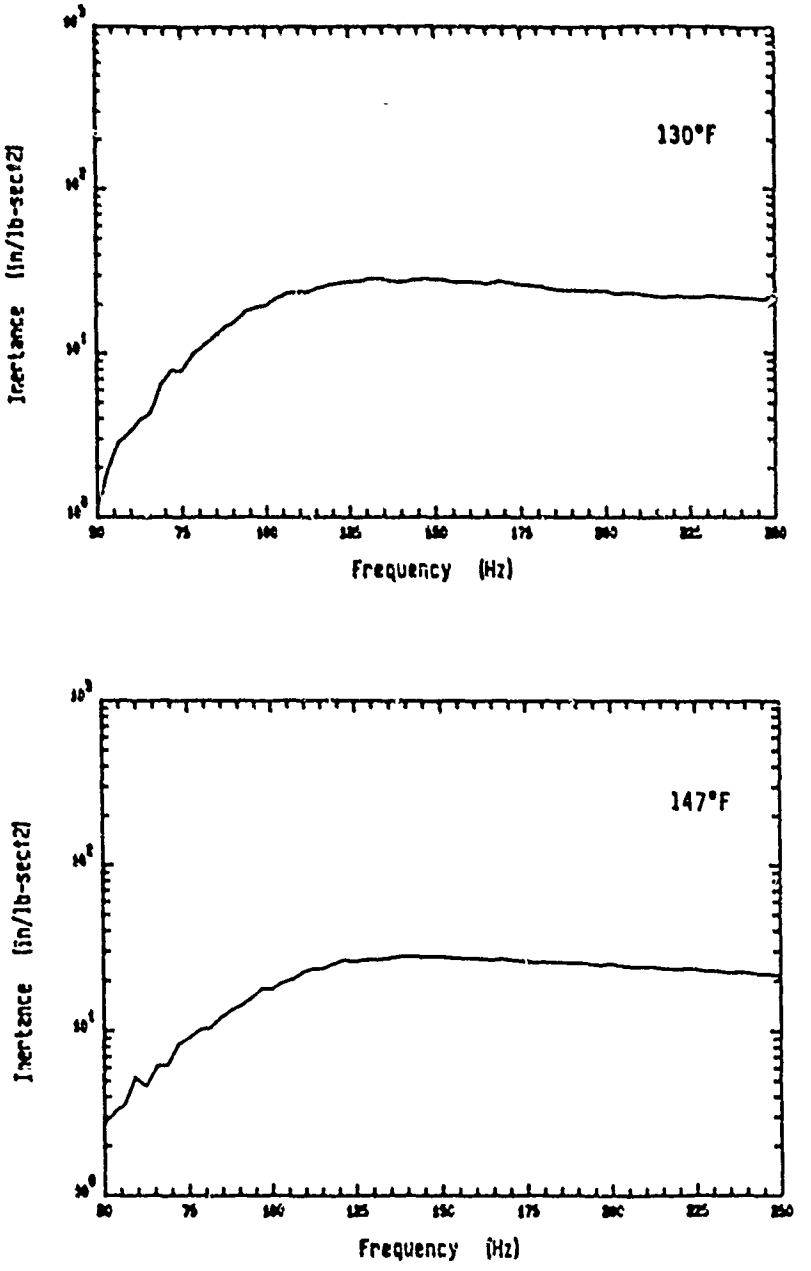


Figure 38: Frequency Response Measurements used in the Shear Impedance Technique for 3M Co. 966

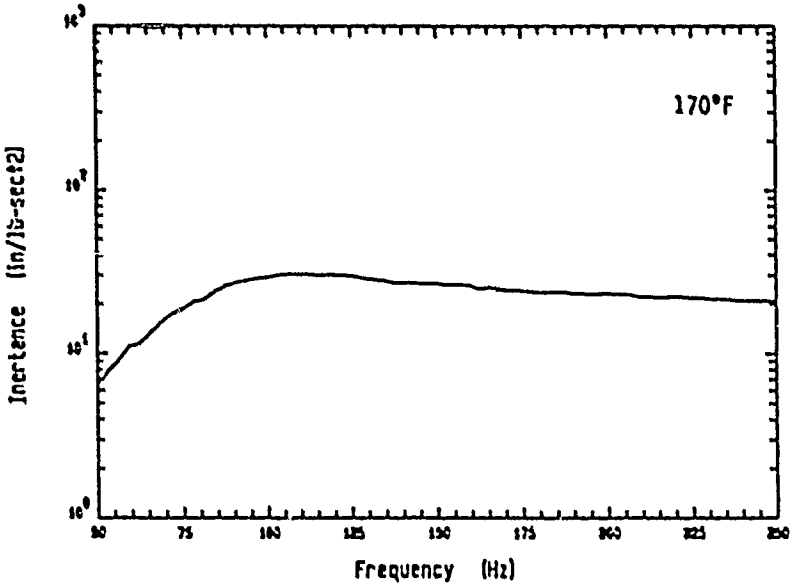
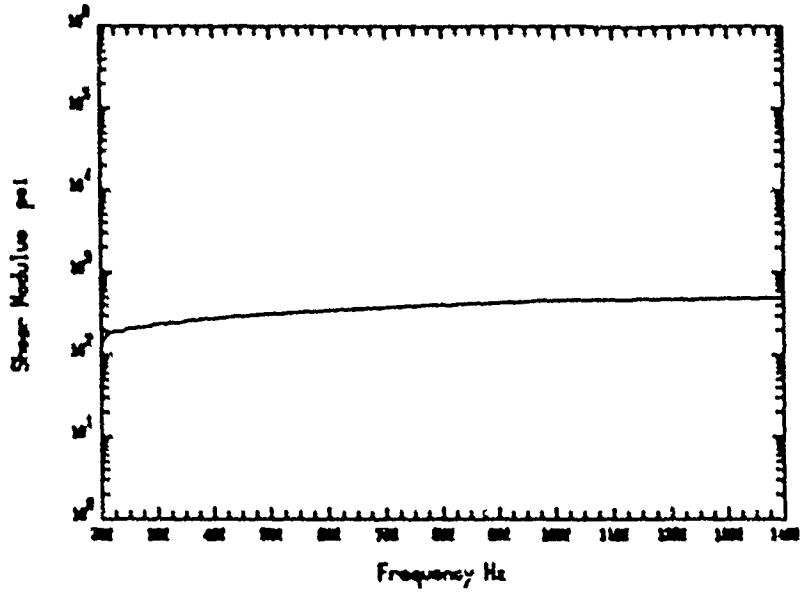


Figure 39: Frequency Response Measurements used in the Shear Impedance Technique for 966



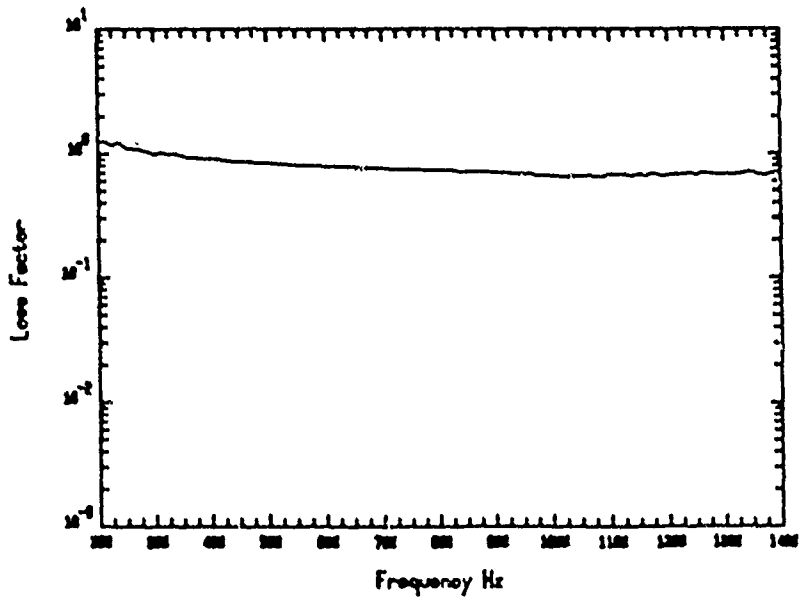
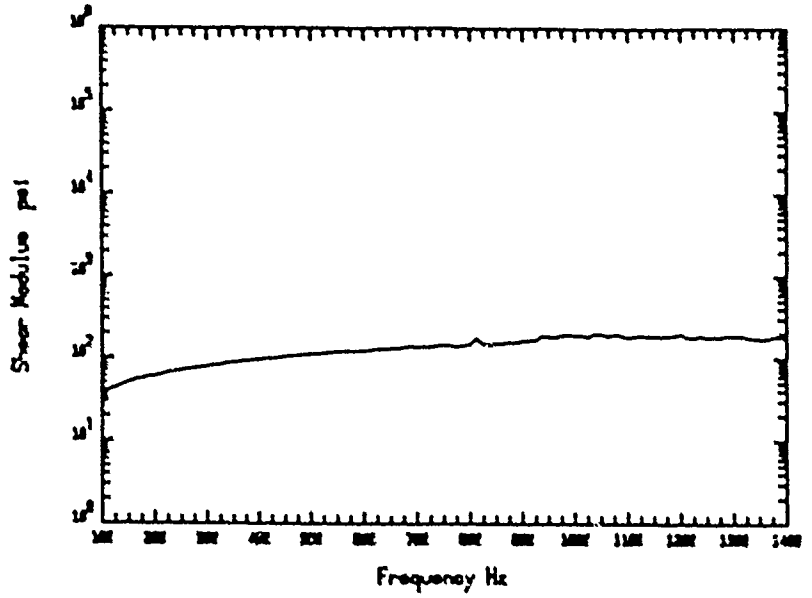


Figure 40: Material Properties at 74°F using the Shear Impedance Technique for 966



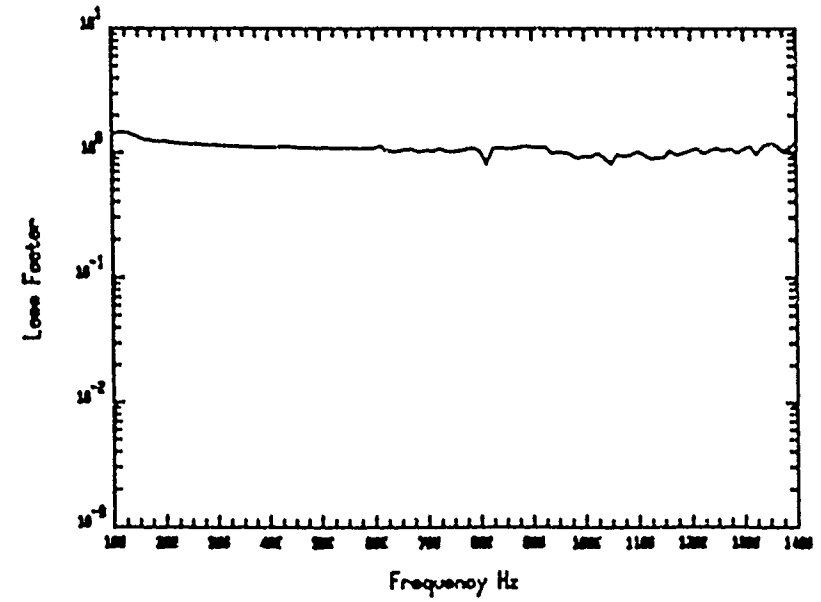


Figure 41: Material Properties at 98°F using the Shear Impedance Technique for 966

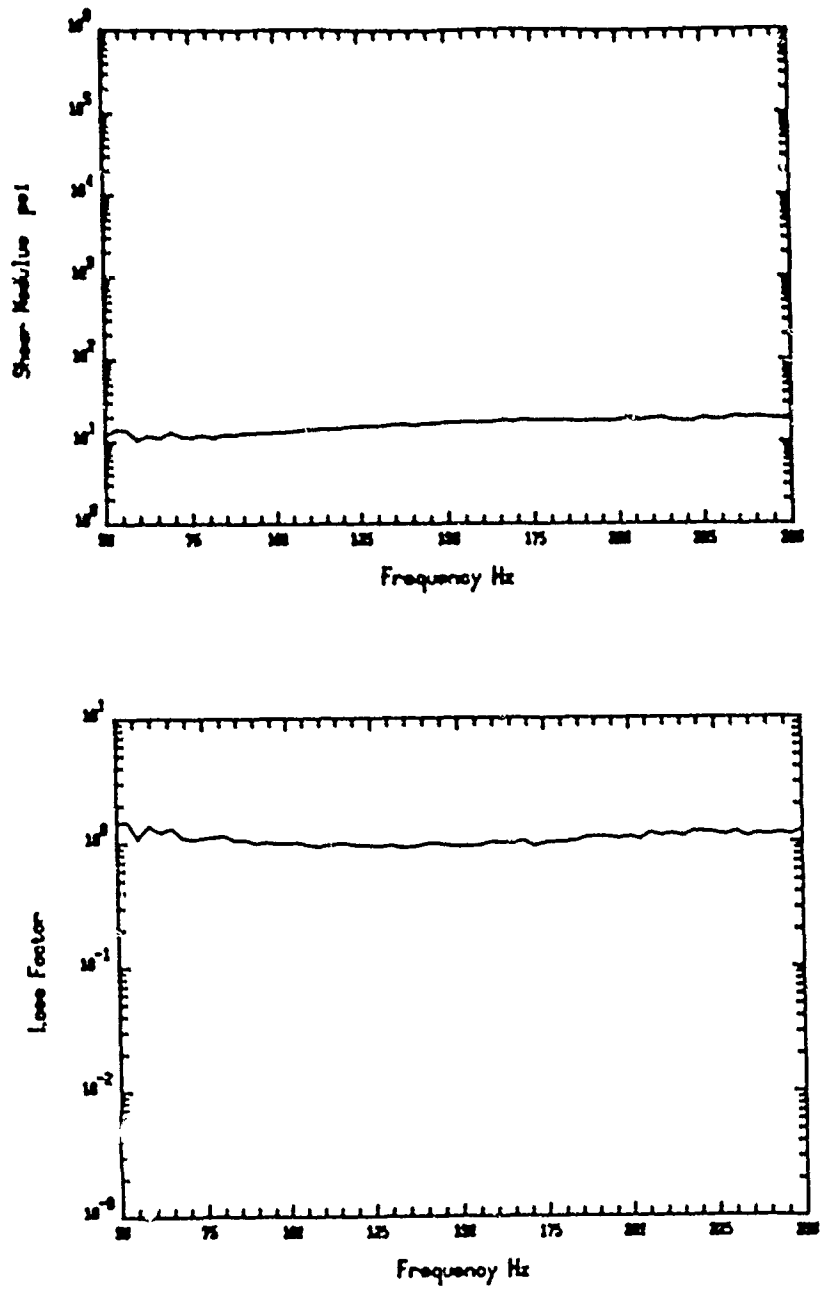
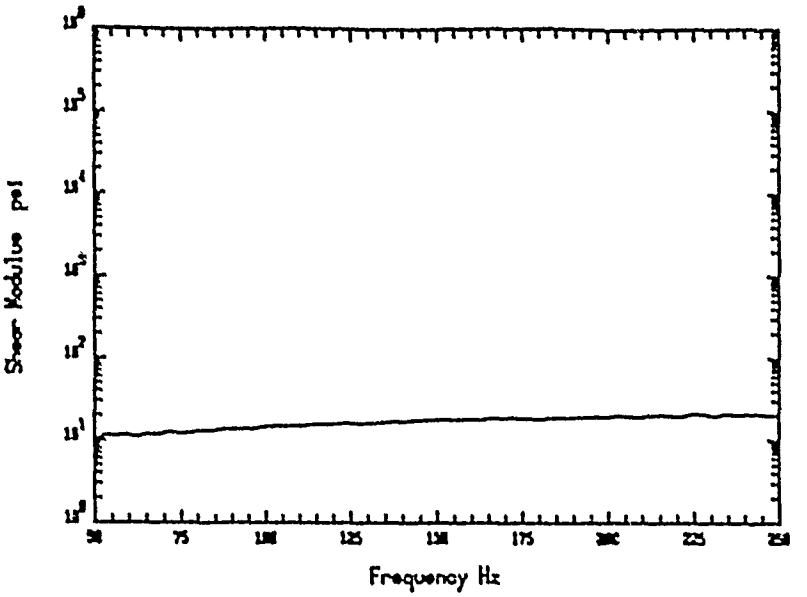


Figure 42: Material Properties at 130°F using the Shear Impedance Technique for 966



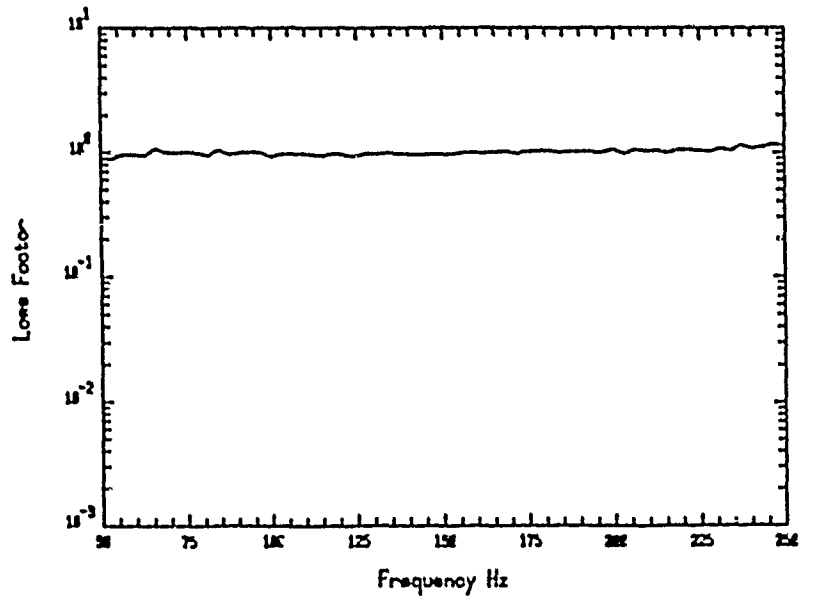
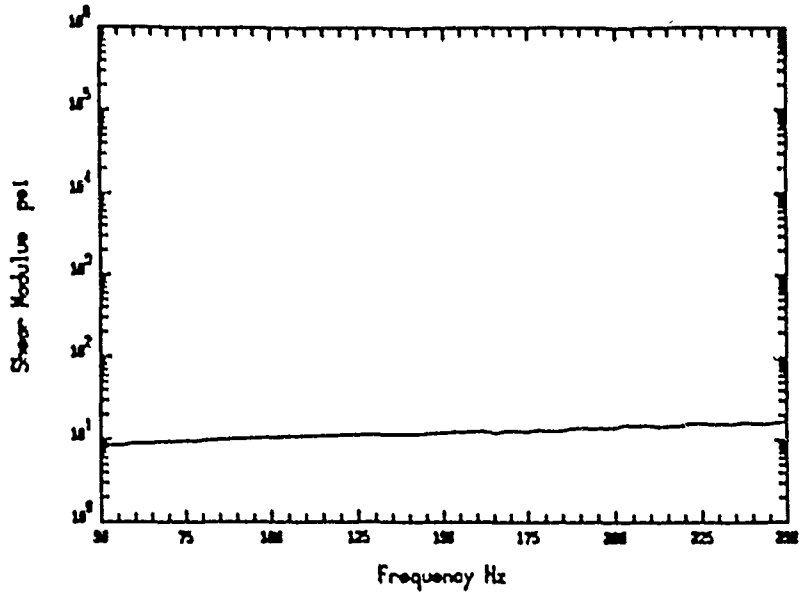


Figure 43: Material Properties at 147°F using the Shear Impedance Technique for 966



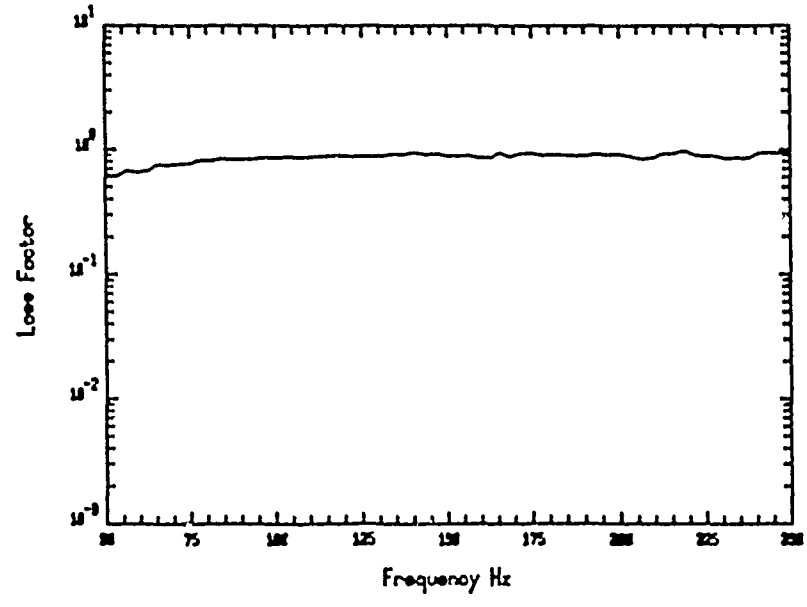


Figure 44: Material Properties at 170°F using the Shear Impedance Technique for 966

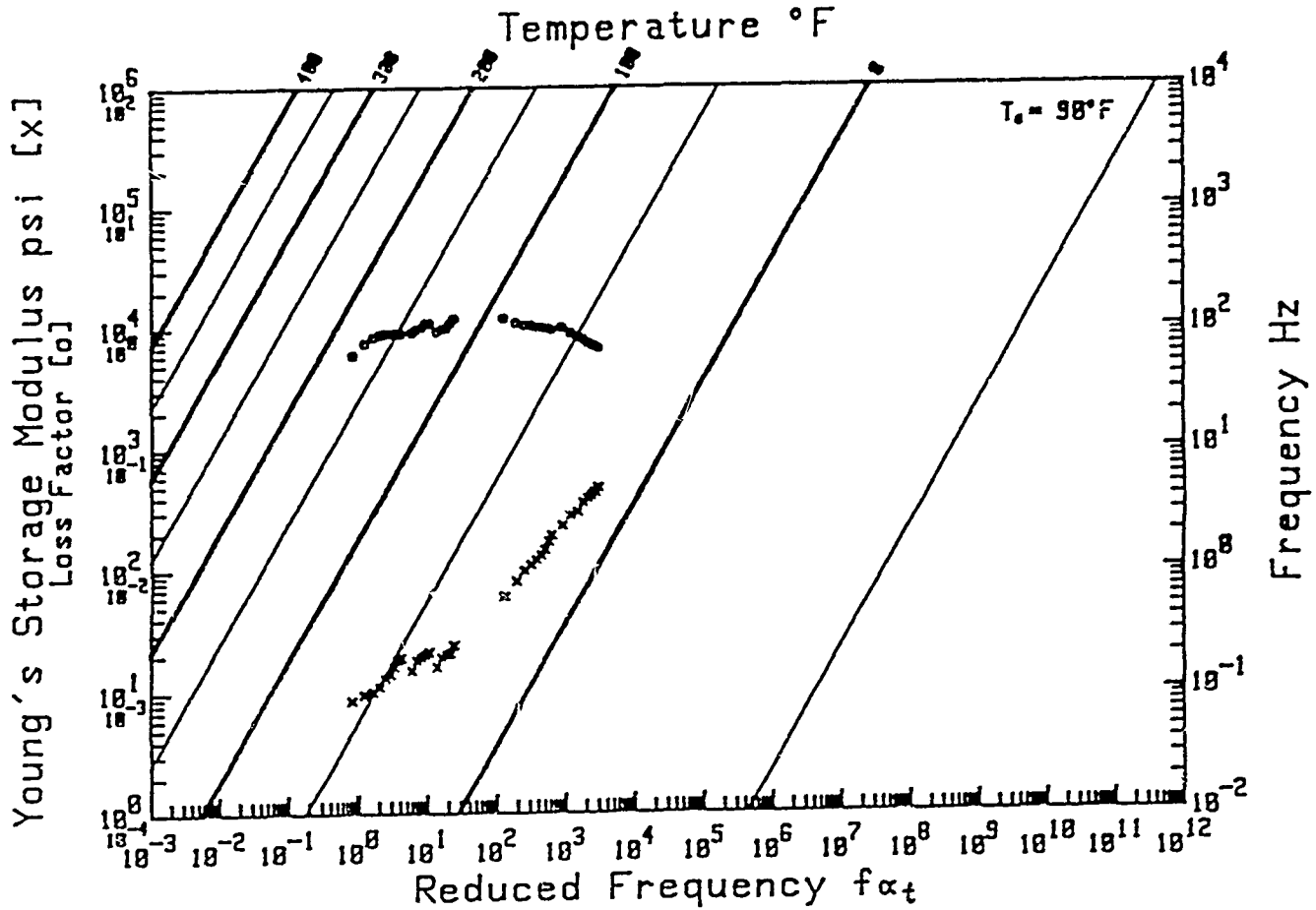


Figure 45: Reduced Frequency Nomogram for 966 using the Shear Impedance Technique

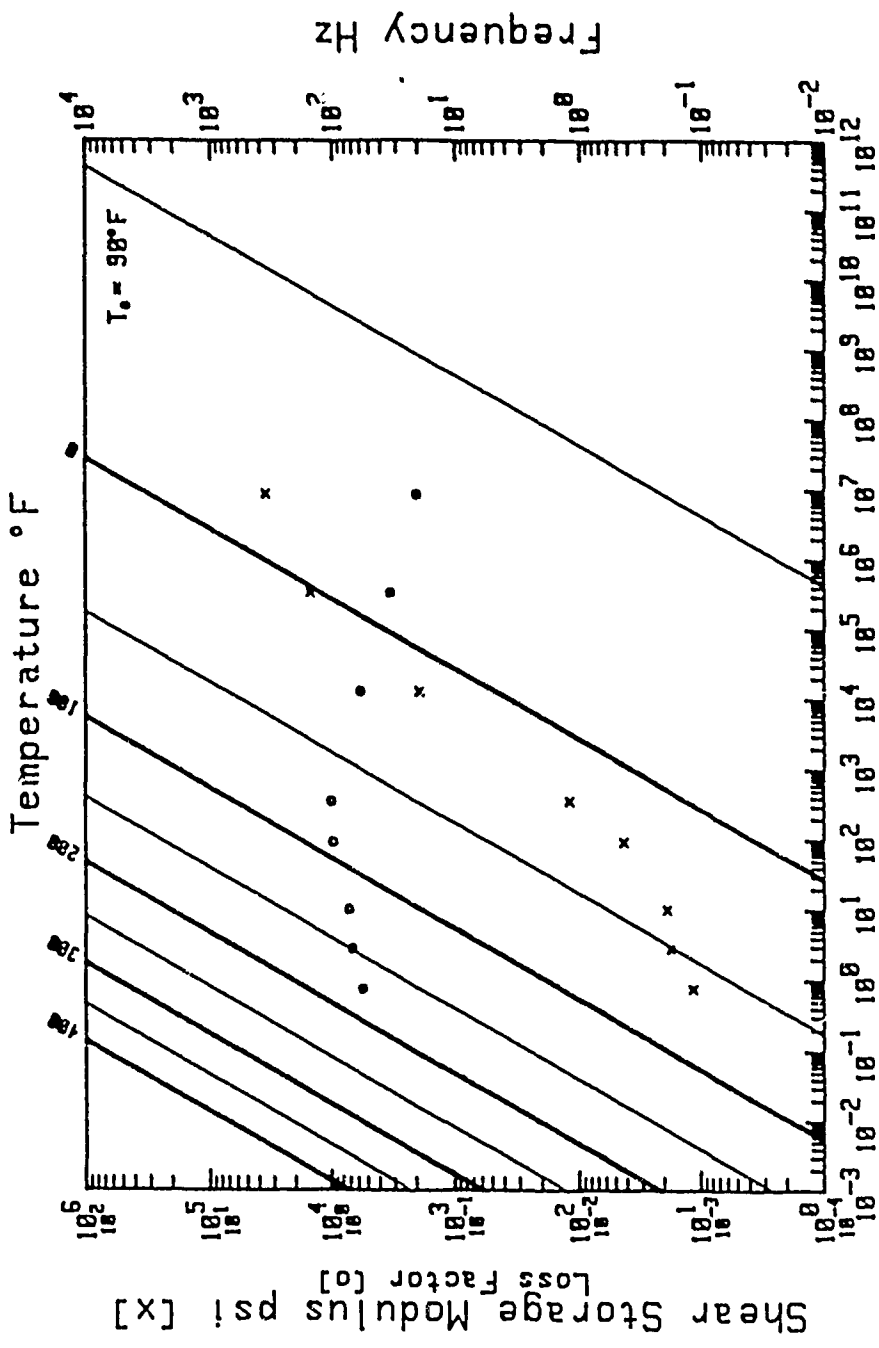
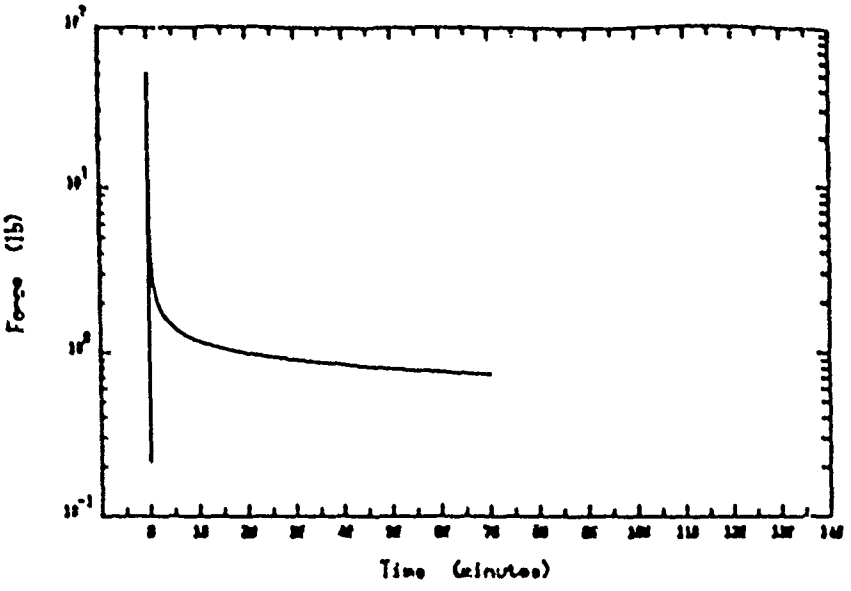


Figure 46: Reduced Frequency Nomogram for 966 using the Shear Resonance Technique



Variation of Relaxation Force with Time

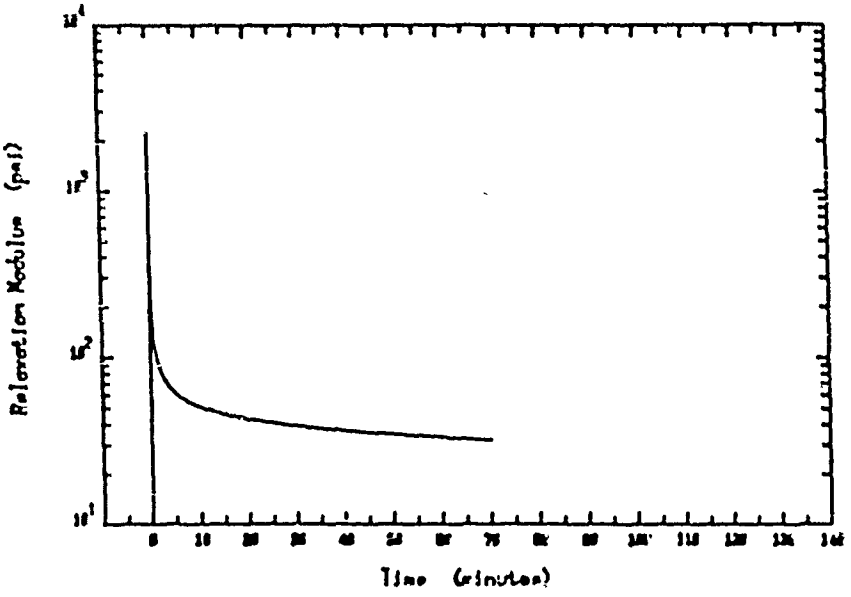
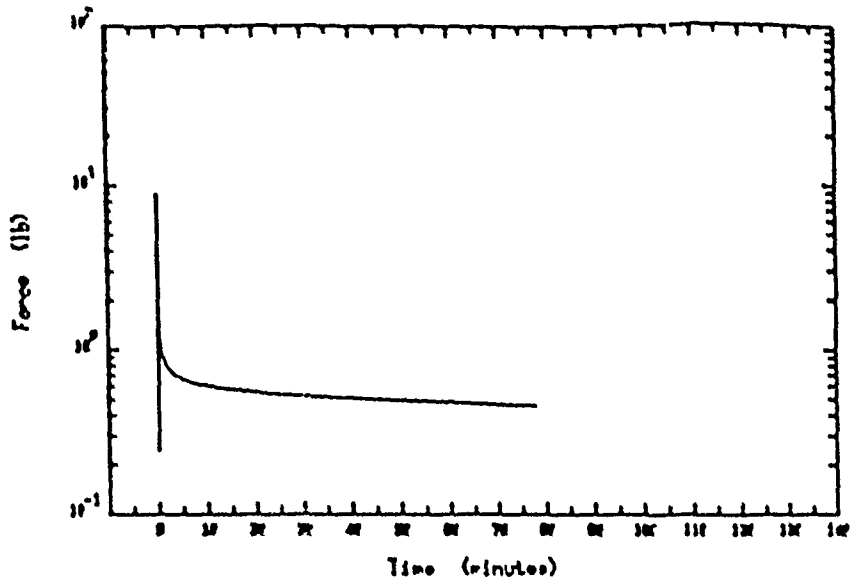


Figure 47:
Variation of Relaxation Modulus with Time

966 Tension-Compression Specimen: Relaxation Data at 0°F



Variation of Relaxation Force with Time

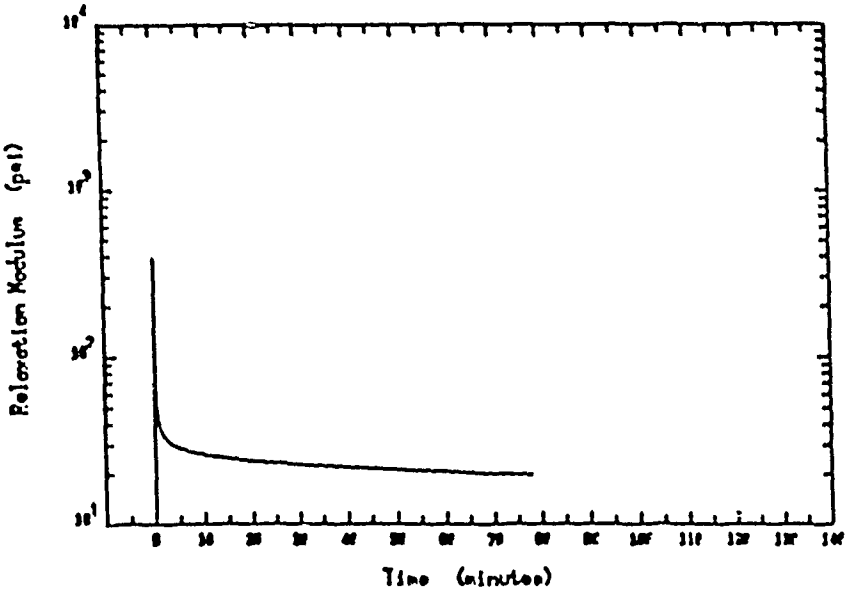


Figure 48:
Variation of Relaxation Modulus with Time

966 Tension-Compression Specimen: Relaxation Data at 25°F

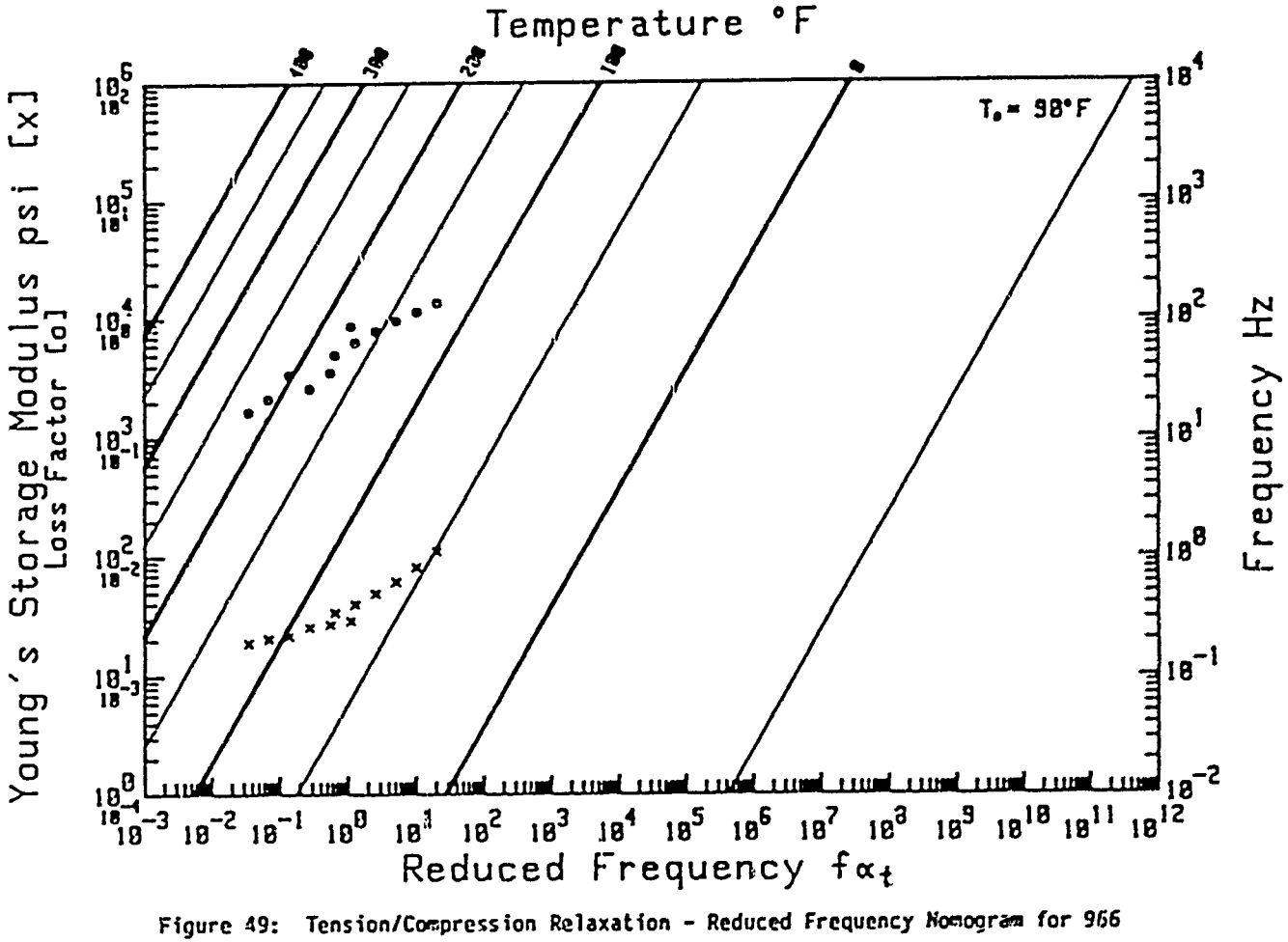
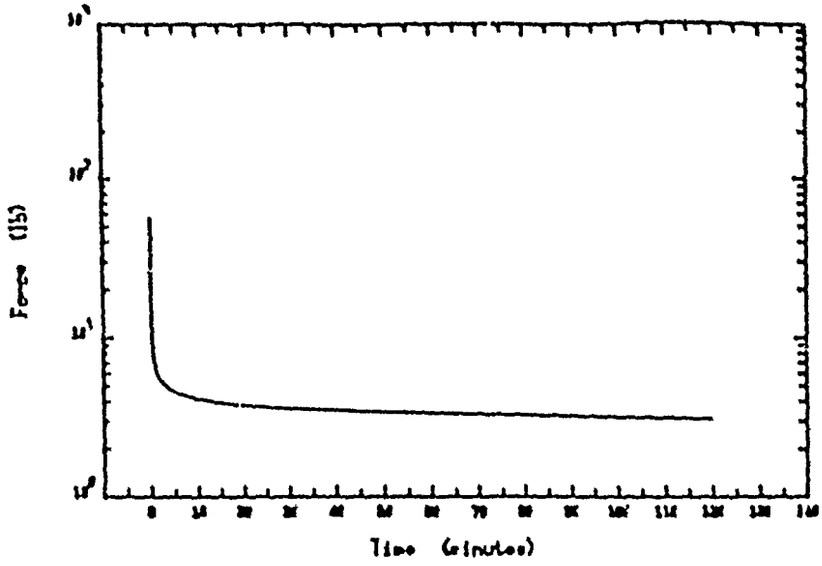


Figure 49: Tension/Compression Relaxation - Reduced Frequency Nomogram for 966



Variation of Relaxation Force with Time

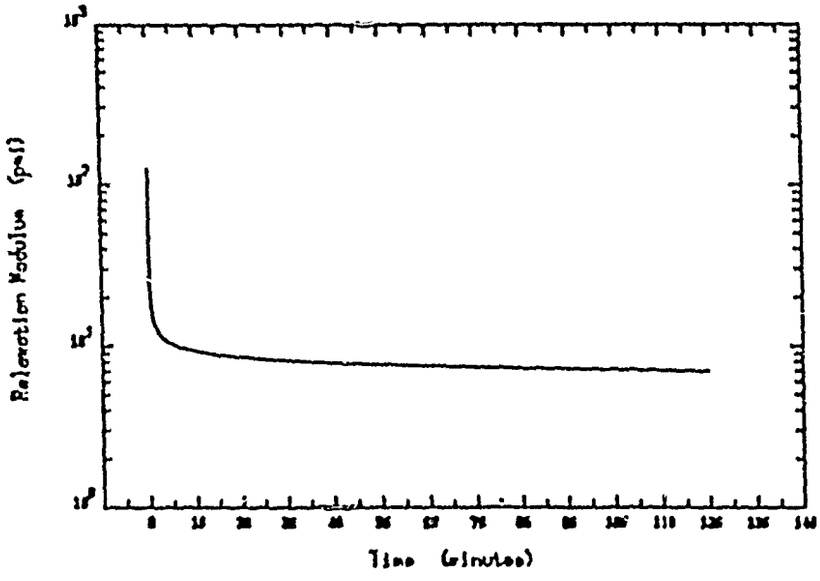
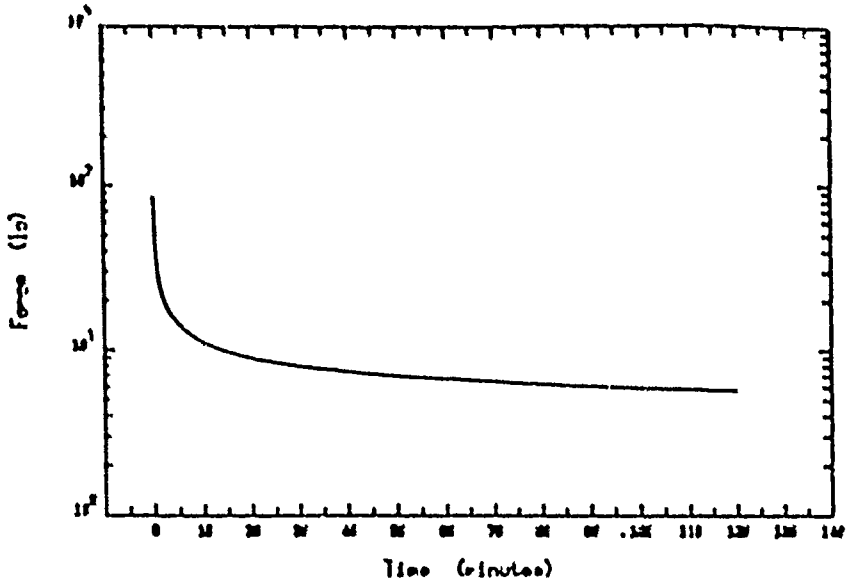


Figure 50:
Variation of Relaxation Modulus with Time

966 Shear Specimen: Relaxation Data at 25°F



Variation of Relaxation Force with Time

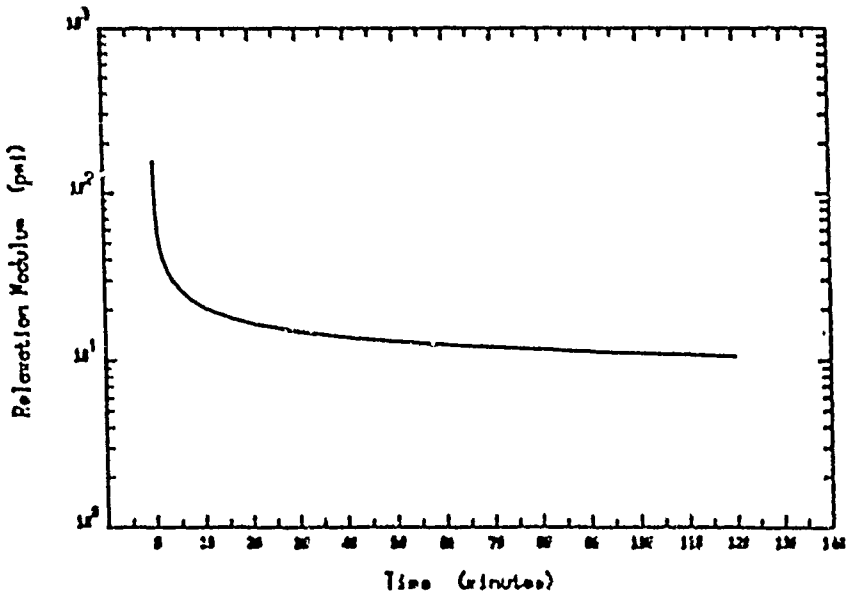


Figure 51:
Variation of Relaxation Modulus with Time

966 Shear Specimen : Relaxation Data at 0°F

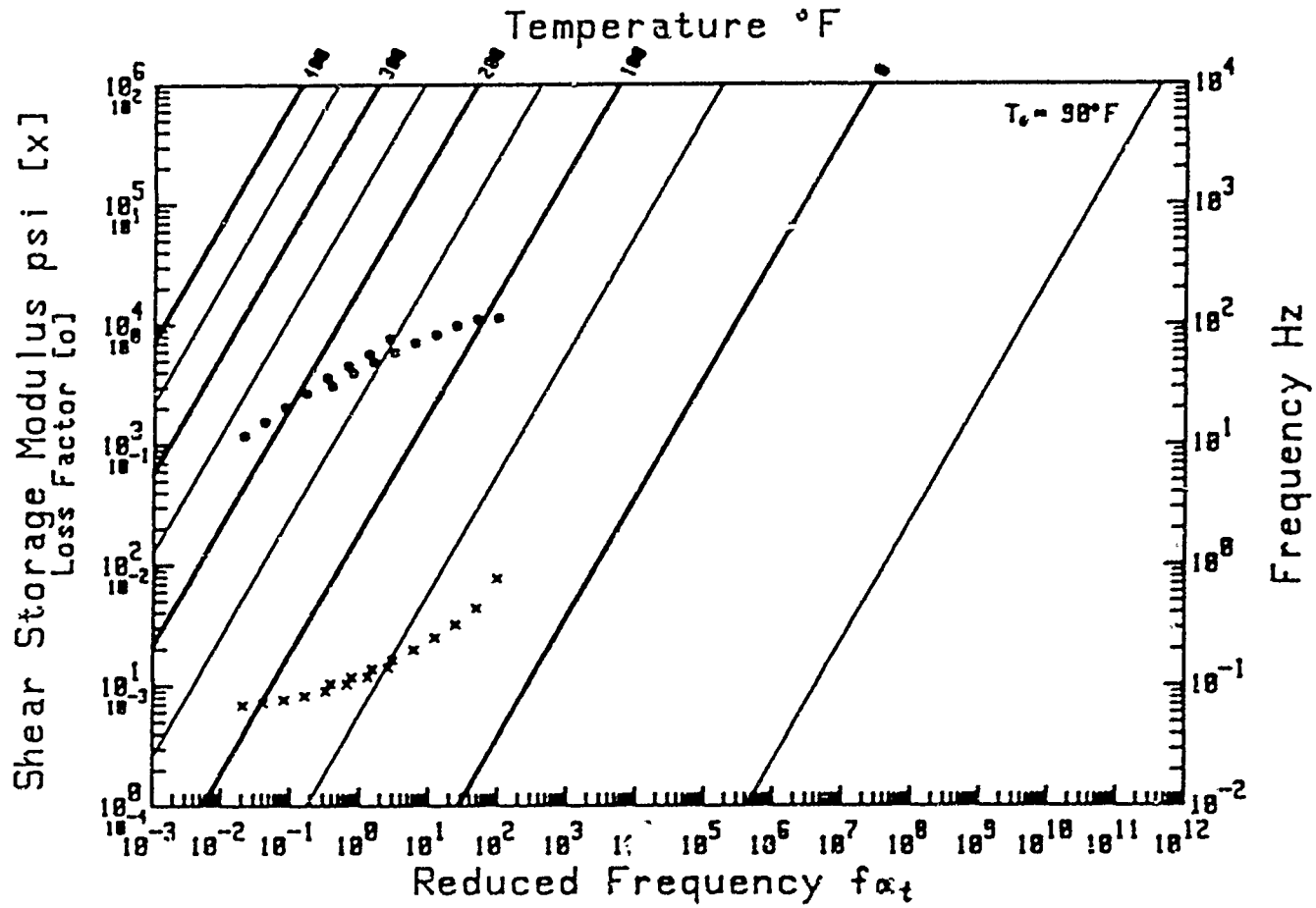


Figure 52: Shear Relaxation - Reduced Frequency Nomogram for 966

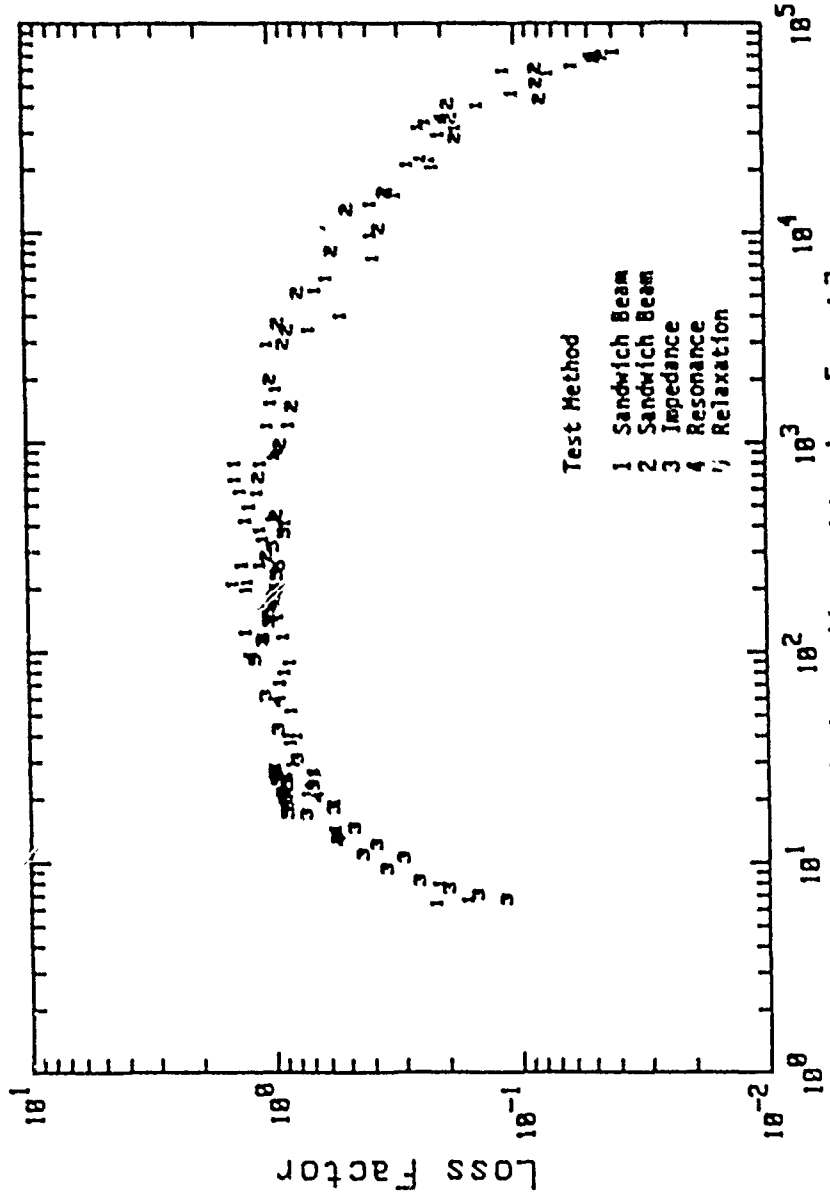


Figure 53: Variation of Loss Factor with Shear Modulus Magnitude for 3M Co. 966

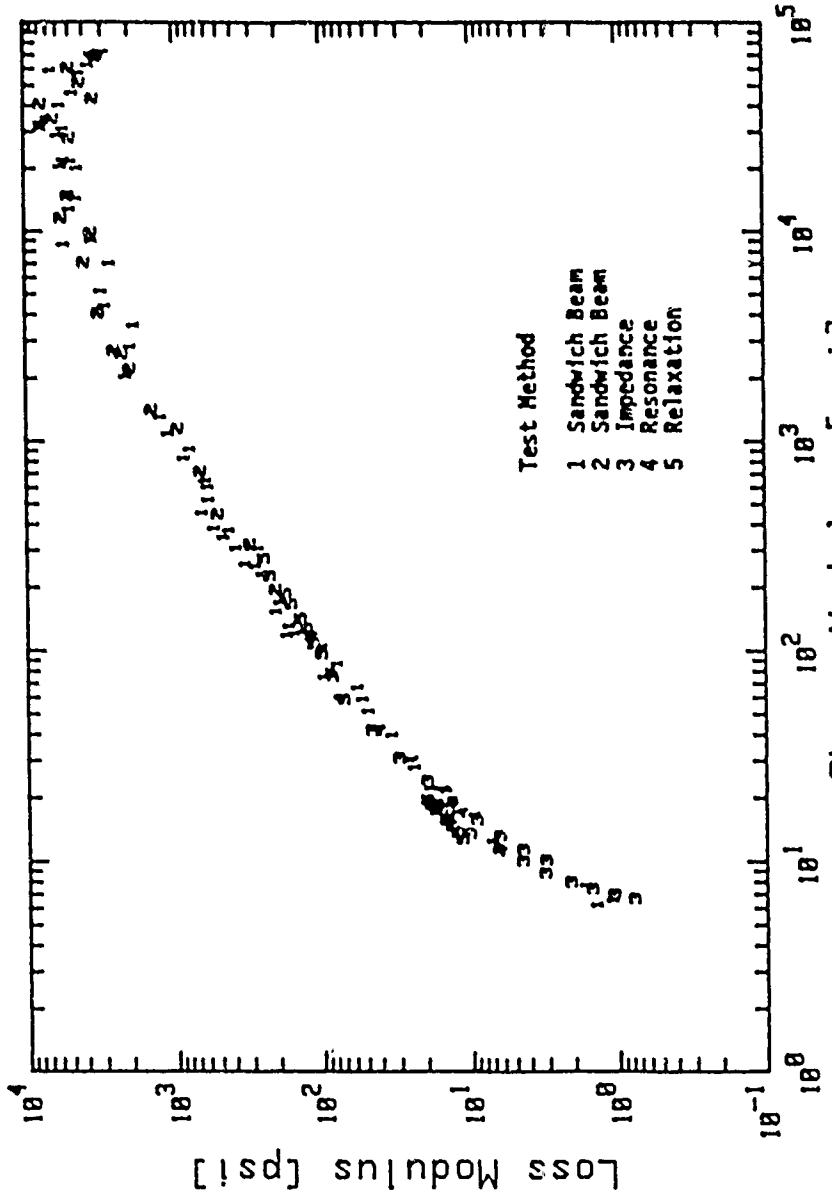


Figure 54: Variation of Loss Modulus with Shear Modulus for 3M Co. 966

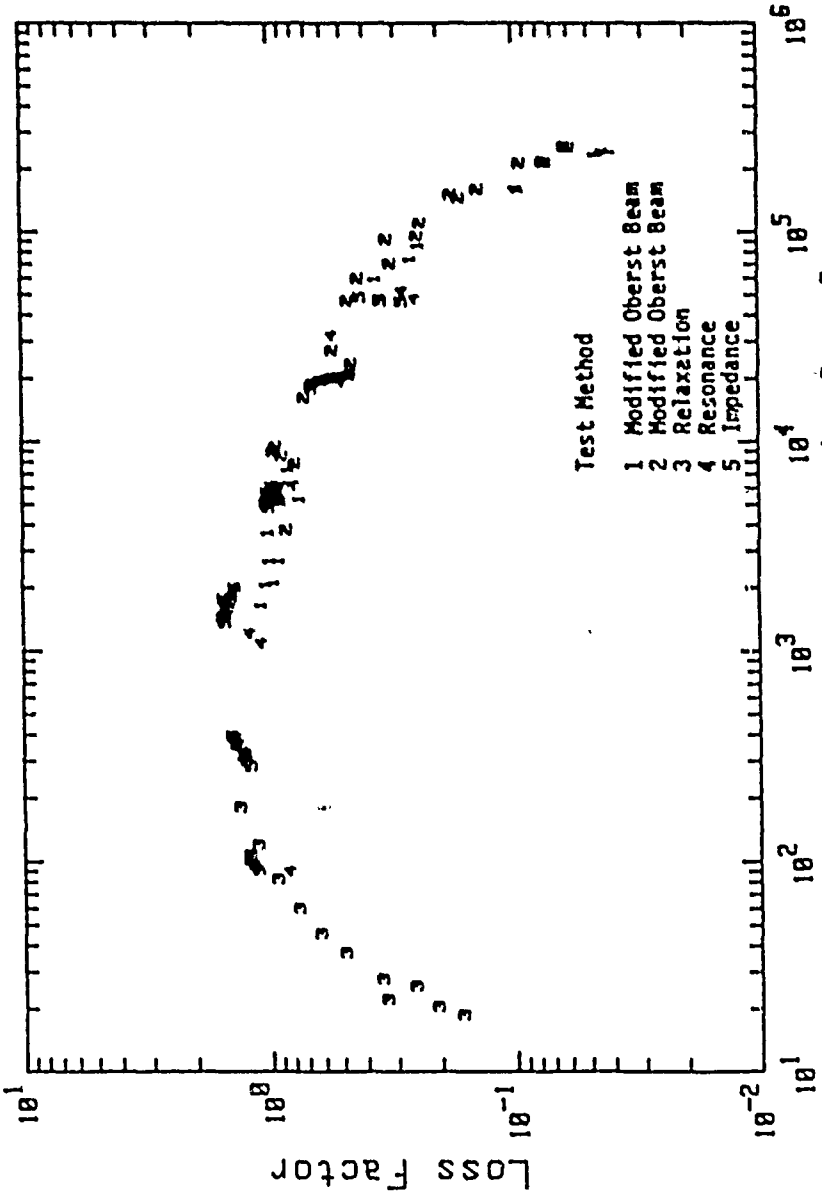


Figure 55: Variation of Loss Factor with Young's Modulus Magnitude for 3M Co. 965

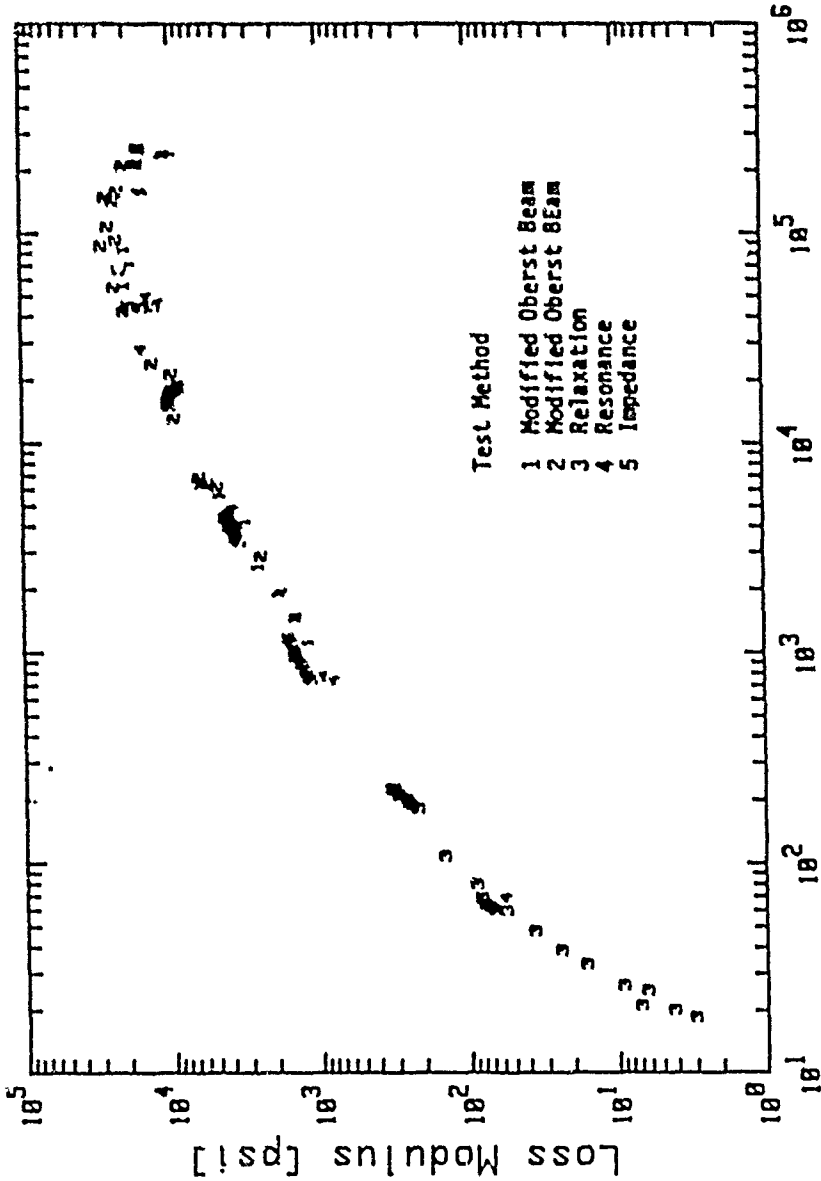


Figure 56: Variation of Loss Modulus with Young's Modulus for 3M Co. 966

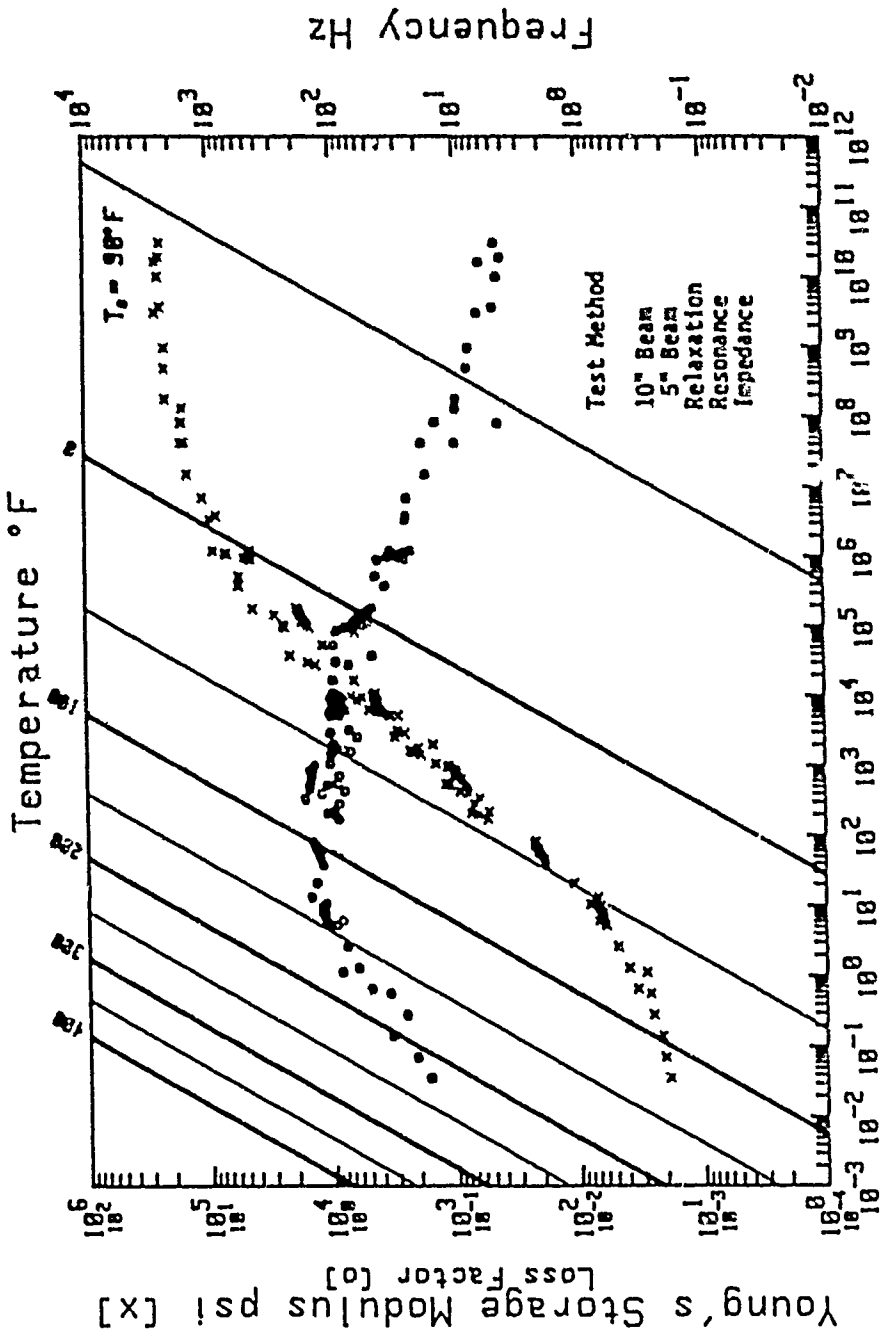


Figure 57: Reduced Frequency Nomogram for 3M Co. 966 Developed from Different Test Method Results

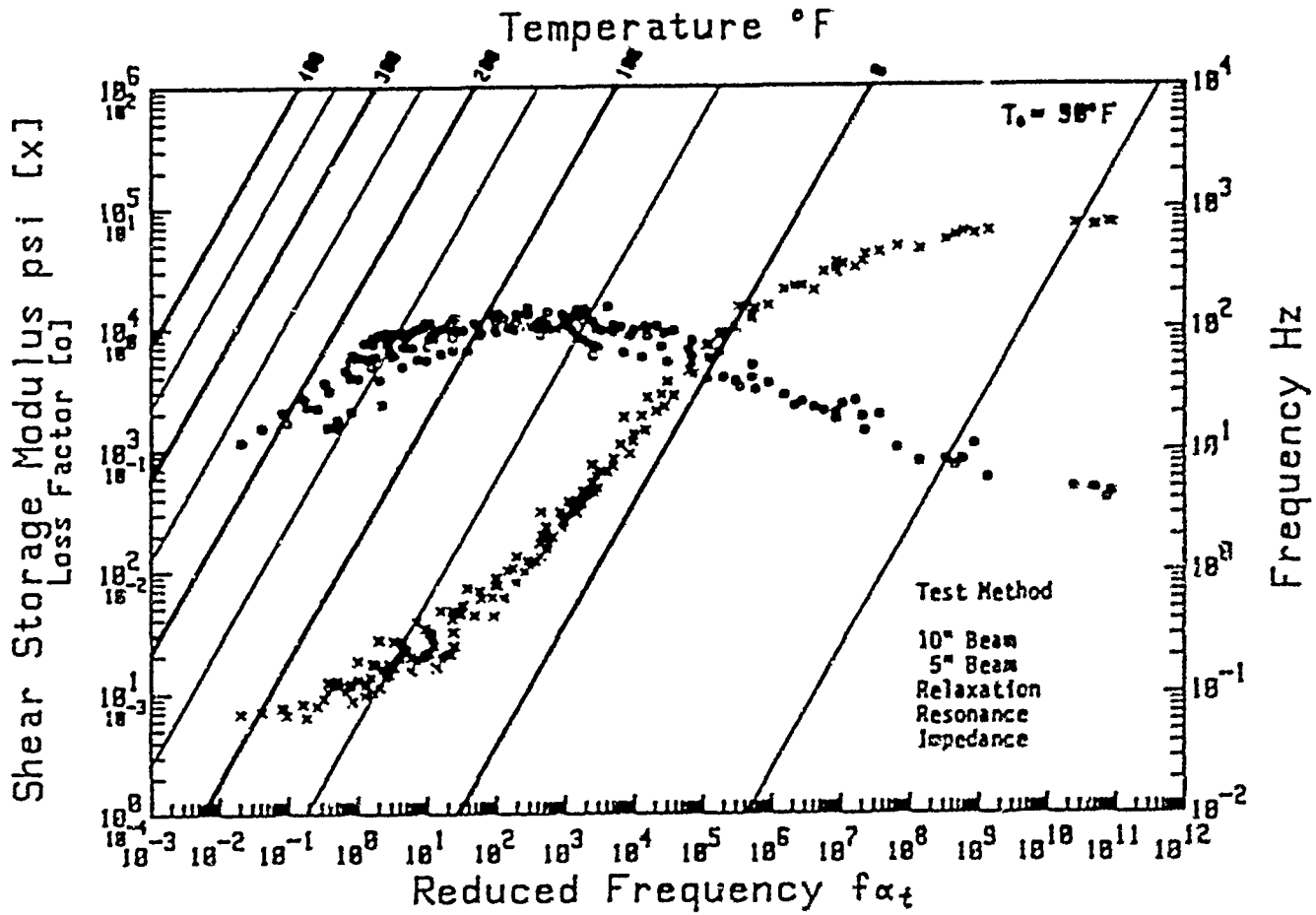


Figure 58: Reduced Frequency Nomogram for 3M Co. 966 Dynamic Shear Modulus and Loss Factor Developed from Different Test Method Results

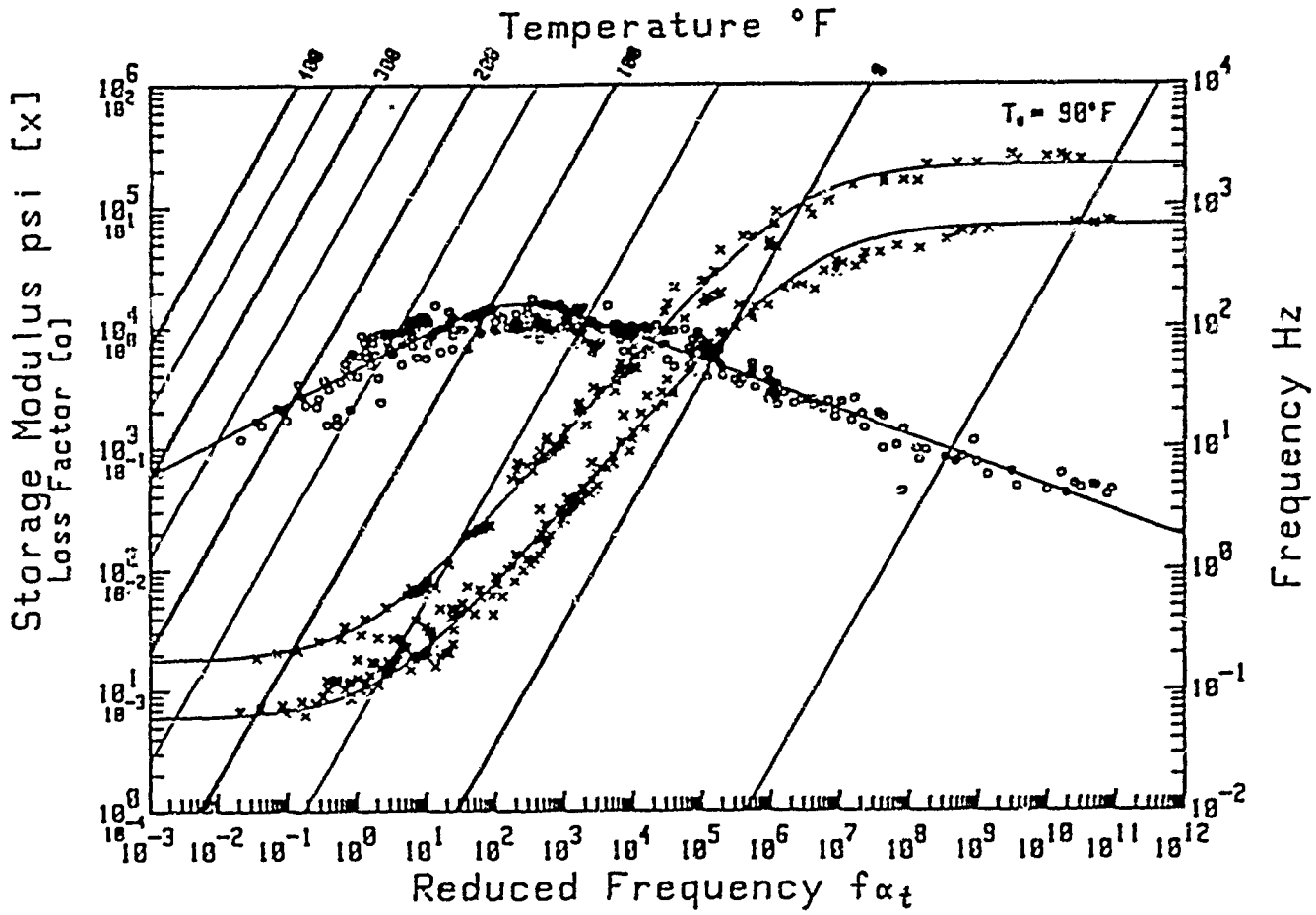


Figure 59: Comparison between Young's Modulus and Shear Modulus as a Function of 3M Co. 966

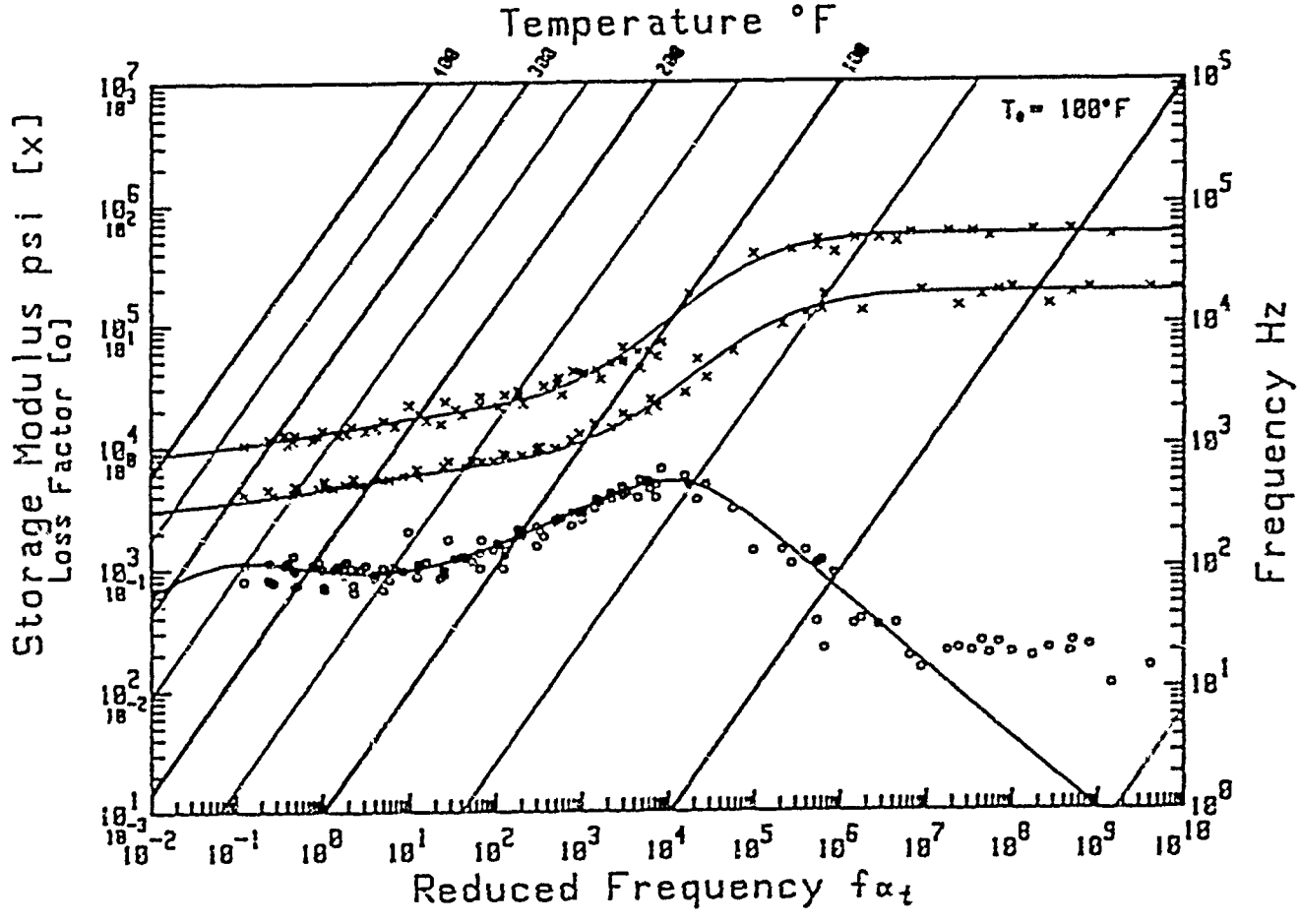


Figure 60: Comparison between Young's Modulus and Shear Modulus for 3M AF-32

PACOSS DAMPING MATERIAL MEASUREMENTS

For
VIBRATION DAMPING WORKSHOP II
"DAMPING 86"

MARCH 5-7, 1986

RIVIERA HOTEL AND CONVENTION CENTER
LAS VEGAS, NV

AUTHORS: M.L. PARIN
A.D. NASHIF
T.M. LEWIS
ANATROL CORPORATION
10895 INDECO DRIVE
CINCINNATI, OH 45241
(513) 793-8844

ABSTRACT

Experimental techniques for measuring the dynamic mechanical properties of two polymeric damping materials are discussed. These include the resonant beam, mechanical impedance, resonance, and relaxation test methods. Test methods are discussed in conjunction with the damping evaluation of 3M Company Acrylic Core Foam No. 4205 and General Electric SMRD 100-F90 for both shear and tension/compression states of stress. It is shown that by using the temperature/frequency superposition principle in conjunction with the experimental data, obtained from these test methods, the dynamic mechanical properties can be generated and correlated over a wide range of frequency and temperature. The storage modulus (both shear and Young's), loss factor, and Poisson's ratio for both materials are presented and discussed.

I. INTRODUCTION

Viscoelastic materials are generally characterized using a number of different experimental test methods that are selected based on the environmental conditions of interest. For example, the vibrating beam approach [1-4] is often used to characterize the linear damping properties in terms of frequency and temperature for both shear and/or extensional types of deformation, while the impedance [5,6] and resonant [2,7,9] techniques are used for determining the non-linear effects of strain amplitude, and static preloads. Long term stability is usually investigated using relaxation and/or creep procedures. The combined results of these different test methods can then be used to develop analytical [10] and also graphical [11,12] representations of the dynamic mechanical properties in terms of the various environmental factors.

This paper discusses the merits and limitations of the resonant beam, mechanical impedance resonance, and relaxation test methods. The damping properties of an acrylic material and a modified epoxy material that were measured by the various techniques will be presented and discussed. The results show that the dynamic mechanical properties can be measured and correlated over a wide range of temperatures and frequencies for different states of stress. From the experimental data, analytical and graphical representations of the material's damping properties can then be developed that include the environmental effects. This will include the dynamic storage modulus (both Young's and shear), loss factor, and Poisson's ratio for both materials.

II. MEASUREMENT TECHNIQUES

Although many techniques have been used to measure the dynamic properties of elastomers, the discussion in this paper will be limited to the vibrating beam, impedance, resonance, and relaxation techniques.

Vibrating Beam Technique

The analysis developed by Ross, Ungar, and Kerwin [13] can be used to calculate the damping properties of elastomeric materials from measurements made on the composite beam system. To use the analysis in its general form, iterative procedures must be used because the equations are coupled. However, for special cases, the equations can be simplified and only these will be presented here.

The technique is based upon utilization of the elastomeric material in conjunction with vibrating metal beams either in shear or extension. If the material is applied to the outside of the metal beam, then the properties can be obtained in extension, whereas if the material is sandwiched between two metal beams, then the properties can be obtained in shear. By studying the various resonances of the damped beam, the effect of frequency on the properties of the material can be established. Also, by placing the system inside an environmental chamber, the effects of temperature can be investigated.

This procedure has been adopted by the American Standard Testing Material as the preferred method for determining the damping properties of materials. The details of this procedure are found in ASTM E-756-83.

Description of Specimens

Although any type of beam specimens can in principle be used to make measurements on the dynamic properties of elastomeric materials, previous experience has concentrated mainly on cantilever beams. This is because of the simplicity of the set-ups for such beams, and also because at least one end can be simulated properly, namely the free end. This implies that careful attention must be applied to insure that the boundary condition at the other end is fully fixed. The same approach is used for other types of beams, with clamped-clamped, simply supported, or free-free boundary conditions. In making dynamic measurements on materials, using vibrating beam tests, it is necessary to apply the elastomeric material on the metal beam and make measurements on the composite system. Usually the

elastomeric material is combined with a metal beam in different configurations depending on the properties of the material of interest. The four main combinations, illustrated in Figure 1 are:

1. The homogeneous beam. This type is used for measuring the dynamic properties of metal alloys and composites. Such materials are usually stiff on their own and do not require combination with a metal beam.

2. The Oberst or externally coated beam, named for Dr. Oberst [14] who developed this technique for making measurements on the dynamic properties of stiff elastomeric materials under extensional deformation.

3. The symmetric free layer beam. This is a modified Oberst beam, where the material is coated on both sides. Again, the properties are determined for extensional deformation. This beam allows for a simplification in the equations and data reduction, and it circumvents some experimental difficulties.

4. The sandwich beam. This technique is used to determine the dynamic properties of elastomeric materials under shear deformation, and is usually employed for soft materials.

From Figure 1, it can be seen that all beams have massive roots, necessary to properly simulate the fixed boundary condition at the root of the cantilever beam, which is usually clamped in a rigid fixture. These roots can be either integrally machined as part of the beam, welded to the beam, or epoxied to the beam. It is emphasized that, for most measurements, the roots are essential for generating useful and accurate data.

The damping material is usually bonded to the metal beam by means of an epoxy adhesive which must have a modulus higher than that of the viscoelastic material. Also, the thickness of the epoxy layer must be kept to a minimum in general and small in comparison with the thickness of the damping material. If these two rules are not followed [15], deformation will occur in the epoxy layer as well as in the elastomeric layer, and erroneous data will result. In some cases the elastomeric material is, or can be, of the self-adhesive type and in that case there will be no need of an epoxy layer.

The type of metal used for the beams is usually steel or aluminum. Typical dimensions, used previously, and found to be successful, are a width of 0.5 inches, a free length of 7 to 10 inches, a root length of 1 inch, and a thickness of 0.04 to 0.125

inches. The thickness of the elastomeric material can vary according to the specific properties of the material and the temperatures and frequencies of interest.

Instrumentation and Set-up

When using the beam specimens of Figure 1 to make measurements of the dynamic properties of materials one usually requires two types of transducer. One is needed to apply the excitation force, and the other to measure the response of the beam. Because, when making such measurements, it is necessary to minimize all extraneous sources of damping, apart from that of the material to be investigated, it is essential to use transducers that are light in weight or of the non-contacting type.

The beam is mounted in a heavy, rigid, fixture which can provide sufficient clamping force around the root of the beam to simulate a fixed end boundary condition. Either a sinusoidal or random signal can be applied to the excitation transducer via a power amplifier. The response of the beam is measured by the second transducer, and is processed through signal conditioning equipment, and the resulting response is stored in a computer or on an X-Y recorder plot for later analysis. The set-up is usually mounted inside an environmental chamber in order to study such environmental factors as temperature, vacuum, etc. A schematic of such a set-up is illustrated in Figure 2.

Data Reduction

For all types of beams, the response of the specimen is measured as a function of frequency. From such a response spectrum, the frequencies and damping values of the various modes of vibration of the specimen are determined at each selected temperature. By varying the temperature of the environmental chamber, these tests are repeated at various temperatures to investigate the effects of temperature. The response of the undamped beam is also needed. Before this data can be processed, it is necessary to have three sets of information, as follows:

1. The frequency and the loss factor of the damped beam for each mode of vibration.

2. The frequencies of the undamped beam for the same modes of vibration, as for the damped beam.

3. The geometrical properties of the damped and undamped beams, along with the densities of the materials.

The following data reduction process is used to calculate the damping properties of materials from measurements conducted on the four types of beams outlined previously.

Homogeneous Beam Technique

The system loss factor η and Young's modulus E of the beam can be calculated from

$$\eta = \Delta f_n / f_n \tag{1}$$

and

$$E = \rho b H L^4 \omega_n^2 / (a_n^2 I) \tag{2}$$

where f_n is the nth natural frequency, ω_n is the nth circular frequency ($2\pi f_n$), ρ is the mass density, L is the length of beam, a_n is the characteristic number of the nth mode, I is the second moment of area and Δf_n is the half-power bandwidth.

Oberst Beam Technique

The properties of the damping material are computed from the measured values of the composite beam using the following equations:

$$(\omega_n/\omega_{1n})^2(1+h_2\rho_r) = \frac{1 + 2e_2h_2(2+3h_2+2h_2^2) + e_2^2h_2^4}{1 + e_2h_2} \tag{3}$$

$$\eta/\eta_2 = \frac{e_2h_2(3 + 6h_2 + 4h_2^2 + 2e_2h_2^3 + e_2^2h_2^4}{(1+e_2h_2)\ (1+4e_2h_2+6e_2h_2^2+4e_2h_2^3+e_2^2h_2^4)} \tag{4}$$

where $e_2 = E_2/E_1$, E_1 is the Young's modulus of the metal beam, $h_2 = H_2/H_1$, H_2 is the thickness of the damping material, H_1 is the thickness of the metal beam, $\rho_r = \rho_2/\rho_1$, ρ_2 is the density of the damping material, ρ_1 is the density of metal beam, η is the loss factor of the composite beam in the nth mode, η_2 is the loss factor of the damping material, ω_{1n} is the nth circular frequency of the metal beam and ω_n is the nth circular frequency of composite beam.

Symmetric Free Layer Beam Technique

The equations used for symmetric beams are:

$$E_2 = \frac{[(\omega_n/\omega_{1n})^2(1+2h_2\rho_r) - 1]\, E_1}{(8h_2^3 + 12\, h_2^2 + 6h_2)} \tag{5}$$

$$\eta_2/\eta = \frac{E_1}{(8h_2^3 + 12\, h_2^2 + 6h_2)\, E_2} + 1 \tag{6}$$

Sandwich Beam Technique

The following relations for the shear modulus and loss factor of the damping material are used for sandwiched beams:

$$G_2 = \frac{(A-B) - 2(A-B)^2 - 2(An)^2}{(1-2A+2B)^2 + 4(An)^2} \times \frac{E_1 H_1 H_2 a_n}{L^2} \tag{7}$$

$$\eta_2 = \frac{An}{A - B - 2(A-B)^2 - 2(An)^2} \tag{8}$$

where

$$A = (\omega_n/\omega_{1n})^2\ (2 + \rho_r h_2)\ (B/2) \tag{9}$$

$$B = 1/6(1+h_2)^2 \tag{10}$$

and G_2 is the shear modulus of the damping material

Since the properties of damping materials can be computed for different modes of vibration, and at different temperatures, the effects of both frequency and temperature can be established.

Usually, the loss factor of the composite beam is measured by the half-power bandwidth method. This is not the only method to measure the damping for a given resonant condition of the beam, and other techniques can be used equally well, within their limitations, such as decay, modal curve-fitting, Nyquist diagrams, etc.

Assumptions and Precautions

Assumptions

As with all techniques and analyses, certain important assumptions have to be made and are listed here. They should be kept in mind when making damping measurements on materials.

1. All damping measurements made by beam tests must be made in the linear range. It is important to select a force level that will be meaningful, because the analysis for the data reduction will otherwise not be applicable.

2. It is important to keep the amplitude of the force signal, applied to the excitation transducer, constant with frequency. This is particularly important when making bandwidth measurements on modes of vibration with high damping. If the force cannot be kept constant, then the response of the beam must be divided by the input force in order to obtain the normalized transfer functions.

3. For the Oberst and symmetric free layer specimens, the analysis is the classical analysis for beams. It does not include the effects of rotatory inertia or shear deformation. The analysis assumes that plane sections remain plane and, therefore, care must be taken not to use specimens with a damping material thickness that is greatly exceeds that of the metal beam.

4. The equations presented for computing the properties of damping materials in shear do not include the extensional terms of the damping layer. This is a good assumption as long as the stiffness of the damping layer is considerably lower than that of the metal beam. Also, these equations were developed and solved using sinusoidal expansions for the mode shapes. For cantilever beams, this approximation is good only for the higher modes. For the first mode, it does

not apply and an equivalent wavelength of vibration must be assumed empirically, to generate useful data. It has been the common practice to ignore the first mode results for sandwich cantilever beams.

5. The loss factor of the metal beam(s) is assumed to be zero. This is usually a good assumption because steel and aluminum have loss factors of the order of 0.0001 or less, which is significantly lower than those of the composite damped beams. This point should be kept in mind if other beam materials are used, such as plastic or epoxy.

6. The damping introduced by the mounting conditions is also assumed to be very low. This is usually a good assumption provided: a) the clamping configuration has sufficient mass and stiffness to counteract the moments introduced by the specimen; and b) the clamping surfaces are flat and paralled so that the clamping forces are uniformly distributed and minimize slip.

Precautions

The following is a list of precautions that must be observed as a result of the geometry of the specimen, instrumentation, and assumptions mentioned above. It is very important to pay close attention to these precautions, for good measurements to be taken at all times and for all conditions.

1. The first point is rather general in nature. Making measurements on the damping properties of materials is usually a very complex and involved process because it involves materials, vibration, instrumentation, computers, and so on. It is necessary to pay close attention to all details of the experiment from the fabrication of the specimen to the actual data reduction and analysis. Good and careful experimentalists are needed to work successfully in this area.

2. The first mode of vibration of the cantilever beam should not be used, unless extreme care is taken, to calculate the properties of the material being investigated. This precaution is necessary because, in the first mode, high amplitudes usually result which may introduce nonlinear effects into the measurements. Also, the assumptions made in the analysis of the sandwich beams are not well duplicated for this mode.

3. The damping of the metal beam is set to zero in the analysis. This is usually true because metal damping is considerably lower than that of good damping materials.

4. When applying a good damping material on a metal beam, the resulting response is usually well damped and the signal-to-noise ratio is not very high. Therefore, it is important to select an appropriate ratio of the thickness of the damping material to that of the metal beam so as to end up with moderate amounts of modal damping. Also, extremely low damping in the system should be avoided, because the differences between the damped and undamped systems will then be too small.

5. With the exception of the homogeneous beam technique, all other techniques are based upon measurements on the damped and undamped systems and making use of the differences, which are often small. The expressions for such differences are in the denominator of the equations used for data reduction, so if small errors are made during the measurements, or in the geometry of the beam, then those small errors will be magnified considerably during the data reduction process. This will lead to erroneous results. As a general guideline to prevent such conditions from occurring, it is usually recommended that:

   a. For the Oberst beam the term $(\omega_n/\omega_{1n})^2(1+\rho_r h_2)$ must be at least equal to or greater than 1.1.

   b. For the symmetric free layer beam, the same precaution as that of the Oberst beam applies for the expression $(\omega_n/\omega_{1n})^2(1+2\rho_r h_2)\geq 1.10$.

   c. For the sandwich beam technique, the same precaution applies for the expression $(\omega_n/\omega_{1n})^2(2+\rho_r h_2)$.

6. The Oberst and symmetric free-layer beam techniques are usually used for stiff materials (Young's modulus of 10^4 psi or higher), where the properties are measured in the glassy and transition regions. These materials are usually applied as free-layer treatments, and include enamels, loaded vinyls, and so on.

7. The sandwich and symmetric constrained layer beam techniques are usually used for softer viscoelastic materials, with moduli of the order of 10^3 psi or less. For temperatures and frequencies for which the material's moduli is less than 80 psi the sandwich beam technique is usually less viable.

Impedance Technique

The impedance technique is usually used to generate the material properties continuously with frequency and is especially useful to investigate the effects of preloads on the dynamic properties. By this technique, a known force is applied to a given specimen and the resulting displacement is measured. The amplitudes of the two signals and the phase angle between them are then used to compute the material properties.

Since most of today's vibration testing is carried out using fast Fourier analyzer systems, it is necessary to adapt the impedance technique to such systems. Of particular importance is that the vibration data is processed on the analyzer using complex algebra. Thus to compute the dynamic properties of elastomers it is necessary to work with the real and imaginary components of the frequency response measurements made on the material of interest. To illustrate this, consider the single degree-of-freedom system illustrated in Figure 3. The compliance X/F for such a system can be written as:

$$\frac{X}{F} = \frac{1}{k - m\omega^2 + ik\eta} \tag{11}$$

If the compliance is defined in terms of its real part R and its imaginary part I then equation (11) can be rewritten as:

$$R + iI = \frac{1}{k - m\omega^2 + ik\eta} \tag{12}$$

The real and imaginary parts of equation (12) can now be used to solve for the two unknowns k and η or:

$$k = m\omega^2 + \frac{R}{R^2 + I^2} \tag{13}$$

$$\eta = \frac{-I}{m\omega^2(R^2+I^2)+R} \tag{14}$$

Description of Specimens

Elastomeric materials are usually tested in tension-compression or in shear states of stress by the impedance technique. Figures 4 and 5 represent some of the ways for combining the material and the mass to simulate a single degree-of-freedom system. Although the cross section of the elastomeric material could be of any shape, it has been common to use specimens having retangular or circular sections.

Instrumentation and Setup

Similar instrumentation to that of the vibrating beam technique is used for the impedance technique in order to apply a force to the specimen and measure its response. Typically, the force is applied by a shaker or an impact transducer while the response is measured by an accelerometer. By controlling the amplitude of the applied force, the non-linear effects on the dynamic properties can be investigated. Also by preloading the specimens, such effects can be studied.

Data Reduction

Equations (13) and (14) can be used to compute the dynamic properties of elastomeric materials when tested either in shear or tension-compression states of stress as illustrated for both specimens of Figures 4 and 5. For either type the loss factor is computed directly from equation (14) while the modulus needs to be computed from the specimen stiffness k of equation (13).

Shear Specimen

The shear modulus of the elastomeric material is determined after the stiffness value k has been established by using the following expression:

$$G = \frac{kH}{A} \qquad (15)$$

where H is the height of the specimen and A is its cross-sectional area.

Tension-compression Specimen

Shape factors are usually considered [16] in reducing the data generated on tension-compression specimens to account for the Poisson's effects. In such cases Young's modulus, E, of the elastomeric material is given by:

$$E = \frac{kH}{A[1+\beta(A/A')^2]}$$

where A' is unloaded area of the specimen and β is a material constant equal to 1.5 or 2.0, depending on whether the material is filled or an unfilled elastomer, respectively.

Assumptions and Precautions

The major point for consideration in making impedance measurements is that the state of stress should be well defined. Unfortunately, this is difficult unless extreme care is taken in designing the specimen and making measurements on it. Specifically, the following points should be kept in mind.

1. To minimize the effects of free edges on the measured values for the shear specimen it is recommended that the height to thickness ratio of the specimen be greater than 4.

2. To minimize the effects of shape factors on tension-compression specimens it is necessary to make the loaded area small in comparison with the unloaded area.

3. The type of excitation and pickup methods and locations should be selected to avoid rocking motions.

4. Although measurements could be made over a wide frequency range using the impedance technique, it has been found that in order to minimize the effects of error magnification factors on the computed properties it is necessary to limit the frequency range to that around the resonance frequency only. Practically, it has been demonstrated, with current equipment, that the frequency range could be as wide as a decade with the specimen resonant frequency approximately in its center. Thus different masses are needed to consider different frequency ranges.

Resonance Technique

The resonance technique is a special case of the impedance one where measurements and analysis of the data is restricted to the resonant frequency. Thus different masses and/or specimen geometries are needed to investigate the frequency effects. Although this technique is restricted to one frequency it is very useful because of its simplicity and the fact that high amplification at resonance help in studying the effects of dynamic nonlinearities on the material properties.
As far as the analysis for this technique, it is sufficient to keep in mind that at resonance:

$$\omega_n = \frac{k}{m} \tag{16}$$

in order to compute the specimen stiffness. The loss factor of the specimen can be measured by many methods such as the half-power bandwidth method or by the following formula:

$$\eta = \frac{1}{\sqrt{Q^2 - 1}} \tag{17}$$

where Q is the amplification factor at resonance.

All points considered for the impedance technique apply equally well for the resonance one.

Relaxation Technique

By this technique the material is subjected to a constant displacement and the change in the force is monitored over a period of time. The time interval where a noticeable change in force occurs depends on the temperature range where the material is being tested. For example, if the material is tested in its rubbery region, then the force can reach equilibrium in a short time. However, as the test temperature causes the material to reach its transition and glassy regions, longer time periods will be needed since the force will continue to change with time for longer periods.

Figure 6 illustrates the measurements made by the relaxation technique. The elastomeric sample having a length of L is mounted to a rigid fixture on end and to a force transducer on the other. The specimen is stretched by displacement ΔL and the force signal can thus be monitored with time and recorded.

The time domain relaxation modulus can then be described as

$$E(t) = \frac{F(t)\,L}{A\,\Delta L} \tag{18}$$

where F(t) is the load, A is the loaded area, L is the sample length, and ΔL is the displacement.

The time domain relaxation modulus can then be transformed into the frequency domain by [17].

$$E(i\omega) = i\omega \int E(\theta)\, e^{-i\omega\theta}\, d\theta \tag{19}$$

where

$$\theta = (t-t') \tag{20}$$

and t' is some past time and t is present time. Rewriting this equation for the storage (E_R) and loss modulus (E_I) gives:

$$E_R(\omega) = \omega \int E(\theta) \sin\omega\theta d\theta \tag{21}$$

$$E_I(\omega) = \omega \int E(\theta) \cos\omega\theta d\theta \tag{22}$$

Equations (21) and (22) can then be used, along with the time domain loading history and specimen geometry, to compute the dynamic properties for viscoelastic materials in either shear or tension-compression states of stress by applying numerical integration procedures. The loss factor is then determined by taking the ratio of equation (22) to equation (21).

III. RESULTS AND DISCUSSION

The experimental data taken for SMRD 100-F90 and Acrylic Core Foam 4205 was analyzed using the equation presented in Section II. The data is presented in Figures 10, 11, 21, 28, 33, 34, 35, and 36 in terms of reduced frequency using the Nashif empirically derived shift factor:

$$a_t = \left[1 - \frac{T-T_o}{175.707}\right]^{t(-11)} \qquad (23)$$

For comparison purposes, the SMRD and the Acrylic Core Foam data have been plotted in Figures 35 and 36 for both the shear and the tension-compression states of stress. These plots include data taken from all of the test methods described in Section II.

By comparison the reduced frequency nomogram for SMRD in Figures 11 and 36, it can be seen that two different reference temperatures were used to shift the data. The Figure 11 plot is composed of data taken from the beam test method. This test method have a test frequency range of approximately 50 Hz up to 15,000 Hz, or less than 3 decades, and this data was used as the basis for selecting a reference temperature suitable for collapsing the available data onto a master curve. Figure 36 is composed of test data generated from the beam, impedance, and resonant methods plus data generatetd from the time domain relaxation test. The relaxation test data has a frequency range of approximately 10^{-5} Hz up to .02 Hz. By including the test data generated for all the different test methods gives the damping properties over a frequency range, covering in excess of 9 decades, from $1x10^{-5}$ Hz up to 15,000 Hz. When all the test data was combined, it was necessary to select a "new" reference temperature in order to collapse the data onto a continuous master curve in the reduced frequency domain.

This same explanation is applicable to the acrylic core foam data presented in Figures 10 and 35. Again, the difference in the selected reference temperature (T_o) between these two plots is due to the expanded frequency range that is available when the time domain test data is transformed to the frequency domain and then coupled with the direct frequency domain damping properties obtained from the beam, mechanical impedance, and resonant test methods.

It can be seen from the above figures, that there exists good correlation between the different techniques over wide frequency ranges. Also, the loss factor measured in shear is essentially the same as that measured in tension-compression. It can also be seen that for acrylic core foam the Young's modulus is approximately three times the shear modulus in the rubbery and transition region and only about 2.7 times in the glassy region, indicating that Poisson's ratio is close to 0.5 in the rubbery and transition regions and about 0.35 in the glassy one.

For SMRD the Young's modulus is also approximately three times the shear modulus in the rubbery and transition regions and only about 2.5 times in the glassy region, thus indicating that Poisson's ratio is again close to 0.5 in the rubbery and transition regions but about .30 in the glassy zone.

IV. SUMMARY AND CONCLUSIONS

Different techniques for measuring the dynamic properties of elastomers have been presented and discussed. The dynamic properties for the elastomer have been measured by the various techniques and correlated over wide frequency and temperature ranges. It was found that there is good agreemen in the results of the various techniques.

The test results also revealed the importance of having experimental data over a wide frequency range in order to properly imply the temperature/frequency superposition principle. It was found that with approximately 8 decades of frequency data the damping properties for the test methods could be collapsed onto master curves.

REFERENCES

1. "Standard for measuring vibration damping properties of materials," American Society for Testing and Materials, E756-80.

2. D.I.G. Jones, "Temperature-frequency dependence of dynamic properties of damping materials," J. Sound Vib., 33(4), pp 451-470, 1974.

3. A.D. Nashif, "A new method for determining the damping properties of viscoelastic materials," Shock and Vibration Bulletin, 36, pp 37-47, 1967.

4. F.S. Owens, "Elastomers for damping over wide temperature ranges," Shock and Vibration Bulletin, 36, Part 4, pp 25-35, 1967.

5. J.L. Edwards and D.R. Hicks, "Useful range of a mechanical impedance technique for measurement of dynamic properties of materials," J.A.S.A., 52, pp 1053-1056, 1972.

6. D.I.G. Jones and A. Muszynska, "On the modal identification of multiple degree of freedom systems from experimental data," Shock and Vibration Bulletin, 53, 1983.

7. C.M. Cannon, A.D. Nashif, and D.I.G. Jones, "Damping measurements on soft viscoelastic materials using a tuned damper technique," Shock and Vibration Bulletin, 38, Part 3, pp 151-163, 1968.

8. D.L. Hunston, W.D. Bascom, E.E. Wells, F.D. Fahey, and J.L. Bitner, "Viscoelastic characterization of structural adhesive via forced oscillation experiments," Adhesion and Absorption of Polymers (ed. Lieng-Huang Lee), Plenum Publishing Corporation, New York, 1980.

9. G.E. Warnaka and H.T. Miller, "Strain-frequency temperature relationships in polymers," J. Eng. for Industry, Tran. ASME, 1967.

10. L.C. Rogers, "Operators and fractional derivatives for viscoelastic constitutive equations," Journal of Rheology, 27(4), pp 351-372, 1983.

11. D.I.G. Jones, "A reduced-temperature nomogram for characterization of damping material behavior," Shock and Vibration Bulletin, 48, Part 2, pp 13-22, 1978.

12. D.I.G. Jones, "An attractive method for displaying material damping data," AIAA Journal, 18(8), pp 644-649, 1981.

13. D. Ross, E.E. Ungar, and E.M. Kerwin, Jr., "Damping of Plate Flexural Vibrations by Means of Viscoelastic Laminate," Section III of Structural Damping, ASME, pp. 49-88, 1959.

14. H. Oberst and K. Frankenfeld, "Uber die Dampfung der Biegeschwingungen dunner Bleche durch festhaftende Belage," Acustica, Vol. 2, pp. 181-194, 1952.

15. G.E. Warnaka, "Effect of Adhesive Stiffness on Extensional Damping" ASME, 1967.

16. J.C. Snowdon, Vibration and Shock in Damped Mechanical Systems, Wiley, New York, 1968.

17. M.P. Blake, and W.S. Mitchell, Vibration and Acoustic Measurement Handbook, pp. 214-224.

18. L.C. Rogers, J. Eichenlaub, and J.B. Layton, "Standard Graphical Presentation of Complex Modulus and Processing Methodology," Damping 1986, AFWAL Technical Report.

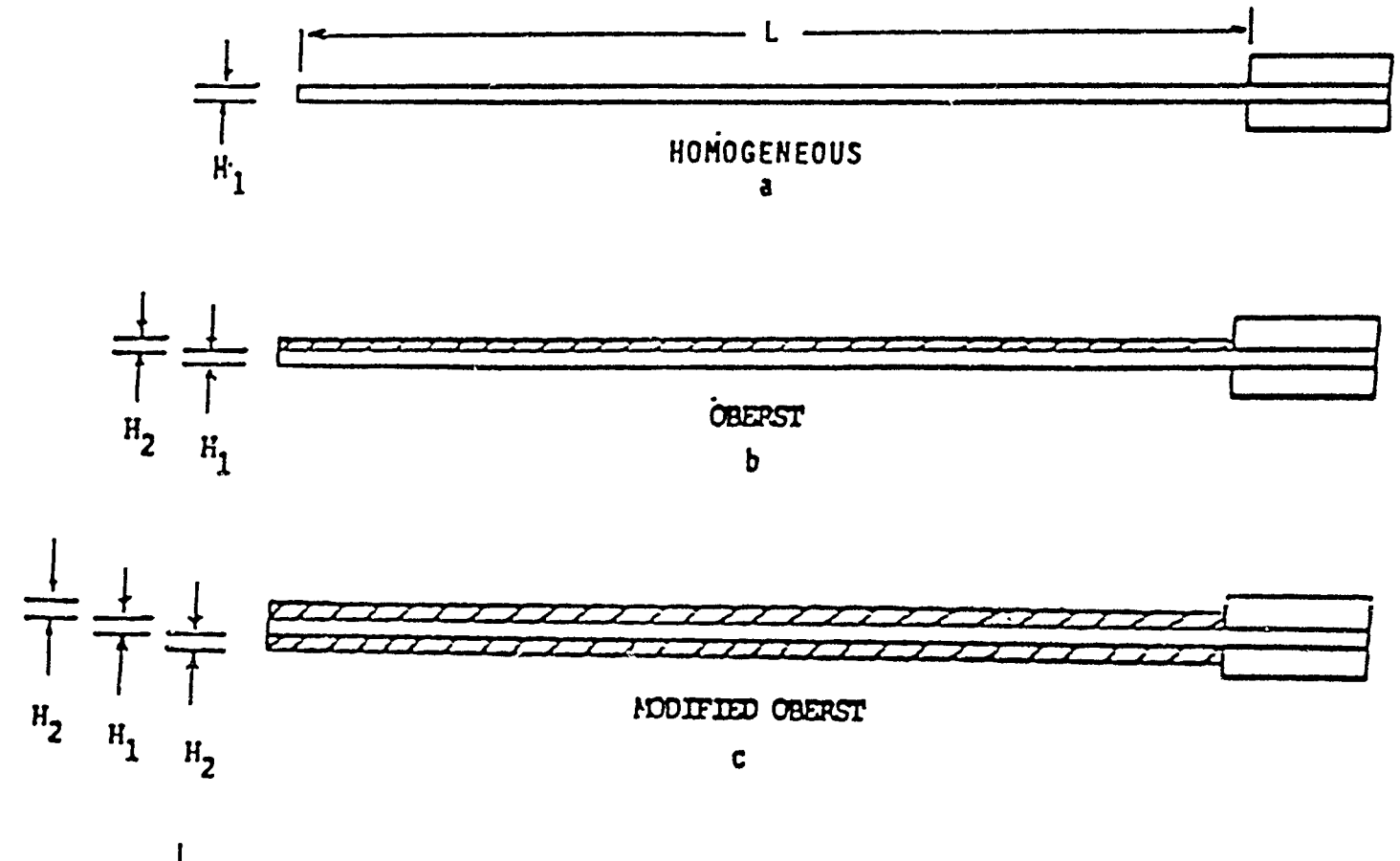


Figure 1: Beam Test Specimen Configuration

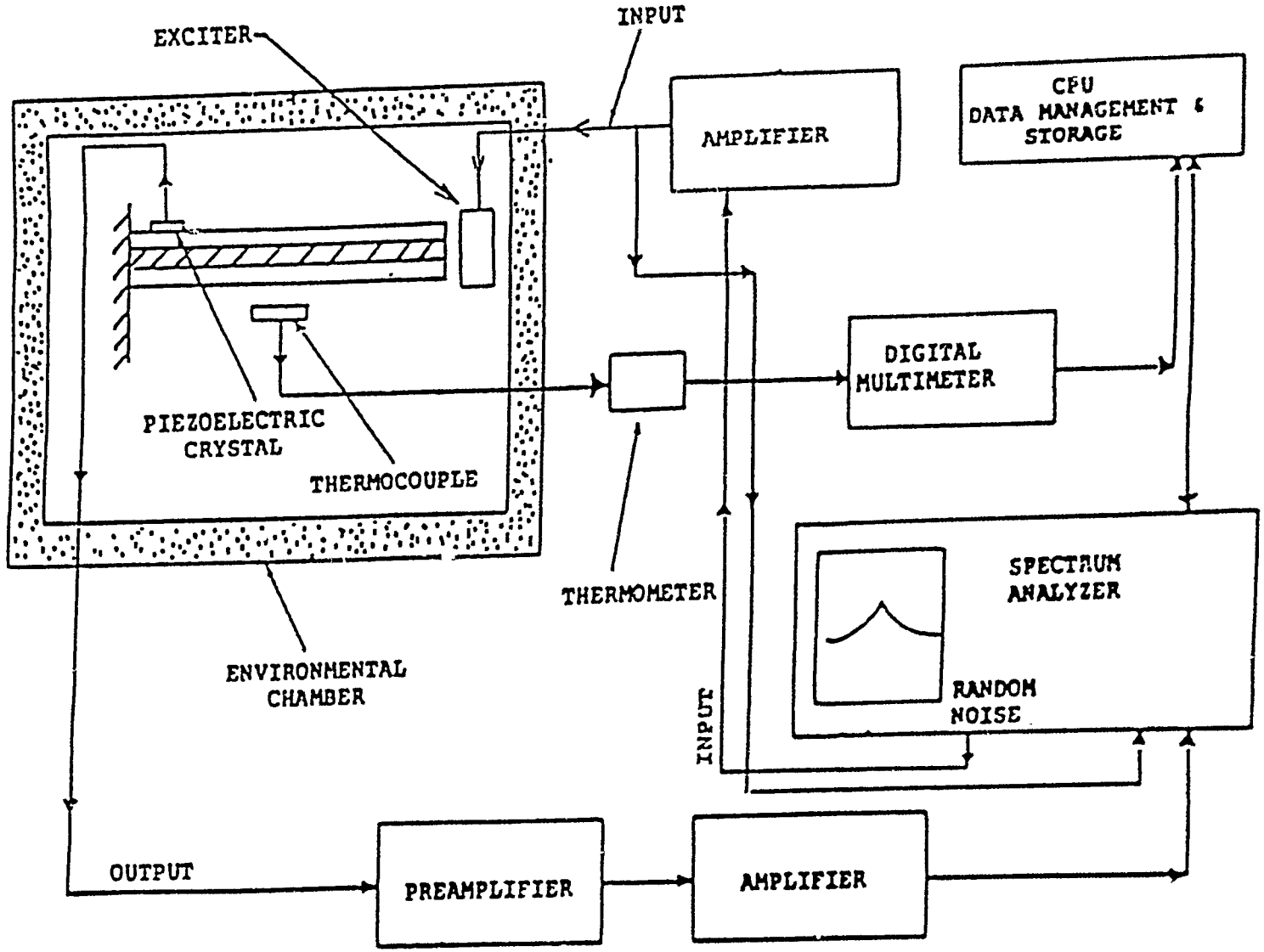


Figure 2: Block Diagram of Typical Laboratory Test Setup for Vibration Beam Tests

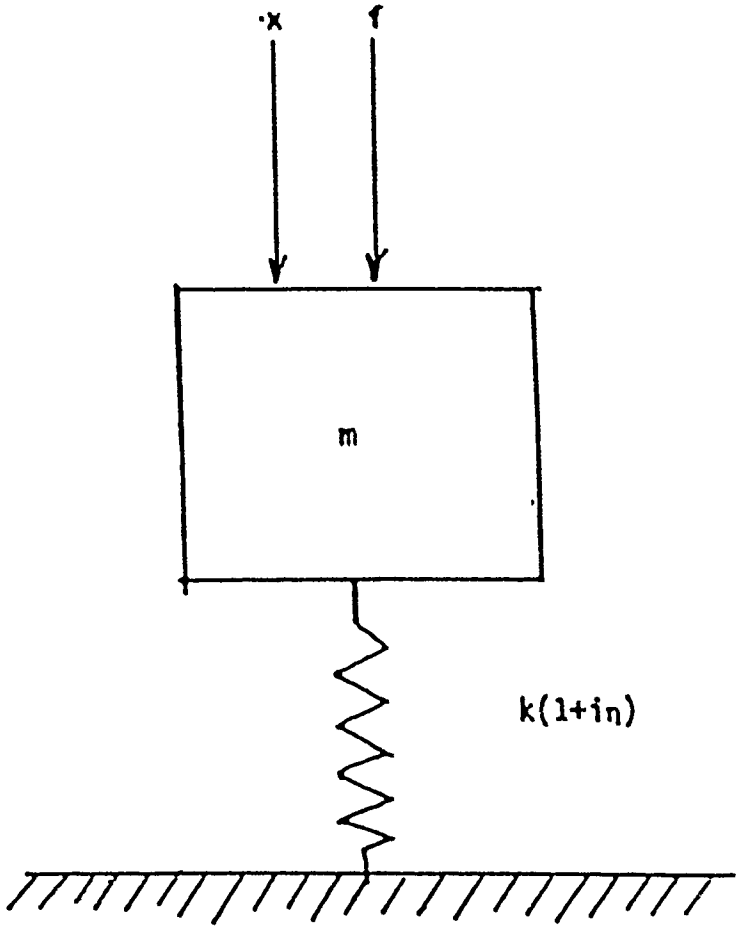
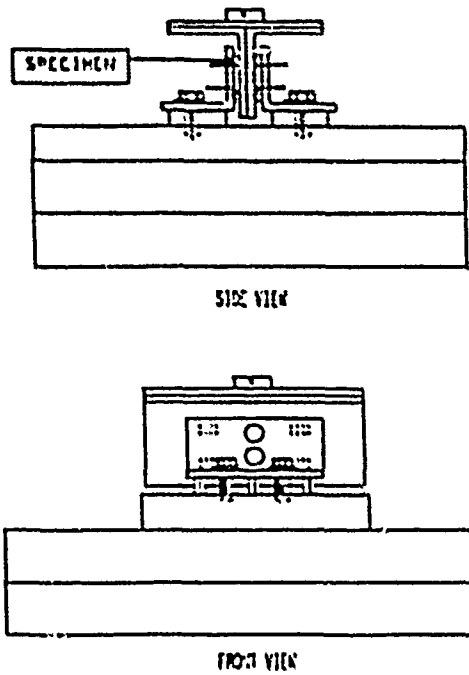


Figure 3: Schematic of Impedance Measurement

SHEAR MECHANICAL IMPEDANCE BREAKDOWN



SHEAR MECHANICAL IMPEDANCE SETUP

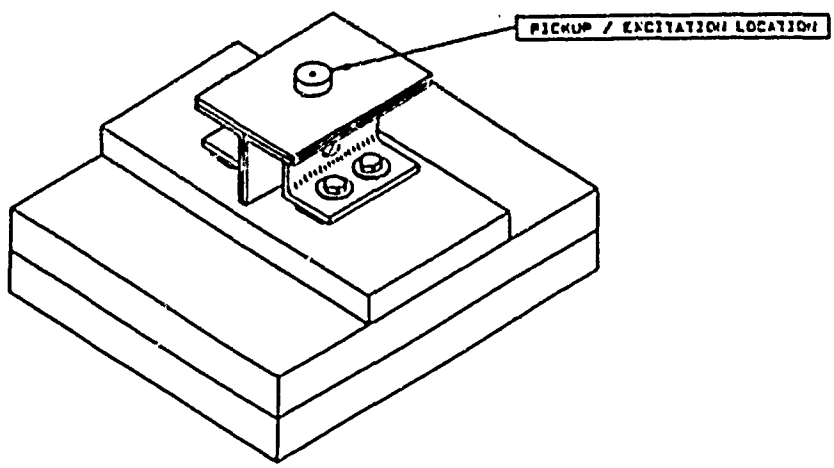


Figure 4: Typical Test Specimen Setup for Resonant and Mechanical Impedance Shear Test Techniques

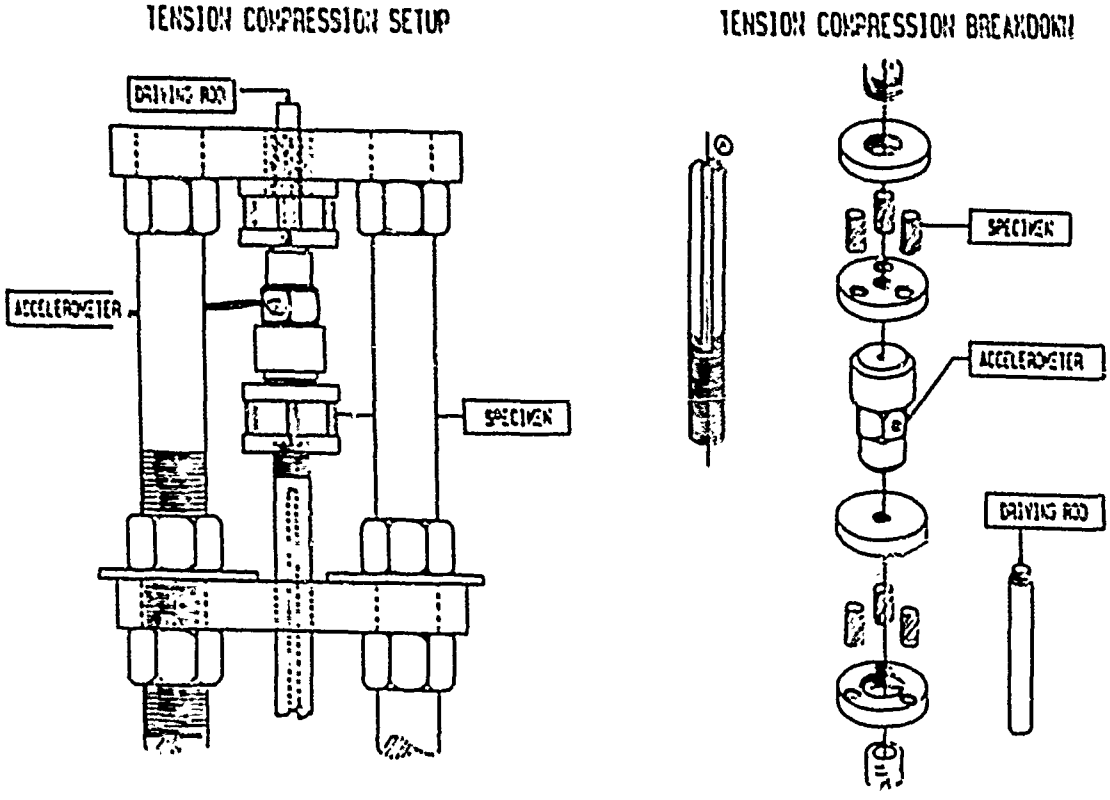


Figure 5: Test Setup for Resonant and Mechanical Impedance Tension-Compression Test Techniques

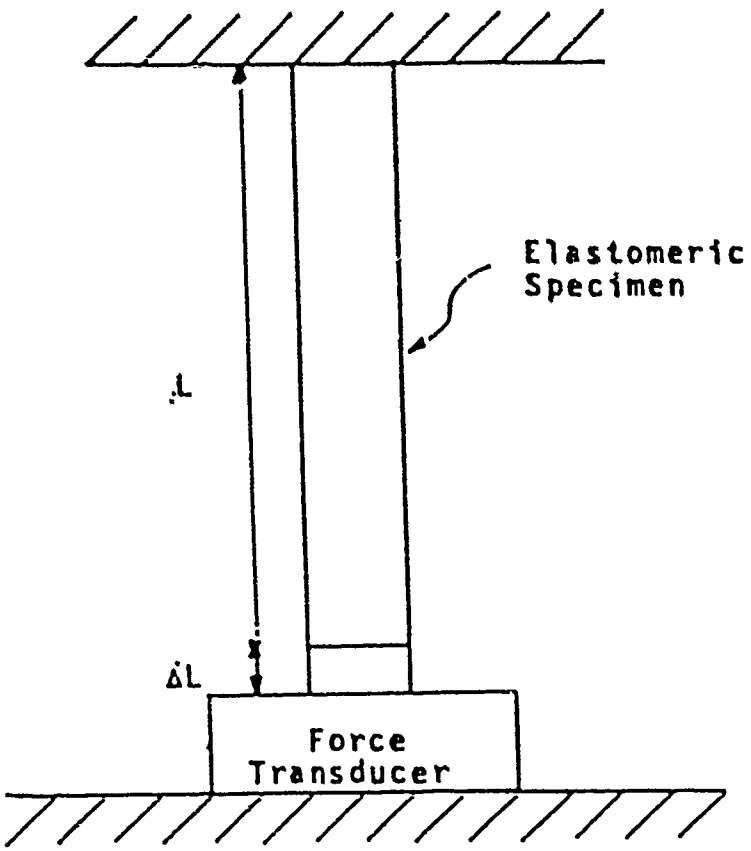


Figure 6: Schematic of Relaxation Measurements

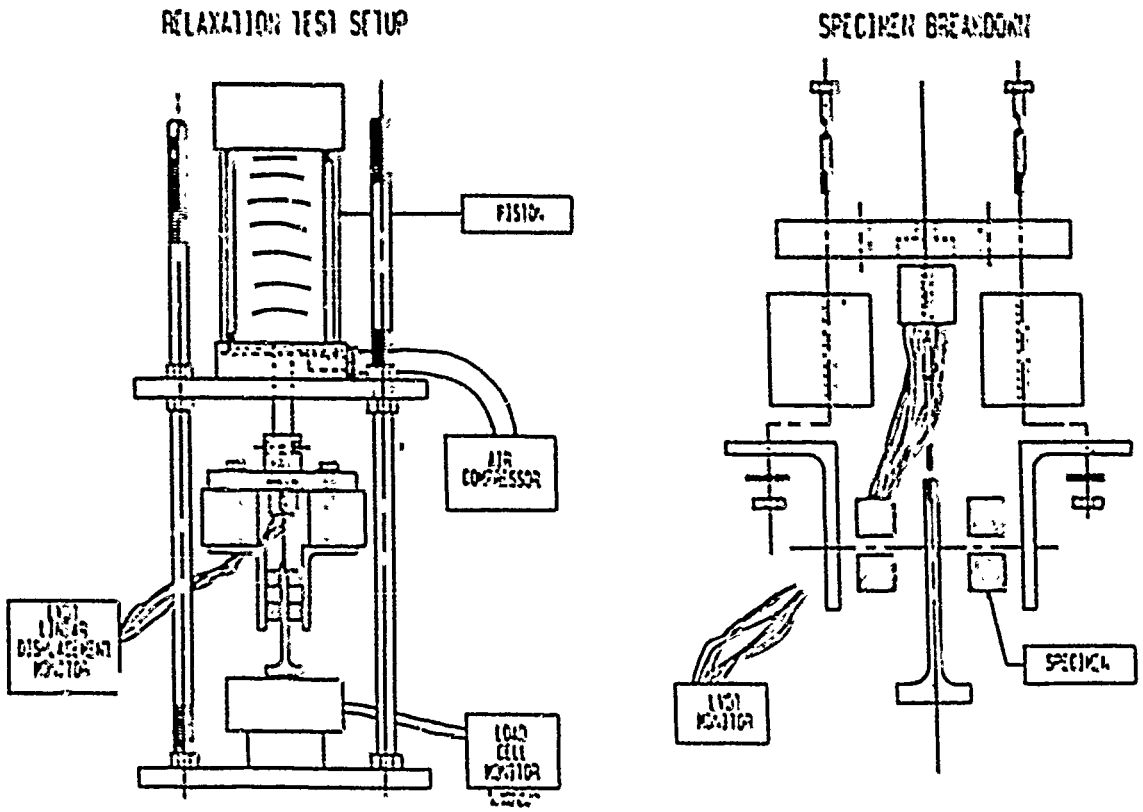


Figure 7: Shear Relaxation Test Measurement System

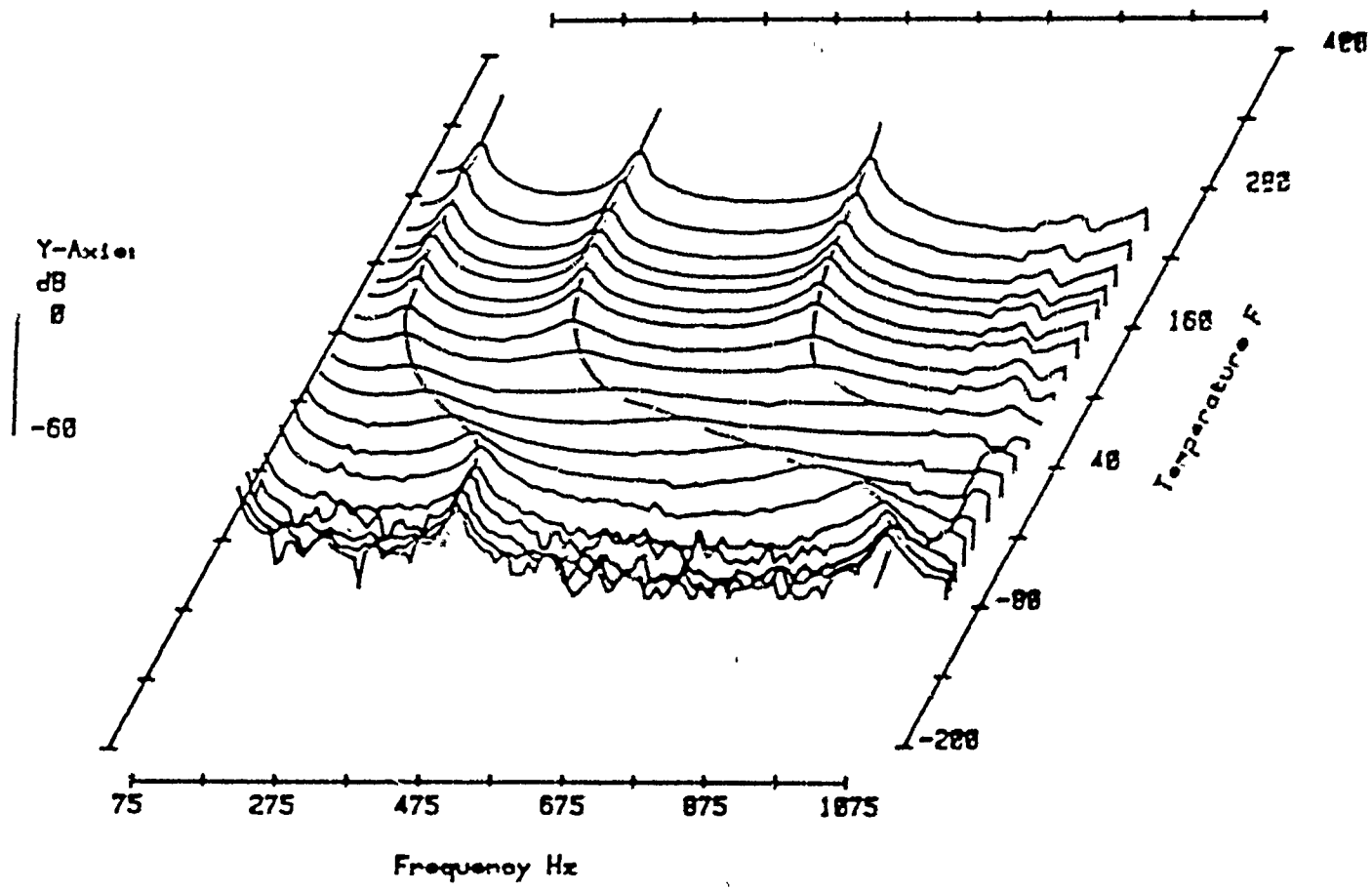
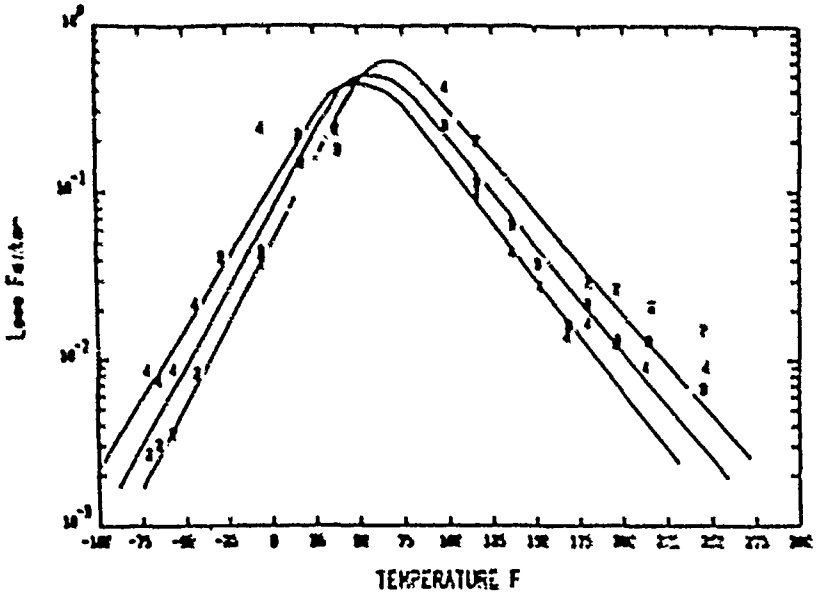


Figure 8: 10" Sandwich Beam: Temperature Spectrum Map



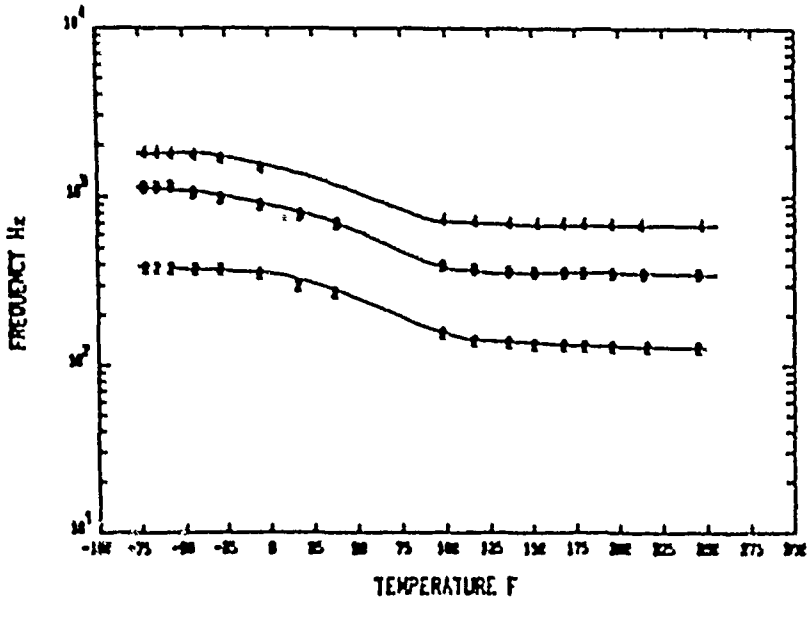


Figure 9: 10" Sandwich Beam: Variation of Loss Factor and Resonance Frequency with Temperature for Acrylic Core Foam

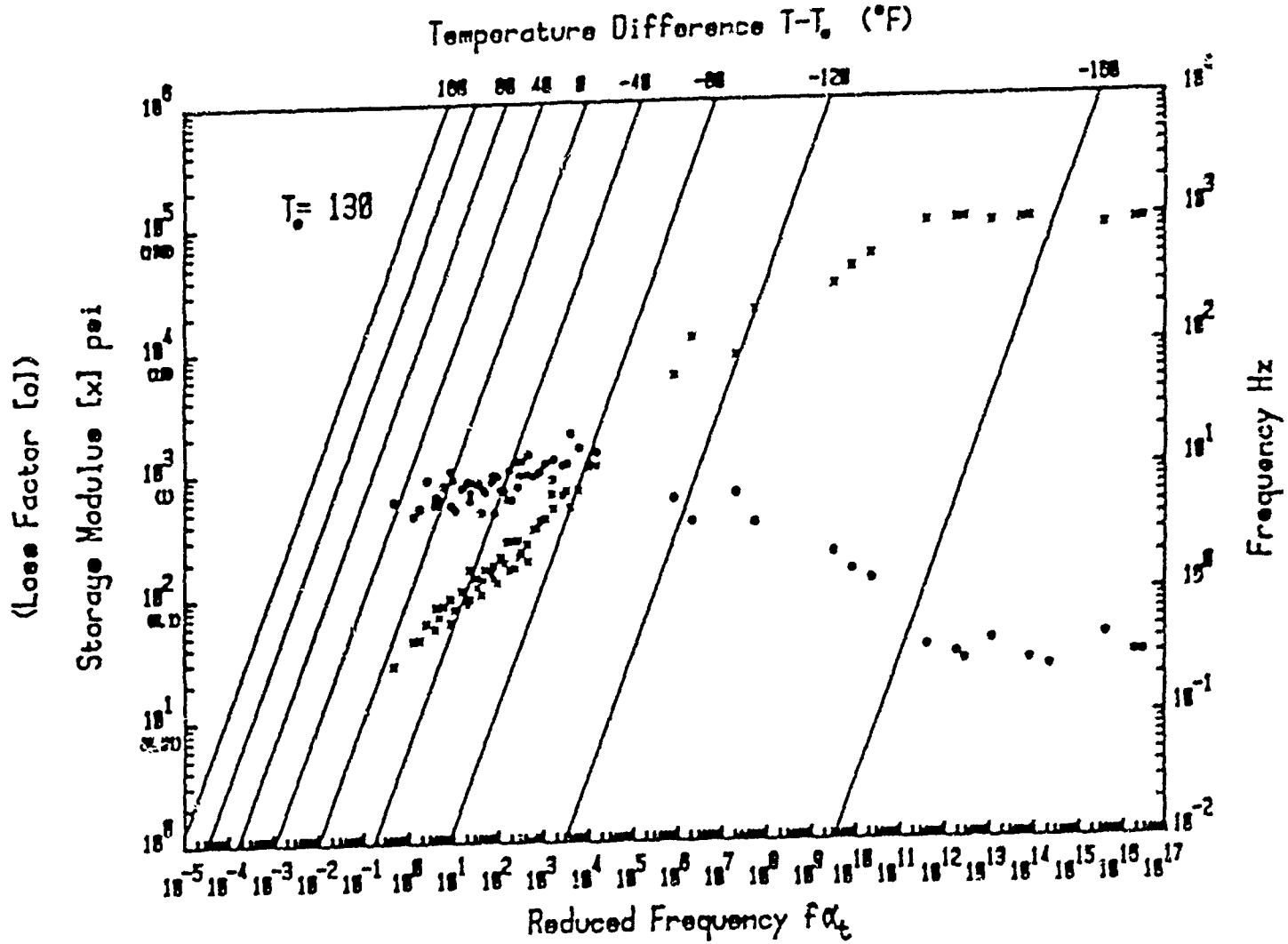


Figure 10: 10" Sandwich Beam: Temperature/Frequency Nomogram for Acrylic Core Foam

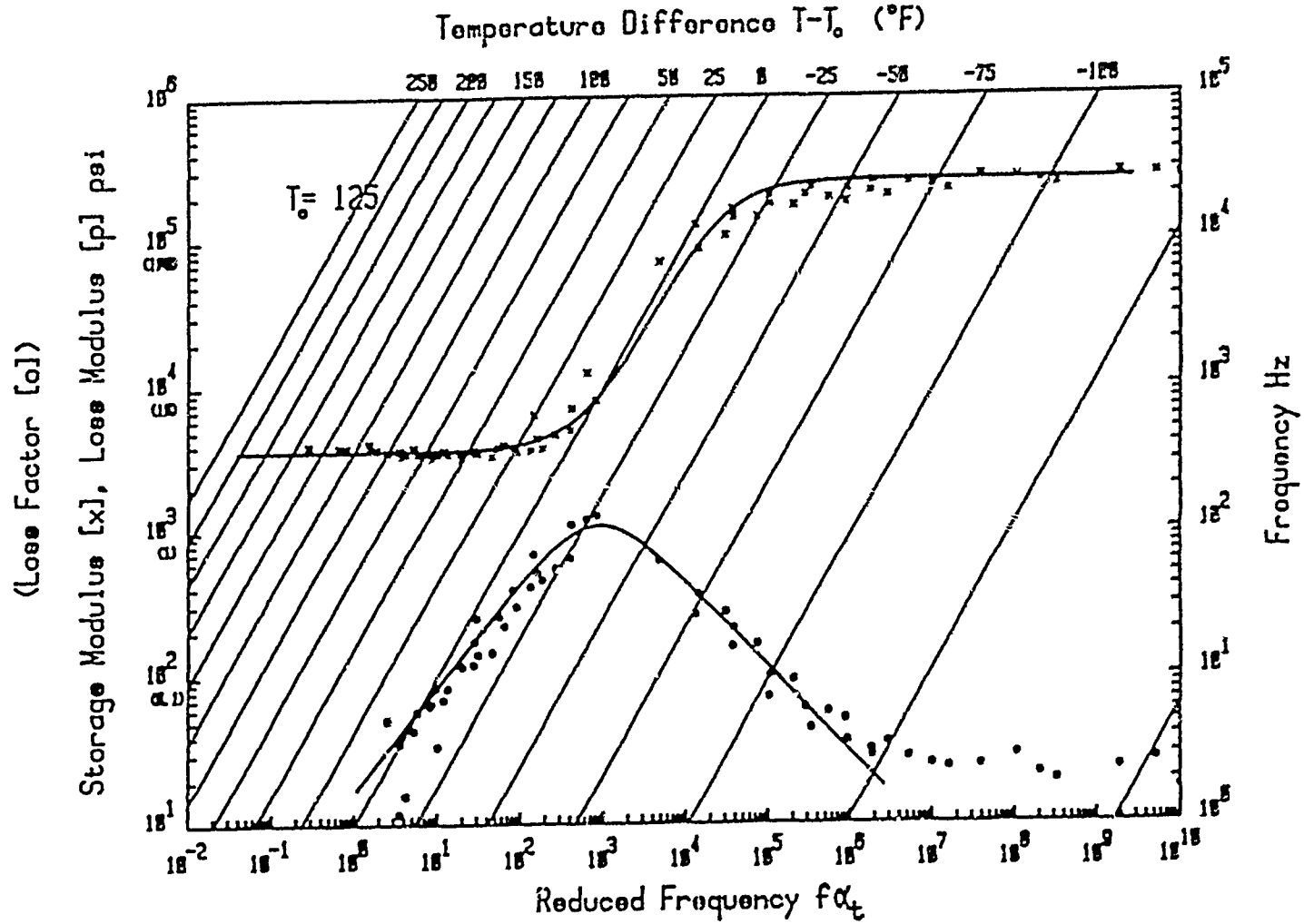


Figure 11: SMRD 100-F90 10" Modified Oberst Beam - Temperature/ Frequency Nomogram

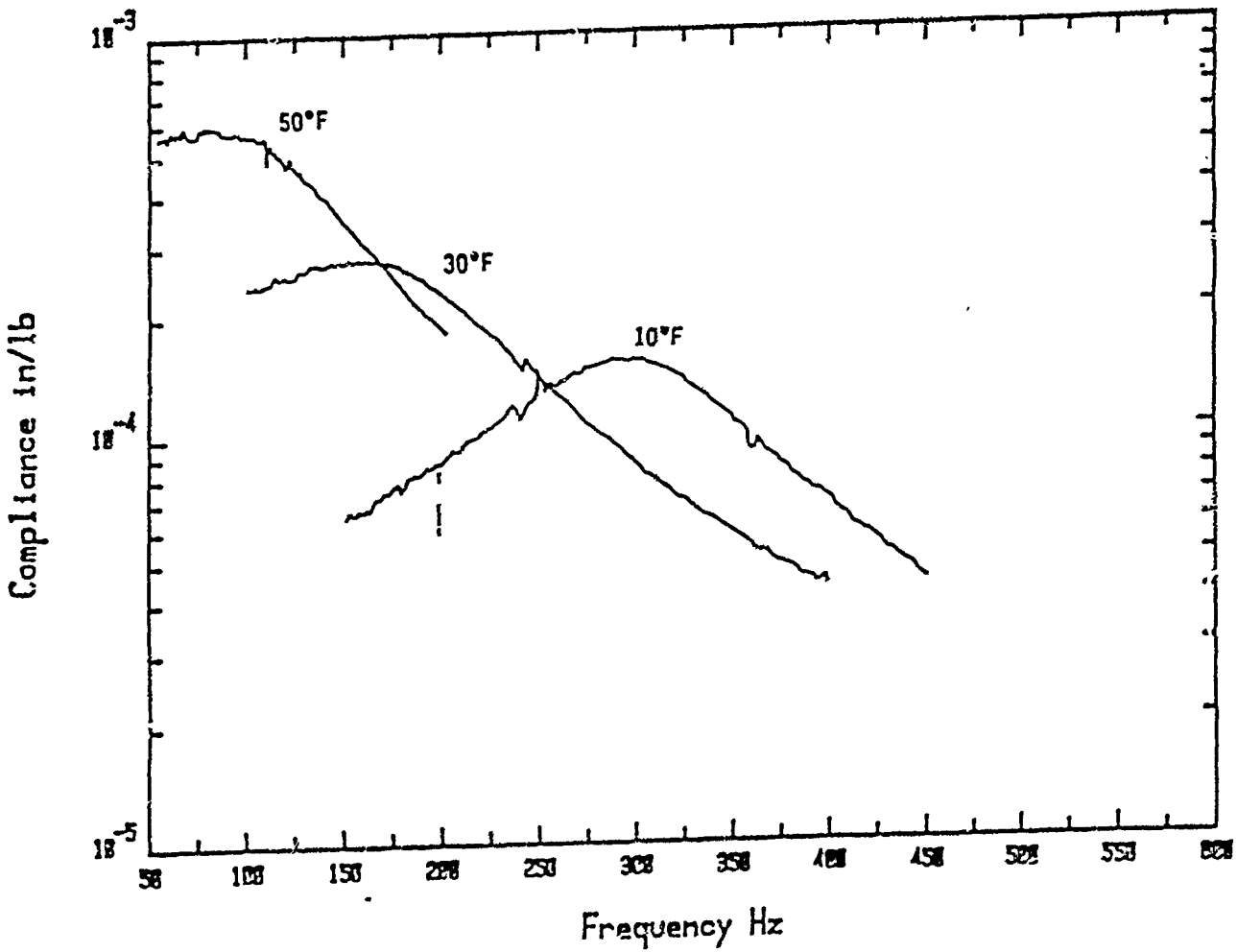


Figure 12: Resonance and Impedance: Compliance vs. Frequency for Acrylic Core Foam at Various Temperatures in Shear

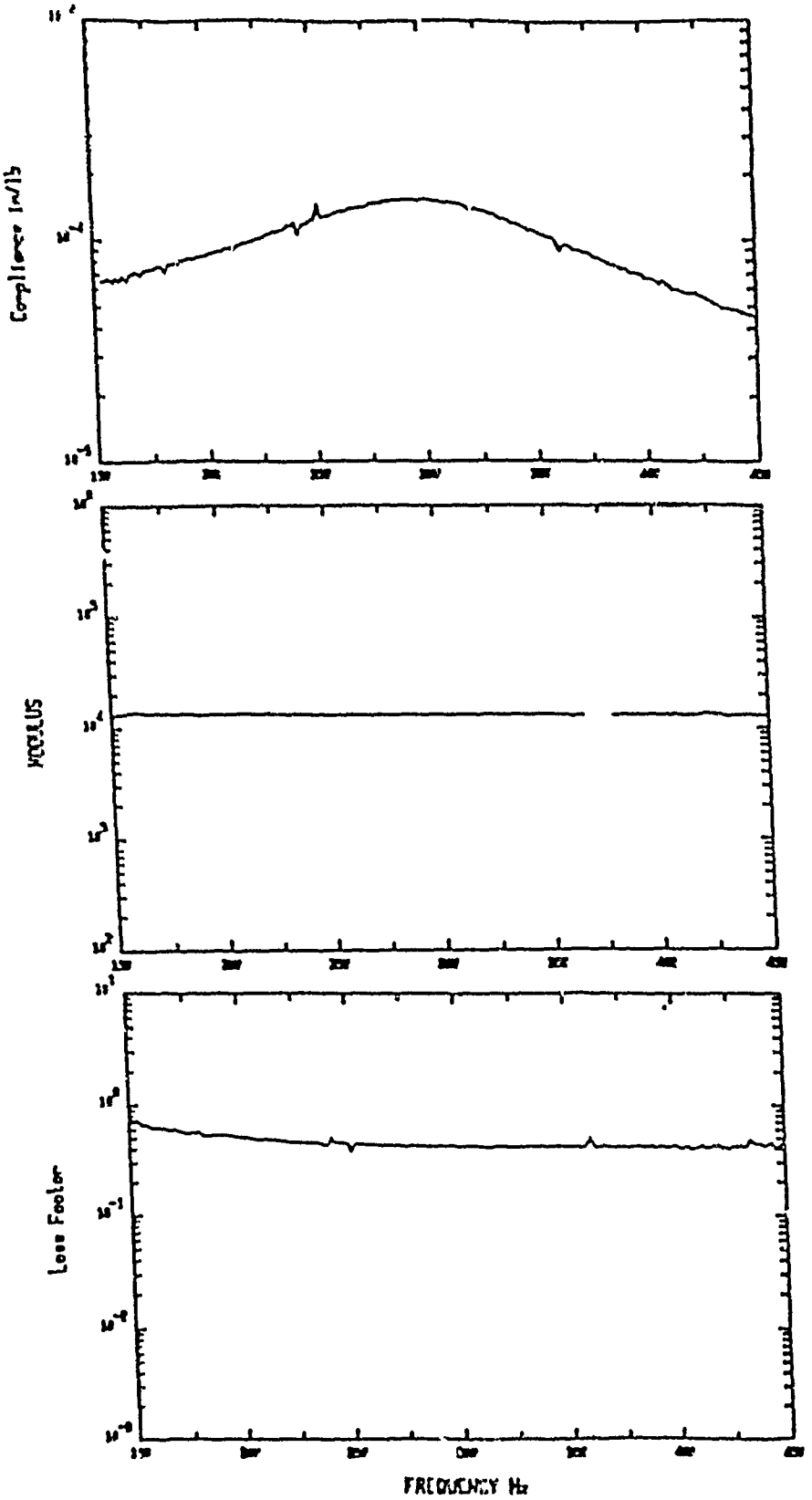


Figure 13: Material Properties in Shear @ 10°F Using the Impedance Technique for Acrylic Core Foam

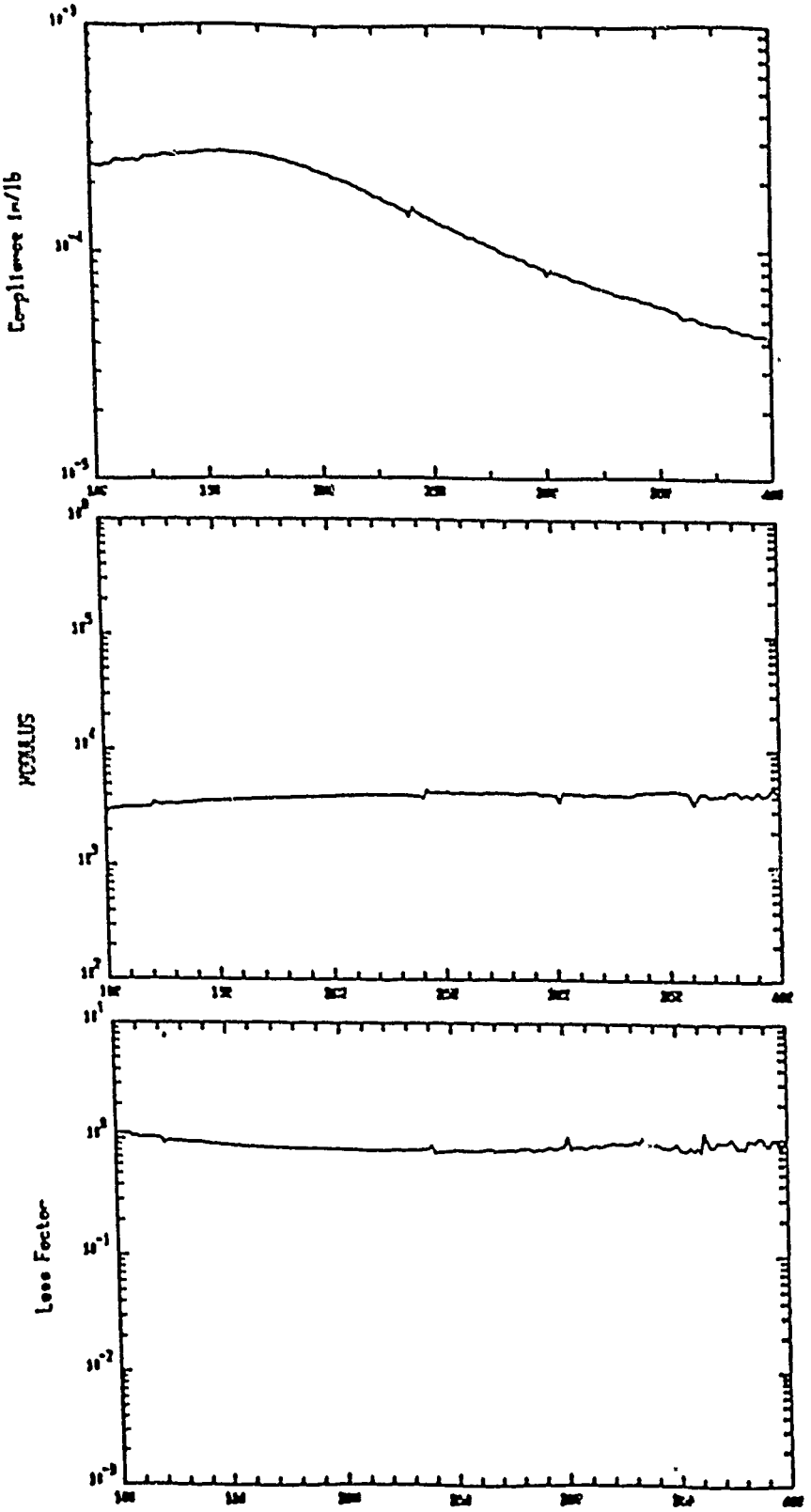


Figure 14: Material Properties in Shear @ 30 °F Using the Impedance Technique for Acrylic Core Foam

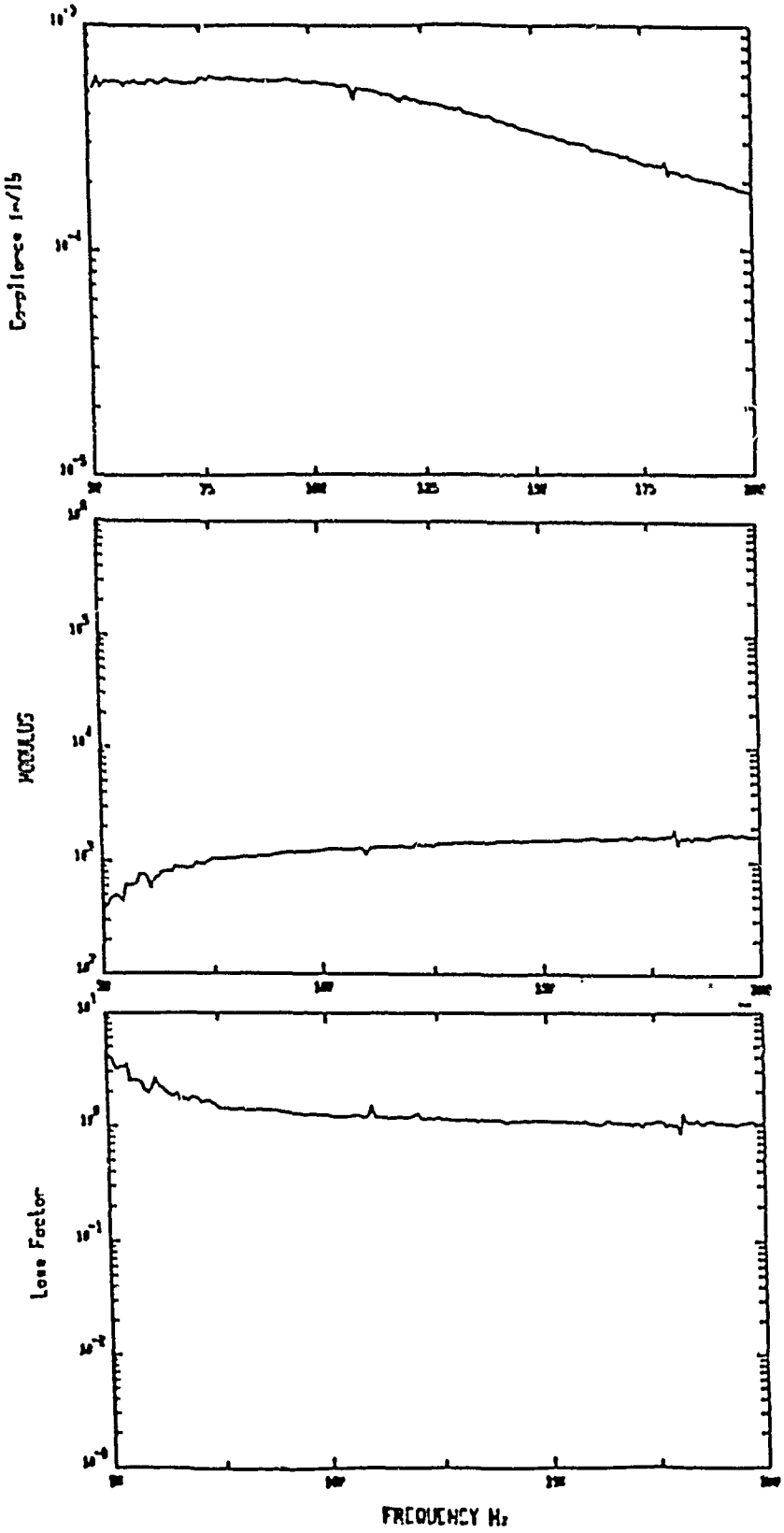


Figure 15: Material Properties in Shear @ 50°F Using the Impedance Technique for Acrylic Core Foam

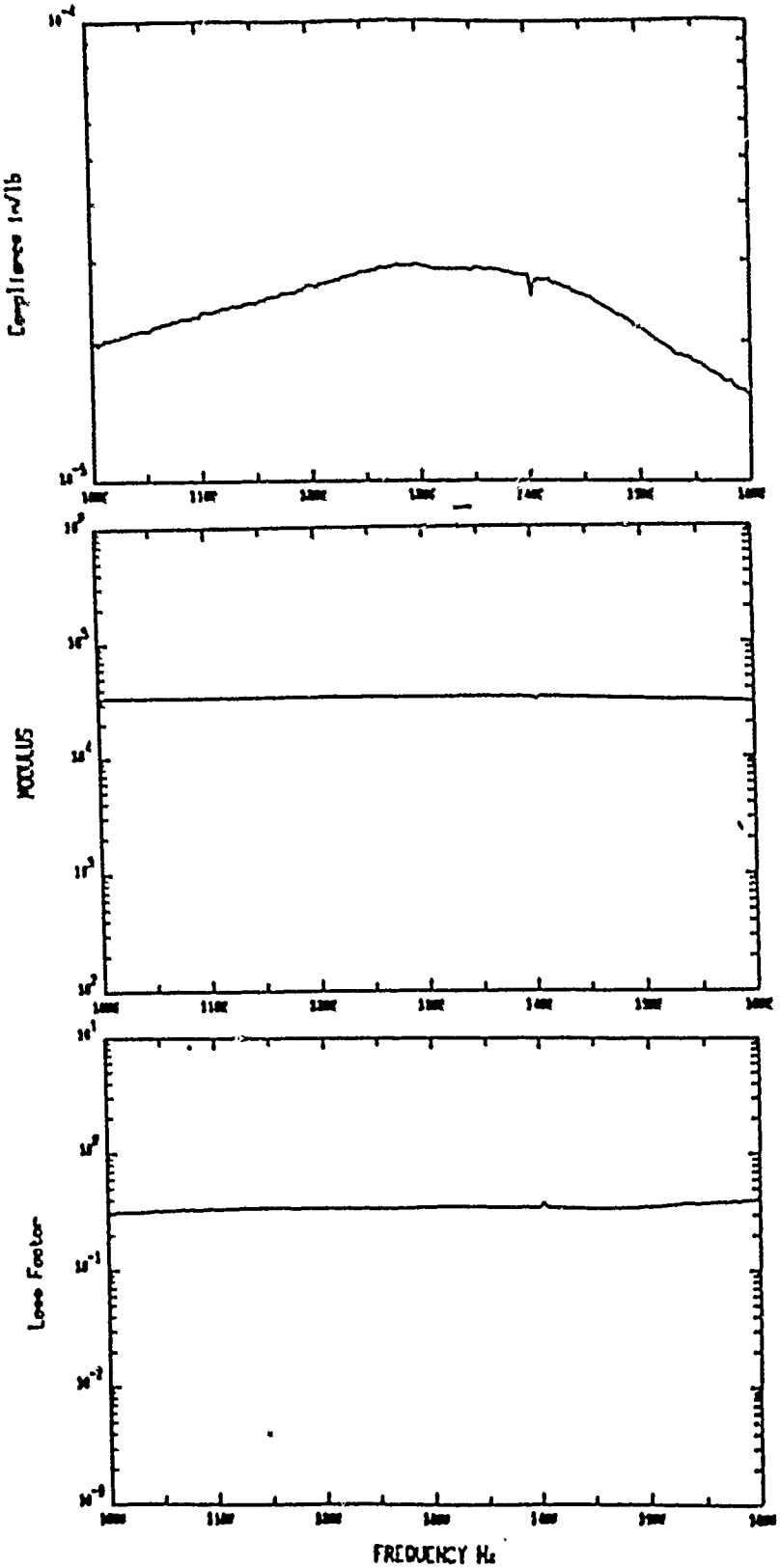


Figure 16: Material Properties in Tension-Compression @ 30°F Using the Impedance Technique for Acrylic Core Foam

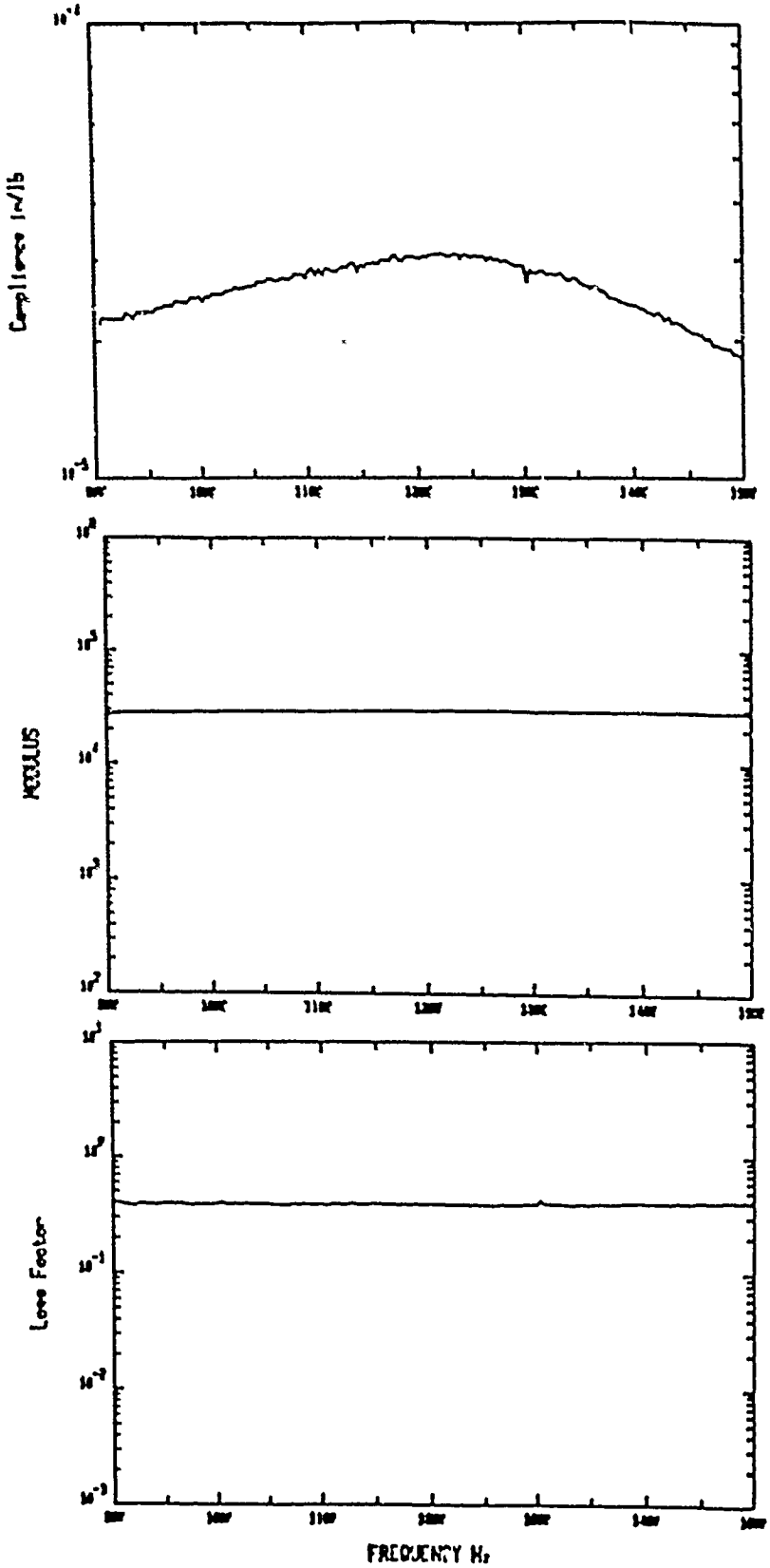


Figure 17: Material Properties in Tension-Compression @ 44°F Using the Impedance Technique for Acrylic Core Foam

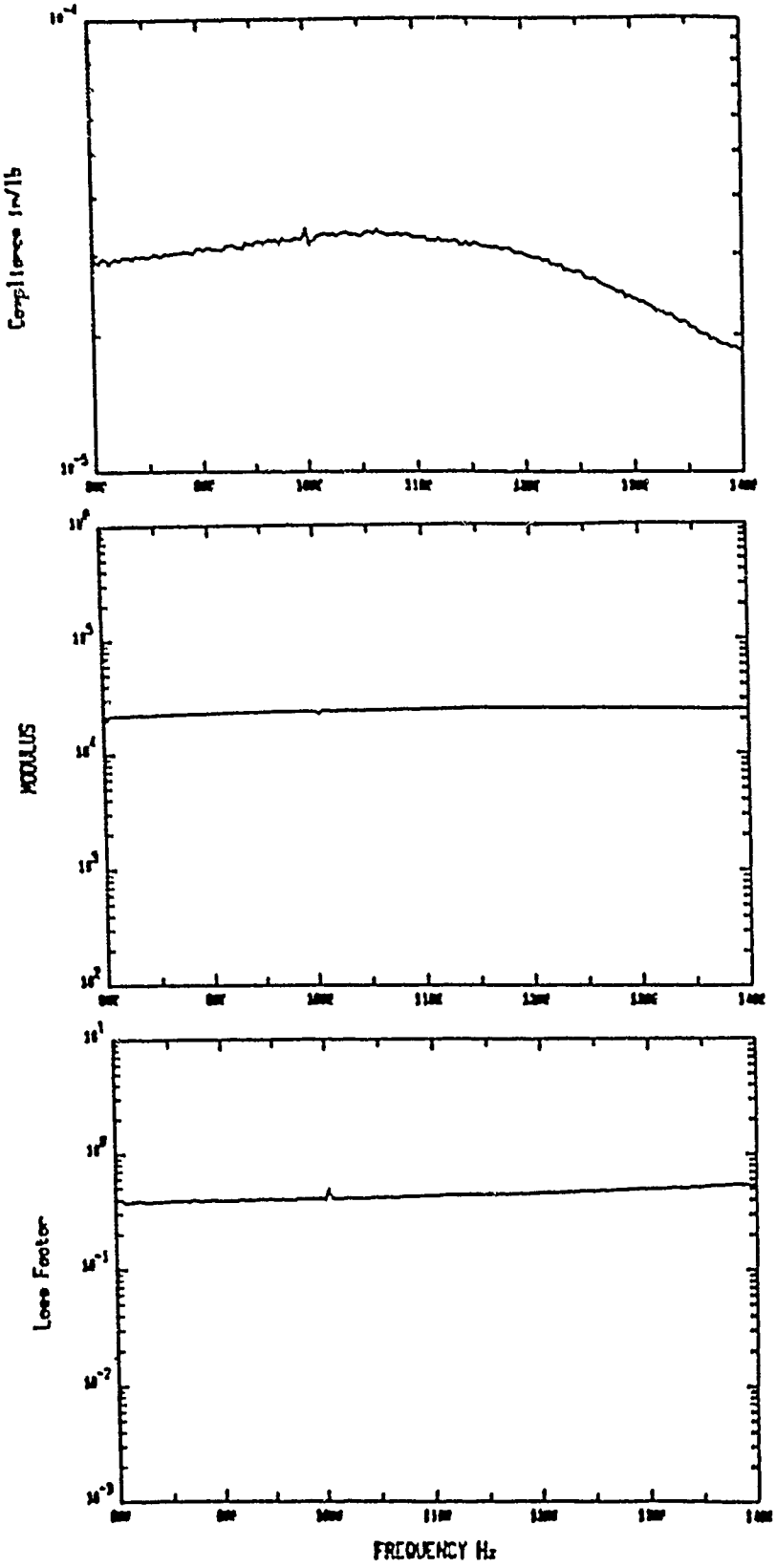


Figure 18: Material Properties in Tension-Compression @ 53°F Using the Impedance Technique for Acrylic Core Foam

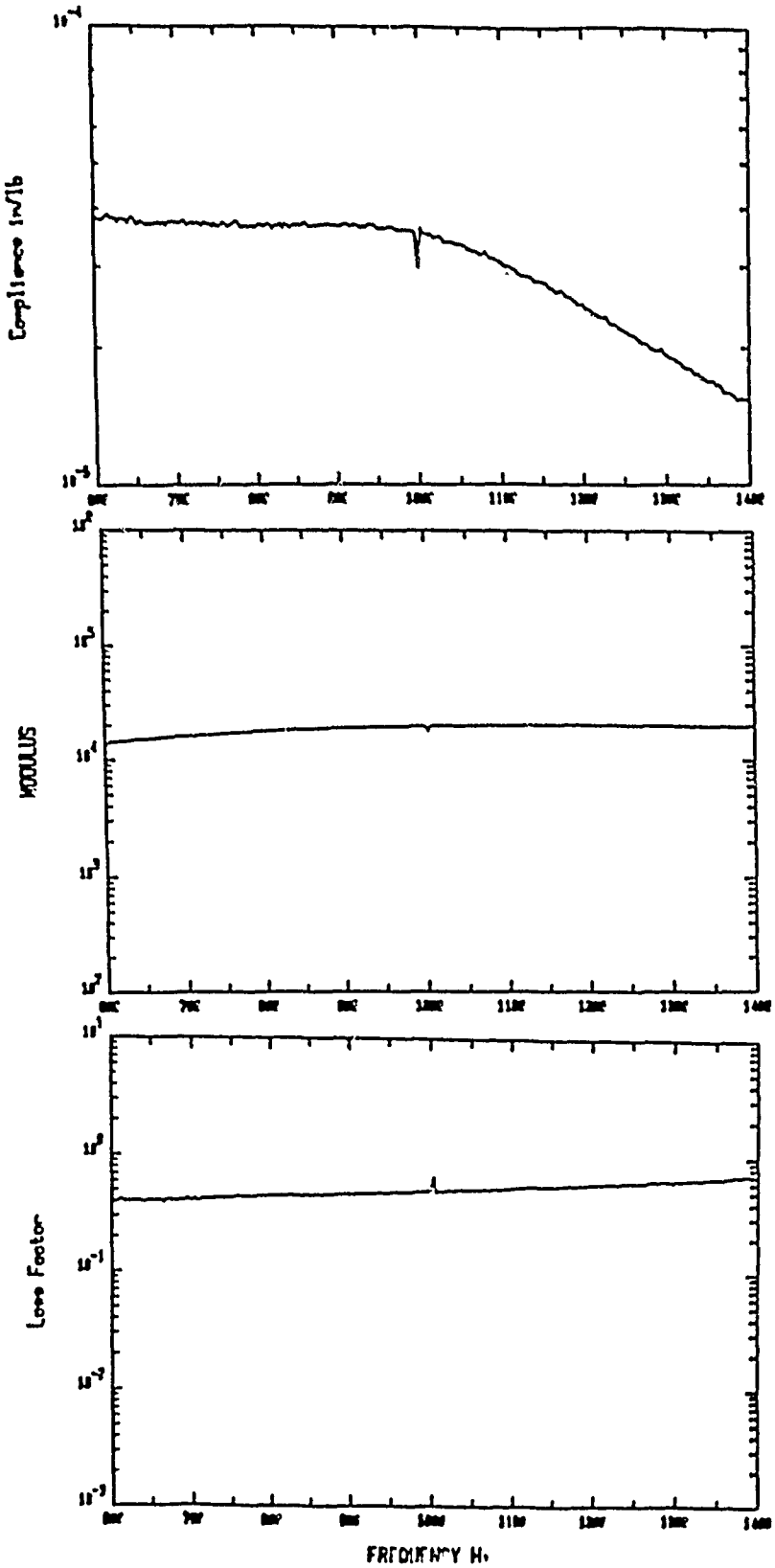


Figure 19: Material Properties in Tension-Compression @ 63°F Using the Impedance Technique for Acrylic Core Foam

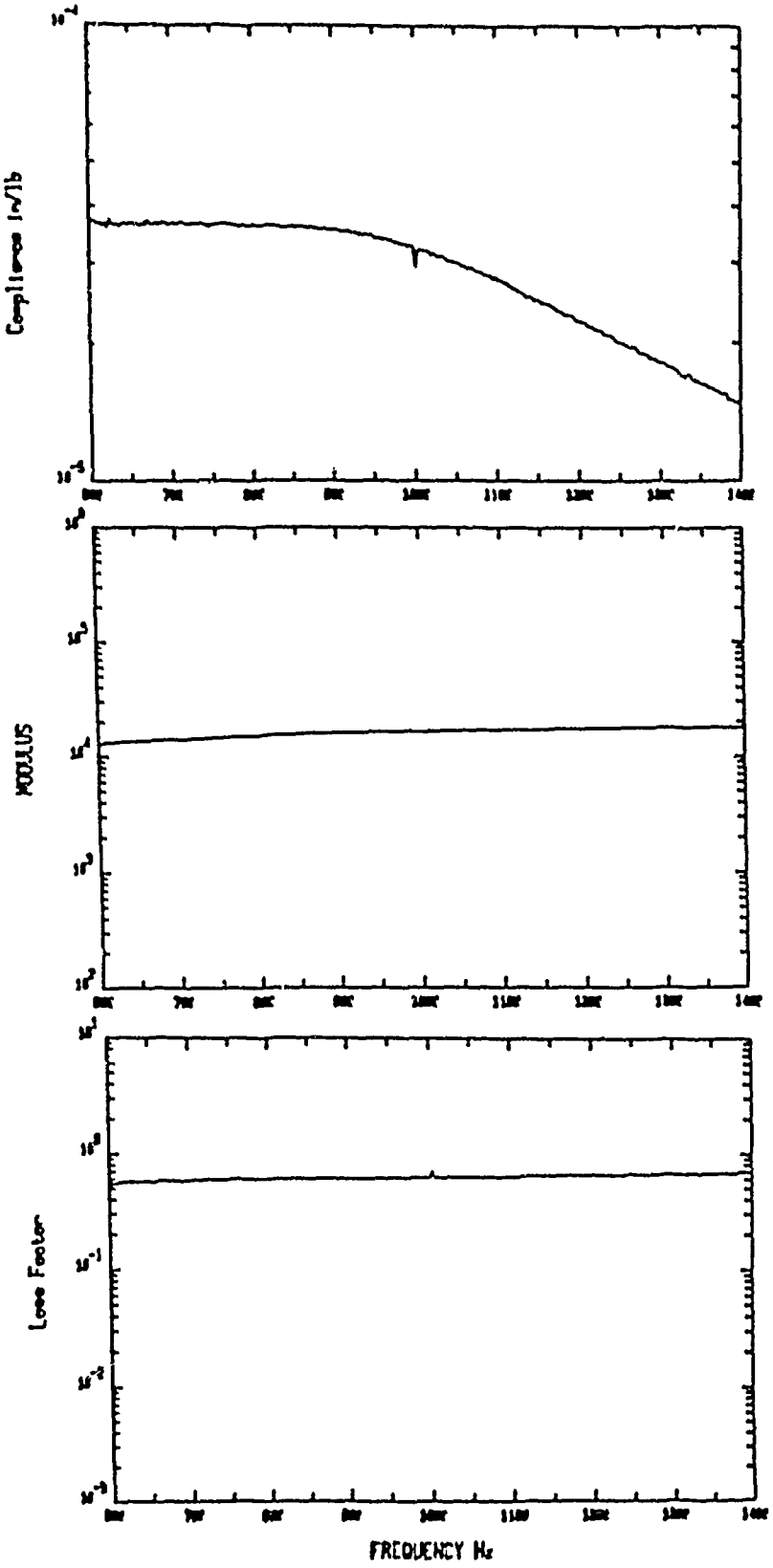


Figure 20: Material Properties in Tension-Compression @ 71°F Using the Impedance Technique for Acrylic Core Foam

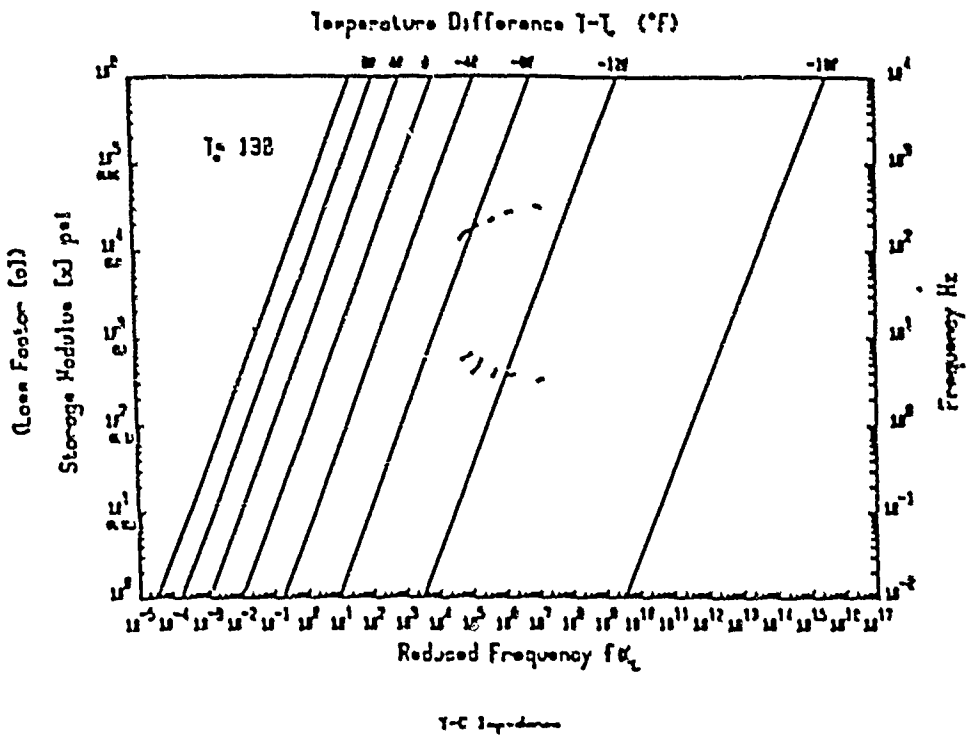


Figure 21: Material Properties in Tension-Compression Derived from Resonance and Impedance Techniques for Acrylic Core Foam

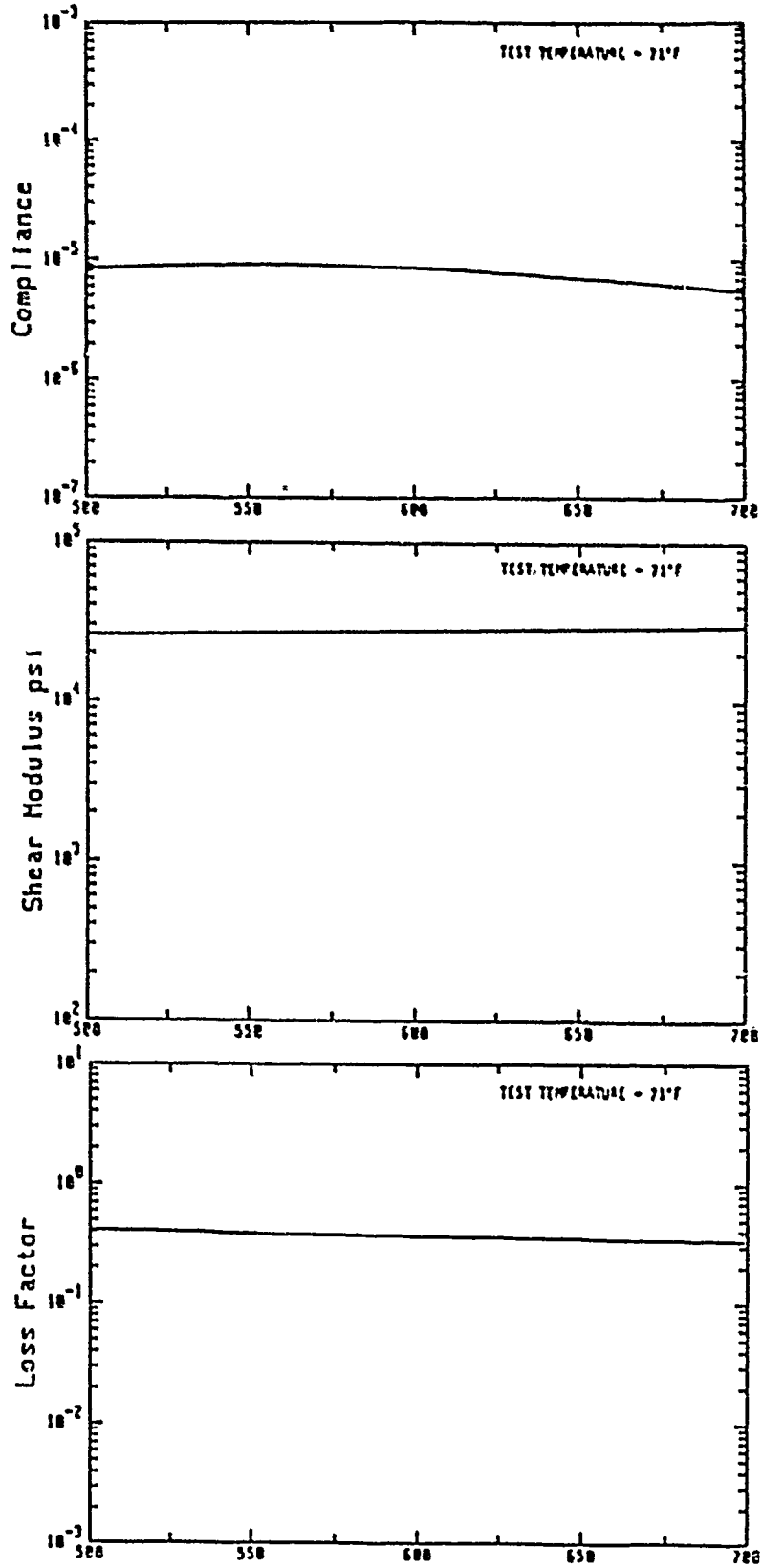


Figure 22: Material Properties in Shear at 71°F Using Mechanical Impedance for SMRD 100-F90

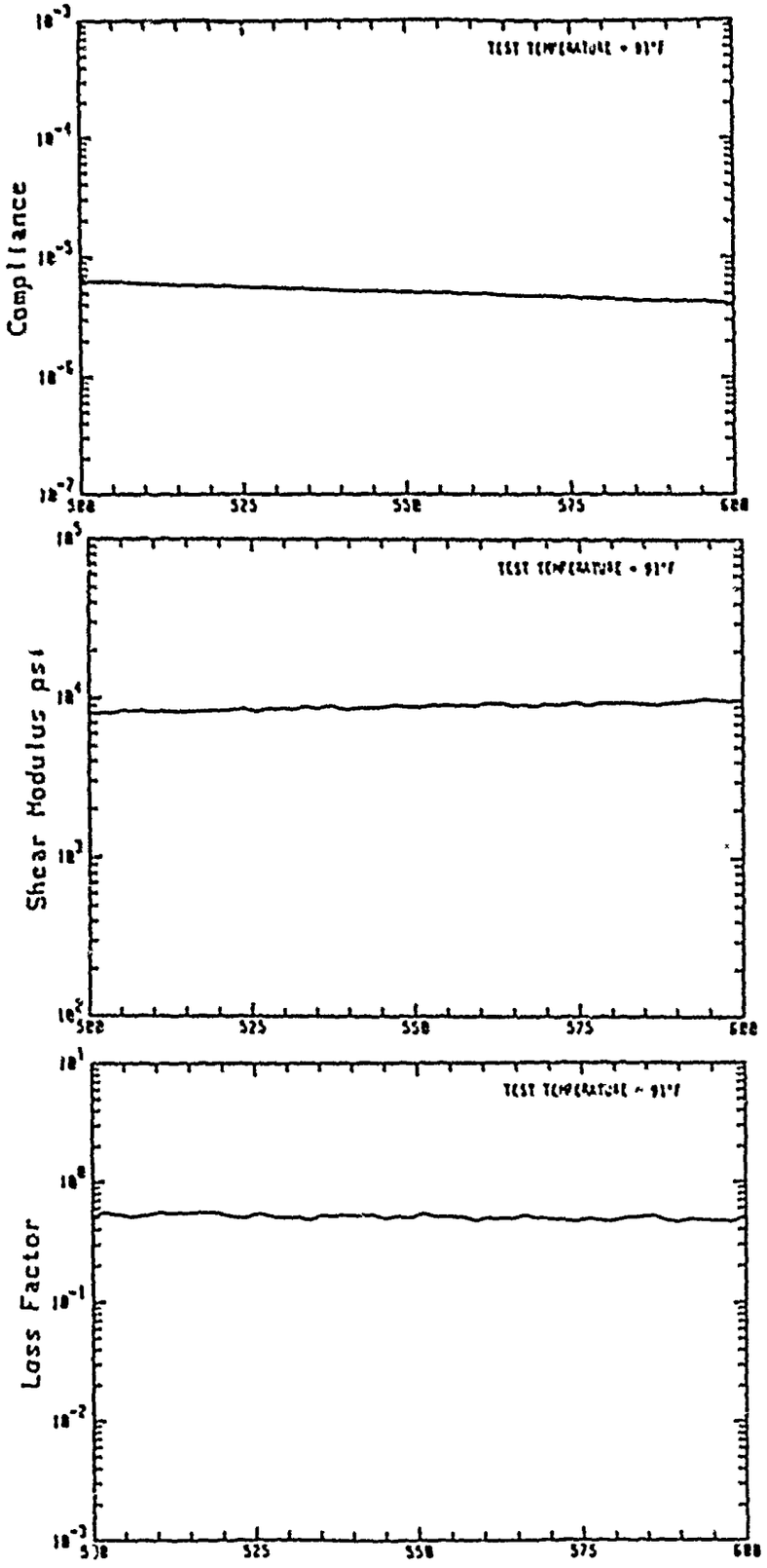


Figure 23: Material Properties in Shear at 91°F Using Mechanical Impedance for SMRD 100-F90

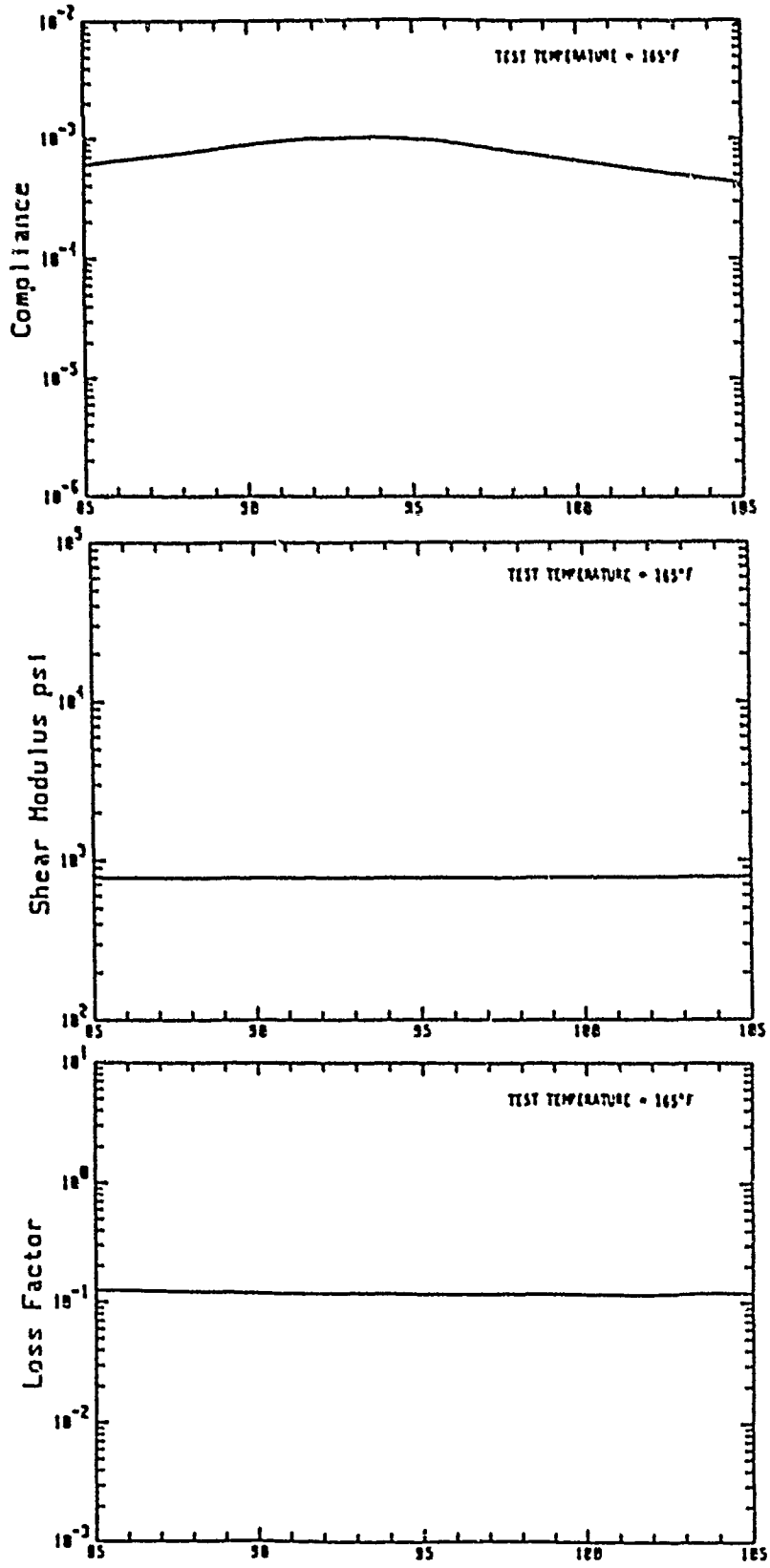


Figure 24: Material Properties in Shear at 165°F Using Mechanical Impedance for SMRD 100-F90

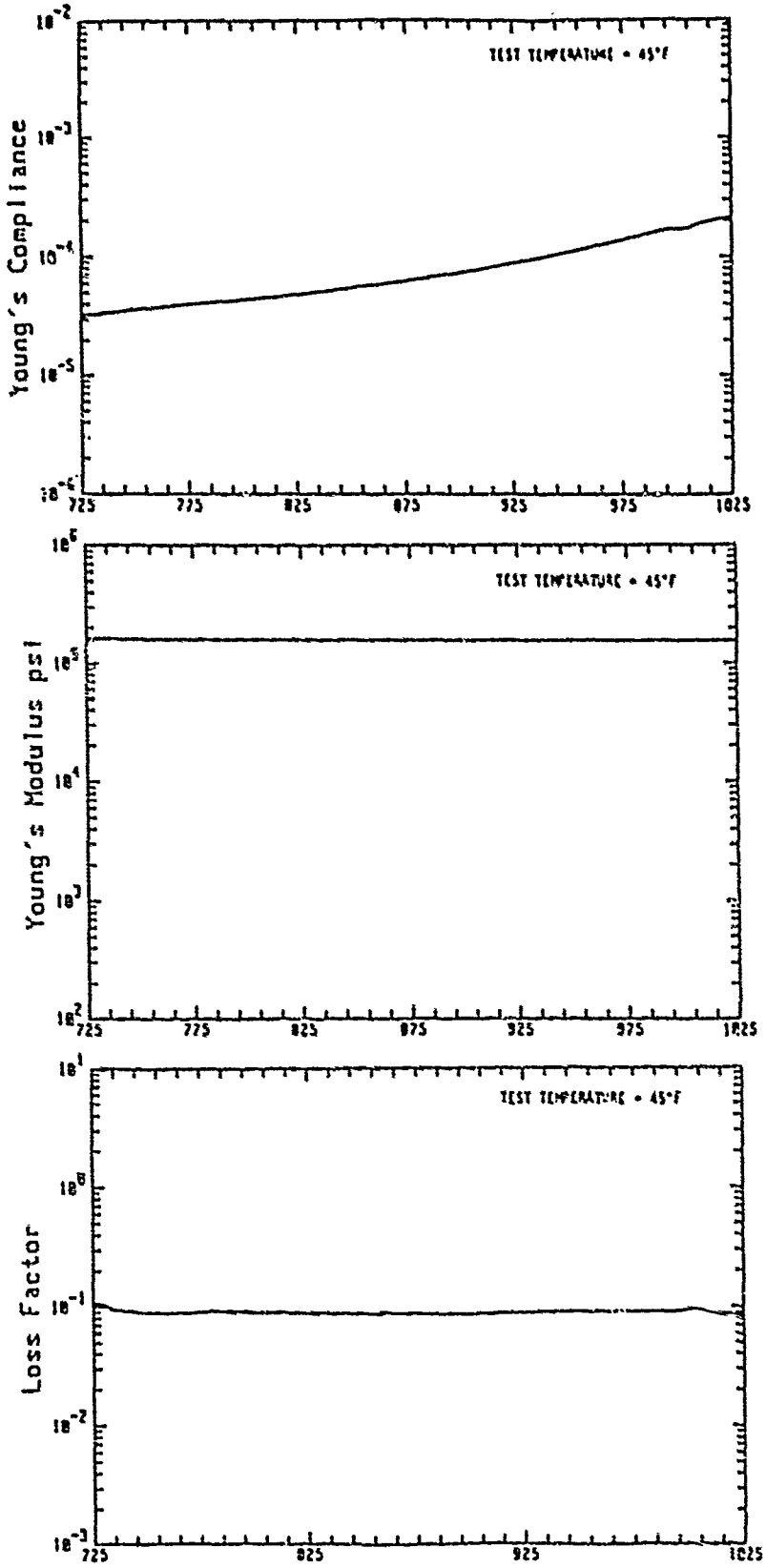


Figure 25: Material Properties in Tension-Compression at 45°F for SMRD 100-F90

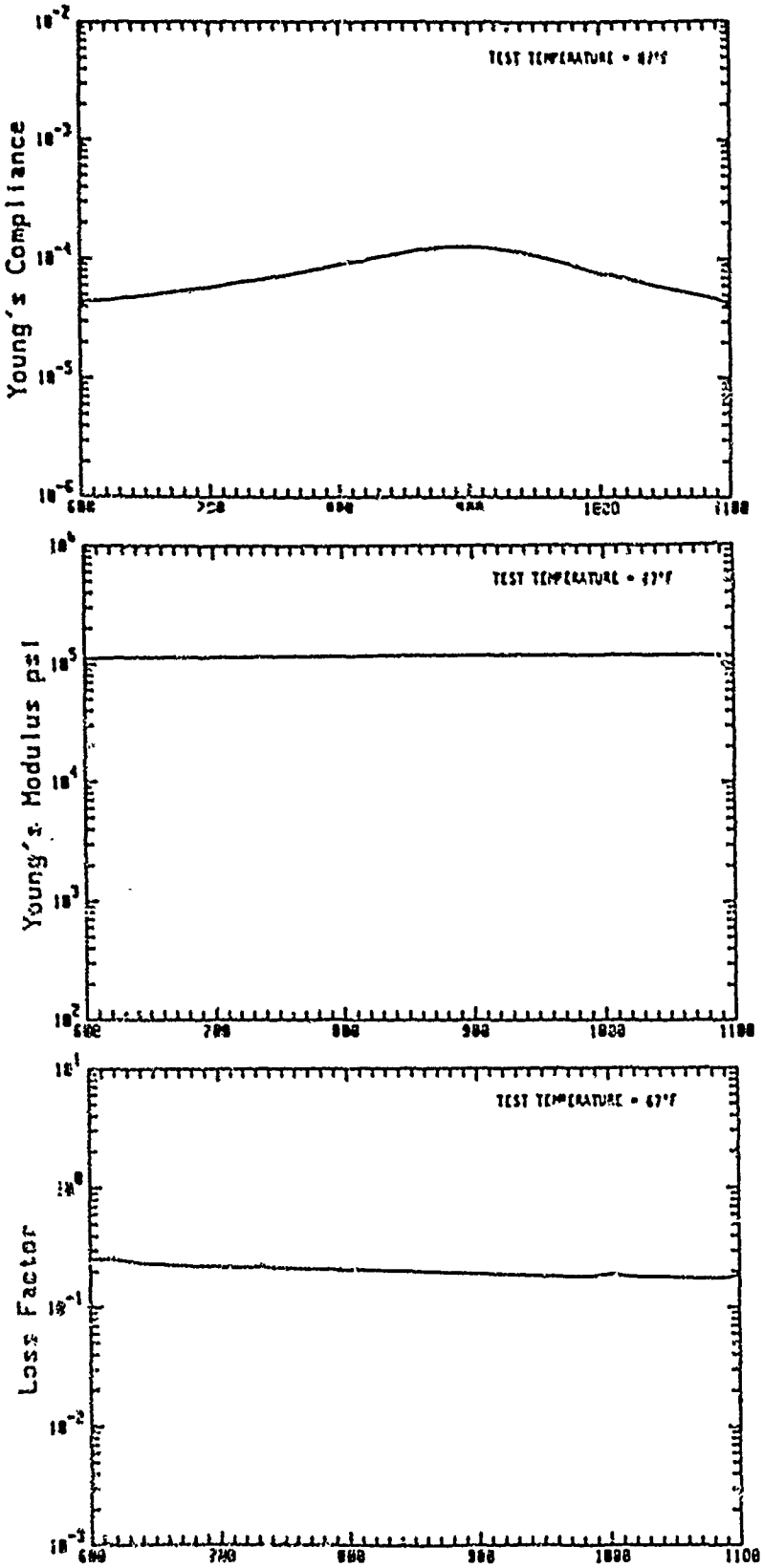


Figure 26: Material Properties in Tension-Compression at 67°F for SMRD 100-F90

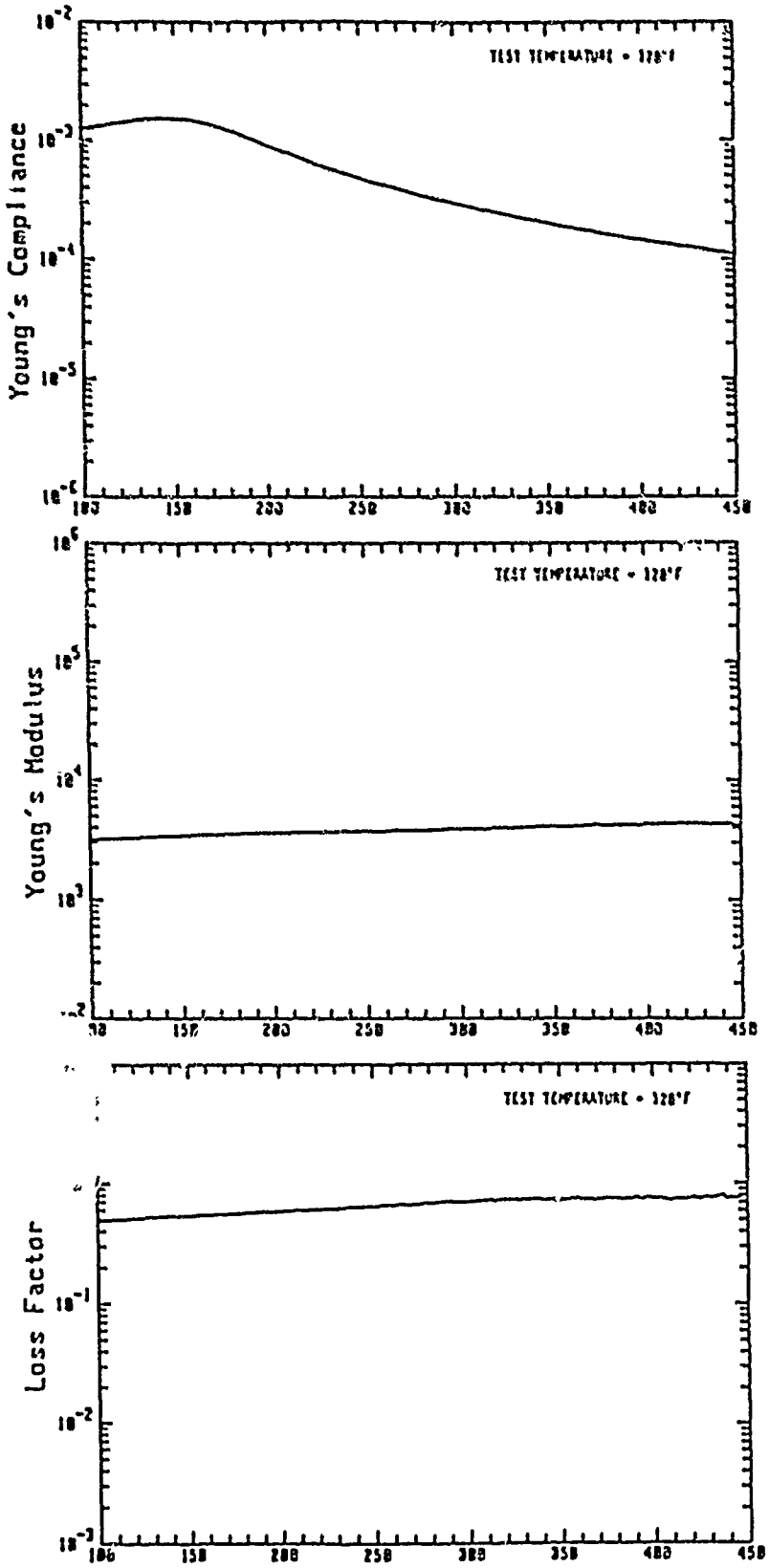


Figure 27: Material Properties in Tension-Compression at 128°F for SMRD 100-F90

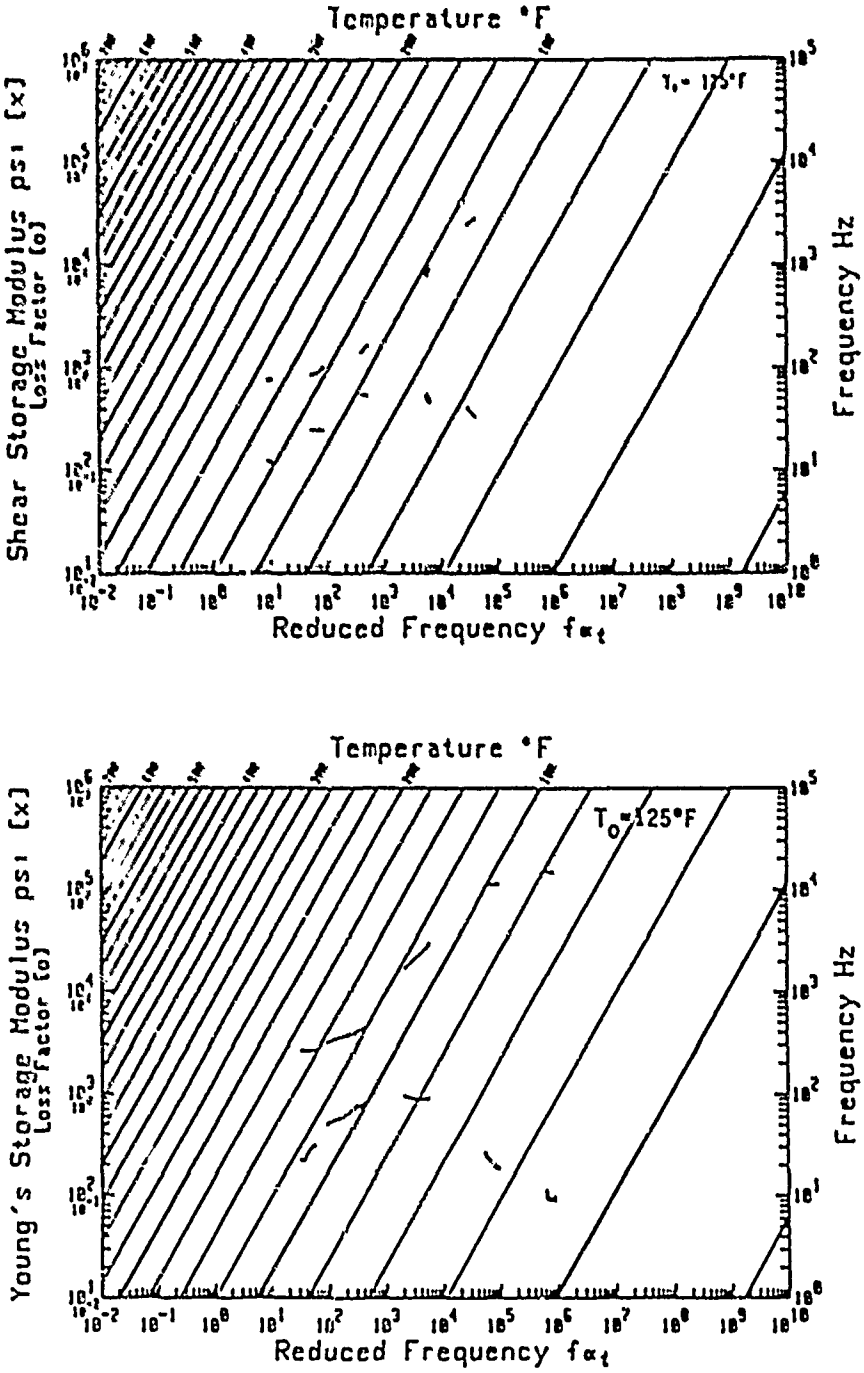


Figure 28: Material Properties in Shear and Tension-Compression States of Stress From Resonant and Mechanical Impedance Techniques for SMRD 100-F90

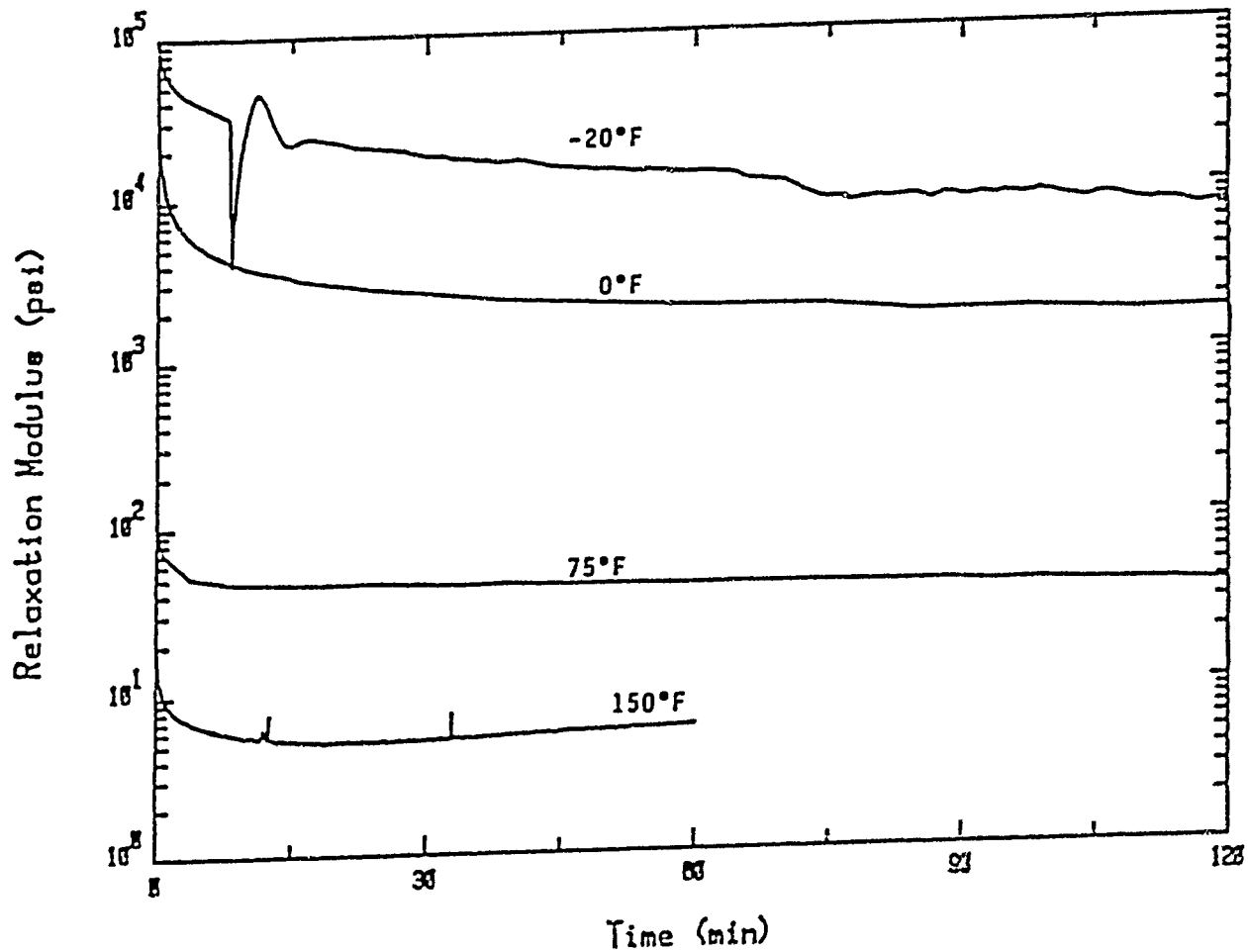


Figure 29: Tension-Compression Specimen: Relaxation Modulus Vs. Time

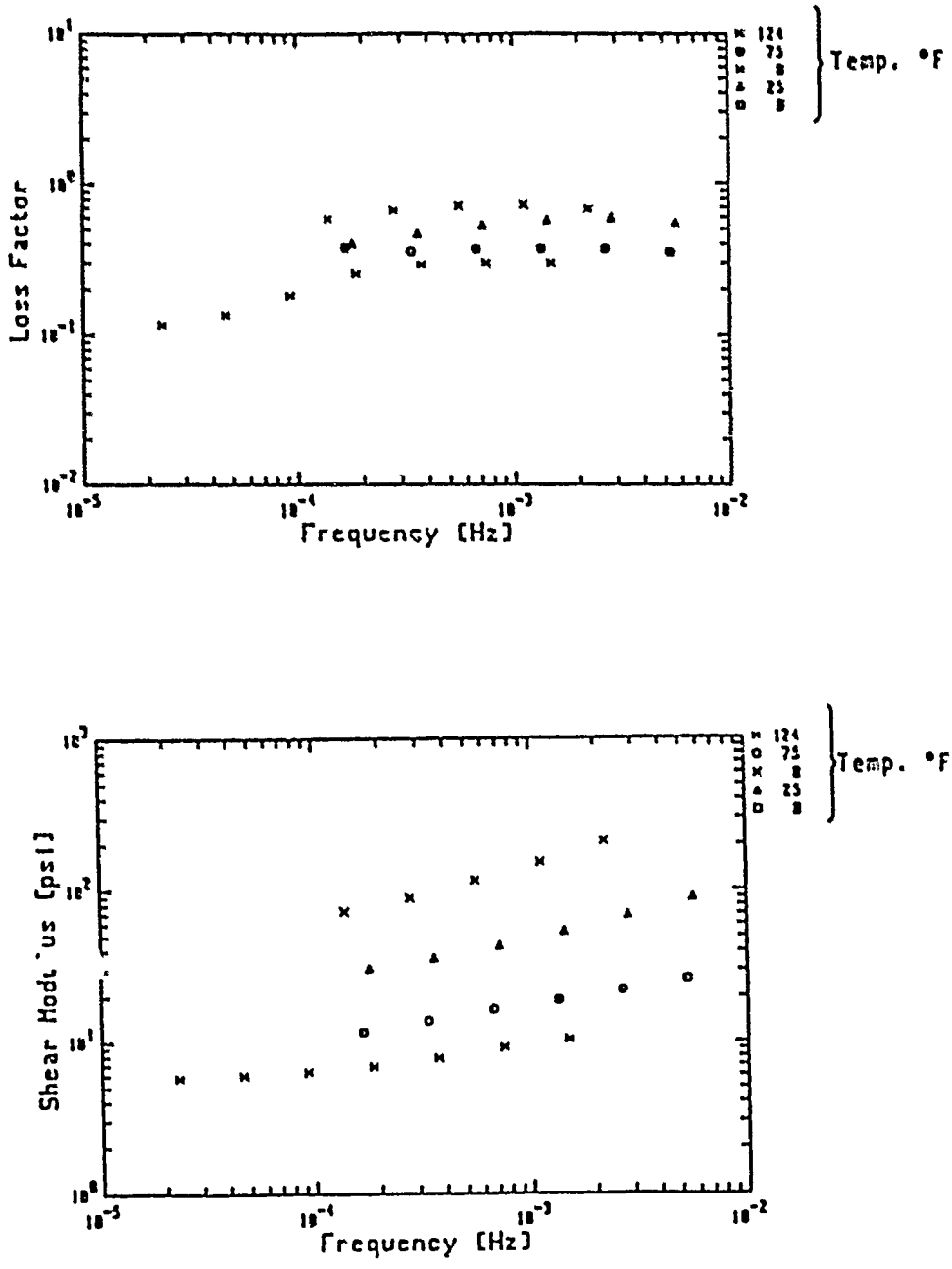


Figure 30: Variation of Shear Modulus and Loss Factor Vs. Frequency for Acrylic Core Foam Calculated from Relaxation Modulus

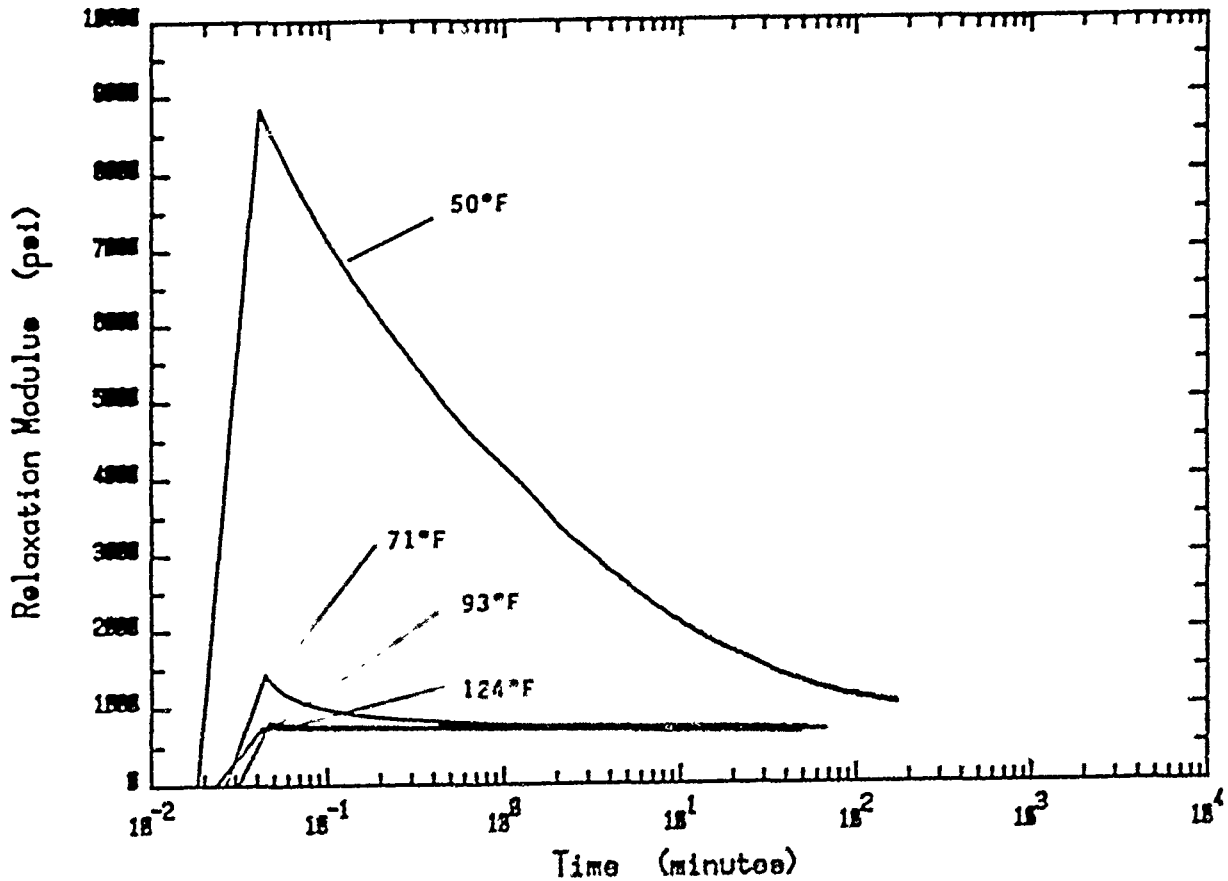


Figure 31: Shear Specimen: Relaxation Modulus Vs. Time for SMRD 100-F90

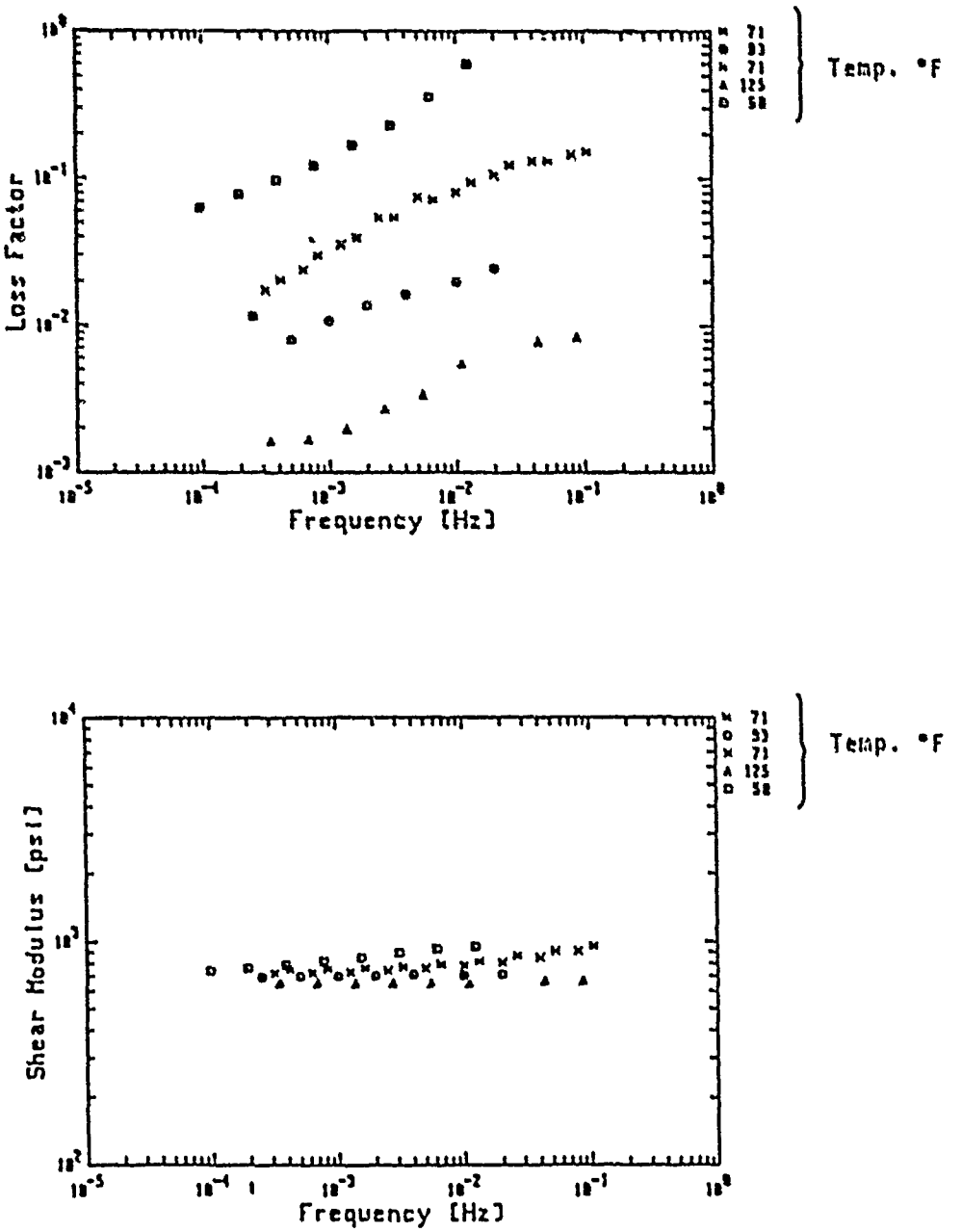


Figure 32: Variation of Shear Modulus and Loss Factor Vs. Frequency for SMRD 100-F90 Calculated from Relaxation Modulus

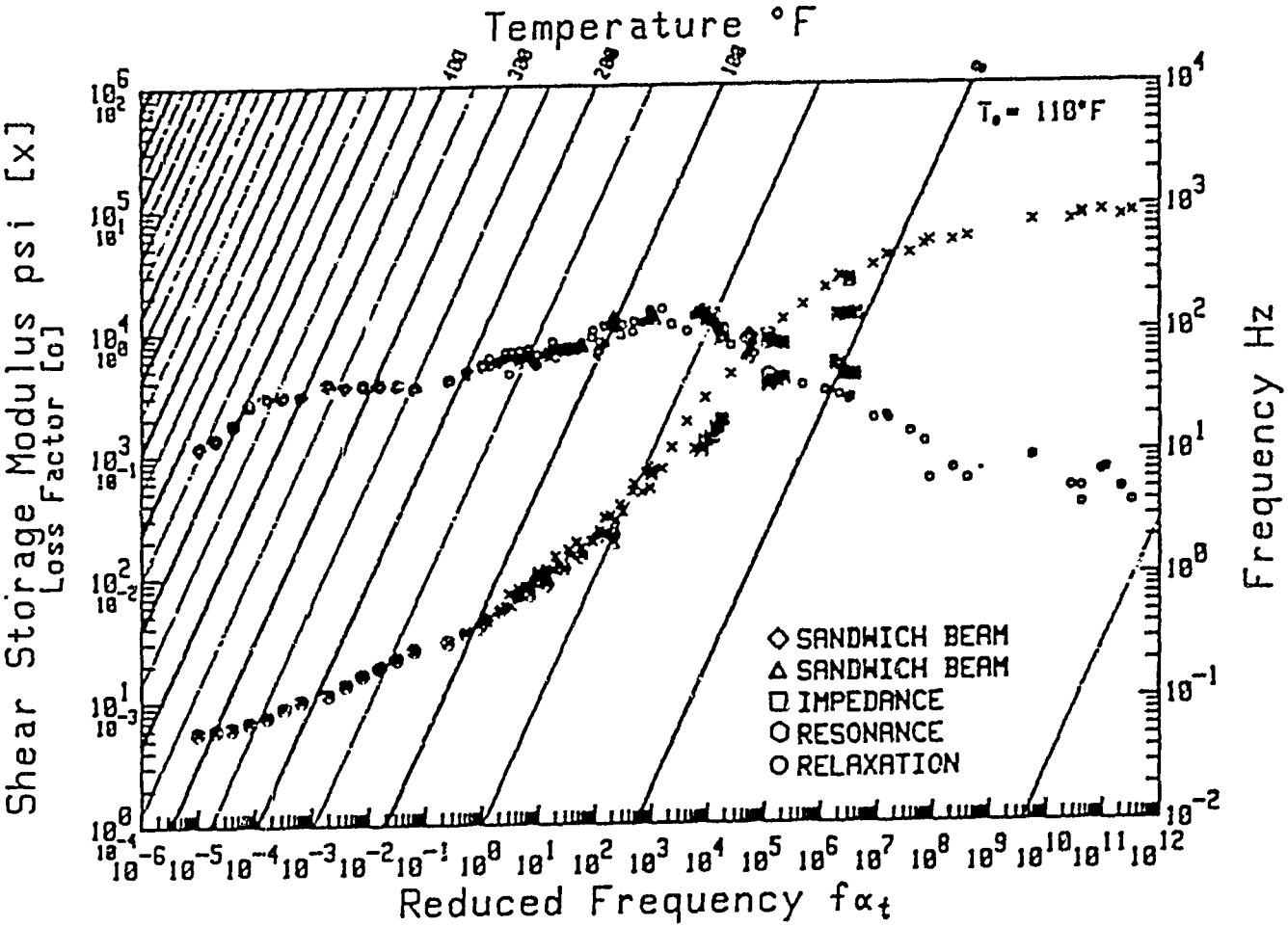


Figure 33: Comparison of Vibrating Beam, Relaxation, Impedance, and Resonance Techniques 4205

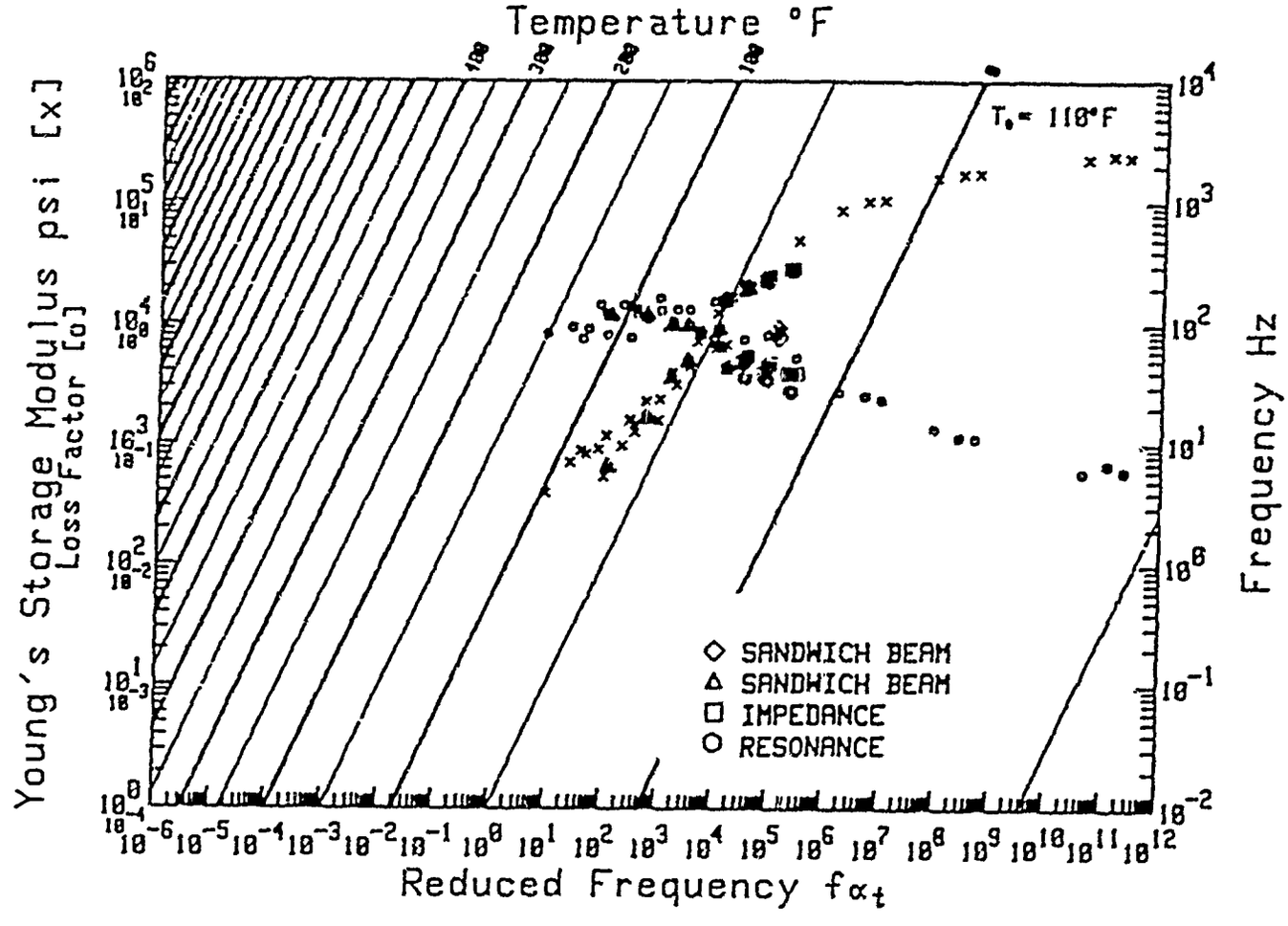


Figure 34: Comparison of Vibrating Beam, Relaxation, Impedance, and Resonance Techniques 4205

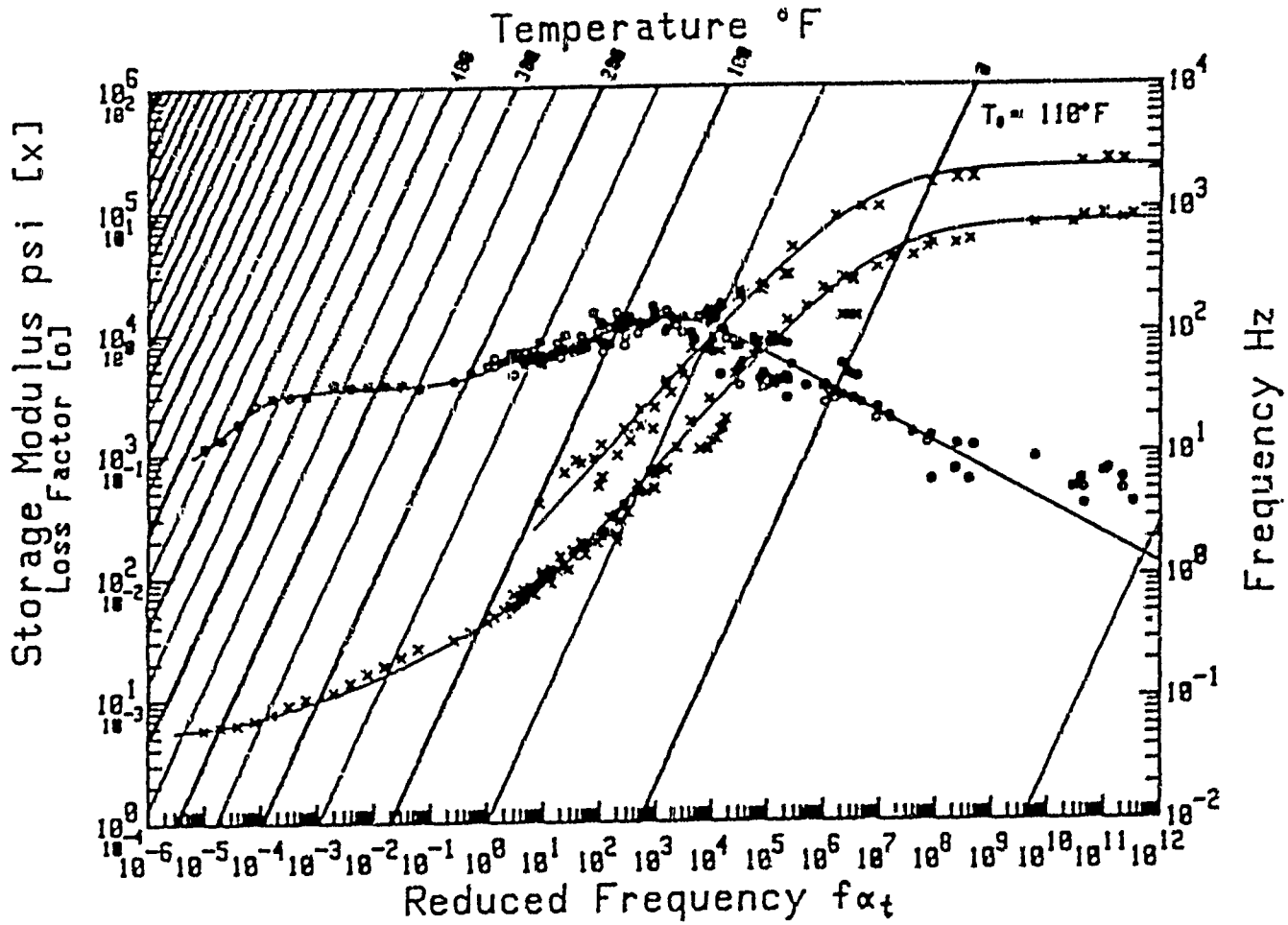


Figure 35: Comparison of Tension-Compression Material Properties with Shear Material Properties for 3M Y-4205 Acrylic Core Foam

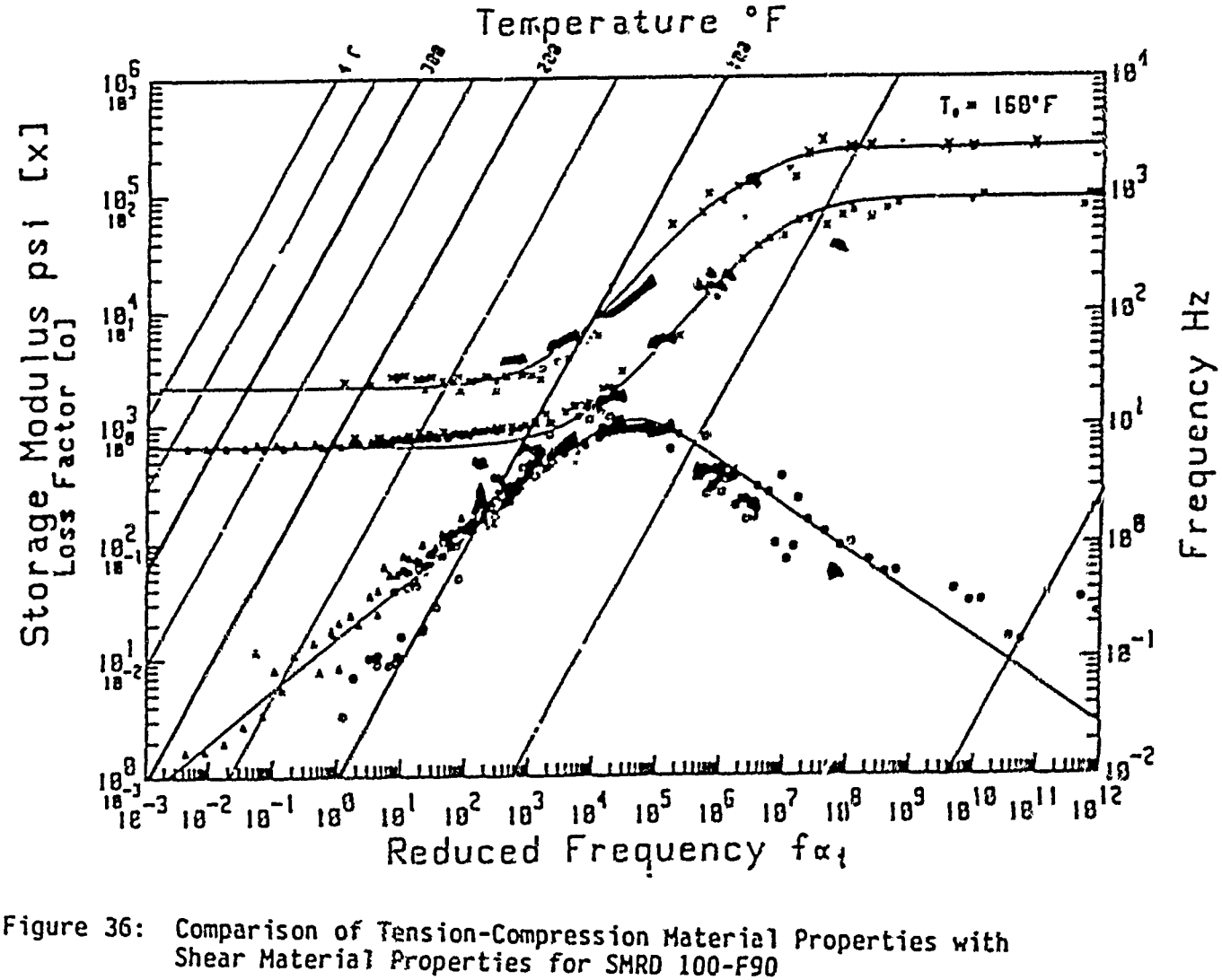


Figure 36: Comparison of Tension-Compression Material Properties with Shear Material Properties for SMRD 100-F90

DESIGN ORIENTED MEASURING PROCEDURES FOR DETERMINING THE MECHANICAL PROPERTIES OF RUBBER MATERIALS

presented at damping vibration workshop
las vegas march 1986

authors: Prof. dr. h.c. J. Peters
Catholic University Leuven Belgium
Dr. Ir. C. De Meersman
Bergougnan Benelux Belgium
Dr. Ir. B. Devis
Bergougnan Instruments Belgium

1. SCOPE

Rubber is a composite material of an elastomeric matrix and filler parts (carbon black, fibres, textiles, ...). Although it seems to be a conventional, wellknown material to outsiders, the study of its properties is still a major subject of research efforts for rubber producers and rubber users. Moreover, there is a series of new rubber(y) materials which have been developed in recent years. In general one can state that these new materials deal with synthetic polymers which show a high internal damping behaviour. Obviously, the field of applications of these new materials is much larger than it was for conventional (natural) rubber materials.
They can generally be called visco-elastic materials: materials which show to have an elastic property as well as an important viscous (damping) property in their mechanical behaviour.

Depending on the composition (and process parameters) of visco-elastic materials a broad variation in mechanical properties can be obtained. In other terms, a visco-elastic material can actually be designed and optimized in function of a specific application.

The mechanical characterisation of visco-elastic materials is most often made by means of its dynamic properties: dynamic stiffness and dynamic damping. The knowledge of these dynamic properties is important, not only for design purposes, but also for quality and process control, for reception control, and for research and development purposes.

The presented text concerns measuring procedures for determining the dynamic properties of visco-elastic materials. The basic principles which are mentioned are valid for all visco-elastic materials. The experimental testplans only have been carried out for a set of industrial natural and synthetic rubber compounds.
Its aim is to correlate the readings of different measuring procedures and test principles. It will also be demonstrated that relaxation tests (stepwise excitation) present a lot more advantages and qualities from the practical point of view than classical dynamic (harmonic excitation) tests. Still, there is very few information in literature about relaxation tests and there are practically no commercially available devices which operate on basis of the relaxation principle.

Indeed, what rubber industry and- more specifically- rubber users need are fast, accurate and simple measuring procedures which characterise the dynamic properties of visco-elastic materials in a fast, simple and reproducible way.
The major problem however is that the dynamic properties of visco-elastic materials are importantly influenced by measuring conditions. The consequences with respect to the implementation of dynamic measuring techniques are important:

- devices which operate with different measuring principles, show incoherent readings.
- devices which operate with similar measuring principles but at other relevant measuring conditions will produce different (however coherent) readings.
- rubber industry uses a broad set of varying testing equipment mostly technological simulation tests.

All these consequences result in a hugh waist of time, efforts and money.

2. STATEMENT

The presented text will prove that the readings of different measuring procedures are coherent, when extrapolated to a set of reference measuring conditions.
In order to confirm this statement, a number of different- currently used- measuring set-ups have been realised:

- dynamical tests:
  - with compression load
  - with free shear load
  - with tension load
- relaxation tests:
  - with compression load
  - with tension load
  - with indentation load
- pseudo-statical tests:
  - with compression load
  - with tension load

The instrumentation which has been used to realise these measuring set-ups are:

1) the dynamic tester: an elektro-hydraulical test equipment with full computer control (programmable function generator: DC, AC, frequency, signal mode) and modular sensor configuration; suited for dynamical, relaxation and pseudo-statical tests with compression, free shear and tension load.
2) the dynaliser: a test equipment for digital analysis of relaxation properties by means of a fast indentation (strain controlled) load.

Both devices have been developed at the Catholic University of Leuven and are now commercialised by Bergougnan Benelux, Gent, Belgium.

3. DEFINITIONS

a) DISPLACEMENT & FORCE CONTROLLED TEST PROCEDURES:
In the first case, the visco-elastic material is loaded with a specific strain load cycle; in the latter, the visco-elastic material is loaded with a specific stress load cycle. Due to the fact that often large deformations are involved when testing visco-elastic materials, the influence of the strain field of the element on the readings will not be neglectible (as it is the case for classical materials). Therefore, in order to make sure that a specific measuring procedure always imposes a specific (reproducible)

deformation field on the tested material, the measuring procedures treated in this text always operate on a strain controlled basis.

b) DYNAMIC TEST:
A dynamic test is defined as a strain controlled test with harmonic excitation. The displacement is imposed on the moving anvil, the induced force is measured on the fixed anvil.

c) RELAXATION TEST:
A relaxation test is defined as a strain controlled impact test. The displacement is imposed in a small time lapse, the induced force is measured during a specific time period, during and after the final strain level has been realised.

d) PSEUDO-STATICAL TEST:
A pseudo-statical test is defined as a test with continuously increasing strain load, applied with a constant strain velocity.

e) SHAPE-FACTOR:
The shape-factor is a coefficient, expressing the degree of freedom of a rubber element to deform freely when loaded in a specific way. The shape-factor will therefore be dependent upon the load set-up.

f) SYSTEM-ELEMENT AND MATERIAL CHARACTERISTICS:
When using a visco-elastic material to design isolators or damper elements, one is most often interested in the natural frequency and the damping ratio of the system. Besides the dynamic properties (stiffness and damping) of the visco-elastic element, the equivalent mass of the system intervenes to determine the systems' behaviour. The natural frequency and the damping ratio are called "system characteristics", while the dynamic stiffness and damping properties of the visco-elastic element are "element characteristics", which depend, not only upon the material used, but also upon the element shape, the load set-up, the static and the dynamic load. It is therefore quite important to know the characteristics of the visco-elastic element in some reference conditions and to express the modification of its properties due to the working conditions. The characteristics in reference conditions will be called "material characteristics".

4. GENERAL METHOD FOR OPTIMISING A MEASURING PROCEDURE

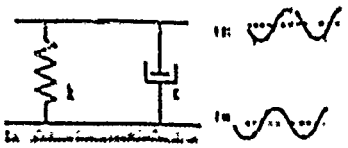
In this paragraph a general method will be described for optimising a specific measuring procedure. This method will be used in next paragraphs in order to develop the different measuring procedures which will be treated.

1) what properties have to be measured?
answering this question will result in an interpretation method and a suited mathematical model.
2) what measuring conditions will influence these properties?
answering this question will result in a series of relevant (controllable) measuring conditions and a series of non-relevant (non-controllable) measuring conditions.
3) implementation of a standard measuring procedure which will eliminate the influence of non-relevant (or non-controllable) measuring conditions.
4) redaction of analytical formulas which express the influence of the different relevant measuring conditions.
5) check on the validity of the expressions: redaction of limits of validity.

5. DYNAMIC TEST

5.1 Basics

The properties to be measured are dynamic stiffness and damping of a rubber element. The model which is best suited for characterizing these properties is the Kelvin-Voight model (fig.5.1), because of its simpliness and since it is commonly used (and standardised).



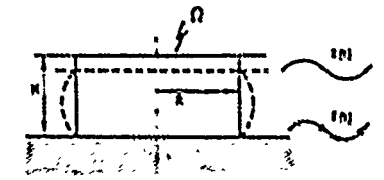
$$\left(\frac{F}{X}(\omega)\right) = k + c\omega j$$

fig. 5.1

5.2 Influencing measuring conditions

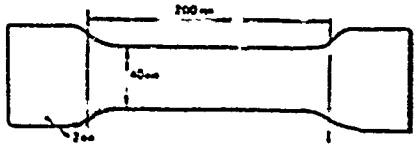
5.2.a. set-up

The set-up (the way how an element is loaded) will importantly influence the readings. For this reason, the set-up has to be characterised accurately and has to be reproducible for all materials which are included in the testplan.
Fig. 5.2, 5.3, 5.4 show the three different set-ups for dynamic tests which will be treated, together with the properties which need to be measured.



transferfunction: $\left(\frac{F/\Pi}{X/H}\right) = E'_c + jE''_c$

fig. 5.2

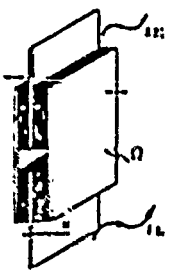


transferfunction: $\left(\frac{F/\Pi}{e}\right) = E'_T + jE''_T$

fig. 5.3

$$G'\,[N/mm^2] = \frac{k\,H}{\Pi}$$

$$G''\,[N/mm^2] = \frac{c\,H\,\omega}{\Pi}$$



transferfunction: $\left(\frac{F/2\Pi}{b\,g\,tg(X/2H)}\right) = G' + jG''$

fig. 5.4

5.2.b characteristics of the driving displacement
prestrain (pr) = mean displacement / initial height [ ]
amplitude (am) = stroke/(2*initial height) [ ]
frequency (f) = 1/harmonic period [Hz]

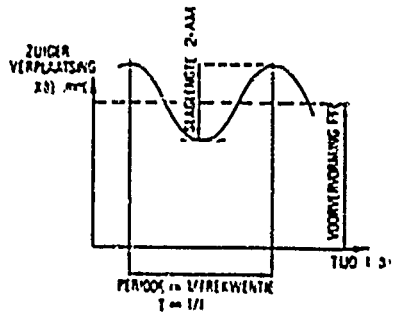


fig. 5.5

5.2.c strain history

Due to the important relaxation phenomenon which is characteristical for visco-elastic materials, the dynamic stiffness and damping properties will vary in time when measured continuously. One the other hand, it is not allowed to test the material until stabilisation occurs in vue of the large internal damping, which would cause internal heat build-up and consequently involve a temperature shift. Therefore, the standard measuring procedure will eliminate the relaxation phenomenon statically, as shown on the right hand graph.

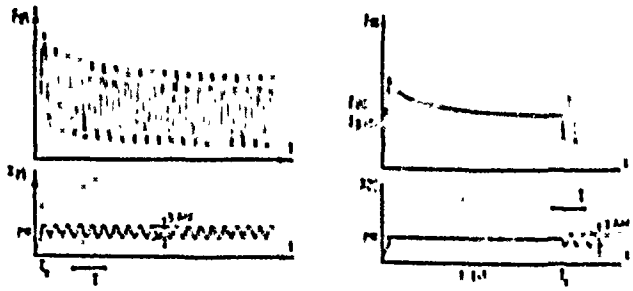


fig. 5.6

5.2.d shape factor S

The shape factor S expresses the degree of freedom with which a rubber element is alloved to deform freely when loaded in a specific vay. The shape factor will therefore not only depend upon the dimensions of the element, but also on the specific load set-up (fig. 5.7).
It is defined as:

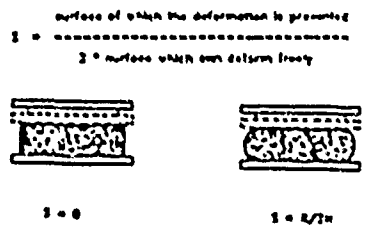


fig. 5.7

5.2.e influence of temperature

The temperature in a rubber element can vary as a consequence of two phenomena:

a) internal heat build-up: due to the large internal damping of visco-elastic materials, a temperature change might occur in the rubber element while loadings dynamically. This phenomenon is non-controllable (however measurable) and therefore must be eliminated maximally. For this reason, the standard test procedure will load the tested element with a minimal number of cycles. Once the transferfunction at a certain set of measuring conditions has been measured, it will the measuring procedure will stop the dynamic load and continue with another set of measuring conditions.

b) external heating: when incorporating the test set-up in a temperature chamber (avoiding all temperature gradients), one can perform measurements at temperatures, different from ambient temperature. The important influence of temperature on dynamic properties of visco-elastic materials is well known. However, determining this temperature influence accurately is still causing problems from the point of accuracy of temperature control and testing speed.

In order to avoid these problems, most constructors of dynamic testing devices with temperature control limit the dimensions of the samples thus alloving to implement small, fast temperature chambers. However, these small sample dimensions will often have a devastating influence on the reproducibility of the dynamic readings (influence of clamps, anvils, internal machine damping, etc.). Moreover, most of these classical dynamic testing devices only operate in a limited range of temperatures and frequencies.

For many years the classical frequency-temperature transformations have been implemented in literature and in practice to overcome these instrumentational problems. However the validity of these frequency-temperature transformations can be questioned:

- they are only valid for thermo-rheological simple materials; a condition which limits the field of applications drastically. For each group of these thermo-rheological materials some constants are given, on basis of which the frequency-temperature transformations are implemented: a procedure which is doubtfull in viev of the very broad range of materials involved (influence of processing parameters on these thermo-rheological constants f.i.).
- the data which are available in literature do not show much information on reproducibility: they are often plotted on logarithmic scales (a technique which masks inaccuracies) and only in a few cases, the validity of the transformation (and the validity of the used thermo-rheological constants) is checked by actually carrying out the dynamic readings for different combinations of frequencies and temperatures.

The solution to all these problems would be to develop a simple, fast and accurate test for determining the dynamic properties over the frequency range of interest and to implement this test-procedure in a high quality temperature chamber. Since most (mechanical) applications can be situated in a frequency range from 0 to 100 Hz, and a temperature range from -40oC to 170oC, this would be the optimal range of operating conditions for such a test procedure.
The presented text will not deal with experimental data on the influence of temperature on the dynamic properties of visco-elastic materials. The experimental data all were obtained at a constant ambient temperature. However it will proove that relaxation tests present a lot more advantages compared to dynamic test procedures. Relaxation test will therefore be much easier to implement in a temperature chamber compared to classical dynamic tests. In fact the Dynalimer device equipment has been build into a high quality temperature chamber with a broad temperature range (-60oC to 170oC): the relaxation measuring procedure shows indeed to function perfectly at varying temperatures with a high degree of high reproducibility and accuracy!

5.3 implementation of a standard measuring procedure

5.3.1 notations

The dynamic moduli at different (relevant) measuring conditions will be noted as following:

compression: $E_{s,pr,am,f}$ & $E_{s,pr,am,f}$

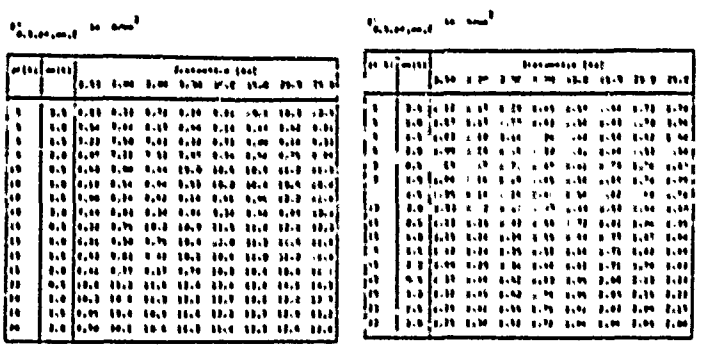
free shear: $G_{s,pr,am,f}$ & $G_{s,pr,am,f}$

tension: $E_{t,pr,am,f}$ & $E_{t,pr,am,f}$

5.3.2 standard measuring procedure

- setting the anvil at reference position (zero force level)
- setting the prestrain i: 1 to 4 (4 levels of prestrain)
- elimination of relaxation phenomenon (fig. 5.6)
- setting the amplitude j: 1 to 4 (4 levels of amplitude)
- setting the frequency k: 1 to 8 (8 levels of frequency)
- measuring force and displacement during N cycles (N < 5)
- setting frequency <1 (intermediate frequency)
- calculation of the transferfunction
- check on the amplitude (measured am = set am?)
- check on the minimum force (for compression and tension)
- next frequency
- next amplitude
- next prestrain
- listing of 128 transferfunctions (testperiod: 35')

5.3.3 example of listing



5.4. reduction of analytical expressions

It has been found that the influence of measuring conditions on both real and imaginary part of the transferfunction (for all 3 set-ups) can be expressed analytically by means of 3 influence functions:

$$\varphi_1(S,pr) * \varphi_2(f) * \varphi_3(am)$$

in which

$\varphi_1(S,pr)$ = element property : dependent of load situation

$\varphi_2(f)$ = material property: independent of load situation

$\varphi_3(am)$ = material property: independent of load situation

ELEMENT INFLUENCE FUNCTION:

compression:
$$\varphi_1(S,pr) = e^{S}\left(1+\frac{(1+2S)pr}{(1-pr)}\right)$$

free shear
$$\varphi_1(S,pr) = 1$$

tension
$$\varphi_1(pr) = \frac{1}{1+pr}$$

FREQUENCY INFLUENCE FUNCTION:

for all load situations:
$$\varphi_2(f) = \left(1+\beta f^{\gamma}\right)$$

AMPLITUDE INFLUENCE FUNCTION:

for all load situations:
$$\varphi_3(am) = \left(1+.1\,e^{-100.1\,am}\right)$$

general expressions:

$$E'_{S,pr,am,f} = E'_o \cdot v_{1S}(S,pr) \cdot v_2(am) \cdot v_3(f)$$

$$G'_{S,pr,am,f} = G'_o \cdot v_{1G}(S,pr) \cdot v_2(am) \cdot v_3(f)$$

$$E'_{T,pr,am,f} = E'_o \cdot v_{1T}(S,pr) \cdot v_2(am) \cdot v_3(f)$$

element reference conditions:

$S = 0$, $pr = 0$

material reference conditions:

$am \gg$, $f = 0$

validity of expressions (limits of experimental plans):
- element shapes: cilinders, cubes and beams with S<2
- prestrain range: 0 ---> 20%
- amplitude range: 0 ---> 10%
- frequency range: 0 ---> 100 Hz
- material range: NR - SBR - EPDM - NBR and blends

6. RELAXATION TEST

With the same methodology as for the dynamic test procedure (paragraph 5), this paragraph will deal with relaxation tests:

6.1 Basics

The property to be measured is the relaxation modulus of a rubber element, loaded in a specific way. The model which is best suited for characterizing this relaxation modulus is the generalised Maxvell-model (fig.6.1) with a continuous distribution of time-constants.
The transferfunction of such a model for a strain-controlled impact test is a power function of time (fig. 6.1), in which A, B and alfa are called 'parameters of the relaxation characteristic' and show to be dependent upon the used measuring conditions (cfr. references).

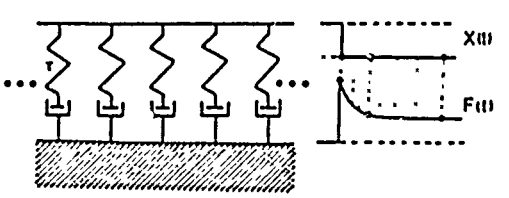


fig. 6.1

6.2 Influencing measuring conditions

6.2.a set-up

The set-ups, considered for relaxation tests are compression (fig. 5.2), tension (fig. 5.4) and indentation load (fig. 6.2). The indentation load has several advantges compared to the other load situations:

- readings on homogenity
- lower force levels
- simplier set-up

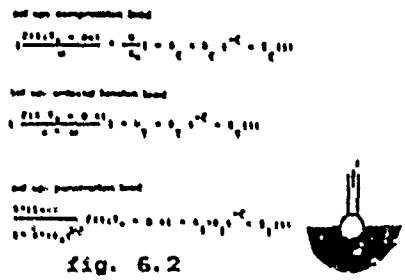


fig. 6.2

6.2.b strain level

Depending upon the strain level which has been realised after impact, the relaxation modulus will be situated at different levels.
Fig 6.3 shows different relaxation moduli at different strain levels.

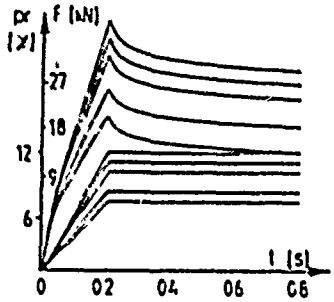


fig. 6.3

6.2.c strain history

Due to the fact that the impact load cannot be applied immediately, the influence of the displacement time Tm has to be eliminated analytically. This is done by shifting the relaxation modulus of a specific time period, which is proportional to the displacement time Tm.

for displacement time Tm=0s: $E(Tm = 0s) = A + B\ t^{-alfa}$

for displacement time Tm≠0s: $E(Tm \neq 0s) = A + B\ (t - \theta\ Tm)^{-alfa}$

6.2.d shape factor

cfr. paragraph 5.2.d of dynamic tests.

6.2.e temperature

No internal heat build up will occur since an impact test is concerned. With respect ot external heating, the relaxation modulus can be curve-fitted on all temperatures (even at transient temperature) by means of an the analytical expression mentioned above (pover function of time). The parameters of the relaxation characteristic will hovever vary as of function of temperature.
This text will only deal with relaxation readings at ambient temperatures.

6.3 implementation of a standard measuring procedure

6.3.a notations

compression: $E_C(t) = A_{S,pr} + B\ t^{***}_{S,pr}$

tension: $E_T(t) = A_{T,pr} + B\ t^{***}_{T,pr}$

indentation: $E_I(t) = A_I + B\ t^{***}_I$

6.3.b standard measuring procedure
- setting the reference (zero-force) position
- setting the strain level (linear displacement)
- recording the force-variation over a 15m time period
- curve-fit of the relaxation force
- calculation of the relaxation modulus (1 transferfunction per strain level)

6.4 redaction of analytical expressions

$$E(t)_{S,pr} = A \cdot {}_{1s}(S,pr) \cdot (1 + B/A \cdot t^{n})$$

$$E(t)_{f,pr} = A \cdot {}_{1f}(S,pr) \cdot (1 + B/A \cdot t^{n})$$

$$E(t) = A \cdot {}_{11}(S,pr) \cdot (1 + B/A \cdot t^{n})$$

element reference conditions:

$S = 0 , pr = 0$

material reference conditions:

$t = \infty$

validity of expression:
- element shape: cilinders, cubes and beams with S<2
- displacement level: 0 ---> 20%
- material range: NR - SBR - EPDM - NBR and blends

7. CORRELATION DYNAMIC TEST - RELAXATION TEST

RELAXATION MODULUS AT REFERENCE ELEMENT PROPERTIES:

$$E(t) = A(1 + B/A\, t^{n})$$

DYNAMICAL MODULUS AT REFERENCE ELEMENT PROPERTIES:

$$E' = E'(1 + \beta f^{n})$$

In other terms: there is a unique relationship betveen the dynamic moduli E'(f) for varying frequencies, measured at reference conditions, and the relaxation modulus E(t), measured at reference conditions.
Both identities can be yielded analytically by making the time-frequency transformation on basis of the generalised Maxvell-model (fig. 6.1) (reference literature) and has been confirmed for extended experimental plans, within the limits of validity which have been mentioned.
It has been proved that:

$$B/A \cdot (2\pi)^{n} \cdot \frac{\Gamma(1-n/2)\,\Gamma(n/2)}{2\,\Gamma(1+n)} = \beta$$

8. PSEUDO-STATICAL TESTS

With the same methodology as used for dynamic tests and relaxation tests, it can be proved that for a pseudo-statical test made with a constant velocity dx/dt, the relation between the measured force F (x, dx/dt≠0 mm/s) and the true statical force F(x, dx/dt=0 mm/s) equals:

$$F_v(X) = \frac{F_m(X, dX/dt)}{\left[1 + B/A \cdot \left((1 - \theta(1))\frac{X}{dX/dt}\right)^{-\alpha}\right]}$$

In which A, B and alfa equal the parameters from the relaxation characteristic (cfr. para. 6).

9. CONCLUSIONS

It has been proved that there is a perfect correlation between the readings of dynamic tests (dynamic moduli) and the readings of a relaxation test (relaxation modulus) and of a pseudo-statical test (force-displacement characteristic), on condition that the dynamic and pseudo-statical readings are extrapolated to reference conditions.
In other terms, the dynamic moduli and pseudo-statical characteristic of simple shape elements can be predicted by means of the relaxation parameters A, B and alfa!
The relaxation test set-up presents of a lot of advantages compared to dynamic test and pseudo-statical tests: speed, accuracy, influence of heat build-up, complexity of set-up, etc. ...

REFERENCES

Peters, J. 'The measurement of the elastic and loss moduli of rubber and rubberlike materials'
De Heersman, C. 'Analyse van de mechanische eigenschappen van rubber i.f.v. hun samenstelling'.

SELECTED COMPLEX MODULUS DATA

Chris CHESNEAU
Bernard DUPERRAY

Société METRAVIB RDS
64 chemin des Mouilles - BP 182 -
69132 ECULLY CEDEX
(FRANCE)

ABSTRACT

In this paper, we present complex modulus Data for a series of materials exhibiting interesting vibration damping characteristics. The measurement equipment used is also presented.

I - INTRODUCTION

The field of material characterization is relatively new and, in many cases, manufacturers of polymeric materials are satisfied with an incomplete set of data when presenting their products. In the area of vibration damping, a critical piece of information is complex modulus, yet it is often forgotten by manufacturers. For this reason, we provide herein complex modulus information for a selected group of vibration damping materials.

Of course, it is necessary to include in this paper the means by which this information was obtained and a descriptive presentation of the test equipment utilized is given as a prelude to the modulus master curves.

II - TEST EQUIPMENT

The bulk of the data presented here was obtained using METRAVIB's own VISCOELASTICIMETER. Simply stated, this instrument measures the force and the displacement acting on a sample submitted to an oscillatory regime. The schematic diagram of figure 1 illustrates the basic mechanics of the instrument. From the sample outward this diagram runs as follows. The sample is placed on a rigid column, incorporating a force transducer, which links it to a fixed, solid, metallic base. The sample is surrounded by a furnace, capable of temperatures of up to 350°C using electric heating elements, and of temperatures as low as - 100°C obtained by liquid nitrogen cooling. The upper part of the sample is attached to an electrodynamic shaker via a rigid column similar to the lower one. The shaker is fastened to a fixed upper chassis. The displacement of the upper column is recorded by a transducer.

The height of the upper chassis can be adjusted, as well as the pre-strain on the specimen.

Even though many different test heads exist, allowing characterization is shear, 3 point bending or the characterization of molten plastics, the materials presented herein were tested in simple tension-compression. The actual measurement principle can now be described.

A viscoelastic sample has a dynamic stiffness K* defined by its response to sinusoïdal sollicitation :

$$K^* = \frac{F^*}{U^*} \qquad (1)$$

where F* is the forcing function :

$$F^* = F_0 \exp i\,(\omega t + \delta) \qquad (2)$$

and U* the harmonic displacement :

$$U^* = U_0 \exp i\omega t \qquad (3)$$

The phase shift, δ, is linked to the vibration damping characteristics of the material and its tangent, $\tan \delta$, is often called the loss factor and denoted η.

From equations (1) (3), the stiffness K* becomes :

$$K^* = (F_0 / U_0) \exp i\delta$$

The real and imaginary parts of K*, K' and K'' respectively, are thus given by :

$$K' = F_0 / U_0 \cos \delta$$
$$K'' = F_0 / U_0 \sin \delta$$

The VISCOELASTICIMETER yields directly F_0/U_0 and δ.

YOUNG's modulus can be obtained using the dimensional parameters of the sample. Using figure 2 as a definition diagram, the following expressions of stress and strain are obtained :

$$\varepsilon^* = U^*/h$$
$$\text{and } \sigma^* = F^*/S_e$$

The magnetude of YOUNG's modulus is given by :

$$|E^*| = \frac{|\sigma^*|}{|\varepsilon^*|} \frac{h}{S_e} \left\{ \frac{1}{1 + 2 \frac{S_e^2}{S_1^2}} \right\}$$

where $\left[1 + 2 \left(\frac{S_e}{S_1} \right)^2 \right]^{-1}$ is a shape factor.

The real part of the modulus E', or storage modulus is given by :

$$E' = |E^*| \cos \delta$$

and the imaginary part, E'', or the loss modulus, is given by :

$$E'' = |E^*| \sin \delta.$$

The VISCOELASTICIMETER's technical characteristics are given in annex A. These are accompanied by the VISCOANALYSER's characteristics, an upmarket fully automated version of the same instrument.

III - MATERIALS

There are so many materials in production exhibiting a vibration damping character, or having a high loss factor, that some sort of criterion for selection had to be used.

The first and most obvious one is that it belonged in our files. This means that we have tested it. This reduces the number of available sources significantly and, in fact, we are mostly concerned here with materials of European manufacture.

The next criterion is one of availability. These materials must be available to the general public everywhere.

Finally, we have chosen samples from various manufacturers wich exhibit a variety of stiffness and temperature-frequency utilization ranges.

We have represented materials by master curves. Shift factors, storage modulus and loss tangents are represented on separate graphs. These are shown in figures 3 to 9. They are, by order of figure :

1 - Epoxy resin, ref. EP 5020 with 10 % hardener ref. HY 956.

Address : S.N.P.E., Société Nationale des Poudres et Explosifs
12 quai Henri IV
75181 PARIS CEDEX 04 (FRANCE)

Tel. (1) 42 77 15 70 - Telex : 220 356.

Figure 3.A : Shift factor V/S temperature and storage modulus V/S reduced frequency.

Figure 3.B : Loss factor V/S reduced frequency.

2 - Epoxy resin, ref. EP 5072 with 20 % hardener ref. HY 956.

Address : S.N.P.E., Société Nationale des Poudres et Explosifs
12 quai Henri IV
75181 PARIS CEDEX 04 (FRANCE)

Tel. (1) 42 77 15 70 - Telex : 220 356.

Figure 4.A : Shift factor V/S temperature and storage modulus V/S reduced frequency.

Figure 4.B : Loss factor V/S reduced frequency.

3 - Reference : 11.112 A

Address : VIBRACHOC
12 route de Milly
91820 BOUTIGNY

Tel. (1) 64 57 90 56 - Telex : 600 415.

Figure 5.A : Shift factor V/S temperature and storage modulus V/S reduced frequency

Figure 5.B : Loss factor V/S reduced frequency.

4 - Reference : 14/59 AI

Address : VIBRACHOC
12 route de Milly
91820 BOUTIGNY

Tel. (1) 64 57 90 56 - Telex : 600 415.

Figure 6.A : Storage modulus V/S reduced frequency and shift factor V/S temperature.

Figure 6.B : Loss factor V/S reduced frequency.

5 - NORSOREX

Address : CdF CHIMIE S.A.
Département NORSOREX
Tour Aurore
18 place des Reflets
Cedex n° 5
92080 PARIS LA DEFENSE (FRANCE)

Tel. (1) 47 78 64 15 - Telex : 610 826

North American Agent :

Address : Paul NELSON (ChemMark)
Factory Lane
MIDDLESEX
New Jersey 08846 (U.S.A)

Tel. (201) 469 7274 - Telex : 752 227

Figure 7.A : Shear Modulus V/S reduced frequency and shift factor V/S temperature.

Figure 7.B : Loss factor V/S reduced frequency.

6 - FASSON ISOTACK

Address : AVERY INTERNATIONAL RESEARCH CENTER
325 North Albaden Drive
PASADENA
California 91107 (U.S.A)

Figure 8 : Shear Modulus and loss factor V/S reduced frequency
Shift factor V/S temperature.

7 - SORBOTHANE S 50

Address : LEYLAND and BIRMINGHAM RUBBER COMPANY Ltd
Golden Hill Lane
Leyland, Preston PR5 IUB
Lancashire (ENGLAND)

Tel. 07724-21434 - Telex : 67126

Figure 9.A : Storage modulus V/S reduced frequency and shift factor V/S temperature.

Figure 9.B : Loss factor V/S reduced frequency and loss modulus V/S reduced frequency.

IV - CONCLUDING REMARKS

The VISCOELASTICIMETER is an instrument designed to study viscoelastic properties of materials in the transition region where loss factors are large. One cannot expect much accuracy below loss factors of 0.01. Thus for metallic materials or glass plateau secondary transition peaks in the loss factor, another METRAVIB instrument is more appropriate. This instrument, called MICROMECANALYSER, is an inversed torsion pendulum, working in forced oscillations below resonance. This can give the instrument a very wide frequency range, from 10^{-5} Hz to 1 Hz. The general specifications are given in annex B, along with a comparison of results obtained with both the VISCOELASTICIMETER and the MICROMECANALYSER (figures 10.A and 10.B).

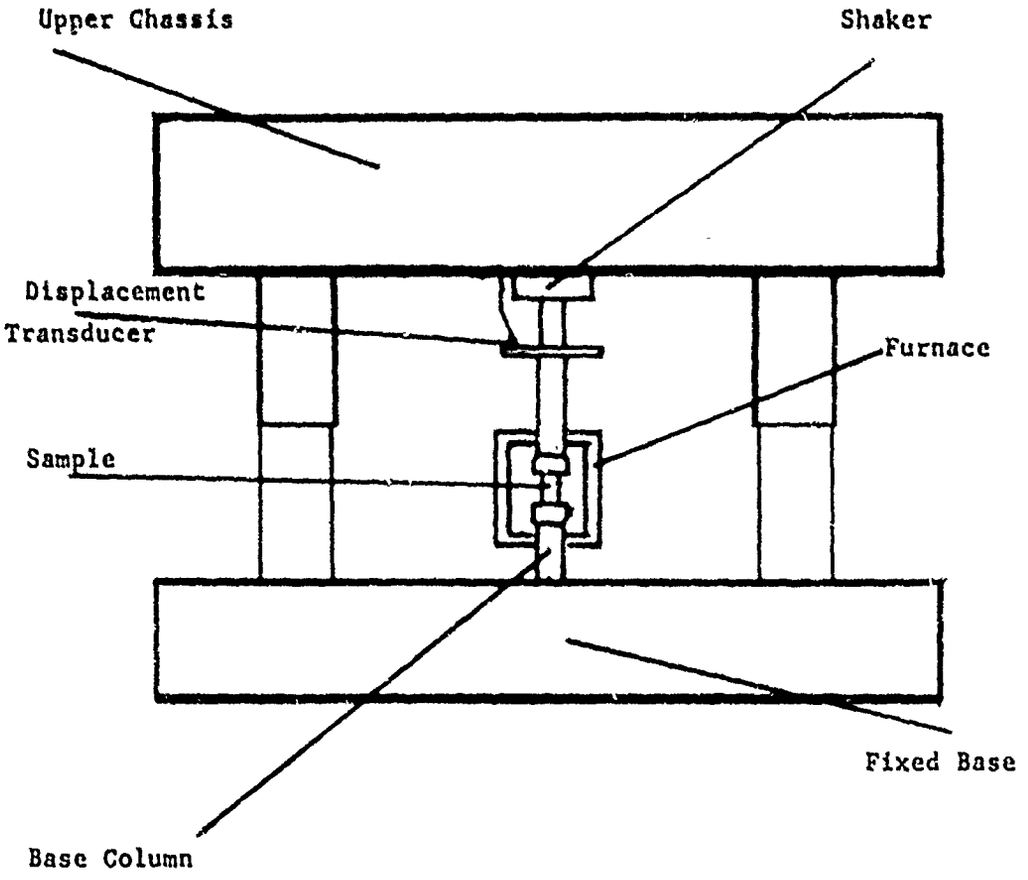


Figure 1 : VISCOELASTICIMETER : Mechanical Section

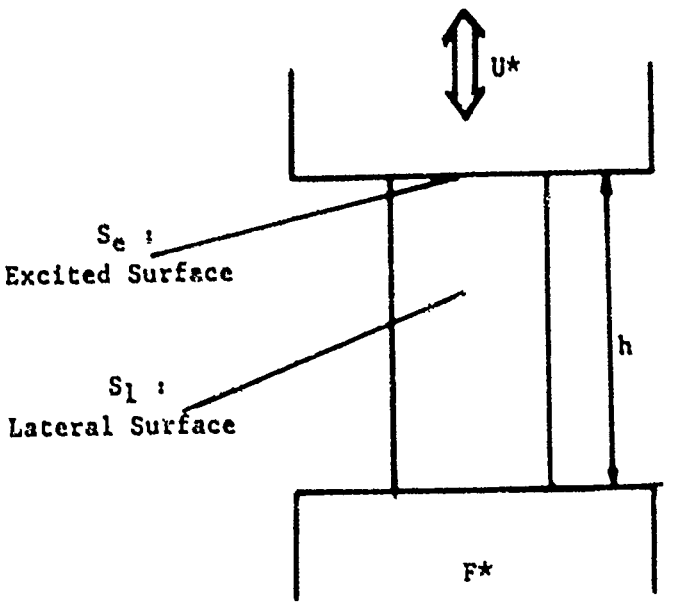
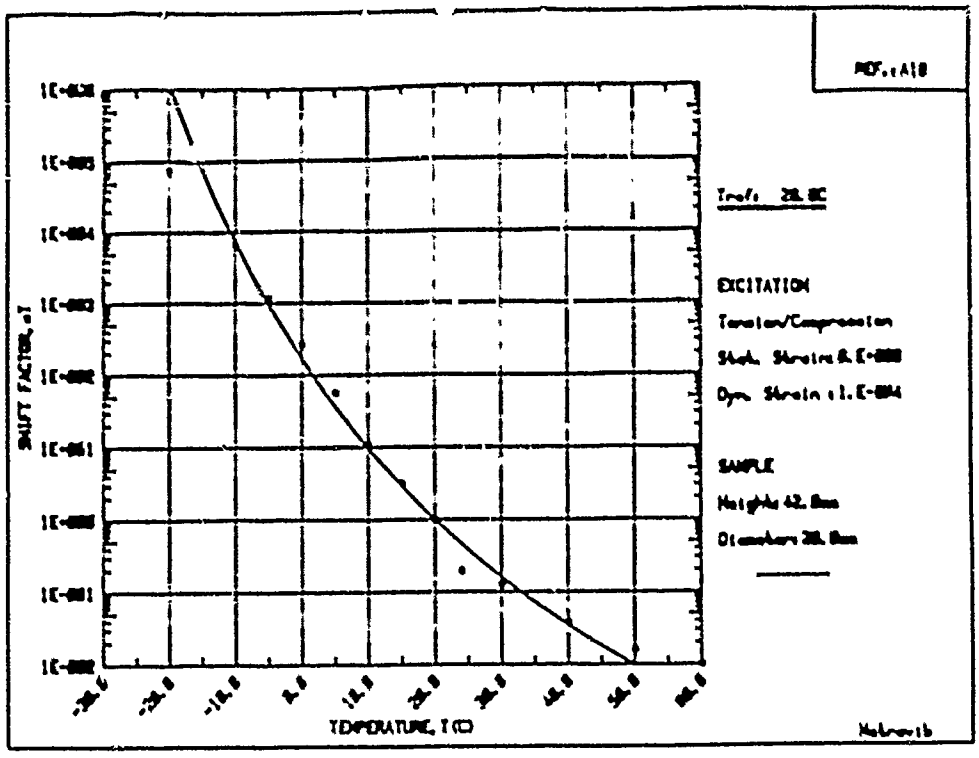


Figure 2 : Measurement - A Definition Diagram

Figure 3.A



EP 5020 - 10 % HY 956

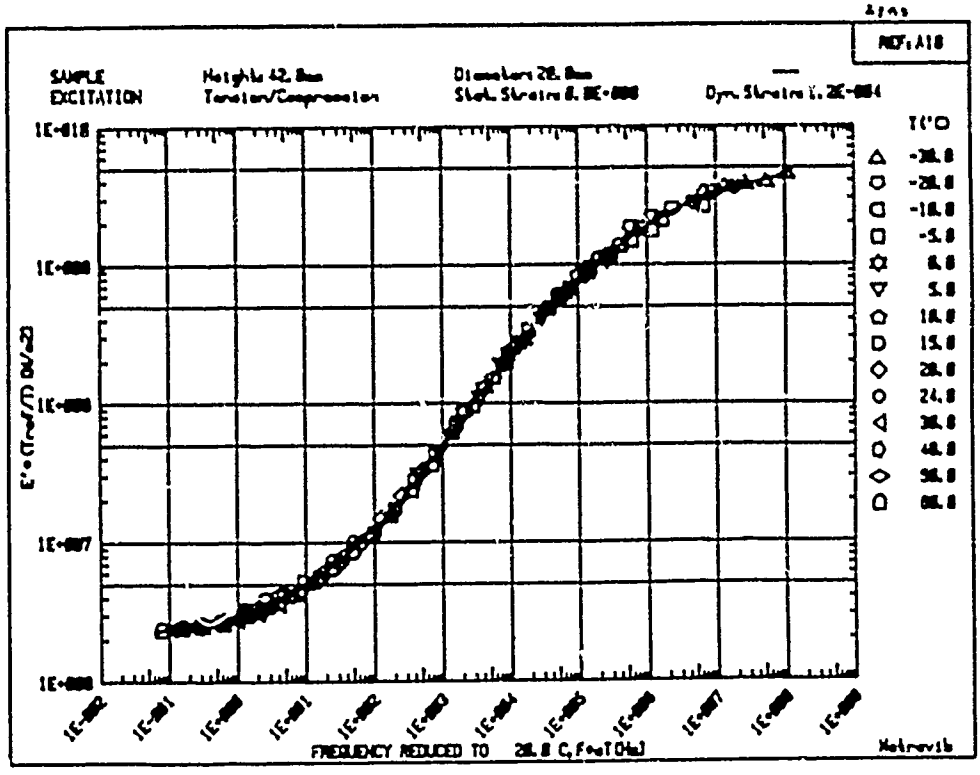
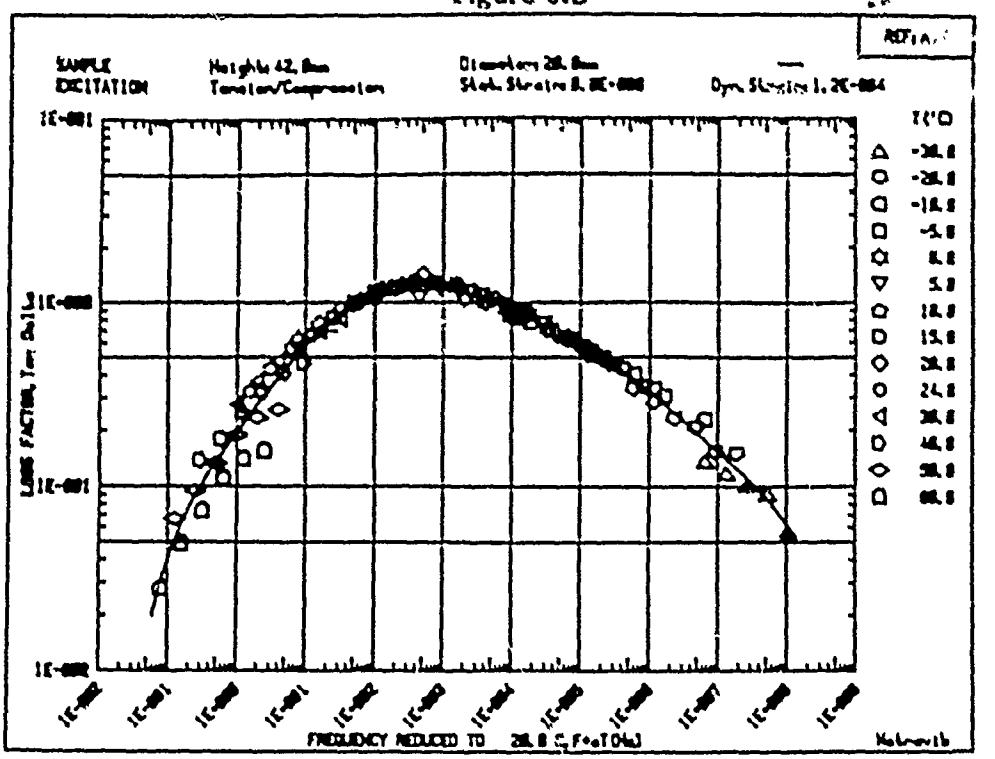
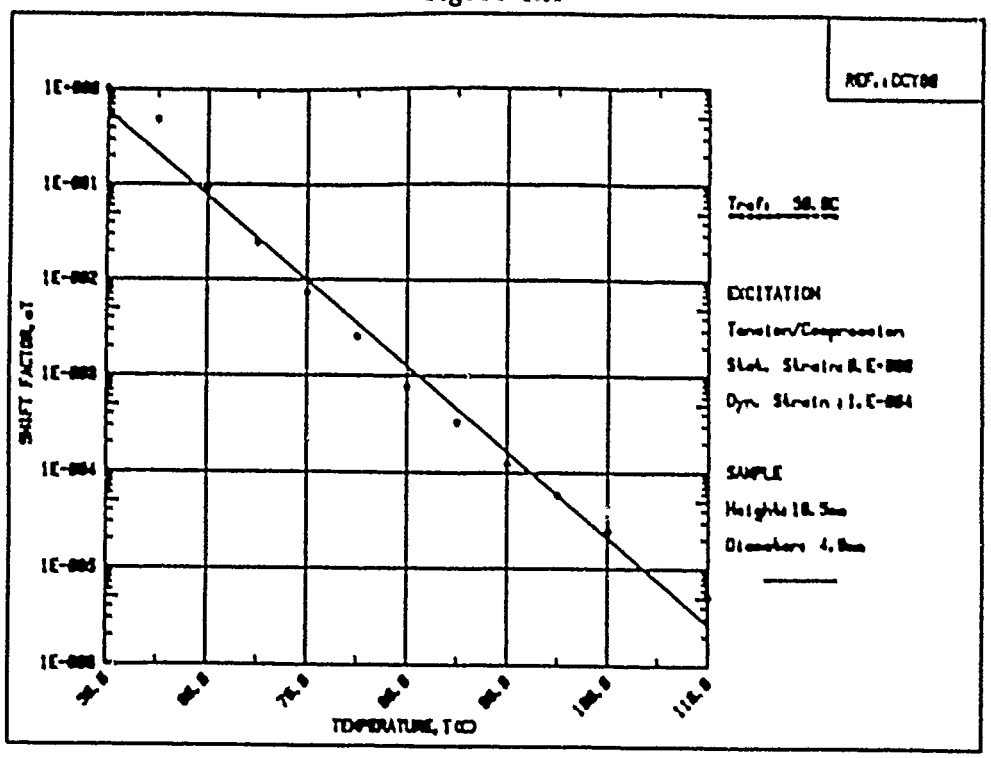


Figure 3.B



EP 5020 - 10 % HY 956

Figure 4.A



EP 5072 - 20 % HY 956

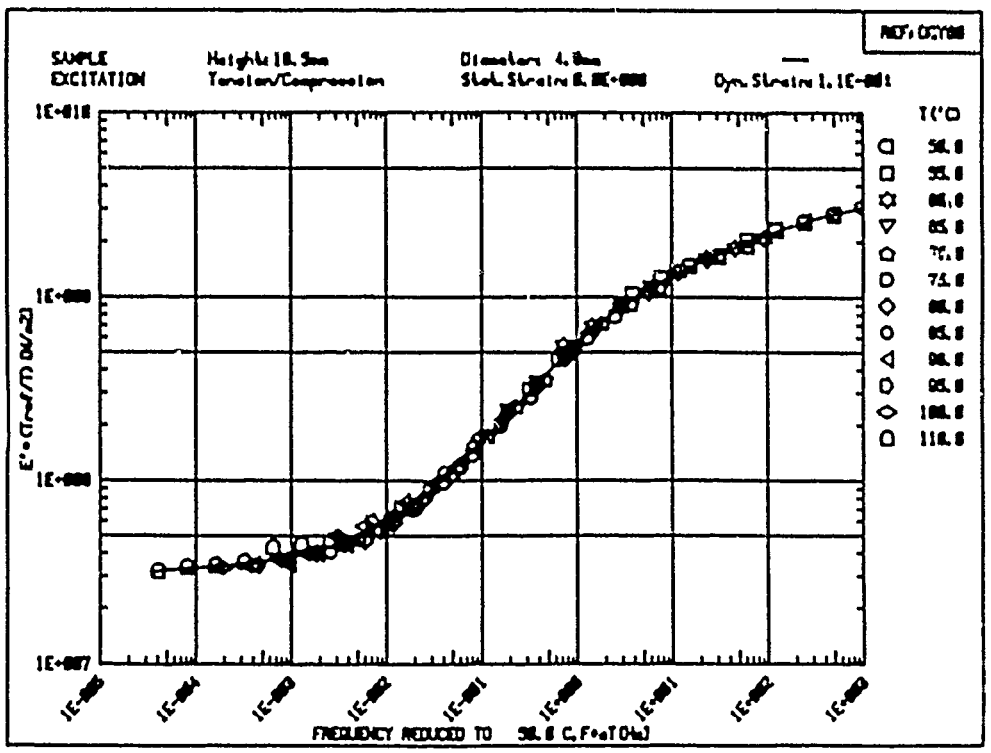
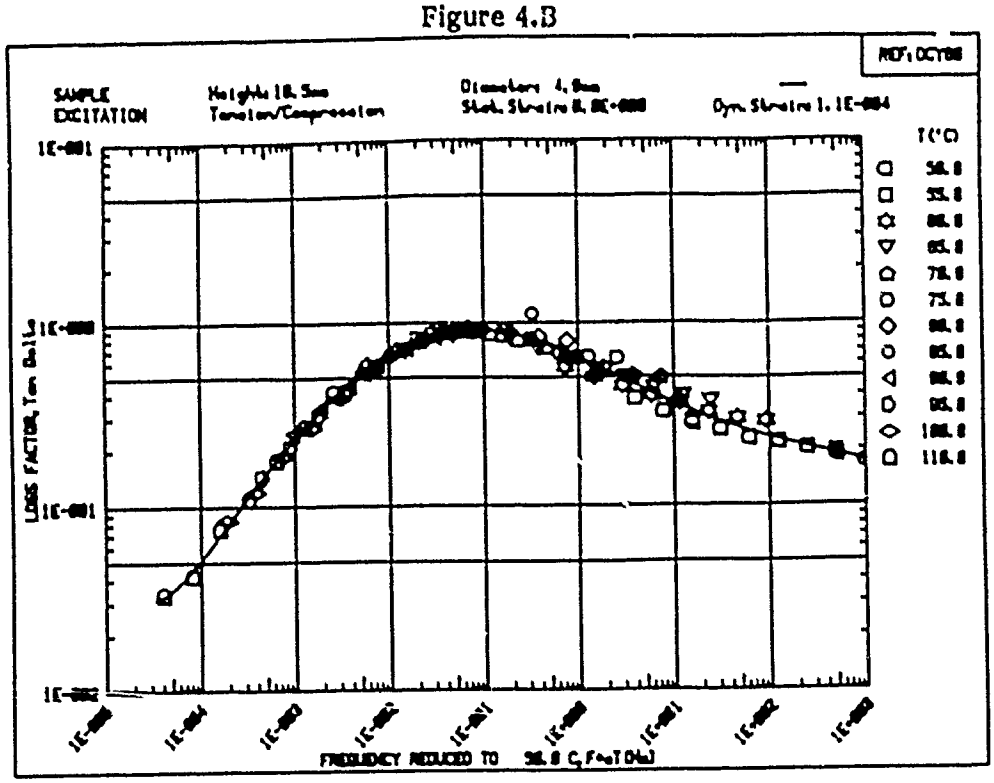
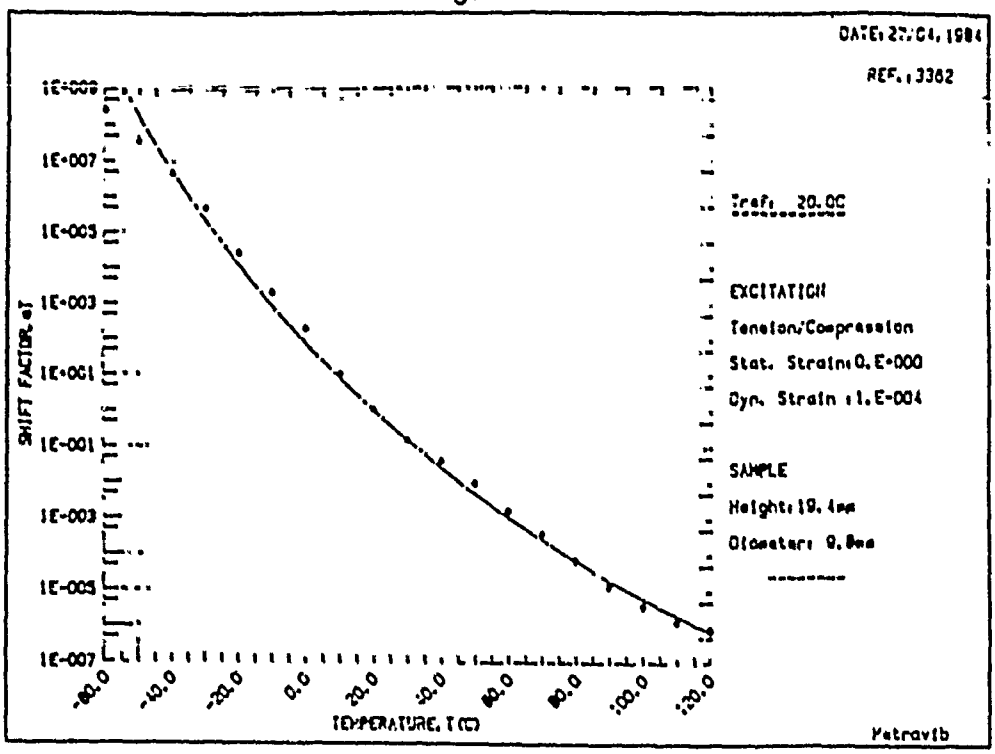


Figure 4.B



EP 5072 - 20 % HY 956

Figure 5.A



VIBRACHOC 11.112 A

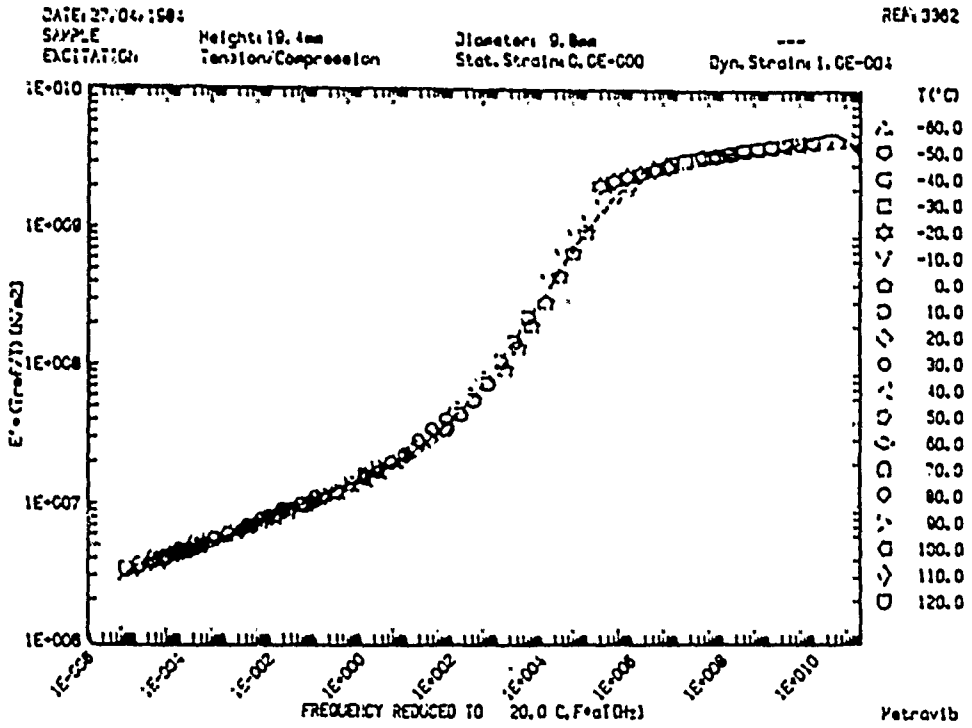
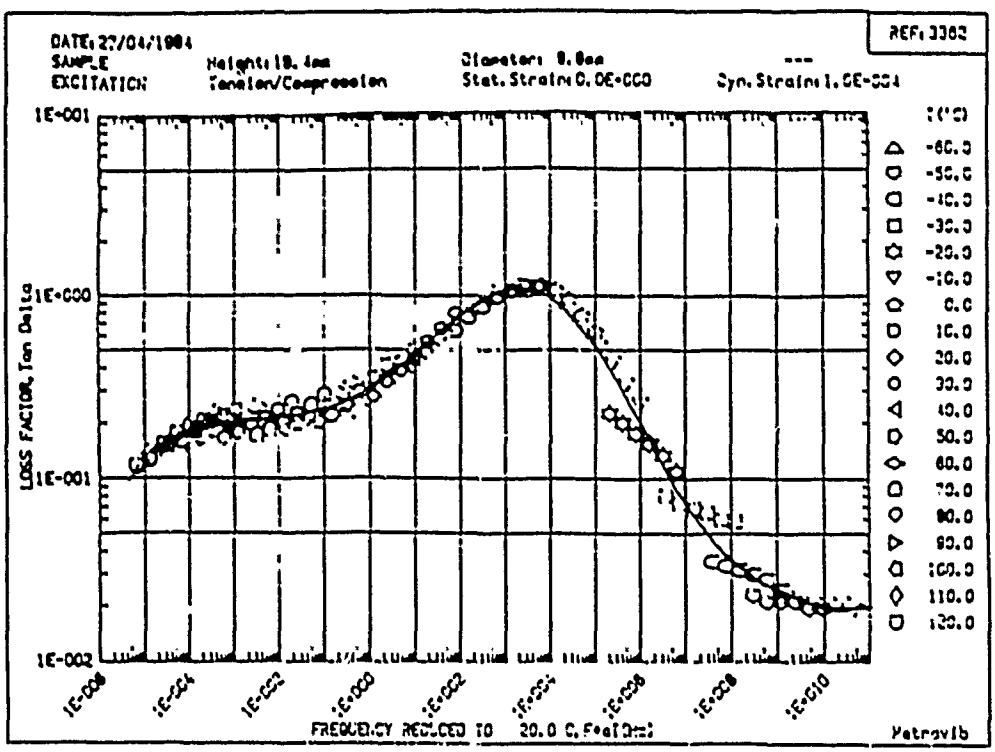
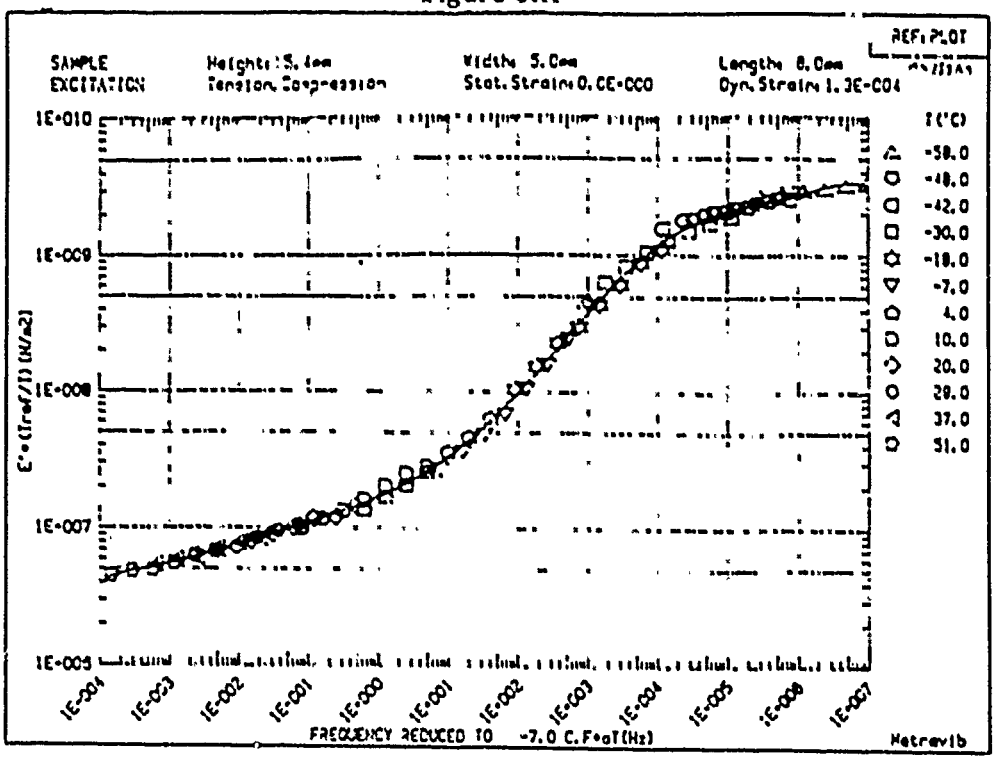


Figure 5.B

VIBRACHOC 11.112 A



- Figure 6.A



VIBRACHOC 14/59 AI

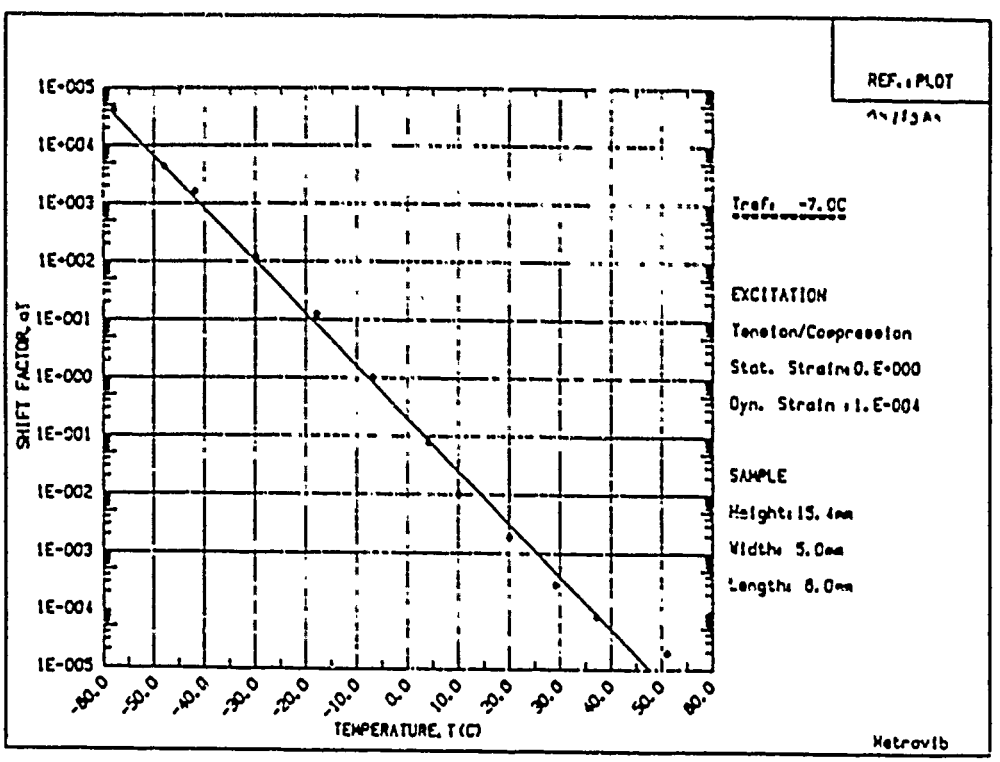
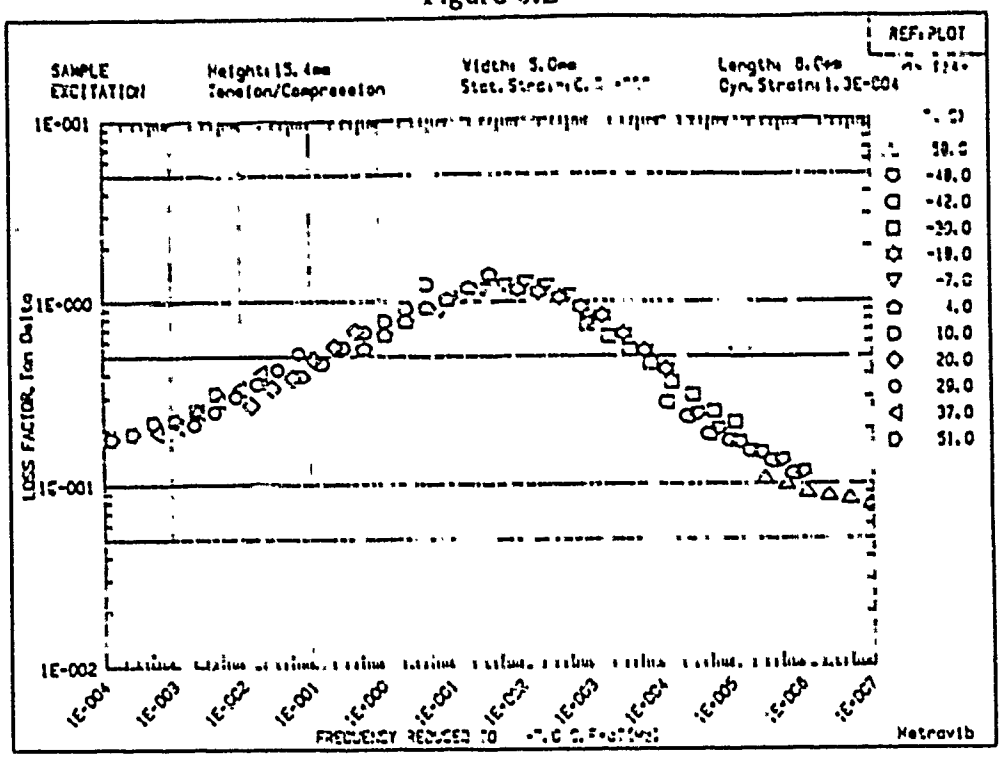
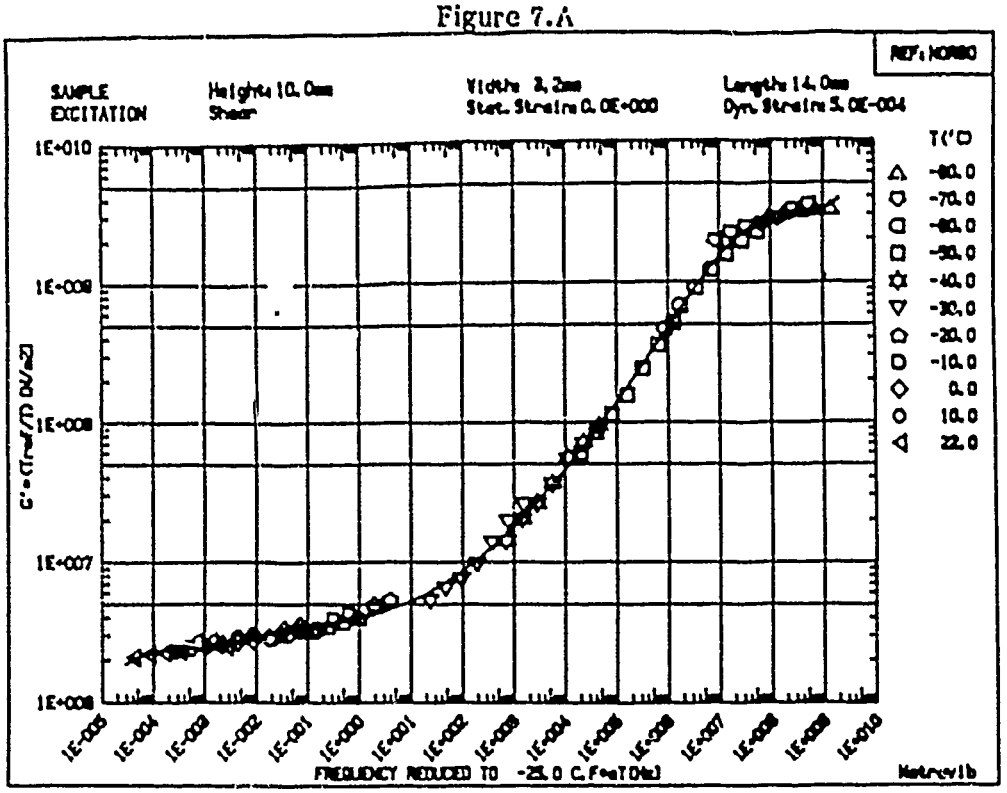


Figure 6.B



VIBRACHOC 14/59 AI

Figure 7.A



NORSOREX

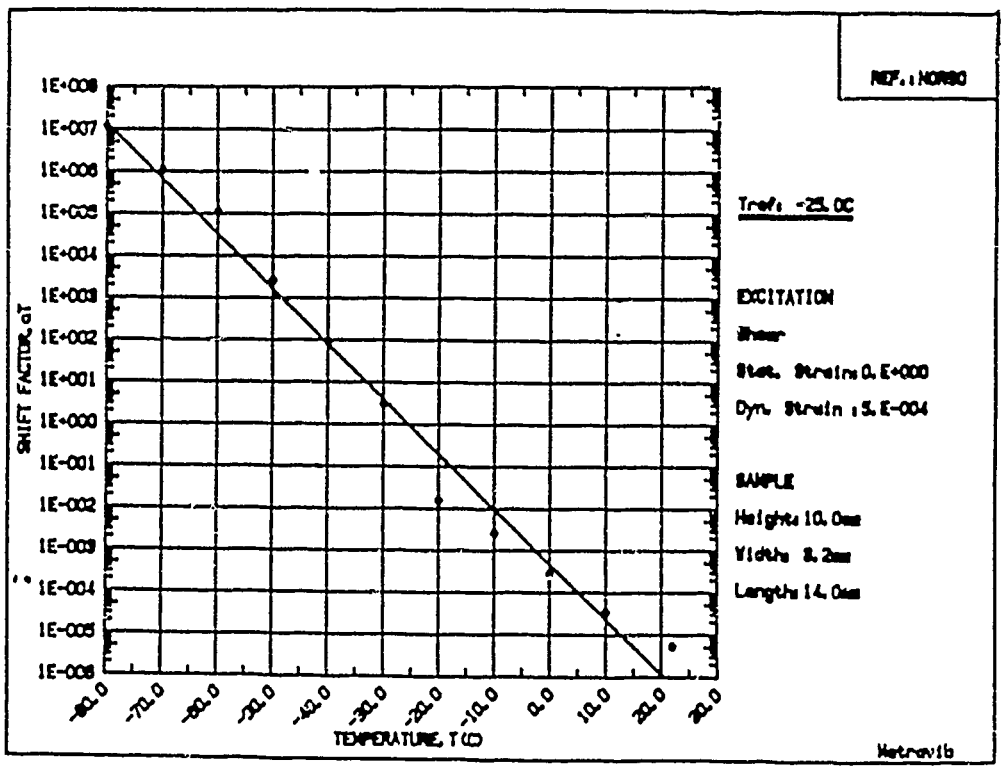


Figure 7.B

NORSOREX

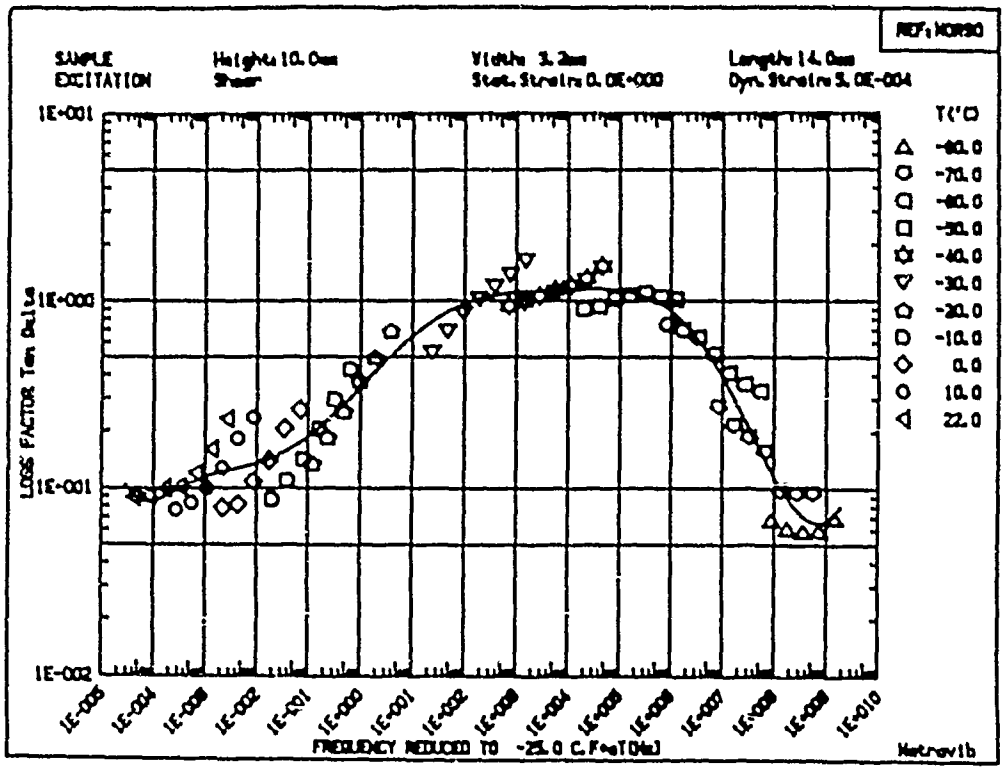
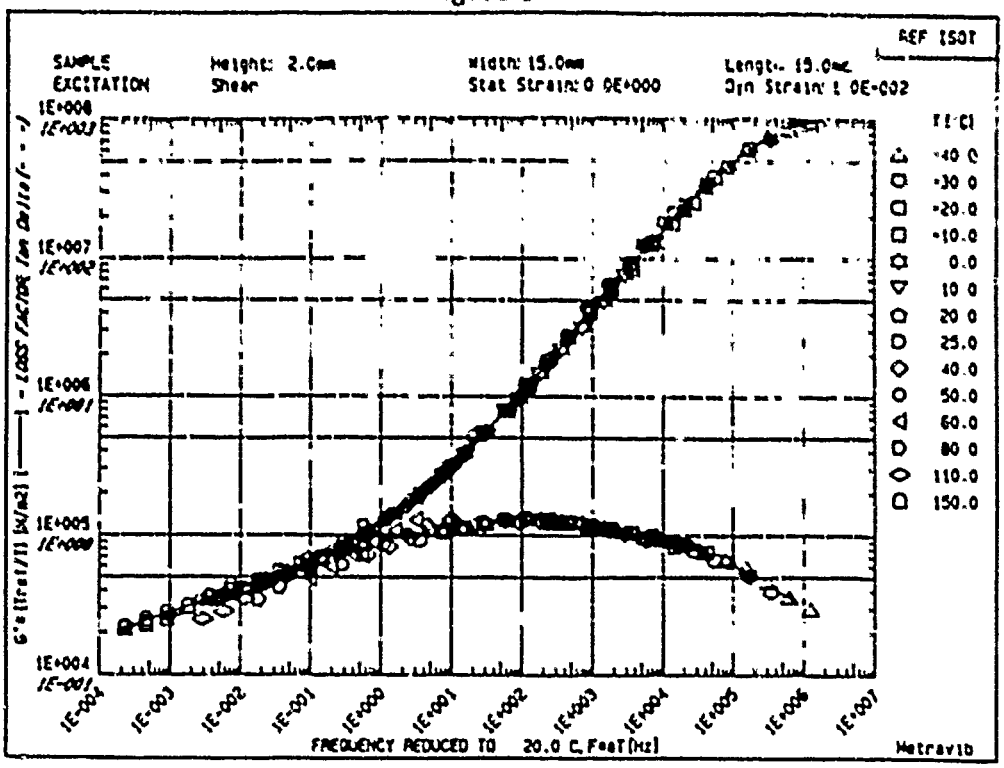


Figure 8



FASSON ISOTACK

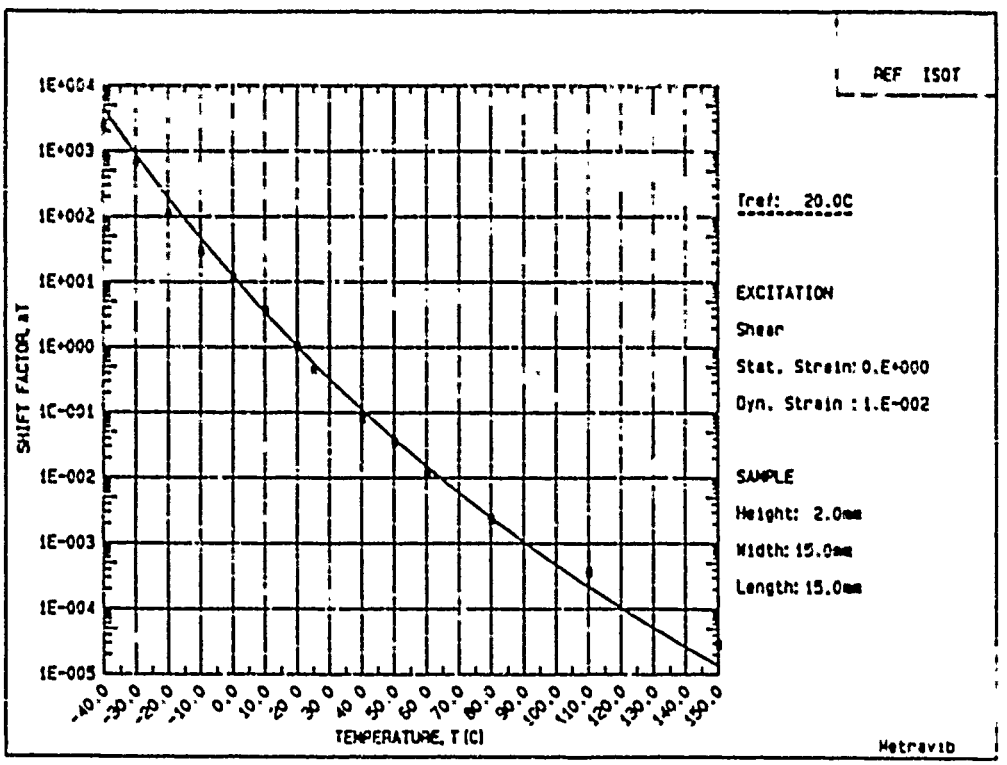
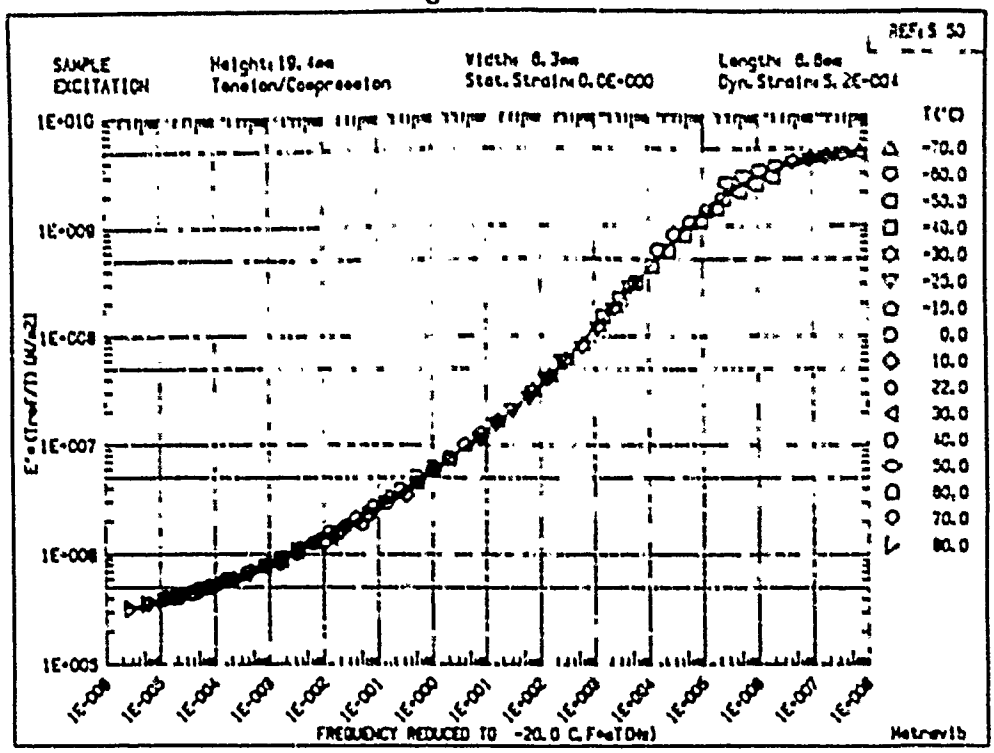


Figure 9.A.



SORBOTHANE S 50

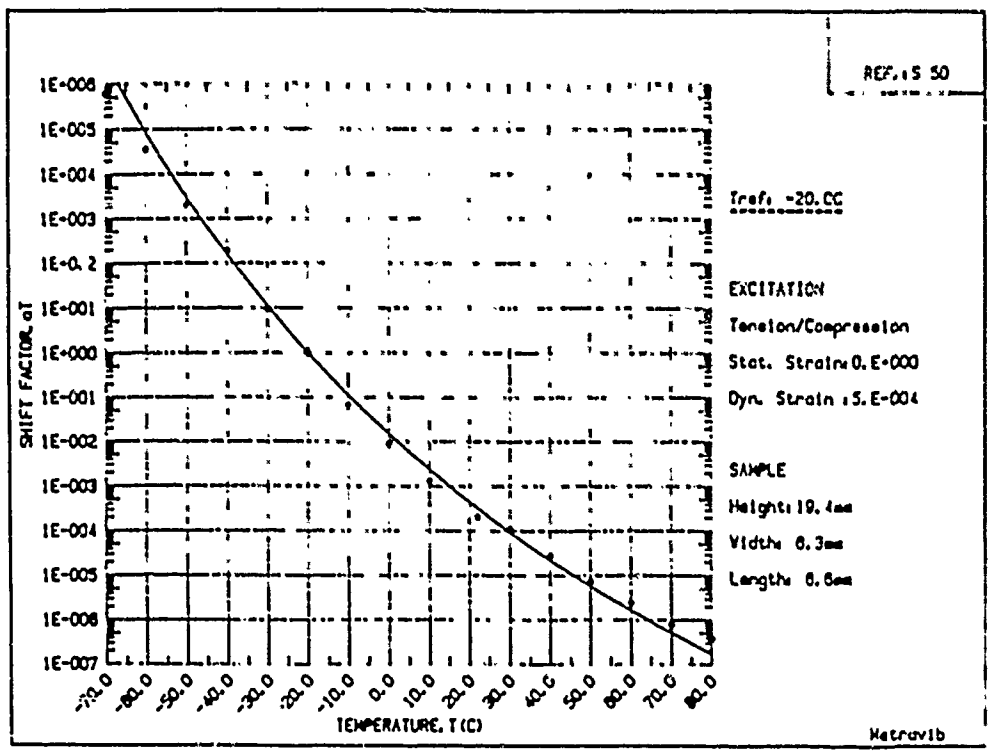
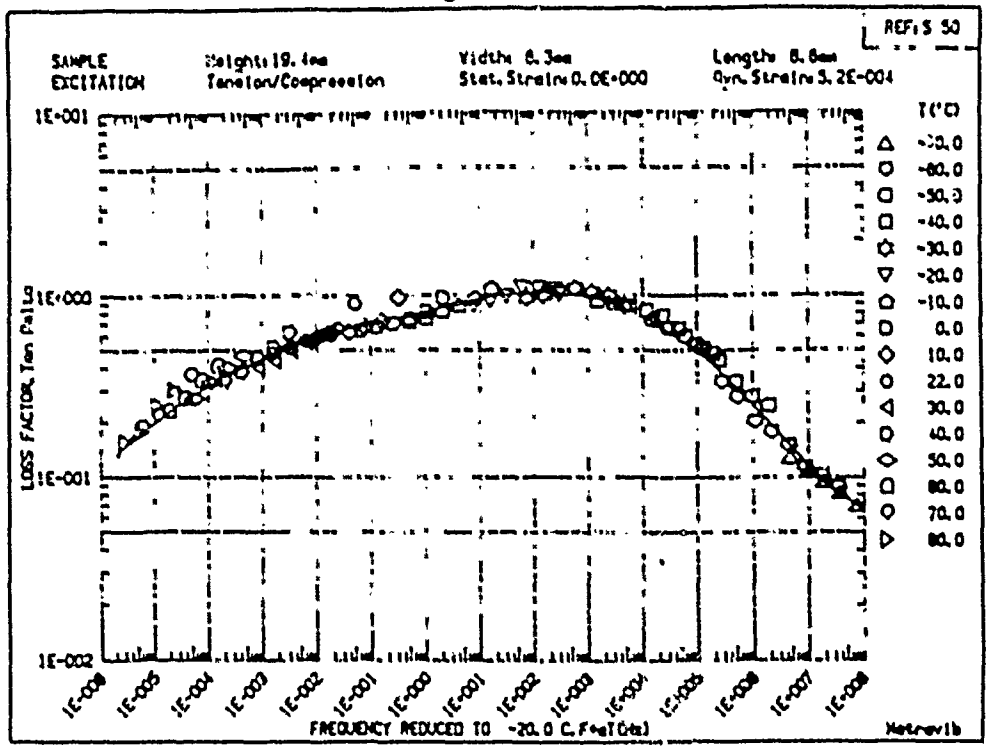
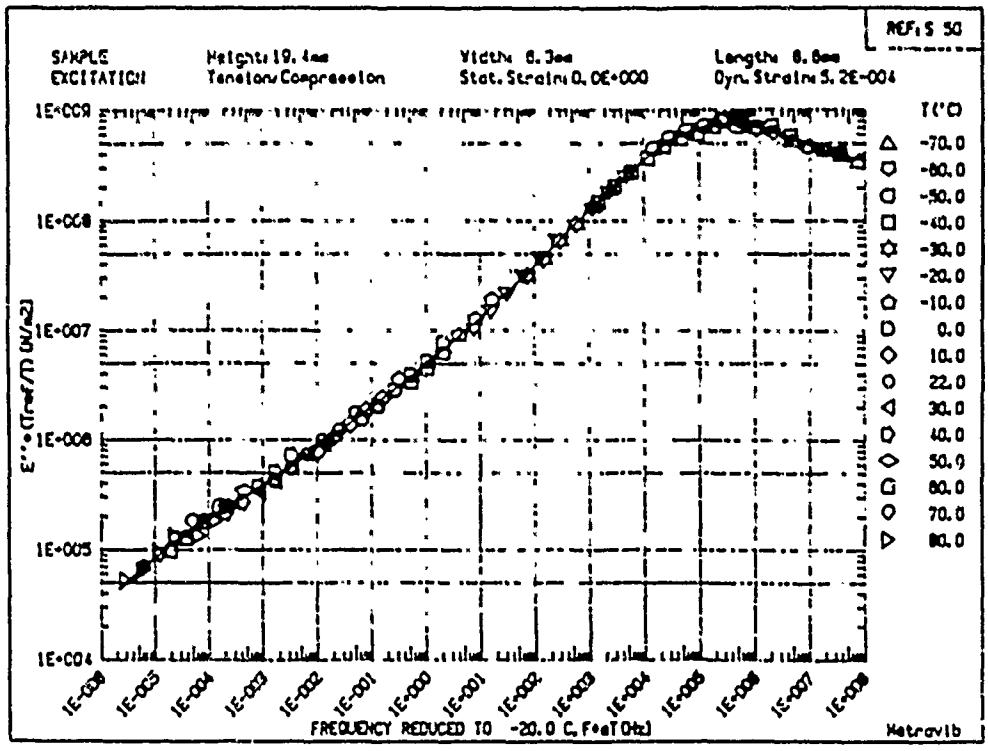


Figure 9.B



SORBOTHANE S 50



A N N E X A

GENERAL AND TECHNICAL CHARACTERISTICS

OF THE VISCOELASTICIMETER AND THE VISCOANALYSER

TEST EQUIPMENT

VISCOELASTICIMETER/VISCOANALYSER

OPERATING PRINCIPLE : FORCED OSCILLATIONS OFF-RESONANCE

GENERAL CHARACTERISTICS

	VISCOELASTICIMETER	VISCOANALYSER
DIMENSIONS	2 m x 1 m	2,5 m x 1 m
WEIGHT : . mechanical frame	200 kg	200 kg
. electronic cabinet	130 kg	200 kg
POWER REQUIREMENTS	220 V/50 - 60 Hz 1,5 kVA	220 V/50 - 60 Hz 2,5 kVA
CRYOGENIC SOURCE *	liquid nitrogen	liquid nitrogen

* (not included in the standard model)

TECHNICAL CHARACTERISTICS

	VISCOELASTICIMETER	VISCOANALYSER
. FREQUENCY	7.8 Hz to 1 000 Hz 7.8 Hz - 15.6 Hz 31.2 Hz - 62.5 Hz 125 Hz - 250 Hz 500 Hz - 1000 Hz	5 Hz to 1 000 Hz up to 100 points in the chosen range between those values
		0.01 Hz to 100 Hz
. DYNAMIC FORCE	0.1 N to 40 N	0.1 N to 100 N
OPTION :	0.1 N to 100 N or 150 N	0.1 N to 150 N
. DYNAMIC DISPLACEMENT	± 0.1 µm to ± 500 µm	± 0.1 µm to ± 500 µm
OPTION :	± 100 µm to ± 3000 µm	± 100 µm to ± 3000 µm
. TEMPERATURE	- 70°C to + 180°C	- 70°C to + 180°C
OPTION :	- 100°C to + 350°C	- 100°C to + 350°C
. RANGE OF MEASUREMENT - YOUNG'S MODULUS - SHEAR MODULUS - VISCOSITY	ALL MATERIALS IN THE RANGE $10^3 N/m^2$ - $10^{12} N/m^2$	ALL MATERIALS IN THE RANGE $10^3 N/m^2$ - $10^{12} N/m^2$
- PHASE ANGLE	from 0 to 90° ± 0.1°	from 0 to 90° ± 0.1°
OPTIONS : - CRYOGENIC SOURCE	PERMITS WORK BETWEEN AMBIENT AND NEGATIVE TEMPERATURES	PERMITS WORK BETWEEN AMBIENT AND NEGATIVE TEMPERATURES
- MULTI-CHANNEL PLOTTER	ALLOWS THE EVOLUTION OF CHARACTERISTICS OF A SAMPLE TO BE RECORDED OVER TIME	
- DATA ANALYSIS	THE HP 85 DOES NOT AFFECT THE RUNNING OF THE EXPERIMENT IN ANY WAY. THIS ALSO MEANS THAT ANY PHENOMENA EVOLVING OVER TIME CAN BE ANALYSED (i.e. thermoset kinetics)	DATA GENERAL COMPUTER INTEGRATED INTO THE SYSTEM : THE EXPERIMENT AND THE DATA PROCESSING BECOME AUTOMATED
- SPECIAL PROGRAMS	KINETICS MONITORING, WLF	KINETICS MONITORING, WLF
- STANDARD TESTING		AFNOR, ISO, DIN, ASTM

A N N E X B

MICROMECANALYSER

GENERAL SPECIFICATIONS,

WITH VISCOELASTICIMETER/MICROMECANALYSER

COMPARATIVE RESULTS

Figure 10.A : Shift factor V/S temperature

Figure 10.b : Shear modulus V/S reduced frequency

GENERAL SPECIFICATIONS

FREQUENCY RANGE : 10^{-5} Hz TO 1 Hz

STRAIN RANGE : 0 TO 10^{-3}

TORQUE : 0 TO 1.5×10^{-2} N.m

TEMPERATURE : 100 K TO 670 K

INTERNAL FRICTION RESOLUTION $\approx 10^{-4}$

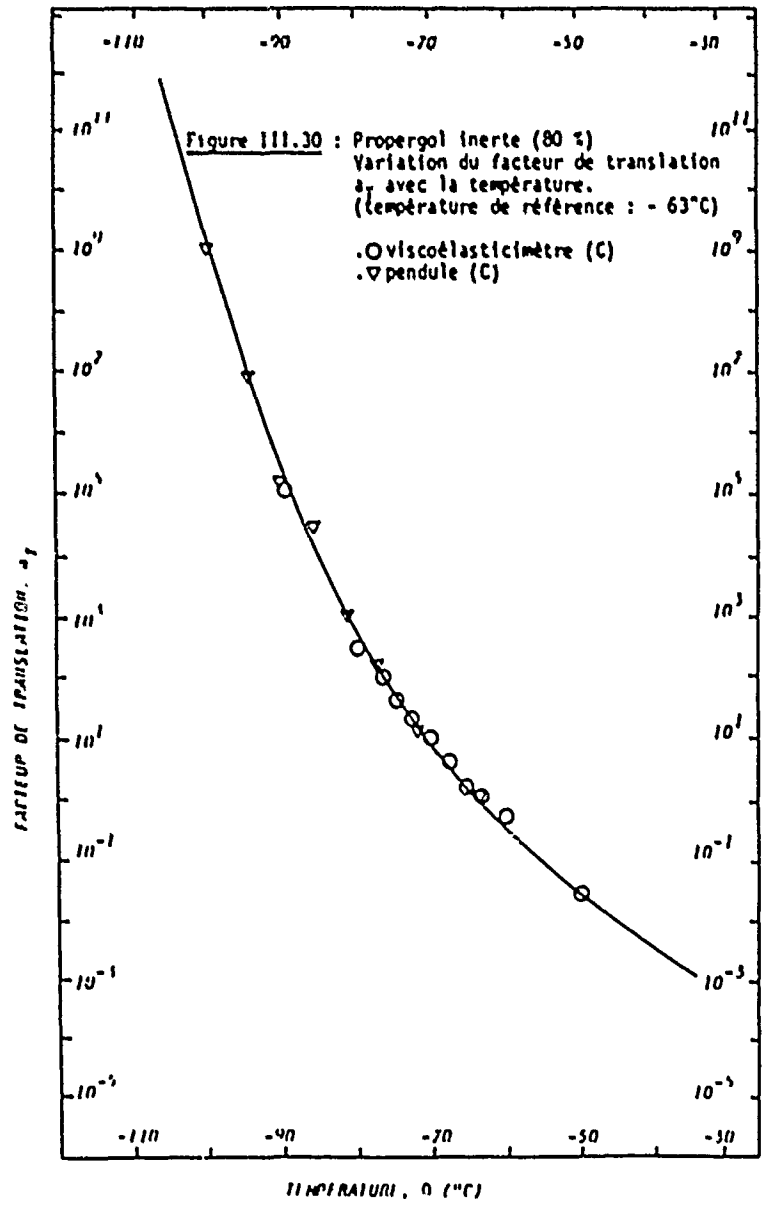


Figure III.30 : Propergol inerte (80 %)
Variation du facteur de translation a_T avec la température.
(température de référence : - 63°C)

.○ viscoélasticimètre (C)
.▽ pendule (C)

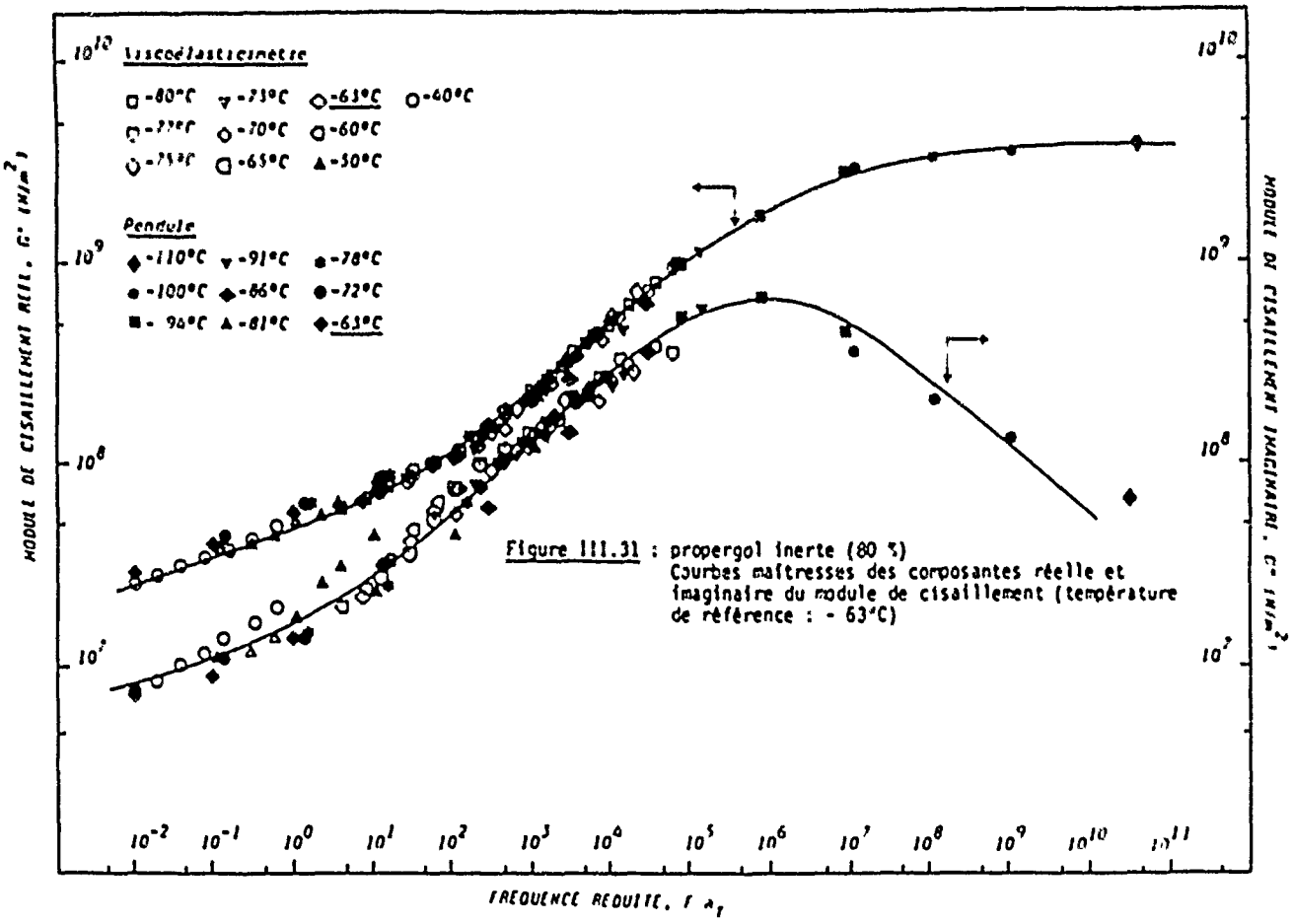


Figure III.31 : propergol inerte (80 %)
Courbes maîtresses des composantes réelle et imaginaire du module de cisaillement (température de référence : - 63°C)

ON THE FRACTIONAL CALCULUS MODEL OF VISCOELASTIC BEHAVIOR

Maj R.L. Bagley and Prof P.J. Torvik

Paper is published:
J. of Rheology, 30(1), 133-155(1986)

CRITIQUE OF COMPLEX MODULUS TEST METHODS

by

David I.G. Jones
Materials Laboratory (AFWAL/MLLN)
Wright-Patterson Air Force Base, Ohio

ABSTRACT

This paper represents a critical review of test methods and data obtained for the complex modulus properties of damping materials. Brief summaries of the test techniques considered are followed by detailed evaluation of the test data, with particular emphasis on processes for evaluating the self-consistency of the test data and culling unacceptable points. A summary of the usable modulus and frequency ranges of several test techniques is given, based on the test data. Steps which can readily be taken to improve the reliability of test results are recommended.

CRITIQUE OF COMPLEX MODULUS TEST METHODS

by

David I.G. Jones
Materials Laboratory (AFWAL/MLLN)
Wright-Patterson Air Force Base, Ohio

ABSTRACT

This paper represents a critical review of test methods and data obtained for the complex modulus properties of damping materials. Brief summaries of the test techniques considered are followed by detailed evaluation of the test data, with particular emphasis on processes for evaluating the self-consistency of the test data and culling unacceptable points. A summary of the usable modulus and frequency ranges of several test techniques is given, based on the test data. Steps which can readily be taken to improve the reliability of test results are recommended.

1. INTRODUCTION

Many test techinques have been devised to measure the complex modulus properties of polymeric damping materials, each of which must be used with great care to ensure that the test data obtained is reliable. In particular, each test technique, for usual specimen sizes and types, has its own particular frequency and modulus ranges within which the most reliable results are obtained. Now that the data base of viscoelastic damping material complex modulus properties is expanding rapidly, it has become possible to review and compare data obtained from several sources and by several test techniques, so as to quantify some of the limits of test techinques. In this paper, such an evaluation is conducted for several damping materials, and recommendations made.

2. PROPERTIES TO BE MEASURED/COMPLEX STRESS-STRAIN BEHAVIOR

The goal of most currently used test systems and methods for measuring polymeric material behavior is to establish the relationship between stress and strain in the time or frequency domains. The moduli ideally required are the shear, extensional and bulk moduli. In the frequency domain, these moduli are complex numbers, being functions of frequency, temperature, cyclic strain amplitude and applied static load in addition to the specimen composition and processing and storage histories. For any given material sample, supposed homogeneous and isotropic on a macroscopic scale, the shear, extensional and bulk moduli, and Poisson's ratio, are interrelated in the frequency domain by the complex number generalization of the classical theory of elasticity. Some of the relevant linear relationships, for low cyclic strain levels are:

$$\sigma_s = G(1 + i\eta_s)\varepsilon_s$$
$$\sigma_e = E(1 + i\eta_e)\varepsilon_e \qquad (1)$$
$$E = 2(1 + \nu)\, G$$
$$\eta_s \doteq \eta_e = \eta$$

G, E, η and ν are functions of frequency and temperature, in particular. For low cyclic strain levels the behavior is linear. The properties are measured for particular samples by deforming specimens cyclically in shear and extension and calculating G, E and η from the measured loads and displacements. It is difficult to measure the bulk modulus K or Poisson's ratio ν but these can be inferred from measured values of E and G.

Many precautions must be observed in the measurement of E, G and η. Specimens must be designed so that the mode of deformation accurately reflects the parameters to be measured, so that effects of finite specimen size, end effects etc. are reduced to a minimum. Tests must be conducted in such a way that the extreme sensitivity to temperature of the material properties is taken into account - this often means that specimens must be soaked at the measurement temperature for extended periods of time, fifteen minutes or more being not unusual. Efforts to reduce test time by sweeping temperature at rates of several degrees a minute are usually counterproductive, since thermal equilibrium is not obtained and the measured data cannot readily be related to the supposed temperature. Temperature sweep procedures may well be useful for other purposes, such as monitoring curing processes, but they are totally unusable for accurate complex modulus measurements. Other precautions must also be taken, on a regular basis, including checking for non-linear behavior, noise and distortion in the excitation and response electronic signals, dimensional stability of the specimens, irreversible degradation of the specimen at extremes of the test environment, proper identification and storage of specimens for possible repeat tests, proper measurement and recording of relevant specimen characteristics such as density, dimensions, composition and processing (when known), test system settings when relevant, date of the test etc. Proper recording and storage of the measured data, before data processing, is an absolute necessity to ensure the possibility, at a later date, of re-examining the test data for possible sources of discrepancies and inconsistencies. In the absence of such records, data may often be unusable at a later date.

3. TEST TECHNIQUES AND TEST SPECIMENS

Most measurement techniques used for determining damping material stress-strain properties apply oscillatory, transient or random loads to a specimen and measure the corresponding response. Differences in techniques reflect the points at which loads are applied, the manner in which the loads are measured and controlled, the points at which the response is measured, the manner in which the response is measured, the magnitudes and types of deformations induced in the specimen, the frequencies at which the measurements are conducted and the particular sets of equations used to

derive the required material properties from the observed behavior. It is an implicit assumption that all methods of measurement, when properly used on samples from the same material batch, will lead to equivalent properties. To assume otherwise would be to admit the impossibility of the measurement process. However, in practice, many sources of error exist for each measurement technique and only the most careful evaluation of an adequate set of measured data over a wide band of frequencies and temperatures, even for materials exhibiting linear viscoelastic behavior, can ensure that a reasonable level of confidence can be placed on the results.

Test techniques can be placed in four major groups; direct or resonant techniques in the frequency domain, or travelling wave and relaxation techniques in the time domain. These in turn may be further subdivided according to whether shear or extensional properties are measured. Direct frequency domain techniques are quite commonly used at the present time and many commercial configurations are available [1-7]. Resonance techniques may be used for simple specimens having uniform states of stress [8-11] or for resonating beams with complex states of stress and several modes of vibration [8,10,12,13] or a torsional pendulum with non-uniform shear stress distributions [11]. Relaxation and travelling wave technique are usually conducted for simple uniform specimens.

Figures 1 to 8 illustrate some idealized forms of the direct, resonance, resonant beam, torsional pendulum and stress-relaxation test configurations, and idealized indications of the types of response behavior observed. Much has been written on the process of obtaining response data, and reduction of this data to obtain complex modulus properties, so the descriptions given here will be brief.

3.1 Direct Techniques

Direct measurement techniques are those in which cyclic loads are applied to a specimen and the resulting cyclic deformations are directly measured in some way. Specimen deformation can be extension, shear, torsion or more complex deformation patterns such as flexure. Figure 1 illustrates some of the possibilities. Commercial systems based on direct measurement include the Autovibron [12], Viscoelasticimetre [3] and the MTS systems [4]. A low frequency direct measurement system is described by Whittier [5]. The stress-strain behavior is ideally represented by two sinusoidal signals:

$$\sigma = \sigma_0 \sin(\omega t)$$
$$\varepsilon = \varepsilon_0 \sin(\omega t + \phi) \qquad (2)$$

as illustrated in Figure 2 .

The complex modulus is obtained from these observed signals by trigonometric expansion of Sin $(\omega t + \phi)$ to give, in shear for example:

$$\sigma = G(1 + i\eta)\,\varepsilon \qquad (3)$$

$$G = \sigma_0 \cos\phi \,/\, \varepsilon_0 \qquad (4)$$

$$\eta = \tan\phi \qquad (5)$$

In the direct measurement techniques, it is important to ensure that the stress and strain signal to noise ratios are high. If, for example, the load measuring transducer is designed to measure up to 5000 lb, and the actual specimen loading forces are of the order of 10 to 100 Lb, then one may expect inaccurate measurements and high electronic noise levels. Equally, errors may be encountered in measuring specimen deformations, and care must be taken to ensure proper choice of transducers. This means that any given instrument, having given load and response transducers, will give reliable data over a very limited range of values of the modulus G and a limited frequency range, although the ranges may vary from configuration to configuration. The extreme range seems to be $1 < G < 10^5$ Lb/in^2 and $10^{-2} < f < 10^2$ Hz, but any specific apparatus will cover only a fraction of this range.

3.2 Resonance Techniques

Simple resonance techniques are those in which the viscoelastic material specimen forms the resilient element of a single degree of freedom system, which is excited harmonically at its resonant frequency [8,9]. Figure 3 illustrates some of the simplest possibilities. If the base of the system is excited harmonically with acceleration amplitude A_1 at frequency ω, then the amplitude A_2 of response of the inertial element behaves as illustrated in Figure 4 . The loss factor η of the material at the resonant frequency ω_r is determined by:

$$\eta = 1 \,/\sqrt{(A_2/A_1)^2 - 1} \qquad (6)$$

and the stiffness of the resilient element from:

$$k + k_0 = M\omega_r^2 \qquad (7)$$

The relationship between k and the specimen geometry varies with the type of specimen. For extensional deformation, $k = ES/h(1+\beta S^2/S_1^2)$ where S is the load-carrying cross sectional area and S_1 is the non-load carrying area and β is a constant between 1.5 and 2. For shear deformation, $k=2GS/h$ where S is the load carrying area and h is the thickness. The resonance techniques can give reliable results, but the range of frequencies and moduli over which these results can be obtained is rather limited, ranging typically from $100 < f < 1000$ Hz in frequency and $10 < G < 3000$ Lb/in^2 for modulus, though other values can be accomodated with extreme effort. Few commercial resonance systems are available, but simple configurations can readily be built up, and are used most often for obtaining additional data to supplement other techniques, or to examine effects of amplitude of vibration. Other types of resonance test system utilize flexural deformations of the specimen. One such setup, illustrated in Figure 3 , is useful for determining complex moduli of stiff plastic materials or

composites. A commercial flexural resonance system is the DuPont DMA system [14]. In this case, the range of moduli and frequencies is still narrow, but different from the simple resonance techniques, ranging from about $1 < f < 100$ Hz with respect to frequency and $10^3 < G < 10^5$ Lb/in^2 with respect to modulus.

3.3 Resonant beam techniques

The resonant beam techniques are quite widely used for measuring damping material complex modulus properties. Some of the most commonly used beam configurations are illustrated in Figure 5. Properties are measured in extension or shear, but the stress distribution is not uniform so data is usually taken only within the linear behavior zone of a given material. The beam techniques have been widely discussed elsewhere [8,9,10,12,13], so we shall not go into details here. Suffice it to say that from measured response data, as illustrated in Figure 6, along with similar data for the metallic or plastic supporting beam or beams, one may deduce the modulus G or E, and the loss factor η, at the discrete frequencies corresponding to each mode and at the discrete temperatures for which each test is performed. It is important to ensure that temperatures are well stabilized and uniform throughout the specimen and that errors and magnification of errors which arise from poorly selected specimen dimensions or too high or too low a material modulus be avoided.

3.4 Stress-relaxation methods

Stress relaxation generally gives modulus data in the time domain, but the application of digital transform techniques to the measured data can give moduli in the frequency domain. Some typical idealized test configurations are illustrated in Figure 7. The strain increment is applied to the specimen as suddenly as possible and the force measured by the force gage is a descriptor of the behavior of the material, once the start-up transients have died away, as illustrated in Figure 8. Beyond this zone, the stress can be represented as a function of time by [15]:

$$(t) = A + B\, t^{-\alpha} \tag{8}$$

The application of transform theory to this gives the complex shear or Young's modulus (according to the test) in the forms:

$$\begin{aligned} G'(\omega) &= A + \alpha B \omega^{\alpha} \Gamma(1-\alpha/2)\Gamma(\alpha/2) \,/\, 2\Gamma(1+\alpha) \\ G''(\omega) &= \alpha B \omega^{\alpha} \Gamma(1-\alpha/2)\Gamma(1+\alpha/2) \,/ 2\Gamma(1+\alpha) \end{aligned} \tag{9}$$

These equations are valid only for small values of ω within the rubbery zone of the damping material. Thus it is possible to determine complex moduli, particularly at low frequencies and for moderate values of G or E, in a fairly accurate and unambiguous way. However, as always, care must be taken to avoid errors, which include the transients, at short times after application of the strain.

4.0 DATA REDUCTION PROCESSES

4.1 Minimization of test errors

Ideally, all the measurement techniques used to determine complex modulus properties of a specific sample of a damping material would complement each other and agree closely in numerical values. In the real world, many sources of error exist which are not always evident during a specific test and many not come to light at all if great care is not taken. Such errors may include errors of calibration in the test equipment, discrepancies between indications of sensors (accelerometers, force gages etc) and the true values of the relevant parameters arising from deficiencies of the test apparatus used outside of its optimum range, errors from too rapid sweeping of frequency in the case of sine-sweep testing, errors from improper time-domain testing, and errors from too rapid sweep rates of temperature. The temptation to sweep temperature at rates of 1°C a minute or more is often irresistible, yet it can lead to large discrepancies between indicated temperature and true specimen temperature. Unless very special techniques are devised to reduce thermal "inertia", only periods of up to 30 minutes to change temperature from one setting to another, along with temperature "dwells" of 15 minutes or more, can ensure freedom from error in this most important respect. Rapid sweep may be acceptable for some purposes, such as following rapid chemical reactions, but is is not acceptable for steady state complex modulus measurements on stable materials.

4.2 Checking the self consistency of test data

Given that some errors will unavoidably remain, one must have some "recipe" for culling out the errors remaining after all recognized test errors have already been eliminated. At present, the best way to accomplish this goal is to examine the collected data on each given material in the form of three plots:

(a) Quadrature modulus (G" or E") versus direct modulus G' or E' for all frequencies, temperatures and test methods, as illustrated in Figure 9. [16]

(b) Loss factor η versus direct modulus G' or E', as illustrated in Figure 10.

(c) Plots of loss factor η, direct modulus G' or E', and quadrature (loss) modulus G" or E" versus frequency at each temperature, as illustrated in Figure 11.

Items (a) and (b) reflect the fact that, in the complete absence of errors, G"(or E") and η should be unique functions of G' (or E') and all test points should be near to this unique curve and be scattered randomly around it, possibly in a normal distribution as illustrated in Figures 9 and 10. Points which fall more than one standard deviation away from the mean curve can be expected to be in error and should be "culled" from the data set. Of course, this process does not identify the reason for the error and one should, where possible, trace back to find that reason. Unfortunately, most often the original test data is not available some time after a test

program is complete, nor is it usually available to other users of the data, so this may indicate that more careful attention should be paid to recording raw data along with finished plots of complex modulus data.

Item (c) illustrates a very important point, namely that such plots can be made only if the test data is recorded at common temperatures. Again this ideal is rarely followed, the test temperatures used in one test often being different from those used in another. Again, investigators should ponder this point and perhaps take greater care to approach closer to the ideal.

These three steps in the process of cleaning up the test data will improve the data set. They are not at all infallible, since it is not at all impossible to get consistent but wrong data. If the number of test methods used is expanded (two or more methods) and the range of frequencies expanded as far as possible (two or more decades), then the best results will be obtained. Only then can one safely assume that low scatter is the same as high accuracy. Spurious precision is always achieveable by conducting only one test, using one test method, over a narrow frequency range at each temperature, and this can be compounded further by sweeping the temperature steadily but rapidly.

5. ILLUSTRATIONS

5.1 3M-ISD-112 [17]

The first material selected was an aerospace viscoelastic adhesive. The material was evaluated by several of the test techniques reviewed earlier, and available test data is summarized in Tables 1 to 8 [12,13,18,19]. Some of the test methods were used in conditions not likely to yield accurate data, in order to establish limits, so some scatter was expected. Figure 12 shows the plot of quadrature (loss) shear modulus G" versus direct shear modulus G' for all the test points. The scatter is evident, giving an indication of the usable range of modului for each test method and specific configuration. The shaded band indicates the range of usable data, though no effort was made to perform a precise statistical analysis. Figure 13 shows the corresponding graph of loss factor η versus direct shear modulus G', again illuminating the acceptable and unacceptable points. Figures 14 and 15 illustrate some plots of G' and η versus frequency at specific temperatures. Unfortunately, common temperatures for comparison between different test methods were not selected as carefully as would have been desirable. Once the "smoothed" data was culled from the total data set, it was possible to produce the usual graphs of modulus G' and η versus reduced frequency as in Figure 16, and the corresponding graphs of shift factor a_T versus temperature as in Figure 17 and versus 1/T as in Figure 18. There is still some scatter, but there is no way of reducing that except through additional testing with more care taken to minimize all possible errors.

The shaded bands in Figures 14 and 15 represent the shaded bands in Figure 16 transferred back to the particular temperatures.

5.2 3M-467 Adhesive [17]

This material has damping and many mechanical properties which are very similar to 3M-ISD-112, but the test data available has been obtained by some different test techniques and over a much larger period of time. The available data is summarized in Tables 9 to 14 [5,8,9,10,16]. Figure 19 shows the graph of quadrature (loss) shear modulus G" versus direct shear modulus G', and Figure 20 shows the graph of loss factor η versus direct shear modulus G'. The scatter is less than for ISD 112 because the test methods were used within their recommended range, so very little data has to be culled. Figure 21 gives the plots of G' and η versus reduced frequency, Figure 22 the plot of shift factor α_T versus temperature and Figure 23 the shift factor α_T versus 1/T.

5.3 GE SMRD 100 F90 [20]

The third material evaluated is a space-qualified viscoelastic material, stiffer than the adhesives and not self-adhesive. Again, several tests were conducted to evaluate various test techniques; the results are summarized in Tables 15 to 18 [18]. Figure 26 shows the plot of quadrature shear modulus G" versus the direct shear modulus G' and Figure 25 shows the plot of loss factor η versus direct shear modulus G'. Figure 26 gives the plot of G' and η versus reduced frequency, Figure 27 gives the plot of α_T versus temperature and Figure 28 the plot of α_T versus 1/T.

5.4 Summary

The test results for the three materials evaluated give us some insight into the effectiveness of each of the test techniques used. The points which were accepted as valid, after the culling process described was applied, cover a range of frequencies and shear modulus values. When plotted as a graph of modulus versus frequency, a very clear indication emerges of the most effective range for each technique used. Figure 29 represents this summary. It is seen that each technique, labelled (1) through (9), has its own range of effective operation. Some ranges overlap, some do not. While one may conduct measurements by each technique outside of the range indicated, valid results can be obtained only with extreme care and payment of full attention to specimen dimensions. For example, the resonance techniques (3) are shown to be useful from 100 to 1000 hertz and G=10 to 1000 Lb/in^2. One can conduct resonance tests as low as 1 Hz by making very massively loaded specimens but this requires extraordinary efforts to avoid straining the specimen excessively, and accelerometers would be difficult to use at such low frequencies because the signals are low. Similarly, at frequencies well above 1000 Hz, internal resonances in the specimen are difficult to avoid.

The studies so far have been limited to examination of particular sets of data. Further efforts to examine additional data sources, such as in reference [21], are needed. Also, efforts to apply these techniques to other materials, including those having multiple transition zones, is needed.

6. CONCLUSIONS

This paper has shown that great care must be taken when conducting complex modulus measurements on damping materials. After every effort has been made to minimize experimental errors, further evaluation of the numerical data are needed to establish the self-consistency of all the data. This is done through plots of quadrature modulus and loss factor versus direct modulus, and of modulus and loss factor versus frequency at fixed, closely controlled temperatures. Finally, the remaining data, after this culling process is complete, can be used to define the complex modulus properties of the material as a function of reduced frequency, and to create nomogram of properties as a function of frequency and temperature. Examination of the results has also given a graphical definition of the modulus and frequency range of useful operation of several test techniques.

Several specific recommendations concerning future measurements of damping material complex modulus properties are particularly important:

(1) All tests should be conducted within the "useful range" of the chosen test technique. Any points lying outside those ranges need to be justified.

(2) All tests should be conducted at fixed temperatures, with the temperatures allowed enough time to change from one test value to the next, along with enough dwell time at each test temperature. No tests in which temperature is swept should be used for property measurement, though the sweep process may be allowable for other purposes. Furthermore, the fixed temperatures should be the same for the different techniques used, so that proper modulus and loss factor plots versus frequency can be made.

(3) The test techniques used should be selected to complement each other. For example, a high frequency technique should be used in conjunction with a low frequency technique whenever possible.

(4) All test data should be culled of "non-self-consistent" points by using the three plots of quadrature modulus versus direct modulus, loss factor versus direct modulus and modulus and loss factor versus frequency at varous temperatures.

REFERENCES

1. Company Literature, "Rheometrics Dynamic Spectrometer Model LA" (tension/shear; 0.006 Hz to 80 Hz; direct load/displacement measurement; Rheometrics Inc., 2438 US Hwy #22, Union, NJ 07083), 1985.

2. Company Literature, "Dynaliser" (relaxation/inversion; direct load-displacement measurement; c/o Leverett A. Anderson Co, PO Box 5400, Akron, Ohio 44313), 1985.

3. Company Literature, "Viscoelasticimetre" (direct load/displacement measurement; tension, shear and flexure, Metravib, 24 Chemin des Mouilles, 69130 Ecully, France; c/o Ceeris International Inc, 1055 Thomas Jefferson St, NW Suite 414, Washington, DC 20007), 1985.

4. Company Literature, MTS Systems.

5. J.S. Wittier, "Rheological Properties of Adhesives Considered for Interface Damping", WADD Technical Report 60-280, Wright Air Development Division, June 1960. [Test data on 3M-467 by cyclic shear test and Fitzgerald methods].

6. D.L. Hunston, et al, "Viscoelastic Characterization of Structural Adhesive via Forced Oscillation Experiments", Adhesion and Adsorption of Polymers, ed Lieng-Huang Lee, pp. 321-339, Plenum Publishing Co, New York, 1980. (impedance, forced vibration test).

7. C. Pillot, et al, "A critical review of the different methods of measurements of dynamic moduli and loss factors of viscoelastic materials", paper presented at Acoustical Society Meeting, Atlanta, 22 April 1980.

8. D.I.G. Jones, "Measurement of linear damping material properties", Dynamika Maszyn, ed. A. Muszynska, Polish Academy of Sciences, Warsaw, pp. 199-230, March 1978. [Data for 3M-467, resonance, beam methods; Polymer blend].

9. D.I.G. Jones, "Temperature-frequency dependence of dynamic properties of damping materials", J. Sound Vib. 33(4), pp. 451-470, 1974. [Test results by resonance and beam methods for 3M-467 and polymer blend].

10. A.D. Nashif, D.I.G. Jones and J.P. Henderson, Vibration Damping, Wiley Interscience, 1985.

11. A. Malkin, A. Askadsky, A. Chalykh and V. Korriga, Experimental Methods of Polymer Physics, MIR Publishers, Moscow, English Edition, 1983.

12. M. Ruddel, et al, "Damping Materials, Finite elements and special projects", AFWAL-TR-82-4167, Dec 1982 [Test data on 3M-467 by vibrating 3-layer beam test method].

13. M.L. Drake and G.E. Terborg, "Polymeric material testing procedures to determine damping properties and the results of selected commercial material", AFML-TR-79-4093, July 1980 [ISD-112, 3 layer beam test data, pp. 200-204].

14. Company Literature, Dupont "DMA" (resonance technique; flexural specimen; single frequency in 3 to 150 Hz range; DuPont Instruments, Wilmington, DE 19898), 1985.

15. J. Peters, C. DeMeersman and P. Vanherck, "The measurement of the elastic and loss moduli of rubber and rubberlike materials", Klasse der Wetenshapen, Brussels, 43(3), pp 1-112, 1981.

16. L.C. Rogers, "Graphical presentation of damping material complex modulus", Proposed Standard ASA/S2-73, ISO/TC108/WG13, AFWAL/FIBA, WPAFB, Ohio, 1986.

17. Company Literature, 3M Company, Minneapolis, Minnesota, 1985.

18. M.F. Kluesener, "Comparisons of damping material properties by various test methods", Proc. Vibration Damping Workshop II, 1986, this report.

19. A.D. Nashif, Anatrol Corporation, Cincinnati, Ohio, unpublished data.

20. Company Literature, "SMRD, A GE developed flight proven damping compound", General Electric Space Systems Division, Philadelphia, PA19101, 1985.

21. M.L. Parin, "PACOSS and RELSAT damping material measurements", Proc. Vibration Damping Workshop II, 1986, this report.

ACKNOWLEDGEMENTS

Thanks are particularly due to Lois Staton for typing the manuscript of this paper, and to Dr D.K. Rao, Systran Corporation, for conducting the tests summarized in Table 4.

NOMENCLATURE

A, B	constants
A_1	base acceleration
A_2	Amplitude of acceleration of resonance specimen mass
b	breadth of specimen
E	Young's modulus
f	frequency (Hz)
F, F_1	driving force amplitude
F_2	shear force at base of vibrating beam
G, G'	shear modulus
G''	shear loss modulus
h	thickness of viscoelastic material
h_1	thickness of base beam
h_2	Thickness of viscoelastic sandwich layer
i	$\sqrt{-1}$
k	stiffness of specimen
k_o	flanking stiffness
ℓ	length of specimen
M	mass of resonance specimen
α	constant
α_T	temperature shift factor
$\Delta\ell$	change in length
ε	strain
ε_s	shear strain
ε_e	extensional strain
ε_o	cyclic strain amplitude
ϕ	phase angle
Γ	Gamma function
η	loss factor
η_s	shear loss factor
η_e	extensional loss factor
σ	stress
σ_e	extensional stress
σ_s	shear stress
σ_o	cyclic stress amplitude
ν	Poisson's ratio
ω	frequency
ω_r	resonance frequency

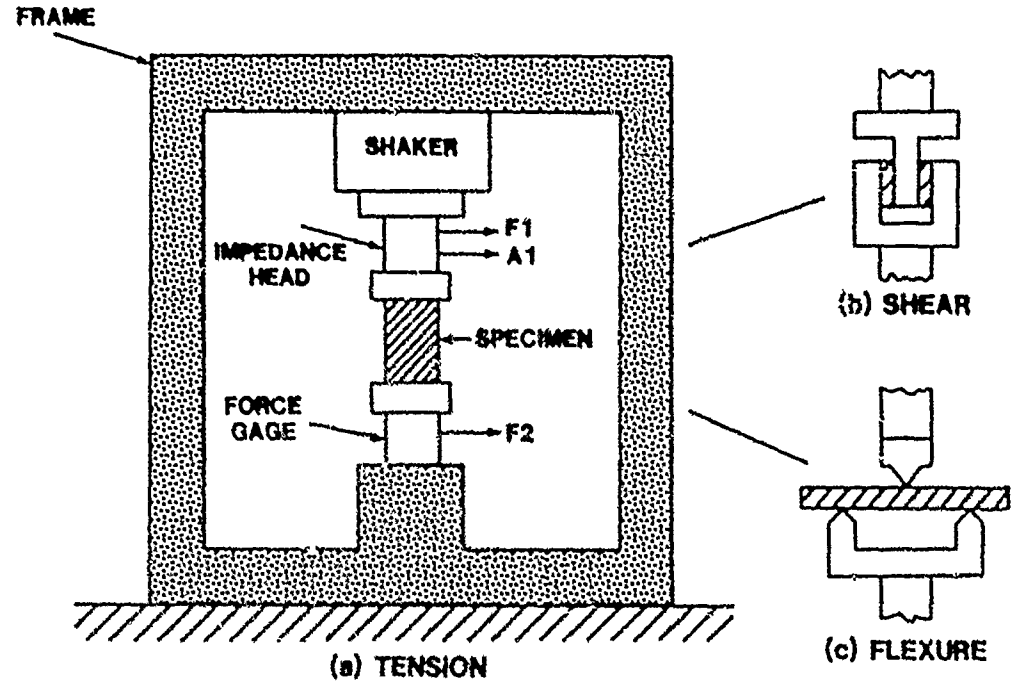


Figure 1 Ideal direct measurement system

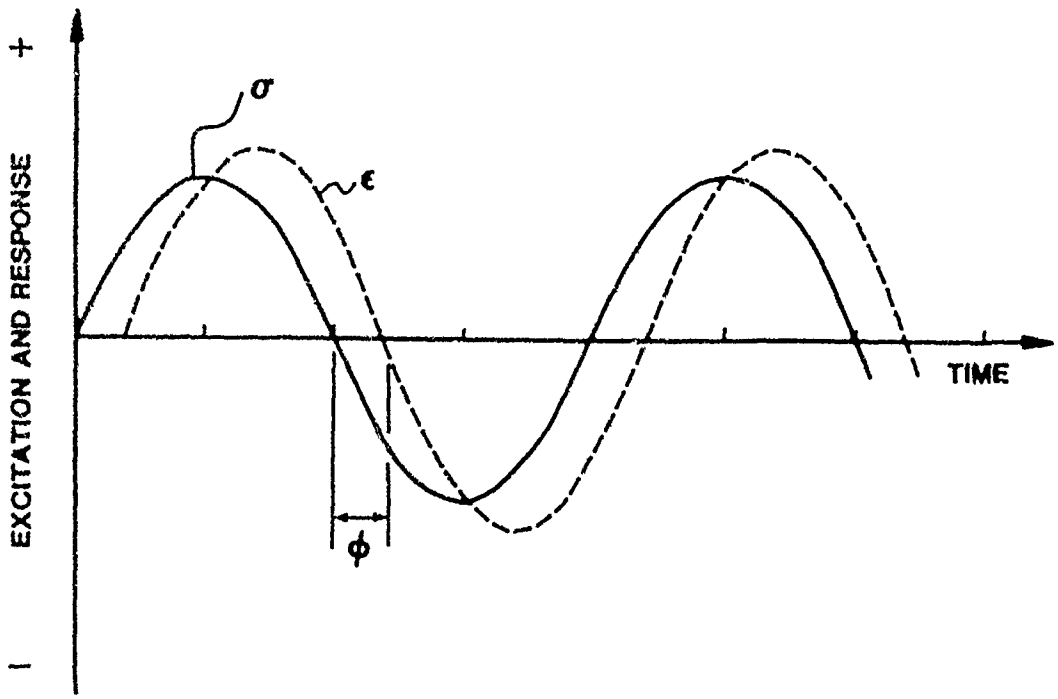


Figure 2 Typical response of direct measurement system

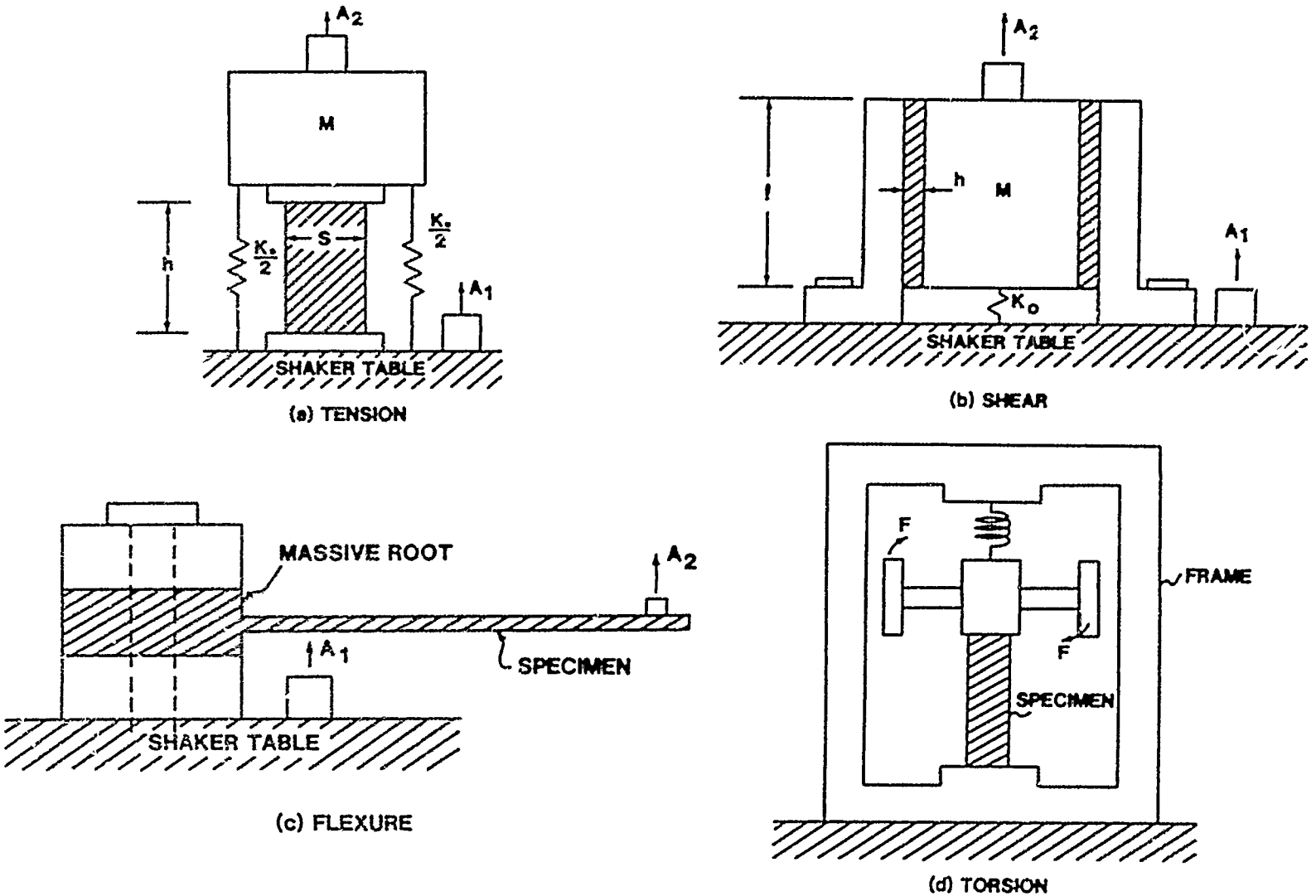


Figure 3 Ideal resonance test techniques for simple specimens

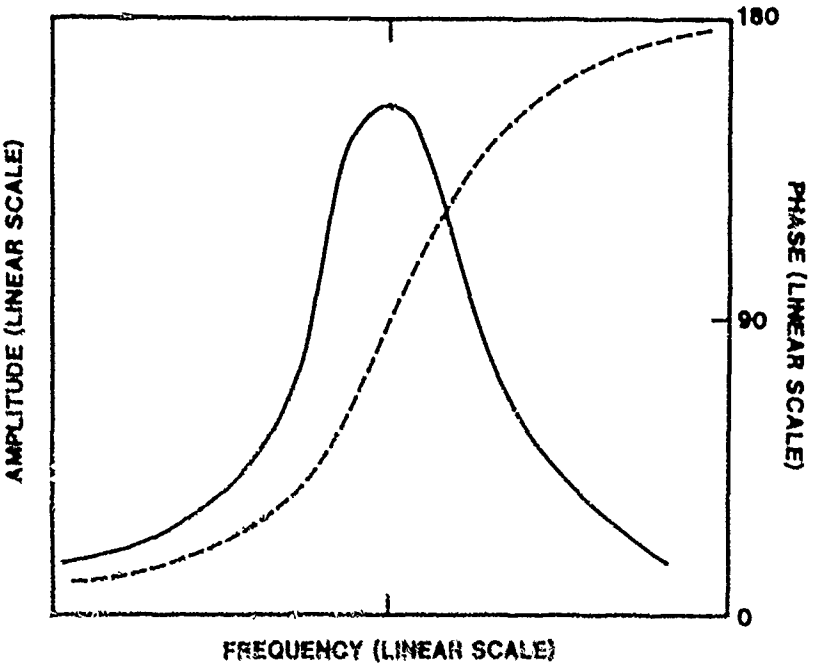


Figure 4 Typical response of resonance system

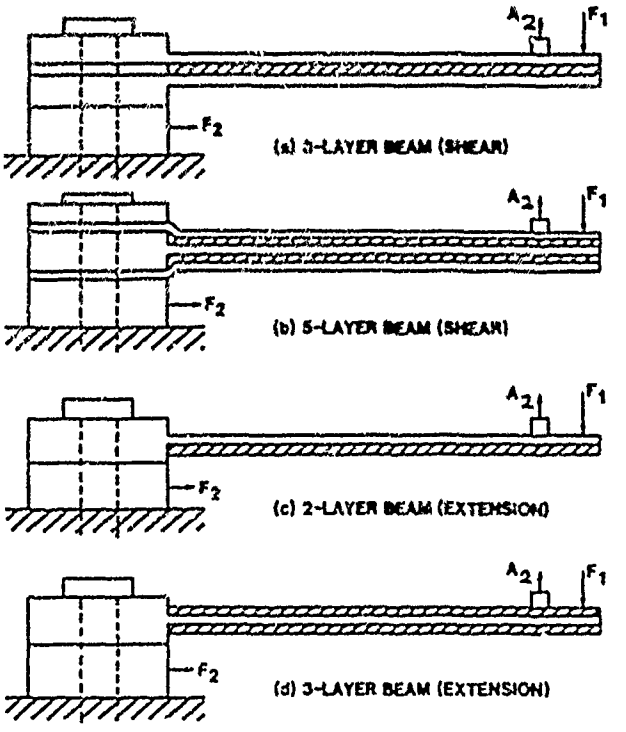


Figure 5 Ideal resonant beam test techniques

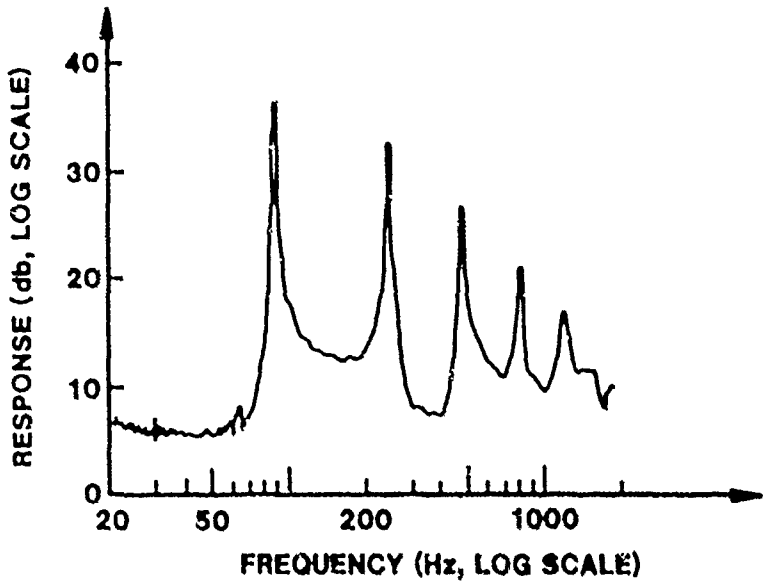


Figure 6 Typical response of resonant beam system

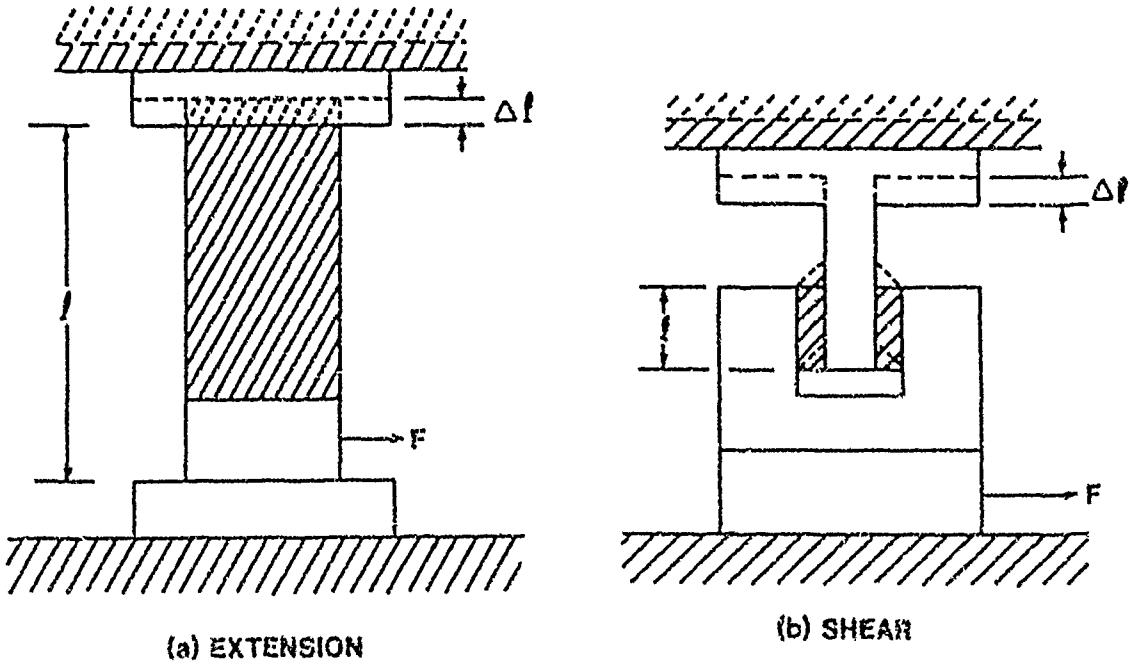


Figure 7 Ideal Stress-relaxation test techiques

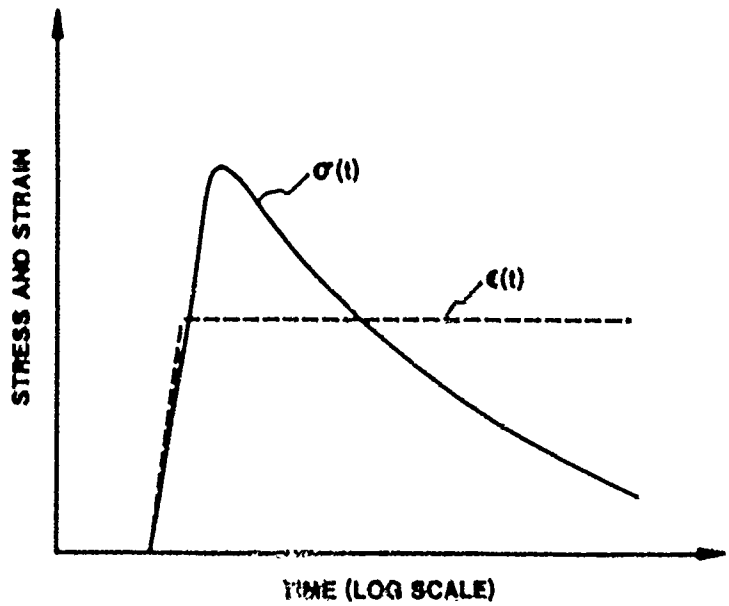


Figure 8 Typical transient response of stress-relaxation system

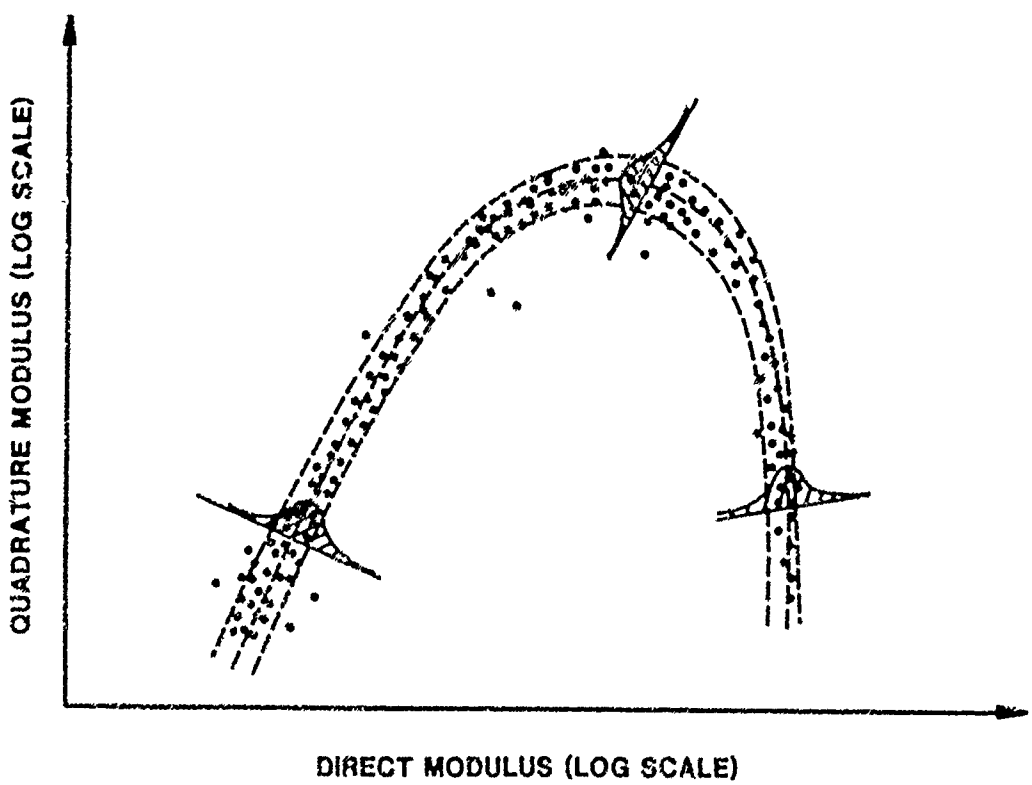


Figure 9 Ideal plot of quadrature modulus versus direct modulus

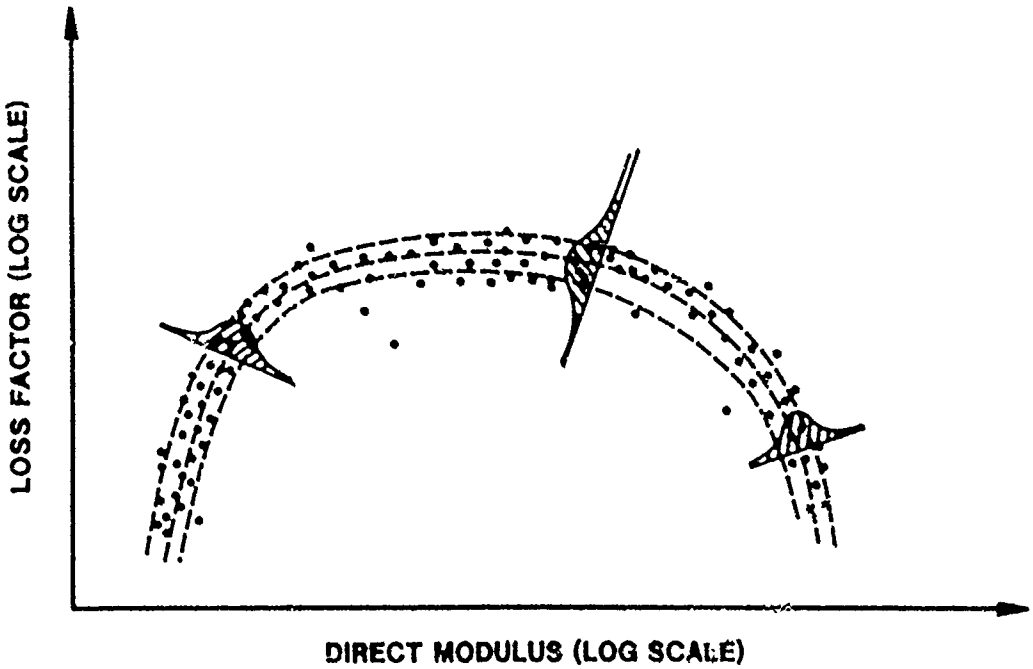


Figure 10 Ideal plot of loss factor versus direct modulus

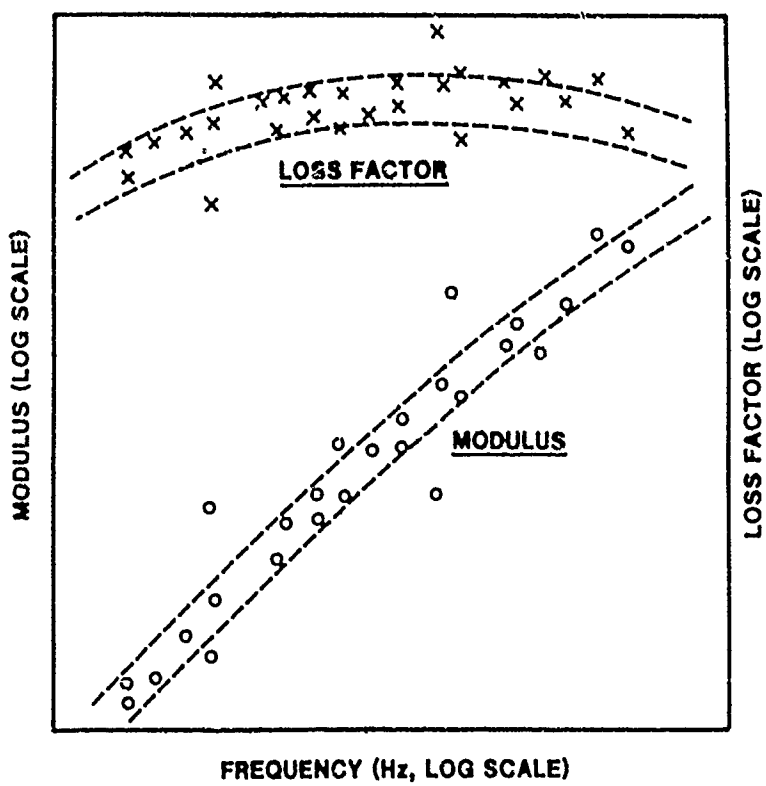


Figure 11 Ideal plot of modulus and loss factor versus frequency

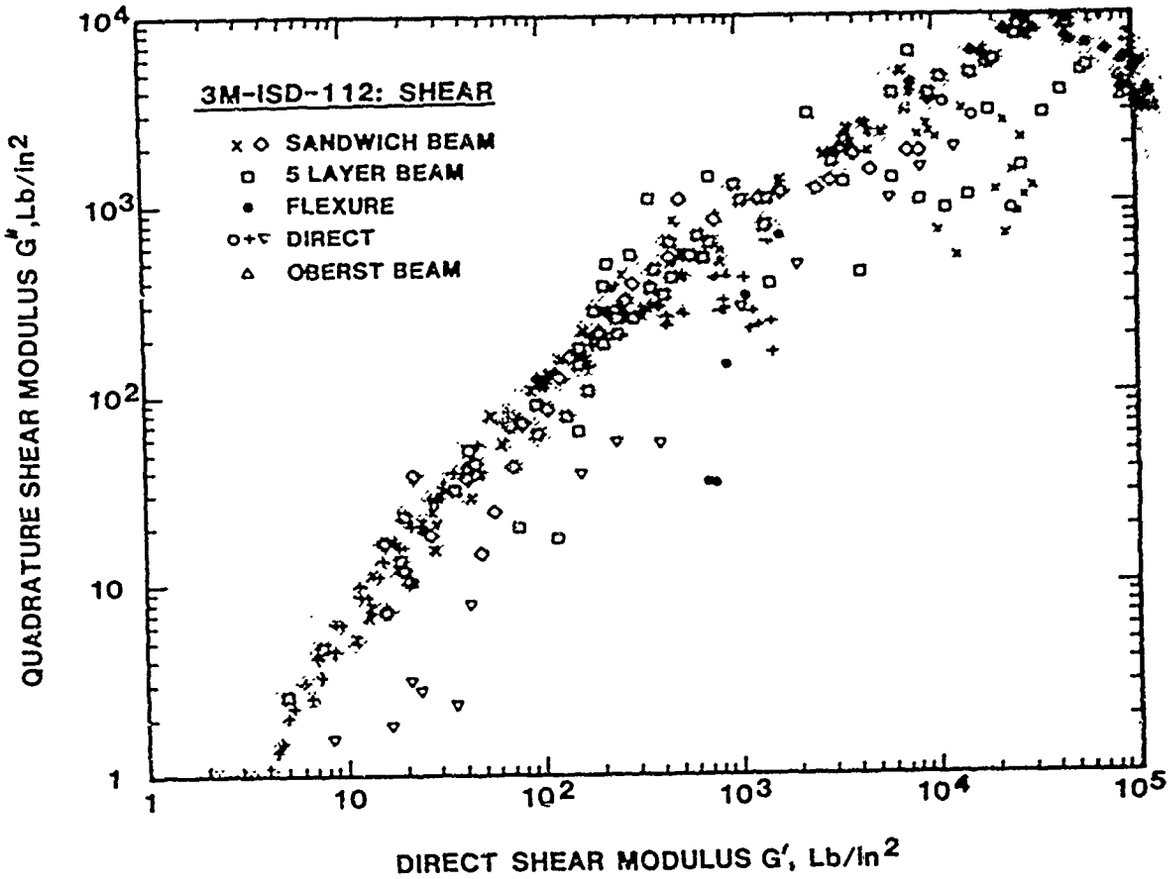


Figure 12 Plot of quadrature shear modulus versus direct shear modulus for 3M-ISD-112 adhesive

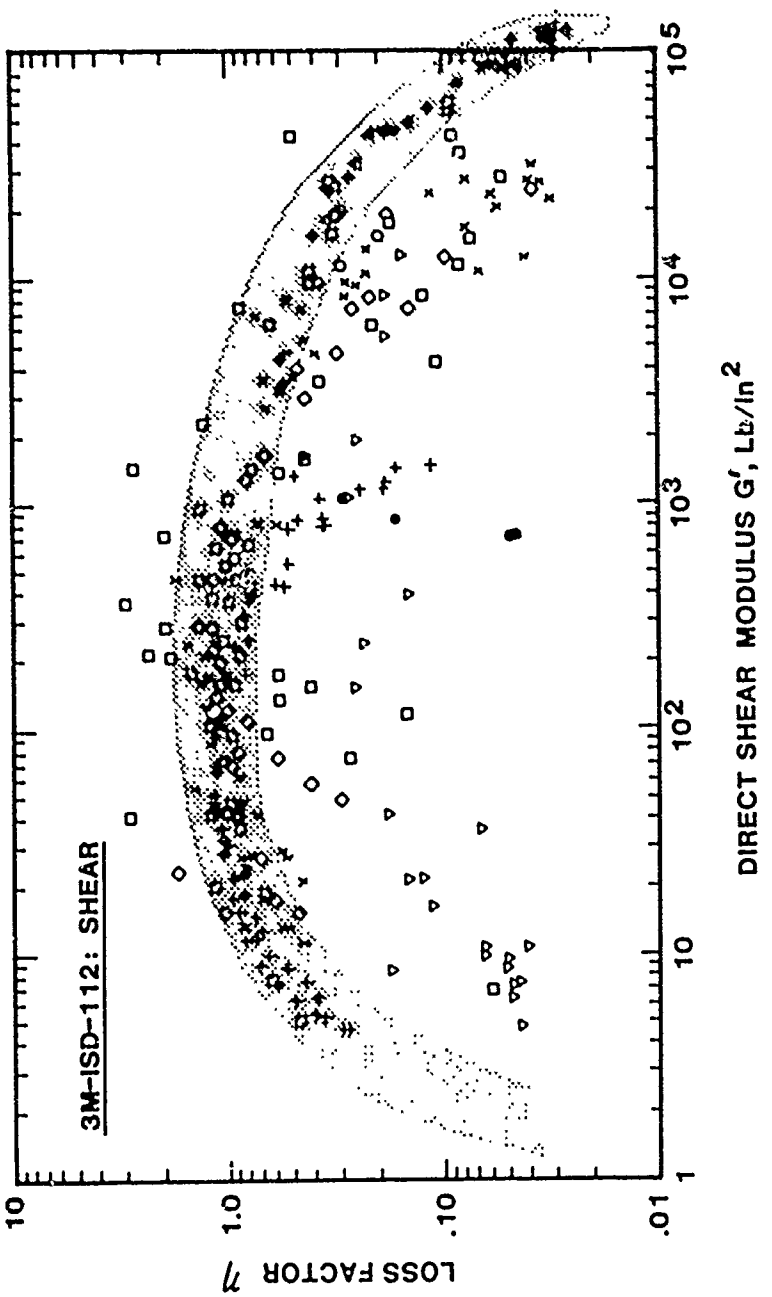


Figure 13 Plot of loss factor versus direct shear modulus for 3M-ISD-112 adhesive

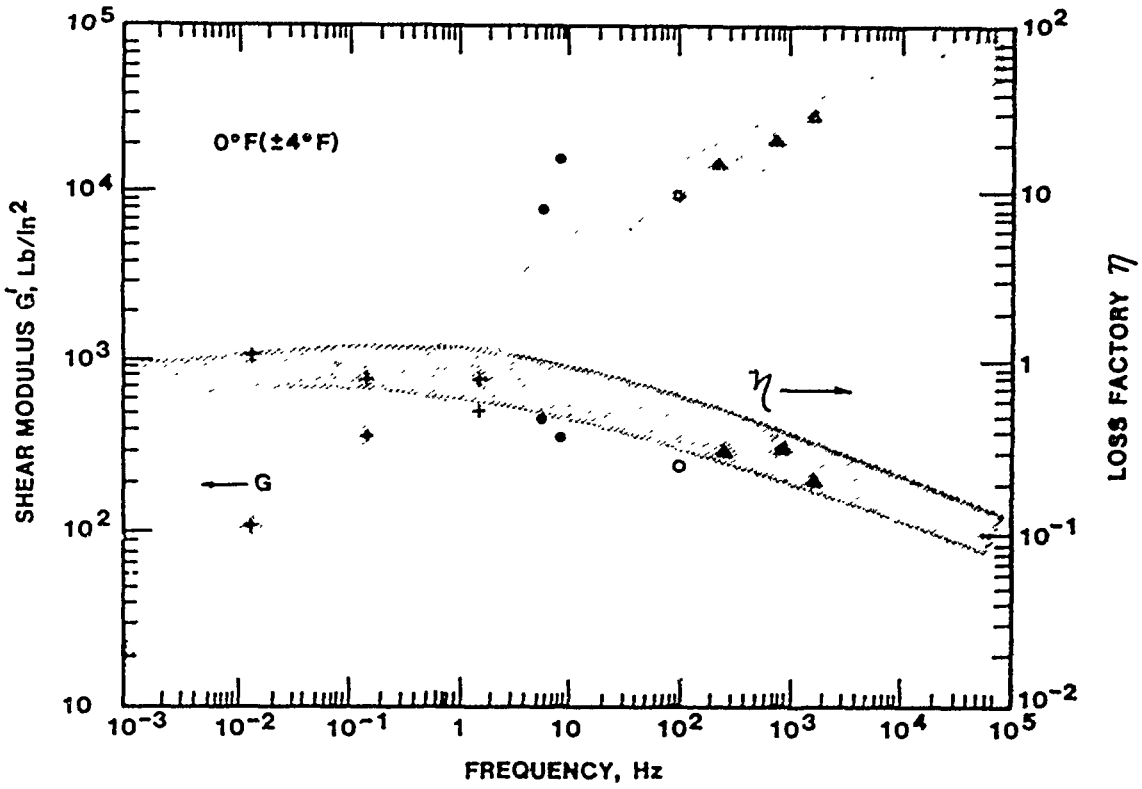


Figure 14 Plot of shear modulus and loss factor versus frequency (3M-ISD-112, 0°F)

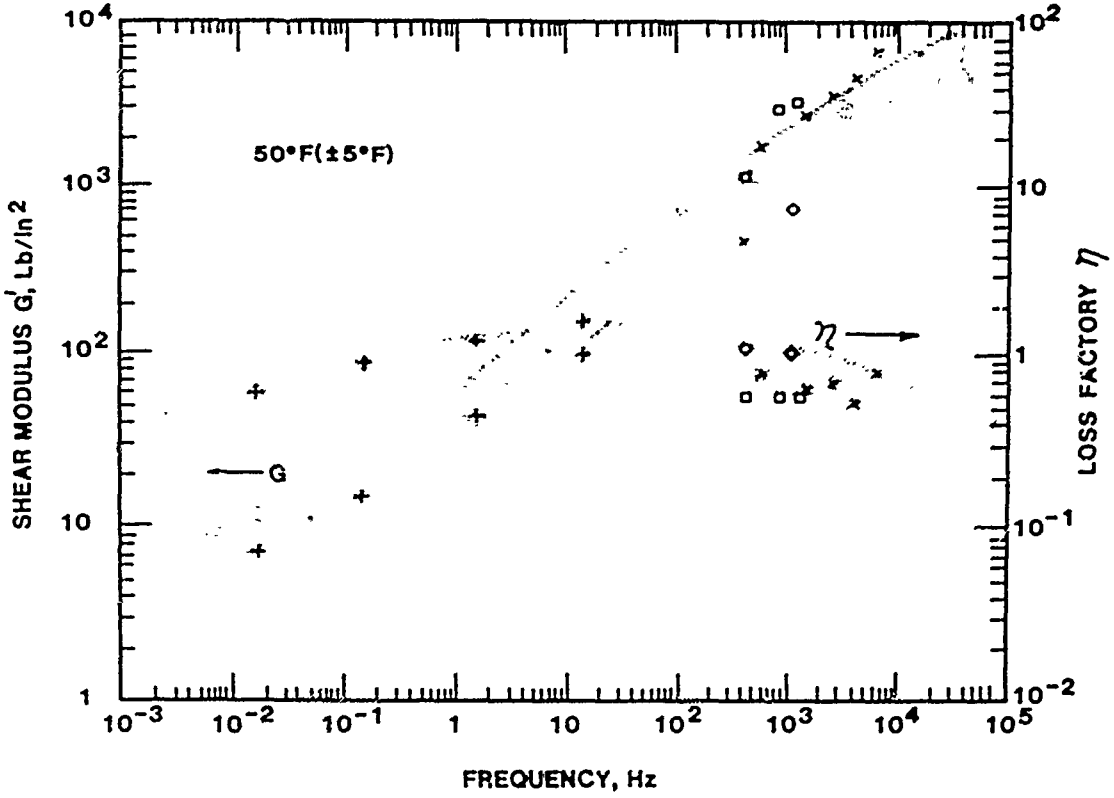
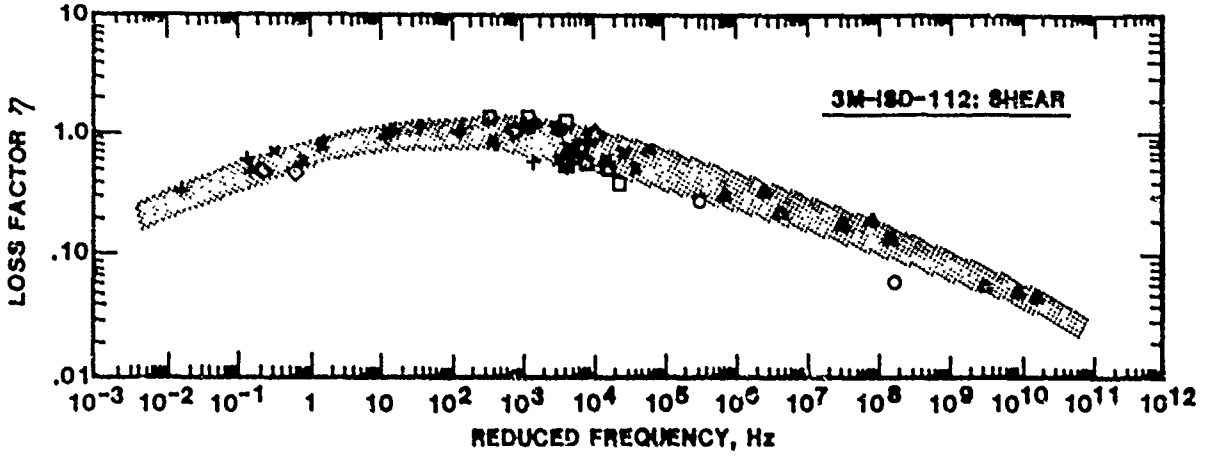


Figure 15 Plot of shear modulus and loss factor versus frequency (3M-ISD-112, 50°F)



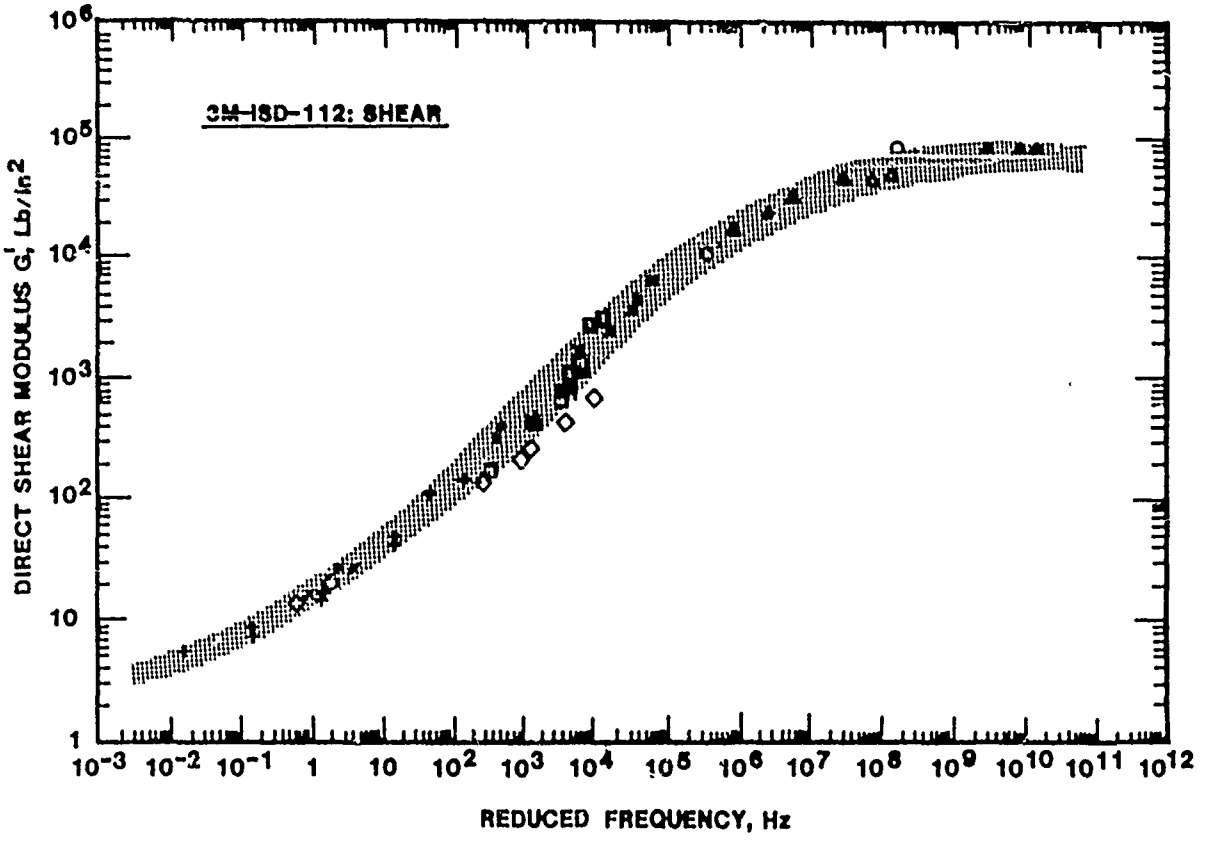


Figure 16 Plot of shear modulus and loss factor versus reduced frequency for 3M-ISD-112

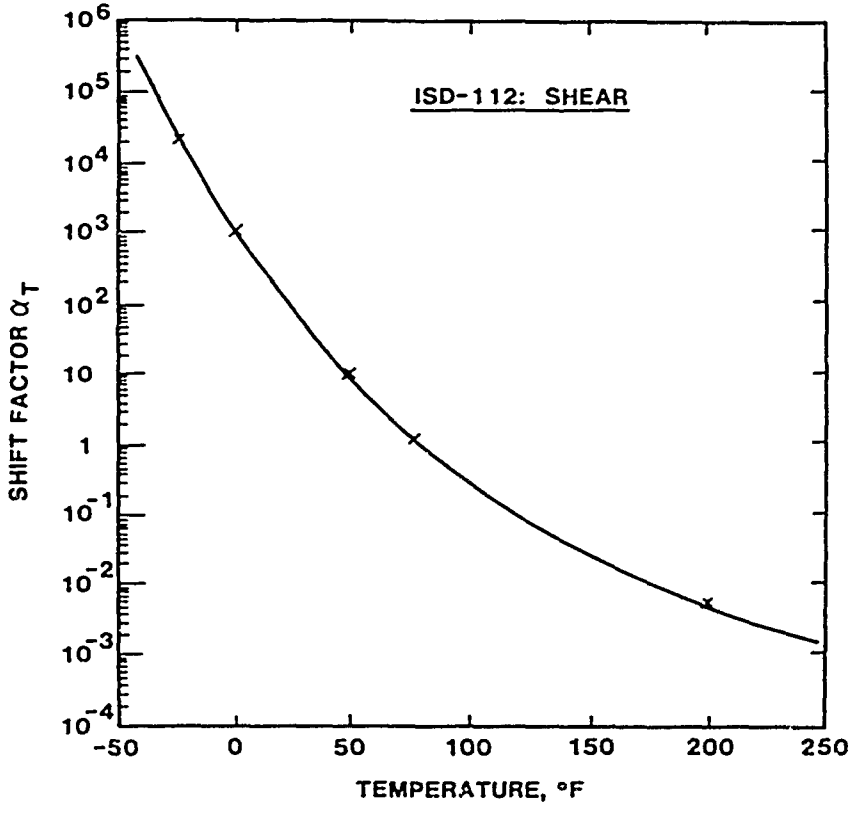


Figure 17 Plot of shift factor α_T versus temperature for 3M-ISD-112

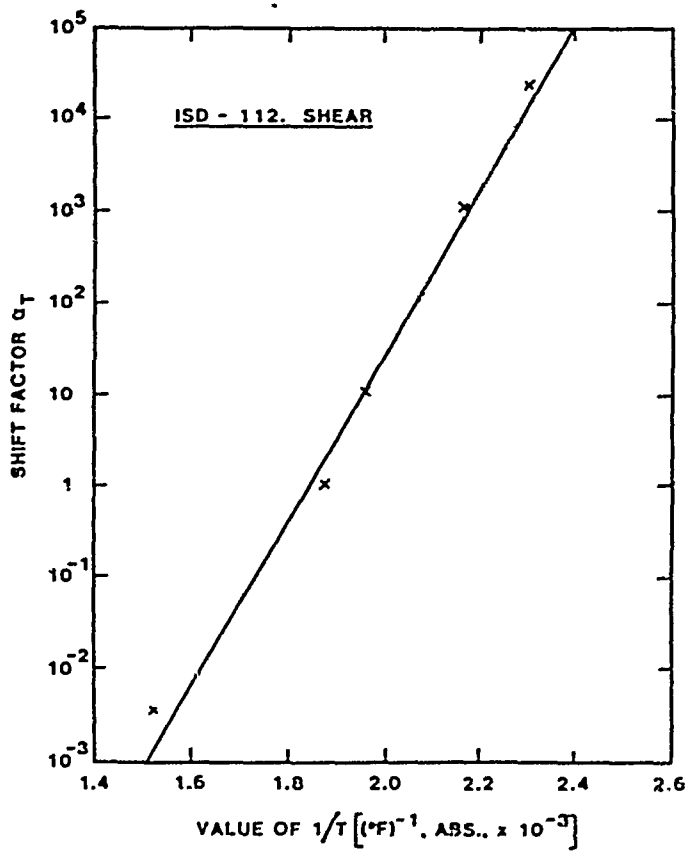


Figure 18 Plot of shift factor a_T versus 1/T for 3M-ISD-112

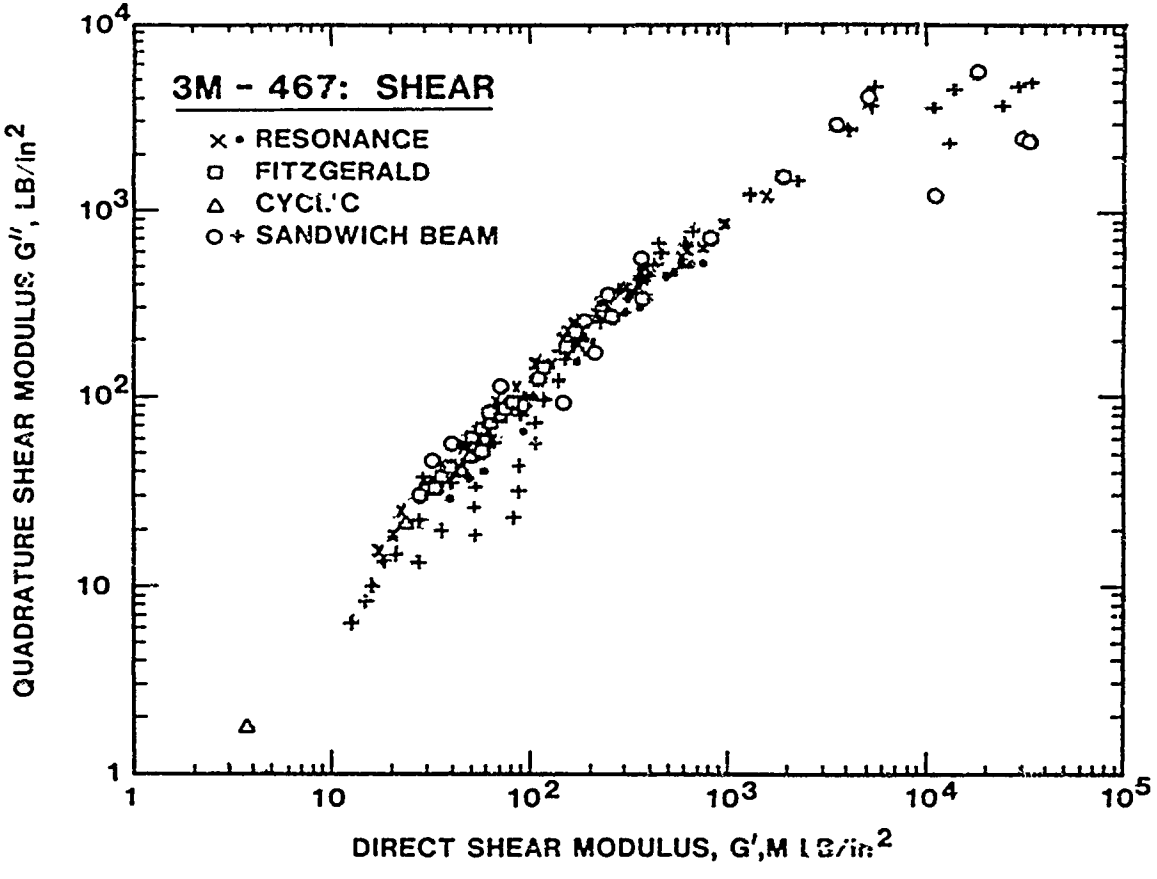


Figure 19 Plot of quadrature shear modulus versus direct shear modulus for 3M-467 adhesive

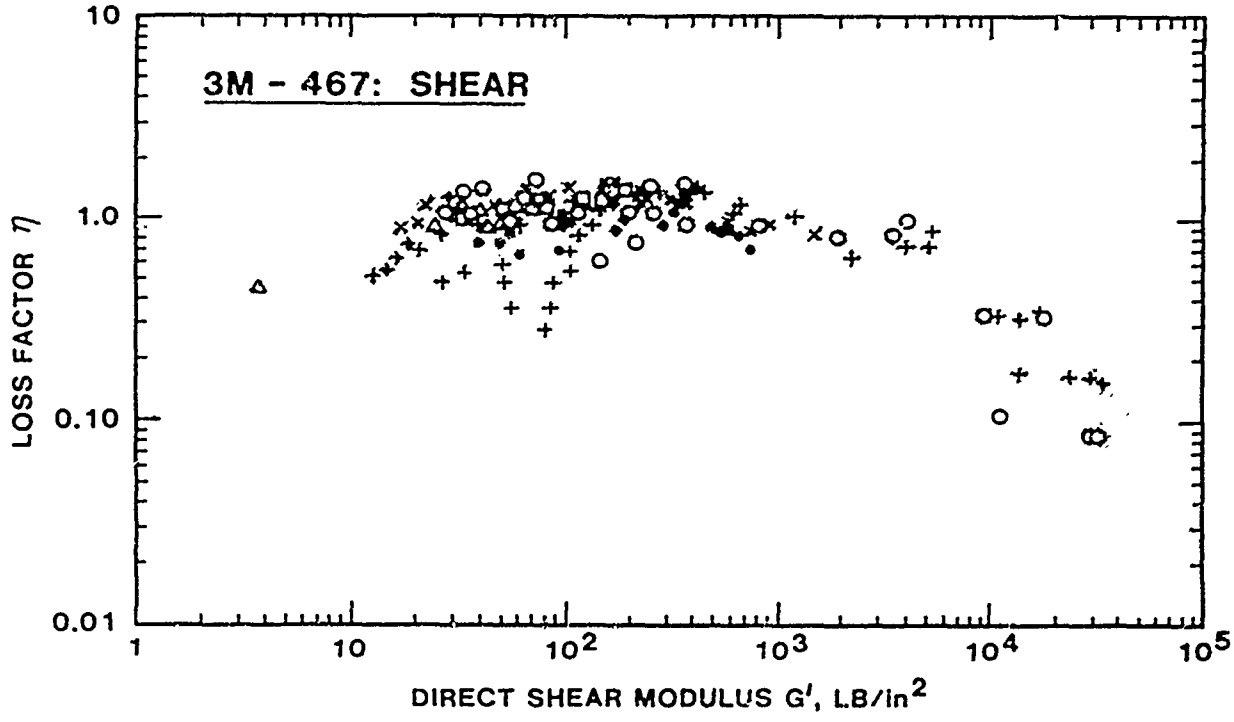


Figure 20 Plot of loss factor versus direct shear modulus for 3M-467 adhesive

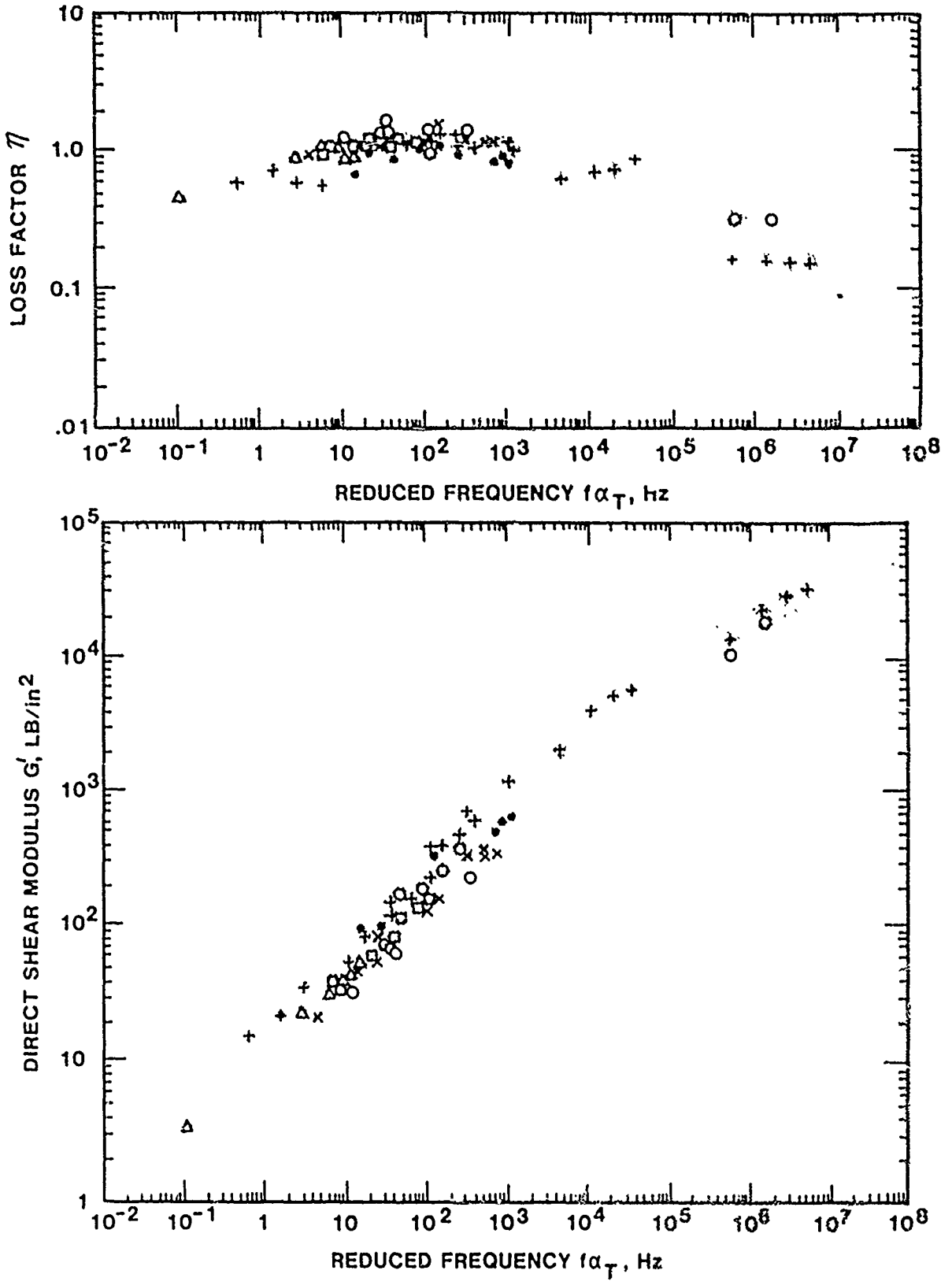


Figure 21 Plot of shear modulus and loss factor versus reduced frequency for 3M-467

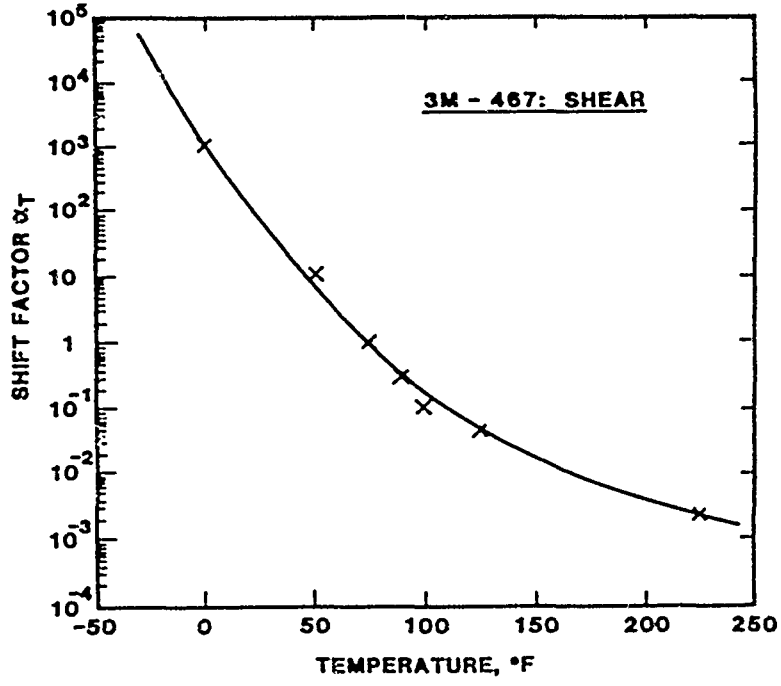


Figure 22 Plot of shift factor α_T versus temperature for 3M-467

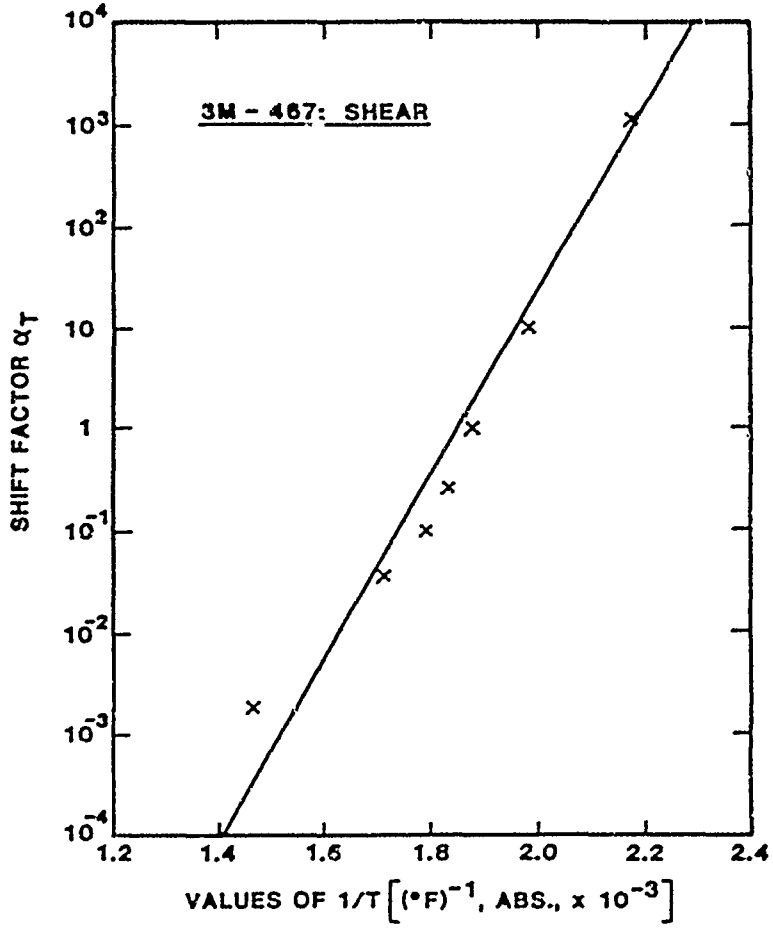


Figure 23 Plot of shift factor α_T versus 1/T for 3M-467

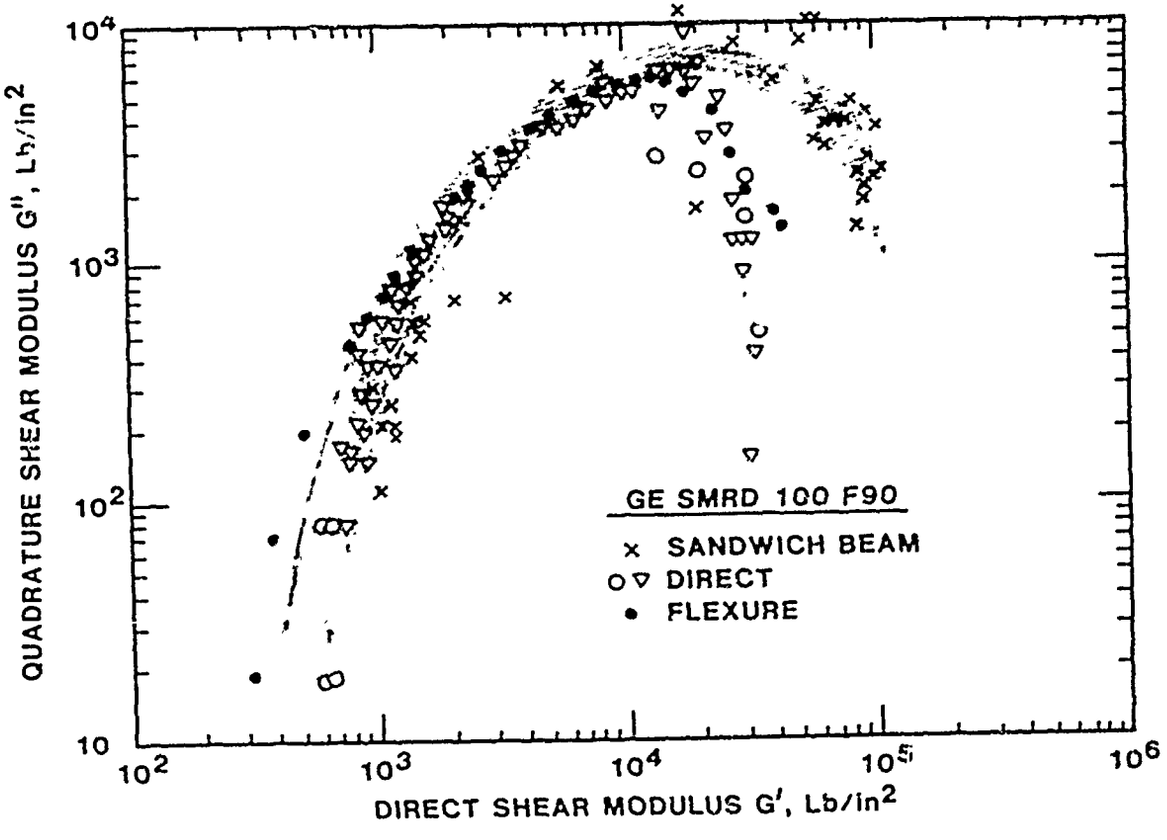


Figure 24 Plot of quadrature shear modulus versus direct shear modulus for GE SMRD 100F90

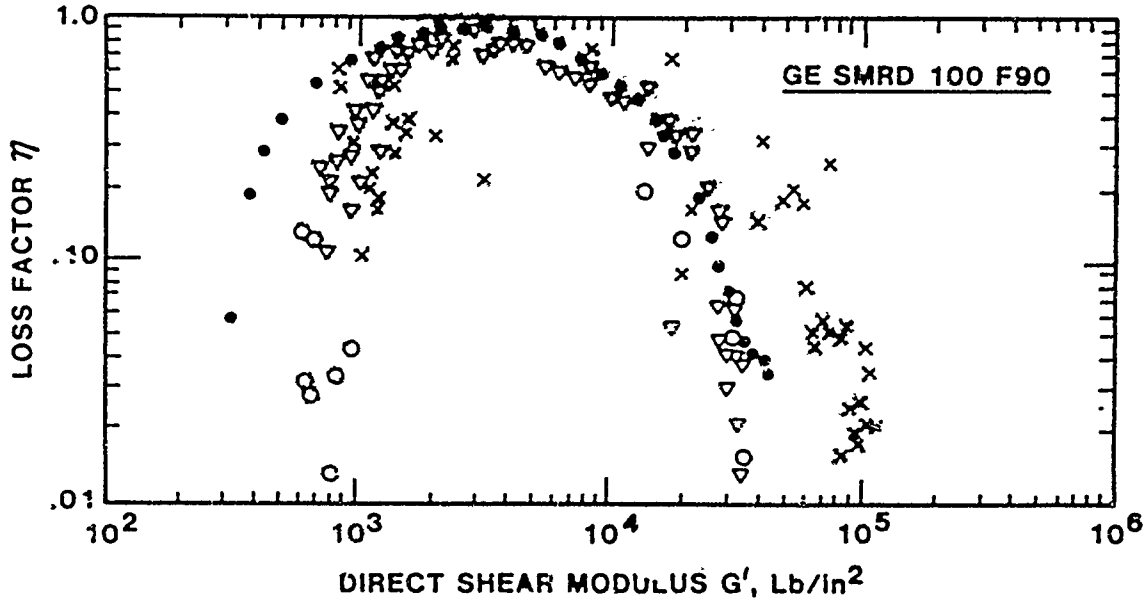


Figure 25 Plot of loss factor versus direct shear modulus for GE SMRD 100F90

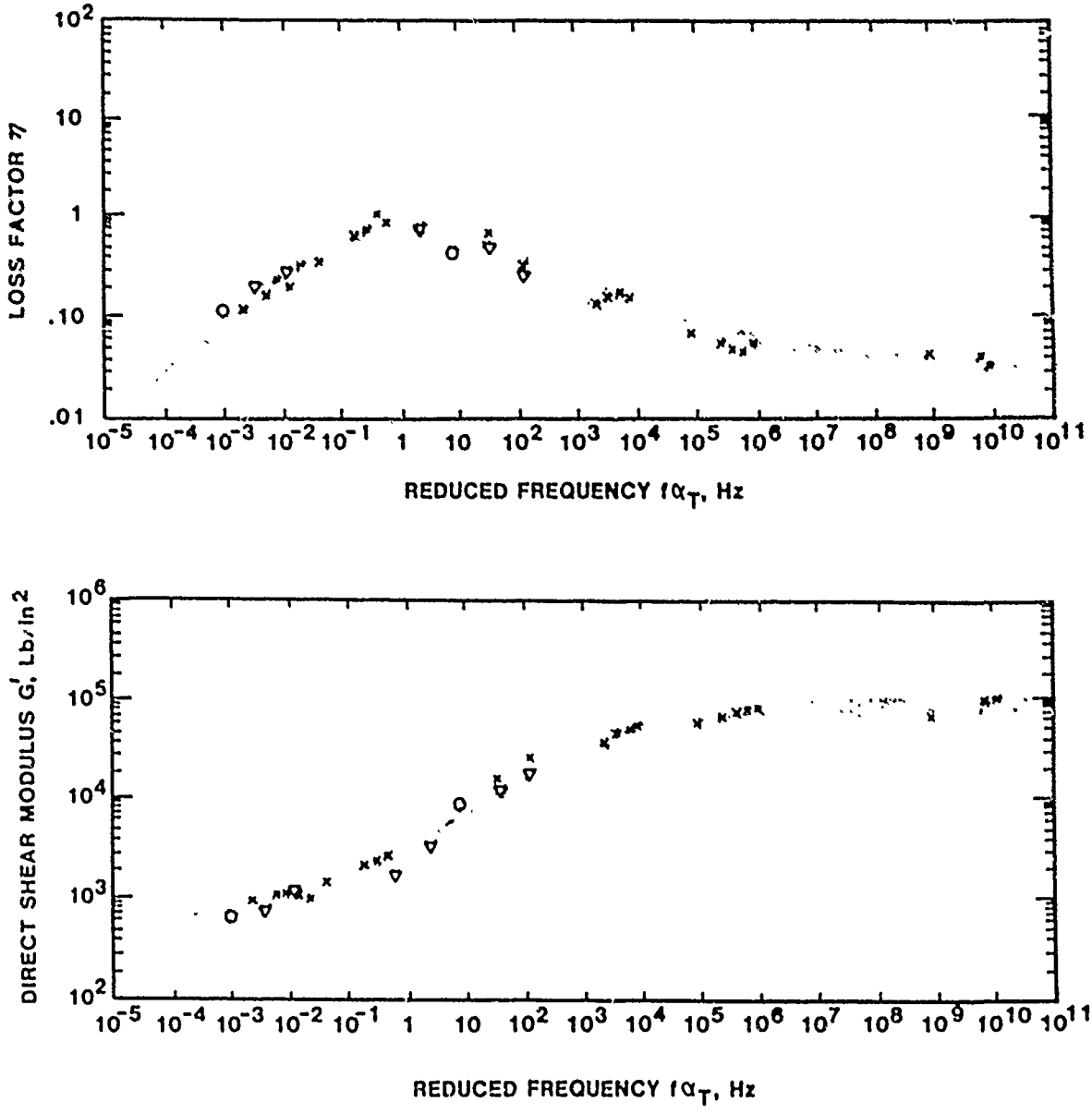


Figure 26 Plot of shear modulus and loss factor versus reduced frequency for GE SMRD 100F90

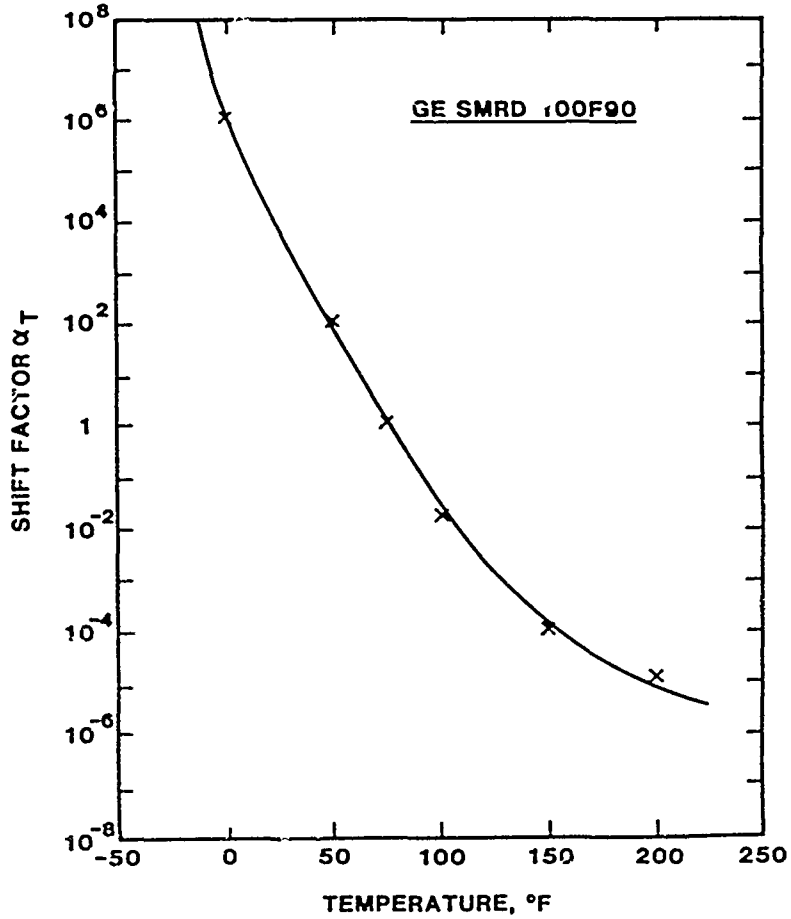


Figure 27 Plot of shift factor α_T versus temperature for GE SMRD 100F90

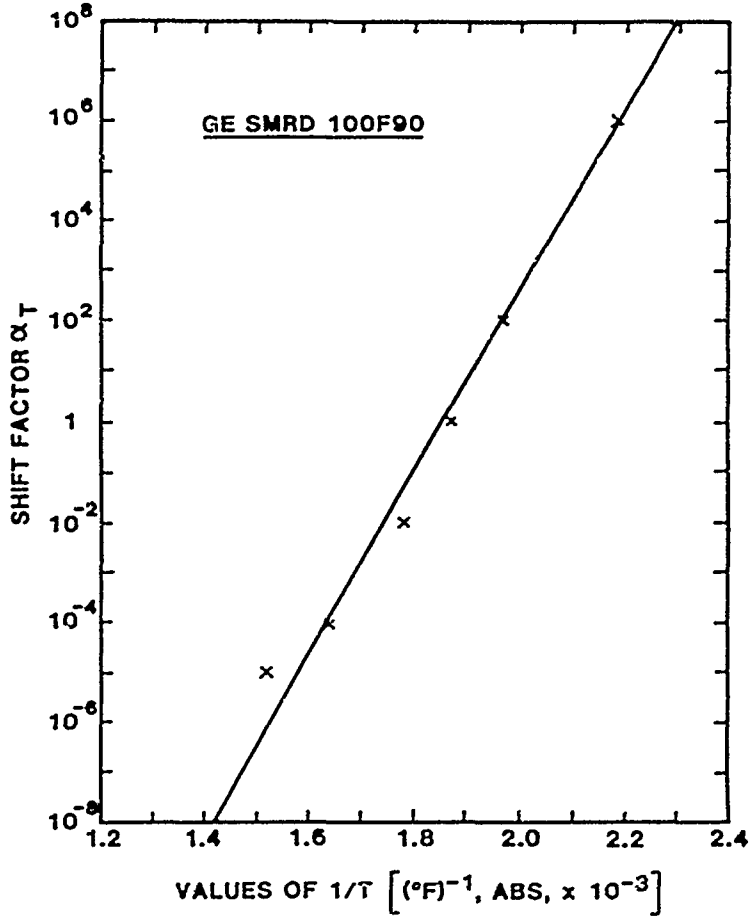


Figure 28 Plot of shift factor α_T versus 1/T for GE SMRD 100F90

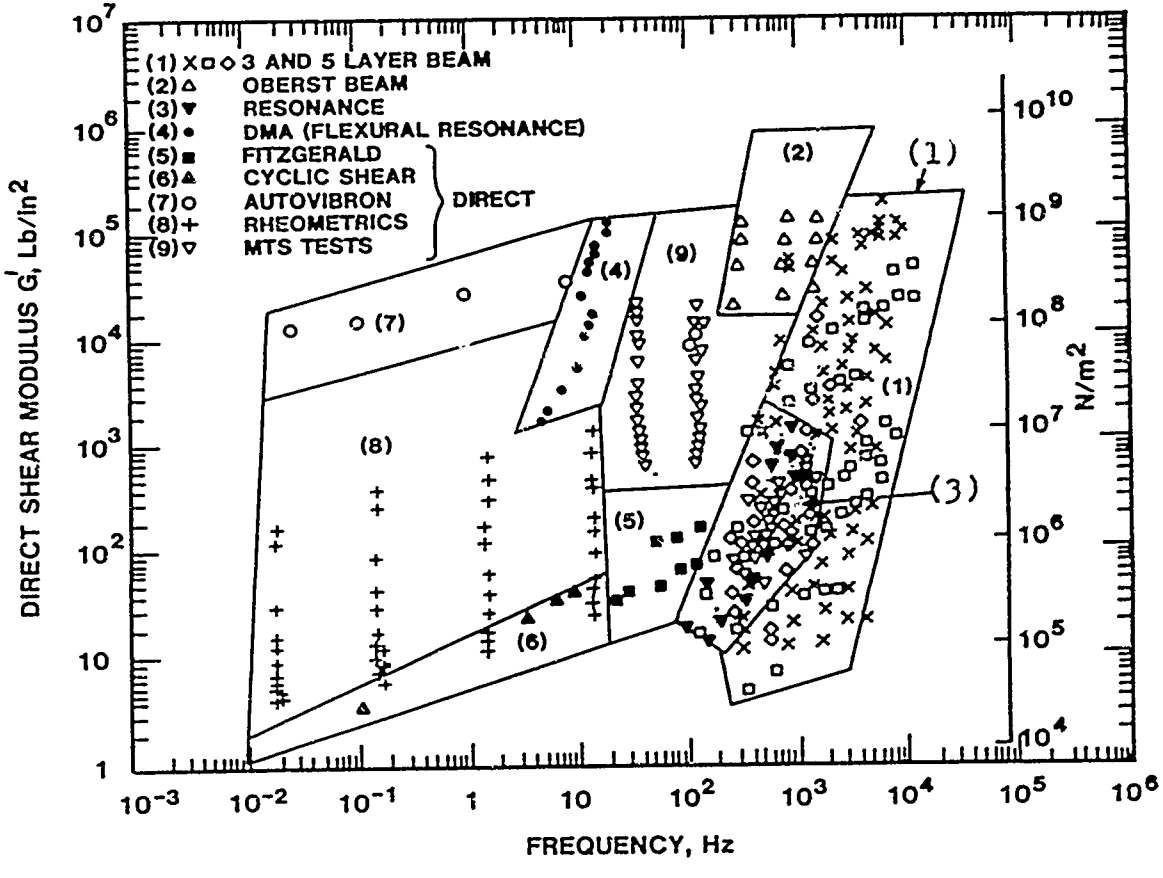


Figure 29 Summary of modulus and frequency zones of effective operation for several test systems

Table 1 Sandwich Beam Test data for 3M-ISD-112 [18] (x)

(ℓ = 7 in, $h_1 = h_3$ = 0.080 in, h_2 = 0.005 in)

TEMPERATURE		MODE	FREQUENCY	G_2'	η_2	G_2''	ACC/REJ
^oC	^oF		(Hz)	Lb/in^2		Lb/in^2	
-45.6	-50	2	668.5	12734	.0409	520.8	r
		3	1840.0	22837	.0302	689.7	r
		4	3517.0	26144	.0342	894.1	r
		5	5640.6	27440	.0390	1070.1	r
		6	8211.0	31107	.0383	1191.4	r
-31.7	-25	2	660.0	9115.9	.2563	2336.4	a
		3	1826.0	20301	.0549	1114.5	r
		4	3483.0	23218	.1142	2451.5	r
		5	5566.4	24317	.0591	1437.1	r
		6	8084.8	27450	.0784	2152.1	r
-17.8	0	2	641.7	4687.7	.3905	1830.5	a
		3	1732.2	8485.3	.2716	2304.6	a
		4	3202.5	9145.5	.2781	2543.4	a
		5	5014.3	10331.3	.0687	709.8	r
		6	7395.1	13853.9	.2220	3075.6	a
- 3.9	25	2	631.1	3540.7	.4978	1762.5	a
		3	1668.6	5449.6	.4336	2363.0	a
		4	3113.9	7056.9	.4381	3091.6	a
		5	4994.6	10016.0	.2201	2204.5	r
		6	6764.1	7618.3	.4994	3804.6	a
10.0	50	2	600.0	1683.5	.7794	1312.0	a
		3	1564.0	2773.2	.6331	1755.7	a
		4	2830.0	3504.3	.6871	2407.8	a
		5	4440.0	4615.7	.5058	2334.6	a
		6	6716.1	6798.8	.7347	4995.1	a
23.9	75	2	455.4	319.6	.8145	260.3	a
		3	1139.3	464.8	1.0465	486.4	a
		4	2060.1	470.4	1.7216	483.7	r
		5	3351.9	811.6	.5961	483.7	a
		6	4814.0	808.2	.7074	571.7	a
43.9	111	3	993.0	166.6	1.2994	216.5	a
		4	1884.0	218.0	1.2729	277.5	a
		5	3050.0	235.0	1.5497	364.1	a
		6	4499.0	258.1	1.6608	428.7	a

TABLE 1 (CONTINUED)

TEMPERATURE		MODE	FREQUENCY	G_2'	η_2	G_2''	ACC/REJ
^oC	^oF		(Hz)	Lb/in^2		Lb/in^2	
51.7	125	2	353.2	55.4	1.423	78.75	a
		3	952.0	101.9	1.070	109.0	a
		4	1826.6	125.0	1.233	154.0	a
		5	3002.6	171.2	1.212	207.5	a
65.6	150	3	926.4	63.8	.894	57.0	a
		4	1789.0	76.4	1.024	74.2	a
		5	2943.1	89.2	1.186	105.8	a
		6	4378.6	104.4	1.180	123.3	a
79.4	175	2	331.2	24.1	.840	20.2	a
		3	909.9	42.3	.703	29.7	a
		4	1764.8	48.2	.859	38.8	a
		5	2904.3	45.2	1.169	52.8	a
93.3	200	2	326.0	17.2	.699	12.0	a
		3	898.2	28.7	.559	16.1	a
		4	1747.2	27.3	.765	20.9	a
107.2	225	2	322.5	13.1	.524	6.85	a
		3	891.3	22.4	.462	10.4	a
		4	1739.4	28.1	.530	15.3	a
		5	2868.9	23.1	.844	19.5	a
		6	4281.3	27.7	.884	24.5	a
120.0	248	2	320.3	11.3	.455	5.15	a
		3	882.8	13.5	.553	7.45	a
		4	1724.2	13.3	.864	11.4	a

Table 2 Sandwich Beam Test data for 3M-ISD-112 [13] (◇)

(ℓ = 7 in, $h_1 = h_3$ = 0.06 in, h_2 = 0.005 in)

TEMPERATURE		MODE	FREQUENCY	G_2'	η_2	G_2^*	ACC/REJ
°C	°F		(Hz)	Lb/in^2		Lb/in^2	
-31.7	-25	2	503.5	7229.9	.144	1042.6	r
		3	1362.0	18498	.184	3403.6	a
		4	2560.9	12079	.098	1178.9	r
-18.9	- 2	2	494.7	4762.9	.304	1449.8	r
		3	1323.3	7066.5	.265	1869.8	r
		4	2463.7	8172.0	.224	1833.0	r
- 5.6	22	2	469.7	1664.3	.676	1124.7	a
		3	1223.2	2955.2	.440	1300.0	a
		4	2251.2	3727.7	.487	1815.0	a
4.4	40	2	426.9	693.7	.949	658.3	a
		3	1092.2	1267.7	.806	1028.5	a
10.0	50	2	401.6	450.3	1.117	502.8	a
		3	1005.8	764.5	1.061	810.9	a
18.3	65	2	352.4	244.6	1.076	253.1	a
		3	894.3	431.3	1.087	468.6	a
24.4	76	2	315.1	139.6	1.120	156.4	a
		3	797.4	216.7	1.169	253.2	a
		4	1488.2	281.2	1.375	386.6	a
29.4	85	2	304.4.	118.7	1.013	120.2	a
		3	782.1	192.7	1.087	209.5	a
		4	1471.1	262.4	1.198	314.4	a
37.8	100	2	284.3	79.1	.898	71.1	a
		3	733.9	106.8	1.135	121.2	a
51.7	125	2	263.5	40.5	.908	36.7	a
		3	708.9	68.7	.984	67.5	a
		4	1369.9	106.1	.801	85.0	a
66.7	152	2	254.3	26.0	.706	18.4	a
		3	678.8	22.5	1.703	38.3	r
		4	1344.8	70.4	.584	41.1	a
80.0	176	2	249.0	18.4	.612	11.2	a
		3	676.4	15.3	1.066	16.3	a
		4	1331.5	57.2	.424	24.3	r
93.9	201	2	246.0	15.3	.473	7.23	a
		3	673.3	21.6	.473	10.2	a
		4	1321.4	49.4	.302	14.9	r

Table 3 Five-Layer Beam Test data for 3M-ISD-112 [19] (□)

(ℓ = 7 in, h_1 = 0.062 in (St), h_2 = 0.005 in, h_3 = 0.010 in (Al))

TEMPERATURE		MODE	FREQUENCY	G_2'	η_2	G_2''	ACC/REJ
°C	°F		(Hz)	Lb/in^2		Lb/in^2	
- 34	- 30	2	424	4224	.103	437	r
		3	832	11300	.085	964	r
		4	1372	14900	.074	1109	r
		5	2043	17300	.174	3010	a
		6	2781	8332	.122	1016	r
		7	3831	28980	.054	1566	r
		8	4893	35710	.082	2922	r
		9	6081	42983	.089	3821	r
		11	8913	55000	.091	4994	a
		12	10477	58680	.091	5360	a
- 11	12	1	149.3	212	2.26	480	r
		2	423	2374	1.250	2958	r
		3	827	6180	.612	3783	a
		4	1361	9051	.409	3703	a
		5	2025	10768	.427	4602	a
		6	2743	6114	.219	1340	r
		7	3778	15019	.322	4837	a
		8	4817	18100	.305	5516	a
		9	5968	19600	.291	5711	a
		10	7361	44700	.499	22300	r
		11	8751	26130	.329	8600	a
		12	10238	25700	.304	7827	a
5.6	42	2	414	1327	.573	760	a
		3	814	3000	.562	1686	a
		4	1332	3444	.575	1979	a
		6	2679	3500	.368	1287	a
		7	3574	3476	.595	2068	a
		8	4717	7329	.866	6348	r
27	80	1	137.7	41	2.78	114	r
		2	387	187	1.48	275	a
		3	736	208	1.86	386	r
		4	1224	458	1.36	625	a
		5	1747	283	1.92	542	r
		6	2464	359	2.98	1070	r
		7	3205	643	1.10	697	a
		8	4222	977	1.23	1203	a
		9	5162	712	1.92	1365	r
		10	6318	1416	.750	1063	a
		11	7568	1423	.267	380	r

TABLE 3 (CONTINUED)

TEMPERATURE		MODE	FREQUENCY	G_2'	η_2	G_2''	ACC/REJ
°C	°F		(Hz)	Lb/in^2		Lb/in^2	
29	84	2	137	95	.64	61	a
		3	382	205	.88	181	a
		4	730	248	1.11	275	a
		5	1194	366	.97	354	a
		6	1754	383	1.17	449	a
		7	2434	531	1.00	531	a
		8	3242	575	.92	531	a
		9	4134	722	.92	664	a
		11	6138	671	.78	524	a
		12	7514	1043	.98	1018	a
47	116	1	131	41.6	.99	41	a
		2	364	94	.946	89	a
		3	696	105	1.19	126	a
		4	1142	157	.936	147	a
		5	1686	159	1.07	171	a
		6	2352	240	1.032	248	a
		7	3155	293	.855	250	a
		8	4043	415	.793	329	a
		10	6071	456	.890	408	a
		11	7575	1546	.423	655	a
74	165	1	125	18.5	.687	13	a
		2	344	20	1.11	23	a
		3	672	36	.877	31	a
		4	1106	43	.885	38	a
		5	1645	45	.954	43	a
		6	2284	42	1.200	51	a
		7	3078	154	.404	62	r
		8	3944	133	.570	77	r
		10	5961	178	.589	105	r
127	260	1	121	7.0	.059	0.4	r
		2	337	5.0	.468	2.5	a
		3	658	7.6	.613	4.7	a
		7	3055	120	.146	17.6	r
		8	3889	75	.266	20	r

Table 4 OBERST Beam Test data for 3M-ISD-112 (A)

(ℓ = 6.625 in, h_1 = 0.069 in, h_2 = 0.064 in)

TEMPERATURE °C	TEMPERATURE °F	MODE	FREQUENCY (Hz)	G_2'* Lb/in^2	η_2	G_2'' Lb/in^2	ACC/REJ
- 73.3	-100	1	51.7	128540	.067	8612	r
		2	327.1	115840	.028	3244	a
		3	917.0	117140	.030	3514	a
		4	1789.6	115360	.034	3922	a
- 59.4	- 75	1	50.6	122000	.077	9394	r
		2	323.3	107877	.033	3560	a
		3	903.5	106070	.031	3288	a
		4	1768.8	107120	.033	3535	a
- 46.7	- 50	1	48.2	832430	.108	89902	r
		2	312.9	81787	.052	4253	a
		3	876.8	82729	.051	4219	a
		4	1708.6	80110	.048	3845	a
- 31.8	- 25	1	44.9	29820	.474	14135	r
		2	297.0	45763	.199	9107	a
		3	826.8	44390	.208	9233	a
		4	1621.5	48857	.148	7231	a
- 17.9	0	1	43.5	511	18.96	9689	r
		2	284.9	18741	.326	6110	a
		3	802.1	25665	.344	8829	a
		4	1574.6	31284	.276	8634	a
23.9	75	1	42.7	21512	.109	2345	r
		2	274.8	887	.585	519	r
		3	768.6	4412	.166	732	r
		4	1498.7	6047	.204	1417	r

* $G_2' \doteq E_2' / 3$

Table 5 Rheometrics Mechanical Spectrometer data for 3M-ISD-112 [18] (+)

TEMPERATURE		FREQUENCY	G_2'	η_2	G_2''	ACC/REJ
^oC	^oF	(Hz)	Lb/in^2		Lb/in^2	
- 37	- 35	.0159	862.5	.336	306.8	r
		.159	1244.1	.187	232.5	r
		1.59	1499.6	.112	168.6	r
- 32	-25.6	.0159	435.6	.586	255.6	a
		.159	826.7	.347	286.5	r
		1.59	1191.7	.189	225.1	r
		15.9	1482.2	.163	241.9	r
- 27	- 17	.0159	175.2	.807	141.4	a
		.159	438.6	.537	235.5	r
		1.59	807.7	.336	271.0	r
		15.9	1155.9	.243	281.4	r
- 22	- 7.6	.159	250.3	.801	200.4	a
		1.59	524.6	.504	264.4	a
		15.9	1058.6	.380	401.8	r
- 17	1.4	.0159	105.4	1.152	121.4	a
		.159	375.5	.793	297.7	a
		1.59	773.9	.518	401.0	a
		15.9	1346.5	.480	646.8	a
- 8	17.6	.0159	27.1	1.067	28.9	a
		.159	90.0	1.136	103.2	a
		1.59	322.8	.860	277.5	a
		15.9	875.4	.472	413.1	r
- 3	26.6	.0159	17.0	.968	16.5	a
		.159	50.0	1.147	57.3	a
		1.59	182.6	1.001	182.8	a
		15.9	516.3	.793	409.6	a
0	32	.0159	11.9	.834	9.87	a
		.159	32.0	1.058	33.9	a
		1.59	104.9	1.097	115.1	a
		15.9	396.7	.735	291.7	a
5	41	.0159	8.9	.705	6.27	a
		.159	21.7	.952	20.7	a
		1.59	64.7	1.138	73.7	a
		15.9	232.6	.919	213.7	a
9	48	.0159	7.03	.585	4.11	a
		.159	15.2	.884	13.4	a
		1.59	42.8	1.107	47.4	a
		15.9	160.7	.993	159.6	a

TABLE 5 (CONTINUED)

TEMPERATURE		FREQUENCY	G_2'	η_2	G_2''	ACC/REJ
°C	°F	(Hz)	Lb/in^2		Lb/in^2	
9	48	.0159	7.03	.585	4.11	a
		.159	15.2	.884	13.4	a
		1.59	42.8	1.107	47.4	a
		15.9	160.7	.993	159.6	a
14	57	.0159	6.21	.482	2.99	a
		.159	12.0	.745	8.91	a
		1.59	30.7	1.027	31.5	a
		15.9	98.4	1.156	113.8	a
19	66	.0159	5.58	.393	2.22	a
		.159	9.70	.641	6.21	a
		15.9	68.3	1.173	80.1	a
23	73	.0159	5.29	.361	1.91	a
		.159	8.75	.502	4.39	a
		1.59	18.5	.848	15.7	a
		15.9	49.6	1.104	54.8	a
28	82	.0159	4.70	.300	1.41	a
		.159	7.63	.443	3.38	a
		1.59	14.7	.749	11.0	a
		15.9	36.4	1.078	39.3	a
33	91	.0159	4.66	.281	1.31	a
		.159	6.65	.387	2.57	a
		1.59	12.1	.691	8.37	a
		15.9	29.3	.989	29.0	a

Table 6 MTS Forced Vibration Test Data for 3M-ISD-112 [18] (▽)

TEMPERATURE		FREQUENCY	G_2'	η_2	G_2''	ACC/REJ
°C	°F	(Hz)	Lb/in^2		Lb/in^2	
- 17.8	0	.025	1016.4	.286	290.7	r
		.10	1975.1	.250	493.8	r
		1.0	5669.5	.182	1031.9	r
		3.0	8130.6	.189	1536.7	r
		10.0	12551.3	.153	1920.4	r
10	50	.025	21.4	.148	3.16	r
		.10	42.1	.186	7.83	r
		1.0	152.9	.257	39.3	r
		3.0	238.0	.234	55.6	r
		10.0	390.5	.141	55.1	r
37.8	100	.025	8.64	.050	0.43	r
		.10	10.2	.064	0.65	r
		1.0	16.6	.112	1.86	r
		3.0	22.7	.122	2.77	r
		10.0	35.0	.066	2.31	r
65.6	150	.025	6.23	.048	0.30	r
		.10	7.26	.046	0.33	r
		1.0	9.31	.050	0.47	r
		3.0	10.8	.040	0.43	r
93.3	200	.025	4.89	.044	0.22	r
		.10	5.18	.044	0.23	r
		1.0	7.54	.043	0.32	r
		3.0	8.38	.180	1.51	r
		10.0	9.70	.065	0.63	r

Table 7 DMA Test Data for 3M-ISD-112 [18] (•)

TEMPERATURE		FREQUENCY	G_2'	η_2	G_2''	ACC/REJ
°C	°F	(Hz)	Lb/in^2		Lb/in^2	
-68	- 90	20.1	111964	.047	5228.7	a
-54	-65	19.2	100507	.050	4995.2	a
-46	- 51	18.1	87309	.064	5614.C	a
-39	- 38	16.7	72371	.085	6151.5	a
-34	- 29	15.2	59028	.116	6847.2	a
-30	- 22	13.5	45395	.165	7490.2	a
-25	- 13	10.9	28861	.263	7590.5	a
-20	- 4	8.2	15953	.394	6285.7	a
-15	5	5.8	7948	.521	4140.8	a
-11	12	4.4	4423	.568	2512.5	a
- 9	16	3.8	3408	.562	1915.4	a
- 8	17.6	3.6	3017	.563	1698.4	a
- 3	26.6	2.6	1552	.437	678.2	r
- 1	30	2.2	1098	.297	326.1	r
0	32	1.9	863	.164	141.5	r
1	34	1.8	744	.046	34.3	r
5	42	1.8	719	.048	34.3	r

Table 8 Autovibron Tests on 3M-ISD-112 [18] (o)

TEMPERATURE		FREQUENCY	G_2'	η_2	G_2''	ACC/REJ
°C	°F	(Hz)	Lb/in^2		Lb/in^2	
- 46.8	-52	110	24593	.037	909.9	r
- 21.8	- 7	110	15059	.195	2936.5	a
- 17	1.4	110	11390	.298	3394.2	a
- 14.4	6	110	9461	.376	3557.3	a

Table 9 Shear Resonance Test data for 3M-467 [8,9] (x)

(o= 0.93 in, h = 0.099 in, ℓ = 1.25 in, Various values of M)

TEMPERATURE		FREQUENCY	G_2'	η_2	G_2''	ACC/REJ
°C	°F	(Hz)	Lb/in^2		Lb/in^2	
10.0	50	822	1560	.804	1254	a
14.4	58	627	905	.940	851	a
16.1	61	523	630	.980	617	a
17.2	63	510	600	.970	582	a
21.1	70	1067	750	.860	645	a
22.8	73	377	329	1.180	388	a
23.3	74	539	365	1.170	427	a
23.9	75	501	318	1.220	388	a
25.0	77	724	348	1.200	417	a
27.2	81	737	360	1.280	461	a
27.2	81	417	220	1.280	282	a
28.3	83	272	171	1.250	214	a
		605	240	1.260	302	a
28.9	84	588	228	1.380	315	a
		346	152	1.150	175	a
30.6	87	499	165	1.510	249	a
31.1	88	324	127	1.150	146	a
32.2	90	477	150	1.380	207	a
32.8	91	478	152	1.460	222	a
34.4	94	258	85	1.290	110	a
34.4	94	403	107	1.380	148	a
37.2	99	259	85	1.200	102	a
37.8	100	211	56.0	1.070	60.0	a
38.9	102	143	47.0	1.400	54.0	a
43.3	110	319	67.0	1.400	94.0	a
55.0	131	94	20.5	.910	18.7	a
57.2	135	117	17.4	.885	15.4	a
58.3	137	184	22.5	1.120	25.2	a

Table 10 Shear Resonance Test data for 3M-467 [8,9] (•)

(15 layers, h = 0.0024 in x 15, b = 0.88 in, ℓ = 1.27 in)

TEMPERATURE		FREQUENCY	G_2'	η_2	G_2''	ACC/REJ
^oC	^oF	(Hz)	Lb/in^2		Lb/in^2	
17.8	64	915	750	.700	525	a
22.8	73	1118	652	.810	528	a
23.3	74	804	582	.900	524	a
23.9	75	770	530	.880	466	a
27.8	82	1337	491	.910	447	a
28.3	83	634	360	.850	306	a
33.9	93	757	298	.940	280	a
35.0	95	483	188	1.000	188	a
38.9	102	1124	318	1.100	350	a
40.6	105	438	171	.880	151	a
47.2	117	338	104	.960	100	a
		435	94.0	.950	89.3	a
49.4	121	323	93.0	.700	65.1	a
		583	94.0	1.050	99.0	a
57.2	135	234	49.0	.760	37.0	a
60.0	140	274	39.0	.760	29.6	a
60.6	141	443	54.0	.860	46.4	a
61.1	142	259	60.0	.670	40.2	a

Table 11 Sandwich beam test data for 3M-467 [13] (o)

(h_1 = 0.070 in, h_2 = 0.008 in, ℓ = 7.00 in)

TEMPERATURE		MODE	FREQUENCY	G_2'	η_2	G_2''	ACC/REJ
°C	°F		(Hz)	Lb/in^2		Lb/in^2	
- 31.7	- 25	2	600.0	11336	.107	1213	r
		3	1649.0	29608	.085	2517	a
- 17.8	0	2	597.0	9636	.328	3160	a
		3	1609.0	17521	.335	5869	a
- 3.9	25	2	537.0	1954	.803	1569	a
		3	1397.0	3581	.825	2954	a
		4	2521.0	4100	.992	4068	a
18.9	66	2	414.0	369	1.495	552	a
		3	1042.0	801	.905	725	a
23.9	75	2	374.0	236	1.470	347	a
40	104	2	313.0	71.5	1.610	115.1	a
		3	854.0	189	1.028	194	a
		4	1629.0	251	1.076	270	a
		5	2645.0	359	.916	329	a
51.7	125		296.0	33.0	1.394	46.0	a
			804.0	63.3	1.280	81.0	a
56.1	133		299.0	40.9	1.375	56.3	a
			814.0	91.0	.987	89.8	a
		4	1572.0	116	1.093	127	a
		5	2583.0	219	.765	168	a
67.2	153	2	293.0	28.1	1.077	30.3	a
		3	798.0	54.9	.916	50.3	a
		5	2550.0	148	.622	92.1	a

Table 12 Sandwich beam test data for 3M-467 [12] (+)

TEMPERATURE		MODE	FREQUENCY	G_2'	η_2	G_2''	ACC/REJ
°C	°F		(Hz)	Lb/in^2		Lb/in^2	
- 18.3	-1	2	510	13890	.171	2375	r
		3	1402	23700	.163	3863	a
		4	2699	29080	.166	4827	a
		5	4380	31870	.155	4940	a
- 3.9	25	3	1368	10880	.333	3623	a
		4	2605	13850	.328	4543	a
		5	4188	17210	.343	5903	a
10	50	2	477	2275	.644	1465	a
		3	1280	4025	.723	2896	a
		4	2388	5132	.744	3818	a
		5	3742	5494	.878	4824	a
23.9	75	2	423	629.6	1.063	669.3	a
		3	1097	1201	1.025	1231	a
30.6	87	2	390	375.2	1.213	455.1	a
		3	988	677.9	1.177	797.9	a
37.8	100	2	319	144.7	1.274	184.3	a
		4	1526	383.1	1.325	507.6	a
		5	2444	447.7	1.350	603.9	a
44.2	112	2	329	168.7	1.254	211.5	a
		3	833	280.0	1.340	375.2	a
		4	1539	384.5	1.317	506.4	a
		5	2444	445.7	1.440	641.8	a
51.0	124	3	738	115.8	1.220	141.3	a
		4	1407	164.3	1.209	198.6	a
		5	2302	228.0	1.167	266.1	a
65.6	150	2	262	39.3	.916	36.0	a
		3	700	57.5	1.091	62.7	a
		4	1356	89.0	1.009	89.8	a
		5	2235	131.7	.938	123.5	a
		6	3326	147.6	1.139	168.1	a
79.4	175	2	254	27.4	.812	22.3	a
		3	685	28.8	1.297	37.3	a
		4	1335	62.6	.932	58.3	a
		5	2208	104.6	.683	71.4	a
		6	3294	116.5	.840	97.9	a

TABLE 12 (CONTINUED)

TEMPERATURE		MODE	FREQUENCY	G_2'	η_2	G_2''	ACC/REJ
°C	°F		(Hz)	Lb/in^2		Lb/in^2	
93.3	200	2	248	18.8	.742	13.9	a
		4	1325	54.2	.591	32.0	a
		5	2188	87.1	.488	42.5	r
		6	3267	107.0	.535	57.3	r
109	225	2	245	15.0	.577	8.3	a
		3	670	20.4	.698	14.3	a
		4	1308	35.3	.542	19.2	a
		5	2165	52.8	.494	26.1	r
		6	3237	87.4	.353	30.9	r
120	248	2	242	12.7	.507	6.4	a
		3	664	15.9	.622	9.9	a
		4	1297	27.7	.480	13.3	a
		5	2145	52.7	.356	18.8	r
		6	3213	82.7	.283	23.4	r

Table 13 Fitzgerald data for 3M-467 [5] (□)

TEMPERATURE		FREQUENCY	G_2'	η_2	G_2''	ACC/REJ
°C	°F	(Hz)	Lb/in^2		Lb/in^2	
25	77	46	118	1.24	146	a
		78	147	1.28	188	a
		90	164	1.38	226	a
		110	185	1.38	255	a
31	87	20	33	1.00	33	a
		25	40	1.04	41.6	a
		45	52	1.11	57.7	a
		64	59	1.15	67.9	a
		98	71	1.15	81.7	a
		117	80	1.15	92.0	a
31	88	20	31	1.04	32.2	a
		25	36	1.07	38.5	a
		45	52	1.15	59.8	a
		64	58	1.15	66.7	a
		80	64	1.15	73.6	a
		98	70	1.15	80.5	a
		110	72	1.19	85.7	a
		120	74	1.19	88.1	a

Table 14 Cyclic Shear test data for 3M-467 [5] (△)

TEMPERATURE		FREQUENCY	G_2'	η_2	G_2''	ACC/REJ
°C	°F	(Hz)	Lb/in^2		Lb/in^2	
24	75	0.1	3.8	.466	1.8	a
		3.0	23.9	.913	21.8	a
		6.0	32.0	1.095	35.0	a
		9.0	39.7	1.046	41.5	a
		12.0	44.3	.910	40.3	a
		15.0	50.0	.966	48.3	a

Table 15 Sandwich beam test data for GE SMRD 100F90 [18] (x)

($h_1 = h_3 = 0.080$ in, $h_2 = 0.039$ in, $\ell = 7.0$ in)

TEMPERATURE		MODE	FREQUENCY	G_2'	η_2	G_2''	ACC/REJ
°C	°F		(Hz)	Lb/in^2		Lb/in^2	
- 31.7	-25	3	2237	85440	.016	1359	a
		4	4153	96210	.017	1664	a
		5	6487	103800	.021	2149	a
		6	9141	110200	.020	2216	a
- 19.4	-2.9	2	836	66000	.044	2911	a
		5	6427	99740	.042	4159	a
		6	9029	104700	.033	3475	a
- 3.9	25	2	830	61030	.051	3131	a
		3	2212	76880	.249	19170	r
		4	4096	90240	.024	2202	a
		5	6380	96740	.020	1915	a
		6	8917	99160	.026	2608	a
10	50	2	827	59310	.077	4537	a
		3	2169	66790	.056	3707	a
		4	3990	75160	.049	3668	a
		5	6164	79830	.047	3744	a
		6	8624	84410	.054	4550	a
23.9	75	2	759	19040	.087	1653	r
		3	2039	39480	.146	5753	a
		4	3721	48140	.180	8669	r
		5	5709	53160	.195	10370	r
		6	7926	56840	.173	9838	r
39.4	103	2	708	8407	.763	6414	a
		3	1828	17200	.656	11290	r
		6	6682	2722	.303	8234	a
51.7	125	2	551	3273	.216	708	r
		4	2365	5479	1.011	5540	a
65.6	150	2	460	1509	.329	496	a
		3	1113	2099	.324	680	r
		4	1988	2208	.693	1529	a
		5	3144	2432	.763	1856	a
		6	4571	2646	1.026	2714	a
79.4	175	2	433	1168	.172	201	a
		3	1036	1384	.286	396	a
		4	1881	1413	.385	545	a
		5	2995	1400	.512	716	a
		6	4391	1489	.387	577	a

TABLE 15 (CONTINUED)

TEMPERATURE °C	TEMPERATURE °F	MODE	FREQUENCY (Hz)	G_2' Lb/in^2	η_2	G_2'' Lb/in^2	ACC/REJ
93.3	200	2	420	1020	.107	109	a
		3	1009	1171	.164	192	a
		4	1839	1119	.234	262	a
		5	2949	1063	.196	208	a
		6	4310	972	.303	294	a

Table 16 DMA Test Data for GE SMRD 100F90 [18] (•)

TEMPERATURE		FREQUENCY	G_2'	η_2	G_2''	ACC/REJ
°C	°F	(Hz)	Lb/in^2		Lb/in^2	
- 68	- 90	23.4	42990	.033	1419	r
- 63	- 81	23.3	42800	.033	1404	r
- 58	- 72	23.2	42020	.034	1446	r
- 53	- 63	23.0	41300	.037	1528	r
- 48	- 54	22.8	40380	.040	1599	r
- 43	- 45	22.6	39360	.041	1610	r
- 39	- 38	22.4	38440	.042	1607	r
- 35	- 31	22.2	37670	.043	1609	r
- 30	- 22	22.0	36850	.043	1573	r
- 25	- 13	21.8	35980	.043	1547	r
- 20	- 4	21.6	25110	.044	1538	r
- 16	3	21.4	34430	.045	1539	r
- 12	10	21.2	33660	.046	1562	r
- 8	17.6	21.0	32980	.049	1629	r
- 6	21	20.9	32550	.052	1683	r
- 4	25	20.8	32060	.055	1747	r
- 2	28	20.6	31530	.058	1826	r
0	32	20.4	30850	.063	1944	r
2	35.6	20.2	30030	.070	2093	r
5	41	19.7	28340	.085	2417	r
8	46.4	19.1	26450	.104	2751	r
10	50	18.8	25240	.127	3206	r
12	53.6	18.3	25740	.163	3870	r
15	59	16.9	19880	.247	4909	a
18	64	14.9	14750	.387	5708	a
20	68	13.1	11170	.518	5786	a
23	73.4	10.1	6335	.761	4821	a
25	77	8.2	4101	.881	3613	a
28	82	6.4	2331	.930	2168	a
30	86	5.6	1760	.876	1542	a
33	91	4.5	1040	.721	750	a
35	95	4.0	783	.603	472	a
38	100	3.5	561	.443	249	r
40	104	3.3	468	.341	160	r
43	109	3.1	375	.193	72.3	r
45	113	3.0	332	.102	33.9	r
46	115	2.9	316	.060	18.8	r

Table 17 Autovibron Test Data for GE SMRD 100F90 [18] (▽)

TEMPERATURE		FREQUENCY	G_2'	η_2	G_2''	ACC/REJ
°C	°F	(Hz)	Lb/in^2		Lb/in^2	
3.0	37	110	32510	.021	683	r
12.8	55		30450	.063	1918	r
13.6	56		28010	.044	1232	r
15.0	59		29470	.043	1267	r
18.7	66		26030	.157	4086	r
21.6	71		23290	.207	4821	r
23.7	75		19820	.274	5431	a
25.5	78		18970	.286	5424	a
27.4	81		15310	.392	6002	r
29.4	85		14430	.294	4244	a
31.2	88		10860	.483	5246	a
33.1	92		8666	.552	4784	a
35.0	95		7292	.599	4368	a
36.9	98		5634	.658	3707	a
38.9	102		3956	.793	3137	a
40.7	105		3396	.755	2564	a
42.5	109		3102	.701	2174	a
44.5	112		1970	.810	1601	a
46.3	115		1894	.762	1443	a
48.3	119		1487	.738	1097	a
50.1	122		1457	.615	896	a
52.1	126		1238	.575	712	a
53.9	129		1136	.715	812	a
55.8	132		1158	.423	490	a
57.7	136		981	.374	367	a
60.5	141		952	.396	377	a
62.3	144		827	.525	434	a
64.3	148		1230	.290	357	a
71.8	161		704	.244	172	a
74.6	166		913	.166	152	a
78.3	173		767	.194	149	a
- 25.6	- 14	35	29160	.005	146	r
- 10.9	12.4		32240	.013	419	r
0.2	32		31960	.038	1214	r
4.4	40		29180	.030	875	r
10.3	50		26590	.046	1223	r
12.1	54		26960	.067	1807	r
13.9	57		25530	.141	3599	a
15.7	60		20330	.163	3314	a
17.5	64		20240	.330	6679	a
19.3	67		18250	.329	6003	a

TABLE 17 (CONTINUED)

TEMPERATURE		FREQUENCY	G_2'	η_2	G_2''	ACC/REJ
°C	°F	(Hz)	Lb/in^2		Lb/in^2	
22.3	72	35	16450	.378	6217	a
25.2	77		13180	.517	6815	a
27.0	81		10500	.490	5147	a
29.0	84		8293	.675	5598	a
30.9	88		6504	.616	4007	a
32.7	91		4693	.795	3731	a
34.7	94		3618	.786	2844	a
36.5	98		2657	.928	2466	a
39.4	103		1971	.852	1679	a
41.3	106		1640	.778	1276	a
43.2	110		1457	.710	1034	a
52.5	127		859	.655	563	a
56.4	134		854	.343	293	a
60.1	140		888	.216	192	a
62.9	145		813	.263	2.4	a
66.7	152		760	.203	154	a
70.7	159		728	.114	83.0	a

Table 18 MTS Forced Vibration Test Data for GE SMRD 100F90 [18] (o)

TEMPERATURE		FREQUENCY	G_2'	η_2	G_2''	ACC/REJ
°C	°F	(Hz)	Lb/in^2		Lb/in^2	
10	50	.025	13710	.199	2729	a
		.10	19360	.122	2362	a
		1.0	30490	.049	1494	a
		3.0	33560	.015	503	r
		10.0	30540	.071	2168	a
37.8	100	.025	726	.009	6.5	r
		.10	743	.013	9.6	r
		1.0	825	.033	27.2	r
		3.0	939	.044	41.3	r
65.6	150	.025	620	.005	3.1	r
		.10	643	.004	2.6	r
		1.0	636	.005	3.2	r
		3.0	639	.028	17.9	r
		10.0	653	.128	83.6	r
93.3	200	.025	579	.006	3.5	r
		.10	585	.007	4.1	r
		1.0	593	.005	3.0	r
		3.0	599	.031	18.6	r
		10.0	603	.135	81.4	r

HUBBLE SPACE TELESCOPE REACTION WHEEL ASSEMBLY VIBRATION ISOLATION SYSTEM

L. P. Davis, J. F. Wilson
Sperry Corporation
Aerospace & Marine Group
Phoenix, Arizona 85036

R. E. Jewell
National Aeronautics and Space Administration
George C. Marshall Space Flight Center
Marshall Space Flight Center, Alabama 35812

J. J. Rodon
Lockheed Missiles and Space Co., Inc.
Space Systems Division
Sunnyvale, CA 94086

ABSTRACT

The Hubble Space Telescope features the most exacting line of sight jitter requirement thus far imposed on a spacecraft pointing system. Consideration of the fine pointing requirements prompted an attempt to isolate the telescope from the low level vibration disturbances generated by the attitude control system reaction wheels. The primary goal was to provide isolation from axial component of wheel disturbance without compromising the control system bandwidth. At Sperry Corporation, a passive isolation system employing metal springs in parallel with viscous fluid dampers was designed, fabricated, and space qualified. Stiffness and damping characteristics are deterministic, controlled independently, and have been demonstrated to remain constant over at least five orders of input disturbance magnitude. The damping remained purely viscous even at the data collection threshold of $.16 \times 10^{-6}$ in input displacement, a level much lower than the anticipated Hubble Space Telescope disturbance amplitude. Vibration attenuation goals were obtained and ground test of the vehicle has demonstrated the isolators are transparent to the attitude control system.

ABSTRACT

The Hubble Space Telescope features the most exacting line of sight jitter requirement thus far imposed on a spacecraft pointing system. Consideration of the fine pointing requirements prompted an attempt to isolate the telescope from the low level vibration disturbances generated by the attitude control system reaction wheels. The primary goal was to provide isolation from axial component of wheel disturbance without compromising the control system bandwidth. At Sperry Corporation, a passive isolation system employing metal springs in parallel with viscous fluid dampers was designed, fabricated, and space qualified. Stiffness and damping characteristics are deterministic, controlled independently, and have been demonstrated to remain constant over at least five orders of input disturbance magnitude. The damping remained purely viscous even at the data collection threshold of $.16 \times 10^{-6}$ in input displacement, a level much lower than the anticipated Hubble Space Telescope disturbance amplitude. Vibration attenuation goals were obtained and ground test of the vehicle has demonstrated the isolators are transparent to the attitude control system.

INTRODUCTION

The Hubble Space Telescope (hST), shown in Figure 1, provides an optical image for five scientific instruments and three Fine Guidance Sensors. The vehicle is approximately 44 feet long and weighs 24,000 pounds. It is designed for STS insertion into a circular orbit of 320 NM for a 15-year mission. On-orbit maintenance and new technology upgrades during the mission are anticipated. To preclude the possibility of contamination of the optical elements no chemical reaction propulsion systems are onboard. Attitude control is provided by the Reaction Wheel Assemblies (RWAs) and the magnetic momentum control system. Reboost following orbital decay will be provided by the orbiter.

POINTING CONTROL SYSTEM

The primary elements of the Pointing Control System (PCS) used for fine pointing are the digital computer, reaction wheels, magnetic momentum system, rate gyro complement, and two of the Fine Guidance Sensors. Pointing torques are applied with the RWAs. The magnetic momentum system is used to desaturate the RWAs and minimize the wheel speed excursions. The four RWAs are positioned with their spin axes inclined at 20 degrees to the telescope optical axis as in Figure 2. Two RWAs provide torque along the pitch and roll axes and two provide torque along the yaw and roll axes. The array is thus redundant in that it can provide control at reduced capacity following the loss of any one RWA. Additional coarse pointing attitude information is available from fixed head star trackers and sun sensors. Finally, a backup control system with backup rate gyros is provided for increased mission reliability.

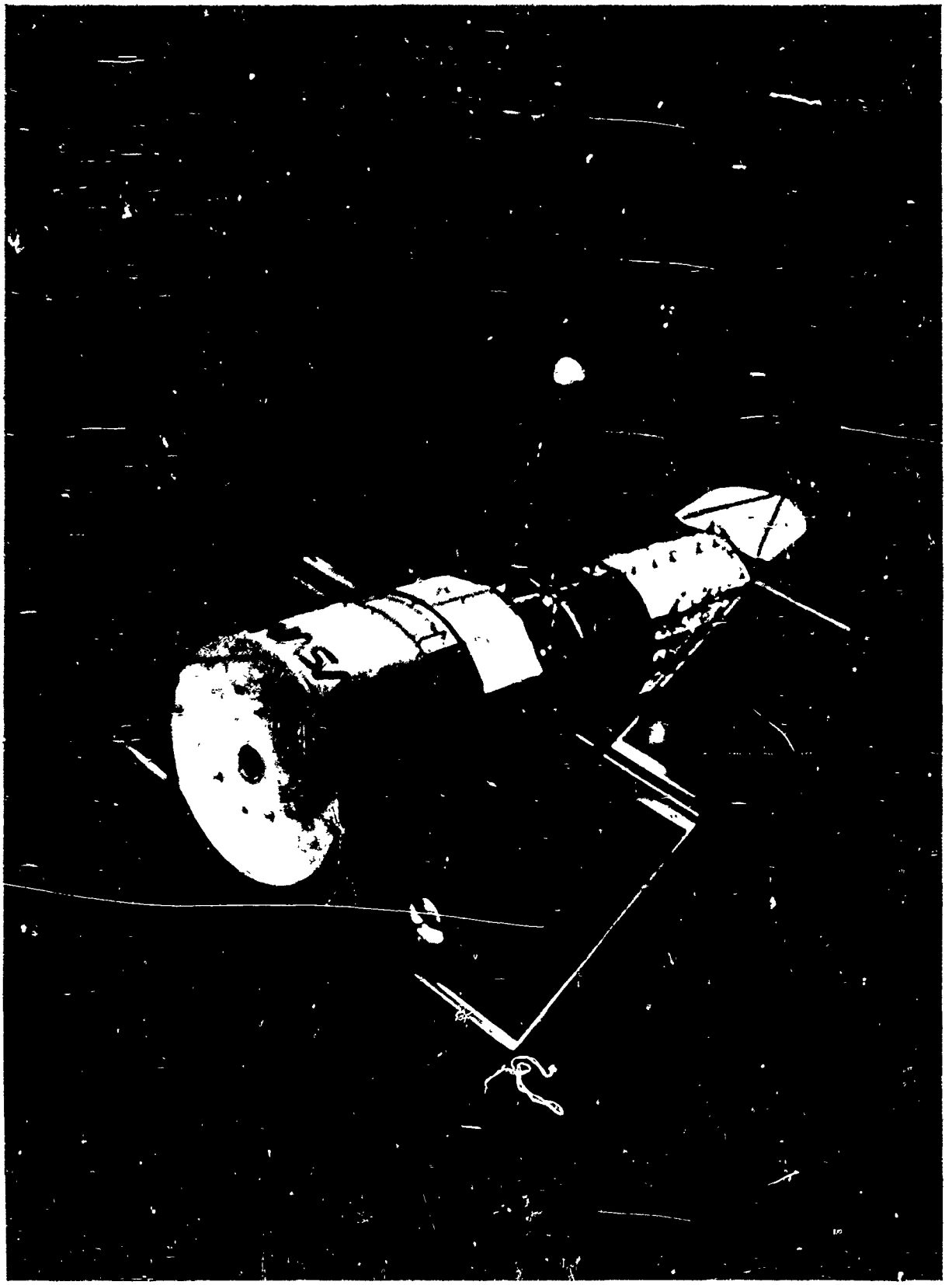


Figure 1

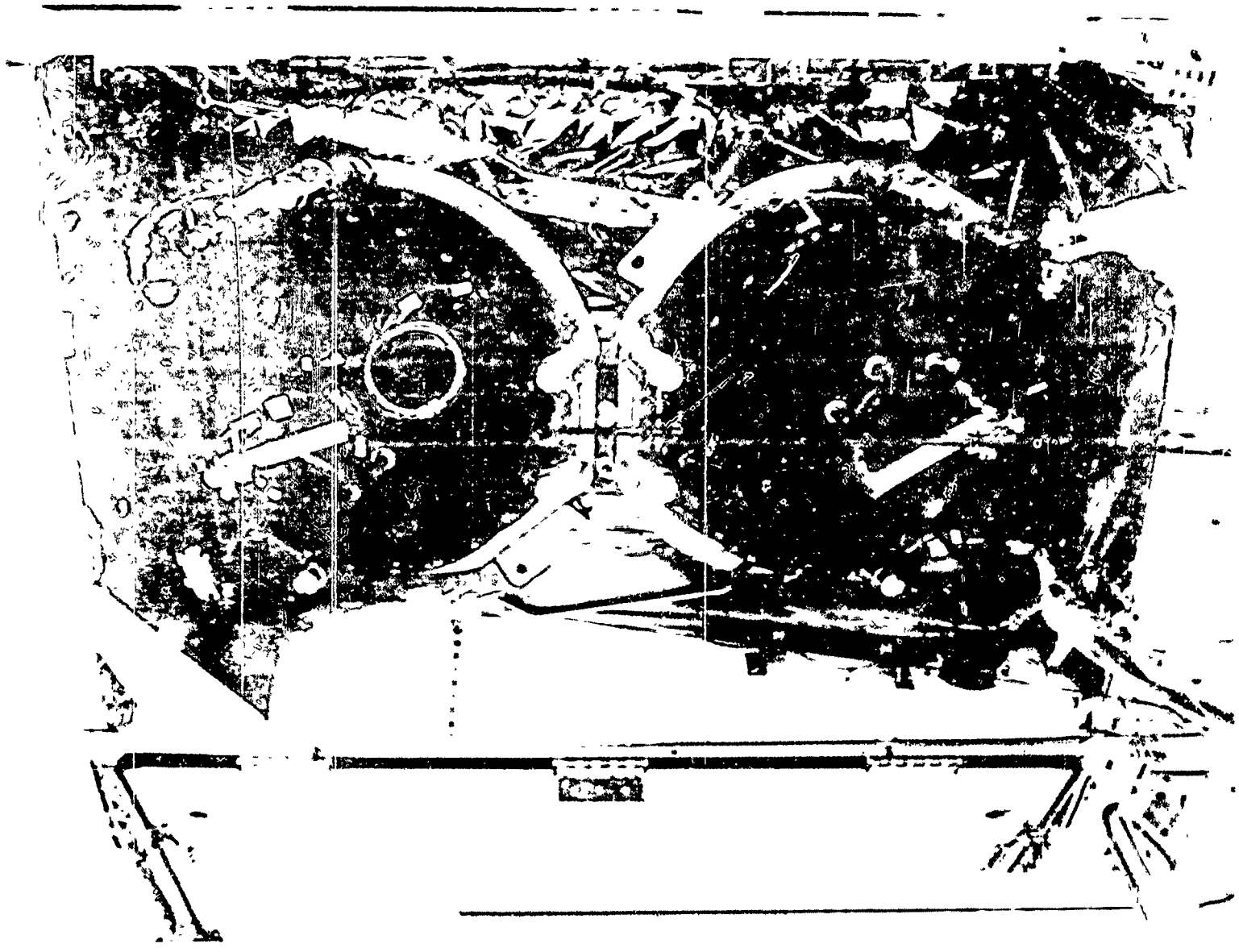


Figure 2

HST pointing accuracy and stability are defined in terms of Line Of Sight (LOS) error of the principal ray at the final imaging element, which includes the errors from all the optical elements in the path. Jitter predictions involve modeling of the disturbance sources, the HST structural transmissivities, and ray tracing between the various optical elements. The HST image stability requirement for periods up to 24 hours is .007 arcsec rms. This requirement is also to be maintained in any period as short as 10 seconds, which limits the averaging of short duration disturbances. The HST pointing repeatability requirement for periods up to 100 hours is .01 arcsec. Pointing performance of a satellite at these levels has not been previously obtained. LOS jitter sources include random sensor noise, coherent sources due to rotating machinery, thermal gradient effects, and residual transients due to recent large amplitude maneuvers. Since the RWAs are the most massive rotating machines onboard and must be operated continuously during science acquisition they received considerable attention in the jitter reduction effort. Jitter models indicated that the LOS was most sensitive to axial RWA disturbances owing to the vehicle configuration.

REACTION WHEEL INDUCED VIBRATION

An RWA produces vibration disturbances when it rotates due to imperfections in the electromagnetics and their drive electronics, unbalance of the rotor, and imperfections in the spin bearings. In the case of the HST RWA, the electromagnetics and electronics were designed to produce negligible disturbances relative to the latter sources. The rotors were balanced to the point that the unbalance was at least as small as and indistinguishable from disturbances due to geometric imperfections in the spin bearings. The bearing geometry disturbances occur at many harmonics of wheel speed, and balancing alters only the once per revolution harmonic, so further improvements in balance are unproductive. The bearing geometry disturbances were minimized through the use of bearings with nearly perfect geometry (equivalent of ABEC 9) and by selectively matching the bearings for lowest net disturbance. This procedure is thought to result in state-of-the-art vibration reduction.

Some of the lower frequency first order disturbances are shown in Figure 3. These are the maximum, average, and minimum force levels for the five flight RWAs and the engineering unit while running at 1500 rpm. Also shown is a table summarizing the sources of these harmonics. In the HST bearing the ball groups rotate .35 times as fast as the rotor so harmonics of 1.0, .35 and their difference occur.

In Figure 4 measured data is shown for the axial force at once per revolution as wheel speed is varied from 0 to 3000 rpm. Also shown is the least square curve fit to the data based on the assumption that force is proportional to the square of wheel speed. A similar correlation with wheel speed squared is found for other harmonics at frequencies below the first resonance of the RWA and test fixture. This correlation suggests that at low frequency the disturbances have the form $f = M\Delta(NW)2$ where f is the disturbance force, M is the mass of the rotor, Δ is the geometrical runout in the bearing, N is the harmonic number, and W is the wheel speed. Using this assumption, Δ for each harmonic may be determined in the least square sense. This was done for the flight units and is tabulated in Figure 4. Since the predicted geometry errors are within the bearing specification and are not practically measurable this model of the bearing disturbance was accepted.

BALL BEARING DISTURBANCES

- 0.35 HARMONIC (BALL RETAINER)
- 1.0 HARMONIC (MASS UNBALANCE)
- 2.0 HARMONIC (RACE TO RACE MISALIGNMENT)
- 2.8 HARMONIC (OUTER RACE DEFECTS)
- 5.2 HARMONIC (INNER RACE DEFECTS)
- 5.6 HARMONIC (OUTER RACE DEFECTS)

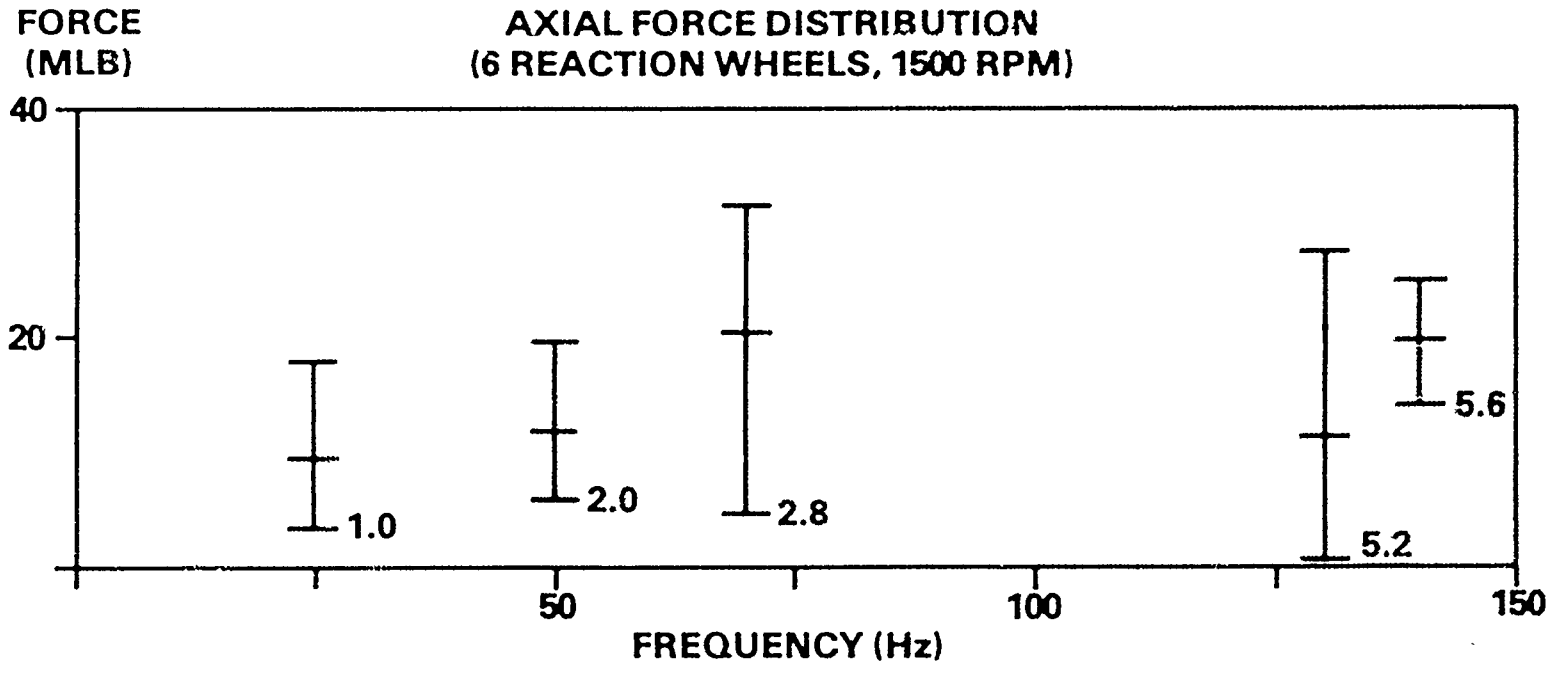


Figure 3

1g Hardmount Axial
1.0 Component

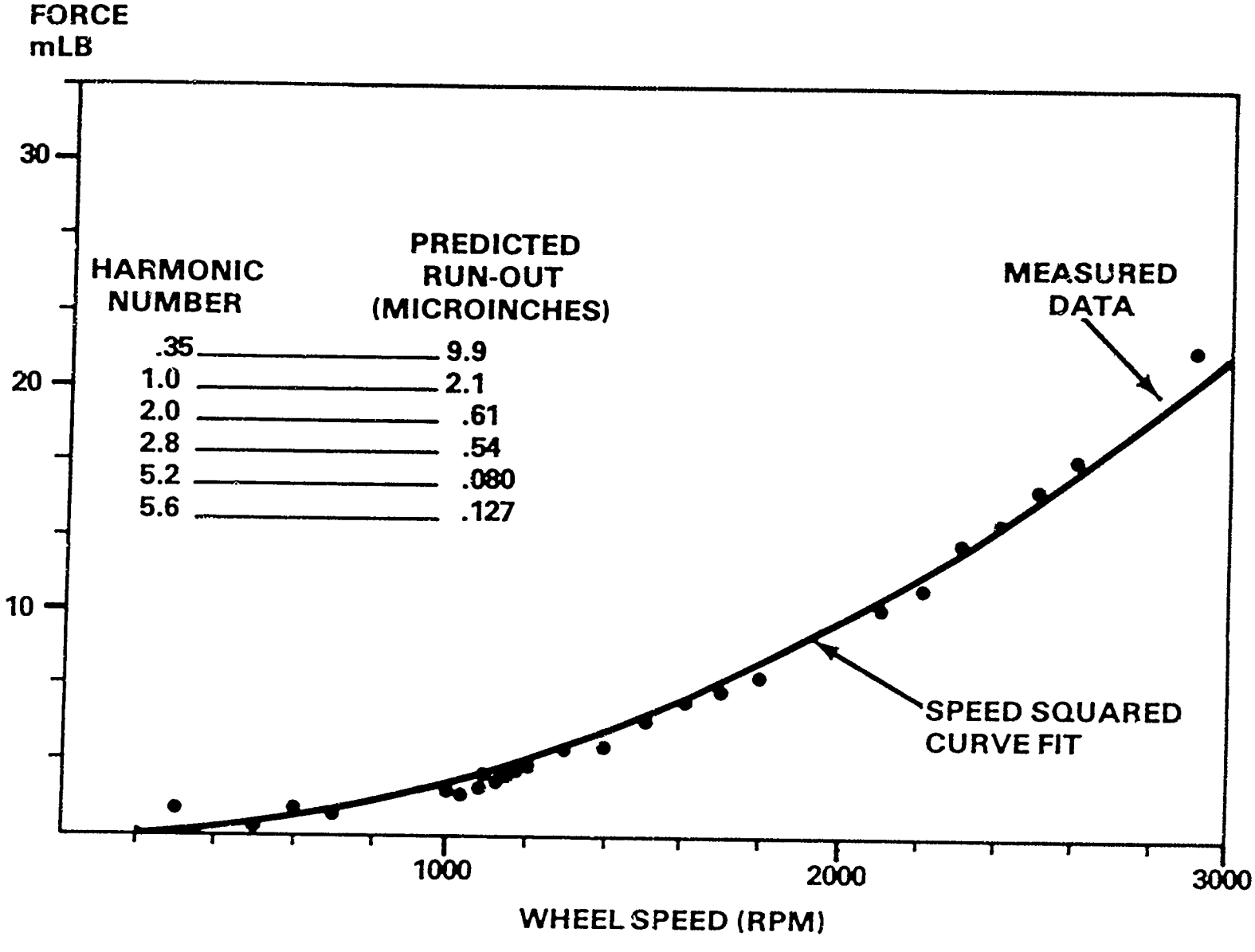


Figure 4

VIBRATION ISOLATION SYSTEM

The nature of the RWA vibration disturbances is that there are many harmonics, sweeping a wide frequency range as wheel speed is run up and down, with amplitudes increasing as the square of speed. LOS jitter models predicted marginal performance due to axial disturbances at the higher wheel speeds above 10 Hz (600 RPM) so passive isolation of the RWAs was a logical approach. Initial evaluations were made with wire rope isolators. The PSD of acceleration response due to force input for this isolator is shown in Figure 5. The input force level was varied from .0045 to .750 pound. The transfer function is nonlinear in stiffness and damping as a function of disturbance amplitude. Both these tendencies are explained to the first order by the loss of sliding friction in the wire rope as the amplitude is reduced. These nonlinearities make accurate modeling of the isolator very difficult. An additional drawback is the lack of strict determinism in the design of the stiffness and damping properties since these characteristics cannot be independently controlled.

These difficulties led to the development of the viscous fluid damped isolator shown in Figure 6. A simplified schematic and a cutaway of the flight design are shown. In the dual chamber schematic damping fluid is contained by two metal bellows supporting the center isolated portion. When the center portion moves axially fluid must flow from one bellows chamber to the other, incurring viscous losses as it flows. The damping value is determined by the viscosity of the fluid and the dimensions of the annular passage between the chambers. The stiffness is determined by the bellows design. These characteristics are deterministic and independent. For radial motion the stiffness is also deterministic although the damping is less so due to the complex flow. The flight design works on the same principal but acquired additional complexity. Coil springs were added in parallel with the bellows which effectively determine the spring rates. A third preloaded bellows chamber was added outboard to accommodate thermal expansion of the fluid. Mechanical stops were built in to limit maximum displacements and a redundant leak-proof seal was added to minimize the chance of fluid escape.

The equivalent lumped mass model and its theoretical transfer function were determined from volume balance equations for the three chambers. Finite element models of the metal parts gave translational and volumetric spring rates. The fluid contributions taken into account were its bulk modulus and viscous loss in the damping chamber. The isolator was assumed to be massless for this model. The equivalent lumped mass model and its theoretical transfer function are shown in Figure 7. It may be seen from the transfer function that high frequency roll-off takes place with a slope of two rather than one as with a simple parallel spring and dashpot. Physically, this is because high frequency motion can be accommodated by volumetric changes in the chambers with no corresponding flow through the damping chamber and hence very low damping. The double peak in the transfer function occurs because with very low damping only k1 is effective whereas with very high damping k1 acts in parallel with the series combination of k2 and k3. The PSD of axial acceleration at various force levels for the viscous isolator are shown in Figure 8. Both stiffness and damping are constant for the range of input considered. Transfer function tests down to the lowest threshold input attainable (.16 μ in.) indicated linear behavior. The damping properties of the isolator and the internal fluid pressure are a function of temperature. The pressure variation is controlled by the design of the thermal compensation bellows. A positive pressure margin is maintained to prevent

Wire Rope Isolator PSD

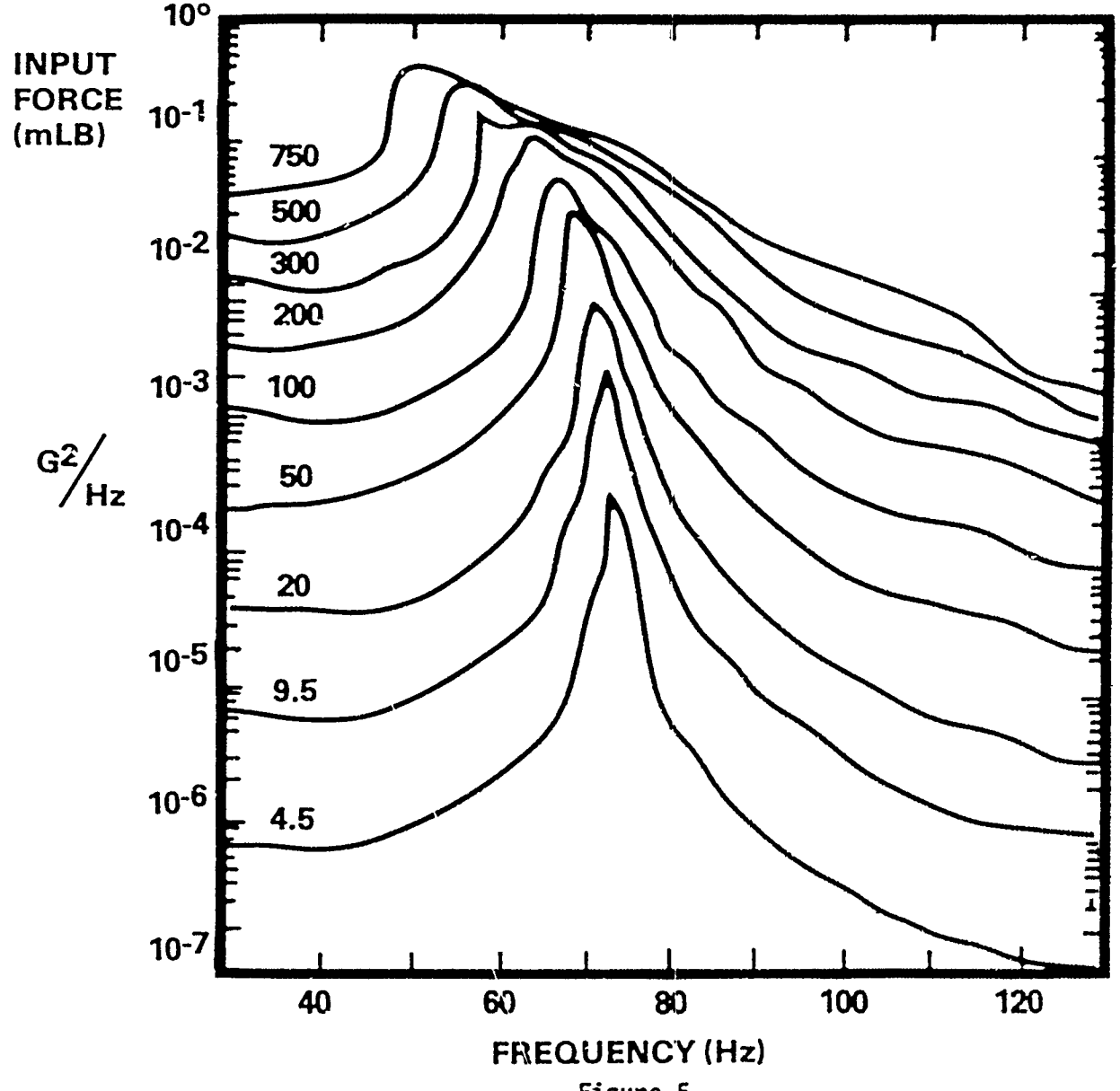


Figure 5

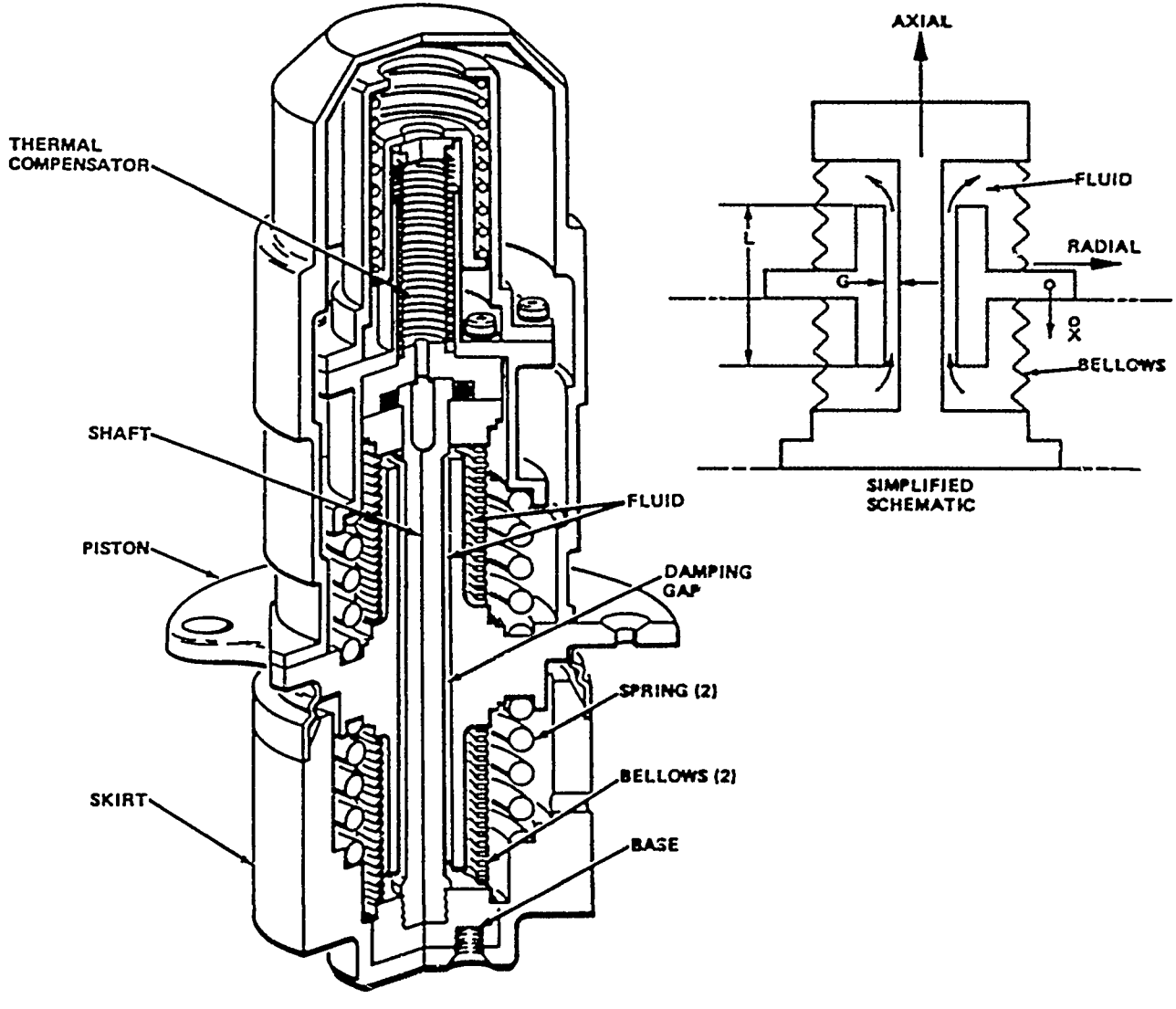
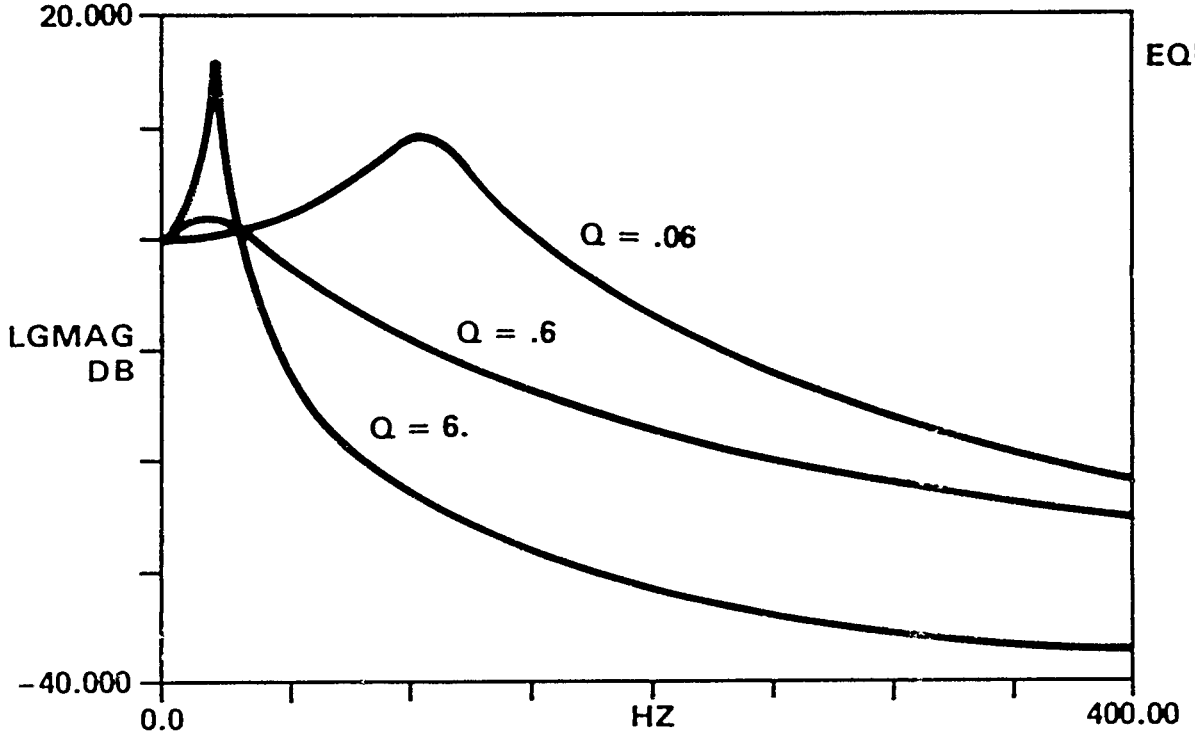

THERMAL COMPENSATOR
SHAFT
PISTON
SKIRT
FLUID
DAMPING GAP
SPRING (2)
BELLOWS (2)
BASE
AXIAL
FLUID
RADIAL
L
G
X
BELLOWS
SIMPLIFIED SCHEMATIC

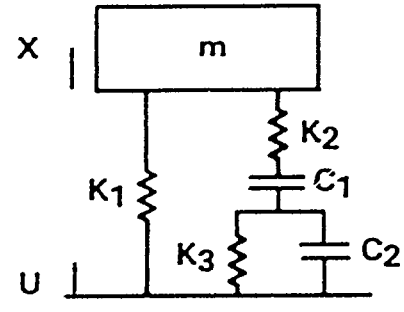
Figure 6

Theoretical Isolator Transfer Function

$$T = \frac{1 + \left(\frac{MN + LN + M + N}{MNQ}\right)\left(\frac{S}{P}\right) + \frac{L(N+1)}{NMQ^2}\left(\frac{S}{P}\right)^2}{1 + \left(\frac{MN + LN + M + N}{MNQ}\right)\left(\frac{S}{P}\right) + \left(\frac{NMQ^2 + L(N+1)}{NMQ^2}\right)\left(\frac{S}{P}\right)^2 + \left(\frac{LN + M + N}{NMQ}\right)\left(\frac{S}{P}\right)^3 + \frac{L}{NMQ^2}\left(\frac{S}{P}\right)^4}$$



EQUIVALENT LUMPED MASS MODEL



$T = X/U$

$N = K_2/K_1$

$M = K_3/K_1$

$L = C_2/C_1$

$Q = \sqrt{K_1 m/c_1}$

$P = \sqrt{K_1 m/c_1}$

Figure 7

Axial Displacement Power Spectral Density

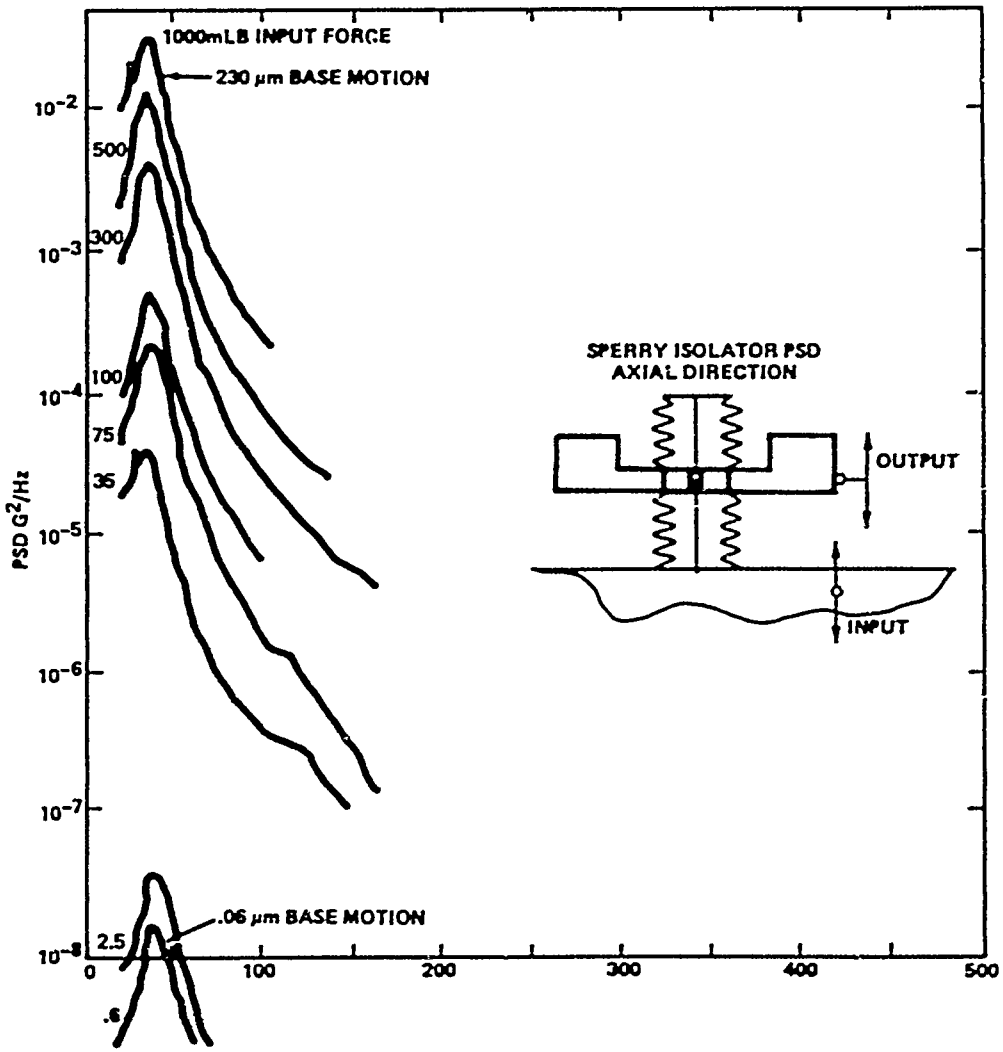


Figure 8

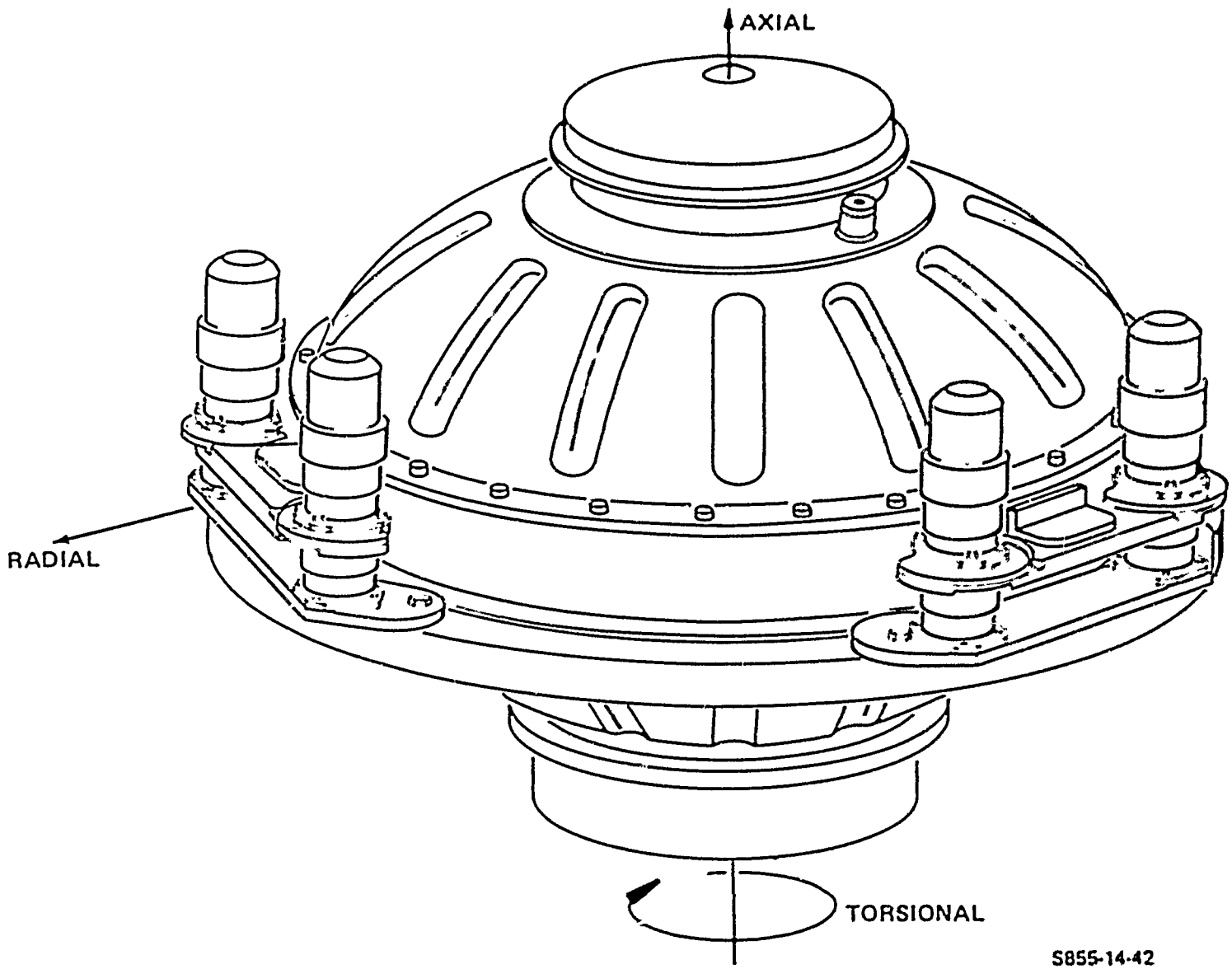
cavitation in the isolator. The variation in damping was deemed acceptable from a dynamic standpoint. An HST RWA mounted on an isolation system is shown in Figure 9. Three sets of two rigidly coupled isolator units are used to support the RWA at three points. For this application, the isolators are aligned for maximum damping in the axial direction. The structural attachments have been designed for on-orbit replacement of the isolation system, RWA, or RWA plus isolation system.

COMPONENT VIBRATION CHARACTERIZATION

The test configuration for characterizing RWAs and isolation systems is shown in Figure 10. The RWA is mounted to a holding fixture through the isolators. The holding fixture is mounted to a large isolation mass through very stiff piezoelectric load cells. The holding fixture is supported by low friction gas bearings to ensure that the preponderance of force transmitted to the isolation block passes through the load cells. Summing networks permit measurements of forces and torques. The holding fixture can be rotated 90 degrees to measure axial or radial disturbances. Radial force measured during a wheel speed rundown without isolation is shown in Figure 11. This plot is a composite of force spectra taken at 16 second intervals during a 1600 second RWA rundown from 3000 rpm to zero wheel speed. The RWA was back-driven with constant torque so the wheel speed varied linearly. In the plot, harmonic disturbances occur at linearly varying frequencies whereas resonances in the RWA and test fixture occur at constant frequency. Peaking occurs where the two coincide. A resonance is evident around 105 Hz. A similar rundown plot for axial force is shown in Figure 12. The peak axial force recorded during the rundown was 3.390 pounds, when the 2X harmonic passed through a resonance at 80 Hz. An axial rundown with the wire rope isolators installed is given in Figure 13. Resonances from 20 to 50 Hz are present. The peak force recorded was .248 pound when the 1X harmonic passed through a resonance near 50 Hz. The ratios of these peaks are not a measure of the isolator attenuation but reflect the ratio of the Q of the RWA at its resonance to the Q of the isolator at its resonance, and also the square of the frequency ratio since force is proportional to speed squared. An axial rundown is plotted in Figure 14 for the Sperry viscous isolator with 200 centistoke damping fluid. An axial resonance lies at 20 Hz and a peak force of .053 pound was measured when the 1X harmonic crossed it. Again the ratio of the peak forces reflects the ratio of the Qs and speeds squared rather than isolator attenuation. When 350 centistoke fluid is used, the peak force is .025 pound. The difference in transmitted energy with and without isolation is dramatic. The LOS jitter predictions show a similar level of improvement with the isolation system.

The HST in dynamic test configuration is shown in Figure 15. It is suspended by three cables from air bags to simulate zero g conditions. The transfer function of vehicle angle response to control system torque was measured with RWAs isolated and nonisolated. The isolators did not alter the transfer characteristic. Figure 16 shows a close-up of the isolators in the test vehicle.

RWA on Isolation System



S855-14-42

Figure 9

Induced Vibration Measurement System

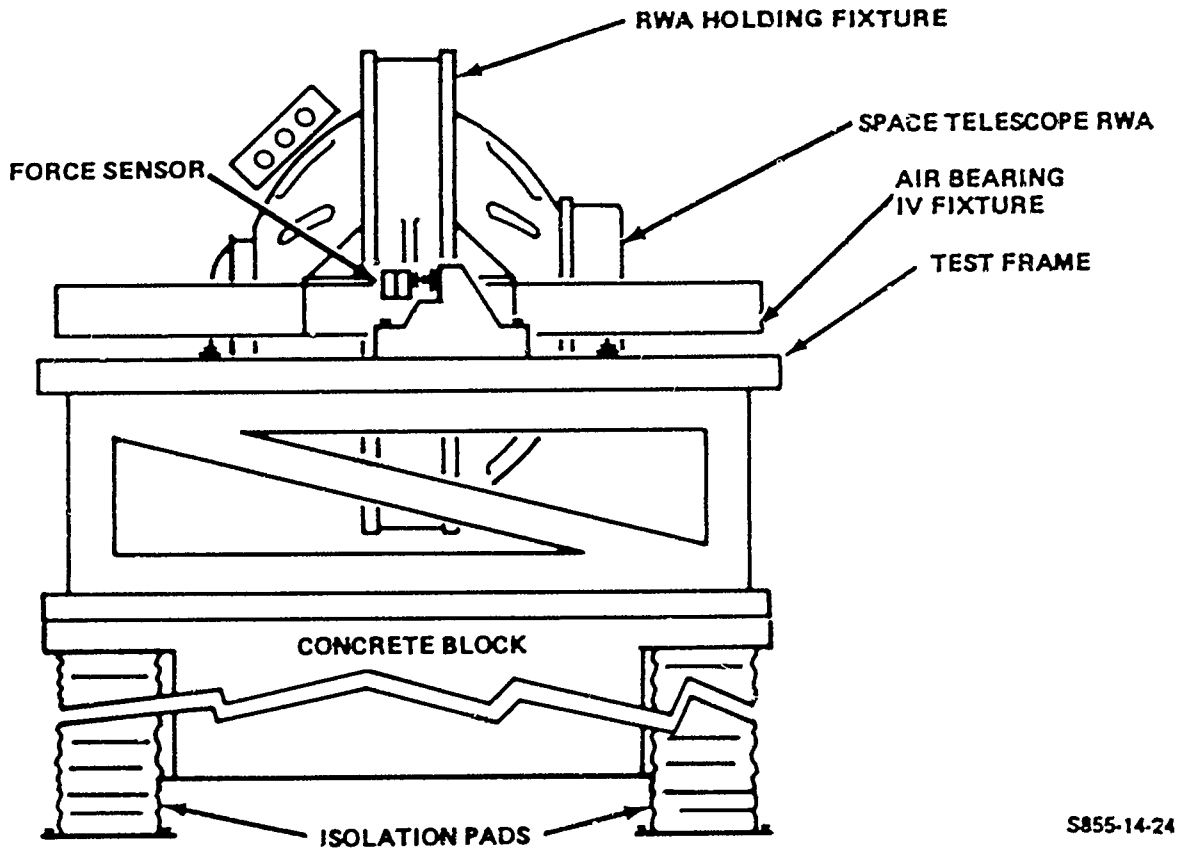


Figure 10

HARD MOUNTED REACTION WHEEL RADIAL FORCE (.782 LB PEAK)

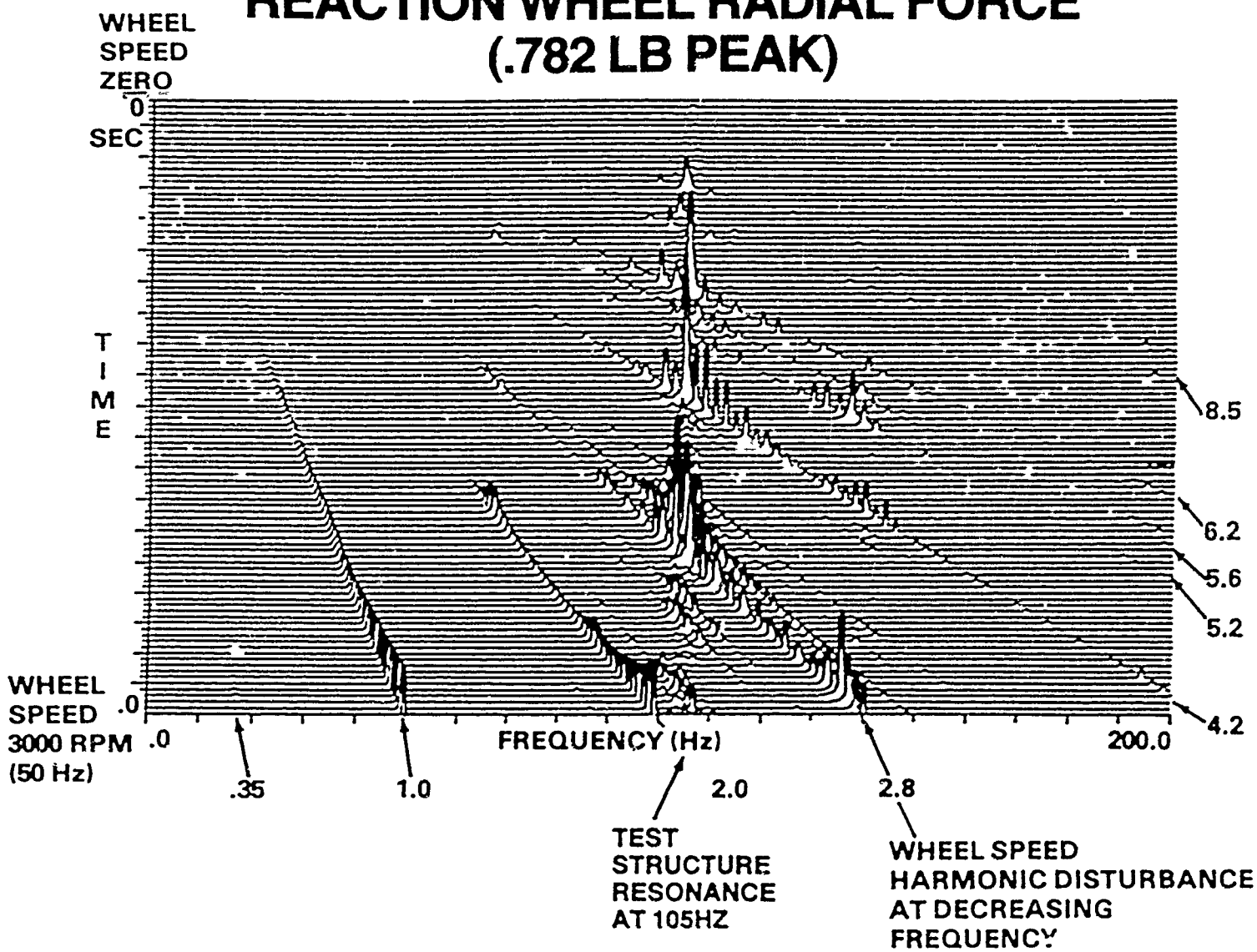


Figure 11

HARD MOUNTED
REACTION WHEEL AXIAL FORCE
(3.39 LB PEAK)

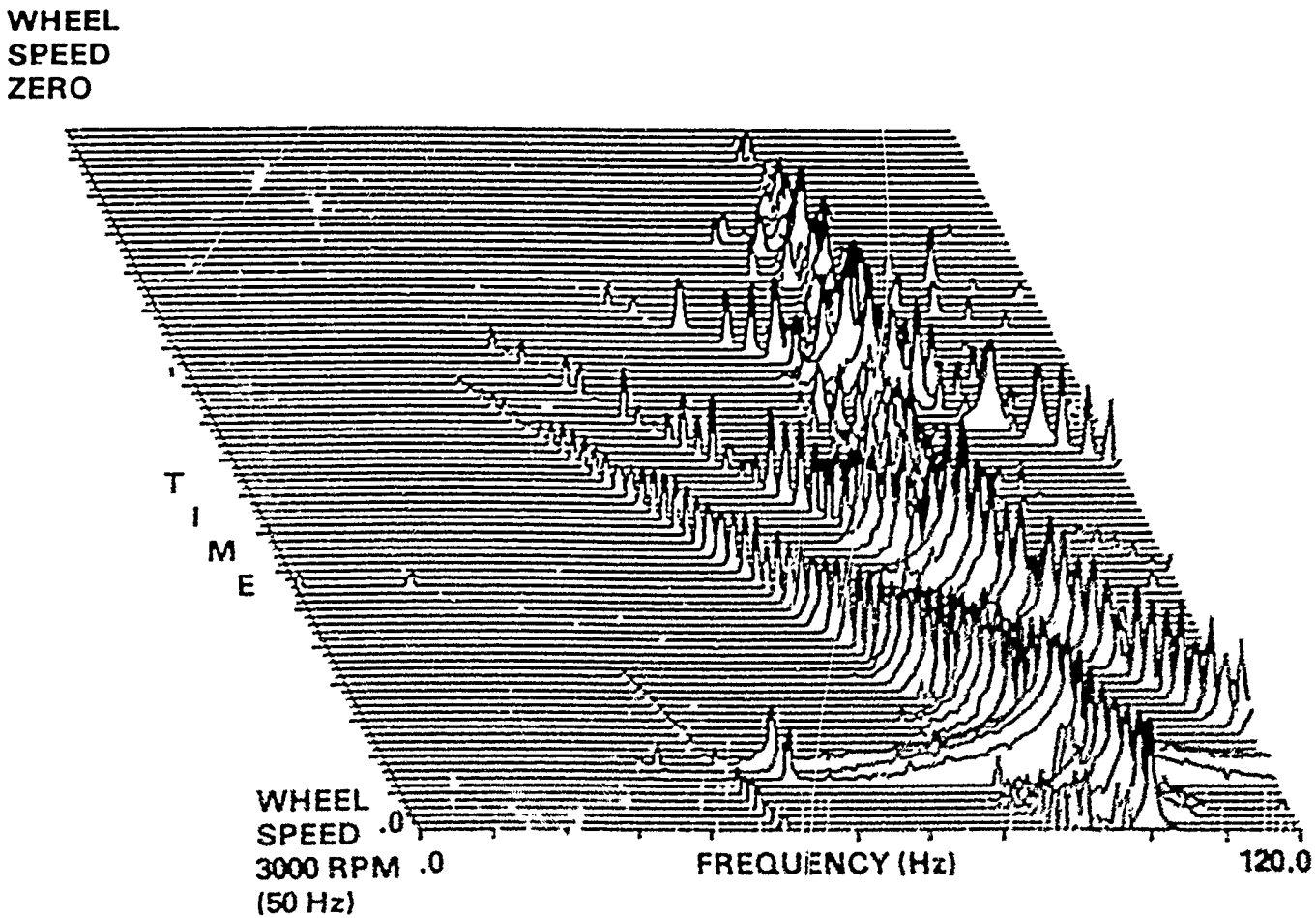


Figure 12

ISOLATED
(WIRE ROPE ISOLATOR)
REACTION WHEEL AXIAL FORCE
(.284 LB PEAK)

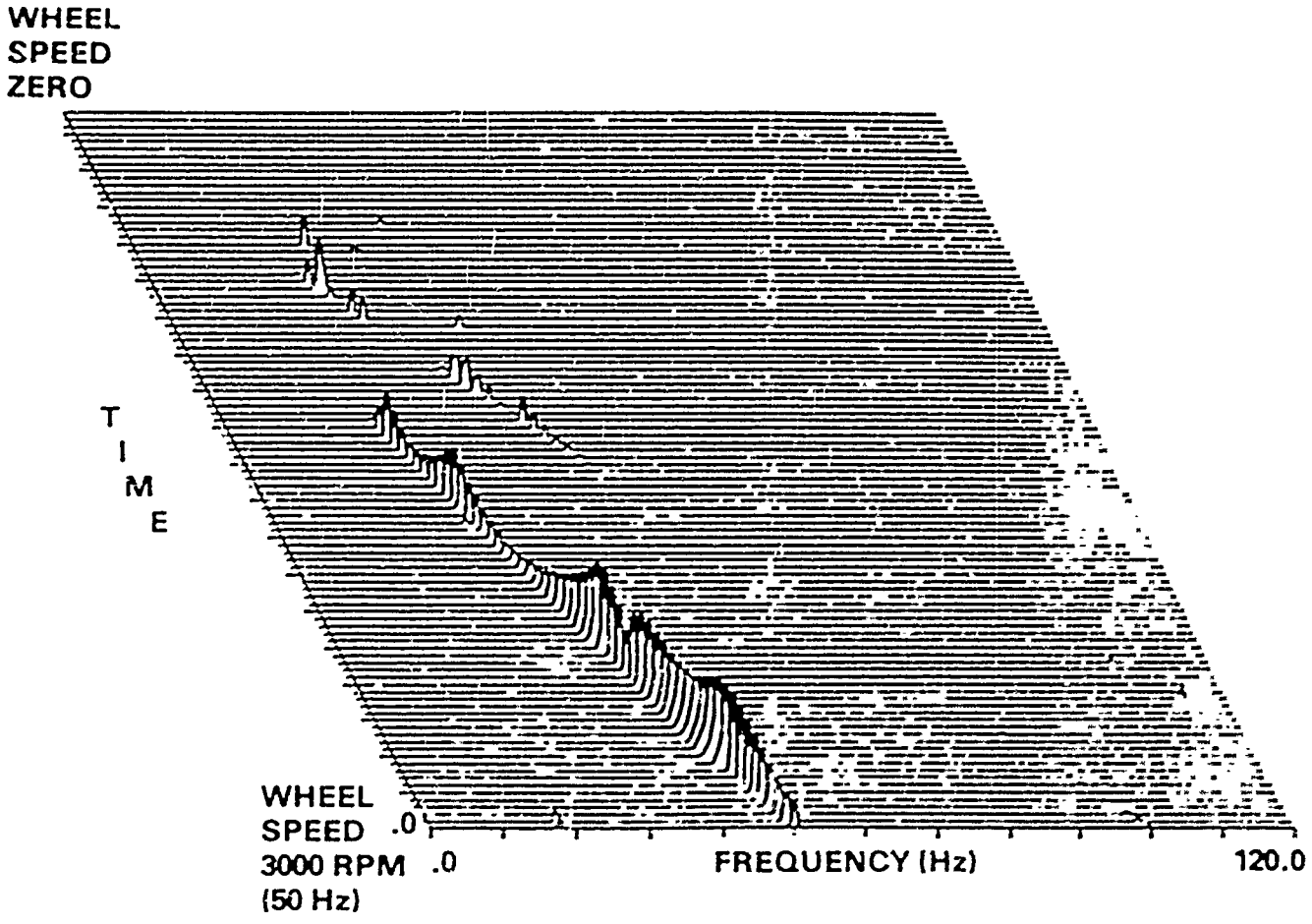


Figure 13

ISOLATED
(SPERRY VISCOUS ISOLATOR)
REACTION SHEEL AXIAL FORCE
(.052 LB PEAK)
200 cs FLUID

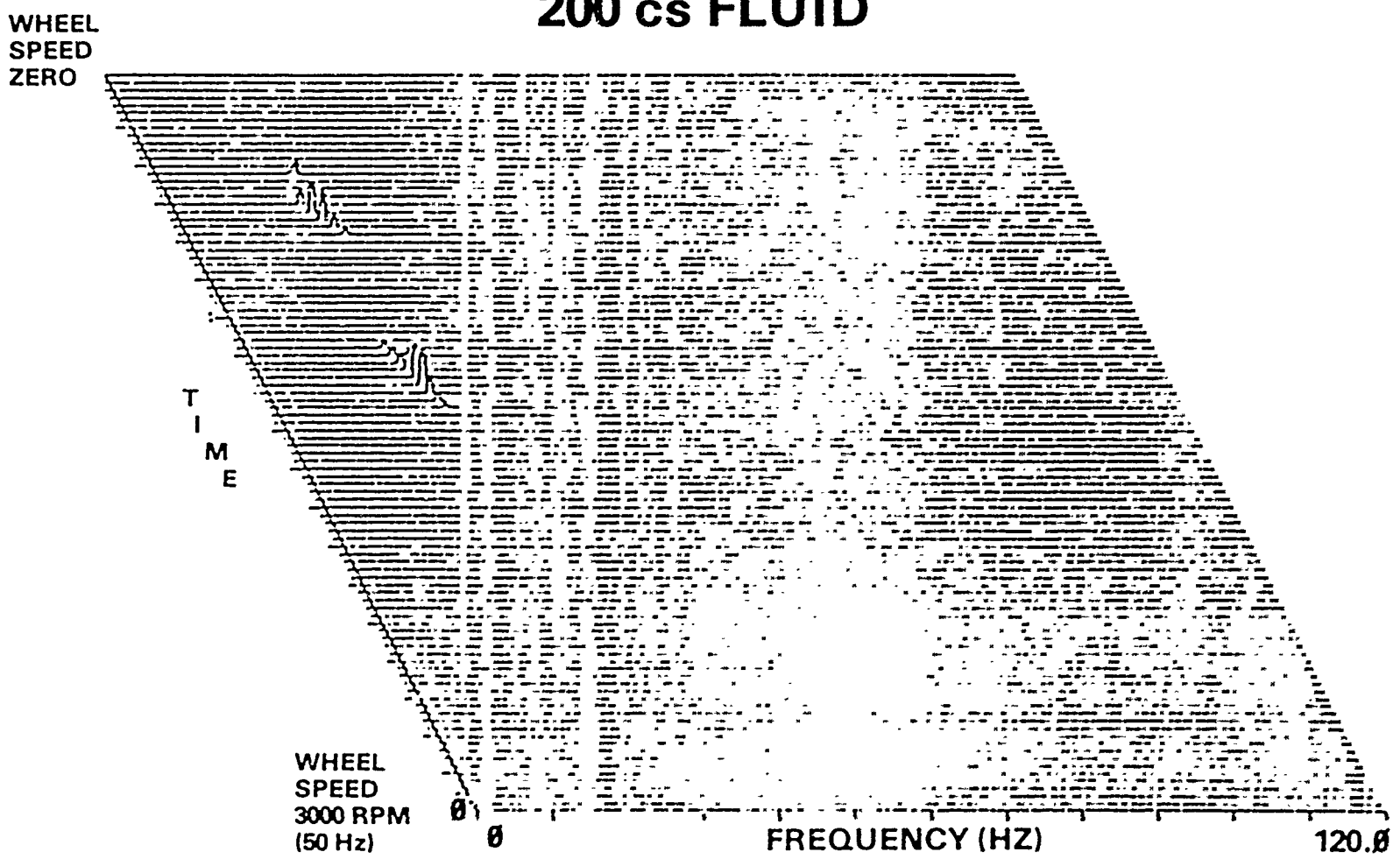


Figure 14

SUMMARY

The Hubble Space Telescope is a spacecraft with unique sensitivity to vibration disturbances. Its Reaction Wheel Assemblies cause coherent frequency disturbances in the millipound range. There are many harmonics of wheel speed and the disturbances are proportional to the square of wheel speed. A passive isolation system was developed to attenuate the higher frequency disturbances. The isolators utilize a metal spring in parallel with a viscous fluid damper, providing independent, deterministic control of the stiffness and damping characteristics. Second order roll-off of the transfer characteristic is obtained due to the volumetric spring rate of the isolator. Stiffness and damping were found constant over a disturbance amplitude range from .2 X 10-6 to .04 inch of input amplitude. Damping is a function of temperature but for this application no compensation was required. The design has been space qualified and subjected to four times life fatigue testing. Component testing has demonstrated greater than two orders of magnitude reduction in peak axial force transmitted by an RWA. Ground testing has been conducted with the spacecraft suspended by cables from three air bags. Frequency response measurements of vehicle angle due to torque commanded have verified the flexibility of the isolators does not compromise the attitude control loop.

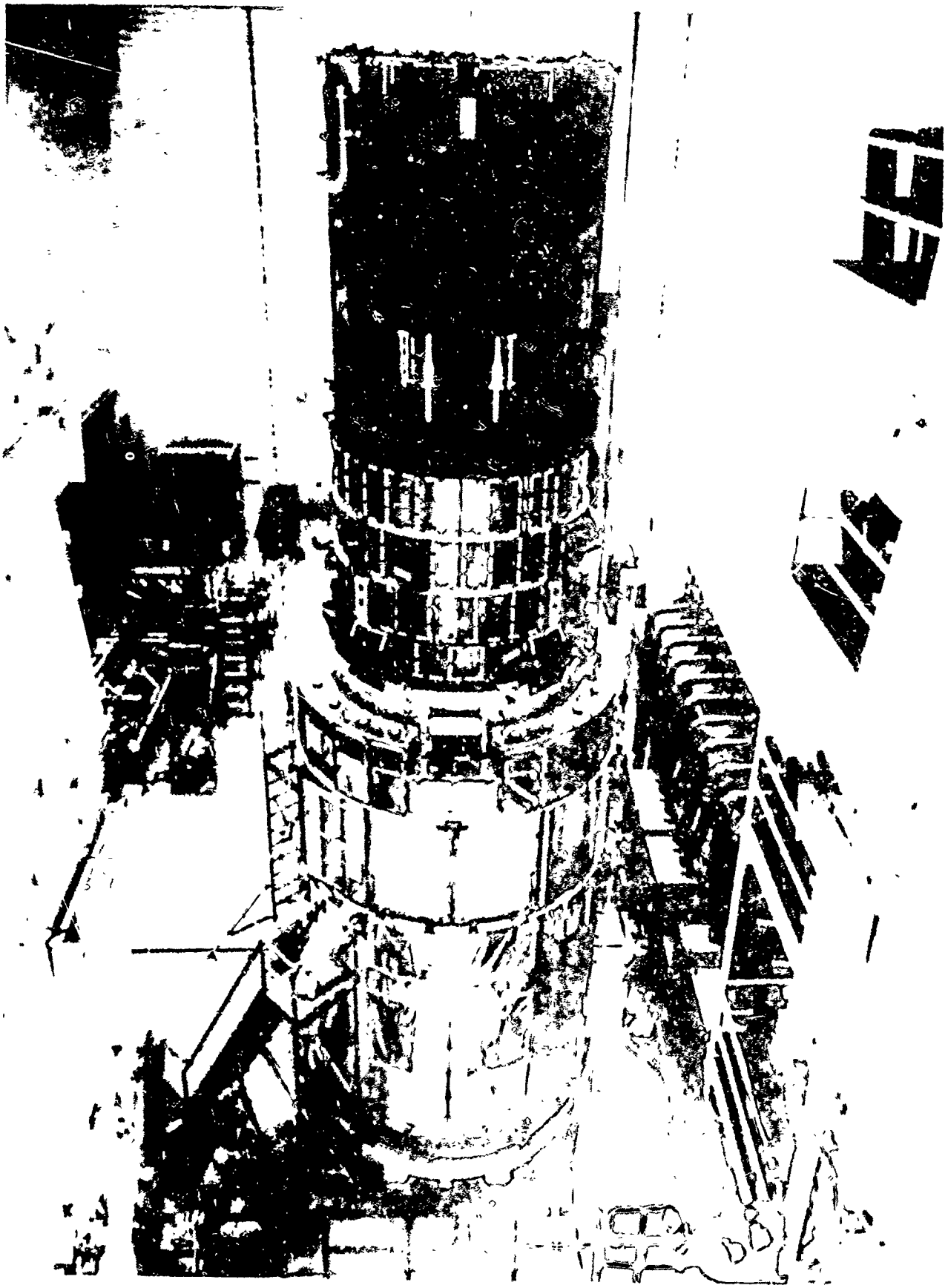


Figure 15

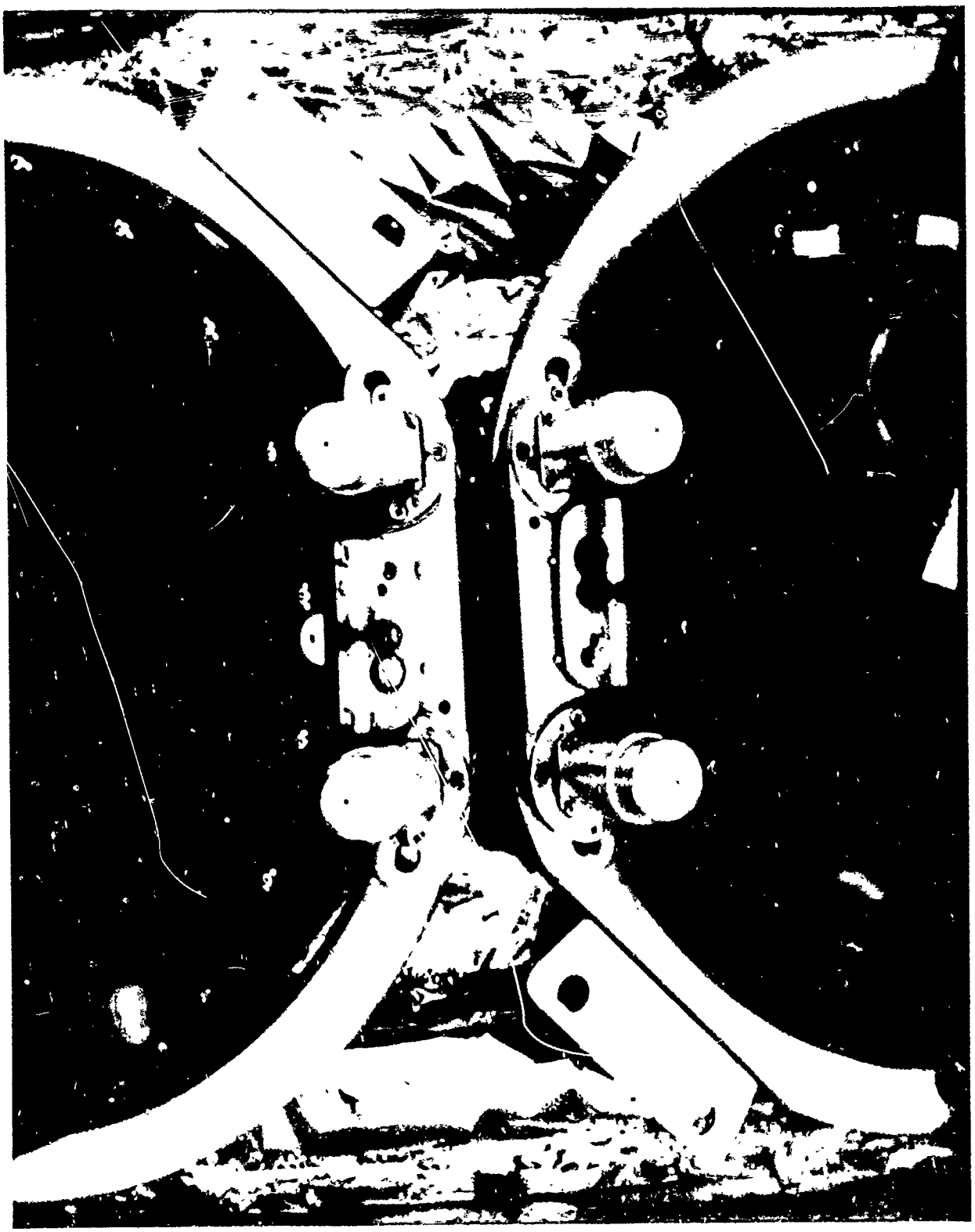


Figure 16

Stress Technology Incorporated
1800 Brighton-Henrietta Town Line Road
Rochester, New York 14623

GASDYNAMIC DAMPING PROPERTIES OF STEAM TURBINE BLADES

Neville F. Rieger
Technical Manager

ABSTRACT

A theory for determining the gasdynamic damping values of turbine blades is presented, which has special application to steam turbine blades. This theory is based on the pumping work which is done on the main gas stream by such blades during their vibration. This theory is suitable for blades of any airfoil cross-section under non-separated flow conditions, during any blade mode of vibration. Knowledge of the power output of a typical blade is needed, together with details of the blade mode shape. Details of the theory are given, together with a simple application to a practical case.

Paper presented at the Vibrations Damping Workshop II, sponsored by Air Force Wright Aeronautical Laboratories. Workshop held at the Riviera Hotel, Las Vegas, Nevada, March 5-7, 1986.

INTRODUCTION

This paper presents a general theory for the prediction of gasdynamic damping of turbine blades. The contribution of gasdynamic damping to the suppression of blade resonant vibrations is widely recognized, though few attempts appear to have been made to evaluate its magnitude in practice. To some extent this may be due to difficulties which surround the development of a satisfactory predictive theory for damping in turbine blades. These difficulties arise from the obscure and variable structural assembly conditions with which the blades are secured to the disk, and they are also due to the lack of solid test data to guide the application of conventional damping theories to structural components within the turbine environment. Gasdynamic damping is often seen by turbine engineers as a minor contributor to the small overall damping values which blade systems possess. It is argued that such minor damping is not worth considering, as its value falls within the error band for structural damping. Specific values for gasdynamic damping are, however, difficult to obtain to test this idea.

More generally, it appears that the mechanism of gasdynamic damping itself is not widely understood, and discussions of this mechanism are not readily located within the subject literature. For these reasons the theory presented here is comprehensive in nature, to address the need for a discussion of the mechanics of gasdynamic damping, and to provide a procedure for obtaining numerical values of gasdynamic damping coefficients for particular stage geometry and power level details. The theory presented is suitable for the computer analysis of general blade geometries. It is shown that the gasdynamic damping mechanism is viscous and linear in nature for the relatively small vibration amplitudes associated with turbine blades.

PREVIOUS WORK

There appears to have been little previous work published in the open literature on the gasdynamic damping properties of steam turbine blades. Legendre [1], [2], presented two surveys of aerodynamic damping between 1967 and 1972. These surveys were directed toward compressor blades, with some reference to turbine blades. Hammons [3] included gasdynamic damping in his computer analyses of decay of torsional oscillations in turbine-generator systems, but gave no details of the theory upon which his coefficients were based. Subsequent work by Rieger [4] showed close correlation between Hammon's results and the theory described herein.

An extensive literature exists worldwide on the gasdynamic properties of compressor blades, which in recent years has focused on damping and dynamic response of long fan stage blades. This literature is primarily concerned with the influence of all primary damping sources, including the likely damping contributions of special devices, to the prediction of the instability threshold for such blades (rotating stall, flutter). It is less concerned with the identification of damping coefficients under the stable, forced vibration conditions addressed in this paper, although

some gasdynamic damping data for selected airfoil operating conditions has been presented: see Legendre [1], [2], Fleeter [5], and others. The results obtained by these authors are in general accordance with the numerical values for gasdynamic damping presented in this paper. Further work on gasdynamic damping is needed, to compare predicted damping values with test data from steam turbine blades.

NOTATION

A,B	Integral Angles
C	Velocity Damping
D	(Superscript) Dynamic Component
F	Blade Force
$\underline{F}$	Force Vector
L	Length of Blade
N	Speed, rpm
S	(Superscript) Steady Component
$\underline{T}$	Torque Vector
W	Work Done
$\underline{i}$, $\underline{j}$, $\underline{k}$	Unit Vectors
m	Modal Response Harmonic
o	Excitation Harmonic
p	Pressure
$\underline{p}$	Pressure Vector
$\underline{q}$	Lift Force Vector
r	Radius
s	Blade
t	Time
u	Amplitude of Vibration
$\dot{u}$	Velocity of Vibration

$\underline{z}$	Radial Coordinate
α	Constant
γ	Frequency Rad/Sec
λ	Phase Angle Between Force and Displacement
$\underline{\omega}$	Disk Rotational Speed Vector
ϕ	Phase Angle From Time Datum
θ	Angle of Rotation
$\dot{\theta}$	Angular Velocity

THEORY

Consider the elemental section ds.dz of the airfoil surface shown in figure 1 which is situated at radius z from the axis of rotation. The net lift force $\underline{q}$ which acts on this surface during operation arises from the variation of the pressure $\underline{p}$ around this surface, and is given by:

$$\underline{q} = \oint \underline{p}\ ds.dz$$

If the gas pressure $\underline{p}$ contains both a steady component $\underline{p}^S$ and a fluctuating component $\underline{p}^D \sin\gamma t$ of frequency γ, the net lift force per unit length can be written as:

$$\underline{q} = \oint (\underline{p}^S + \underline{p}^D \sin \gamma t)\ ds.dz$$

$$= \underline{q}^S + \underline{q}^D \sin \gamma t$$

where $$\underline{q}^S = \underline{q}_T^S + \underline{q}_A^S = q_T^S\, \underline{i} + q_A^S\, \underline{j}$$

$$\underline{q}^D = \underline{q}_T^D + \underline{q}_A^D = q_T^D\, \underline{i} + q_A^D\, \underline{j}$$

and $\underline{i}$ and $\underline{j}$ are unit vectors aligned as shown in figure 2.

More generally, the blade is responding to a forcing spectrum which contains m harmonic components. The net gas force per unit length of blade is then:

$$\underline{q} = \underline{q}^S + \sum \underline{q}^D_m \sin (\gamma_m t + \phi_m)$$

and ϕ_m is the phase angle of the nth harmonic referred to some arbitrary time datum.

The blade responds to this forcing in each of its n modes of vibration.

The blade amplitude of vibration at radius z may be written:

$$\underline{u} = \underline{u}^S + \sum_{m=1} \sum_{n=1} \underline{u}^D_{mn} \sin (\gamma_m t + \phi_m - \lambda_{mn})$$

where λ_{mn} is the phase angle between the mth forcing harmonic and the nth modal amplitude.

The blade velocity $\dot{\underline{u}}$ at radius z is then:

$$\dot{\underline{u}} = \dot{\underline{u}}^S + \sum_{m=1} \sum_{n=1} \gamma_m \, u^D_{mn} \cos (\gamma_m t + \phi_m - \lambda_{mn})$$

$$= \underline{\omega}^S z + \sum_{m=1} \sum_{n=1} \gamma_m \, u^D_{mn} \cos (\gamma_m t + \phi_m - \lambda_{mn})$$

where $\underline{\omega}^S$ is the steady angular velocity of rotation of the rotor.

The torque $\underline{T}$ about the axis of rotation due to the total lift force $\underline{F}$ is given by:

$$\underline{T} = \underline{F} \times \underline{z} = (F_T \underline{i} + F_A \underline{j}) \times (r \, \underline{k})$$

$$= T_A \underline{i} - T_T \underline{j}$$

The total force due to the gas load $\underline{q}$ on the blade is:

$$\underline{F} = \int_{r_o}^{r_o+L} \underline{q} \, dz = \int_{r_o}^{r_o+L} \{q^S(z) + \sum_{m=1} q^D_m (z) \sin (\gamma_m t + \phi_m)\} \, dz$$

The work done per cycle due to the total torque $\underline{T}$ oscillating through the total angle θ is given by:

$$W = \oint \underline{T} \cdot d\underline{\theta} = \oint T \cdot \frac{d\theta}{dt}\, dt = \oint \underline{T} \cdot \dot{\theta}\, dt$$

$$= \oint (\underline{F} \times \underline{z}) \cdot (\dot{\underline{u}} \times \frac{\underline{1}}{z})\, dt = \oint \underline{F} \cdot \dot{\underline{u}}\, dt$$

Substituting gives:

$$W = \frac{1}{\gamma_m} \int_0^{2\pi} \left[\int_{r_o}^{r_o+L} (\underline{q}^S(z) + \sum_{m=1} \underline{q}_m^D(z) \sin(\gamma_m t + \phi_m))\, dz \right] \cdot$$

$$\left[\dot{u}^S(z) + \sum_{m=1} \sum_{n=1} \gamma_m \underline{u}_m(z) \cos(\gamma_m t + \phi - \lambda_{mn}) \right] d(\gamma_m t)$$

$$= W^S(z) + W^D(z)$$

where $W^S(z)$ is the steady component, and $W^D(z)$ is the harmonic component of the total work. Considering $W^S(z)$, and writing $\underline{q}^S(z) = q_t^S(z)\underline{i}$ for the work-producing component, and $\underline{\dot{u}}^S(z) = \omega^S z\underline{i}$ for the steady velocity gives, upon expansion:

$$W^S(z) = \frac{1}{\gamma_m} \int_0^{2\pi} \left[\int_{r_o}^{r_o+L} q_t^S(z)\underline{i}\, dz \right] \cdot \left[\omega^S z\underline{i} \right] d(\gamma_m t)$$

For the simplest case $q_t^S(z) = q_t^S$, i.e., constant along the blade length. Integrating gives:

$$W^S(z) = \frac{2\pi}{\gamma_m} q_t^S L\, \omega^S \left(r_o + \frac{L}{2}\right)$$

The period of integration $\gamma_m t$ is arbitrary and so may be extended to $\omega^S t$, the duration of one revolution of the shaft, i.e., one work-cycle. In this manner, the steady-state work expression becomes:

$$W^S(z) = 2\pi\ (q_t^S L)(r_o + \frac{L}{2})$$

which is the product of the steam force in the direction of motion times the distance moved in the direction of motion during one revolution, measured at the point of application of this force, as would be expected from elementary considerations.

The expression for the harmonic work term $W^D(z)$ is:

$$W^D(z) = \frac{1}{\gamma_m} \int_0^{2\pi} \int_{r_o}^{r_o+L} \sum_{m=1} q_m^D(z) \sin(\gamma_m t + \phi_m) \cdot$$

$$\sum_{m=1} \sum_{n=1} \gamma_m \underline{u}(z)_{mn} \cos(\gamma_m t + \phi_m - \lambda_{mn})\ dz.d(\gamma_m t)$$

Each of the remaining products in the work integral involves terms which are constant in time, and which therefore represent zero harmonic work. The terms $q_m^D(z)$ and $u(z)_{mn}$ respectively describe the unit vector force and the vector velocity at location z along the blade. Expanding both terms into their components, and taking the scalar product gives the following work integrals for the tangential and axial directions:

$$W_T^D(z) = \frac{1}{\gamma_m} \int_0^{2\pi} \int_{r_o}^{r_o+L} \sum_{m=1} q_{T,m}^D(z) \sin(\gamma_m t + \phi_m).$$

$$\sum_{m=1} \sum_{n=1} \gamma_m\ u_{T,mn}(z) \cos(\gamma_m t + \phi_m - \lambda_{mn})\ dz\ d(\gamma_m t)$$

$$W_A^D(z) = \frac{1}{\gamma_m} \int_0^{2\pi} \int_{r_o}^{r_o+L} \sum q_{A,m}^D(z) \sin(\gamma_m t + \phi_m).$$

$$\sum_{m=1} \sum_{n=1} \gamma_m \, u_{A,mn}(z) \cos (\gamma_m t + \phi_m - \lambda_{mn}) \, dz \, d(\gamma_m t)$$

Recalling that:

$$\int_0^{2\pi} \sin A \cos (A - B) \, dA = \pi \sin B$$

allows the above expressions for tangential and axial harmonic work to be reduced to:

$$W_T^D(z) = \pi \int_{r_o}^{r_o+L} \sum_{m=1} q_{T,m}^D(z) \sum_{m=1} \sum_{n=1} u_{T,mn}(z) \, dz \, . \sin \lambda_{mn}$$

$$W_A^D(z) = \pi \int_{r_o}^{r_o+L} \sum_{m=1} q_{A,m}^D(z) \sum_{m=1} \sum_{n=1} u_{A,mn}(z) \, dz \, . \sin \lambda_{mn}$$

These expressions indicate that gasdynamic damping in a given mode depends upon the phase angle λ_{mn} between the nth gas harmonic forcing component and the response of the blade in the nth mode. For all practical cases the gasdynamic damping is evidently negligible unless the phase angle $\lambda_{mn} = \pi/2$, i.e., blade resonance exists between the forcing harmonic m and the vibration mode n.

The magnitude of the resonant gasdynamic damping may therefore be determined mode by mode for individual resonant modes, once the radial distributions of the tangential and axial forcing $q_T^D(z)$ and $q_A^D(z)$ are known, together with the associated mode shapes $u_T(z)$ and $u_A(z)$.

With the above concepts included the general work integrals for each resonant mode n become:

$$W_{T,mn}^D = \pi \int_{r_o}^{r_o+L} q_{T,m}^D(z) \, u_{T,mn}(z) \, dz$$

$$W^D_{A,mn} = \pi \int_{r_o}^{r_o+L} q^D_{A,m}(z)\, u_{A,mn}(z)\, dz$$

To establish the practical meaning of these expressions, consider the simple case of the uniform cantilever blade shown in figure 1 which rotates at ω^S rad/sec while vibrating in its lowest mode at γ_1 rad/sec. Assuming that the first mode of vibration in the tangential direction has the form:

$$u_{T,1}(z) = u^0_{T,1}\left(1 - \cos\frac{\pi z}{2L}\right)$$

where u^0_T is the vibration amplitude of the tip of the cantilever In this instance the blade is encastre' at its attachment to the disk, and so,

$$u_{A1}(0) = 0.$$

For convenience the gasdynamic force per unit length along the blade is assumed to be constant, i.e., $q^D_T(z) = q^D_T = \text{Const.}$ The work integral is therefore obtained between 0 and L, as the cantilever base has no harmonic motion. Then

$$W^D_{T,1} = \pi \int_0^L q^D_T\, u^0_{T,1}\left(1 - \cos\frac{\pi z}{2L}\right) dz$$

$$= 0.3634\, \pi\, q^D_T\, L\, u^0_{T,1}$$

This expression indicates that the work product of the total excitation harmonic force $q^D_T L$ and the blade tip vibration amplitude $u^0_{T,1}$ must be modified by the factor 0.3634, to allow for the effect of the mode shape in assessing the damping work of this case.

MAGNITUDE OF HARMONIC GASDYNAMIC FORCE

The magnitude of the gasdynamic damping force which develops in response to blade oscillatory motions may be determined from the stage power (or torque vs. speed) curve. A typical stage power curve is shown in figure

3, in which the constant power characteristic shown is described by the relation:

$$\alpha P = TN,$$

where P is the output horsepower, T is the stage driving torque in lb.in., and N is the shaft speed in rpm. With these units the constant α has the value 63025.

Under conditions which involve small fluctuations of speed and torque but with constant power output, the differential relationship between these quantities is:

$$\alpha dP = NdT + TdN$$

For constant P, dP = 0 and so:

$$0 = NdT + TdN,$$

i.e., $$\frac{dT}{dN} = -\frac{T}{N} = -\frac{\alpha P}{N^2},$$

thus $$dT = -\frac{T}{N}\,dN = -9.55\,\frac{T}{N}\,d\dot{\theta},$$

$$= -C_S^{\theta}\,d\dot{\theta},$$

where $$C_S^{\theta} = 9.55\ T/N$$

The fluctuating blade torque is governed by oscillations in the gasdynamic force along the length of the blade. For convenience this force may be referred to the blade mid-height by writing

$$dT = (r_o + \frac{1}{2}L)\,dF = -C_s^{\theta}\,d\dot{\theta}$$

$$= -C_S^{\theta}\,\dot{u}_T^D\,(L)\ /\ (r_o + L),$$

i.e., $$dF = -C_S^u\,\dot{u}_T^D(L) = -C_S^u\,\gamma\,u_T^D(L),$$

where $$C_S^u = C_S^\theta \,/\, (r_o + \tfrac{1}{2} L)\ (r_o + L) = 9.55\ \frac{T}{N}\ \frac{1}{(r_o + \frac{1}{2} L)\ (r_o + L)}$$

This expression is suitable for modes in which the maximum modal amplitude occurs at the tip of the blade.

The total gasdynamic force on the blade dF is also given by the expression:

$$dF = \int_{r_o}^{r_o+L} q_D(z)\ z\ dz \,/\, (r_o + \tfrac{1}{2} L)$$

In low-order modes where the blade is motionless at the base, and where the gasdynamic force is of constant magnitude along the blade length, integration gives:

$$dF = q_D L, = - C_S^u\ \gamma\ u_T^D.$$

Recalling the expression for the gasdynamic work and substituting for dF therein gives:

$$W_{T,1}^D = - 0.3634\ \pi\ C_S^u\ \gamma\ \{u_T^D\ (L)\}^2$$

where C_S^u is given by the formula stated above, and $\{u_T^D(L)\}$ is the blade tip amplitude. This shows that the gasdynamic work on the blade is negative, i.e., dissipative, and that the form of the work expression is the same as the well-known form for viscous dissipation, i.e., $W = - (\text{const.})\ \pi\ C_D\ \gamma\ u^2$. A similar expression can be obtained for the axial gasdynamic work $W_{A,1}^D$, once the modal equation $u(z)_{A,1}$ is specified, and the distribution of the gas force along the length of the blade is known. The damping work for higher modes, and for coupled vibrations in both the axial and tangential directions, likewise depends upon the availability of information on the mode shapes, and on the lengthwise gas force distribution.

REFERENCES

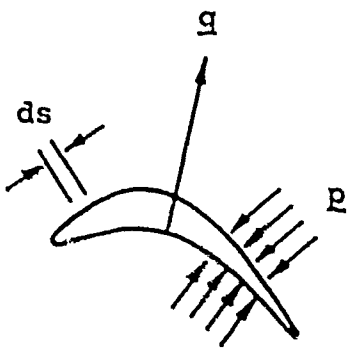
1) Legendre, R., 'Aerodynamic Damping of Compressor Blades and Turbine Buckets,' Proceedings of Colloquium on Turbomachinery , Cambridge (U.K.), July 1967. Published by I.Mech.E., London, pp. 111-116.

2) Legendre, R., Aerodynamic Damping of Two-Mode Vibrations, Colloquium on Flow Research on Blading. Elsevier Publishing Company, 1970, pp. 197-207.

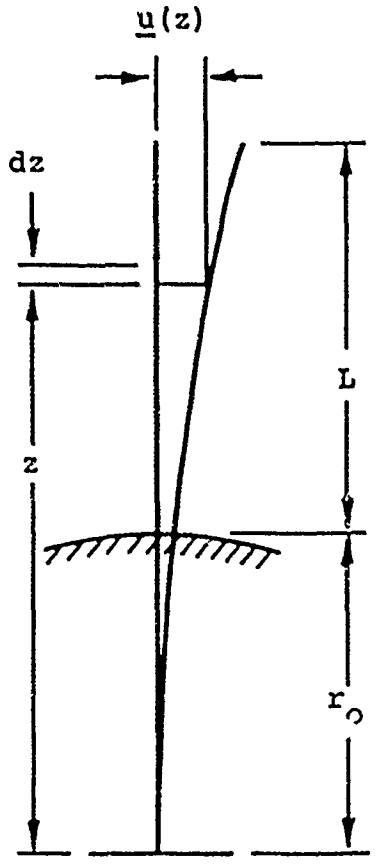
3) Hammons, T. J., 'Accumulative Fatigue Life Expenditure of Turbine Generator Shafts Following Worst-Case System Disturbances,' Transactions IEEE Winter Annual Meeting, Preprint - February 1983.

4) Rieger, N. F., Vibrations of Rotating Machinery - Part 2: Blading and Torsional Vibrations, The Vibration Institute, Clarendon Hills, IL, Chapter 7, p. 130.

5) Fleeter, S., Proceedings, AGARD Conference on High Speed Flow Through Turbomachine Blading.



a. Details of gas loading on airfoil at radius z.



b. Blade geometry on disk.

Figure 1 Blade Loading and Geometry Details

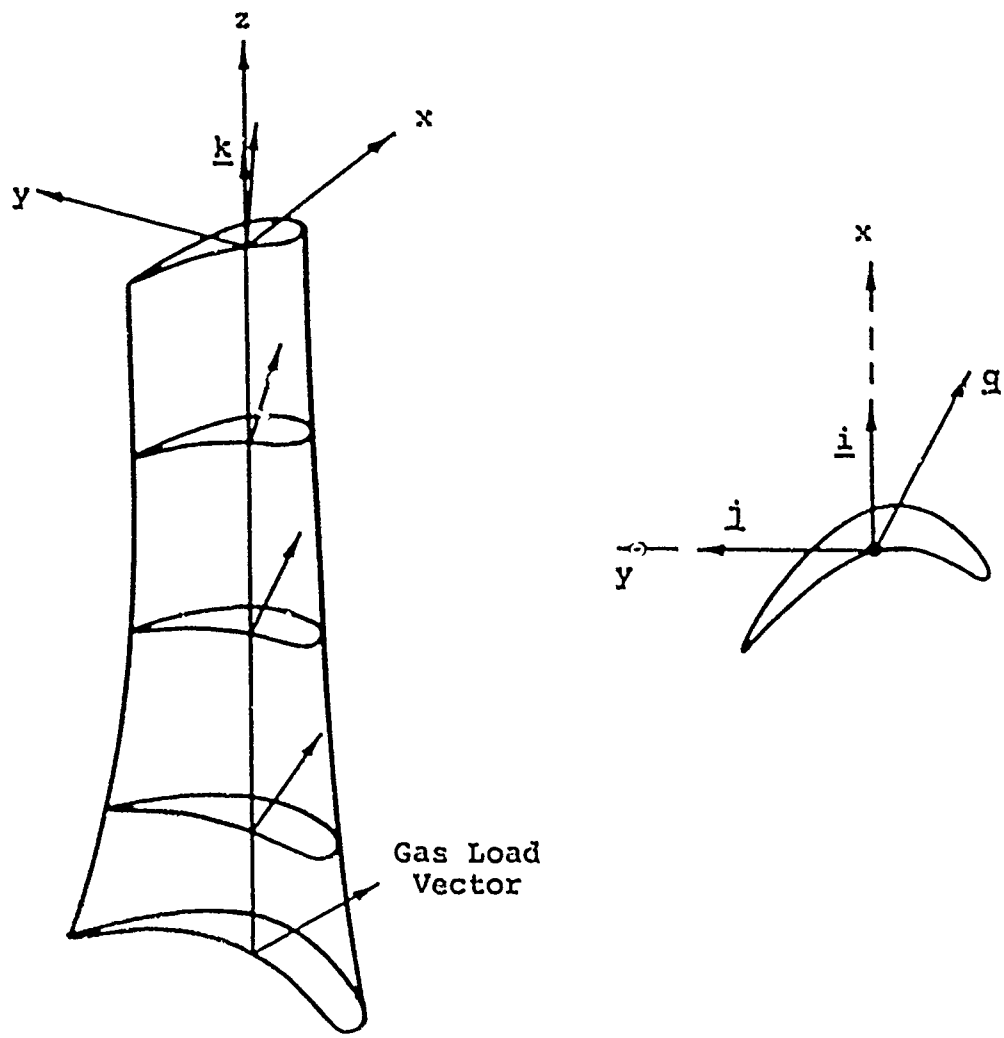


Figure 2 Blade Coordinates and Load Vectors

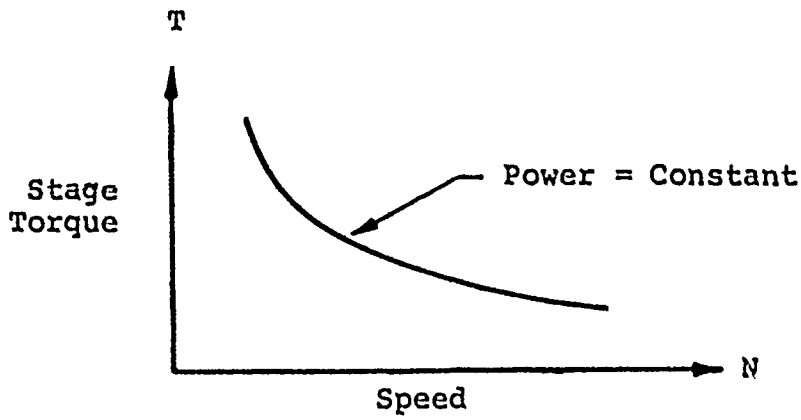


Figure 3 Stage Power Curve

A LAYERED NOTCH FILTER FOR HIGH-FREQUENCY ISOLATION

J. L. Sackman
J. M. Kelly
University of California, Berkeley

and

A. E. Javid
IBM Corporation

ABSTRACT

An efficient method of isolation from high-frequency vibrations is the use of periodically layered composites acting as a mechanical filter. This device is a periodically layered stack of alternating materials with widely different densities and stiffnesses. The working principle of the device is wave reflection, and the device becomes increasingly effective when there is a large impedance mismatch which leads to rapid attenuation of an input wave for certain frequency ranges. This filter acts only in specific frequency bands. At other frequencies, it will transmit the vibratory energy unmodified, thus acting as a mechanical notch filter.

The theoretical development of the mechanical notch filter is based on the theory of waves in periodically layered media. Floquet theory is used to solve the equations for the propagation of plane waves through a laminated system of parallel plates of different materials when the direction of propagation is normal to the plates. Several experiments were conducted to prove the validity of the mechanical notch filter concept. These experiments demonstrated that the theory is correct and that the results have practical application.

1. INTRODUCTION

In the design of machinery the control of undesirable vibrations is frequently handled by the use of isolation concepts. In most cases the frequency of these vibrations is low, e.g. less than 100 Hz, and the principles of vibration isolation for this range of frequency are relatively well understood[1]. In some cases, however, there may be a need to protect very sensitive components from higher frequencies and the standard techniques may not be appropriate due to the presence of wave effects. To deal with high-frequency vibration problems it was suggested by Javid[2] that the device known as a mechanical filter[3-5] be used. This device is a periodically layered stack of alternating materials which have wide differences in density and stiffness. The working principle of the device is wave reflection and the device becomes increasingly effective when there is a large impedance mismatch between materials. La.ge differences in impedance can lead to rapid attenuation of an input wave for certain frequency ranges. This filter acts only in specific frequency bands. At other frequencies it will transmit the vibrations unmodified (as in the case of steady-state vibrations)

The theoretical development of this system is based on the theory of waves in periodically layered media. The equations for the propagation of plane waves through a laminated system of parallel plates of different materials when the direction of propagation is normal to the plates are treated by what is called Floquet theory[4-6] The problem of a shear wave propagating through an infinite stack of plates each of which is infinite in extent allows a very simple solution which can provide insight into the existence of stopping bands and an understanding of the attenuation of a mechanical filter of this kind. An analysis has been given by Lee and Wang[7] and Lee[8] for cells containing two layers and by Karim-Panahi[9] for cells with three layers.

The fact that real filters have plates of finite extent does not appear to affect the response generally, possibly due to the fact that in shear waves the errors introduced by the assumption of infinite plates are due to the presence of shear stresses in the free surfaces at the edge of each plate If the width-to-thickness ratio of each plate is very large, this error will be small. This supposition appears to be supported by the results of the experimental program conducted at IBM. In addition, the theory predicts extremely rapid attenuation of the waves when the frequency of input is in the center of the stopping bands and thus the waves are effectively blocked after only a finite number of layers are traversed. The fact that the real stack is finite, as opposed to infinite as assumed in the theory, seems therefore not to obviate the existence of stopping bands although it may modify their details.

2. THEORETICAL BACKGROUND

In what follows we use terminology common in the theory of periodically layered composites in which each cell, of thickness a, is made up of two layers of different materials. We refer to that layer which is composed of the denser and stiffer material as the filament, and the other as the matrix. The filament layer is taken to be of thickness b and the matrix of thickness $a-b$. The direction of propagation of plane waves through an infinite stack of these cells is normal to the layering and distance is denoted

by x (Figure 1). The displacement in the parallel direction is denoted by $w(x,t)$ and it is assumed that:

$$w(x,t) = u(x)e^{-i\omega t} \tag{1}$$

where ω is the frequency of steady-state oscillatory input. The densities and shear moduli of the filament and matrix materials will be denoted by ρ_f, ρ_m and G_f, G_m.

The only non-zero strain and stress components are:

$$\gamma = \frac{\partial w}{\partial x} \qquad \tau(x,t) = G(x)\gamma(x,t) \tag{2}$$

The equation of motion takes the form:

$$\frac{d}{dx}[G(x)\frac{du}{dx}] + \rho(x)\omega^2 u = 0 \tag{3}$$

The functions $G(x)$ and $\rho(x)$ are periodic functions with period a, the cell thickness, and according to Floquet theory the solution takes the form.

$$u(x) = v(x)e^{iqx} \tag{4}$$

where $v(x)$ is periodic with period a, and q is a constant wave number. The displacement $w(x,t)$ thus takes the form of a Floquet wave propagating through the stack:

$$w(x,t) = v(x)e^{i(qx-\omega t)} \tag{5}$$

The second order differential equation requires two boundary conditions, which in the Floquet theory are supplied by the quasi-periodic boundary conditions:

$$u(\frac{a}{2}) = u(-\frac{a}{2})e^{iqa} \tag{6}$$

$$u'(\frac{a}{2}) = u'(-\frac{a}{2})e^{iqa} \tag{7}$$

It should be noted that these equations arise from the periodicity of $v(x)$ and the requirement of continuity of displacement and shear stress across cell boundaries. The ordinary differential equation (3) and the quasi-periodic boundary conditions constitute a Sturm-Liouville (or eigenvalue) system. Here, the eigenvalue is the wave number q.

The eigenvalue equation is most conveniently obtained by considering two linearly independent solutions of equation (3), which we can denote by u_1 and u_2, and taking the eigenfunction as $u_1 + \alpha u_2$ where α is a constant to be determined from the boundary conditions. Since the functions G and ρ in (3) are constant in each layer in a cell, the basic solutions u_1 and u_2 take particularly simple forms. In the filament, the first solution u_1 is taken to be:

$$u_1 = \cos\frac{\omega x}{c_f} \qquad -\frac{b}{2} \le x \le \frac{b}{2} \tag{8}$$

where $c_f = \sqrt{G_f/\rho_f}$. In the matrix material, $b/2 \le x \le a/2$, and u_1 takes the form:

$$u_1 = A^+\cos\frac{\omega x}{c_m} + B^+\sin\frac{\omega x}{c_m} \tag{9}$$

where A^+, B^+ are determined from continuity of displacement and stress at the interface between filament and matrix at $x = b/2$. These lead to the solution for u_1 for the matrix in the form:

$$u_1 = \cos\frac{\omega b}{2c_f}\cos\frac{\omega(x-\frac{b}{2})}{c_m} - p\sin\frac{\omega b}{2c_f}\sin\frac{\omega(x-\frac{b}{2})}{c_m}$$

$$\frac{b}{2} \leq x \leq \frac{a}{2} \tag{10}$$

where

$$p = \frac{G_f}{c_f} \times \frac{c_m}{G_m} = \frac{\rho_f c_f}{\rho_m c_m} \tag{11}$$

The solution for u_1 in the region $-(a/2) \leq x \leq -(b/2)$ is given by the above using symmetry.

The second solution is obtained by taking:

$$u_2 = \sin\frac{\omega x}{c_f} \qquad -\frac{b}{2} \leq x \leq \frac{b}{2} \tag{12}$$

in the filament material and using the same technique to extend it to the matrix material in the regions $b/2 \leq x \leq a/2$, $-a/2 \leq x \leq -b/2$. When we take both solutions in the form

$$u = u_1 + \alpha u_2 \tag{13}$$

and use the first quasi-periodic boundary condition we obtain α and the solution for u in the form:

$$u = \cos\frac{\omega x}{c_f} + \frac{i\left[\cos\frac{\omega b}{2c_f}\cos\frac{\omega(a-b)}{2c_m} - p\sin\frac{\omega b}{2c_f}\sin\frac{\omega(a-b)}{2c_m}\right]}{\left[\sin\frac{\omega b}{2c_f}\cos\frac{\omega(a-b)}{2c_m} + p\cos\frac{\omega b}{2c_f}\sin\frac{\omega(a-b)}{2c_m}\right]} \times \tan\frac{qa}{2}\sin\frac{\omega x}{c_f} \tag{14}$$

for the filament region $-b/2 \leq x \leq b/2$ with a corresponding expression in the matrix region. When these two solutions are substituted into the second quasi-periodic boundary condition, we obtain the final eigenvalue equation relating the eigenvalue q to the input frequency ω:

$$\cos qa = \cos\frac{\omega(a-b)}{c_m}\cos\frac{\omega b}{c_f} - \frac{1}{2}(p + \frac{1}{p})\sin\frac{\omega(a-b)}{c_m}\sin\frac{\omega b}{c_f} \tag{15}$$

It is this basic equation which reveals the existence of a wave-blocking filter. In order that the composite system transmit waves of a specific frequency ω, the eigenvalue q must be real. If for some value of ω the right-hand side of equation (15) is of magnitude greater than 1, then q will be complex and the imaginary part will give a solution in the form of a decaying exponential. Under these circumstances, a wave will penetrate in effect only a finite distance into the stack. It is clear from equation (15) that if p is large enough, the value of the right-hand side can exceed 1 for a wide range of ω. The design of the filter follows from this equation and a detailed

analysis of equation (15) is given in the next section.

3. APPLICATION TO FILTER DESIGN

In the design of practical filters, it is essential that there be a large impedance mismatch between the two materials and this means that the parameter p in

$$\cos qa = \cos\frac{\omega(a-b)}{c_m}\cos\frac{\omega b}{c_f} - \frac{1}{2}\left(p+\frac{1}{p}\right)\sin\frac{\omega(a-b)}{c_m}\sin\frac{\omega b}{c_f} \tag{15}$$

will be very large. We will also be considering very thin layers of either material. It follows that the quantity

$$\frac{\omega b}{c_f} = \pi\left|\frac{\frac{\omega}{2\pi}}{\frac{c_f}{2b}}\right| \tag{16}$$

is the ratio of two frequencies: the first, $\omega/2\pi$, is the input frequency, and $c_f/2b$ is the natural frequency of the first thickness shear mode of the filament layer. This ratio will be very small in most realistic designs and we thus will approximate $\sin\omega b/c_f$ by $\omega b/c_f$ and $\cos\omega b/c_f$ by 1. If $1/p$ with respect to p is neglected, then equation (15) becomes:

$$\cos qa = \cos\frac{\omega(a-b)}{c_m} - \frac{1}{2}p\,\frac{\omega b}{c_f}\sin\frac{\omega(a-b)}{c_m} \tag{17}$$

It is convenient to rewrite this equation in the form:

$$\cos qa = \cos z - \alpha z \sin z \tag{18}$$

where

$$\alpha = \frac{1}{2}\frac{\rho_f b}{\rho_m(a-b)} = \frac{1}{2}\frac{\rho_f}{\rho_m}S \tag{19}$$

$$S = \frac{b}{(a-b)} \tag{20}$$

$$z = \frac{\omega(a-b)}{c_m} = \pi\left|\frac{\frac{\omega}{2\pi}}{\frac{c_m}{2(a-b)}}\right| \tag{21}$$

In the above, S is a thickness ratio (viz., the ratio of the thickness of the filament layer to that of the matrix layer), and z is essentially the ratio of the input frequency $\omega/2\pi$ to that of the natural frequency of the first thickness shear mode of the compliant layer, $c_m/2(a-b)$. For the regime of practical interest, equation (18) is the key relationship and the basis for the design of the band-stopping mechanical filters.

The design concepts involved are quite straightforward. Given that one wishes to block frequencies in a certain band, the material properties and the thicknesses of the layers making up each cell must be chosen so that the right-hand side of equation (18) has a magnitude greater than 1 in the frequency band of interest. Thus, the edges of the stop bands will be given by the condition that $\cos qa = -1$ or $+1$. We see from the right-hand side of

equation (18) that for small values of z (corresponding to small values of ω), $\cos qa$ will be positive and slightly less than 1. As ω (and therefore z) increase, $\cos qa$ diminishes, becoming negative, reaching the value -1, which is the start of the first stop band, and then decreasing from -1 to a minimum and increasing back to -1 when $z = \pi$, which is the end of the first stop band. As ω (and z) increase, $\cos qa$ will become positive, then attain the value +1, which is the start of the second stop band, then increase from +1 to a maximum, and then decrease back to +1 at $z = 2\pi$, which is the end of the second stop band. In this way, an infinite sequence of stop bands is generated, each terminating at an integral multiple of π.

The start of each stop band must be determined numerically from equation (18). In practice, we would be interested in only the lowest few bands, and also in designing the system in such a way that the start of the first stop band is as low as possible. This will produce the widest possible first stop band.

Considering the stop bands produced by $\cos qa = -1$, the corresponding values of z are, from equation (18), given by roots of:

$$\alpha z \sin z = 1 + \cos z \tag{22}$$

shown graphically in the sketch, Figure 2. For the stop bands produced by $\cos qa = +1$, we get the equation:

$$\alpha z \sin z = -1 + \cos z \tag{23}$$

whose roots are also shown in Figure 2.

The specific roots giving the beginning of each stop band may be determined numerically by a relatively simple procedure. However, for certain conditions it is possible to obtain closed-form approximations for the first root. For example, if α is small, the first band is narrow and the first root for z is close to π and a simple approximation is

$$z = \pi(1 - 2\alpha) \tag{24}$$

More pertinent to filter design are large values of α; here, the band is wide and the first root is approximately given by:

$$z = \sqrt{2/\alpha} \tag{25}$$

Most real filter designs will involve intermediate values of α, necessitating a numerical analysis of equation (18). Examples will be given in a subsequent section.

In any real filter we will have a finite (and probably a relatively small) number of cells. It is important to know how much decay will take place as the wave propagates through the filter. For a filter of infinite extent this is given by q_I, the imaginary part of $\cos qa$ when this has a magnitude greater than 1. For a filter of finite extent, wave reflections will occur at the free surfaces at the top and bottom of the filter so that the q_I mentioned above will no longer be the exact measure of the decay. Nevertheless, we can use this as an indicator of how effectively waves are blocked by the finite filter when they are in a stopping band. For a fixed-frequency ω and $\cos qa < -1$, we obtain:

$$q = \frac{\pi}{a} + iq_I \tag{26}$$

where

$$q_f a = \cosh^{-1}[-\cos z + \alpha z \sin z] \tag{27}$$

Since $w(x,t) = v(x)e^{i(qx-\omega t)}$ and $v(x)$ is periodic with period a:

$$\frac{|w(na,t)|_{max}}{|w(0,t)|_{max}} = e^{-nq_f a} \tag{28}$$

where n is the number of cells in the filter. We interpret the left-hand side of equation (28) as measuring the ratio of the maximum of the response at the top of the filter to the maximum of the input at the bottom of the filter. We denote this ratio as $1/R$, where R is the reduction factor associated with the filter. The number of cells required to obtain a reduction of R is thus given by:

$$n = \frac{\ln R}{q_f a} \tag{29}$$

which is an important relationship for filter design. For a given choice of cell materials and geometry, the number of layers can be selected to provide the necessary degree of attenuation, and therefore reduction, at the prescribed frequency. This frequency must lie within the stop band, since when $|\cos qa| \leq 1$, there is no attenuation, and hence no reduction.

The degree of attenuation for fixed n will vary with frequency within the stop band. By determining how the reduction factor R diminishes as ω approaches either edge of the stop band ($R=1$ at any edge of the stop band) we can define the *effective* range of the stop band, i.e. that range of the frequency ω within the stop band for which $R \geq R^*$, where R^* would be the desired degree of reduction for the filter. Once a filter has been designed, it is relatively easy to determine its effective range by a straightforward numerical evaluation of equation (18), also using equation (28). An illustration of this will be given later.

4. EXAMPLE

To verify physically the fundamental phenomenon of interest, namely the existence of stop bands in a periodically layered medium, some experiments were performed at IBM San Jose by Ahmad E. Javid on a block of such material. The block, a square 8 inches on edge in planform, was 13 cells deep. each cell was 1/2 inch thick and consisted of a 3/8 inch thick layer of rubber bonded to a steel layer of 1/8 inch thickness. The properties of these materials were:

$$G_m = 200\ psi \quad , \quad \rho_m = 1.16\ gm/cm^3$$

$$G_f = 12 \times 10^6\ psi \quad , \quad \rho_f = 7.7\ gm/cm^3$$

for the rubber and steel materials, respectively.

Before experiments were commenced at the IBM site, computations were performed to determine the first (lowest frequency) stop band. This required the use of the following quantities:

$$c_m = \sqrt{G_m/\rho_m} = 1358 \quad \text{inches per second}$$

$$c_f = \sqrt{G_f/\rho_f} = 129.1 \times 10^3 \quad \text{inches per second}$$

$$p = \frac{G_f c_m}{G_m c_f} = 631 \gg \frac{1}{p}$$

$$f_f = \frac{c_f}{2b} = 516.5 \times 10^3 \text{ Hz}$$

We expected that the lowest stop band of this system would have a frequency f of order 10^3 Hz. Therefore, $f/f_f \ll 1$, so that we are justified in using the simplified equation (17), or equivalently equation (18), rather than the more complex equation (15). Thus, we have to find the lowest root z of the equation:

$$\cos qa = \cos z - \alpha z \sin z = -1 \tag{30}$$

where α is given by equation (19) and in this case has the value 1.106.

A simple numerical solution of equation (30) by the elementary scheme of the method of chords gives for the lowest root, z, a value of 1.2515, which represents the start of the first stop band. As mentioned previously, the end of the first stop band is given by $z = \pi$. From equation (21), we recall that:

$$f = \frac{\omega}{2\pi} = \frac{z}{\pi} f_m \tag{31}$$

where f is the frequency of vibration in Hz, and

$$f_m = \frac{c_m}{2(a-b)} \tag{32}$$

is the natural frequency of the lowest thickness shear mode of the rubber layer. This yields for the beginning of the first stop band the frequency $f_B = 722$ Hz, and for the end of the first stop band the frequency $f_E = 1808$ Hz. The frequency f_M at the middle of the first stop band is 1265 Hz. Thus, our preliminary estimate that the frequency of the first stop band would be of order 10^3 is correct.

To see how large the attenuation is when the frequency of the vibration f is within the stop band, we examine the situation at the middle of the stop band where $f = f_M = 1265$ Hz. Using (31), we compute for the right-hand side of (18) that $\cos qa = -2.55$, whence, from (27), $q_I a = 1.59$.

For a filter n cells deep, this gives a reduction factor R of $\exp[nq_I a]$ (see equation (28)). Thus, we have:

n	13	7	3
R	9.48×10^9	68,200	118

Even for a filter of only 3 cells, we get a considerable reduction (over 100).

Experiments were performed for $n = 13$, then $n = 7$, and finally for $n = 3$. The beginning and end of the first stop band occurred at frequencies very close to the predicted ones given above.

It is important to see how the quantity $q_I a$, which controls the reduction factor R, varies as we approach the edges of the stop band. As discussed previously, this will define the *effective* width of the stop band. We have determined $q_I a$ and the corresponding values of R for 3 layers (i.e., $n = 3$) at the 1/8-*th* point of the stop band (where f = 858 Hz) and at the 7/8-*th* point of the stop band (where f = 1672 Hz). We obtain:

f (Hz)	722	858	1265	1672	1808
$q_I a$	0	1.012	1.59	1.141	0
R	1	20.8	118	30.6	1

Thus, we see that even when we are close to the edges of the stop band, a three-cell filter gives a considerable degree of reduction.

A certain amount of reduction, unaccounted for in the present theory, will also occur due to the viscoelastic nature of the rubber. This reduction due to material damping can be estimated and compared to that caused by wave trapping produced by the layering. A shear wave propagating through the rubber alone would have a displacement field given by:

$$w(x,t) = e^{i(qx - \omega t)} \tag{33}$$

with

$$q = q_R + iq_D \tag{34}$$

where q_R is the real part of the wave number and q_D represents the attenuation factor due to material damping. This factor can be written in terms of the real (G_R) and imaginary (G_I) parts of the shear modulus of the rubber as:

$$q_D = \frac{\omega}{\sqrt{G_R/\rho}} \sin\left(\frac{\vartheta}{2}\right) \left[1 + \left(\frac{G_I}{G_R}\right)^2\right]^{-\frac{1}{4}} \tag{35}$$

with:

$$\vartheta = \arctan \delta \tag{36}$$

$$\delta = \frac{G_I}{G_R} \tag{37}$$

and ρ is the density of the rubber. Since $G_R \gg G_I$ for the rubber used in the bearing, we get:

$$q_D = \frac{\omega \delta}{2c} \tag{38}$$

where $c = \sqrt{G_R/\rho}$ is the speed of shear waves in the rubber. For this rubber, δ = 0.15, and if we consider a filter with three cells, the reduction factor, R_D, due to damping is at the midpoint frequency of the stop band

(1265 Hz):

$$R_D = e^{3\eta_D(a-b)} = e^{(3)(.439)(.376)} = 1.64 \tag{39}$$

The reduction factor R due to wave trapping was, for 3 cells, at this frequency, 118. Clearly, material damping plays a negligible role in reducing the magnitude of the output, the major reduction is caused by wave trapping.

The block was also cut so that its dimension in the y-direction was halved, and vibration experiments were performed on this reduced block. This reduction in the planform of the block should have no effect on its performance as a filter since all planes where y is equal to a constant are traction free. Experiments appear to bear out this conclusion.

The block was then cut along the plane z equal to a constant (see Figure 1) so that its dimension in the z direction was halved. This reduction could have an effect on its performance since the planes for which z is a constant are not traction free. As discussed in the Introduction to this report, edge effects will thus be present. It was the purpose of these experiments to get a preliminary estimate of the importance of edge effects.

The experimental results will be discussed in Section 6.

5. ILLUSTRATION OF FILTER DESIGN: OPTIMAL DESIGN

As an example, we will consider first the design of a filter with a relatively low-frequency stop band. It is desired to design a filter that will block a frequency of 400 Hz. The dimensions of the filter are to be 1.5 inches x 4 inches in planform and 1 inch deep. To get an effective filter, we want to design it so that 400 Hz will fall near the middle of the first stop band.

We begin by assuming that we will get a sufficiently high reduction factor by using 3 cells. Each cell will be composed of a layer of rubber bonded to a layer of steel. Since we are trying to block frequencies which are relatively low, we want to make the frequency at which the first stop band begins as low as possible. Thus, the most compliant rubber available must be used. An oil-extended rubber has been produced with the following properties[10]:

$$G_m = 37.7\ psi \quad ; \quad \rho_m = 0.93\ gm/cm^3$$

For steel, we have the following properties:

$$G_f = 12 \times 10^6\ psi \quad ; \quad \rho_m = 7.7\ gm/cm^3$$

This yields:

$$c_f = 129.1 \times 10^3 \quad \text{inches per second}$$

$$c_m = 658.6 \quad \text{inches per second}$$

$$p = 1623 \gg \frac{1}{p}$$

We note that $\omega b/c_f \approx 0.02 \ll 1$, so that we are justified in using the approximate relation (18).

For our first design attempt we chose $S = b/a - b = 1/2$. Thus, since $a = 1/3$ inch, $b = 1/9$ inch and $a - b = 2/9$ inch. Then, $\alpha = 2.07$ and solving equation (18) with this value of α, we obtain for the lowest root z_B, $z_B =$

0.945. Then, $f_B = 0.945/\pi f_m$, $f_m = c_m/2(a-b) = 1482$ Hz, which yields the value $f_B = 446$ Hz. The 400-Hz frequency is not within this stop band, and thus the design is not appropriate.

For our second attempt, we try $S = 1/3$. Going through the same procedure as above, we obtain $z_B = 1.136$, which yields $f_B = 476$ Hz, a value even larger than the first attempt. Thus, we are moving in the wrong direction, and we have to try a value of S larger than $1/2$.

In our third attempt, we use $S = 1$. This leads to $z_B = 0.6815$ and $f_B = 429$ Hz, which is an improvement over our two previous designs, but is still not suitable. Therefore, we again move to a larger value of S.

For our fourth attempt we use $S = 3$, which leads to $z_B = 0.3986$ and $f_B = 501$ Hz, which makes this design worse than any of the previous three. However, these four designs indicated that there must be some particular value of S which, for a given cell size a, minimizes f_B. We now wish to determine that value of S and the corresponding minimum value of f_B. For our purposes, this would be the optimal filter.

There are several ways in which we could investigate the question of what is the optimal value of S so as to minimize f_B. We begin with the simplest approach. It is clear from equation (18) and Figure 2, that one way to obtain a small value of f_B is to choose material properties and a value of S which make α as large as possible. This can be accomplished for values of S of order unity by choosing materials such that $\rho_f/\rho_m \gg 1$.

Let us assume that $\rho_f/\rho_m \to \infty$ which implies that $\alpha \to \infty$. As $\alpha \to \infty$, $z_B \to 0$, and we get

$$f(z) = \cos z - \alpha z \sin z \to (1 - \frac{1}{2}z^2) - \alpha z^2$$

that is,

$$f(z) \to 1 - \alpha z^2$$

since $\alpha \gg 1$. The beginning of the first stop band, z_B, occurs when $f(z) = -1$. Thus, we get,

$$-1 = 1 - \alpha z^2$$

whence, $z_B = \sqrt{2/\alpha}$. Now,

$$f_B = \frac{z_B}{\pi}\frac{c_m}{2(a-b)} = \frac{z_B}{\pi} f_m^* \frac{a}{a-b}$$

where $f_m^* = \frac{c_m}{2a}$ is the natural frequency of vibration of the first thickness shear mode of a layer of the rubber used in the filter with a depth equal to a, the cell depth. The factor f_B may be rewritten as:

$$f_B = \frac{f_m^*}{\pi}[z_B(1+S)]$$

But $z_B = \sqrt{2/\alpha}$ with $\alpha = \frac{1}{2}\frac{\rho_f}{\rho_m} \times S$. Putting this into the expression for f_B, we obtain:

$$f_B = \left[\frac{2}{\pi}\sqrt{\rho_m/\rho_f}\, f_m^*\right]\left[\sqrt{S} + \frac{1}{\sqrt{S}}\right]$$

36

We note that once the materials and cell thickness have been chosen, the first bracket is a constant. The dependence of f_B on the thickness ratio S is expressed solely in the second bracket. Therefore, in order to minimize f_B, that value of $S > 0$ which minimizes the second bracket must be selected The second bracket is a well-known function whose minimum can be found by elementary means, and it occurs when $S = 1$. This is an interesting result, and certainly not an obvious one. The optimal filter occurs when the layers of rubber and steel are of equal thickness.

However, it must be kept in mind that the preceding analysis is correct only when $\alpha \gg 1$. For our choice of materials, if we set $S = 1$, we get $\alpha = 4.14$, which is *not* $\gg 1$. Thus, we can use $S = 1$ only as a rough guide to optimal design when α is not $\gg 1$. Our four previous design attempts bear out the validity of $S = 1$ leading to a near optimal design. Of all our designs, the one which gave the lowest value for f_B was the one where $S = 1$.

We can now try to deal with the optimal problem in a more general manner. Let us attempt to construct an algorithm that will lead to an optimal design for any value of $\alpha > 0$. We have:

$$f_B(S) = \frac{f_m^*}{\pi} z_B(S)[1 + S] \tag{39}$$

where $z_B(S)$ is the lowest root of equation (18) with $\cos qa = -1$:

$$\cos z - \frac{1}{2}\left[\frac{\rho_f}{\rho_m}\right] S z \sin z + 1 = 0 \tag{40}$$

In the sequel as a matter of convenience we will drop the subscript B on z_B. For a minimum value of f_B we must have:

$$\frac{df_B}{dS} = 0 \quad \text{which implies that} \quad (1 + S)\frac{dz(S)}{dS} + z(S) = 0 \tag{41}$$

From equation (40) we get:

$$\frac{dz}{dS} = \frac{-z \sin z}{S \sin z + S z \cos z + 2\dfrac{\rho_f}{\rho_m} \sin z} \tag{42}$$

Substituting (42) into (41), and simplifying, we obtain as the optimality condition:

$$S = [1 - 2(\rho_m / \rho_f)]\left[\frac{\tan z}{z}\right] \tag{43}$$

It is important to recall the meaning of z: it is the lowest root of equation (40).

Based on the optimality condition, equation (43), we can now construct a simple iterative design procedure which will lead to the optimal value for S. Say that we have arrived at the i-*th* design attempt. It is associated with the value S_i. We obtain the root z_i which is the lowest root of equation (40) with $S = S_i$. How do we choose S_{i+1} to give us a better design? We use the optimality condition, equation (43). In the right-hand side of equation (43) we substitute for z the value z_i. This then produces the value S_{i+1}. That is.

$$S_{i+1} = [1 - 2(\rho_f / \rho_m)]\left[\frac{\tan z_i}{z_i}\right] \tag{44}$$

We continue this process until we converge to the optimal value of S. As a partial check on the validity of this formula, consider what happens as $\rho_f/\rho_m \to \infty$ which implies that $\alpha \to \infty$. Then, equation (43) yields $S = 1$, which was the result previously obtained by a direct solution.

We now apply this method to the example that we were discussing previously. Starting with the first case, we had $S_1 = 1/2$ with $z_1 = 0.945$. Equation (44) yields for S_2 the value 1.11, which is a move in the right direction. For the second case, we had $S_1 = 1/3$ with $z_1 = 1.136$. This gives for S_2 the value of 1.45 which again is a move in the right direction. For the third case, we had $S_1 = 1$ with $z_1 = 0.6815$. This results in $S_2 = 0.9027$. For the fourth case, we had $S_1 = 3$ with $z_1 = 0.3986$, which leads to $S_2 = 0.80$. Thus, in all four cases, the optimality condition drives the next value of S (i.e., S_2) closer to the optimal value than S_1 was.

Let us continue with case 3 (where $S_1 = 1$) because our crude criterion states that $S = 1$ is the optimal condition. We can use this as input to the more refined criterion, equation (44). We have seen that $S_1 = 1$ gives $z_1 = 0.6815$ and $f_B = 429$ Hz, which leads to $S_2 = 0.9027$. With this value of S_2 we obtain for z_2 the value 0.7157 and for f_B, 429 Hz. This then leads to $S_3 = 0.9214$, which then gives $z_3 = 0.7075$ and $f_B = 429$ Hz. At this stage we see that the iterative optimization scheme has converged. We find that f_B is not very sensitive to small changes in S when we are near the optimal point. For $S = 1$ or 0.9027 or 0.9214, we get $f_B = 429$ Hz. There is no point in trying to seek greater accuracy. (The true properties of the rubber are not known all that accurately.) From a practical point of view, the easiest filter to manufacture would be for $S = 1$, i.e., equal thicknesses of steel and rubber. (If there are slight errors in the manufacturing process, so that S is not exactly equal to 1, but close to it, then our previous results tell us that it is not critical, since when S is near 1, f_B is insensitive to small changes in S.) The lowest value of f_B attainable for the materials utilized and a cell thickness of 1/3 inch is 429 Hz. Thus, such a filter cannot be used to stop transmission of a disturbance with a frequency of 400 Hz. Therefore we must try a larger cell size, which implies, for the fixed-depth dimension of 1 inch, a smaller number of cells.

We next choose a filter with 2 cells, so that $a = 1/2$ inch. Based on our previous work, we also choose $S = 1$. This leads to $z_B = 0.6815$, as for our previous case 3. But now this leads to $f_B = 286$ Hz. We know that z_E, the root associated with the end of the first stop band, is $z_E = \pi$, which leads to $f_E = 1317$ Hz. Thus, the frequency of interest, 400 Hz, lies within the stop band, and this design is potentially acceptable.

Now, we must check to see if the reduction factor for this design is sufficiently high for practical purposes. For this design, we obtain $q_f a = 1.627$. Thus, for a filter with 2 cells, we have:

$$R = e^{nq_f a} = 26$$

If this is not a sufficiently high reduction factor, then the filter cannot be designed successfully with this choice of materials. One would have to find more suitable materials, e.g., the stiff material should have a larger density and a larger shear wave speed while the compliant material should have a lower density and a slower shear wave speed.

It is interesting to note that if we could make the filter 1 cell thicker (i.e., 1.5 inches instead of 1 inch), the reduction factor R would increase to the value 132. This value would appear to be sufficiently high to meet most practical requirements.

Next, we consider the design of a high-frequency filter to block disturbances with a frequency of 5000 Hz. Experience with the previous design attempts for a low-frequency filter show that the thickness of the rubber in a layer in a cell should be chosen such that the natural frequency of the first thickness shear mode, f_m, is somewhat higher than the frequency to be blocked, since the first thickness shear mode frequency is equal to f_B, the end of the lowest stop band of the filter.

In this design, it is not necessary to use the special, highly compliant, oil-extended rubber previously employed. We can use an ordinary carbon-filled rubber of the type used in the filter that was studied experimentally at the IBM site. Thus, we will use the material properties listed in Section 4. Let us choose for f_m an approximate value of 10000 Hz. But $f_m = c_m/2(a-b)$, so that $a-b \approx 0.0679$. Therefore, we choose $a-b = 1/16$ inch = 0.0625 inch. We also choose $S = 1$ for optimal design (to get a *broad* band for the stop band), so that $b = 1/16$ inch and $a = 1/8$ inch. This yields $f_m = 10866$ Hz, $\alpha = 3.319$, $z_B = 0.7573$, and $f_B = 2619$ Hz. This puts the 5000-Hz frequency near the center of the stop band, which indicates a good design (i.e., large attenuation).

At 5000 Hz, the value of $q_f a$ is 2.215, a quite high value, which is desirable. Thus, we get $R = 9.16$ for a single-cell filter, $R = 83.9$ for a two-cell filter, and $R = 769$ for a three-cell filter. In some applications, a single-cell filter might suffice.

As a final check on our design, we look at the quantity $\omega b/c_f$ whose value, 0.0152, is $\ll 1$, in accordance with our initial, simplifying hypothesis

6. EXPERIMENTAL RESULTS

To verify certain aspects of the theoretical results presented above, a series of experiments were performed at IBM in San Jose on several specimens of periodically layered composites. Due to time and cost constraints, only a limited program could be pursued. The purpose of these experiments was to ascertain whether the wave stopping phenomenon predicted for the infinite composite medium would be observed in a block, or mechanical filter, of finite dimensions. If wave blocking were observed in the finite filter, we then wanted to determine whether the frequencies of the start and end of the observed stopping band were adequately predicted by the theory based on the infinite medium.

Two composites were used in the experiments. The first was the composite described in Section 4 and the second was made of alternating steel and rubber layers, each with a thickness of 1/4 in. The rubber employed was an oil-extended one as described in Section 5. The experiments were performed by attaching the bottom of a specimen (or filter) to the rigid base of a vibration table which was then excited, first by a sine sweep input and next by a random input. A transducer attached to the rigid base of the vibration table measured the input at the bottom of the specimen, and one attached to the top of the specimen measured the output there. These measurements were fed into a Fourier analyzer which then displayed and

plotted the transmissibility of the specimen filter. In this way we could directly observe whether any wave stopping occurred.

The tests performed on the first composite were with a specimen having 13 cells and a planform of 8 in. by 8 in. Wave stopping was observed in a frequency band close to that of the lowest predicted from the theory for the infinite medium. To assess whether decreasing the planform of the filter would obviate the wave-stopping action, the specimen was cut in half to produce a filter of 4 in. by 8 in. The behavior of this filter was essentially the same as that of the larger one. Next, this filter was cut so as to remove 3 cells, leaving a filter of 7 cells. Tests on that specimen yielded a stopping band whose starting and ending frequencies differed little from those obtained in the previous test. This 7-cell filter was then cut to reduce its planform to a square 4 in. on edge. Again, tests demonstrated wave blocking with essentially the same frequency interval for the stopping band. For the final series of tests on this composite, the 7 cells of the 4-in. specimen were shaved to 3. Tests on this filter yielded results similar to those described above.

Typical experimental data are shown in Figures 3 and 4 for the 3-cell filter. The input and output oscilloscope traces under sinusoidal excitation at a frequency below that of the first stopping band are shown in Figure 3. The output is not reduced. The input and output traces when the excitation frequency is within the stopping band of the filter are shown in Figure 4 and the reduction in the output is marked. The transmissibility (output/input) versus the frequency of this filter are shown in Figure 5 in which the stopping band is obvious. Within the stopping band, this filter can produce a drop in the transmissibility of as much as 40 dB.

Tests on the second composite were performed on a specimen with 3 cells and a planform of 3 in. by 5 in. The results were similar to those for the first specimen except, of course, that different stopping bands and attenuation values were obtained. The transmissibility versus frequency for this filter is plotted in Figure 6 where a reduction of as much as 60 dB is observed.

These results demonstrate that the fundamental wave-stopping phenomenon predicted by the theory for a mechanical filter of infinite extent composed of a periodically layered composite is not obviated when the filter is of finite extent. By reducing the filter to finite extent, the details of its behavior are modified, but its basic action is not.

7. CONCLUDING REMARKS

The study summarized in this paper indicates that it may be feasible to use periodically layered composites as mechanical filters for a variety of vibration isolation purposes. In comparison to conventional vibration isolation methods, the use of such mechanical filters would be primarily in the higher ranges of frequency.

The theory employed in this study is based on wave propagation in a periodically layered composite of infinite extent and composed of two materials. Given such a medium, the prediction of frequencies of the stop b nds of any particular composite is quite straightforward. These stop bands define the mechanical filtering action of the medium. Theoretical predictions of the beginning and ending frequencies of stop bands appear.

to be corroborated by experiments carried out at IBM.

However, in practical applications, mechanical filters are of finite extent. This then introduces edge effects and reflections from the top and bottom face of the filter the consequences of which have not been explored analytically. Such studies appear to be nontrivial. The limited results from the small experimental program at IBM seem to indicate that these effects do not obviate the basic physical phenomenon in the layered composite. The filtering effects (i.e., the stop bands) still appear to exist as the size of the mechanical filter is reduced to reasonable dimensions. This is an area of study which needs further investigation, both analytically and experimentally.

The inverse problem, that of designing a mechanical filter to produce a desired stop band, does not appear to be difficult if it is based on a model of a periodically layered medium of infinite extent (i.e., assuming that edge effects are negligible and that reflections from the top and bottom faces of the filter are negligible.) The equation upon which mechanical filter design is based can, for a large class of problems of interest, be simplified so that it is easy to use in practice.

REFERENCES

[1] J. C. Snowden, *Vibration Isolation: Use and Characterization*, NBS Handbook 128, National Bureau of Standards, Washington, D.C. (1979).

[2] A. E. Javid, Personal Communication, April 1985.

[3] Vincent, *Phil. Mag.*, Vol. 46, 537 (1898).

[4] L. Brillouin, *Wave Propagation in Periodic Structures*, McGraw-Hill Book Company, Inc., New York (1946).

[5] T. J. Delph, G. Herrmann, and R. K. Kaul, "Harmonic Wave Propagation in a Periodically Layered, Infinite Elastic Body: Antiplane Strain," *Journal of Applied Mechanics*, Vol. 45, 343-349 (1978).

[6] G. Floquet, *Ann. Ec. Norm.* (2) Vol. 13, 47 (1883).

[7] E. H. Lee and W. H. Wang, "On Waves in Composite Materials with Periodic Structures," *SIAM J. Appl. Math.*, Vol. 25, No. 3, 492-499 (1973).

[8] E. H. Lee, "Wave Propagation in Composites with Periodic Structures," *Proceedings of the Fifth Canadian Congress of Applied Mechanics*, G49-G59 (1975).

[9] K. Karim-Panahi, "Antiplane Strain Harmonic Waves in Infinite, Elastic, Periodically Triple-Layered Media," *Journal of the Acoustical Society of America*, Vol. 74, No. 1, 314-319 (1983).

[10] C. J. Derham, *et al.*, *New Rubber Technology*, Vol. 8, Part 3, 63 (1977).

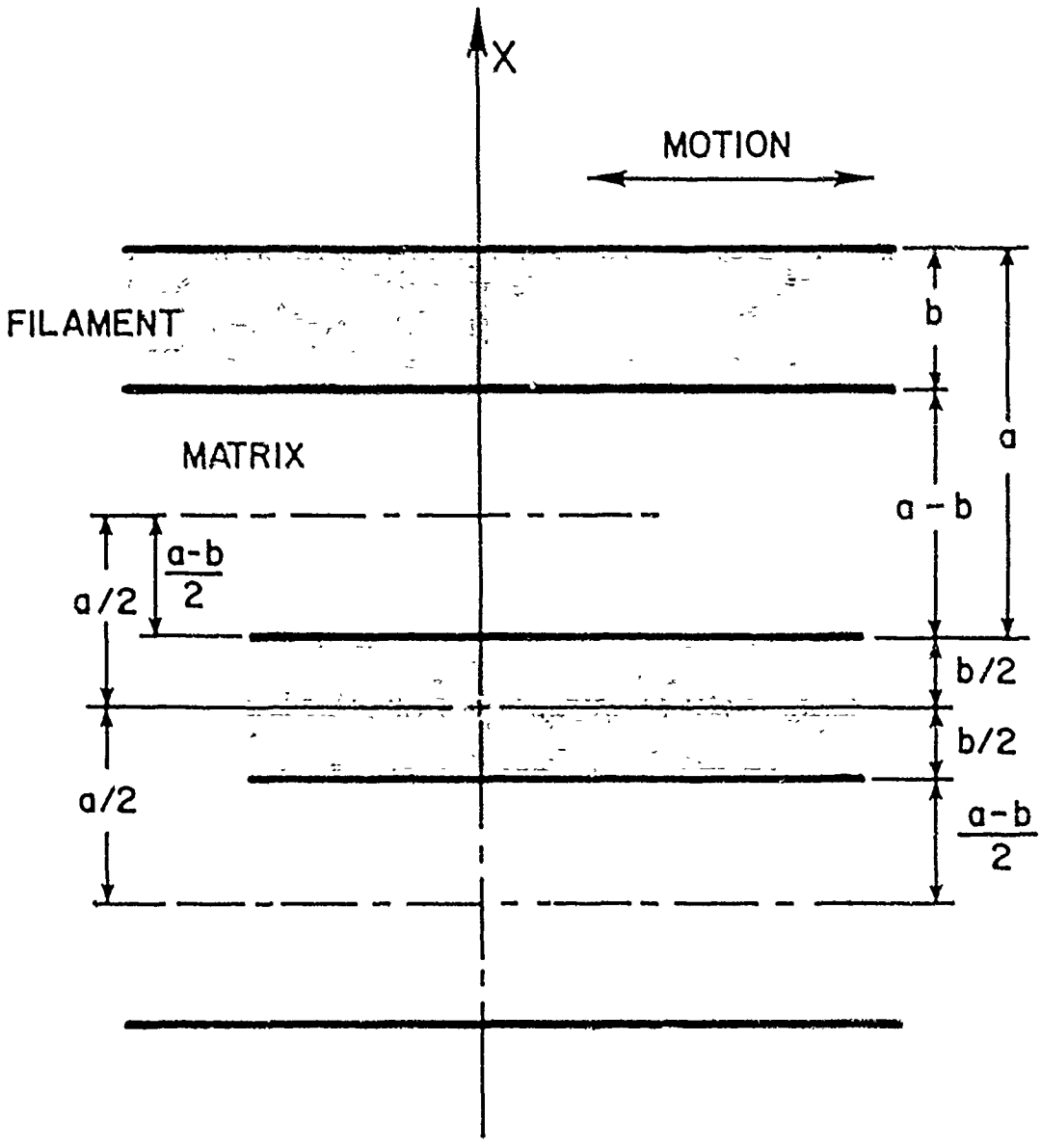


FIGURE 1. INFINITE, PERIODICALLY LAYERED COMPOSITE

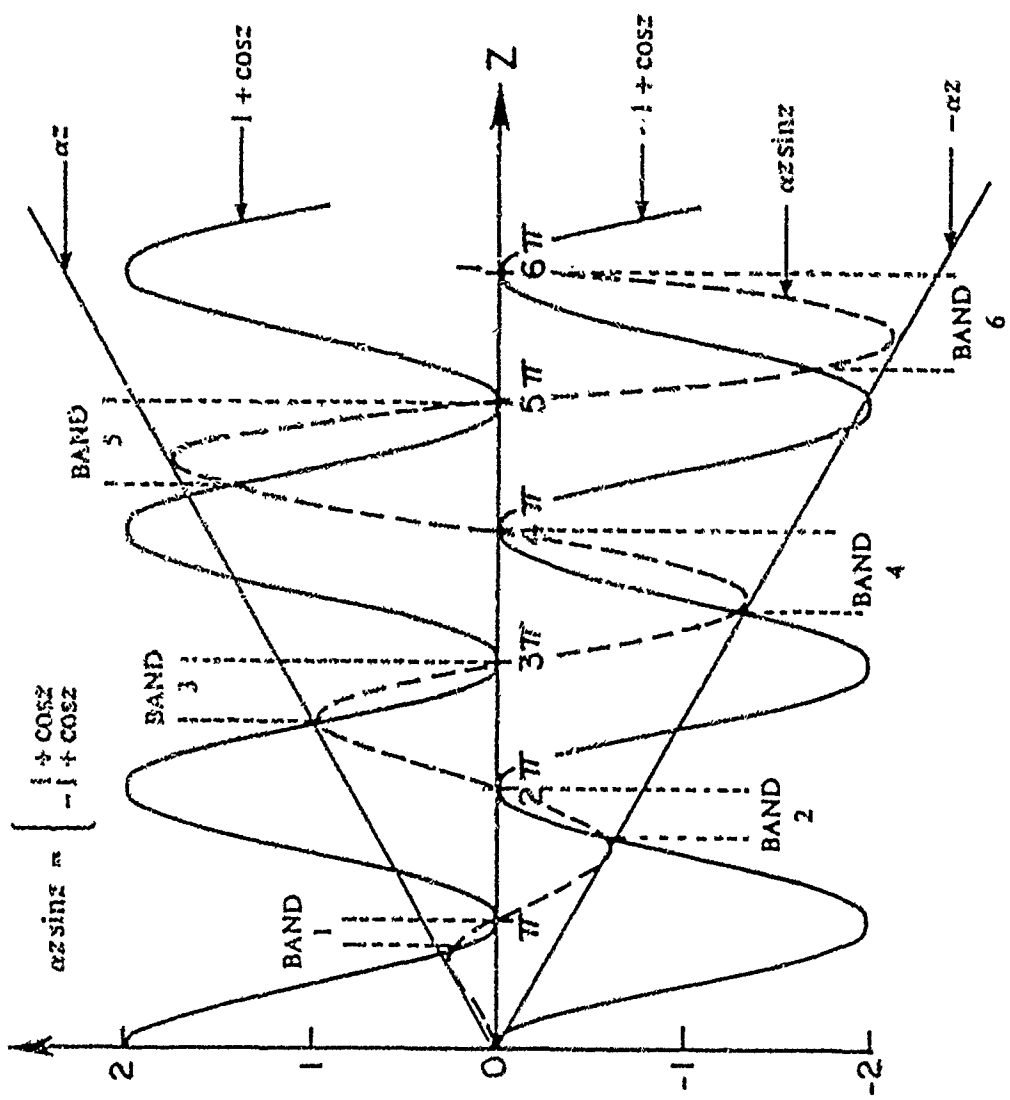


FIGURE 2. DETERMINATION OF STOPPING BANDS

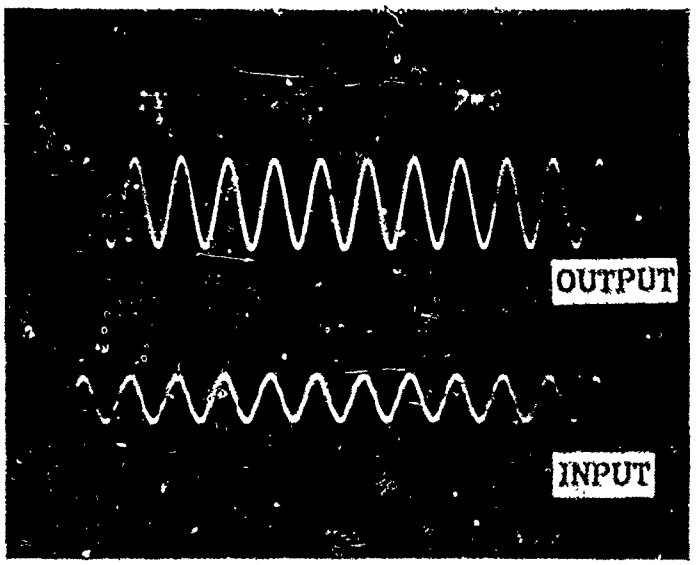


FIGURE 3. INPUT AND OUTPUT FOR FILTER WHEN FREQUENCY OF VIBRATON IS BELOW FIRST STOPPING BAND

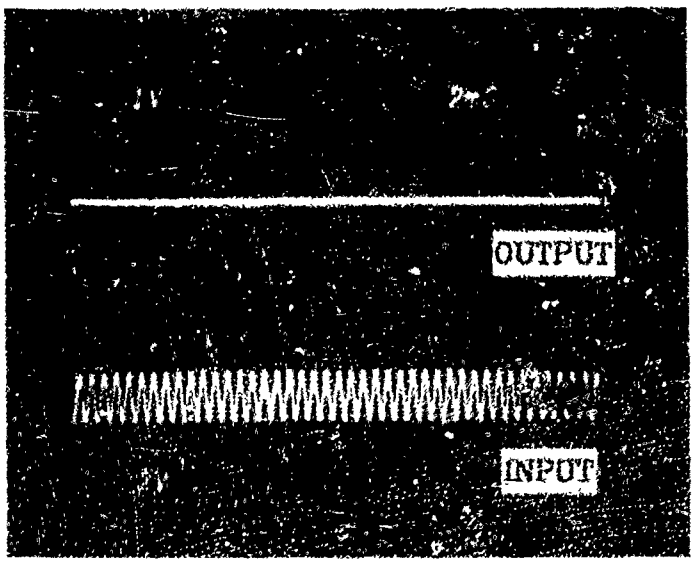


FIGURE 4. INPUT AND OUTPUT FOR FILTER WHEN FREQUENCY OF VIBRATION IS WITHIN FIRST STOPPING BAND

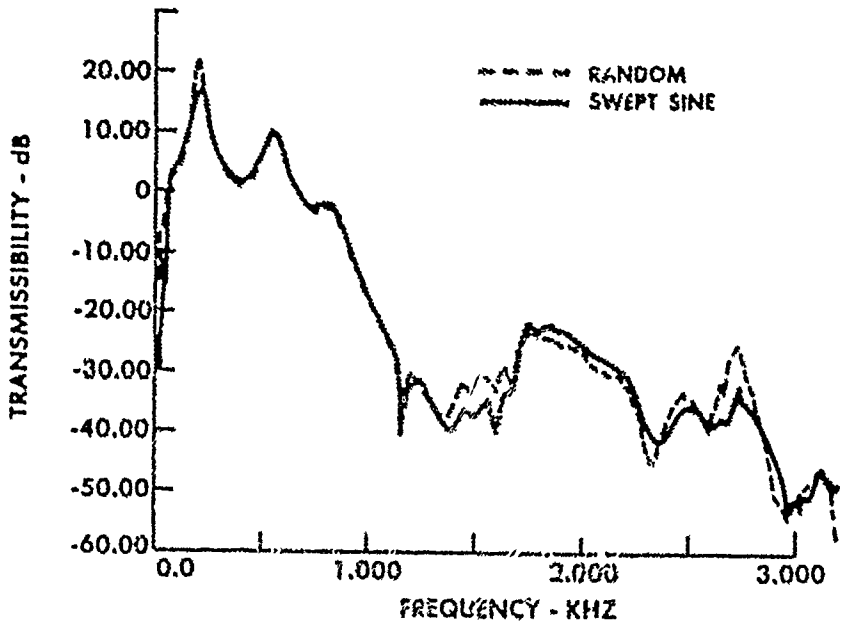


FIGURE 5. TRANSMISSIBILITY VERSUS FREQUENCY FOR FIRST COMPOSITE (a = 1/2 in., b = 1/8 in.)

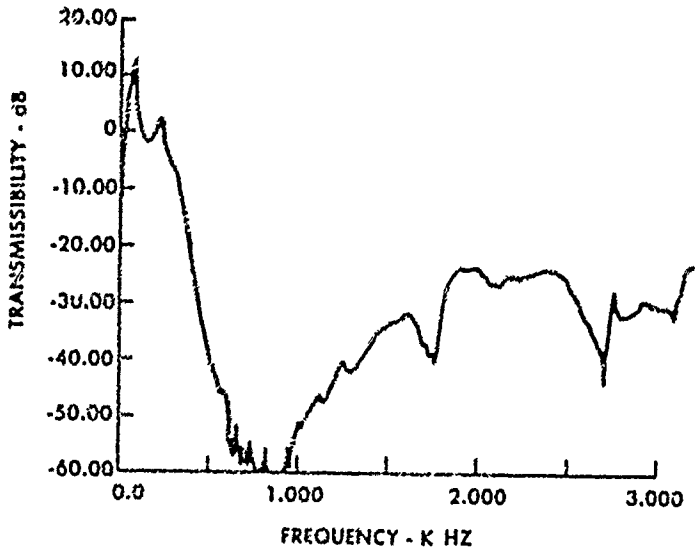


FIGURE 6. TRANSMISSIBILITY VERSUS FREQUENCY FOR SECOND COMPOSITE (a = 1/2 in., b = 1/4 in.)

Analytical and Experimental Studies of Structures with Coulomb Friction Elements

Prof. S. F. Masri
O. T. Hata
J. A. Malthan

(Not available for publication)

IS IT DAMPING OR NONLINEARITY?

R.A. Ibrahim, Professor

Texas Tech University
Department of Mechanical Engineering
Lubbock, Texas 79409

ABSTRACT

This paper sheds some light on adversary effects of damping on the response characteristics of mechanical systems. While damping is regarded as a passive source for vibration control, it can cause instability to an originally stable system. Nonlinearity, on the other hand, is found to control vibrations especially in dangerous regions of parametric instability.

INTRODUCTION

Velocity dependent forces are classified as conservative or nonconservative. Gyroscopic forces for example are conservative and they exert no work. Damping forces, on the other hand, are nonconservative and the work done by these forces is non-zero. If the work done is negative the damping is a source of energy dissipation. If it is positive the damping becomes a sources of energy and may cause a noise or self-excited vibration. The general concept of positive damping is that it controls vibration since it transforms a portion of the system kinetic energy into another form. The damping is an important parameter in the study of dynamic stability of elastic systems. In most cases, stability criteria indicate that the damping is very favorable in stabilizing dynamic systems. However, in certain situations the damping may result in dynamic instability of the system response.[1-7] For elastic systems there are several criteria involved to examine their stability. These are:[1]

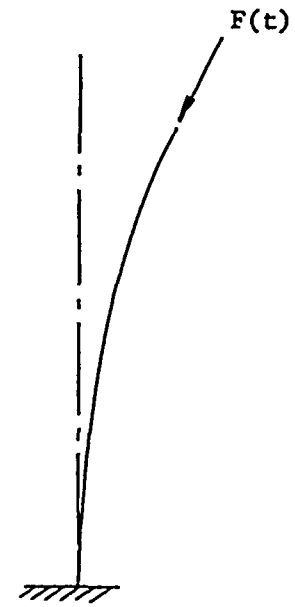
i. The static criterion due to Euler: This method predicts the critical loads above which bifurcation of equilibrium occurs.

ii. The energy criterion: The total potential energy of the system is examined to define the critical load which is associated with the transition of the value of the potential energy from positive de finite form.

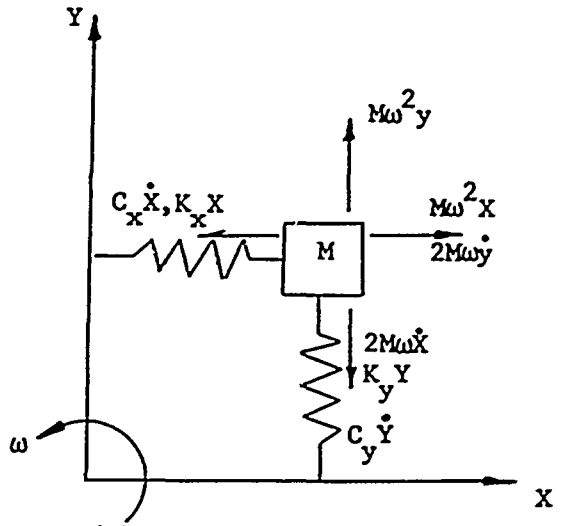
iii. The dynamic criterion: This method predicts free motions in the vicinity of the static equilibrium position.

Hermann and Bungay[2] established two instability mechanisms. The first is known as divergenc (or static buckling) which is identified by a bifurcation of equilibrium configuration. The second is called flutter and is characterized by oscillatory motion. It was found that a conservative system can be examined by either the static or dynamic criteria, while a non-conservative system can only be treated by using the dynamic criterion. However, the static approach is usually inadequate for stability analysis of elastic systems especially those which are subjected to tangential forces (known also as follower or circulatory forces). This fact was first realized by Pflüger[3] who investigated the stability of a cantilever column under a follower compressive load by using the static criterion. He found that the Euler method does not provide any value for the critical load. Later, Beck[4] and Ziegler[5,6] considered Pflüger's problem and employed the dynamic method and obtained bounded values for the critical load.

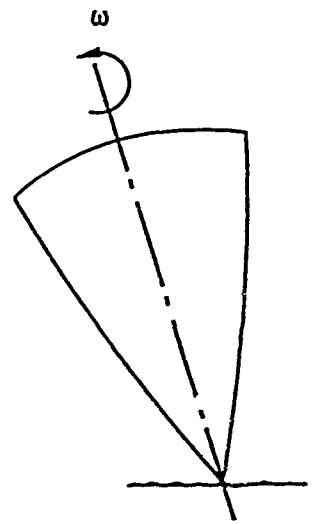
The introduction of energy dissipation such as linear damping is one form to control vibration. While this is always true for most dynamic systems, the damping is known to be unfavorable for vibration isolation and could have a destabilizing effect in some cases such as gyroscopic motion or systems under follower forces. Figure (1) shows three mechanical systems which become dynamically unstable if the damping is included in the equations of motion. The destabilizing effect of damping was first discovered by Ziegler[5,6] and Bolotin[7] in two-degree-of-freedom systems. Fu and



(a) Column under periodic follower force



(b) Mass - Spring system under rotating motion



(c) Rotating top on rough surface

Fig.(1) Examples of mechanical systems which become unstable due to damping.

Nemat-Nasser[8] showed that if an undamped autonomous linear system with a Jordan canonical stiffness matrix is unstable it can be made stable by adding suitable terms with harmonic coefficients of small amplitude. If damping is included the system becomes totally unstable. On the other hand, if the stiffness matrix has a diagonal form the system may or may not be stable.

The noise and vibration in shipboard stern tube occur mainly due to negative damping. Experimental investigations of Krauter and Brower[9] have shown that rotor speed, load, and temperature are very important in governing the frictional properties at the shaft-bearing contact zone. The mechanism of stick-slip can occur when the friction coefficient decreases with increasing the speed. Experimental measurements of damping coefficient revealed that the damping changed continously with time because the friction force was changing continously. It was concluded that the occurrence of squeal which occurred synchronously with shaft rotation is due to variations in structural damping. This variation was found random and for certain levels it causes squeal or chatter.

PARAMETRIC INSTABILITY AND DAMPING

Parametric instability is one form of undesirable vibratory motion of dynamic systems and occurs when the external excitation is normal to the direction of the system response. Mathematically, the exciation appears in the equations of motion as a time-dependent coefficient. Parametric instability differs from the familiar types of instability, such as forced vibration resonance in various fundamental aspects. It may occur at axial loads considerably lower than the lowest static Euler buckling load over some regions of excitation frequency and amplitude. For linear systems parametric instability is a very dangerous phenomenon even in the presence of damping. The inclusion of damping imposes a threshold value of the excitation amplitude. However, in certain situations the damping enhances parametric instability and results in wider instability regions.

Evan-Iwanowski[10] demonstrated the damping destabilizing effect in a cantilever column subjected to a dynamic follower force F(t) as shown in fig. (1a). Two types of damping were considered in the mathematical model; these were a linear viscous damping and a Kelvin-type internal dissipative mechanism. Evan-Iwanowski found that for suitable values of the system parameters, the column exhibit parametric principal resonances, combination resonance of the summed and difference types. It was shown that if the damped system were unstable under a static load, it can be stabilized by the introduction of a dynamic component whose frequency is very close to the sum of the two natural frequencies of the column. Another interesting result revealed that under certain conditions of the applied load the column internal damping acted as a destabilizing effect. Figure (2) shows a sample of the stability/instability boundaries for various values of the internal resonance parameter R.

The influence of time dependent aerodynamic forces upon the dynamic behavior of a flat plate of infinite length was examined by Dzygadlo[11-13] for subsonic and supersonic flow regimes. Dzygadlo found that the form of

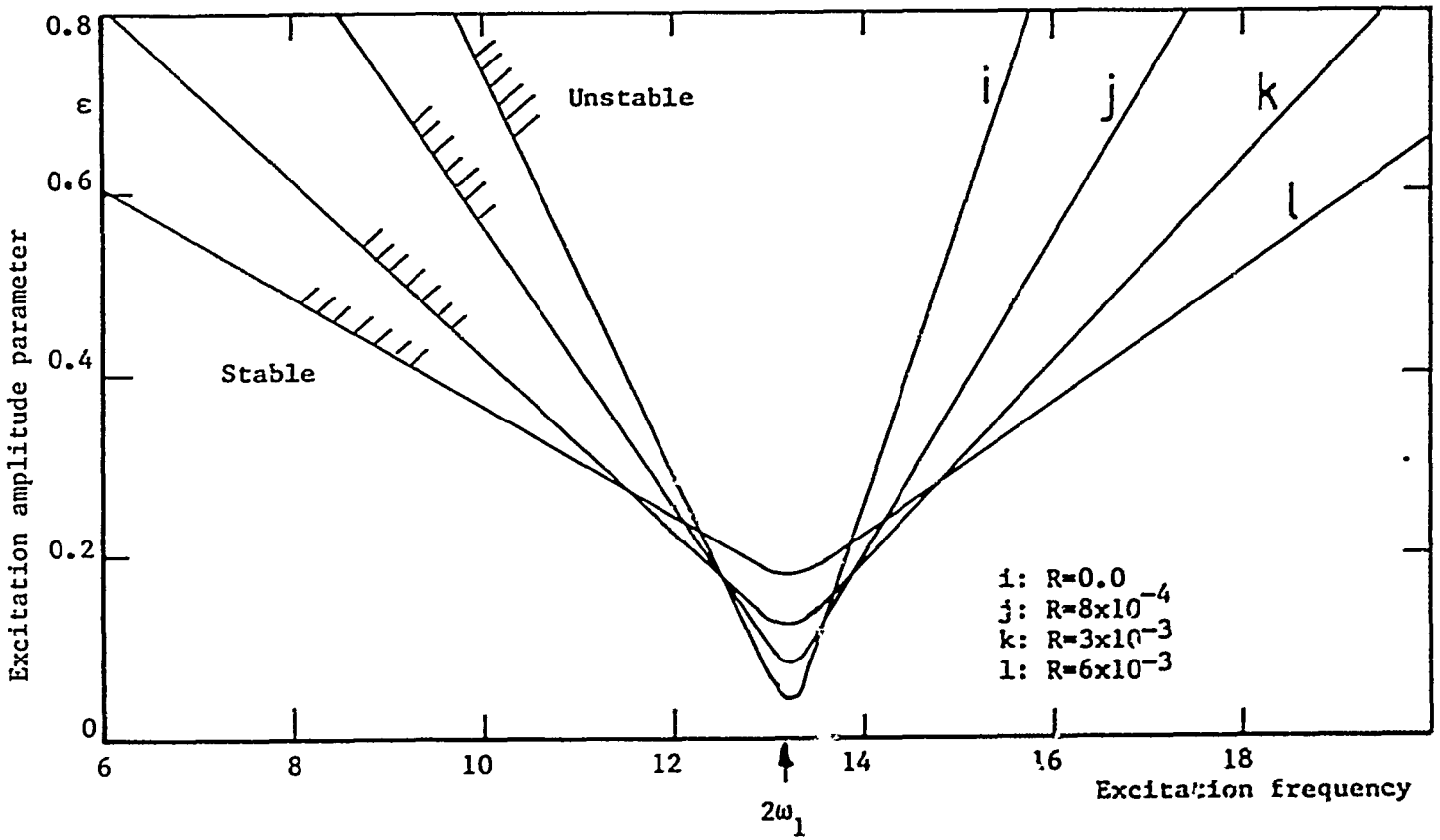


Fig.(2) Instability regions of a cantilever column subjected to periodic follower force 10 (R = internal damping parameter, ω_1 first eigenvalue of the column).

instability regions of parametric resonance is influenced by the subsonic flow in such a way that the regions became wider and move towards lower regions of parametric excitation frequencies. For post-flutter speeds these regions were found to shift away from the frequency axis, in a manner similar to the damping stability effect. The regions of parametric instability do not exist if the flow becomes supersonic as long as the flat plate has infinite length. For the case of a plate with finite length exposed to supersonic flow, Dzygadlo found that the presence of air flow would change the location and shape of the regions of parametric instability. The airflow was found to create aerodynamic damping and coupling between the plate normal modes as indicted by the set of equations of motion

$$Y_n'' + C_n Y_n' + \omega_n^2 (1 - 2\varepsilon a_n \cos\Omega\tau) Y_n = -\frac{\bar{\lambda}}{M} [Y_n' + \sum_{\ell=1}^{n} b_{\ell n} Y_\ell] \qquad (1)$$

where $Y_n = y_n/L$, y_n is the plate maximum deflection of mode n

L = Length of the plate,

$$\bar{\lambda} = \frac{L \rho_a}{h \rho_p}, \qquad \varepsilon = \varepsilon_o/[2(\pi^2 - S_o)], \qquad a_n = \frac{2}{n^2\pi^2 - S_o}$$

$$C_n = \frac{n^4\pi^4 C}{\lambda_1 M^2}, \quad \omega_n^2 = \frac{n^4\pi^4}{\lambda_1 M^2}\left(1 - \frac{S_o}{n^2\pi^2}\right)$$

$$b_{\ell n} = \begin{cases} \dfrac{2\ell n}{n^2 - \ell^2}\,[1 - (-1)^{\ell+n}] & \text{for } \ell \neq n \\ 0 & \text{for } \ell = n \end{cases}$$

ε_o = amplitude of parametric load (inplane component)

a = speed of sound, $\tau = tU/L$

ρ_a = density of the air, ρ_p = density of the plate

C = damping coefficient of the plate material

U = air speed,

$\lambda_1 = 12(1 - \nu^2)\ (L/h)^2\ \rho_p a^2/E$

ν = Poisson's ratio, E = Young's modulus

h = thickness of the plate

It was assumed that $|\varepsilon| < 1$, $S_o < S_{cr} = \pi^2$

The coupling coefficients $b_{\ell n}$ satisfy the skew-symmetric condition $b_{\ell n}=b_{\ell n}$ The stability boundaries as obtained by Dzygadlo are shown in Fig. (3). Two dotted curves show the parametric instability boundaries under parametric loading and no airflow $\bar{\lambda}=0$. The first is located at excitation frequency parameter $r = 1$. It is seen that as the Mach number increases the first region diminishes and moves towards high values of excitation frequency and amplitude. This trend is reversed for the second instability region. For lower values of Mach number this region is displaced away from the frequency axis due to the effect of aerodynamic damping. If the Mach number increases further the second stability region starts to expand and moves towards smaller values of excitation frequency and amplitude until the Mach number reaches a critical value where the parametric instability region becomes maximum and touches the frequency axis. For $M > M_{cr}$ the instability region shrinks again.

The aerodynamic damping is found to play an important role in the aeroelastic flutter and parametric vibration of helicpoter rotor blades. Friedman[13] examined the stability boundaries of a hingeless helicopter blade. He indicated that the physical reason for flap-lag instability is the combination of the destabilizing aerodynamic damping and inertial coupling of the flap and lead-lag degree-of-freedom, together with the low aerodynamic damping in the lag degree-of-freedom.

PARAMETRIC VIBRATION AND NONLINEARITY

When the excitation parameters are located in one of the parametric instability regions the system will vibrate with an amplitude which grows exponential by growth amplitude until it collapses in spite of the presence of damping. In reality the system does not fail because as the response amplitude increases the system behavior is no longer governed by the linear differential equations of motion. The system nonlinearities start to play an important role and bring the system response into a limit bounded limit cycle or cause a number of complex characteristics which cannot be interpreted within the framework of the linear theory. These response characterisites include multiple solutions, amplitude jump, internal resonance, limit cycle and chaotic motion. In this regard the dynamicist must include the various sources of nonlinearities in his predictive model.

The nonlinearities may arise from two main sources:

1. Geometric nonlinearities due to large deformations such as large curvature, end shortening effect, and inertias of concentrated or distributed masses.

2. Material properties which exhibit nonlinear or multivalued stress-strain relationships.

Parametric vibration of dynamic systems has been examined by several investigators.[10,14,15] Hsu[16] pointed out that parametric excitation could play a significant role in the dynamic behavior of shells, sometimes directly (as in the case of external parametric excitation) and sometimes indirectly, as in the case of autoparametric coupling. Autoparametric

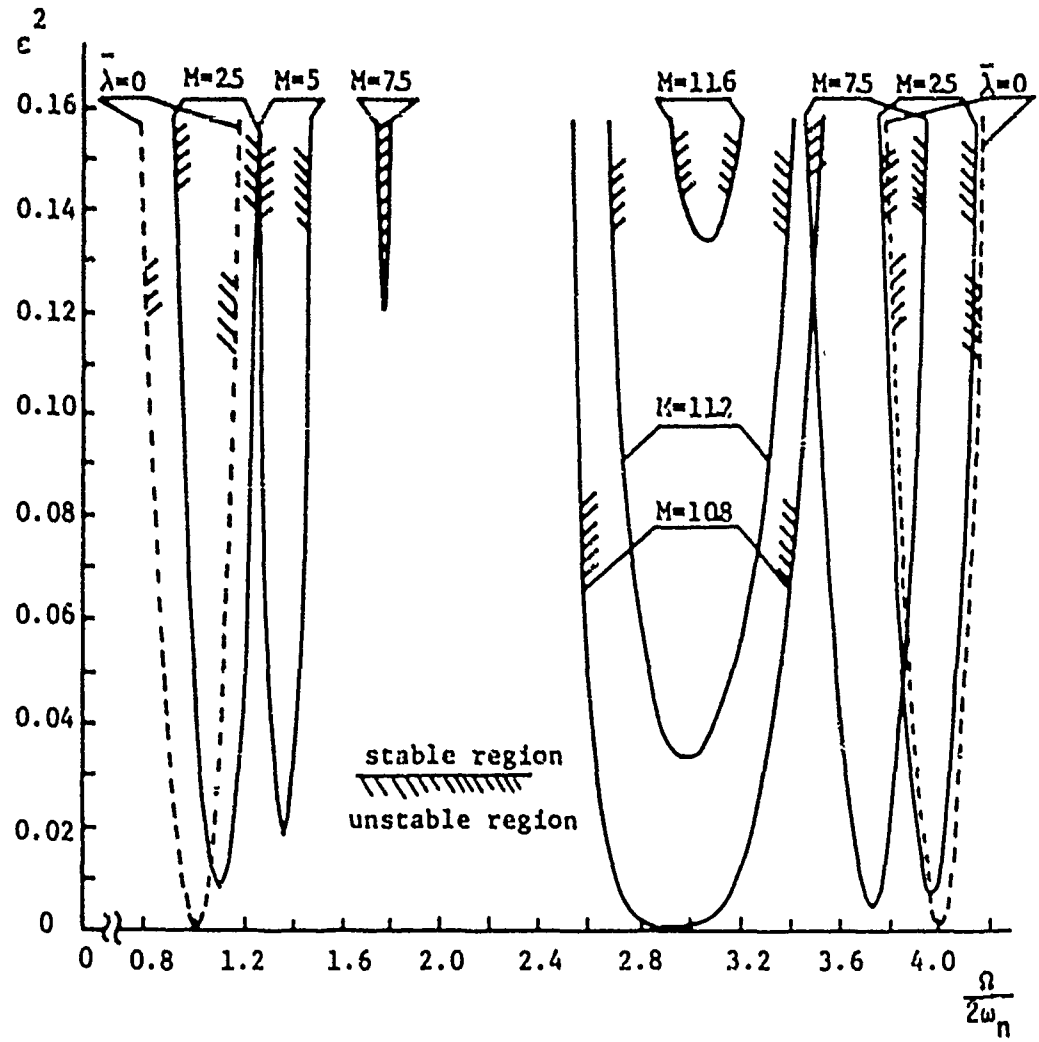


Fig.(3) Effect of Mach number on the regions of parametric instability (λ = 0 no airflow, L/h = 150).

coupling refers to a nonlinear coupling of the system normal modes and becomes significant when the relationship between the normal mode frequencies is linear.

The autoparametric interaction of liquid sloshing modes with elastic motion of a supporting structure has been examined when the normal modes of such systems are coupled through quadratic non-linearity. It was shown that with principal internal resonance ($\omega_2=2\omega_1$, where ω_1 and ω_2 are the first two normal mode frequencies) the system experiences a complete steady state response. With three-mode interaction, however, the system may not achieve a steady-state when the three modes have the frequency relation $\omega_3 = |\omega_1 \pm \omega_2|$. Additional modes may also be included and their inclusion may give rise to the multiple internal resonance where the interaction involves irregular beating motions.

The system shown in fig. (4) consists of a rigid tank partially filled with a liquid. The tank is supported on an elastic structure that can move laterally under parametric or autoparametric resonance conditions. The system equations of motion in terms of normal coordinates are found to involve cubic nonlinearities:

$$\left.\begin{aligned} &\ddot{Y}_1 + 2\zeta_1\omega_1\dot{Y}_1 + \omega_1^2 Y_1 = Y_o\cos(\Omega t+\phi)\,[C_{11}Y_1 + C_{12}Y_2] + \phi_1(\underset{\sim}{Y},\underset{\sim}{\dot{Y}},\underset{\sim}{\ddot{Y}}) \\ &\ddot{Y}_2 + 2\zeta_2\omega_2\dot{Y}_2 + \omega_2^2 Y_2 = Y_o\cos(\Omega t+\phi)\,[C_{21}Y_1 + C_{22}Y_2] + \phi_2(\underset{\sim}{Y},\underset{\sim}{\dot{Y}},\underset{\sim}{\ddot{Y}}) \end{aligned}\right\} \quad (2)$$

where Y_i are the normal coordinates of the system responses

ζ_i damping ratios

ω_i normal mode frequencies

Y_o vertical amplitude of base motion

Ω excitation frequency

ϕ phase angle of the excitation

ϕ_i ( ) nonlinear cubic terms

C_{ij} constant coefficients

The system dynamic response is determined when the supporting structure is subjected to vertical harmonic motion. The effect of cubic nonlinearity on the system parametric responses under prinicpal and combination parametic resonance condition are examined by using the asympototic approximation technique of Struble.[18]

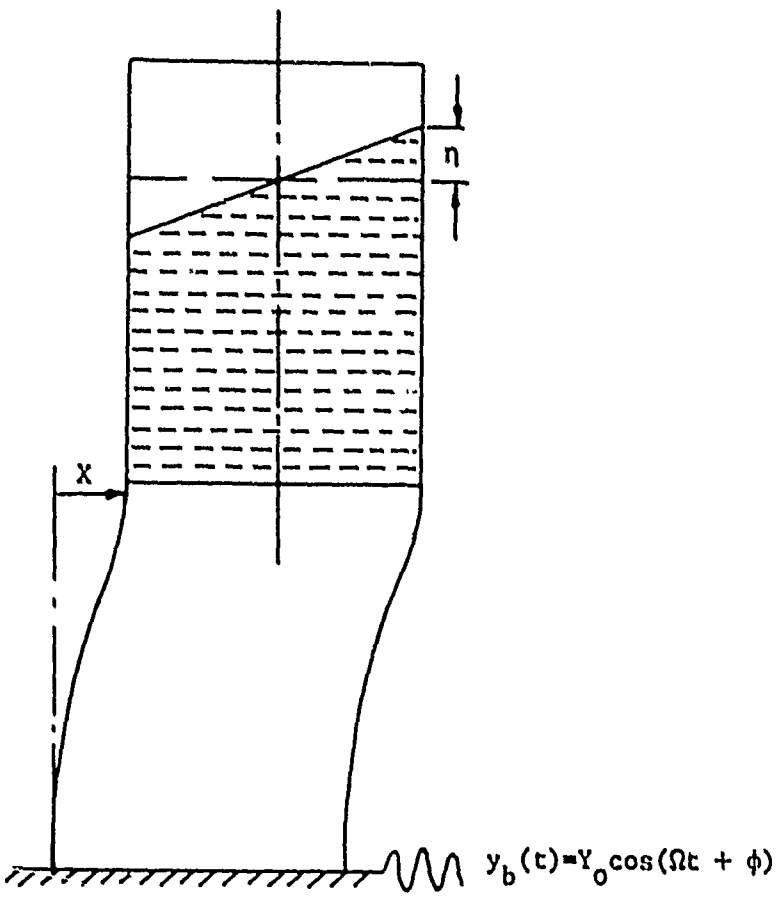


Fig.(4) Elevated water tower subjected to vertical harmonic excitation.

$$\begin{Bmatrix} X \\ \eta \end{Bmatrix} = [R] \begin{Bmatrix} y_1 \\ y_2 \end{Bmatrix}$$

[R] = modal matrix

y_i = normal coordinates

The steady state amplitude response of the system in the neighborhood of the first normal mode parametric resonance condition $\Omega = 2\omega_1$ is shown in fig. (5) for various values of damping coefficients. It is seen that the response amplitude increases as the excitation frequency increases in a manner similar to the characteristics of hard nonlinear systems. This means that the parametric response of the first mode is governed mainly by the structure nonlinearity. The system response near the second mode parametric resonance condition $\Omega = 2\omega_2$ is shown in fig. (6). The response curves follow the characteristics of hard nonlinear systems. Fig. (7) shows the response amplitude curves near combination parametric resonance $\Omega = \omega_1 + \omega_2$ where ω_1 and ω_2 are the two normal mode frequencies.

The three figures (5-7) exhibit the jump and collapse phenonmena of the response amplitudes at excitation frequencies above or below the condition of parametric resonance depending on whether the system is hard or soft. While the nonlinearity brings the originally unstable system into a bounded limit cycle the damping decreases the response amplitude magnitude and causes the amplitude to collapse at points of vertical tangency on the response curves. Under parametric resonance it is found that the damping is not adequate to control the vibration. It is the nonlinearity which is responsible for the limitation of amplitude growth.

Reference

1. Hermann, G., "Stability of Equilibrium of Elastic Systems Subjected to Nonconservative Forces," ASME Applied Mech. Reviews 20(2), pp. 103-108, 1967.

2. Hermann, G. and Bungay, R.W., "On the Stability of Enlstic Systems Subjected to Nonconservative Forces," ASME J. Appl. Mech. 31, pp. 435-440, 1964.

3. Pflüger, A., "Stabilitatsprobleme der Elastomechanik," Julius Springer, Berlin 1950.

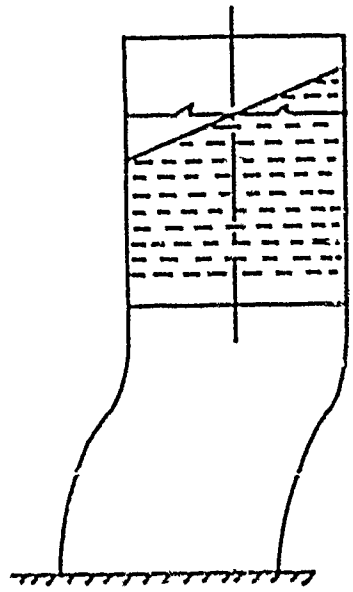
4. Beck, M., "Die Knicklast des einseitig eingespannten, tangential gedruckten Stabs," Zeitschrift fur angewandte Mathematik und Physik 3, pp. 225-228, 1952.

5. Ziegler, H., "Die Stabilitatskriterium der Elastomechanik," Ingenieur-Archiv 20, pp. 49-56, 1952.

6. Ziegler, H., "Linear Elastic Stability,". Zeitschrift fur angewandte Mathematik und Physik 4, pp. 89-121, 168-185, 1953.

7. Bolotin, V.V., Nonconservative Problems of the Theory of Elastic Stability, Macmillan Company, New York, 1963.

8. Fu, F.C.L. and Nemat Nasser, S., "Stability of Solution of Linear Differential Equations with Harmonic Coefficients," AIAA Journal 10(1), pp. 30-36, 1972.



$\Omega = 2\omega_1$

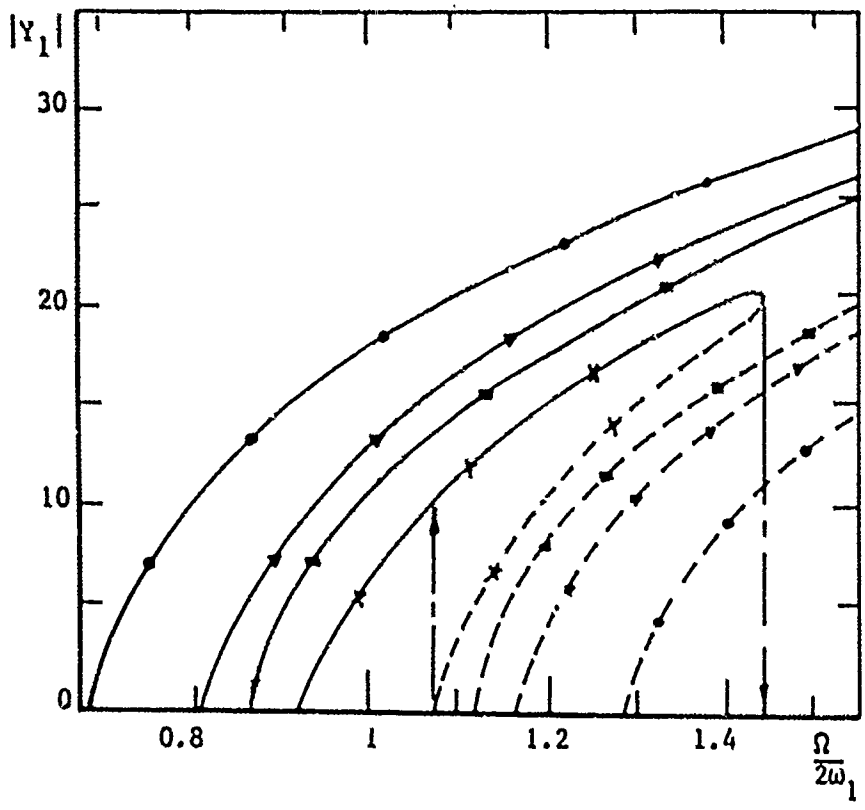


Fig.(5) Amplitude frequency response curves of first mode parametric excitation for various values of damping values ($\bullet\zeta_1$=0, $\blacktriangledown\zeta_1$=0.0001, $\blacksquare\zeta_1$=0.001, $x\zeta$=0.08), ε=0.008.

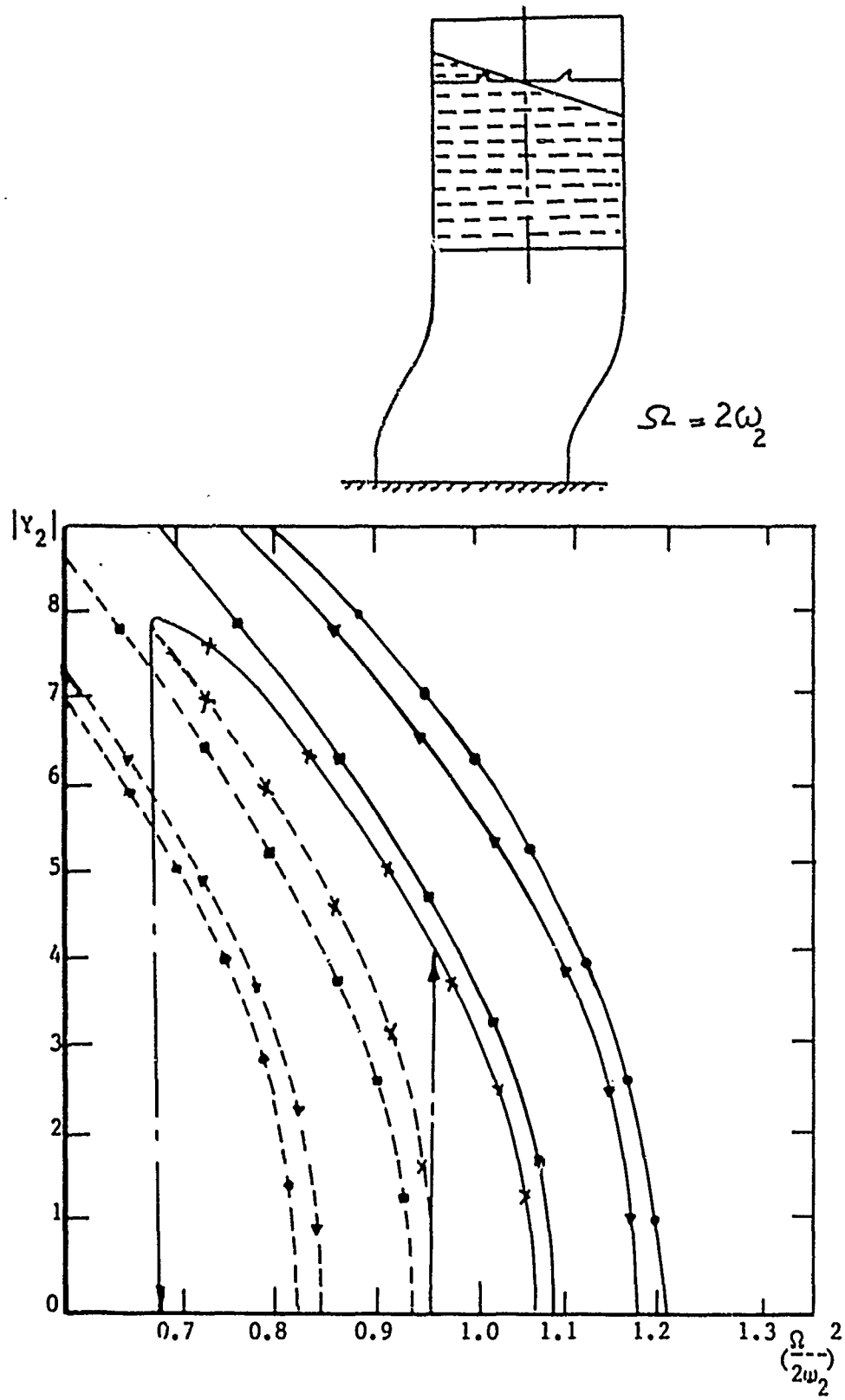


Fig. (6) Amplitude frequency response curves of second mode parametric excitation ($\bullet\zeta_2=0, \blacktriangledown\zeta_2=0.004, \blacksquare\zeta_2=0.008, \times\zeta_2=.04$) $\varepsilon=0.004$

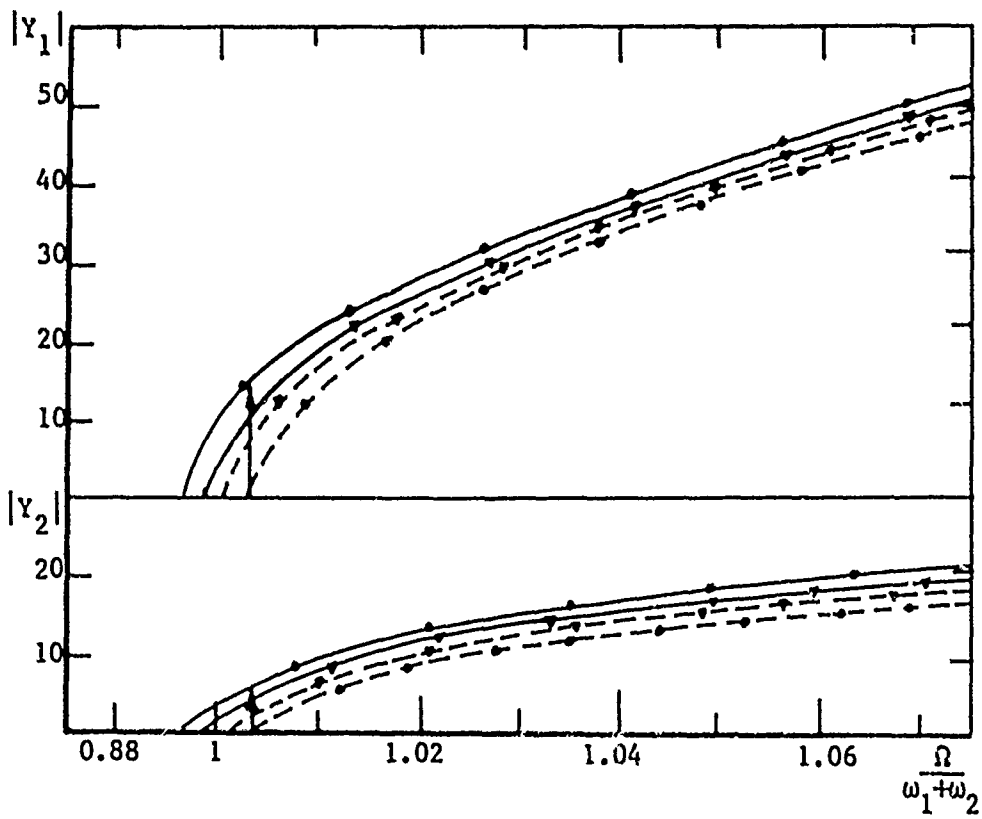


Fig. (7) Amplitude frequency response curves near combination parametric resonance $\Omega=\omega_1+\omega_2$ ($\bullet\ \zeta_1=\zeta_2=0.0005$, $\blacktriangledown\ \zeta_1=\zeta_2=0.002$) $\varepsilon=0.005$.

9. Krauter, A.I. and Brower, D.C., Squeal of Water-Lubricated Elastomeric Bearings - A Quantiative Laboratory Investigation, Technical Report SRC 78-TR-26, Shaker Research Corp., Ballston Lake, New York, 1978.

10. Evan-Iwanowski, R.M., Resonance Oscillations in Mechanical Systems, Elsevier Scientific Publishing Company, Amsterdam, 1976.

11. Dzygadlo, Z. "Parametric Self-Excited Vibration of a Simply Supported Plate in Supersonic Flow," Proceedings of Vibration Problems 4(6), pp. 353-365, 1965.

12. Dzygadlo, Z. and Kaliski, S., "Parametric Self-Excited Vibrations of Elastic and Aeroelastic Systems with Travelling Waves," Bull. Acad. Polon. Sci., Series des Sci. Tech. 14(1), pp. 1-10, 1966.

13. Dzygadlo, A. and Kaliski, S., "Instability Limits of Parametric Self-Excited Vibrations of Elastic and Aeroelastic Systems with Travelling Waves," Arc. Mech. Stosowanej 20(4), pp. 461-471, 1968.

14. Friedman, P., "Aeroelastic Instability of Hingless Helicopter Blades," J. Aircraft 10(10), 1973.

15. Bolotin, V.V., The Dynamic Stability of Elastic Systems, Holden-Day, Inc., San Francisco, 1964.

16. Schmidt, G., Parametric Oscillations, (in German) VEB Deutscher Verlag der Wissenschaften, Berlin, 1975.

17. Hsu, C.S., On Parametric Excitation and Snap-Through Stability Problems of Shells, in Thin Shells Structures: Theory, Experiment and Design, Edited by E.E. Sechler and Y.C., Fung, Prentice Hall, pp. 103-131,1973.

18. Struble, R.A., Nonlinear Differential Equations, McGraw-Hill, New York, 1962.

Damping in Elastic Systems

Prof. E. Dowell

(Not available for publication)

VISCOSITY AND DAMPING AS THE DIABOLIC AND ROGUISH CAUSE FOR INSTABILITY

Prof.Dr.rer.nat.Helmut F.Bauer

Universität der Bundeswehr
Fakultät Luft- und Raumfahrttechnik
Institut für Raumfahrttechnik
Werner-Heisenberg-Weg 39
D-8014 Neubiberg

Abstract

The statement, that the introduction or increase of damping or viscosity will by all means lead a dynamical system to stability, is in many cases not true. For this reason some engineering examples have been shown, where damping is the cause of instability or where its increase even accelerates such an instability. This shows, that the introduction of damping or viscosity into an unstable system has to be performed with great care, if one wants to obtain with it a stable system.

1. Introduction

The statement of the decrease of vibration amplitudes by damping or viscosity inherent in a mechanical or liquid system is in many cases superficial and will lead to wrong conclusions concerning the stability of such systems. The fact, that there exist many examples in engineering where this is not the case should be made aware to any engineering investigator. A few of such systems will be treated here, where the first system is that of a rotating mechanical two-degree-of-freedom oscillator consisting of a mass attached to springs and dashpots, where the increase of the magnitude of damping leads for natural frequencies below the rotational angular velocity (spin) to accelerating instability. The vibration amplitudes increase with larger damping. The same is true for a satellite boom in the axis of rotation of a spin stabilized satellite. In addition a spin-stabilized satellite with a liquid ring damper may be unstable if not designed properly, i.e. if the moments of inertia do not satisfy the condition $I_z > I_x$, meaning that the moment of inertia about the spin-axis must be larger than that about a perpendicular axis through the center of mass. If this condition is not satisfied the angle of nutation increases, thus any damper and increase of its damping enhances instability. So will a linearly damped mass in an orbiting space laboratory under the action of the residual inhomogeneous micro-gravity field perform motions, which exhibit unstable behavior, depending on the initial conditions and the magnitude of the damping. This means, that in this case of free fall the mass point increases its distance to the original location during the orbiting of the space laboratory a fact, which may be of importance during space walks and other experimental activities in a space laboratory. For two specific liquid systems the fact, that damping leads to instability shall also be presented. This means, that viscous liquid exhibits instabilities where frictionless liquid do show stability. The first system is a solidly rotating liquid column with a free outer surface in zero-gravity environment. In such a state the cylindrical liquid surface, being able to oscillate, will be held together by the surface tension force, which counteracts the centrifugal force. It can be shown, that for frictionless liquid the cylindrical liquid column rotating about its axis with a constant angular velocity Ω_o is stable for a much larger angular velocity than a column consisting of viscous liquid. Writing for the rotational Bond number $\tilde{Bo} = \rho\Omega_o^2 a^3/T$, where ρ is the mass density of the liquid, T the surface tension and 2a the diameter of the liquid column, one obtains in the case of frictionless liquid, that for $\tilde{Bo}_i \leq m(m+1)$, and in the case of viscous liquid, that for $\tilde{Bo}_\nu \leq (m^2-1)$ stability is guaranteed. The value m is the mode at which the system oscillates, indicating that m=2 deforms the cross-section of the liquid column to an elliptic form. For m=2 it is $\tilde{Bo}_i \leq 6$ and $\tilde{Bo}_\nu \leq 3$. We notice also, that the stability boundary for viscous liquid is independent of the magnitude of the viscosity. Determining the roots $s=\sigma+i\omega$ of such a system yields, that the instability grows with increasing rotational Reynoldsnumber $\tilde{Re} = \Omega_o a^2/\nu$ and decreases with larger surface tension parameter $Ta/\rho\nu^2$, meaning, that the diverging oscillation amplitudes increase rapidly and that the oscillation frequency increases. A more viscous liquid enhances the instability. While the wave in the opposite direction of spin becomes more unstable, the wave in direction of spin exhibits more stability, as is expressed by larger decay magnitude for increased rotational Reynolds number. Increase of the surface tension parameter renders increased oscillatior frequency and slightly decreased decay magnitude. The second liquid system, that has been investigated, is an annular liquid column around an elastic center shell. This system also holds quite a few surprises, in as much as if the liquid is treated as frictionless liquid the coupled hydro-elastic frequencies are all conjugate imaginary.

This means, that the system oscillates in its real coupled frequencies without decay or increase of amplitude. For a viscous annular liquid column around the elastic shell instability appears in the motion of the free liquid surface as well as in the shell motion. For a less rigid shell the liquid becomes unstable if it is a very thin layer, while the structural root concerning the motion of the shell becomes strongly unstable, exhibiting diverging instability for thick liquid layers and for very thin viscous liquid layers the shell shows an oscillatory instability. Since viscosity introduces phase shifts and additional excitation through the no-slip condition in form of angular motion, instability occurs in a few situations which are not present for frictionless liquid, which renders, of course, a quite different flow behavior of the liquid.

2. Instability of Damped Mechanical- and of viscous Liquid Systems

In many cases where one would think, that the introduction of damping in form of an energy dissipating dashpot or in a liquid system the use of a more viscous liquid would eliminate or at least ease an instability, one may be surprised, that the opposite will occur. On the contrary the increase of damping increase the growth of the unstable motion, i.e. renders increased diverging amplitude of the motion. This is not only true in some mechanical cases, but also appears in fluid systems, where similar effects have been detected. Some of these cases will be treated in the following.

2.1. Rotating Oscillator

A solidly rotating oscillator of two-degrees-of-freedom consisting of two equal springs of stiffness k/2, dashpots with damping coefficients c/2 each in perpendicular direction (Figure 1) renders with the kinetic energy

$$T = \frac{m}{2}\{\dot{\vec{r}} + [\vec{\Omega}_0 \times \vec{r}]\}^2 \tag{1}$$

where $\vec{\Omega}_0 = \Omega_0 \vec{k}$ and $\vec{r} = x\vec{i} + y\vec{j}$, the dissipation function

$$D = \frac{c}{2}[\dot{x}^2 + \dot{y}^2] \tag{2}$$

and the potential energy

$$V = \frac{k}{2}(x^2 + y^2) \tag{3}$$

and no exterior forces with the Lagrange equation

$$\frac{d}{dt}\left(\frac{\partial T}{\partial \dot{q}_\lambda}\right) - \frac{\partial T}{\partial q_\lambda} + \frac{\partial D}{\partial \dot{q}_\lambda} + \frac{\partial V}{\partial q_\lambda} = 0, \quad q_\lambda = x \text{ and } y$$

the equations of motion of the mass point

$$m[\ddot{x} - 2\Omega_0\dot{y} - \Omega_0^2 x] + c\dot{x} + kx = 0 \tag{4a}$$

$$m[\ddot{y} + 2\Omega_0\dot{x} - \Omega_0^2 y] + c\dot{y} + ky = 0 \tag{4b}$$

With $\omega^2 = \frac{k}{m}$ and $2\zeta\omega = \frac{c}{m}$ we obtain with $x = Xe^{(s/\Omega_0)t}$, $y = Ye^{(s/\Omega_0)t}$ as the solution of

the system the characteristic equation ($S \equiv \frac{s}{\Omega_0}$, $\bar{\omega} \equiv \frac{\omega}{\Omega_0}$)

$$S^4+4\zeta\bar{\omega}S^3+2[2\zeta^2\bar{\omega}^2+\bar{\omega}^2+1]S^2+4\zeta\bar{\omega}(\bar{\omega}^2-1)S+(\bar{\omega}^2-1)^2=0 \qquad (5)$$

With the Hurwitz-Criteria for stability, it may be found, that instability occurs in the strip region $0<\bar{\omega}<1$ and $\zeta>0$ in the $(\bar{\omega},\zeta)$-plane. The coupled four roots of the frequency equation (5) ($s=\sigma+i\omega$) are presented in Figure 2a,b for $1 \leq (\omega/\Omega_0) \leq 10$ and Figure 2c,d for $0 < (\omega/\Omega_0) < 1$ and various small damping factors ζ. It may be seen that the vibrator becomes, for $0 < (\omega/\Omega_0) < 1$ with damping unstable. The increase of damping accelerates the instability of two roots in as much as it increases the amplitudes of oscillation. If the frequency ω is larger Ω_0 all four roots are stable and exhibit with increasing damping damped oscillations with increased decay magnitude. So it may be noticed, that with decreasing spin velocity Ω_0 and increasing damping factor ζ the roots for $\omega/\Omega_0 > 1$ become more stable, indicating stronger decay at a higher frequency (see s-plane, Fig. 2a,b). If the angular velocity of spin Ω_0 is larger then $\omega = \sqrt{k/m}$ two roots remain stable and exhibit the same behavior as those in the case $\Omega_0 < \omega$, i.e. show increased stability as ζ increases and Ω_0/ω decreases, while the other two roots become unstable and exhibit with increasing damping larger instability. This means, that the diverging amplitude increases much faster at slightly decreased frequency. This is more pronounced, if the spin magnitude Ω_0 moves away from the natural frequency ω of the spring-mass-system. For larger damping factors $\zeta > 1$ the roots are exhibited in Figure 3a through 3e. For $\Omega_0 < \omega$ the results are given in Figure 3a and 3b, where again only the upper-half-plane is shown, since the roots represent conjungate complex couples. With the increase of Ω_0 the oscillation frequency magnitude reduces drastically, which also happens for an increase of the damping factor ζ. The decay magnitude also reduces considerably with the increase of the velocity of spin (Figure 3a). For increasing damping the oscillation shows a frequency, which decreases at enlarged decay magnitude. If, however, the spin Ω_0 is larger than $\omega(\Omega_0 > \omega)$ one couple of the roots become unstable. The stable roots are shown in Figure 3d and express for increasing damping $\zeta > 0$ a slight increase of the oscillation frequency at a stronger decay. Increasing Ω_0 further means reduced oscillation frequency at lesser decay. The unstable root couple is presented in Figure 3e, where an increase of damping $\zeta > 1$ yields first an increase of diverging at smaller frequency and for even larger ζ-values a decrease of the oscillation frequency at a decreased divergence. Increasing the spin magnitude Ω_0 further renders increased divergence at higher oscillation frequencies. This is also true for a satellite boom oriented in the rotational axis of a spin-stabilized satellite, for which the equations of motion read for a symmetric circular cross-section of the boom [1,2]

$$\frac{\partial^2\xi}{\partial t^2} - 2\Omega_0\frac{\partial\eta}{\partial t} - \Omega_0^2\xi + 2\zeta\omega\frac{\partial\xi}{\partial t} + \frac{EI}{\rho A}\frac{\partial^4\xi}{\partial z^4} = 0 \qquad (6a)$$

$$\frac{\partial^2\eta}{\partial t^2} + 2\Omega_0\frac{\partial\xi}{\partial t} - \Omega_0^2\eta + 2\zeta\omega\frac{\partial\eta}{\partial t} + \frac{EI}{\rho A}\frac{\partial^4\eta}{\partial z^4} = 0 \qquad (6b)$$

where $\xi(z,t)$, $\eta(z,t)$ are the bending deflections in x- and y-direction resp.. EI is the constant stiffness of the boom and ρA its constant mass per unit length, while Ω_0 is the constant angular velocity (spin) of the satellite about the z-axis (Figure 1). This system is also unstable for $\lambda_n^2\sqrt{(EI/\rho A\ell^4)} < \Omega_0$, where λ_n

are the eigenvalues of the bending problem. In this case of a cantilever beam $\lambda_1 = 1.8751$, $\lambda_2 = 4.6941$, $\lambda_3 = 7.8541$ etc..

2.2. Spin-stabilized Satellite

A spin-stabilized rigid satellite may, once disturbed, perform undesirable nutational oscillations. In order to dampen this nutational motion the satellite has to be equipped with a damping device, consisting usually of a damped vibrator of one or the other kind (also liquid damper). The provision of damping, however, is by no means a guarantee for the decay of the nutational oscillations, unless the satellite exhibits by its proper design the largest moment of inertia about the axis of spin. If this is not the case, the nutational angle will increase until the satellite spins about its axis of maximum moment of inertia, a fact, which for the orientation of the original spin axis is of disastrous consequences. This may be seen from the simple treatment of the problem. If the satellite is supposed to be spin-stabilized about the z-axis, where the satellite exhibits $I_z < I_x = I_y$ the equations of motion are given by the Euler equations (Figure 1)

$$I_x\dot{\Omega}_x + (I_z - I_x)\Omega_y\Omega_z = 0 \tag{7a}$$

$$I_x\dot{\Omega}_y + [I_x - I_z]\Omega_x\Omega_z = 0 \tag{7b}$$

$$I_z\dot{\Omega}_z = 0 \tag{7c}$$

with the solution

$$\Omega_x = N\cos(\nu t + \varepsilon); \quad \Omega_y = N\sin(\nu t + \varepsilon), \quad \Omega_z = \Omega_{z_0} \tag{8}$$

N being the amplitude and ν the frequency of the nutational motion.
The kinetic energy of the satellite is

$$T = \frac{1}{2}[I_x N^2 + I_z \Omega_{z_0}^2], \tag{9}$$

while the angular momentum D is given by

$$D^2 = I_x^2 N^2 + I_z^2 \Omega_{z_0}^2 \tag{10}$$

Elimination of Ω_z^2 yields with $I_x N = D\sin\delta$ (δ being the nutational angle)

$$2T = \frac{D^2}{I_z}\{1 + \frac{I_z - I_x}{I_x}\sin^2\delta\} \tag{11}$$

which is exactly valid for a rigid satellite. Since, however, a damping device should be light and small, this relation may also be employed for a satellite with a damping device. Thus the kinetic energy will render a function of time now, i.e. $T = T(t)$. The time derivative yields

$$\dot{T} = \frac{D^2}{I_x I_z}(I_z - I_x)\sin\delta\cos\delta\cdot\dot{\delta} \tag{12}$$

which for the dissipation of energy through the damping device renders a negative value, i.e. $\dot{T} < o$. Thus for the above mentioned satellite $I_z - I_x < o$, the

value $\dot{\delta}$ must be larger zero ($\dot{\delta}>0$), indicating inspite of the damping a growth of the nutational angle δ. The satellite must therefore be designed in such a way, that $I_z > I_x$, meaning, that the moment of inertia about the spin axis should be the largest. Then $\dot{\delta}<0$, which means, that the nutational angle decreases with time, bringing the spin axis back to its original orientation.

2.3. Linearly Damped Mass in a Space-laboratory in Orbit

The case of the free fall with linear velocity dependent friction in an orbiting space laboratory[3] renders without exterior forces the equations for relative motion with respect to the center of mass of the space laboratory ($c/m = 2\zeta\Omega_0$)

$$\ddot{x} + 2\Omega_0\dot{z} + 2\zeta\Omega_0\dot{x} = 0 \tag{13a}$$

$$\ddot{y} + 2\zeta\Omega_0\dot{y} + \Omega_0^2 y = 0 \tag{13b}$$

$$\ddot{z} - 2\Omega_0\dot{x} - 3\Omega_0^2 z + 2\zeta\Omega_0\dot{z} = 0 \tag{13c}$$

The coordinates (x,y,z) are connected to the center of mass with x in the flight direction, y perpendicular to the orbit plane and z in the orbit plane pointing from the center of the earth into space [Fig.4]. The above equations are obtained from the Lagrange equation with the kinetic energy (1), where $\vec{r}=x\vec{i}+y\vec{j}+(r_0+z)\vec{k}$, $\vec{\Omega}_0=\Omega_0\vec{j}$ (r_0 being the radius of the circular orbit), the dissipation function $D=(c/2)(\dot{x}^2+\dot{y}^2+\dot{z}^2)$ and Newton's attraction potential

$$V(x,y,z) \approx -\frac{\mu m}{r_0}\left(1 - \frac{z}{r_0} - \frac{x^2+y^2}{2r_0^2} + \frac{z^2}{r_0^2}\right)$$

in which μ represents the gravitation parameter $\mu=\gamma M$ (M as mass of the earth and γ as the gravitational constant). It may be noticed that the motion in y-direction is independent from that in x- and z-direction and performs a damped motion. The coupled motion in x and z depends on the damping magnitude ζ and the initial conditions. The characteristic equation reads

$$s\left(\frac{s}{\Omega_0}\right)^3 + 4\zeta\left(\frac{s}{\Omega_0}\right)^2 + (1+4\zeta^2)\left(\frac{s}{\Omega_0}\right) - 6\zeta = 0 \tag{14}$$

The solution is given by the expression

$$x = A + Be^{s_2 t} + Ce^{s_3 t} + De^{s_4 t} \tag{15a}$$

$$z = -B\left[\frac{1}{2}\left(\frac{s_2}{\Omega_0}\right)+\zeta\right]e^{s_2 t} - C\left[\frac{1}{2}\left(\frac{s_3}{\Omega}\right)+\zeta\right]e^{s_3 t} - D\left[\frac{1}{2}\left(\frac{s_4}{\Omega_0}\right)+\zeta\right]e^{s_4 t} \tag{15b}$$

$$y = e^{-\zeta\Omega_0 t}\left[y_0\cos\left(\sqrt{1-\zeta^2}\,\Omega_0 t\right) + \frac{\dot{y}_0+\zeta\Omega_0\varphi_0}{\Omega_0\sqrt{1-\zeta^2}}\sin\left(\sqrt{1-\zeta^2}\,\Omega_0 t\right)\right] \tag{15c}$$

where the integration constants are given with the initial conditions (x_0, y_0, z_0), $(\dot{x}_0, \dot{y}_0, \dot{z}_0)$ by

$$A = x_0 + (z_0 + \frac{1}{2}\frac{\dot{x}_0}{\Omega_0})/\zeta \tag{16a}$$

$$B = -\frac{1}{[\frac{s_2}{\Omega_0} - \frac{s_3}{\Omega_0}]} \cdot \frac{1}{[\frac{s_2}{\Omega_0} - \frac{s_4}{\Omega_0}]} \{\frac{s_3}{\Omega_0}\frac{s_4}{\Omega_0}\frac{1}{\zeta}(z_0 + \frac{1}{2}\frac{\dot{x}_0}{\Omega_0}) + (\frac{s_3}{\Omega_0} + \frac{s_4}{\Omega_0})\frac{\dot{x}_0}{\Omega_0} + 2(\frac{\dot{z}_0}{\Omega_0} + \zeta\frac{\dot{x}_0}{\Omega_0})\} \tag{16b}$$

$$C = \frac{1}{[\frac{s_2}{\Omega_0} - \frac{s_3}{\Omega_0}]} \frac{1}{[\frac{s_3}{\Omega_0} - \frac{s_4}{\Omega_0}]} \{\frac{s_2}{\Omega_0}\frac{s_4}{\Omega_0}\frac{1}{\zeta}(z_0 + \frac{1}{2}\frac{\dot{x}_0}{\Omega_0}) + (\frac{s_2}{\Omega_0} + \frac{s_4}{\Omega_0})\frac{\dot{x}_0}{\Omega_0} + 2(\frac{\dot{z}_0}{\Omega_0} + \zeta\frac{\dot{x}_0}{\Omega_0})\} \tag{16c}$$

$$D = \frac{1}{[\frac{s_2}{\Omega_0} - \frac{s_4}{\Omega_0}]} \frac{1}{[\frac{s_3}{\Omega_0} - \frac{s_4}{\Omega_0}]} \{\frac{s_2}{\Omega_0}\frac{s_3}{\Omega_0}\frac{1}{\zeta}(z_0 + \frac{1}{2}\frac{\dot{x}_0}{\Omega_0}) + (\frac{s_2}{\Omega_0} + \frac{s_3}{\Omega_0})\frac{\dot{x}_0}{\Omega_0} + 2(\frac{\dot{z}_0}{\Omega_0} + \zeta\frac{\dot{x}_0}{\Omega_0})\} \tag{16d}$$

The result of the motion of an object (space walking astronaut, satellite or structural part of a space station to be assembled in orbit) is shown for the "free fall"-case, i.e. without initial velocities ($\dot{x}_0 = \dot{z}_0 = o$) in Figure 5 for various dampings. We may see, that without damping, the object performs during each orbit a "hopping" motion and lags for an initial $z_0 > o$ behind the space shuttle, while for $z_0 < o$ it will move ahead of the vehicle. Including a linear damping force will not make the object move less far away from the space shuttle during one orbit, as one may expect, but it will move it with an increased magnitude of damping ζ farther away from the vehicle, as may be seen in Figure 5. This is contrary to what happens in free fall on earth, as may be seen from the free fall results ($\dot{z}_0 = o$)

$$z = z_0 - \frac{g_0}{z} t^2 \quad \text{without friction}$$

and

$$z = z_0 - \frac{g_0}{c/m} t + \frac{g_0}{(c/m)^2}(1 - e^{-(c/m)t}) \quad \text{with friction.}$$

After one orbit the object is without experiencing friction about 349 m away from the center-of-mass of the space shuttle, while for $\zeta = o.o5$ the distance is already 777 m, if the object was set out at $z_0 = 1o$ m. This also is quite a surprising result.

2.4. Rotating Liquid Column

An infinitely long liquid column exhibiting no z-dependency (two-dimensional case) is rotating solidly about its axis of symmetry (z-axis) with the angular velocity Ω_0 [4,5]. The free liquid surface at r=a is held together by surface tension T(Fig.6), which provides the restoring force, if the surface is disturbed. The equations of motion for frictionless liquid in body-fixed coordinates are the Euler equations for a rotating system, which are in linearized form in a zero-gravity environment given by

$$\frac{\partial \vec{v}}{\partial t} + 2[\vec{\Omega}_0 x \vec{v}] + [\vec{\Omega}_0 x (\vec{\Omega}_0 x \vec{r})] + \frac{1}{\rho} \text{grad } p = o \tag{17}$$

Since the liquid is considered incompressible the continuity equation reads ($\vec{v} = u\vec{e}_r + v\vec{e}_\varphi$)

$$\operatorname{div} \vec{v} = 0 \tag{18}$$

The introduction of an acceleration potential

$$\chi = \frac{p}{\rho} - \frac{1}{2}\Omega_0^2 r^2 \tag{19}$$

yields with the free surface condition

$$\rho \frac{\partial \chi}{\partial t} + \rho \Omega_0^2 a u + \frac{T}{a^2}\left(u + \frac{\partial^2 u}{\partial \varphi^2}\right) = 0 \quad \text{at } r=a \tag{20}$$

and with the velocities and acceleration potential in form of

$$\begin{aligned} u(r,\varphi,t) &= U(r)\sin(\omega t + m\varphi) \\ v(r,\varphi,t) &= V(r)\cos(\omega t + m\varphi) \\ \chi(r,\varphi,t) &= P(r)\cos(\omega t + m\varphi) \end{aligned} \tag{21}$$

where $P(r) = \bar{A}_m r^m$

finally the natural frequencies of the system. They are

$$\frac{\omega_m}{2\Omega_0} = \frac{1}{2}\left(1 \pm \sqrt{1 + m\left[\frac{T(m^2-1)}{\rho a^3 \Omega_0^2} - 1\right]}\right) \tag{22}$$

which exhibits for

$$\Omega_0^2 \geq \frac{Tm}{\rho a^3}(m+1) \quad \text{or} \quad \tilde{Bo} = \frac{\rho \Omega_0^2 a^3}{T} \geq m(m+1) \tag{23}$$

instability where $\tilde{Bo}$ is the Bondnumber. For a viscous liquid the Euler equation (17) has to be substituted by[4] the Stokes equation

$$\frac{\partial \vec{v}}{\partial t} + 2[\vec{\Omega}_0 \times \vec{v}] + [\vec{\Omega}_0 \times (\vec{\Omega}_0 \times \vec{r})] + \frac{1}{\rho} \operatorname{grad} p + \nu \operatorname{curl} \operatorname{curl} \vec{v} = 0 \tag{24}$$

The centrifugal- and Coriolis acceleration term may be written as

$$[\vec{\Omega}_0 \times (\vec{\Omega}_0 \times \vec{r})] = -\operatorname{grad}\left(\frac{1}{2}\Omega_0^2 r^2\right) \tag{25}$$

and

$$2[\vec{\Omega}_0 \times \vec{v}] = -\operatorname{grad}(2\Omega_0 \Psi) \tag{26}$$

where Ψ represents the streamfunction and renders

$$u = -\frac{1}{r}\frac{\partial \Psi}{\partial \varphi} \text{ and } \quad v = \frac{\partial \Psi}{\partial r} \tag{27}$$

We finally have to solve the differential equation

$$\Delta(\Delta \Psi - \frac{1}{\nu}\frac{\partial \Psi}{\partial t}) = 0 \tag{28}$$

where Δ represents the Laplace operation in polar coordinates.
The boundary conditions are

$$\tau_{r\varphi} = \eta[r\frac{\partial}{\partial r}(\frac{v}{r}) + \frac{1}{r}\frac{\partial u}{\partial \varphi}] = 0 \quad \text{for } r=a \tag{29}$$

and the free surface condition

$$\frac{\partial p}{\partial t} + \rho a \Omega_0^2 u + 2\rho\Omega_0 \frac{\partial \Psi}{\partial t} - 2\eta \frac{\partial^2 u}{\partial r \partial t} + \frac{T}{a^2}[u + \frac{\partial^2 u}{\partial \varphi^2}] = 0 \qquad \text{at } r=a \tag{30}$$

With the stream function

$$\Psi(r,\varphi,t) = e^{st} \sum_{m=1}^{\infty} \{A_m r^m + B_m I_m(\sqrt{\frac{s}{\nu}}\, r)\} e^{im\varphi} \tag{31}$$

we obtain finally the frequency equation

$$I_m(x)\{x^6 + 4m^2x^4 + m(m^2-1)x^2[8m + \frac{Ta}{\rho\nu^2}] + \frac{4Ta}{\rho\nu^2}m^2(m^2-1) - (4m+x^2)[m(\frac{\Omega_0 a^2}{\nu})^2 +$$

$$+ 2i(\frac{\Omega_0 a^2}{\nu})x^2]\} = 2xI_{m-1}(x) \cdot \{x^4 + 2x^2m(m^2-1) + \frac{Ta}{\rho\nu^2}m(m^2-1) - 2ix^2(\frac{\Omega_0 a^2}{\nu}) - m(\frac{\Omega_0 a^2}{\nu})^2\} \tag{32}$$

where $x = a\sqrt{\frac{s}{\nu}}$. For vanishing viscosity $\nu \to 0$, we obtain the above result (22) for the natural frequencies of the frictionless liquid. From the complex frequency equation of the viscous liquid the stability boundary is found to be ($s \to 0$)

$$\frac{Ta}{\rho\nu^2}(m^2-1) = \tilde{Re}^2 = \tilde{Ta} \tag{33}$$

where $\tilde{Re} = \frac{\Omega_0 a^2}{\nu}$ is the rotational Reynolds number or $\tilde{Re}^2 = \tilde{Ta}$ the Taylor number. This means, that for

$$\Omega_0^2 \geq \frac{T}{\rho a^3}(m^2-1) \quad \text{or} \quad \tilde{Bo} \geq m^2-1 \tag{34}$$

the rotating liquid column exhibits instability. It may be noticed that this condition is independent of the viscosity and that the existence of viscosity, whatever magnitude it may have, renders instability at a much lower rotational speed, than for a frictionless liquid. It may be noticed from the results, that due to the rotation of the liquid column, the roots are no longer symmetrical to the real axis.

This means, that the surface waves in the direction of spin exhibit a different frequency than those in the opposite direction of spin (Fig.7). This latter wave becomes due to the Coriolis force finally with the increase of the rotational Reynolds number unstable, while the root in the direction of spin renders even better stability by the increase of spin (Fig.7a). It performs for increased $\tilde{R}e = (\Omega_0 a^2/\nu)$ oscillations of larger frequency with a faster decay. For larger surface tension the frequency of oscillation increases, while the decay magnitude decreases. The root in the third quadrant, representing the wave behavior in the direction opposite to the spinning of the viscous liquid column decreases at first its frequency and decay magnitude with increasing spin Ω_0 and becomes finally unstable (Fig.7c), i.e. the root migrates across the origine of the s-plane into the first quadrant. With increasing rotational speed the oscillatory instability increases, exhibiting larger oscillation frequency and larger diverging magnitude. For increased surface tension parameter $Ta/\rho\nu^2$ we obtain a smaller oscillation frequency with a much less strongly diverging magnitude of amplitudes. For a more viscous liquid both the surfacetension parameter and the rotational Reynoldsnumber decrease, indicating that the unstable root renders a slightly decreased oscillation frequency at less diverging amplitudes. For the stable root we obtain with the increase of viscosity an oscillation with increased frequency at less decaying amplitudes (Fig.7a). The results are also presented as real- (Figure 8a) and imaginary part of the roots for the elliptic cross-sectional mode m=2 (Fig.8b) as a function of the rotational Reynoldsnumber $\tilde{R}e = (\Omega_0 a^2/\nu)$. For the root representing the wave in the direction of spin we notice, that with increasing Reynoldsnumber the real part of the root for m=2 is negative (stable root) and increases its magnitude, indicating, that stronger decay (Fig.8a) appears with a higher oscillation frequency (Fig.8b). For increasing tension parameter $Ta/\rho\nu^2$ the oscillation frequency increases at a lesser decay. In Figure 8c we see the real- and imaginary part of the root, representing the wave opposite to the direction of spin. We notice, that at the given value (33) the root becomes unstable. Both real- and imaginary part vanish at this location. With the increase of the Reynoldsnumber the oscillation frequency increases in the unstable region with increasing divergence. With larger tension parameter, instability happens at a larger $\tilde{R}e$ and renders smaller oscillation frequency at a lesser divergence. For an increase of the viscosity we observe higher oscillation frequency at a stronger divergence.

2.5. Hydroelastic Vibrations

Perturbations in an annular liquid system around an elastic center structure leads to a coupling of the elastic shell and the liquid with a free surface (Fig.6). This hydroelastic system will exhibit coupled frequencies, that shall be determined for ideal (frictionless) liquid [6], as well as for viscous liquid [7]. The liquid is considered incompressible, i.e. div $\vec{v}$=o, and the shell shall exhibit in a perturbed state only small displacements and velocity components. For frictionless liquid ($\vec{v}$=grad Φ) we have to solve the Laplace equation

$$\Delta \Phi = 0 \tag{35}$$

while for viscous liquid, we need to solve the Stokes equation

$$\frac{\partial \vec{v}}{\partial t} + \frac{1}{\rho} \text{grad } p + \nu \text{ curl curl } \vec{v} = 0 \tag{36}$$

We treat the two-dimensional case, i.e. observe z-independence of the velocity $\underline{v}=u\underline{e}_r+v\underline{e}_\varphi$. With the kinematic condition $u=(\partial\zeta/\partial t)$, where $\zeta(\varphi,t)$ is the free liquid surface elevation, the dynamic condition at the free liquid surface at r=a reads

$$\frac{\partial^2\Phi}{\partial t^2}-\frac{T}{\rho a^2}\left[u+\frac{\partial^2 u}{\partial\varphi^2}\right]=0 \qquad \text{for frictionless liquid} \tag{37}$$

or

$$\frac{\partial p}{\partial t}-2\mu\frac{\partial^2 u}{\partial r\partial t}+T\left[u+\frac{\partial^2 u}{\partial\varphi^2}\right]=0 \quad \text{for viscous liquid} \tag{38}$$

For viscous liquid the additional condition at the free liquid surface of vanishing shear stress $\tau_{r\varphi}=0$ yields

$$r\frac{\partial}{\partial r}\left(\frac{v}{r}\right)+\frac{1}{r}\frac{\partial u}{\partial\varphi}=0 \quad \text{at } r=a \tag{39}$$

In these equations T represents the liquid surface tension, μ the dynamic viscosity, p the pressure and ρ the density of the liquid. If we denote the elastic deflection of the shell structure by ξ in radial- and η in angular direction, the cylindrical shell of infinite length renders under the assumption of no motion in the z-direction the equations

$$\xi+\frac{h^2}{12b^2}\left[\xi+2\frac{\partial^2\xi}{\partial\varphi^2}+\frac{\partial^4\xi}{\partial\varphi^4}\right]+\frac{\partial\eta}{\partial\varphi}+\frac{\bar{\rho}(1-\bar{\nu}^2)b^2}{E}\frac{\partial^2\xi}{\partial t^2}=\begin{cases}\dfrac{\rho b^2}{D}\dfrac{\partial\Phi}{\partial t} & \text{for frictionless liquid} \quad (40a)\\[2ex] -\dfrac{b^2}{D}\left(p-2\mu\dfrac{\partial u}{\partial r}\right) & \text{for viscous liquid} \quad (40b)\end{cases}$$

$$\frac{\partial\xi}{\partial\varphi}+\frac{\partial^2\eta}{\partial\varphi^2}-\frac{\bar{\rho}(1-\nu^2)b^2}{E}\frac{\partial^2\eta}{\partial t^2}=\begin{cases}0 \text{ for frictionless liquid} & (40c)\\[2ex] \dfrac{b^2\mu}{D}\left[r\dfrac{\partial}{\partial r}\left(\dfrac{v}{r}\right)+\dfrac{1}{r}\dfrac{\partial u}{\partial\varphi}\right] \quad \text{for viscous liquid} & (40d)\end{cases}$$

These are the Donnell-Mushtari shell equations, in which h is the thickness of the shell, $\bar{\nu}$ the Poisson ratio, E the modulus of elasticity, b the radius of the shell, $\bar{\rho}$ its material density and $\bar{D}=Eh/(1-\bar{\nu}^2)$. It may be noticed, that these equations are coupled with the liquid motion by the terms on the right-hand side, where the viscous liquid exhibits a stronger coupling. The coupling of the shell to the liquid is performed by the boundary conditions

$$\frac{\partial\xi}{\partial t}=u \text{ and } \frac{\partial\eta}{\partial t}=v \text{ (additional for viscous liquid) at } r=b \tag{41}$$

The solution for <u>frictionless</u> liquid is given by the velocity potential

$$\Phi(r,\varphi,t) = \sum_{m=1}^{\infty} [A_m r^m + B_m r^{-m}] e^{im\varphi + st}, \tag{42}$$

with which $u = (\partial\Phi/\partial r)$ and $v = (\partial\Phi/r\partial\varphi)$ may be obtained. For viscous liquid the stream function ($u = -(1/r)(\partial\Psi/\partial\varphi)$, $v = (\partial\Psi/\partial r)$) renders the expression

$$\Psi(r,\varphi,t) = \sum_{m=1}^{\infty} (\bar{A}_m r^m + \bar{B}_m I_m(\sqrt{\frac{s}{\nu}} r) + \bar{C}_m r^{-m} + \bar{D}_m K_m(\sqrt{\frac{s}{\nu}} r)) e^{im\varphi + st} \tag{43}$$

where $s = \sigma + i\omega$ is the complex frequency. The deflections of the shell are

$$\xi(\varphi,t) = \sum_{m=1}^{\infty} X_m e^{im\varphi + st} \tag{44a}$$

$$\eta(\varphi,t) = \sum_{m=1}^{\infty} Y_m e^{im\varphi + st} \tag{44b}$$

Introducing the above given boundary conditions (37), (41) into the equations (40a) and (40') renders for the frictionless case four equations for the unknowns A_m, B_m, X_m and Y_m and for the viscous case six equations for the determination of the constants $\bar{A}_m$, $\bar{B}_m$, $\bar{C}_m$, $\bar{D}_m$, X_m and Y_m. The vanishing coefficient determinant represents in either case the frequency equation. From these frequency equations the special cases of a liquid around a rigid center core[4], a simple elastic shell (without liquid)[8], may be easily obtained. The frequency equation has been evaluated numerically for the various parameters of surface tension $T_0 a/\rho\nu^2$, of density ratio $\bar{\rho}/\rho$, shell wall thickness ratio h/a, diameter ratio k = (b/a) and stiffness parameter $\gamma = \bar{\rho}(1-\bar{\nu}^2)\nu^2 k^2/Ea^2$. The results are given as real- (——) and imaginary part (---) of $S = (\bar{\sigma}a^2/\nu) + (i\bar{\omega}a^2/\nu)$ as a function of the ratio of the shell diameter to the liquid diameter k=(b/a). This means, that if k is in the vicinity of k=1 the liquid column is a very thin one, while with decreasing magnitude of k the annular liquid column becomes thicker. The numerical evaluation has been restricted to the mode m=2, for which the natural frequency for a frictionless liquid around a rigid center shell is represented in the following figures. The natural frequencies of the non-viscous liquid are proportional to the square root of the surface tension T_0, proportional to the inverse of the square root of the density of the liquid. It decreases with increasing diameter ratio k=(b/a). The uncoupled natural frequencies for m=2 and viscous liquid around a rigid center shell is marked with $\gamma = 0$, which expresses nothing but the limit case of the modulus of elasticity $E \to \infty$. The uncoupled frequencies of the elastic shell with no liquid around it, are shown as horizontal lines (-.-.-), exhibiting only an imaginary part. We are now interested in the coupled frequencies of the system, which yield for each mode two coupled liquid frequencies and four coupled structural frequencies. The coupled liquid roots are presented in Figure 9 for the density ratio $\bar{\rho}/\rho = 2$, i.e. a shell density $\bar{\rho}$ of twice the density ρ of the liquid, for a thickness ratio of the shell of h=0.01a and a tension parameter $T_0 a/\rho\nu^2 = 1000$. The mode shown here is that of m=2, which means the vibration in an elliptic geometry. The parameter γ was taken to be 10^{-8} and 10^{-4}. The roots for a non-viscous liquid around a rigid shell are given by S_0, which is a pure conjugate imaginary root. It shows for increasing diameter ratio k=(b/a) first a slight

decrease of frequency, which for larger k-values ($k<1$) then rapidly decreases to zero. The curve marked with $\gamma=o$ is the oscillatory root of the viscous liquid for a rigid center shell, since $\gamma\to o$ means, that the elasticity parameter $(Ea^2/\bar{\rho}(1-\bar{\nu}^2)\nu^2k^2)\to\infty$. This renders the roots as obtained already by Bauer in[8]. It exhibits a damped oscillatory root with a decay magnitude shown for the real part (——) marked with $\gamma=o$. With decreasing liquid thickness the decay magnitude increases, while the oscillatory part (---), i.e. the frequency, decreases. At about $k=(b/a)\approx 0.83$ the frequency of this damped oscillation becomes zero, indicating that in the range of $0.83<k<1$, i.e. for the smaller liquid thicknesses, the liquid layer is no longer able to oscillate, but merely performs an aperiodic motion, which with increasing k-magnitude exhibits less decay. For thin liquid layers therefore the aperiodic motion of the liquid persists for a long time, but it does not oscillate. For a rather stiff shell with $\gamma=10^{-8}$ the coupled liquid frequency increases with decreasing layer thickness and shows at $k\gtrsim 0.8$ that the liquid motion becomes unstable. Similar results are obtained for a less stiffer shell ($\gamma=10^{-4}$), where with increasing k-value the oscillatory frequency increases, while at $k\gtrsim 0.97$ the liquid becomes unstable. Figure 9a exhibits the real- and imaginary part of S for $\gamma=10^{-8}$ as a function of the diameter ratio k. The values S_o of the frictionless liquid (-.-.-) and the damped frequency for the viscous liquid around a rigid center shell ($\gamma=o$) are shown again for convenience. In addition the coupled structural frequencies are presented. The -.-.- line represents the uncoupled structural frequency, which decreases with increasing shell radius b. We notice that the coupled liquid frequency increases with increasing k, while its decay decreases slightly until at $k\gtrsim 0.8$ the real part of this root becomes positive, indicating an oscillation of high frequency with increasing amplitude, i.e. oscillatory instability. The coupled structural root exhibits for a thick liquid layer a very strong decay at a high oscillation frequency. With decreasing thickness of the liquid layer the decay magnitude decreases rapidly, indicating a longer oscillatory decay motion with a much smaller frequency. It may be noticed, that the oscillation frequency of the coupled structural motion is much lower than that of the uncoupled shell motion. Finally at about $k>0.73$ the shell ceases to oscillate and perform for $k>0.73$ an aperiodically damped motion. The second structural frequency is very large and not in the range of the numerical values presented in Figure 9a. In Figure 9b and 9c we present the coupled roots for an elasticity parameter $\gamma=10^{-4}$. The uncoupled structural frequencies are both shown by the -.-.- lines. The liquid frequencies S_o for frictionless liquid and that for a viscous liquid around a rigid shell ($\gamma=o$) are again presented for convenience. It may be noticed that the structural frequency is unstable for all k-values and that it is a diverging instability along nearly all the range of k. In Figure 9c the range of $0.97<k<1$ is shown in addition. It is seen that the coupled structural frequency (marked as (2)) is divergingly unstable and becomes oscillatory unstable above $k\approx 0.977$. The coupled liquid root is shown and marked as (1). We dectect the previously mentioned instability and a strong decrease of the frequency. The physical significance of the here obtained results calls for some discussion. The main interest appears in that we observe a case where viscosity provides instability, where as an ideal liquid renders always stability. Small perturbations of the structure lead to perturbations of the liquid surface and vice versa, where in the case of a viscous liquid (for which different phase relations appear) the flow field of the liquid is quite different to ideal liquid, which exhibit a slipping in angular direction. These perturbations result into liquid surface displacements, thus changing the surface tension restoring force, which in the case of viscous liquid through the additional

41

disturbance in angular direction by the motion of the elastic shell is not adequate to dampen out the perturbation. A similar explanation of the instability of the coupled motion of the elastic shell may be stated. Figure 9b shows that the root belonging to the angular η-motion becomes unstable and that the instability flips from a diverging one to an oscillatory instability for thin liquid layers, where the oscillatory interaction of the liquid motion is more pronounced. These effects (phase shifts and additional excitation of the liquid through the angular motion of the elastic shell and vice versa), which are not present for frictionless liquid seem to be responsible for such instabilities.

In conclusion, we may state:

a) that for a less stiffer shell ($\gamma=10^{-4}$) the coupled liquid root becomes unstable for very thin liquid layers $k \gtrsim 0.97$,

b) that for a stiffer shell ($\gamma=10^{-8}$) the coupled liquid root exhibits an instability for thin layers $k>0.8$ and becomes stronger unstable for thinner layers,

c) that for a less stiffer shell ($\gamma=10^{-4}$) the structural root for the angular direction becomes strongly unstable, exhibiting diverging instability till $k=0.977$ and then for even thinner liquid layers $k>0.977$ an oscillatory instability.

References

1. Bauer,H.F.: Vibration of a rotating uniform beam. Part I: Orientation in the axis of rotation. Journal of Sound and Vibration (1980), 72(2), 177-189.

2. Bauer,H.F.: Biegeschwingungen von homogenen um die Achse rotierenden Satellitenauslegern und zeitlich veränderlichen Randbedingungen. Z.Flugwiss. Weltraumforschung 4(1980),Heft 3, 121-128.

3. Bauer,H.F.: Motion behavior of particles relative to a space laboratory in orbit. Forschungsbericht FB-WE-9-FB-8-1985. UniBw.,8014 Neubiberg.

4. Bauer,H.F.: Coupled Oscillations of a solidly rotating and non-rotating finite and infinite liquid bridge of immiscible liquids in zero-gravity. Acta Astronautica 9(1982), 547-563.

5. Bauer,H.F.: Surface- and interface oscillations of a rotating viscous liquid column of immiscible liquids. Forsch.Ing.Wes.50 (1984), Nr.1, 21-31.

6. Bauer,H.F.: Coupled frequencies of a frictionless hydroelastic system. Forschungsbericht der UniBw. Institut für Raumfahrttechnik, 8014 Neubiberg (1985) (to be published).

7. Bauer,H.F.: Coupled frequencies of a hydroelastic viscous liquid system. Forschungsbericht der UniBw. Institut für Raumfahrttechnik, 8014 Neubiberg, (1985) (to be published).

8. Bauer,H.F.: Coupled frequencies of a hydroelastic viscous liquid system. Forschungsbericht FB-WE-9-FB-5(1985). UniBw., 8014 Neubiberg

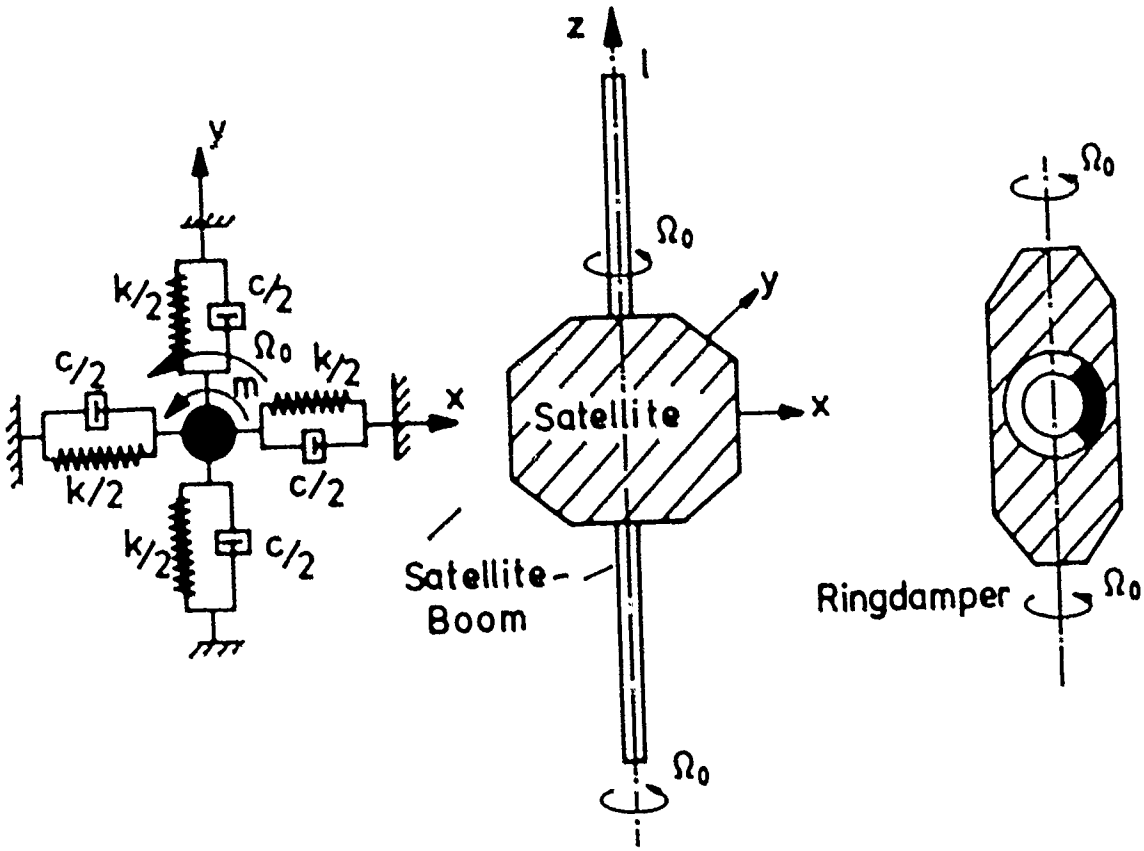


Fig. 1 Rotating systems:
a) damped oscillating mass point
b) satellite boom
c) spin-stabilized satellite

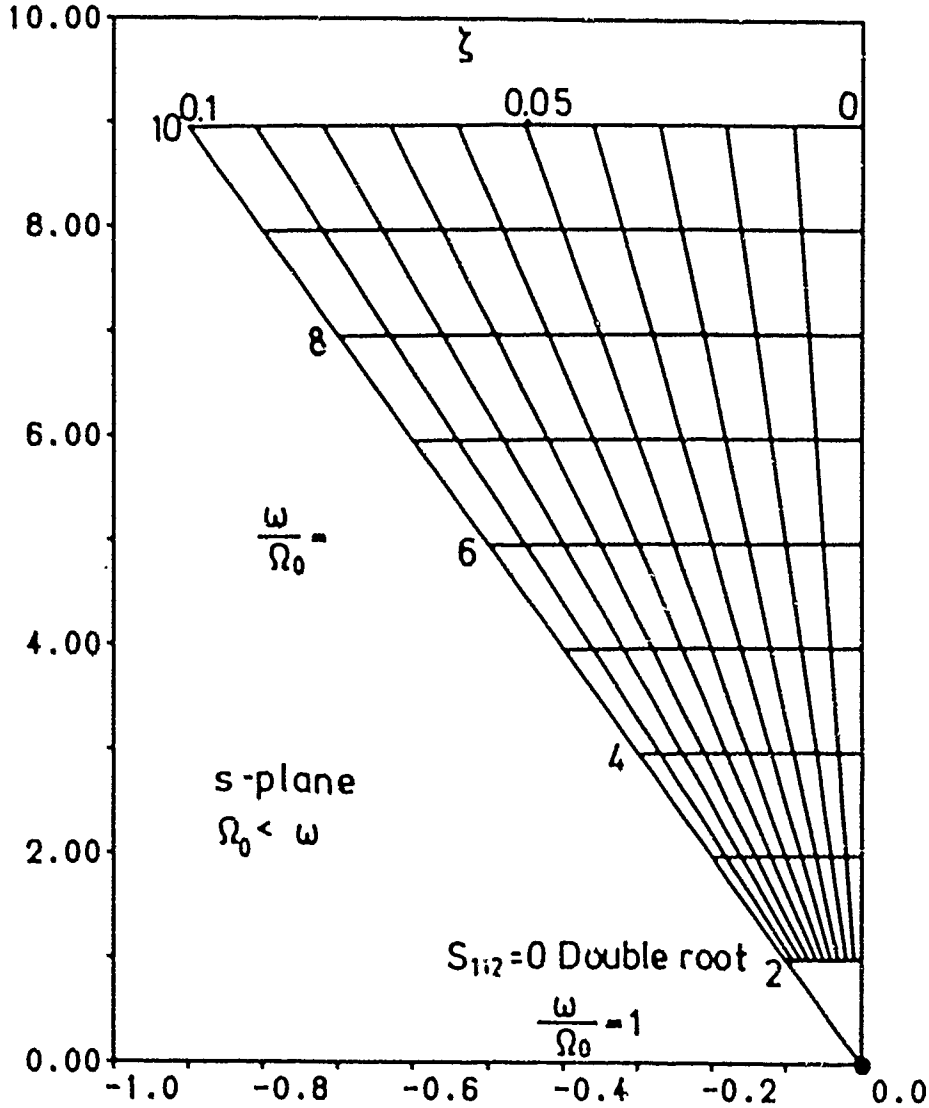


Fig. 2a Roots in complex s-plane for rotating mass-point system

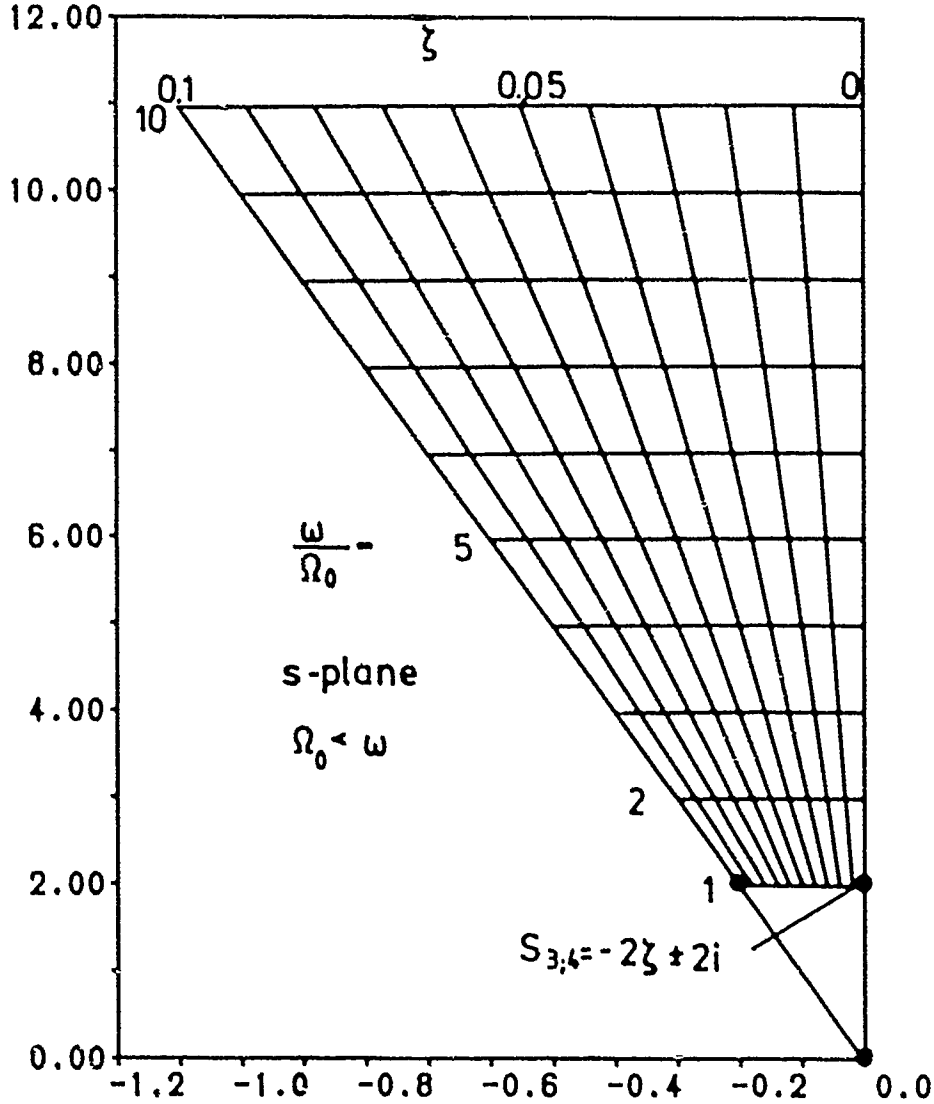


Fig. 2b Roots in complex s-plane for rotating mass-point system

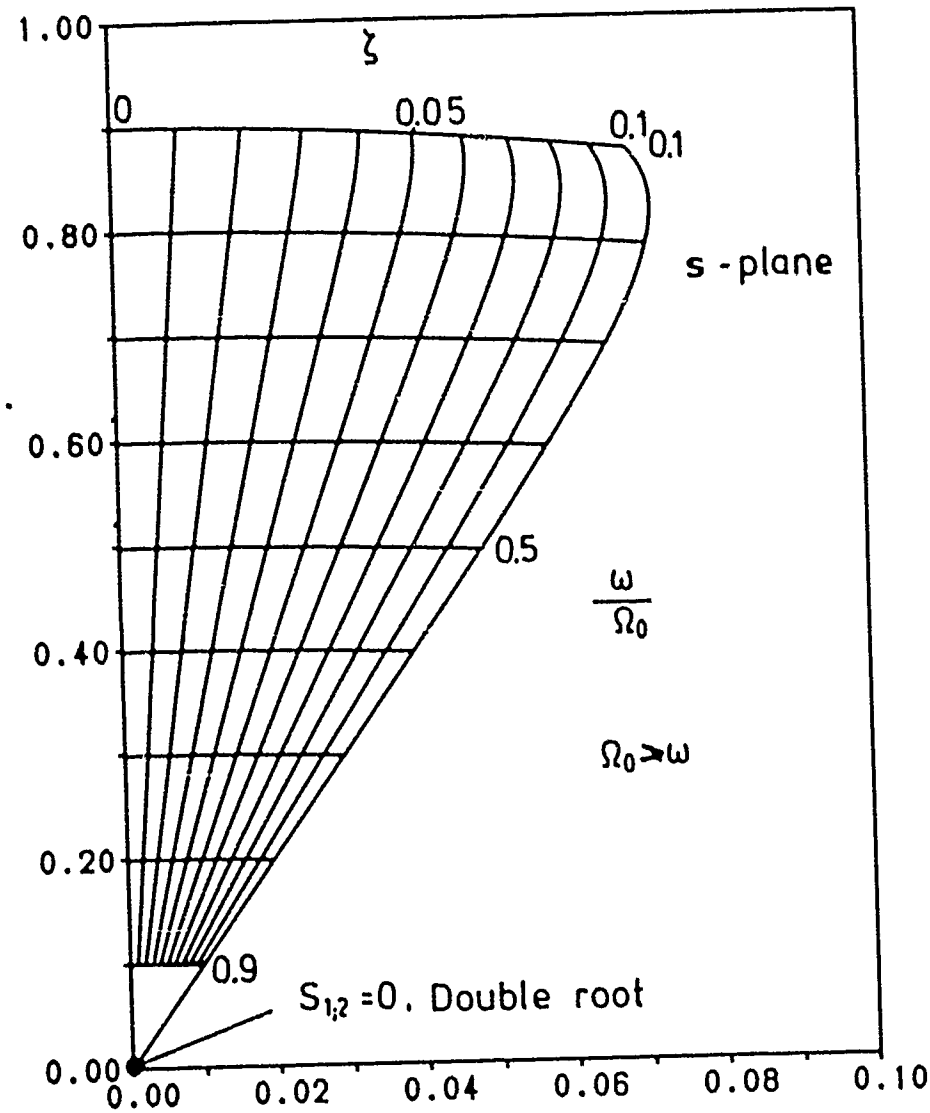


Fig. 2c Roots in complex s-plane for rotating mass-point system

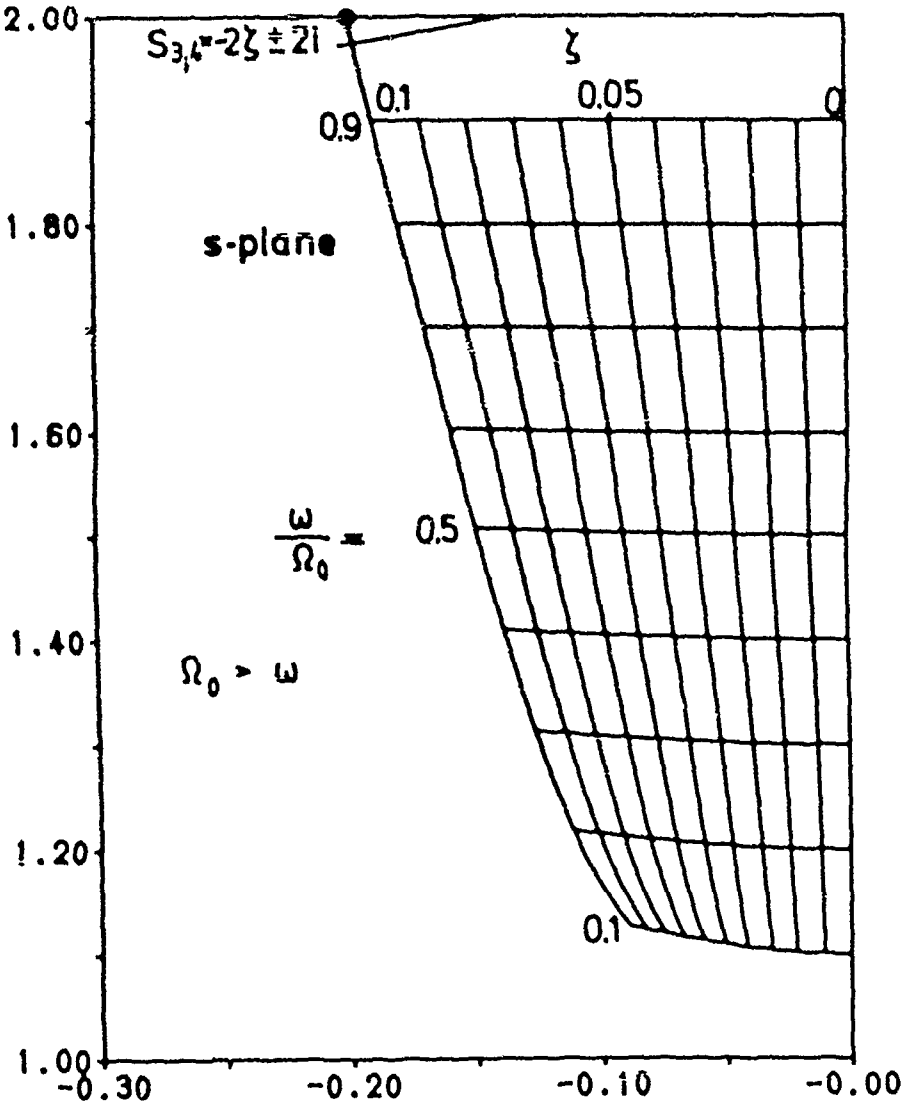


Fig. 2d Roots in complex s-plane for rotating mass-point system

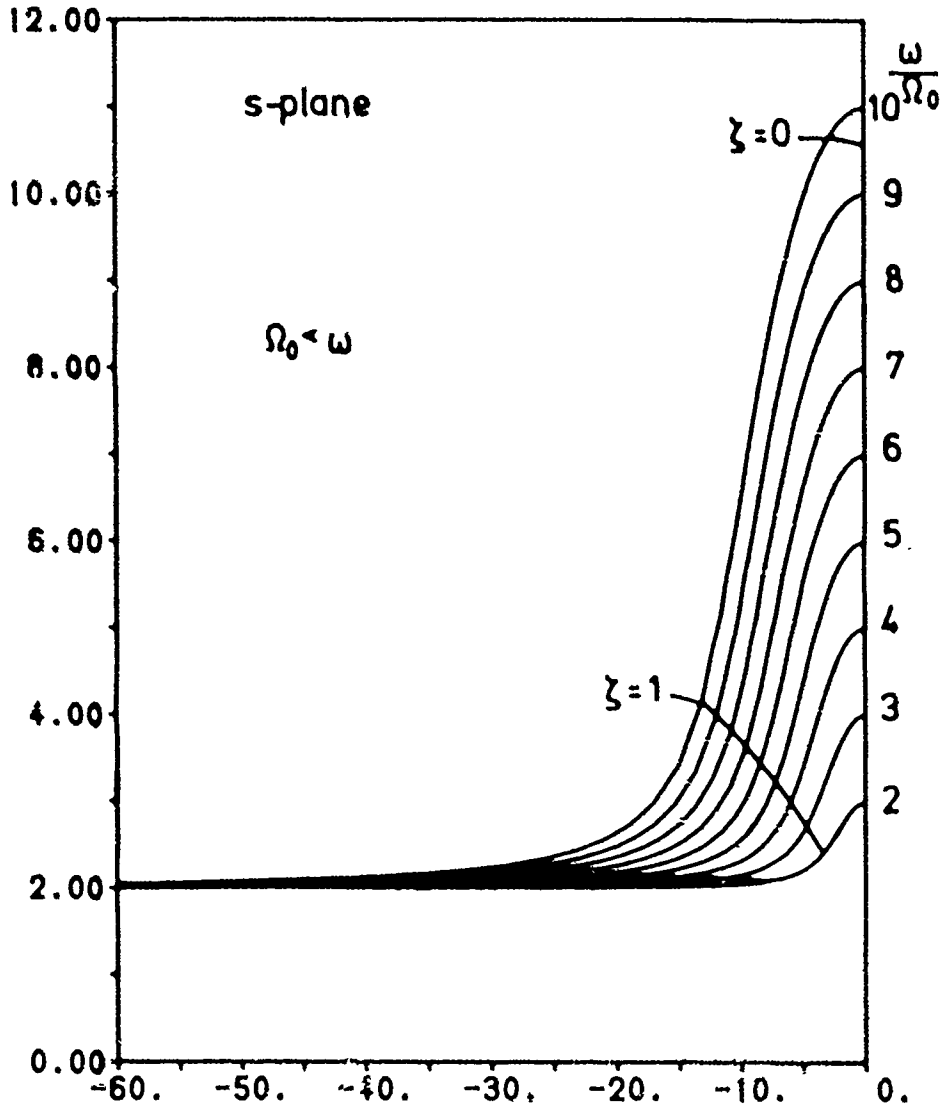


Fig. 3a Roots in complex s-plane for rotating mass-point system

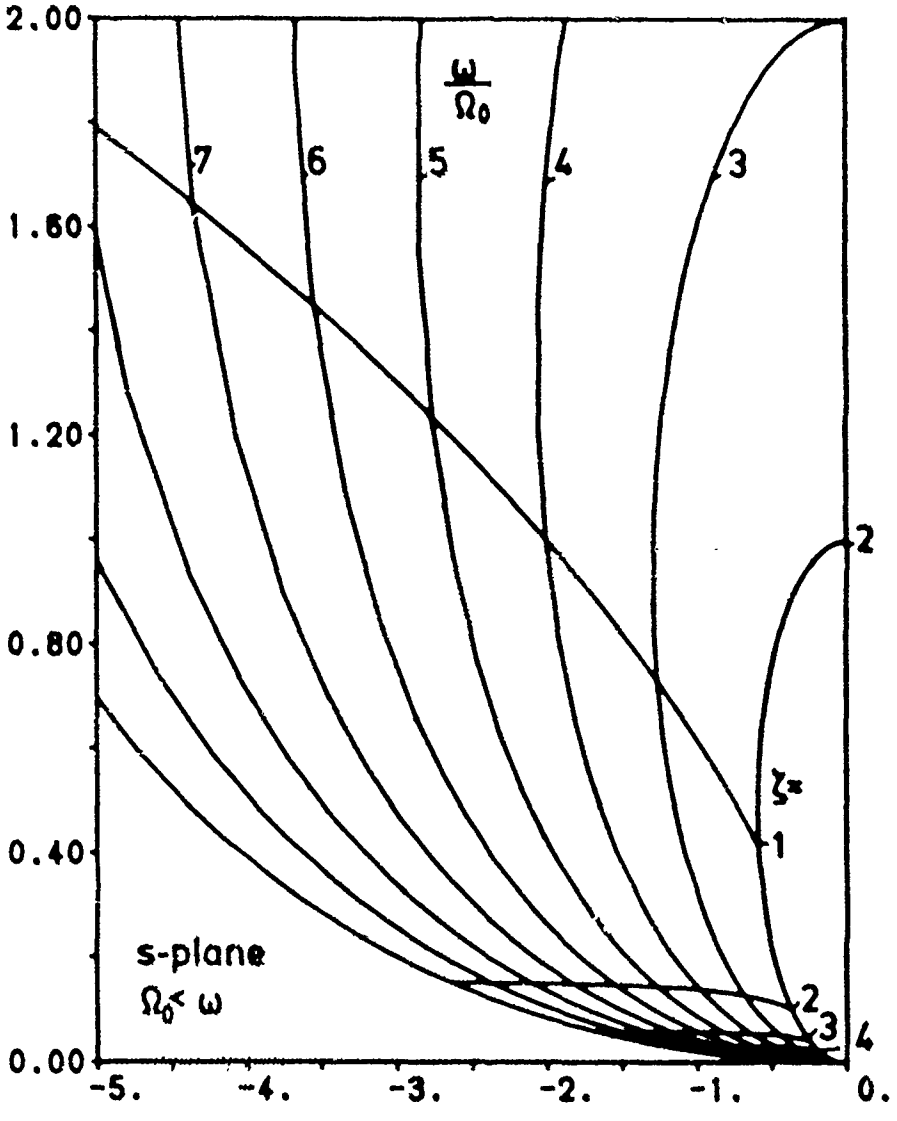


Fig. 3b Roots in complex s-plane for rotating mass-point system

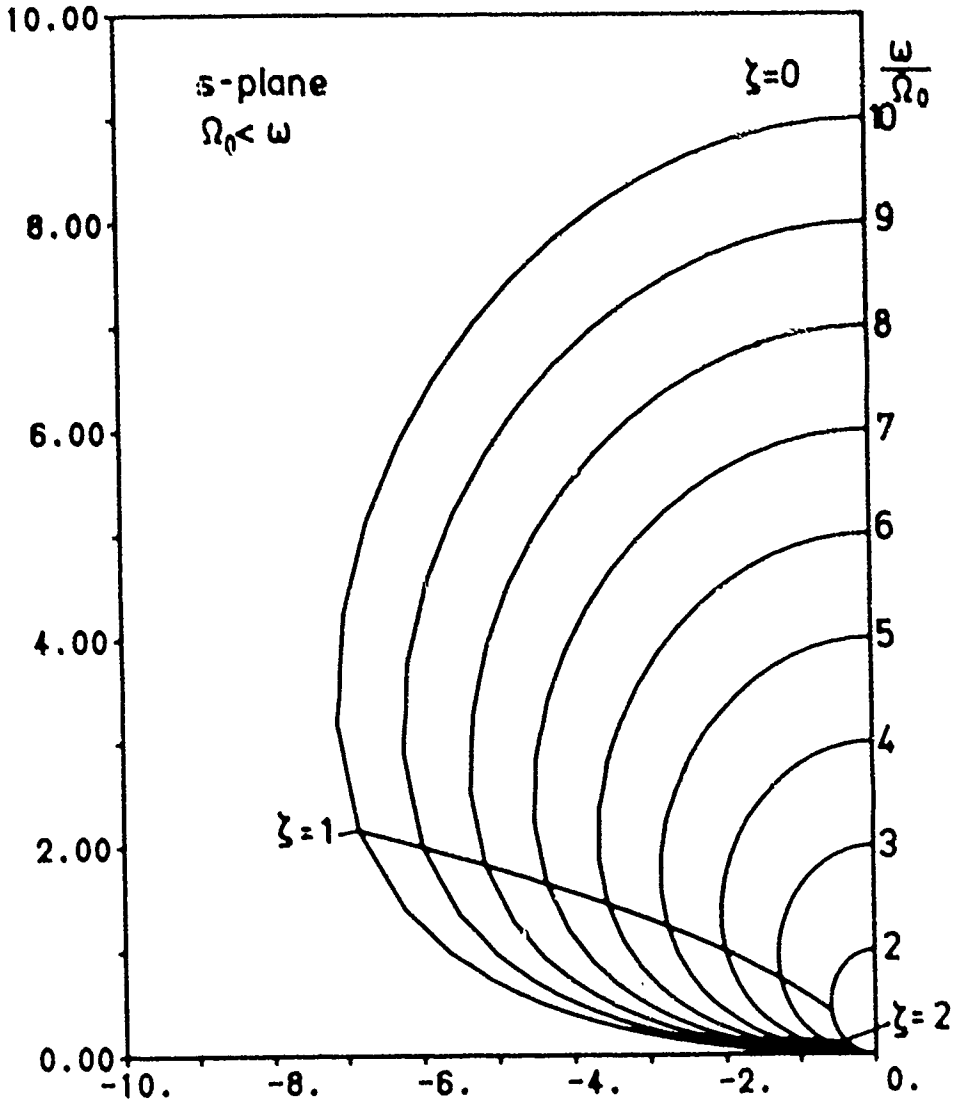


Fig. 3c Roots in complex s-plane for rotating mass-point system

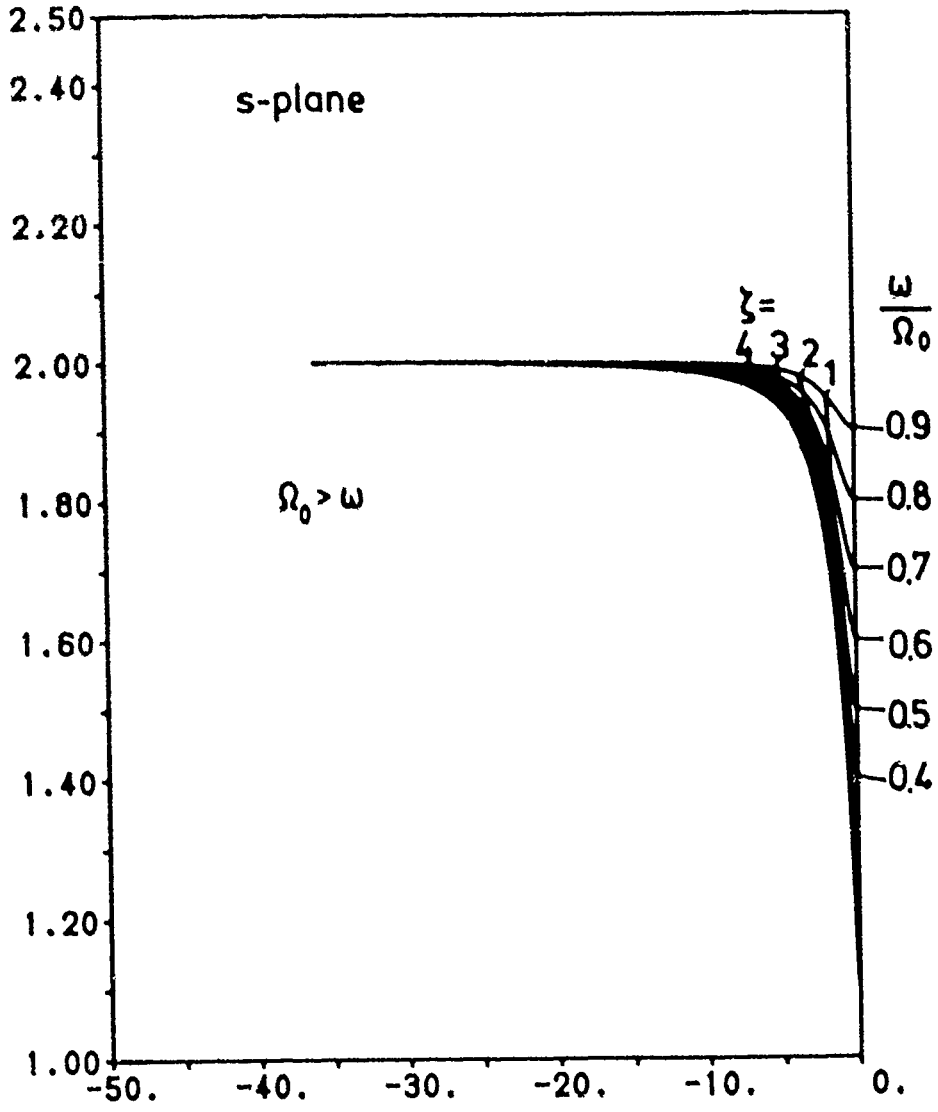


Fig. 3d Roots in complex s-plane for rotating mass-point system

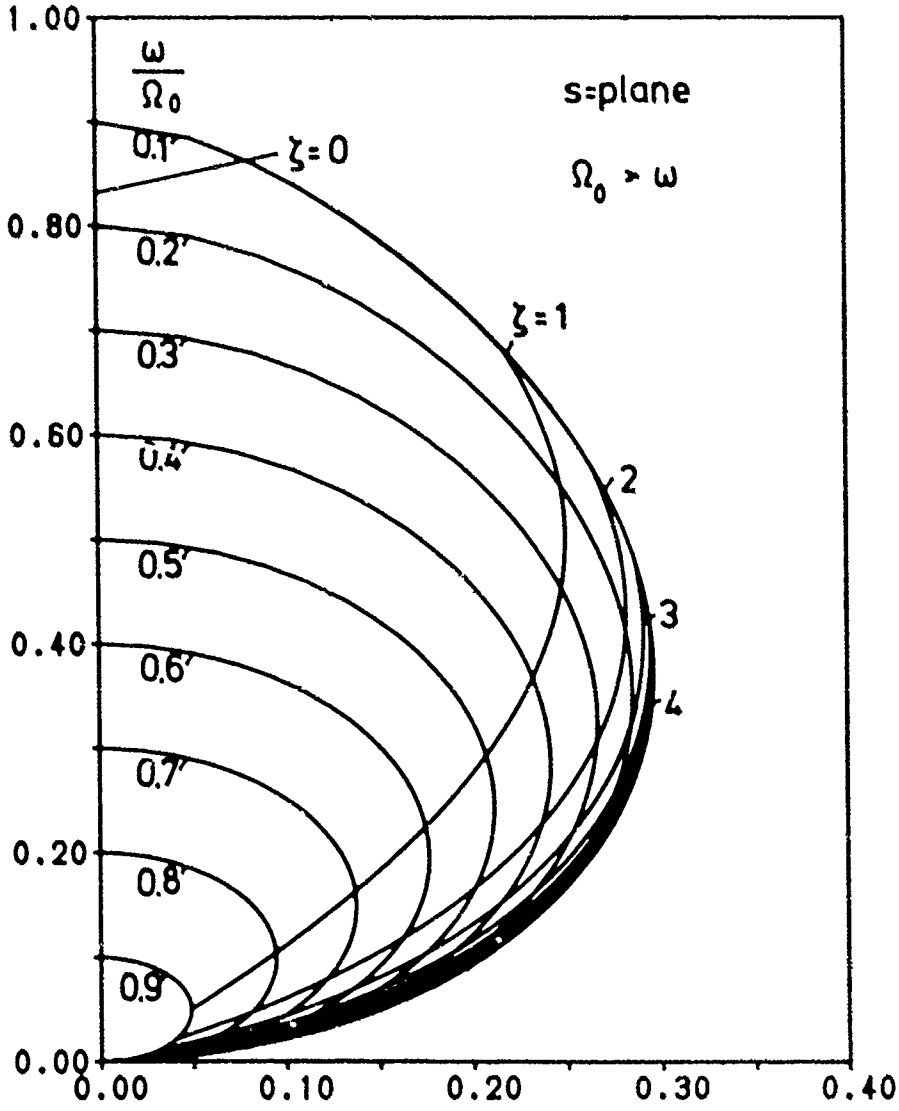


Fig. 3e Roots in complex s-plane for rotating mass-point system

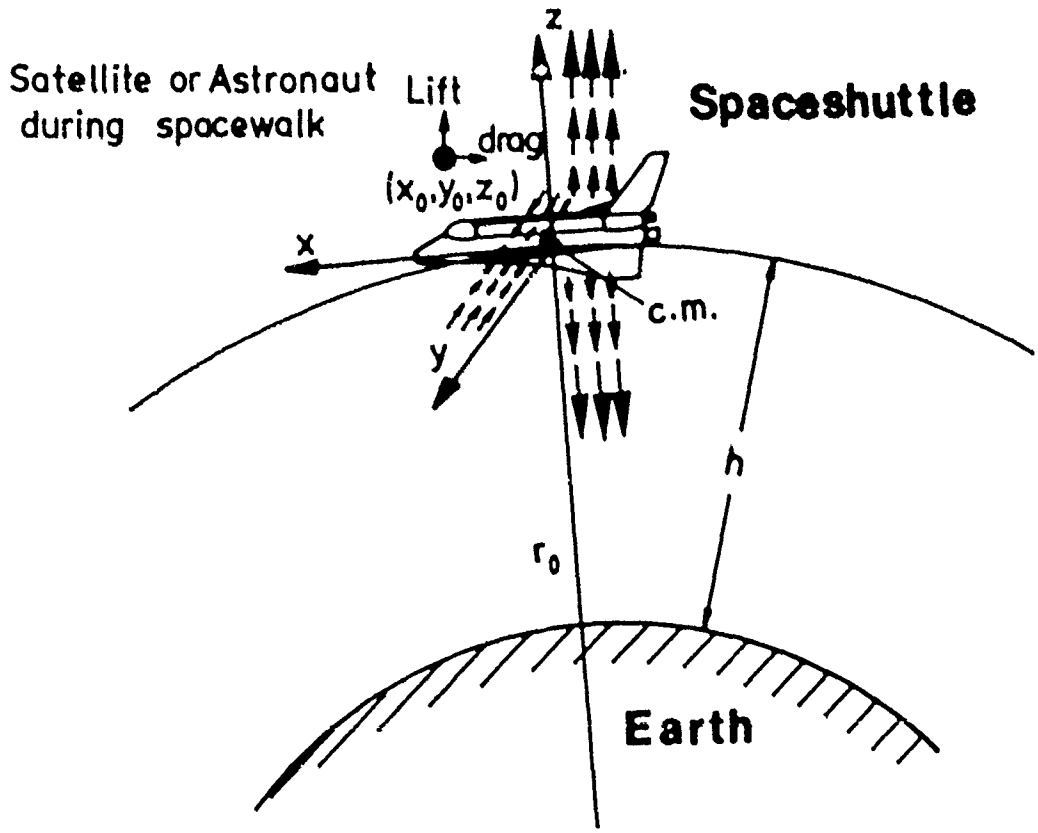


Fig. 4 Residual gravity field for orbiting Space shuttle

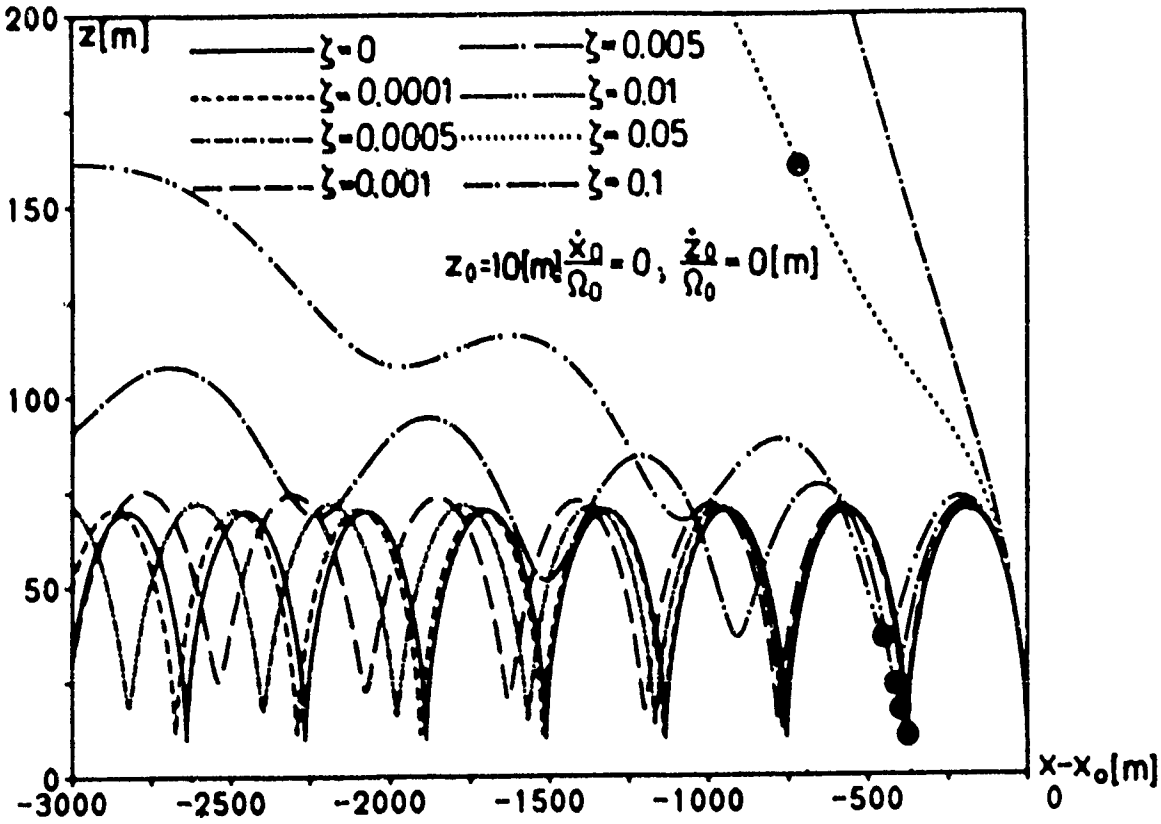


Fig. 5 Motion of mass point outside orbiting Space shuttle

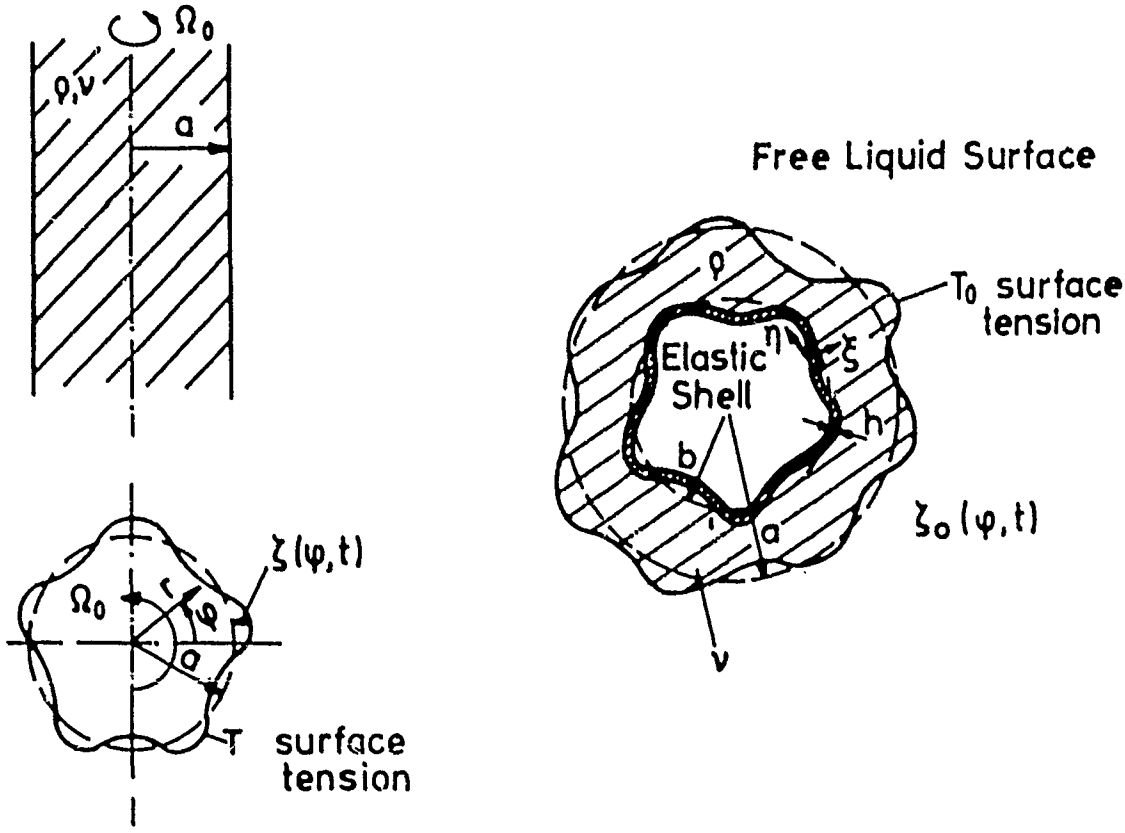


Fig. 6 a) Rotating liquid column
b) elastic shell with liquid layer

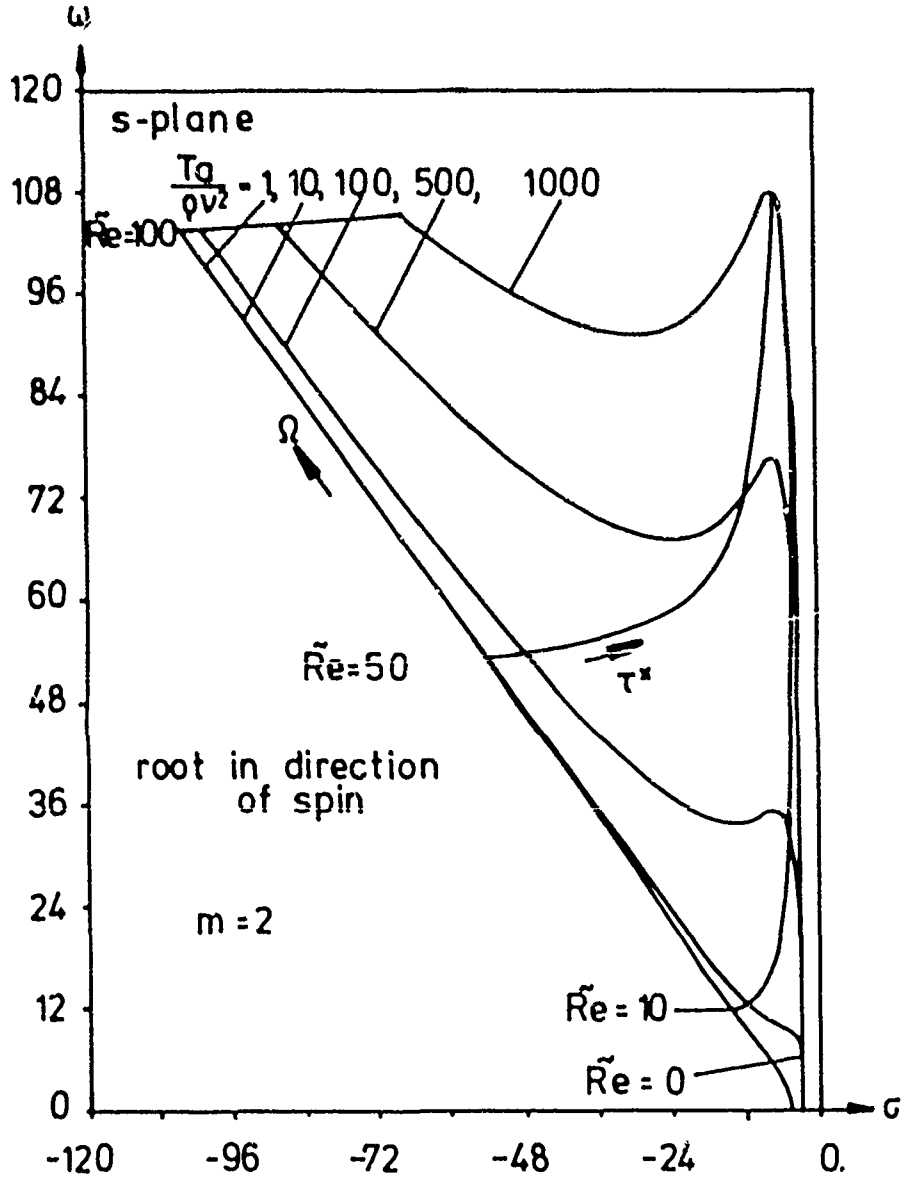


Fig. 7a Roots in complex s-plane for rotating viscous liquid column

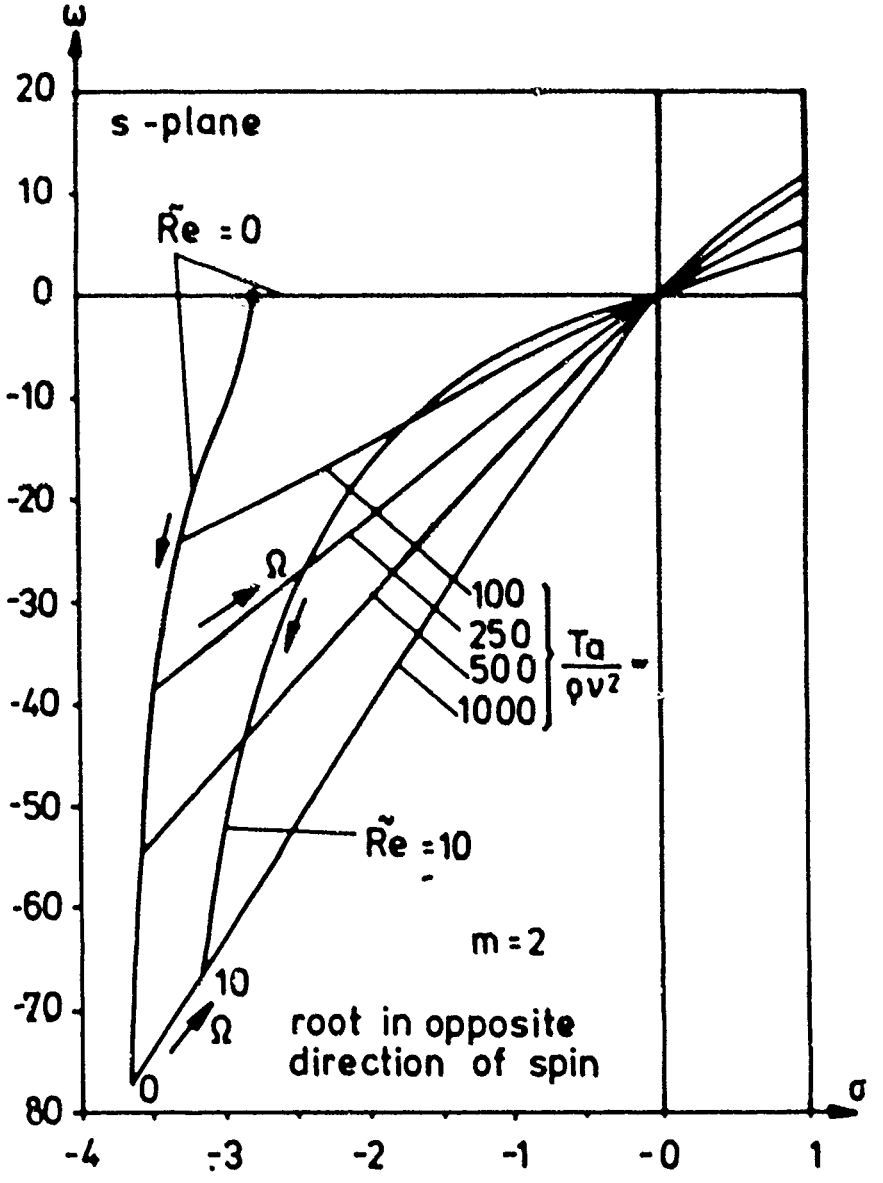


Fig. 7b Roots in complex s-plane for rotating viscous liquid column

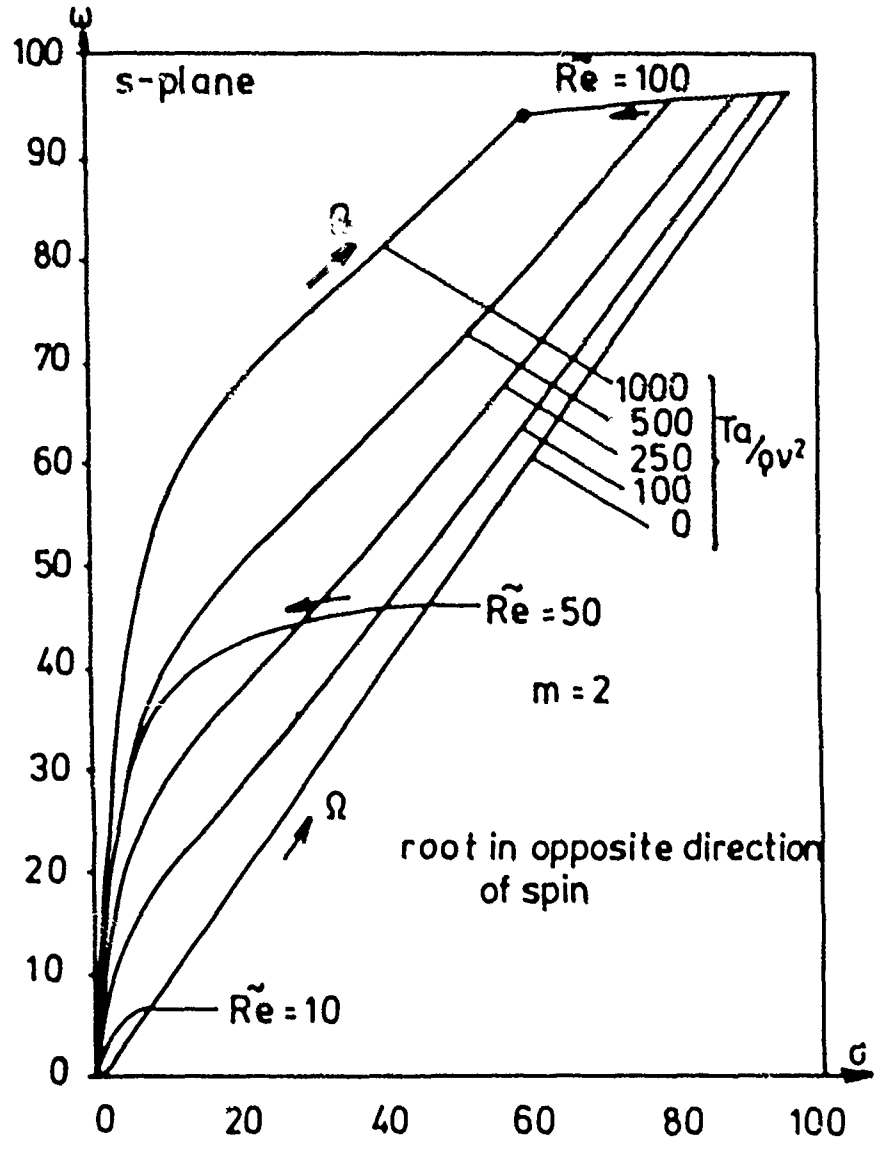


Fig. 7c Roots in complex s-plane for rotating viscous liquid column

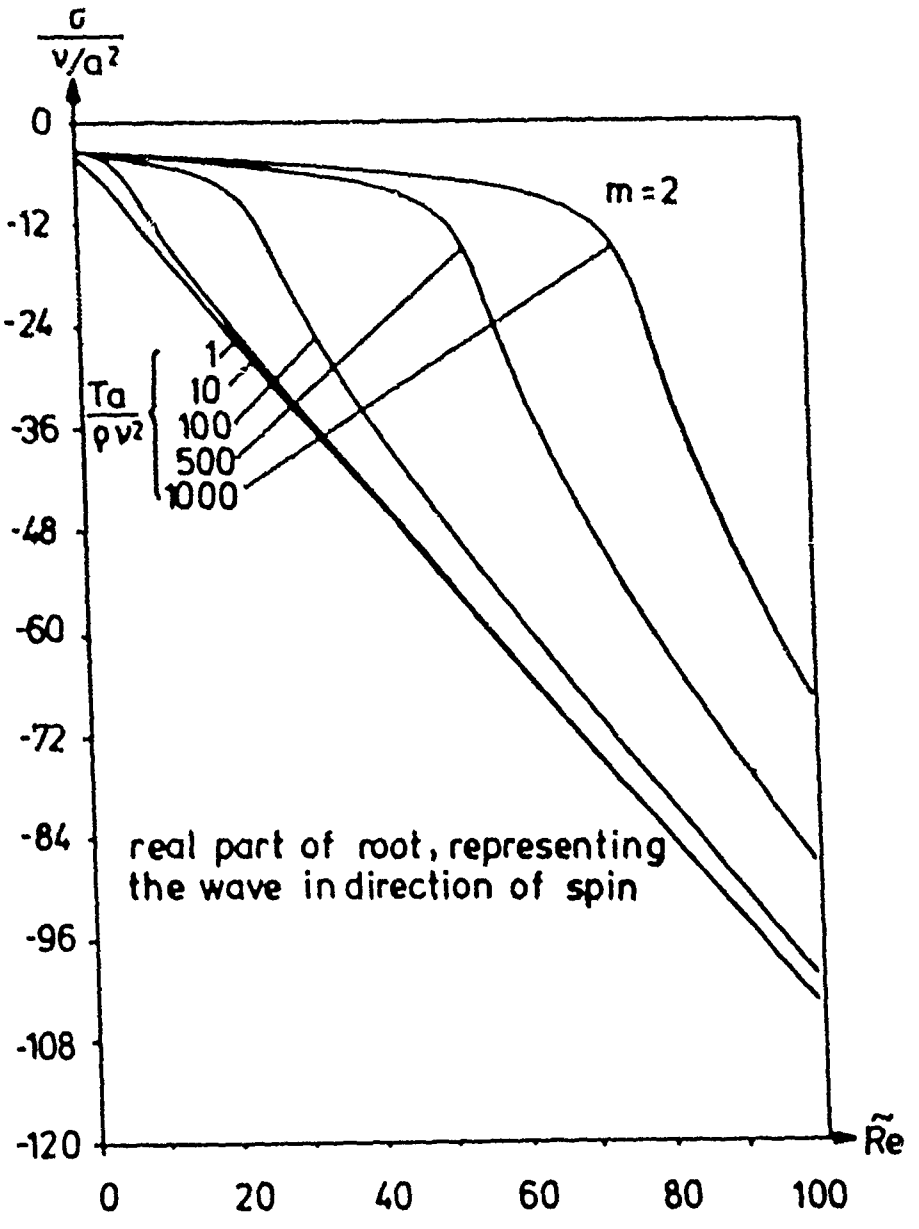


Fig. 8a Roots of rotating liquid column

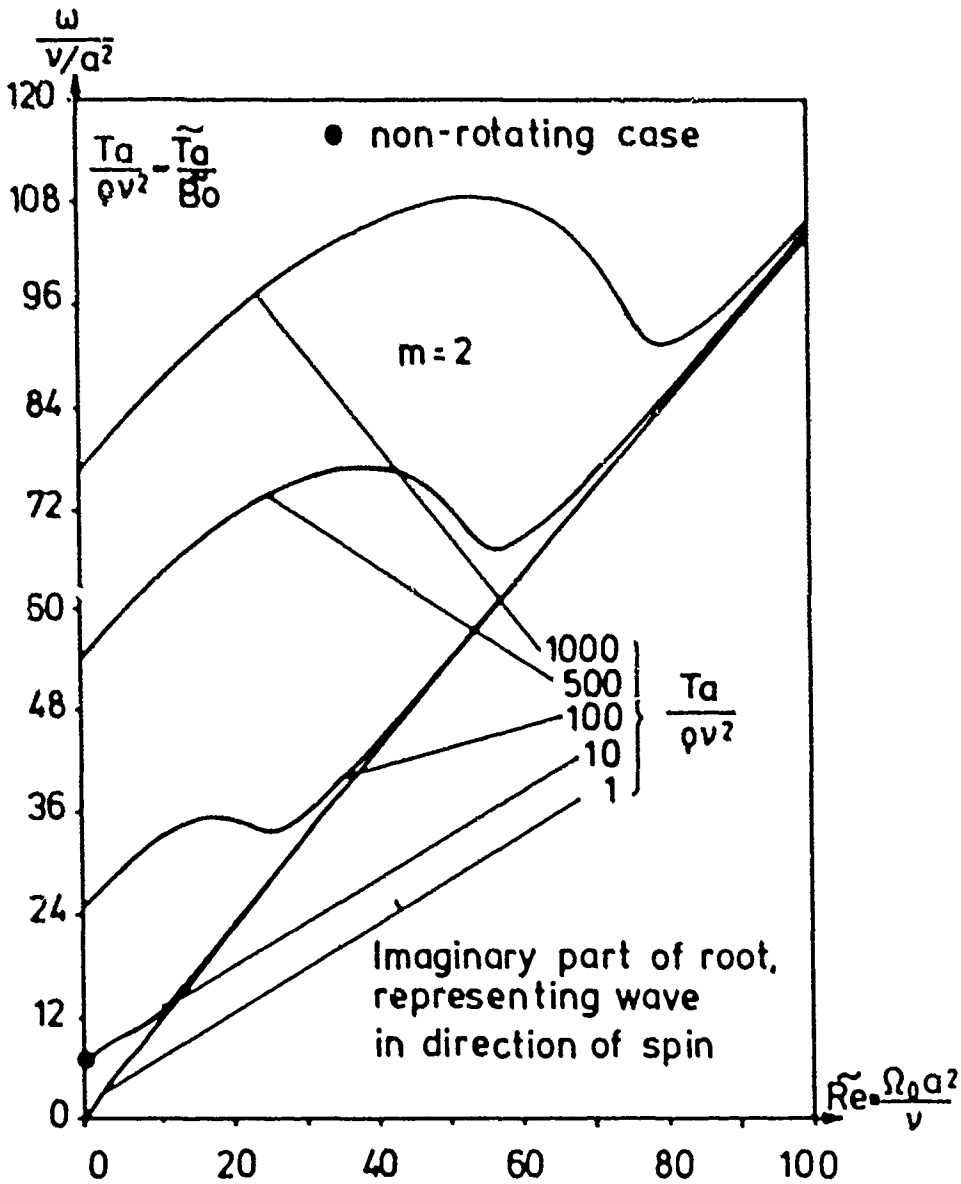


Fig. 8b Roots of rotating liquid column

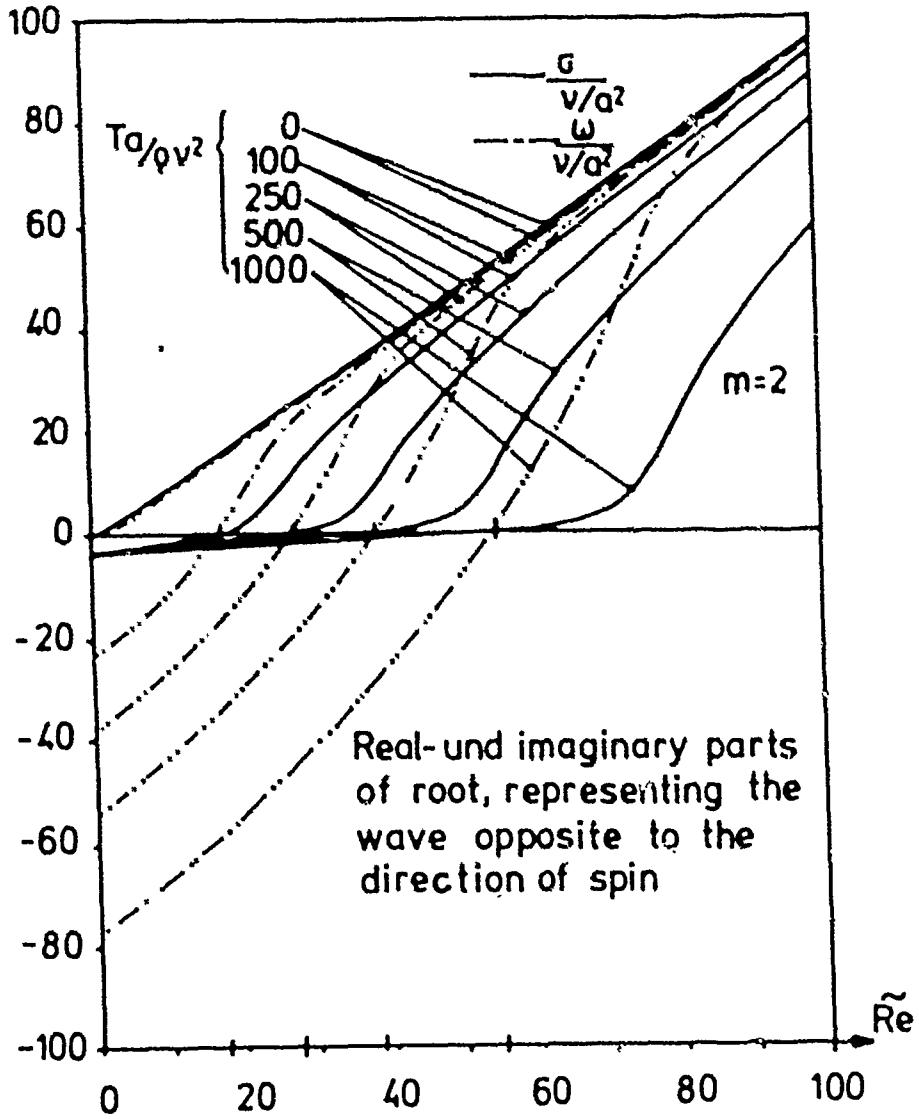


Fig. 8c Roots of rotating liquid column

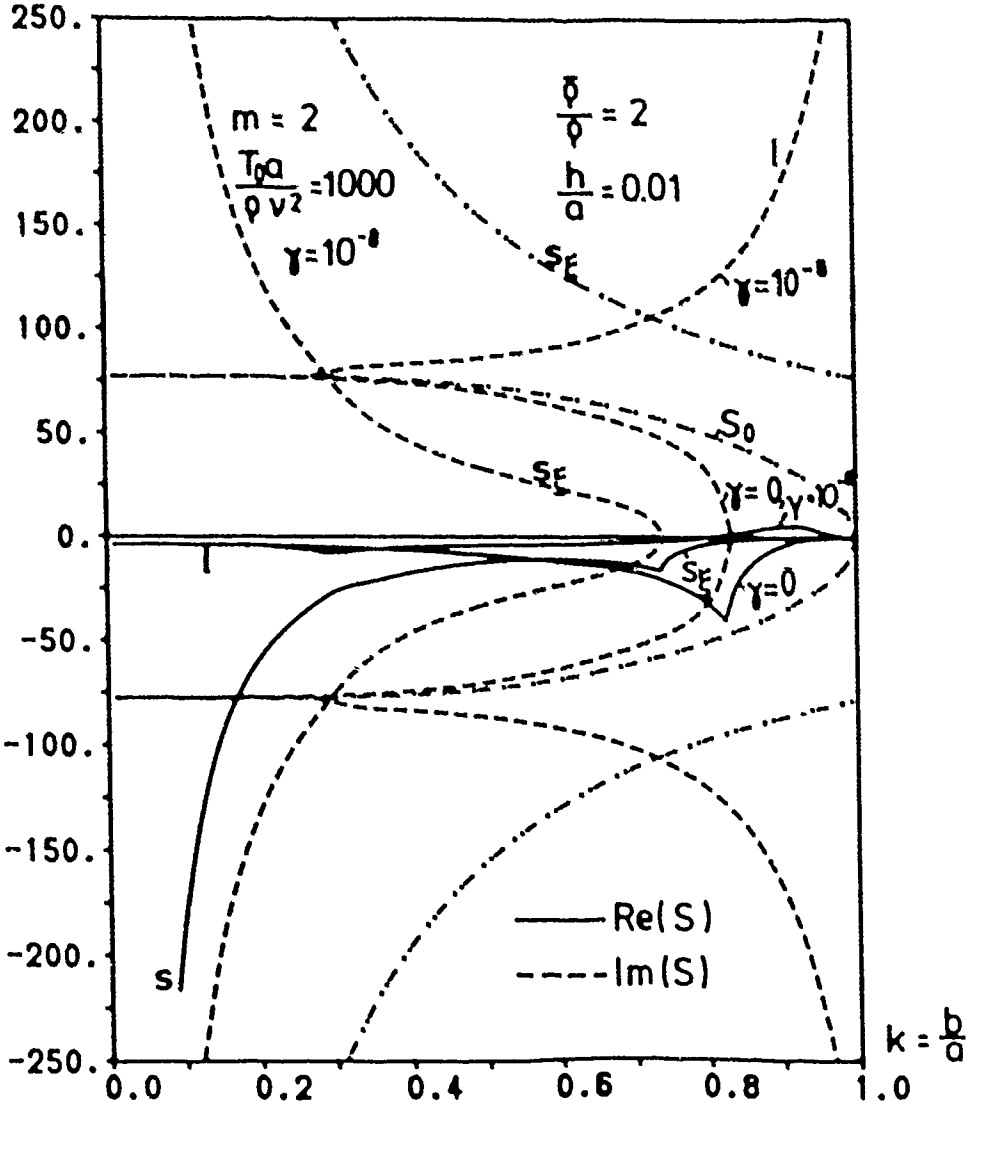


Fig. 9a Coupled roots of hydroelastic system

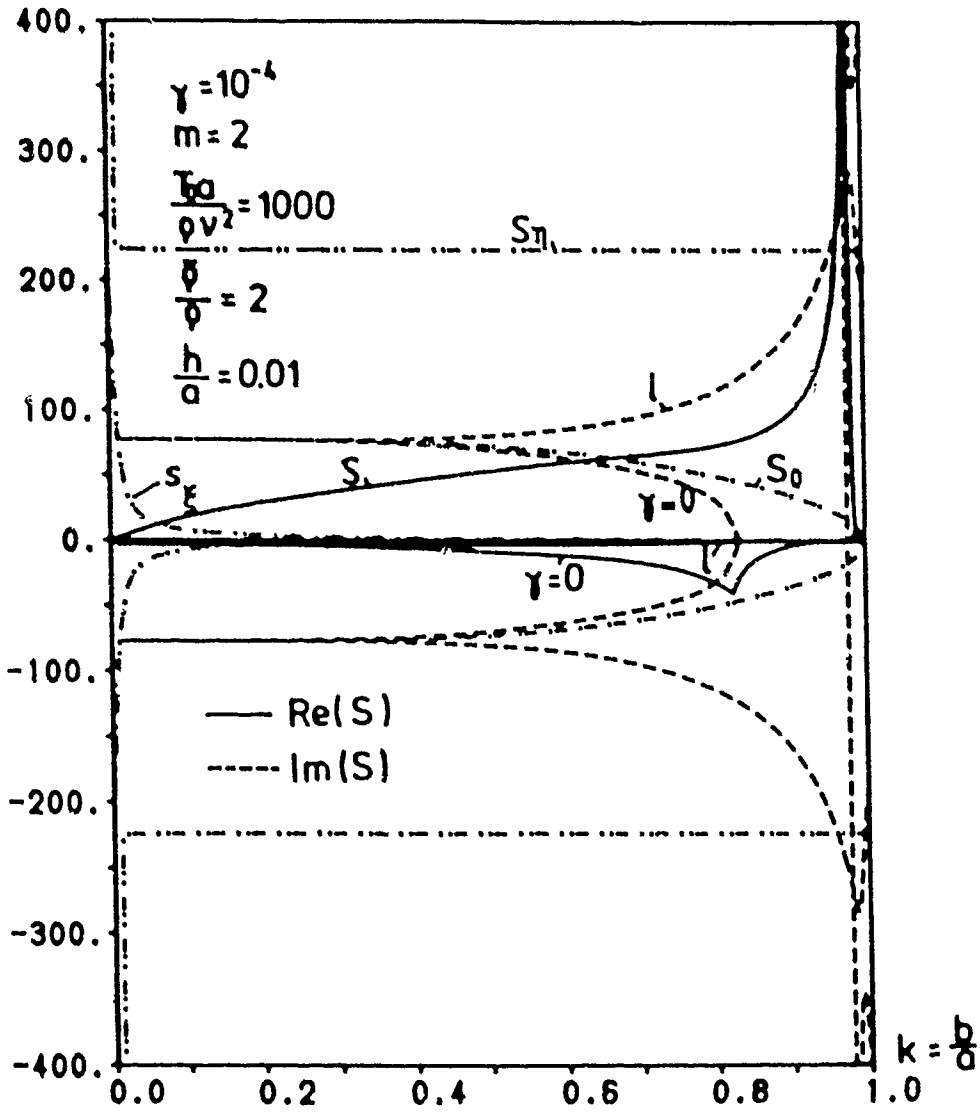


Fig. 9b Coupled roots of hydroelastic system

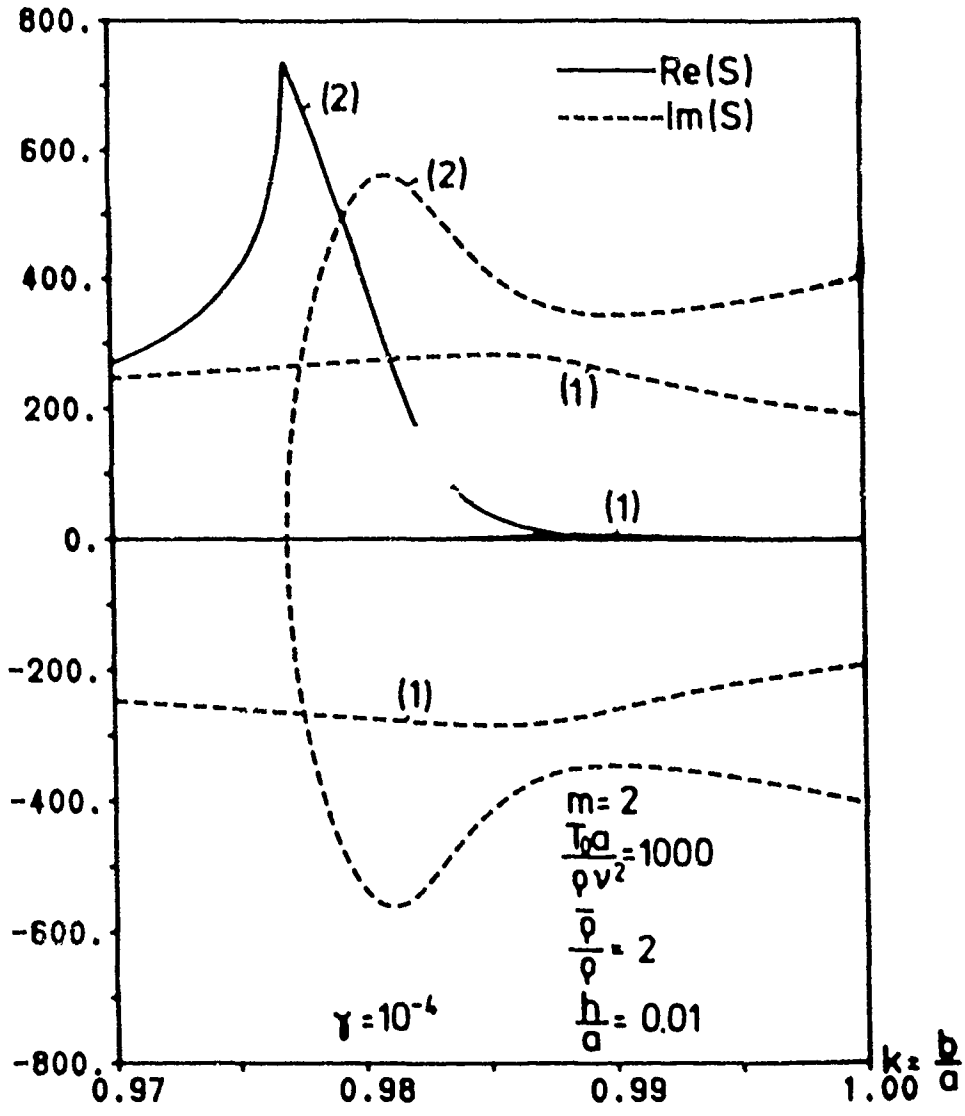


Fig. 9c Coupled roots of hydroelastic system

DAMPED OPTICS DESIGN

By

M. J. LAUGHLIN

UNITED TECHNOLOGIES RESEARCH CENTER
OPTICS AND APPLIED TECHNOLOGY LABORATORY
P. O. DRAWER 4181
WEST PALM BEACH, FLORIDA 33402

ABSTRACT

Optical systems used in advanced technology devices are required to provide mirror planar and angular stability to the micro-inch or micro-radian level. These systems may also be exposed to dynamic, impulsive disturbances that produce responses that must be damped out in a few milli-seconds to meet system performance requirements. This presentation will discuss the detailed design, fabrication, and testing of a set of molybdenum mirrors that employed viscoelastic constrained layer damping to produce the required dynamic performance levels. The mirrors were designed using finite element analyses to obtain modal properties that were utilized to predict dynamic response of the mirror. The damping material was applied in two orthogonal planes in order to provide the required damping for the complex modes identified. Design constraints required that the damping material be applied to only 55% of the mirror surface area and in non-optimal locations. Damping levels were predicted from the finite element model using modal strain energy techniques. Structural damping levels of approximately 10% were predicted from this analysis. Following fabrication of the mirrors, impact tests of the assembled mirror were conducted to verify the predicted damping levels. Excellent agreement with the predicted damping levels was obtained, and the validity of the design approach was confirmed.

INTRODUCTION

Optical systems used in advanced technology devices are required to provide mirror planar and angular stability to the micro inch or micro-radian level. These systems may also be required to resist impulsive pressure loads that can produce very large surface distortions that must be eliminated very rapidly to meet system performance requirements. Only two viable solutions have been found to deal with this situation. Either enough stiffness must be introduced into the system to prevent the initial distortion, or enough damping must be incorporated into the design to eliminate residual vibration within a few milliseconds before succeeding impulses occur. While the stiffness approach is the more conventional and easily implemented one, the job of limiting the initial distortion of a large surface exposed to a sizeable pressure to microinches is formidable. If, for example, the mirror cross section were made very thick to prevent bending distortion, deflection in the thickness direction due to compression longitudinal modes could become a problem. Furthermore, the mass of such a concept can become so large that supporting structure cannot be designed stiffly enough to prevent low frequency rigid body modes from occurring. The damping approach, however, offers the potential of reducing distortions to acceptable levels before the following pressure pulse is applied, even though initial distortions are thousands of times larger than allowable levels. The two primary challenges to implementing this strategy are the very high level of damping required to succeed, and the difficulty of incorporating this damping into a structure which must exhibit creep stability to a few microinches.

This paper will discuss the details of the design, fabrication, and testing of a set of molybdenum mirrors that employed viscoelastic constrained layer damping to achieve the required dynamic performance levels. The mirrors were designed using finite element and modal strain energy analyses to obtain the modal damping values required to predict the dynamic response of the mirror. The damping material was applied in two orthogonal planes to control coupled bending and rigid body vibratory modes in all six degrees of freedom. Design constraints required that the damping material be applied to only 55% of the mirror surface area and in non-optimal locations. Furthermore, mirror shapes were irregular and of variable thickness, adding to the complexity of the analysis task. Modal loss factors of approximately 10% were calculated for the critical low frequency modes of the final configuration, leading to predictions that performance specifications would be met. Following fabrication of the mirrors, impact tests of the assembled mirror were conducted to verify the predicted damping levels and transient response to impulsive loads. Excellent agreement with the predicted damping levels was obtained, and the validity of the design approach was confirmed.

DISCUSSION

Dynamic Pressure Loads

The environment in which the optical elements of the system must live is illustrated in Figure 1. The plot of pressure as a function of time indicates that the pressure suddenly increases abruptly, decays irregularly for about 2 ms., is quiescent for about 15 ms., and then repeats the pattern. The diagram of the mirror and incident pressure wave indicates that a plane wave strikes the surface in a correlated fashion. The exact duration of the rise time of the pressure pulse is unknown and varies from pulse to pulse, but it is known to be short compared to critical mirror vibratory periods. Thus, for the purpose of analysis, it was assumed that the rise time is zero. This assumption, of course, means that all vibratory modes will be excited no matter how high the frequency. For higher order bending modes this assumption can significantly overestimate the dynamic response, but the higher frequency modes decay more severely in a fixed time period and tend to be less problematic. In order to account for the manner in which the shape of the pressure pulse couples with the shape of a particular vibratory mode, the generalized force concept is used. The procedure involves weighting the pressure at a particular location with the magnitude of a particular modal vibratory response and integrating over the mirror surface to determine an effective force. Equation (1) describes the exact procedure used[1] :

$$Q_i = \int_0^a \int_0^b P(x,y,t)\, W_i(x,y)\, dx\, dy \qquad (1)$$

where Q_i = generalized force for mode i.

$P(x,y,t)$ = pressure at position x, y for time t

$W_i(x,y)$ = mode shape at position x,y for mode i

Figure 2, for example, shows the mirror second bending mode excited by the incident pressure wave. Due to its symmetric nature, equation (1) would indicate a zero magnitude generalized force for this mode. However, in reality, modal coupling usually precludes exact symmetry, and generalized forces of some magnitude exist for all modes.

The initial deflection of a mirror surface after exposure to a single pressure pulse is large and takes the shape of the vibratory modes. Figure 2 shows that the initial deflection is on the order of 1000 times the allowable residual, and that parent material damping is inadequate even for a very thick mirror. However, the .05 loss factor curve shows that if 5% structural damping could be incorporated into the mirror, the distortion goal could be met with a reasonable mirror thickness.

A trade study was carried out to balance the required structural stiffness, the resulting system weight, and fabrication cost. The result of that study was a decision to utilize conventional optical construction to minimize weight and fabrication cost, and rely heavily on a well-designed effective damping scheme.

Design Constraints

The design constraints imposed on a dynamic optical structure are unprecedented in severity or either damped structures or optical structures. The performance requirements for the damping concept are so severe that the final design must take full advantage of the constrained layer operational concept, and yet must satisfy all standard optical structural criteria such as long term stability and the absence of creep. The primary design criteria are the following:

1. Total allowable distortion from vibration, thermal, polishing, gravity, and creep must be <4 μin.

2. Damping must attenuate an initial 4000 μin. distortion to 0.4 μin. in 15 ms.

3. The optical mount must isolate the mirror thermally, but also damp rigid body bounce and tilt modes effectively.

4. Polishing must not affect the damping material or cause any permanent structural shift.

5. Gravity loading must not cause significant distortion when mounted in any position.

6. Creep of the viscoelastic material (VEM) must not result in figure change exceeding 0.5 μin.

The first step in designing the damped optic was to select the mount configuration, because the mirror/mount system geometrical constraints are affected and the mount itself must be damped. Figure 3 illustrates the results of a thermal sensitivity study which was carried out to select the mount concept. Both a three point mount and a tangent mount were considered because both are determinate and both provide thermal isolation from the environment. Isolation is defined here as an attenuation of support structure deflection due to small room temperature changes before it reaches the mirror surface. Figure 3 clearly indicates that only the tangent mount concept can limit thermal distortions below the 4 μin. allowable.

Having selected the tangent mount configuration, it is clear that the damping constraining layer effectiveness must be significantly compromised. Figure 4 shows the tangent mount concept, and it is evident that the cylindrical shape correlates poorly with the rectangularly shaped mirrors. The tangent mount's cylindrical shape is dictated by the cylinder die-out phenomenon, in which a displacement or load imposed at the base dies out along the cylinder axis. A rectangular mount shaped to fit the mirror configuration would provide desireable flexibility at the walls, but would be too stiff at the corners. Thus a circularly shaped mount is required and the constraining layer must be somehow fitted in. To achieve maximum stiffness, the constraining layer should be continuous. Such continuity, however, would require penetrating the tangent mount cylinder, severely reducing the ability of the mount to resist rigid body mirror vibration. If the mirror surface were to be completely covered it would have to be done in a discontinuous

fashion. That is, a circular piece of constraining layer could be fitted inside the tangent mount cylinder, and an additional piece could be added outside the mount cylinder. However, finite element analysis indicated that such a segmented concept was not as effective as one where a single circular piece was used inside the tangent mount. The portion of the constraining layer outside the tangent mount was ineffective structurally and served primarily as parasitic mass, which caused a deleterious reduction in resonant frequency. Thus the most effective configuration of mirror, mount, and constraining layer relegates as much as 45% of some mirror surfaces to a free layer damping concept, a much less effective scheme, or to no damping at all.

Design Analysis

The need for an accurate cost-effective analysis scheme is all the more necessary because of the constraints placed on the damping design. Not only is a high level of overall modal damping required, but whatever scheme is employed will inevitably be compromised by the partial coverage requirement. It is essential, therefore, that the analysis method employed to calculate modal damping be accurate enough to account for the VEM partial coverage, the irregular mirror and constraining layer shapes, and the variable thickness mirror geometry. Only then would the designer have the necessary information to know whether a particular concept is good enough or whether redesign is required. Figure 4 illustrates and summarizes the difficulties of predicting modal damping accurately for a potential configuration.

Closed form formulae were found to be adequate and very useful for the conceptual design phase. The objective for this phase was to carry out trade studies to optimize the thicknesses of the mirror and constraining layer, and to optimize the thickness, modulus, and loss factor of the VEM. For this purpose, equations similar to equation (2) below were ultilized[2] :

$$\eta = \frac{B_2 Y x}{1 + (2 + Y)x + (1 + Y)(1 + B_2^2)x^2} \qquad (2)$$

where η = loss factor of the composite panel

Y = a stiffness parameter dependent on the modulii and thickness of elastic layers

x = a shear parameter

An additional factor which constrained the conceptual design was the inability to inexpensively fabricate lightweight configurations of the primary mirror material, molybdenum. Lightweight configurations can enhance damping performance by increasing resonant response frequencies and strain levels of the VEM. However, it is not a simple matter to fabricate a lightweight sandwich core from molybdenum, so all designs were confined to configurations using solid plate stock.

During the detailed design phase, it was necessary to determine the actual dynamic performance of the concept selected during conceptual design. The analytical assessment must be accurate and must account for the actual geometry and location of all components of the damped optical structure. In addition, funding constraints did not allow expensive and time consuming techniques such as complex frequency-dependent eigenvalue analysis using a high density 3-D finite element mesh. To accomplish these conflicting objectives, it was decided to use real eigenvalue finite element analysis to calculate frequencies and mode shapes, and to employ the modal strain energy (MSE) method to determine the overall effective damping for each vibratory mode. Figure 5 shows a typical mode shape for a 3-D model employing reflective symmetry. The MSE approach allows the use of real eigenvectors to calculate modal damping, and has been widely used successfully[3,4,5]. The actual MSE procedure is characterized by equation (3) below[6]:

$$n^{(r)} = n_i \frac{SE_i^{(r)}}{SE^{(r)}} \qquad (3)$$

where n_i = material loss factor for the i'th material

$SE_i(r)$ = strain energy in the i'th material when the structure deforms in the r'th mode

$SE^{(r)}$ = total strain energy for the r'th mode

The use of the MSE method produced some performance predictions which were, at times, surprising. But in all cases where calculations indicated worse performance than desired, application of the constrained layer formulae corroborated the prediction. For example, when MSE analysis predicted poor damping performance of the tangent mount in the bounce mode, hand analysis revealed that the constraining layer was too thin to constrain the VEM being used. So the mount constraining layer was properly resized, and MSE reanalysis predicted an improved and adequate result.

The pressure time history was handled by assuming a step function with zero rise time and a duration of 2 ms. Coupling between the deflected mirror shape and the plane wave pressure pulse was determined using the generalized force described in equation (1). Since the pulse duration was long compared to mirror vibratory periods, static analysis with the generalized force was used to calculate the initial deflection for each vibratory mode. Then the rate of decay and residual vibration for each mode was determined using modal properties and the single degree of freedom transient response expression listed in equation (4) below[1,7]:

$$y(t) = \frac{F_o}{K} e^{-zw_n t} \left[\cos(w_d t) + \frac{zw_n}{w_d} \sin(w_d t) \right] \qquad (4)$$

where $y(t)$ = response of single d.o.f. at time t

F_o = magnitude of force step function

K = modal stiffness

W_d, W_n = damped, undamped natural frequencies

z = percent viscous critical damping.

Finally, the total mirror response was determined using superposition of the individial modal responses :

$$Y(x,t) = W_i(x)\, q_i(t) \qquad (5)$$

where $y(x,t)$ = physical response at position x, time t

$W_i(x)$ = modal response of i'th mode at position x

$q_i(t)$ = generalized coordinate of the i'th mode at time t

This method of calculating total mirror response neglects any mode transformations which may occur due to coupling of complex vibration modes. However, it was felt that neglecting such coupling would be conservative, and the cost of complex transient response analysis was avoided.

Final Configuration

The final configuration of one of the damped optics being designed is illustrated in Figure 6. This figure shows the outline of the circular tangent mount, the bolt pattern attaching the constraining layer to the mirror, and the large amount of undamped mirror surface area located outside of the tangent mount cylinder. Also shown are the variable mirror thickness, large constraining layer inside the tangent mount cylinder, tangent mount, tangent mount constraining layer, and viscoelastic damping material on the mirror and mount surfaces. The mirror constraining layer thickness was made equal to the mirror thickness for maximum efficiency, and was bolted to the mirror with spacers and Bellville washers to control creep effects. The metal spacers were made slightly thinner than the 0.002 in.ISD 112 damping layer to allow full contact when the attaching bolts are torqued to specification, but to eliminate loosening of the assembly as the VEM stress-relaxes. The Bellville washers are used to retain bolt preload in the face of a creeping VEM. The mount constraining layer is unusually thick compared to the mount thickness due to the difficulty in damping the longitudinal bounce mode. This constraining layer is segmented to allow assembly after permanent attachment of the tangent mount to the mirror. Bolts are used for attachment to the mount to ensure the long term integrity of the constraining layer, VEM, and mount assembly. The rear plate is used to evenly distribute loads due to thermal mismatch between the molybdenum mount and steel support structure.

Performance predictions are summarized in Table 1 below:

Table 1

Frequency, Hz.	Mode	Modal Structural Damping, %	Displacement, μin. Initial	Final
980	Shear + Bending	15	100	0.10
1360	Bounce + Bending	11	1060	1.20
1630	Bending	16	270	0.001
2670	Bending	10	630	0.002

Overall residual deflections after 15 ms. following the previous pressure pulse were estimated to be 1.2 μin., or about 30% of the total allowable deflection.

Performance Tests

To confirm predictions for the dynamic performance of the damped mirror, dynamic impact testing was carried out on the final delivered configuration. An impact hammer was used to excite the mirror locally, simulating the impulsive loading to be expected in service. Damping was determined using a conventional curve fitting algorithm employed by the HP 5423A FFT structural dynamic analyzer. Figure 7 illustrates a typical frequency response function, the calculated damping, and an actual response time history before and after application of the damping treatment. The response curve cannot be assumed to estimate the actual transient response of the mirror because all modes are not excited to the correct level. But the damped response curve does illustrate that an initial impulsive response is damped to the noise level in about 10-15 ms., within the allocated time span.

An additional comparison between tested and predicted performance is shown in Figure 8. Here the overall modal damping is plotted as a function of frequency for different modes; both test data and analytical predictions are shown. Figure 8 shows that more modes were detected from test than were predicted over the same frequency range, an effect that was probably due to the limited finite element model density. For those modes that were predicted, however, the correlation between test results and predictions is quite good. Certainly the predictions were better than would be necessary to justify using the relatively simple and cost-effective analytical design techniques employed to design such a complex optical structure; their continued use is recommended to the community.

CONCLUSIONS

The following conclusions summarize the significant results of the damped optics program:

1. Optics subjected to dynamic pressure load require very high damping to meet optical distortion criteria.

2. Complete VEM coverage of the mirror surface is not necessary if resonant frequencies are sufficiently high.

3. The Modal Strain Energy (MSE) analysis method can be an accurate and cost-effective design tool.

4. Test results correlate well with analytical predictions.

5. State-of-the-art damping can be successfully applied to modern high precision optics through careful design practice as outlined herein.

REFERENCES

1. Thompson, W. T. "Theory of Vibration with Applications", 2nd ed., Prentice-Hall Inc., Englewood Cliffs, New Jersey

2. Ungar, E. E. "Loss Factors of Vicoelastically Damped Beam Structures," J. Acoust. Soc. Am., Vol. 34, pp. 1082-1089, 1962.

3. Johnson, C. D., Kienholz, D. A., and Rogers, L. C. "Finite Element Prediction of Damping in Beams with Constrained Viscoelastic Layers," Shock and Vibration Bulletin, No. 51, May 1981, pp. 71-82.

4. Johnson, C. D. and Kienholz, D. A. "Finite Element Prediction of Damping in Structures with Constrained Viscoelastic Layers," AIAA Journal, Vol. 20, No. 9, Sept. 1982.

5. Ungar, E. E. and Kerwin, E. M. Jr., "Loss Factors of Viscoelastic Systems in Terms of Energy Concepts," Acoust. Soc. of Am., Vol. 34, July 1962, pp. 954-957.

6. Johnson, C. D., Kienholz, D. A., Austin, E. M. and Schneider, M. E. "Finite Element Design of Viscoelastically Damped Structures." Vibration Damping 1984 Workshop Proceedings, Nov. 1984.

7. Harris, C. M. and Crede, C. E. "Shock and Vibration Handbook", 2nd Edition, McGraw Hill, N.Y., 1976, Chapter 8.

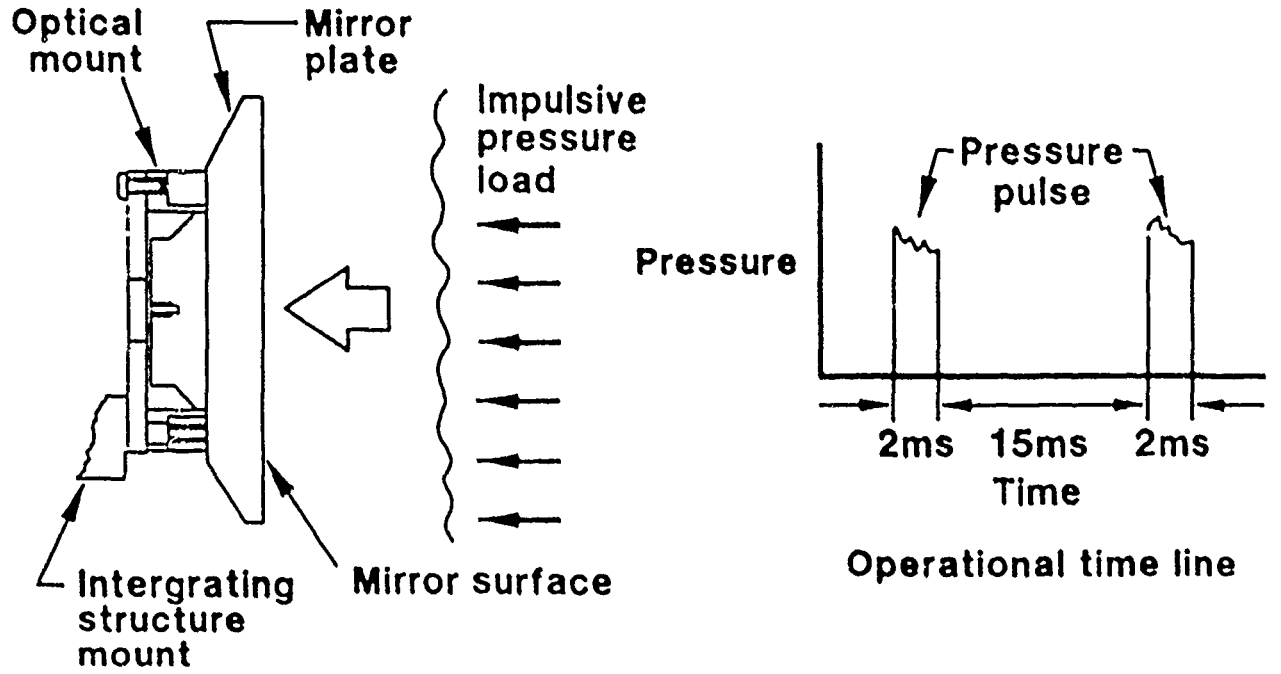


FIGURE 1 MIRROR SURFACE IS EXPOSED TO SEVERE DYNAMIC ENVIRONMENT

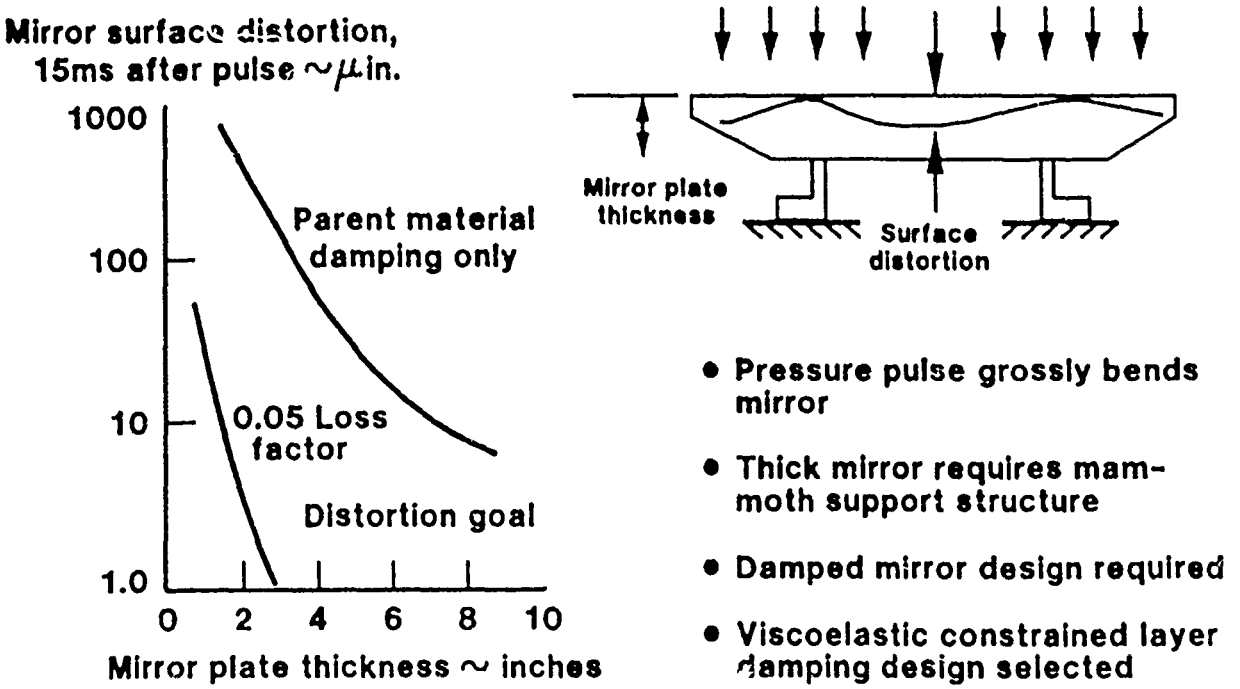


FIGURE 2 DAMPING IS REQUIRED TO MEET DISTORTION GOAL

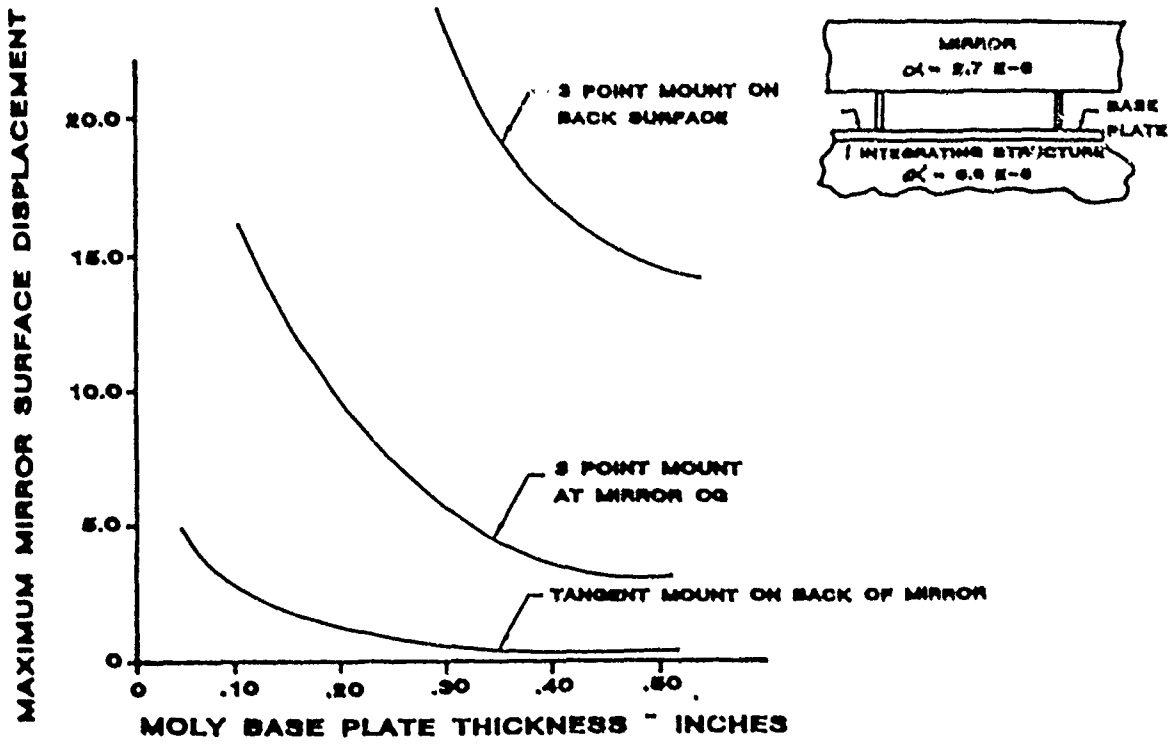
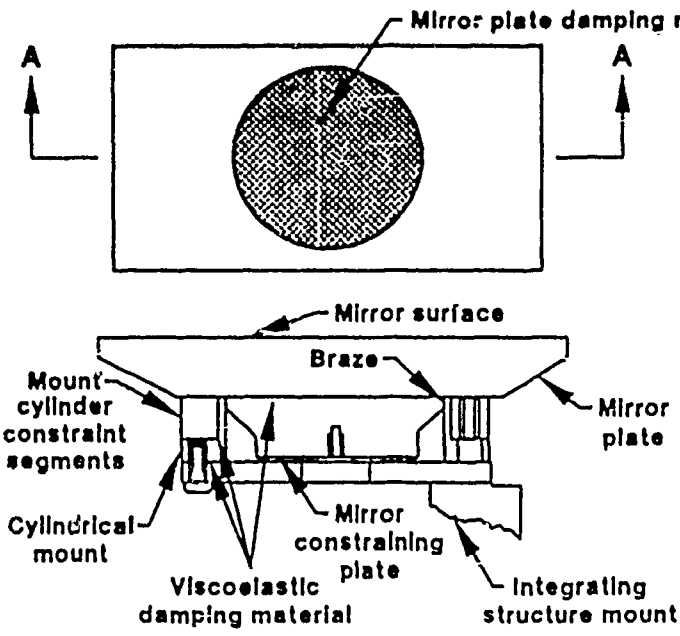


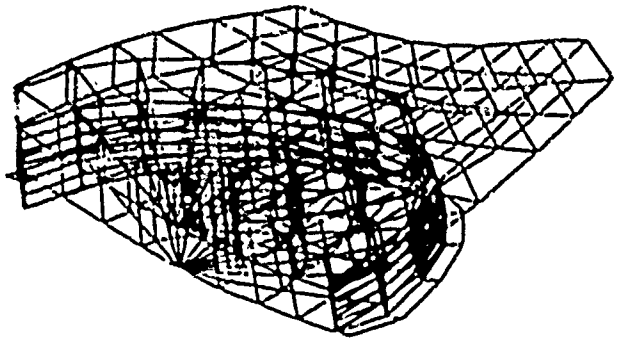
FIGURE 3 CIRCULAR TANGENT MOUNT SHOWS LOWEST SENSITIVITY TO AMBIENT TEMPERATURE CHANGE WITH MOLY BASE



- VEM covers only 55% of some configurations
- Bending modes not optimally treated by placement of damping material
- Cylindrical mount selected to provide thermal isolation
- Cylindrical mount must be damped for rigid body mode control
- Accurate analysis is required to determine effective modal damping for all modes

FIGURE 4 PREDICTION OF MODAL DAMPING IS DIFFICULT

'3-D HEXA' elements used to model mirror and VEM



- Finite element model predicts mode shapes and frequencies
- MSE method predicts modal damping
- Transient forced response predicted using generalized forces (zero rise time)
- Higher frequency modes have less VEM participation but oscillate through more cycles
- Loss factors of 0.05 to 0.15 predicted
- Residual response after 15 ms calculated to be ≤ 44% of allowable

FIGURE 5 ANALYSIS RESULTS PREDICT HIGH DAMPING

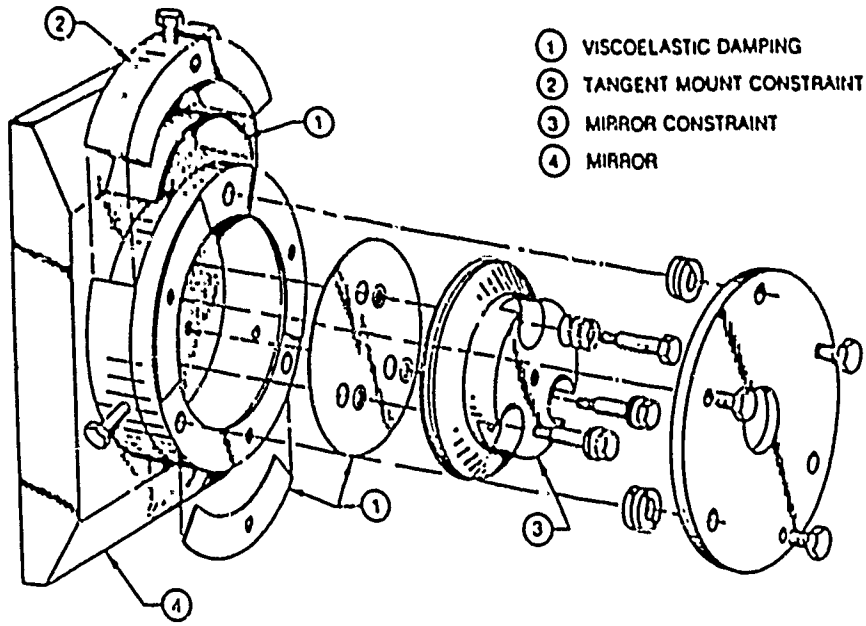


FIGURE 6 FINAL DESIGN EMPLOYS CONSTRAINED LAYER VEM DAMPING IN BOTH MIRROR AND MOUNT

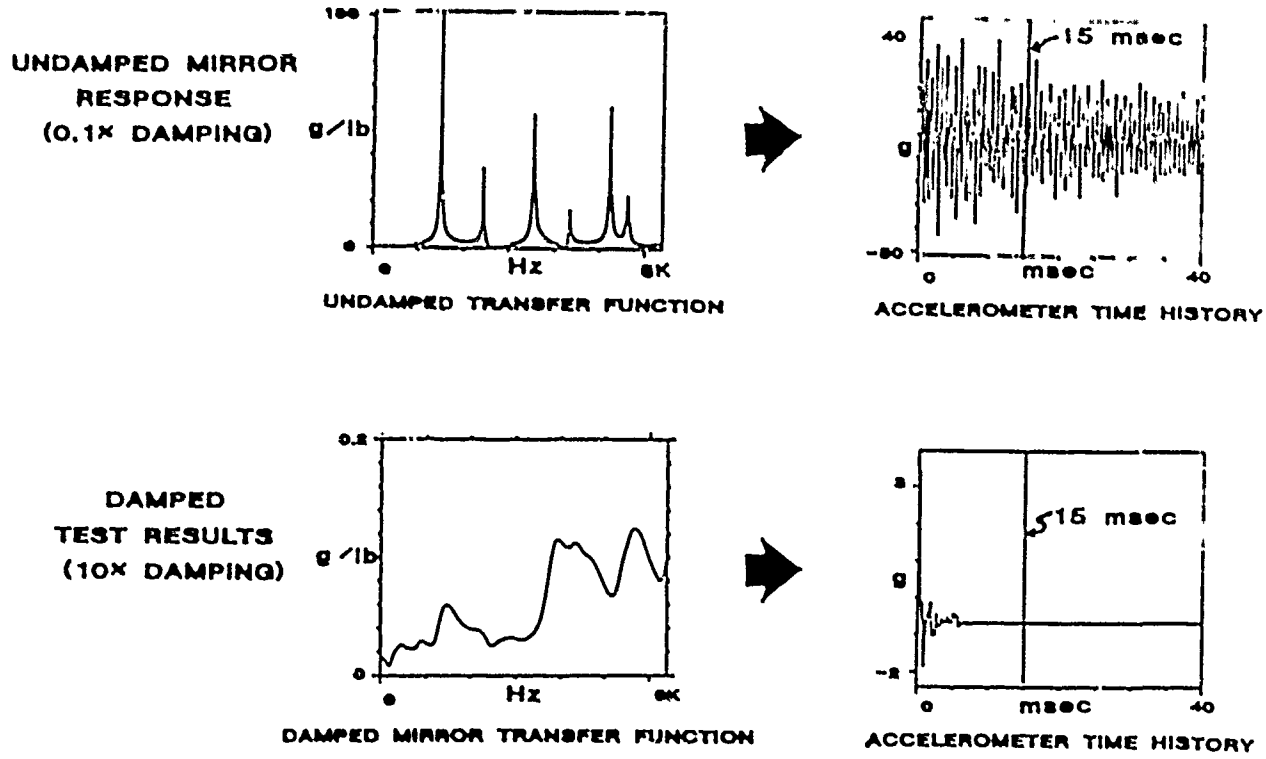
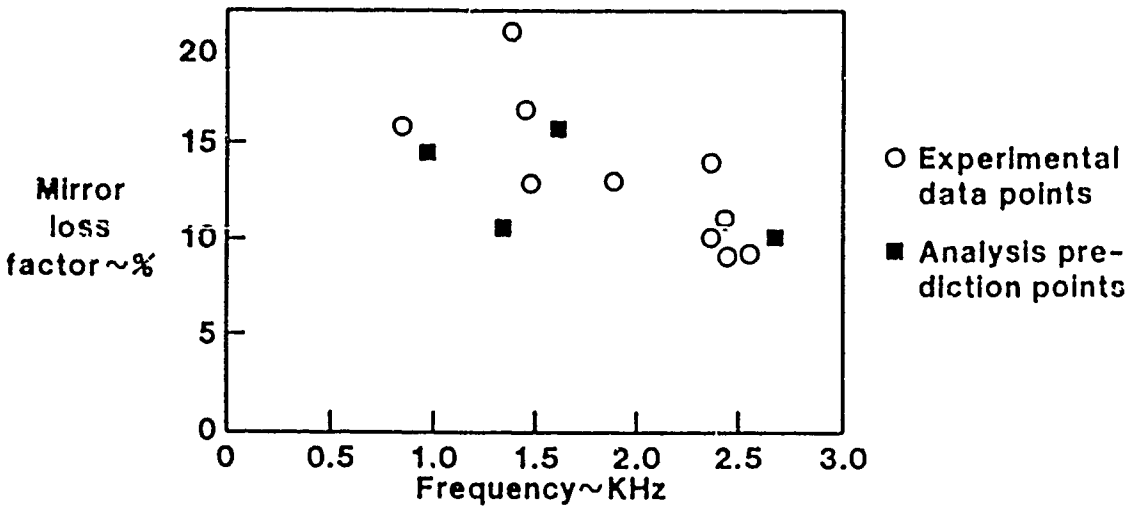


FIGURE 7 MIRROR IMPACT RESPONSE DRAMATICALLY REDUCED AFTER ADDITION OF DAMPING



- Impact testing used to obtain modal damping
- Micro strain levels from pressure pulses simulated
- Experimental loss factors ranged from 0.09 to >0.20
- Worst correlation at higher frequencies where finite element model density affects analysis accuracy

FIGURE 8 TEST RESULTS CORRELATE WELL WITH PREDICTIONS

METAL DAMPER ANALYSIS AND TEST

Charles W. White
Martin Marietta Denver Aerospace
Denver, Colorado

ABSTRACT

A series-type viscoelastic damper was used as the damping treatment on the PACOSS Twin Towers experiment. This damper unit was connected to the towers in series with Plexiglas tubes. Although the results of the twin tower tests showed this Plexiglas unit added significant damping, it was learned by analysis that installation of the unit in series with aluminum tubes would about double the observed tower damping. In addition, the metal damper unit has the potential of being space qualifiable. Therefore, a metal damper unit has been built and tested as a component to verify the analytical prediction of increased damping. The purpose of this paper is to present the results of the tests that were conducted and to evaluate the ability to predict future damper designs.

The paper describes the metal damper unit and the testing that was done. Test results are present in tabular and graphical form. An analytical model of the damper unit is described and used to calculate the shear modulus and loss factor of the viscoelastic material used in the unit. A comparison of these results with those obtained by other investigators show general good agreement. It was concluded that the general scatter in viscoelastic material characteristic descriptions, although adequate for preliminary design, warrants testing of specific damping treatments at the component level to evaluate the final design.

INTRODUCTION

The primary purpose of this paper is to present the results of hysteresis testing conducted to determine the damping characteristics of the series-type viscoelastic damper shown in Figure 1. The secondary purpose is to evaluate the ability to predict damper stiffness and loss factor using an analytical model and generic viscoelastic material characteristics. Figures 2 and 3, respectively, show a partially assembled view and a disassembled view of Figure 1 to facilitate the following description of how the damper works.

Part A is an aluminum cylinder having female threads at both ends which mate with parts D and E. Part D seals cylinder A at one end. Parts B1 and B2 are two halves of another cylinder. B1 and B2 are fastened to the outer surface of two rings of viscoelastic material (VEM) by adhesive. The inner surface of the VEM rings is fastened by adhesive to part C. Each VEM ring is 1.0-inch wide and 0.1875-inch thick. The damper unit is assembled by sliding the cylinder, B, formed by B1 and B2, into cylinder A. Then part E is mated with part A to complete the assembly. The outer diameter of B mates with a snug sliding fit to the inside diameter of A. The length of B is such that one end butts against part D and the other against p[illegible] E. Thus, parts A, B, D and E virtually form a single part attached to the outer surface of the VEM rings, while part C is attached to the inner surface of the VEM rings. Parts C and D provide interfaces for connecting the damper unit to the structure in which it will operate. This damper design was inspired by the success of the PACOSS Twin Tower dampers. It is superior to the PACOSS Twin Towers damper in three ways: 1) The metal construction of all but the VEM part drives most (85% to 98%) of the operating strain energy into the VEM material, thus increasing the damper unit loss factor; 2) The metal housing (part A) provides the potential for space qualification by adding a bellows connecting parts C and E and plugging the D end of tube C to eliminate outgassing of the unit; and 3) The bellows connecting parts C and E could be designed to provide whatever stiffness is required for dimensional stability.

The bellows modification has not been completed yet. This paper addresses only the measurement of damping to demonstrate the improvement of performance (item 1 above). The contents of this paper are organized in the following manner: The hysteresis test data and the method of data reduction are presented first. Next, an analytical model to predict damper behavior using known VEM material properties is developed. Finally, the comparison of test and analysis is discussed, using the analytical model to back out VEM material properties to compare with the "known" values.

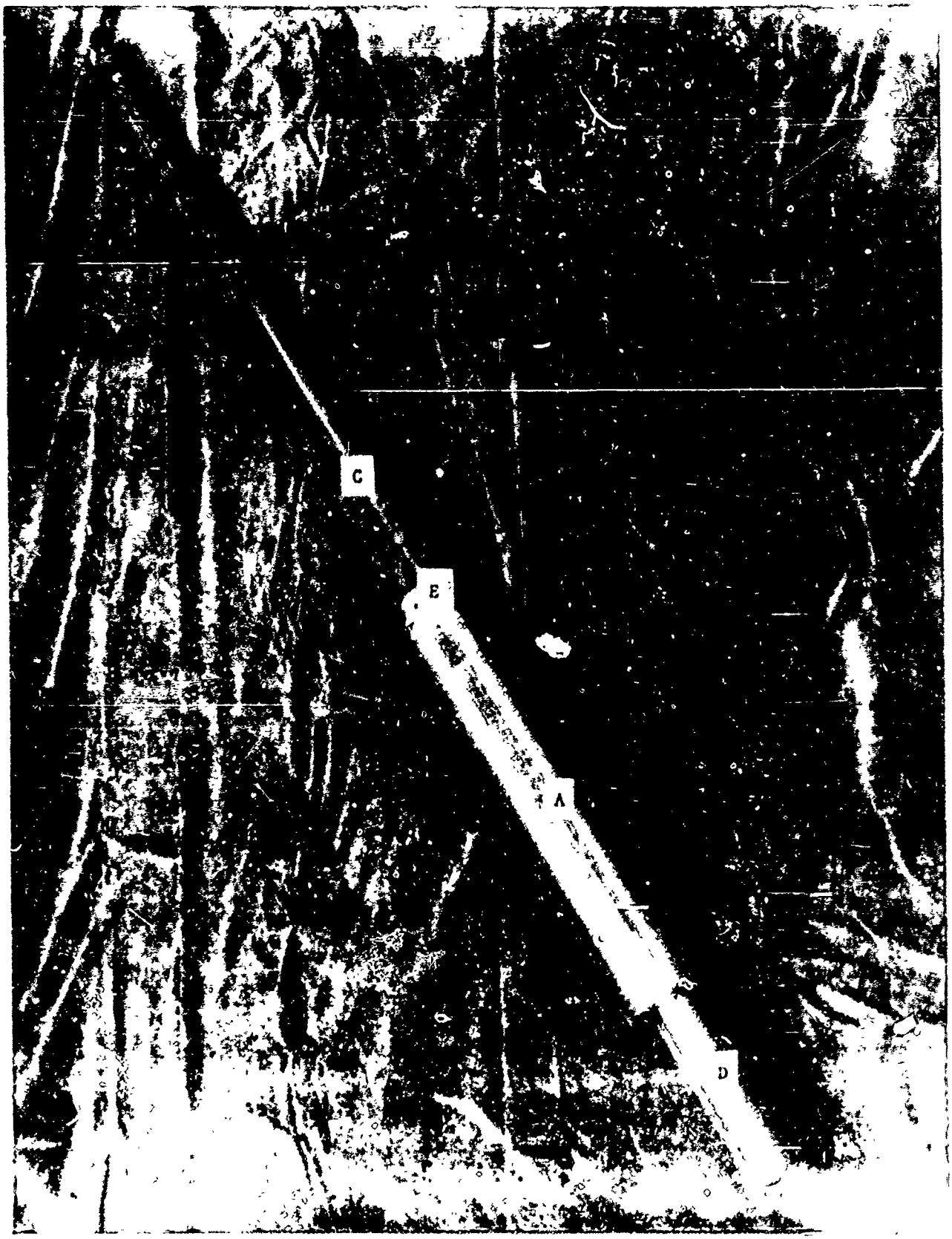


Figure 1 Series-Type Viscoelastic Damper (Assembled)

CB-3



Figure 2 Series-Type Viscoelastic Damper (Partial Assembly)

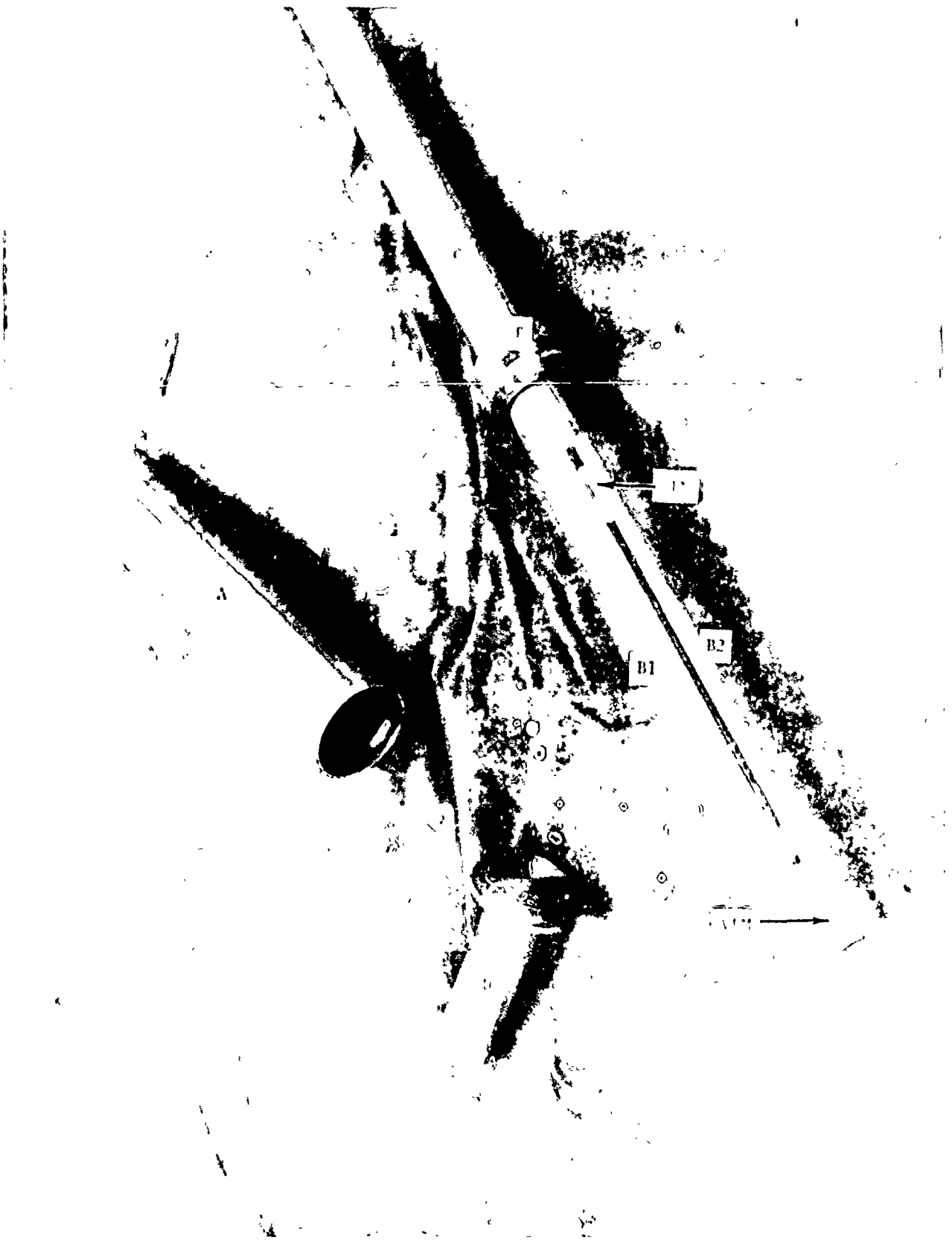


Figure 3 Series-Type Viscoelastic Damper (Disassembled)

HYSTERESIS TEST RESULTS

To perform the tests the test article was fastened into a materials testing machine, and a chamber to control temperature was placed around the test article. Temperature was observed on a strip recorder and a digital meter. Testing began only after the desired temperature was stabilized. Each hysteresis test was conducted by setting the desired frequency and maximum stroke amplitude on the materials testing machine and plotting the resulting force versus displacement. Figure 4 represents a typical hysteresis plot.

The information contained in a hysteresis plot is easily identified by a discussion of the elementary diagram of the rotating force vectors that describe the force balance in a sinusoidally excited single- degree-of-freedom system. Figure 5 shows such a diagram. (The mathematics leading up to the diagram are detailed in many elementary vibration textbooks*.) At a constant excitation frequency the diagram in Figure 5 rotates at ω radians per second with a constant phase angle, θ, between applied force, F, and displacement, X_o. The values of F and X recorded by the hysteresis plot of Figure 4 are

$$F = F_o \sin \omega t \tag{1}$$

and

$$X = X_o \sin (\omega t - \theta) \tag{2}$$

Therefore, when $\omega t = \theta$

$$F = F_o \sin \theta = C\omega X_o \tag{3}$$

and

$$X = 0 \tag{4}$$

Thus, in Figure 4, the force, $F = C\omega X_o$ at $X = 0$, is highlighted as of special interest. Furthermore, it is clear from Figure 5 that

$$F_o \cos \theta = KX_o - M\omega^2 X_o \tag{5}$$

At the low frequencies of these hysteresis tests $M\omega^2 X_o$ is negligible, so Eq. (5) gives

$$K \simeq F_o \cos \theta / X_o \tag{6}$$

By reading the peak force, F_o, (when $\omega t = 0$) and maximum displacement, X_o, (when $\omega t - \theta = 0$) as indicated on Figure 4, one can determine θ from Eq. (3) and then K from Eq. (6). Finally, using the definition that the component loss factor, η, is the ratio of the energy loss over the energy stored, the equivalent ratio can be obtained from Figure 5 as

$$\eta = C\omega X_o / [KX_o - M\omega^2 X_o] = \tan \theta \tag{7}$$

*Thomson, W. T., "Mechanical Vibrations," Prentice-Hall, Inc., Englewood Cliffs, New Jersey, 1956, p. 52.

Figure 4 Viscoelastic Damping Hysteresis Loop

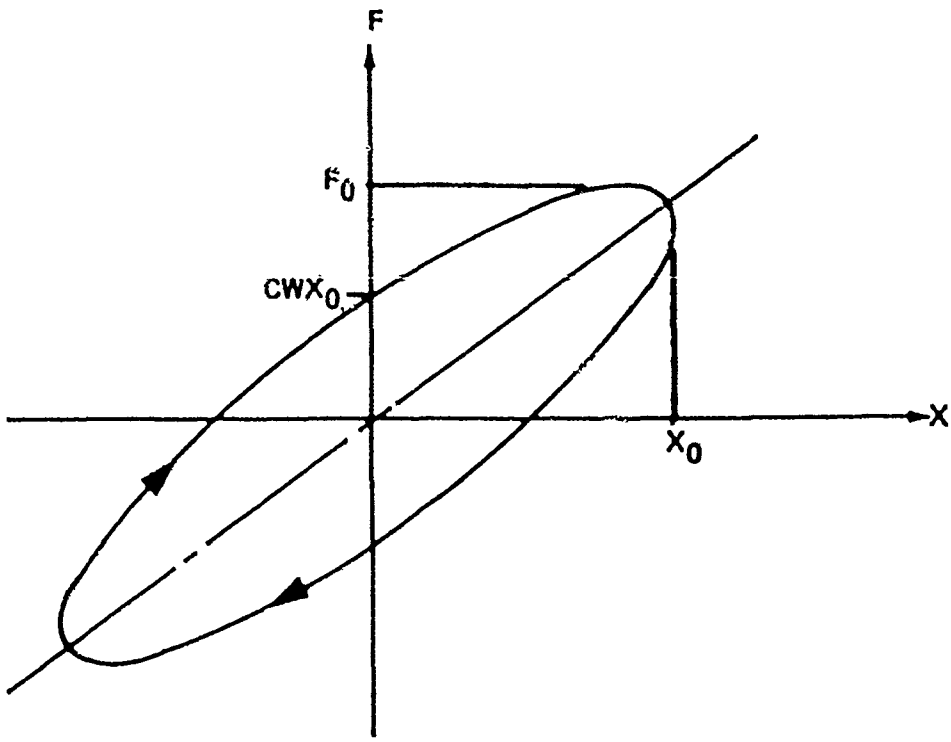


Figure 5 Vector Representation of Forced Vibration with Viscous Damping

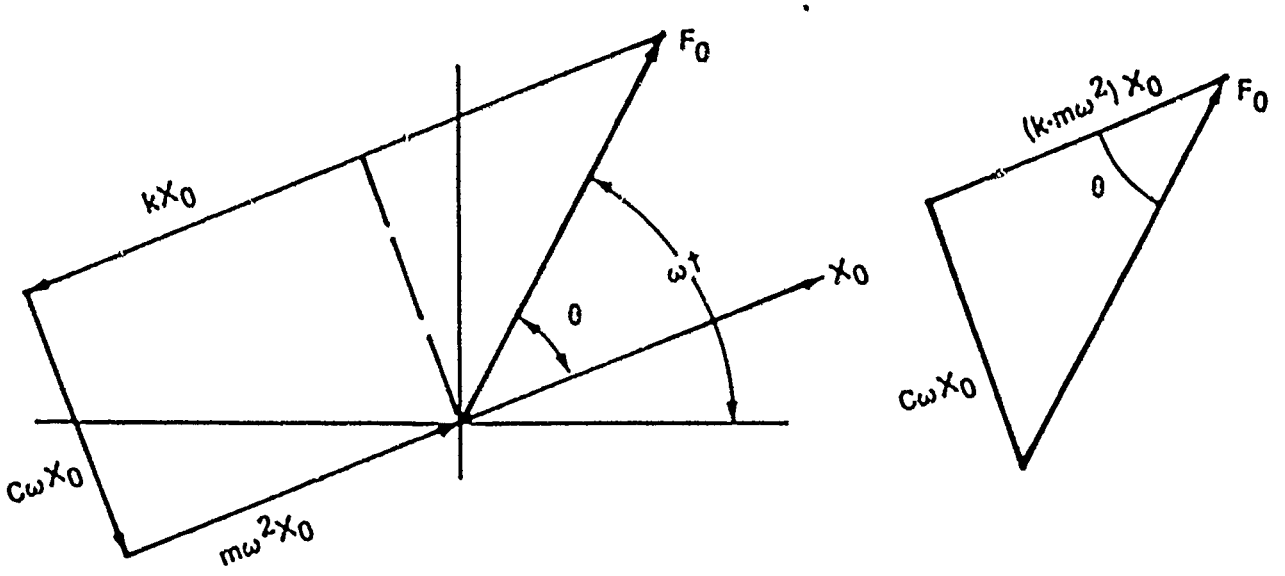


Table 1 tabulates the measured values of $C\omega X_o$, F_o and X_o and corresponding calculated values of θ, η and K for each of 24 tests. They have been categorized into six cases, A through F. Each case is for a particular temperature and maximum displacement of the unit. Tests were conducted at four different frequencies (0.5 Hz, 1.0 Hz, 1.4 Hz and 2.0 Hz) for each case.

The calculated values of K and η shown in Table 1 are plotted as a function of frequency in Figure 6. Two anomalies are evident in Figure 6: 1) The loss factor calculated for the 50°F test at 0.0005-inch displacement (case A) does not follow the trend of the other 50°F results. The reason for this anomaly is the scale used to plot the test force was too small to allow an accurate reading, e.g., a 0.25-mm reading error, decreasing damping force and increasing maximum force, would make the 2-Hz data of case A have the same trend as cases B and C; and 2) The loss factors calculated for 50°F data decreases with increasing frequency. The reason for this trend has not been found. However, the loss factor of the VEM does display this trend at lower temperatures as will be discussed in the Theoretical Experimental Correlation section of this paper.

The following section describes the analytical model generated to predict the damper characteristics.

ANALYTICAL MODELS

The analytical model of the metal damper was a simple lumped model based on the assumption of constant strain between displacement coordinates.

The damper unit weighs approximately 25 lbs so the maximum inertia force, $M\omega^2$, is less than 10 1/4 lbs per inch of test deflection. (Because one end is fixed, the actual force is half of this value.) The lowest damper spring rates, as will be shown, is about 2,000 lbs per inch of test deflection. Therefore, the analytical model described below consists only of stiffness terms.

Figure 7 is a sketch of a section view of the damper and an idealized five-element model. The stiffness matrix for this model was generated from the triple matrix product:

$$\begin{bmatrix} 1 & & & & \\ -1 & 1 & & & -1 \\ & -1 & 1 & & \\ & & -1 & 1 & \\ & & & -1 & 1 \end{bmatrix} \begin{bmatrix} K_1 & & & & \\ & K_2 & & & \\ & & K_{V1} & & \\ & & & K_3 & \\ & & & & K_{V2} \end{bmatrix} \begin{bmatrix} 1 & -1 & & & \\ & 1 & -1 & & \\ & & 1 & -1 & \\ & & & 1 & -1 \\ -1 & & & & 1 \end{bmatrix}$$

$$= \left[\begin{array}{c|c|c|c|c} K_1 & -K_1 & & & \\ -K_1 & K_1+K_2+K_{V2} & -K_2 & & -K_{V2} \\ \hline & -K_2 & K_2+K_{V1} & -K_{V1} & \\ \hline & & -K_{V1} & K_3+K_{V1} & -K_3 \\ \hline & -K_{V1} & & -K_3 & K_3+K_{V2} \end{array}\right] \qquad (8)$$

Table 1 Measured Damper Properties

TEMP(°F)	FREQ(Hz)	$C\omega X_o$ DAMPER FORCE(LBS)	F_o MAX FORCE(LBS)	X_o MAX DISP(IN.)	θ PHASE (DEG)	K_D DAMPER STIFF(LBS/IN.)	η_D DAMPER LOSS FACT
	.5	5.75	8.5	.00052	42.57	12,038.	.9138
50.2	1.0	7.6	11.2	.000525	44.72	14,616.	.9238
(Case A)	1.5	8.75	13.5	.000507	40.40	20,277.	.8511
	2.0	9.9	14.75	.000484	42.51	22,311.	.9115
	.5	24.375	36.875	.0024	41.38	11,529.	.8809
50.2	1.0	33.75	51.875	.0024	40.59	16,415.	.8567
(Case B)	1.5	39.0	61.45	.002375	39.39	19,995.	.8213
	2.0	41.875	66.875	.00225	38.77	23,174.	.803
	.5	54.5	82.0	.005225	41.65	11,782.	.8895
50.2	1.0	73.5	112.5	.005175	40.79	16,458.	.863
(Case C)	1.5	83.75	133.75	.005025	38.77	20,753.	.8031
	2.0	87.5	145.0	.00477	37.12	24,240.	.7567
	.5	6.75	11.55	.0025	35.06	3,847.	.7018
76.4	1.0	9.4	15.5	.0025	37.3	4,930.	.7627
(Case D)	1.5	11.75	18.5	.002425	39.43	5,893.	.8223
	2.0	12.625	20.05	.0023	39.03	6,772.	.8105
	.5	14.5	26.75	.0053	32.82	4,241.	.6450
76.4	1.0	20.5	34.0	.00525	35.85	5,403.	.7226
(Case E)	1.5	24.38	39.5	.0051	38.1	6,095.	.7842
	2.0	27.0	42.75	.00485	39.17	6,834.	.8146
	.5	6.25	11.9	.0052	31.68	1,947.	.6172
99.4	1.0	7.75	14.85	.0052	31.46	2,436.	.6118
(Case F)	1.5	9.0	17.0	.0050	31.97	2,884.	.6240
	2.0	9.75	17.9	.0049	33.00	3,064.	.6495

Figure 6 Damper Stiffness and Loss Factor vs. Frequency

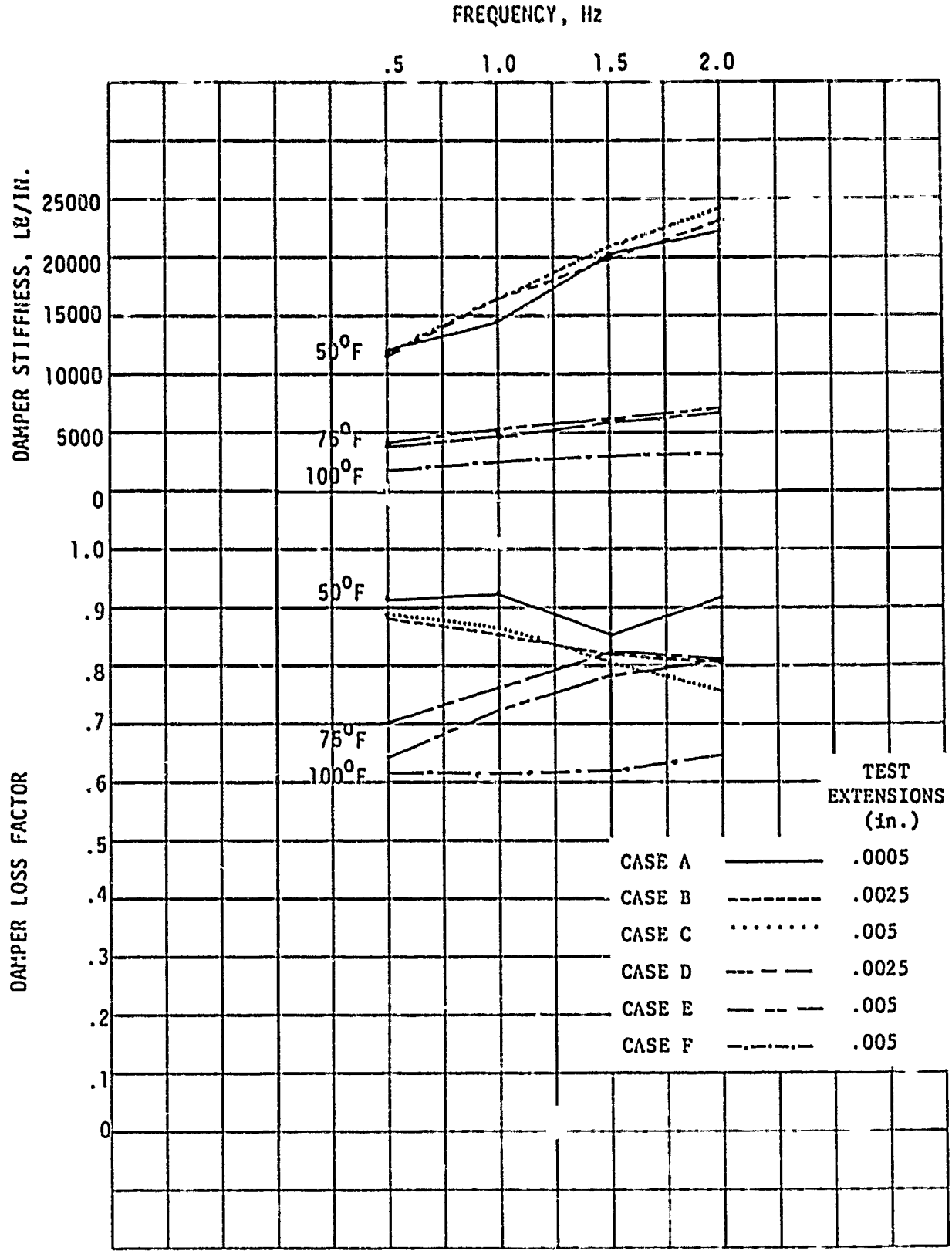
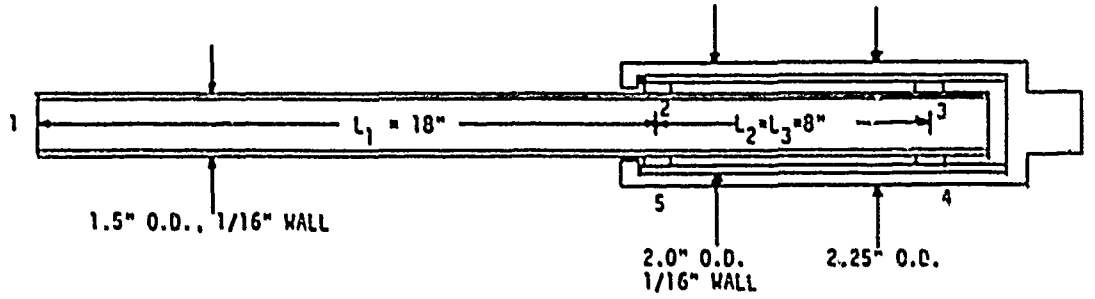
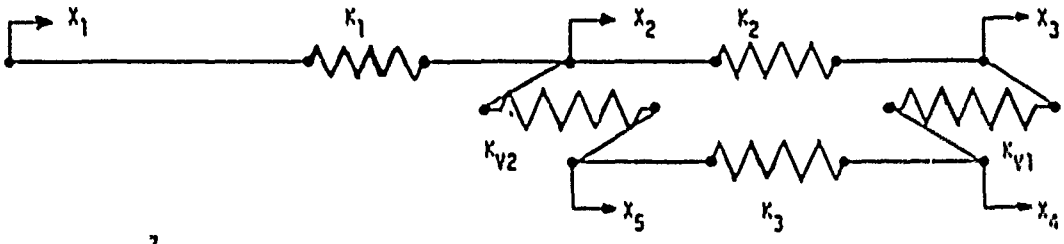


Figure 7 Elements of Damper Model





$E = 10^7$; G_V = (SEE FIGURE 8)

$$K_1 = \frac{(\pi D_1 t_1)}{L_1} E; \quad K_1 = 1.704\ (10)^5, \quad K_2 = 3.835\ (10)^5, \quad K_3 = 3.037\ (10)^6$$

$$K_V = \frac{A_V G_V}{t_V} - \frac{(\pi D_V L_V) G_V}{L_V}, \quad K_{V1} = K_{V2} = 28.27\ G_V$$

The hysteresis tests were conducted by grounding one end of the damper and displacing the other. Therefore, it is necessary to ground one end of the model to make it representative of the test. When this is done, the solution for deflections (neglecting inertia effects) can be written,

$$\begin{Bmatrix} X_1 \\ X_2 \\ X_3 \\ X_5 \end{Bmatrix} = \left[\begin{array}{c|c|c|c} K_1 & -K_1 & & \\ \hline -K_1 & K_1+K_2+K_{V2} & -K_2 & -K_{V2} \\ \hline & -K_2 & K_2+K_{V1} & \\ \hline & -K_{V2} & & K_3+K_{V2} \end{array}\right]^{-1} \begin{Bmatrix} F_1 \\ 0 \\ 0 \\ 0 \end{Bmatrix} = [K]^{-1}\{f\} = [E]\{f\} \qquad (9)$$

The inverse of the flexibility, E_{11}, provides the expression for the end-to-end stiffness, K_D, of the model. Assuming $K_{V1} = K_{V2} = K_V$, the desired stiffness can be written as,

$$K_D = F_1/X_1 = 1/E_{1,1} = |K|\ (\text{Adjoint}[K])_{1,1}$$

$$= \frac{K_1[(K_1+K_2+K_V)(K_2+K_V)(K_3+K_V) - K_2^2(K_3+K_V) - K_V^2(K_2+K_V)] - K_1^2(K_2+K_V)(K_3+K_V)}{[(K_1+K_2+K_V)(K_2+K_V)(K_3+K_V) - K_2^2(K_3+K_V) - K_V^2(K_2+K_V)]} \qquad (10)$$

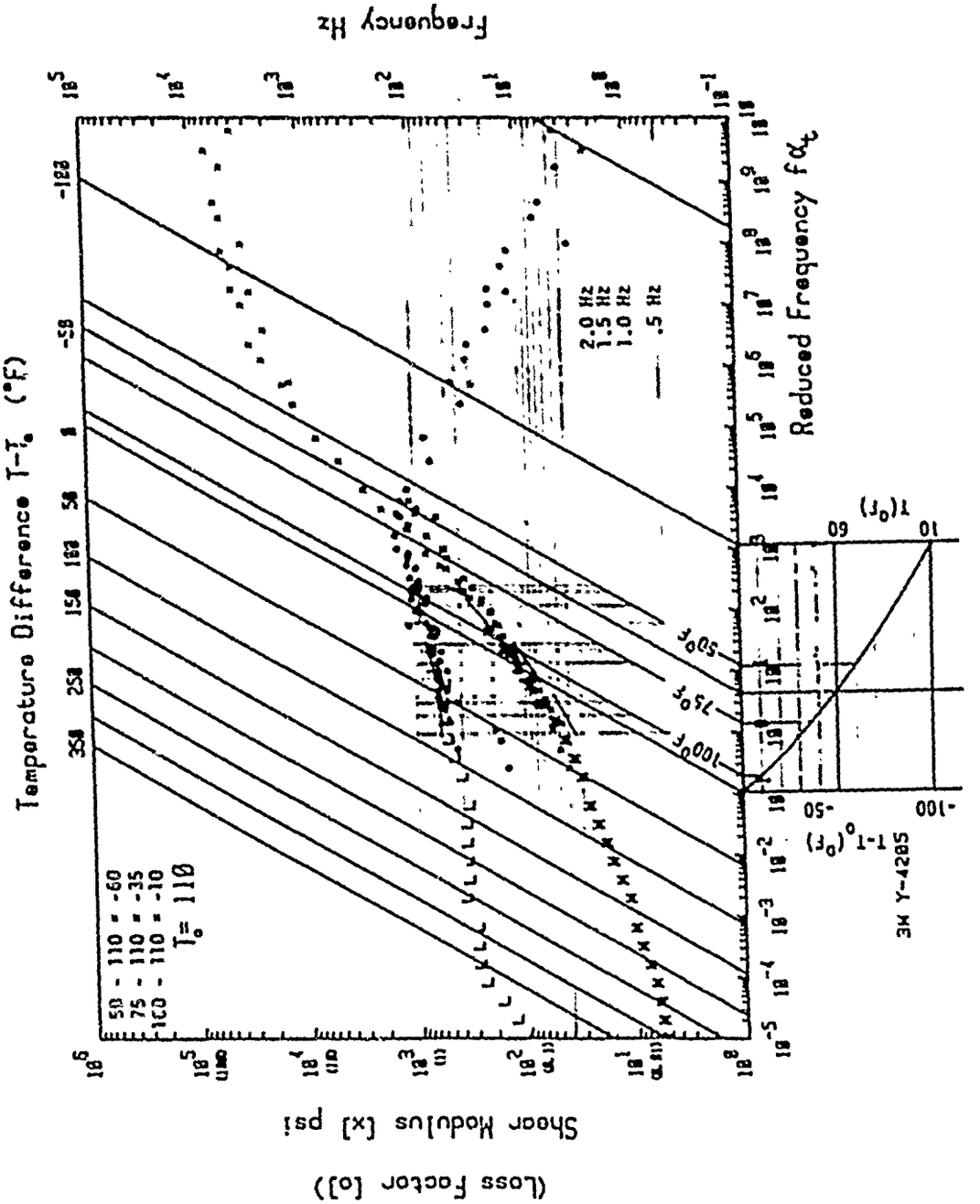
or, after some algebraic rearrangement,

$$K_D = K_1 - \frac{K_1^2}{K_1 + \dfrac{K_V}{1+\dfrac{K_V}{K_3}} + \dfrac{K_V}{1+\dfrac{K_V}{K_2}}} \qquad (11)$$

$$\text{and} \quad \lim_{K_2 \to K_3 \to \infty} K_D = \frac{2K_1K_V}{K_1 + 2K_V} \qquad (12)$$

The values of K_1, K_2, and K_3 are given in Figure 7. Values of K_V depend on values of G_V which must be read from the 3MY-4205 viscoelastic material characteristics plot presented as Figure 8. As Figure 8 shows, both material shear modulus, G_V, and loss factor, η_V, are functions of temperature and frequency. To read values of G_V and η_V at a particular temperature and frequency, one must construct a horizontal line at the desired frequency and find the intersect of that line with the desired

Figure 8 Comparison of Hysteresis Test Results
With 3MY-4205 Viscoelastic Characteristics



temperature. (If the desired temperature line does not appear on the plot, it must be constructed. This may be done by cross-plotting reduced frequency against temperature on a linear scale as shown in Figure 8.) At the intersect of frequency and temperature, construct a vertical line which intersects the G_V and η_V data. Finally, at the intersect of the vertical line and the VEM data, construct a horizontal line to the G_V and/or η_V scale. Thus, it can be seen that values of G_V range from 40 psi to 400 psi in the temperature and frequency of intersect. Therefore, the highest value of K_V is $400(28.27) = 1.1308(10)^4$. So, $K_V/K_2 \leq 0.295$, and $K_V/K_3 \leq 0.00372$. Consequently,

$$\frac{1}{1 + K_V/K_2} + \frac{1}{1 + K_V/K_3} = 1.968 \qquad (13)$$

and

$$K_D = \frac{1.968\ K_1 K_V}{K_1 + 1.968\ K_V} \qquad (14)$$

That is, Eq. (12) appears to provide a good model for preliminary design calculation. Because the lumped model from which Eq. (12) was derived prohibits local distortion due to the split in Part B and does not allow variations in stress through the VEM due to local loading of the aluminum, the lumped model predictions were compared with those of a more detailed finite element model (FEM). This comparison confirmed the adequacy of the simple lumped model.

However, when using Figure 8, the difficulty of accurate construction and the scatter of data in the range of interest result in a broad range of possible values of G_V (easily 10% to 20% variation) to use in either Eq. (11) or Eq. (12) for prediction of damper stiffness. Therefore, an alternative method of using the analytical model to compare the damper hysteresis test results with the 3MY-4205 data (also test results) was used. This is discussed in the following section.

THEORETICAL/EXPERIMENTAL CORRELATION

Because of the difficulties of selecting single values of G_V and η_V from Figure 8 which allow a fair evaluation of the ability to predict damper characteristics, it was decided to back out values of G_V and η_V from the hysteresis test results for direct comparison with test data presented in Figure 8.

Equation (10) is used to determine an expression for G_V from the model. After some algebraic manipulation it can be arranged in the form,

$$\left(1 - \frac{K_D K_1}{K_1 - K_D}\left(\frac{1}{K_2 + K_3}\right)\right)K_V^2 - \left(\frac{K_D K_1}{K_1 - K_D} - \frac{2K_2 K_3}{K_2 + K_3}\right)K_V - \left(\frac{K_2 K_3}{K_2 + K_3}\right)\left(\frac{K_D K_1}{K_1 - K_D}\right) = 0 \qquad (15)$$

This quadratic equation is solved for K_V, then G_V is obtained from

$$K_V = G_V A_V/t \tag{16}$$

where the value of A_V/t for a single VEM ring is given in Figure 8.

Table 2 presents the calculated values of G_V for all hysteresis test results contained in Table 1. Table 2 also presents values of η_V calculated from the relationship

$$\eta_d = \eta_{AL}\,(SE_{AL}/SE_D) + \eta_V(SE_V/SE_D) \tag{17}$$

where

η_d = the measured damper loss factor

η_{AL} = loss factor of aluminum (0.005)

η_V = VEM loss factor to be calculated

SE_V, SE_{AL}, SE_D = strain energy of VEM, aluminum and total damper, respectively.

The strain energy terms were calculated using the element values defined in Figure 7 and the K_V values calculated using Eq. (13) to form the terms of the 4x4 stiffness matrix defined in Eq. (9). From these stiffness terms the first column of the adjoint matrix (corresponding to applied force F_1) was calculated. That is, the first column of Eq. (9) was calculated from:

$$\{X\} \equiv \begin{Bmatrix} X_1 \\ X_2 \\ X_3 \\ X_5 \end{Bmatrix} = \begin{Bmatrix} (K_1+K_2+K_V)(K_2+K_V)(K_3+K_V) - K_2^2(K_3+K_V) - K_V^2(K_2+K_V) \\ K_1(K_2+K_V)(K_3+K_V) \\ K_1K_2(K_3+K_V) \\ K_1K_V(K_2+K_V) \end{Bmatrix} F_1/\Delta \tag{18}$$

Table 2 3MY-4205 Shear Modulus, G_{V1} and Loss Factor, η_V, Backed Out of Hysteresis Test Results

TEMP (°F)	FREQ (Hz)	DAMPER STIFFNESS	DAMPER LOSS FACTOR	VEM SHEAR MODULUS	S.E. RATIO	VEM LOSS FACTOR
	.5	12,038.	.9183	232.	.92	.99
50.2	1.0	14,616.	.9238	287.	.90	1.0
(Case A)	1.5	20,277.	.8511	417.	.86	.98
	2.0	22,311.	.9165	466.	.85	1.08
	.5	11,529.	.8809	221.	.92	.95
50.2	1.0	16,415.	.8567	327.	.89	.96
(Case B)	1.5	19,995.	.8213	410.	.86	.94
	2.0	23,174.	.8030	488.	.84	.94
	.5	11,782.	.8895	227.	.92	.96
50.2	1.0	16,458.	.8630	328.	.89	.96
(Case C)	1.5	20,753.	.8031	428.	.86	.93
	2.0	24,240.	.7567	514.	.83	.90
	.5	3,847.	.7018	69.9	.97	.72
76.4	1.0	4,930.	.7627	90.3	.96	.78
(Case D)	1.5	5,893.	.8223	109.	.96	.85
	2.0	6,772.	.8105	126.	.95	.84
	.5	4,241.	.6450	77.3	.97	.66
76.4	1.0	5,403.	.7226	99.3	.96	.74
(Case E)	1.5	6,095.	.7842	113.	.95	.81
	2.0	6,834.	.8146	127.	.95	.85
	.5	1,947.	.6172	34.9	.98	.62
99.4	1.0	2,436.	.6118	43.8	.98	.62
(Case F)	1.5	2,884.	.6240	52.0	.98	.63
	2.0	3,064.	.6495	55.4	.97	.66

These displacements were used to calculate the strain energy in each of the elements. Equation (8) defines the strain transformations, SE, with the fourth degree of freedom grounded, used in these calculations. If each strain energy term is written:

$$(SE)_i = \lfloor X \rfloor \{\psi_i\} K_i \lfloor \psi_i \rfloor \{X\} (F_i/\Delta)^2 \qquad (19)$$

the desired strain energy ratios can be expressed in terms of appropriate sums of these terms. Note that $(F_i/\Delta)^2$ constant cancels out. These ratios also are included in Table 2.

To compare the hysteresis test determined values of G_y and η_y with the general 3MY-4205 viscoelastic characteristics, data in Table 2 were plotted on Figure 8. The hysteresis derived shear modulus and loss factor data are connected by solid lines to distinguish them from the generic data scatter.

CONCLUSIONS

1. Agreement of hysteresis test derived 3MY-4205 viscoelastic material characteristics with prior test results verifies the results reported herein.

2. Use of stiff links in series with viscoelastic material produces a damper mechanism whose loss factor is a large fraction of the viscoelastic material loss factor.

3. Generic viscoelastic material characteristics, in the form shown in Figure 8, are invaluable for use in preliminary design of a viscoelastic damping treatment. However, because of the scatter of data and the difficulty of accurate reading of data from viscoelastic material characteristics temperature-frequency plots, final prediction of system level frequency and loss factor should reflect component test results of the final damping treatment.

THE EFFECTS OF BOND IMPERFECTIONS ON THE STRENGTH AND DYNAMIC RESPONSE OF LAMINATED BEAMS

P.G. Reinhall and R.N. Miles
Department of Mechanical Engineering
University of Washington
Seattle, Washington 98195

Abstract

Constrained layer dampers have been applied to a wide variety of vibrating structures in order to reduce resonant vibration. Even though substantial vibration reduction is achieved by the application of constrained layer dampers, there is often a concern that the bonding adhesive will fail and that the structure will delaminate due to high vibration levels. The situation is aggravated by the fact that defects or gaps are always present in the adhesive layer. These defects lead to stress concentrations which may enhance the tendency for the structure to delaminate. While a very large number of analytical studies have considered the optimum design for damping performance, very little is known about the durability of a given design. The main purpose of this paper is to present an accurate and practical scheme for predicting the strength of a constrained layer damper.

Approximate solutions based on the Ritz method are obtained for the maximum stresses in the adhesive layer of a vibrating laminated beam. Results are presented for both the damping performance and the maximum stresses when parts of the adhesive have been removed to simulate defects in the bond. A correction to the approximate stresses due to the effect of stress concentrations around the defects is then determined in order to facilitate a direct comparison with the measured strength of the adhesive as determined by a standard shear lap test. A detailed finite element analysis is carried out to examine the stress fields of the adhesives in both the laminated beam and the shear lap test specimen. This analysis indicates that the approximate method will yield accurate results.

1. Introduction

The concept of reducing the amplitude of vibration of a structure by bonding a stiff thin member to the structure with soft viscoelastic material has been used in a wide range of applications during the last decades. Considerable attention has been given in the recent literature [1-12] to the damping characteristics of a range of different contrained layer damping configurations. Traditionally, these configurations have nearly always been constructed such that damping will occur mostly through shear strain in the viscoelastic layer. This will be the case if the two layers, the primary structure and the constraining layer, do not deflect relative to each other, therebye preventing any deformation of the adhesive in the thickness direction. It has been shown by the authors [13], however, that a design which incorporates the thickness deformation of the adhesive can be more effective in increasing the loss factor of a structure. The thickness deformation also becomes more important as the excitation frequencies are increased and should therefore also be considered in configurations designed with only shear in mind.

In this paper we consider how defects in the adhesive layer affect the performance and the strength of the constrained layer damping treatment applied to a simply supported beam. Both shear and thickness deformations of the adhesive are accounted for. The inclusion of the thickness deformation is especially important close to the defect since the constraining layer is not bonded to the primary beam along the defect. Numerical solutions for the natural frequencies, loss factors, and forced response are obtained by the use of the Ritz method for a range of defect sizes located both at the middle and at the end of the beam. It is assumed that there is perfect bonding between all layers except along the defect where the adhesive has been removed. All deformations are assumed to be small so that nonlinear effects can be neglected. It is also assumed that the effect of stress concentrations due to defect geometries on the dynamical response can be neglected. A finite element analysis of the adhesive stresses is presented in support of this assumption.

In contrast to the dynamical response, the strength of the laminated beam is severely affected by the stress singularities in the adhesive layer. For a design engineer, it is probably as important to know that the chosen treatment will remain bonded to the structure as it is to know that he has chosen the highest performing damping treatment. While the optimization of the performance of constrained layer dampers has been given considerable attention, few analytical studies have considered the structural strength of these damping treatments. It is desirable to know how we can relate the traditional adhesive testing methods to the case of dynamic delamination of laminated structures. Most adhesive testing is done statically (or quasi-statically in the case of fatigue testing) by the use

of a simple shear lap testing technique. Using the Ritz solution as the far field solution in conjunction with a finite element analysis, we compare the dynamically induced stress singularities in the adhesive layer with the stress field in a static shear lap test specimen. Criteria are then developed to relate shear lap test data to the case of vibrating laminated structures.

2. Damping Effectivness

Consider a simple supported beam with a bonded free-free constraining layer as shown in Figure 1. The equations of motion and the boundary conditions are obtained by the use of Hamilton's Principle.

The strain and kinetic energies can be written, respectively:

$$V=\frac{1}{2}\int_0^l \Big\{ E_1 I_1\Big(\frac{\partial^2 w_1}{\partial x^2}\Big)^2 + E_3 I_3\Big(\frac{\partial^2 w_3}{\partial x^2}\Big)^2 + E_1 A_1\Big(\frac{\partial u_1}{\partial x}\Big)^2 + E_3 I_3\Big(\frac{\partial u_3}{\partial x}\Big)^2 + \frac{1}{2} G_2 b_2 H_2\Big[\gamma_1\gamma_2 + \Big(\frac{\gamma_2+\gamma_1}{3}\Big)^2\Big] + E_2\frac{1-\nu}{1-\nu-2\nu^2} A_2\Big(\frac{w_3-w_1}{H_2}\Big)^2\Big\} dx \qquad (1)$$

$$T=\frac{1}{2}\int_0^l \Big\{\Big(\rho_1 A_1 + \frac{\rho_2 A_2}{2}\Big)\Big[\Big(\frac{\partial w_1}{\partial t}\Big)^2 + \Big(\frac{\partial u_1}{\partial t}\Big)^2\Big] + \Big(\rho_3 A_3 + \frac{\rho_2 A_2}{2}\Big)\Big[\Big(\frac{\partial w_3}{\partial t}\Big)^2 + \Big(\frac{\partial u_3}{\partial t}\Big)^2\Big]\Big\} dx$$

where

$$\gamma_1=\frac{\partial w_1}{\partial x}\Big(1+\frac{H_1}{2H_2}\Big)+\frac{\partial w_3}{\partial x}\frac{H_3}{2H_2}+\frac{u_1-u_3}{H_2}, \quad \gamma_2=\frac{\partial w_3}{\partial x}\Big(1+\frac{H_3}{2H_2}\Big)+\frac{\partial w_1}{\partial x}\frac{H_1}{2H_2}+\frac{u_1-u_3}{H_2}$$

and where the integration is over the beam length l. The subscripts correspond to the different layers, 1 being the primary beam, 2 the adhesive layer, and 3 the constraining layer. E_i, I_i, A_i and ρ_i are the Young's Modulus, the bending moment of inertia, the cross-sectional area, and the density of the i^{th} layer, respectively. w_1 and w_3 are the transverse displacements of the primary beam and the constraining layer. u_1 and u_3 are the longitudinal displacements of the layers. H_i is the nominal thickness of the i^{th} layer. Both the adhesive shear modulus, $G_2(x)$, and $E_2(x)$ are set equal to zero along the defect. We now proceed by substituting the kinetic and potential energy expressions into Hamilton's principle and assuming harmonic time dependence of the form $e^{i\omega t}$. w_1 and w_3 are expanded in the eigenfunctions of a simple Euler-Bernoulli beam and u_1 and u_3 are expanded in the eigenfunctions for longitudinal vibration in a uniform rod. This leads to a standard eigenvalue problem,

$$K A = \omega^2 M A \qquad (2)$$

where K and M are the stiffness and mass matrices, respectively. The evaluation of these matrices is outlined in [13]. The solution of this eigenvalue problem yields the natural frequencies, ω , and the normal modes of the structure in terms of an expansion of the chosen shape functions. The coefficients of this expansion make up vector A. The steady state forced response of the structure subjected to a sinusoidal point load can now be obtained as a linear combination of the normal modes (see [14]).

The effect of defects in the adhesive on the response is indicated in Figure 2. The magnitude of response to a 1 lbf point load at the center of the beam is here shown as a function of excitation frequency close to the first mode of the structure. In this case, we see a decrease of the damping and the frequency of the first mode as the defect is introduced in the adhesive layer. It can also be seen that the damping performance is sensitive to the location of the defect. The decrease of the loss factor is more severe if the gap is in the middle of the beam rather than at the end.

Figure 3 shows the loss factor versus the shear parameter, g , for adhesive defects of various sizes, at the center of the beam. The parameter g depends on the geometry and the material properties of the beam.

$$g = \frac{G_2}{H_2}\left(\frac{1}{E_1 H_1} + \frac{1}{E_3 H_3}\right) \qquad (3)$$

It can be seen in Figure 3 that the loss factor is sensitive to the size of the defect. The beam, with an optimal choice of adhesive, experiences a 80% decrease in the loss factor when the defect length is increased from 1 to 5 inches.

If the defect occurs at the end of the beam, a much smaller decrease in the loss factor occurs as indicated in Figure 4. In this case the loss factor is almost independent of the gap length.

3. Approximate Solutions for Adhesive Stress in a Vibrating Beam

In order to study the strength of a laminated beam we need to consider the stress state in the adhesive. The shear stress and the normal stress in the thickness direction are given by

$$\tau_{xy} = G\left\{\frac{1}{2}\left[\frac{\partial w_1}{\partial x}\left(1+\frac{H_1}{H_2}\right)+\frac{\partial w_3}{\partial x}\left(1+\frac{H_3}{H_2}\right)\right]+\frac{u_1-u_3}{H_2}\right. \qquad (4)$$

$$\sigma_y = \frac{E(1-\nu)}{1-\nu-2\nu^2}\,\frac{w_2-w_1}{H_2}$$

It should be noted that these equations are not valid in the region close to a defect due to stress concentrations created by the chosen defect geometry. We will show in the next section, however, that these stress concentrations decay rapidly with distance, making equation (4) valid along most of the length of the adhesive. The stresses given by this equation will be referred to in the following as the far field stresses.

Figures 5 and 6 show the normal and shear stresses close to the defect as a function of the shear pararameter g for different gap sizes when the structure oscillates in its first mode. It is seen that both stresses are directly proportional to the the defect length . Hence, the strength of the structure is significantly decreased by an increase of the defect size. This is in sharp contrast to the static case where the strength of the adhesive joint has been found to be proportional to the adhesive thickness, not the defect size [15]. The far field stresses in Figures 5 and 6 will be used in the next section in order to obtain an estimate of the magnitudes of the stress concentrations at the end of a defect.

The stresses next to a defect (again ignoring stress concentration affects) located at the end of the beam are shown in Figures 7 and 8. The shear stress is no longer sensitive to the gap length. The shear and normal stress in the adhesive layer are plotted in Figures 9 and 10. Both stresses grow significantly as the defect is approached. It should also be noted that the far field stresses at the free ends are significant since the constraining layer is free and the primary beam is simply supported resulting in a considerable thickness deformation in the adhesive. Similarly, the stresses for the case where the defect is at the end of the beam are shown in Figures 11 and 12.

4. Predictions of Strength Using Lap Test Results.

To determine the strength of laminated structures adhesive strength data is needed. The ultimate strength of a specific adhesive is usually estimated using a static lap joint test (as depicted in Figure 13). The lap test creates mainly shear strain in the adhesive while we know from the above discussion that both shear and normal stresses are present in the adhesive of a vibrating beam. Care must therefore bee taken in applying the results of a lap test during the determination of the strength of a vibrating beam. Since the failure of the

adhesive is due to stress concentrations in both the static lap test [16] and the vibrating beam, we need to make a detailed comparison of the stress fields between the two systems. In this section the stress concentrations are analyzed using a finite element technique. A scheme is then presented which enables the use of lap test data in the determination of the strength of a laminated beam. The method depends only on estimates of the far field stresses which may easily be obtained experimentally in the case of the lap test and by the Ritz method and equation (4) in the case of the beam.

4.1 Approximate Stresses Neglecting Singularities

If the effects of the stress concentrations are neglected at the ends of the adhesive it is not difficult to determine the normal and shear stresses in both the lap test specimen and the vibrating beam. In the lap test the ultimate shear stress of the adhesive is simply taken to be

$$\tau_{Av} = \frac{F}{A} \qquad (\ )$$

where F is the measured applied force and A is the area of the bonded surface. The stresses away from the discontinuities (the far field stresses) in the vibrating beam may be predicted using the Ritz method as described in sections 2 and 3.

4.2 Detailed Stress Fields by Ritz/Finite Element Model

To obtain a detailed description of the stresses near a defect in the adhesive layer of the laminated beam a hybrid Ritz/Finite element method was used. The maximum far field stress state at the end of the defect, over one cycle of vibration, was determined using the Ritz solution as described in Section 3. This result was then used to obtain boundary conditions for a static finite element model of the region near the end of the adhesive. A small region, close to the discontinuity, can in this manner be analyzed in detail with a very fine finite element mesh while the overall response is efficiently accounted for by the Ritz method.

An alternative to this approach would be to model the entire beam using the finite element method. Unfortunately, in order to obtain sufficient resolution in the region close to the singularity it is necessary to have a large number of elements across the adhesive thickness. Since the aspect ratio of each element needs to be within acceptable limits, the number of degrees of freedom required to accurately model the complete structure would become very large. The use of the Ritz method to account for the global response produces a more efficient formulation since it allows us to model only a small part of the adhesive (see Figure 14).

Results of this analysis, given in Figure 15 show the normalized shear stress as a function of distance from the edge of the defect. τ_0 is the far field shear stress, i.e. the shear stress at the end of the mesh as given by the Ritz method. It can be seen that the shear stress rapidly decays toward τ_0 as the distance from the defect is increased. In fact, the stress intensity due to the defect can be seen to be neglible at a distance equal to one adhesive thickness away from the defect. The stress intensity factor, τ_{xy}/τ_0, ranges from 0.6 to 2.0 for the five cases considered. The normal stress intensity factors are more severe as shown in Figure 16 where σ_3/σ_1 is plotted versus the distance from the defect. σ_3 is the normal stess in the thickness direction and σ_1 is the largest principle stress. The magnitude of the normal stress intensity grows to values significantly larger than the shear stress intensity factors. It is worth noting that the spatial region where the intensified normal stress has any influence is small due to its fast decay. This supports the assumption that the increased stress level around the defects does not influence the global dynamic behavior of the structure.

To obtain a detailed description of the stress field in a lap joint specimen a finite element model was constructed where two horizontal surfaces were displaced relative to each other in the horizontal direction. An adhesive connecting these two surfaces was modeled using solid elements with a fine mesh.

A comparison between the predicted maximum shear stresses (the difference between the maximum and the minimum principal stresses) in the lap test specimen and in the beam are given in Figure 17. The maximum shear stress is plotted as a function of distance from the end of the adhesive. It should be emphasized that both thickness and shear deformations are present in the "far field region" of the adhesive layer in the vibrating laminated beam. As discussed in Section 2, thickness deformations, and hence, normal stresses are more pronounced as the defect size increases. In the case of the lap joint specimen, however, the predominant adhesive deformation mode in the far field is shear.

It would be very helpful if an approximate procedure could be constructed where the true maximum shear stress at the end of the adhesive in a vibrating beam could be compared to that obtained in a lap test specimen without resorting to a detailed finite element analysis as performed here. These two configruations cannot be directly compared due to the significant difference in their far field stress state. However, the configurations may be indirectly compared to each other by first calculating the maximum far field shear stresses, $\tau_{\max}$, from equations (4) and (5). In the case of the shear lap test specimen this maximum shear stress is simply equal to τ_{AV} given by equation (5). For the beam it is equal to half the difference between the maximum and the minimum far field principle stresses which are easily obtained from equation (4) and the Ritz method.

By using this approach the maximum far field shear stress in the adhesive layer of the laminated beam can be directly related to the average shear stress, τ_{Av}, which can be measured during a static shear lap test. The results of our detailed finite element analysis given in Figure 17 show that approximately the same maximum stresses for both cases are obtained if we put τ_{Av} equal to τ_i of the beam due to similar growth of the shear stresses at the end of the adhesive. Hence, this approach allows the use of static lap test data in the prediction of the maximum acceptable excitation levels during the design of constrained layer damping treatments if τ_{Av} is set equal to τ_i .

Conclusions and Summary

A mathematical model of a laminated beam with defects in the bonding adhesive has been presented. The model allows for thickness as well as shear deformation of the adhesive. It was shown that defects have a significant effect on the loss factor of a constrained layer damper. The natural frequecies of the beam are decreased with introduction of adhesive defects. It was also shown that the location of a defect along the beam significantly affects the loss factor . The change of the dynamical behavior of the beam due to defects has mainly three implications. First, in the context of constrained layer damping, it points out the importance of correct and careful applications of the adhesive and the constraining layer. Secondly, the location of the treatment on the strucure becomes critical when the bonding of a constraining layer on the whole structure is not possible (due to weight considerations, for example). This is indicated indirectly in this paper in that the change of the dynamical behavior is sensitive to the defect location. The problem of optimal damping placement is an important one and should be given more attention in future designs as weight considerations become more important. Thirdly, the sensitivity of the modal parameters on the existence of defects in the adhesive could possibly be used in on-line detection of defects in laminated structures. Research in this area is underway and will be the subject of a future paper.

Defects are always present in the adhesive layer of constrained layer damped structures. The stresses are intensified around each defect resulting in significantly larger maximum stress levels than for the case of a continuous adhesive without defects. In order to obtain an estimate of the stress levels around the defects a hybrid Ritz/Finite element method was employed. It was concluded that the stress intensification only become significant within a distance from the edge of the defect approximately equal to the thickness of the adhesive layer. It was also shown that these stress singularities are very similar in intensity and spatial variation to the singularities occuring at both ends of the adhesive in a simple shear lap test specimen. This will potentially enable us to

use the already existing adhesive data, which have been obtained by static shear lap testing, in the design of laminated structures undergoing vibratory motion.

References

1) Douglas, B.E. and Yang, J.C.S., "Transverse Compressional Damping in the Vibratory Response of Elastic-Viscoelastic Beams", AIAA Journal, Vol.16, No.9, 1978, pp. 925-930.

2) Saito, H. and Tani, H., "Vibration of Bonded Beams with a Single Lap Adhesive Joint", Journal of Sound and Vibration, Vol.92, No. 2, 1984, pp. 229-309.

3) Swallow, W., "An Improved Method of Damping Panel Vibrations", British Patent Specification 513, 171, 1939.

4) Ross, D., Ungar, E. and Kerwin, E.M., "Damping of Plate Flexural Vibrations by Means of Viscoelastic Laminae", Struuctural Damping, ASME, New York.

5) Whittier, J.S., "The Effect of Configurational Additions Using Viscoelastic Interfaces on the Damping of a Cantilevered Beam", WADC Technical Report 58-568, May 1959, Wright Air Development Center.

6) DiTaranto, R.A., "Theory of the Vibratory Bending for Elastic and Viscoelastic Finite Length Beams" , ASME Journal of Applied Mechanics, Vol. 32, 1965.

7) Mead, D.J. and Markus, S., "The Forced Vibration of a Three-Layer, Damped Sandwich Beam With Arbitrary Boundary Conditions", Vol.10(2), 1969, pp. 163-175.

8) Yan, M.J. and Dowell, E.H., "Governing Equations for Vibrating Constrained Layer Damping of Sandwich Beams and Plates", ASME Journal of Applied Mechanics, Vol.94, 1972, pp.1041-1047.

9) Mead, D.J., "A Comparison of Some Equations for the Flexural of Vibration of Damped Sandwich Beams", Journal of Sound of Vibration, Vol. 83, No.3, 1982, pp. 363-377.

10) Johnson, C.D. and Kienholtz, D.A., "Finite Element Design of Viscoelasticaly Damped Structures - Methods", AFWAL-TR-84-3064, Vibration Damping Workshop, 1984.

11) Miles, R.N., United States Patent 4,425,980,"Beam Dampers for Damping the Vibrations of the Skin of Reinforced Structures", 1984.

12) Miles, R.N., "Beam Dampers for Skin Vibration and Noise Reduction in the 747", AFWAL-TR-84-3064, Vibration Damping Workshop 1984, Proceedings, Long Beach, Calif.

13) Miles, R.N. and Reinhall P.G., "An Analytical Model for the Vibration of Laminated Beams Including the Effects of Both Shear and Thickness Deformation in the Adhesive Layer", ASME Journal of Vibration, Acoustic, Stress, and Reliability in Design, Vol.108, No.1, 1986.

14) Meirovitch, L., "Analytical Methods in Vibrations", The Macmillan Company, New York

15) Knauss, W.G., "Fracture Mechanics and Time Dependent Strength of Adhesive Joints, "Journal of Composite Materials, Vol. 5, 1971, pp.176.

16) Botha, L.R., Jones, R.M., and Brinson H.F., "Viscoelastic Analysis of Adhesive Stresses in Bonded Joints", Report VPI-E-83-17, College of Engineering, Virginia Polytechnic Institute and State University, Virginia, 1983.

Figure 1 BEAM GEOMETRY

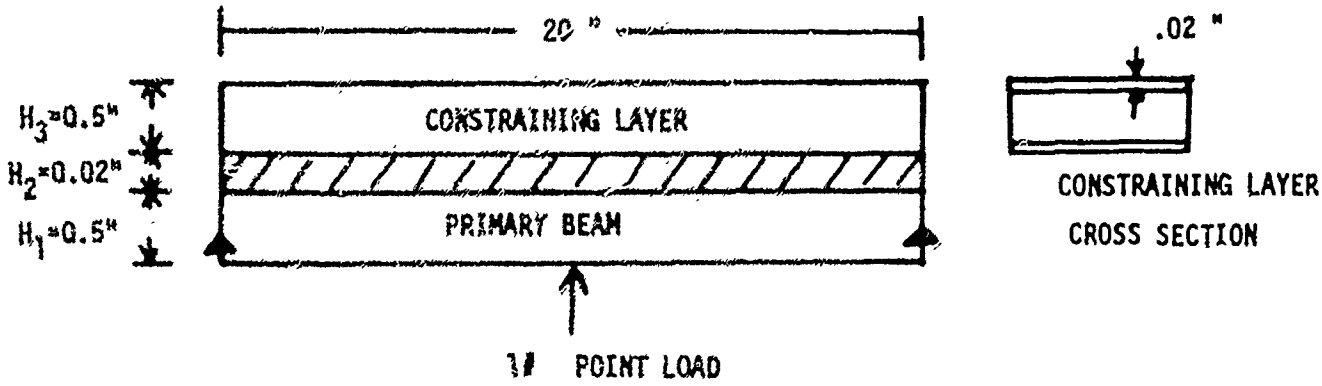


Figure 2 EFFECT OF ADHESIVE GAPS ON RESPONSE

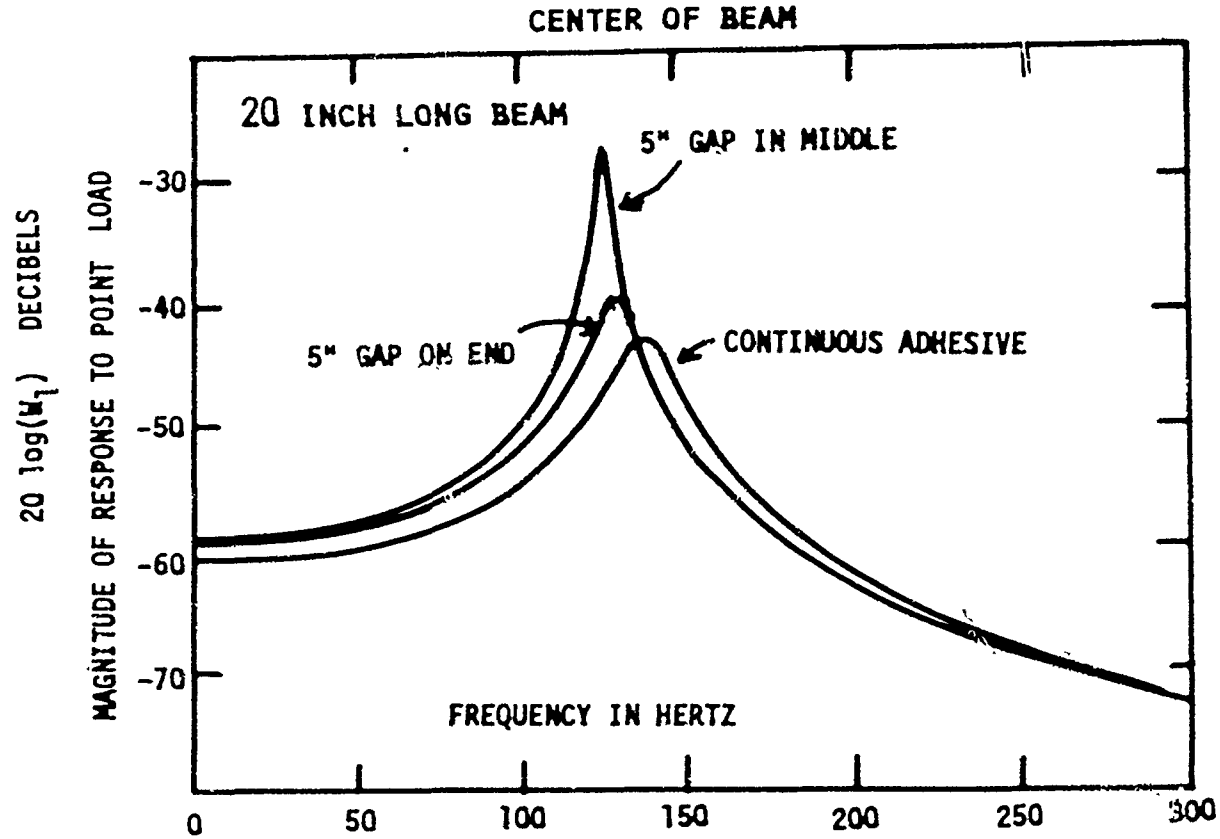


Figure 3 EFFECT OF GAP SIZE ON LOSS FACTOR

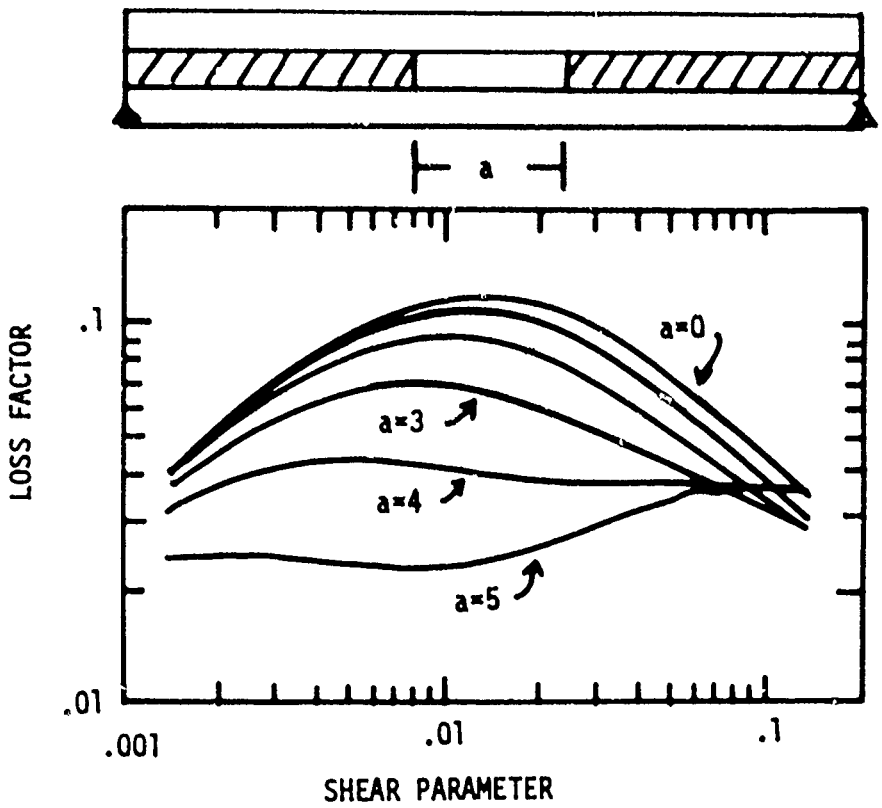
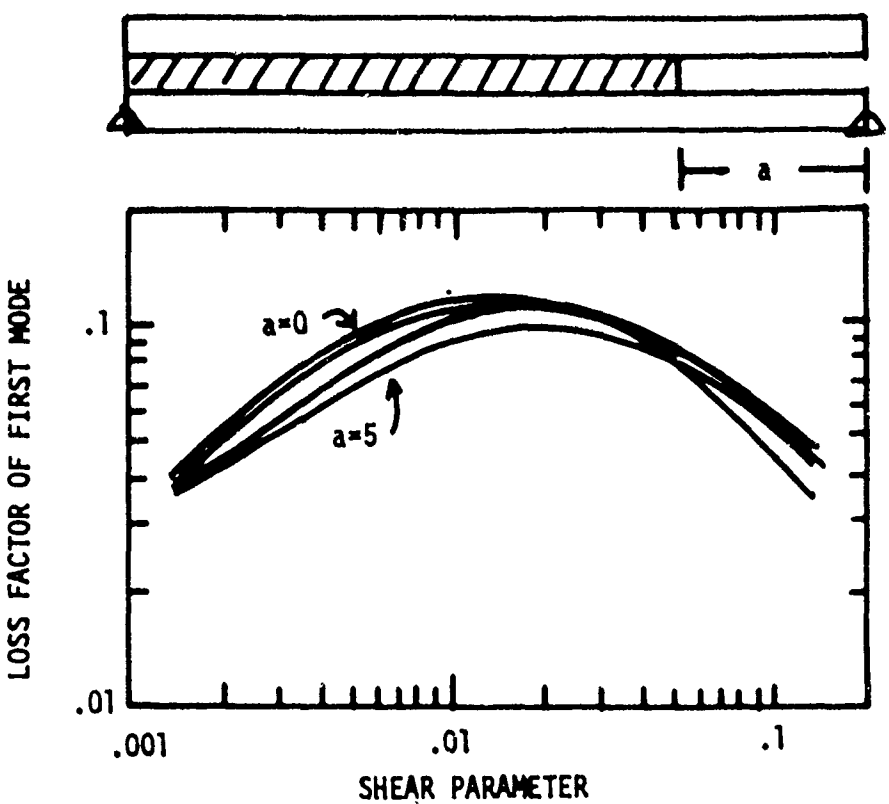


Figure 4 EFFECT OF GAP SIZE ON LOSS FACTOR



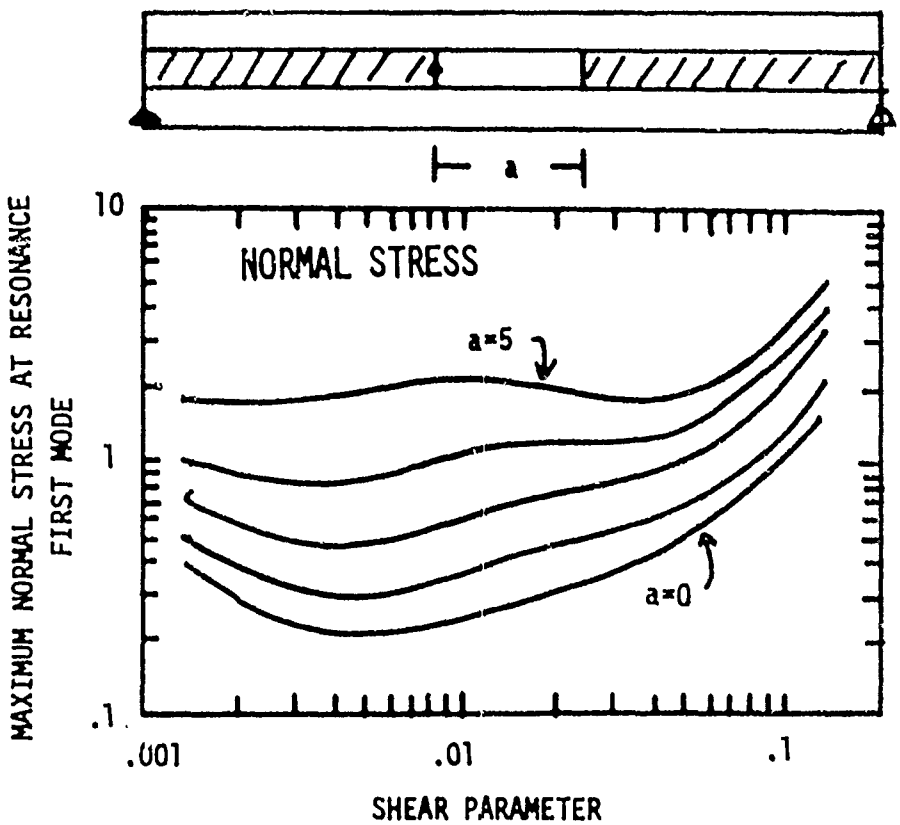

a
NORMAL STRESS
a=5
a=0
10
1
.1
.001
.01
.1
MAXIMUM NORMAL STRESS AT RESONANCE
FIRST MODE
SHEAR PARAMETER

Figure 5

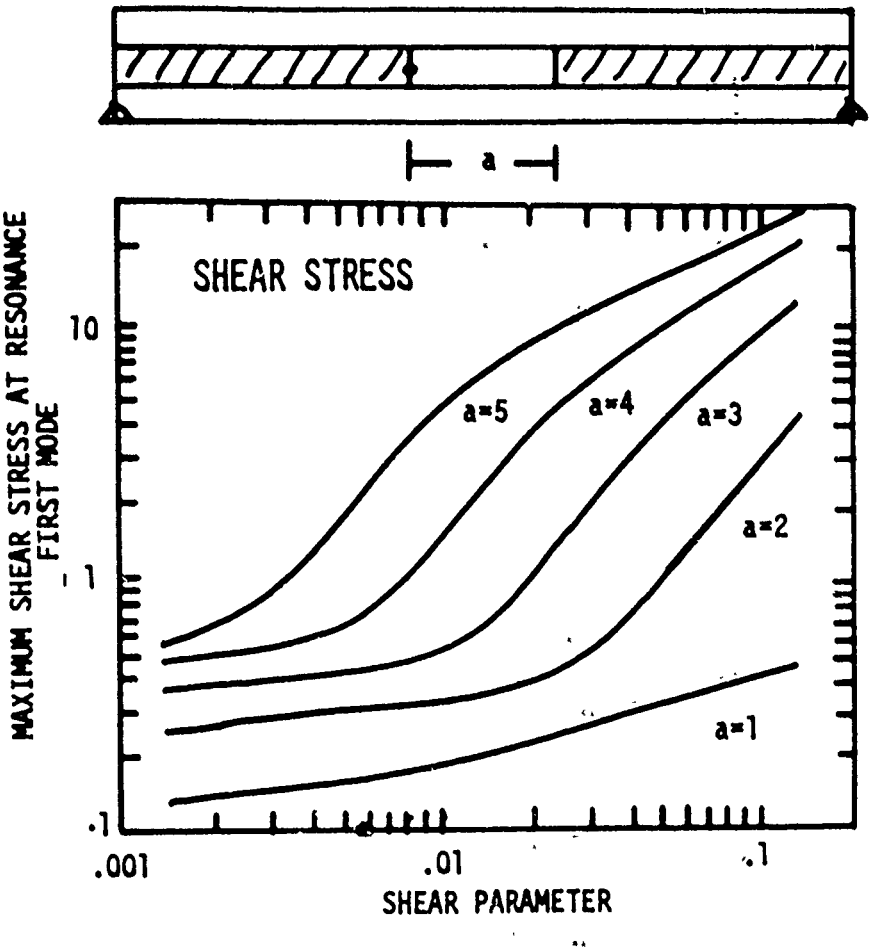

a
SHEAR STRESS
MAXIMUM SHEAR STRESS AT RESONANCE
FIRST MODE
10
1
.1
a=5
a=4
a=3
a=2
a=1
.001
.01
.1
SHEAR PARAMETER

Figure 6

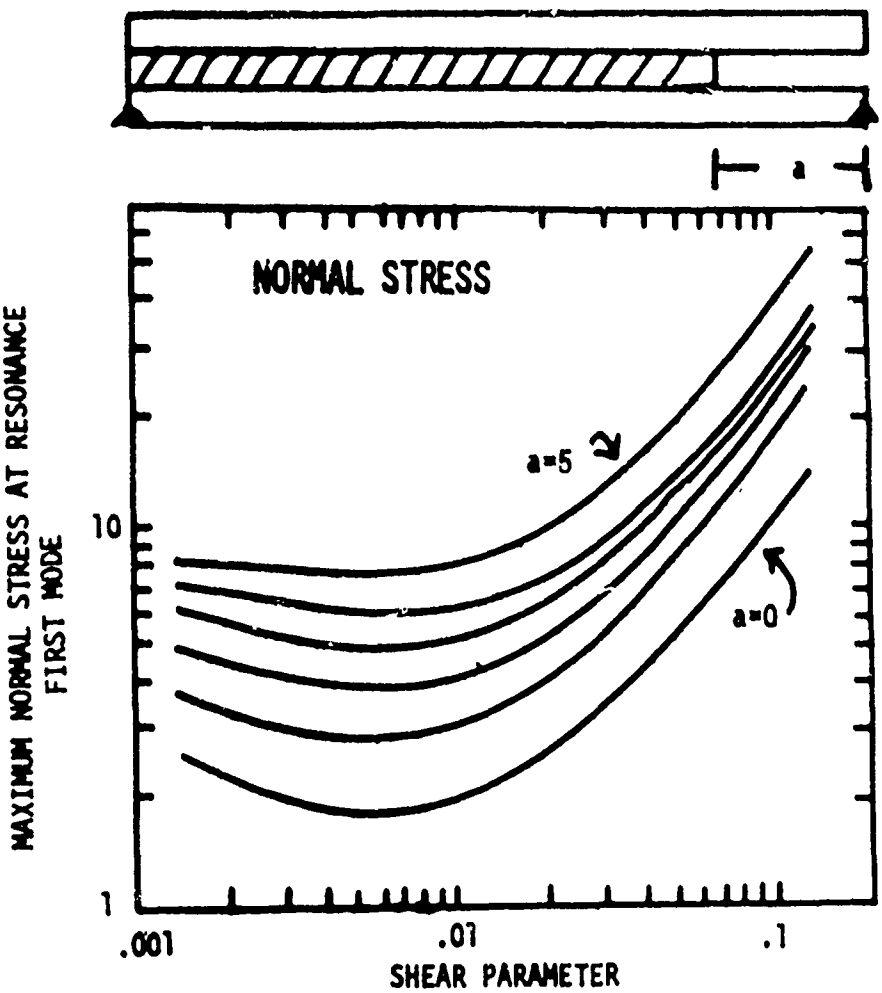

a
NORMAL STRESS
a=5
a=0
MAXIMUM NORMAL STRESS AT RESONANCE
FIRST MODE
10
1
.001
.01
.1
SHEAR PARAMETER

Figure 7

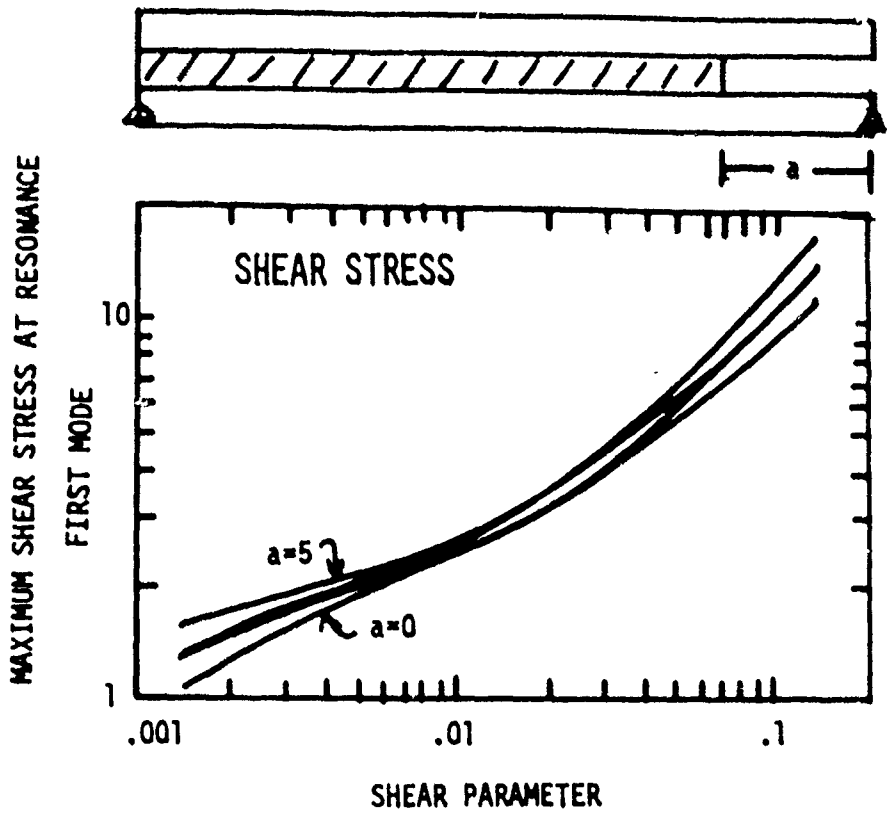
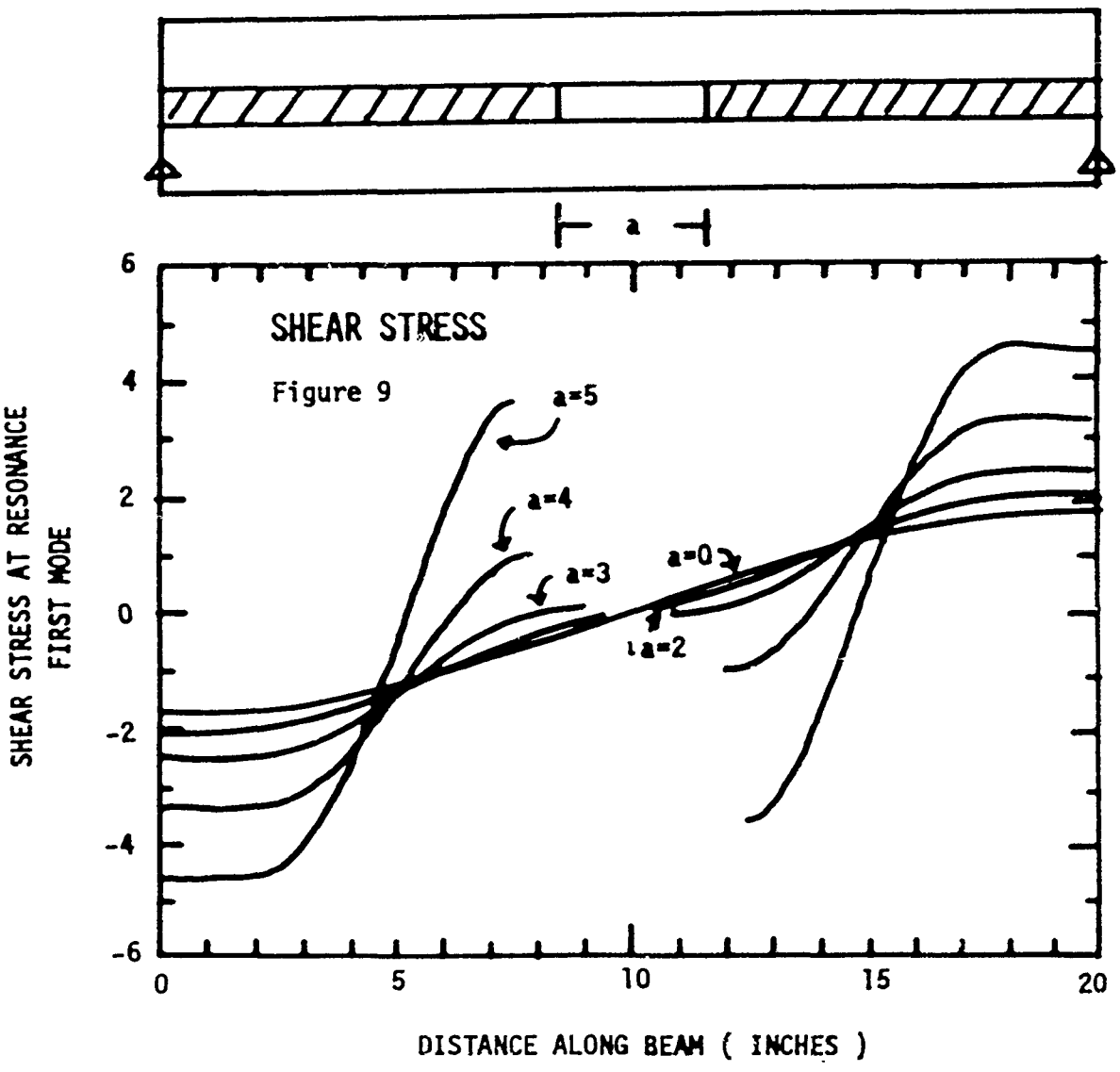
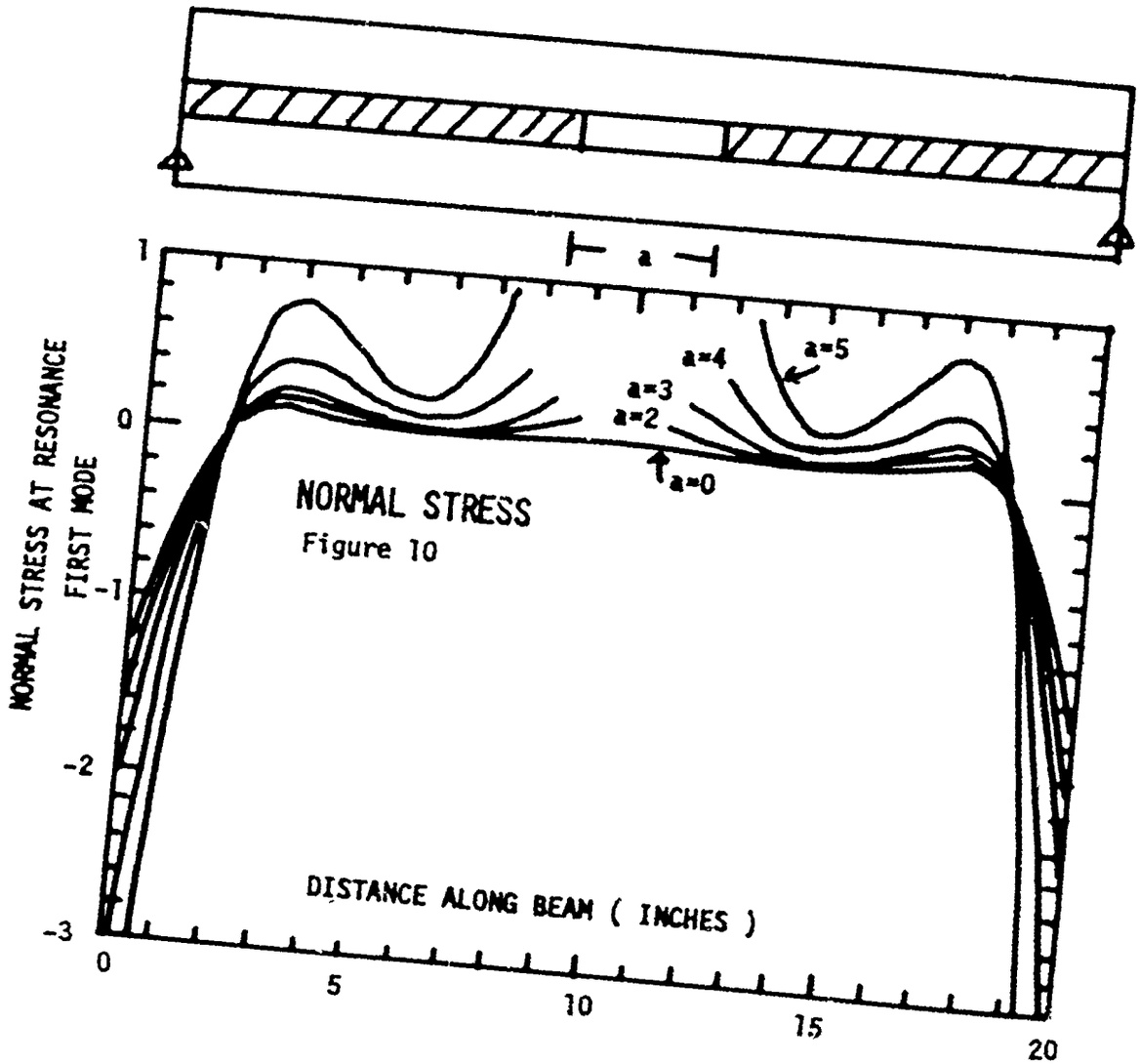

a
SHEAR STRESS
10
1
a=5
a=0
.001
.01
.1
MAXIMUM SHEAR STRESS AT RESONANCE
FIRST MODE
SHEAR PARAMETER

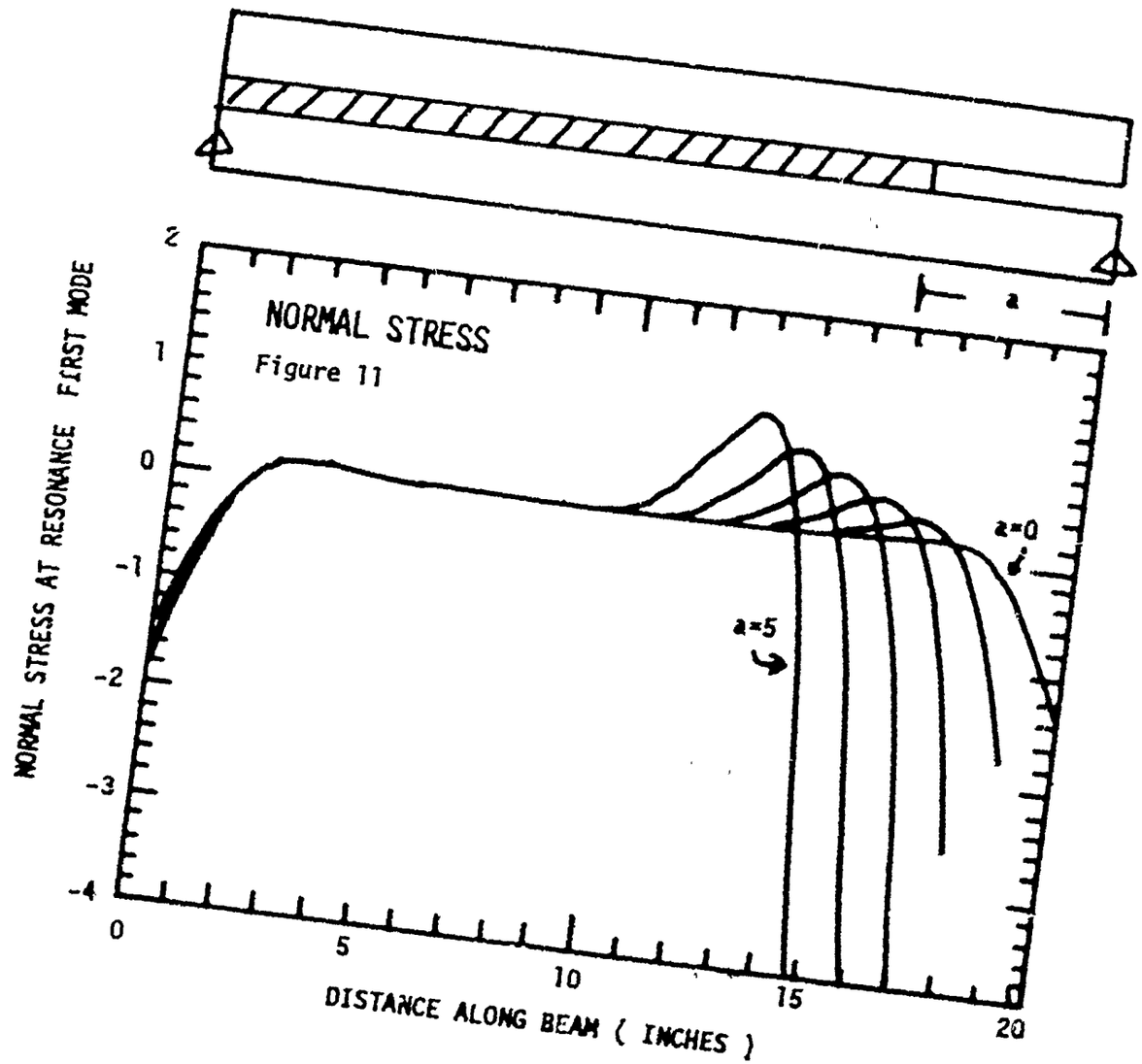
Figure 8

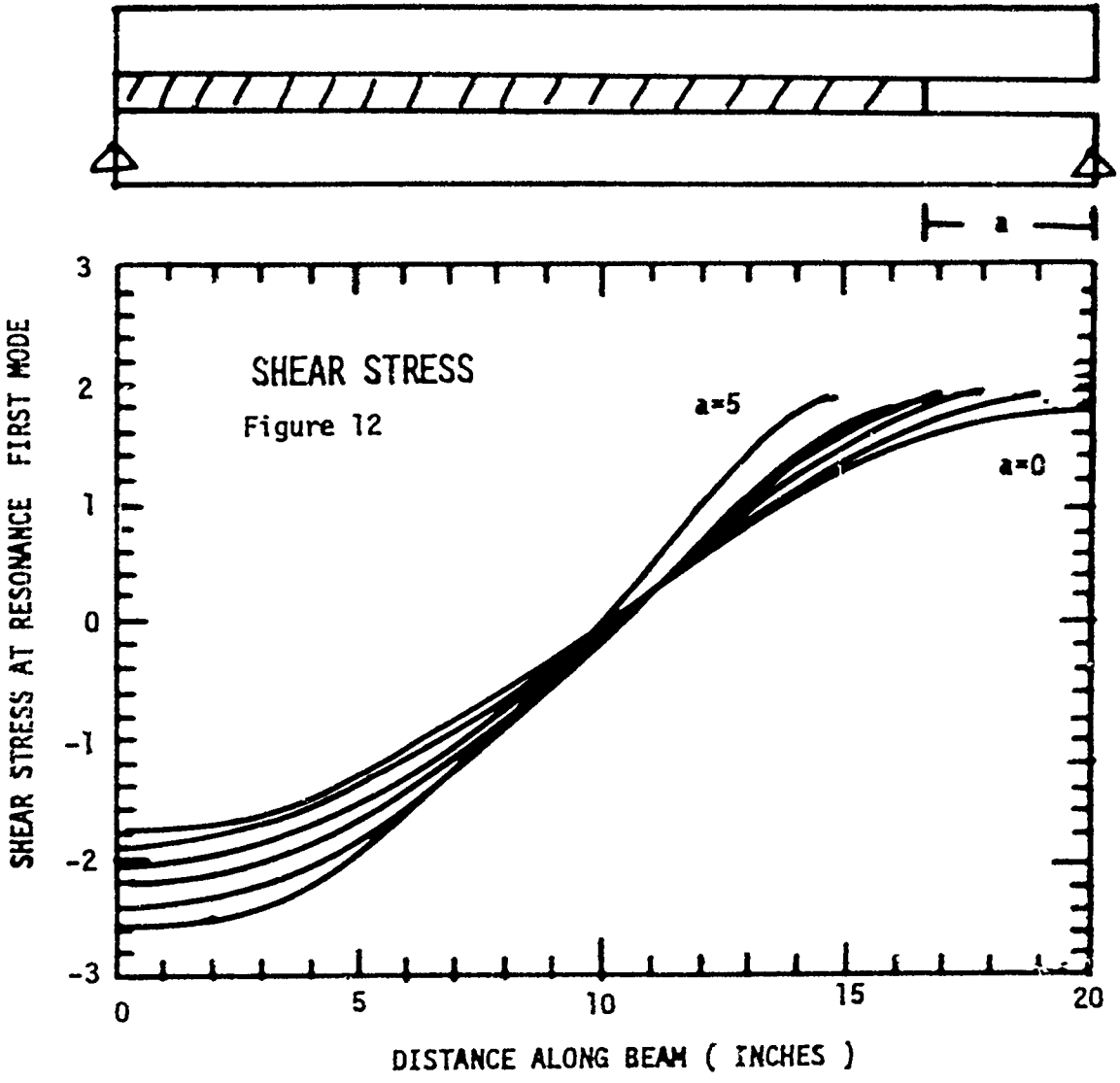

a
SHEAR STRESS
Figure 9
a=5
a=4
a=3
a=0
a=2
SHEAR STRESS AT RESONANCE
FIRST MODE
6
4
2
0
-2
-4
-6
0
5
10
15
20
DISTANCE ALONG BEAM (INCHES)



NORMAL STRESS

Figure 10


a
NORMAL STRESS
Figure 11
NORMAL STRESS AT RESONANCE FIRST MODE
2
1
0
-1
-2
-3
-4
0
5
10
15
20
DISTANCE ALONG BEAM (INCHES)
a=0
a=5


a
SHEAR STRESS
Figure 12
a=5
a=0
SHEAR STRESS AT RESONANCE FIRST MODE
3
2
1
0
-1
-2
-3
0
5
10
15
20
DISTANCE ALONG BEAM (INCHES)

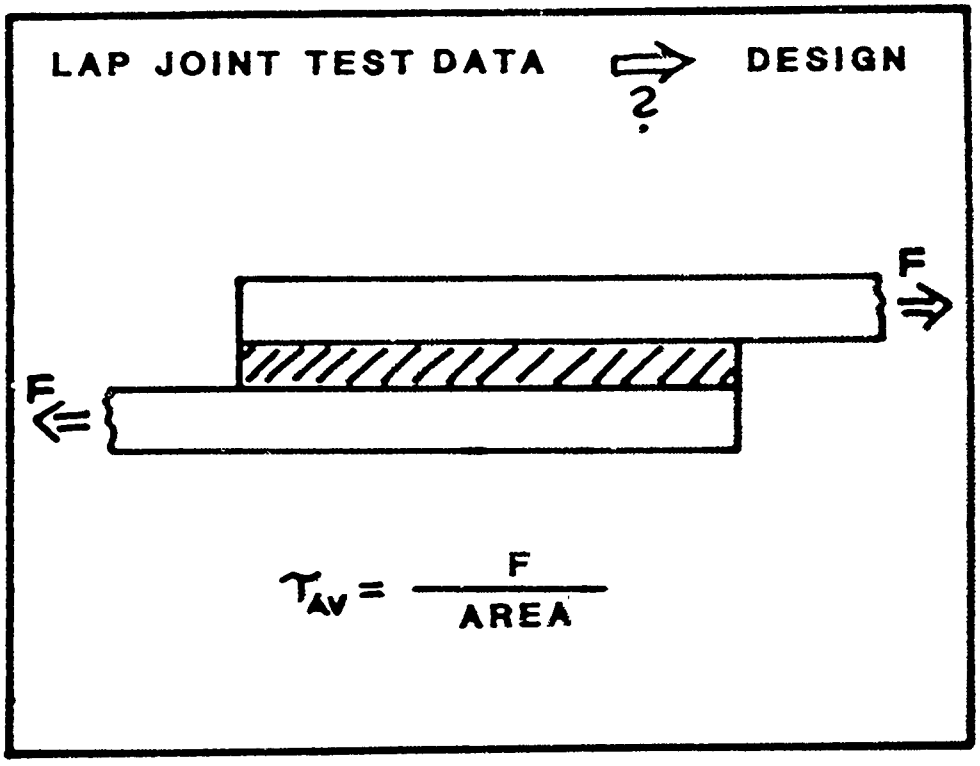


Figure 13

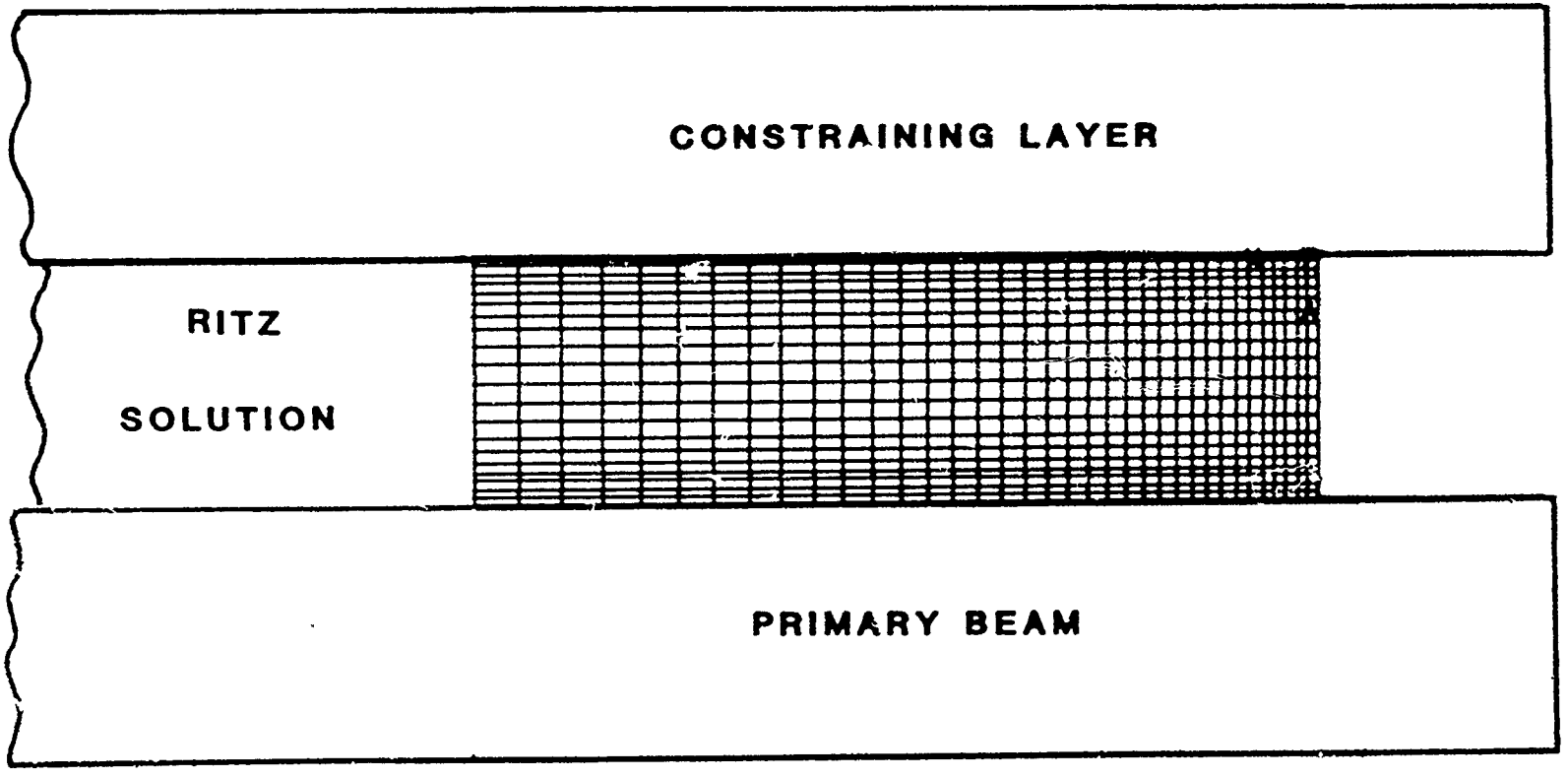


Figure 14

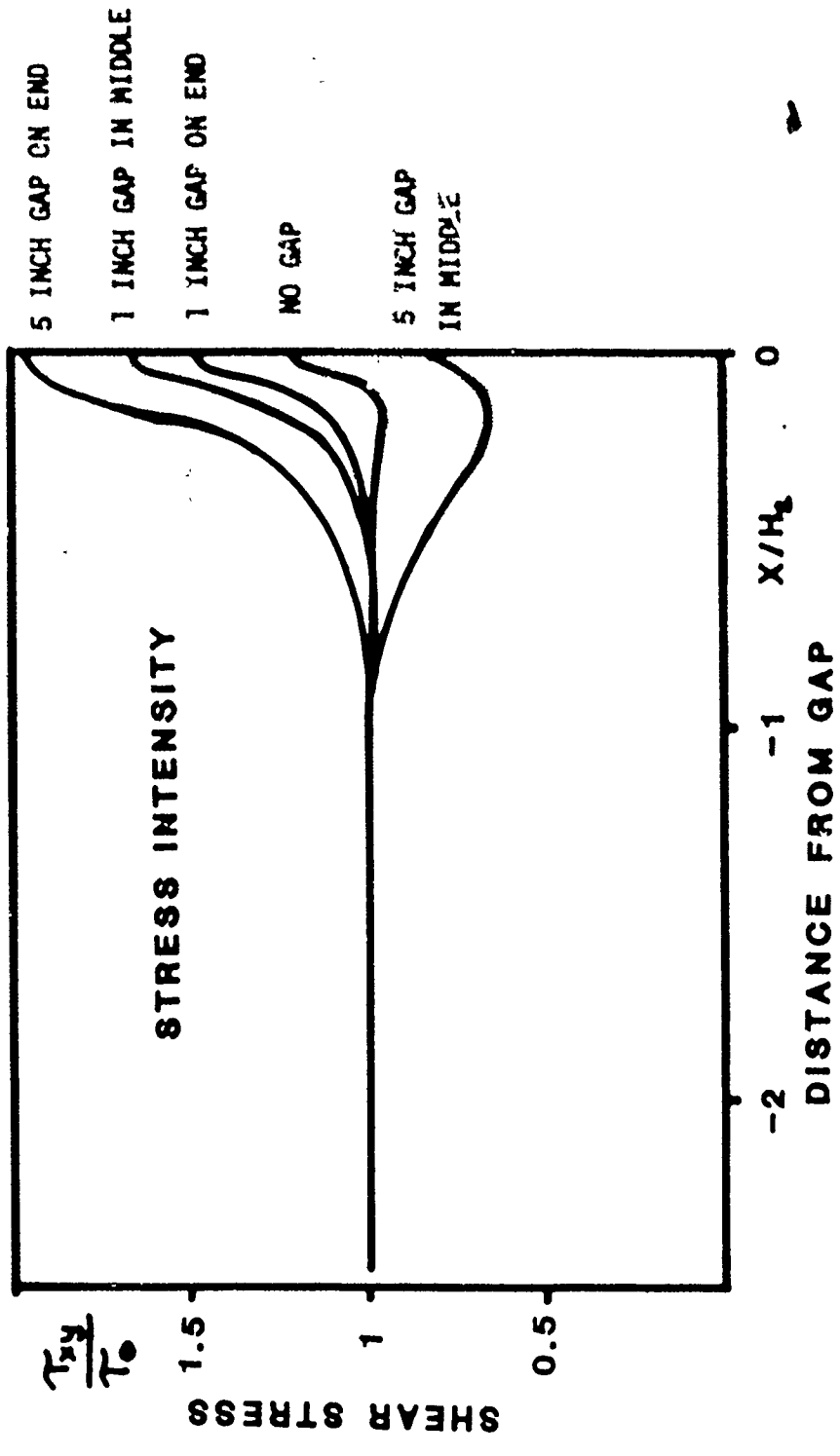

5 INCH GAP ON END
1 INCH GAP IN MIDDLE
1 INCH GAP ON END
NO GAP
5 INCH GAP IN MIDDLE
STRESS INTENSITY
SHEAR STRESS
$\frac{\tau_{xy}}{\tau_0}$
1.5
1
0.5
0
-1
-2
X/H_2
DISTANCE FROM GAP

Figure 15

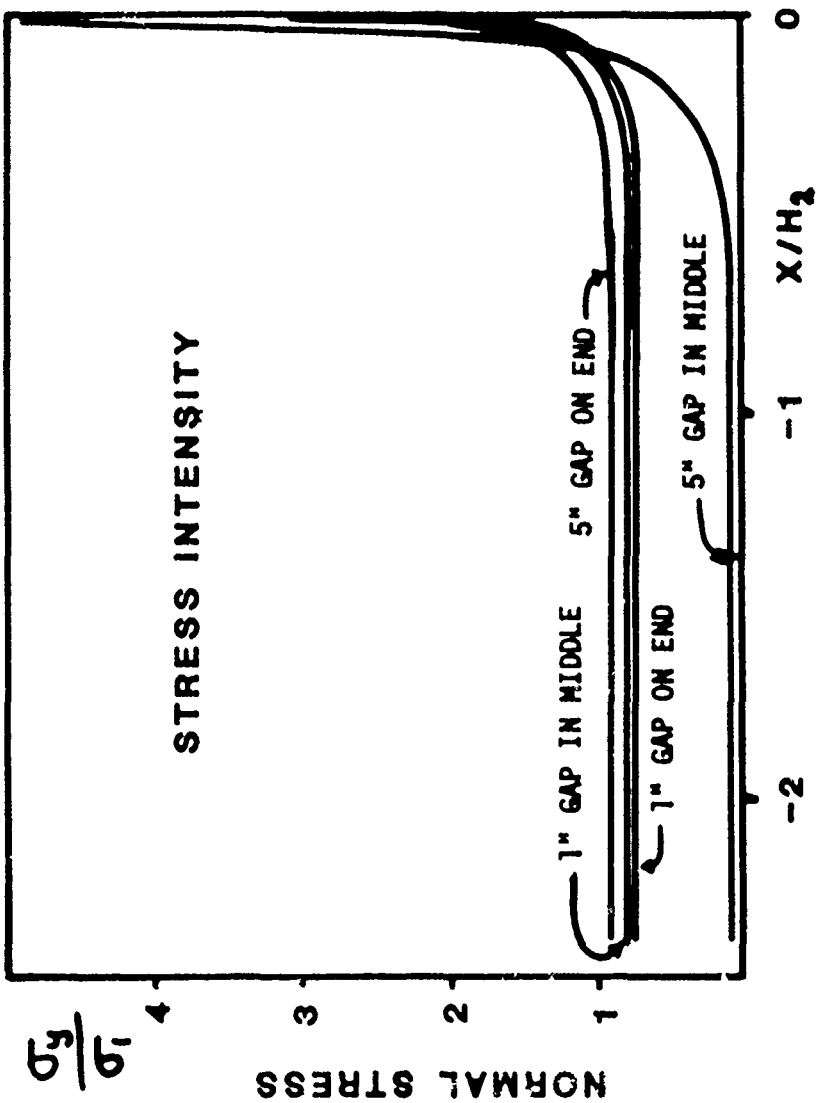
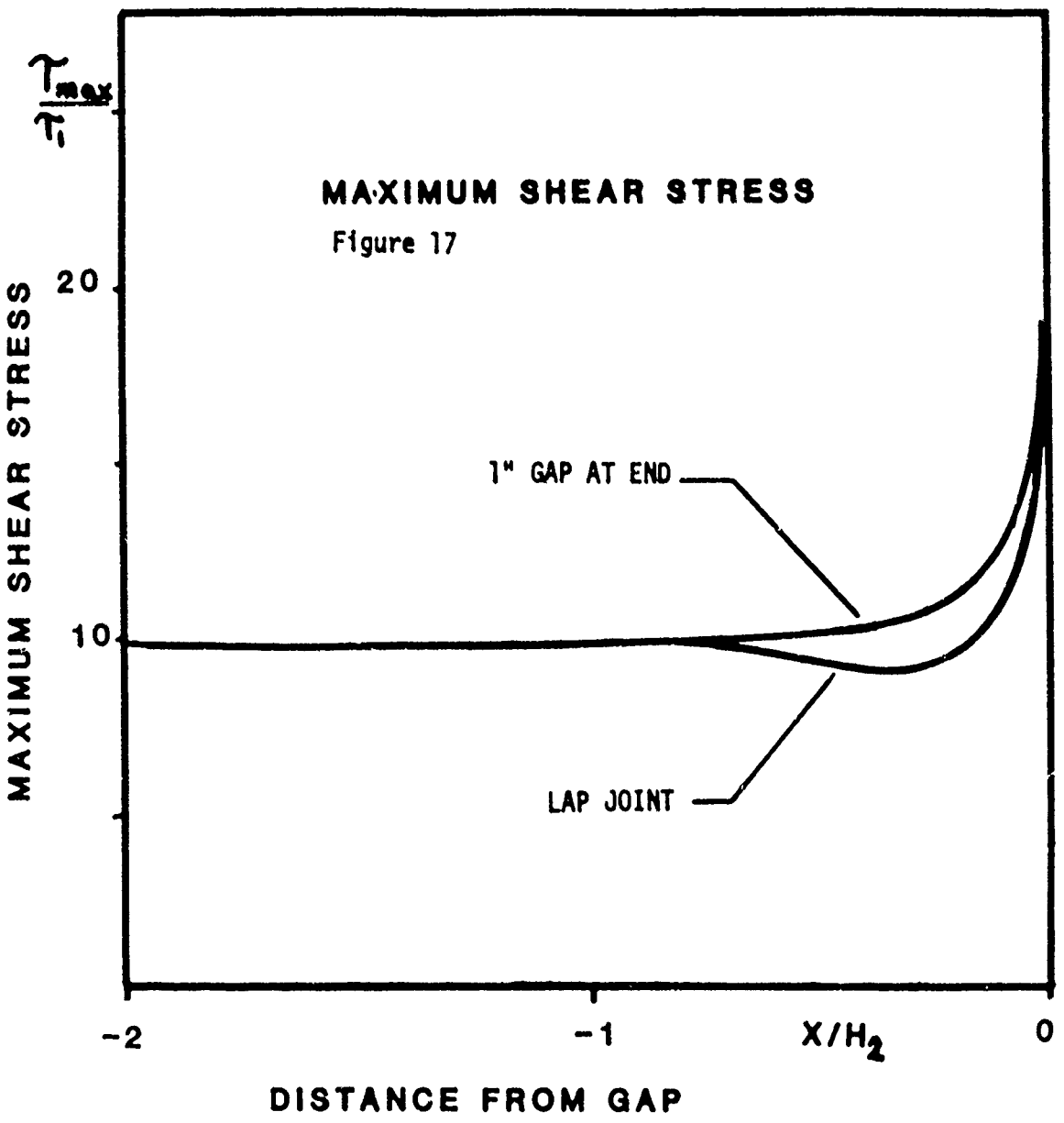

STRESS INTENSITY
NORMAL STRESS
σ_y/σ_∞
4
3
2
1
0
-1
-2
X/H_2
DISTANCE FROM GAP
1" GAP IN MIDDLE
5" GAP ON END
1" GAP ON END
5" GAP IN MIDDLE

Figure 16


$\frac{\tau}{\tau_{max}}$
MAXIMUM SHEAR STRESS
Figure 17
20
10
MAXIMUM SHEAR STRESS
1" GAP AT END
LAP JOINT
-2
-1
X/H_2
0
DISTANCE FROM GAP

METHOD OF PREDICTING THE DAMPING IN STIFFENED STRUCTURES

J. SOOVERE
LOCKHEED-CALIFORNIA COMPANY
BURBANK, CALIFORNIA

ABSTRACT

The viscous damping ratio, in the fundamental mode of stiffened panel type aircraft structures, has been assumed to vary inversely with the resonant frequency, when plotted on a log-log graph. It is shown, in this paper, that the fundamental mode viscous damping ratio is in fact a constant, independent of the structural resonant frequency, for a given panel design. A method for predicting the damping in stiffened panels has been developed which exhibits good correlation with test data. A new analytical model, representing the contribution to the damping from friction at the fastener lines, is included in the above method. It is also shown that the dominant contribution to the stiffened panel damping is, generally, due to acoustic radiation.

INTRODUCTION

The currently used representation[1,2,3] of the fundamental mode damping, for a variety of stiffened panel type aircraft structures, is illustrated in Figure 1. Most of these damping data have been measured[1] during sonic fatigue testing of representative multi-bay panels where the emphasis has been placed on measuring the response in the fundamental mode. Dominant fundamental mode response is usually assumed in sonic fatigue analysis[3,4]. The damping curves, in Figure 1, were obtained[1] by forcing the assumed inverse resonant frequency curve fit the measured damping data, Figure 2, when plotted on a log-log graph. This ion of the viscous damping ratio with resonant frequency, was derived fre gle degree-of-freedom system response theory, in which the resonant vib i. ampli-tude was kept constant.

When Hay first presented the damping data[1] at an AGARD Conference in Toulouse, France, in 1972, he mentioned that there was no real justification for assuming the inverse frequency type of variation for the damping. He indicated that there was an equal justification for drawing a horizontal line through the measured data points such as illustrated in Figure 2. This comment was considered humorous at the time. However, the results in this paper indicate that it was, actually, a very valid comment.

The accepted mechanisms[5], contributing to the damping of stiffened panels, include acoustic radiation, friction damping and gas pumping at the fastener lines, material damping, and energy loss to the surrounding structure. The friction damping has been assumed to be the dominant damping mechanisms, but attempts at modelling this damping analytically have failed to produce the expected correlation with test data[6]. The acoustic radiation has been assumed, on the other hand, to provide only a small contribution to the damping[7]. The material damping is small for most aerospace structural materials. The gas pumping at the fastener lines provides a contribution to the panel damping only in the higher order panel modes[8]. This contribution can, however, be minimized through the use of jointing compound. The energy loss to the surrounding structure is, however, very difficult to establish, both experimentally and analytically[9].

TEST PROGRAM

The acoustic radiation damping is proportional to the panel area[7,10], while the friction damping at the fastener line is proportional to the panel periphery. Large honeycomb panels were selected for the test program in an attempt to isolate the contributions from the above two mechanisms by taking advantage of their different natures. The large honeycomb panels were made from graphite/epoxy and Kevlar to study, at the same time, the behavior of composite materials[11]. The graphite/epoxy composite was known to have a very low material damping[12,13] whereas Kevlar has significant material damping, Figure 3.

Most of the composite honeycomb panels were tested in the free-free mode, prior to installation in the test frames, to obtain an estimate of the material damping. The free-free honeycomb panels were suspended by two strings, positioned at the nodal lines, and excited by a concentric coil and magnet driver having a very low damping. Some free-free beams were also tested using a plate attachment to a

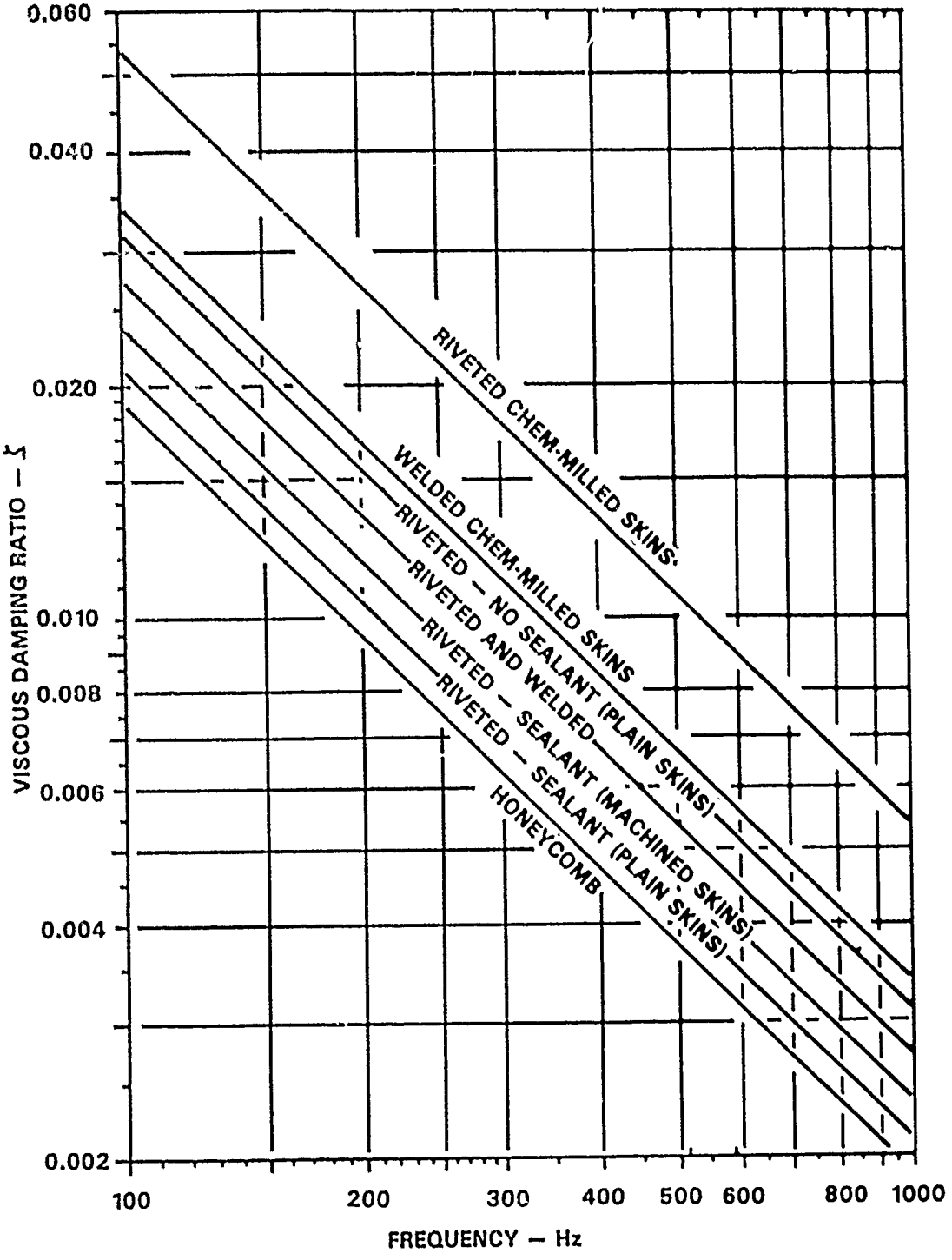


FIGURE 1. CURRENT REPRESENTATION OF STIFFENED PANEL DAMPING

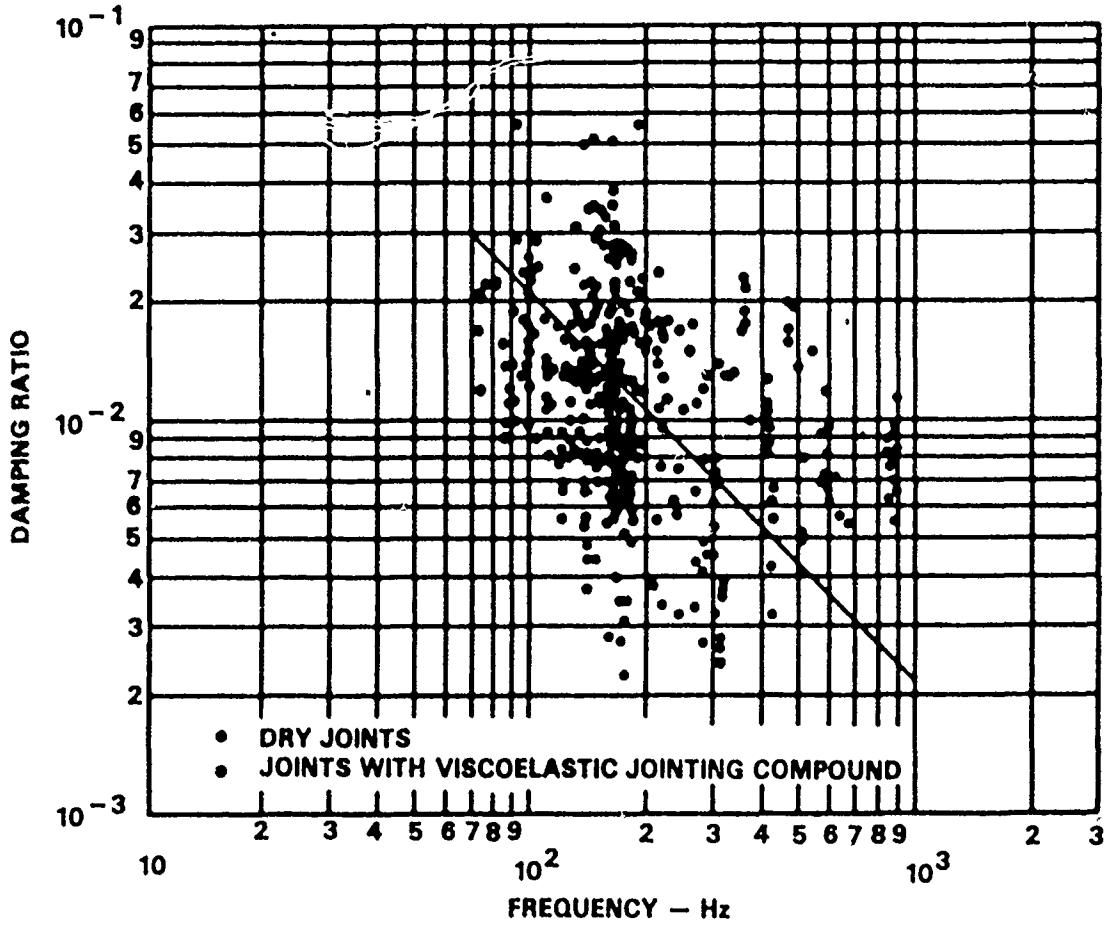


FIGURE 2. MEASURED DAMPING IN FLAT SKIN-STRINGER PANELS

small electrodynamic shaker to excite the beams through the air coupling between the beam and the plate. The response was measured by a non-contacting optical vibration transducer[13]. The free-free edge conditions minimize the contribution from air damping (acoustic radiation). The viscous damping ratio measured on the free-free graphite/epoxy beams and in many of the free-free graphite/epoxy honeycomb panel modes were below 0.001, a value that can be ignored in subsequent stiffened panel damping predictions, in air. As previously stated, the material damping values, Figure 3, were significant for the Kevlar panels and beams and should be included in the analysis. The free-free beam tests were conducted to determine the influence of the Kevlar cloth on the material damping. No such influence was found. The material damping was mainly a function of the resin damping and the fiber orientation.

Thereafter, the composite honeycomb panels were installed in the aluminum test frame with countersunk fasteners. Jointing compound was applied to the frame and panel interface to minimize the effect from gas pumping on the panel damping.

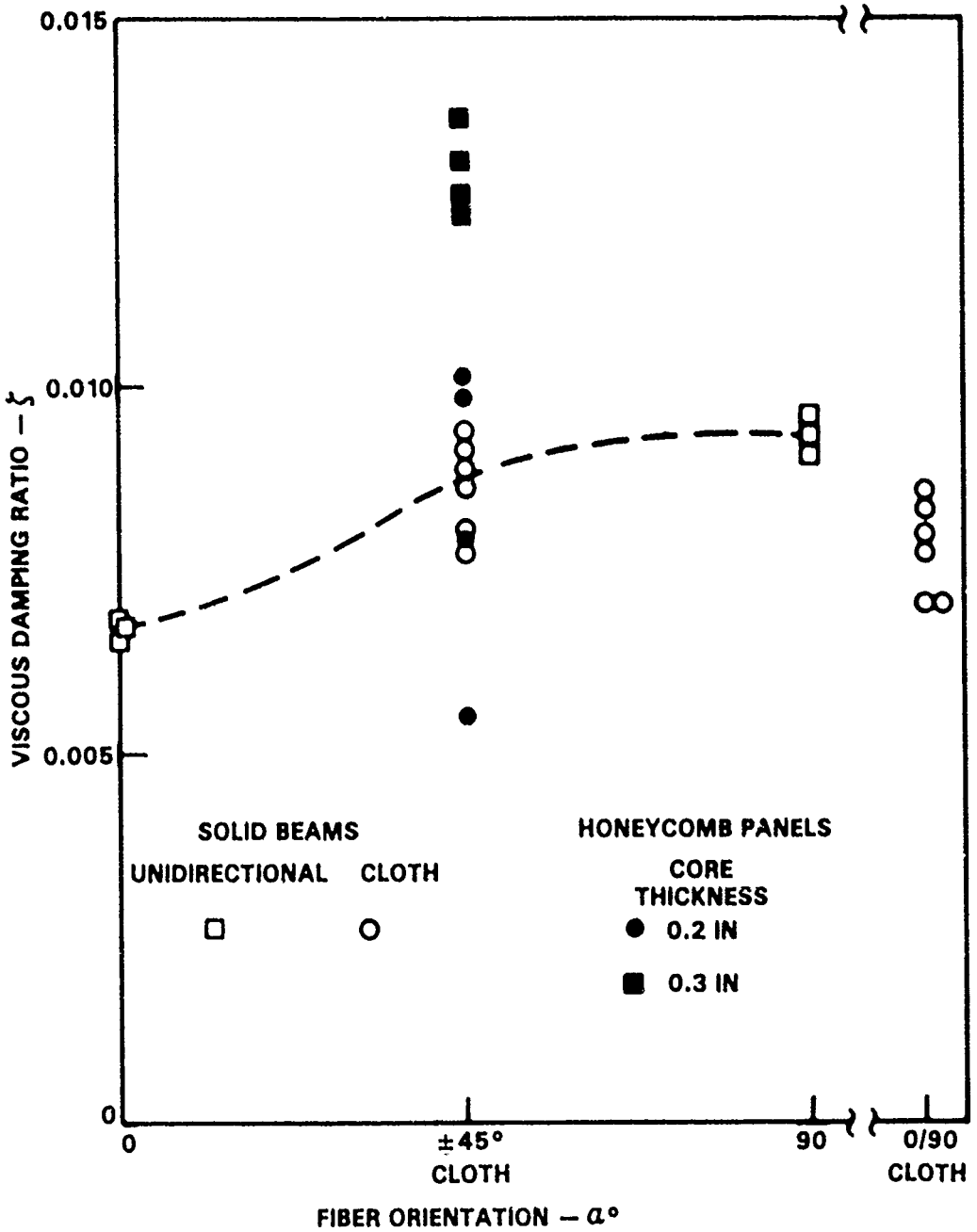


FIGURE 3. DAMPING IN FREE-FREE KEVLAR BEAMS AND HONEYCOMB PANELS

The stiffened honeycomb panels were mounted, in turn, horizontally on four wishbone springs, Figure 4, for modal studies. The wishbone springs were designed to simulate the stiffness of the two wire panel suspensions to be used later in the large baffle test facility. The damping data measured in the modal study tests are illustrated in Figure 5. The measured damping values, at the lower resonant frequencies in Figure 5, indicate that the contribution to the panel damping from fastener line friction must be less than a viscous damping ratio of, approximately 0.003, since acoustic radiation damping is also present in these data. The effect of acoustic radiation can be seen more clearly at the higher mode frequencies, where edge radiation effects start to dominate.

The composite honeycomb panels were then mounted, one-at-a-time, in the large baffle test facility, illustrated in Figure 6. The test facility was itself located in an anechoic room. The baffle extended from the floor to the ceiling and over one fundamental mode wavelength beyond the panel in the lengthwise

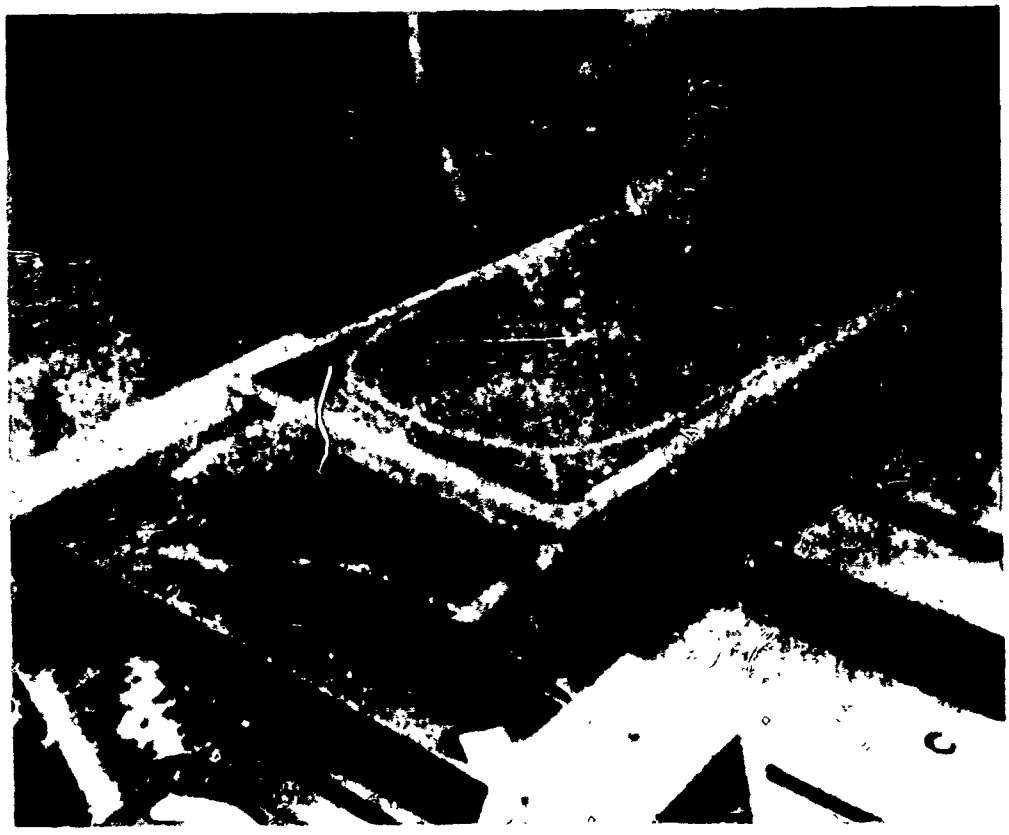


FIGURE 4. MODAL STUDY TEST FACILITY

direction. The frame-mounted test panels were supported vertically in the test aperture by two wires to minimize the energy loss to the surrounding structure. The honeycomb panel acoustic, but not the structural edge conditions, were changed in going to this test facility from the modal study facility. The viscous damping ratios, measured in the large baffle test facility, are illustrated in Figure 7. Care was taken to minimize the error from all sources, including those introduced by the data analysis techniques. As a consequence, good modal grouping was obtained in the measured damping data. These damping data were also repeatable within a plus or minus ten percent error after dismantling and reassembling the test set-up, a year later. These data indicate that the damping, in large stiffened honeycomb panels, is due predominantly to acoustic radiation. The highest damping is measured in the fundamental mode, as predicted by acoustic radiation theory[7]. This result has also been observed in integrally stiffened graphite/epoxy panels[14,15], where the damping is entirely due to acoustic radiation, except for the very small contribution from the material damping.

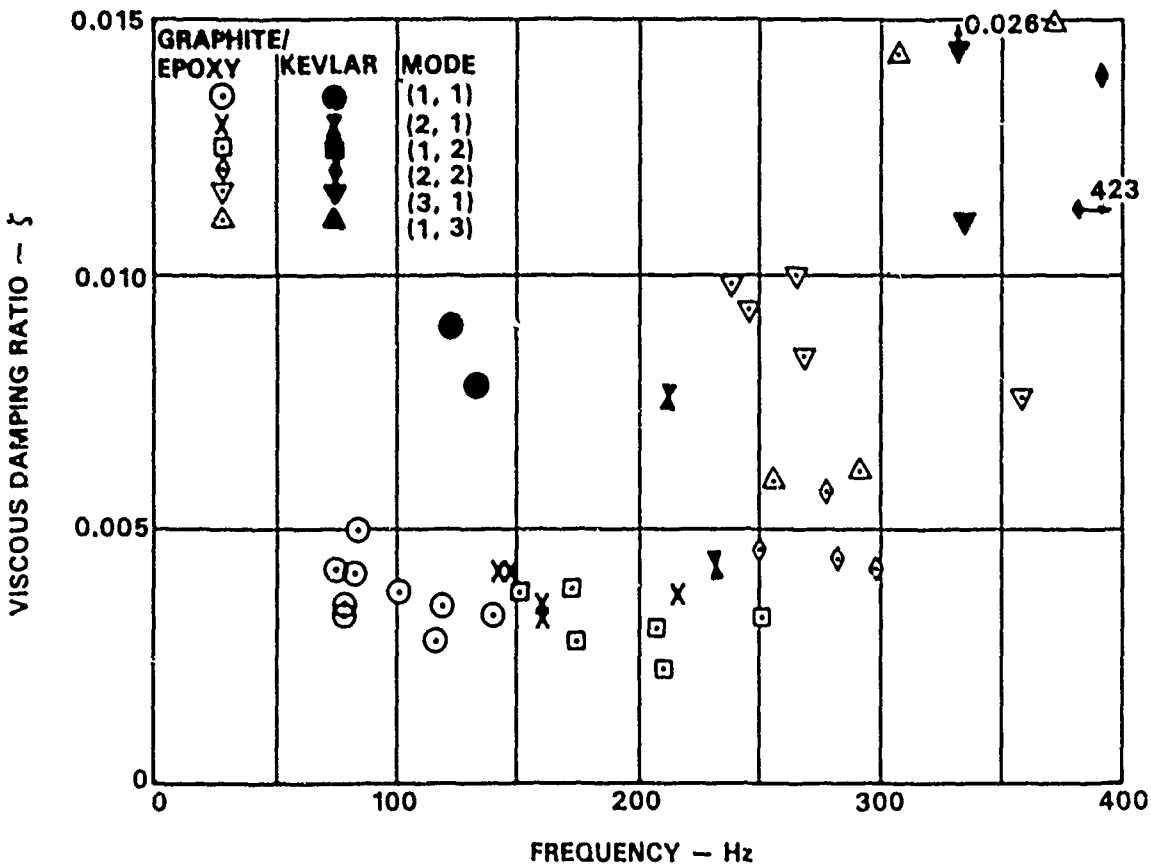
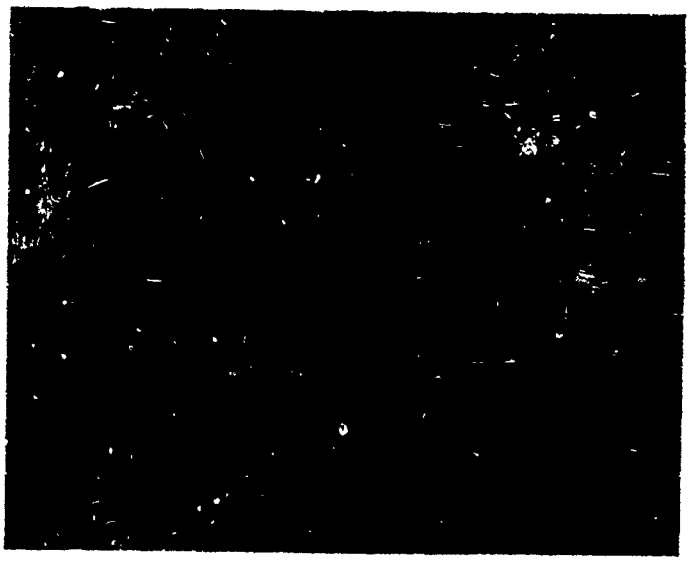


FIGURE 5. COMPOSITE HONEYCOMB PANEL DAMPING MEASURED DURING MODAL STUDIES



(a) Front View



(b) Rear View

FIGURE 6. LARGE BAFFLE TEST FACILITY

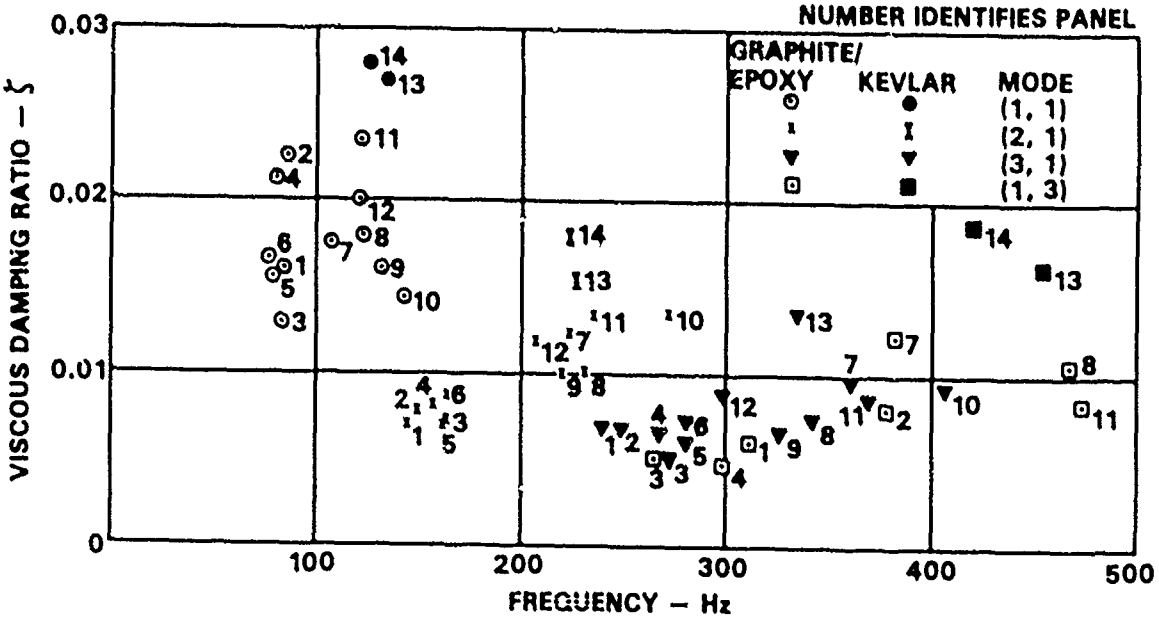


FIGURE 7. COMPOSITE HONEYCOMB PANEL DAMPING MEASURED IN A LARGE BAFFLE TEST FACILITY

DISCUSSION OF THE DAMPING DATA

The fundamental mode damping data, for the composite honeycomb panels, have been plotted in Figure 8, together with similar data measured two decades ago on comparable size aluminum honeycomb panels[16]. A horizontal line can be drawn through all of these data points. The experimental test set-up was totally different in the two tests, but the results are very consistent, including the scatter in the data. Also damping data for the 3,1 composite honeycomb panel mode are included in the above figure. The damping in this mode is different for the two types of graphite/epoxy honeycomb panels fabricated with either ultra-high modulus or intermediate modulus graphite/epoxy face sheets. This result indicates that the viscous damping ratio in the higher panel modes may be dependent on the stiffness characteristics of the panels.

The same constant fundamental mode damping behavior is obtained for other types of stiffened panels, based on individual panel damping data available in the literature. These damping data are summarized in Figure 9 for riveted[16] and bonded[17] aluminum skin-stringer panels, in Figure 10 for aluminum box structures[18,19] and multi-bay panels[18] and in Figure 11 for corrugated, hat-stiffened and built-up integrally stiffened panels[20]. The metallic material, used in the construction of the multi-bay stiffened panels[21], does not make a difference to the measured damping, Figure 12. The horizontal line drawn through the damping data in Figures 9, 10, and 12, corresponds to a constant viscous damping ratio of 0.015. The average viscous damping ratio for the fundamental mode of stiffened

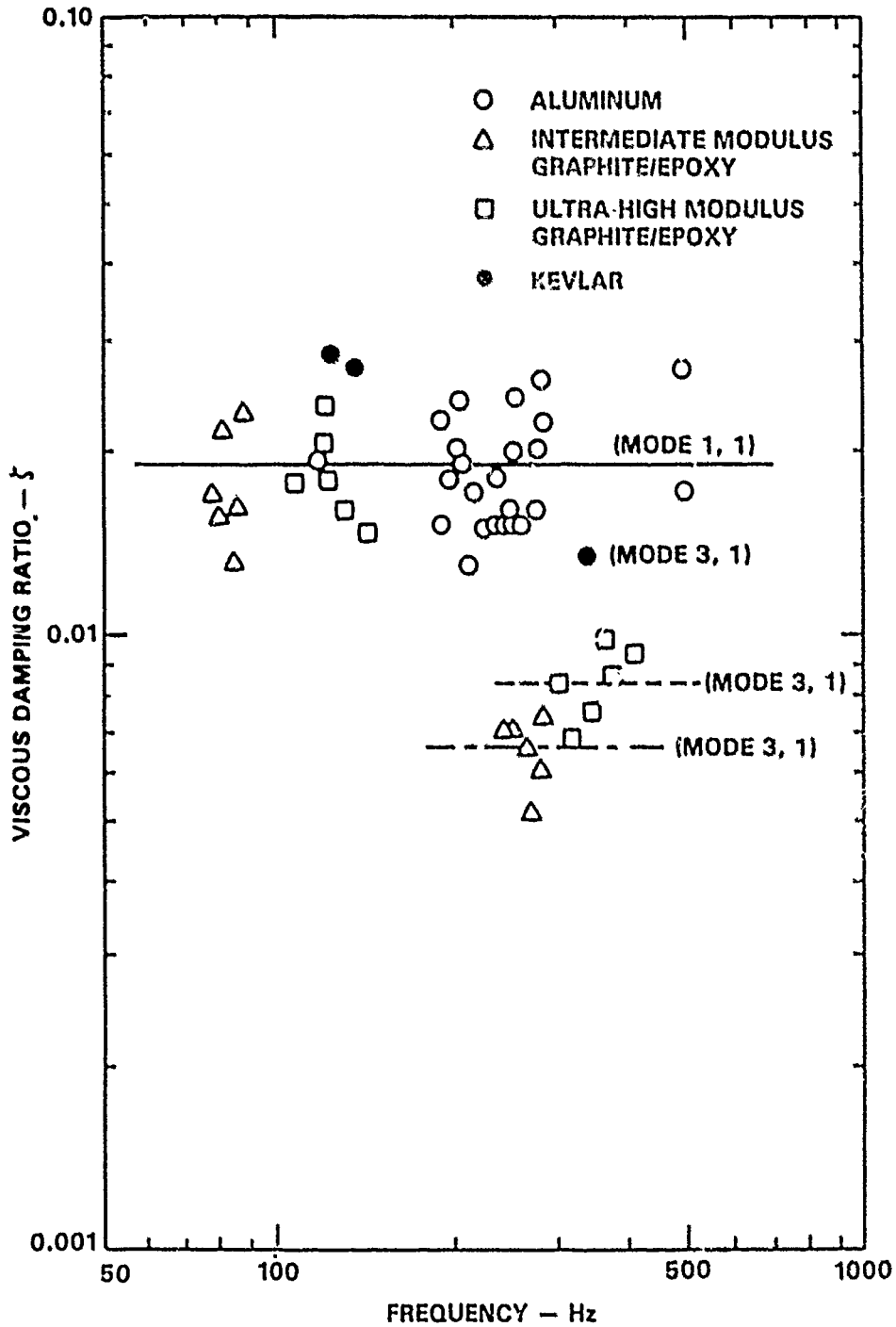


FIGURE 8. VARIATION OF MEASURED DAMPING WITH FREQUENCY FOR STIFFENED HONEYCOMB PANELS

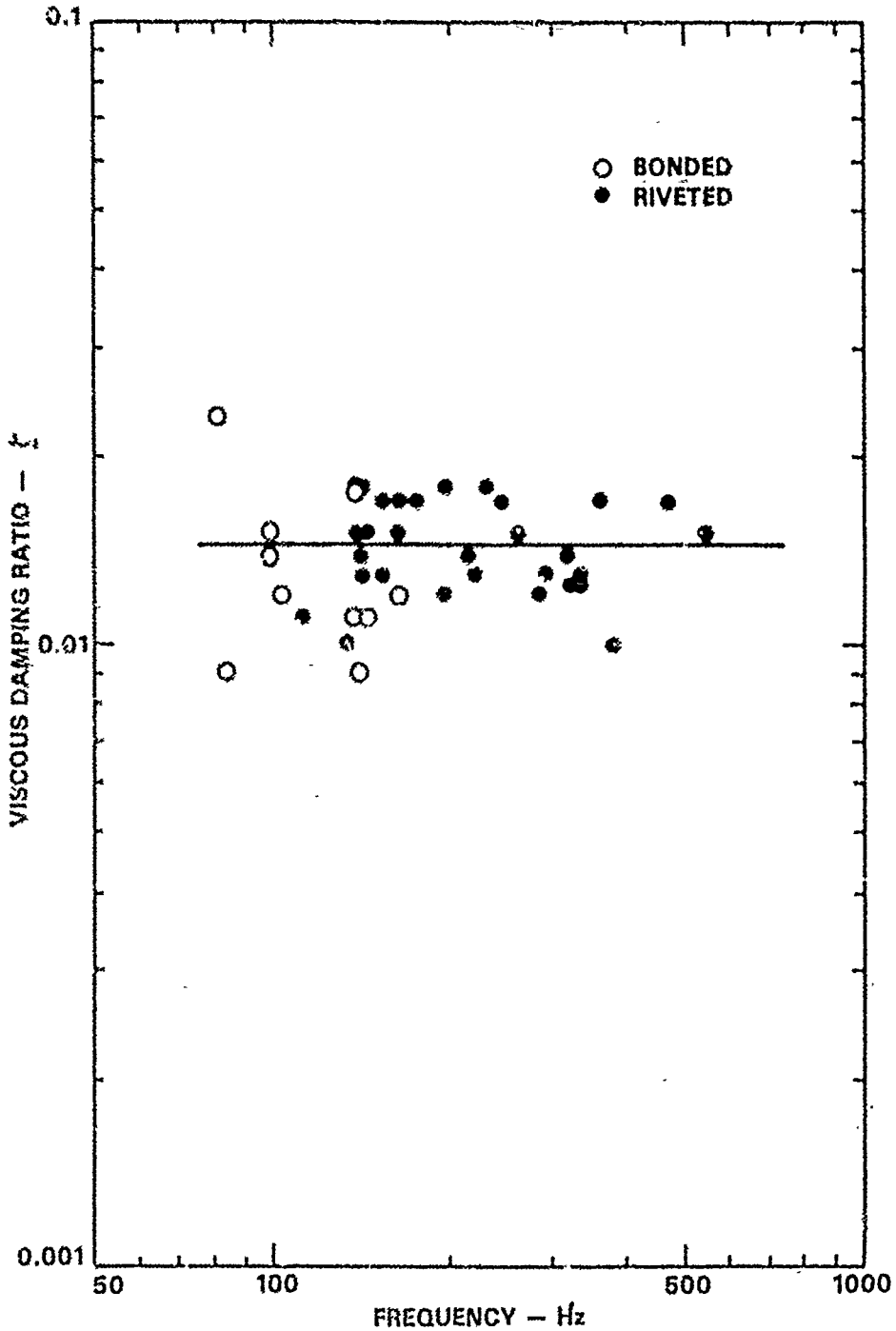


FIGURE 9. MEASURED DAMPING IN THE FUNDAMENTAL MODE OF SKIN-STRINGER ALUMINUM PANELS

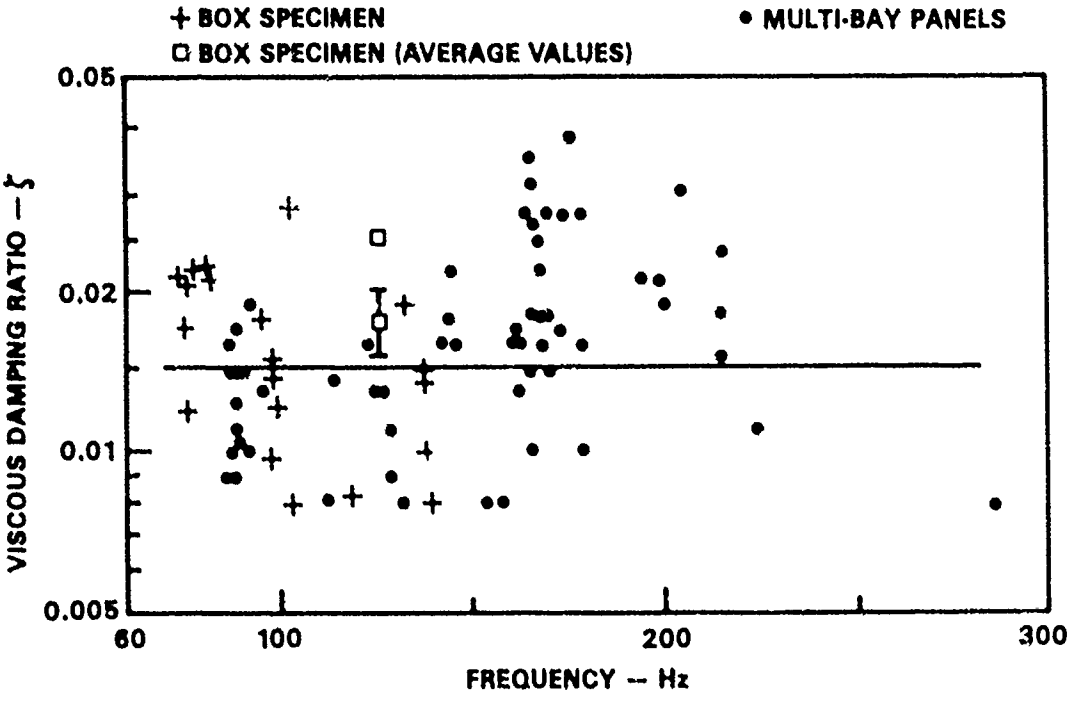


FIGURE 10. MEASURED STIFFENED PANEL AND BOX SPECIMEN DAMPING

curved panels is also constant with resonant frequency and equal to 0.015, the same as obtained for the stiffened flat panels. The curved panel resonant frequencies are higher than those of the flat panels on account of the stiffening effect from curvature. The average viscous damping ratio of 0.012, for the bonded panels in Figure 9, is slightly lower than the corresponding value for the riveted panels, indicating a relatively small contribution of 0.003 to the panel viscous damping ratio from fastener line friction. Bonding, while eliminating the contribution from friction to the panel damping, does not, itself, provide any damping to the panel.

Unfortunately, there are no damping data reported in the literature for the higher modes of the above stiffened panels, except for the data presented in this paper on the stiffened composite honeycomb panels. The variation of the higher mode damping with resonant frequency is illustrated in Figure 13 for only six of these composite honeycomb panels for purposes of clarity. The average damping trend lines do seem to vary almost inversely with the resonant frequency. However, there is a different trend line for each composite honeycomb panel design. Thus, the trend lines are a function of the panel stiffness, the material damping and the panel geometry. Consequently, it is necessary to develop an analytical model for the modal damping, which includes the above parameters, if sense is to be made of all the modal damping data. This analytical model must also include the contribution from friction damping at the fastener lines.

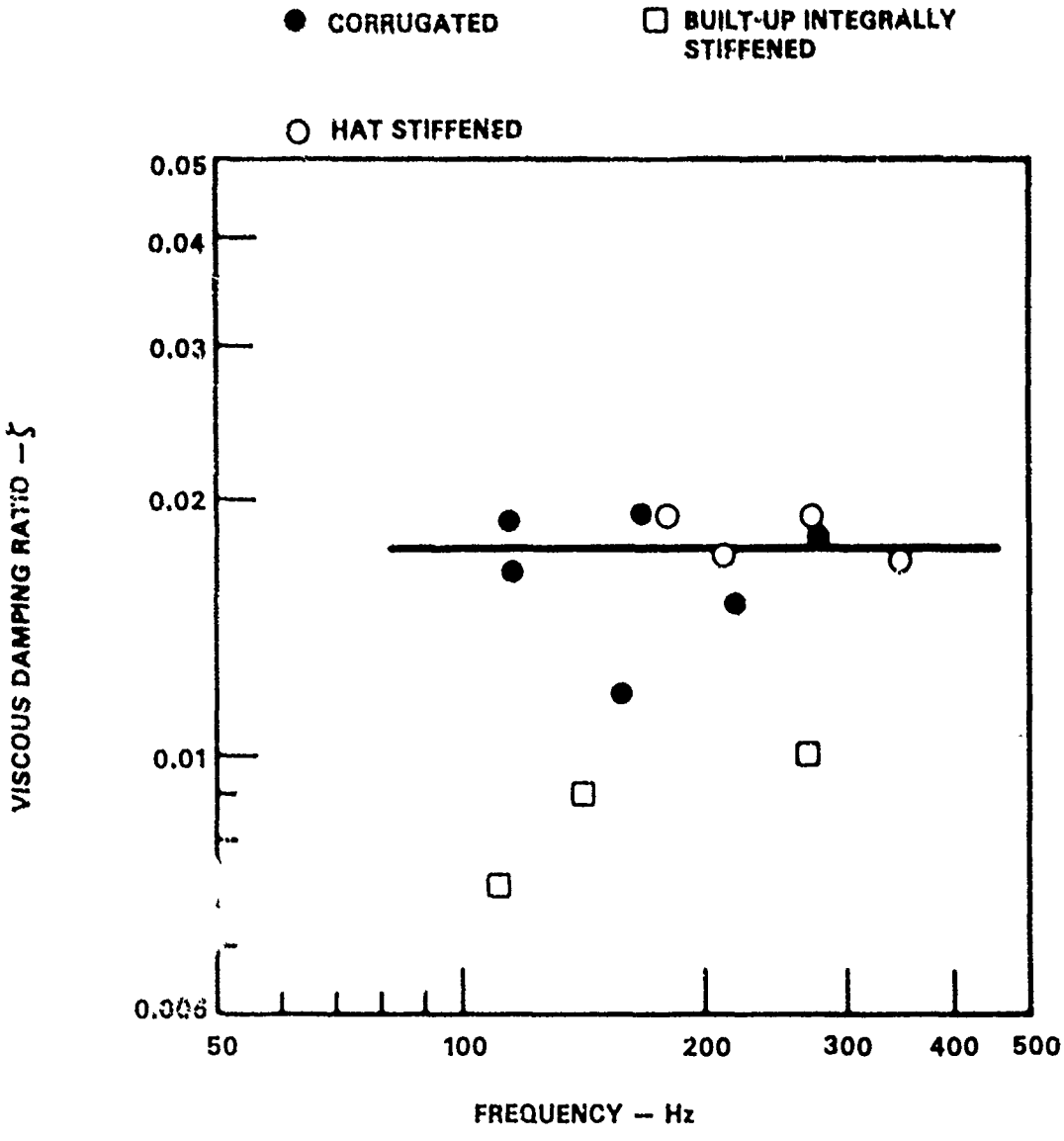


FIGURE 11. MEASURED DAMPING RATIOS FOR DIFFERENT STRUCTURES

FASTENER LINE FRICTION DAMPING MODEL

Friction or Coulomb damping is generated by slippage between two contacting surfaces. The damping force is, generally, assumed to be equal to the product of the coefficient of sliding friction and the normal force, but independent of the velocity. In an experiment, described in Reference 22, the equivalent coefficient of sliding friction was shown to be independent of both frequency and maximum velocity, but dependent on the normal force.

Friction damping, at the fastener lines of stiffened panels, was first investigated many years ago[23,24] and continues to be a source of interest in more recent years[5,6]. The earlier studies revealed a complicated behavior depending on the load amplitude at the joint. In a more recent study[6], damping measurements were made on a wire suspended panel array in near vacuum conditions and on simple

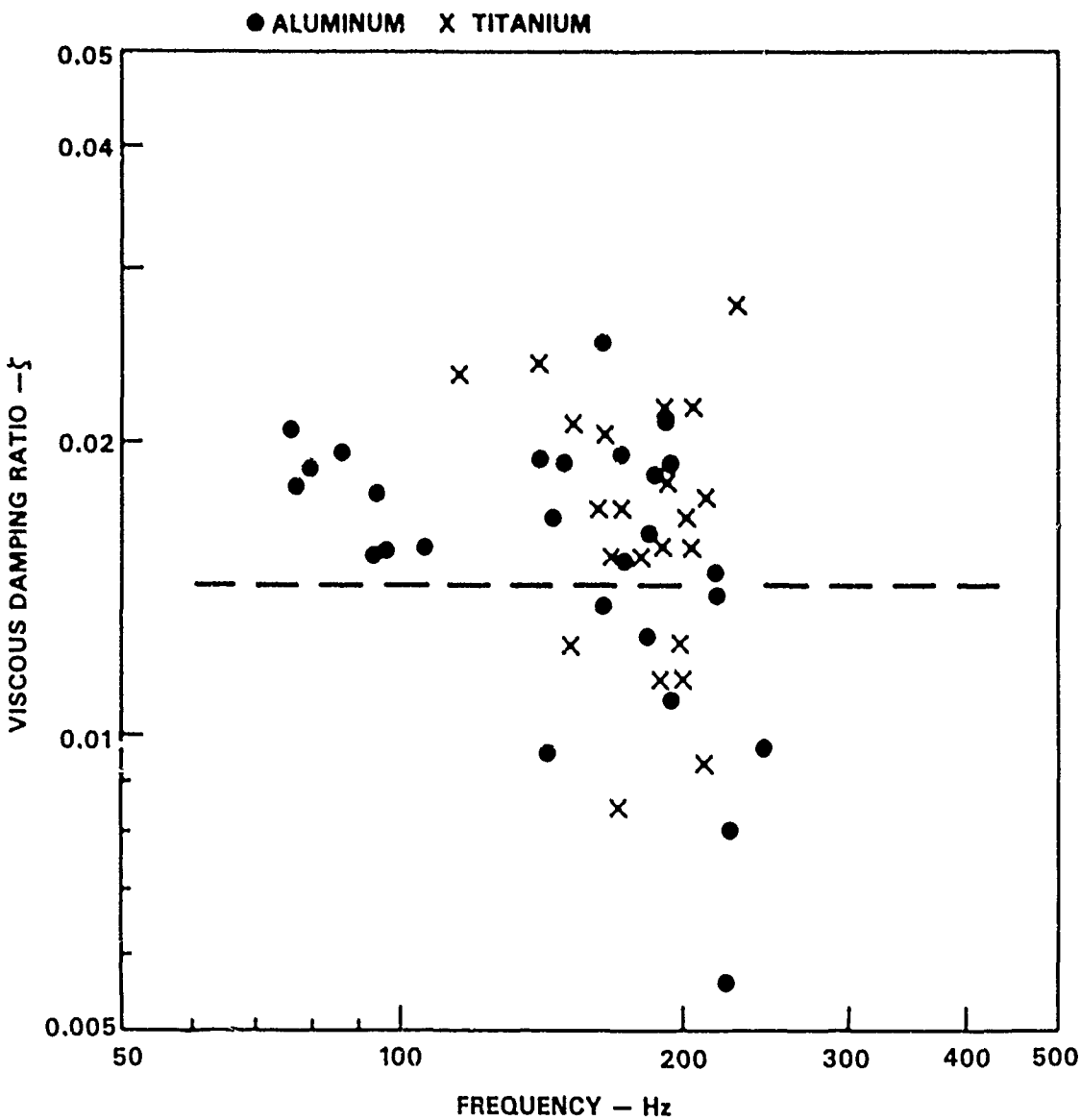


FIGURE 12. MEASURED STIFFENED ALUMINUM AND TITANIUM PANEL DAMPING

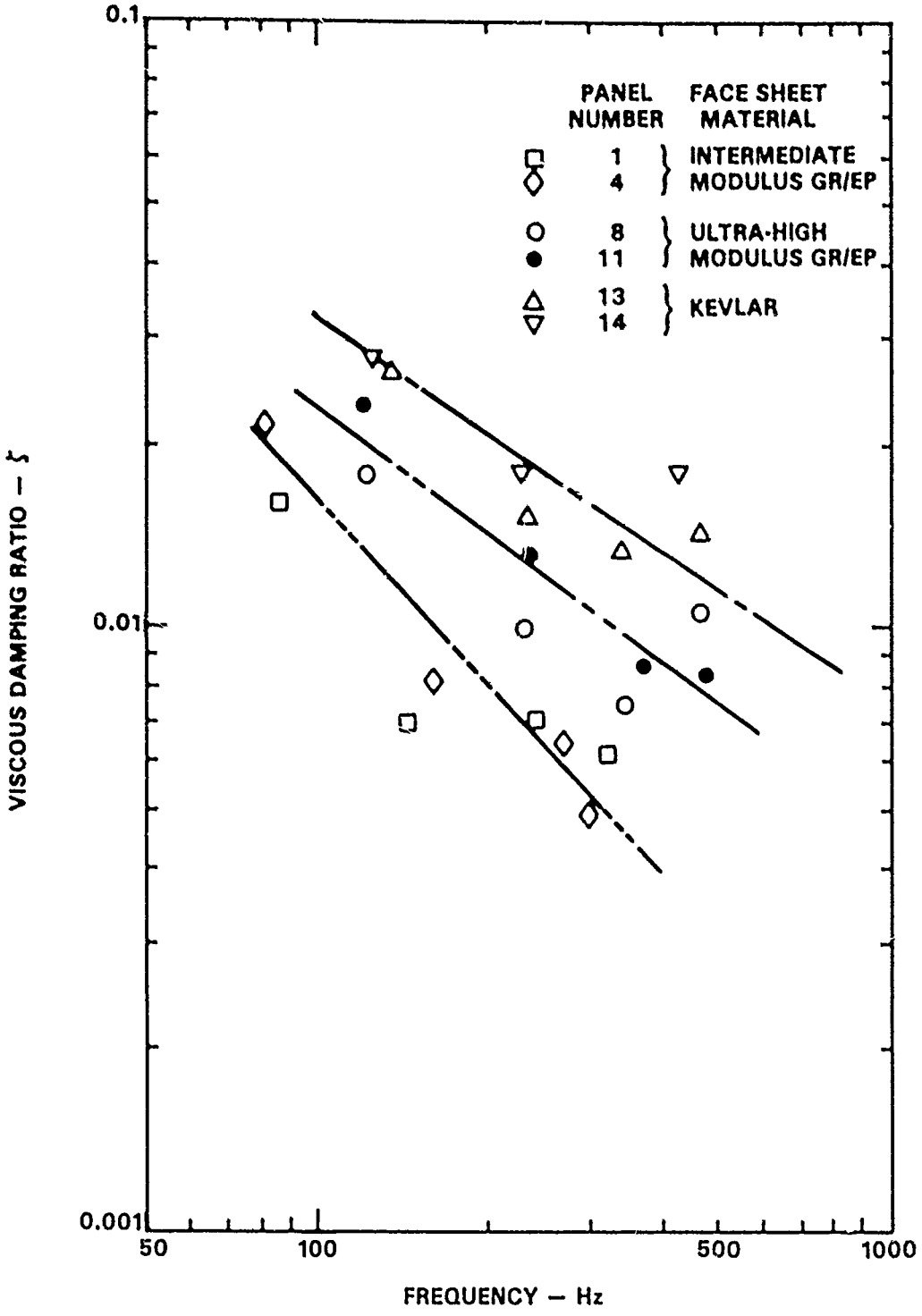


FIGURE 13. TYPICAL MULTI-MODE VARIATION OF DAMPING WITH FREQUENCY

riveted crossed double cantilever coupons. The coupon data revealed that the measured friction related joint dissipation coefficient, which is proportional to the loss factor, was found to be constant with the joint load amplitude.

The test results, in Reference 22, show that the sliding friction coefficient is independent of frequency and velocity. The test results, in Reference 6, indicate that the loss factor is independent of the load amplitude at the fastener line, at least for skin-stiffener type panels. It is, therefore, reasonable to conclude that the friction damping at the fastener line of stiffened panels is indeed a constant, dependent only on the number of fasteners along the panel periphery. The viscous damping ratio of 0.0085, measured in a panel array under near vacuum conditions[6], is assumed to be representative of the friction damping in stiffened panels. It is further assumed that the fasteners at the corners of the panel and at nodal lines that cross the panel, do not contribute anything to the friction damping. Based on these two assumptions the following approximate expression is obtained for the equivalent viscous damping ratio, ζ_F, representing the fastener line friction damping:

$$\zeta_F = 0.0253 \frac{\left[s(a+b) - \frac{n}{s} - \frac{m}{s}\right]}{ab} \qquad (1)$$

where

a,b = the panel length and width in inches

m,n = the mode number in the length and width directions, respectively

s = the number of fasteners per inch.

The damping predicted by equation (1) decreases with increasing mode number. Also, the half wave length of the higher order panel modes is assumed to be greater than the fastener spacing which is, typically, around one inch for most lightweight aerospace structures.

Since the viscous friction damping ratio is proportional to the number of effective fasteners around the panel periphery divided by the panel generalized mass, the above equation is equally applicable to each active panel in a panel array. The same viscous friction damping ratio is obtained for a three-by-three panel array when all of the equal bays are participating in the vibration or if a larger center bay is vibrating by itself, provided that the active bay dimensions and fastener spacings are the same. However, the acoustic radiation damping could differ significantly under the above circumstances, depending on the phase relationship between the active bays in the array.

ACOUSTIC RADIATION DAMPING

Acoustic radiation from stiffened aircraft panel type structures, has been investigated for more than two decades and has, consequently, been the subject of very many papers. The simplest of the theories for predicting the acoustic radiation damping, is given in Reference 7 for both simply supported and clamped single

panels when mounted in an infinite baffle. An expression was developed in this theory for the generalized acoustic damping coefficient, from the instantaneous acoustic pressure generated by an elemental piston within the panel. The viscous acoustic damping ratio, ζ_a, was obtained by dividing the generalized damping coefficient by the critical generalized damping coefficient. The resulting viscous damping ratio, for double-sided acoustic radiation, is given by

$$\zeta_a = \frac{f_n}{cM} \frac{\int_0^a \int_0^b w(x',y') \int_0^a \int_0^b \frac{\sin(2\pi r/\lambda)}{2\pi r/\lambda} w(x,y)\, dy\, dx\, dy'\, dx'}{\int_0^a \int_0^b w^2(x,y)\, dy\, dx} \qquad (2)$$

where

ρ = density of air

c = speed of sound in air

λ = acoustic wave length

f_n = natural frequency of the m,nth panel mode

$w(x,y)$ = panel mode shape

M = panel mass per unit area

a = panel length

b = panel width

x,y and x',y' = coordinates of two elemental panels in the panel surface

$$r = \left\{(x - x')^2 + (y - y')^2\right\}^{1/2}$$

On assuming that the acoustic wave length is much greater than panel dimensions[7], and, therefore, that

$$\frac{\sin(2\pi r/\lambda)}{2\pi r/\lambda} \simeq 1 \qquad (3)$$

equation (2) reduces to

$$\zeta_a = \frac{f_n}{cM} \frac{\left\{\int_0^a \int_0^b w(x,y)\, dy\, dx\right\}^2}{\int_0^a \int_0^b w^2(x,y)\, dy\, dx} \qquad (4)$$

For a simply supported panel, equation (4) becomes simply

$$\zeta_a = \frac{64}{\pi^4} \frac{\rho}{c} \frac{f_n}{M} \frac{a\ b}{m^2 n^2} \tag{5}$$

Mead[7] indicated, through numerical integration of equation (2), that equation (5) overestimates the acoustic damping ratio of comparatively small panels with aspect ratios of three or less, by approximately eight percent.

The assumption made in equation (3) may not be valid for honeycomb panels because of their larger size. An improvement in the accuracy can be obtained[25] by expanding the $\sin(2\pi r/\lambda)/(2\pi r/\lambda)$ term in the numerator of equation (2) as a series and then retaining the first two terms of the series in the integration. Equation (2) now becomes

$$\zeta_a = \frac{\rho}{c} \frac{f_n}{M} \left\{ \int_0^a \int_0^b w(x'y') \int_0^a \int_0^b \left\{ 1 - \frac{1}{6} \left(\frac{2 f_n}{c} \right)^2 \left[(x - x')^2 + (y - y')^2 \right] \right\} w(x,y)\, dx\, dy\, dx'\, dy' \right\} \Bigg/ \left\{ \int_0^a \int_0^b w^2(x,y)\, dx\, dy \right\} \tag{6}$$

A closed form solution can be obtained for equation (6), which, for the fundamental mode of a simply supported panel, becomes

$$\zeta_a = \frac{64}{\pi^4} \frac{\rho}{c} \frac{f_1}{M} a\ b \left\{ 1 - \frac{\pi^2 - 8}{3} \left(\frac{f_1}{c} \right)^2 \left(a^2 + b^2 \right) \right\} \tag{7}$$

where f_1 is the natural frequency of the fundamental mode. This equation is the same as equation (5) for the fundamental mode, except for the added term in the parentheses.

Equation (7) was used[25] to predict the damping in the fundamental mode of the aluminum honeycomb panels in Reference 16. These panels were mounted in very stiff test frames. Equivalent simply supported mode shapes[25,26] were used in the above analysis. The damping predicted by equation (7), however, overestimated the measured damping. Reasonable correlation was obtained between the theory and test data (Figure 14) when the predicted damping values were reduced by a factor of two. The same factor of two was used in a similar, but more complex, analysis[25] for predicting the fundamental mode damping of the composite honeycomb panels. The test frame torsional and flexural flexibilities were included in this analysis. The degree of correlation achieved is illustrated in Figure 15. The average measured material damping values from Figure 3, were added to the

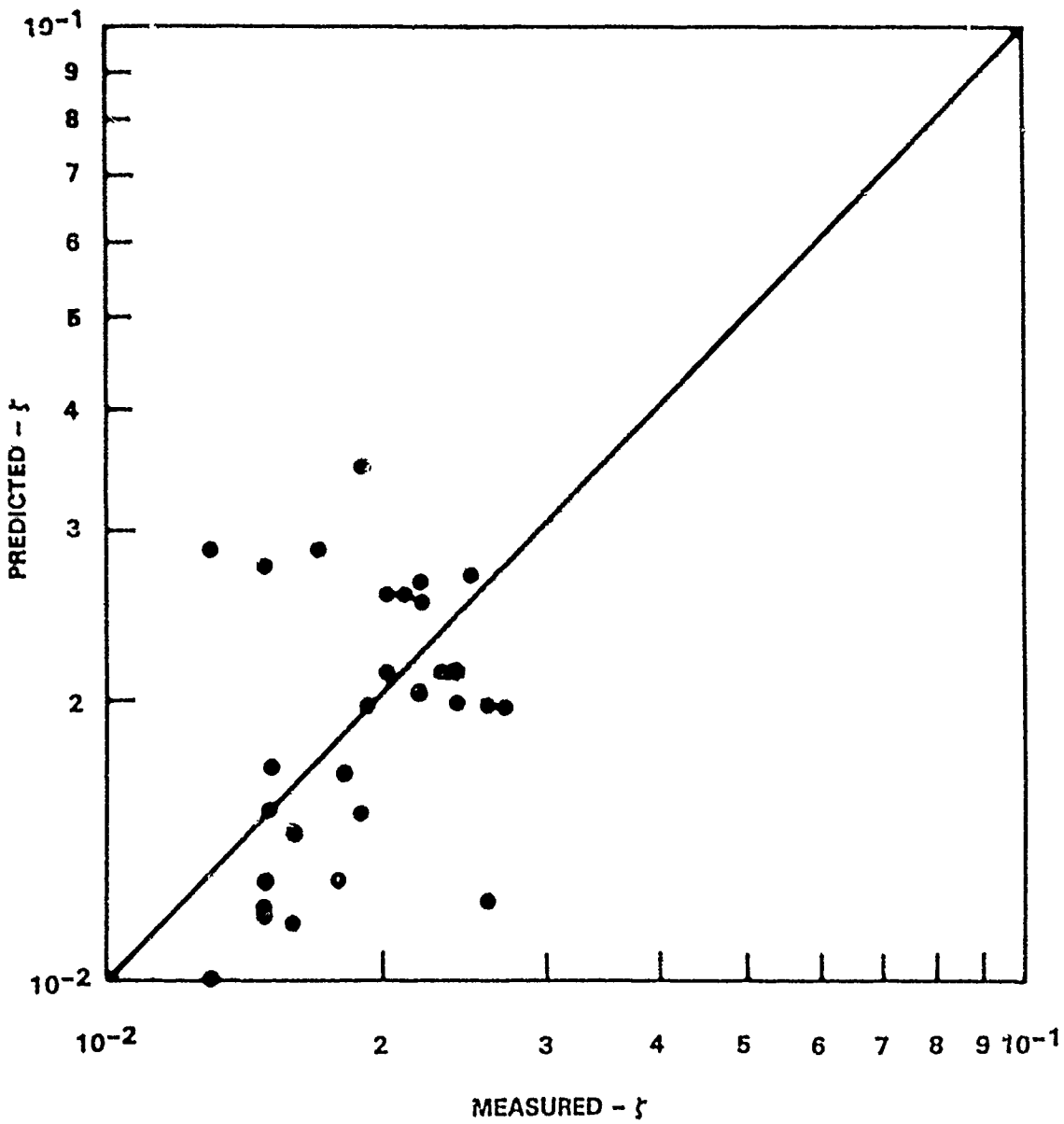


FIGURE 14. COMPARISON OF THEORETICALLY PREDICTED AND MEASURED VISCOUS DAMPING RATIOS FOR FUNDAMENTA MODE OF STIFFENED ALUMINUM HONEYCOMB PANELS.

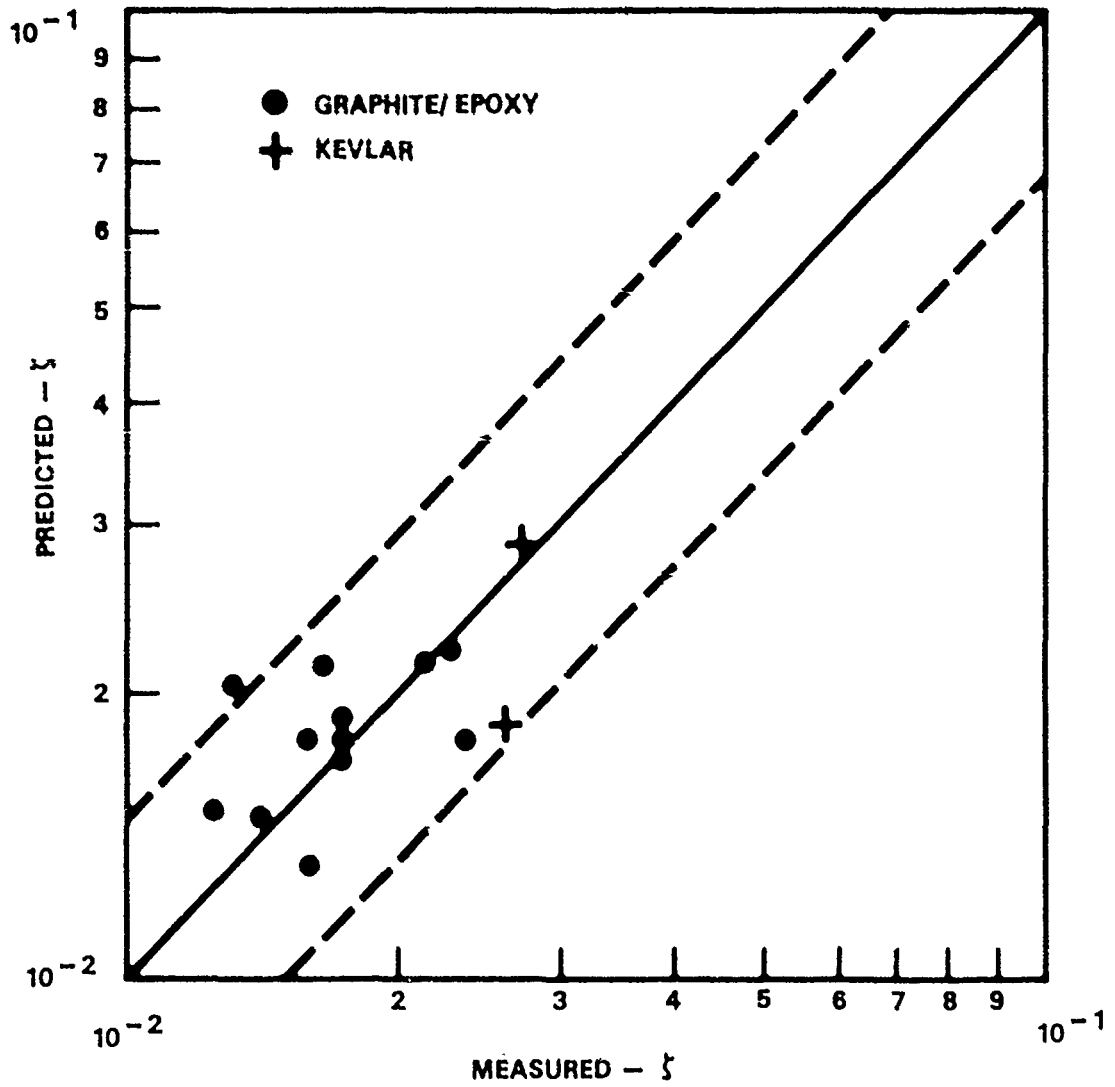


FIGURE 15. COMPARISON OF PREDICTED AND MEASURED VISCOUS DAMPING RATIOS FOR HONEYCOMB PANELS

theoretically predicted values only for the Kevlar panels. The contribution from friction damping at the fastener line was not included in the above analysis. However, when equation (5) was used to predict the damping of an integrally blade stiffened graphite/epoxy minisandwich panels, reasonable correlation was achieved with the measured damping, Figure 16, without having to use any empirical factor. Clearly, the use of single-sided acoustic radiation, as suggested by Mead[7] cannot be justified for the honeycomb panels because of the test setup used. The reason for the above discrepancy remains to be discovered. Nevertheless, a theoretical basis for predicting the damping of stiffened panels has been established.

METHOD FOR PREDICTING STIFFENED PANEL DAMPING

The viscous damping ratio, ζ_{mn}, for the m,nth mode of a single panel is simply

$$\zeta_{mn} = \zeta_a + \zeta_F + \zeta_M \tag{8}$$

where the viscous damping ratios for fastener line friction and acoustic radiation are given by equations (1) and (5), respectively, and where ζ_M is the material viscous damping ratio that needs to be established experimentally. The expression for the acoustic radiation damping of honeycomb panels (Equations (5) or (7)) needs to be divided by a factor of 2. Equation (8) can be applied directly to a single panel vibrating in a panel array. Most of the multi-bay test panels consist of 9-bays with a large center bay. Thus, the dominant response tends to occur in the center bay vibrating alone. For a panel array with equal bays, equation (5) has to be modified to account for the number of bays vibrating in-phase and out-of-phase in the panel array. If all of the adjacent bays are vibrating out-of-phase, then the expression for the acoustic radiation damping becomes

$$\zeta_a = \frac{64}{\pi^4} \frac{\rho}{c} \frac{f_n}{M} \frac{a\ b}{m^2 n^2} \frac{1}{\bar{M}\ \bar{N}} \tag{9}$$

where $\bar{M}$ and $\bar{N}$ are number of axial and lateral bays in the panel array. If, on the other hand, all of the bays are vibrating in phase, then equation (5) can be used directly since the viscous damping ratio will be the same for each bay. The length, a, and width, b, in equations (5) and (9) refer to the corresponding dimensions of the individual bays.

Equations (1), (8) and (9) were used to predict the damping in a number of riveted and bonded multi-bay panels [16,17], based on equivalent sinusoidal mode shapes. The degree of correlation achieved between the measured and predicted damping is illustrated in Figure 17. The material damping was assumed to be zero for all of the panels while the friction damping was assumed to be zero for the bonded panels. Although no damping data were available for the higher panel modes, the theory was used to predict the fundamental and higher mode damping for two panel arrays[16], with different dimensions, to illustrate (Figure 18) the behavior of the predicted damping in the higher modes.

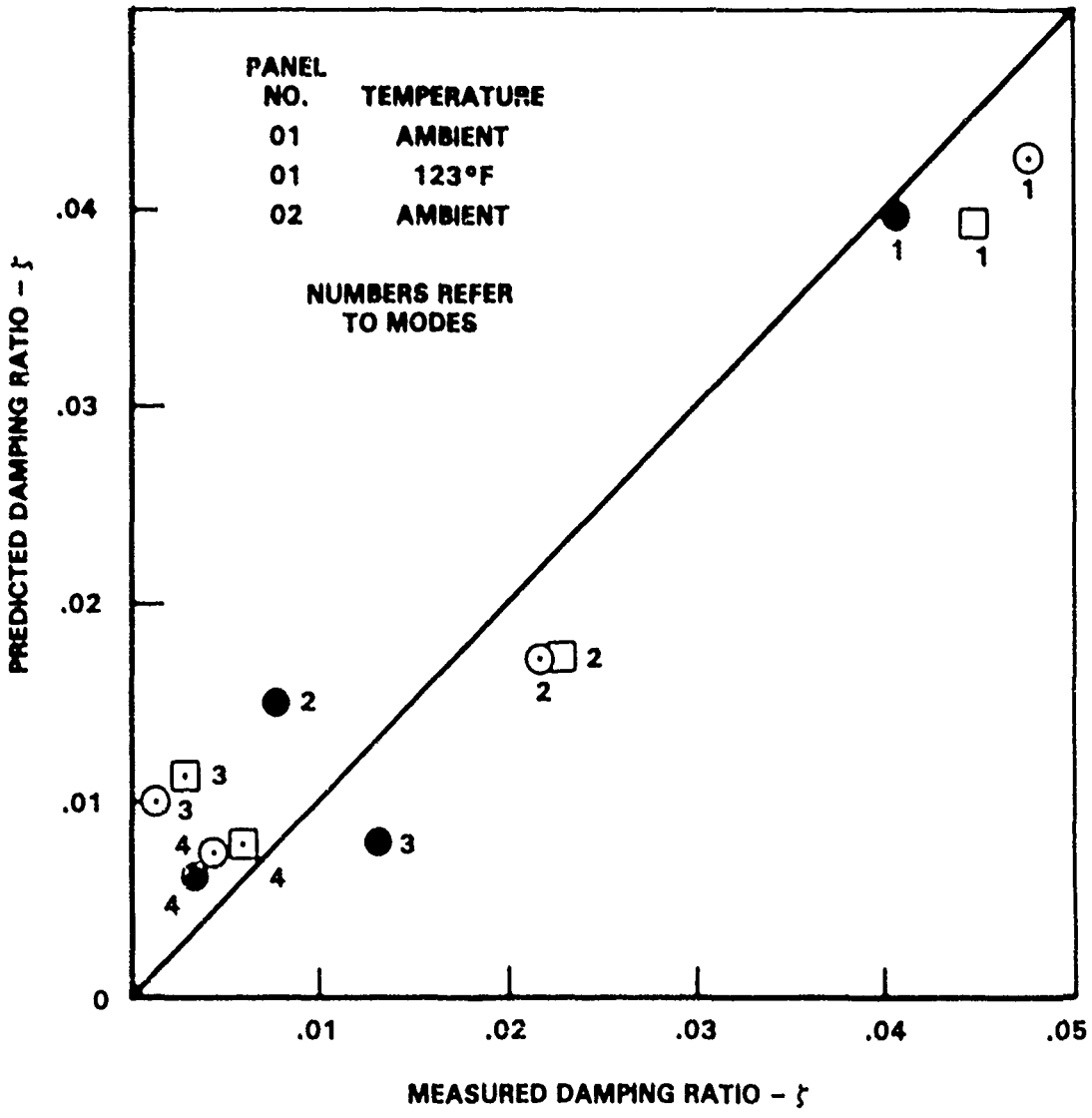


FIGURE 16. COMPARISON OF THEORETICALLY PREDICTED AND MEASURED VISCOUS DAMPING RATIOS OF BLADE STIFFENED MINISANDWICH GRAPHITE/EPOXY PANEL.

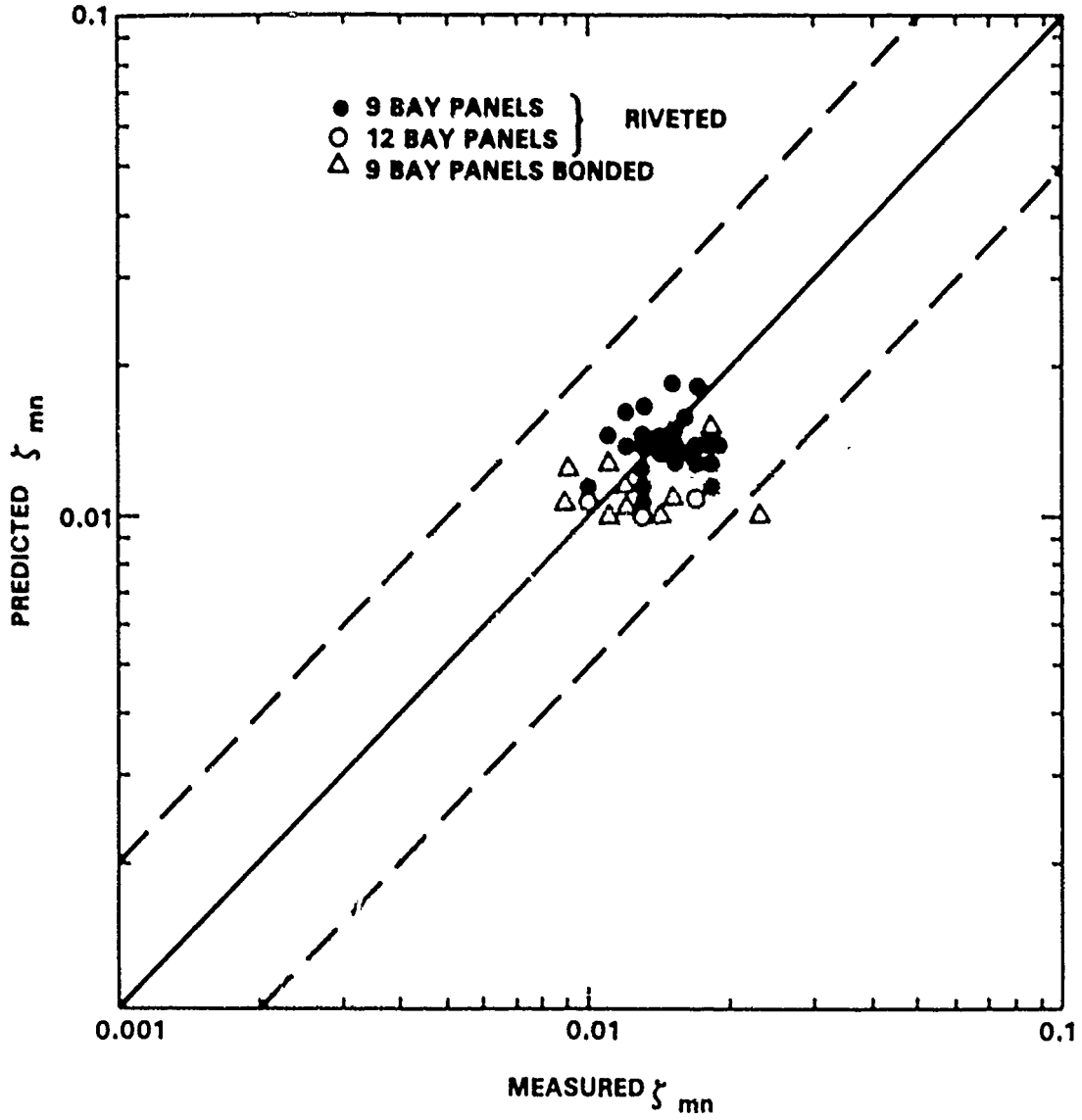


FIGURE 17. COMPARISON OF MEASURED AND PREDICTED DAMPING

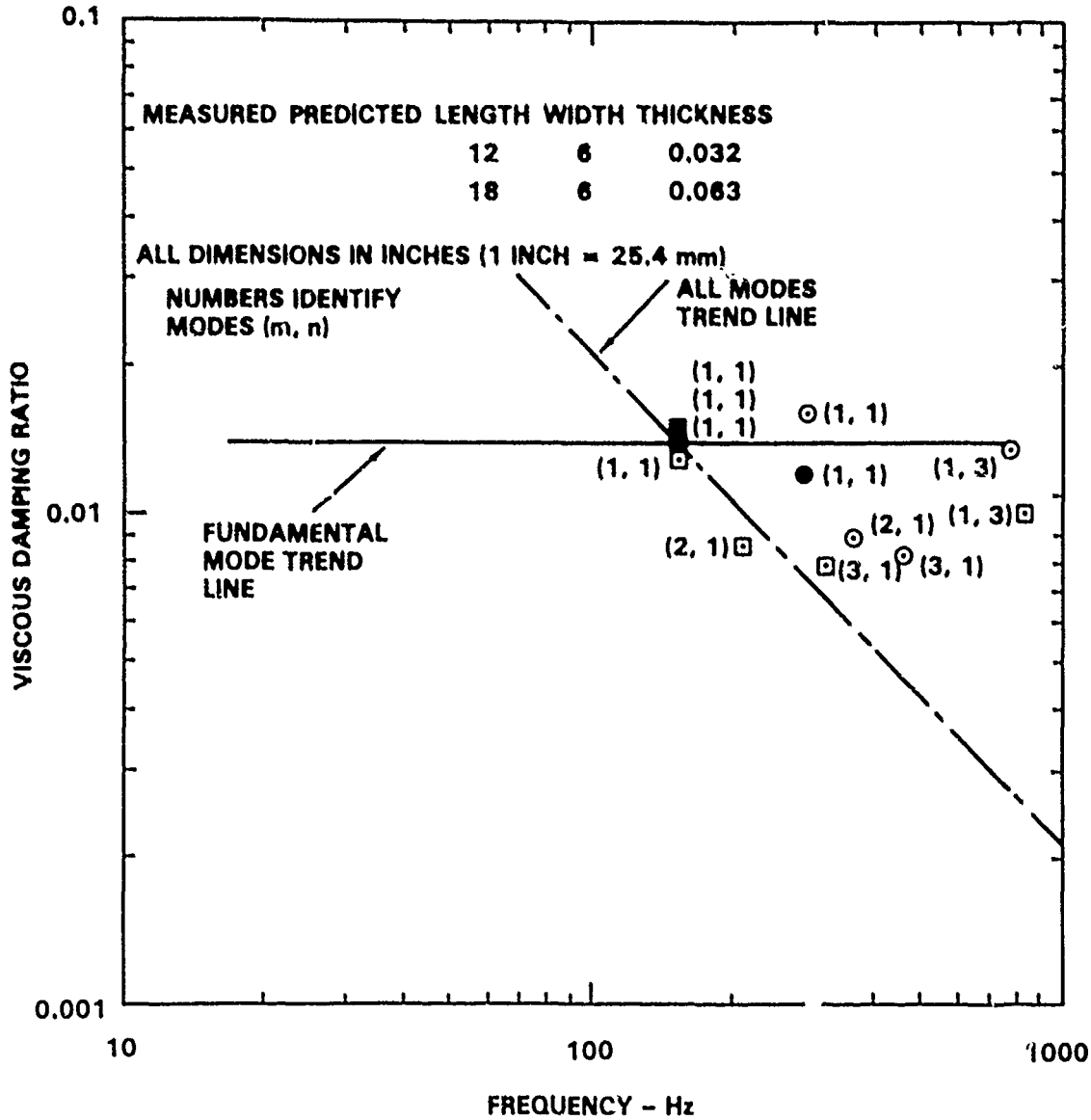


FIGURE 18. COMPARISON OF MEASURED AND PREDICTED DAMPING OF RIVETED MULTI-BAY ALUMINUM PANELS WITH PREDICTIONS FOR HIGHER MODE DAMPING.

The predicted fundamental mode damping was in reasonable agreement with the measured damping and the horizontal fundamental mode trend line at a viscous damping ratio of 0.015. The inverse frequency trend line from Figure 2 is also included for comparison purposes. It has been labelled the all modes trend line since it is suspected that some higher mode damping may also be included in Figure 2.

There is a large amount of damping data available in literature for the fundamental mode of stiffened panels but not for the higher panel modes, for the reasons already discussed in this paper. Scatter is present in the measured damping data that cannot be explained by theory alone. It is reasonable to assume that the mechanisms responsible for producing the scatter in the fundamental mode damping will produce a comparable change in the higher mode damping. A great benefit can be gained, if it is possible to predict the damping in the higher order panel modes from the fundamental mode damping. Sonic fatigue is moving towards adopting multimodal analysis, especially for composites. The approach used is to first subtract out the estimated friction and material damping from the measured fundamental mode damping, ratio the remaining damping on the basis of equation (5) and reintroduce the friction and material damping. Thus, the resulting expression for the viscous damping ratio, ζ_{mn}, for the m,nth mode is simply

$$\zeta_{mn} = (\zeta_{11} - \zeta_M - \zeta_{Fl}) \frac{f_n}{f_1} \cdot \frac{1}{m^2 n^2} + \zeta_M + \zeta_F \qquad (10)$$

where ζ_{11} is the measured fundamental mode viscous damping ratio and ζ_{Fl} is the contribution from rivet line friction damping in the fundamental mode. Thus, only the frequency and mode number of the higher mode need to be known, in addition to the fundamental mode data, in order to predict the higher mode damping.

The degree of correlation achieved between the predicted and measured higher mode data is illustrated in Figure 19 for the stiffened composite honeycomb panels. No friction damping was assumed in the analysis. Also, a material viscous damping ratio of 0.008 and zero were used for the Kevlar and graphite/epoxy panels, respectively. The correlation appears to be reasonable. There is a suggestion of the presence of some friction damping in the ultra-high modulus graphite/epoxy panel damping data. The amount of the friction damping is comparable to that predicted by equation (1). The presence of friction damping in the Kevlar panels is probably masked by the value assumed for the material damping. Some panel mounting problems were encountered with the intermediate modulus graphite/epoxy honeycomb panels that affected the measured fastener line dynamic strains and, it is suspected, also reduced the friction damping. This problem was corrected in the design of the other composite honeycomb panels. The reasonable correlation achieved in predicting the higher mode damping in the composite honeycomb panels, tends to validate the use of equations (8) and (10) for predicting the damping in the higher order modes of other types of stiffened panels, pending future experimental verification.

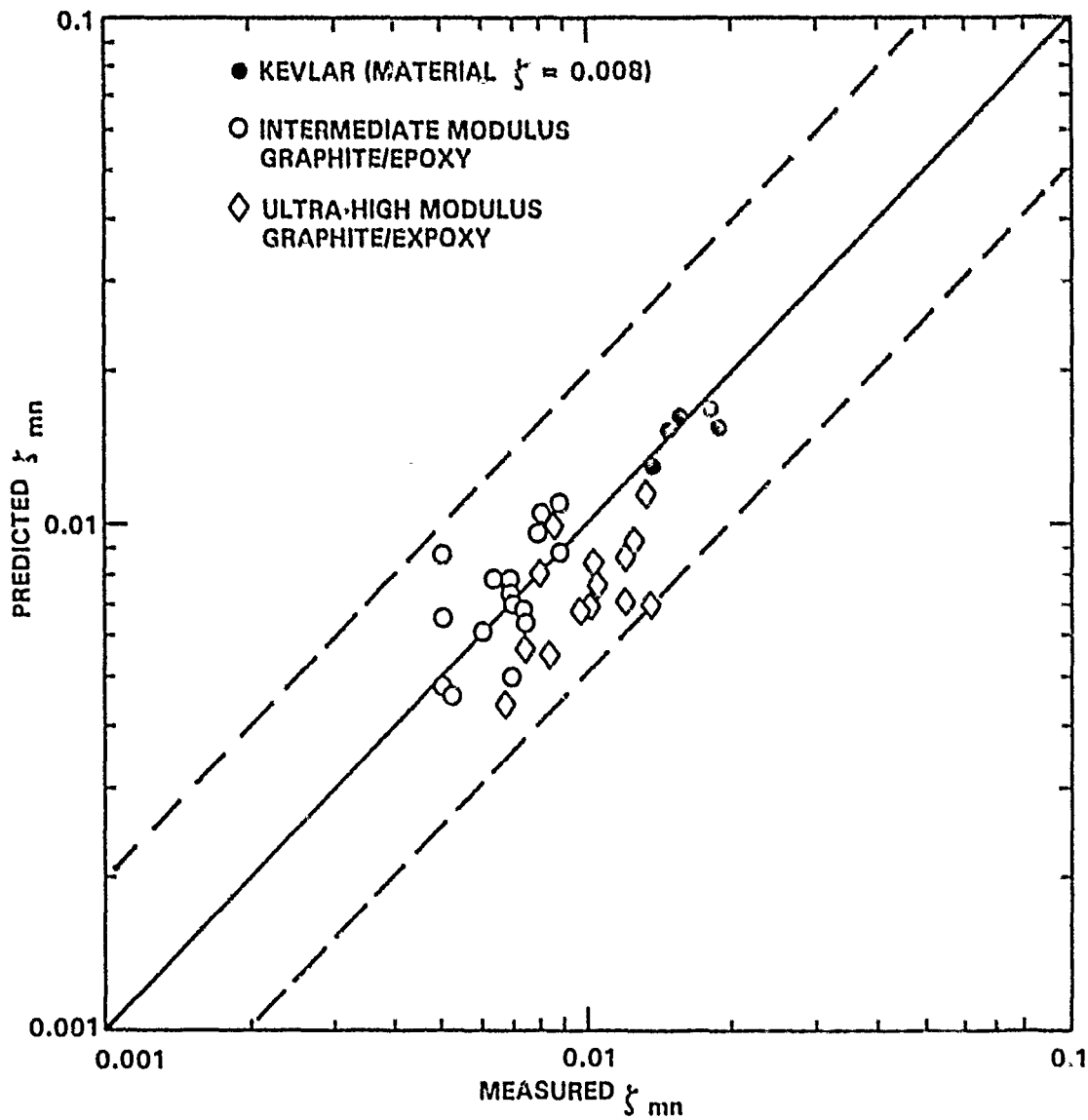


FIGURE 19. HIGHER MODE DAMPING PREDICTED FROM FUNDAMENTAL MODE DAMPING.

CONCLUSIONS

The fundamental mode viscous damping ratio is constant, independent of the resonant frequency, for a given stiffened panel design. Methods have been developed that can be used to predict the damping in stiffened panels with reasonable confidence. The methods have been verified against test data and a variety of stiffened metal and composite panels including honeycomb panels. Additional confirmation is required for the higher order modes of riveted metal panels.

REFERENCES

1. May, J.A., "Experimentally Determined Damping Factors", Symposium on Acoustic Fatigue, AGARD-CP-113, May 1973.

2. Thomson, A.G.R. and Lambert, R.F., "Acoustic Fatigue Design Data", AGARD-AG-196 - Part III, December 1973.

3. Rudder, F.F. and Plumblee, H.E., "Sonic Fatigue Design Guide for Military Aircraft", AFFDL-TR-74-112, May 1975.

4. Clarkson, B.L., "Stress in Skin Panels Subjected to Random Acoustic Loading", AFML-TR-67-199, June 1967.

5. Ungar, E.E., "The Status of Engineering Knowledge Concerning the Damping of Built-Up Structures", Journal of Sound and Vibration, Vol. 26, No. 1, 1973.

6. Mead, D.J., "Prediction of the Structural Damping of a Vibrating Stiffened Plate", AGARD-CP-277, October 1979, p. 2-1.

7. Mead, D.J., "The Effect of Certain Damping Treatments on the Response of Idealized Aeroplane Structures Excited by Noise", AFML-TR-65-284, August 1965.

8. Maidanik, G. and Ungar, E.E., "Panel Loss Factor Due to Gas-Pumping at Structural Joints", NASA CR-854, November 1967.

9. Beranek, L.L.,"Noise and Vibration Control", McGraw Hill, 1971.

10. Kerwin, E.M., "Acoustic Damping Mechanisms", WADC-TR-59-676, March 1961.

11. Soovere, J., "Dynamic Properties of Graphite Fibre Honeycomb Panels", AIAA Dynamics Specialists Conference, Williamsburg, Virginia, March 1973, Paper No. 73-326.

12. Adams, R.D., Fox, M.A.O., Flood, M.J.L, Friend, R.J. and Hewitt, R.L., "The Dynamic Properties of Unidirectional Carbon and Glass Fiber Reinforced Plastics in Torsion and Flexure", Composite Materials, Vol. 3, October 1969, p. 594.

13. Wright, G.C., "The Dynamic Properties of Fiber Reinforced Beams", ISVR Technical Report 51, September 1971.

14. Soovere, J., "Effect of Acoustic/Thermal Environments on Advanced Composite Fuselage Panels", Journal of Aircraft, Volume 22, No. 4, April 1985.

15. Soovere, J., "Dynamic Response and Acoustic Fatigue of Stiffened Composite Structures", Proceeding of the Second International Conference on Recent Advances in Structural Dynamics, M. Petyt and H.F. Wolfe, Editors, University of Southampton, 9-13 April, 1984, p. 775.

16. Ballentine, J.R., Rudder, F.F., Mathis, J.T. and Plumbless, H.E., "Refinement of Sonic Fatigue Structural Design Criteria", AFFDL-TR-67-156, January 1968.

17. Jacobson, M.J., "Sonic Fatigue Design Data for Bonded Aluminum Aircraft Structures", AFFDL-TR-77-45, June 1977.

18. Rudder, F.F., "Acoustic Fatigue Resistance of Internal Airframe Structure", AFFDL-TR-71-107, July 1971.

19. Clarkson, B.L., "Extraction of the Response of Box Type Structures to Acoustic Loading", Symposium on Acoustic Fatigue, AGARD-CP-113, May 1973.

20. Baird, E.F., Bernstein, M. and Arcas, N., "Sonic Fatigue Failure Mechanisms in Potential Space Shuttle Orbiter Designs", AIAA/ASME/SAE 15th Structures, Structural Dynamics and Materials Conference, Las Vegas, Neveda, April 17-19, 1974.

21. Schneider, C.W., "Acoustic Fatigue of Aircraft Structures at Elevated Temperatures", AFFDL-TR-73-155 - Part I, March 1974.

22. Srinivasan, A.V., Cassenti, B.N. and Cutts, D.G., "Characteristics of Dry Friction Damping", Vibration Damping 1984 Workshop Proceedings, Dr. Lynn Rogers, Editor, AFWAL-TR-84-3064, p. I-3.

23. Mead, D.J., "The Damping, Stiffness and Fatigue Properties of Joints and Configurations Representative of Aircraft Structures", NADC-TR-59-676, March 1961, p. 235.

24. Ungar, E.E., "Energy Dissipation of Structural Joints, Mechanisms and Magnitude", FDL-TDR-64-98, August 1964.

25. Soovere, J., "Dynamic Response of Acoustically Excited Stiffened Composite Honeycomb Panels", Ph.D. Thesis, Institute of Sound and Vibration Research, Southampton University, England, March 1984.

26. Soovere, J., "Random Vibration Analysis of Stiffened Panels with Beveled Edges", to be published in the AIAA Journal of Aircraft, 1986.

Implementation of Modal Strain Energy Method Using MSC/NASTRAN and Post-processing Utility Programs

Norman K. Frater

International Business Machines Corporation
General Products Division
San Jose, California

ABSTRACT

The modal strain energy method has been semi-automated by using a set of post-processing programs with MSC/NASTRAN. These programs extract, tabulate and reorder modal strain energy data from MSC/NASTRAN eigenvalue analysis runs. The modal strain energy data is then interpolated mode by mode to find iterative solutions for frequency and modulus using viscoelastic material properties data stored in a database. Damped frequency and structural loss factor for each mode are tabulated and formatted into loss factor (TABDMP1) and eigenvalue shift factor (DMI) tables for subsequent MSC/NASTRAN dynamic response analysis. An MSC/NASTRAN DMAP alter is presented which shifts the eigenvalues computed for a fixed viscoelastic modulus to the damped eigenvalues using the DMI shift factors. Comparison of modal frequency response analysis to direct frequency response analysis was made for a cantilever beam example with a constrained layer damper using 3M ISD-112 viscoelastic material.

Frequency response plots agree very well for 0°, 50° and 100° F cases over a frequency range of 10 to 10,000 Hz including 13 structural modes. The addition of frequency shift factors to modal frequency response improved agreement in resonance frequencies by a factor of twelve and in resonance amplitudes by a factor of two. The mean differences in resonance frequencies and amplitudes were 0.5 percent and 10.3 percent, respectively, over the entire temperature and frequency range.

Introduction

The finite element method provides a powerful evaluation tool for viscoelastic (VE) material damping designs. The modal strain energy method presented by Johnson and Kienholz[1,2] is an efficient means of predicting structural frequency and loss factor. In practice a series of finite element runs must be made to investigate the modal frequency and strain energy ratios as a function of VE material modulus. Plotting modal strain energy ratio vs. VE material modulus shows clearly the range of VE material modulus needed to obtain effective damping. If the strain energy ratio is low or the peak occurs in a range in which no VE material can be found, then the damping design is modified and the analysis process begins again.

To evaluate the use of a specific VE material using the modal strain energy method requires iteration and interpolation between the finite element results and the VE material properties. The procedure presented here improves the basic modal strain energy process by linking the MSC/NASTRAN finite element results and a VE materials database using a set of IBM internally developed post-processing programs[5]

The link is divided into three logical programs shown in Fig. 1 which perform the following functions:

1. DAMPED: extracts modal frequency and strain energy data from several MSC/NASTRAN eigenvalue analysis runs in which VE modulus is varied.

2. DAMPRO: reorders data extracted from the eigenvalue runs into a table of frequency and strain energy ratio vs. VE material modulus and checks for correct tracking of modes.

3. DAMPIT(a): interpolates frequency and strain energy data, finds iterative solution for frequency using VE material data, computes modal loss factors.

4. DAMPIT(b): formats appropriate MSC/NASTRAN data tables defining modal loss factors and eigenvalue frequency shift factors for subsequent dynamic response analysis.

An MSC/NASTRAN DMAP alter is presented in Fig. 2 which allows the iterative solution for damped frequencies to be substituted into MSC/NASTRAN for modal frequency or transient response analysis. With the iterative solutions for modal frequency as well as modal loss factor inserted into MSC/NASTRAN, a definite improvement in response prediction using the strain energy method can be expected.

The goals of the present study were to (1) evaluate the effectiveness of the post-processing programs for a simple problem which exhibits a variety of modes, (2) determine weaknesses of the implementation to direct further development, and (3) compare results against the direct frequency response method in MSC/NASTRAN over a wide range of temperature and frequency.

Example

A steel cantilever beam 100 by 10 by 1 mm was used for this study. A damper made from 0.5 mm of 3M-ISD-112 viscoelastic material and a 0.25 mm steel constraining layer covered 90 percent of the beam as shown in Fig. 3a. An MSC/NASTRAN finite element model was constructed using two layers of offset CQUAD4 elements and one layer of CHEXA elements[1] as shown in Fig. 3b. A grid mesh of 3 by 11 was used, resulting in 300 degrees of freedom (base grid points and all Z rotations constrained). Using a viscoelastic shear modulus of 10 N/mm^2, the computed MSC/NASTRAN eigenvalues are:

No.	Frequency, hz	Description
1	81.0	1 bending
2	565.5	2 bending
3	747.4	1 transverse
4	1211.5	1 torsion
5	1402.4	3 bending
6	2598.0	4 bending
7	3618.0	2 torsion/transverse
8	4188.0	5 bending
9	4806.0	2 transverse/torsion
10	6141.0	6 bending
11	6318.0	3 torsion
12	8390.0	7 bending
13	9253.0	4 torsion

This model exhibits a variety of modes and exhibits coupling between torsion and transverse bending modes due to the asymmetry of the damping treatment. All modes can therefore be excited by applying a dynamic force to the corner of the beam tip shown in Fig. 4. This dynamic force is used to compare modal (strain energy method) frequency response with direct frequency response analysis (the benchmark).

Discussion

Step 1 - Eigenvalue Analysis

The first step is the modal strain energy procedure (Fig. 1) is to make a series of eigenvalue runs in which the strain energy in the VE material (CHEXA elements) and the total strain energy is calculated for each mode. Each run is made using a different VE material modulus in logarithmic steps through approximately three orders of magnitude. The modulus range must be selected considering the intended VE material properties, the structural frequencies and the temperatures of interest:

Minimum modulus: lowest modulus material at highest temperature and lowest frequency

Maximum modulus: highest modulus material at lowest temperature and highest frequency

Step 2 - Extraction of Data

After each eigenvalue run is made, the modal frequency and strain energy data is extracted by the first utility program called "DAMPED." This program extracts data from the output print file of MSC/NASTRAN by scanning for job and run descriptions, eigenvalues, eigenvectors and strain energies using overlaid PL/I structure variables. FORTRAN programs could also be used to read "OUTPUT2" files generated by MSC/NASTRAN.

The data is formatted into a sequential file as shown in Fig. 5. It is important to append to this data the correct VE material modulus and units that were used for the eigenvalue run. In order to correctly track modes in Step 3, it is also necessary to extract subsets of each eigenvector. The number of displacement components selected should not be less than the number of modes used for damping analysis and they should be distributed to differentiate the types of modes present. Twelve components shown in Fig. 6 were selected for the example beam to differentiate higher order bending modes, torsion modes, transverse modes and shear modes of the constraining layer.

Step 3 - Reordering of Data

The sequential data extracted by "DAMPED" from several MSC/NASTRAN eigenvalue runs must be collected into table form, then reordered by ascending VE modulus and by mode type. The initial strain energy table formatted by the second utility program called "DAMPRO" is shown in Fig. 7. The first task then is to shift the table columns into ascending VE modulus order. This means that the order of eigenvalue runs made and extracted by "DAMPED" is unimportant. If additional runs need be made to better define a particular region, they can be made at any time, extracted by "DAMPED" then reordered by "DAMPRO."

The second and hardest task of reordering is to ensure that each row represents a single mode. This is harder than may first appear because different types of modes are affected differently by VE material modulus. The shift in frequency of thirteen modes with modulus is shown in Fig. 8. Since MSC/NASTRAN sorts modes by frequency, it is obvious that some modes shift order between VE modulus values of 0.1 and 250 N/mm^2. Tracking modes is further complicated by changes in mode shapes across the wide variation of VE material modulus. An example is shown in Fig. 9 where the fifth bending mode has clearly changed at low VE modulus. By examining eigenvectors, one can see that in fact all mode shapes change, even if only subtly, across such a wide range of VE modulus. This fact has implications to dynamic response prediction accuracy in step 5 as well as to the mode tracking task now at hand.

Two other problems must be addressed by the mode tracking algorithm. Often new modes involving only shearing of the constrained layer damper appears at very low VE modulus (see "invasion" in Fig. 8). Because the strain energy ratio approaches unity for these modes, they are probably well damped and thus unimportant in dynamic response prediction. It is the invasion of the new modes that is problematic since the important structural modes we desire to track have been shifted upward in sequence and could be lost from our tracking table.

The second problem involves coupling of modes such as the second torsion and second transverse bending modes. In the VE modulus range of 0.6 to 1.0 N/mm^2, these modes track as shown in Fig. 8 according to frequency (an additional eigenvalue run was made at a VE modulus of 0.8 N/mm^2 for verification). The mode shapes shown in Fig. 10 show a dramatic change in this modulus range such that an apparent crossover in mode shape occurs. The second torsion/second transverse bending mode at high VE modulus looks like the second transverse bending/second torsion mode at low VE modulus. With such large

changes in mode shape, the dynamic response prediction for these modes may be inaccurate. Examination of the strain energy ratio vs. modulus for these modes in Fig. 11 shows a dramatic increase toward unity for both modes. Thus in VE modulus ranges where eigenvalues and mode shapes are rapidly changing, one must be cautious in accepting dynamic response predictions. This is one area where the larger expense of using the *direct* response method is warranted.

Mode Tracking Algorithm

Considering the above difficulties -- namely, (1) changing mode shapes, (2) invasion of damper shear modes at low VE modulus, and (3) apparent crossover of coupled modes -- the following mode tracking algorithm has been employed.

First of all, the VE modulus columns of the initial strain energy table (Fig. 7) are arranged into ascending order; i.e., 0.12, 0.25, 0.6, 1, 3, 10, 50 and 250. Secondly, each of the tracking eigenvectors extracted from MSC/NASTRAN by "DAMPED" are normalized to unit length.

The mode tracking algorithm uses dot products of these unit tracking vectors as a measure of how well a given mode for one VE modulus agrees with a candidate matching mode for another VE modulus. If the modes are identical, then the dot product must be unity (by definition of unit length). Considering that MSC/NASTRAN may normalize a given mode with a (+) or (-) sense, we must examine the absolute value of the dot products. Thus, two modes which are indeed different will have an absolute value of their dot product smaller than 1 (they will not be zero because subsets of orthogonal eigenvectors do not retain orthogonality).

The only definitive statement one can and must make is that the highest absolute valued dot product of one tracking vector with a set of other tracking vectors is the best match of mode shapes. This assumption is the basis for the mode tracking algorithm.

The algorithm is illustrated in Fig. 12. Because of the likely invasion of damper shear modes at low VE modulus, the algorithm will always start with the highest VE modulus column and work downwards. The modes in the next to the highest VE modulus column are first matched to the order of modes in the highest VE modulus column. Then the modes in the next lower VE modulus column are matched to the modes in the next to the highest VE modulus column and so on until the lowest VE modulus column

is reached. The reordered strain energy table is shown in Fig. 13. Notice that several of the modes have shifted sequence

Check of Mode Tracking

It is likely that the highest modes will not track as well as lower modes because of (1) changing mode shapes, and (2) invasion of damper shear modes at lower VE modulus. Also in the case of coupled modes mentioned earlier, the mode shape can change rapidly with VE modulus and may be difficult to track. One needs to have an independent check of how well the mode tracking algorithm has worked. Figure 14 shows an evaluation of mode tracking using two measurements of proper tracking:

1. frequency ratio = frequency for mode i at VE modulus j divided by frequency for mode i at VE modulus j + i.

2. dot product = dot product of tracking vector for mode i at VE modulus j with tracking vector for mode i at VE modulus j + i.

   If the mode has been tracked properly, both frequency ratio and dot product will be nearly unity. Arbitrary clipping levels can be used to flag modes which are questionable and to count the lowest number of "error-free modes" as shown in Fig. 14. Poor tracking can be improved by adding new eigenvalue runs at intermediate VE modulus values, but always is a warning of rapidly changing modes.

Step 4 - Damping Iteration

The reformatted strain energy table (Fig. 13) can be readily interpolated to give mode frequency or strain energy ratio for any intermediate value of VE material modulus. No additional finite element runs need be made to evaluate the damping of the structure for any temperature and any VE material. This is accomplished by the utility program called "DAMPIT" shown in Fig. 1 which iterates to a convergent solution for each mode between the finite element data and VE material property data.

The VE material properties database can use any analytical form to describe the VE material modulus and loss factor as functions of frequency and temperature. In fact, many different forms may co-exist in

the database depending on the source of the properties data. The most general form is a tabulation of the reduced frequency format(8X10) as shown in Fig. 15a. It has been found that about seven points are adequate to define the alpha T (temperature shift factor) vs. temperature as well as the modulus and loss factor vs. reduced frequency (alpha T times frequency). all points are read from the standard reduced frequency plot as shown in Fig. 15b. Third order Lagrangian polynomial interpolation is used in program "DAMPIT" to interpolate first $\log_{10}$(alpha T) vs. temperature, then $\log_{10}$(modulus) and (loss factor) vs. $\log_{10}$ (reduced frequency).

When executing program "DAMPIT," the user is asked to select a material number from the database and select a starting temperature for analysis. The iteration strategy shown in Fig. 16 is to reach convergence to frequency and VE material modulus for each mode, then calculate structural loss factor. The structural loss factor for each mode is the product of the strain energy ratio interpolated from the reformatted strain energy table (Fig. 13) and the material loss factor obtained from the material database.

$$\eta^{(r)} = \eta_v \left[V_v^{(r)} / V^{(r)} \right]$$

where $\eta^{(r)}$ is the structurrl loss factor for the rth mode, η_v is the material loss factor at the frequency of the rth mode and temperature selected, and $V_v^{(r)} / V^{(r)}$ is the ratio of strain energy in the viscoelastic material to the total strain energy for the rth mode.[1]

After all modes have been processed, the user may select another temperature for analysis or select another material from the database. All results for a given material are summarized in a table of frequency and structural loss factor for each mode vs. temperature as shown in Fig. 17. These tables may be the end result of analysis because damping effectiveness can be evaluated for any material in the database and across any range of temperature. Frequency and structural loss factor are plotted vs. temperature in Figs. 18 and 19. Of course one must not extrapolate from the tabulated finite element data (Fig. 13) or VE material data (Fig. 15), so an extrapolation error count is needed to determine the relative validity of the derived data. Occasionally, a negative value of structural loss factor is computed which is an interpolation error! This could occur if a given row of the reformatted strain energy table (Fig. 13) does not represent a single mode or if the mode shape changes drastically such as for the coupled second torsion/second tangential modes (see Figs. 11 and 19).

Discussion

Finally, two types of data cards for subsequent MSC/NASTRAN modal transient or frequency response analysis are prepared by "DAMPIT." The tabulated damping table "TABDMP1" and a direct input matrix "DMI" which contains frequency shift factors are both prepared for each VE material and temperature analyzed. Examples of these data cards are shown in Fig. 20. The frequency shift is actually accomplished by a three-statement DMAP alter in the MSC/NASTRAN modal transient or frequency response procedure. The MSC/NASTRAN module called "LAMX" shifts each computed modal frequency according to the following relationship.[9]

$$f_{new} = f_{old} * (1 + \text{shift factor})$$

Step 5 - Dynamic Analysis

One of the recognized deficiencies of using modal dynamic analysis is that the eigenvalues and eigenvectors are calculated using a stiffness matrix which is constant with respect to frequency.[1] Thus the eigenvalues and eigenvectors are correct for at most one mode. Even though the calculated structural loss factors are input to MSC/NASTRAN on "TABDMP1" data cards, the eigenvalues and eigenvectors are in error.

The greater the difference between the assumed constant VE modulus used for modal analysis with the actual VE modulus vs. frequency, the greater is the error in eigenvalues and eigenvectors. One of these errors can be eliminated by the use of the LAMX module in MSC/NASTRAN as mentioned earlier. By knowing the exact eigenvalues extracted by MSC/NASTRAN for a fixed "reference" VE modulus, one can calculate appropriate factors to shift these eigenvalues to the iterative solution for damped frequencies. When one executes an MSC/NASTRAN modal dynamic analysis run, the eigenvalues are computed using the fixed reference VE modulus. But then, MSC/NASTRAN uses the DMAP alter and DMI factors to shift these frequencies to match the damped frequencies.

Finally, MSC/NASTRAN computes the modal dynamic response using the shifted eigenvalues. The only error left is that the eigenvectors have been computed for the fixed VE modulus. Thus the reference VE modulus must still be thoughtfully chosen to most nearly represent the actual range of VE modulus over frequency and temperature.

In preparing the TABDMP1 and DMI tables, careful attention must be paid to the ordering of the modes. Since a reordering step was necessary to prepare the table used for interpolation (Fig. 13), the order of

modes (in general) no longer matches the original order extracted by MSC/NASTRAN (Fig. 7). One must keep track of this correspondence so that the DMI factors (Fig. 20) apply to the original order of modes extracted by MSC/NASTRAN using a fixed "reference" VE modulus. On the other hand, the tabulation of modal loss factors in the TABDMP1 table (Fig. 20) must appear in ascending damped frequency order to be interpolated by MSC/NASTRAN modal dynamic analysis. It is wise to ensure that the second listing of the eigenvalue table -- the one written by the DMAP after following the eigenvalue shift -- matches the frequencies tabulated in the modal damping table TABDMP1 (Fig. 20).

The reference VE modulus should be chosen considering the temperature and frequency range of interest for dynamic analysis. Figure 21 shows the variation of modulus with frequency and temperature for 3M ISD-112 VE material. A temperature range 0° to 100° F and a frequency range 10 to 10,000 Hz has been selected to perform modal frequency response. Thus, a median shear modulus of 10 N/mm^2 was chosen for the reference VE modulus.

Modal frequency response analysis was performed using the force and displacement definitions shown in Fig. 4. The TABDMP1 modal loss factor and DMI eigenvalue shift factor tables produced by DAMPIT for 0°, 25°, 50° (Fig. 20), 75° and 100° F were inserted into the MSC/NASTRAN modal frequency response deck. Response was computed from 10 to 10,000 hz as shown in Fig. 22. The frequency and damping shift with temperature can be seen in the second bending mode (450 to 700 hz). Thus the computed damped frequencies and loss factors have been properly incorporated into the modal dynamic response analysis.

Comparison to Direct Frequency Response

Because the variation of VE modulus with frequency is accounted for in the direct frequency response method in MSC/NASTRAN,[4] it is a benchmark by which the approximate modal strain energy method can be compared. Furthermore, since the identical finite element model of the damped beam, the same mathematical description of the VE material from the database and the same finite element program is used, this comparison is valid. On the other hand, the validity of the finite element model in representing the actual damped cantilever beam description given in Fig. 3a is not considered and is not related to the purpose of this paper. The finite element model is a valid mathematical model used only to compare two analysis techniques.

For comparison with modal analysis using frequency shifts, MSC/NASTRAN direct frequency response analysis was performed using only the 0°, 50° and 100° F cases. The real and imaginary parts of the shear modulus for 3M ISD-112 VE material were computed from the VE material database and entered on DMI data cards[4] as shown in Fig. 23. Two other response methods were also compared: (1) modal analysis usig only the calculated loss factors, and (2) modal analysis using adjusted loss factors suggested by Johnson and Kienholz.[1,2] These four frequency response plots are compared in Figs. 24 to 26 for the three temperatures. For each temperature modal analysis with frequency shifts shows excellent agreement to the direct method. Modal analysis with only calculated loss factors appears somewhat different due to frequency errors, especially for the 0° and 100° F cases i which the actual VE material modulus varies significantly from the chosen reference modulus of G = 10 (see Fig. 21). Modal analysis with adjusted loss factors differs significantly from the other methods at 0° and 100° F due to loss factor errors caused by the large adjustments.

To quantify these comparisons, refined frequency response analyses were performed around each resonance peak. The delta frequency to resonant frequency ratio was chosen small enough to guarantee a peak amplitude error of less than 0.2 percent. The quantitative comparisons are tabulated in Figs. 27 to 29 for the three temperatures. These tables can be further condensed by computing mean values of absolute errors for each column of frequency and amplitude. the final condensed comparison is shown in Fig. 30 along with a CPU time comparison as well. The following observations can be made:

1. As expected, all modal methods have best agreement at 50° F where the reference VE modulus agrees most closely with the actual VE modulus.

2. The modal method with calculated loss factors and frequency shifts shows the best agreement with direct frequency response method.

3. Inclusion of frequency shifts improved agreement of the modal method to the direct method:

    a. 12 times better in frequency
    b. 2 times better in amplitude
    c. 5 times better in number of peaks (only one resonance peak missing compared with four extra and one missing peaks)

Discussion

4. The modal method with adjusted loss factors did not improve agreement over the modal method with only calculated loss factors.

5. The modal method used seven times less CPU time than the direct method.

Conclusions

The development of a set of utility programs as described in this paper is not a trivial undertaking. However, the benefits of having a semi-automated implementation of the modal strain energy method are tremendous. The following specific conclusions can be drawn from this work:

1. Post-processing utilities are valuable to extract, reorder and tabulate modal strain energy data from MSC/NASTRAN.

2. Iterative technique is successful to reach solution between finite element data and viscoelastic material properties (both interpolated).

3. Modal frequency response using tabulated eigenvalue shift factors and modal loss factors agrees very well with direct frequency response using MSC/NASTRAN.

4. The use of eigenvalue shift factors has improved agreement to direct frequency response by a factor of 12 for frequencies and a factor of 2 for amplitudes of resonant peaks.

5. The modal strain energy method is very cost effective compared to direct response analysis and gives valuable intermediate design data not available using the direct method.

Further Work

Three of the weaknesses of the semi-automated implementation of the modal strain energy method described here are mode tracking, selection of the reference viscoelastic modulus and interpolation errors for strain energy ratio. It is recommended that further work be directed to the following areas:

1. Develop better ways to track modes across large range of viscoelastic modulus considering:

a. changing mode shapes
b. invasion of new modes at low viscoelastic modulus
c. apparent crossover of coupled modes

2. Determine optimal reference modulus for a given material and temperature to achieve best agreement to direct frequency response method.

3. Determine the most accurate methods to use for interpolating tabulated finite element frequencies and strain energy ratios, considering the rapid changes possible in certain viscoelastic modulus ranges.

Bibliography

1. Johnson, C. D., and D. A. Kienholz, "Finite Element Prediction of Damping in Structures with Constrained Viscoelastic Layers,", *AIAA Journal,* Vol. 20, No. 9 (Sept. 1982).

2. Johnson, C. D., D. A. Kienholz, E. M. Austin, and M. E. Schneider, "Design and Analysis of Damped Structures Using Finite Element Techniques," CSA Engineering, Inc., (Palo Alto, CA, circa 1984).

3. Ungar, E. E., and E. M. Kerwin, Jr., "Loss Factors of Viscoelastic Systems in Terms of Energy Concepts", *Acoustic Society of America,* Vol. 34 (July 1962) pp. 954-7.

4. Joseph, J. A. (Ed), *MSC/NASTRAN Applications Manual,* MacNeal-Schwendler Corp., Vol. I, Sec. 2.11 (Los Angeles, CA., June 1983).

5. Frater, N. K., and T. B. Loutzenheiser, "Modeling Viscoelastic Constrained Layer Damping Treatments Using MSC/NASTRAN," 8th IBM Finite Element Methods Conference, IBM Corporation, General Technology Division, Endicott, NY, (Sept. 27-29, 1983).

6. Wilke, P. S., "Direct Frequency Response Analysis with Viscoelastic Materials in MSC/NASTRAN," IBM Corporation, General Products Division, (San Jose, CA, Jan. 3, 1986).

7. Nashif, A. D., D. I. G. Jones, and J. P. Henderson, *Vibration Damping,* John Wiley & Sons (New York, 1985).

8. Rogers, L. C., "Graphical Presentation of Damping Material Complex Modulus, Proposed Standard," AFWAL/FIBA, Wright-Patterson AFB, Ohio, (Nov. 11, 1985).

9. McCormick, C. W. (Ed), *MSC/NASTRAN User's Manual,* MacNeal-Schwendler Corp. Vol. II, Sec. 5.4 "LAMX" (Los Angeles, Feb. 1981).

10. "Product Information: Scotchdamp SJ2015X Viscoelastic Polymer Types 110, 112, 113, 830 Material Damping Properties," Structural Products Department, 3M Corporation, St. Paul,

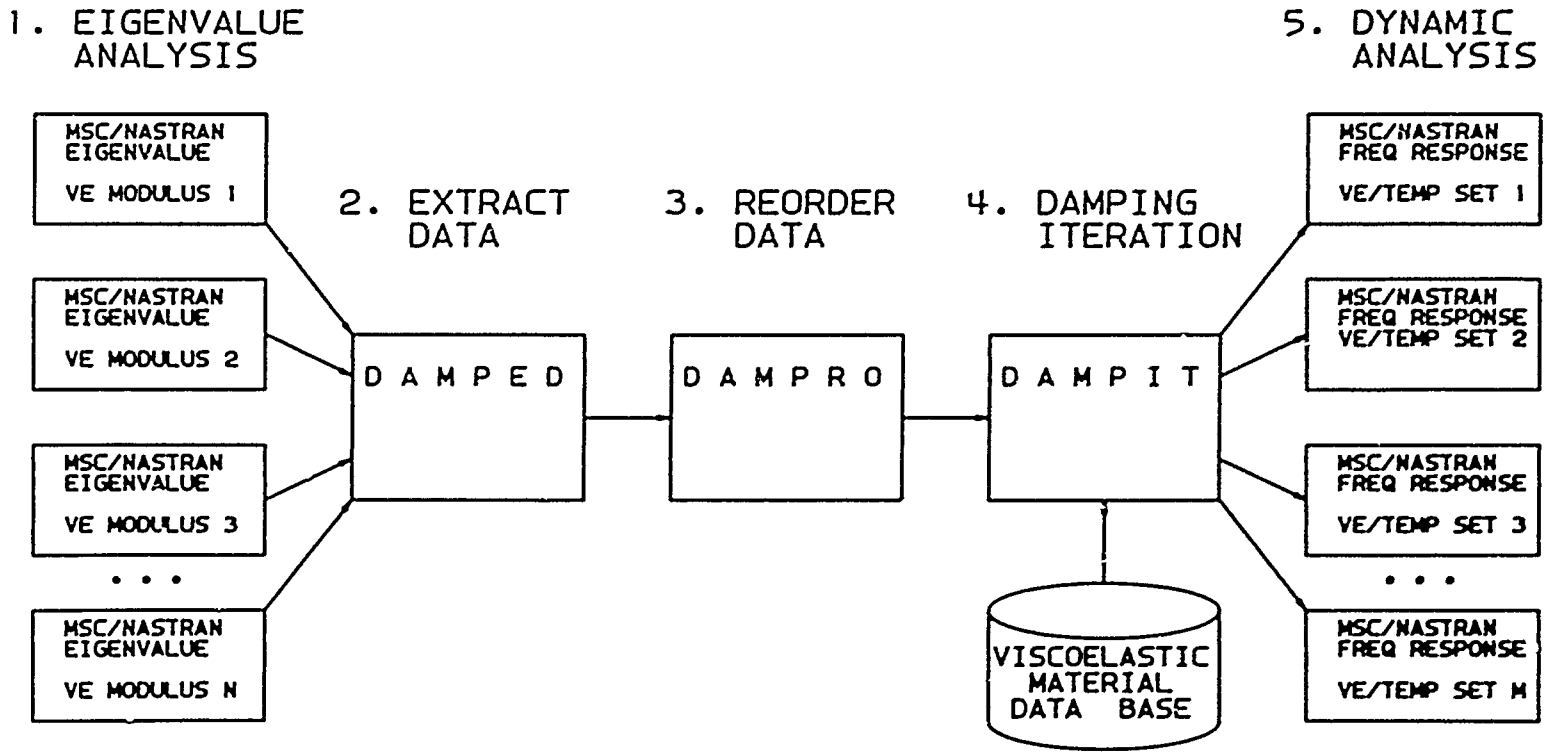


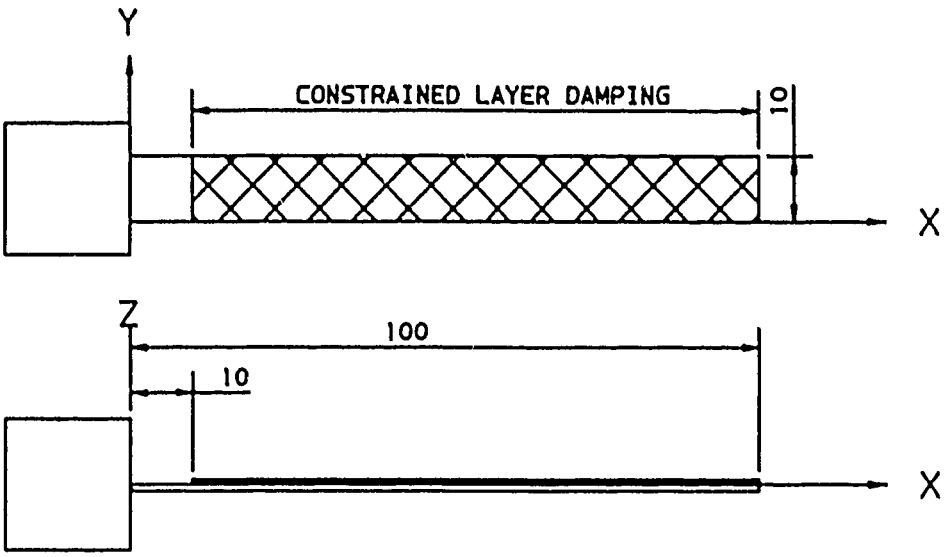
Figure 1 MODAL STRAIN ENERGY PROCESSING SEQUENCE

```
$-----------------------------------------------------------------------
$ ALTER TO SHIFT EIGENVALUES USING DMI TABLE FROM PROGRAM "D A M P I T"
$ INSERT ALTER AFTER NASTRAN   "READ . . . . . "
$                      AND     "OFP LAMA,OEIGS//$"
$ STATEMENTS IN DMAP PROCEDURE BEING USED.
$-----------------------------------------------------------------------
$ ALTER 429   - FOR MSC SOLUTION 30
$ ALTER 830   - FOR MSC SOLUTION 71
$ LAMX          "NAME"      ,LAMA/LAMB/0$ MODIFY EIGENVALUE TABLE
$ EQUIV         LAMB,LAMA/TRUE$  EQUIV LAMA TABLE TO MODIFIED LAMA TABLE
$ OFP           LAMA,OEIGS//$  PRINT MODIFIED EIGENVALUE TABLE
$ ENDALTER $
$-----------------------------------------------------------------------
$ REFERENCE MSC USERS MANUAL SECTION 5.4 FOR DESCRIPTION OF LAMX DMAP
$ MODULE.  DMI MATRIX CONTAINS DELTA FACTORS USED IN DMAP ALTER
$ TO CHANGE REFERENCE FREQUENCIES TO CALCULATED DAMPED FREQUENCIES:
$    MODIFIED FREQUENCY = REFERENCE FREQUENCY * (1.0 + DELTA)
$       NAME    MODE            DELTA
DMI     "NAME"  0       2       1       1               3       40
DMI     "NAME"  1       2       .049943
DMI     "NAME"  2       2       .2329187
DMI     "NAME"  3       2       .0168533
DMI     "NAME"  4       2       .0784683
DMI     "NAME"  5       2       .2862368

        . . .                   . . .
```

Figure 2 MSC/NASTRAN DMAP ALTER FOR SHIFTING EIGENVALUES

A. BEAM DIMENSIONS (NOTE: ALL DIMENSIONS IN MM)



B. FINITE ELEMENT MODEL

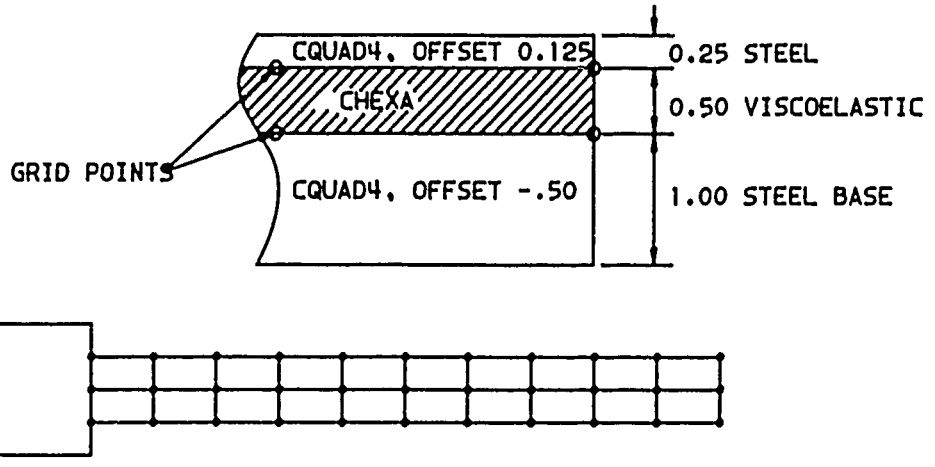


Figure 3 DAMPED CANTILEVER BEAM EXAMPLE

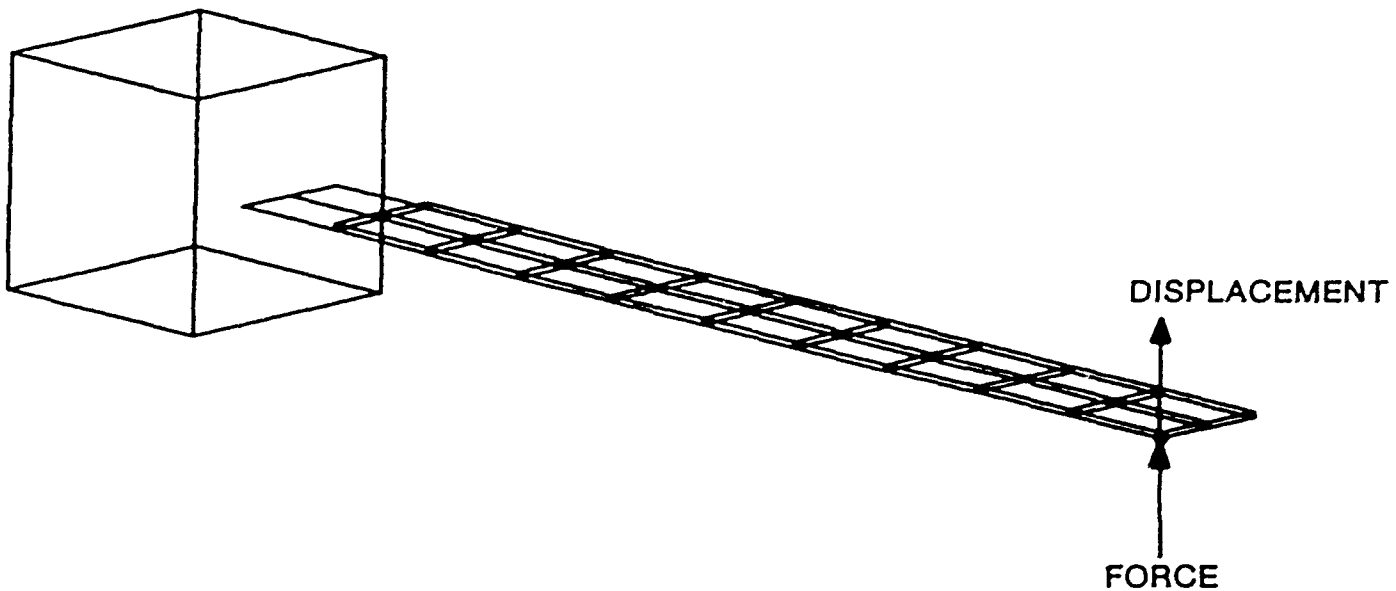


Figure 4 DYNAMIC RESPONSE FORCE AND DISPLACEMENT DEFINITION

```
1
IBM DAMPING POSTPROCESSOR (PGM=DAMPED, LEVEL 2.0, RELEASED 02/25/86)

NASTRAN JOB IDENTIFICATION --
  24 FEB 86 JOB EXECUTION DATE
  //BUH10     JOB (F332472,'D=E34,B=026,O=B64,A=CH15,L=300'),        JOB 2114
  TITLE = REFERENCE VISCOELASTIC MODULUS G=10.     N/MM 2
  SUBTT = CANTILEVER BEAM WITH CONSTRAINED LAYER DAMPING
  LABEL = MSC/NASTRAN SOL = 3

DAMPING MATERIAL IDENTIFICATION --
  SHEAR (G) MODULUS =  10.      NEWTON/MM**2

STRAIN ENERGY TABLE --
  MODE NUMBER  FREQUENCY(HZ)   STRAIN ENERGY    STRAIN ENERGY
                               RATIO (%)        MODE TOTAL
       1        81.01099        10.06082        2.11486E+05
       2        565.4978        24.11002        9.43175E+06
       3        747.4214        1.698758        3.74039E+07
       4        1211.478        2.447206        6.90292E+07
       5        1402.418        15.55614        5.37383E+07
       6        2598.088        8.341353        3.63942E+08
       7        3617.91         2.827587        3.19740E+08
       8        4188.648        4.654436        3.73853E+08
       9        4806.43         1.463042        5.06536E+08
      10        6141.172        2.671567        1.42389E+09
      11        6318.324        2.961023        1.48926E+09
      12        8389.977        1.973407        1.45966E+09
      13        9253.113        2.982493        2.00080E+09
      14        10617.46        18.28062        2.59109E+09
      15        10758.3         9.403651        3.20064E+09

EIGENVECTOR TABLE --
  POINT/COMPONENT DEFINITIONS
                    5    -2    5    -3    9    -3    25   -3    29   -3
                    33   -2    33   -3    114  -2    114  -3    121  -1
                    121  -2    121  -3
  MODE NUMBER     EIGENVECTOR
       1          -.060412    202.5733    576.7153    59.16064    383.5242
                  -.002533    770.4272    -6.742-9    59.99623    -8.49911
                  4.6980-7    673.7563
       2          .6546926    529.197     -74.1774    244.844     429.3921
                  -.004109    -734.734    2.8437-7    245.1604    10.97636
                  9.4164-7    -400.966
       3          274.8813    75.54501    119.3818    -33.3325    -103.306
                  1119.52     -126.089    84.73872    -1.772-6    3 1817-7
                  982.7751    1.5068-7
       4          9.973927    -537.458    -930.275    244.163     774.584
                  157.7955    994.5684    -35.0723    5.4223-8    -2.801-7
                  29.44481    1.5779-7
       5          -1.32108    -376.073    304.3408    -439.529    353.0525
                  -.383221    -698.505    3.4976-7    -434.592    7.092246
                  1.8026-6    -144.877
       . . .                                  . . .

END OF DATA -- EXECUTED 02/27/86
```

Figure 5 SEQUENTIAL DATA EXTRACTED FROM MSC/NASTRAN BY PROGRAM "DAMPED"

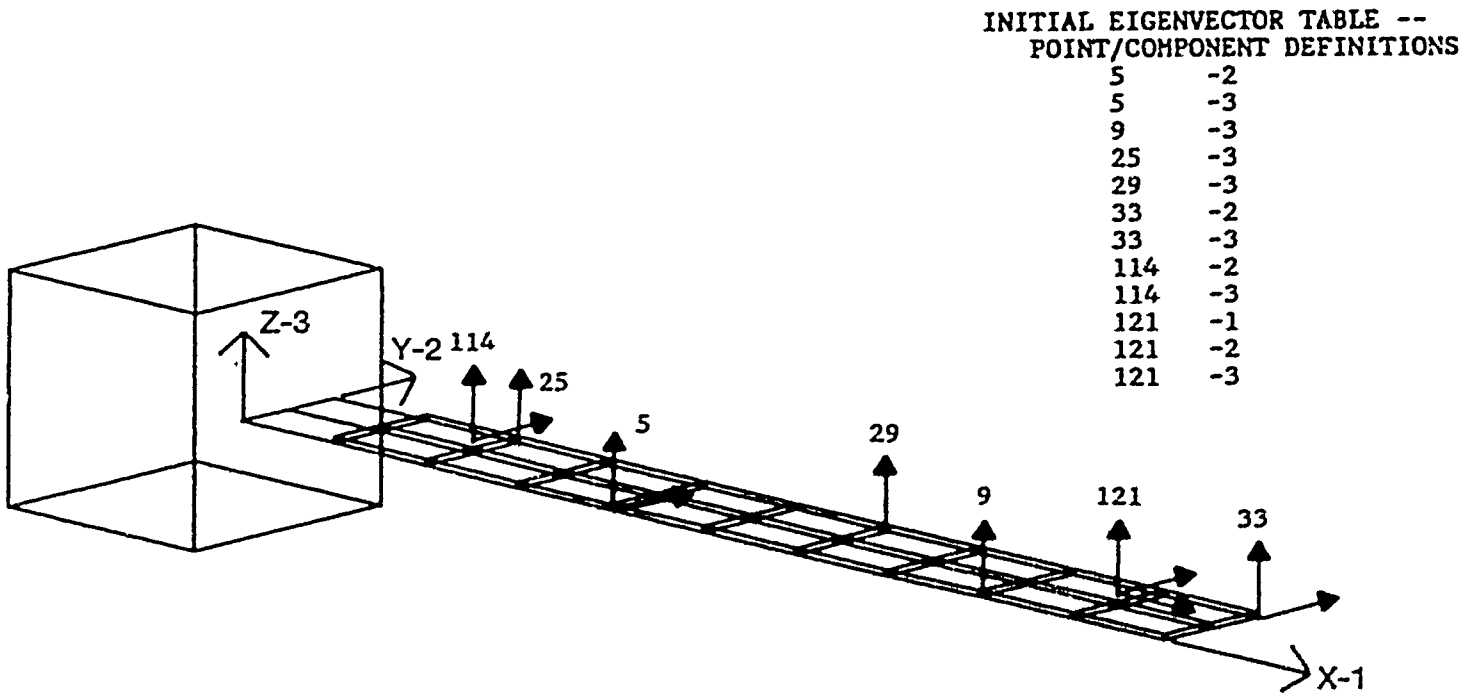


Figure 6 MODE TRACKING EIGENVECTOR COMPONENT DEFINITION

```
IBM DAMPING POSTPROCESSOR 03/15/86 (PGM=DAMPRO, LEVEL 2.0, RELEASED 02/22/86)


INITIAL STRAIN ENERGY TABLE --
        DIMENSIONS =   20      BY      8
        FREQ = FREQUENCY (HZ)
        SRAT = STRAIN ENERGY RATIO (%)

        SHEAR (G) MODULUS NEWTON/MM**2
MODE    10.00000 1.000000 3.000000 50.00000 250.0000 .3500000 .1199999 .6000000

1  FREQ 81.01099 74.93581 76.94753 88.11200 94.11731 74.10669 73.77985 74.43924
   SRAT 10.06082 3.183024 6.655131 9.925859 6.239918 1.294053 .4869074 2.084820

2  FREQ 565.4976 473.2930 501.1592 679.5989 745.7134 462.7322 458.7327 466.8997
   SRAT 24.11002 6.586548 14.92709 18.06717 6.151307 2.567349 .9476755 4.212360

3  FREQ 747.4214 732.5198 739.7637 757.9043 768.7947 724.7710 710.9480 728.9683
   SRAT 1.698757 1.849461 1.741594 1.780812 1.676847 2.375887 5.699574 1.978114

4  FREQ 1211.478 1195.979 1200.371 1265.132 1450.998 1193.366 1190.426 1194.614
   SRAT 2.447206 .4934389 .9168777 9.800516 24.22101 .3774102 .6820608 .4088800

5  FREQ 1402.418 1286.441 1315.845 1672.962 2001.493 1275.982 1271.141 1280.144
   SRAT 15.55614 2.404302 6.414805 25.80225 16.16312 .9590149 .5969006 1.511392

6  FREQ 2598.088 2491.371 2517.480 2929.946 3551.776 2478.715 1636.334 2484.846
   SRAT 8.341352 1.183848 2.944893 21.83730 21.95978 1.047980 97.33635 .9152036

7  FREQ 3617.910 3496.282 3569.131 3773.671 4250.008 2707.013 1667.188 3294.888
   SRAT 2.827586 6.707702 2.115437 8.961308 19.41367 87.09995 99.52921 48.52541

8  FREQ 4188.645 4084.515 4115.340 4511.426 4911.895 2836.193 1922.995 3694.564
   SRAT 4.654435 1.271439 1.749221 15.10740 4.297153 98.46718 94.66066 97.52567

9  FREQ 4806.430 4230.898 4713.805 4841.355 5310.105 3230.562 2464.917 3774.724
   SRAT 1.463041 42.50336 6.576258 .7807012 22.40555 98.28783 1.638659 32.86893

10 FREQ 6141.172 4729.316 6071.625 6419.102 7256.445 3617.482 3528.381 4069.917
   SRAT 2.671567 95.49686 1.570565 9.623496 19.73346 6.920527 5.029649 1.702738

11 FREQ 6318.320 5420.813 6229.719 6586.309 7404.195 4045.215 3838.236 4215.000
   SRAT 2.961022 97.34575 2.188929 8.490968 21.22614 3.093491 22.35677 98.77625

12 FREQ 8389.977 5796.625 7751.602 8619.520 9371.445 4862.230 4045.559 5359.148
   SRAT 1.973407 43.54810 79.77216 5.775795 15.39141 44.03835 40.78534 19.10245

13 FREQ 9253.109 5995.941 8266.563 9612.066 10640.90 5181.336 4174.855 5555.477
   SRAT 2.982492 5.444666 4.833425 7.470983 18.63564 8.024192 21.11139 53.43187

14 FREQ 10617.46 6249.266 8619.813 10927.70 11507.39 5486.547 5052.758 5959.613
   SRAT 18.28061 8.545834 73.30417 3.497725 9.933507 54.95708 2.954040 12.25559

15 FREQ 10758.30 6539.934 9158.344 11709.70 12066.03 6101.418 5224.152 6174.512
   SRAT 9.403650 62.71068 7.584310 5.381584 3.165833 18.59659 59.55423 3.695704

. . .                                                    . . .
```

Figure 7 INITIAL STRAIN ENERGY TABLE AS READ BY PROGRAM "DAMPRO"

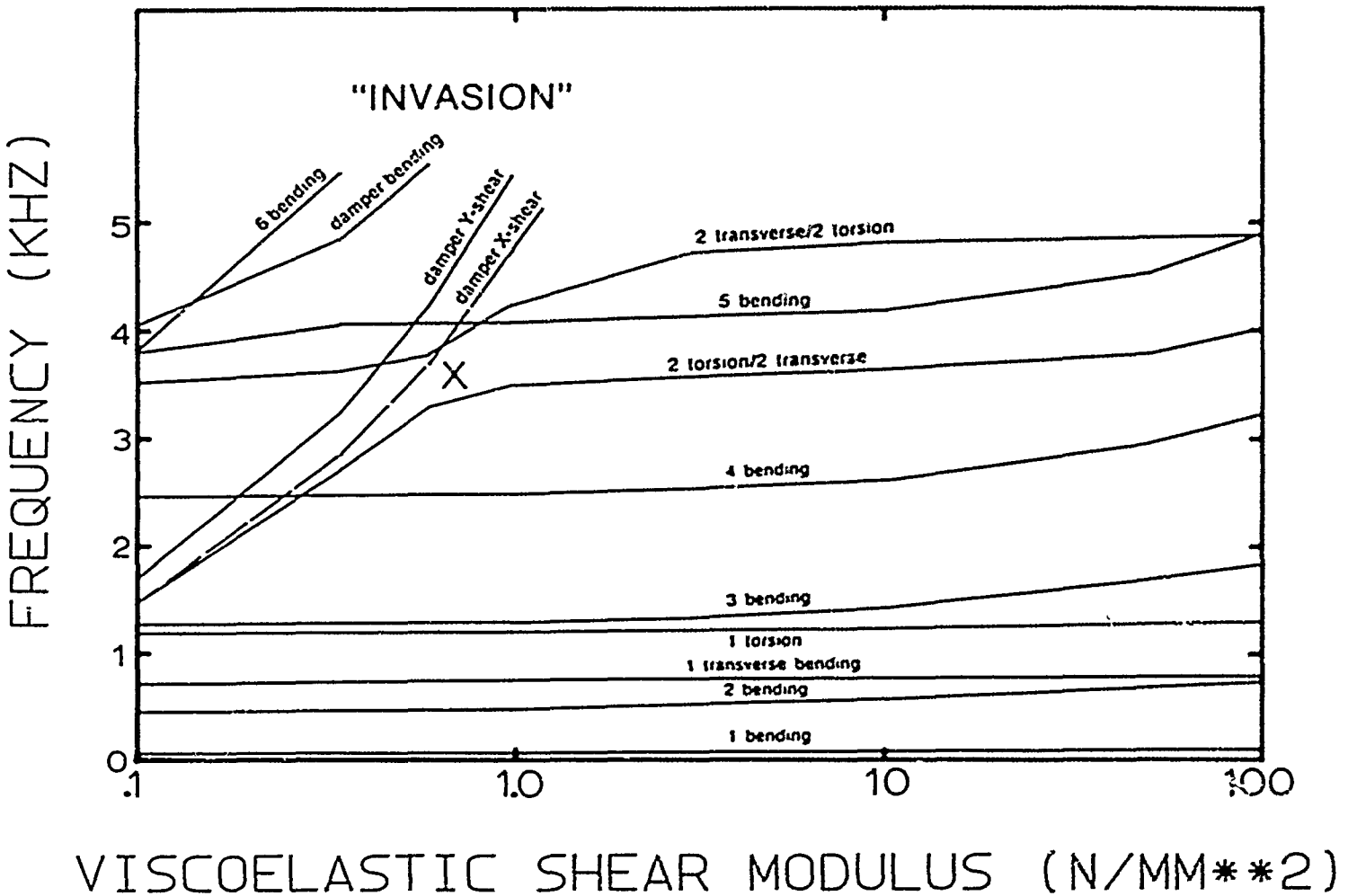


Figure 8 FREQUENCY VS. VISCOELASTIC SHEAR MODULUS

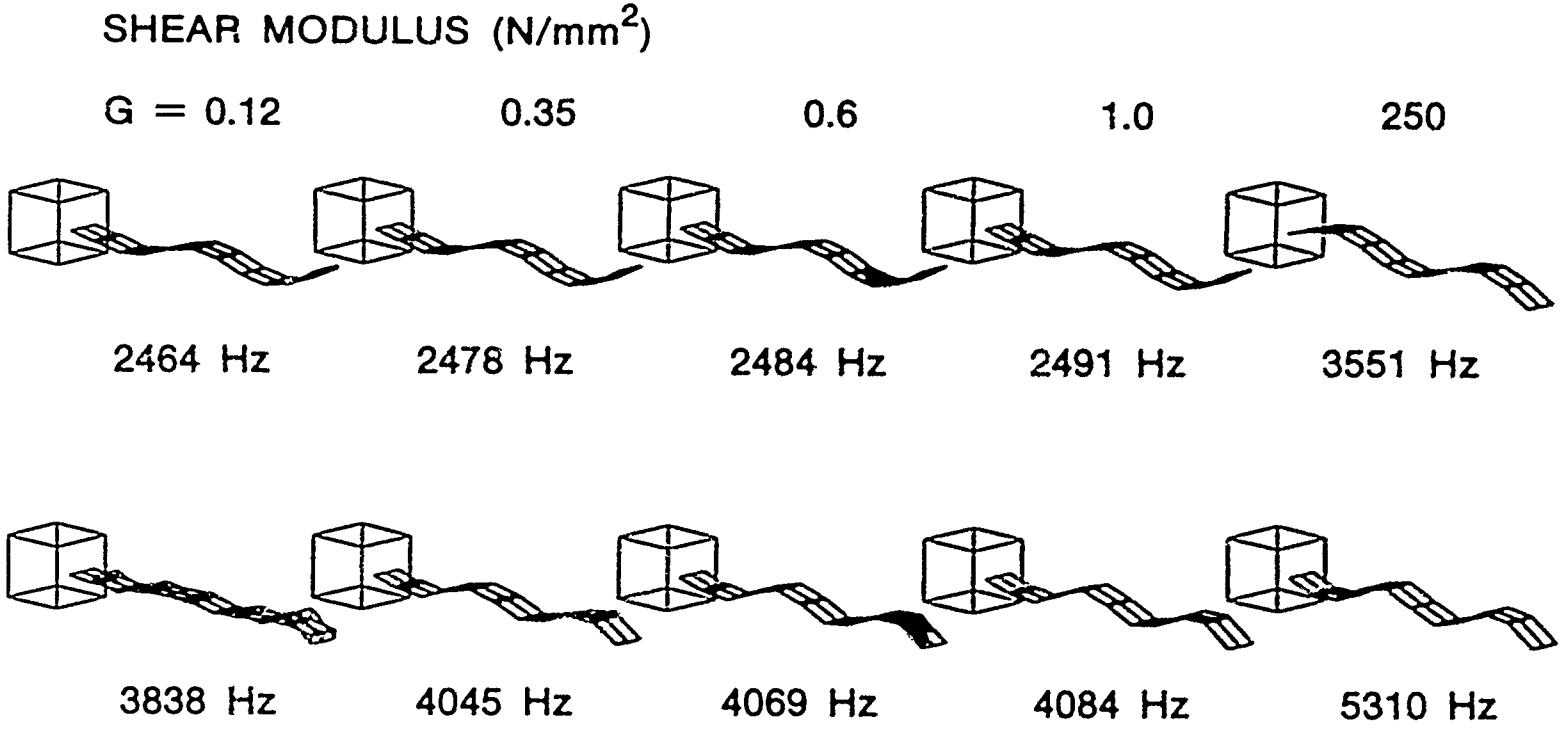


Figure 9 CHANGING MODE SHAPES: 4 BENDING AND 5 BENDING

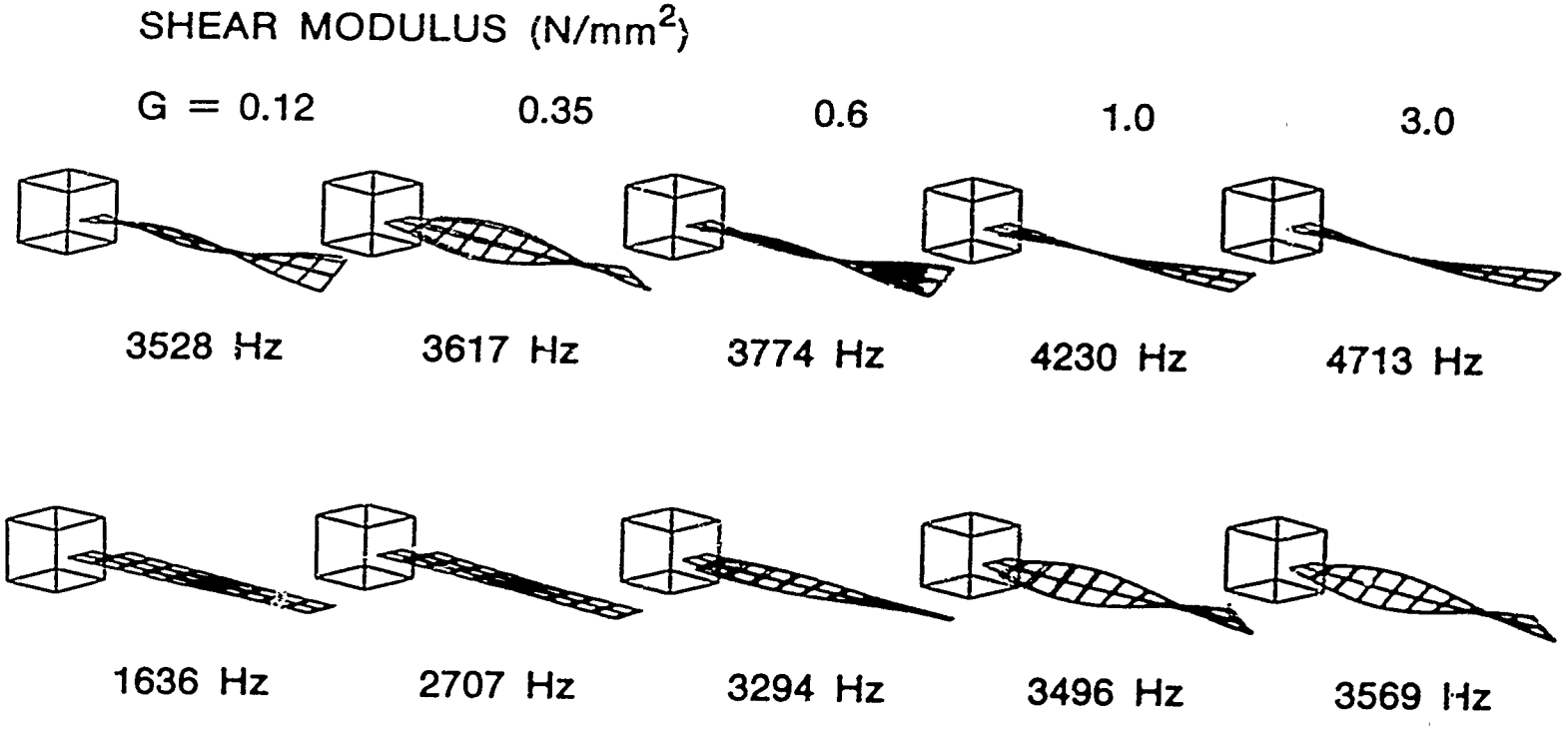


Figure 10 CROSSOVER OF COUPLED MODES: 2 TORSION/2 TRANSVERSE BENDING

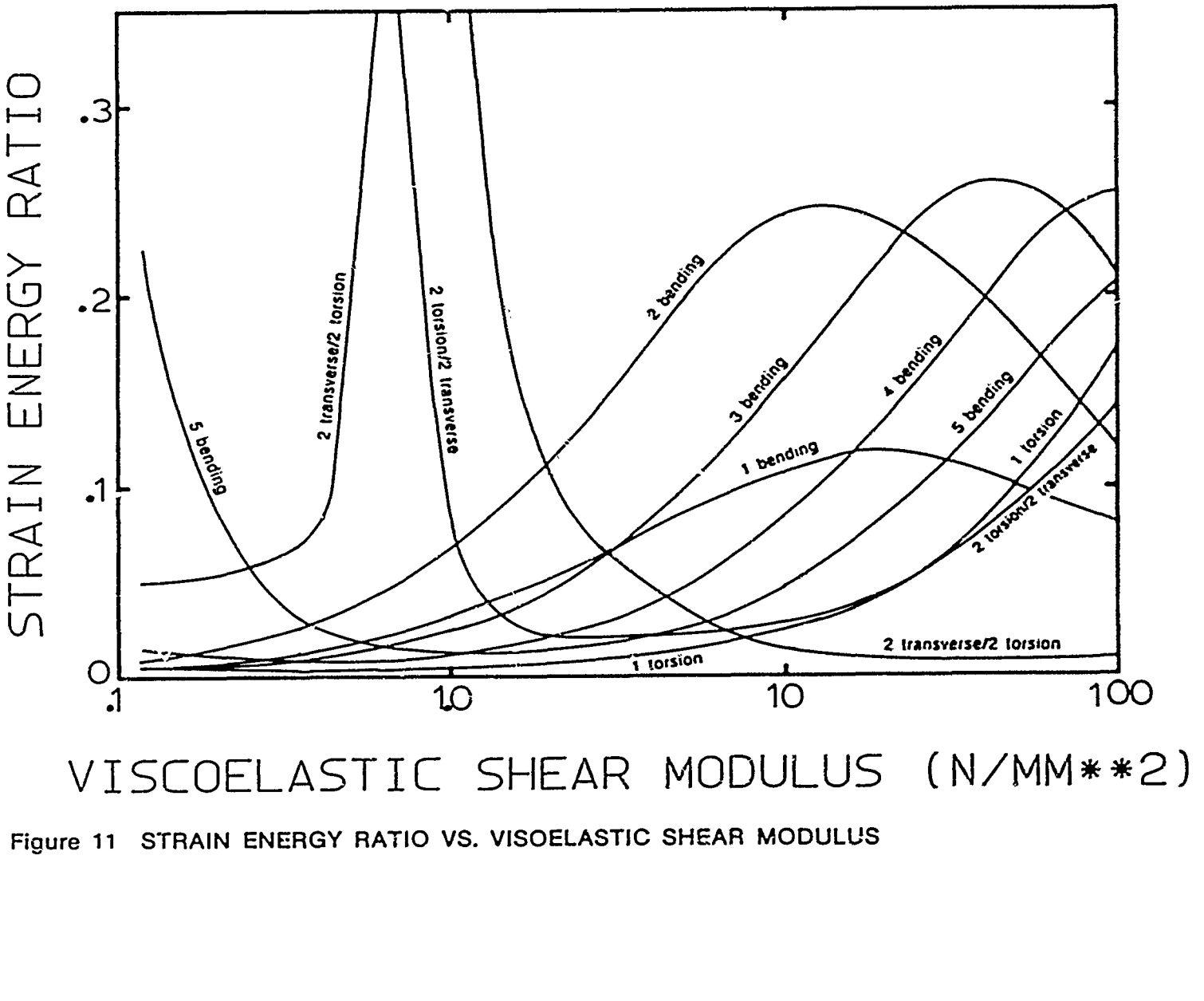


Figure 11 STRAIN ENERGY RATIO VS. VISOELASTIC SHEAR MODULUS

Step 1: Match modes in VE modulus column Gn-1 mode for mode with order of modes in VE modulus column Gn

	Viscoelastic Modulus:	Gn-2	Gn-1	Gn
1.1 Compute dot product of tracking vector C1 with tracking vectors B1, B2, B3, B4 ... Bm	Mode 1	A1	B1	C1
	Mode 2	A2	B2	C2
	Mode 3	A3	B3	C3
1.2 Switch tracking vector for Gn-1 which has the largest absolute valued dot product into row 1 (assume this is vector B2)	Mode 4	A4	B4	C4
	. . .			
	Mode m	Am	Bm	Cm

	Viscoelastic Modulus:	Gn-2	Gn-1	Gn
1.3 Compute dot product of tracking vector C2 with remaining tracking vectors B1, B3, B4 ... Bm	Mode 1	A1	B2 =	C1
	Mode 2	A2	B1	C2
	Mode 3	A3	B3	C3
1.4 Switch tracking vector for Gn-1 which has the largest absolute valued dot product into row 2 (assume this is vector B1)	Mode 4	A4	B4	C4
	. . .			
	Mode m	Am	Bm	Cm

	Viscoelastic Modulus:	Gn-2	Gn-1	Gn
1.5 Compute dot product of tracking vector C3 with remaining tracking vectors B3, B4 ... Bm	Mode 1	A1	B2 =	C1
	Mode 2	A2	B1 =	C2
	Mode 3	A3	B3	C3
1.6 Switch tracking vector for Gn-1 which has the largest absolute valued dot product into row 3 (assume this is vector B4)	Mode 4	A4	B4	C4
	. . .			
	Mode m	Am	Bm	Cm

	Viscoelastic Modulus:	Gn-2	Gn-1	Gn
1.7 Compute dot product of tracking vector C4 with remaining tracking vectors B3 ... Bm	Mode 1	A1	B2 =	C1
	Mode 2	A2	B1 =	C2
	Mode 3	A3	B4 =	C3
1.8 Continue sequence until all modes for VE modulus Gn-1 have been matched row for row with modes for VE modulus Gn	Mode 4	A4	B3	C4
	. . .			
	Mode n	Am	Bm	Cm

Step 2: Match modes in VE modulus column Gn-2 mode for mode with order of modes (as reordered) in VE modulus column Gn-1

	Viscoelastic Modulus:	Gn-2	Gn-1	Gn
2.1 Compute dot product of tracking vector B2 with tracking vectors A1, A2, A3, A4 ... Am	Mode 1	A1	B2 =	C1
	Mode 2	A2	B1 =	C2
	Mode 3	A3	B4 =	C3
2.2 Continue sequence until all modes for VE modulus Gn-2 have been matched row for row with modes for VE modulus Gn-1	Mode 4	A4	B3 =	C4
	. . .			
	Mode n	Am	Bm =	Cm

Figure 12 MODE TRACKING ALGORITHM PROCESSING SEQUENCE

```
IBM DAMPING POSTPROCESSOR 03/15/86 (PGM=DAMPRO, LEVEL 2.0, RELEASED 02/22/86)


REFORMATTED STRAIN ENERGY TABLE --
        DIMENSIONS =   20      BY      8        NO. ERROR FREE MODES = 6
        FREQ = FREQUENCY (HZ)
        SRAT = STRAIN ENERGY RATIO (%)

        SHEAR (G) MODULUS NEWTON/MM**2
MODE    .1199999 .3500000 .6000000 1.000000 3.000000 10.00000 50.00000 250.0000

1  FREQ 73.77985 74.10669 74.43924 74.93581 76.94753 81.01099 88.11200 94.11731
   SRAT .4869074 1.294053 2.084820 3.183024 6.655131 10.06082 9.925859 6.239918

2  FREQ 458.7327 462.7322 466.8997 473.2930 501.1592 565.4976 679.5989 745.7134
   SRAT .9476755 2.567349 4.212360 6.588548 14.92709 24.11002 18.06717 6.151307

3  FREQ 710.9480 724.7710 728.9683 732.5198 739.7637 747.4214 757.9043 768.7947
   SRAT 5.699574 2.375887 1.978114 1.849461 1.741594 1.698757 1.780812 1.676847

4  FREQ 1190.426 1193.366 1194.614 1195.979 1200.371 1211.478 1265.132 1450.998
   SRAT .6820608 .3774102 .4088800 .4934389 .9168777 2.447206 9.800516 24.22101

5  FREQ 1271.141 1275.982 1280.144 1286.441 1315.845 1402.418 1672.962 2091.493
   SRAT .5969006 .9590149 1.511392 2.404302 6.414805 15.55614 25.80225 16.16312

6  FREQ 2464.917 2478.715 2484.846 2491.371 2517.480 2598.088 2929.946 3551.776
   SRAT 1.638659 1.047980 .9152036 1.183848 2.944893 8.341352 21.83730 21.95978

7  FREQ 1636.334 2707.013 3294.888 3496.282 3569.131 3617.910 3773.671 4250.008
   SRAT 97.33635 87.09995 48.52541 8.707702 2.115437 2.827586 8.961308 19.41367

8  FREQ 3528.381 3617.482 3774.724 4230.898 4713.805 4806.430 4841.355 4911.895
   SRAT 5.029649 6.920527 32.86893 42.50336 6.576258 1.463041 .7807012 4.297153

9  FREQ 3838.236 4045.215 4069.917 4084.515 4115.340 4188.645 4511.426 5310.105
   SRAT 22.35677 3.093491 1.702738 1.271439 1.749221 4.654435 15.10740 22.40555

10 FREQ 4045.559 5486.547 5959.613 5995.941 6071.625 6141.172 6419.102 7256.445
   SRAT 40.78534 54.95708 12.25559 5.444666 1.570565 2.671567 9.623496 19.73346

11 FREQ 5726.645 6102.387 6174.512 6249.266 6229.719 6318.320 6586.309 7404.195
   SRAT 22.76021 5.495537 3.695704 8.545834 2.188929 2.961022 8.490968 21.22614

12 FREQ 6405.063 6101.418 6886.363 8026.793 8266.563 8389.977 8619.520 9371.445
   SRAT 58.70917 18.59659 65.55086 34.57300 4.833425 1.973407 5.775795 15.39141

13 FREQ 6430.480 8249.309 8772.133 8957.254 9158.344 9253.109 9612.066 10640.90
   SRAT 50.44959 36.12852 12.02825 5.465423 7.584310 2.982492 7.470983 18.63564

14 FREQ 5646.352 8201.543 9151.281 9797.852 10587.64 10758.30 10927.70 11507.39
   SRAT 30.04520 37.69179 24.43390 31.42531 15.46460 9.403650 3.497725 9.933507

15 FREQ 1667.188 2836.193 3694.564 4729.316 7751.602 10617.46 11709.70 12066.03
   SRAT 99.52921 98.46718 97.52567 95.49686 79.77216 18.28061 5.381584 3.165833

. . .                                                    . . .
```

Figure 13 REORDERED STRAIN ENERGY TABLE PREPARED BY PROGRAM "DAMPRO"

```
IBM DAMPING POSTPROCESSOR 03/15/86 (PGM=DAMPRO, LEVEL 2.0, RELEASED 02/22/86)


MODE TRACKING SUMMARY TABLE --
        DIMENSIONS =   20      BY      8
6       NUMBER OF LOWEST ERROR FREE MODES
28      TOTAL NUMBER OF TRACKING ERRORS
.85     TRACKING DOT PRODUCT CRITERIA
.70     TRACKING FREQUENCY RATIO CRITERIA
        DOTP = DOT PRODUCT OF ADJACENT EIGENVECTORS
        FRAT = FREQUENCY RATIO OF ADJACENT EIGENVALUES

        SHEAR (G) MODULUS NEWTON/MM**2
MODE    .1199999 .3500000 .6000000 1.000000 3.000000 10.00000 50.00000 250.0000

1  FREQ 73.77985 74.10669 74.43924 74.93581 76.94753 81.01099 88.11200 94.11731
   FRAT .9955896 .9955326 .9933734 .9738559 .9498406 .9194092 .9361933 1.000000
   DOTP .9999986 .9999986 .9999971 .9999570 .9998582 .9997843 .9999446 .9999997

2  FREQ 458.7327 462.7322 466.8997 473.2930 501.1592 565.4976 679.5989 745.7134
   FRAT .9913567 .9910741 .9864918 .9443964 .8862270 .8321049 .9113406 1.000000
   DOTP .9999973 .9999971 .9999934 .9998870 .9994853 .9991254 .9998338 .9999998

3  FREQ 710.9480 724.7710 728.9683 732.5198 739.7637 747.4214 757.9043 768.7947
   FRAT .9809278 .9942421 .9951516 .9902078 .9897544 .9861685 .9858344 1.000000
   DOTP .9978669 .9999191 .9999753 .9999554 .9999816 .9997800 .9987368 .9999999

4  FREQ 1190.426 1193.366 1194.614 1195.979 1200.371 1211.478 1265.132 1450.998
   FRAT .9975362 .9989554 .9988586 .9963410 .9908319 .9575901 .8719047 1.000000
   DOTP .9995483 .9999883 .9999930 .9999794 .9999933 .9999048 .9993286 .9999997

5  FREQ 1271.141 1275.982 1280.144 1286.441 1315.845 1402.418 1672.962 2001.493
   FRAT .9962060 .9967489 .9951050 .9776539 .9382687 .8382844 .8358570 1.000000
   DOTP .9999652 .9999961 .9999945 .9999135 .9995143 .9978691 .9991608 .9999996

6  FREQ 2464.917 2478.715 2484.846 2491.371 2517.480 2598.088 2929.946 3551.776
   FRAT .9944335 .9975325 .9973810 .9896289 .9689741 .8867358 .8249242 1.000000
   DOTP .9982092 .9997253 .9999732 .9999428 .9997735 .9980615 .9979444 .9999996

7  FREQ 1636.334 2707.013 3294.888 3496.282 3569.131 3617.910 3773.671 4250.008
   FRAT .6044796 .8215796 .9423977 .9795892 .9865173 .9587243 .8879209 1.000000
   DOTP .9900776 .9073795 .8472357 .9746227 .9990134 .9996517 .9865994 .9999997
        XXXXXXXX          XXXXXXXX

8  FREQ 3528.381 3617.482 3774.724 4230.898 4713.805 4806.430 4841.355 4911.895
   FRAT .9753693 .9583434 .8921802  8975549 .9807289 .9927859 .9856391 1.000000
   DOTP .9851416 .8977492 .8809471 .8613190 .9874995 .9983051 .9706597 .9999998

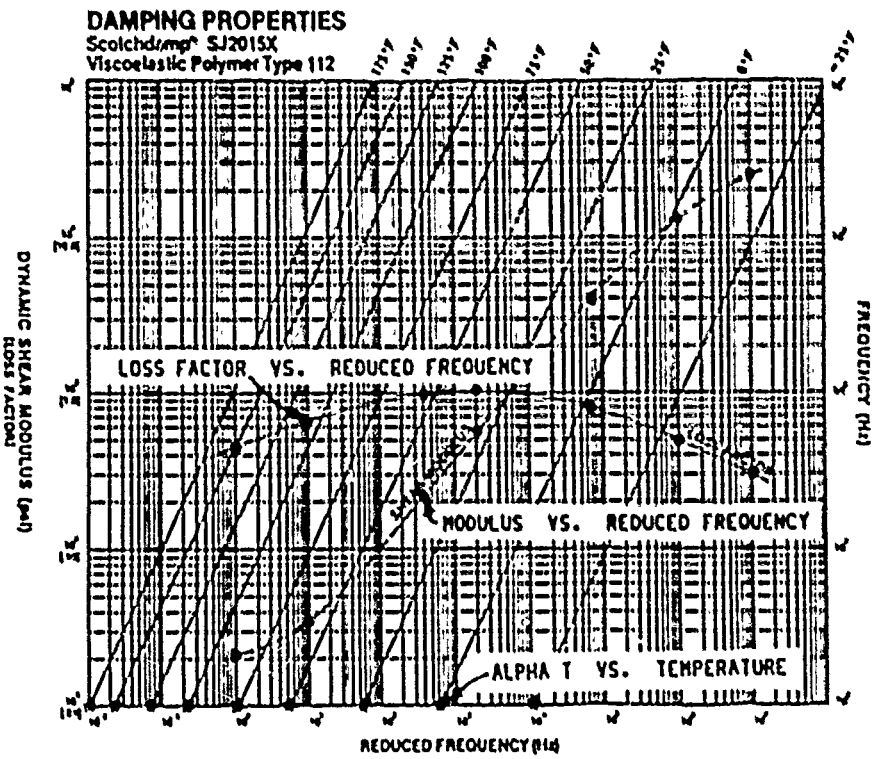
9  FREQ 3838.236 4045.215 4069.917 4084.515 4115.340 4188.645 4511.426 5310.105
   FRAT .9488336 .9939305 .9964260 .9925097 .9824992 .9284525 .8495924 1.000000
   DOTP .8444715 .9969354 .9992452 .9995112 .9998357 .9990709 .9984518 .9999996
        XXXXXXXX

10 FREQ 4045.559 5486.547 5959.613 5995.941 6071.625 6141.172 6419.102 7256.445
   FRAT .7373597 .9206213 .9939412 .9875348 .9886753 .9567027 .8846068 1.000000
   DOTP .8720858 .9013605 .8567947 .9739401 .9990695 .9962218 .9729924 .9999996

. . .                                                  . . .
```

Figure 14 MODE TRACKING SUMMARY TABLE

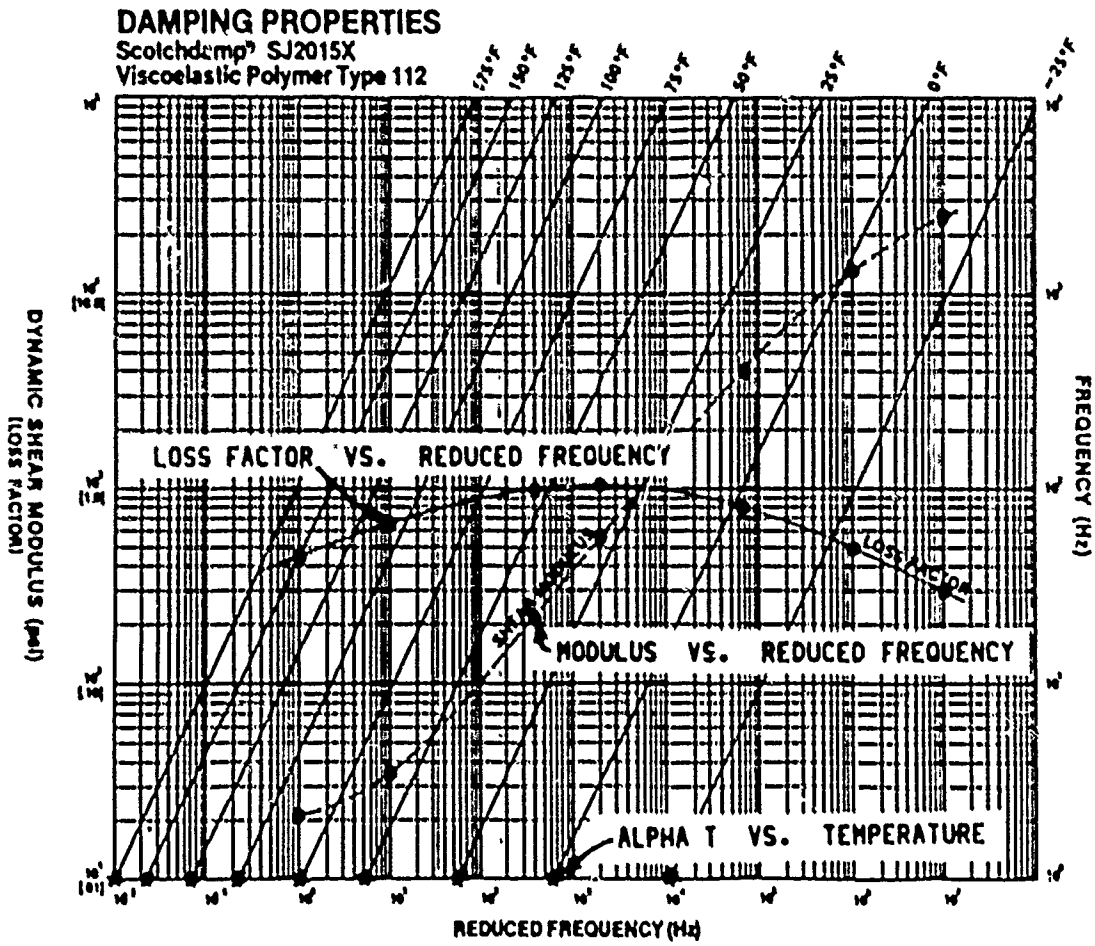
a Reduced Frequency Plot[1]



b Tabulation of Properties in Material Data Base

3M 112M	DATA ENTERED 7/01/85 BY NORMAN K. FRATER							
MATERIAL IDENT	3M SCOTCHDAMP(R) SJ2015X VISCOELASTIC POLYMER TYPE 112							
MATERIAL TYPE	ACRYLIC							
THICKNESS	0.002	INCHES						
DENSITY	.0348	LB/IN3						
BONDING	PRESSURE ONLY							
MANUFACTURER	3M COMPANY, MINNEAPOLIS, MINN.							
DATA SOURCE	SCOTCHDAMP SJ2015X VISCOELASTIC POLYMER: TYPES 110, 112, & 113 PRODUCT INFORMATION, 3M COMPANY							
DATA FORMAT	MASTER G							
DATA UNITS	DEGF	PSI (POUND/INCH**2)						
POISSONS RATIO	0.49							
NO.TEMPERATURE	9							
TEMP	-25	0	25	50	75	100	125	+
	150	175						
ALPHAT	1100.	650.	50.	5.5	1.1	0.23	0.07	+
	0.023	0.0095						
NO.FREQUENCY	7							
FREQ	1.0	10.	400.	2.0E3	6.5E4	1.0E6	1.0E7	+
G	21.	25.	220.	550.	4.0E3	1.3E4	2.5E4	+
ADA	0.44	0.65	1.00	1.06	0.80	0.50	0.30	+

Figure 15 VISCOELASTIC MATERIAL PROPERTIES FOR 3M ISD-112




```
1-------------------------------------------------------------------------
3M 112M          DATA ENTERED 7/01/85 BY NORMAN K. FRATER
MATERIAL IDENT   3M SCOTCHDAMP(R) SJ2015X VISCOELASTIC POLYMER TYPE 112
MATERIAL TYPE    ACRYLIC
THICKNESS        0.002    INCHES
DENSITY          .0348    LB/IN3
BONDING          PRESSURE ONLY
MANUFACTURER     3M COMPANY, MINNEAPOLIS, MINN.

DATA SOURCE      SCOTCHDAMP SJ2015X VISCOELASTIC POLYMER: TYPES 110, 112,
                 & 113 PRODUCT INFORMATION, 3M COMPANY
DATA FORMAT      MASTER   G
DATA UNITS       DEGF     PSI (POUND/INCH**2)
POISSONS RATIO   0.49
NO.TEMPERATURE   9
TEMP             -25      0        25       50       75       100      125      +
                 150      175
ALPHAT           1100.    650.     50.      5.5      1.1      0.23     0.07     +
                 0.023    0.0095
NO.FREQUENCY     7
FREQ             1.0      10.      400.     2.0E3    6.5E4    1.0E6    1.0E7    +
G                21.      25.      220.     550.     4.0E3    1.3E4    2.5E4    +
ADA              0.44     0.65     1.00     1.06     0.60     0.50     0.30     +
1-------------------------------------------------------------------------
```

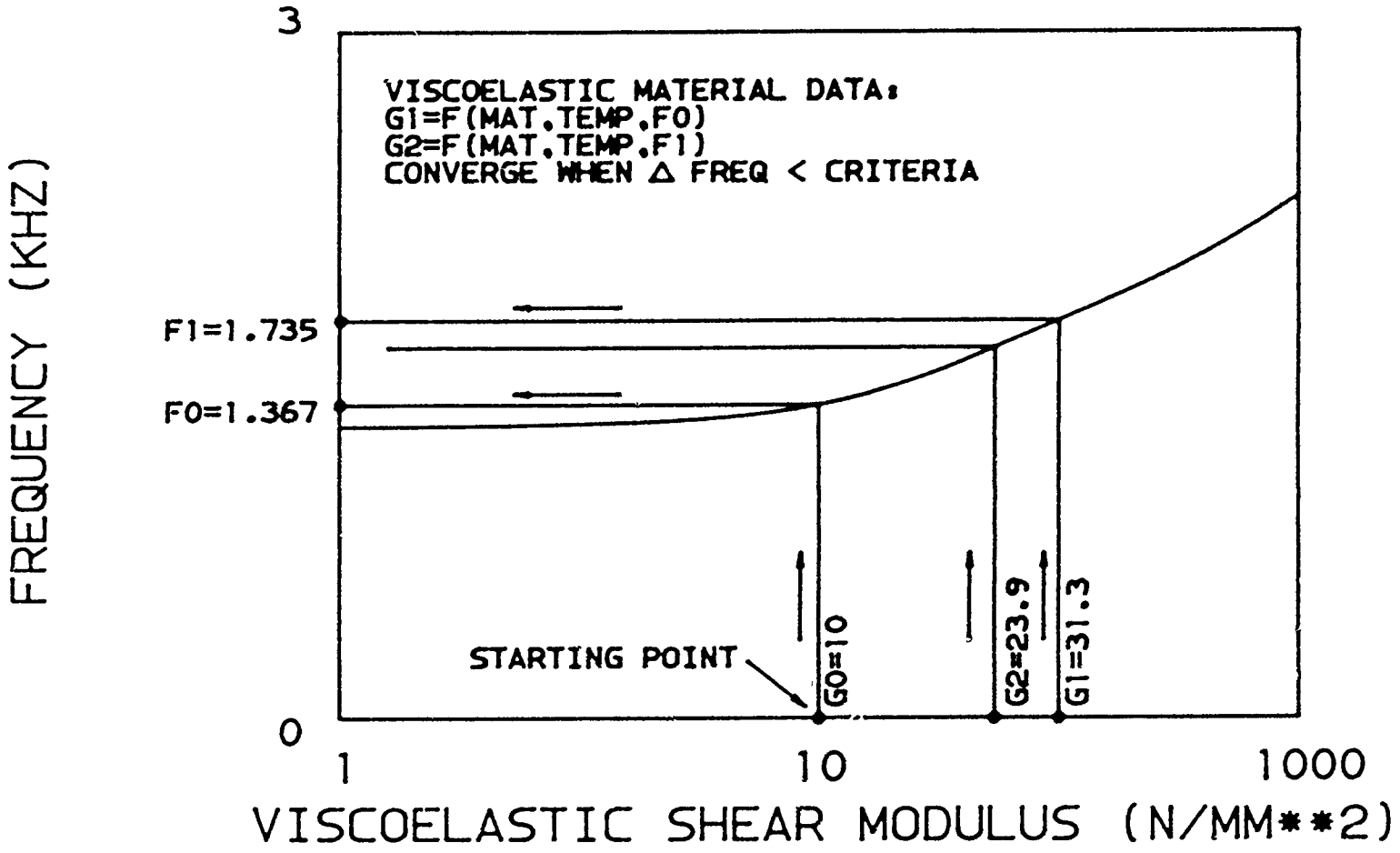


Figure 16 ITERATIVE SOLUTION STRATEGY FOR VISCOELASTIC MODULUS AND FREQUENCY

1 SUMMARY OF RESULTS

EXTRAPOLATION ERROR COUNT = 0

MATERIAL: 3M SCOTCHDAMP(R) SJ2015X VISCOELASTIC POLYMER TYPE 112

G MODULUS NEWTON/MM**2

		TEMPERATURE (DEG.F) 0.00	25.00	50.00	75.00	100.00
MODE 1	DAMPED FREQ=	85.057	78.892	75.571	74.349	73.924
	LOSS FACTOR=	0.086028	0.089168	0.044752	0.016406	0.005905
	G MODULUS =	25.3386	5.6536	1.5505	0.5314	0.2159
MODE 2	DAMPED FREQ=	697.213	608.634	521.681	485.151	467.473
	LOSS FACTOR=	0.092640	0.206621	0.197478	0.108714	0.039911
	G MODULUS =	66.3863	18.3555	4.6872	1.7888	0.6354
MODE 3	DAMPED FREQ=	760.018	752.090	743.941	737.968	731.466
	LOSS FACTOR=	0.010231	0.014849	0.017589	0.018266	0.017556
	G MODULUS =	68.7124	20.6118	5.7768	2.2722	0.8556
MODE 4	DAMPED FREQ=	1306.542	1233.969	1207.665	1200.363	1196.478
	LOSS FACTOR=	0.070602	0.049777	0.019173	0.009674	0.005154
	G MODULUS =	84.4936	26.8401	7.6810	2.9962	1.1875
MODE 5	DAMPED FREQ=	1803.842	1576.739	1384.025	1318.146	1290.091
	LOSS FACTOR=	0.123134	0.185484	0.139476	0.071335	0.028998
	G MODULUS =	94.7903	30.3465	8.3193	3.1597	1.2481
MODE 6	DAMPED FREQ=	3211.979	2869.946	2622.897	2536.011	2502.771
	LOSS FACTOR=	0.107329	0.144087	0.093152	0.046492	0.019636
	G MODULUS =	114.6290	40.3740	12.0528	4.6102	1.8678
MODE 7	DAMPED FREQ=	3983.923	3758.535	3637.901	3593.907	3576.307
	LOSS FACTOR=	0.058863	0.057541	0.034544	0.017866	-0.018887
	G MODULUS =	122.4055	45.6501	14.5216	5.6609	2.2893
MODE 8	DAMPED FREQ=	4869.246	4841.711	4823.238	4804.793	4687.285
	LOSS FACTOR=	0.010031	0.005240	0.005185	0.009211	0.119369
	G MODULUS =	129.7791	51.0567	17.0109	6.7163	2.6702
MODE 9	DAMPED FREQ=	4913.348	4508.086	4246.262	4148.438	4108.746
	LOSS FACTOR=	0.080547	0.098945	0.065689	0.031642	0.015939
	G MODULUS =	130.1127	49.4872	15.8424	6.1601	2.4775
MODE 10	DAMPED FREQ=	6877.258	6465.832	6213.406	6121.762	6073.086
	LOSS FACTOR=	0.058304	0.064618	0.043004	0.020621	0.016245
	G MODULUS =	142.6435	57.7825	19.5636	7.7431	3.0934
MODE 11	DAMPED FREQ=	7034.137	6634.719	6391.898	6292.305	6231.059
	LOSS FACTOR=	0.057340	0.057663	0.039540	0.023781	0.022200
	G MODULUS =	143.4880	58.4109	19.8689	7.8688	3.1388
MODE 12	DAMPED FREQ=	9057.117	8694.855	8474.570	8383.684	8293.758
	LOSS FACTOR=	0.040969	0.041338	0.025327	0.016544	0.029121
	G MODULUS =	152.9413	65.2840	23.1424	9.3051	3.6917
MODE 13	DAMPED FREQ=	10251.441	9745.656	9396.020	9251.742	9182.184
	LOSS FACTOR=	0.049950	0.053397	0.035387	0.029462	0.071623
	G MODULUS =	157.5495	68.3392	24.4501	9.8537	3.9150

Figure 17 SOLUTION SUMMARY FOR FREQUENCY AND LOSS FACTOR FROM PROGRAM "DAMPIT"

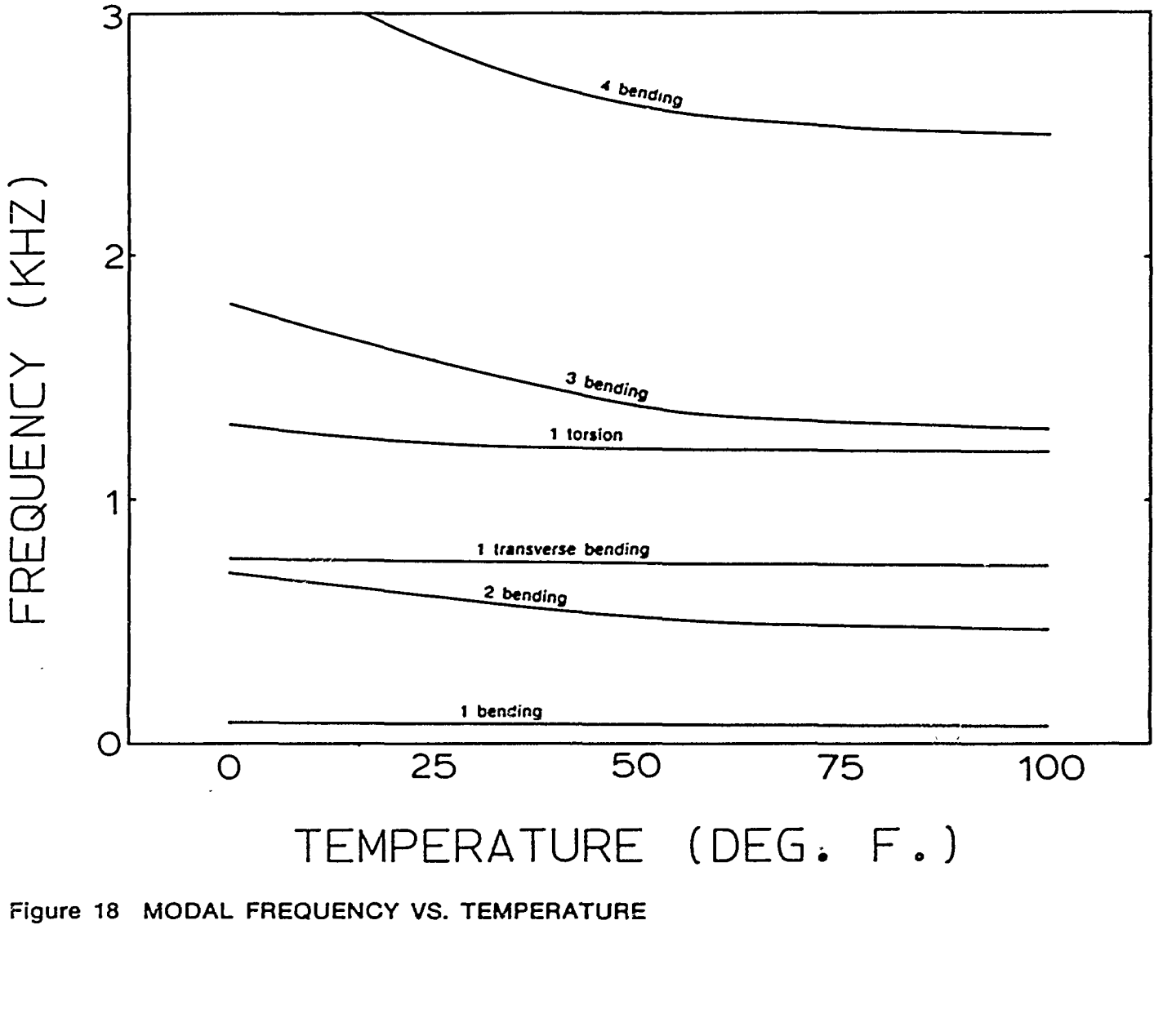


Figure 18 MODAL FREQUENCY VS. TEMPERATURE

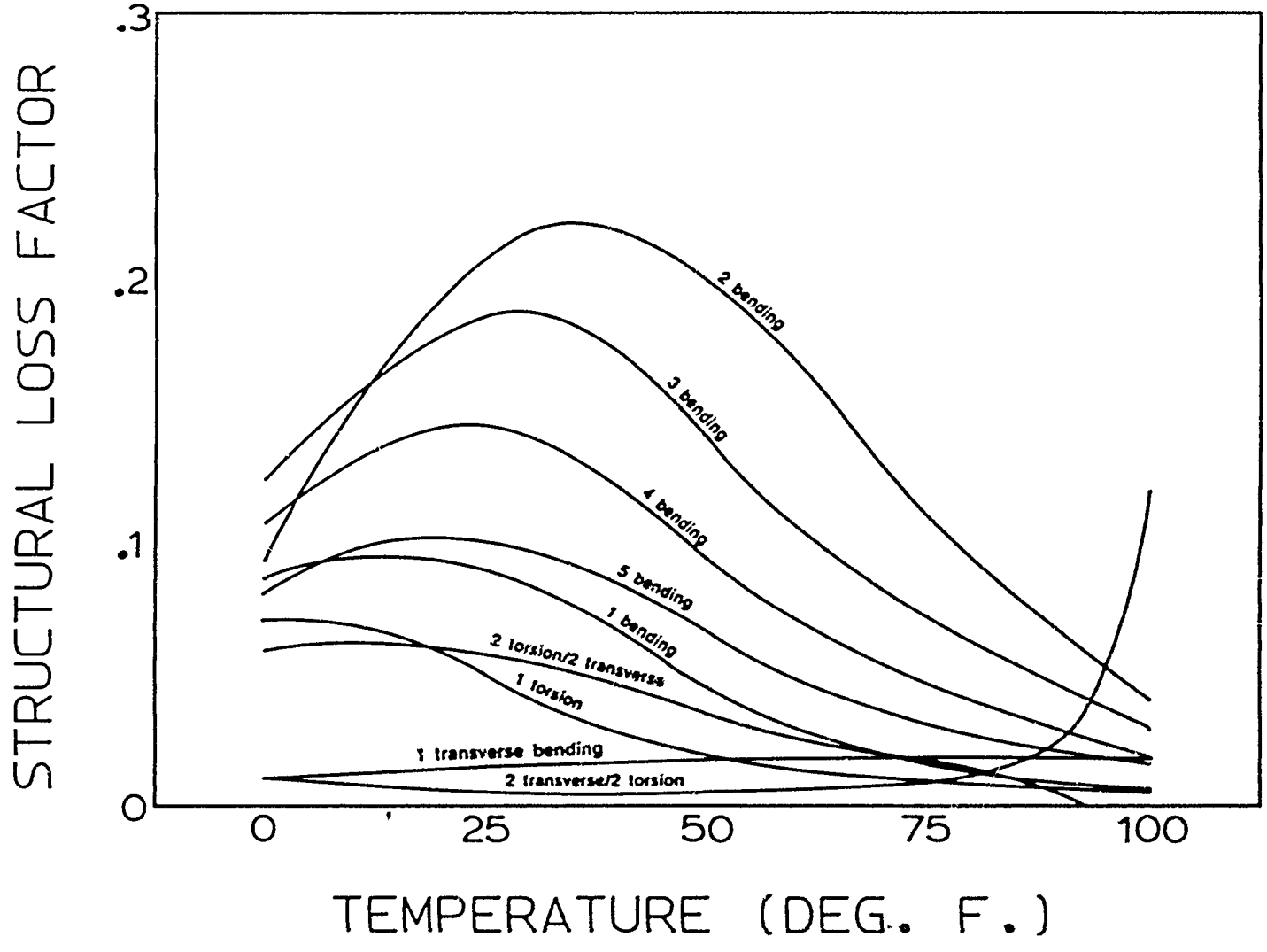


Figure 19 MODAL LOSS FACTOR VS. TEMPERATURE

```
$-----------------------------------------------------------------------
$ LAMA SHIFT DMI DATA CARDS GENERATED 03/15/86 BY PROGRAM "D A M P I T"
$ D A M P I T   PROGRAM 2.0  FEBRUARY 1986 (03/15/86)
$ MATERIAL SELECTED:  3M SCOTCHDAMP(R) SJ2015X VISCOELASTIC POLYMER TYPE 112
$ REFERENCE G MODULUS SELECTED: 1.00000E+01 NEWTON/MM**2
$ TEMPERATURE SELECTED: 5.00000E+01 DEG. F
$-----------------------------------------------------------------------
$ ALTER TO SHIFT EIGENVALUES USING DMI TABLE FROM PROGRAM "D A M P I T"
$ INSERT ALTER AFTER NASTRAN    "READ . . . . . "
$                       AND     "OFP LAMA,OEIGS//$"
$ STATEMENTS IN DMAP PROCEDURE BEING USED.
$-----------------------------------------------------------------------
$ ALTER 429  - FOR MSC SOLUTION 30
$ ALTER 830  - FOR MSC SOLUTION 71
$ LAMX         "NAME"      ,LAMA/LAMB/0$ MODIFY EIGENVALUE TABLE
$ EQUIV        LAMB,LAMA/TRUE$  EQUIV LAMA TABLE TO MODIFIED LAMA TABLE
$ OFP          LAMA,OEIGS//$  PRINT MODIFIED EIGENVALUE TABLE
$ ENDALTER $
$-----------------------------------------------------------------------
$ REFERENCE MSC USERS MANUAL SECTION 5.4 FOR DESCRIPTION OF LAMX DMAP
$ MODULE.  DMI MATRIX CONTAINS DELTA FACTORS USED IN DMAP ALTER
$ TO CHANGE REFERENCE FREQUENCIES TO CALCULATED DAMPED FREQUENCIES:
$    MODIFIED FREQUENCY = REFERENCE FREQUENCY * (1.0 + DELTA)
$       NAME    MODE            DELTA
DMI     EIG3050 0       2       1       1               3       40
DMI     EIG3050 1       2       -.067151
DMI     EIG3050 2       2       -.077483
DMI     EIG3050 3       2       -.004656
DMI     EIG3050 4       2       -.003147
DMI     EIG3050 5       2       -.013115
DMI     EIG3050 6       2       .0095482
DMI     EIG3050 7       2       .0055256
DMI     EIG3050 8       2       .0137548
DMI     EIG3050 9       2       .0034962
DMI     EIG3050 10      2       .0117617
DMI     EIG3050 11      2       .0116453
DMI     EIG3050 12      2       .0100822
DMI     EIG3050 13      2       .0154448
DMI     EIG3050 14      2       .0854578
DMI     EIG3050 15      2       .0076189
DMI     EIG3050 16      2       .0588007
DMI     EIG3050 17      2       .0376177
DMI     EIG3050 18      2       .0233402
DMI     EIG3050 19      2       .0760527
DMI     EIG3050 20      2       .064477
$
$ TABDMP1 DATA CARDS GENERATED 03/15/86 BY PROGRAM "D A M P I T"
$       FREQ    ADA     FREQ    ADA     FREQ    ADA     FREQ    ADA
TABDMP1 3050                                                    +3050 1
+3050 1 0.0     0.0     75.57103.0447521521.6812.1974777743.9414.0175893+3050 2
+3050 2 1207.665.019173 1384.025.13947552622.897.093152 3637.901.034544 +3050 3
+3050 3 4246.262.06568884823.238.00518496213.406.043004 6391.898.0395399+3050 4
+3050 4 8474.57 .02532759396.02 .035386910840.27.040186511524.81.0397828+3050 5
+3050 5 12678.04.035406312951.37.016625812979.83-.00410414278.41.0293295+3050 6
+3050 6 16525.21-.03811218177.71.043970533050.41.0439705ENDT
$       FREQ    ADA     FREQ    ADA     FREQ    ADA     FREQ    ADA
$-----------------------------------------------------------------------
```

Figure 20 MSC/NASTRAN DMI EIGENVALUE SHIFT AND TABDMP1 DAMPING TABLES PRODUCED BY PROGRAM "DAMPIT"

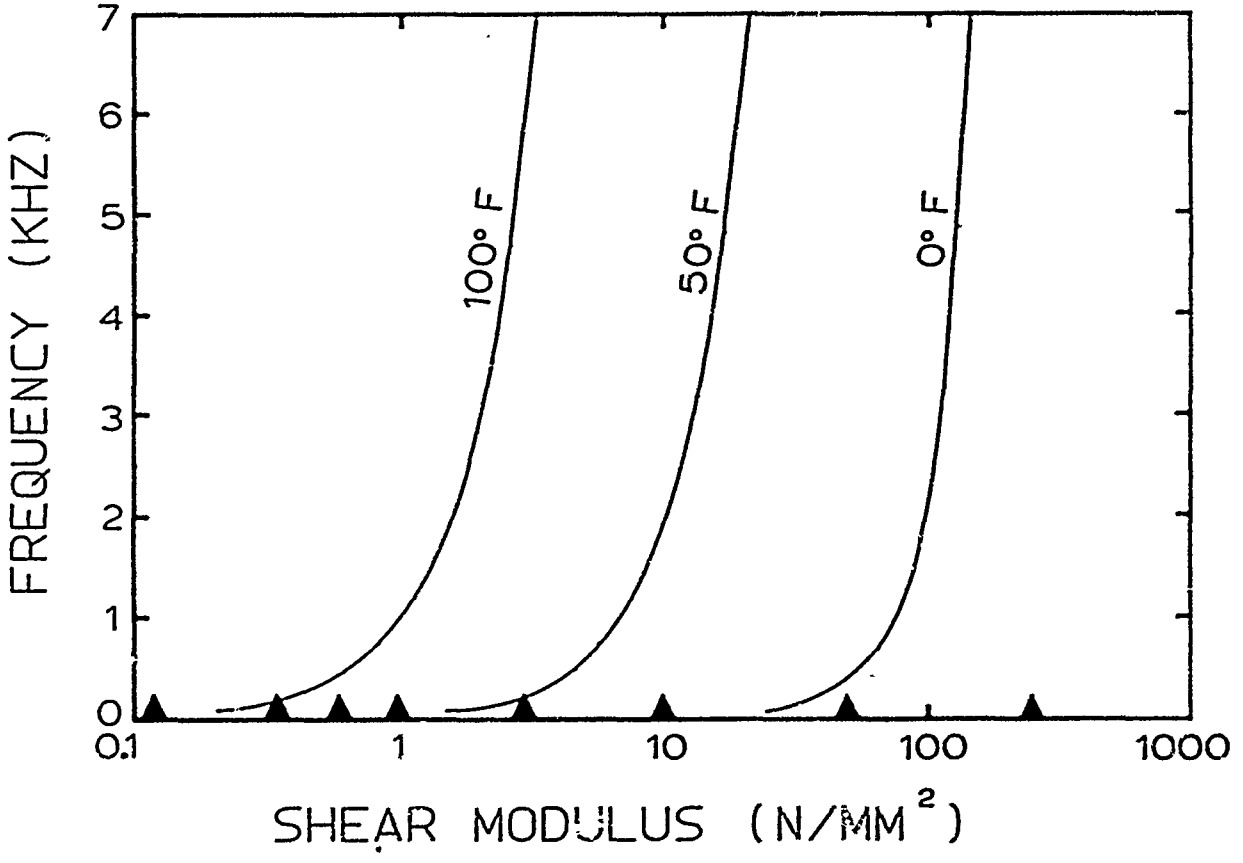


Figure 21 SHEAR MODULUS VS. FREQUENCY AND TEMPERATURE FOR 3M ISD-112

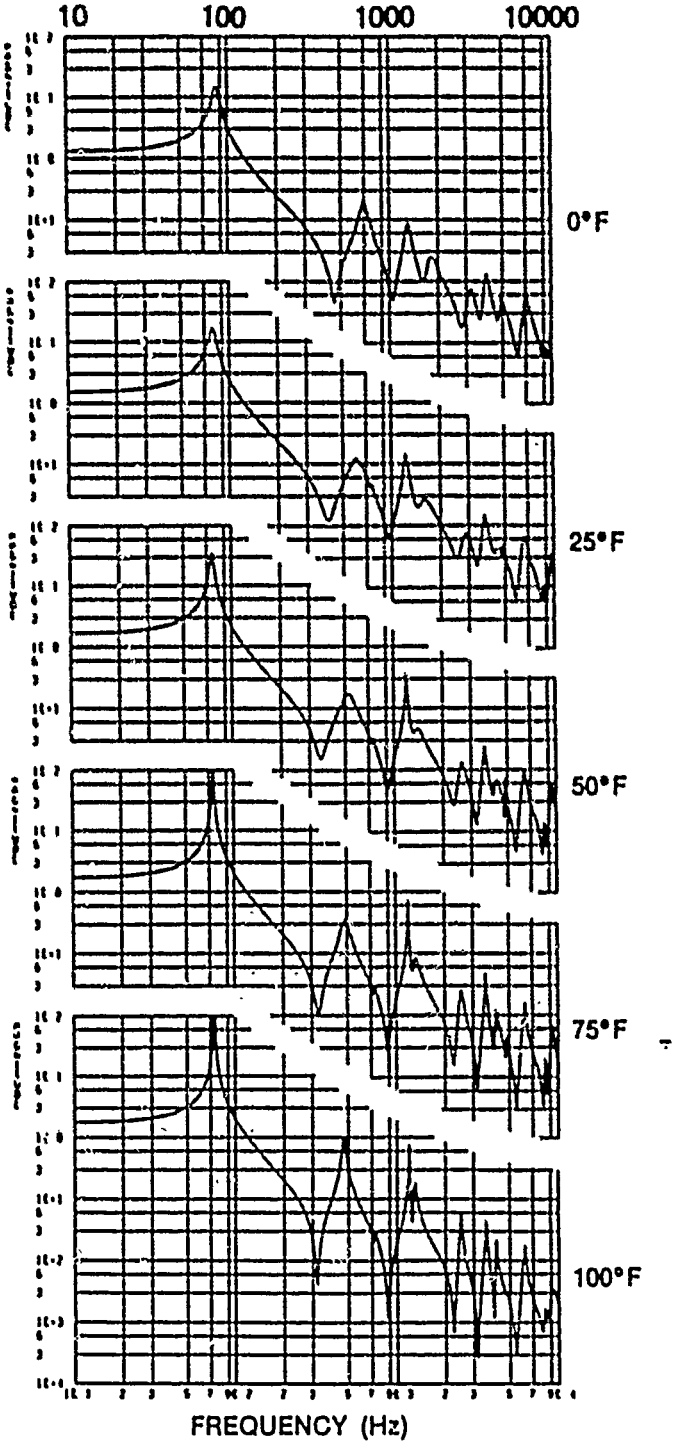


Figure 22 MODAL FREQUENCY RESPONSES, 0° TO 100°F

```
$-------2-------3-------4-------5-------6-------7-------8-------9-------
$ MATERIAL PROPERTIES FOR CONSTRAINED DAMPING MATERIAL
$    REFERENCE MODULUS = 1.0,              REFERENCE LOSS FACTOR = 1.0
$    UNITS = NEWTON/MM**2
MAT1     2               1.0     0.49    9.633-10                 1.0
$-------2-------3-------4-------5-------6-------7-------8-------9-------
$ 3M TYPE 112 VISCOELASTIC DAMPING MATERIAL
$ REAL PART OF COMPLEX MODULUS, TR(F), TEMP =  50.0 DEGREES F.
$    G REF =      1.0000, ETA REF =      1.0000, ETA STRUC =      0.0000
$    UNITS = NEWTON/MM**2
$-------2-------3-------4-------5-------6-------7-------8-------9-------
TABLED1 3050
        50.     0.187   75.     0.544   100.    0.820   150.    1.293
        200.    1.701   300.    2.400   400.    3.009   600.    4.089
        800.    5.029   1200.   6.652   1600.   8.054   2400.   10.452
        3200.   12.502  4800.   15.964  6400.   18.882  9600.   23.728
        12800.  27.695  ENDT
$-------2-------3-------4-------5-------6-------7-------8-------9-------
$ 3M TYPE 112 VISCOELASTIC DAMPING MATERIAL
$ IMAGINARY PART OF COMPLEX MODULUS, TI(F), TEMP = 50.0 DEGREES F.
$    G REF =      1.0000, ETA REF =      1.0000, ETA STRUC =      0.0000
$    UNITS = NEWTON/MM**2
$-------2-------3-------4-------5-------6-------7-------8-------9-------
TABLED1 3051
        50.     1.158   75.     1.547   100.    1.858   150.    2.389
        200.    2.841   300.    3.602   400.    4.237   600.    5.295
        800.    6.186   1200.   7.667   1600.   8.892   2400.   10.892
        3200.   12.515  4800.   15.103  6400.   17.150  9600.   20.319
        12800.  22.692  ENDT
$-------2-------3-------4-------5-------6-------7-------8-------9-------
```

Figure 23 COMPLEX MODULUS TABLES USED IN MSC/NASTRAN DIRECT FREQUENCY RESPONSE ANALYSIS

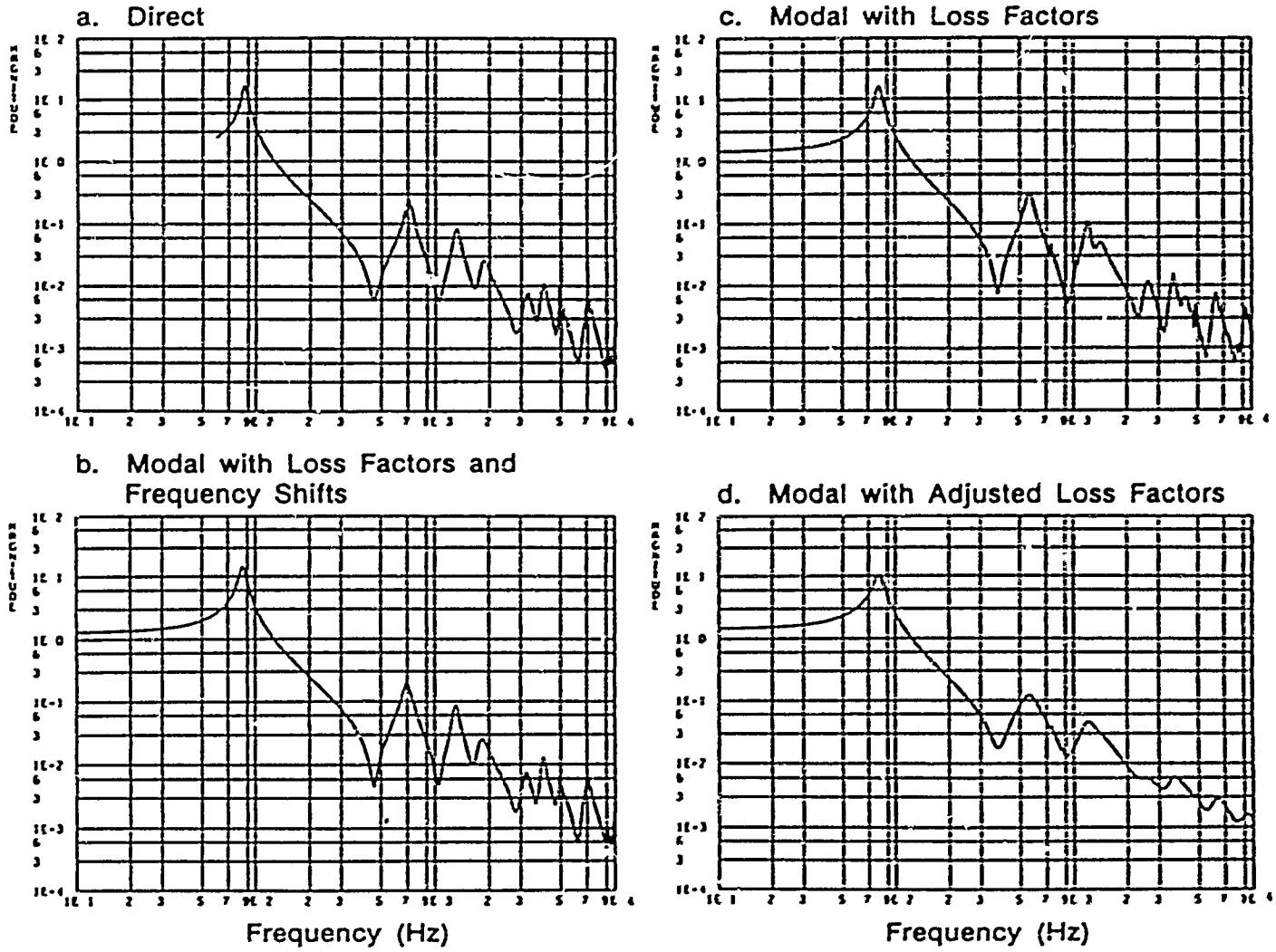


Figure 24 GRAPHICAL FREQUENCY RESPONSE METHODS COMPARISON AT 0°F

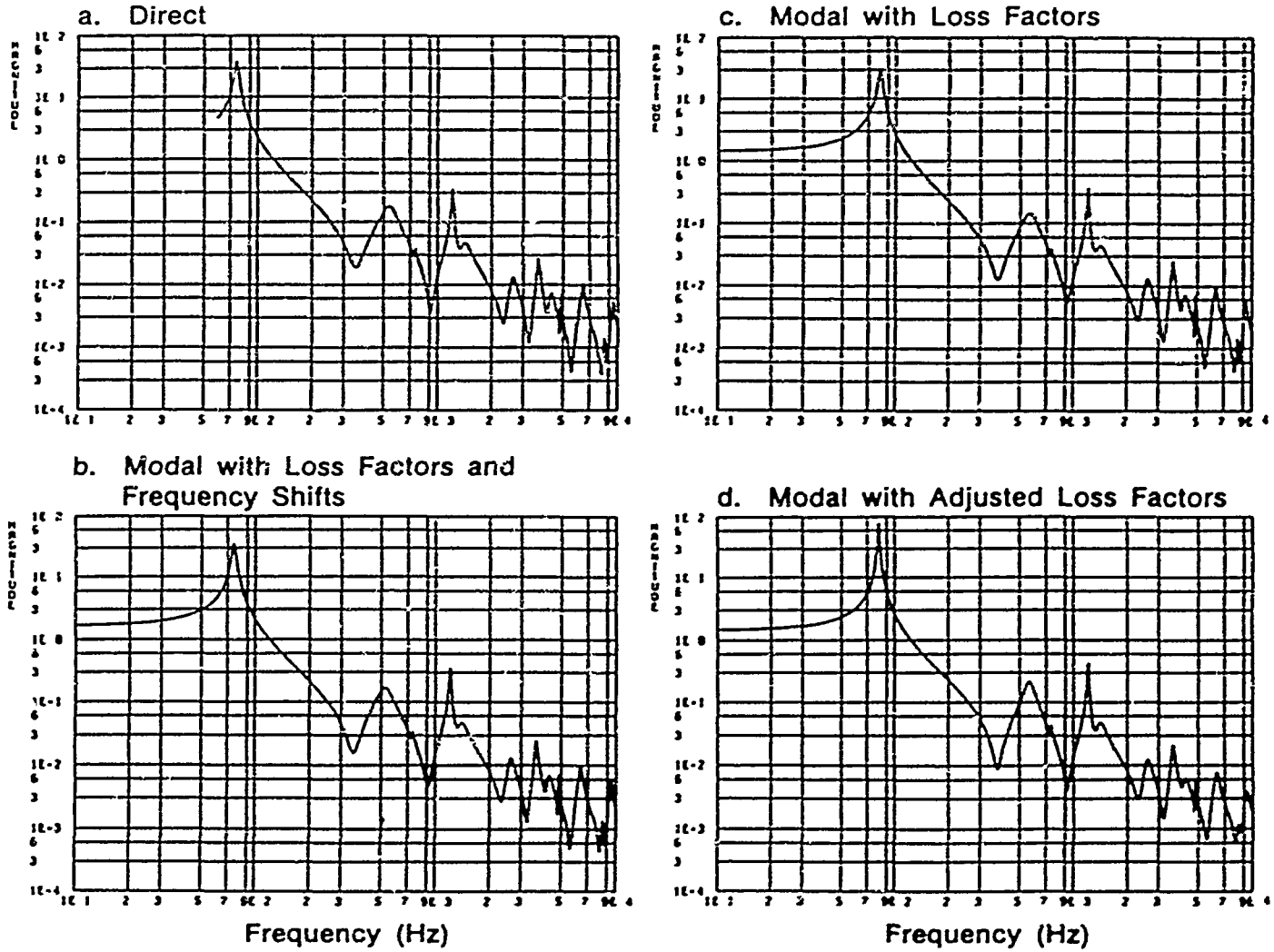


Figure 25 GRAPHICAL FREQUENCY RESPONSE METHODS COMPARISON AT 50°F

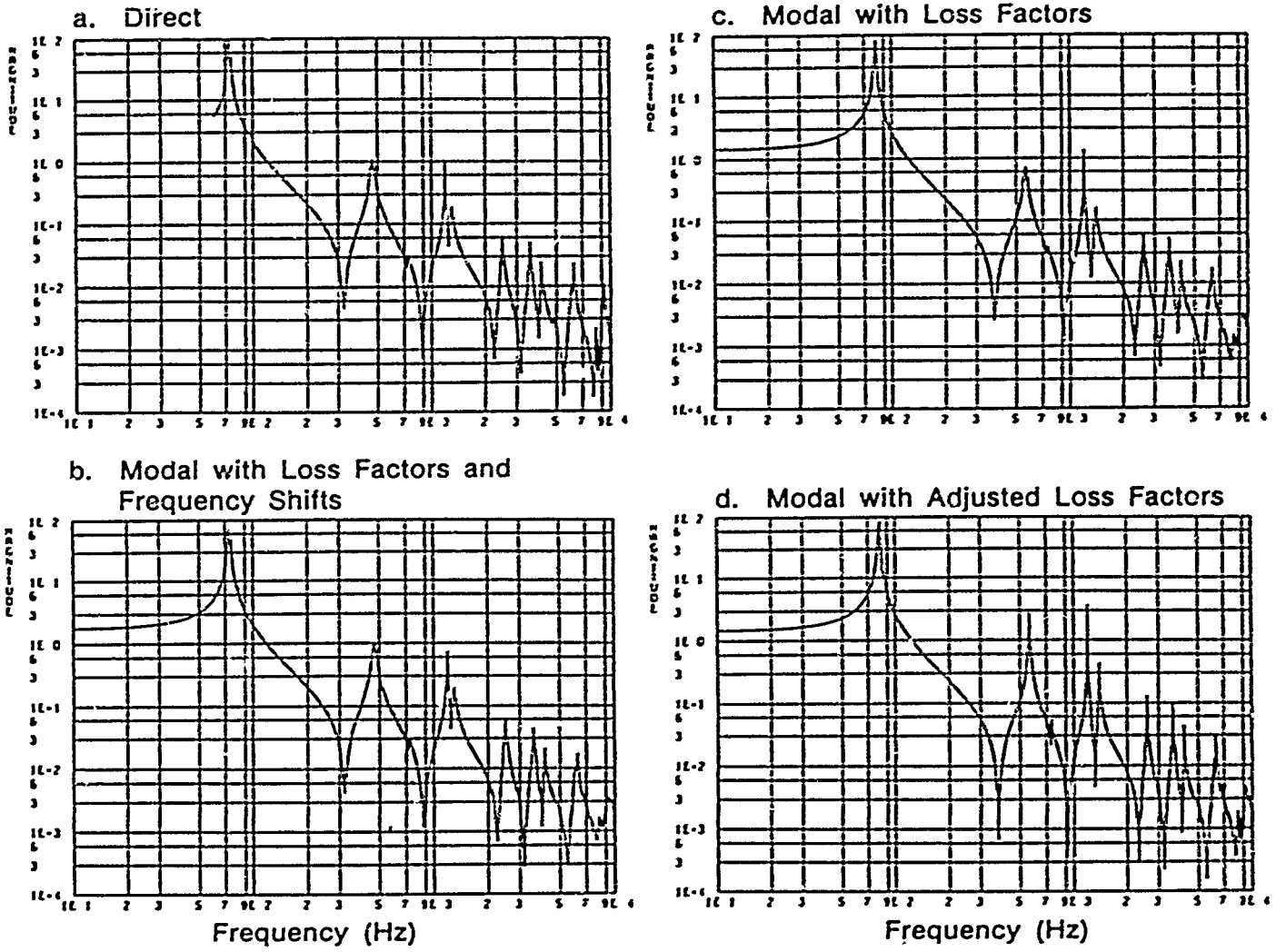


Figure 26 GRAPHICAL FREQUENCY RESPONSE METHODS COMPARISON AT 100°F

Figure 27 Tabulated Frequency Response Methods Comparison at 0 deg. F.

	Frequency Response Method							
	I.		II.		III.		IV.	
	Direct Method		Modal With Loss Factors & Freq. Shifts		Modal With Loss Factors		Modal With Adjusted Loss Factors	
Mode Description	Direct (REF.)		Modal	% Diff.	Modal	%Diff.	Modal	%Diff.
1 Bending	F =	86.23	84.96	-1.5	80.85	-6.2	80.50	-6.6
	DISP =	16.46	14.81	-10.0	16.33	-0.8	10.28	-37.5
2 Bending	F =	706.8	696.7	-1.4	565.3	-20.0	563.0	-20.3
	DISP =	.2417	.2043	-15.5	.3103	+28.4	.1233	-48.9
1 Transverse Bending	F =	---	---	---	749.5	---	749.9	---
	DISP =	---	---	---	.04727	---	.03940	---
1 Torsion	F =	1311.	1307.	-0.3	1210.	-7.7	1220.	-6.9
	DISP =	.08478	.08906	+5.0	.1087	+28.2	.04543	-46.4
3 Bending	F =	1866.	1830.	-1.9	1419.	-23.9	---	---
	DISP =	.02615	.02599	-0.6	.05052	+93.2	---	---
4 Bending	F =	3279.	3226.	-1.6	2621.	-20.0	---	---
	DISP =	.007489	.007507	+0.2	.01174	+56.8	---	---
2 Torsion/2 Trans Bend	F =	4011.	3995.	-0.4	3627.	-9.6	3673.	-8.4
	DISP =	.01104	.01283	+16.2	.01535	+39.0	.00618	-44.0
5 Bending	F =	---	---	---	4238.	---	---	---
	DISP =	---	---	---	.00653	---	---	---
2 Trans Bend/ 2 Torsion	F =	4869.	4875.	+0.1	4817.	-1.0	4825.	-0.9
	DISP =	.01033	.00670	-35.1	.00494	-52.2	.00331	-67.9
6 Bending	F =	7049.	7052.	0.0	6338.	-10.1	6383.	-9.4
	DISP =	.006082	.006176	+1.5	.007493	+23.2	.002785	-54.2
3 Torsion	F =	---	---	---	---	---	---	---
	DISP =	---	---	---	---	---	---	---
7 Bending	F =	9104.	9100.	0.0	8416.	-7.6	---	---
	DISP =	.001059	.000993	-6.2	.001112	+5.0	---	---
4 Torsion	F =	#	#	---	9297.	---	9365.	---
	DISP =	---	---	---	.004307	---	.001582	---

Note: # Mode is above 10,000 Hz

Figure 28 Tabulated Frequency Response Methods Comparison at 50 deg. F.

	Frequency Response Method							
	I.		II.		III.		IV.	
	Direct Method		Modal With Loss Factors & Freq. Shifts		Modal With Loss Factors		Modal With Adjusted Loss Factors	
Mode Description	Direct (REF.)		Modal	% Diff.	Modal	%Diff.	Modal	%Diff.
1 Bending	F =	75.75	75.60	-0.2	80.97	+6.9	81.00	+6.8
	DISP =	38.96	36.02	-7.5	31.37	-19.5	79.64	+104.4
2 Bending	F =	532.3	521.8	-2.0	564.2	+6.0	564.9	+6.1
	DISP =	.1792	.1718	-4.1	.1461	-18.5	.2125	+18.6
1 Transverse Bending	F =	748.6	747.2	-0.2	750.2	+0.2	749.9	+0.2
	DISP =	.04040	.03532	-12.6	.04038	0.0	.04340	+7.4
1 Torsion	F =	1209.	1207.	-0.2	1211.	+0.2	1211.	+0.1
	DISP =	.3879	.3850	-0.7	.3818	-1.6	.4338	+11.8
3 Bending	F =	1417.	1403.	-1.0	1424.	+0.5	1424.	+0.5
	DISP =	.04732	.04723	-0.2	.04515	-4.6	.04776	+0.9
4 Bending	F =	2653.	2642.	-0.4	2618.	-1.3	2620.	-1.2
	DISP =	.01322	.01291	-2.3	.01320	-0.1	.01216	-8.0
2 Torsion/2 Trans Bend	F =	3648.	3640.	-0.2	3621.	-0.7	3623.	-0.7
	DISP =	.02785	.02509	-9.9	.02540	-8.8	.02129	-23.5
5 Bending	F =	4294.	4294.	0.0	4233.	-1.4	4240.	-1.2
	DISP =	.007291	.006967	-4.4	.007263	-0.4	.006383	-12.4
2 Trans Bend/ 2 Torsion	F =	4834.	4828.	-0.1	4811.	-0.5	4813.	-0.4
	DISP =	.007107	.007393	+4.0	.007345	+3.3	.006181	-13.0
6 Bending	F =	---	---	---	---	---	---	---
	DISP =	---	---	---	---	---	---	---
3 Torsion	F =	6425.	6407.	-0.3	6334.	-1.4	6339.	-1.3
	DISP =	.01049	.00998	-4.8	.01022	-2.6	.00765	-27.0
7 Bending	F =	8496.	8491.	0.0	8403.	-1.1	8416.	-0.9
	DISP =	.001450	.001402	-3.3	.001437	-0.9	.001183	-18.4
4 Torsion	F =	#	#	---	9277.	---	9305.	---
	DISP =	---	---	---	.005892	---	.003935	---

Note: # Mode is above 10,000 Hz

Figure 29 Tabulated Frequency Response Methods Comparison at 100 deg. F.

	Frequency Response Method							
	I.		II.		III.		IV.	
	Direct Method		Modal With Loss Factors & Freq. Shifts		Modal With Loss Factors		Modal With Adjusted Loss Factors	
Mode Description	Direct (REF.)		Modal	% Diff.	Modal	%Diff.	Modal	%Diff.
1 Bending	F = 73.90		73.90	0.0	81.00	+9.6	81.00	+9.6
	DISP = 307.2		285.1	-7.2	237.6	-22.6	1614.	+425.4
2 Bending	F = 467.8		467.6	0.0	565.4	+20.9	565.5	+20.9
	DISP = 1.089		1.050	-3.6	.7173	-34.1	2.844	+161.1
1 Transverse Bending	F = 736.7		735.4	-0.2	751.3	+2.0	748.5	+1.6
	DISP = .03368		.02984	-11.4	.03947	+17.2	.06037	+79.2
1 Torsion	F = 1197.		1196.	-0.1	1212.	+1.2	1211.	+1.2
	DISP = 1.585		1.428	-9.9	1.392	-12.2	4.035	+154.5
3 Bending	F = 1295.		1294.	-0.1	1405.	+8.5	1403.	+8.3
	DISP = .1968		.1988	+1.0	.1613	-18.0	.4448	+126.0
4 Bending	F = 2505.		2505.	0.0	2599.	+3.7	2598.	+3.7
	DISP = .06161		.06232	+1.1	.05790	-6.0	.1334	+116.5
2 Torsion/2 Trans Bend	F = 3574.		3577.	+0.1	3618.	+1.2	3618.	+1.2
	DISP = .05865		.04614	-21.3	.05361	-8.6	.1069	+82.2
5 Bending	F = 4118.		4114.	-0.1	4194.	+1.8	4190.	+1.7
	DISP = .02399		.02263	-5.7	.02200	-8.3	.04276	+78.2
2 Trans Bend/ 2 Torsion	F = 4814.		---	---	---	---	---	---
	DISP = .003095		---	---	---	---	---	---
6 Bending	F = 6076.		6066.	-0.2	6133.	+0.9	6135.	+0.9
	DISP = .01189		.01029	-13.5	.00945	-20.5	.01369	+15.1
3 Torsion	F = 6256.		6241.	-0.2	6327.	+1.1	6321.	+1.0
	DISP = .02364		.01750	-26.0	.01685	-28.7	.02903	+22.8
7 Bending	F = 8353.		8316.	-0.4	8412.	+0.7	8398.	+0.5
	DISP = .002188		.001665	-23.9	.001463	-33.1	.001935	-11.6
4 Torsion	F = 9185.		9263.	+0.8	9332.	+1.6	9291.	+1.1
	DISP = .01072		.00346	-67.7	.003138	-70.7	.004715	-56.0

Figure 30 Response Method Summary: Mean Errors and CPU Time

a. Mean Absolute Frequency and Displacement Magnitude Errors Summarized from Figures 27, 28 and 29.

Frequency Response Method	Comparison (10-10000 Hz)	Temperature (Deg. F.) 0	50	100	Mean Error For 0,50,100
I. Direct Method	Freq Error =	0.0	0.0	0.0	0.0
	Disp Error =	0.0	0.0	0.0	0.0
	No. Peaks =	9	11	13	---
	Mismatch # =	0	0	0	0/33
II. Modal Method With Loss Factors and Freq. Shifts	Freq Error =	0.8 %	0.4 %	0.2 %	0.5 %
	Disp Error =	10.0 %	4.9 %	16.0 %	10.3 %
	No. Peaks =	9	11	12	---
	Mismatch # =	0	0	1	1/33
III. Modal Method With Loss Factors	Freq Error =	11.8 %	1.8 %	4.4 %	6.0 %
	Disp Error =	36.3 %	5.5 %	23.3 %	21.7 %
	No. Peaks =	12	12	12	---
	Mismatch # =	3	1	1	5/33
IV. Modal Method With Adjusted Loss Factors	Freq Error =	8.7 %	1.7 %	4.3 %	4.9 %
	Disp Error =	49.8 %	22.3 %	110.7 %	60.9 %
	No. Peaks =	8	12	12	---
	Mismatch # =	5	1	1	7/33

Note: # number of resonance peaks mismatched (extra or missing)

b. CPU Time Comparison for Modal vs. Direct Frequency Response Methods (five frequency response plots using 500 frequency increments each)

(1) Modal Strain Energy and Modal Frequency Response Method with Loss Factors and Frequency Shifts

MSC/NASTRAN Eigenvalue Runs (8 x 52) - - - -	416 sec.	
DAMPED, DAMPRO, DAMPIT - - - - - - - - - -	12 sec.	
MSC/NASTRAN Modal Freq Response (5 x 28) - -	140 sec.	
TOTAL	568 sec.	(1X)

(2) Direct Frequency Response Method

MSC/NASTRAN Direct Freq Response (5 x 803) -	4015 sec.	
TOTAL	4015 sec.	(7X)

INFLUENCE OF TEMPERATURE ON STRUCTURAL JOINTS WITH DESIGNED-IN DAMPING

Jacky C. Prucz
West Virginia University

Philip Smith and Lawrence W. Rehfield
Georgia Institute of Technology

Ambur D. Reddy
Lockheed-Georgia Company

ABSTRACT

An innovative means to enhance the inherent damping in structures is provided by the designed-in incorporation of viscoelastic materials in joints. The joints, as envisioned, are double-lap shear joints that dissipate energy when worked in an axial direction. The damping and stiffness characteristics of such joints have been evaluated experimentally at various temperatures and frequencies which are expected to be representative for large space structures. A new, non-resonant experimental technique has been utilized for this investigation. It provides the complex stiffness of the test specimen at extremely low strain levels and accounts for elastic deformations in the test set-up by means of carefully measured calibration factors. The temperature and frequency variations of the overall joint properties follow, in general, the same trends as the corresponding properties of the particular viscoelastic material used in the joint. The test data show that properly selected viscoelastic materials and design configurations can reduce the dependence of the joint properties on temperature and frequency variations. Significant damping benefits are possible without unacceptable stiffness penalties.

INTRODUCTION

Mission requirements for future space structures dictate extremely large dimensions by today's standards. Several important missions, such as defense systems, orbiting telescopes or large antennae require very tight orientation tolerances, short settling times and low vibration levels. The stringent controllability requirements of large space structures have spawned intensive research and development efforts in the vibration control area. They are generally divided in two basic approaches - active modal control and passive damping enhancement. A balanced approach, that properly combines active and passive means, is widely accepted today as the most realistic and practical solution to motion control of large space structures. High passive damping not only limits vibration amplitudes and shortens transient decay times, but also has favorable synergistic effects when it is combined with active controls[1].

An innovative means to enhance the inherent damping in structures is provided by the designed-in incorporation of viscoelastic materials in joints. It combines the well-known damping capability of viscoelastic materials[2] with the predominant influence that joints and supports have on the overall damping of most structures[3]. As opposed to the commonly used add-on approach for damping treatments, the designed-in approach provides a promising opportunity to maximize the damping benefit while minimizing the associated penalties in other structural properties.

Preliminary theoretical and experimental research for the development of passively damped joining concepts has been a recent cooperative undertaking of McDonnell Douglas Astronautics Company and Georgia Institute of Technology under the sponsorship of the Air Force Office of Scientific Research. Two new experimental techniques developed during the initial phase of the program for dynamic characterization of such joints have been presented at the "Vibration Damping Workshop I."[4] They are referred to as the "simplified steady state" and the "sine pulse propagation" methods. The first yields the complex stiffness by using a non-resonant forced vibration approach whereas the second provides the energy dissipated by damping by using a stress wave propagation approach. Their application to room temperature testing of passively damped joint specimens and the corresponding results have been described in Ref. 5. A detailed description of the test specimens, their design criteria, assumptions and methodologies and their fabrication procedures appears in Ref. 6. Two new analytical models have been developed during this research program for design analyses of passively damped joints of double-lap configuration. The first is a fully elastic model presented in Refs. 4 and 6 whereas the second is a quasi-static model that employs the complex modulus concept to describe the viscoelastic behavior of the adhesive layers[7]. Good correlation has been obtained between the two models as well as between analytical predictions and experimental results[7]. A detailed presentation of the room temperature tests, the analytical modeling and parametric studies is given in Ref. 8. A complete overview of the entire program, including low and high temperature tests, is reported in Ref. 9.

This paper deals only with the low and high temperature tests on representative specimens of passively damped joints. Its objective is to complete the reporting of results generated by the research program mentioned above. It is associated primarily with Ref. 5 since it shows how some of the room temperature damping and stiffness properties presented in that reference may change when measured either at low or high temperatures. The environmental temperature tests have been conducted on 8 specimens at temperatures of -50, 25, 75 and 200°F, at four of the test frequencies investigated in Ref. 5, namely 0.25, 1.0, 25.0 and 100.0 Hz. Since damping enhancement in large space structures was the primary motivation of this program, the tests have been confined to low strain levels and frequency and temperature ranges considered to be representative for such structures[1,5].

TEST SPECIMENS

The passively damped joint specimens selected for low and high temperature tests are listed in Table 1. Six different types of viscoelastic materials, which are considered to be suitable for space applications, have been used in these specimens. Their density, manufacturer, trade names and chemical base are given in Table 1.

All the specimens are based upon the symmetric double-lap configuration of bonded joints in which the conventional elastic adhesive is replaced by viscoelastic material. The damping enhancement is achieved by shear deformation of the viscoelastic adhesive layers when the joint members are loaded in their axial direction (Fig. 1). The use of this joining concept is based upon the hypothesis that it is possible to obtain a favorable trade-off when structural stiffness is exchanged for increased structural damping. The need to accept a stiffness penalty arises from the requirement to make the joints somewhat flexible so that a reasonable amount of strain energy is resident in the joints. This strain energy is then available for dissipation by the viscoelastic material selected expressly for this purpose.

A slightly different configuration of a double-lap joint has also been investigated as a possible way to achieve better trade-offs between the damping benefit and the associated stiffness penalty. It includes a direct glass-fiber connection between the members of the joint, as shown in Fig. 2. In addition to higher axial stiffness, this elastic link provides structural redundancy at elevated temperatures and in the case of viscoelastic materials with poor creep resistance. Two of the specimens listed in Table 1 include such elastic connection elements. They are specimens 15 and 18 that use the same viscoelastic materials as the regular double-lap specimens 3 and 5, respectively. The analytical models developed for passively damped joints (Refs. 6 and 7) account for the effect of these elastic links on the overall properties of the joint.

The dimensions shown in Figs. 1 and 2 are typical for all the test specimens. The only geometric parameter that varies significantly from one specimen to another is the thickness of the adhesive layers. Its value is about 0.007 in. for specimens 1 and 11, about 0.05 in. for specimens 5, 9, 15 and 21, and about 0.125 in. for specimen 3. The axial stiffness of certain specimens could have been increased by using thinner adhesive layers when feasible from the manufacturing standpoint.

Table 1. Specimens for Environmental Temperature Tests

Specimen Number	Viscoelastic Material			
	Density (lb/in^3)	Manufacturer	Name	Type
1	0.035	3M	ISD 110	Acrylic
3	0.046	3M	EC 2216	Epoxy
5	0.035	Soundcoat	DYAD 606	Polyurethane
9	0.029	GE	SMRD 100F90	Epoxy
11	0.046	GE	RTV 630	Silicone
15*	0.046	3M	EC 2216	Epoxy
18*	0.035	Soundcoat	DYAD 606	Polyurethane
21		MDAC		Rubber Plastic

* Includes Elastic Connection Elements

SUMMARY OF ROOM TEMPERATURE

EXPERIMENTS

The damping and stiffness characteristics of selected joint specimens have been measured at room temperature (75°F) and 8 different frequencies - 0.1, 0.25, 0.5, 1.0, 10, 25, 50 and 100 Hz. Since the primary candidates for large space structures are repetitive lattice trusses, the main loading direction considered in the design and testing of these specimens was the axial one. The main experimental procedures and results are presented in Ref. 5.

Three different experimental methods have been used for the room temperature tests. Two methods are new and have been developed during this research program. They are referred to as the simplified steady state and the sine pulse propagation techniques, respectively. In addition, the classical hysteresis-loop approach has been applied on all the specimens in order to enhance the data base at very low frequencies. New and innovative data acquisition and reduction procedures, based on advanced digital instrumentation, have been utilized for all the three testing techniques. Good correlation has been obtained among the data generated by different methods in the same testing conditions, as shown in Figs. 3 and 4 which are reproduced here from Ref. 5. A least-square fitting routine is used in these figures in order to draw the "best fit" line between the data points generated by the same method.

The frequency effect on room temperature damping and stiffness characteristics of selected specimens is shown in Figs. 5 and 6, respectively, which are reproduced from Ref. 5. Again, the continuous lines represent the "best fit" generated by a least-square routine for all the data points of the same specimen. The results shown in these figures have been obtained by the simplified steady state approach. Specimen 14, which is not listed in Table 1, is a standard double-lap bonded joint with a rigid EA 956 epoxy used as adhesive.

The results show that favorable trade-offs between the damping benefit and the associated stiffness penalty can be achieved if the designed-in approach is adopted. This possibility is well reflected in the test data for specimen 15, although better tradeoffs can be achieved with improved design configurations.

It should be emphasized that the damping data in Figure 5 are expressed in terms of the measured loss factor of the joint rather than the material loss factor of the viscoelastic layers. The damping characteristics of soft joints, like specimen 1, are dominated by those of the adhesive materials, but as these materials become stiffer the joint loss factor is reduced from the damping material loss factor since the viscoelastic layers share less of the total strain energy stored in the joint[7]. The stiffness increase with frequency, as illustrated in Figure 6, may yield, therefore, a

reduction in the damping performance of the joint at higher frequencies over for a viscoelastic material with a relatively flat loss factor-frequency behavior.

LOW AND HIGH TEMPERATURE TESTS

The environmental temperature tests have been performed on all the specimens listed in Table 1 at four different temperatures within the range expected for space structures: -50, 25, 75 and 200°F. These tests have been confined to four of the eight frequencies used in the room temperature tests, namely 0.25, 1.0, 25.0 and 100 Hz.

Only the simplified steady state technique has been utilized for the environmental temperature tests since it is expedient and correlates well with the other two methods applied in the room temperature experiments. The hysteresis-loop approach has been excluded since it is applicable only for very low frequencies, usually below 0.5 Hz. The sine-pulse propagation approach is preferable in the case of multiple-branch joints or when accurate absolute values of damping in transient phenomena are needed. It does not require a custom-made, piezoelectric motion transducer as needed for the simplified steady state method. However, the fact that all the equipment required for the simplified steady state method was already available from the room-temperature tests, has facilitated its selection for low and high temperature tests. In addition, this approach is more closely related to conventional measurement and interpretation concepts of damping data and it permits a faster data reduction procedure than the sine pulse propagation method.

The simplified steady state method is described in Refs. 4, 5 and 8. The only difference between the experimental set-up of the room temperature tests and that of the environmental temperature tests is the placement of the test fixture inside an environmental chamber, as shown in Fig. 7. This is a BLUE-M LN-270C-1 constant temperature environmental chamber with mechanical convection horizontal airflow. It uses liquid nitrogen as the cryogenic agent. Due to the highly corrosive nature of this cooling medium, the test fixture and the dynamic response pick-ups had to be made of stainless steel. The chamber can provide a temperature range from -180°F to 550°F, which has not been fully utilized in these tests in order to avoid any potential irreversible damage to the joint specimens.

When a harmonic voltage is applied to the piezoelectric exciter, it generates a small axial harmonic motion which is transmitted through the test specimen and results in an axial harmonic force measured by the piezoelectric load cell. If the displacement output of the exciter in unloaded condition, i.e., with no specimen attached to it, is expressed as

$$x_u(t) = A \cos wt \qquad (1)$$

where w is the circular frequency (rad/sec), then the force signal measured by the load cell is

$$P(t) = B \cos (wt + \theta) \qquad (2)$$

where the phase lag • is caused by the viscoelastic behavior of the test specimen. By using the complex stiffness concept of viscoelasticity[10] the following equations are developed for the real and imaginary stiffness components of the specimen[4]:

$$Re(K) = \frac{1}{A}\left(\frac{B}{A}\cos \bullet - \frac{B^2}{A^2} C\right) \tag{3}$$

$$Im(K) = \frac{1}{A}\frac{B}{A}\sin \bullet \tag{4}$$

where:

$$A = 1 - 2C\frac{B}{A}\cos \bullet + C^2\left(\frac{B}{A}\right)^2 \tag{5}$$

$$C = \frac{1}{K_1} + \frac{1}{K_2} + \frac{1}{K_3} \tag{6}$$

In the loaded condition, the displacement amplitude of the exciter departs from A because its internal stiffness, K_1, is not infinite. The actual axial motion can be determined from the equilibrium condition between the external reaction force and the internal force generated by the piezoelectric effect. Its expression is

$$x_L(t) = P(t)\left(\frac{1}{K} + \frac{1}{K_2} + \frac{1}{K_3}\right) \tag{7}$$

...hich is derived by assuming that the total external force is the resultant of three elastic restoring elements connected in series, namely the specimen, the load cell and the test fixture whose stiffnesses are K, K_2, and K_3, respectively. The equivalent compliance C in the above equations is a correction term that accounts for the stiffness contributions of the test fixture, load cell and displacement transducer. It can be neglected when the stiffness of the specimen is much lower than the combined stiffness of these elements.

The elastic stiffness of the test specimen is calculated from Eq. (3) whereas its overall loss factor is given by:

$$\eta = \frac{Im(K)}{Re(K)} \tag{8}$$

The parameters A, B and • are determined from the two harmonic signals acquired in each test - the input voltage applied to the piezoelectric exciter and the response of the load cell. These signals are averaged, stored and analyzed on separate channels of a NICOLET 4094A digital oscilloscope. The load phase lag •, with respect to the applied displacement, is determined by the difference between the zero-crossings of the corresponding time waves.

After possible DC components are eliminated from the two signals, the displacement amplitude A and the force amplitude B are calculated by using the appropriate calibration factor. The sensitivity of the PCB piezoelectric load cell was about 17 pC/lb, whereas the sensitivity of the piezoelectric exciter in unloaded condition was about 0.2 μ inch/volt. The latter was measured in preliminary calibration tests at each of the selected test frequencies and the exact value corresponding to each frequency has been used in calculating A.[8] Since the amplitude of the input voltage to the motion transducer was about 300 volts in all tests, its maximum stroke was about 60 μ inch, with the exact value varying slightly from one frequency to another.[8] A schematic of the data analysis procedure in the simplified steady state method is shown in Fig. 8.

The primary drawback of the simplified steady state approach utilized in these experiments is the tedious preliminary calibration tests which are required for measuring the equivalent compliance C. They include two different sets of experiments - one in unloaded configuration of the piezoelectric motion transducer and the other in its loaded configuration. A reference aluminum specimen whose axial stiffness is 225,000 lb/in is mounted in the test fixture when the loaded sensitivity of the exciter is measured. A piezoelectric ENDEVCO accelerometer with high sensitivity (about 500 pC/g) is used to measure the displacement output of the motion transducer in the calibration tests. The data analysis for these tests is performed in the frequency domain by using a HP 5423A Dynamic Analyzer, as described in detail in Ref. 8.

The equivalent compliance C is calculated from the equation

$$C = \frac{A}{B} - \frac{1}{K_{ref}} \qquad (9)$$

where K_{ref} is the stiffness of the reference specimen (K_{ref} = 225,000 lb/in in the present case). Eq. (9) is obtained from Eqs. (3) and (5) by substituting Re(K) by K_{ref} and assuming that the reference specimen has no damping, i.e., $\bullet$=o. Since repeated measurements of C revealed a yet unexplained sensitivity to both frequency and temperature, its value has been determined separately for each combination of frequency and temperature selected for the tests. These values are shown in Table 2. For each test, only the corresponding value of C from Table 2 has been used in the data analysis according to Eqs. (3-6). One may notice that the stiffness contributions included in the parameter C, Eq. (6), become more significant as the temperature increases or the frequency decreases. This behavior can possibly be related to improper mounting and preloading of the stack of piezoelectric crystals in the motion transducer. However, a thorough analysis of the exciter is needed before the problem can be clearly identified and corrected.

Table 2. Equivalent Compliance Values for Test Frequencies and Temperatures (in/lb x 10^6).

Freq. (Hz) / Temp (°F)	0.25	1.0	25.0	100.0
- 50	1.84	1.77	0.98	0.69
25	1.97	1.97	1.22	0.91
75	2.53	2.57	1.80	1.45
200	4.49	4.87	3.94	3.79

RESULTS AND DISCUSSION

The low and high temperature test results are presented here in the same format as the room temperature test results in Refs. 5 and 8. The conventional format of reduced frequency monograms[11] is not necessary in this case because of the low number of data points. Although the number of data points is not sufficient to determine exact numerical values over the whole test temperature and frequency ranges, general trends can be established. The "best fit" of a given set of data points is obtained, like in the room temperature tests, by using a least square fitting routine and is shown as a line in the following figures.

Figures 9-12 show that the damping performance of regular double-lap joints with EC 2216, SMRD 100 F90, ISD 110 and DYAD 606 viscoelastic materials respectively, varies strongly with temperature. In most cases the loss factor peaks at room temperature, approximately, but drops sharply at low and high temperatures. Such a behavior is expected since the viscoelastic materials used in the joints are usually designed to perform best at room temperature. It should be emphasized that, similarly to Fig. 5, the damping data shown in Figs. 9-12 are expressed in terms of the overall loss factor of the joint system rather than the material loss factor of its adhesive. The analytical model described in Ref. 7 provides a uniquely defined relationship between these two loss factors. Material properties of the EC 2216 and the GE SMRD viscoelastic adhesives are illustrated in Figs. 13 and 14, respectively. One may notice that the joint damping shown in Fig. 9 follows the same trends as the corresponding material damping in Fig. 13. A similar conclusion can be drawn by comparing Fig. 10 with Fig. 14.

For all the specimens shown in Figs. 9-12, the loss factor dependence on frequency is much weaker than its sensitivity to temperature changes. This observation agrees with Figs. 13 and 14 and with the room temperature test results, as shown in Fig. 5. At low temperatures, the loss factor tends to decrease as the frequency increases. At high temperatures, however, the loss factor increases with frequency. These trends are illustrated in Figs. 15 and 16 for specimens 3 and 9, respectively.

Since the design trade-offs between potential damping benefits and the stiffness penalties associated with them are an important topic of this research, the stiffness characteristics of specimens 3 and 9 are shown in Figs. 17 and 18, respectively. If Fig. 17 is analyzed in conjunction with Fig. 15 and Fig. 18 is analyzed in conjunction with Fig. 16 one may identify a certain temperature range for each viscoelastic material within which a favorable trade-off between damping and stiffness may be achieved. Figs. 17 and 18 show a significant stiffness reduction with increasing temperature, but a much lower sensitivity to frequency changes. The "relative stiffness" parameter used in these figures is the ratio between the axial stiffness of the actual joint specimen and that of a continuous reference specimen whose stiffness if 585,000 lb/in.

Two of the viscoelastic materials listed in Table 1 seem to be more suitable to applications in which good damping performance is required over a wide temperature range. One is RTV 630 used in specimen 11 and the other is a new rubber plastic material manufactured by McDonnell Douglas Astronautics Company[9] and used in specimen 21. The foregoing conclusion is based upon the relatively flat behavior displayed by these specimens in Figs. 19 and 20 over the test temperature range. Small peaks can still be observed in the room temperature region.

The effect of the elastic connection elements between the members of the joint (Fig. 2), upon its overall loss factor can be analyzed by comparing Fig. 21 to Fig. 9 for the EC 2216 viscoelastic material, or by comparing Fig. 22 to Fig. 12 for the DYAD 606 viscoelastic material. In both cases, as expected, the elastic links reduce the damping benefit, but they also reduce its variations with temperature and frequency changes. This is due to the fact that the influence of the viscoelastic material properties on the overall properties of the joint is reduced with such a configuration and the structural interactions among the joint constituents become more pronounced.[7]

A good indication as to the reliability of the test data generated by the simplified steady state method can be obtained by comparing the results obtained on certain specimens during the environmental temperature tests with those measured on the same specimens at the same frequencies during the room temperature tests. Since the two series of tests have been performed at a time interval of about one year with no temperature measurement during the room temperature tests, an approximate agreement among the results should be considered satisfactory. Such an agreement is indeed observed by comparing the data measured at 75°F on specimen 3 (compare Fig. 9 with Fig. 5 and Fig. 17 with Fig. 6), specimen 1 (compare Fig. 11 with Fig. 5) or specimen 15 (compare Fig. 21 with Fig. 5).

CONCLUDING REMARKS

Passively damped joints provide a cheap, simple and efficient means to enhance the inherent damping in space structures. However, careful consideration should be given to their design configuration and material selection in order to achieve favorable trade-offs between the damping benefit and the associated stiffness penalty. Potential penalties that have not been analyzed in this research, like strength, weight, and cost must also be considered.

The test results show, in general, that the overall damping and stiffness characteristics of axially loaded double-lap joints are determined primarily by the material properties of their viscoelastic adhesive layers. For instance, the temperature variations of the joint properties follow the same qualitative trends as the corresponding properties of the particular viscoelastic material used in the joint. These variations can be reduced by tailoring the material selection to the temperature range within which the joint is expected to operate. When it is not possible to choose viscoelastic materials with relatively weak temperature dependence, like RTV 630 or the rubber plastic alloy of McDonnell-Douglas Co., the use of thermal protection on the joints may be considered for wide temperature range applications.

The simplified steady state technique provides a reliable characterization of passively damped joint specimens if sufficient care is taken in measuring and using the various calibration factors included in its equations. The accuracy of the test data generated by this method is extremely sensitive to possible errors in the calibration factors. Since some of these factors may change not only with the test frequency and temperature, but also because of slight mounting inconsistencies of the specimens in the test fixture, the calibration factors should be rechecked any time a new specimen is mounted in the fixture. The calibration problem is greatly reduced in the sine-pulse propagation approach, which may be considered a good alternative to the simplified steady state method when sufficient time is available for data reduction.

ACKNOWLEDGMENT

This effort was supported by the Air Force Office of Scientific Research on Contract F49620-83-C-0017. The contribution of Mr. R. W. Trudell from McDonnell Douglas Company to the initiation and successful completion of this research program is gratefully acknowledged.

REFERENCES

1. Trudell, R. W., Curley, R. C., and Rogers, L. C., "Passive Damping in Large Precision Space Structures," Paper No. 80-0677, AIAA/ASME/ASCE/AHS Structures, Structural Dynamics and Materials Conference, Seattle, WA, May 1980, pp. 124-136.

2. Nakra, B. C., "Vibration Control with Viscoelastic Materials," Shock and Vibration Digest, Vol. 8, No. 6, June 1975.

3. Beards, C. F., "Damping in Structural Joints," Shock and Vibration Digest, Vol. 11, No. 9, September 1979.

4. Trudell, R. W., Rohfield, L. W., Reddy, A. D., Prucz, J., and Peebles, J., "Passively Damped Joints for Advanced Space Structures," Presented at the Vibration Damping Workshop sponsored by the Air Force Flight Dynamics Laboratory, Long Beach, CA, February 27-29, 1984, and published in the Proceedings.

5. Prucz, J., Reddy, A. D., Rohfield, L. W., and Trudell, R. W., "Experimental Characterization of Passively Damped Joints for Space Structures," Paper No. 85-0756, AIAA/ASME/ASCE/AHS 26th Structures, Structural Dynamics and Materials Conference, Orlando, FL, April 1985. To appear in the September-October 1986 issue of the Journal of Spacecraft and Rockets.

6. Trudell, R. W. and Blevins, C. E., "Passively Damped Joints for Advanced Space Structures," McDonnell Douglas Astronautics Company, Huntington Beach, Annual Technical Report MDC H1178, June 1984.

7. Prucz, J., "Analysis of Design Tradeoffs for Passively Damped Structural Joints," Paper 85-0780 AIAA/ASME/ASCE/AHS 26th Structures, Structural Dynamics and Materials Conference, Orlando, FL, April 1985. To appear in the September-October 1986 issue of the Journal of Spacecraft and Rockets.

8. Prucz, J., "Analytical and Experimental Methodology for Evaluating Passively Damped Structural Joints," Ph.D. Dissertation, Georgia Institute of Technology, June 1985.

9. Peebles, J. H., Trudell, R. W., Blevins, C. E., Prucz, J. C., and Rohfield, L. W., "Passively Damped Joints for Advanced Space Structures," Final Report to AFOSR, McDonnell-Douglas Report MDC H2334, March 1986.

10. Christensen, R. M., Theory of Viscoelasticity, An Introduction, Academic Press, New York, 1971.

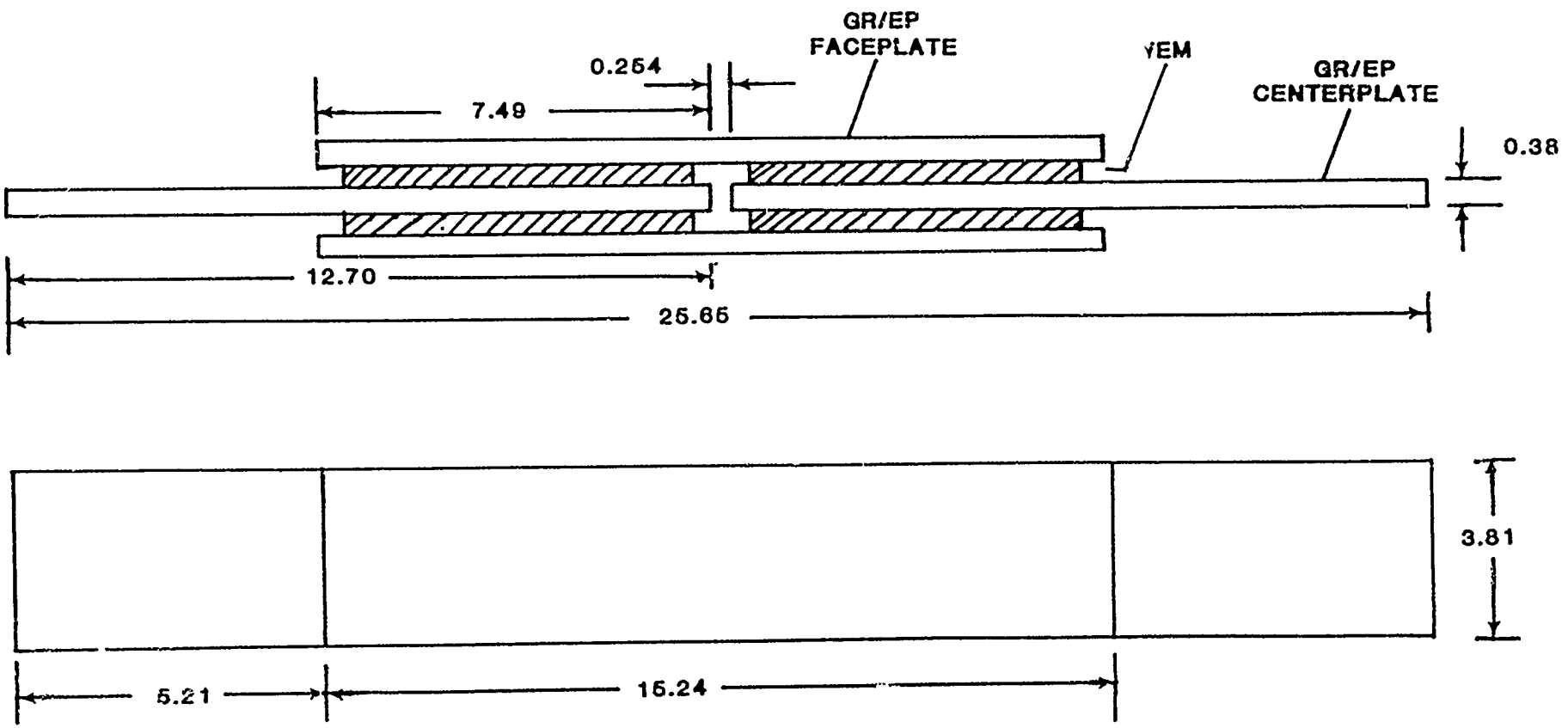
11. Jones, D.I.G., "A Reduced-Temperature Nomogram for Characterization of Damping Material Behavior," The Shock and Vibration Bulletin, No. 48, Part 2, Sept. 1978, pp. 13-22.

NOTES

1 DIMENSIONS GIVEN IN CENTIMETERS

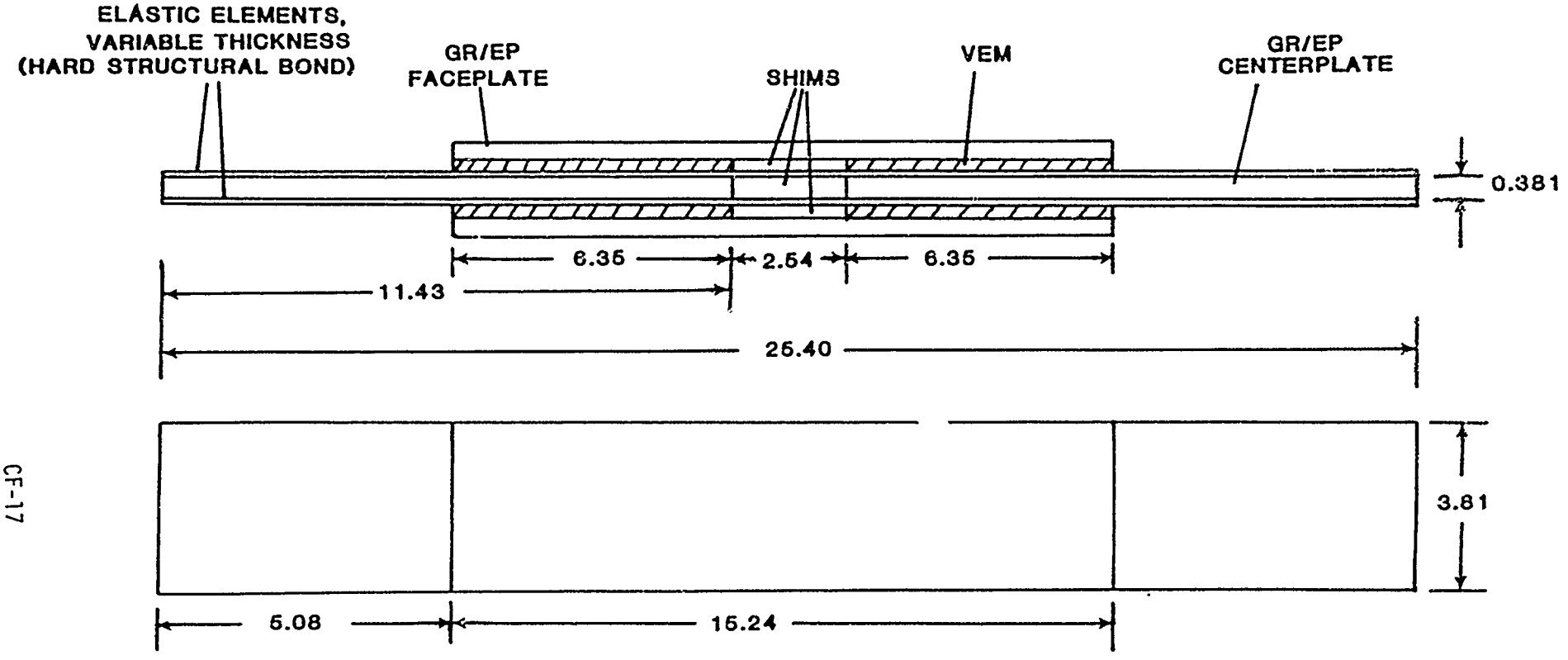
2 ABBREVIATIONS: VEM - VISCOELASTIC MATERIAL

GR/EP - GRAPHITE EPOXY



CF-16

Fig. 1 - PASSIVELY DAMPED JOINT SPECIMEN WITHOUT ELASTIC LINK BETWEEN MEMBERS



CF-17

Fig.2 - PASSIVELY DAMPED JOINT SPECIMEN WITH ELASTIC ELEMENTS

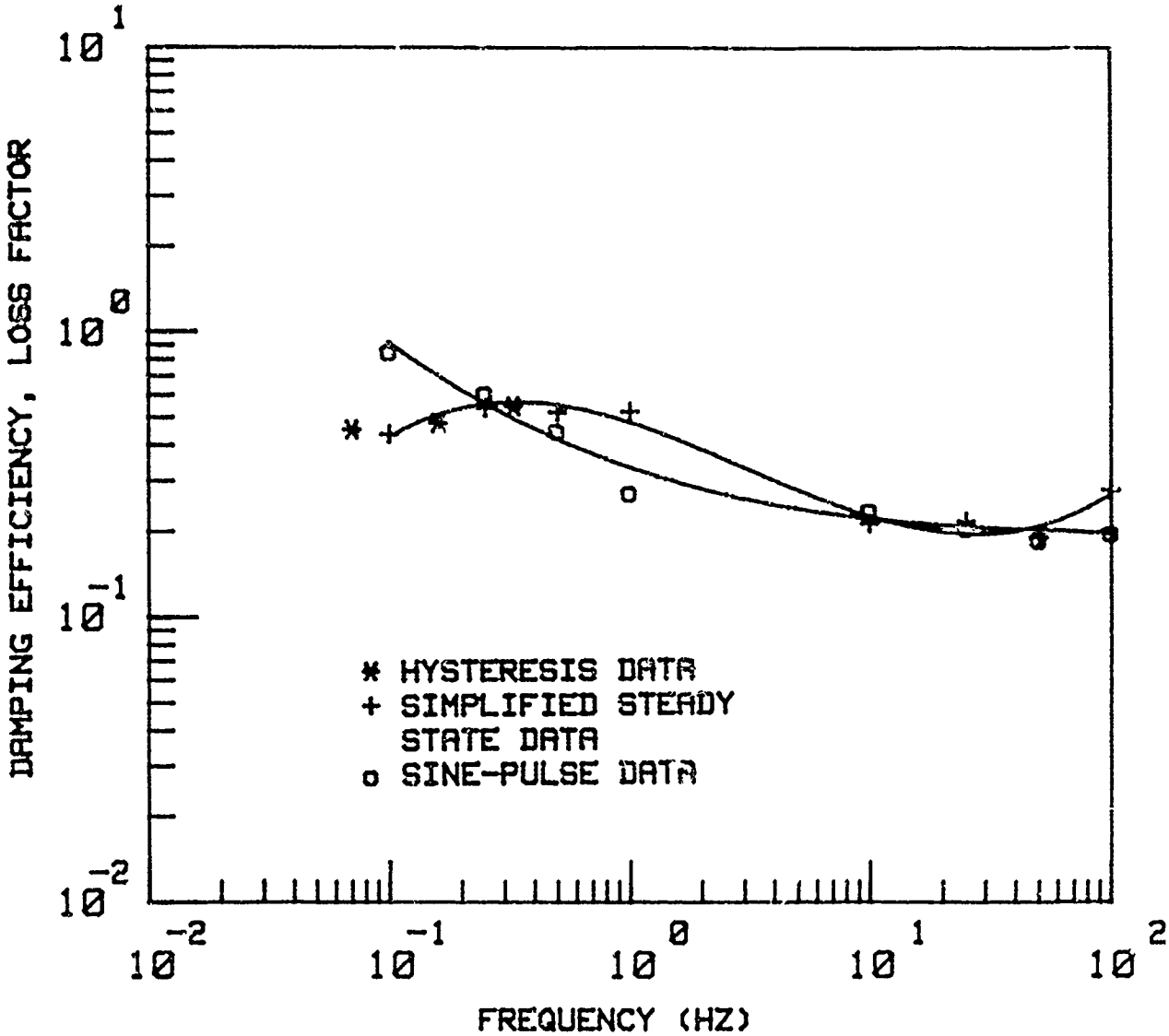
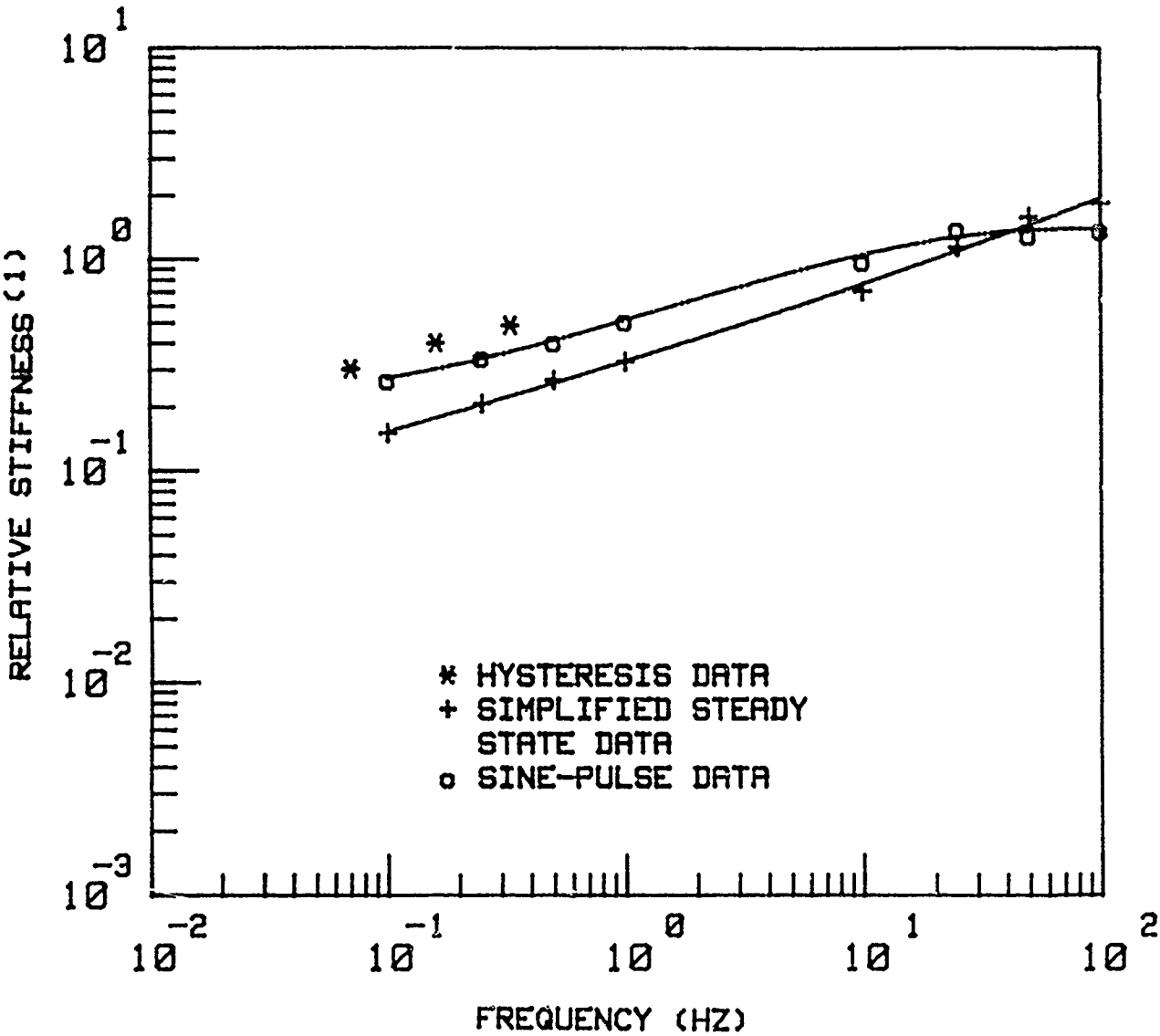


Fig. 3 – DAMPING DATA CORRELATION FOR SPECIMEN No. 3



(1) - REFERENCE STIFFNESS EQUAL TO 1,024,902 N/cm (585,000 lb/in)

Fig.4 - STIFFNESS DATA CORRELATION FOR SPECIMEN No. 3

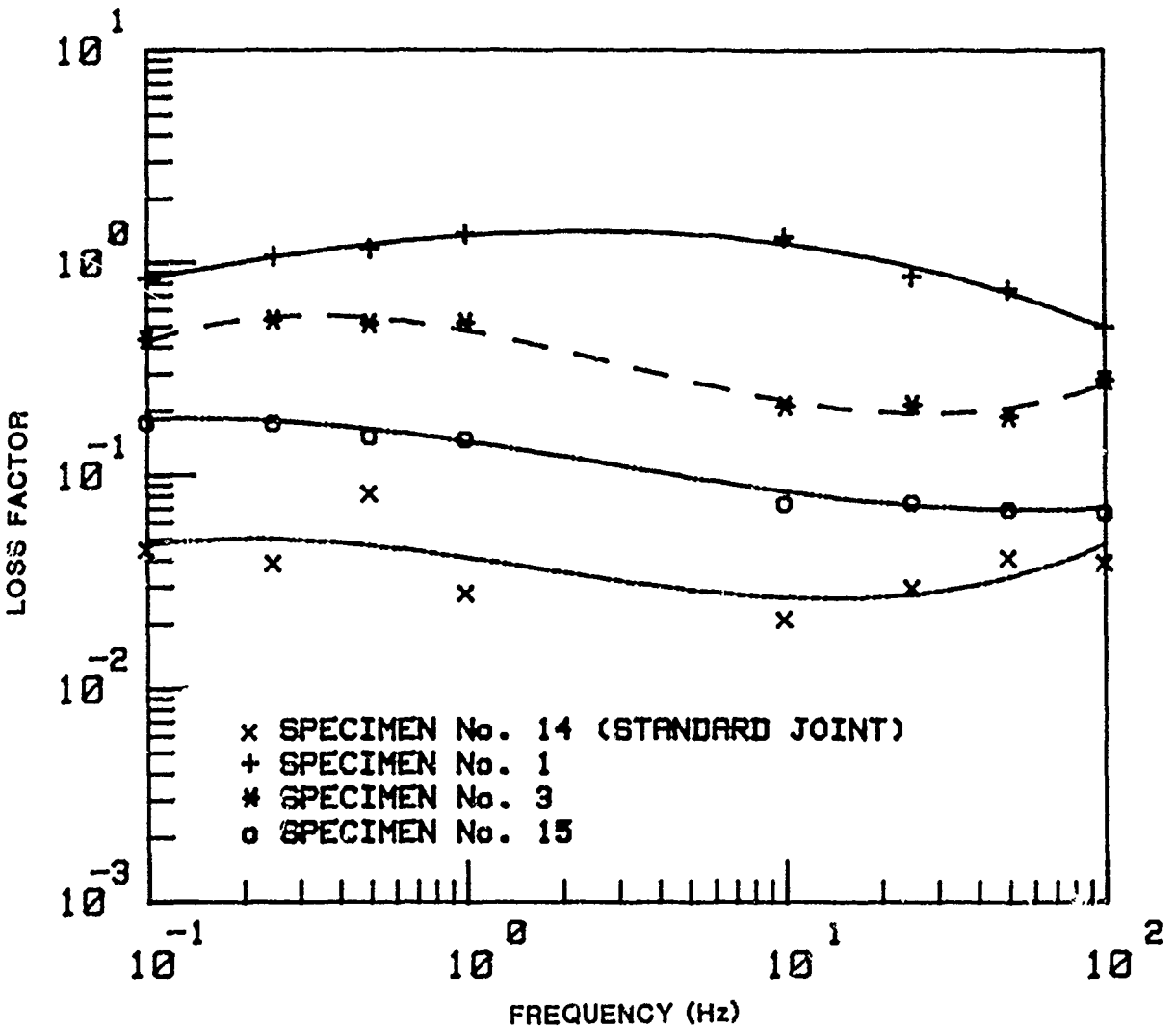
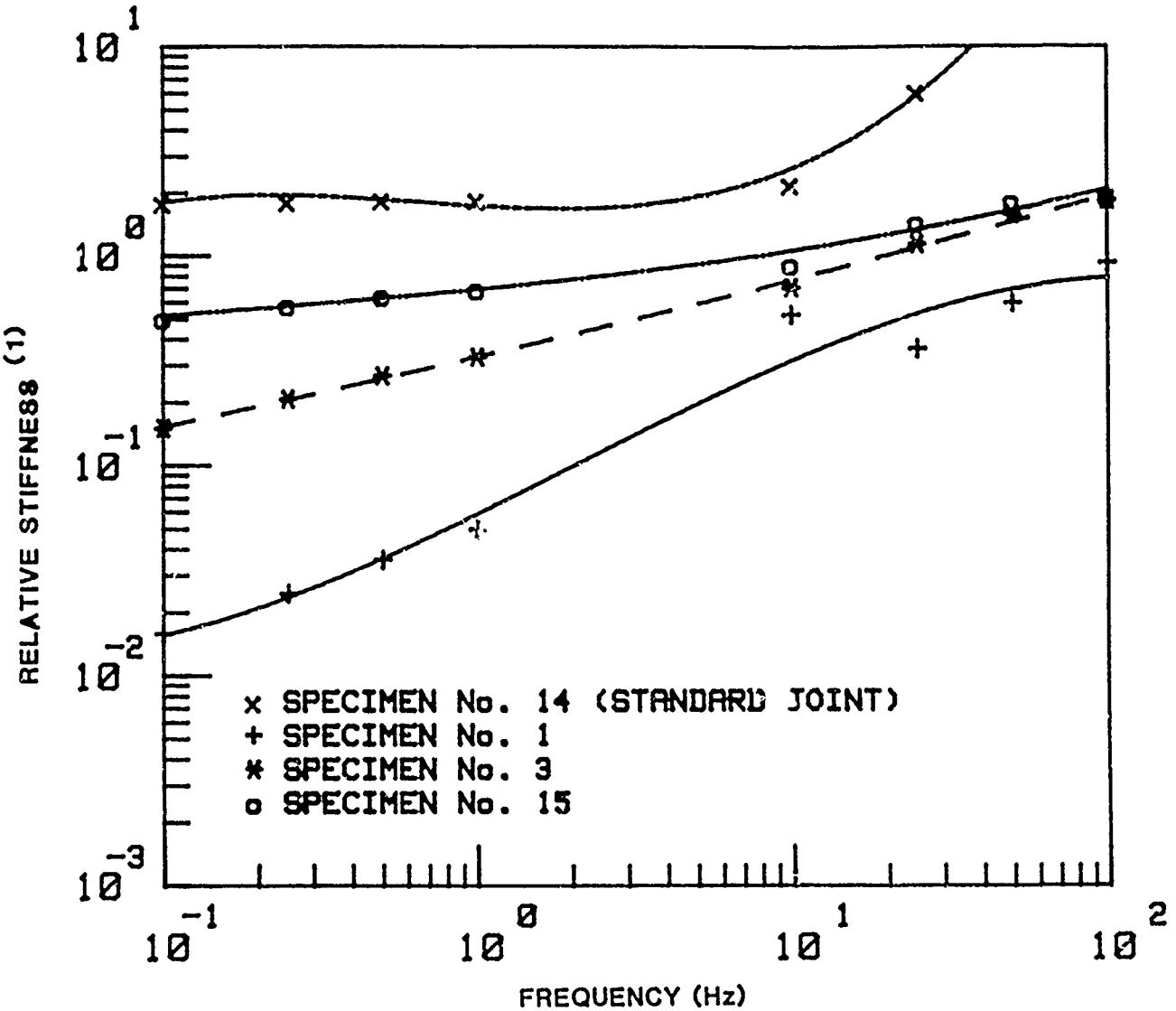
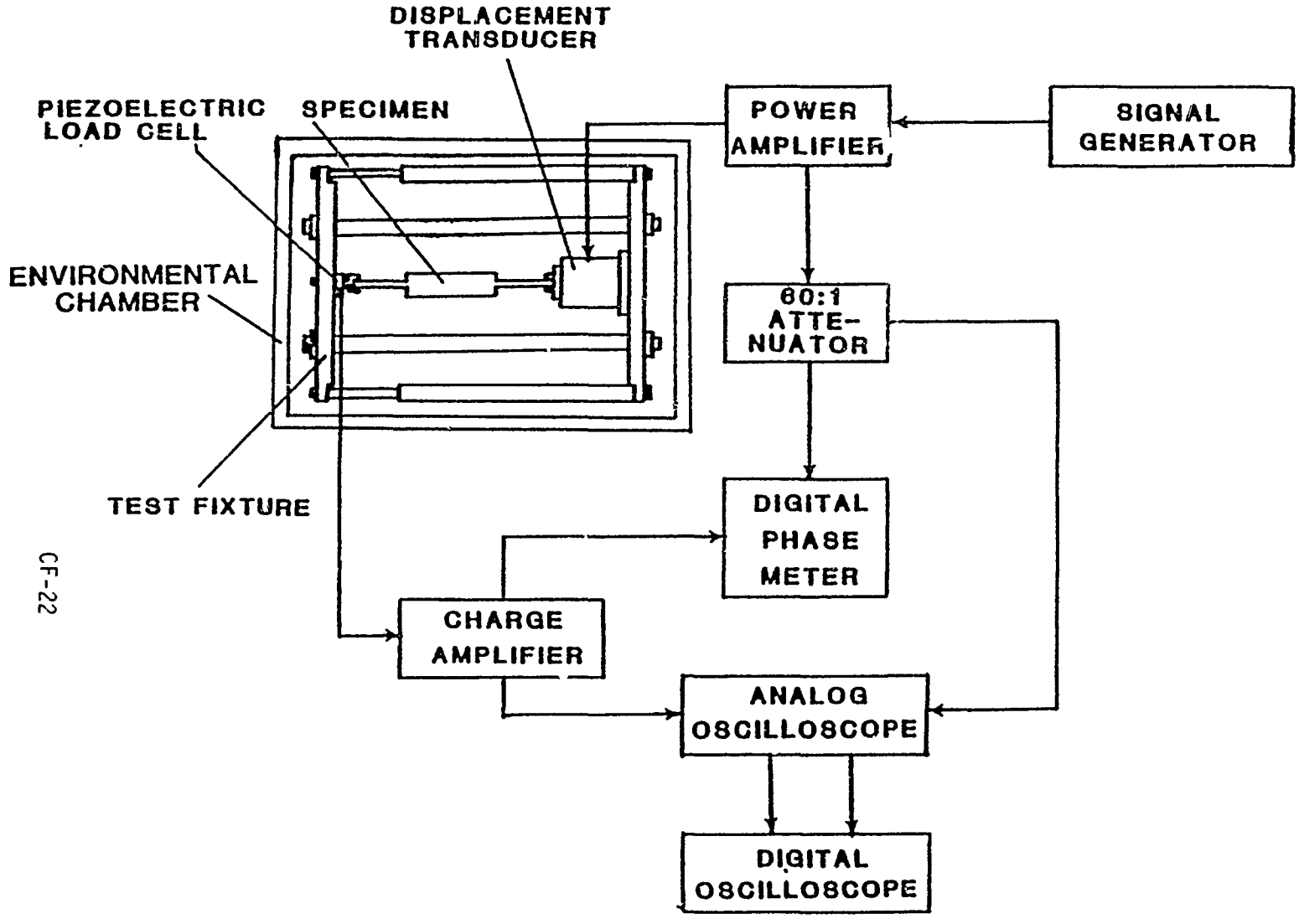


Fig. 5 - FREQUENCY EFFECT ON LOSS FACTOR OF JOINT SPECIMENS



(1) - THE REFERENCE STIFFNESS IS 1,024,902 N/cm (585,000 lb/in)

Fig. 6 - FREQUENCY EFFECT ON AXIAL STIFFNESS OF JOINT SPECIMENS



CF-22

Fig. 7 -- EXPERIMENTAL SET-UP FOR THE SIMPLIFIED STEADY STATE APPROACH

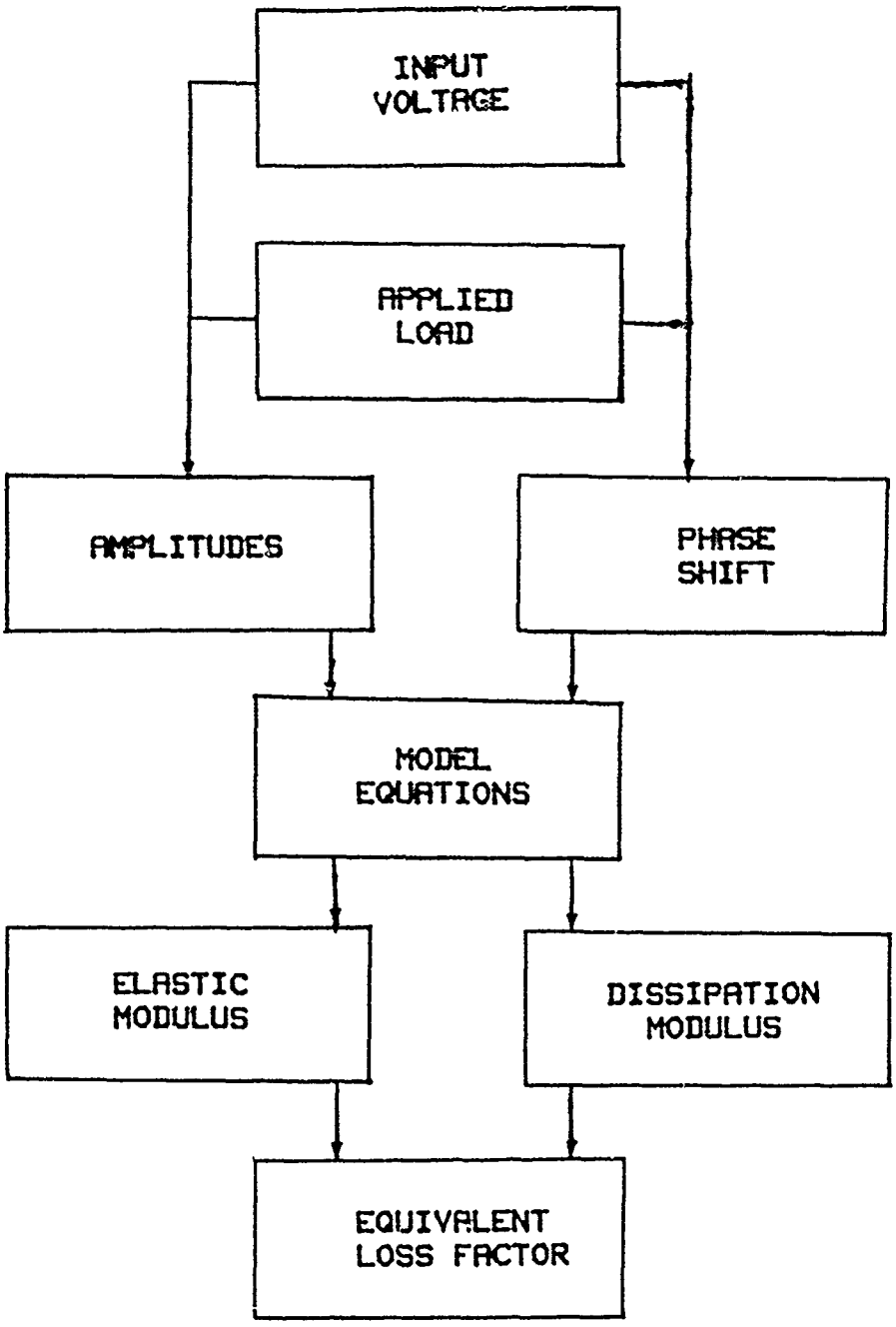


Fig. 8 - DATA ANALYSIS DIAGRAM FOR THE SIMPLIFIED STEADY STATE APPROACH

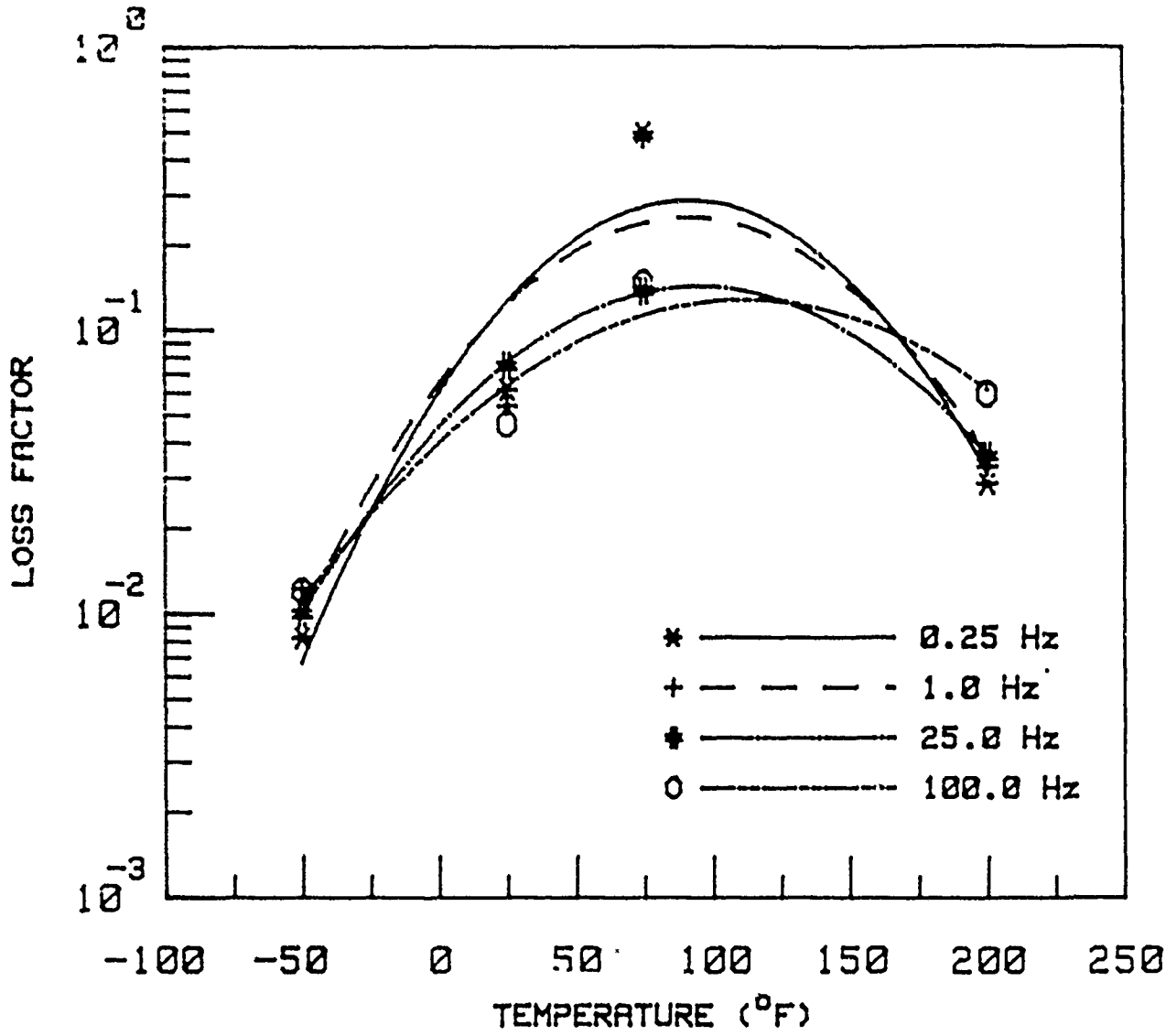


Fig. 9 - TEMPERATURE EFFECT ON LOSS FACTOR OF SPECIMEN No. 3

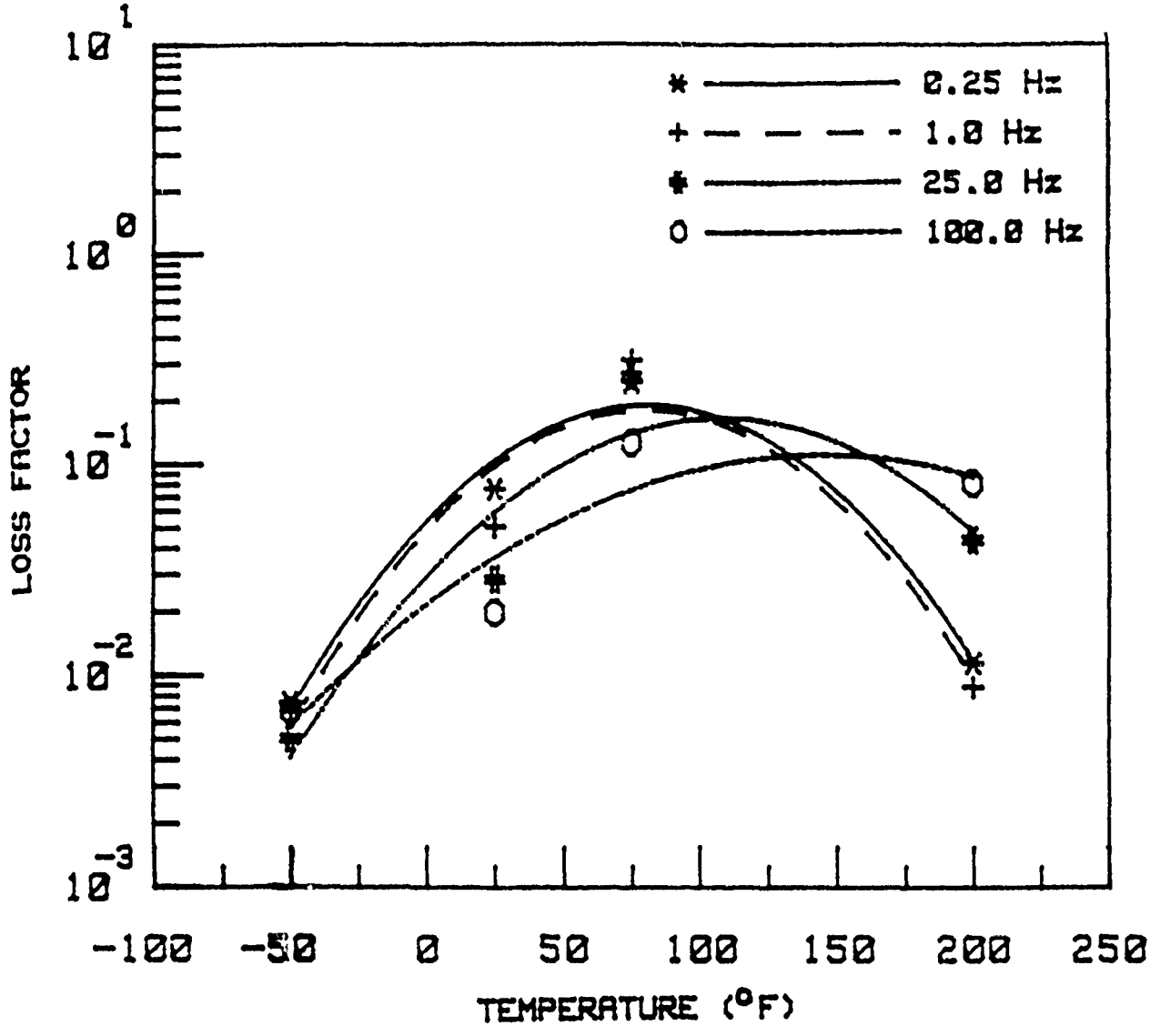


Fig.10 - TEMPERATURE EFFECT ON LOSS FACTOR OF SPECIMEN No. 9

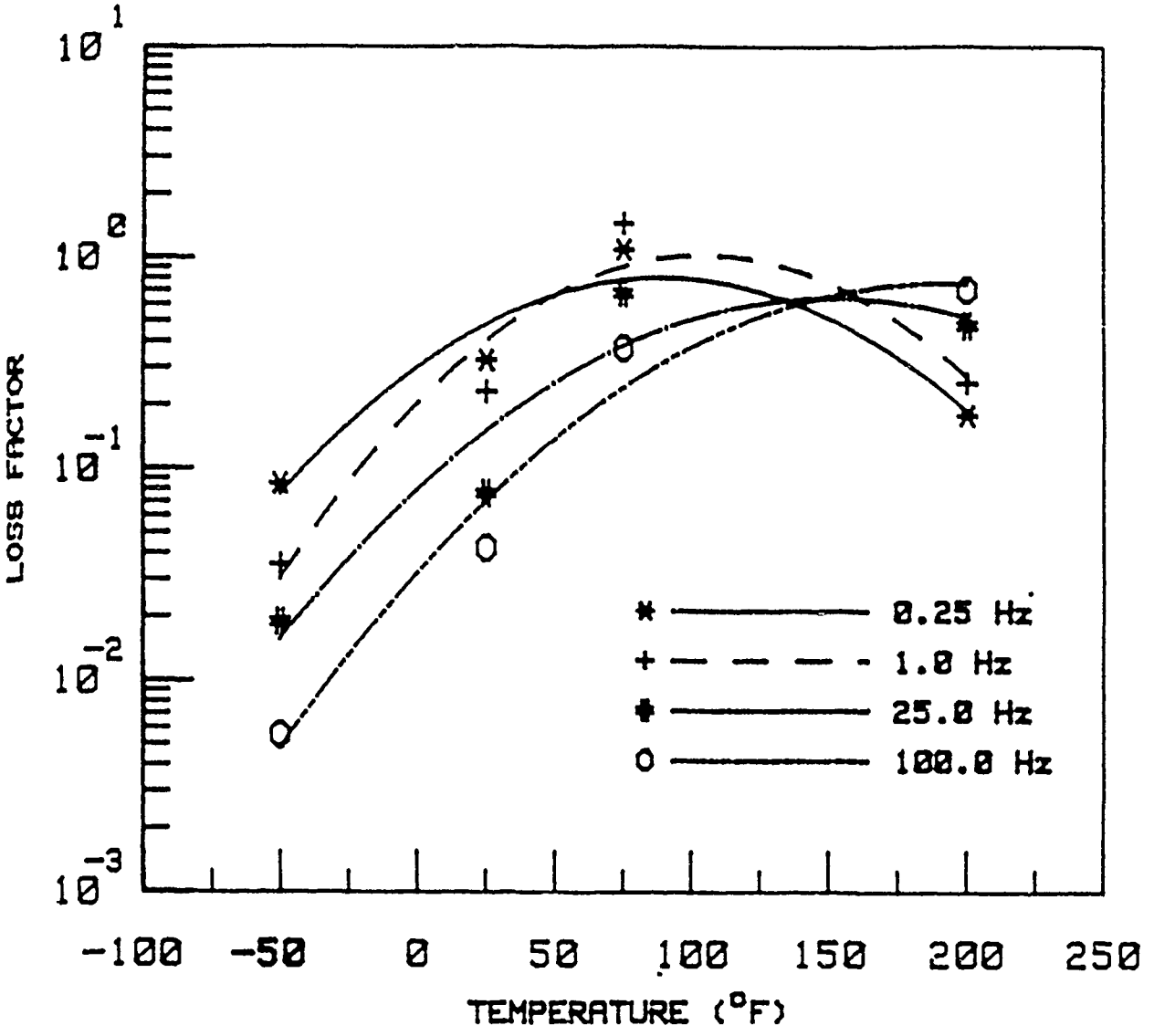


Fig. 11 - TEMPERATURE EFFECT ON LOSS FACTOR OF SPECIMEN No. 1

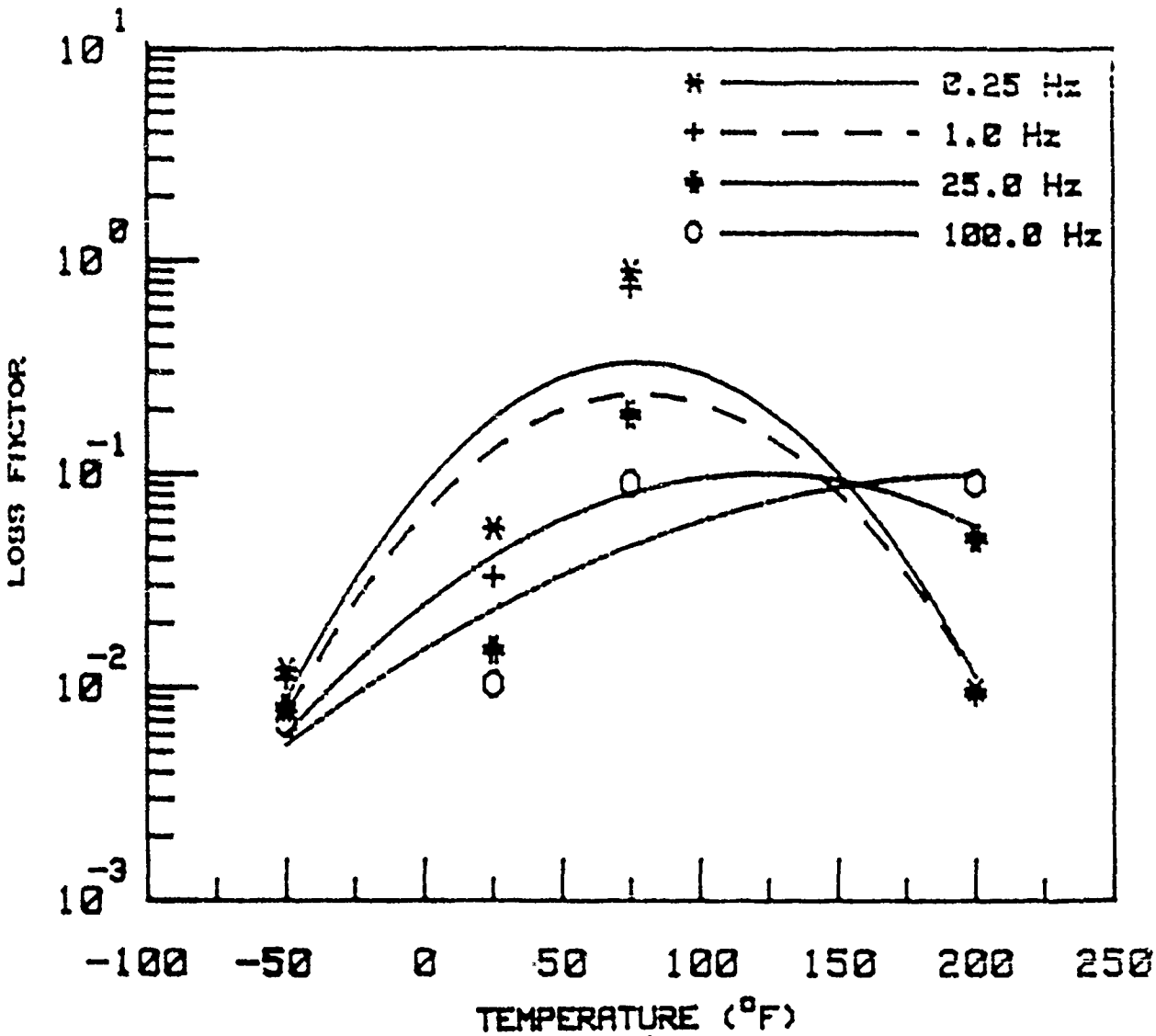


Fig. 12 - TEMPERATURE EFFECT ON LOSS FACTOR OF SPECIMEN No. 5

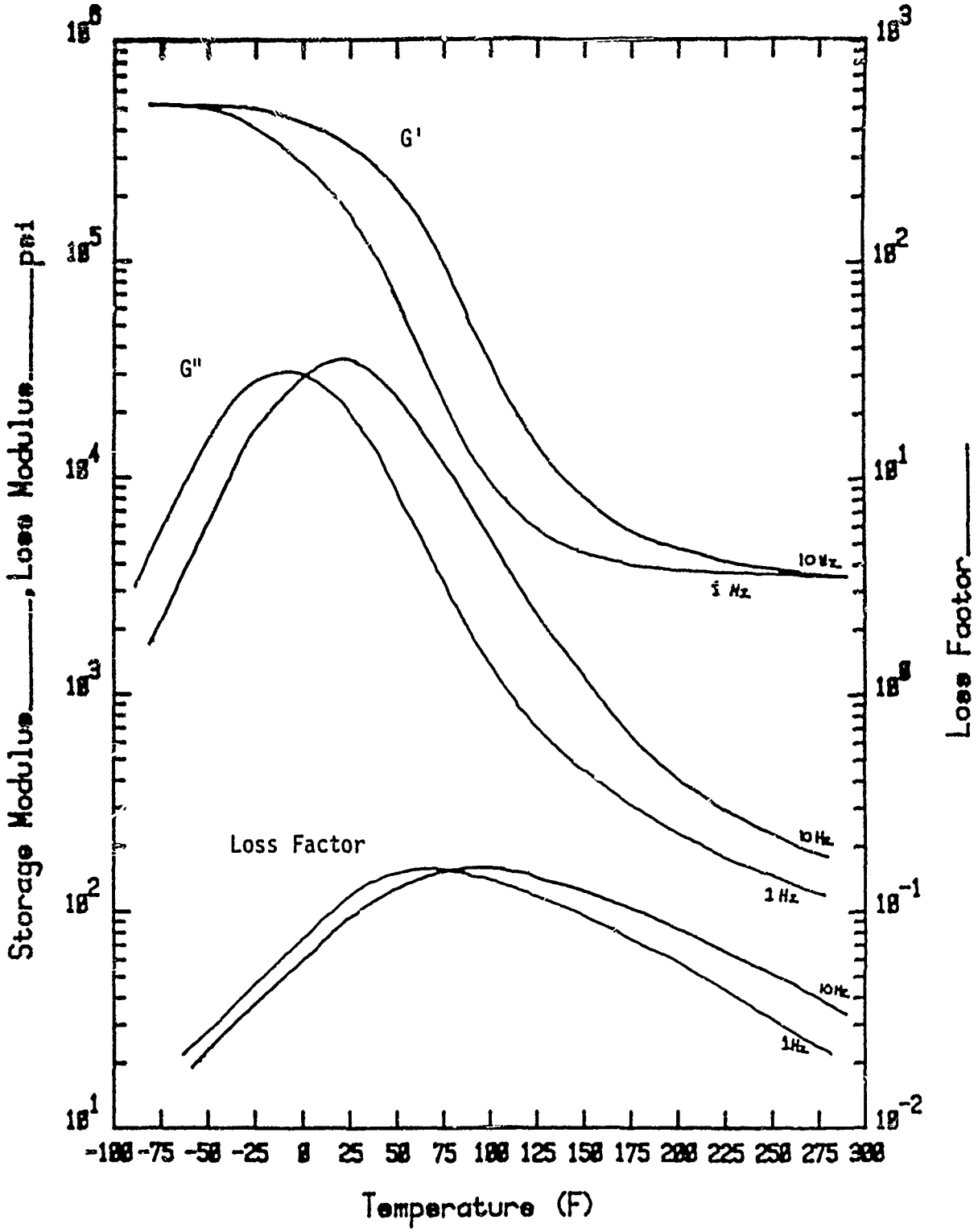


FIGURE 13. DAMPING PROPERTIES OF EC 2216 (ANATROL, INC.)

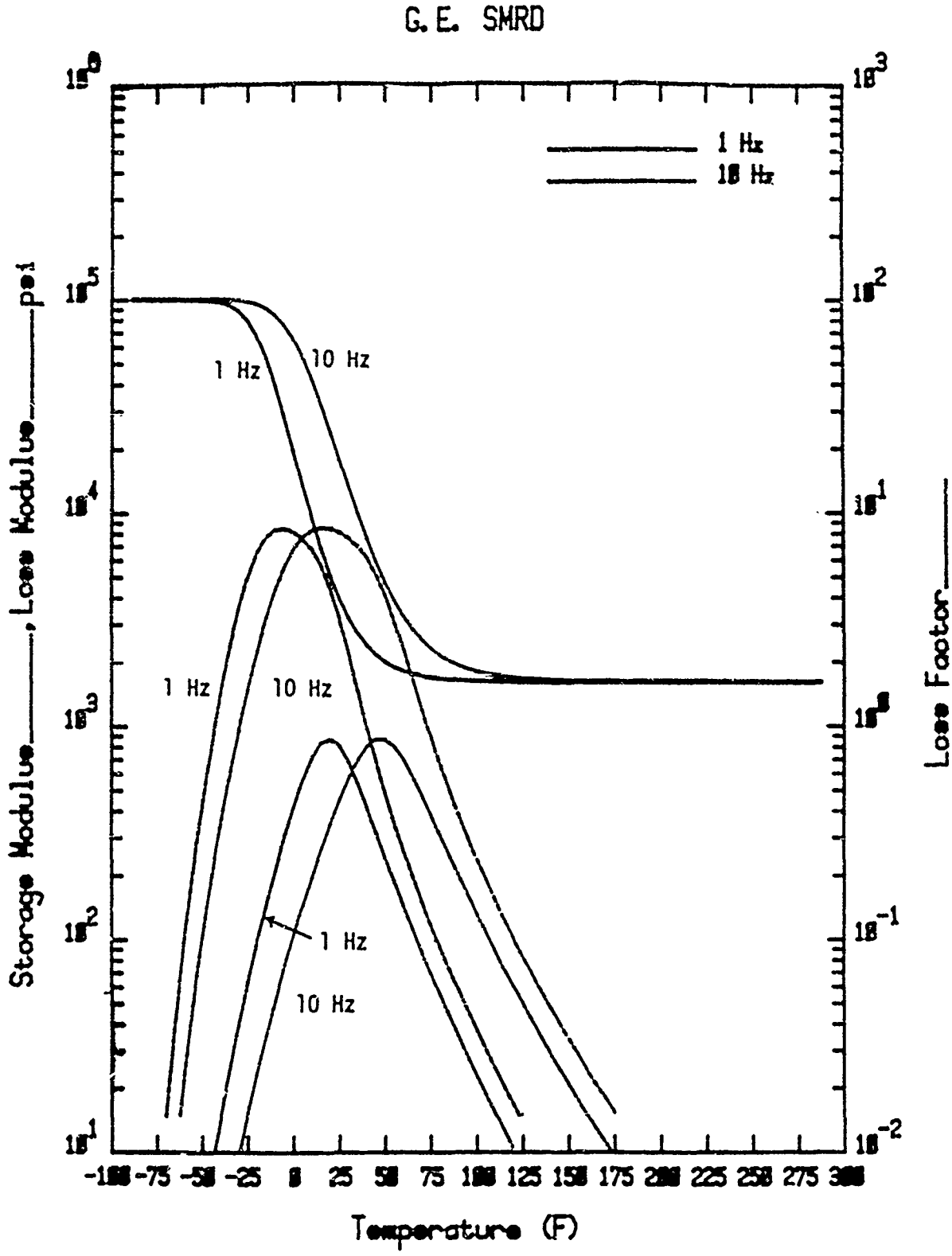


FIGURE 14. DAMPING PROPERTIES OF SMRD 100F90 (ANATROL, INC.)

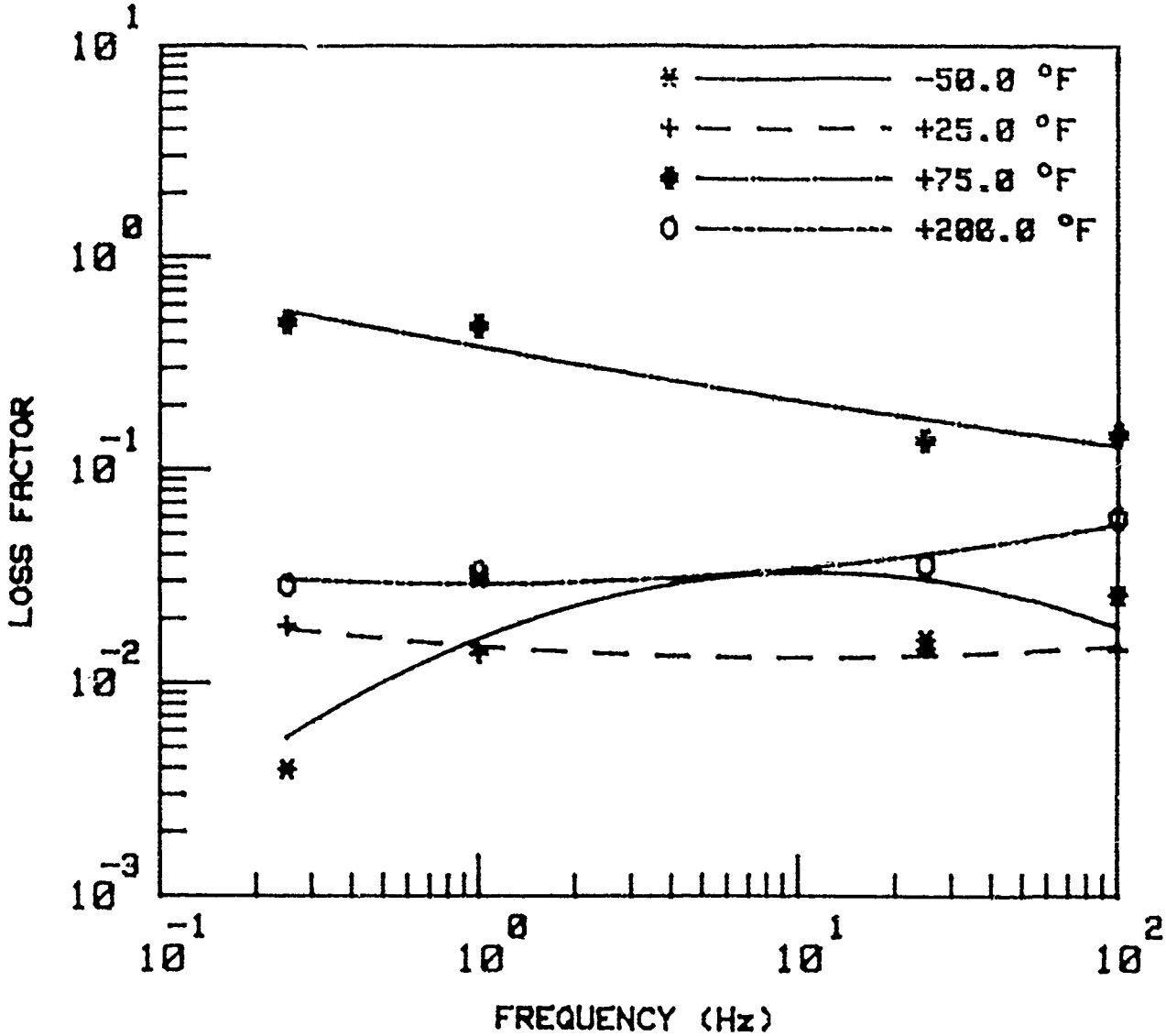


FIG. 15 - FREQUENCY EFFECT ON LOSS FACTOR OF SPECIMEN 3

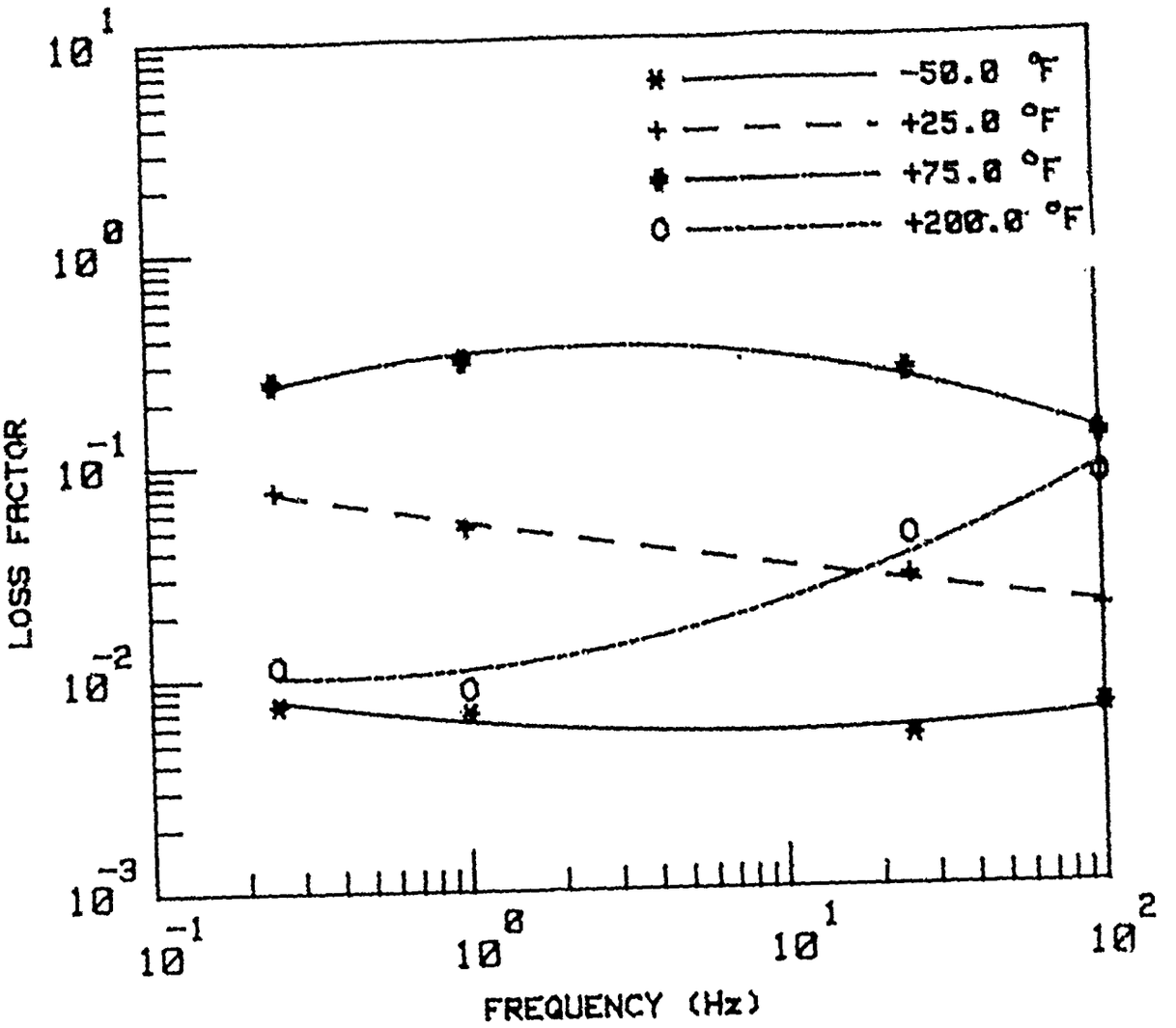


FIG. 16 - FREQUENCY EFFECT ON LOSS FACTOR OF SPECIMEN 9

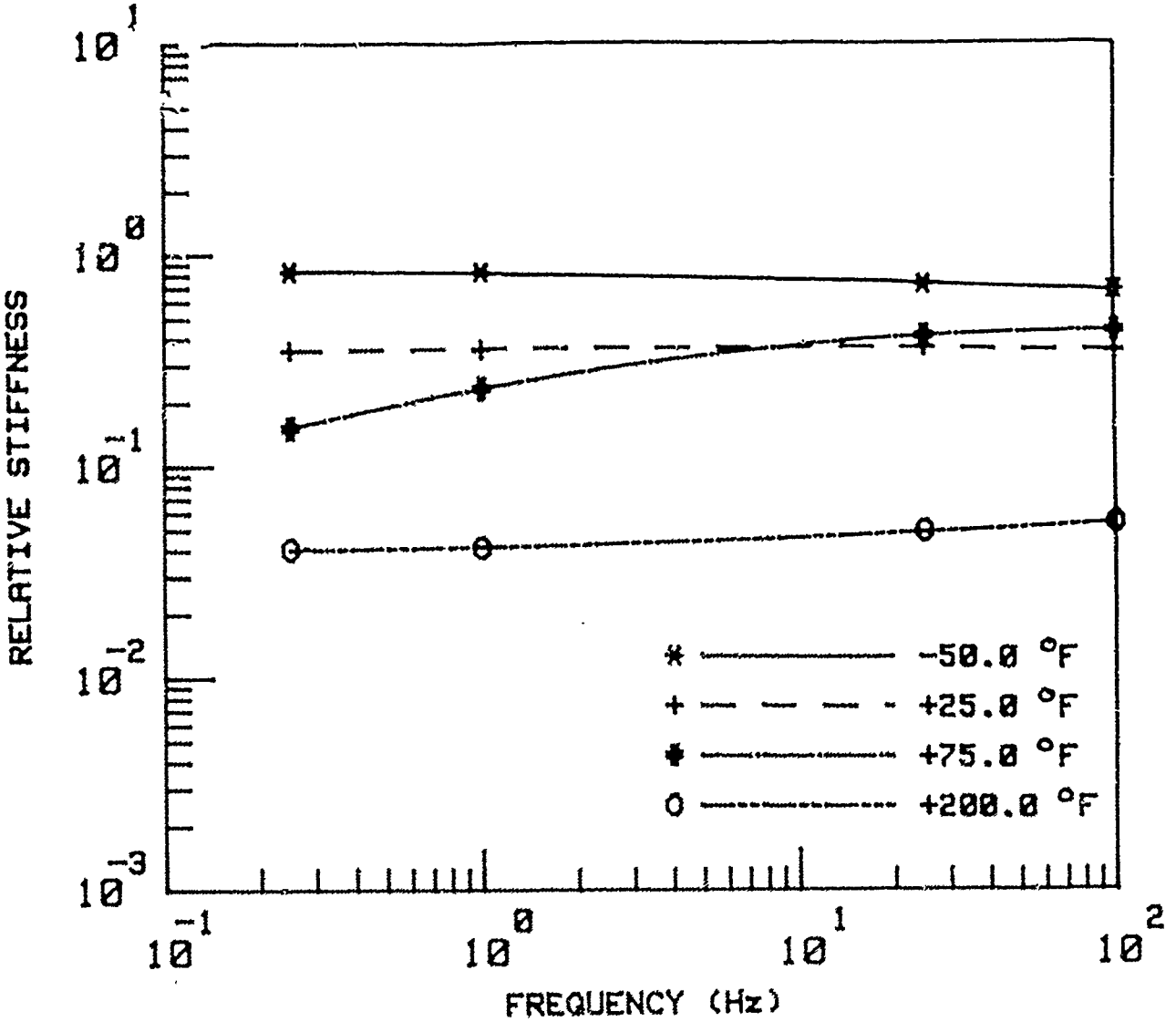


FIG. 17 - FREQUENCY EFFECT ON STIFFNESS OF SPECIMEN 3

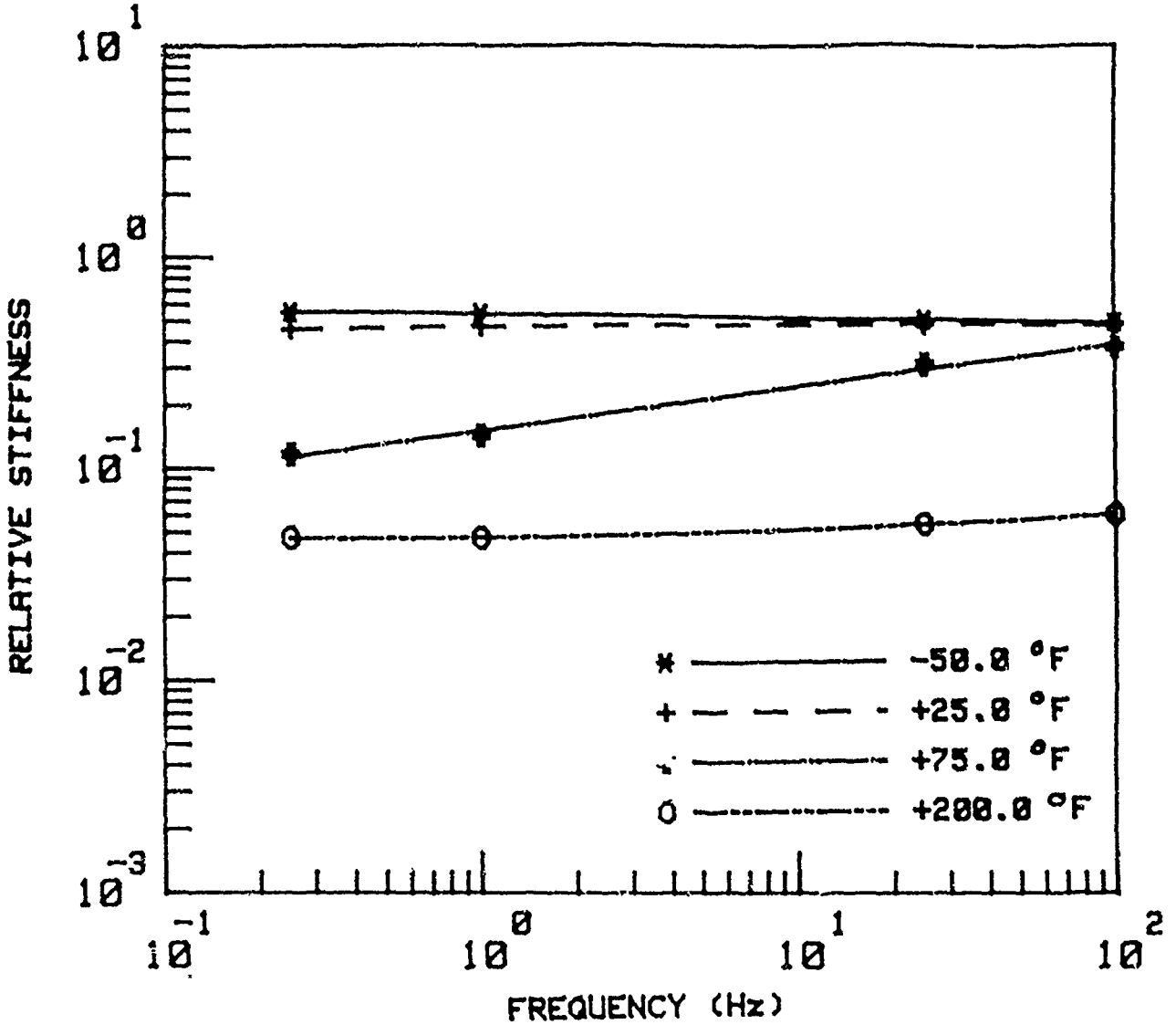


FIG. 18 - FREQUENCY EFFECT ON STIFFNESS OF SPECIMEN 9

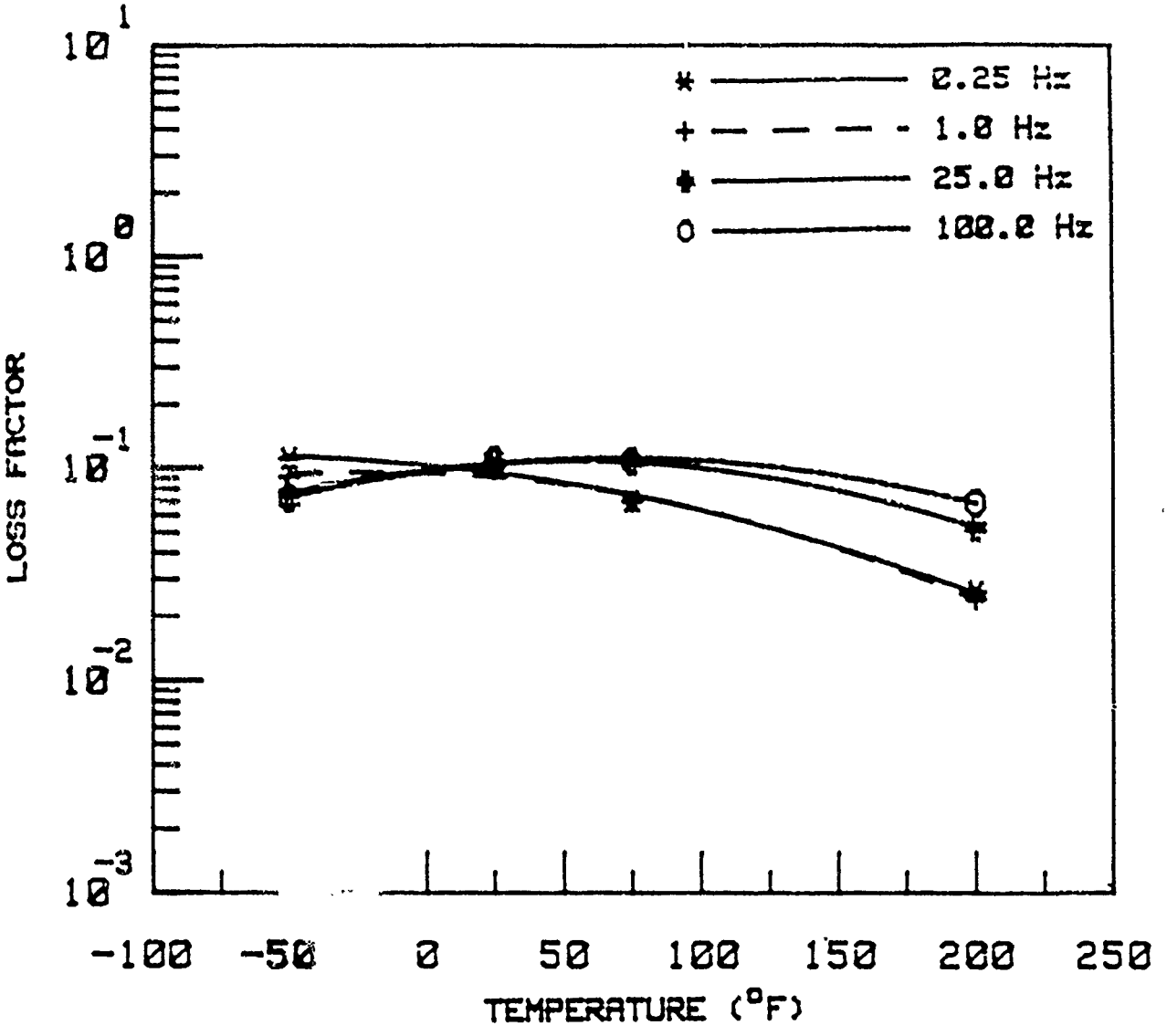


Fig. 19 - TEMPERATURE EFFECT ON LOSS FACTOR OF SPECIMEN No. 11

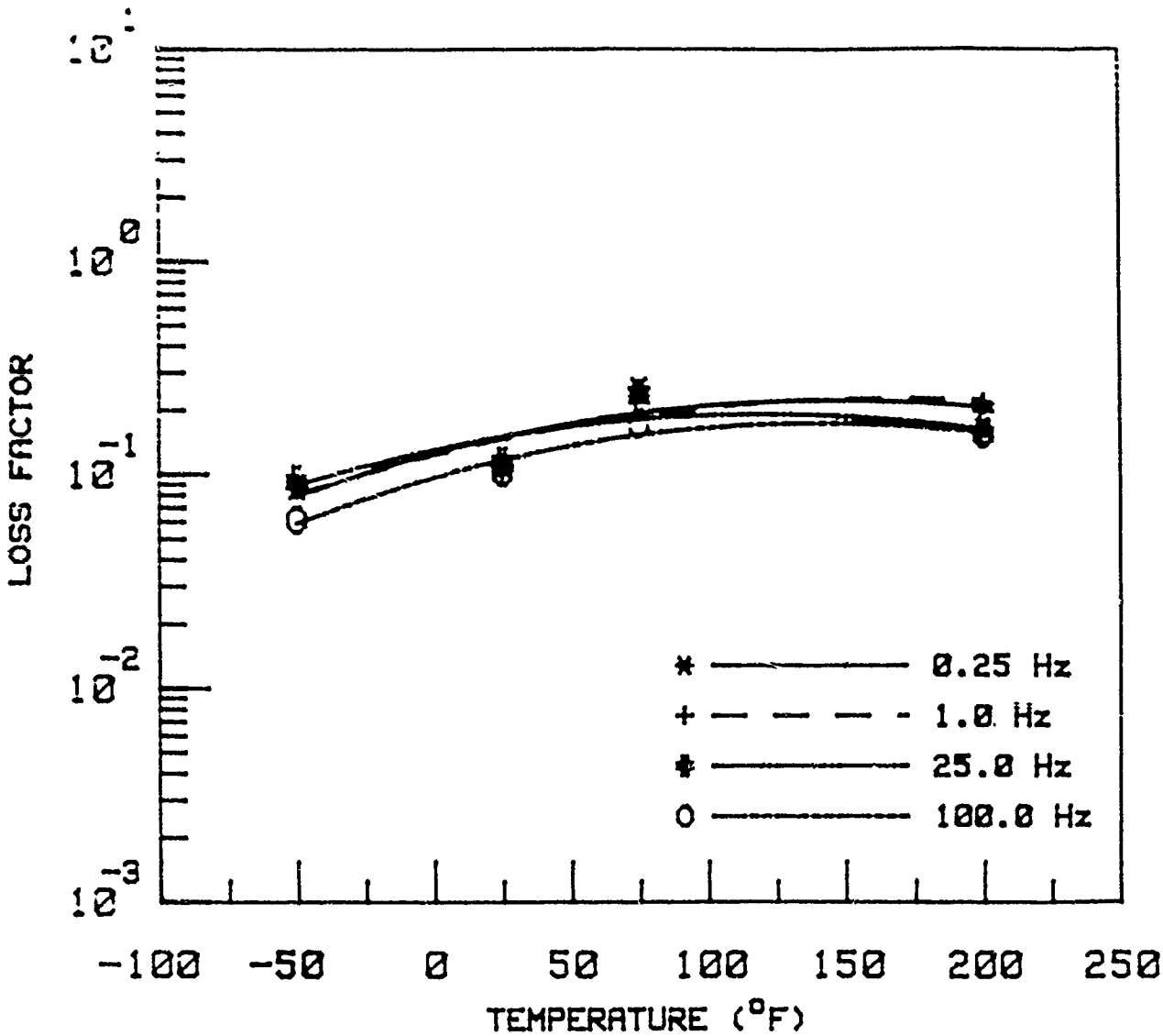


Fig. 20 - TEMPERATURE EFFECT ON LOSS FACTOR OF SPECIMEN No. 21

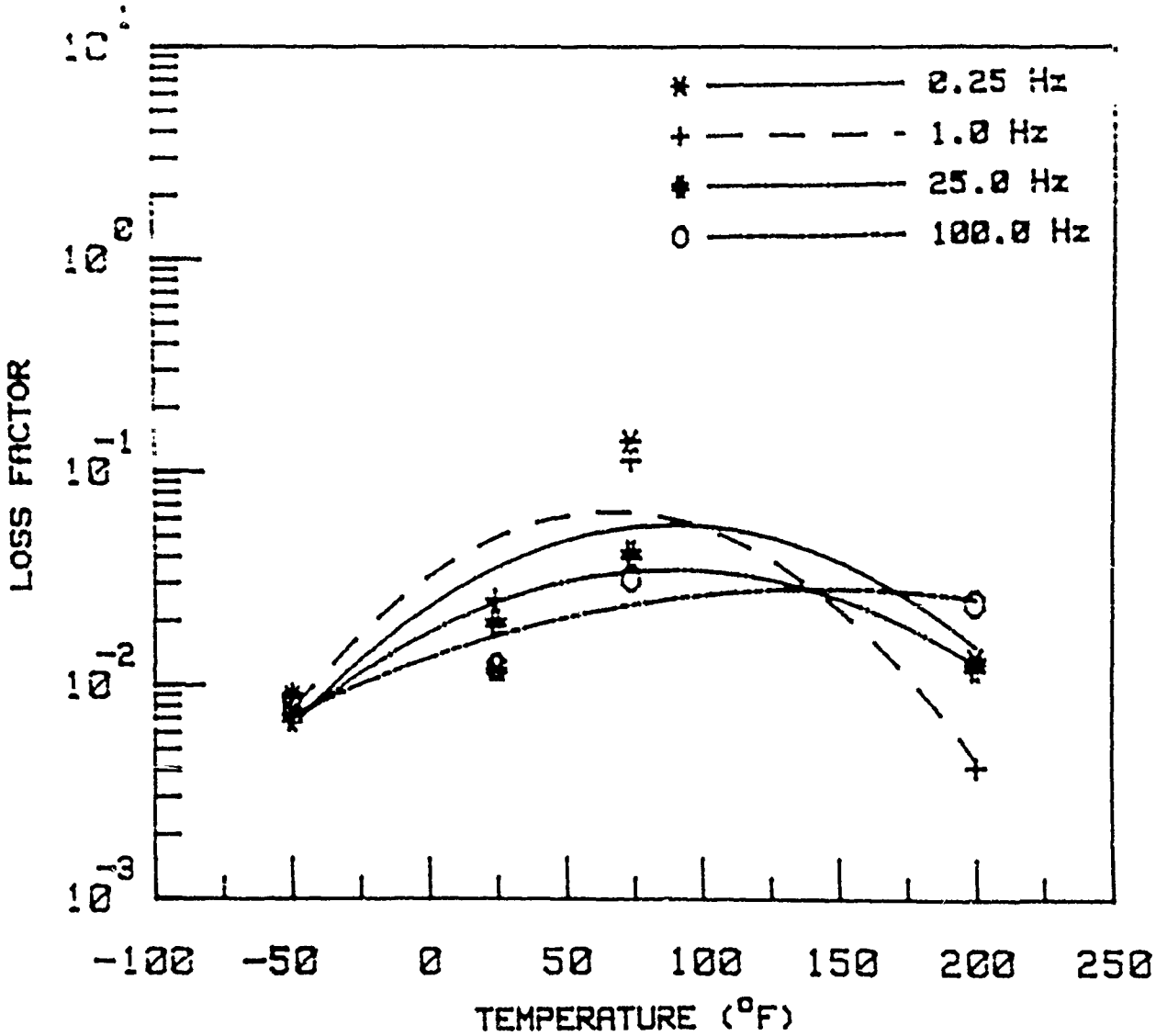


Fig. 21 - TEMPERATURE EFFECT ON LOSS FACTOR OF SPECIMEN No. 15

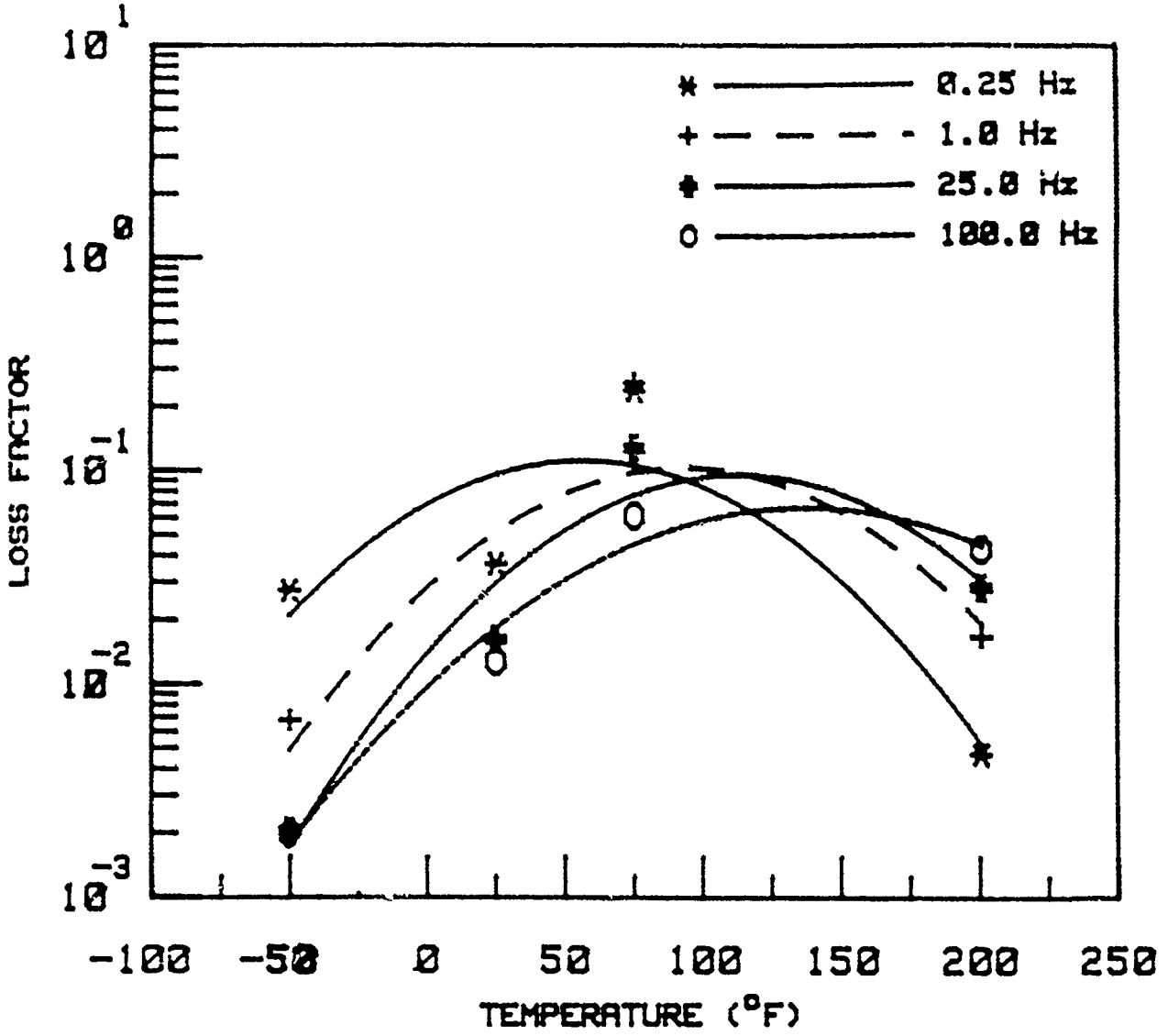


Fig. 22 - TEMPERATURE EFFECT ON LOSS FACTOR OF SPECIMEN No. 18

DYNAMICS OF VISCOELASTIC STRUCTURES

K. J. BUHARIWALA and J. S. HANSEN

Institute for Aerospace Studies
University of Toronto

ABSTRACT

In this paper we present a general method for modeling material damping in dynamical systems. The work is primarily concerned with a dissipation model based on viscoelastic assumptions. First, linear constitutive relations are briefly reviewed. Motion equations are then formulated in operator form for a structure constructed from an anisotropic, viscoelastic material. The mass, damping and stiffness operators are developed consistently in the formulation. Basic operator properties are discussed and orthonormality conditions are derived for the viscoelastic system. Modal identities are derived for a constrained viscoelastic structure. These identities provide criteria which are useful in order reduction of finite element models. An example of a viscoelastic beam in pure flexure is illustrated.

1 Introduction

The analysis of most structural dynamics problems can be undertaken with considerable confidence owing to the powerful numerical and analytical techniques currently available. Damping models are, however, usually the weakest link in a structural dynamics analysis. Hence, the primary objective of our work is to present a consistent material damping model. A number of techniques exist for identifying the damping matrix from a given set of information about the dynamic behavior of the system. For example, Caravani et al. [1] have outlined a time domain recursive least squares technique to identify the general damping matrix. Similarly, Yun and Shinozuka [2] describe a nonlinear Kalman filtering technique for the problem. Another method as given by Caravani and Thompson [3] of characterizing systems with nonproportional damping is to work in the frequency domain. The drawback of identifying the system damping matrix from a given set of information about the dynamic behavior of the system is that the damping matrix is not known at the design stage. Also, alterations in the parameters of the system require a remeasurement of the dynamic behavior to identify the damping matrix for the altered system. Of course, identifying the damping matrix by measuring the dynamic response may be impractical for some structures such as large flexible space structures. The present approach to the problem is to construct a consistent damping matrix, without any knowlwdge of the dynamic behavior of the system.

The underlying assumption in deriving the motion equation is that the stress-strain and the strain-displacement relations behave linearly. Otherwise, the material damping model is quite general and can be applied for any material with an arbitrary degree of anisotropy. The dynamics of an arbitrary structure is studied by formulating the motion equation using an operator notation.

A consistent damping model is developed using a linear viscoelastic constitutive relation. In Section Two, we briefly review various forms of viscoelastic stress-strain relations. We then use one specific form in Section Three to develop the motion equation. The assumption of linearity permits us to formulate the eigenproblem by taking the Laplace transform. Orthonormality conditions are the topic of discussion of Secton Five: first, the elastic problem is reviewed; the remainder of the section is devoted to the orthonormality conditions of the viscoelastic problem. The previous results are the basis for the derivation of modal identities; these provide a useful guide for establishing a hierarchy of the the system modes. Finally, the general results are illustrated in a cantilevered viscoleastic beam problem.

2 Some Aspects of Linear viscoelasticity

Structural models based on purely elastic constitutive relations cannot account for energy dissipation. For a comprehensive development, we require constitutive relations which allow the time rate of change of energy to be negative. This condition is met by viscoelastic constitutive relations. Here, a brief review of viscoelastic stress-strain relations is presented.

The standard viscoelastic model for a uniaxial constitutive relation as suggested by Bland and Lee [4] is

$$\sum_{r=0}^{n_p} p_r \frac{d^r \sigma}{dt^r} = \sum_{r=0}^{n_q} q_r \frac{d^r \epsilon}{dt^r} \qquad (1)$$

where p_r and q_r are material constants. A generalization of this form is to use fractional derivatives in the constitutive relation, as suggested by Caputo [5]

$$p_0\sigma(t) + \sum_{r=1}^{n_p} p_r D^{\alpha_r}[\sigma(t)] = q_0\epsilon(t) + \sum_{r=1}^{n_q} q_r D^{\beta_r}[\epsilon(t)] \qquad (2)$$

where the fractional derivative operator of real order α is defined by

$$D^{\alpha}[x(t)] \triangleq \frac{1}{\Gamma(1-\alpha)} \frac{d}{dt} \int_0^t \frac{x(\tau)}{(t-\tau)^{\alpha}} d\tau \quad 0 < \alpha < 1 \qquad (3)$$

Constitutive relation (2) is a generalization of the standard model (1) in the sense that the order of the derivatives are no longer limited to the set of positive integers.

The major drawback to the above forms is that they are not readily amenable to analysis, since many terms may be required to describe a material adequately. Before use, the model requires experimental determination of material constants p_r and q_r, and fractional orders α_r and β_r.

An equivalent form for viscoelastic constitutive relations of an anisotropic material can be given in terms of the Boltzmann hereditary superposition integral where the stress depends on the entire strain history:

$$\sigma_{ij}(t) = \int_0^t \sum_{k,l=1}^{3} C_{ij}^{kl}(\underline{r}, t-\tau) \frac{\partial \epsilon_{kl}}{\partial \tau} d\tau \qquad i,j = 1,2,3 \qquad (4)$$

Here the usual tensor notation followed by Sokolnikoff [6] is used. The tensor quantities refer to a dextral orthogonal set of Cartesian axes (x_1, x_2, x_3), $\underline{r}$ is the position vector, C_{ij}^{kl}, which are functions of $\underline{r}$ and t, are termed the relaxation moduli and σ_{ij} are the components of the stress tensor acting on a face whose normal points in the "i" direction and which acts in the "j" direction, Fig. 1.

It is assumed that the stress and strain vanish for $t < 0$. This restriction may be removed by a translation of variable t or using $(-\infty)$ as the lower limit of integration in (4). From the symmetric nature of σ_{ij} and c_{ij} the symmetry properties

$$C_{ij}^{kl}(\underline{r},t) = C_{ji}^{kl}(\underline{r},t) = C_{ji}^{lk}(\underline{r},t) \tag{5}$$

can be deduced. Biot [7] has shown that when Onsager's reciprocity relations apply, the relaxation moduli satisfy

$$C_{ij}^{kl}(\underline{r},t) = C_{kl}^{ij}(\underline{r},t) \tag{6}$$

Hence the relaxation moduli are completely symmetric (symmetric in all four indices), like the moduli of elastic media.

In addition, the time dependence of the relaxation moduli is taken as a series of exponentials (Staverman and Schwarzl [8])

$$C_{ij}^{kl}(\underline{r},t) = \sum_{s=1}^{n} C_{ij}^{kl(s)}(\underline{r})e^{-t/\rho_s} + C_{ij}^{kl}(\underline{r}) \tag{7}$$

which is the harbinger of the more general relation to follow. The exponential series in (7) implies that the stress-strain relation can be represented by an array of springs and dashpots [7]. In (7), ρ_s are the material relaxation (decay) constants and all fourth order tensors on the right hand side are independent of t, completely symmetric, real and are positive—semidefinite.

The problem of determining a possibly large number of moduli C_{ij}^{kl} and relaxation constants ρ_s in (7) still remains when using the Boltzmann superposition integral (4) to describe a viscoelastic material. To overcome this dilemma, Biot [9] considered an almost continuous distribution of relaxation constants. Hence the discrete relaxation constants are treated in the form of a continuous relaxation density distribution function $\gamma(\theta)$. Therefore, the viscoelastic constitutive relation takes the form

$$\sigma_{ij}(t) = \int_o^t \sum_{k,l=1}^{3} [G_{ij}^{kl}(\underline{r},t-\tau) + C_{ij}^{kl}(\underline{r})] \frac{\partial \varepsilon_{kl}}{\partial \tau} d\tau \tag{8}$$

$$G_{ij}^{kl}(\underline{r},t) = \int_o^\infty C_{ij}^{kl(*)}(\underline{r},\theta)\gamma(\theta)e^{-\theta t}d\theta \qquad (9)$$

where G_{ij}^{kl} are completely symmetric and positive-semidefinite and $C_{ij}^{kl(*)}$ is a function of $\underline{r}$ and $\theta = 1/\rho$. The summation in (7) is replaced by an integral in (9), and in so doing we account for the possibility of $C_{ij}^{kl}(\underline{r},\theta)$ being a discontinuous function in θ.

It will be convenient in our formulation to separate the elastic term, hence we integrate the second component (time independent moduli) in (8). Integrating (8) and taking

$$G_{ij}^{kl} \equiv 0 \qquad (10)$$

we recover the linear anisotropic elastic constitutive relation

$$\sigma_{ij} = \sum_{k,l=1}^{3} C_{ij}^{kl}(\underline{r})\,\epsilon_{kl} \qquad (11)$$

otherwise, for non-vanishing relaxation moduli we have the linear anisotropic viscoelastic constitutive relation

$$\sigma_{ij}(t) = \int_o^t \sum_{k,l=1}^{3} G_{ij}^{kl}(\underline{r},t-\tau)\frac{\partial \epsilon_{kl}}{\partial \tau}\,d\tau + \sum_{k,l=1}^{3} C_{ij}^{kl}(\underline{r})\,\epsilon_{kl} \qquad (12)$$

This relation will be the building block in our development of the motion equations of a viscoelastic body.

3 Theory

We are now in a position to formulate the motion equations of a viscoelastic body. The motion equations for a viscoelastic continuum, Fig. 2, are developed in operator form; in so doing we apply the principle of virtual work which can stated as follows:

It is a necessary and sufficient condition for equilibrium of a system if the total work done by all the external forces plus the work done by all the internal forces is equal to zero for a virtual displacement.

This principle can be generalized to include dynamical systems by appealing to d'Alembert's principle. Hence, the principle of virtual work can

be stated as

$$\int_V \sum_{i=1}^{3} f_i \, \delta u_i \, dV = \int_V \sum_{i=1}^{3} \left(\sum_{j=1}^{3} \sigma_{ij} \, \delta \varepsilon_{ij} + \dot{p}_i \, \delta u_i \right) dV \tag{13}$$

where f_i are the components of the externally applied force vector

$$\underline{f}^T = [\, f_1(\underline{r}) \quad f_2(\underline{r}) \quad f_3(\underline{r}) \,] \tag{14}$$

taken as force per unit volume; p_i are the components of the momentum vector

$$\underline{p}^T = [\, p_1(\underline{r}) \quad p_2(\underline{r}) \quad p_3(\underline{r}) \,] \tag{15}$$

and are defined as

$$p_i \triangleq \rho(\underline{r}) \dot{u}_i \tag{16}$$

$$(\dot{}) \triangleq \frac{\partial}{\partial t} \tag{17}$$

where $\rho(\underline{r})$ is the material density of the viscoelastic continuum, taken to be time-independent, but in general nonuniform. The linear strain tensor is

$$\varepsilon_{ij} \triangleq \frac{1}{2} (u_{i,j} + u_{j,i}) \tag{18}$$

where u_i are components of the displacement vector

$$\underline{u}^T = [\, u_1(\underline{r},t) \quad u_2(\underline{r},t) \quad u_3(\underline{r},t) \,] \tag{19}$$

We have used δu_i in (13) to denote the components of virtual displacements in contrast to the components of real displacements u_i.

Using (12) and (18) in (13) gives

$$\int_V \sum_{i=1}^{3} \bar{r}_i \, \delta u_i \, dV = \int_V \sum_{i=1}^{3} \left\{ \frac{1}{4} \sum_{j=1}^{3} \left[\int_o^t \sum_{k,l=1}^{3} G_{ij}^{kl}(\underline{r}, t-\tau) \cdot \right. \right.$$

$$\left. \frac{\partial}{\partial \tau}(u_{k,l} + u_{l,k}) d\tau + \sum_{k,l=1}^{3} C_{ij}^{kl}(\underline{r})(u_{k,l} + u_{l,k}) \right] \cdot$$

$$\left. \delta(u_{i,j} + u_{j,i}) + \dot{p}_i \delta u_i \right\} dV \qquad (20)$$

Applying the divergence theorem to the volume integral and making use of the symmetry properties of moduli G_{ij}^{kl} and C_{ij}^{kl} gives

$$\int_V \sum_{i=1}^{3} \left\{ \dot{p}_i - \sum_{j,k,l=1}^{3} \frac{\partial}{\partial x_j} \left[\int_o^t G_{ij}^{kl}(\underline{r}, t-\tau) \frac{\partial u_{l,k}}{\partial \tau} \, d\tau + \right. \right.$$

$$\left. \left. C_{ij}^{kl}(\underline{r}) u_{l,k} \right] - f_i \right\} \delta u_i dV = 0 \qquad (21)$$

with the appropriate boundary terms compatible with the boundary conditions of the problem. Since the components of the virtual displacements are arbitrary and independent of one another it follows that

$$\dot{p}_i - \sum_{j,k,l=1}^{3} \frac{\partial}{\partial x_j} \left[\int_o^t G_{ij}^{kl}(\underline{r}, t-\tau) \frac{\partial u_{l,k}}{\partial \tau} \, d\tau + \right.$$

$$\left. C_{ij}^{kl}(\underline{r}) u_{l,k} \right] - \bar{r}_i = 0 \quad , \quad i=1,2,3 \qquad (22)$$

Therefore in operator form the motion equation can be written as an integro-differential equation

$$\underset{\sim}{M} \, \ddot{\underline{u}} + \int_o^t \underset{\sim}{R}(\underline{r}, t-\tau) \frac{\partial \underline{u}}{\partial \tau} \, d\tau + \underset{\sim}{K} \, \underline{u} = \underline{f} \qquad (23)$$

where the operators are identified as follows:

$$\underset{\sim}{M} \triangleq \underset{\sim}{M}_{ij} = \rho(\underline{r})\delta_{ij} \tag{24}$$

$$\underset{\sim}{R} \triangleq \underset{\sim}{R}_{ij} = -\sum_{k,l=1}^{3} \frac{\partial}{\partial x_k} \left[G_{ij}^{kl}(\underline{r} \quad \bar{x}_l \right] \tag{25}$$

$$\underset{\sim}{K} \triangleq \underset{\sim}{K}_{ij} = -\sum_{k,l=1}^{3} \frac{\partial}{\partial x_k} \left[C_{ij}^{kl}(\underline{r}) \frac{\partial}{\partial x_l} \right] \tag{26}$$

and the externally applied force vector $\underline{f}$ and displacement $\underline{u}$ are defined in (14) and (19). Here the symbol $\underset{\sim}{R}$ is used to distinguish between the damping operator derived consistently from the constitutive relation, and the more commonly used damping operator symbol $\underset{\sim}{C}$ or $\underset{\sim}{D}$. It is observed from (25) and (26) that the form of the damping and the stiffness operators is the same. This means that in a spatial discretization procedure such as the finite element method, the algorithm for developing the stiffness matrix $\underline{K}$ and the damping matrix $\underline{R}(t)$ is the same. Therefore the extension of a dynamical elastic model to a dynamical viscoelastic model is relatively simple, and if a computer code for a particular elastic structure already exists, it needs to be modified only slightly to account for viscoelastic effects.

From (25) it is observed that the damping operator $\underset{\sim}{R}$ is time dependent, unlike the mass and stiffness operators. In addition, the functional relationship is such that the damping operator tends to zero as time increases arbitrarily; this is in keeping with the fading memory property, that is

$$\lim_{t \to \infty} \underset{\sim}{R}(\underline{r},t) = \underset{\sim}{0} \tag{27}$$

The response $\underline{u}$ at time t, as obtained from the integro-differential eqn. (23) is dependent on the entire history of the response up to time t, and can be determined uniquely in conjunction with the initial conditions

$$\underline{u}(0) = \underline{u}_0 \text{ and } \dot{\underline{u}}(0) = \underline{v}_0 \tag{28}$$

For the undamped problem when

$$G_{ij}^{kl} \equiv 0 \tag{29}$$

the damping operator vanishes,

$$\underset{\sim}{R} \equiv \underset{\sim}{0} \tag{30}$$

as expected and we obtain the standard undamped differential motion equation

$$\underset{\sim}{M}\,\ddot{\underline{u}}^0 + \underset{\sim}{K}\,\underline{u}^0 = \underline{r} \tag{31}$$

Here superscript $(.)^0$ is used to differentiate between the elastic and viscoelastic representation.

4 Properties of Operators

The mass, damping and stiffness operators satisfy certain properties. From (24)-(26), we have the self-adjoint properties with respect to space, (but not with respect to time),

$$(\underline{u}_1, \underset{\sim}{M}\underline{u}_2) = (\underline{u}_2, \underset{\sim}{M}\underline{u}_1) \tag{32}$$

$$(\underline{u}_1, \underset{\sim}{R}\underline{u}_2) = (\underline{u}_2, \underset{\sim}{R}\underline{u}_1) \tag{33}$$

$$(\underline{u}_1, \underset{\sim}{K}\underline{u}_2) = (\underline{u}_2, \underset{\sim}{K}\underline{u}_1) \tag{34}$$

and the definiteness properties

$$(\underline{u}, \underset{\sim}{M}\underline{u}) > 0 \tag{35}$$

$$(\underline{u}, \underset{\sim}{R}\underline{u}) > 0 \tag{36}$$

$$(\underline{u}, \underset{\sim}{K}\underline{u}) > 0 \tag{37}$$

for any $\underline{u} \neq \underline{0}$, that is, the mass operator is positive-definite while the damping and stiffness operators are positive-semidefinite in general, and the product $(.\ ,\ .)$ is given by

$$(\underline{u}_1,\underline{u}_2) \triangleq \int_V \underline{u}_1^T \underline{u}_2 \, dV \tag{38}$$

5 Eigenproblem

We wish to study the free vibration problem; in particular we wish to analyze the decaying oscillatory motion of a viscoelastic structure in the absence of external forces after it has undergone a small perturbation from equilibrium. The response to an arbitrary loading $\underline{f}$ can then be expanded in terms of the time independent eigenfunctions. Hence we seek a transformation in the formulation of the eigenproblem which removes the integro-differential operator in (23), that is, we wish to transform (23) into

$$\lambda \underset{\sim}{A} \underline{y} = \underset{\sim}{B} \underline{y} \tag{39}$$

The convolution integral in the motion equations (23) suggests the application of the Laplace or Fourier transform; either is applicable, but we choose the Laplace representation.

Taking the Laplace transform (Laplace variable p) of the integro-differential motion equation (23) yields

$$(p^2 \underset{\sim}{M} + p\underset{\sim}{\tilde{R}}(\underline{r},p) + \underset{\sim}{K})\underline{\tilde{u}} = \underline{\tilde{f}} + \underset{\sim}{M}\left(\frac{\partial \underline{u}(\underline{r},0)}{\partial t} + p\underline{u}(\underline{r},0)\right) + \underset{\sim}{\tilde{R}}\,\underline{u}(\underline{r},0) \tag{40}$$

where

$$\underset{\sim}{\tilde{R}}(\underline{r},p) = -\sum_{k,l=1}^{3} \frac{\partial}{\partial x_k}\left[\tilde{G}_{ij}^{kl}(\underline{r},p)\frac{\partial}{\partial x_l}\right] \tag{41}$$

$$\tilde{G}_{ij}^{kl}(\underline{r},p) = \int_0^\infty \frac{C_{ij}^{kl(*)}(\underline{r},\theta)\gamma(\theta)}{p+\theta}\, d\theta \tag{42}$$

Laplace transformed quantities are denoted by $(\tilde{\cdot})$.

We shall expand the solution for an arbitrary loading $\underline{f}$ in terms of the eigenfunctions $\underline{v}(\underline{r})$ which are space dependent, but independent of initial conditions. Therefore, we consider the homogeneous counterpart of (40); that is, free vibration of a viscoelastic structure and zero initial conditions,

$$\underline{f} \equiv \underline{0}\ , \quad \underline{u}(\underline{r},0) = \frac{\partial}{\partial t}\,\underline{u}(\underline{r},0) = \underline{0} \tag{43}$$

and obtain the eigenproblem

$$(p^2\underset{\sim}{M} + p\underset{\sim}{\tilde{K}}(\underline{r},p) + \underset{\sim}{K})\underline{v} = \underline{0} \tag{44}$$

In the analysis to follow it is convenient to work in first order form, so the eigenproblem (44) is expressed as

$$p\underset{\sim}{A}\underline{q} + \underset{\sim}{\tilde{B}}(p)\underline{q} = \underline{0} \tag{45}$$

where

$$\underset{\sim}{A} = \begin{vmatrix} \underset{\sim}{M} & \underset{\sim}{0} \\ \underset{\sim}{0} & -\underset{\sim}{K} \end{vmatrix} \tag{46}$$

$$\underset{\sim}{\tilde{B}}(p) = \begin{vmatrix} \underset{\sim}{\tilde{K}}(p) & \underset{\sim}{K} \\ \underset{\sim}{K} & \underset{\sim}{0} \end{vmatrix} \tag{47}$$

$$\underline{q}^T = [p\underline{v} \quad \underline{v}] \tag{48}$$

Here operators $\underset{\sim}{M}$, $\underset{\sim}{\tilde{K}}$, and $\underset{\sim}{K}$ and consequently $\underset{\sim}{A}$ and $\underset{\sim}{\tilde{B}}$ are all functions of the spatial coordinates; however, for simplicity this dependence is not noted explicitly in (45) - (48). From (46) it is observed that operator $\underset{\sim}{A}$ is real, symmetric and self-adjoint

$$(\underline{q}_1, \underset{\sim}{A}\underline{q}_2) = (\underset{\sim}{A}\underline{q}_1, \underline{q}_2) \tag{49}$$

Also operator $\underset{\sim}{\tilde{B}}$ is complex, symmetric and self-adjoint

$$(\underline{q}_1, \underset{\sim}{\tilde{B}}\underline{q}_2) = (\underset{\sim}{\tilde{B}}\underline{q}_1, \underline{q}_2) \tag{50}$$

The symmetric nature of $\underset{\sim}{\tilde{B}}$ implies

$$\underset{\sim}{\tilde{B}}^H = (\overline{\underset{\sim}{\tilde{B}}}) \tag{51}$$

where H denotes the Hermitian of the matrix operator, that is, the transpose of the complex conjugate (denoted by an overscore). Property (51) follows directly from expressions (41), (42), and (47). It is observed that neither $\underset{\sim}{A}$ nor $\underset{\sim}{\tilde{B}}$ exhibits definiteness properties.

For the undamped problem, when

$$\underset{\sim}{\tilde{K}} \equiv \underset{\sim}{0} \tag{52}$$

the eigenproblem becomes

$$p^0 \underset{\sim}{A}\underline{q}^0 + \underset{\sim}{B}^0\underline{q}^0 = \underline{0} \tag{53}$$

where the matrix operator $\underset{\sim}{B}^0$ is symmetric as before but is now real.

$$\underset{\sim}{B}^0 = \begin{bmatrix} \underset{\sim}{0} & \underset{\sim}{K} \\ \underset{\sim}{K} & \underset{\sim}{0} \end{bmatrix} \qquad \underline{q}^T = [\, p^0\underline{v}^0 \quad \underline{v}^0 \,] \tag{54}$$

The eigenvalues and eigenfunctions for the undamped problem are denoted by p^0 and $\underline{q}^0$. Superscript $(.)^0$ is used for the undamped elastic eigenproblem to distinguish it from the damped viscoelastic problem. It is noted that the matrix operator $\underset{\sim}{A}$ defined by (46) does not involve the damping operator $\underset{\sim}{\tilde{K}}(p)$, hence the matrix operator $\underset{\sim}{A}^0$ of the undamped problem is identical to the matrix operator $\underset{\sim}{A}$ of the damped problem.

6 Orthonormality Conditions

Before we derive the orthonormality conditions for the eigenfunctions of the viscoelastic problem, let us first review the classical orthonormality conditions for the eigenfunctions of the undamped eigenproblem (53). For the α^{th} mode we have

$$p_\alpha^0 \underset{\sim}{A} \underline{q}_\alpha^0 + \underset{\sim}{B}^0 \underline{q}_\alpha^0 = \underline{0} \quad , \quad \alpha = 1,2,3,... \tag{55}$$

From this we observe that eigenvalues p^0 and eigenfunctions $\underline{q}^0$ occur in complex conjugate pairs. Now performing $(\underline{q}_\beta^0,.)$ on (55) and using the self-adjoint properties of $\underset{\sim}{A}$ and $\underset{\sim}{B}^0$, we obtain the orthogonality relation

$$(\underline{q}_\alpha^0, \underset{\sim}{A}\underline{q}_\beta^0) = 0, \quad p_\alpha^0 \neq p_\beta^0 \tag{56}$$

Also, let us take the normalizing factor A_α^0, given by

$$(\underline{q}_\alpha^0, \underset{\sim}{A}\underline{q}_\alpha^0) = A_\alpha^0 \tag{57}$$

Then conditions (56) and (57) can then be expressed as

$$(\underline{q}_\alpha^0, \underset{\sim}{A}\underline{q}_\beta^0) = A_\alpha^0 \delta_{\alpha\beta} \tag{58}$$

The eigenfunctions are also orthogonal to $\underset{\sim}{B}^0$, i.e.,

$$(\underline{q}_\alpha^0, \underset{\sim}{B}^0 \underline{q}_\beta^0) = - p_\alpha^0 A_\alpha^0 \delta_{\alpha\beta} \tag{59}$$

We now turn to the task of finding the orthogonality conditions for the damped viscoelastic problem whose eigenproblem is

$$p_\alpha \underset{\sim}{A}\underline{q}_\alpha + \tilde{\underset{\sim}{B}}_\alpha \underline{q}_\alpha = \underline{0}, \quad \alpha = 1,2,3,... \tag{60}$$

where for simplicity and convenience, the notation

$$\underset{\sim}{\tilde{B}}_\alpha \triangleq \underset{\sim}{\tilde{B}}(p_\alpha) \tag{61}$$

is adopted. From (60) it is observed that the eigenvalues and eigenfunctions for the damped problem, also, occur in complex conjugate pairs, since from (42) we have

$$\bar{\tilde{G}}^{kl}_{ij}(\underline{r},p) = \tilde{G}^{kl}_{ij}(\underline{r},\bar{p}) \tag{62}$$

Applying $(\underline{q}_\beta,.)$ to (60), we obtain

$$p_\alpha(\underline{q}_\beta,\underset{\sim}{A}\underline{q}_\alpha) + (\underline{q}_\beta,\underset{\sim}{\tilde{B}}_\alpha\underline{q}_\alpha) = 0 \tag{63}$$

Utilizing, the self-adjoint properties of $\underset{\sim}{A}$ and $\underset{\sim}{\tilde{B}}$ (49) and (50), equation (63) becomes

$$p_\alpha(\underline{q}_\alpha,\underset{\sim}{A}\underline{q}_\beta) + (\underline{q}_\alpha,\underset{\sim}{\tilde{B}}_\alpha\underline{q}_\beta) = 0 \tag{64}$$

Interchanging indices α and β in (63), gives

$$p_\beta(\underline{q}_\alpha,\underset{\sim}{A}\underline{q}_\beta) + (\underline{q}_\alpha,\underset{\sim}{\tilde{B}}_\beta\underline{q}_\beta) = 0 \tag{65}$$

and so combining (64) and (65) yields the orthogonality condition

$$(p_\alpha - p_\beta)(\underline{q}_\alpha,\underset{\sim}{A}\underline{q}_\beta) + (\underline{q}_\alpha,[\underset{\sim}{\tilde{B}}_\alpha - \underset{\sim}{\tilde{B}}_\beta]\underline{q}_\beta) = 0, \qquad p_\alpha \neq p_\beta \tag{66}$$

Hence the eigenfunctions are not orthogonal to $\underset{\sim}{A}$ unlike (56) for the undamped problem. For the normality condition we shall take

$$(\underline{q}_\alpha, \underline{\underline{A}}\underline{q}_\alpha) = A_\alpha \tag{67}$$

$$p_\alpha p_\beta (\underline{q}_\beta, \underline{\underline{A}}\underline{q}_\alpha) + p_\beta (\underline{q}_\beta, \underline{\underline{B}}_\alpha \underline{q}_\alpha) = 0 \tag{68}$$

and realizing the symmetric nature of $\underline{\underline{A}}$ and $\underline{\underline{B}}$ yields

$$p_\alpha p_\beta (\underline{q}_\alpha, \underline{\underline{A}}\underline{q}_\beta) + p_\beta (\underline{q}_\alpha, \underline{\underline{B}}_\alpha \underline{q}_\beta) = 0 \tag{69}$$

Interchanging the indices α and β in (68), we obtain

$$p_\alpha p_\beta (\underline{q}_\alpha, \underline{\underline{A}}\underline{q}_\beta) + p_\alpha (\underline{q}_\alpha, \underline{\underline{B}}_\beta \underline{q}_\beta) = 0 \tag{70}$$

Upon combining (69) and (70) gives the second orthogonality condition,

$$(\underline{q}_\alpha, [p_\beta \underline{\underline{B}}_\alpha - p_\alpha \underline{\underline{B}}_\beta] \underline{q}_\beta) = 0, \quad p_\alpha \neq p_\beta \tag{71}$$

Equations (66) and (71) are two orthogonality relations for the viscoelastic problem. The former relation (66) is important in the derivation of modal identities which is the subject of discussion of the next section.

7 Modal Identities

It has been a traditional practice of dynamicists to analyze a flexible structure in terms of its eigenvalues and eigenfunctions. Hughes [10] has shown that in analysis of elastic structures, the complete set of eigenfunctions are not needed per se, but, two integrals of the eigenfunctions $\underline{P}_\alpha$ and $\underline{H}_\alpha$, which correspond to the linear and angular momenta of mode α. Once modal parameters are identified they can be shown to satisfy many identities. These identities provide a guide for establishing the importance of various modes, and also provide a numerical check on the completeness of a reduced (truncated) model. Several ideas put forth by Likins et al. [11] and Hughes and Skelton [12] are available for mode selection and the ones that rely solely on the structural dynamics are those that depend on the eigenvalues p_α, and modal coefficients $\underline{P}_\alpha$, and $\underline{H}_\alpha$.

We now extend Hughes' results for a constrained viscoelastic structure as shown in Fig. 3. It is constrained at point 0 to eliminate rigid body motion. First, we shall find an expansion of the inverse of the mass, damping and stiffness operators in terms of the eigenmodes. The identities for the modal

coefficients $\underline{P}_\alpha$ and $\underline{H}_\alpha$ are then established using the expansion of $(\underline{M}^{-1}, \underline{K}^{-1}, \underline{Q})$.

The constraint condition makes the stiffness operator $\underline{K}$ positive-definite, thus the inverse of operator $\underline{A}$, (eqn. (46)) exists. Expanding $\underline{A}^{-1}$ in terms of its eigenfunctions,

$$\underline{A}^{-1} \triangleq \sum_{\alpha,\beta=1}^{\infty} c_{\alpha\beta}(\underline{q}_\alpha)(\underline{q}_\beta \tag{72}$$

where the notation for the product $.)(.$ is defined explicitly by

$$\underline{A}^{-1}\underline{x} \triangleq \sum_{\alpha,\beta=1}^{\infty} c_{\alpha\beta}\underline{q}_\alpha(\underline{q}_\beta,\underline{x}) \tag{73}$$

and $c_{\alpha\beta}$ are unknown coefficients to be determined. Now for (72) to be a valid expansion, $\underline{A}^{-1}$ must satisfy the eigenproblem

$$p_\gamma \underline{q}_\gamma + \underline{A}^{-1}\underline{B}\underline{q}_\gamma = \underline{0} \tag{74}$$

Thus substituting (72) in the above equation and using (63) gives

$$p_\gamma[\underline{q}_\gamma - \sum_{\alpha,\beta=1}^{\infty} c_{\alpha\beta}(\underline{q}_\beta,\underline{A}\underline{q}_\gamma)\underline{q}_\alpha] = \underline{0}\ , \qquad \gamma = 1, 2, \ldots \tag{75}$$

For a constrained structure

$$p_\gamma \neq 0\ , \quad \gamma = 1, 2, 3, \ldots \tag{76}$$

and since $\underline{q}_\alpha$ are eigenfunctions, from (75) we obtain

$$\sum_{\beta=1}^{\infty} c_{\alpha\beta}(\underline{q}_\beta,\underline{A}\underline{q}_\gamma) = \delta_{\alpha\gamma}, \qquad \alpha,\gamma = 1,2,3,\ldots \tag{77}$$

or in matrix form we can write

$$\underline{C}\,\underline{D} = \underline{1} \tag{78}$$

where the elements of the matrices are identified as follows:

$$\underline{C} = c_{\alpha\beta} \tag{79}$$

$$\underline{D} = (\underline{q}_\beta, \underline{\underline{A}}\underline{q}_\gamma) \tag{80}$$

$$\underline{1} = \delta_{\alpha\gamma} \tag{81}$$

Equation (78) is sufficient to solve for the unknown coefficients $c_{\alpha\beta}$ provided $\underline{D}$ is non-singular. It should be noted that matrix $\underline{D}$ as defined in (80) is not diagonal since the eigenfunctions of a viscoelastic structure are not orthogonal to $\underline{\underline{A}}$ as is evident from (66). This is unlike the elastic problem where the orthogonality condition (58) makes $\underline{D}$ diagonal.

Three more expansions from $\underline{\underline{A}}^{-1}$ can be obtained. For this we, first, rewrite $\underline{q}$ in terms of $\underline{v}$ using (48). The expansion for $\underline{\underline{A}}^{-1}$ then becomes

$$\underline{\underline{A}}^{-1} = \sum_{\alpha,\beta=1}^{\infty} c_{\alpha\beta} \begin{bmatrix} p_\alpha p_\beta \underline{v}_\alpha)(\underline{v}_\beta & p_\alpha \underline{v}_\alpha)(\underline{v}_\beta \\ p_\beta \underline{v}_\alpha)(\underline{v}_\beta & \underline{v}_\alpha)(\underline{v}_\beta \end{bmatrix} \tag{82}$$

Also from (46) we have

$$\underline{\underline{A}}^{-1} = \begin{bmatrix} \underline{\underline{M}}^{-1} & \underline{\underline{0}} \\ \underline{\underline{0}} & -\underline{\underline{K}}^{-1} \end{bmatrix} \tag{83}$$

Operator $\underline{\underline{K}}$ is invertible since the structure is constrained. So comparing the two expressions for $\underline{\underline{A}}^{-1}$ (82) and (83), we obtain

$$\underset{\sim}{M}^{-1} = \sum_{\alpha,\beta=1}^{\infty} c_{\alpha\beta}\, p_\alpha p_\beta \underline{v}_\alpha)(\underline{v}_\beta \tag{84}$$

$$\underset{\sim}{K}^{-1} = -\sum_{\alpha,\beta=1}^{\infty} c_{\alpha\beta} \underline{v}_\alpha)(\underline{v}_\beta \tag{85}$$

$$\underline{0} = \sum_{\alpha,\beta=1}^{\infty} c_{\alpha\beta} p_\alpha \underline{v}_\alpha)(\underline{v}_\beta \tag{86}$$

The above expressions can be used to establish identities in terms of the modal coefficients which are identified as follows. First, consider the reaction force and torque at the constrained point O of the viscoelastic body, Fig. 3,

$$\underline{F}_R(t) = -\int_V \underline{y}(\underline{r},t)dV \tag{87}$$

$$\underline{T}_R(t) = -\int_V \underline{r}^X \underline{y}(\underline{r},t)dV \tag{88}$$

where

$$\underline{y} \triangleq \underset{\sim}{K}\,\underline{u} = \underline{f} - \underset{\sim}{M}\,\ddot{\underline{u}} - \int_o^t \underset{\sim}{R}(\underline{r},t-\tau)\frac{\partial \underline{u}}{\partial \tau}\, d\tau \tag{89}$$

and $(\cdot)^X$ is the skew-symmetric 3x3 matrix associated with the cross product. The displacement function under our assumption of linearity can be taken to be separable in the spatial coordinates and the variable t. So

$$\underline{u}(\underline{r},t) = \sum_{\alpha=1}^{\infty} \underline{v}_\alpha(\underline{r}) v_\alpha(t) \tag{90}$$

where $\underline{v}_\alpha(\underline{r})$ and $v_\alpha(t)$ are in general complex. The reaction force and torque can then be written as

$$\underline{F}_R(t) = -\underline{F}_E(t) + \sum_{\alpha=1}^{\infty} \left(\underline{P}_\alpha \ddot{v}_\alpha + \int_o^t \underline{R}_\alpha(t-\tau)\frac{dv_\alpha}{d\tau}\, d\tau\right) \tag{91}$$

$$\underline{T}_R(t) = -\underline{T}_E(t) + \sum_{\alpha=1}^{\infty} \left(\underline{H}_\alpha \ddot{v}_\alpha + \int_0^t \underline{Q}_\alpha(t-\tau)\frac{dv_\alpha}{d\tau}\, d\tau\right) \tag{92}$$

where

$$\underline{F}_E(t) \triangleq \int_V \underline{f}(\underline{r},t)dV \tag{93}$$

$$\underline{T}_E(t) \triangleq \int_V \underline{r}^X \underline{f}(\underline{r},t)dV \tag{94}$$

$$\underline{P}_\alpha \triangleq \int_V \rho(\underline{r})\, \underline{v}_\alpha(r)dV$$

$$= (\rho\underline{1}, \underline{v}_\alpha) \tag{95}$$

$$\underline{H}_\alpha \triangleq \int_V \rho(\underline{r})\underline{r}^X \underline{v}_\alpha(\underline{r})dV$$

$$= -(\rho\underline{r}^X, \underline{v}_\alpha) \tag{96}$$

$$\underline{R}_\alpha(t) \triangleq \int_V \underline{\underline{R}}\,(\underline{r},t)\underline{v}_\alpha(\underline{r})dV$$

$$= (\underline{\underline{R}}, \underline{v}_\alpha) \tag{97}$$

$$\underline{Q}_\alpha(t) \triangleq \int_V \underline{r}^X \underline{\underline{R}}(\underline{r},t)\underline{v}_\alpha(\underline{r})dV$$

$$= -(\underline{\underline{R}}\underline{r}^X, \underline{v}_\alpha) \tag{98}$$

The constants $\underline{P}_\alpha$ and $\underline{H}_\alpha$ are termed the modal momentum and modal angular momentum coefficients since the momentum and angular momentum of the viscoelastic body are $\sum_{\alpha=1}^{\infty} \underline{P}_\alpha \dot{v}_\alpha$ and $\sum_{\alpha=1}^{\infty} \underline{H}_\alpha \dot{v}_\alpha$ respectively. Coefficients $\underline{R}_\alpha(t)$ and $\underline{Q}_\alpha(t)$ are identified as the time dependent modal linear and angular coefficients associated with the damping operator $\underline{\underline{R}}$.

The modal identities can now be set up in terms of the modal coefficients. Using (24) we have

$$(\rho \underline{1}, \underset{\sim}{M}^{-1} \rho \underline{1}) = m \underline{1} \tag{99}$$

where m is the total mass of the viscoelastic body. If the expansion for $\underset{\sim}{M}^{-1}$ as given by (84) is used we obtain

$$(\rho \underline{1}, \underset{\sim}{M}^{-1} \rho \underline{1}) = \sum_{\alpha,\beta=1}^{\infty} c_{\alpha\beta} p_\alpha p_\beta (\rho \underline{1}, \underline{v}_\alpha)(\underline{v}_\beta, \rho \underline{1})$$

$$= \sum_{\alpha,\beta=1}^{\infty} c_{\alpha\beta} p_\alpha p_\beta \underline{P}_\alpha \underline{P}_\beta^T \tag{100}$$

Comparison of expressions (99) and (100) yields the matrix identity

$$\sum_{\alpha,\beta=1}^{\infty} c_{\alpha\beta} p_\alpha p_\beta \underline{P}_\alpha \underline{P}_\beta^T = m \underline{1} \tag{101}$$

It should be noted that the double sum in (101) is real since the coefficients $c_{\alpha\beta}$, the eigenvalues, the eigenfunctions and thus the modal coefficients all appear in complex conjugate pairs.

Similarly, two more identities involving the expansion for $\underset{\sim}{M}^{-1}$ can be established. These are

$$\sum_{\alpha,\beta=1}^{\infty} c_{\alpha\beta} p_\alpha p_\beta \underline{H}_\alpha \underline{H}_\beta^T = \underline{J} \tag{102}$$

$$\sum_{\alpha,\beta=1}^{\infty} c_{\alpha\beta} p_\alpha p_\beta \underline{H}_\alpha \underline{P}_\beta^T = \underline{c}^X \tag{103}$$

where $\underline{c}$ and $\underline{J}$ are first and second moments of inertia respectively,

$$\underline{c}^x \triangleq -(\rho \underline{r}^x, \underline{\underline{M}}^{-1} \rho \underline{1}) \tag{104}$$

$$\underline{J} \triangleq (\rho \underline{r}^x, \underline{\underline{M}}^{-1} \rho \, \underline{r}^x) \tag{105}$$

Proceeding in the manner outlined above, using the expansion (85) for operator $\underline{\underline{K}}^{-1}$, we can establish three more identities. For this we require the flexibility operator, which can be expressed as an integral operator

$$\underline{\underline{F}}[f(\underline{r})] \triangleq \underline{\underline{K}}^{-1}[f(\underline{r})] = \int_V \underline{\underline{F}}(\underline{r},\underline{\xi}) f(\underline{\xi}) dV \tag{106}$$

where $\underline{\underline{F}}$ is symmetric and positive-definite and thus $\underline{\underline{F}}$ is symmetric and positive-definite. Therefore

$$\sum_{\alpha,\beta=1}^{\infty} c_{\alpha\beta} \underline{P}_\alpha \underline{P}_\beta^T = -\int_V \int_V \rho(\underline{r}) \underline{\underline{F}}(\underline{r},\underline{\xi}) \rho(\underline{\xi}) dV dV \tag{107}$$

$$\sum_{\alpha,\beta=1}^{\infty} c_{\alpha\beta} \underline{H}_\alpha \underline{H}_\beta^T = -\int_V \int_V \rho(\underline{r}) \underline{r}^x \underline{\underline{F}}(\underline{r},\underline{\xi}) \rho(\underline{\xi}) \underline{\xi}^x dV dV \tag{108}$$

$$\sum_{\alpha,\beta=1}^{\infty} c_{\alpha\beta} \underline{H}_\alpha \underline{P}_\beta^T = -\int_V \int_V \rho(\underline{r}) \underline{r}^x \underline{\underline{F}}(\underline{r},\underline{\xi}) \rho(\underline{\xi}) dV dV \tag{109}$$

Using expansion (86) for the null operator, we obtain

$$\sum_{\alpha,\beta=1}^{\infty} c_{\alpha\beta} p_\beta \underline{P}_\alpha \underline{P}_\beta^T = \underline{0} \tag{110}$$

$$\sum_{\alpha,\beta=1}^{\infty} c_{\alpha\beta} p_\beta \underline{H}_\alpha \underline{H}_\beta^T = \underline{0} \tag{111}$$

$$\sum_{\alpha,\beta=1}^{\infty} c_{\alpha\beta} p_\beta \underline{H}_\alpha \underline{P}_\beta^T = \underline{0} \tag{112}$$

This completes the derivation of the modal identities, (101)-(103), (107)-(109) and (110)-(112). These can be used as a numerical check on the solution of the eigenproblem or more importantly for mode selection as shown in [11] and [12]. For completeness a parallel axis theorem for the momentum coefficients as given by Hughes [10] is included here. As shown in Fig. 4 consider two reference points, A and B. The locations with respect to A and B are denoted by $\underline{r}_A$ and $\underline{r}_B$, and related by

$$\underline{r}_A = \underline{r}_B + \underline{r}_{AB} \tag{113}$$

where vector $\underline{r}_{AB}$ is the constant location of B with respect to A. Also, we take

$$dV_A = dV_B = dV \tag{114}$$

Modal linear momentum coefficients $\underline{P}_\alpha$ are independent of the reference point, while the angular momentum coefficients $\underline{H}_\alpha$ are defined as

$$\underline{H}_{A\alpha} \triangleq \int_V \underline{r}_A^{\times} \underline{v}_\alpha \rho(\underline{r}) dV, \quad \underline{H}_{B\alpha} \triangleq \int_V \underline{r}_B^{\times} \underline{v}_\alpha \rho(\underline{r}) dV \tag{115}$$

which implies

$$\underline{H}_{A\alpha} = \underline{H}_{B\alpha} + \underline{r}_{AB}^{\times} \underline{P}_\alpha \tag{116}$$

This result is particularly useful when adding a flexible body of known characteristics to a structure. Modal coefficients $\underline{H}_\alpha$ for the entire structure can be computed using expression (116), rather than using the primitive definition, (96).

The modal identities for the elastic (undamped) problem can be shown to involve only a single sum. The eigenfunctions $\underline{q}^0$ are orthogonal to $\underline{A}$ as seen from (58) and so matrix $\underline{D}$ in (80) becomes

$$\begin{aligned} \underline{D}^0 &= (\underline{q}_\beta^0, \underline{A}\underline{q}_\gamma^0) \\ &= A_\beta^0 \, \delta_{\beta\gamma} \end{aligned} \tag{117}$$

and from (78) we obtain

$$c_{\alpha\beta} = A_{\beta}^{0-1}\delta_{\alpha\beta} \tag{118}$$

So the double sum in the modal identities derived earlier reduces to a single sum, i.e. (101) becomes

$$\sum_{\alpha=1}^{\infty} A_{\alpha}^{0-1}\, p_{\alpha}^{0}\, p_{\alpha}^{0}\, \underline{p}_{\alpha}^{0}\, \underline{p}_{\alpha}^{0T} = m\, \underline{1} \tag{119}$$

In keeping with the notation used earlier, superscript $(.)^0$ is used for all quantities (normalizing factor A_{α}^{0}, eigenvalues p_{α}^{0}, and modal coefficient $\underline{p}_{\alpha}^{0}$) of the elastic problem. Similarly, the double sum in identities (102)-(103), (107)-(109), and (110)-(112) reduces to a single sum (cf. Hughes [7]).

8 Example - Cantilevered Viscoelastic Beam

This section illustrates the concepts discussed earlier on a simple one-dimensional problem; a cantilevered viscoelastic beam in pure flexure, Fig. 5. The stress-strain relation for the one dimensional problem is

$$\sigma = \int_{0}^{t} G(t-s)\frac{\partial \varepsilon}{\partial s}\, ds + C\varepsilon$$

$$G(t) = \int_{0}^{\infty} C^{(*)}(\theta)\gamma(\theta)e^{-\theta t}d\theta \tag{120}$$

Using this in the principle of virtual work, in the absence of external forces, the equation of motion of the viscoelastic beam is

$$\rho\ddot{w} + I\Big(\int_{0}^{t} G(t-\tau)\frac{\partial w''''}{\partial \tau}\, d\tau + C\, w''''\Big) = 0 \tag{121}$$

where ρ is the material mass/length and I is the second moment of the cross-sectional area. To formulate the eigenproblem, we first take the Laplace transform. This gives

$$p^2\, \rho\, \tilde{w} + I\Big(p\tilde{G}(p) + C\Big)\frac{\partial^4 \tilde{w}}{\partial x^4} = \rho\Big(\frac{\partial w(0)}{\partial t} + pw(0)\Big) + \tilde{G}\, w(0)$$

$$\tilde{G}(p) = \int_0^\infty \frac{C^{(*)}(\theta)\gamma(\theta)}{p + \theta}\, d\theta \tag{122}$$

The corresponding eigenproblem becomes

$$p^2\rho\phi + I(p\tilde{G}(p) + C)\phi'''' = 0 \tag{123}$$

and the eigenmodes ϕ_j are obtained from the differential equation

$$\phi_j'''' - z_j^4 \rho\, \phi_j = 0, \qquad z_j \text{ - separation constant}, \quad j = 1,2,\ldots \tag{124}$$

and satisfy the orthonormality condition,

$$\int_0^l \phi_i(x)\phi_j(x)dx = 1 \tag{125}$$

The eigenmodes which satisfy (124) and (125) are

$$\phi_j(x) = \frac{1}{l^{1/2}}[(\cos z_j x - \cosh z_j x) - \alpha_j(\sin z_j x - \sinh z_j x)] \tag{126}$$

where

$$z_j = \frac{\varepsilon_j}{l}, \qquad \varepsilon_j^4 = \frac{\omega_j^2 l^4}{CI} \tag{127}$$

$$\alpha_j = \frac{\cos \varepsilon_j + \cosh \varepsilon_j}{\sin \varepsilon_j + \sinh \varepsilon_j} \tag{128}$$

ε_j are the roots of the transcendental equation

$$\cosh \varepsilon_j \cos \varepsilon_j + 1 = 0 \tag{129}$$

and the integro-differential equation for the modal coordinate, f_j is

$$\ddot{f}_j + \omega_j^2 (g_j(t) + f_j) = 0 \tag{130}$$

$$g_j(t) \triangleq \frac{1}{C} \int_0^t G(t - \tau) \frac{df_j}{d\tau} d\tau \tag{131}$$

$$w(x,t) = \sum_{j=1}^{\infty} \phi_j(x) \, f_j(t) \tag{132}$$

The reaction force and torque at the fixed end of the beam can be obtained from

$$F_R(t) = \sum_{j=1}^{\infty} (P_j \ddot{f}_j + CI \, z_j^4 \, P_j \, g_j(t)) \tag{133}$$

$$T_R(t) = \sum_{j=1}^{\infty} (H_j \ddot{f}_j + CI \, z_j^4 \, H_j \, g_j(t)) \tag{134}$$

Here the damping force $(= CI \sum_{j=1}^{\infty} z_j^4 P_j \, g_j(t))$ is a linear combination of the momentum coefficients P_j. Using (126) the modal momentum coefficients as given by (95) and (96) for the beam become

$$P_i = \rho \int_0^l \phi_i(x) dx$$

$$= 2(\rho l)^{1/2} \frac{\alpha_i}{\varepsilon_i} \tag{135}$$

$$H_i = \rho \int_0^l x \phi_i(x) dx$$

$$= \frac{2(\rho l^3)^{1/2}}{\varepsilon_i^2} \tag{136}$$

The non-dimensionalized modal coefficients are shown in Figure 6. The modal parameters P_i and H_i are seen to decrease monotonically with mode number i, with H_i's decreasing faster than P_i's. Therefore, identities involving parameter H_i converge faster than the ones involving P_i. This result was shown by Hughes [13] for the same elastic problem, i.e. $G(t) \equiv 0$.

9 Closing Remarks

In this paper a general dynamical model for material damping based on viscoelastic assumptions is introduced. As observed from the flowchart for the viscoelastic model depicted in Figure 7, the motion equations are no longer differential, but rather integro-differential in nature. All operators (mass, damping and stiffness) are completely defined and arise consistently in the formulation.

The eigenproblem is formulated by taking the Laplace transform of the equation of motion. The eigenmodes are shown to satisfy orthogonality conditions and these conditions have been obtained for the elastic and viscoelastic problem. The eigenproblem for this class of problem is non-standard and cannot be solved numerically by standard algorithms. It is demonstrated, however, that the eigenproblem can be solved using a perturbation analysis. The accuracy of the numerical solution of the eigenproblem can be checked by the modal identities derived in this paper.

The only aspect remaining to be determined is the viscous moduli and decay distribution function $\gamma(\theta)$. The viscous moduli can be determined from a creep test as shown by Smith [14] for an orthotropic graphite reinforced epoxy. As for the decay distribution function $\gamma(\theta)$, one approach of determining it could involve correlating the analytical and experimental response (displacement) for a simple structure, such as a beam. Once the distribution is established, a consistent damping study can be incorporated in a dynamical model at the design stage.

In closing, the work can be summarized by the following remarks:

1) A damping operator is formulated, consistent with viscoelastic stress-strain relations.

2) The eigenproblem cannot be solved numerically by standard algorithms.

3) Modal coefficients for a viscoelastic problem satisfy certain identities. The identities can be used as a guide in modal reduction as shown by Hughes and Skelton [12].

4) Viscous moduli and distribution function $\gamma(\theta)$ need to be established for different materials.

REFERENCES

[1] Caravani, P., Watson, M.L., and Thompson. W.T., "Recursive Least-Squares Time Domain Identification of Structural Parameters", Journal of Applied Mechanics, Vol. 44, No. 1, March 1977, pp. 135-140.

[2] Yun, C.B., and Shinozuka, M., "Identification of Nonlinear Structural Dynamic Systems", Journal of Structural Mechanics, Vol. 8, No. 2, 1980, pp. 187-203.

[3] Caravani, P., and Thompson, W.T., "Identification of Damping Coefficients in Multidimensional Linear Systems", Journal of Applied

Mechanics, Vol. 41, No. 2, June 1974, pp. 379-382.

[4] Bland, D.R., and Lee, E.H., "Calculation of the Compliance Modulus of Linear Viscoelastic Materials from Vibrating Reed Measurements", 1955, Journal Applied Physics, 26, pp. 1497-1503.

[5] Caputo, M., "Linear Models of Dissipation whose Q is Almost Frequency Independent", Annali di Geofisica, XIX (4), 1966, pp. 383-393.

[6] Sokolinokoff, I.S., Mathematical Theory of Elasticity, McGraw-Hill, 1956.

[7] Biot, M.A., "Linear Thermodynamics and the Mechanics of Solids", Proceedings 3rd U.S. Natl. Congr. Appl. Mech., ASME (1958), pp. 1-18.

[8] Staverman, A.J. and Schwarzl, F., "Non-Equilibrium Thermodynamics of Viscoelastic Behaviour", Koninklijke Nederlandse Akademie Van Wetenschappen, Proceedings of the Section of Sciences, Vol. 55, Series B, 1952, pp. 486-492.

[9] Biot, M.A., "Theory of Stress-St.. Relations in Anisotropic Viscoelasticity and Relaxation Phenomena", Journal of Applied Physics, Vol. 25, No. 11, 1954, pp. 1385-1391.

[10] Hughes, P.C., "Modal Identities for Elastic Bodies, with Application to Vehicle Dynamics and Control", Journal of Appl. Mech., vol. 47, No. 1, March 1980, pp. 177-184.

[11] Likins, P.W., Ohkami, Y., and Wong, C., "Appendage Modal Coordinate Dynamic Analysis", Journal Spacecraft and Rockets, Vol. 15, Oct. 1976, pp. 611-617.

[12] Hughes, P.C. and Skelton, R.E., "Modal Truncation for Flexible Spacecraft", Journal Guid. and Control, Vol. 4, No. 3, May-June 1981, pp. 291-297.

[13] Hughes, P.C., "Space Structure Vibration Modes: How Many Exist? Which Ones Are Important?", University of Toronto, Institute for Aerospace Studies, Technical Note No. 252, April 1984.

[14] Smith, B.A.W., "Polymer Matrix Composite Materials in Simulated Space Environment: Ultraviolet and Vacuum Effects", Thesis for the degree of Master of Applied Science, University of Toronto, Department of Aerospace Science, 1981.

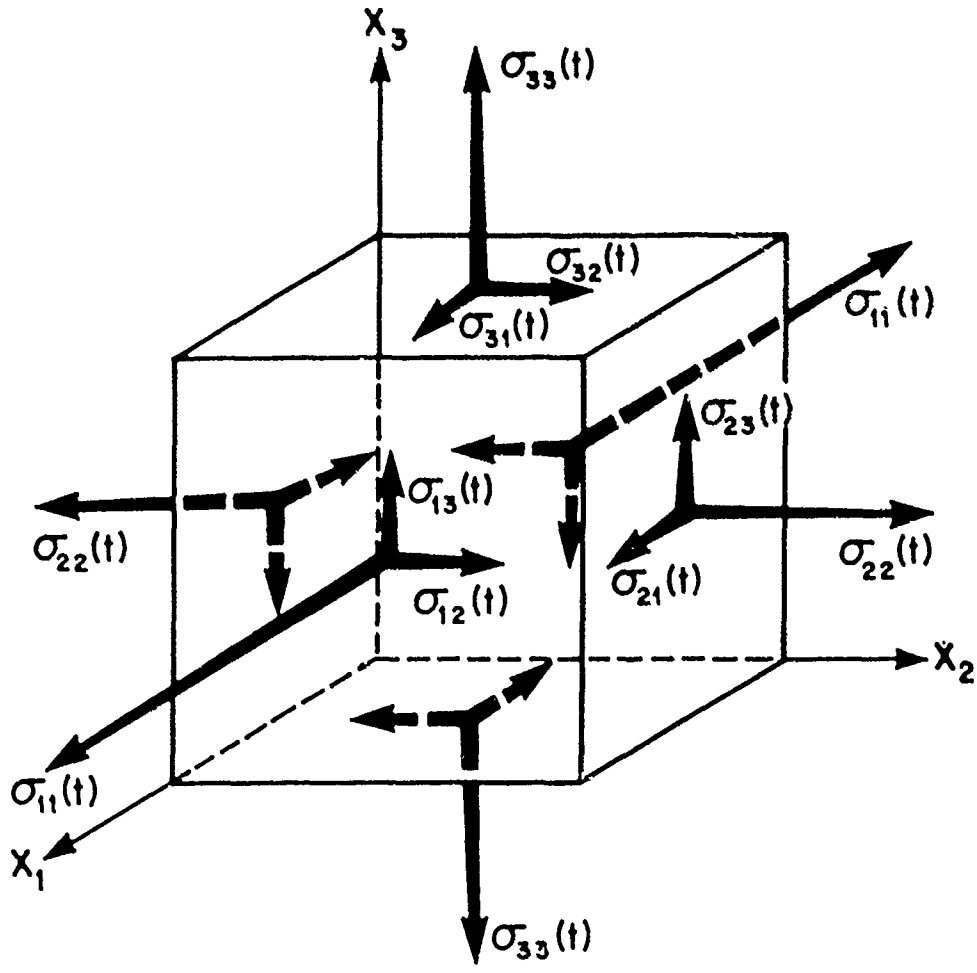


Fig. 1 A General State of Stress Acting on a Viscoelastic Element

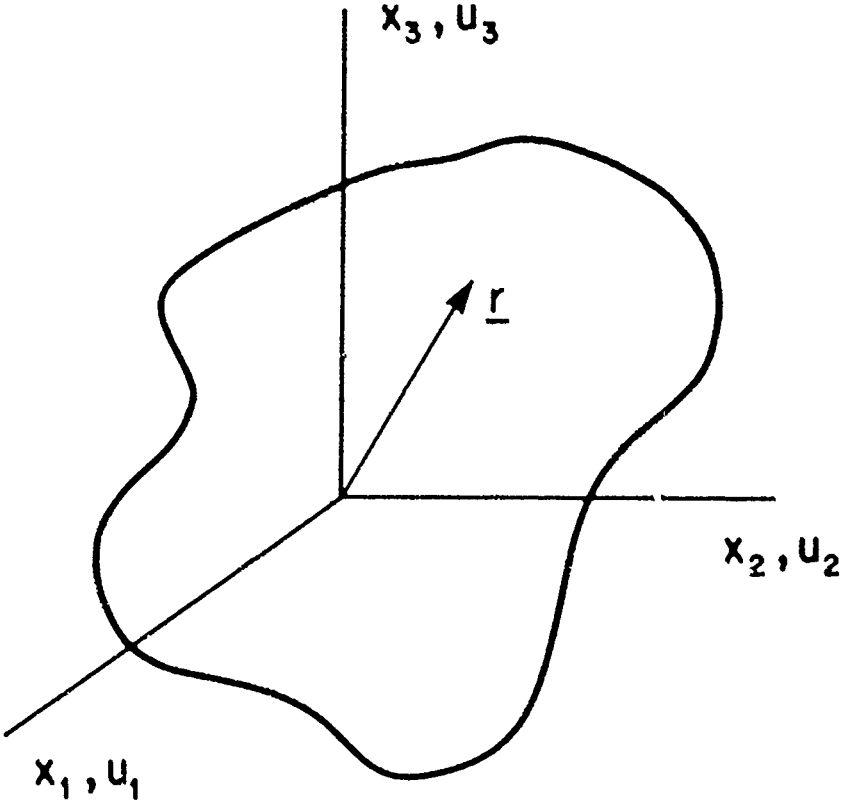


Fig. 2 Viscoelastic Body

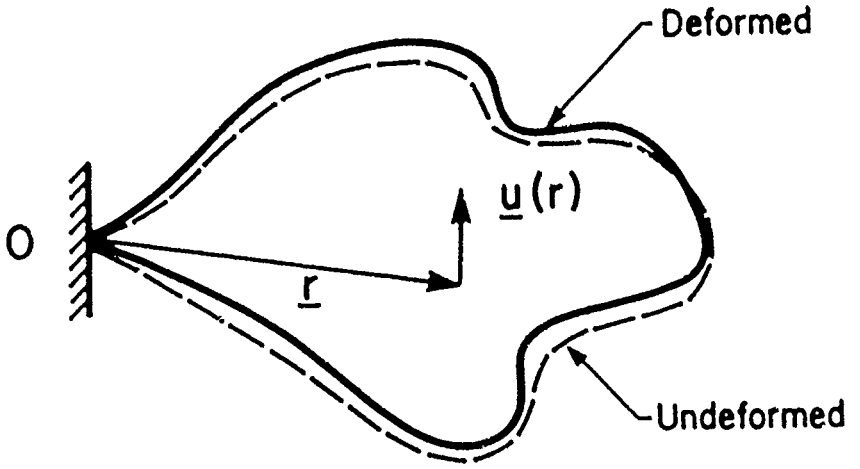


Fig. 3 Constrained Viscoelastic Body

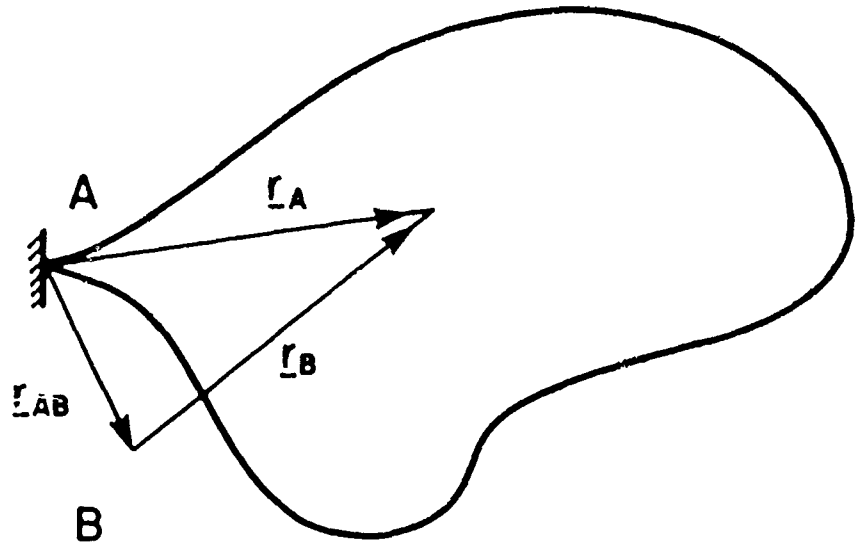


Fig. 4 Geometry of Parallel-AXIS Theorem for Modal Momentum Coefficients

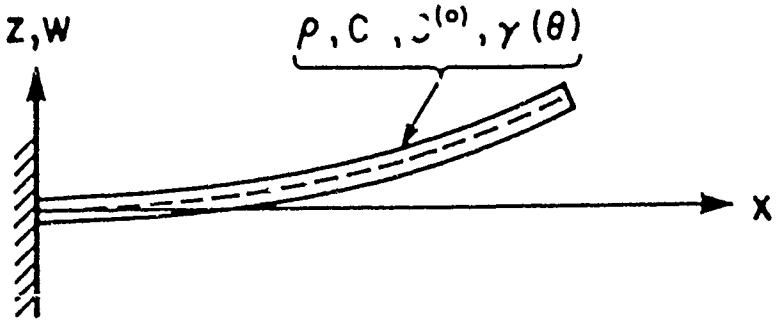


Fig. 5 Cantilevered Viscoelastic Beam in Pure Flexure

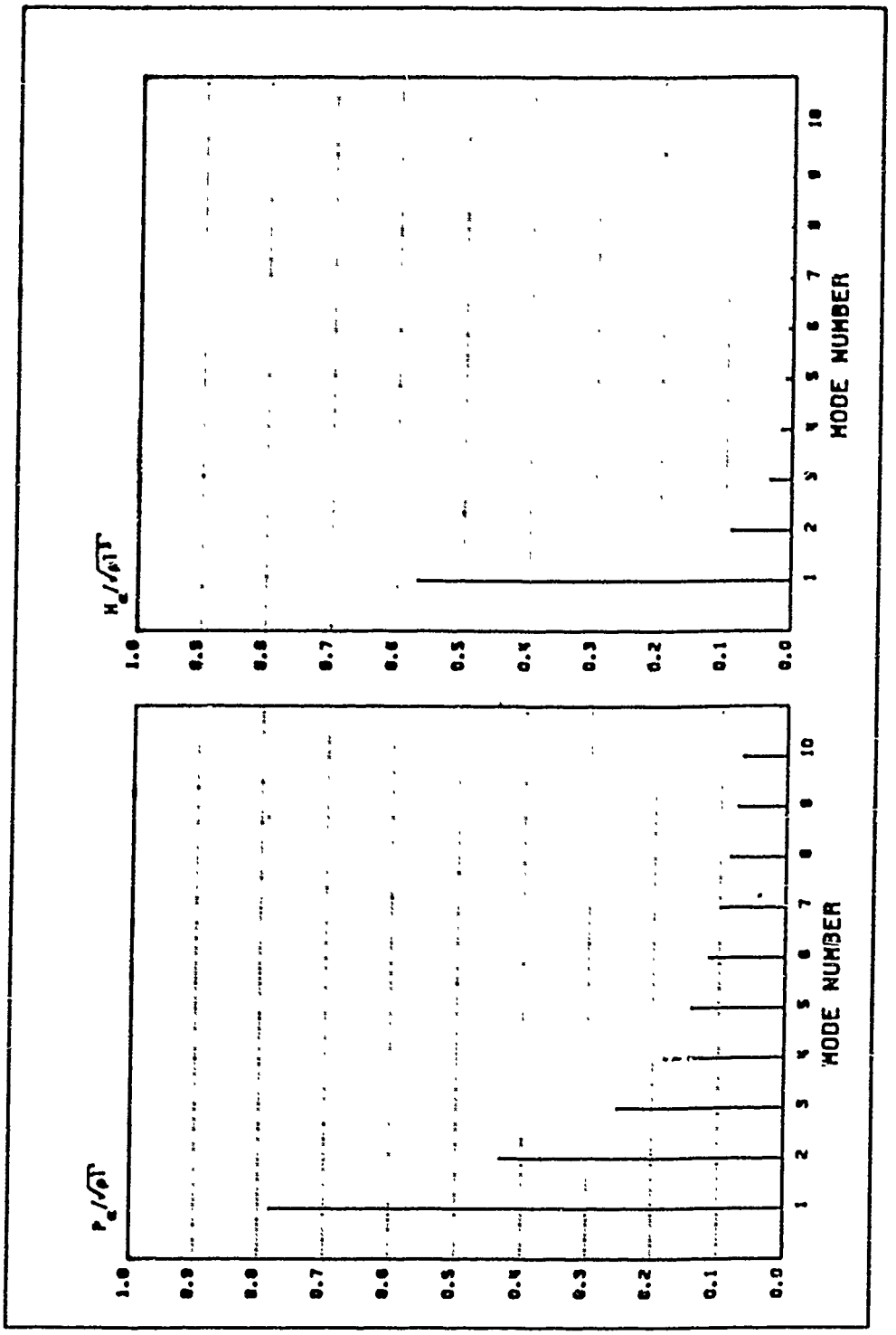


Fig. 6 Non-Dimensionalized Modal Coefficients

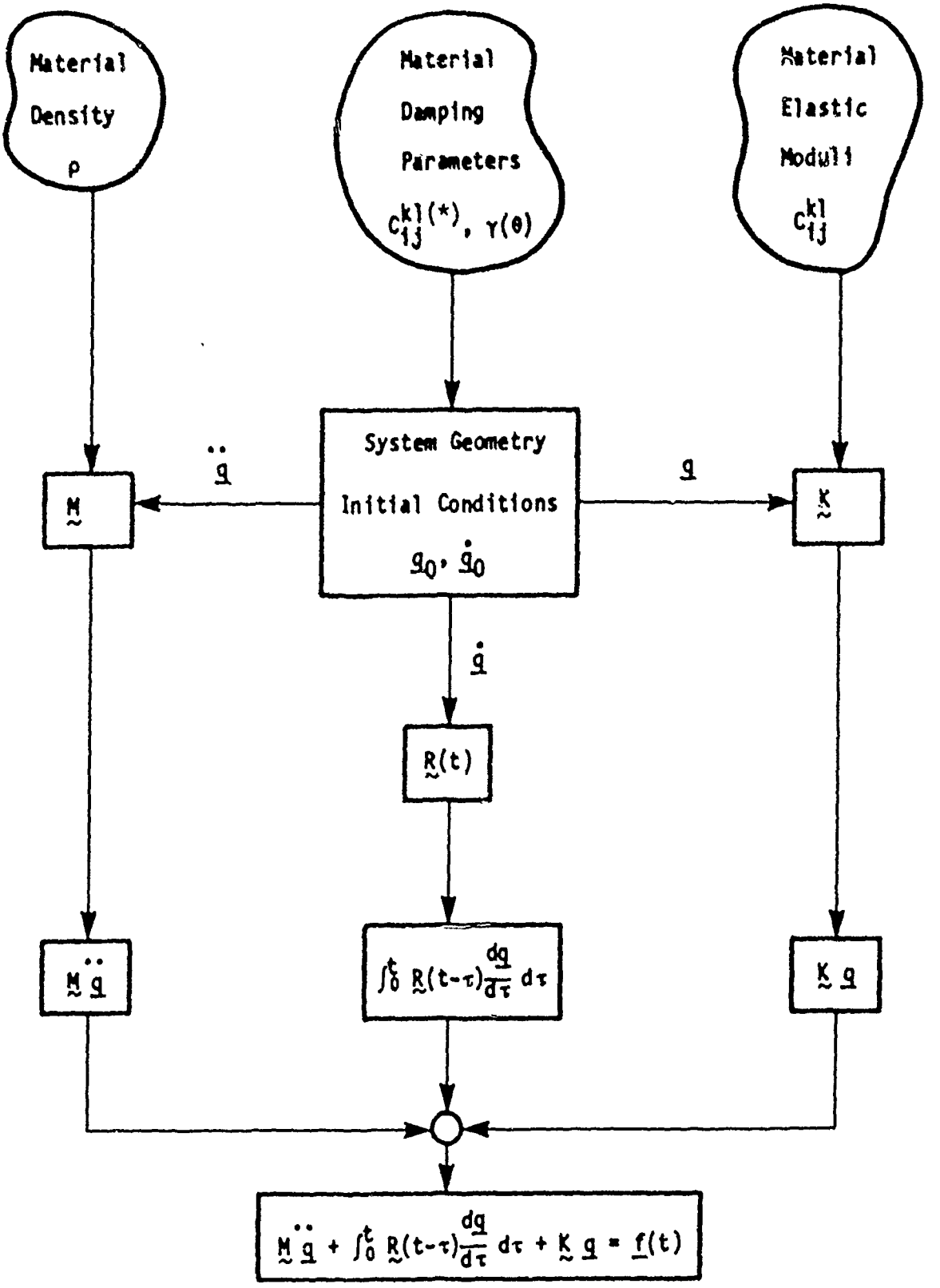


Fig. 7 Flow Chart for a Dynamical Viscoelastic Model

ON THE VIRTUES AND PROSPECTS FOR PASSIVE DAMPING IN LARGE SPACE STRUCTURES

By

Holt Ashley
Department of Aeronautics and Astronautics
Stanford University

and

Donald L. Edberg
Applied Technologies Section
Jet Propulsion Laboratory
California Institute of Technology
Pasadena, CA

ABSTRACT

Damping requirements estimated by the designers of active control systems for typical large structures deployed in orbit are compared with what might be expected to be available inherently in such structures. An attempt is made to draw on the best published experience from both tests made in space and modal decay measurements involving components, aircraft and other systems supported on the ground. With defined exceptions, it is concluded that in the majority of cases the available passive damping will meet or exceed the needs. Therefore, special provisions for augmenting energy dissipation will not be useful unless they offer a clear advantage, in cost, weight or simplicity.

INTRODUCTION

The objective of this paper is simple: to advance the claim that the modal damping naturally available in most large structures deployed in space will be more than adequate to permit the successful design of active control systems, without the use of special measures to augment passive energy dissipation. It is hoped to stimulate discussion and thoughtful reflection by this rather controversial conclusion.

One assumption must be clearly stated at the outset, because it represents a limitation on the classes and the purposes of space systems to which this study applies. It is assumed that space itself and the operations conducted therein constitute a relatively benign dynamic environment. Ruled out are such things as very rapid slewing maneuvers of large platforms or reflectors. The docking of Shuttle orbiters and other orbital transfer vehicles must be confined to "soft landings", as was the case with Apollo. Impulsive inputs such as impact by a large meteoroid are regarded as accidents rather than normal design conditions.

In summary, damping as a means of reducing the severity of very large responses is not included here. The emphasis is on the stability and effective performance of the controlled spacecraft. Furthermore, non-linearities cannot be so prominent as to negate the use of normal mode superposition as a means of representing dynamic behavior. (It is remarked that this appears to be the preferred approach to LSS control system analysis as can be seen, for example, by reference to the majority of papers at the latest Blacksburg Symposium[1].)

The program of the paper is to compare statements by informed specialists about what is needed against best estimates, derived from tests reported in the literature, of what will almost certainly be present. The critical damping ratio ζ for free motion in a "pure" natural mode of vibration is used as the primary measure of energy - dissipation capability in the structure or uncontrolled system. When the values are small, say $\leq 10^{-2}$, ζ is close to exactly half the "structural damping parameter" g or the "loss factor" η

Needs of the Control System Designer

It is, of source, impossible to quantify what is required in terms of a single value of ζ or even a range not involving powers of 10. The authors have discussed the issue with several well - informed specialists. The extensive literature has been carefully examined. About the only broad generalization that one can derive therefrom is that damping is usually neglected (see e.g., Hughes and Skelton[2]) within the control system bandwidth; with regard to both stability and performance, this is believed to be a conservative approximation.

The general answer to the question "how much ζ?" clearly depends on a variety of factors. They include the complexity and frequency spectrum of the plant being controlled; the bandwidth itself; the numbers and locations of sensors and actuators; the controllability and observability of all significant modes; and finally the specifications which are to be met. It is prima facie that the designer must be provided with an adequate model in terms of eigenvalues and frequency eigenvectors of the flexible structure. One observes, however, that past experience indicates that this last requirement can be fulfilled, so long as the system development process provides opportunities for periodic updating and for the ultimate experimental verification of these data.

Let it be assumed that the designer has the aforementioned adequate resources to do his job. In particular, measuring instruments and "effectors" of sufficient performance can be deployed throughout the structure so that problems can be avoided due to inadequate frequency ranges, controllability or observability. Under these circumstances, the authors have found no lacks of consensus* regarding the following conclusions suggested by Bryson[3]:

> For elastic modes with frequencies well within the system bandwidth, any ζ greater than zero is satisfactory.
>
> Above the system bandwidth, where such phenomena as "spillover" instability must be avoided, the range
>
> $$10^{-3} < \zeta \leq (10^{-2} \text{ or more}) \qquad (1)$$
>
> can be accepted. In general, the higher the (small) values the easier the design tasks.

It is the criterion of Equation (1) that should be borne in mind as the data in the next section are studied.

Damping Likely to be Available

The approach taken is to compare the numbers in Equation (1) against what is believed to be a relevant and carefully-made selection from the enormous literature on modal damping measurements. (One need only look to Lazan[4] or to the 102 literature citations in the 1973 review by Graham[5] in order to appreciate the meaning of "enormous.")

Several, but not all, of the data sets presented are felt to be representative of the highest experimental precision attained to date. Although difficult to prove rigorously, this claim of

---

*For instance, they proved acceptable to Professor P. C. Hughes, University of Toronto, during discussion at Vibration Damping Workshop II.

accuracy is based on personal knowledge and/or scrutizing of the methodology and details of error estimates furnished by the experimenters themselves. Two decimal places --- that is, RMS errors of $O(\pm 1\%)$ --- are felt to constitute a level of accuracy at the limit or beyond what has been accomplished to date.

The selection begins with a search for lower bounds on ζ through the study of measurements in vacuum on simple, monolithic components. It then proceeds to test data for complete structures --- first in the orbital environment, where very few have been published, and finally in ground facilities on various aerospace systems. In the first category, the most precise measurements are believed to be those of Crawley and collaborators (see Crawley and Mohr[6] among several references), as well as the thesis[7,8] of one of the present authors. Some values of ζ from that thesis are reproduced and discussed here; there is good agreement between comparable numbers from the two sources.

Table 1 lists all the specimens employed by Edberg[7]. The experimental technique, which was designed both to eliminate "air damping" and to minimize such other sources of extraneous energy dissipation as mechanical supports, is fully described in [7]. Table 2 and Figures 1 through 6 present typical results. Most of the data points actually summarize ten or more individual experiments. Their precision can be inferred from the vertical bars, which estimate the $\pm 1\sigma$ probable errors, and from the extreme values plotted as diamonds.

Figure 1 shows that, in a range of natural frequencies above the peak of the so-called "Debye curve" (cf. Zener[9] or Lee[10]), aluminum free-free beams reproduce quite well the predictions[9,10] of thermoelastic theory. For composite beams with epoxy matrix and three types of reinforcements, Figures 2, 3 and 4 show ζ to be almost independent of frequency. Various graphite and fiberglass specimens yielded values in a range 4 to 9×10^{-4}. Remarkably the ζ's for the Kevlar* - reinforced epoxy beams (Figure 4) turned out to be five to ten times higher than those for the other two reinforcements. This difference must be attributed to greater energy dissipation in the Kevlar. Since the Figure 4 ζ- values already meet the test of Equation (1) and this is suitable for many space applications, one concludes that Kevlar/epoxy constitutes a very desirable material from the standpoint of the present study.

Table 2 lists typical results from tests on aluminum and composite rectangular plates. Since there were no indications of any non-linear effects of vibration amplitude on these data, it is observed that the ratios between plate and beam damping for the aluminum and graphite are unexpectedly large. For instance, thermoelastic theory as developed by Lee[10] predicts a plate-to-

*"Kevlar" is a registered trademark of the DuPont Company.

beam ratio for metals dependent on Poisson's ratio and gives about 1.8 for aluminum. The same surprising underpredictions can be seen for monolithic, rectangular, aluminum trusses in Figures 5 and 6. Indeed, the disagreements implicit in Table 2 and Figures 5 and 6 remain unexplained. They are regarded by the authors as a challenge to those conducting theoretical research on vibratory energy dissipation in crystalline solids like metallic alloys.

Table 3 presents the only modal damping ratios from tests on orbit that could be found in the literature prior to the present Workshop. For the first out-of-plane bending mode of the 100%-deployed OAST-1 (or SAFE) solar array, Brumfield, Pappa, Miller and Adams[11] actually cite measurements of ζ between 3 and 4×10^{-2}, increasing with amplitude. What is especially significant, however, is the comparison between these numbers and a pre-flight estimate of 0.5×10^{-2} quoted by Venneri[12] at the Workshop.

The paper by Lips and Vigneron[13] contains the rest of the data in Table 3; it was telemetered from orbital tests on the Canadian communications satellite Hermes. No advance predictions or indications of experimental error are given for the ζ-values in Reference 13. It should be noted that the modal frequencies in the table are quite low compared to most ground test results and fall in the range estimated for the first generation of LSS. They suggest that the decrease of damping with increasing scale, forecast for instance in the paper by Ashley[14], may be too pessimistic.

The remaining examples are drawn from ground testing. Figure 7 is reproduced from Chen's article[16] (see also Stroud[15]), which summarizes an extensive series of vibration tests conducted on the Galileo spacecraft in its stowed configuration for launch to earth orbit. Altogether nine combinations of excitations and data-reduction procedures were employed in this program. As indicated, three of these are represented on the figure. Only nine of the approximately 25 modes for which ζ vs. frequency are plotted are identified by Chen[16] as "global" - in the sense that they have primary significance for the design of active controls. Described as "chaotic" in Reference 16, these damping ratios are difficult to characterize in terms of accuracy or of which method of excitation should be considered most reliable. They are shown here mainly as an indication of the levels to be expected on multi-component spacecraft. Observe that, if ζ is averaged between the three values given for each mode, none is found to be less than 5×10^{-3} and the majority exceed 10^{-2} significantly. Thus the criterion of Equation (1) is certainly met.

Figure 8 is taken from Jensen[17] as an example of full-scale measurements made in 1977-1978 on the Space Shuttle. These ζ-values are from the complete stack, in the launch configuration ("begin stage 1") and in a lighter condition corresponding to burnout of the solid rocket boosters. Three of the points on Figure 8 fall below the "control system design value" of $\zeta = 5 \times 10^{-3}$ The average up to a frequency of 80 rad/sec. is

calculated to be 1.7×10^{-2}. This may be compared with averages[17] of 2.1×10^{-2} for the orbiter/external tank combination and 3.2×10^{-2} for the orbiter alone.

Commenting about Jensen's results, one observes, on the one hand, that many of the ζ - values he presents are higher than what would probably be encountered in vacuum because of the combined effects of "air damping" and energy dissipation in the supports. On the other hand, substantial aerodynamic damping is available during boost to augment what is provided by the stack structure. Furthermore, no difficulties have been reported involving either the stability or performance of the Space Shuttle active controls.

Table 4 is from DiValentin[18] and summarizes damping ratios from low-frequency modal measurements on the large wind turbine WTS-4, built by Hamilton Standard Division and operating at Medicine Bow, WY. These data were obtained during natural excitation by atmospheric turbulence and are believed to be as accurate as any published for such machines. The fiberglass rotor blade is supported so as to teeter freely at its center, so that the symmetric modes (S1, S2) have effectively cantilever root boundary conditions whereas A1 and A2 relate to a free-free beam pinned at its midpoint. The tower is of welded steel construction, and relatively little energy can be dissipated at joints either in it or in the blade. The blade is subjected to some "air damping". Nevertheless, one sees that all the observed ζ fall well above the range of Equation (1).

Two samples are reproduced from the extensive literature of ground vibration tests on aircraft. In the late 1960's AGARD (NATO Advisory Group for Aerospace Research and Development) sponsored a very thorough program on the Lockheed F-104G, measurements being carried out independently in France by a group from O.N.E.R.A. and in Federal Republic of Germany of D.F.V.L.R. specialists. All results are summarized in a supplement by Küssner[19] to Vol. VI of the AGARD Manual on Aeroelasticity. Frequencies and damping ratios, in a range from the fundamental up to 100 Hz, were obtained by both organizations using variants of the sine-dwell technique[16,19]. There is far from close agreement between the reported sets of ζ's, but because of the extreme care taken in analyzing modal decays by the German Group their data are believed to be representative of the greatest accuracy obtained to date in aircraft tests of this type.

Figure 9 plots vs. modal frequency all of the damping ratios reported by the Germans on F-104G. The scatter of these points is, by no means, an indication of probable errors. Rather it reflects the fact that wide variations in ζ from mode to mode are to be expected in complicated structure. One comment must be made regarding the very low apparent damping ratios in two antisymmetrical modes at around 56 and 68 Hz. Both of these modes are concentrated in the empennage and include considerable rudder rotation. Because the hydraulic system, which powers the rudder and other control surface actuators, was active during these

tests, it is believed that this external energy source caused these ζ's (and perhaps some others) to be lower than what would have been obtained on a wholly passive structure. If this hypothesis is accepted, then Figure 9 can be said to bear out a phenomenon observed by the authors on other aircraft as well: that damping ratios tend generally to increase as one proceeds up the frequency scale.

Table 5 lists similar data for the first three modes of the ring of the DO-24TT, an experimental amphibian built by Dornier. The source is a paper by Artmann[20] at a recent symposium on aeroelasticity. He indicates that, as in the case of Figure 9, these were very careful measurements. Again one sees that the criterion of Equation (1) is satisfied and that ζ tends to increase with increasing frequency.

The final example chosen for presentation involves not a complete, built-up structural system but rather a large component typical of what the members of a LSS will look like. The LSS/IGTV measurements described by Tollison and Waites[21] were made on a 45-ft. "Astromast" truss, supported as a cantilever at its upper end and hanging free at the lower. Tests were made with an without an x-shaped "cruciform" frame attached at the bottom; this added a large rotary inertia whose main influence was to lower the torsional frequencies. Table 6 summarizes all data[21] that included reported ζ - values. Except for fundamental bending and three of the four torsion modes, these results also exceed the 10^{-2} limit of Equation (1). It is difficult to account for the ζ - increase in first torsion, which is associated with the large cruciform appendage. Second torsion, however, behaves just as one might anticipate from augmenting the kinetic and potential energies of the vibration while making no change in the capacity for energy dissipation.

CONCLUDING REMARKS

What one hopes is an unbiased selection has been offered from the literature on measured modal damping ratios of aerospace systems and components. Careful examination of these data is believed to support the initially - stated conclusion that, for the majority of large structures deployed in space, the naturally available damping will be enough to ensure the stability and acceptable performance of the controlled space vehicle.

ACKNOWLEDGEMENTS

This research was supported in part, by the Air Force Office of Scientific Research under Contract AFOSR 82-0062, and in part by the NASA Office of Aeronautics and Space Technology under Contract NAS7-918.

REFERENCES

1. Many authors, "Proceedings of the Fifth VPI&SU/AIAA Symposium on Dynamics and Control of Large Structures", Blacksburg, VA, June 1985.

2. Hughes, P. C., and Skelton, R. E., "Controllability and Observability for Flexible Spacecraft", J. Guidance and Control, Vol. 3, No. 5, September-October 1980, pp. 452-459.

3. Bryson, A. E., Jr., Private communication, Stanford University, February 1986.

4. Lazan, B. J., Damping of Materials and Members in Structural Mechanics, Pergamon Press, London, 1968.

5. Graham, W. B., "Material Damping and its Role in Linear Dynamic Equations", Institute for Aerospace Studies, University of Toronto, March 1973.

6. Crawley, E. F., and Mohr, D. G, "Experimental Measurements of Material Damping in Free-Fall with Tuneable excitation", AIAA Paper No. 83-0850, AIAA/ASME/ASCE/AHS 24th Structures, Structural Dynamics and Materials Conference, Lake Tahoe, Nevada, May 1983.

7. Edberg, D. L., "Measurement of Material Damping in a Simulated Space Environment", SUDAAR Report No. 546, Department of Aeronautics and Astronautics, Stanford University, December 1984.

8. Edberg, D. L., "Material Damping of Simple Structures in a Simulated Space Environment", presented at ASME Winter Annual Meeting, New Orleans, December 1984.

9. Zener, C. M., Elasticity and Anelasticity of Metals, University of Chicago Press, Chicago, IL, 1948.

10. Lee, U., "Thermal and Electromagnetic Damping Analysis and its Application", SUDAAR 543, Departments of Aeronautics/Astronautics and Mechanical Engineering, Stanford University, August 1984.

11. Brumfield, B., Pappa, M. L., Miller, J. B., and Adams, R. R., "Orbital Dynamics of the OAST-1 Solar Array Using Video Measurements", AIAA Paper 85-0758-CP, AIAA/ASME/ASCE/AHS 26th Structures, Structural Dynamics and Materials Conference, Orlando, FL, April 1985.

12. Venneri, S. L., "NASA Perspective for Passive and Active Damping Requirements", invited lecture, Vibration Damping Workshop II, Las Vegas, Nevada, March 4-6, 1986.

13. Lips, K. W., and Vigneron, F. R., "Damping Synthesis for a Spacecraft Using Substructure and Component Data", AIAA Paper No. 84-1053, AIAA/ASME/ASCE/AHS 25th Structures, Structural Dynamics and Materials Conference, Palm Springs, CA, May 1984.

14. Ashley, H., "On Passive Damping Mechanisms in Large Space Structures", Journal of Spacecraft and Rockets, Vol. 21, No. 5, September/October 1984, pp. 448-455.

15. Stroud, R. C., "The Modal Survey of the Galileo Spacecraft", Sound and Vibration, April 1984, pp. 28-34.

16. Chen, J. C., "Evaluation of Modal Testing Methods", AIAA Paper No. 84-1071, AIAA/ASME/ASCE/AHS 25th Structures, Structural Dynamics and Materials Conference, Palm Springs, CA, May 1984.

17. Jensen, D. L., "Structural Damping of Shuttle Orbiter and Ascent Vehicles", Paper Z, Vibration Damping 1984 Workshop Proceedings, AFWAL-TR-84-3064, Long Beach, CA, 1984.

18. DiValentin, E., "Variable Frequency Modal Response Testing of the WTS-4", Report 11SER9577, Hamilton Standard Div., United Technologies Corp., Wintson Locks, Conn., March 1985.

19. Küssner, H. G., "A Comparison of Methods Used in Flutter Research", AGARD Report No. 592, NATO Advisory Group for Aerospace Research and Development, August 1972.

20. Artmann, J., "Determination of Both Complex Characteristic Structural Values and Normal Mode Parameters from Harmonic Excitation Near Resonance", Second International Symposium on Aeroelasticity and Structural Dynamics, Aachen, April 1985, pp. 512-522.

21. Tollison, D. K., and Waites, H. B., "Dynamic Verification of Large Space Structures", proceedings of Conference on Large Space Antenna Systems Technology, NASA Conference Publication 2368, Part 2, Hampton, VA, December 1984, pp. 591-601.

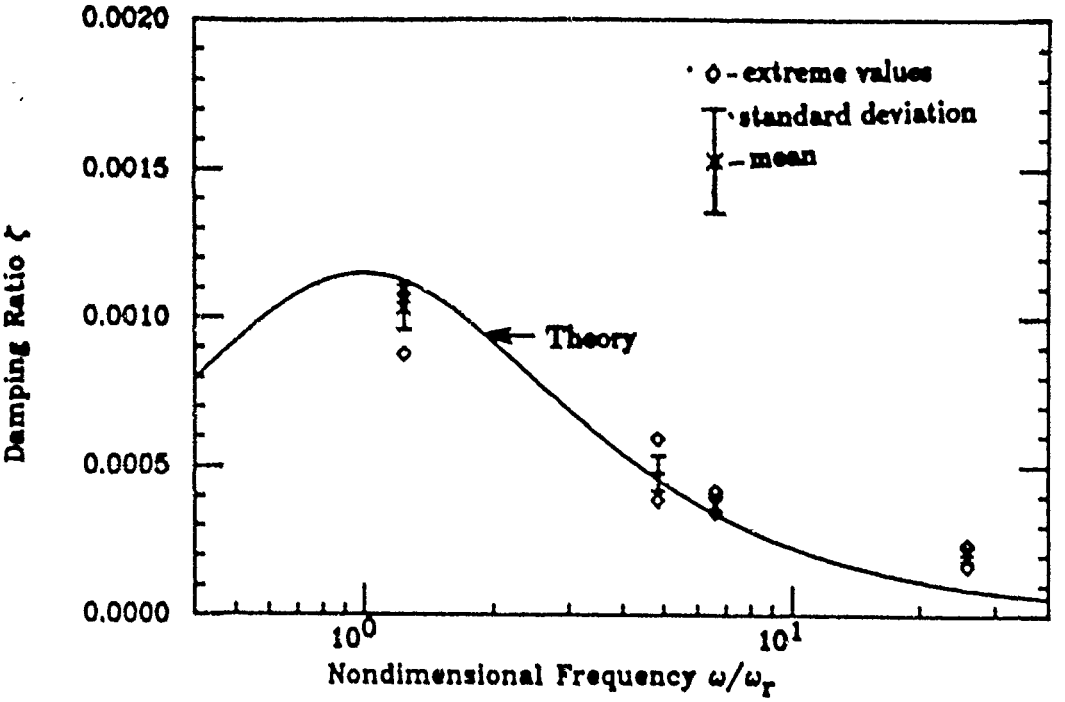


Figure 1. Damping ratios measured on Aluminum beams[7], as compared with thermoelastic predictions[9,10] (solid curve).

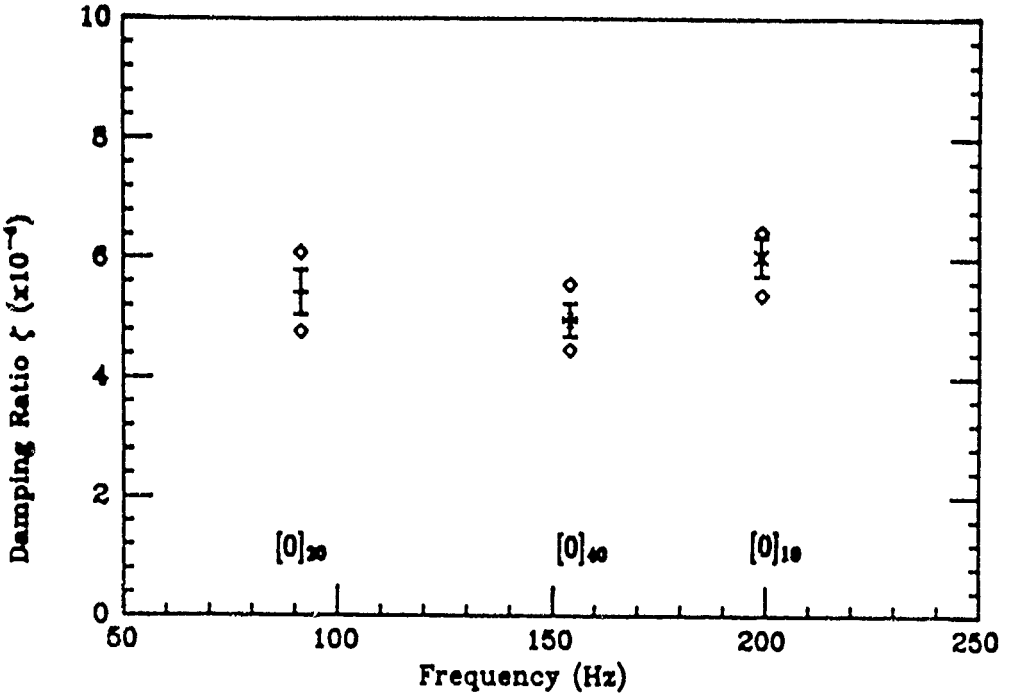


Figure 2. Damping ratios for unidirectional Graphite/Epoxy beams as a function of frequency[7].

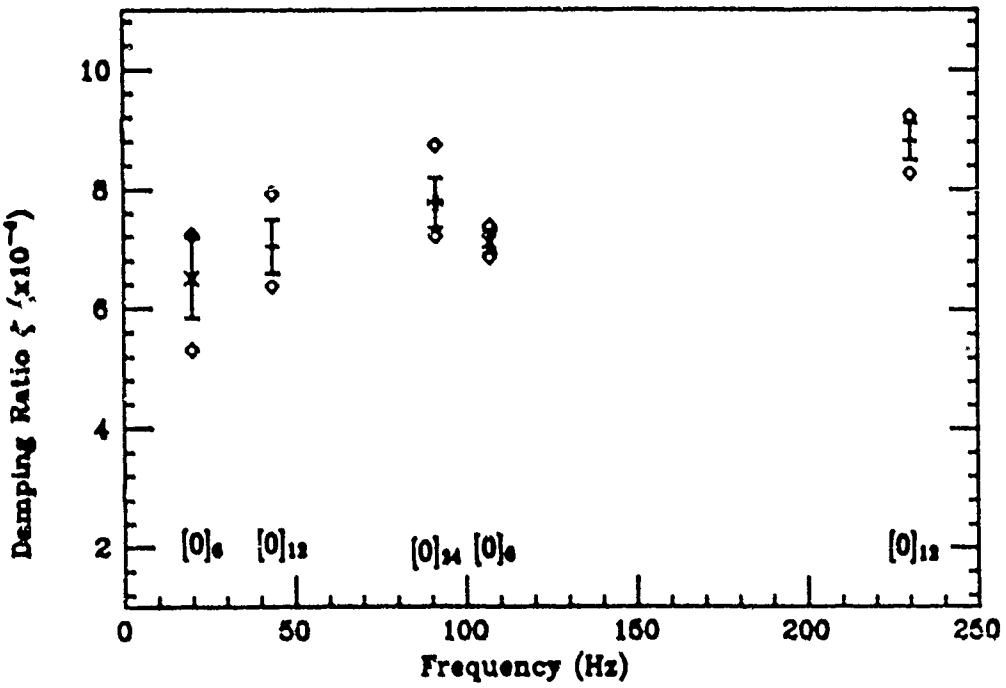


Figure 3. Damping ratio for unidirectional Fiberglass/Epoxy beams as a function of frequency[7].

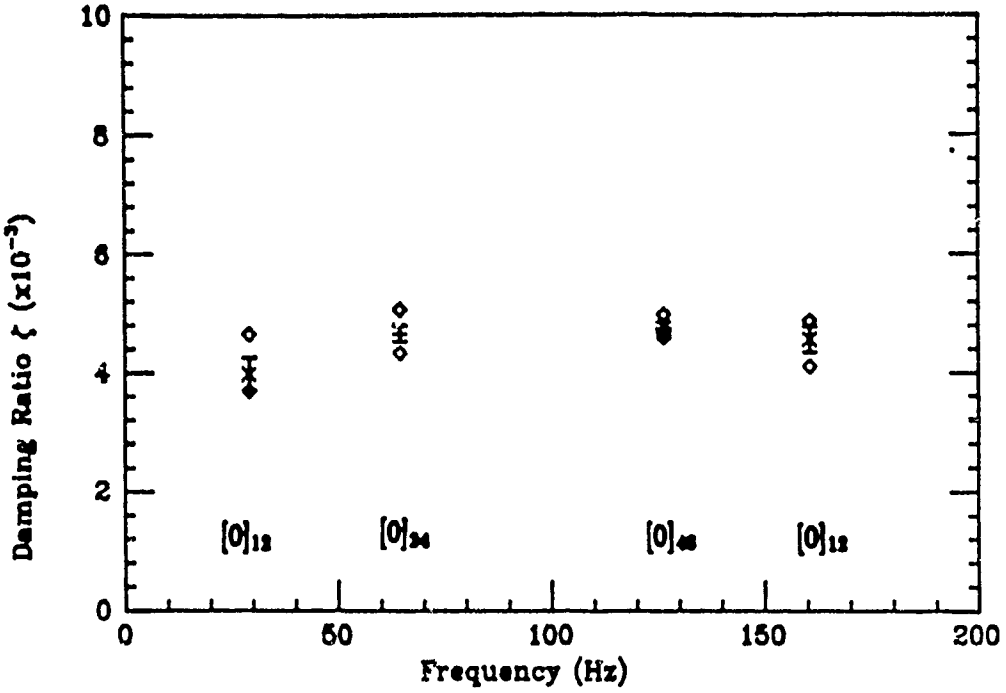


Figure 4. Damping of unidirectional Kevlar/Epoxy beams as a function of frequency[7].

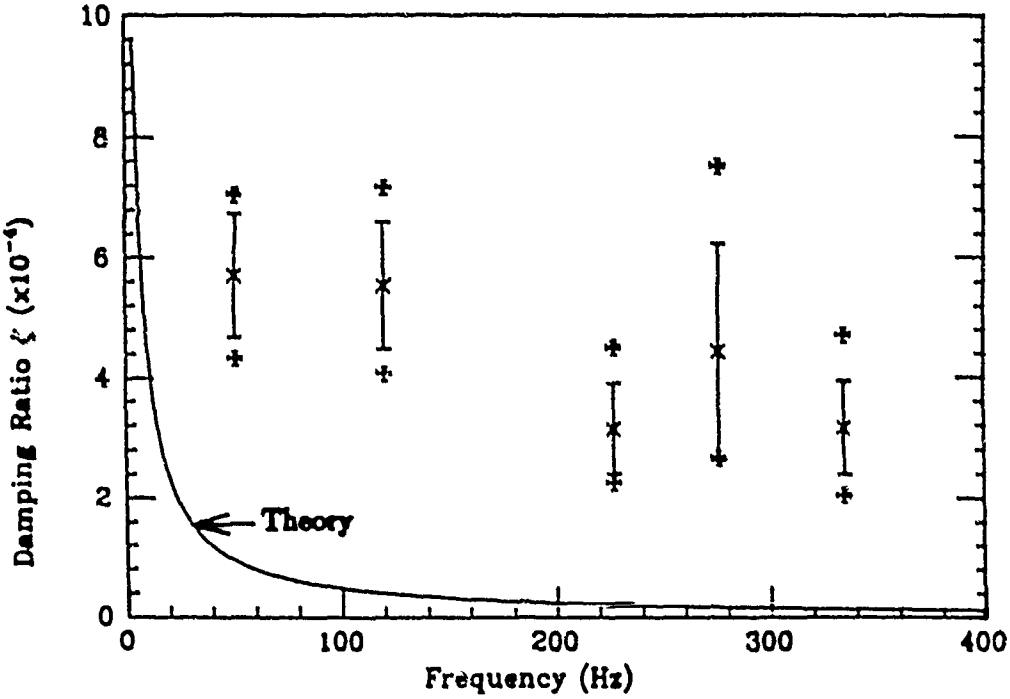


Figure 5. Damping ratio vs. frequency for 5 Bay Planar Truss under in-plane vibration[7] (the solid line is the theoretical thermoelastic damping based on the thickness of the spanwise members).

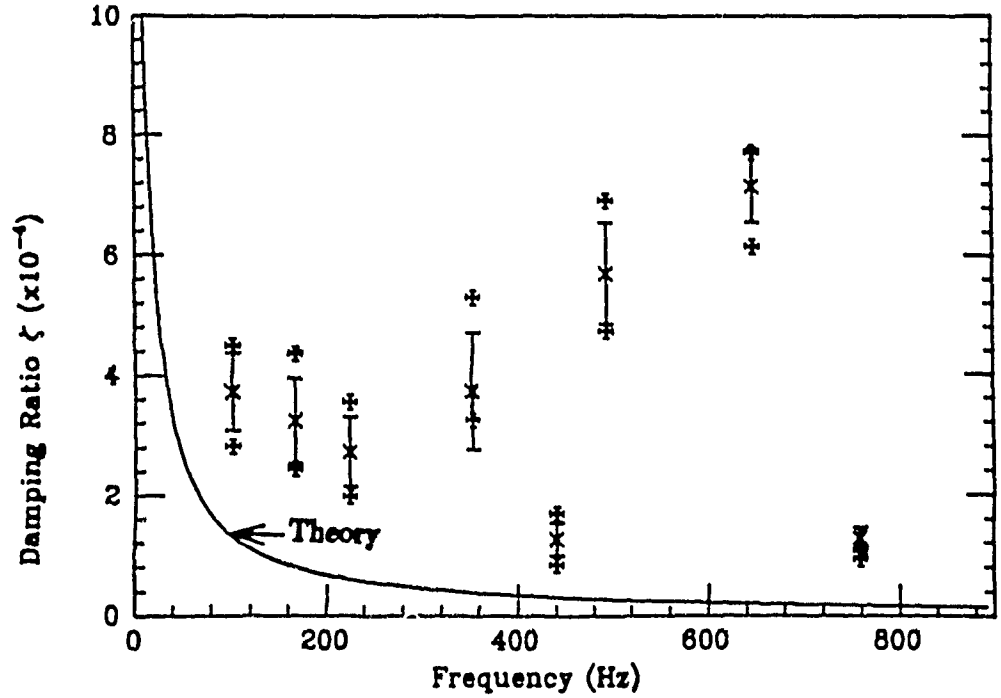


Figure 6. Damping ratio vs. frequency for 22 Bay Planar Truss under in-plane vibration[7].

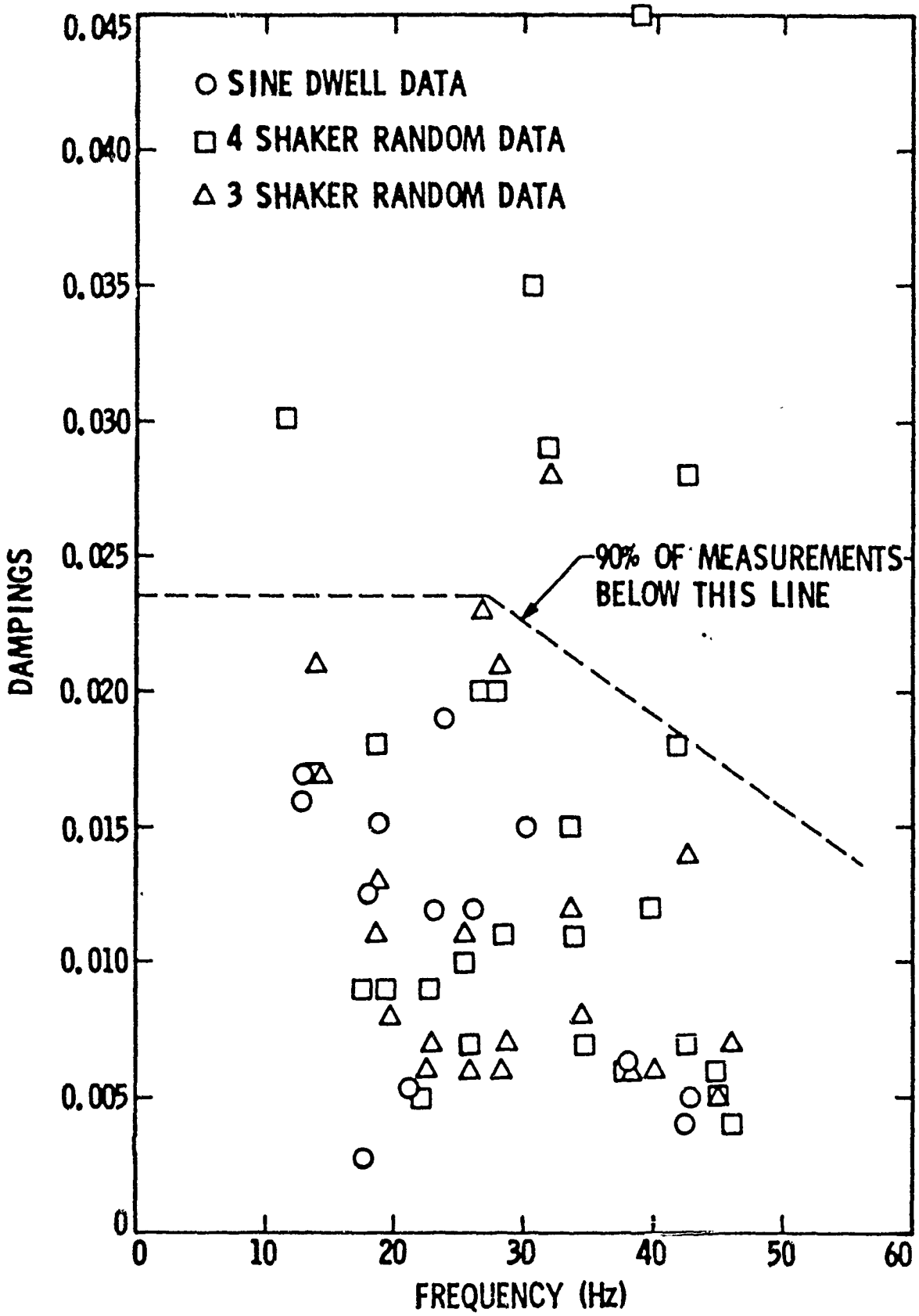


Figure 7. Measured damping ratios for the Galileo spacecraft[16].

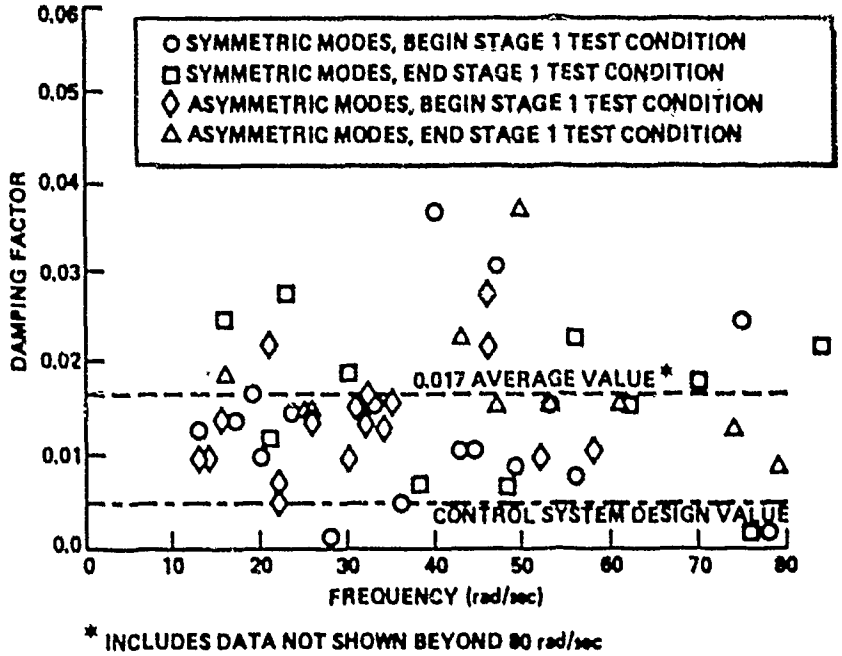


Figure 8. Damping ratios measured during Orbiter/ET/SRB mated vehicle vibration tests[17].

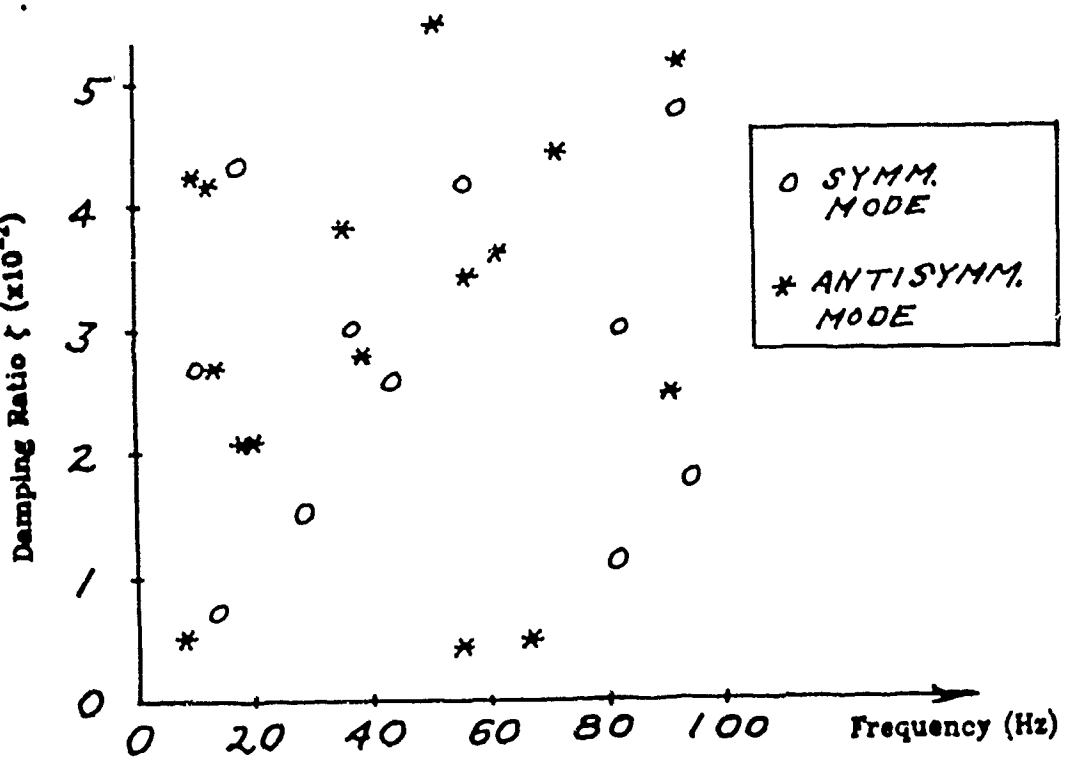


Figure 9. Damping ratio plotted vs. frequency from German tests on F-104G reported by Küssner[19].

Table 1
Typical Specimens (tested by Edberg[7])

Type	# Plies	L (in)	W (in)	t (in)
2024-T3 Beam	--	30.9	1.867	.0924
2024-T3 Beam	--	23.9	1.865	.1222
2024-T3 Plate	--	23.9	16.0	.090
Fiberglass/Epoxy Beam	6	25.1	1.728	.075
Fiberglass/Epoxy Beam	12	24.9	1.939	.148
Fiberglass/Epoxy Beam	24	24.8	1.942	.296
Graphite/Epoxy Beam	10	25.0	2.007	.073
Graphite/Epoxy Beam	20	24.9	1.729	.161
Graphite/Epoxy Beam	40	24.9	1.230	.277
Graphite/Epoxy Plate	20	23.9	16.0	.036
Kevlar/Epoxy Beam	12	25.0	1.750	.072
Kevlar/Epoxy Beam	24	24.95	1.747	.148
Kevlar/Epoxy Beam	48	25.0	1.257	.290
Kevlar/Epoxy Plate	24	23.9	24.0	.090
Aluminum Truss	22 bay	54.3	2.61	.375
Aluminum Truss	5 bay	49.5	10.10	.375

Table 2
Critical Damping Ratios of Plates[7]

Material	ζ	$\zeta_{plate}/\zeta_{beam}$
2024-T3 Aluminum	3.56×10^{-3}	3.95
Graphite/Epoxy (0-90°)	5.03×10^{-3}	9.3
Kevlar/Epoxy (0-90°)	7.32×10^{-3}	1.69

Table 3

Measurements On Orbit

System	Source	f (Hz)	ς
OAST-1 (SAFE) on STS 41-D	Brumfield et al[11]	0.037 Higher Modes	$\sim 3.3\times 10^{-2}$ N/A (Nonlin.)
HERMES	Lips & Vigneron[13]	0.13 0.15 0.30 0.44 0.50 0.82	$8.0 - 9.0\times10^{-2}$ 3.0 - 3.8 3.0 - 3.9 1.5 - 2.2 0.7 - 0.8 1.2 - 1.6

Table 4

WTS-4 Wind Turbine[18] (D = 256 ft)

Mode	f (Hz)	ς
Blade Flatwise (S1)	1.0	3.9×10^{-2}
Blade Flatwise (A1)	1.4	1.9
Blade Flatwise (S2)	2.4	3.2
Blade Flatwise (A2)	3.6	3.5
Tower 2nd Longitudinal	1.9	1.2
Tower 2nd Lateral	2.1	2.8

Table 5

DO-24TT Amphibian Wing Vibration Data[20]

Mode	f (Hz)	ζ
1st Bending	6.104	0.82×10^{-2}
2nd Bending	9.090	1.64×10^{-2}
1st Torsion	15.46	2.05×10^{-2}

Table 6

LSS/GTV (45 ft Suspended Truss)[21]

Mode	Without Cruciform		With Cruciform	
	f (Hz)	ζ	f (Hz)	ζ
1st Bending (x)	0.144	0.35×10^{-2}	N/A	N/A
2nd Bending (x)	1.33	1.33	1.36	1.9×10^{-3}
2nd Bending (y)	1.83	1.38	1.83	1.9
3rd Bending (x)	3.38	1.76	3.24	1.7
3rd Bending (y)	3.90	2.20	3.74	2.0
4th Bending (x)	8.06	2.90	6.36	1.1
4th Bending (y)	8.13	4.50	6.67	1.85
1st Torsion	0.991	0.44	0.377	0.56
2nd Torsion	9.6	1.1	3.02	0.34

INVESTIGATION OF PASSIVE DAMPING OF LARGE SPACE TRUSS STRUCTURES

by

Dr. John M. Hedgepeth
Dr. Mehran Mobrem
Astro Aerospace Corporation
Carpinteria, California

ABSTRACT

The purpose of this paper is to investigate several passive damping design concepts for large space truss structures. The concepts include damping in both the truss members and joints of space truss structures. The effect of local vibration of the individual truss members on the overall space truss response has been investigated. It has been concluded that the local vibration acts as a source of added damping for the overall response. The efficiency of segmented constrained viscoelastic layers on truss members and the effects of tuned dampers are also studied.

INVESTIGATION OF PASSIVE DAMPING OF LARGE SPACE TRUSS STRUCTURES

CATEGORY: PASSIVE DAMPING CONCEPTS

by

Dr. John M. Hedgepeth

Dr. Mehran Mobrem

INTRODUCTION

The augmentation of passive damping in large space structures is an attractive approach to improving the dynamic behavior of such structures. Some of the envisioned missions involve combinations of large size, high precision, and rapid slewing that will demand orders of magnitude better performance than available today. Managing these demands without a structural damping (g) of one percent or greater will severely complicate the problems of active control of these structures.

Not only must the damping be appreciable, but also it must be linear and operative for small structural distortions involving microinch/inch strain levels. Therefore, such seemingly attractive approaches as impact absorbers and nonlinear joints are not available for the solution of the damping problem. Furthermore, the allowable distortions are so small that adding flexible, highly-damped links in the structural load path (a favored approach in the past) is unacceptable.

The present study deals with damping augmentation approaches which do not add structural flexibility and which do not depend on large strains or

nonlinearity for their effectiveness. The type of structure considered is the open truss structure consisting of slender tubular struts of metal or composite, attached with high stiffness, linear joints located at the truss nodes. The interfaces to payloads, propulsion units, and other parts of the spacecraft are assumed to be at the joints. The primary deformation of the struts is therefore axial straining; any local bending would have little effect on the distortions of the nodal points.

The first approach discussed involves the use of segmented constraint layers to produce efficient shear straining of a high-damping elastomeric layer on the struts. The next is to add tuned vibration dampers at the nodes. Finally, the use of the lateral vibration of the struts themselves as the tuned dampers is evaluated.

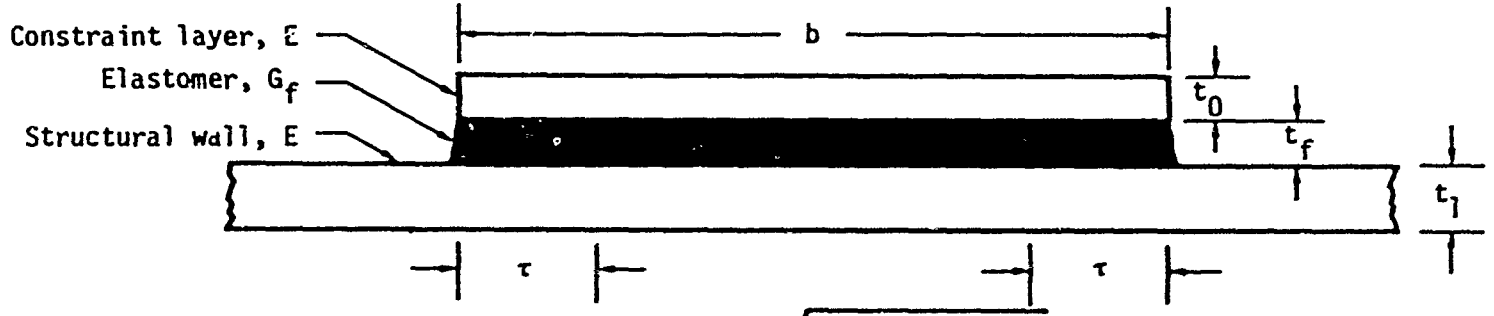
SEGMENTED CONSTRAINT LAYERS

High-damping materials tend to exhibit relatively low stiffness. The constraint layer approach has been used for some time to introduce shear strains into a trapped elastomeric layer. By making the elastomeric layer thin, the strains and, hence, the damping stresses, can be magnified. This technique was applied first to the damping of acoustic vibration in panels. The mismatch in strain between the panel and constraint layer that occurs with sonic waves can be duplicated for the uniformly stressed strut by segmenting the constraint layer.

Consider the segment shown in Figure 1. Let the lengthwise coordinate x be measured from the center of the segment. Let u_0 and u_1 be the lengthwise displacements of the constraint layer and the structural wall, respectively. The shear strain in the elastomer is

$$\gamma = \frac{u_0 - u_1}{t_f} \tag{1}$$

See Figure 1 for the definition of dimensions.



$$\text{Boundary layer thickness, } \tau = \sqrt{\frac{E_0 t_0 t_f}{G_f} \frac{1}{1 + \frac{E_0 t_0}{E_1 t_1}}}$$

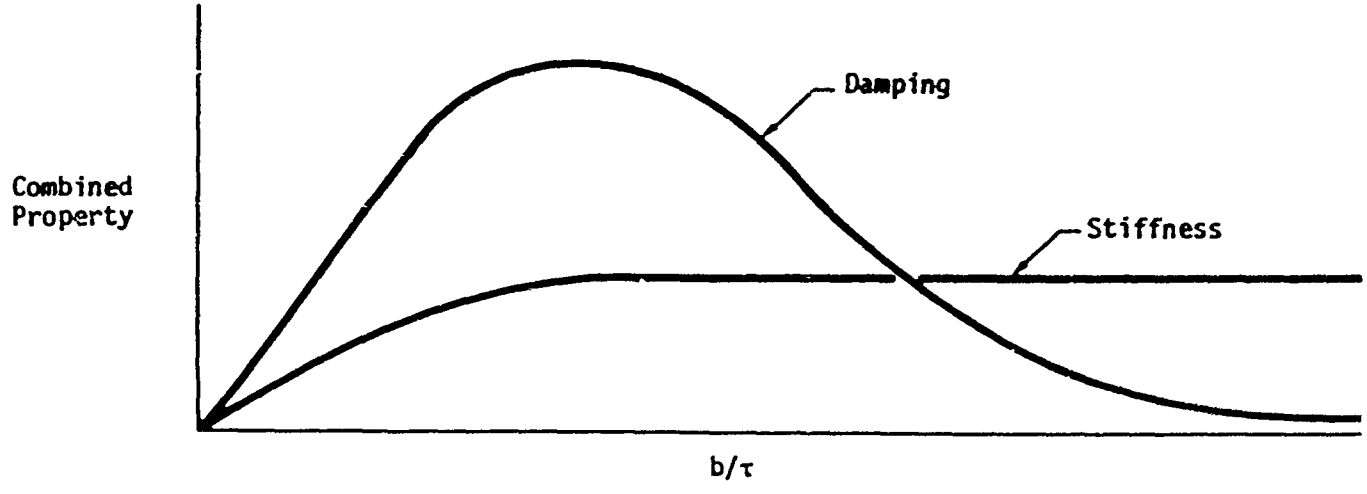


Figure 1. Damping augmentation with constrained high damping elastomer.

The equilibrium equations of the constraint and structural layers are

$$\left.\begin{aligned} Et_0 \frac{d^2 u_0}{dx^2} &= G_f \gamma \\ Et_1 \frac{d^2 u_1}{dx^2} &= -G_f \gamma \end{aligned}\right\} \tag{2}$$

where Et_0 and Et_1 are the extensional stiffness of the outer layers and G_f is the complex shear modulus of the elastomer.

Assume the structural wall is loaded cyclically with an amplitude at $x = \pm b/2$ of $\pm \varepsilon_1 b/2$ so that the average lengthwise strain is ε_1. The solution resulting is

$$u_1 = \varepsilon_1 \frac{x + \frac{Et_0}{Et_1} \tau \frac{\sinh\left(\frac{x}{\tau}\right)}{\cosh\left(\frac{b}{2\tau}\right)}}{1 + \frac{Et_0}{Et_1} \frac{2\tau}{b} \tanh\left(\frac{b}{2\tau}\right)} \tag{3}$$

where the (complex) boundary layer width τ is given in Figure 1.

The combined stiffness of the constrained strut of length b is

$$\overline{Et} = Et_1 \frac{1 + \frac{Et_0}{Et_1}}{1 + \frac{Et_0}{Et_1} \frac{2\tau}{b} \tanh\left(\frac{b}{2\tau}\right)} \tag{4}$$

Note that the effective damping ratio and stiffness ratio are

$$\left.\begin{aligned} g_{eff} &= \frac{\mathrm{Im}\,\overline{Et}}{\mathrm{Re}\,\overline{Et}} \\ R &= \frac{\mathrm{Re}\,\overline{Et}}{Et_1} \end{aligned}\right\} \tag{5}$$

As is indicated in Figure 1, for small values of b, the values of g_{eff} and R approach zero and one, respectively. For large values of b, the value of g_{eff} again tends to zero, but the stiffness tends to the sum of the

stiffnesses of the strut and its constraint layer. For each set of properties, there is an optimum segment length for which g_{eff} is a maximum.

The results of calculating for optimum length segments are shown in Figure 2. Here the damping achieved with various thicknesses of the constraint layer is shown. It is seen that significant damping can be obtained (three percent, for example) with only moderate increases in weight (ten percent). Also shown are results obtained when only 20 percent of the length of the strut is treated. Note that the more effective method is to treat the entire length of strut.

This approach shows great promise and should be investigated further. One potential problem is the need to avoid wide variations in elastomer properties in service so that the boundary layer width does not stray too far away from its design value. Perhaps the breadth of performance could be increased by using different segment lengths in different portions of the truss.

An experimental verification of this approach has been performed by S. S. Sattinger. This careful work is reported in Reference 1, which was unknown to the authors before the Workshop.

TUNED DAMPERS

A well-used approach for vibration absorption is to use tuned dynamic dampers. Such dampers are efficient at their natural frequencies but are not very useful at other frequencies.

In order to evaluate the effect of such dampers on the response of truss stress to dynamic excitation, the idealized structure shown in Figure 3 was analyzed. This is a uniform beam on which tuned mass-spring oscillators are mounted. They are assumed to be so closely spaced as to be considered continuously distributed along the beam. The beam is simply supported a foundation that is vibrated vertically at a constant amplitude. Attention is directed to the amplitude response at the center of the beam.

Let y be the displacement of the beam and y_D that of the sprung masses. The governing equations are

$$(1 + ig)\, EI\, y^{iv} + (1 + ig_D)\, k\, (y - y_D) + m\ddot{y} = 0 \qquad (6)$$

$$m_D \ddot{y}_D + (1 + ig_D)\, k\, (y_D - y) = 0$$

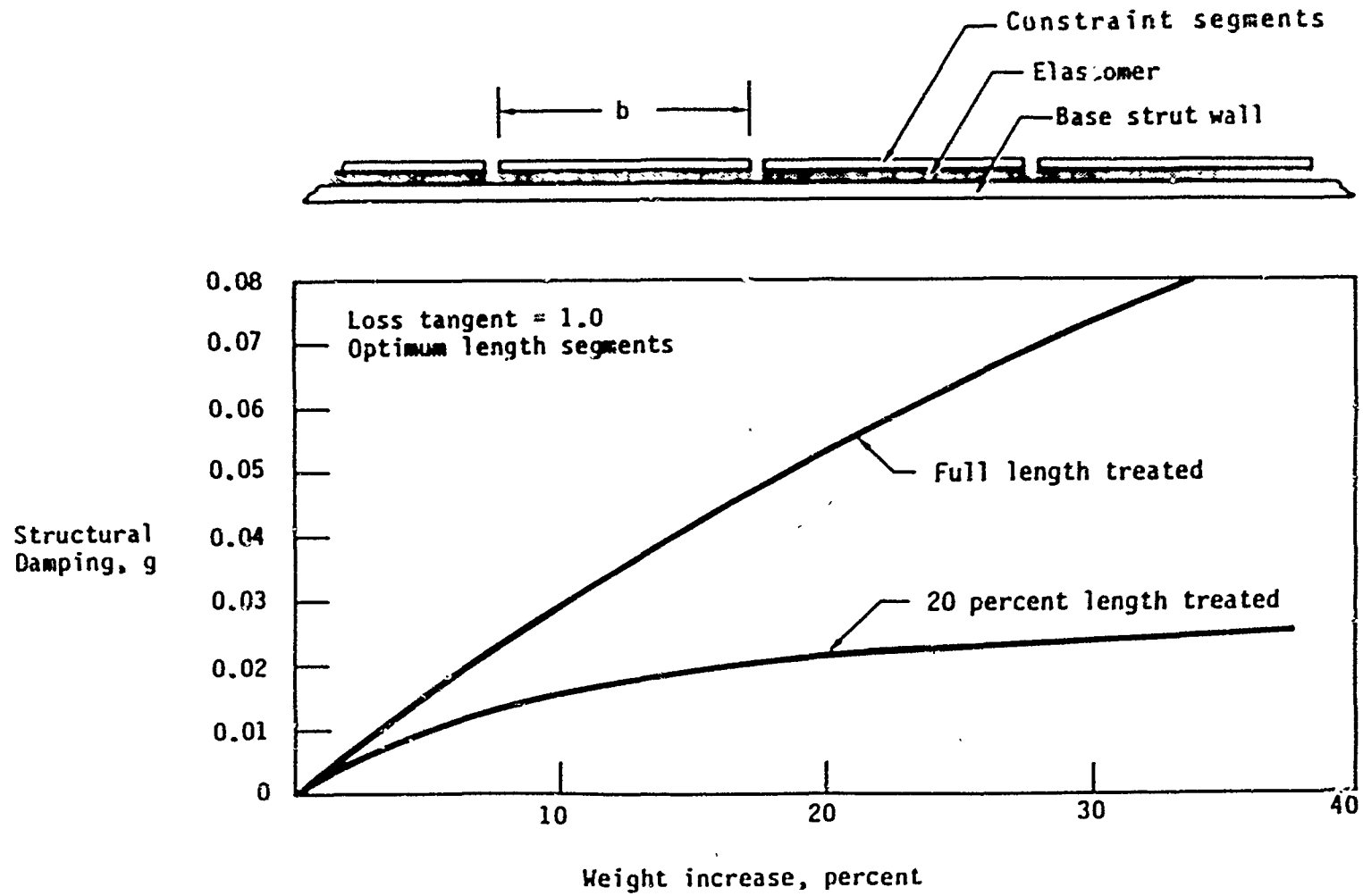


Figure 2. Segmented-constraint-layer damping results.

where EI and k are the beam and spring stiffness, respectively, m and m_D are the mass per unit length of the beam and damper, respectively, and g and g_D are their (structural) damping coefficients.

The boundary conditions at x = 0 and x = L, where L is the length, are

$$y = y_0 \cos \omega t \tag{7}$$

$$y'' = 0$$

where y_0 is the foundation displacement amplitude.

The solution of these equations for the beam displacement is

$$\frac{y}{y_0} = \frac{\sinh \lambda\left(1 - \frac{x}{L}\right) + \sinh \lambda \frac{x}{L}}{2 \sinh \lambda} + \frac{\sin \lambda \left(1 - \frac{x}{L}\right) + \sin \frac{\lambda x}{L}}{2 \sin \lambda} \tag{8}$$

where

$$\lambda^4 = \pi^4 \frac{\omega^2}{(1 + ig)\,\omega_1^2} \left[\frac{1 + \frac{m_D}{m}}{1 + \frac{\omega^2}{(1 + ig_D)\,\omega_D^2}}\right] \tag{9}$$

in which

$$\omega_1 = \pi^2 \sqrt{\frac{EI}{mL^4}} \tag{10}$$

is the first natural frequency of the base beam and

$$\omega_D = \sqrt{\frac{k}{m_D}} \tag{11}$$

is the frequency of the damper.

The vibration response factor at the center of the beam is

$$\frac{y_c}{y_0} = \frac{1}{2}\left(\frac{1}{\cosh\frac{\lambda}{2}} + \frac{1}{\cos\frac{\lambda}{2}}\right) \tag{12}$$

Extensive calculations were made for the response factor for varying values of forcing frequency, natural frequencies and damping. The computer program used for this calculation (written in C language) is given in the Appendix. As could be expected, the peak responses obtained as the forcing frequency was varied occurred at the coupled natural frequencies for which the undamped values of λ were odd integral multiples of π. See Equation (9). The resulting peak values are shown in Figure 3 for a damping ratio of 0.01 (for both the beam and the damper) and a mass ratio of 0.1.

The curves show the responses of two modal branches for each odd integer value of n, coalescing at the natural frequency and then trading roles. The reduction in response is a factor of about two at the notch for each set of modal pairs. This amount of reduction is not very useful in practice.

The influence of change damper mass and damping ratio is shown in Figure 4. In this case, attention is concentrated on the first mode. It can be seen that increasing the mass of the damper broadens the range of effectiveness but does not improve the maximum reduction. On the other hand, increasing the damping factor of the vibration absorber to 0.1 has a strong beneficial effect, reducing the response by an order of magnitude (at optimum) for beam damping g of 0.01, and by two orders of magnitude for a g of 0.001.

Single-frequency vibration absorbers are not very useful for most space applications in which a large range of frequencies must be managed. One possible approach would be to use dampers of differing frequency at various points in the structure. Some attention is paid to such an approach in the next section.

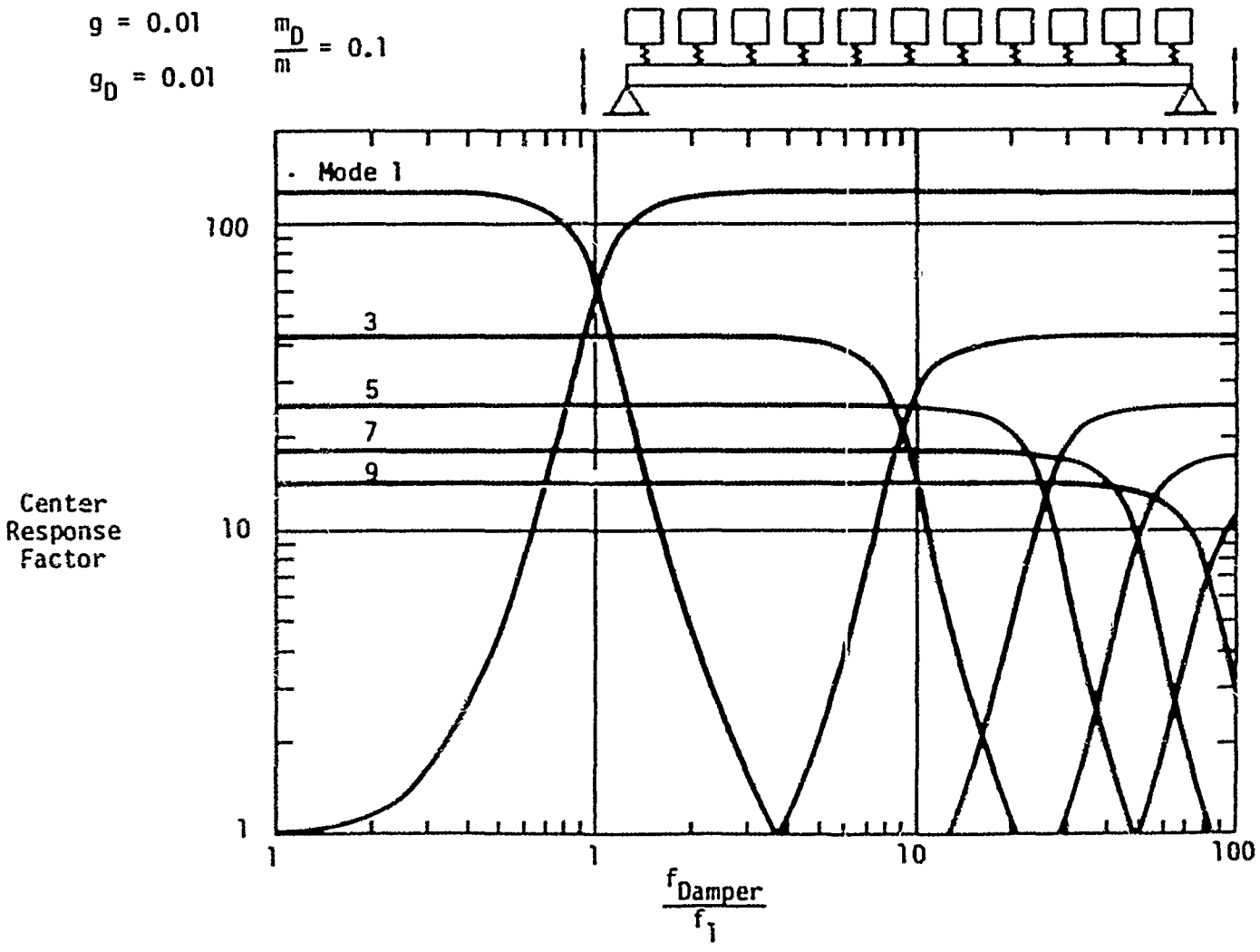


Figure 3. Peak frequency response factors with dynamic dampers.

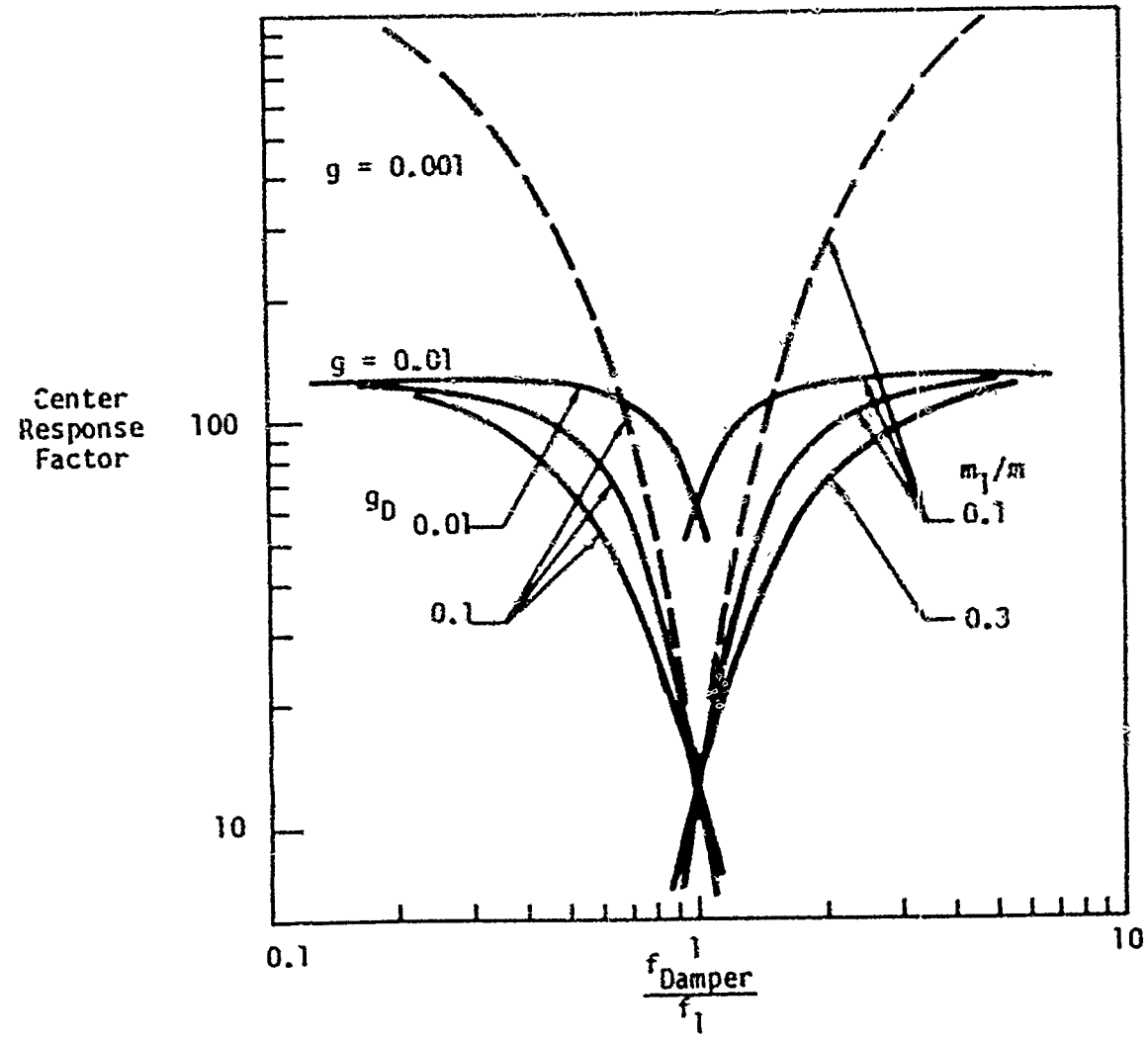


Figure 4. Effects on response factor, first mode.

Another approach would be to use multimode vibration dampers. Some insight into the effectiveness of this method is obtained by analyzing the idealized structure shown in Figure 5. Here the vibration dampers mounted to the simply supported beams are, themselves, simply supported beams. By appropriately tuning the fundamental frequency of the damper beams, effectiveness can be obtained over a wide range of frequencies.

The analysis of this structure follows the same approach as the previous one. It is necessary only to replace the definition of λ, Equation (9), by

$$\lambda^4 = \pi^4 \frac{\omega^2}{(1 + ig)\,\omega_1^2} \left[1 + \frac{m_D/m}{\lambda_D} \left(\tan \frac{\lambda_D}{2} + \tanh \frac{\lambda_D}{2}\right)\right] \tag{13}$$

where

$$\lambda_D^4 = \frac{\pi^4 \omega^2}{(1 + ig_D)\,\omega_D^2} \tag{14}$$

and ω_D is now the fundamental natural frequency of the damper beams.

Results calculated with the computer program DAMPCON.C given in the Appendix are shown in Figure 5. Since a closed-form solution for the resonant frequencies was not available, it was necessary to perform extensive frequency sweeps. The curve shows the response of the base beam with $g = 0.01$. The symbols show the peak responses for a particular design in which $m_D/m = 0.1$ and $f_D/f_1 = 1.05$. Results are given for $g_D = 0.01$ and 0.1.

The effectiveness of the multimode follows the same trends as obtained with the single-mode damper except that all the modes are benefited. Here again, the results for $g_D = 0.01$ are not very good, but increasing the damping of the absorbers to 0.1 yields major reductions.

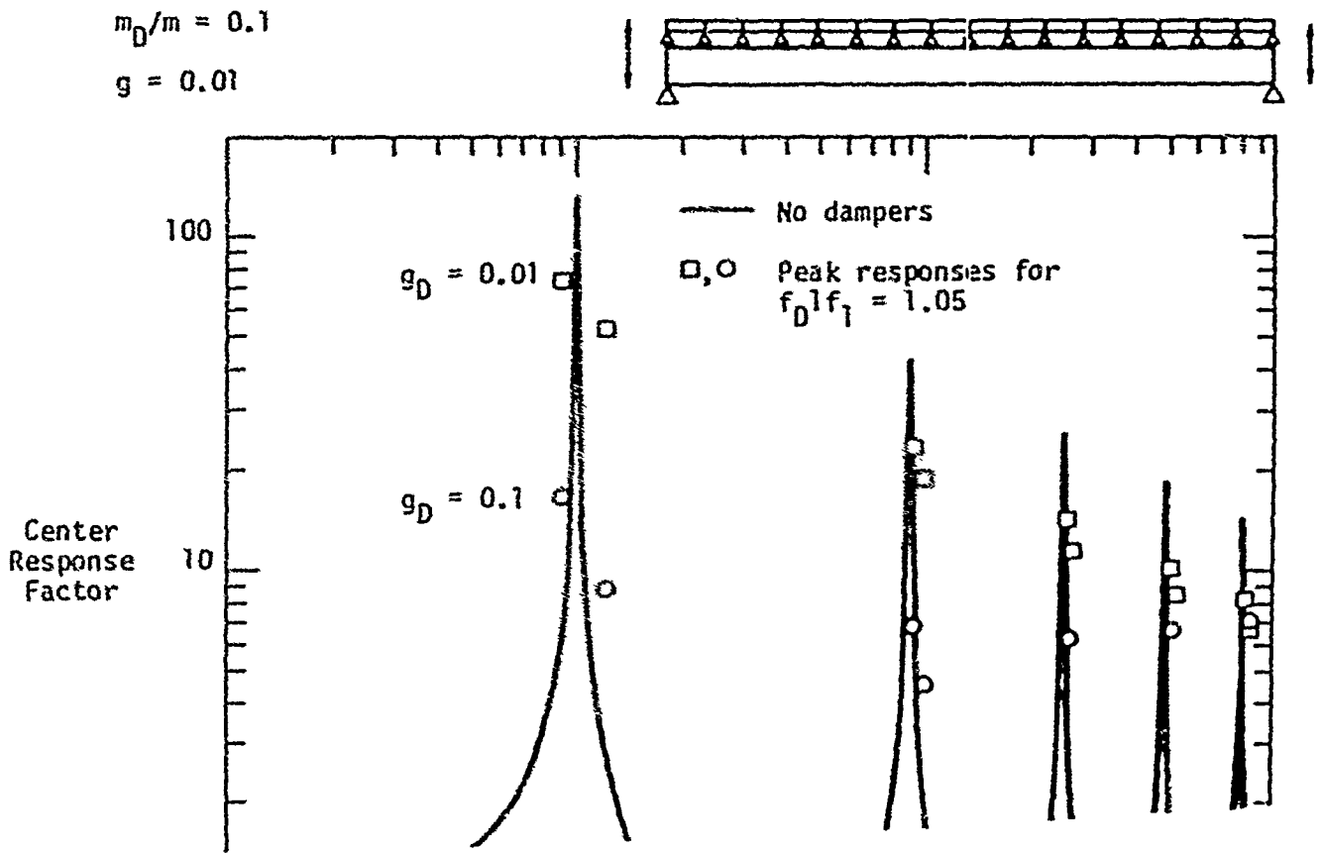


Figure 5. Frequency response with beam dampers.

DAMPING CAUSED BY LOCAL STRUT VIBRATION

The effect of local vibration of the individual struts on the overall truss structure response is analyzed by a finite element method using COSMOS7 software.

The energy needed to excite the local bending vibrations of the struts results in the reduction of applied energy to excite the primary mode of the truss structure. The reduction in the applied energy is more effective when the applied load frequency is in the vicinity of struts' local bending natural frequencies.

The cantilever planar truss structure presented in Figure 6 has been selected for the analysis.

It is customary to model the struts of a truss structure by "truss elements" in which only axial deformations are considered. The use of such truss elements results in an error in the dynamic response of the truss structure since the local bending response of struts is neglected. The error is small if the local strut bending frequency is much higher than that of the truss structure. As the overall natural frequency approaches the local natural frequency, the error increases.

A more accurate modeling is achieved by the use of beam elements which are capable of bending, as well as axial, deformation. For the present analysis, additional nodes were place at the center of the struts. Also, a standard beam element of the COSMOS7 library with the lumped mass option was selected for the analysis.

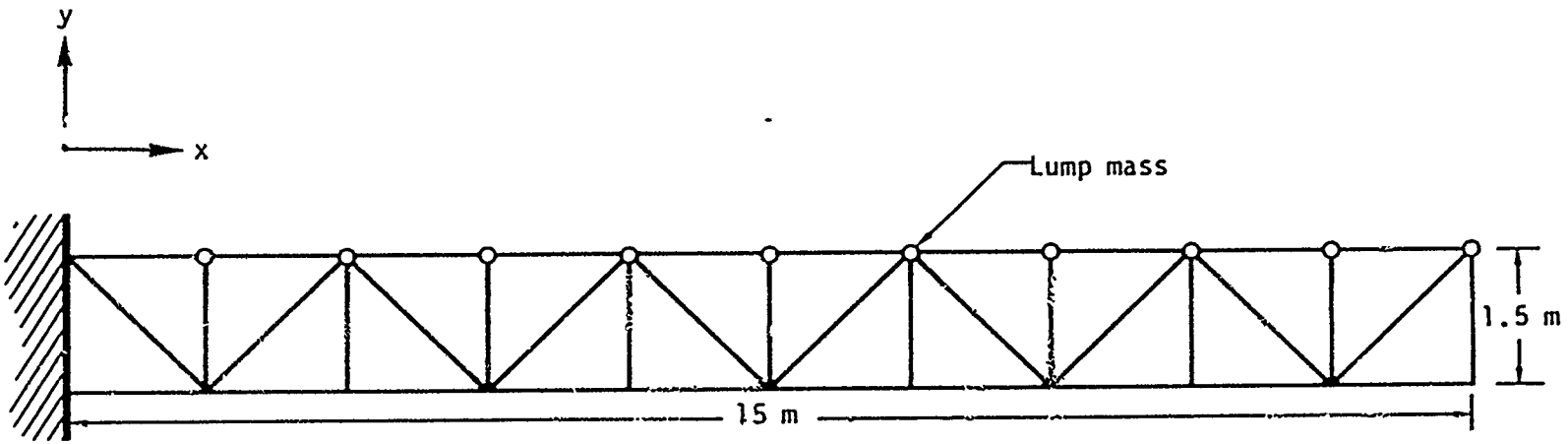
The response $q_n(t)$ of the truss structure at structural node n is

$$q_n(t) = \sum_{r=1}^{m} \phi_r \eta_r(t) \tag{15}$$

where

$$\eta_r(t) = \frac{\phi_r^T F(t)}{\omega_r^2 \left[1 - \left(\frac{\omega}{\omega_r}\right)^2 + ig\right]} \tag{16}$$

$F(t)$ is the applied load; ω_r is the rth natural frequency; ϕ is the rth



a sin ωt

Strut EA = 2.995×10^6 N

Strut uniform mass, m = 0.042 kg/m

Strut structural damping, g = 0.01

Lump mass = 10 kg each

Strut EI = 13,800 Nm^2 or 39.7 Nm^2

DB-15

Figure 6. Truss beam model.

mode shape; g is the structural damping, and m is the number of vibrational modes used in the analysis.

In the case of modal damping, ζ_r, Equation (16) is changed to

$$\eta_r(t) = \frac{\phi_r^T F(t)}{\omega_r^2 \left[1 - \left(\frac{\omega}{\omega_r}\right)^2 + i2\zeta_r \frac{\omega}{\omega_r}\right]} \tag{17}$$

The frequency response of the truss structure at its free end has been computed, subject to a harmonic base excitation, for two different cases. In one case, the bending stiffness EI of struts is purposely increased by 2.5 orders of magnitude, which results in a truss structure with struts exhibiting axial deformation only. For the other case, the actual bending stiffness of struts is used.

In the analysis, the modal damping of $\zeta_r = 0.005$, which corresponds to the structural damping of $g = 0.01$ in the vicinity of natural frequencies, has been used

Presented in Figure 7 is the truss structure tip response factor in the y-direction for the frequency range of zero to 48 Hz. There are eight primary modes corresponding to the structure with stiff struts. For the structure with flexible struts, the number of modes increase to 40 in the above frequency range. The primary mode shapes and some of the local modes are presented in Figures 8 to 18.

The local strut vibration mode has reduced the tip structure response by 26 percent, and 48 percent corresponding to sixth and seventh modes, respectively. The response corresponding to the eighth primary mode is no longer present.

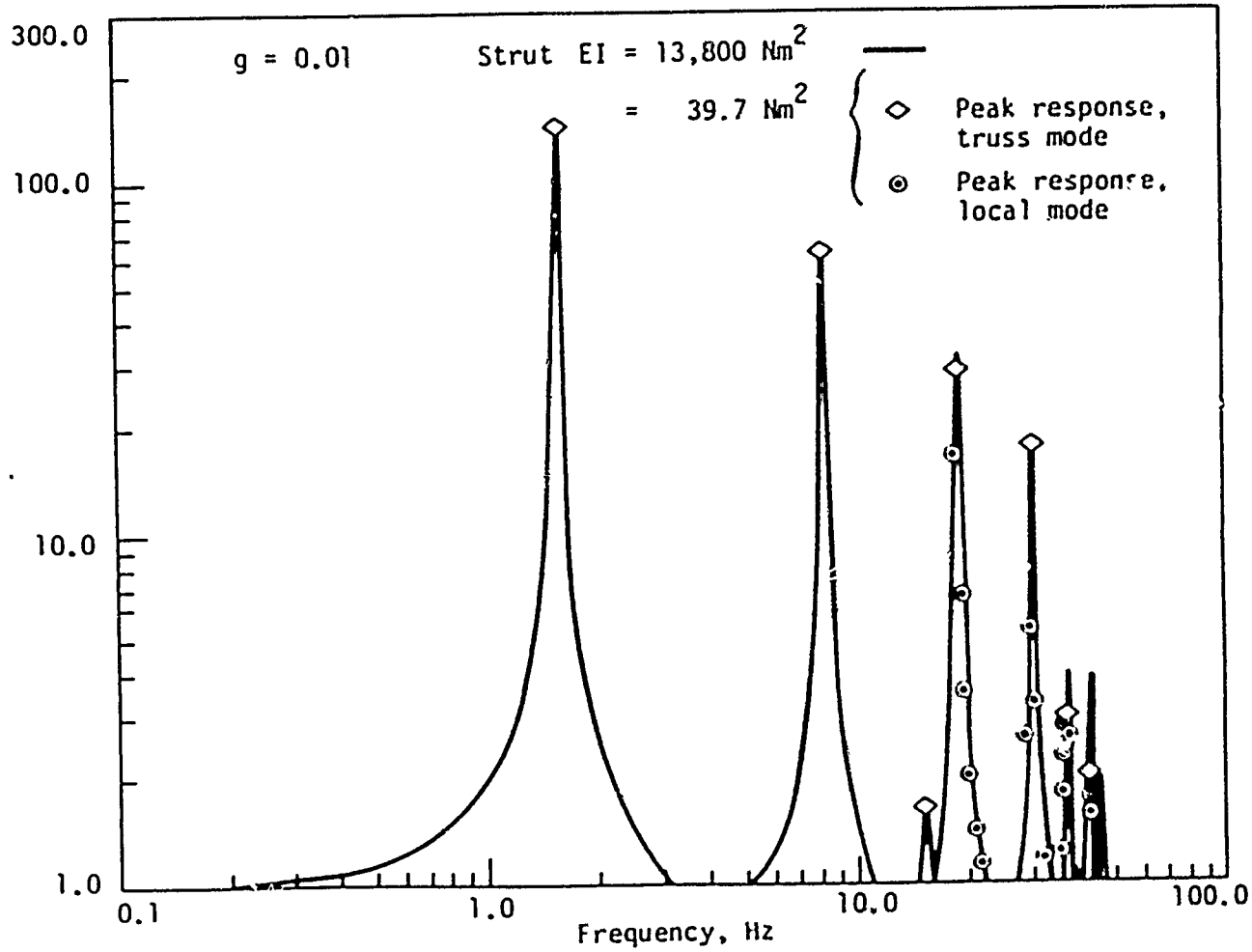


Figure 7. Frequency response of truss beam.

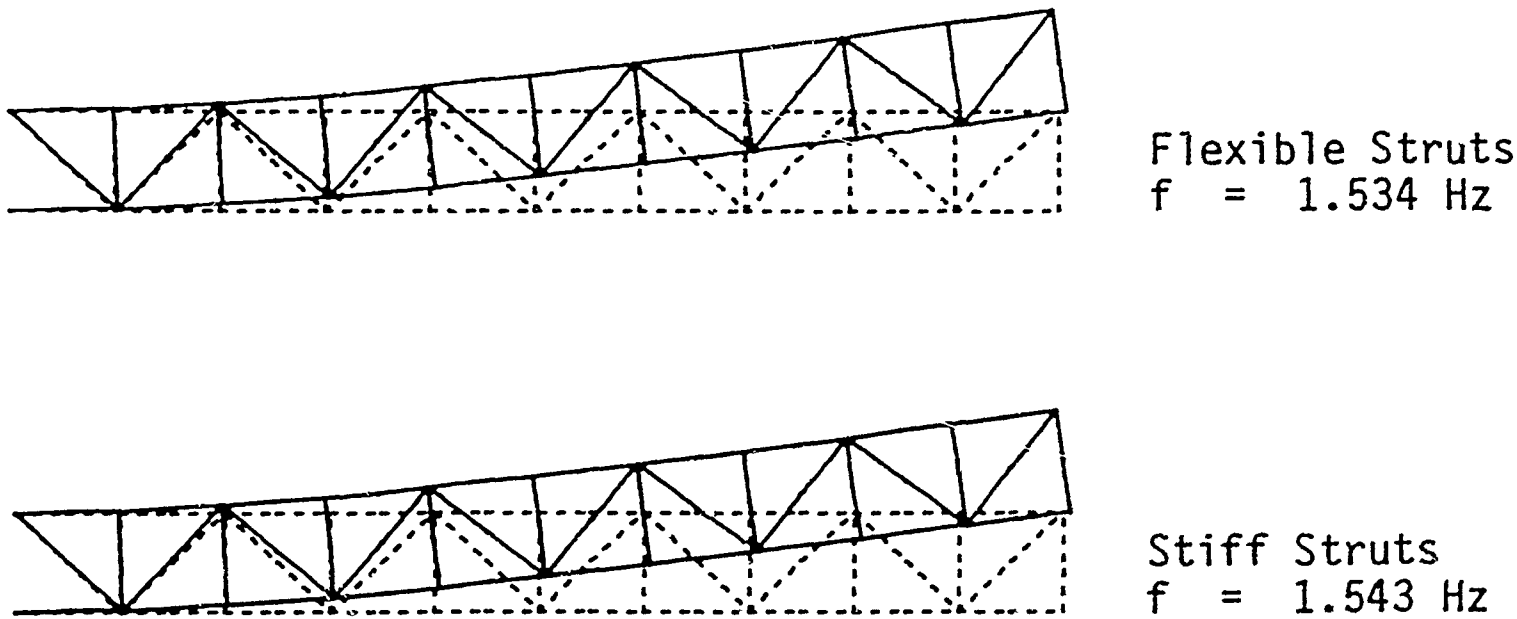


Figure 8. Truss beam mode shapes, 1st truss mode.

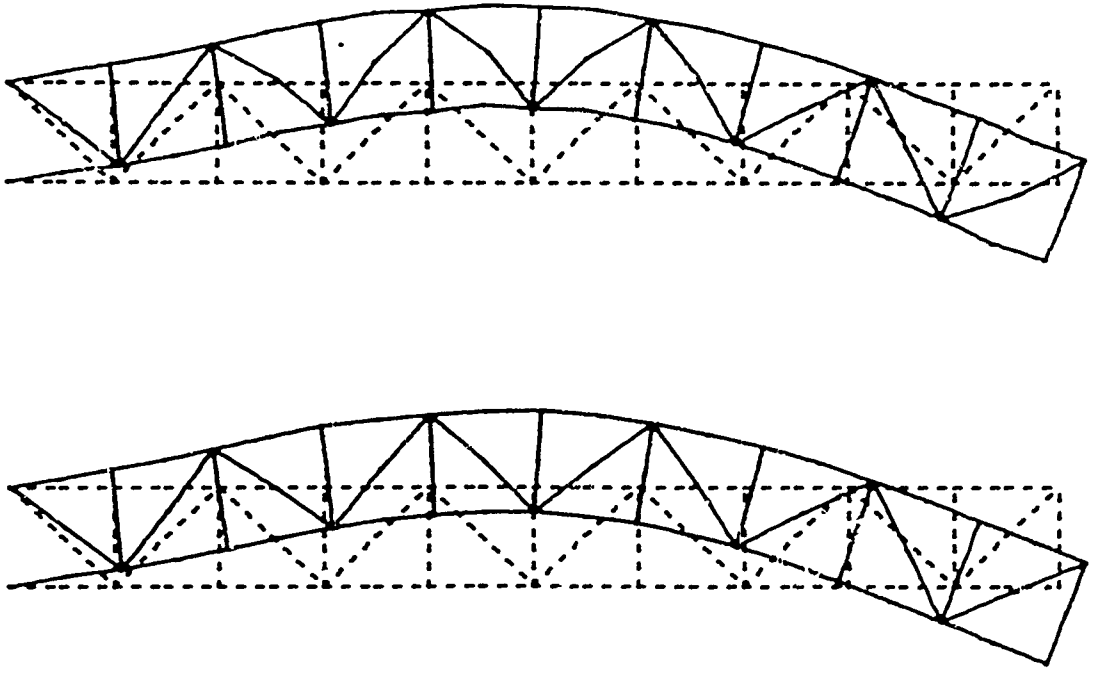
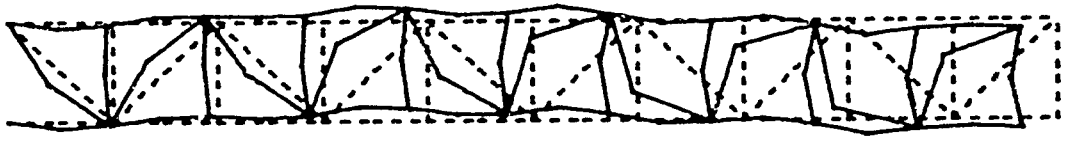
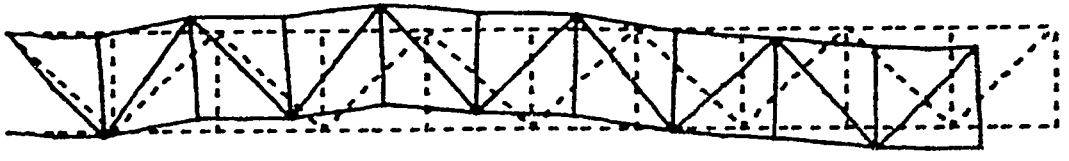


Figure 9. Truss beam mode shapes, 2nd truss mode.

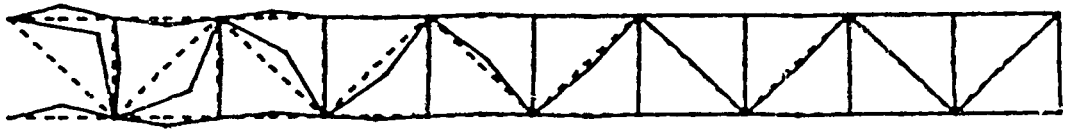


Flexible Struts
f = 14.83 Hz



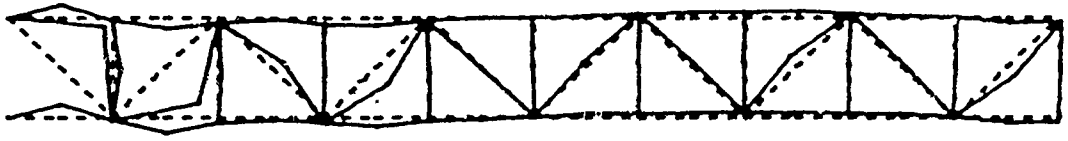
Stiff Struts
f = 15.06 Hz

Figure 10. Truss beam mode shapes,
3rd truss mode.

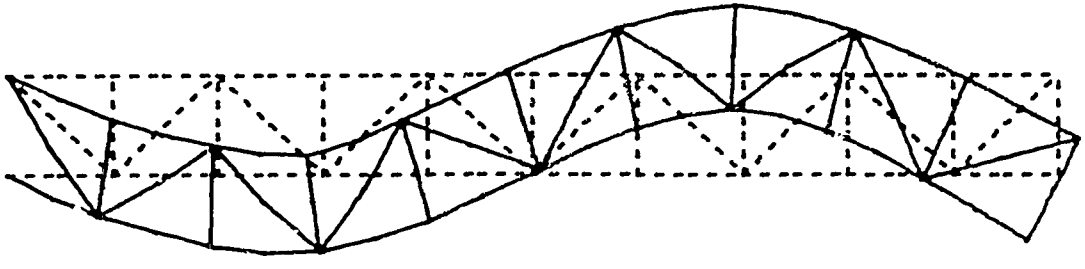


Flexible Struts
f = 18.22 Hz

Figure 11. Truss beam mode shape, local mode.



Flexible Struts
f = 18.37 Hz



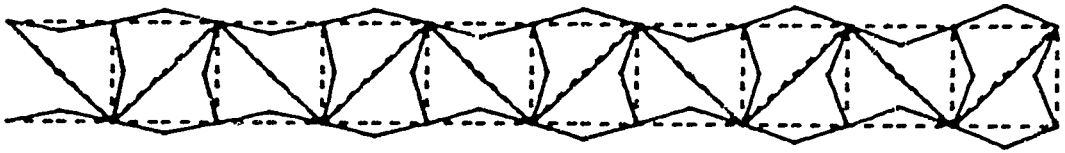
Stiff Struts
f = 18.71 Hz

Figure 12. Truss beam mode shapes, 4th truss mode.



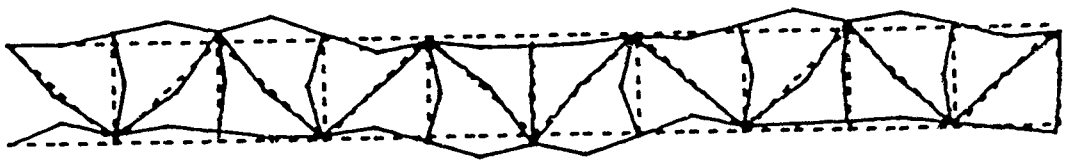
Flexible Struts
f = 23.79 Hz

Figure 13. Truss beam mode shape, local mode.

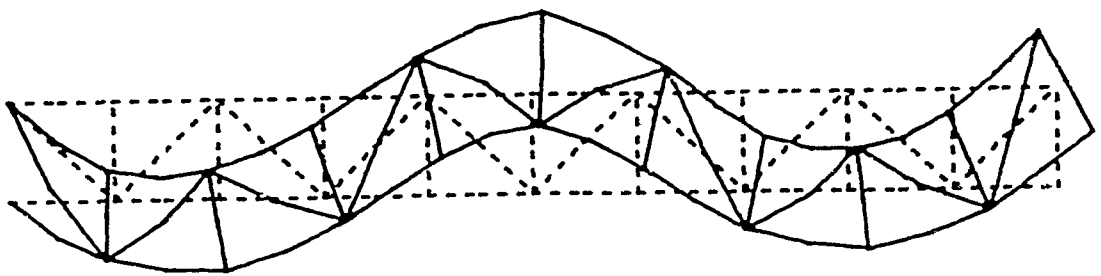


Flexible Struts
f = 28.15 Hz

Figure 14. Truss beam mode shape, local mode.

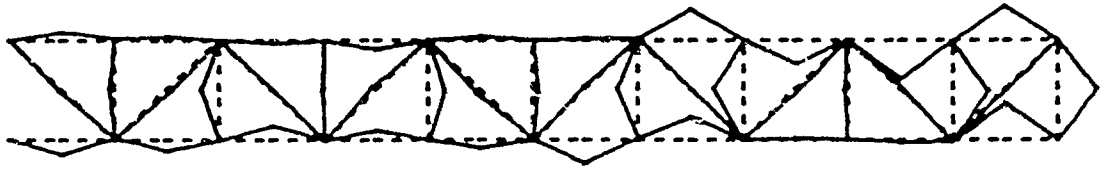


Flexible Struts
f = 29.16 Hz

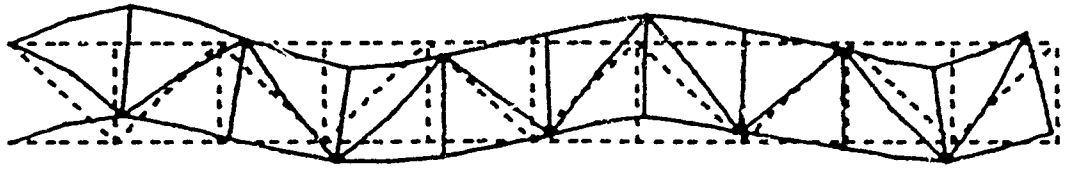


Stiff Struts
f = 29.94 Hz

Figure 15. Truss beam mode shapes, 5th truss mode.

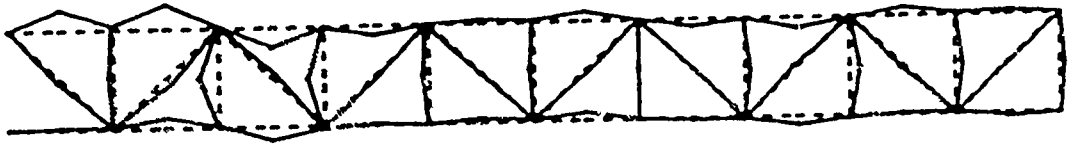


Flexible Struts
f = 36.2 Hz

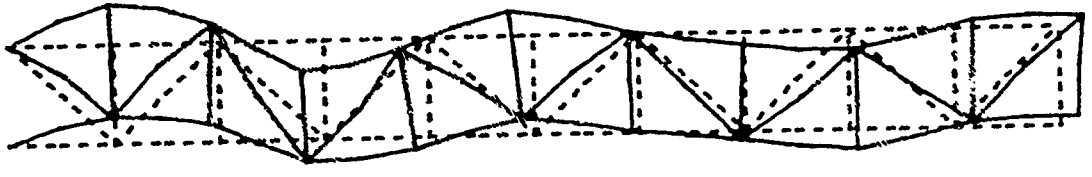


Stiff Struts
f = 37.07 Hz

Figure 16. Truss beam mode shapes,
6th truss mode.

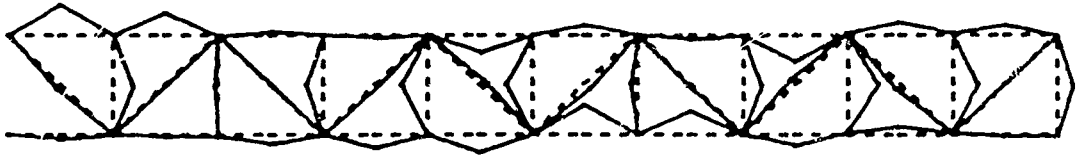


Flexible Struts
f = 41.02 Hz

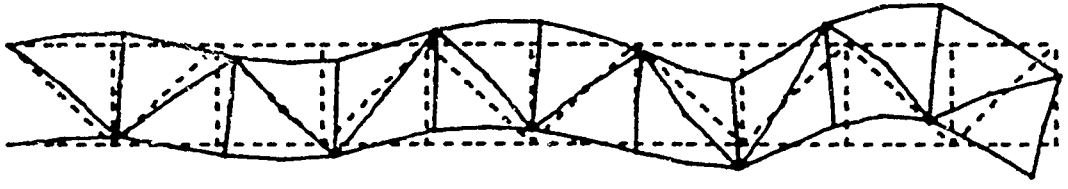


Stiff Struts
f = 42.79 Hz

Figure 17. Truss beam mode shapes, 7th truss mode.



Flexible Struts
f = 43.02 Hz



Stiff Struts
f = 44.5 Hz

Figure 18. Truss beam mode shapes,
8th truss mode.

CONCLUSIONS

The theoretical results obtained in this study indicate that:

- Passive damping can be augmented without reducing stiffness.
- Segmented constraint layers can yield 3% damping with 10% increased mass.
- Need high damping material with constant properties.
- External dampers most effective at their resonant frequency.
- Multi-resonant dampers would enable broad coverage.
- Local strut vibration modes can double the effective damping ratio of truss modes.

The work should be extended. In particular, "area" truss structures should be investigated.

REFERENCES

1. Sattinger, S. S. "Constrained-Layer Damping Effectiveness on Members Under Vibratory Extensional Loading," 27 November 1984, 84-IJ7-DAMPS-P1. Westinghouse R&D Center, Pittsburgh, Pennsylvania.

APPENDIX

```
/* DAMPBEAM.C - Calculate the dynamic response of a simply supported
                damped beam with dynamic dampers continuously distributed
                along its length.


            jmh 2/20/86     */
/*  Note:   void cxarth(x,y,z,n)
            double x[],y[],z[];
            int n;

            is a Wiley Scientific Subroutine Library Function which performs
            arithmetic operations on complex numbers each stored as a two
            element array.  The integer n specifies what operation to make
            on *x and *y to result in *z:
                n = 1   *z = *x + *y
                    2   *z = *x - *y
                    3   *z = *x times *y
                    4   *z = *x/*y
*/

#include "math.h"

double tanh(),cosh(),sinh();
main()
{
    double zeta[2],temp[2],den[2],num[2],g,g1,damp[2],quo[2],m,sign,b,c,nrat,
           damp1[2],omega,omega_s,omega_1,omega_u,eps,fourth,coeff,mag,phase;
    int i,j,n;
    char chr;

    m = 0.1;
    g = 0.01;
    g1 = 0.01;

    puts("\nDetermine Frequency Response for a damped ");
    puts("simply supported beam.  jmh 2/20/86\n");
  while() {
    chr = 0;
    while(chr != 'Y') {
        printf("\nParameters are: Mass ratio = %f, g = %f, g1 = %f\n",m,g,g1);
        printf("\nAre these OK? ");
        if((chr = toupper(getchar())) != 'Y') {
            printf("\nEnter new values separated by commas ?");
            scanf("%lf,%lf,%lf\n",&m,&g,&g1);
        }
    }

    damp[0] = 1.;
    damp[1] = g;

    damp1[0] = 1.;
    damp1[1] = g1;

    while(chr == 'Y') {
        printf("\n\nEnter values of omega_s and limits on omega ?");
        scanf("%lf,%lf,%lf\n",&omega_s,&omega_1,&omega_u);
        if(omega_s < 0)  break;

        eps = (omega_u - omega_1)/20;
```

```
        printf("\n\n\tFrequency\tResponse\tPhase\t\t omega_s = %f\n\n",omega_s);

        omega_s *= omega_s;

        for(i=0,sign=1; i<=20; i++) {
            omega = omega_1 + i*eps;
            omega *= omega;

            if(eps<=0) {
                sign *= -1;
                n = i/2;
                nrat = 2*n+1;
                nrat *= nrat;
                nrat *= nrat;
                b = (1.+m)*(omega_s + nrat)/2.;
                c = (1.+m)*omega_s*nrat;
                omega = b + sign*sqrt(b*b-c);
            }
            num[0] = omega/omega_s;
            num[1]=0;

            cxarth(num,damp1,temp,4);

            den[0] = 1 - temp[0];
            den[1] = -temp[1];
            temp[0] = 1.;
            temp[1] = 0;

            cxarth(temp,den,num,4);

            num[0] = pi*pi*pi*pi*omega/(1+m)/16.*(1. + m*num[0]);
            num[1] = pi*pi*pi*pi*omega/(1+m)/16.*m*num[1];

            cxarth(num,damp,temp,4);

            cxsqrt(temp,num);
            cxsqrt(num,temp);

            deflect(temp,zeta);

            mag = sqrt((zeta[0]*zeta[0] + zeta[1]*zeta[1]));
            phase = 180./pi*atan2(zeta[1],zeta[0]);

            printf("\t%f\t%f\t%f\n",sqrt(omega),mag,phase);
        }
        printf("Continue?");
        chr = toupper(getchar());
    }
}
}

cxsqrt(z,w)
double z[],w[];
{
    double r,thet;

    r = sqrt(sqrt(z[0]*z[0] + z[1]*z[1]));
    if(z[0] == 0) {
        if(z[1]  = 0) thet = pi/4.;
        else thet = -pi/4.;
```

```
        )
        else thet = 0.5*atan(z[1]/z[0]);

        w[0] = r*cos(thet);
        w[1] = r*sin(thet);
    )

    deflect(alfa,z)
    double alfa[],z[];
    {
        double x[2],y[2],temp[2];

        x[0] = 1.;
        x[1] = 0;

        cxcosh(alfa,y);
        cxarth(x,y,z,4);

        y[0] = - alfa[1];
        alfa[1] = alfa[0];
        alfa[0] = y[0];

        cxcosh(alfa,y);
        cxarth(x,y,temp,4);

        z[0] = (z[0] + temp[0])/2.;
        z[1] = (z[1] + temp[1])/2.;
    }


    double cosh(x)
    double x;
    {
        x = exp(x);
        return (x + 1./x)/2.;
    }

    double sinh(x)
    double x;
    {
        x = exp(x);
        return (x - 1./x)/2.;
    }

    double tanh(x)
    double x;
    {
        return sinh(x)/cosh(x);
    }

    cxcosh(z,w)
    double z[],w[];
    {
        w[0] = cosh(z[0])*cos(z[1]);
        w[1] = sinh(z[0])*sin(z[1]);
    }
```

```
/* DAMPCON.C - Calculate the dynamic response of a simply supported
               damped beam with simply supported damper beams continuously
               distributed along its length.

            jmh 2/26/86     */
#include "math.h"
double tanh(),cosh(),sinh();
main()
{
    double zeta[2],temp[2],den[2],num[2],g,g1,damp[2],quo[2],m,sign,b,c,nrat,
           damp1[2],omega,omega_s,omega_1,omega_u,eps,fourth,coeff,mag,phase;
    int i,j,n;
    char chr;

    m = 0.1;
    g = 0.01;
    g1 = 0.01;

    puts("\nDetermine Frequency Response for a damped ");
    puts("simply supported beam.  jmh 2/20/86\n");
  while() {
    chr = 0;
    while(chr != 'Y') {
        printf("\nParameters are: Mass ratio = %f, g = %f, g1 = %f\n",m,g,g1);
        printf("\nAre these OK? ");
        if((chr = toupper(getchar())) != 'Y') {
            printf("\nEnter new values separated by commas ?");
            scanf("%lf,%lf,%lf\n",&m,&g,&g1);
        }
    }

    damp[0] = 1.;
    damp[1] = g;

    damp1[0] = 1.;
    damp1[1] = g1;

    while(chr == 'Y') {
        printf("\n\nEnter values of omega_s and limits on omega ?");
        scanf("%lf,%lf,%lf\n",&omega_s,&omega_1,&omega_u);
        if(omega_s < 0)  break;

        eps = (omega_u - omega_1)/20;

        printf("\n\n\tFrequency\tResponse\tPhase\t\t omega_s = %f\n\n",omega_s);

        omega_s *= omega_s;

        for(i=0,sign=1; i<=20; i++) {
            omega = omega_1 + i*eps;
            omega *= omega;

            if(eps<=0) {
                sign *= -1;
                n = i/2;
                nrat = 2*n+1;
                nrat *= nrat;
                nrat *= nrat;
                b = (1.+m)*(omega_s + nrat)/2.;
```

```
                c = (1.+m)*omega_s*nrat;
                omega = b + sign*sqrt(b*b-c);
            }
            num[0] = pi*pi*pi*pi*omega/omega_s/16.;
            num[1]=0;
            cxarth(num,damp1,temp,4);

            cxsqrt(temp,num);
            cxsqrt(num,temp);

            eff_mass(temp,num);

            num[0] = pi*pi*pi*pi*omega/(1+m)/16.*(1. + m*num[0]);
            num[1] *= pi*pi*pi*pi*omega/(1+m)/16.*m*num[0];

            cxarth(num,damp,temp,4);

            cxsqrt(temp,num);
            cxsqrt(num,temp);

            deflect(temp,zeta);

            mag = sqrt((zeta[0]*zeta[0] + zeta[1]*zeta[1]));
            phase = 180./pi*atan2(zeta[1],zeta[0]);

            printf("\t%f\t%f\t%f\n",sqrt(omega),mag,phase);
        }
        printf("Continue?");
        chr = toupper(getchar());
    }
}
}

cxsqrt(z,w)
double z[],w[];
{
    double r,thet;

    r = sqrt(sqrt(z[0]*z[0] + z[1]*z[1]));
    if(z[0] == 0) {
        if(z[1] >= 0) thet = pi/4.;
        else thet = -pi/4.;
    }
    else thet = 0.5*atan(z[1]/z[0]);

    w[0] = r*cos(thet);
    w[1] = r*sin(thet);
}

deflect(alfa,z)
double alfa[],z[];
{
    double x[2],y[2],temp[2];

    x[0] = 1.;
    x[1] = 0;

    cxcosh(alfa,y);
    cxarth(x,y,z,4);
```

```
    y[0] = - alfa[1];
    alfa[1] = alfa[0];
    alfa[0] = y[0];

    cxcosh(alfa,y);
    cxarth(x,y,temp,4);

    z[0] = (z[0] + temp[0])/2.;
    z[1] = (z[1] + temp[1])/2.;
}

eff_mass(alfa,meff)
double alfa[],meff[];
{
    double y[2],temp[2];

    if(alfa[0]==0 && alfa[1]==0) {
        meff[0] = 1.;
        meff[1] = 0;
        return;
    }

    cxtanh(alfa,y);
    cxarth(y,alfa,meff,4);

    y[0] = - alfa[1];
    alfa[1] = alfa[0];
    alfa[0] = y[0];

    cxtanh(alfa,y);
    cxarth(y,alfa,temp,4);

    meff[0] = (meff[0] + temp[0])/2.;
    meff[1] = (meff[1] + temp[1])/2.;
}



double cosh(x)
double x;
{
    x = exp(x);
    return (x + 1./x)/2.;
}

double sinh(x)
double x;
{
    x = exp(x);
    return (x - 1./x)/2.;
}

double tanh(x)
double x;
{
    return sinh(x)/cosh(x);
}

cxcosh(z,w)
double z[],w[];
```

☆U.S. GOVERNMENT PRINTING OFFICE 1986-646-049